RUSSIAN ACADEMY OF SCIENCES

**SCIENTIFIC COUNCIL
FOR DIRECT ENERGY CONVERSION**

SCIENTIFIC COUNCIL FOR FLUID MECHANICS

THE 3RD WORKSHOP
ON MAGNETO- PLASMA-
AERODYNAMICS
IN AEROSPACE APPLICATIONS

MOSCOW
24 APRIL - 26 APRIL 2001

20021009 047

**Organized by Institute of High Temperatures of RAS
In co-operation and sponsorship by:**
RFBR   EOARD   ILG MHD   SEAM

REPORT DOCUMENTATION PAGE

Form Approved OMB No. 0704-0188

1. REPORT DATE (DD-MM-YYYY)	2. REPORT TYPE	3. DATES COVERED (From – To)
27-06-2002	Conference Proceedings	24 April 2001 - 26 April 2001

4. TITLE AND SUBTITLE

The Third Workshop on Magneto- and Plasma Aerodynamics For AeroSpace Applications

5a. CONTRACT NUMBER
F61775-01-WF033

5b. GRANT NUMBER

5c. PROGRAM ELEMENT NUMBER

6. AUTHOR(S)

Conference Committee

5d. PROJECT NUMBER

5d. TASK NUMBER

5e. WORK UNIT NUMBER

7. PERFORMING ORGANIZATION NAME(S) AND ADDRESS(ES)
Institute of High Temperatures RAS (IVTAN)
Izhorskaya str., 13/19
Moscow 127412
Russia

8. PERFORMING ORGANIZATION REPORT NUMBER
N/A

9. SPONSORING/MONITORING AGENCY NAME(S) AND ADDRESS(ES)

EOARD
PSC 802 BOX 14
FPO 09499-0014

10. SPONSOR/MONITOR'S ACRONYM(S)

11. SPONSOR/MONITOR'S REPORT NUMBER(S)
CSP 01-5033

12. DISTRIBUTION/AVAILABILITY STATEMENT

Approved for public release; distribution is unlimited.

13. SUPPLEMENTARY NOTES

14. ABSTRACT

The Final Proceedings for The Third Workshop on Magneto- and Plasma Aerodynamics For AeroSpace Applications, 24 April 2001 - 26 April 2001

This is an interdisciplinary conference. Topics include 1) MHD and Plasma Aerodynamics flow/flight control; 2) MHD on-board electrical power generation, 3) MHD assisted hypervelocity testing, 4) Plasma Aerodynamics, drag/heat flux/boundary layer control, 5) Shock wave propagation in gas-plasma systems, 6) On-board plasma generators, and related problems.

15. SUBJECT TERMS
EOARD, Magnetohydrodynamic (MHD), Combustion, Plasma Aerodynamic

16. SECURITY CLASSIFICATION OF:			17. LIMITATION OF ABSTRACT	18. NUMBER OF PAGES	19a. NAME OF RESPONSIBLE PERSON
a. REPORT	b. ABSTRACT	c. THIS PAGE	UL	434	Wayne Donaldson
UNCLAS	UNCLAS	UNCLAS			19b. TELEPHONE NUMBER (Include area code) +44 (0)20 7514 4299

Standard Form 298 (Rev. 8/98)
Prescribed by ANSI Std. Z39-18

RUSSIAN ACADEMY OF SCIENCES

**SCIENTIFIC COUNCIL
FOR DIRECT ENERGY CONVERSION**

SCIENTIFIC COUNCIL FOR FLUID MECHANICS

THE 3RD WORKSHOP ON MAGNETO- PLASMA- AERODYNAMICS IN AEROSPACE APPLICATIONS

MOSCOW
24 APRIL - 26 APRIL 2001
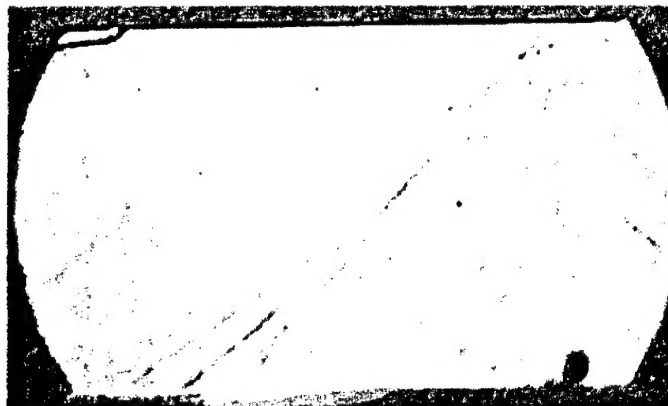
**Organized by Institute of High Temperatures of RAS
In co-operation and sponsorship by:**

RFBR   EOARD   ILG MHD   SEAM

On the front cover the shock wave structure modified by plasma formation excited in the boundary layer is shown (S.B.Leonov, IVTAN).

ACKNOWLEDGMENTS

International Committee

Aleksandrov A.F. (Russia)

Alferov V.I. (Russia)

Batenin V.M. (Russia)

Bazhenova T.V. (Russia)

Bityurin V.A. – Chairman (Russia)

Bobashov S.V. (Russia)

Borghi C. (Italy)

Cherniy G.G. (Russia)

Cole J. (USA)

Harada N. (Japan)

Kelley D. (USA)

Khodataev K.V. (Russia)

Krasilnikov A.V. (Russia)

Kuranov A.L. (Russia)

Levin V.A. (Russia)

Lineberry J. (USA)

Macheret S. (USA)

Van Wie D. (USA)

Vatazhin A.B. (Russia)

Veefkind A. (The Neherland)

Local Committee

Bityurin V.A.

Bocharova E.A.

Klimov A.I.

Kolesnichenko Yu.F.

Kuznetsova T.N.

Leonov S.B.

Semenova T.M.

Sukhov V.N.

Veselovskii A.S.

PREFACE
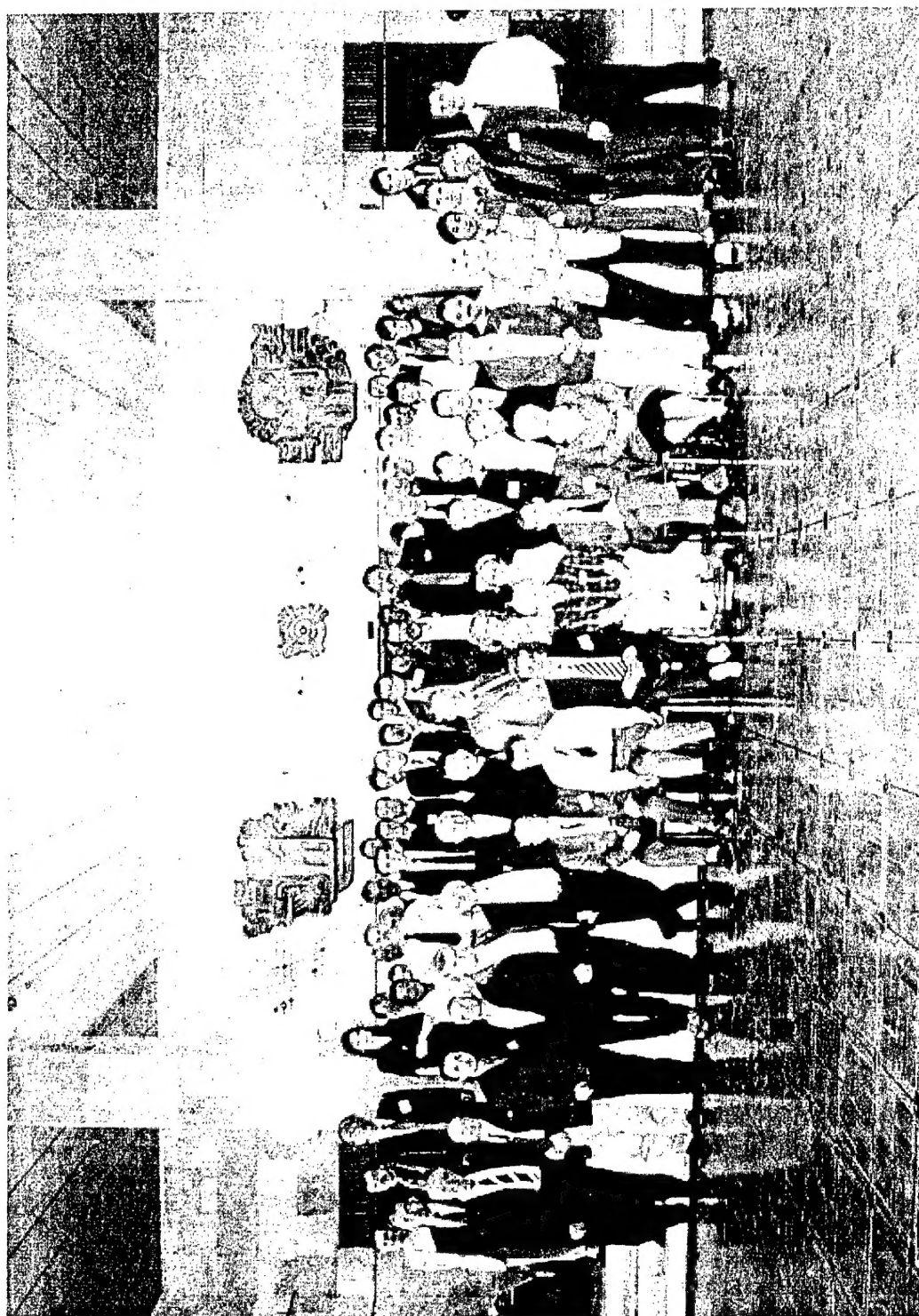
The 3rd Workshop on Magneto-Plasma-Aerodynamics for Aerospace Applications was held in Moscow on April 24-26 at IVTAN (Institute of High temperatures of Russian Academy of Sciences). The Workshop was organized by IVTAN under Scientific Council for Direct Energy Conversion and Scientific Council for Fluid Mechanics both of Russian Academy of Sciences. The Workshop was sponsored by EOARD, RFBR (Russian Foundation for Basic Research), ILG MHD, SEAM (USA), MTC and others organizations.

The Workshop was attended by more than 120 registered participants including 20 specialists from USA, UK, Italy, Japan. Besides of the registered participants more then 50 Russian specialists participated in the scientific sessions. Thus, total number of participants is estimated as much as 170.

The main goal of the Workshop, as in a case of the 3rd Workshop held in April 2001 also at IVTAN, was to discuss fundamental aspects of magneto-plasma aerodynamics in relation to applications of magneto-plasma aerodynamics processes and effects in aero space R&D.

Scientific and technical background in this field was formed during several decades of intensive programs for MHD energy conversion, physics of gas discharge, research and development of miscellaneous gas discharge devices, physical gas dynamics, physics of shock waves and many others related areas. IVTAN as one of the leading organization of Russian Academy of Sciences in many of these fields took an initiative to manage such an international meetings.

Structural the Workshop was organized in several profiled sessions: plenary, MHD flow control, MHD electrical power generation, plasma aerodynamics, plasma generators, shock wave propagation in gas-plasma media, magneto-plasma aerodynamics effects in wind tunnels, related problems.

The results of the 3rd Workshop were discussed and formulated at the round table discussion with 17 speakers. It was recognized a remarkable growth of the quality of the technical presentation as well as the level of the discussions both during the sessions and informal contacts. It was recommended to continue the series of the Workshop, which is in conjunction with US based Weakly Ionized Gas Workshop, becoming fruitfully scientific event.

The next 4th Workshop is expected to be soon announced to be held at IVTAN, Moscow on end of March- beginning of April 2002.

V.Bityurin, PhD, DS
Chairman, Organizing Committee

CONTENTS

8

9

SESSION 7. Plasma Aerodynamics - III

SESSION 8. Plasma Aerodynamics - IV

SESSION 9. Onboard System

11

12

SESSION 12. Plasma Generator

1. CYLINDER WITH CURRENT IN HYPERSONIC FLOW

J.T.Lineberry
LyTec LLC, Tullahoma, TN

V.A.Bityurin, A.N.Botcharov, D.S.Baranov
IVTAN, Moscow, Russia

A.B.Vatazhin, V.I.Kopchenov, O.B.Gouskov
CIAM, Moscow

V.I.Alfyorov, A.S.Boushmin
TsAGI, Zhukovskyi

Abstract. Numerical study of the hypersonic flow over the circular cylinder in the presence of external magnetic field has been carried out. Azimuthal magnetic field is created by the electrical current flowing in the direction of cylinder axis. The study has been performed for the conditions close to that realized in the hypersonic MHD (Magneto-Hydro-Dynamic) facilities: free-stream Mach number equals to 12, static pressure is 40Pa, static temperature is 700K, characteristic magnetic induction magnitude is about 1 Tesla. As consequence of such conditions, the high temperature behind the bow chock takes place (up to 20,000K). This may lead to the high values of electrical conductivity and, in turn, to appearance of feasibility of MHD flow control. Two models were considered. In the first model the MHD-interaction is considered in the entire domain upstream and downstream the magnetic field generating cylinder, the anisotropic electrical conductivity is taken into account, and ionization equilibrium is assumed. Effects of radiation transfer are also taken into account. Second model in which the electrodynamic part of the whole problem was simplified is intended to investigate the MHD flow around the critical point of the cylinder in more details. The wide range of magnitude of MHD interaction factor was considered and the flow fields were calculated. The important integral characteristics were obtained, namely the bow shock stand off distance, total pressure force, friction, magnetic force and total head flux into cylinder surface. It was observed that MHD interaction could lead to reducing the heat flux onto the surface as much as one order of magnitude under the free-stream conditions mentioned above. The specific flow features were revealed such that the presence of cold gas circulation zone near the critical point and the existence of the widely spread region with MHD interaction downstream the blunt body.

Introduction

Since 50th considerable attention has been paid to the flows around blunt body in the presence of external magnetic field. At high magnetic Reynolds number the fluid deforms the magnetic field, rather than passes through it. As a result liquid free cavities are produced near the body, which prevents to appearing of large heat flux into the body surface [1]. The application problems of author's interest are those in which magnetic Reynolds number values are of order of unit or even much less. In this case the feasibility of MHD flow control relies on another principles and should be investigated in more details. The incompressible MHD flows around bodies including cylindrical that were vastly studied in 60th (see, for example, [2]). Many exact and approximate analytical methods were developed for solving problems on the MHD flow over bodies of different shape. The bibliography of earlier studies on the finite conductivity MHD flows can be found in [3]. In one of the first work on the supersonic MHD flow around a body [4] it was shown that increasing

MHD interaction factor leads to increasing of the bow-shock stand-off distance. In hypersonic low-pressure air flows (M>10) the electrical conductivity behind the bow-shock may become sufficient for the strong MHD interaction to appear in the presence of magnetic field of order of one tesla. In calculating the hypersonic flow over blunt body one should take into account the radiation transfer from the high temperature region. Also note that factor M^2/Re (M is the Mach number and Re is the Reynolds number) becomes of order of one, which leads to smearing of the shock wave.

In the current paper the hypersonic flow around the circular cylinder is investigated. This is one of the simplest objects from the view-point of design and from the view-point of studying the specific MHD effects. It is of practical interest since it is used as the diagnostic tool in some hypersonic MHD facilities like MHD shock tube of TSAGI. Finally, the flow over this simplest object is interesting from the scientific point of view since it is characterized by a large set of similarity parameters and by interaction of many physical effects.

15
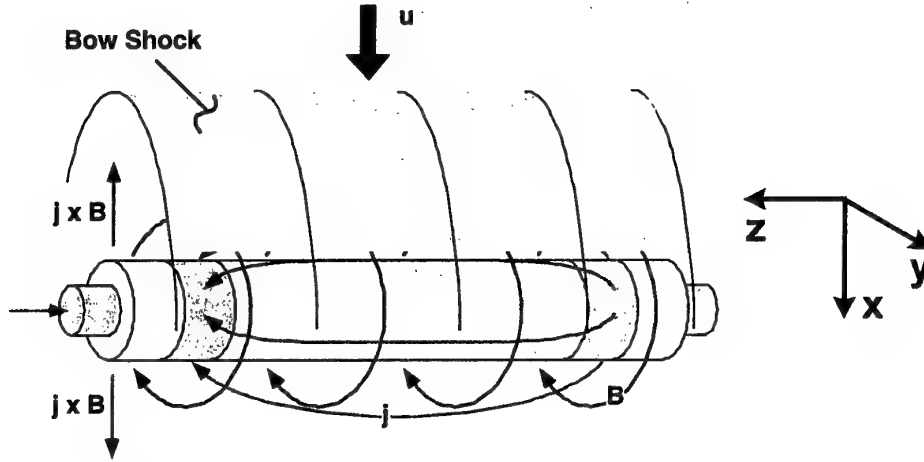
Fig.1. Schematic of MHD flow over the circular cylinder with axial electric current.

Problem formulation

Consider a flow over the circular cylinder of radius of r in which the electric current flows along the cylinder axis (Fig.1). This current produces the circular or azimuthal magnetic field which amplitude can be characterized by the value of magnetic induction on the cylinder surface. Designate the density of the flow as ρ_∞, pressure as P_∞, velocity as v_∞ and the magnetic induction on the cylinder surface as B^*. Outside the cylinder the external electric field $E=(0,0,E_z)$ can be applied. It is assumed that z-directed electric current is provided by the electrodes located at $z=\pm L$ planes (see Fig.1). The surface of cylinder is considered as electrical insulator. The flow over cylinder in the azimuthal magnetic field can be described by the Navier-Stokes equations in which the electromagnetic force $\mathbf{f}=[\mathbf{j}\times\mathbf{B}]$ appears in the momentum equations and the source $\mathbf{J}\cdot\mathbf{E}$ appears in the energy equation. The working gas, air, is assumed to be a perfect gas with constant heat capacity. The transport coefficients of viscosity μ and heat conductivity λ are approximated by the functions of temperature. The radiation from the high temperature region is described by the model of optically thin media. The absorption coefficient is taken to be constant, for simplicity. At the cylinder surface the constant temperature, T_w, is specified.

Electrodynamic part of the whole equation system includes the Maxwell equations enclosed by the generalized Ohm's law in which anisotropy of electric conductivity is accounted for. The conductivity σ and electron mobility factor $\alpha=e\tau_e/m_e$ (e is the electron charge, m_e is the mass of electron, τ_e is the average collision time of electron

with other particles) are assumed to be functions of thermodynamic parameters.

Under assumptions made above the MHD flow is described by the following set of the governing parameters:

$$\rho_\infty, p_\infty, v_\infty, r, c_p, \mu, \lambda, \gamma, T_w, q_R, T, B^*, E_z, \alpha \qquad (1)$$

In (1) c_p is the heat capacity at constant pressure, γ is the ratio of heat capacities, q_R is the characteristic radiation power, or the value of divergence of radiative heat flux, $\alpha=\omega_e\tau_e/B$, $\omega_e\tau_e$ is the Hall parameter.

According to the theory of similarity and dimensionality (see, for example [5]), any dimensionless flow characteristics is the function of the set of the following parameters

$$\Gamma = \{M, Re, \gamma, Pr, \overline{T}_w, \overline{q}_R ; S, K, \beta, Re_m\}, \qquad (2)$$

Here M is the Mach number , Re is the Reynolds number, Pr is the Prandl number, $\overline{T}_w$ is the temperature factor, the ratio of surface temperature and the free-stream stagnation temperature. $\overline{q}_R$ is the characteristic radiation power. S and K are MHD interaction factor and electric load coefficient, respectively. β is the Hall parameter, Re_m is the magnetic Reynolds number. These magnitudes are defined as follows:

$$M^2 = \frac{u_\infty^2 \rho_\infty}{\gamma p_\infty}, \quad Re = \frac{\rho_\infty u_\infty r}{\mu}, \quad Pr = \frac{c_p \mu}{\lambda},$$

$$S = \frac{\sigma B_*^2 r}{\rho_\infty u_\infty}, \quad K = \frac{E_z}{u_\infty B_*}, \quad \beta = \frac{e\tau B_*}{m},$$

$$Re_m = u_\infty r \sigma \mu_0 \qquad (3)$$

(μ_0 is the magnetic permitivity of vacuum). Variety of flow regimes is determined by first six gasdynamic parameters and by four electrodynamic ones.

The flow characteristics of primary interest are: the bow shock stand-off distance $\Delta/r = A_1(\Gamma)$; surface heat flux density $q_w = \mathrm{St}(\Gamma,\theta)\cdot\rho_\infty u_\infty c_p(T_\infty - T_w)$, where St is Stanton number and θ is the angle coordinate along the surface; the total force $\mathbf{F}$ acting on cylinder. The total force $\mathbf{F}$ is calculated as

$$F_i = \int_\Sigma P_{ik} n_k d\Sigma - \int_V [\mathbf{j}\times\mathbf{B}]_i dV \text{ , i=1,2,3} \qquad (4)$$

$\mathbf{n}=(n_1, n_2, n_3)$

Here, V is the volume occupied by the fluid only, Σ is the surface of cylinder, $\mathbf{n}=(n_1, n_2, n_3)$ is the outward unit normal to the surface, P_{ik} is the hydrodynamic stress tensor.

The flow conditions of interest are such that $\mathrm{Re}_m \leq 0.1$ (see below). Therefore induced magnetic field can be neglected and electrodynamic equations can be cast as

$$\begin{aligned}
&\mathrm{div}\,\mathbf{j} = 0 \\
&\mathbf{j} + \alpha[\mathbf{j}\times\mathbf{B}] = \sigma\mathbf{E}^* \qquad (5) \\
&\mathbf{E}^* = \mathbf{E} + [\mathbf{v}\times\mathbf{B}] \\
&\mathbf{E} = -\nabla\varphi, \ \alpha = e\tau_e/m_e = \beta_e/B
\end{aligned}$$

Where $\mathbf{j}$ is the electric current density, $\mathbf{B}$ is the magnetic induction vector, $\mathbf{E}$ is the electric field strength, $\mathbf{v}$ is the fluid velocity vector and φ is the electric potential. The set of equations (5) readily reduces to one elliptic equation for electric potential.

The crucial point in investigating the MHD interaction under conditions discussed above is the question of conductivity and electron mobility distribution. It is seen from (5) that the smaller conductivity and/or higher mobility, the lower is the electromagnetic force [$\mathbf{J}\times\mathbf{B}$] and, hence, the effect of MHD interaction on the flow characteristics. As the first step the equilibrium thermal ionization is assumed in the high temperature region behind the shock. Therefore, the conductivity and electron mobility are determined from the following relationships.

$$\sigma = \frac{e^2 n_e \tau_e}{m_e}, \ \tau_e^{-1} = \sum_K \tau_{eK}^{-1} . \qquad (6)$$

Here, n_e is the electron number density and τ_e^{-1} is the characteristic collision frequency of electron with neutrals and ions. Both are estimated in the usual way, i.e.

$$\tau_{en}^{-1} \sim n_n \langle v\rangle \langle Q_{en}\rangle$$

and

$$\tau_{ei}^{-1} \sim n_e \langle v\rangle \langle Q_{ei}\rangle$$

where n_n is the concentration of neutral particles, $\langle v\rangle$ is the average electron velocity, and $\langle Q\rangle$ is the impact cross-sections. $\langle Q_{en}\rangle$, electron-neutral collision cross-section, is taken as constant, $Q_{en} \sim 10^{-15}\mathrm{cm}^2$.

$$Q_{ei} = C\frac{n_e}{T^{3/2}}\ln\Lambda ,$$

where $\Lambda = BT^{3/2}/n_e^{1/2}$ is the Coulomb' logarithm [15].

The electron concentration is estimated from the Saha' formula [15]

$$\frac{n_e^2}{N} = AT^{3/2}\exp(-I/T), \quad (7)$$

$A = 2.414\cdot10^{15}\mathrm{cm}^{-3}\mathrm{K}^{-3/2}$, $I = 10^5\mathrm{K}$.

Finally,

$$\alpha = \frac{e\tau_e}{m_e} = \frac{\sigma}{en_e}$$

the equilibrium conductivity approach is expected to overestimate the conductivity level.

The Hall effect results in appearance of the x- and y-components of electric current. They in turn generate the force along the cylinder axis and can violate the two-dimensional flow field. However, the calculations showed that total force [$\mathbf{j}\times\mathbf{B}$] is several orders of magnitude less than x- and y-components of electromagnetic force. Therefore the MHD flow field is considered to be two-dimensional. The MHD flow is considered in the domain including both regions upstream and downstream of cylinder. The symmetry is assumed to hold on the $y=0$ line (Fig.1). The "short-circuit" operation mode is mainly studied, i.e. $E=0$ everywhere. The transport coefficients are approximated by functions of temperature. The radiation power is estimated from formula $Q_R = \kappa\cdot\sigma_0 T^4$, where $\kappa=10^{-3}\mathrm{cm}^{-1}$, and σ_0 is the Stefan-

Boltzman constant. For absorption coefficient, approximate estimations were made from the data presented in [14].

The system (5) with conductivity and Hall parameter defined in (6,7) constitute the called Model 2. This is computationally more time-consuming compared to the second model. The preliminary analysis of MHD flow over cylinder based on the model (5-7) showed that the magnitude of electron mobility is of order of unit in the most important region near the cylinder critical point. For qualitative analysis one can omit the Hall effect. The system (5) simplifies to one algebraic equation for j_z current component. This approach will be called as Model 1. This model is intended to analyze MHD flow near the critical point of cylinder. The conductivity is assumed to be zero in the region upstream the shock and in the regions of supersonic flow behind the shock. Near the critical point it is assumed to have the constant value. $E_z=0$ regime is considered.

In the current paper the MHD flow over a circular cylinder is numerically studied for the conditions of TsAGI MHD facility

M=12, p_∞=40Pa, T_∞=700K, T_w=1200K, B_*=0÷1 tesla.

Analysis of MHD flow near the critical point of cylinder

The Model 1 is used in this study to analyze the MHD flow features near the critical point. The conductivity is set to constant value in the subsonic region behind the shock. Hall effect is omitted. The following dimensionless parameters characterize the flow:

M=3÷12, Re=10^2÷10^3, γ=1.4 and 1.2, Pr=0.72, S=0÷20, κ=0, β=0, Re$_m$=0, $\bar{Q}_r$=0   (8)

The temperature factor $\bar{T}_w = T_w/T_\infty^0$ is determined from γ, M, T_w=1200K.

It should be noted that the governing parameters of the flow are such that the ratio $M^2/Re\cong0.7$ is close to unit. According to the theory of gaseous media mechanics (see, for example [13]) the effects of gas rarefaction may become important. In particular, the velocity and temperature slip-effects on the surface may be essential. Moreover, the viscous stress tensor and heat flux vector should be modified in the Navier-Stokes equations to take into account the rarefaction effects. However, in the current study the traditional, "continuum" formulation is applied.

The laminar flow is considered. High-order finite-difference implicit method [6,7] is used to solve gasdynamic part of the total system of equations. The method is the modification of the well-known Godunov method [8]. It was successfully used earlier for solution of several problems on hypersonic MHD flow control in the channels [9-12]. The specific feature of the method is the adaptation of the computational grid to the shock-wave shape.

The Mach number distributions are shown in Figs.2a and 2b for two Reynolds number values: Re=200 (Fig.2a) and Re=1000 (Fig.2b). in the second case the value M2/Re=0.144 is essentially less than unit. Hence, traditional formulation seems to be suitable. Comparison of two fields shows that the width of the bow shock front is larger for case Re=200. This can't be explained only by numerical dissipation. The rarefaction effect makes some contribution to the front width enhancement.

a)   b)
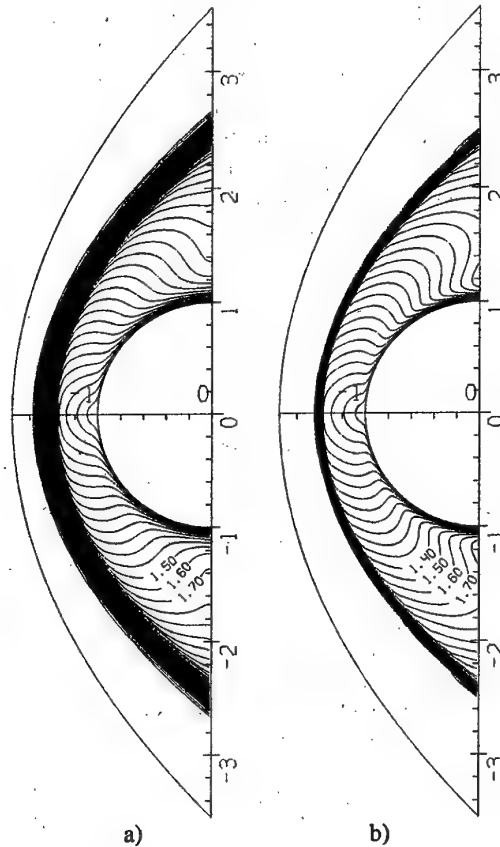
Fig.2. Mach number fields for non-MHD flow, M=12: a) Re=200 (M^2/Re=0.72); b) Re=1000 (M^2/Re=0.144)

The main studies were intended to expose the effect of magnetic field on the flow structure near the critical point, on the surface characteristics

a) Mach number field   b) Pressure field   c) Temperature field
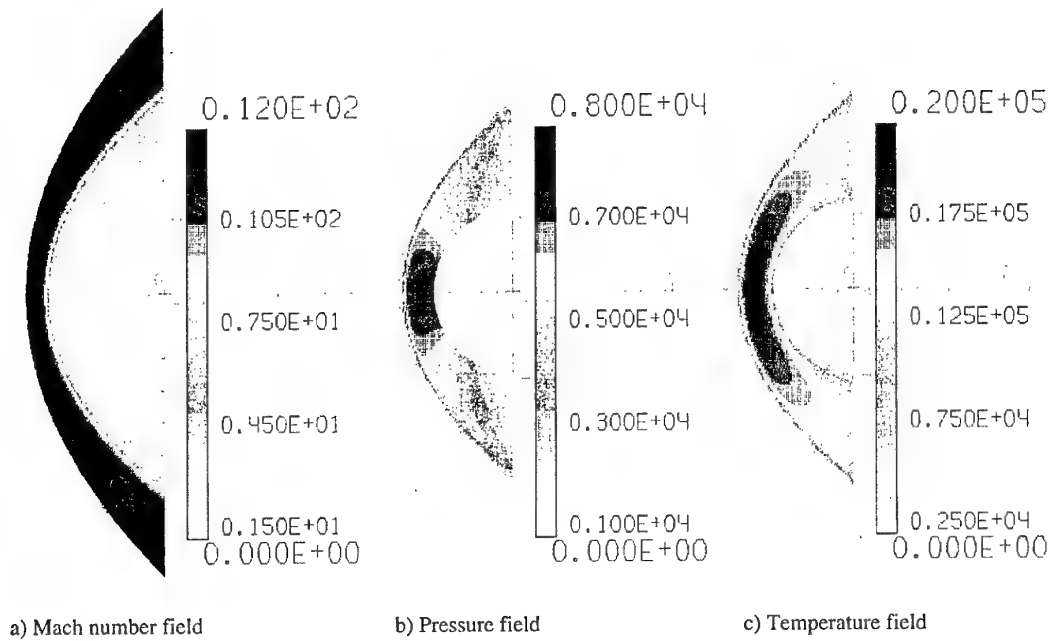
Fig.3. Flow fields for non-MHD case, M=12, Re=200

a)

b)

c)
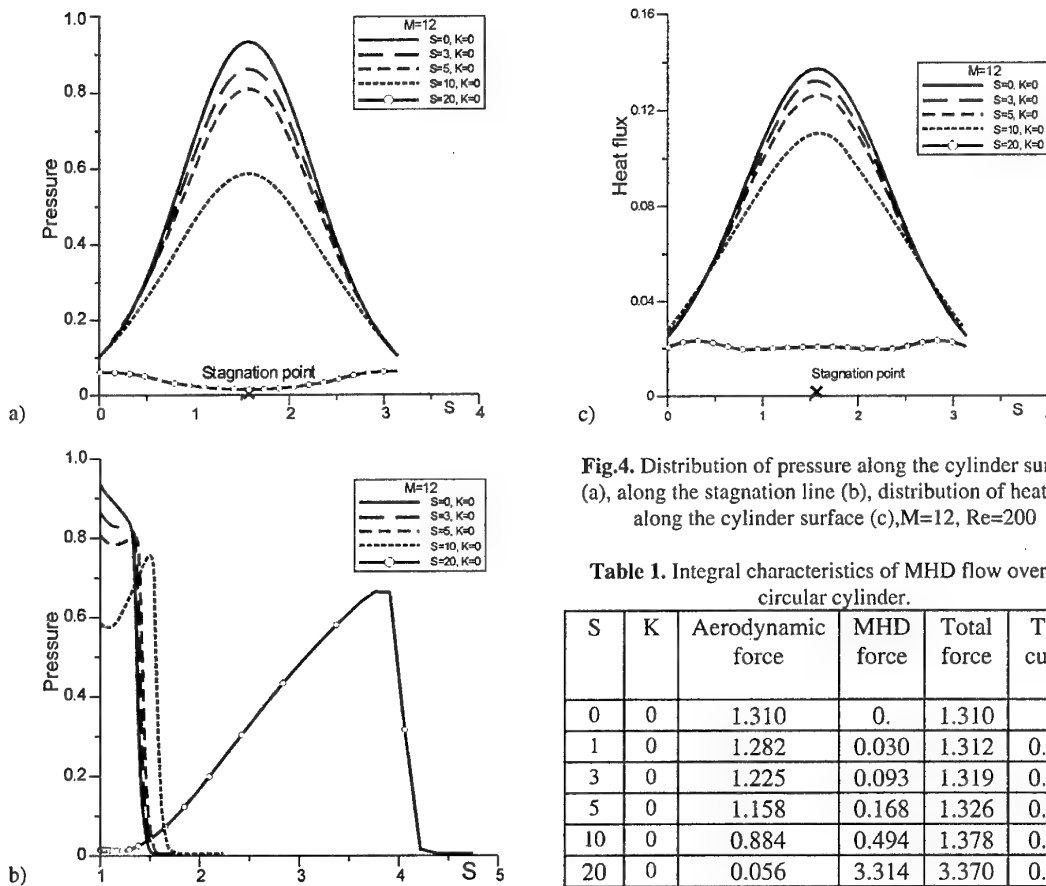
Fig.4. Distribution of pressure along the cylinder surface (a), along the stagnation line (b), distribution of heat flux along the cylinder surface (c),M=12, Re=200

Table 1. Integral characteristics of MHD flow over the circular cylinder.

S	K	Aerodynamic force	MHD force	Total force	Total current
0	0	1.310	0.	1.310	0.
1	0	1.282	0.030	1.312	0.041
3	0	1.225	0.093	1.319	0.043
5	0	1.158	0.168	1.326	0.047
10	0	0.884	0.494	1.378	0.075
20	0	0.056	3.314	3.370	0.617

19

distributions, on the neat flux into the surface, on the body drag. Two specific heat ratio values were considered, $\gamma=1.2$ and $\gamma=1.4$. It was detected that all specific flow features observed for the case $\gamma=1.4$ take place in the flow of gas with $\gamma=1.2$. Therefore, the results for the case $\gamma=1.4$ are mainly presented.

The Mach number, pressure and temperature distributions for non-MHD flow are shown in Fig.3. In this case the highest pressure zone is located near the critical point, in which the pressure takes maximum value. The dimensionless distributions of pressure along the surface, and along the stagnation line directed from the cylinder surface toward the bow shock are shown in Fig.4a and 4b, respectively. In Fig.4c the distribution of the heat flux on the surface in presented. The length is normalized by cylinder radius on all graphs.

Increasing the MHD interaction factor leads to moving the bow shock away from the body. In the range of values $0{\leq}S{\leq}5$ no qualitative change in the flow structure is observed. This is confirmed by the Fig.5 where the distributions of Mach number, pressure and temperature are given for the MHD-interaction factor $S=5$. Starting from this value pressure distribution behind the shock has non-monotonous character, which can be seen in Fig.4b. Moreover, at $S=10$, for example, the maximum of pressure is achieved just behind the

bow shock rather then at critical point of cylinder. Such behavior of pressure corresponds with the beginning of the flow structure changing.

The changes in the flow structure are well seen at $S=20$. The flow pattern shown in Fig.6 confirms that the high pressure region is located just behind the shock but the pressure is essentially lower near the cylinder surface. The shock stand-off distance is several times larger in the case $S=20$ than in any of $0{\leq}S{\leq}10$ cases. In MHD flows characterized by high MHD interaction factors, the region of low Mach number values significantly expands. Moreover, rather large recirculation zone appears near the critical point. This is illustrated by Fig.7, in which the velocity field near the critical point is shown. As a result of changes in the flow structure, the flow splitting point locates at some distance off the surface.

The reformation of the flow results in the radical decrease of the surface heat flux. This heat flux decrease is observed not only near the critical point, but over most of all the cylinder surface considered (Fig.4c).

It is also interesting to estimate the total drag acting on the body. It consists of the hydrodynamic force in x-direction and electromagnetic force, first and second term in relationships (4), respectively. The magnitude of these two forces normalized by $\rho_\infty v_\infty r$ and 1m of

a) Mach number field   b) Pressure field c) Temperature field

Fig.5. Flow fields for MHD flow, M=12, Re=200 S=5

number field   Pressure field   Temperature field
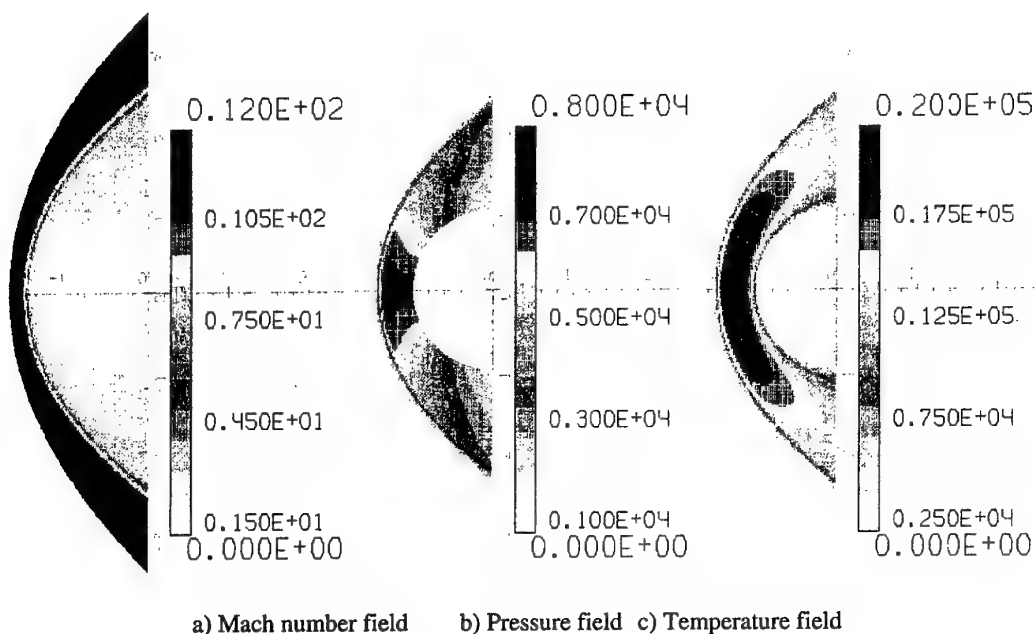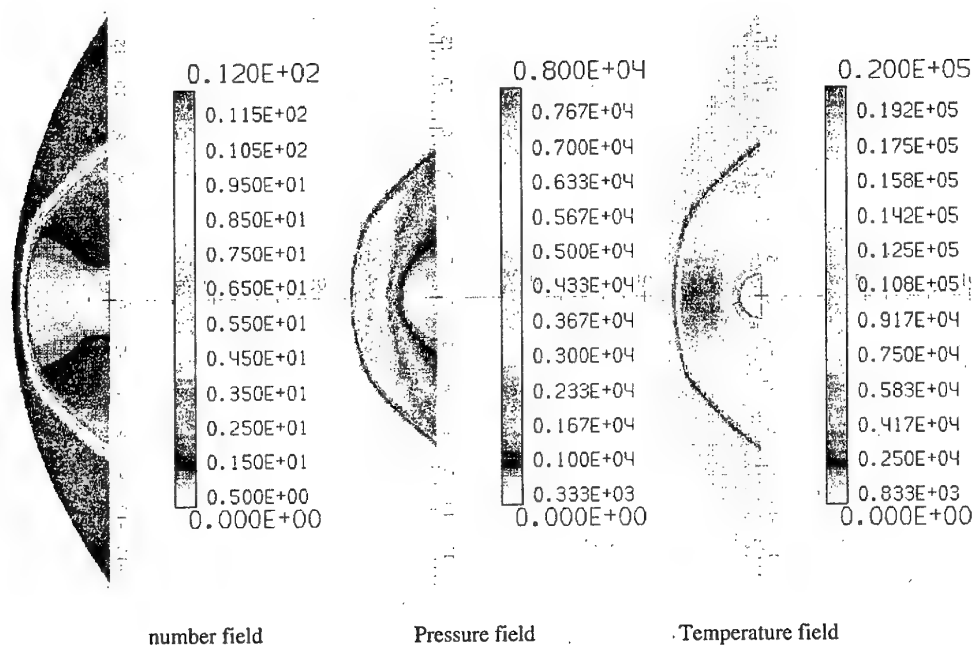
Fig.6. Flow fields for MHD flow, M=12, Re=200 S=20
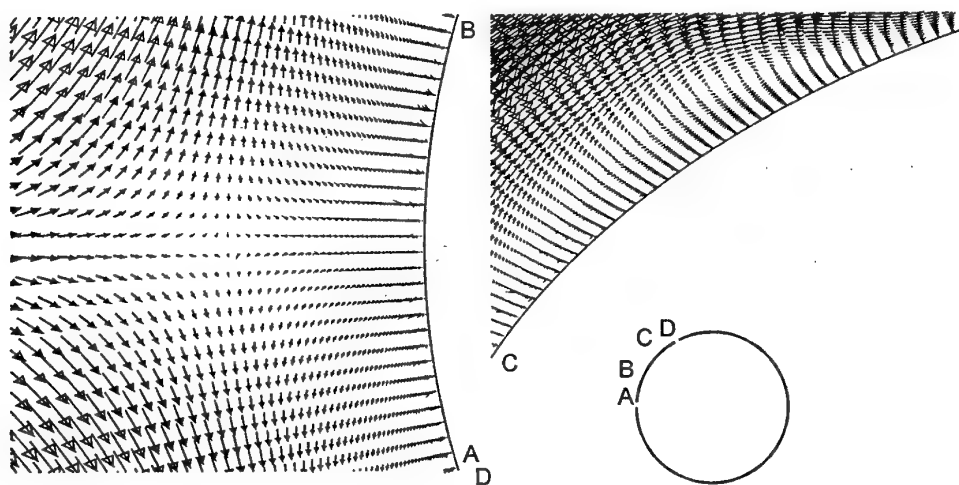
Fig.7. Velocity field near the critical point, M=12, Re=200, S=20.

cylinder span are given in Table 1 as functions of MHD interaction factor S for γ=1.4. Note, that friction is a small part of the hydrodynamic force. When S varies from 0 to 10 the hydrodynamic force decreases while electromagnetic force rises. The total force, sum of these two, slightly rises too. In S=20 flow there is a significant pressure drop near the critical point and significant (more than 20 times) decrease of the hydrodynamic constitutive of the drag.

At the same time the electromagnetic part of the drag increases considerably. The total drag is 2.5 times more than that observed in non-MHD flow.

The results presented above indicate dramatic decrease in the heat fluxes on the cylinder surface and hydrodynamic part of total drag for large MHD interaction factors. At the same time the total cylinder drag increases essentially.

21

MHD flow over cylinder with Hall effect

The possibility of formulation of Model 1 is based on the estimation of the electrical currents in the solution plane. As they generate a force in the axial direction, the two-dimensional formulation can violate. However the violating force is as low as five orders of magnitude in comparison with x- and y-components of electromagnetic force. The local values of axial force component are at least 20 times less than two other components. Therefore, the two-dimensional MHD flow character is assumed to hold.

The electrodynamic part of the entire equation set is described by the equations from (5) to (7). Equ (5) reduces to one equation of elliptic type for electric potential. The boundary conditions suitable for the flow in TsAGI MHD Facility are proposed to be as follows. The cylinder surface is considered as an insulator. On symmetry lines, $y=0$, zero normal derivative of potential is set. On the rest of boundary the $\varphi=0$ condition is specified. The short circuit operation mode is considered, $E_z=0$.

Computational details

The problem (5)-(7) is solved on the exactly same grid as the Navier-Stokes equations. The control-volume conservative formulation is used to discretize the equation for potential expressing the conservation of electric charge. One integration-point was used to calculate the current through any cell-face, while 7-point Gauss quadrature was applied to calculate the at-face average resistance between two cell-centers. The obtained sparse nine-diagonal linear equation set was solved with Additive Correction Multigrid method of Hatchinson and Raithby [16]. Four Grid-Level Flexible-Cycle approach was utilized. Modified Incomplete Choleski method of Gustaffson [17] was used as smoother on any grid-level. One-dimensional Additive Correction procedure was applied to accelerate convergence. From 21 to 25 fine-grid iterations was normally needed to reduce the residual in six orders of magnitude.

Results of Calculations

The influence of MHD interaction on the bow shock stand-off distance is demonstrated by Fig.8 and Fig.9. The pressure distribution along the stagnation line is shown in Fig.8 for several magnetic fields values, $B^*=0 \div 1$ tesla. Increasing the magnetic field increases the stand-off distance while the pressure drops on the cylinder surface. The temperature distribution along stagnation line

vs magnetic field is shown in Fig.9. It is well seen that the temperature gradient decreases significantly in the region between the shock and cylinder surface, as magnetic field rises. As consequence, the conductive heat flux into surface drops when the magnetic field amplitude increases.
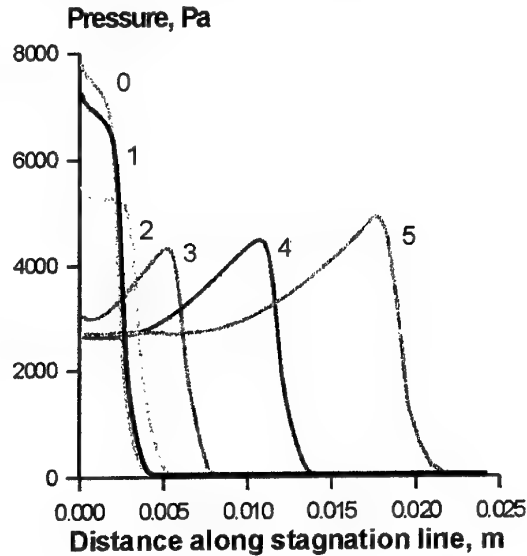
Pressure, Pa

Fig.8. Distribution of pressure along stagnation line. 0– B=0; 1– B=0.2; 2– B=0.4; 3– B=0.6; 4– B=0.8; 5– B=1.0.
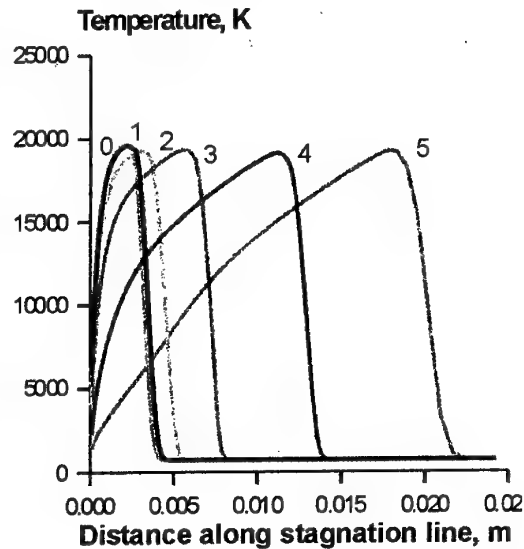
Temperature, K

Fig.9. Distribution of temperature along stagnation line. 0– B=0; 1– B=0.2; 2– B=0.4; 3– B=0.6; 4– B=0.8; 5– B=1.0.

Pressure and heat flux density on the cylinder surface vs magnetic field amplitude are shown in Fig.10 and 11, respectively. Unlike the non-MHD flow, when both pressure and heat flux
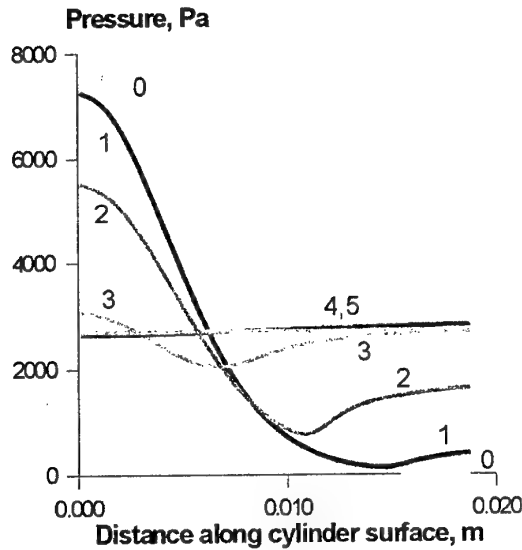
Pressure, Pa

Fig.10. Distribution of pressure along cylinder surface.
0– B=0; 1– B=0.2; 2– B=0.4; 3– B=0.6;
4– B=0.8; 5– B=1.0.
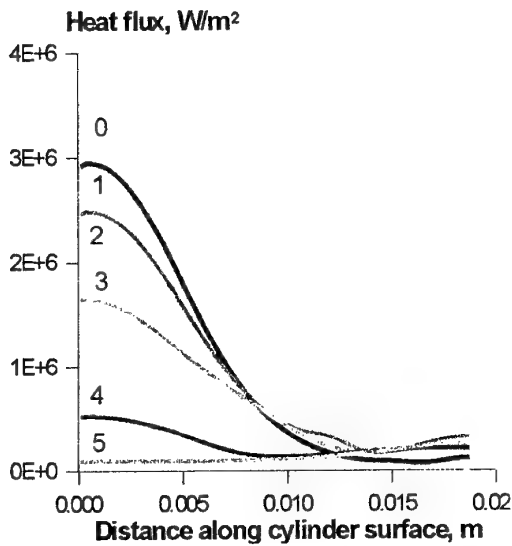
Heat flux, W/m²

Fig.11. Distribution of heat flux along cylinder surface.
0– B=0; 1– B=0.2; 2– B=0.4; 3– B=0.6;
4– B=0.8; 5– B=1.0.

have well-distinguished maximum at critical point, their distributions along the surface become more uniform in MHD-flow. Level out of pressure is also demonstrated by Fig.12, where the pressure field is shown for non-MHD case $B^*=0$, and for $B^*=1$ tesla case. In the second case there is a large zone of nearly constant pressure both downstream and upstream the cylinder. The strongest interaction takes place in the region just behind the shock,

where the velocity vector is still perpendicular to the magnetic field lines. Action of electromagnetic force is similar to the flow over a larger size body. In this case the cylinder itself appears in the region of wake of such effective body, where the lower and uniform pressure takes place.
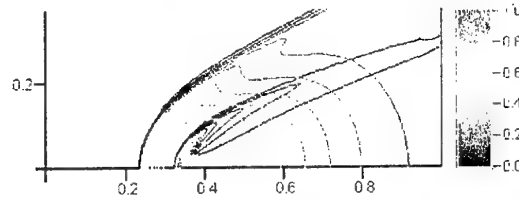
Fig.12. Pressure contour lines for non-MHD flow (B=0) and MHD flow (B=1).

Total pressure force, N   Total heat flux, kW

Total current, kA   Total MHD force, N
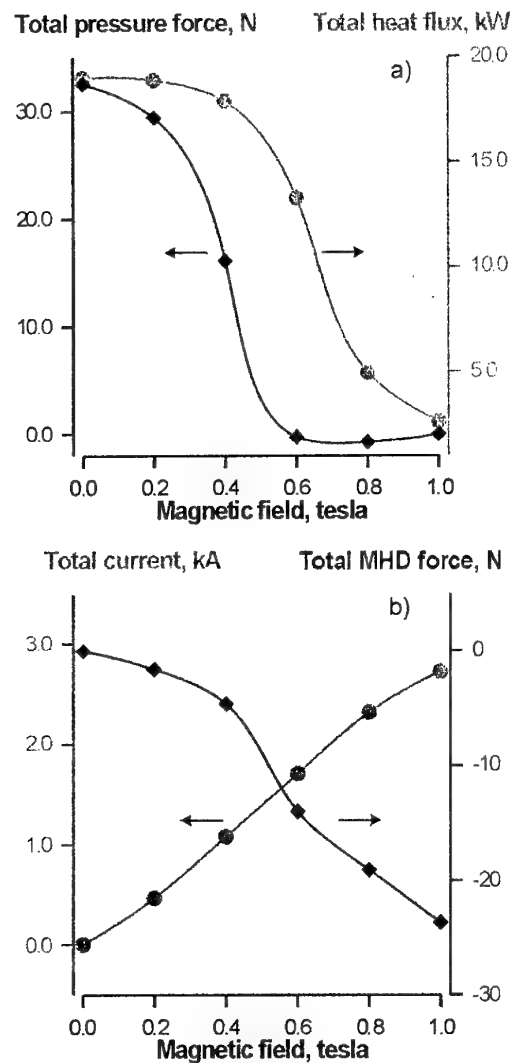
Fig.13. Total pressure force and heat flux (a), total axial current and electromagnetic force (b) versus magnetic field amplitude.

23

The components of total force (4) acting on the cylinder are plotted in Fig.13. Also total conductive heat flux and total axial current are presented. Similar to the no Hall effect flow discussed in the precious section the hydrodynamic part of the total force dramatically decreases compared to the non-MHD flow. The same is valid relative to the total heat flux into cylinder.

NON-MHD (B=0)

MHD (B=1)
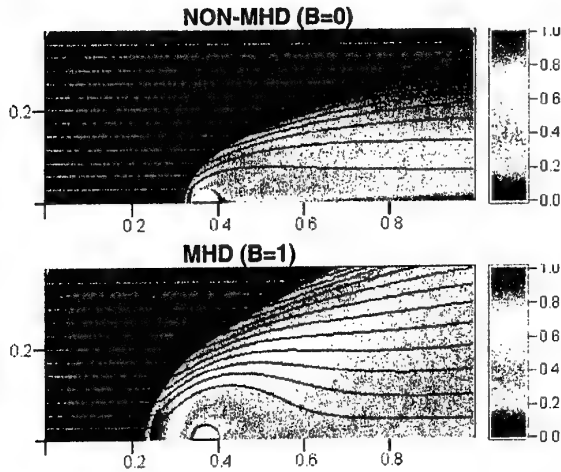
Fig.14. Temperature and flow stream lines for non-MHD flow (upper) and MHD flow (lower).
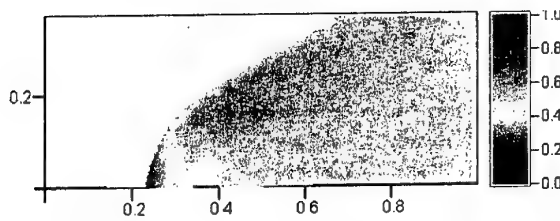
Fig.15. Axial current density distribution, B=1.
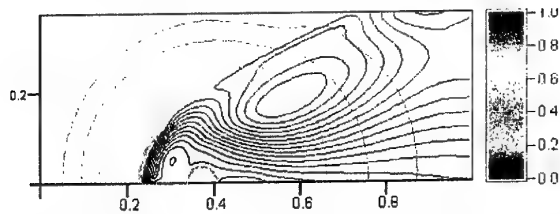
Fig.16. Electric potential and plane current stream lines.

The changes in the flow structure are seen from Fig.14-Fig.16. The temperature fields are shown in Fig.14 for non-MHD case and for the MHD flow with B^*=1 tesla. The highest temperature zone locates just behind the shock, whereas in the rest of the domain rather moderate temperature is observed. The distribution of the axial current, Jz, is shown in Fig.15. It is seen that

there is a small region between the shock and cylinder surface where the current is negative. This current mainly provides the interaction and effects on the position and shape of the bow shock. In the larger part of the entire domain it is positive and electromagnetic force acts in opposite direction, toward the body. However, the amplitude of the opposite force is much smaller then those acting in the front region.

The electric current flow in the solution plane is presented in Fig.16 by the current stream lines. The main interaction zone is also well detected by the "negative" current vortex. In the larger part of the domain the current vortex of opposite sign exists. It should be noted that the amplitude of the "plane" current is essentially smaller than the amplitude of axial one. Therefore, the electromagnetic force it generates in axial direction is much smaller than that created by the axial current component. This allows one to neglect with the three-dimensional flow pattern and to consider the two-dimensional MHD flow. Also note that in the problem considered the Hall effect appeared to be small, which is a consequence of equilibrium conductivity assumption. In the main interaction zone the electron mobility β/B is of order of unit due to high temperature and, hence, sufficiently high electron number density. The Hall parameter, β, appears to be less than unit since the magnetic field amplitude drops with increasing of distance as $B_*\cdot r/L$. The Hall parameter is large in the cold near surface region, but this is compensated by the zero-current boundary condition specified on the cylinder surface. From this follows that under the considered conditions the Hall effect can be neglected and the Model 1 becomes suitable for analyzing the MHD flow over the cylinder.

Conclusions

In this paper the MHD flow over the circular cylinder was studied. It was assumed that external magnetic field is created by the electric current flowing along the cylinder axis. The gas dynamics field and heat transfer on the cylinder surface were numerically analyzed. The analysis was carried out for the conditions typical for the hypersonic MHD-facilities (8). Two MHD flow models were considered, which differ from each other by a number of physical effects taken into account. Both models showed that there is a region near the critical point of the cylinder, in which low speed, relatively low pressure and temperature occur. The MHD interaction results in the increase of bow shock stand-off distance as much as 3-4 times compared with the non-MHD flow. Local heat flux densities and total heat flux into cylinder

24

surface are reduced by one order of magnitude. The total body drag considerably increases, whereas the aerodynamic part of the drag drops.

References

1. Kulikovski A.G., "On the Flow of Conducting Fluid Over the Magnetized Bodies", Doklady of USSR Acagemy of Sciences, 1957, v.17, No.2 (in Russian).
2. Zinober A.B., "Magnetohydrodynamic Flow Around Bodies", Riga, Zinatne, 1970, 291p. (in Russian).
3. Kulikovski A.G., Lyubimov G.A., "Magnetohydrodynamics", M: Fismatgiz, 1962, 246p. (in Russian).
4. Resler E.L., Sears W.R., "The Prospects for Magnetohydrodynamics", JAS, 1958, v.25, No.4, pp.235-245.
5. Sedov L.I., "Similarity and Dimensionality Methods in Mechanics", 10th Edition, M: Nauka, 1987, 432p. (in Russian).
6. Kopchenov V.I., Lomkov K.E., Topekha E.A., "Numerical Methods and Computations of the Viscous Flows in Ducts and Jets", Proc. 7th Soviet Meet. On Theoretical and Applied Mechanics, M., 1991, p.200 (in Russian).
7 Gouskov O.V., Kopchenov V.I., "Numerical Simulation of Duct Flows at Supersonic Entry Conditions", 8th Int. Conf. on the Methods of Aerophysical Research, Proceedings, 1996, Novosibirsk, Russia, p84-89.
8. Godunov S.K., Zabrodin A.V., Ivanov M.Ya., Kraiko A.N., Prokopov G.P., "Numerical Solution of Multidimensional Problems of Gas Dynamics", M:Nauka, 1976, 400p. (in Russian).
9. Vatazhin A.B., Gouskov O.V., Kopchenov V.I., Lichter V.A., "On the Problem of Deceleration of Supersonic Conductive Flow in the Duct by Magnetic Field", Izvest. RAN, MZhG, 1998, No.5, pp.169-181 (in Russian).
10. Vatazhin A.B., Gouskov O.V., Kopchenov V.I., "Peculiarities of Deceleration of Two-Dimensional Hypersonic Flow of Conductive Gas in Channel in MHD Generation Operation Mode", Proc. Of Steklov Mathematical Institute, M.:MAIK Nauka, 1998, v.223, pp.153-162 (in Russian).
11. Vatazhin A.B., Gouskov O.V., Kopchenov V.I., "Assessment of Possibility to Use the MHD Control for Hypersonic Flow Deceleration", AIAA Paper 99-4972, 1999.
12. Vatazhin A.B., Gouskov O.V., Kopchenov V.I., "Assessment of Possibility to Use the MHD Control in Scramjet", AIAA Paper 99-4971, 1999.
13. Loitsyanski L.G., "Mechanics of Fluid and Gas", M.:Nauka, 1973 (in Russian).
14. Avilova I.V., Biberman L.M., Vorob'ev V.S., et.al., "Optical Properties of Hot Air", edited by Biberman L.M., M.:Nauka, 1970, Chapter 10.
15. Sutton D. and Shermann A. "The Principles of Technical Magnetic Gas Dynamics", Russian Translation, M.:Mir, 1968, 492p. (in Russian).
16. Hutchinson B.R. and Raithby G.D. "A Multigrid Method on the Additive Correction Strategy", Numerical Heat Transfer J., 1986, v.9, p.511-537.
17. Gustafsson I. "On Modified Incomplete Factorization Methods", Lecture Notes in Mathematics, Proceedings, Bielefild, 1980, p.968.

2. PLASMA CONTROL OF SHOCK WAVES IN AERODYNAMICS AND SONIC BOOM MITIGATION

R.B. Miles, S.O. Macheret, L. Martinelli, M.N. Shneider, R. Murray, B. McAndrew
Princeton University
Department of Mechanical and Aerospace Engineering
D-414 Engineering Quadrangle, Princeton, NJ 08544, U.S.A.
E-mail: macheret@princeton.edu

J. Kline, and J. Fox
RSI, Inc., Princeton, NJ 08544, U.S.A.

We describe computational and experimental studies of plasma-induced shock attenuation, drag reduction, and off-axis energy addition for vehicle maneuvering. Both computations and experiments performed in a laboratory-scale microwave-driven plasma wind tunnel show that positioning plasma upstream of the shock, shock angles, and pressure distribution can be significantly affected. Theoretical analysis shows that, due to vehicle geometry and structural constraints, drag reduction will be energy-efficient at very high hypersonic Mach numbers. By initiating and controlling plasma location with electron beam or a laser, and sustaining the plasma with a subcritical microwave field, force moments can be generated, which can be useful for rapid-response maneuvering.

The sonic boom mitigation problem is very different from that of near-field aerodynamic control. Even if a shock is completely eliminated in the near field, the shock will emerge again far enough from the vehicle. We discuss an approach to sonic boom control that combines vehicle shape optimization with dynamic off-body energy addition. A key element of this approach is to dynamically change the weaker of the two or more shocks whose coalescence in the far field creates sonic boom. Thus, although a relatively weak shock is being moved, which requires relatively little energy, the position of the resulting coalesced shock can be modulated in time, which could break the boom into weaker wavelets.

3. USING OF MHD SYSTEMS ON HYPERSONIC AIRCRAFT

A.L. Kuranov, E.G. Sheikin
Hypersonic Systems Research Institute
St. Petersburg, Russia

Abstract. Potential application domains of MHD systems on hypersonic aircraft are discussed in the paper. Modern status of investigations of scramjet with MHD control under "AJAX" concept is reviewed. Results obtained by various groups of investigators are analyzed in the paper.

It is necessary to solve set of principal problems in order to realize the long-term atmospheric flight with hypersonic velocities (M>6). Hypersonic aircraft undergoes high power and heat loads, thus it is indispensable to implement an active thermal protection of the aircraft. Engine of hypersonic aircraft must ensure long-term motion of the vehicle at continually changing conditions of free stream flowing around the vehicle (including acceleration and deceleration phases). Scramjet is often considered as perspective engine of hypersonic aircraft because of its capabilities. Potentially it provides the maximal value of specific impulse than other engines. In order to realize this advantage it is necessary to ensure effective functioning of the scramjet in the range of hypersonic flight conditions variation. It requires developing controlled inlet and combustion chamber, which provides steady-state supersonic combustion. The systems approach to realize the long-term atmospheric flight with hypersonic velocities is developed in the "AJAX" concept [1]. In this paper some possible applications of MHD systems in hypersonic vehicles are considered briefly. Problems of using and potentialities of MHD systems for scramjet control, see Fig.1, will be considered more detailed.

improve characteristics of mixing and combustion in not premixed air-fuel streams. More detailed the problem of improving the mixing and combustion of air and fuel streams by means of MHD interaction is discussed in [3]. Influence of magnetic field on stream over blunt body is considered in papers [4-7], where it is shown that MHD control allows one to decrease wall heat flux and to increase the bow shock wave standoff distance from the body. Sufficiently detailed historical review of investigations of magnetic field influence on drag and wall heat fluxes of blunt body at atmospheric entry is presented in the paper [6].

Possibilities of MHD control to improve inlet performance are investigated numerically in papers [8-15]. It is shown in papers [12,13] that MHD influence allows one to increase the flow compression in the inlet. In papers [14,15] it is shown that for flight Mach number M_∞ greater than designed one M_d, flowfield in inlet can be moved near to designed flowfield by using the MHD control methods, see Fig.2. It is shown in papers [8-11] that MHD methods allow one to increase air mass flow rate in inlet when $M_\infty < M_d$. In papers [16,17] it is shown experimentally that MHD interaction modifies flowfield and regulates oblique shock wave position.

Fig.1. Simplified scheme of scramjet with MHD control under "AJAX" concept

One of the possible MHD applications is control of wall heat fluxes on hypersonic aircraft. Potentialities of MHD control to decrease the wall heat flux are discussed in review [2], ibidem it is shown that MHD interaction can be used to
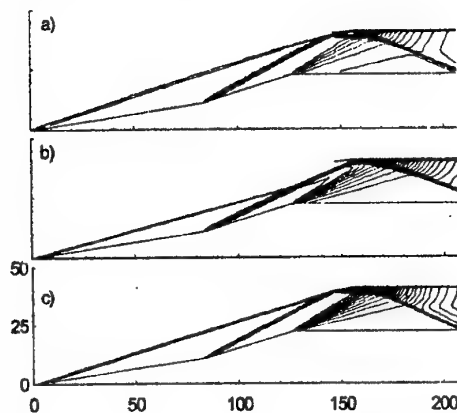
Fig.2. Density contours in supersonic inlet. a)M_∞=6, S_v=0 b) M_∞=8, S_v=0 c) M_∞=8, S_v≠0. From the paper [14].

27

More detailed we will review the papers devoted to investigation of the hypersonic aircraft engine which is originated and developed in Saint-Petersburg in the framework of the "AJAX" concept. The engine is a scramjet in which composition the additional subsystems (such as external and internal MHD generators, MHD accelerator and ionizer) are included in order to control its performance, see Fig.1. Nowadays two alternative titles are generally used in the special literature as a name for such engine: Magneto-Plasma-Chemical Engine (MPCE) [8-11, 18,19] and MHD bypass scramjet [20]. In this work the historically first (author's') title – MPCE – will be used as a name for such engine. Let's consider the functionality of MPCE basic subsystems in brief. The external MHD generator allows one to control a flow field and to regulate the air mass flow rate in a scramjet. The flow compression in MHD controlled inlet is a result of joint actions of multishock gas-dynamic compression and additional MHD compression. The internal MHD generator is used for increasing the static pressure. External and internal MHD generators located upstream the combustion chamber transform a part of the flow enthalpy into the electric power, which is transferred to MHD accelerator located downstream the combustion chamber, for additional acceleration of combustion products. The use of MHD systems in a scramjet allows one to increase effectiveness of a propulsion system thermodynamic cycle and to increase its specific impulse and thrust.

The degree of MHD influence on a flow in MHD generator channel depends on a magnetic induction value and on the flow conductivity. In typical conditions, the scramjet static temperature at a combustion chamber entrance, and, hence, in external and internal MHD generators does not exceed 2000° K. In such situation an equilibrium degree of the air ionization, and, hence, its conductivity are negligible. Therefore to realize the essential MHD influence on a flow it is necessary to ensure nonequilibrium ionization. To reach this one should, in that way or other, to input additional energy into the flow. Electric discharge, MW radiation or charged particle beam of high energies can be considered as probable means of power supply. But it is necessary to consider only the self-sustained operational mode, where the energy put into a flow to increase its conductivity, does not exceed energy produced by MHD generator. The problem of ensuring nonequilibrium conductivity of a cold flow in MHD generator channel is discussed in the works [8-10,15,21-23]. In the paper [24] it is shown that, the most effective is the use of an electron beam as an ionizer in order to minimize energy spent to create a necessary

electron concentration. The ionizer characteristics limitations at which the self-sustained operational mode for MHD generator with nonequilibrium conductivity can be realized are obtained in the works [8,10,21]. The requirement of a self-sustained operational mode of the MHD generator with nonequilibrium ionization and the requirement of realization the essential MHD effect on a flow $S_v > S^*$ (where S_v is MHD interaction parameter) result, in accordance with [21], in a magnetic induction value limitation B_{lim}. The B_{lim} dependencies for the internal MHD generator conditions at a value of a load factor of the MHD generator $k_1 = 0.5$ upon free stream dynamic pressure and MHD interaction parameter are shown in a Fig.3. These results are obtained for MHD generator located downstream the inlet which is characterized by a designed Mach number $M_d = 10$ and by the total turning angle of a flow $\theta_N = 15°$.
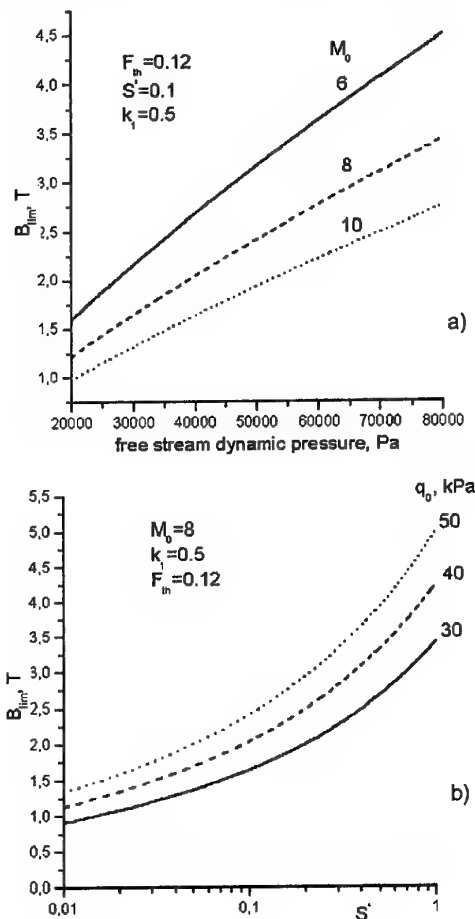
Fig.3. Limiting values of magnetic induction as a function of: a) free stream dynamic pressure, b) MHD interaction parameter.

28

The magnitude F_{th} shown in the Figure determines the relative value of an inlet throat. Limiting values of B_{lim}, according to a Fig.3, are magnified with increasing free stream dynamic pressure and diminished with increasing a flight Mach number. The MHD generator with nonequilibrium conductivity will work in a self-sustained operational mode and will provide the MHD interaction parameter $S_v > S^*$ if the magnetic induction B exceeds B_{lim}.

In the works [,11,13,14,16] the scheme of a scramjet with the internal MHD generator, the MHD accelerator and flow ionizer is analyzed. In 1-D approach the analytical ratios are obtained to calculate specific impulse of this propulsion system. From these ratios the limitations on parameters of a scramjet, ionizer and MHD systems are obtained, at which MHD interaction allows one to increase scramjet specific impulse. In particular according to [21] using of MHD generator with a constant cross-sectional area allows one to increase specific impulse of scramjet when the following inequality is true:

$$\frac{(\gamma-1)(1-k_1)M_1^2+1}{M_1^2-1} - \frac{T_1}{\Delta T}\left(1-\frac{k_1}{k_3}\left(1-\sqrt{\frac{q_{ion}}{q_{cr}}}\right)\right) > 0$$

where γ - is the specific heat ratio, k – is the load factor, M – is the Mach number, T – is the gas temperature, ΔT – is the temperature increase in the combustion chamber, q_{ion} – is the power density put into flow ionization, q_{cr} – is the critical power density (defined in [8]). Subscript 1 corresponds to parameters at MHD generator entrance, subscript 3 corresponds to MHD accelerator.

In a Fig.4 the dependencies of a MPCE specific impulse divided by a scramjet specific impulse (a relative specific impulse) on the enthalpy extraction ratio η for different values of relative inlet throat F_{th} are shown. This figure allows us to conclude, that MHD interaction results in scramjet specific impulse increasing. It should be noticed that the more is the relative inlet throat the greater positive effect can be reached. The dependencies concerning the value of a scramjet specific impulse on the enthalpy extraction ratio for various values of a load factor of MHD generator an MHD accelerator are shown in Figs.5-6.
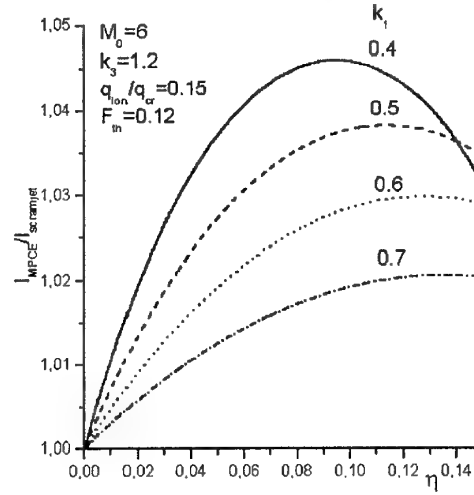
Fig.5. Relative specific impulse of MPCE as a function of the enthalpy extraction ratio for various values of load factor k_1.
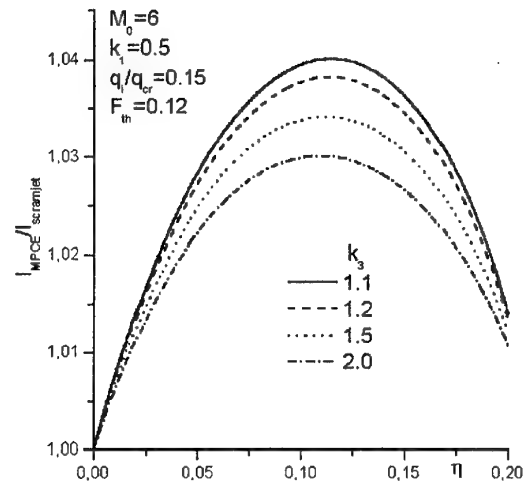
Fig.6. Relative specific impulse of MPCE as a function of the enthalpy extraction ratio for various values of load factor k_3.

Fig.4. Relative specific impulse of MPCE as a function of the enthalpy extraction ratio for various values of inlet throat F_{th}.
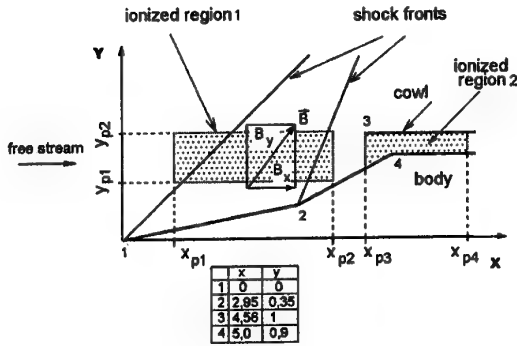
Fig.7. eometry of MPCE inlet with external and internal MHD generators.

a)

b)
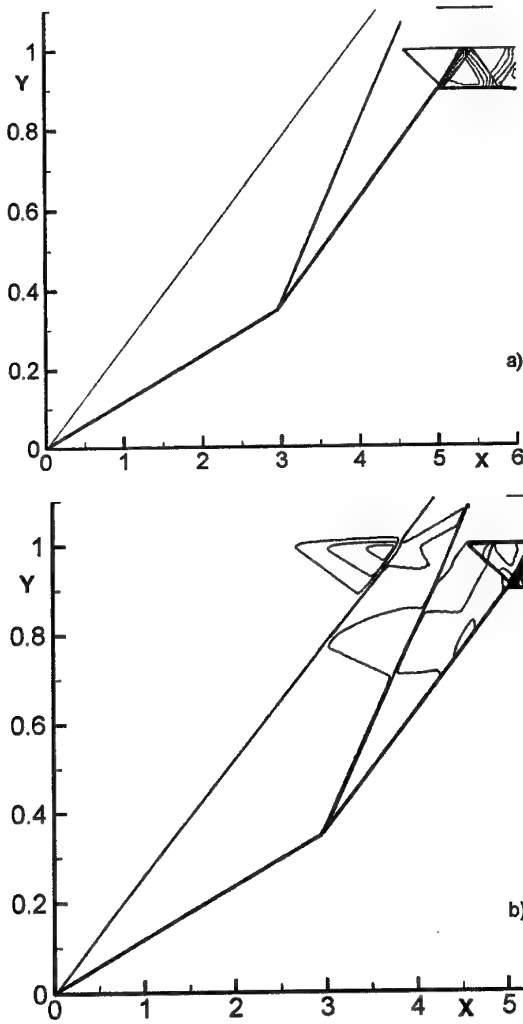
Fig.8. Density contours in MHD controlled inlet. M_d=8, F_{thr}=0.1, M_∞=6. a) q_{ion}=0, b) q_{ion}=1W/cm³

In works [8-11] in 2-D Euler approach the influence of the external MHD generator on a flow field, air mass flow rate and the value of a scramjet

specific impulse is explored. The geometry of MHD controlled inlet with external and internal MHD generators is shown in a Fig.7. The density contours in a scramjet inlet for different values of a power put to the flow ionization q_{ion} are given in a Fig.8. The influence degree comparison of external and internal MHD generators on the thrust value of a scramjet is shown in a Fig.9. Using just external MHD generator increases thrust more than using just internal MHD generator. The maximal thrust increase is observed in the case when the scheme combines external and internal MHD generators. The relative values of air mass flow rate, specific impulse and thrust of MPCE with external MHD generator in case of different relative power values put into flow ionization and for two values of a flight Mach number, which are smaller than the designed Mach number M_d are shown in the Tab.1. It is seen, that the MHD interaction allows one to increase air mass flow rate, specific impulse and thrust. And the more flight Mach number differs from the designed value the more positive effect of MHD influence is reached.
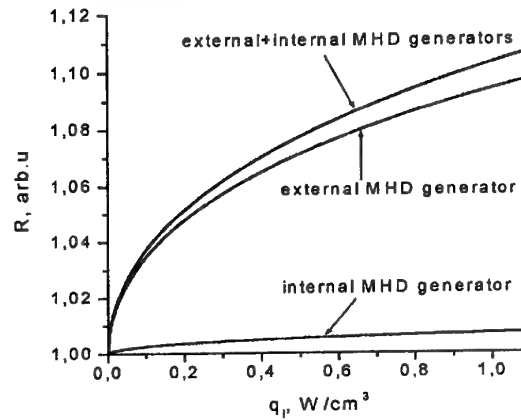
Fig.9. Relative thrust of MPCE with various location of MHD generators.

Table.1. Relative characteristics of MPCE with MHD controlled inlet. M_d=10, F_{thr} = 0.2

M_0	$\dfrac{q_i}{q_{cr}}$	$\dfrac{\dot{m}_{MPCE}}{\dot{m}_{scramjet}}$	$\dfrac{I_{MPCE}}{I_{scramjet}}$	$\dfrac{R_{MPCE}}{R_{scramjet}}$
6	0.05	1.25	1.12	1.40
	0.25	1.32	1.12	1.48
	1.0	1.37	1.10	1.50
8	0.02	1.18	1.02	1.20
	0.08	1.20	1.01	1.21
	0.16	1.23	0.99	1.22

Potentiality of MHD generator as a source of electrical energy on a board of hypersonic aircraft is considered in [8,22,23,25]. In [25] paper two schemes are analyzed: 1) MHD generator is located in scramjet upstream the combustion chamber, conductivity of flow is supposed to be equal 1 Sm/m without discussion of a way of the conductivity creation; 2) MHD generator is located downstream the combustion chamber, in this case conductivity is ensured by put into flow light-ionized additive (K-Na eutectic). In [23] paper MHD generator with nonequilibrium ionization of cold air by electron beam is considered. In particular it is shown in [23] that MHD generator with inlet cross-section $25\times25cm^2$, exit cross-section $75\times75cm^2$, length 3m produces 6 MW of electrical energy at $M_\infty=8$ at flight altitude $h=30km$. Ionization spent in this case is equal only to 97 kilowatt, that is less than 2% of power produced by the MHD generator.

So brief review of modern works shows that there are many possible applications of MHD systems in hypersonic aircraft. Publications count, far from being complete list of them is presented here, demonstrates considerable interest to indicated field of research.

References

1. Kuranov A.L., Korabelnicov A.V., Kuchinskiy V.V. and Sheikin E.G., "Fundamental Techniques of the "AJAX" Concept. Modern State of Research," AIAA paper No 2001-1915.
2. Batenin V.M., Bityurin V.A., Bocharov A.N., Brovkin V.G., Klimov A.I., Kolesnichenko Yu.F., Leonov S.B., "EM Advanced Flow/Flight Control," AIAA paper No 2001-0489
3. Bityurin V.A. and Bocharov A.N., "Advanced MHD Assisted Mixing of Reacting Streams," AIAA paper No 2001-0793
4. MacCormack R.W.,"A Conservation Form Method for Magneto-Fluid Dynamics," AIAA paper No 2001-0195
5. Bityurin V.A., Botcharov A.N., Potebnya V.G. and Lineberry J.T., "MHD Effects in Hypersonic Flows about Blunt Body," in The 2nd Workshop on Magneto-Plasma-Aerodynamics in Aerospace Applications, Moscow, 5-7 April 2000, p. 46
6. Poggie J. And Gaitonde D.V., "Computational Studies of Magnetic Control in Hypersonic Flow," AIAA Paper No 2001-0196
7. Deb P. and Agarawal R., "Numerical Simulation of Compressible Viscous MHD Flows with a Bi-Temperature Model for Reducing Supersonic Drag of Blunt Bodies

and Scramjet Inlets," AIAA paper No 2000-2419
8. Brichkin D.I., Kuranov A.L., and Sheikin E.G., "MHD Technology for Scramjet Control," AIAA paper No 98-1642.
9. Kuranov A.L., and Sheikin E.G., "The Potential of MHD Control for Improving Scramjet Performance," AIAA paper No 99-3535.
10. Brichkin D.I., Kuranov A.L., and Sheikin E.G., "The Potentialities of MHD Control for Improving Scramjet Performance," AIAA paper No 99-4969
11. Kuranov A.L., and Sheikin E.G., "Possibilities of MHD Control in Scramjet," in The 2nd Workshop on Magneto-Plasma-Aerodynamics in Aerospace Applications, Moscow, 5-7 April 2000, p.69
12. Vatazhin A., Kopchenov V., and Gouskov O., "Numerical Investigation of Hypersonic Inlets Control by Magnetic Field," in The 2nd Workshop on Magneto-Plasma-Aerodynamics in Aerospace Applications, Moscow, 5-7 April 2000, p. 56
13. Kopchenov V., Vatazhin A., and Gouskov O., "Estimation of Possibility of Use of MHD Control in Scramjet," AIAA paper No 99-4971
14. Golovachev Yu.P., Suschikh S.Yu., "Weakly Ionized Flows in Supersonic Inlets Subjected to the External Electromagnetic Fields," in Perspectives of MHD and Plasma Technologies in Aerospace Applications, IVTAN, Moscow, March 24-25, 1999, Proceedings, p.105
15. Macheret S.O., Shneider M.N., and Miles R.B., "External Supersonic Flow and Scramjet Inlet Control by MHD with Electron Beam Ionization," AIAA paper No 2001-0492
16. Bobashev S.V., D'yakonova E.A., Erofeev A.V., Lapushkina T.A., Maslennikov V.G., Poniaev S.A., Sakharov V.A., Vasil'eva R.V., and D. Van Wie, "Influence of MHD Interaction on Shock-Wave Structures in Supersonic Diffuser" in The 2nd Workshop on Magneto-Plasma-Aerodynamics in Aerospace Applications, Moscow, 5-7 April 2000, p. 64
17. Manucci M.A.S., Meloney E.O., Nagamatsu H.T., Myrabo L.N., and Bracken R.M., "Experimental Investigation of a 2-D slipstream generator and accelerator with $M\infty=7.6$ and T0=4100 K," AIAA paper No 2000-0446
18. Fraishtadt. V.L., Kuranov A.L., and Sheikin E.G., "Use of MHD Systems in Hypersonic Aircraft," Technical Physics, Vol 43, 1988, p.1309.

31

19. Bityurin V.A., Lineberry J.T., Potebnia V.G., Alferov V.I., Kuranov A.L. and Sheikin E.G., "Assesment of Hypersonic MHD Concept," Paper AIAA-97-2393.

20. Park C., Bogdanoff D.W., and Mehta U.B., "Theoretical Performance of a Nonequilibrium MHD-Bypass Scramjet," Paper AIAA-2001-0792.

21. Brichkin D.I., Kuranov A.L., and Sheikin E.G. ,"Scramjet with MHD Control under "AJAX" Concept. Physical Limitation," AIAA paper No 2001-0381

22. Macheret S.O., Shneider M.N., and Miles R.B., "Potential Performance of Supersonic MHD Power Generators," AIAA paper No 2001-0795

23. Macheret S.O., Shneider M.N., and Miles R.B., "MHD Power Extraction From Cold Hypersonic Air Flows with External Ionizer," AIAA paper No 99-4800

24. Macheret S.O., Shneider M.N., and Miles R.B., "Modeling of Air Plasma Generation by Electron Beams and High-Voltage Pulses," AIAA paper No 2000-2569

25. Zeiagrnic V.A., Novikov V.A., Okunev V.I., Rickman V.Yu., and Kuranov A.L., "Mass-Dimension Optimization of MHD Generators for Hypersonic Aircraft of "AJAX" Concept," in The 2nd Workshop on Magneto-Plasma-Aerodynamics in Aerospace Applications, Moscow, 5-7 April 2000, p. 240

04. PLASMA ASSISTED COMBUSTION

Klimov A., Bityurin V, Brovkin V., Kuznetsov A., Sukovatkin N., Vystavkin N,
Institute of High Temperatures, Russian Academy of Sciences, Moscow, Russia

Van Wie D.M.
Johns Hopkins University, Laurel MD

Main goal of our researches is preparation and realization plasma assisted combustion (PAC) experiment in wind tunnel at airflow parameters closed to scram-jet ones. Flow parameters are the followings: $M \sim 2$, $P_{st} = (0.5-0.8) \times 10^5$ Pa, $T_{0, air} = 300-950K$.

It is well known that there are some difficulties in a scream jet technology, connected with ignition, mixing and combustion of fuel in supersonic airflow. In turns these difficulties are connected with large characteristic times of ignition τ_i and combustion τ_c of hydrocarbon fuel in supersonic airflow at parameters closed to scram jet ones. Additional active radical and vibration exited molecule generation in airflow could decrease these characteristic times dramatically [1,2]. Active radicals O, H, OH, NO and vibration exited molecules play important role in a combustion process [2]. Non- equilibrium discharge can generate these particles effectively. So, PAC study is very important for internal and external gas dynamics.

Generation of non- equilibrium high energetic structural plasma formations (further named non- equilibrium plasmoids, NP) in a gas and a gas flow was studied in [3,4]. High effective plasma generators of these NP were designed in the course of these investigations.

Different types of NP were used in our plasma assisted combustion experiment, namely
- HF streamer plasmoid,
- NP, created by pulse repetitive discharge,
- NP, created by AC discharge and combined discharge.

Note that it is possible to control main plasma parameters N_e and T_e independently in combined discharge namely.

NP characteristics in cold and hot gas flow are studied now and discussed in this paper.

Best experimental results on PAC were obtained by HF streamer plasmoid namely. Remember that ignition, combustion and advanced mixing of propane stimulated by HF streamer plasmoid in airflow at Mach number $M < 2$, $P_{st} \sim 100$ torr were studied in our previous work [4,5].

It was revealed that a small HF power is needed for the propane- air ignition and generation of radicals in this fuel in a supersonic airflow. The value of HF power was closed to minimal threshold of HF discharge generation in airflow (about $\sim 100W$).
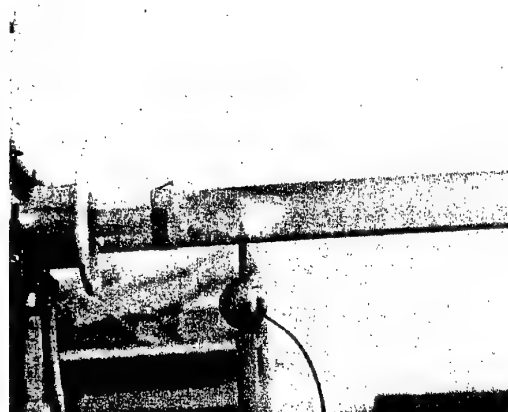
Fig.1. Stable HF streamer discharge in a cold airflow, $M \sim 0,8-1,2$; $P_{st} \sim 1$ Bar, $T_o \sim 300K$
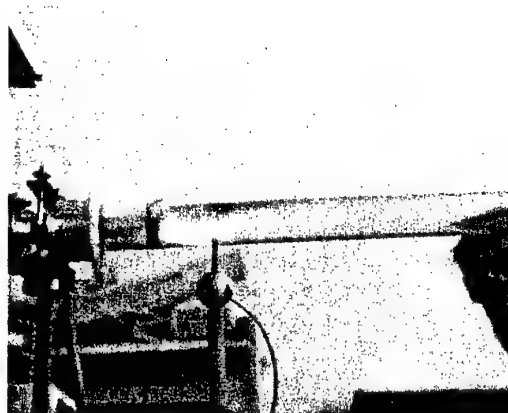
Fig.2. Stable PAC controlled by HF streamer discharge, $M \sim 0,8-1,2$; $P_{st} \sim 1$ Bar, $T_o \sim 300K$

Stable HF streamer discharge in a cold airflow in wind tunnel is shown in Fig.1. Stable PAC created by HF streamer discharge is shown in Fig.2. It was revealed that HF streamer discharge has a number of important positive properties (peculiarities) in PAC experiment (comparing it with other types of electric discharges), namely:

33

1. HF discharge was ignited and burned near a mixing contact surface between propane injection flow and airflow (near a gas density gradient region) as a rule. In Fig.1 one can see that normal position of HF streamer discharge is a region near a hot electrode in a cold supersonic airflow without propane injection. HF streamers are concentrated near airflow separation zone behind hot electrode. On the other hand the HF discharge changes its position and shape considerably with propane injection and its further ignition and burning, Fig.2. One can see that stable HF discharge creation and its burning are near mixing zone (near gas density gradient region) in this case namely. It is very important result (see below).

2. HF streamer discharge can disturb contact mixing surface and stimulate propane- air mixing (advanced mixing). Really it was revealed that streamer HF discharge could increase aerodynamic jet noise and airflow turbulence considerably in our previous experiments [6]. So, these gas dynamic disturbances can stimulate and increase fuel-airflow mixing. It is needed to study this advanced mixing in future experiments.

It was revealed that fuel could penetrate through a HF streamer channels deeply in airflow. So, study of physical and chemical properties of a single HF streamer is very important for advanced mixing and PAC optimization. Propane transportation through streamer is very fast process. Estimations and measurements proved this conclusion. Really it is very easily to obtain (based on characteristic streamer lifetime and its length, see below) that mean velocity of propane transportation inside a streamer channel is about

$$V_{fl} \sim 10^3 \text{ m/s, and more.}$$

3. Characteristic plasma parameters of a single HF streamer are the followings (see our works [4,5]):

- Electron concentration $\qquad >10^{15} \text{ cm}^3$
- Electron temperature $\qquad$ 1-10 eV
- Gas temperature $\qquad$ 1000-1500K,
- Vibration temperature $\qquad$ ~2500K
- Specific energy storage $\qquad$ ~1-10 J/cm^3
- HF streamer length $\qquad L_{str.exp} \sim 50$ mm
- HF streamer characteristic
  lifetime $\qquad T_{str} \sim 50\text{-}100$ mcs
- Velocity of HF streamer
  propagation $\qquad V_{str} \sim 10^3\text{-}10^5$ m/s

This plasma formation is non-equilibrium one. It has high specific energy storage. So, this NP can stimulate plasma chemical reactions and radical generation in a fuel-air mixture.

4. HF plasmoid is very adaptive one and self-organized one. It was revealed that streamer HF discharge is transformed to diffusive torch one in a combustion region at fuel ignition (in a hot gas region, with gas temperature $T_g > 2000$K, see below), Fig.2. This result is very important from the point of view of HF plasma efficiency. There is a good transportation of HF power in HF torch discharge namely. This HF discharge has a small resistance and a very large current density. Main part of HF energy is transformed into gas heating in this discharge. Note that HF torch discharge plasma is very closed to equilibrium one. There is a positive reverse coupling in HF torch discharge. It generates and amplifies hot gas disturbances (after ignition by HF streamer discharge) in a combustion region considerably. It was revealed that PAC luminosity is not stationary in a space and time, Fig.2. It is interesting to note that flame vibration frequency is equaled to streamer generation one. Amplitude of PAC luminosity is much higher than chemical flame one without HF discharge.

5. There is a number of HF NP in airflow, created by HF generator. Here we consider two types of HF NP only:
- NP created by HF torch discharge, Fig.3.
- NP created by HF streamer discharge.Fig.1.

Note that HF torch discharge exists in a cold airflow at small Mach number M<0,1 (or without airflow). Streamer HF discharge exists in a cold airflow at high Mash number (up to M~ 4 and higher).

Experimental results obtained during _HF torch plasma assisted combustion_ (diffuse combustion) are shown in Fig.3. It was revealed considerable intensification and acceleration of propane combustion at HF torch discharge generation near combustion region. Characteristic chemical flame dimension was decreased by factor 5 at HF torch discharge creation. Propane flame stimulated by this discharge was very bright and hot (like arc discharge). So, PAC chemical rate was increased more than factor 5 in HF torch discharge also.
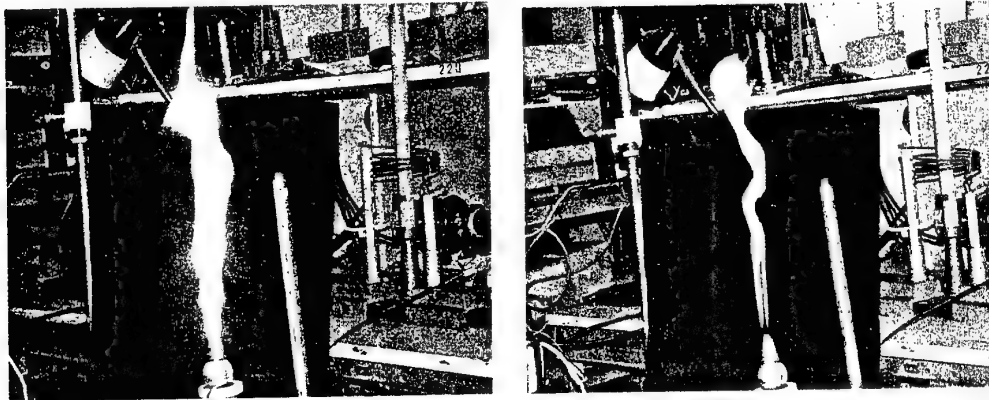
Fig.3. Propane combustion activated by HF torch discharge (left) and one without discharge (right).

HF streamer plasma assisted combustion was created and studied at the following conditions:

- Mach number $0,1 < M < 2$,
- Static pressure $0,1 \text{Bar} < P_{st} < 1 \text{Bar}$,
- Mean HF power $N_d < 2 \text{ kW}$
- Propane mass injection   1-5 g/s

1. It was revealed that stable HF plasma assisted ignition and combustion were created in a cold and hot airflow at described conditions.
2. Characteristic ignition time τ_1 is decreased more than factor 10 in propane- air mixture in subsonic flow ($M < 0.8$, $P_{st} \sim 1 \text{Bar}$, $T_{st} \sim 270 \text{K}$). Minimal value τ_1 reaches up to $\tau_1 \sim 30-50 \text{mcs}$.
3. There is complete PAC of propane- air mixture in a cold airflow. Final products of this PAC were carbon dioxide and water vapor only (without toxic impurities, see below).

For the optimization of HF streamer PG it is need to study HF streamer parameters and characteristics in airflow in detail.

PAC plasma parameters measured by optical spectroscopy.

Characteristic spectrum of HF streamer discharge in airflow ($M < 0.8$; $P_{st} \sim 1$ Bar, $T_0 \sim 300 \text{K}$) is shown in Fig.4. One can see the second positive nitrogen band in this spectrum. There are rotation optical lines of the molecular nitrogen in this spectrum also. Estimation of a rotation (or gas) temperature is possible by using of the relative intensity method [5]. The following optical transitions were studied in our experiment: $(0,0)-$ $\lambda = 3371 \text{A}$; $(1,2)- \lambda = 3536 \text{A}$; $(0,1)- \lambda = 3576.9 \text{A}$; $(2,4)- \lambda = 3710.5 \text{A}$; $(1,3)- \lambda = 3755 \text{A}$; $(0,2)- \lambda = 3805 \text{A}$; $(2,5)- \lambda = 3943 \text{A}$; $(1,4)- \lambda = 3998 \text{A}$; $(0,3)- \lambda = 4059 \text{A}$.
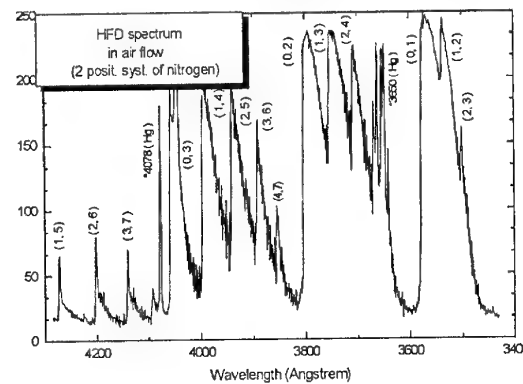
Fig.4. Characteristic optical spectrum obtained in HF streamer discharge in airflow, $M \sim 0.8$: $P_{st} \sim 1 \text{Bar}$, $T_0 \sim 300 \text{K}$, $I_d \sim 0,6 \text{Amp}$
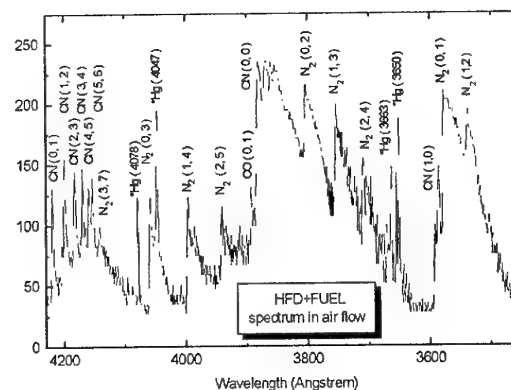
Fig.5. Characteristic optical spectrum of PAC in airflow $(M \sim 0.8)$ with propane injection.

It was revealed that rotational level distribution is closed to Boltzmann's one. So, it is possible to estimate the rotational temperature T_R in

35

discharge plasma. Gas temperature was closed to rotation temperature in our experiment [4,5].

Optical spectrum was changed dramatically in the case of a fuel injection in HF discharge zone. The amplitudes of some molecular nitrogen bands were decreased (or disappeared). Characteristic optical lines of the *CN, CO, OH* and others molecules were appeared in PAC spectrum. Characteristic PAC optical spectrum is shown in Fig.5.

Tabl.1

$I_{a,HF}= 0.5$ A	$I_{a,HF}=0.7$ A	$I_{a,HF}=0.8$ A
T=1000–1200K	T=1200–1400K	T=1600K

Note, that characteristic PAC spectrum in airflow (M<0.8) is very complex. There are many atomic lines in the range of $\Delta\lambda$=3160-4500A and practically continuous spectrum in the range of $\Delta\lambda$=2370-3500A. The atomic lines are corresponded to single ionized iron atoms (evaporated electrode material). There are optical lines of the single ionized atoms of O_1 (λ= 3823.47A; 3973.27A; 4072.15A), N1 (λ= 3830.4A; 3842.2A) and H_1 (λ=3835.4A) in this spectrum also. Now these spectra are analyzed. Rotation temperature inside HF streamer discharge was measured by optical spectroscopy method. Its value was about T_g~1000-1600K. This temperature depended on anode current strongly, Tabl.1. Measured gas temperature in PAC region was about T_g~2600K. This temperature was measured by two independent methods:
- Thermocouple method,
- Optical spectroscopy.

Chemical mass spectroscopy analysis. IR spectroscopy.

Chemical composition of final PAC products was analyzed by mass spectroscopy and IR spectroscopy. PG HF was used in this experiment. Small portion of tested gas was evacuated from gas flow after PAC region.

It was measured that there were increased concentrations of the following components in the tested gas:

- CO_2, M=44 ΔN~ 5-6%
- $CO_2 + H$, M=45 ΔN~ 4%
- NO_2 ΔN~ 0%

where $\Delta N = N_{test\ gas} - N_{air}$, HCN, NO_x, CO molecules were absents in tested gas.

IR spectroscopy proved this conclusion also. Complete combustion of propane in airflow

was realized in a cold airflow by HF streamer discharge. Carbon dioxide molecule optical lines were recorded in IR spectrum only (without propane lines). So, there is complete combustion of propane stimulated by HF streamer discharge in a cold airflow.

Conclusions

Following main results were obtained in PAC experiment:
1. Design and manufacture of different types of HF PG for PAC experiment were fulfilled:
2. These HF PG was tested in airflow at M=0.1-2; $P_{st}<$ 1Bar.
3. Stable PAC of propane- air mixture was created in a cold airflow (M=0.1-2; P_{st}<1Bar, T_0=300K).
4. Different diagnostic instrumentation were used in plasma assisted combustion experiments:

- The spectroscopic diagnostic set up was used to measure the rotational temperature T_{rot} (T_{rot}~T_g) and vibration temperature T_V.
- Mass spectrometer was used for determination of chemical composition of combustion products.
- IR spectroscopy.
- Probe diagnostics was used for electron concentration measure in HF streamer discharge in airflow.

5. Chemical combustion rate of propane- air mixture is increased more than factor 5 in HF discharge.
6. Characteristic ignition time τ_1 was decreased more than factor 10 in propane- air mixture in HF streamer discharge in subsonic flow (M<0.8, P_{st}~1Bar, T_{st}~270K). Minimal value τ_1 was about τ_1~30-50mcs.
7. There is complete combustion of a propane-air mixture stimulated by HF streamer discharge in a cold airflow. Final products of this PAC are carbon dioxide and water vapor only (without toxic impurities).
8. Estimations of plasma efficiency in PAC experiment. Mean HF power used in this experiment was N_d~100-1000W. Total chemical power was about N_{ch}~16-17kW, (it corresponds to propane mass flux m~0,4g/s). So, ratio $\eta=(N_d/N_{ch})$ 100%=0,6-6%. Maximal radical concentration has to be closed this value also.
9. It is necessary to continue a study of the optical spectra in detail in future PAC experiment.
10. It is need to continue measure plasma parameters in combined discharge (HF discharge+ pulse repetitive one) for PG design optimization. and PAC optimization.

36

References

1. Morris R.A., Arnold S.T., Viggano A.A., Maurice L.Q., Carter C., Sutton E.A. "Investigation of the Effects of Ionization on Hydrocarbon-Air Combustion Chemistry". 2nd Weakly Ionized Gases Workshop, Norfolk, 1998.
2. Buriko Yu., Vinogradov, V., Goltsev, V., "Influence of active radical concentration on self-ignition delay of hydrocarbon fuel- air mixture". Appl. Phys., 2000, P.10.
3. Ball Lightning in Laboratory, M. Chemistry, 1994, P.256
4. Report IVTAN, Delivery 1-4; Partner Project #1810P, Description of the experimental set up and diagnostic instrumentation, Moscow, 2000, P.28
5. Biturin V.A., Klimov A.I., Lebedev P.D., et.al. "Study of ignition and burning of fuel-air mixture in supersonic flow stimulated by HF streamer discharge". Report IVT AN, 1998.
6. Klimov A.I., Beaulieu W., Bityurin V., Kuznetsov A., Leonov S., Jet Noise Reduction by Plasma Formations, Proc.2nd Workshop on Magneto-Plasma-Aerodynamics in Aerospace Applications, IVTAN, Moscow, 5-7 April 2000, P.138

05. STRONG ACTION OF MAGNETIC AND ELECTRICAL FIELDS ON INLET SHOCK CONFIGURATION IN DIFFUSER

S.V. Bobashev, A.B.Erofeev, T.A.Lapushkina, S.A.Poniaev, V.A.Sakharov, R.V.Vasil'eva
Ioffe Physico-Technical Institute, Russian Academy of Sciences, St. Petersburg, RUSSIA

D.Van Wie
Johns Hopkins University, Laurel, Maryland, USA

Abstract. This work continues a series of [1,2] initiated under AJAX program [3] with a purpose to study the external effects on the shock-wave structures arising in a diffuser with a total inner flow compression. The main part of the diffuser is a linearly convergent channel. The shock-wave structure incorporates two attached shocks affected by each other in the diffuser. External electric field arranged in such a manner that it enhanced a magneto-induced current. A flow is a result of the MHD interaction itself as well as a gas heating under the external electric field.

Statement of the Problem

A general aim of the work is a treatment of a shock-wave structure's dynamics under the external fields and of what processes and of what part of the diffuser are more important in flow shape changes. For this aim, a comparison is carried out between the flow pictures under effects in a diffuser's bulk and its separate parts with the electric field only or with both the electric and magnetic fields. Solving this problem, the conditions have been established under which a flow in the diffuser's bulk with the external fields is of a mode with strong interaction when arises a MHD deceleration shock, being of a mode with the weak one in its separate parts.

Design o Experiment

A schematic of the experimental setup is presented in [1,2]. It is a working vacuum chamber conjugated with a shock tube. In its turn, the working chamber incorporates a supersonic nozzle accelerating a plasma flow up to M_0=4.3 and a convergent diffuser with a system of electrodes circuited in Faraday's manner. As a working fluid Xe plasma has been used. The initial Xe pressure in the low-pressure chamber of the shock tube is 20 torr, the Mach number of the incident shock wave M=8. As a method of recording a state of the shock-wave structure, it was applied a schlieren technique with two modes of filming. The first presented in [2] gives an opportunity to obtain a flow picture in a given moment of time from the flow beginning with high separation in the one-fold regime. As an illumination source it has been applied a ruby laser OGM-20. The exposure time is 30ns. The second gives an opportunity to record a structural change in the shock-wave structure in a course of a whole process. As an illumination source it has been used the Podmoshensky's source. The recording proceeds with a high-speed

camera VSK-5. To conjugate this camera with a schlieren setup, the entrance of the camera was modified. For comparison, Fig.1 gives a schlieren picture of the flow in a diffuser obtained in the one-fold regime with no external fields as well as a scheme of arising discontinuities. Here, the inlet shocks «a» are well seen with a point of their interaction distanced by X_c=(44±1.5)mm from the diffuser's inlet.
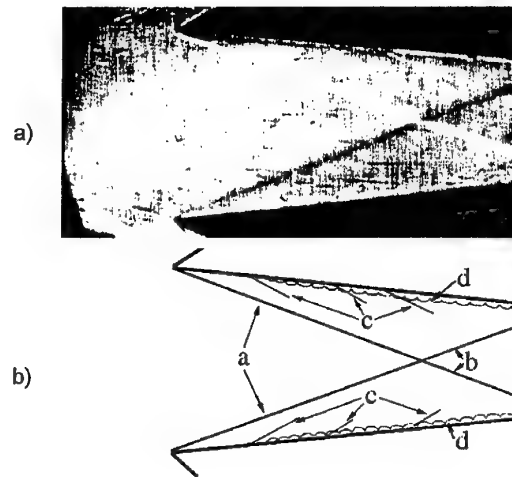
Fig.1. Schlieren picture of a flow and a scheme of HD irregularities with no external fields.

The reflection of the attached shock from each other results in the shocks «b». Note that a near-wall layer «d» is slightly distinct in this case and marked off eventually on accompanied scheme. The additional irregularities «c» seen in the photo arise onto the wall layer.

A point in the developed setup is a need of supplying the electrodes with external electric field for raising a current density sufficient to the MHD magnitudes, short-circuiting the inherent current

38

being in troubles due to existence of a large potential drop through a sheath. Supplying the external electric field is accomplished with a discharge of the long lines through a circuit incorporating a plasma spacing between a pair of the electrodes and a load resistance 0.1 Ω.

The pairs of the electrodes are triggered by the same voltage of 110V. The Ohm law for a circuit with the MHD generator of EMF $\varepsilon=uBh$, an external voltage source V, and a load resistance is $V+uBh=I(R_{eff}+R_L)$, where V is the electrode voltage, u is a flow velocity, B is magnetic induction, h is a spacing between the electrodes, I is a current, R_{eff} is an effective internal resistance of a plasma, including the resistance of a flow core and that of the wall layers, R_L is a load resistance.

Three regions of interaction with the external fields have been distinguished (Fig.2) marked by that the current exists only within separated areas. This has been obtained by triggering the external voltage on the electrodes situated in this area.
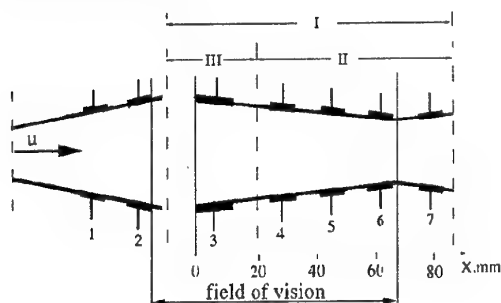
Fig.2. A schematic of a channel with the marked areas of interaction under 3 modes of the external electric field's triggering.

One can see in Fig.2 that the voltage is supplied to all the pairs of the electrodes from 3rd to 7th in the diffuser's bulk under Connection I. The interaction arises in all the diffuser's bulk. A length of the interaction region is about 90mm. Connection II is accomplished excluding the inlet part of the diffuser, the voltage is supplied to 4-7th pairs of the electrodes, a length of the interaction region is 70mm. Connection III is accomplished with 3rd pair of the electrodes, thus, interaction proceeds only within the first part of the diffuser. A length of the interaction region is about 20mm.

In Fig.3, the distributions over a current density along the channel are presented corresponding to three modes of the external voltage connection with no magnetic field and under MHD interaction. Zero point of the abscissa refers to the diffuser's origin. Contrary to the expectations one can see no rise in a current density

in the graphs when triggering the magneto-induced EMF. It occurs probably both on account of Hall effect due to non ideal electrode sectionalization and because of an increase of near-wall layer at MHD interaction. With volt-ampere characteristics the values of R_{eff} have been estimated. At B=0, $R_{eff}\approx0.15\Omega$, at B=1.3T, R_{eff}=0.2-0.4Ω. Then, a load coefficient k=R_L/(R_L+R_{eff}) is within 0.2-0.4 limits.
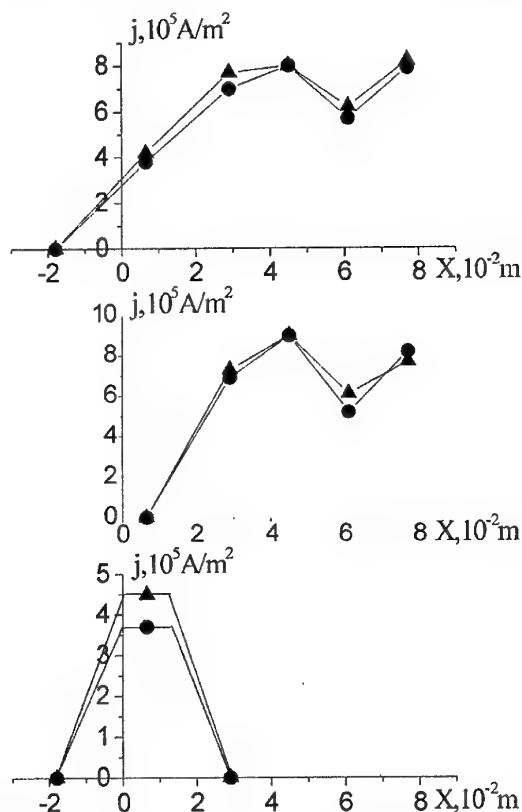
Fig.3. Distribution over a current density along the channel: a) Connection I; b) Connection II; c) Connection III. The triangles refer to B=0, circles refer to B=1.3T.

Comparative Estimations of the Effects of The Magnetic and Electric Fields

The simple effects on the flows include the force and power ones. General force effect on a flow is due to ponderomotive force $F=jB$. A power effect includes two aspects. First, there is an energy outflow into external circuit generated under MHD interaction. Second, there is a heat input from the external source of the electric field. The work of the ponderomotive force and heat input decelerate a supersonic flow, heat output results in the flow acceleration.

Figure 4 gives a calculated Mach number of the flow along the axis of the gasdynamic tract under influence of the magnetic and electric fields. Calculation data have been obtained solving a system of the equation giving the changes in a flow velocity, state parameters, Mach numbers, and Ohm law under conditions nearest to those of the present experiments [4]. Calculation has been carried out when $X=0$ - a critical cross section, $T_{cr}=7700K$, $\rho_{0cr}=2,2kg/m^3$, $a_{cr}=940m/s$. As a value of conductivity in the interaction region it have been used that of effective conductivity obtained experimentally, $\sigma_{eff}=150S/m$. A load coefficient $\kappa=0,3$.
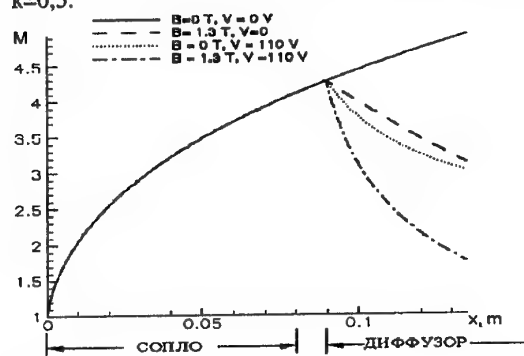
Fig.4. Changes in the Mach number of the flow along the axis of the gasdynamic tract under influence of the magnetic and electric fields.

One can see in Fig.4 that the separated effects of the electric and magnetic fields are strong decreasing Mach number about 25%. A mutual action of the external fields illustrated by the data of calculation results in a sharp drop of the Mach number of the flow over an interaction length.

Interaction with the External Fields in a Bulk of the Diffuser (Connection I)

In Fig.5 are shown the flow pictures in the diffuser obtained with the schlieren technique in one-fold regime as well as a graphic decoding of the shock-wave structures.

Figures 5.1-a and b show a flow structure arising under the electric field effect only. Here, one can see the attached shocks «a», shocks «b» involved under reflection of the attached shocks from each other, and the shocks «f» involved under reflection of the shocks «b» from a wall or wall layer «d». The wall layer is well seen on a schlierengramm. One can see that its thickness is increased along the diffuser and the wall layer are greater with a current than that with no current (Fig.1). The gasdynamic discontinuity «e» has been identified as a contact disruption arising in a region downward the attached shocks due to divergent flow going into the diffuser. A shock «l» mounts the boundary layer. Compared with flow picture with no fields (Fig.1), in this case, a slope angle of the attached shocks grows, an intercept point of the shocks X_c shifts toward the diffuser inlet, $X_c=(37\pm1,5)mm$, and the points of the shocks' reflection from the walls, also, are closer to the inlet. Qualitatively, a flow picture formed under effect of the electric field on the flow is similar to that arisen under a weak MHD interaction.

(5.1)
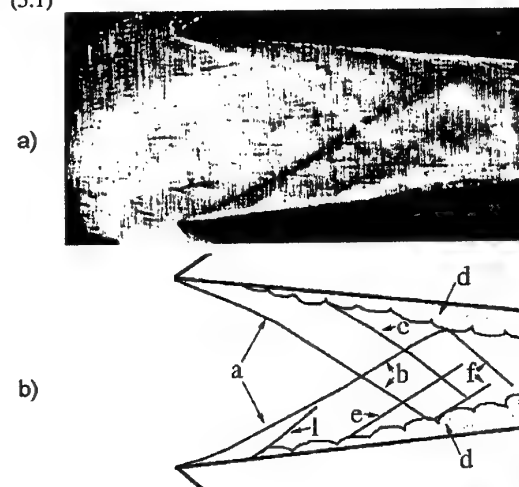
(5.2)
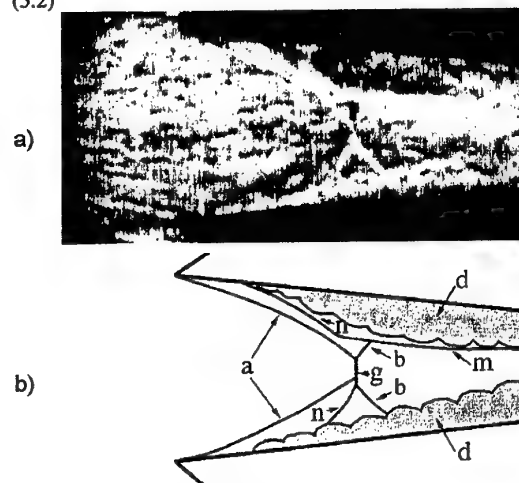
Fig.5. Connection I. Schlieren picture (a) a flow schematic (b). (5.1) $B=0$; (5.2) $B=1,3T$.

Figure 5.2-a demonstrates a schlieren picture of the flow, and Figure 5.2-b demonstrates a scheme of the main observed gasdynamic irregularities arisen in the diffuser as a result both of the electric and magnetic fields. One can see that the flow picture is essentially changed. Attention is to a strong development of the wall layer,

40

N 2

N 6

N 22

N 32

N 44

N 44

N 51
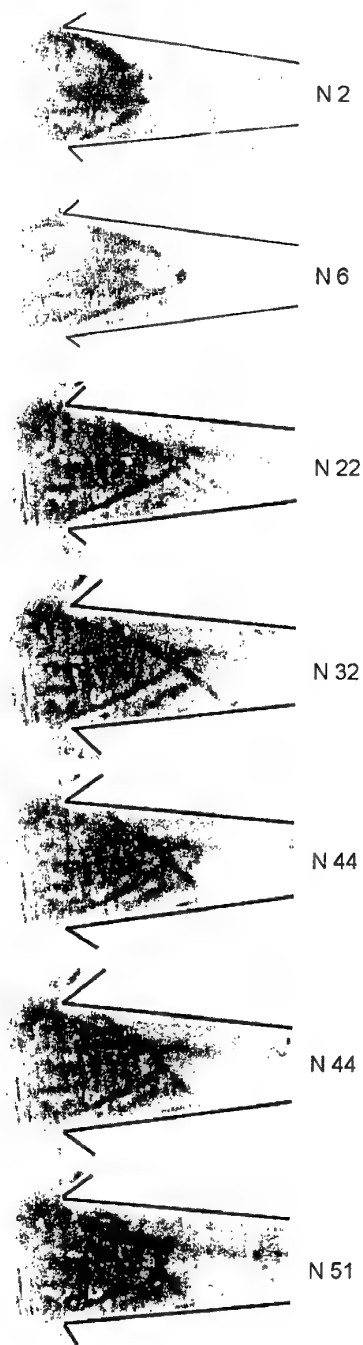
Fig.6. Scanning exposures of schlieren pictures for connection I.

a discontinuity «m» which can be seen near the top wall. Picturing the flow as a whole, we can confirm that it is a pattern of a strong interaction when there is a direct shock of MHD deceleration in the flow core, however, the flow picture is very complicated due to an effect of a highly developed wall layer.

For the presentation of arising the MHD deceleration shock, in Fig.6 given are the separate shots of the schlieren pictures obtained with a high-speed camera. Exposition time is $2\mu s$, time between shots is $5.7\mu s$. Shots 2-6 show the process of the flow entering the diffuser. Shot 22 show formed near-wall layer and second shock near upper wall, which is most probably formed on the near-wall layer. All other shots (23-61) shows that all changes of flow is connected with attached shocks.

Schematically this transformation is shown in Fig.7.

t_1

t_2

t_3 a   g   b   d
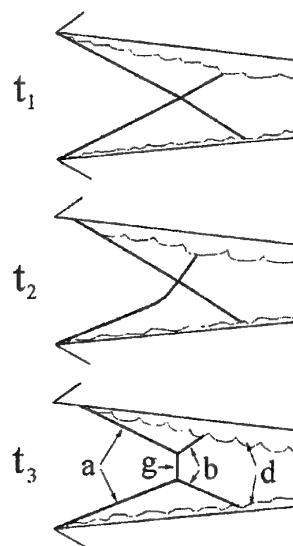
Fig.7. Scheme of formation of MHD deceleration shock.

At time t_1 a regular reflection of the attached shocks from each other proceeds. At the next moment of time t_2 the attached shock becomes more concave, an angle of its inclination increases, being probably related with a decrease in the Mach number of the flow due to deceleration. But the shocks' reflection remains regular. At t_3 shocks' reflection becomes irregular but the Mach's reflection, i.e., a triple configuration shown in Fig.5.2-b arises including an attached shock «a», Mach wave «g» normal to the flow, and a reflected wave «b». Thus, a decelerating MHD shock is built-up due to Mach waves arisen at the Mach reflection of the attached shocks from each other. Note that this way of flow formation is surprising.

especially, near the top wall. It is of importance the principal change in the inlet shocks' structure. Instead of the intercepting oblique shocks we can see a triple structure including a direct shock in the flow core «g» and two oblique shocks «a» and «b». Between them, one distinguishes also the discontinuities «n». Further, we can not yet identify

More expected is way when due to pressure increase at the end of interaction zone compression waves adding up to shock wave and then this shock wave moves upwind and changes inlet shocks configuration.

Interaction on the Various Sections of Diffuser. Connection II

To found the most effective conditions for influence on the shock-wave structures let us consider changes of it when the current exists on the various sections of diffuser. Fig.8 shows the structure of flow at connection II.

(8.1)

a)

b)

(8.2)

a)

b)
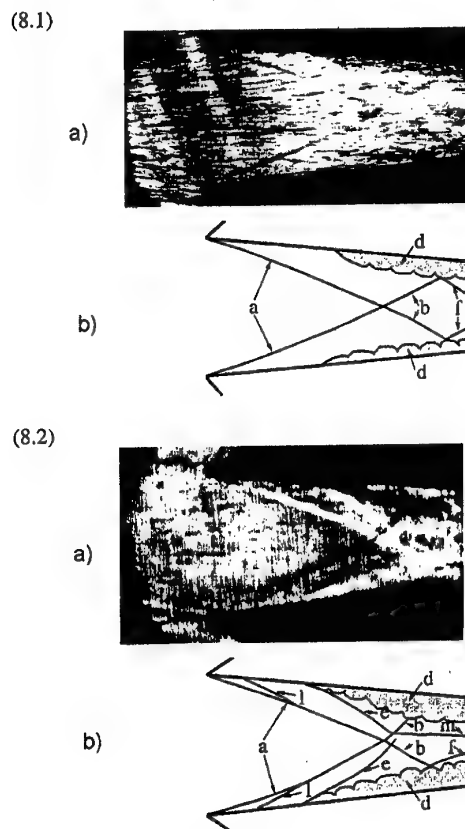
Fig.8. Connection II. Schlieren picture (a) and a scheme of a flow (b). (8.1) $B=0$; (8.2) $B=1,3T$.

An external electric field is connected to all the electrodes excluding the first. The schlieren picture under the electric field only is presented in Fig.8.1-a. Figure 8.1-b demonstrates a scheme of the observed discontinuities. One can see that the slope angles of the attached shocks «a» are slightly changed compared with Fig.1, a distance X_c is not changed in practice. The location of the shocks «b» are slightly changed, their slope angle is greater in such a manner that the shocks «f» reflected from

the wall layer are visible. However a current does effect a growth of the wall layer, its growth being originated near the first electrode under this connection.

Involving additional magnetic field (Fig.8.2-a,b) does not give a noticeable shift of the attached shocks, one can see only a weak distortion and a more pronounced discontinuity «e». Moreover, near a wider wall layer, a gasdynamic discontinuity «m» arises.

Connection III

In a case when the external electric field involves only the first pair of electrodes situated on the diffuser's noses (Connection III) a shock-wave structure arises given in Fig.9.

(9.1)

a)

b)

(9.2)

a)

b)
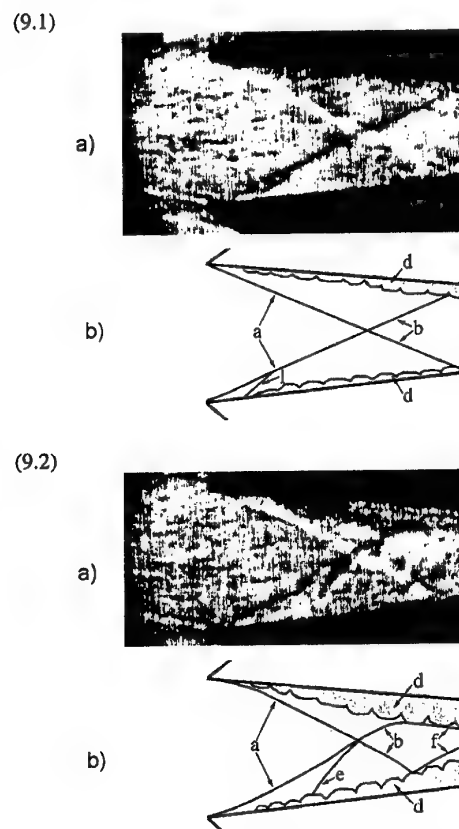
Fig. 9. Connection III. Schlieren picture (a) and a scheme of a flow (b): (9.1) - $B=0$; (9.2) - $B=1,3T$

Already with short-circuiting a current with no magnetic field (Fig.9.1-a, b) a pronounced change in the slope angles of the shocks is observed, a point of their intercept shifts toward the diffuser's inlet, $X_c=(3.6\pm1.5)$mm, also, is noticeable a growth of the wall layer beginning the very inlet of the diffuser. Under MHD interaction (Fig.9.2-a,

b) there is no additional change in X_c but the attached shocks become more concave and the wide wall layers are well seen, a top layer being gather wider that the low one. Well seen is a contact discontinuity «e».

Discussion

This experiment demonstrates that Connection II is of more weak influence on a shock-wave structure than Connection III despite a more stretched interaction region. To compare amounts of energy consumed when changing the flow parameters under two modes of connection, II and III, we estimate a work of the ponderomotive force and gas heating energy under the external electric field. Energy outflow in accordance with estimations is of minor role and out of consideration here. Over a length L a work of the ponderomotive force is $A=jBL$, it is determined via experiment. A measure of its influence on the flow is a Stuart parameter $St=iBL/<\rho u^2>$ determined as a ratio of a work of the ponderomotive force to a mean doubled kinetic energy of the flow in the diffuser's bulk over a length L at $V=0$ and $B=0$. With kinetic energy estimate from the calculations, we obtain a value of a Stuart parameter under Connection II $St_{II}= 0.38$ at III - $St_{III}=0.04$. One can see that a value of St_{II} is about an order higher than St_{III} indicating the stronger MHD interaction in the second part of the channel.

Contribution of plasma heating under the electric field into the flow deceleration at two connections can be compared when estimating a ratio of a Joule heating over a period: $\Delta t=L/u$: $Q_c=(1-k)iLV/uh$ to a mean enthalpy of incoming flow $H=<\rho(\frac{u^2}{2}+C_pT)>$, namely, comparing $P=Q_c/H$. Using the calculation data of a velocity and temperature of the incident flow, we obtain the parameter P for two interaction regions as follows $P_{II}=1.2$, $P_{III}=0.07$. One can see that a Joule heating must be stronger in its effect on the flow when using II mode of supplying a current to the electrodes. But, as it is seen in Figs.8,9, the experiment gives a reverse trend: a stronger force in a region II involves a less pronounced change in the shock-wave structure in a region III, i.e., an external action is of more influence on the attached shocks when applied near diffuser's origin. In connection with this, note a structural difference of the flows in the regions Ii and III.

Region II is closely packed with the dissipative structures. While in region III the main volume is filled by a continuous flow. Naturally, the observed inertia of the shocks in region II can

be related to energy consumed by their formation under interaction between the flow and the diffuser's walls. An amount of irreversible heat Q supplied to the shocks is determined by an entropy jump S. $Q=\int TdS=<T>\Delta S$, where $\Delta S=C_v \ln \frac{p_2\rho_1^{\gamma}}{p_1\rho_2^{\gamma}}$, a suffix 2 refers to the downward parameters, suffix 1 refers to the upward ones. This amount of energy is about two orders of value smaller than a total enthalpy of the flow. In the case when there are several shocks, partially or completely, in the interaction region, energy dissipated in the shocks is probably added. A ratio of this energy to interaction energy could be a measure of inertia of the shocks when tending to change their location under the external factors.

Conclusion

The main results of this work are presented as follows.

An effect of the wall layer on a flow picture in the diffuser is revealed.

A shock of MHD deceleration arises as a result of transition from a regular reflection of the attached shocks to the Mach reflection.

It is maintained that the external effects should be applied to the inlet part of the diffuser with a purpose to control the attached shocks.

It is demonstrated that a flow with shocks has a certain inertia relative to the external effects, being connected with energy dissipated in the shocks during their formation as a result of an interaction of the flow with diffuser's walls.

References

1. S.V.Bobashev, R.V.Vasil'eva, E.A.D'yakono-va, A.V.Erofeev, T.A.Lapushkina, V.G.Mas-lennikov, S.A.Poniaev, V.A.Sakharov and D.Van Wie. The Effect of MHD Interactions on the Input Shock Waves in a Supersonic Diffuser. Technical Physics Letters, Vol. 27, pp. 71-73, 2001
2. S.V.Bobashev, E.A.D'yakonova, A.V.Erofeev, T.A.Lapushkina, V.G.Maslennikov, S.A.Po-niaev, V.A.Sakharov, R.V.Vasil'eva and D.M.Van Wie. Shock-tube facility for MGD supersonic flow control. AIAA Paper No 2000-2647, 2000
3. Gurijanov E.P. and Harada P.T. «AJAX: New Direction in Hipersonic Technoloigy.» AIAA Paper 96-4609. 7th Aerospase Planes and Hipersonic Technology Conference. Norfolk, VA, 1996.
4. L.A.Vulis, A.L.Genkin, B.A.Fomenko. Theory and Calculation of Magnetogas-dynamic Flows in the Channels (in Russian). Atomizdat, Moscow, 384 p., 1971

6. FUNDAMENTAL STUDIES ON AN MHD ACCELERATOR

Nob. HARADA

Department of Electrical Engineering, Nagaoka University of Technology
1603-1 Kamitomioka, Nagaoka 940-2188, Japan
nob@nagaokaut.ac.jp

Abstract. We have a plan to start Magnetohydrodynamic (MHD) acceleration and/or propulsion experiments with a shock tube facility. In this paper, fundamental performance of a non-equilibrium linear MHD accelerator was evaluated using 1-dimensional numerical simulation. As a result of this analysis, it was confirmed that the working gas was successfully accelerated by Lorentz force due to the externally applied voltage. However, at high external voltages in particular, the working gas was decelerated at the entrance. This deceleration could be suppressed by increasing divergence angle and acceleration performance was improved. In this part, negative pressure gradient was larger than Lorentz force and this fact resulted in negative velocity gradient. Therefore, this part of the linear channel acted as an MHD compressor, where gas velocity decreased and pressure increased downstream. Operation mode of an accelerator or a compressor depended on loading factor. In the next step, acceleration and/or compression by MHD effects for the case of aero-plasma should be studied.

Introduction

Basic concept of MHD acceleration has been proposed since about 1960, where the **JxB** Lorentz force produced by the external applied electric and magnetic fields can accelerates working medium. Possible applications are hypersonic wind tunnel with extremely high Mach numbers and high enthalpy flows, MHD thruster for trans-atmospheric vehicles and the AJAX concept or an MHD assisted scramjet.

At the Nagaoka University of Technology, the MHD laboratory plans to start experimental study on these subjects using a shock tube facility. In the present paper, fundamental results of numerical simulation of linear Faraday type MHD accelerator with a non-equilibrium plasma working gas is described. We chose inert gas as working plasma only for simplicity at the first step and should to proceed to use aero-plasma including chemical kinetics in near future.

Experiments

MHD accelerator channel used in the present study is shown in Fig.1. Dimensions are decided the same as experimental facility. Cross sections of the inlet and exit are 24x100mm^2 and 40x100mm^2, respectively. Channel length is 350mm with 35 electrode pairs and their pitch is 10mm. Conditions for numerical analyses are summarize in Table 1. Working gas of argon seeded with potassium is chosen for simplicity.

Basic Equations and Numerical Procedure

Generally, we can apply the two-temperature model to analyze non-equilibrium MHD power generation and acceleration

phenomena where electron temperature may be different and becomes much higher than heavy particle temperature.[1] Electrons are highly heated by Joule heating in an MHD channel and their energy loss is quite small to inert gas due to small collision cross section.
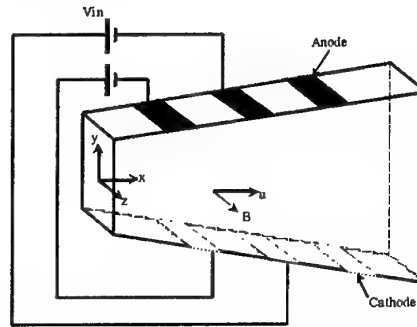
Fig.1. Schematic of the MHD Accelerator Channel.

Table 1. Conditions for Numerical Analyses.

Working gas	Ar + Cs
Seed fraction	1×10^{-5}
Magnetic Field Strength	2.4 T
Inlet Mach Number	2.4
Stagnation pressure	0.2 MPa
Stagnation Temperature	2500 K

Equations for heavy particles

Continuity:

$$\frac{\partial}{\partial t}(\rho A) + \frac{\partial}{\partial x}(\rho u A) = 0 \qquad (1)$$

Momentum equation:

44

$$\frac{\partial}{\partial t}(\rho u A)+\frac{\partial}{\partial x}(\rho u u A)=\left(\vec{J}\times\vec{B}-\nabla p\right)\cdot A \qquad (2)$$

Energy equation:

$$\frac{\partial}{\partial t}(E_S A)+\frac{\partial}{\partial x}[(E_S+p)\cdot uA] \qquad (3)$$
$$= A\vec{J}\cdot\vec{E}-AQ_L$$

where E_S is total energy of unit volume and Q_L denotes heat loss through the channel walls.

· Equations for electrons

Continuity of ions:

$$\frac{\partial}{\partial t}\left(n_i{}^+A\right)+\frac{\partial}{\partial x}\left(n_i{}^+uA\right)=\dot{n}_i{}^+A \qquad (4)$$

Momentum equation (=Generalized Ohm's law)

$$\vec{J}+\frac{\beta}{B}\vec{J}\times\vec{B}=\sigma\left(\vec{E}+\vec{u}\times\vec{B}+\frac{1}{en_e}\nabla p_e\right) \qquad (5)$$

Energy equation:

$$\frac{\partial U_e}{\partial t}\nabla\cdot(U_e u)=\frac{J^2}{\sigma}-(Coll.)-Q_L \qquad (6)$$

where time derivative terms in eq.(5) and eq.(6) are neglected because their characteristic times are much shorter than that of ionization process.

If we assume, for simplicity, infinite electrode segmentation, we can calculate electric fields and current density as;

$$E_y=KuB\ ,\ \ E_x=\beta\left(uB-E_y\right)$$
$$J_y=\sigma\left(uB-E_y\right) \qquad (7)$$

where K is loading factor defined as

$$K=\frac{V_{applied}}{V_{opencircuit}}=\frac{E_y}{uB} \qquad (8)$$

In addition above set equations, the following simplified Maxwell equations are used.

$$\nabla\cdot\vec{E}=0\ ,\ \nabla\cdot\vec{J}=0 \qquad (9)$$

This set of equation can be numerically solved by means of McCormack scheme which is one of the finite difference methods using artificial viscosity under the initial conditions of isentropic flow.

Results and Discussions

Effects of Applied Voltage

At first, we have to confirm the effect of applied electric field on gas flow in an MHD channel. Changes of gas velocity distribution are shown in Fig.2 with no applied electric field and Fig.3 with the applied voltage Vin of 1kV. For the case of no applied field shown in Fig.2, this MHD channel is operated as a generator (or a decelerator) because electrode pairs are short-circuited. And therefore, gas velocity decreases downstream. For

initial velocity distribution, gas velocity increases slightly downstream because the divergent channel cross section increases gas velocity under the isentropic conditions. We can confirm from Fig.3 that the acceleration of gas flow downstream by Lorentz force.
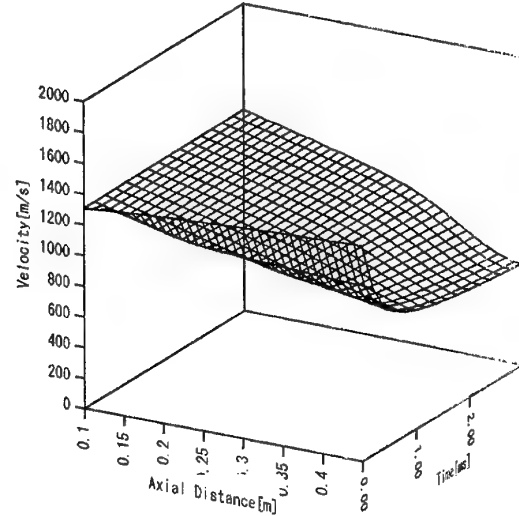
Fig.2. Change of velocity distribution for no applied voltage case. (V_{in}=0)
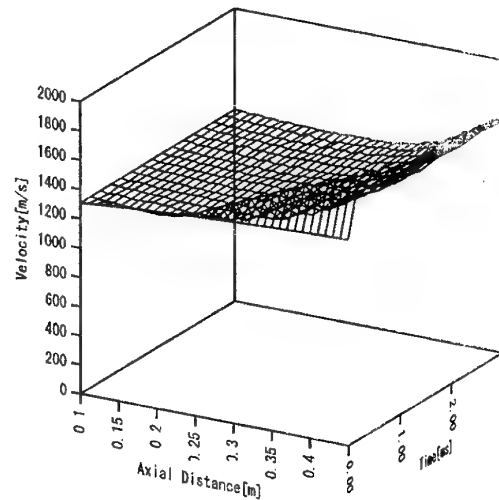
Fig.3. Change of velocity distribution for applied voltage of 1 kV. (V_{in}=1 kV)

Velocity and Mach number distributions for various externally applied voltages are shown in Fig.4 and Fig.5, respectively. Although the velocity at the exit increases with the increase of applied voltage, noticeable reduction in gas velocity at the entrance region is observed at V_{in}=1.2kV. In this

case, Mach number at the inlet part decreases below 1. Applied field operation gives raise to two major effects; 1) acceleration of gas flow due to Lorentz force and 2) gas heating due to Joule heating. The latter, at the same time, may produce the negative pressure gradient to retard the flow.
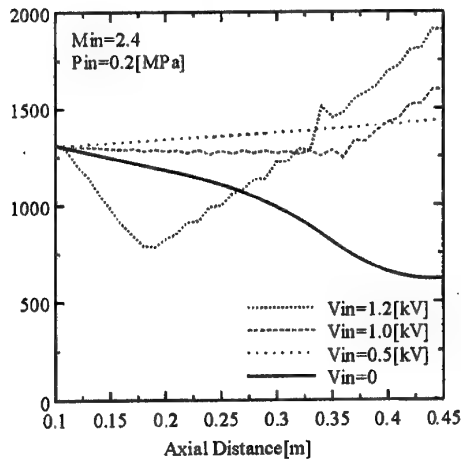
Fig.4. Velocity distributions for various applied voltages.
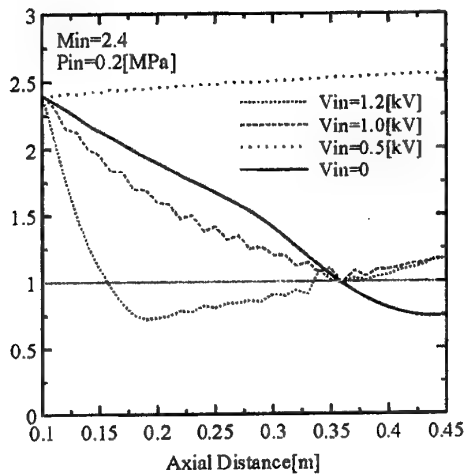
Fig.5. Mach number distributions for various applied voltages.

Force Terms in Momentum Equation

In order to understand this deceleration phenomena even if Lorentz force pushes gas flow to downstream, the right hand side terms of momentum equation (2) are plotted in Fig.6 for V_{in}=0.5kV and in Fig.7 for V_{in}=1.2kV. For the case of V_{in}=0.5kV where gas velocity continuously increases downstream, the net force term, JxB-dp/dx, is positive throughout the channel as can be

seen from Fig.6. Lorentz force is positive and larger than negative pressure gradient –dp/dx. On the other hand, for the case of V_{in}=1.2kV where gas flow is decelerated in the inlet part, the net force term is strongly negative in the flow decelerating region because the negative pressure gradient is larger enough than Lorentz force to makes the net force tern positive. We can understand that Lorentz force decelerates gas flow and increases pressure gradient especially in this inlet region. We can say that this part of the MHD channel acts as a compressor rather than an accelerator. Such a behavior becomes very important to study an MHD assisted scramjet engine where both an MHD compressor and an MHD accelerator must be operated properly over wide range of flight conditions.
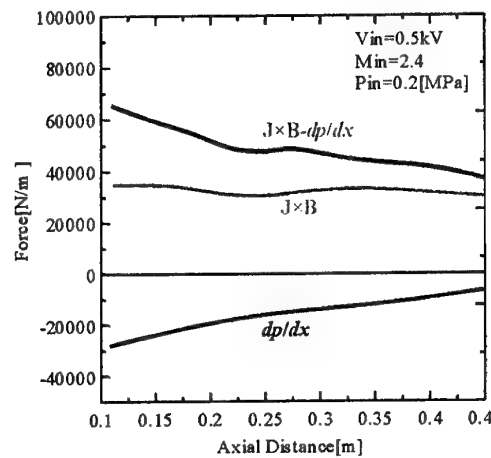
Fig.6. Force terms in right hand side of momentum equation (2). (V_{in}=0.5 kV)
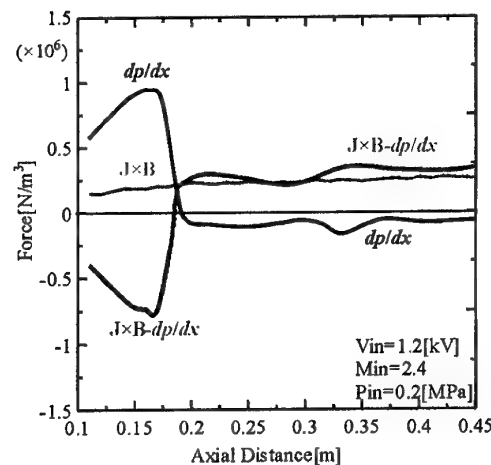
Fig.7. Force terms in right hand side of momentum equation (2). (V_{in}=1.2 kV)

46

Effects of Divergence Angle on Performance

We have pointed out that the inlet part of this channel acts as a compressor for certain condition. It is known that pressure can be converted kinetic energy of gas flow by increase of channel cross section for supersonic condition. Next, we examine effect of divergent angle on acceleration performance. Velocity and Mach number distributions for various divergent angles are shown in Fig.8 and Fig.9, respectively, for the case of applied voltage V_{in}=1.2kV, where velocity decrease in the inlet part is most significant.
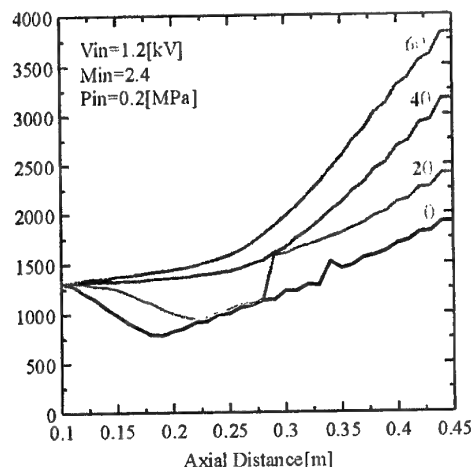
Fig.8. Velocity distributions for various divergence angle. (V_{in}=1.2 kV)
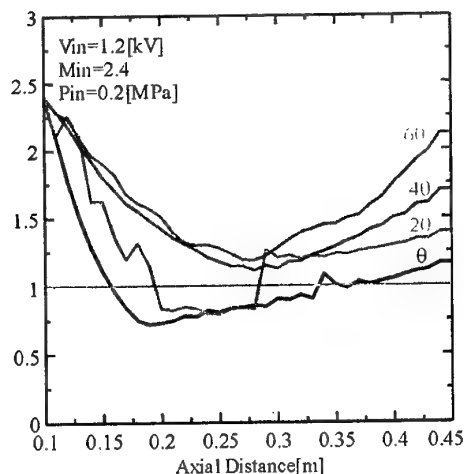
Fig.9. Mach number distributions for various divergence angle. (V_{in}=1.2 kV)

Divergence angle θ is the reference case of the original channel shape shown in Fig.1. We can see that the increase in divergence angle of the channel reduces flow deceleration effect at the inlet part and with the divergence angle of larger than 4θ, flow Mach number can be kept supersonic throughout the channel and no flow deceleration can be seen at the inlet.

Figure 10 shows pressure distributions for various divergence angles. While, for relatively smaller divergence angles of θ and 2θ, pressure gradient at the inlet part looks significant, for relatively larger divergence angles of 4θ and 6θ, pressure gradient does not significant there and this MHD channel acts as an accelerator. Operating mode depends partly on divergence angle.
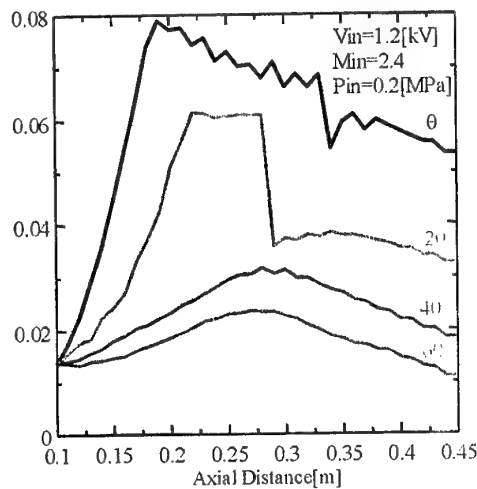
Fig.10. Gas pressure distributions for various divergence angles.

Effects of Loading Factor on Performance

It can be considered that operating mode depends on a loading factor which is an important factor of an MHD generator. Figures 11 and 12 show velocity and gas pressure distributions for various loading factors. We consider constant loading factor case throughout the channel. We can see that gas flow is continuously accelerated and pressure increase in the inlet region is not significant for loading factors of less than 3. On the other hand, if loading factors are larger than 4, flow deceleration and pressure increase in the inlet region become much more significant. Therefore, inlet part of this channel works as a compressor when loading factors are larger than 4 under the present operating conditions. It must be noted that the downstream part works as an accelerator for all cases of loading factor even inlet part works as a compressor for loading factor of less than 3. We could not find the conditions where the entire channel worked as a compressor.

47
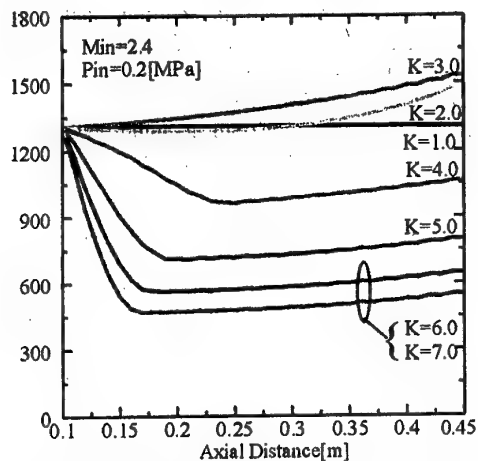
Fig.11. Velocity distributions for various loading factors.
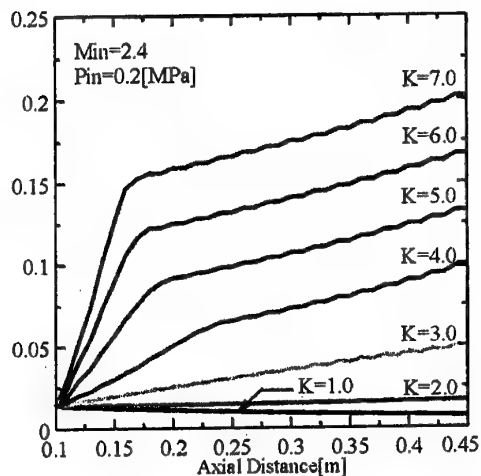
Fig.12. Gas pressure distributions for various loading factors.

We have to clarify operating conditions which decide the operating mode, an MHD compressor or an MHD accelerator for the application to the AJAX concept or an MHD assisted scramjet engine.

Concluding Remarks

We can summarize the present results of numerical simulation as the following remarks:

- We could confirm acceleration of gas flow by MHD effects. For certain case, however, gas was decelerated by applied voltage at the inlet region even the Lorentz force pushed the gas downstream.
- Electric power not only accelerated gas flow but also increased gas pressure downstream, i.e. increased pressure gradient.
- In the inlet part where gas is decelerated, the negative pressure gradient becomes larger than Lorentz force and the net force was negative. So, this part worked as a compressor rather than an accelerator.
- Unfavorable operation could be suppressed by increasing divergence angle of a channel.
- Operation mode was partly decided by divergence angle and loading factor.
- For future applications, we have to clarify effects of channel shape and loading factor on operating mode precisely.

Aknowledgement

References

1. R.J. Rosa, "Magnetohydrodynamic Energy Conversion," McGraw-Hill, 1963.

48

7. EXPERIMENTAL METHODS FOR INVESTIGATION PLASMA-BODY INTERACTION IN SUPERSONIC AIR AND CO₂ FLOWS

Brovkin V.G., Kolesnichenko Yu.F
Institute for High Temperatures of Russian Academy of Sciences,
13/19 Izhorskaya Str., 127412 Moscow, Russia

Krylov A.A., Lashkov V.A., Mashek I.Ch
St-Petersburg University

Ryvkin M.I.
Institute of Radio Apparatus, St-Petersburg

Abstract. Diagnostic methods and results of experimental investigation of plasma formations created by impulse-periodic MW discharge in front of the bow shock wave of blunt body in supersonic flows of air and carbon dioxide are presented. Detailed spatial-temporal data of evolution of the discharge regions at active and glow phases and their interaction with the bow shock wave are given.

Last years research attention was attracted to physics of microwave (MW) discharge in supersonic gas flows [1,2,3]. The main advantages of MW range for modifying the processes in supersonic flows consist in high enough efficiency of generating devices, wide opportunities in transportation of MW-power and control of MW-plasma parameters.

Research team from IHT RAS (Moscow), S-PbSU and VNIIRA (St.-Petersburg) carry out investigations of MW discharge physics in supersonic gas flows since 1997, using experimental installation, which was described previously [3,4]. The general scheme of this installation with the most essential elements of the diagnostic equipment is presented in Fig.1.
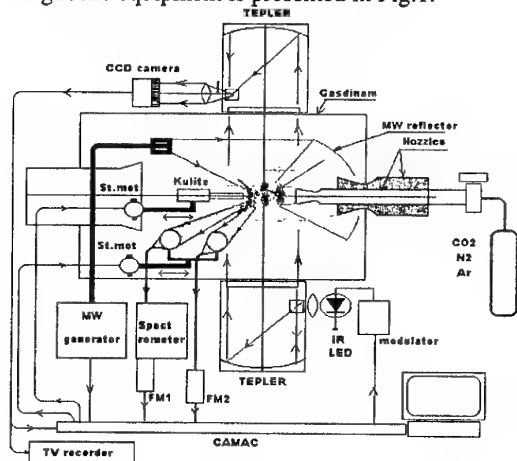
Fig.1. The General scheme of plasma-dynamic installation with basic elements of diagnostics

Electromagnetic radiation with wavelength 3 cm enters the working chamber through a waveguide from MW generator. A parabolic reflector focuses it on an axis of working flow. Pulse duration of generation - 1,5-1,7 μs, repetition frequency - 500 Hz, pulse power about 200 kW. The direction of the field polarization vector in the discharge region at the present arrangement can be only at 90 degree angle in relation to the flow velocity vector. The desirable characteristics of the working flow are approached by the pumping action of external jet [4]. Along with this useful function the jet creates certain difficulties for application of optical and several intrusive methods of diagnostics. The ways of these problems overcoming are discussed below. The diameter of internal working flow is equal to 27mm, Mach number - 1,6-1,7, static temperature - 180-200K, static pressure 50 - 80 Torr, run time in a working mode - 60-90s. Installation is equipped by three-coordinate balances, allowing to provide measurements of integral load on AD model in three directions: X - along flow axis, Y - perpendicular to flow vector in a vertical direction, and Z - perpendicular to flow vector in a horizontal direction [2].

For testing of pure gas flows, such as Ar, CO2, N2, the internal nozzle is connected with a working gas balloons (40 litters, 150 bars). During experiment the pressure of a working gas in the internal nozzle is regulated manually, the control of its pressure being providing by the sensor, located nearly the critical section of the internal nozzle.

The represented work is devoted to the description of complex approach development to the measurements in plasma aerodynamic experiment. Complex diagnostics of the basic processes parameters constitute five groups:
- Gas-dynamic characteristics of the working flow without MW discharge

49

- Parameters of a MW radiation
- Emission characteristics of MW plasma
- Dynamics of stagnation pressure
- Dynamics of flow pictures near the model.

The most important features of the developed measurement methods and results of their application will be considered below exactly in such sequence.

1. Gas-dynamic characteristics of a working flow

Local gas-dynamic characteristics of the working flow without MW discharge are measured by the standard intrusive sensors for stagnation and static pressure and stagnation temperature. Spatial characteristics of the working flow are analysing by the Shlieren system. All these data permit to obtain the density, temperature and velocity distribution fields in investigation area of internal (working flow) [3-6].

2. Microwave radiation parameters control

The spatial distribution of electric field created by parabolic reflector in the working zone is investigated at rather small levels of MW power with the aid of the mobile detector. The circuit of measurements is represented in Fig.2. The signal of the master oscillator on the carrying frequency passes through the preliminary amplifier in which the output radiopulses have power about 30W. Then they are weakened by the variable attenuator up to 30...50mW. This signal passes through a coaxial cable, two coaxial-fiber adapter and MW waveguide to the horn radiator in bypass of the main high power amplifier. MW-power to be tested is radiated by the horn, then is focused by the parabolic reflector in the working area where is received by a MW-probe in the form of small symmetric dipole. The signal, received by the probe is detected, and the videopulses are transmitted to the oscilloscope input. The probe is moving inside the research area by the coordinate device.

For calibration of the measuring circuit for the absolute values of EM-power flow density in the research area several preliminary operations are executed:

1. Measurement of the near MW-field of horn radiator on the VNIIRA stand.
2. Measurement of the near field of the same horn radiator in H-plane at the same distance, by the same probe in gas-dynamic chamber under the circuit of Fig. 2.
3. Measurement of maximum voltage in radiator near field and in focal area.
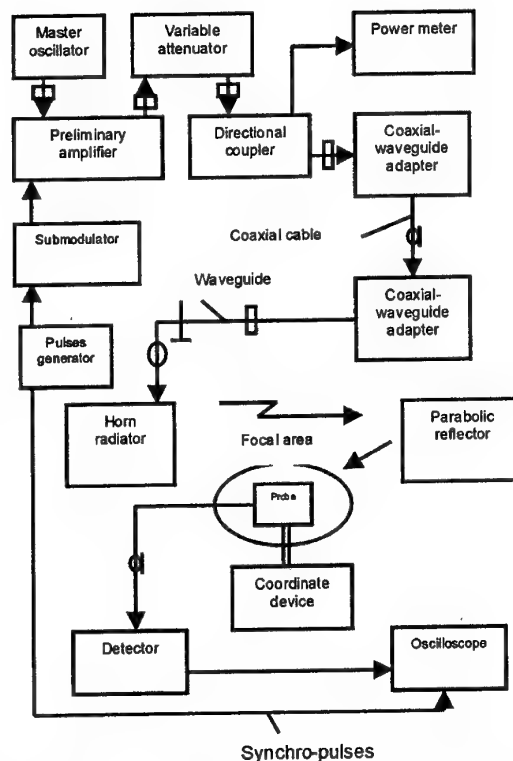
Fig.2. The circuit of MW parameters measurement in the working area
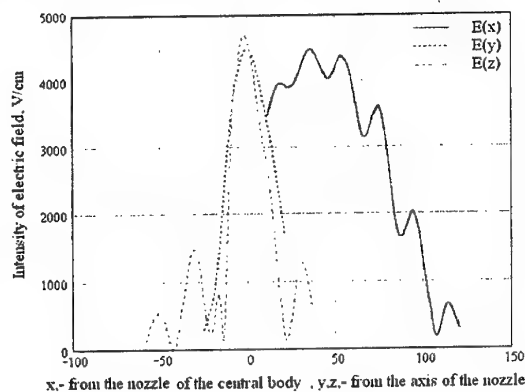
Fig.3. Distribution of electrical field in working area. Dotted line - Y and Z -axis, continuous line - X axis

Spatial distribution of radiator MW-power output, carried out at the near- field stand in VNIIRA has shown, that the radiation levels outside of a zone with radius more than 50mm do not exceed - 25dB from the maximum. It means, that area for calculating radiator fields with dimensions $100 \times 100 mm^2$ is sufficient. Knowing the power level of radiator input in real experiment

50

$(P_0=210\text{kW})$ and data, obtained at performance of items 1) and 2) as well, it is possible to show that the maximal value of electrical field intensity in the focus area is about $4,47\times10^3\text{V/cm}$. Axial distributions of electric field in reflector focal area at radiator input of pulse power 210kW shown in a Fig.3. The axis X is directed along the nozzle axis, the axis Y- is directed from the axis nozzle upwards, and the axis Z - is horizontal.

At the graph of field distribution along X-axis three areas of the maximal intensity are clearly observed. The general view of MW discharge, which corresponds to the given field distribution is presented in Fig.4.
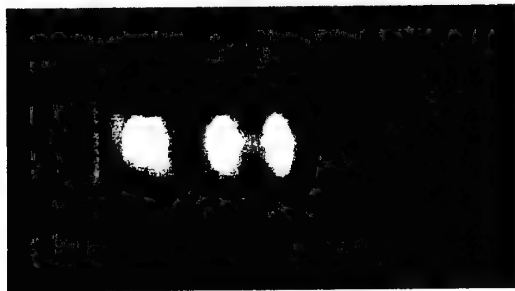
Fig.4. General view of MW discharge
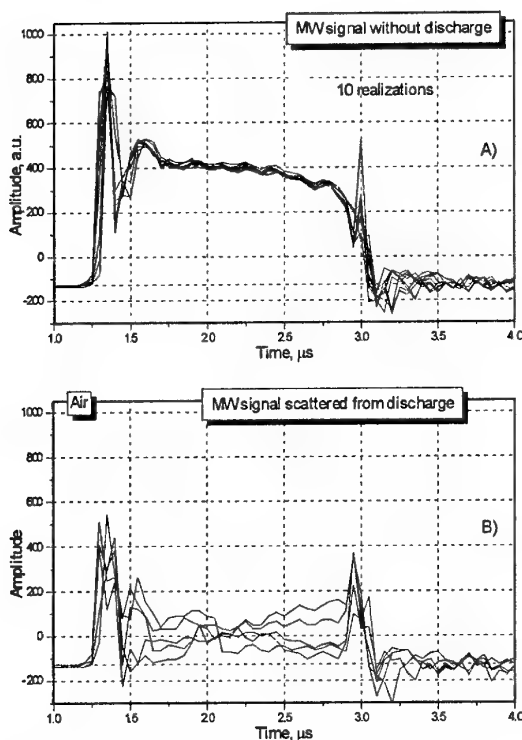
Fig.5. Output signal of the MW detectors. A- detector of input power, B- detector of passed power

The instant values of the input radiator MW power, and the instant values of the power having passed through plasmoids in a flow are registered by standard MW - detectors with a bandpass 50MHz. Their output signals after amplification are analyzed in CAMAC system. The fast Flash ADC F4226 is used for work. They have conversion time about 50ns and internal memory 1kb. In Fig.5 the examples of several single realizations of MW power signals are presented. Fig.5a - signals passed through the chamber at the absence of discharge, Fig.5b - in its presence. The average value of signal amplitude in Fig.5a corresponds to radiator output power equal to 200kW. The decreasing of amplitude in Fig.5b corresponds to absorbing and scattering of MW power in the flow working area.

3. Emission characteristics of MW plasma

Investigation of emission radiation of MW plasma permits to obtain the number of very important plasma characteristics such as different gas temperature (vibrational and rotational), electron concentration, electron temperature and others. All these data are critically necessary for creating of numerical model for processes of plasma - body interaction in supersonic flows.

One of the most difficult problems existing in optical measurements in the presence of MW plasma is strong influence of parasite scattering MW field to sensitive optical sensors – photomultiplyers (FM) and CCD device. For eliminating of this influence, we widely use the fiber optic. This way allows to place the main part of the sensitive measuring devices at comparatively long distance (about 20m, in another room) from MW generator and gas-dynamic installation. The second important advantage - very simple construction of optical signals input/output from the gas-dynamic test section. Only several small orifices are to be made in the vacuum test chamber wall for measuring spectral and spatial characteristics of MW plasmoids.

We use quartz - polymer fibers with numerical aperture 0,4 and core diameters 125 and 400µm. They have spectral range from 300nm to 1100nm. Two identical optical systems are placed on the coordinate device in the vicinity of the working flow inside of the test section. The distance between plasmoids and the input lenses of the both optical systems is chosen as small, as possible - 230mm. The relative orifice of the optical systems is about 1/2, in a good correspondence to the high numerical aperture of the fiber in use. Both channels collect the emitting light from the same area of plasmoids. The distance between the end of the internal nozzle and the

51

investigation point (X coordinate) can be changed by the coordinate device from 0 to 190mm with 0,3mm step and 60mm/s velocity. Dimensions of investigation area, corresponding to core fiber diameter 125μm are 1 mm in diameter and 15mm in length. For core diameter 400μm these dimensions are 3mm and 45mm correspondingly.

3.1. Temporal and spatial characteristics of radiation emitting by MW discharge

The first optical channel is used for temporal and spatial measurements of the emitted light. Its short wave spectral limit is determined by the fiber (300nm), the long wave limit - by sensitivity of using FM (750nm). The angle between the flow axis and the channel optical axis is 81°.

The output signal from FM passes trough the fast amplifier (equivalent load resistor is 1 kOhm, bandpass about 20MHz). Signal from amplifier goes either to the flash-ADC F4226 (temporal measurements in discharge light emitted), or to Sample - Hold (S-H) device (spatial distribution of emitted light in plasmoids). The sample- time of S-H is 100ns, and the delay time - for sample moment - 2,5-3μs. The last corresponds to the maximum level in emitting light for most part of discharge realizations. Instantaneous level of light intensity is converted in ADC FK-72 (12 bit, 70μs) and is stored in PC memory, where the necessary number of realization are summing for achieving of a good level of S/N.

High sensitivity of this optical channel permits to use it both for investigations of integral luminescence processes in supersonic flow and for measurements in comparatively narrow spectral range, for example 5-10nm. In this case, the light being collected by the optical system then passes through the spectrometer. This operation mode permits to investigate the temporal and spatial behaviour of the most essential vibration - rotational spectral bands of discharge radiation.

At Fig.6 the spatial distribution of MW discharge intensity in airflow along the X- axis is presented. Curves correspond to different levels of MW power in discharge. Difference in these levels are less then 5%. The first peak of intensity at 3mm is connected with the discharge on the edge of the nozzle.

It corresponds to 0-2 transition of the second positive system of N_2 for the plasmoid in airflow, placed at 45mm. The spectral width of the spectrometer slits is 4nm. The beginning of MW impulse - at 4,5μs, the end - at 6,25μs (noted by row).

At Fig. 8 the results of weak luminescence investigation of MW discharge in free supersonic

flow are shown. The time - delay of chemi-luminescence signal for different points of the flow axis determines the flow velocity and its dynamic [6].
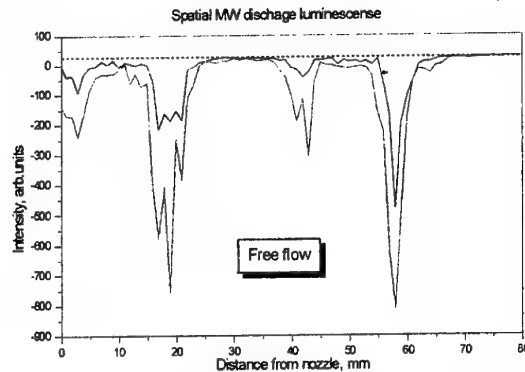
Fig.6. Spatial distribution of MW discharge intensity along the X-axis
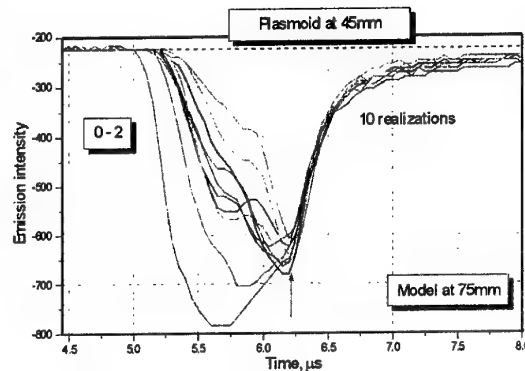
Fig.7. The intensity of 0-2 transition N_2 in MW discharge in supersonic airflow.
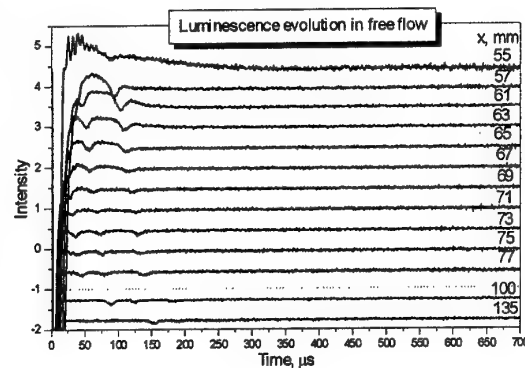
Fig.8. Spatial-temporal dynamics of chemi-luminescent area in air flow for Z-polarization of MW field.

3.2. Spectral investigations of MW discharge in supersonic flows

The second optical system is used for spectral measurements. It operates with high-light gathering power spectrometer MDR-2 which has relative orifice 1/2, grids with 1200 1/mm, dispersion 2nm/mm and spectral width of instrumental profile 0,2nm for slit 100μm. Spectrometer is controlled by the CAMAC system.

One of the serious problems in spectral measurements in supersonic flows is comparatively short run-time of the working gas-dynamic regime. Usually, this time is limited to about 50-70c, and it does not allow to get the spectra with high resolution in wide spectral range. In this situation the spectral velocity of tuning is chosen comparatively fast - 0,03nm/step with step frequency 250Hz. Output light of spectrometer is detected by photo-multiplier (FM FEU79). It can work in two operation modes. The first is the analogue regime, the second – the digital regime (photocounter).

In the analogue regime the output signal of FM passes through trans-impedance transducer (equivalent transducer resistor is 4,7MOhm, bandpass frequency 1MHz) and goes to S-H CAMAC device, mentioned above. Time - delay for this channel corresponds to the maximum of signal on transducer output. The digital regime is used comparatively rear, only for registration with maximal spectral resolution.

Optical axis for this spectral channel is perpendicular to the flow axis. At Fig.9 the review spectrum of MW discharge for plasmoids placed at 60mm is shown. It is registered with wide spectrometer slit and recording time 30s. This spectrum demonstrates the most important analytical emitting lines in the second positive system of N_2 commonly using for diagnostic in our experiments.
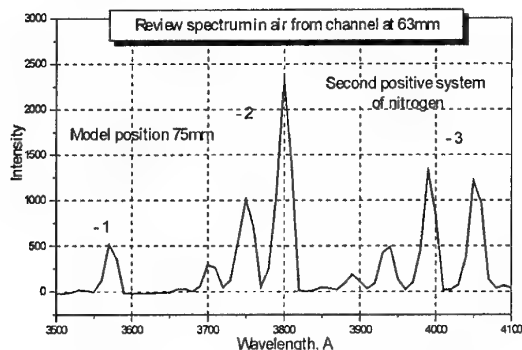
Fig.9. Review spectrum of MW discharge in air supersonic flow

The measurement of gas temperature in airflow is made with using 0-0, 0-3, and 1-4 bands of N_2. As the spectrometer-spread function is 0.15-0.2nm, only partially resolved molecular spectrum can be obtained in experiment. The emission is recorded with time shift corresponding to the back front of MW pulse and maximum in light intensity. The step in wavelength is about 0.1nm. Emission is averaged over 100-200 realisations. The spectra of the bands 0-0, 0-3 for both plasmoids and 1-4 for the second one are recorded. At Fig.10 the example of partially-resolved spectrum for vibration-rotational band of 0-2 N_2 is shown.
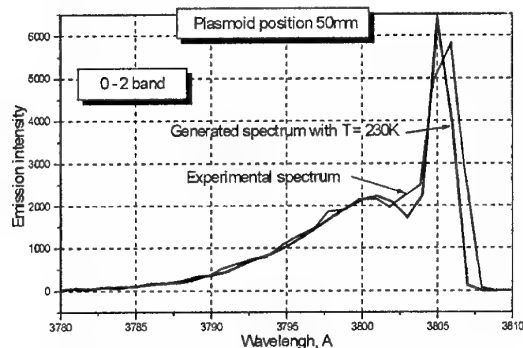
Fig.10. The partially-resolved spectrum for vibration-rotational band of 0-2 N_2 in MW discharge in airflow.

For the determination of gas temperature in a discharge the method of optical emission spectrum shape fitting has been adopted [3,4,6]. The exact full spectrum of 0-0, 0-3 and 1-4 transitions of the second positive nitrogen system, including R-, P- and Q-branches (the last is very weak) is generating under the defined temperature and is then convoluted with the spread function of the spectral device. The synthetic spectrum obtained in such a manner is then compared with the real one. It is made in a procedure of best fitting of the spectrum contour by variation of the defined temperature. In this case the special attention is paid for the best coincidence of the spectral shape at the lower rotational numbers, where the distribution over the rotational levels is known to establish at a temperature practically equal to that of the gas.

The results of such fitting can be summarised as follows:

1st plasmoid (45 mm):

        0-0 transition, T=200K ($\tau = 3.2\mu s$),

        0-3 transition, T=240-250K ($\tau = 3.2\mu s$),

        0-3 transition, T=250-270K ($\tau = 4.0\mu s$).

2nd plasmoid (60 mm):

        0-0 transition, T=270K ($\tau = 4.0\mu s$),

        1-4 transition, T = 300K ($\tau = 4.0\mu s$),

        0-3 transition, T = 320K ($\tau = 4.0\mu s$)
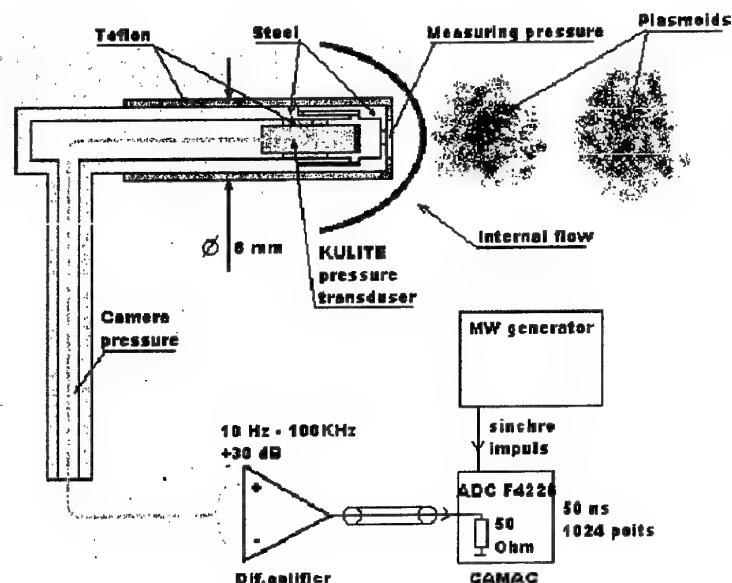
Fig.11. The schema of pressure sensor, which allows to make measurements in strong MW field

The accuracy of temperature determination by this procedure can be estimated in 20K. It should be noted that 0-0 transition has given lower temperature in comparison with *0-3* transition, but the difference between temperatures in the first and the second plasmoids is approximately the same – about 70K.

The data obtained from spectral measurements in MW discharge allow to make estimates for vibration temperature levels as function of energy input and calculate the relative population of N_2 vibration levels [5-9].

4. Dynamics of stagnation pressure at AD body in MW discharge

Two main problems dramatically increase when sensitive pressure transducer is using for stagnation pressure measurements in presented experimental installation. The first is strong (3-4 kV/cm) MW field in the area where transducer is placed, making the essential electromagnetic influence on it. The second is the transition gas-dynamic processes at input and output of the working regime for the both jets - internal (working) and external (pumping). For some moments of these regimes, the pressure level acting on the transducer (more than 5 atm) is essentially higher than its ultimate undamaged level. The schema of pressure sensor, which allows making measurements in conditions, mentioned above, is shown at Fig.11.

The pressure sensor has been created on base of low-impedance wide band tenzo-resistive differential pressure transducer Kulite, XCS-093, 5 PSI (about 260Torr). The up-level frequency for it is 150kHz, static sensitivity - 0.3mV/Torr. Transducer is placed in external steel cylindrical case and isolated from it by the Teflon ring. At the same time, this ring separates the values of measuring pressure and basic pressure (static pressure in working chamber). Internal value of pressure sensor is connected with the flow area under investigation by the orifice in steel case. The orifice diameter is 2mm. Position of the transducer inside the sensor's case determines the bandpass of pressure sensor and has been chosen as a compromise between its maximum meaning and minimum influence from MW impulse field to the measuring circuit. Measurements of dynamic stagnation pressure made in our previous work [3] show that the main harmonic of investigated signals belong to frequency band 8-10kHz. Transition characteristics of our pressure sensor were investigated on the special constructed low-pressure shock tube. The estimates of dynamic error level, making up on this tube had shown that decreasing of amplitude for the main harmonic is not more than 0,7-0,8 and phase shift - less than 10-15µs.

An output transducer signal is analyzed by the differential amplifier with bandpass 0.01-100kHz, and gain level +30dB. The recording of this signal makes up by fast flash ADC F4227 in CAMAC system, mentioned above. Flash ADC

54

begins to work simultaneously with synchro-impulse from MW - generator. It permits to measure both the single realizations of pressure signals with comparatively low level S/N and the averaged signals with excellent level S/N.

As we note above, the second problem, arising in such measurements is connected with a low-level of pressure transducer overload capability. For resolve of this problem, before the beginning of experiment we placed the transducer inside of internal nozzle. In this position the levels of pressure overload essentially less than 0,5atm, and can not damage the transducer. After achievement of the working regime, sensor is moved in the investigation points, where measuring are to be done and after this is returning back to the initial position. Unfortunately, comparatively low speed of coordinate transducer device (about 2mm/s for X-axis) do such measurements very long. For example, the measuring in 8-10 points at the distance 80-100mm from the nozzle exit section have a duration about 100-150s. So long time of gas-dynamic regime makes these experiments rather expensive.
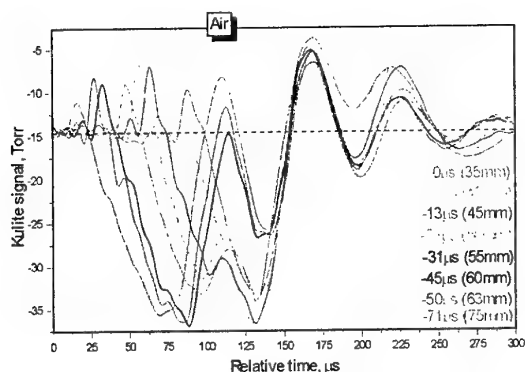
Fig.12. Stagnation pressure for different points of flow with MW discharge.
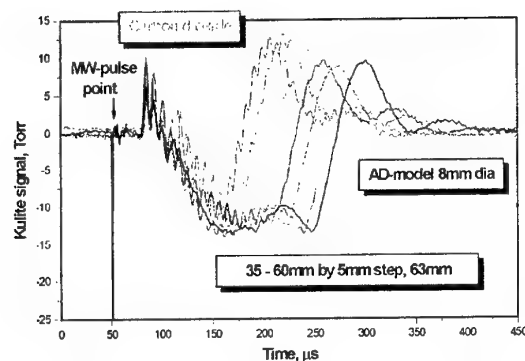
Fig.13. The stagnation pressure signals for Carbon Dioxide flow with MW discharge.

The results of stagnation pressure dynamic measurements in airflow made by the created pressure sensor are shown at Fig.12. They correspond to different position of sensor and have a common point for compare – the back front. Electric field in this seria is Y-polarized. The same signals for Carbon Dioxide flow are presented at Fig.13.

5. Dynamics of flow pictures near the model

The investigation of the bow shock behaviour was conducted with the aid of a specially designed digital Schlieren system, which was based on the serial device IAB-450. An infrared light emitting diode (LED) with output power of about 2W (input impulse current 25A, time duration -2-3μs) was used as the source of radiation. The time delay interval from 1 to 500μs of light impulse was controlled by the program. The spectral band of LED is comparatively narrow (910±10nm) and lies outside the region of maximum spontaneous radiation emitting of MW discharge in air. It has a good correlation with maximal band of spectral sensitivity of the used TV system. The suppression of MW emitting light can be achieved with the interference filter. Incoherent character of LED light and simplicity of its synchronisation makes it very useful for investigation of the dynamics of the flow field around AD model under the influence of impulse - periodic MW discharge.

The presence of an external pumping jet containing the workflow creates the essential problem for Schlieren diagnostic. Turbulent character of this external jet leads to arising of high spatial noises on the Schlieren image. The spatial noises mask an already low-contrast image in workflow (static pressure 50-80Torr, diameter about 25mm). In addition, the prismatic character of external jet shifts the optimal position of analysing knife in Fourier plate of the receiving telescope after achieving the working gas-dynamic regime. For the reasons mentioned above the dynamic diapason of the Schlieren system has to be large. It cannot be achieved with the traditional scheme of Schlieren diagnostics. In the presented work we use the special mask placed in Fourier plate of receiving telescope. Its transmission is linearly dependent on the coordinate [10-11]. The output signal of CCD matrix was recorded onto a VCR and then digitally coded. A collection of consecutive images, based on these recordings, which displays a temporary picture of a flow around the model after MW discharge. Each image in this collection is a result of averaging of more than 50TV images for the fixed value of time-delay. On the Fig.14 the flowpicture in CO_2 for Z-MWpolarisation are shown.

55
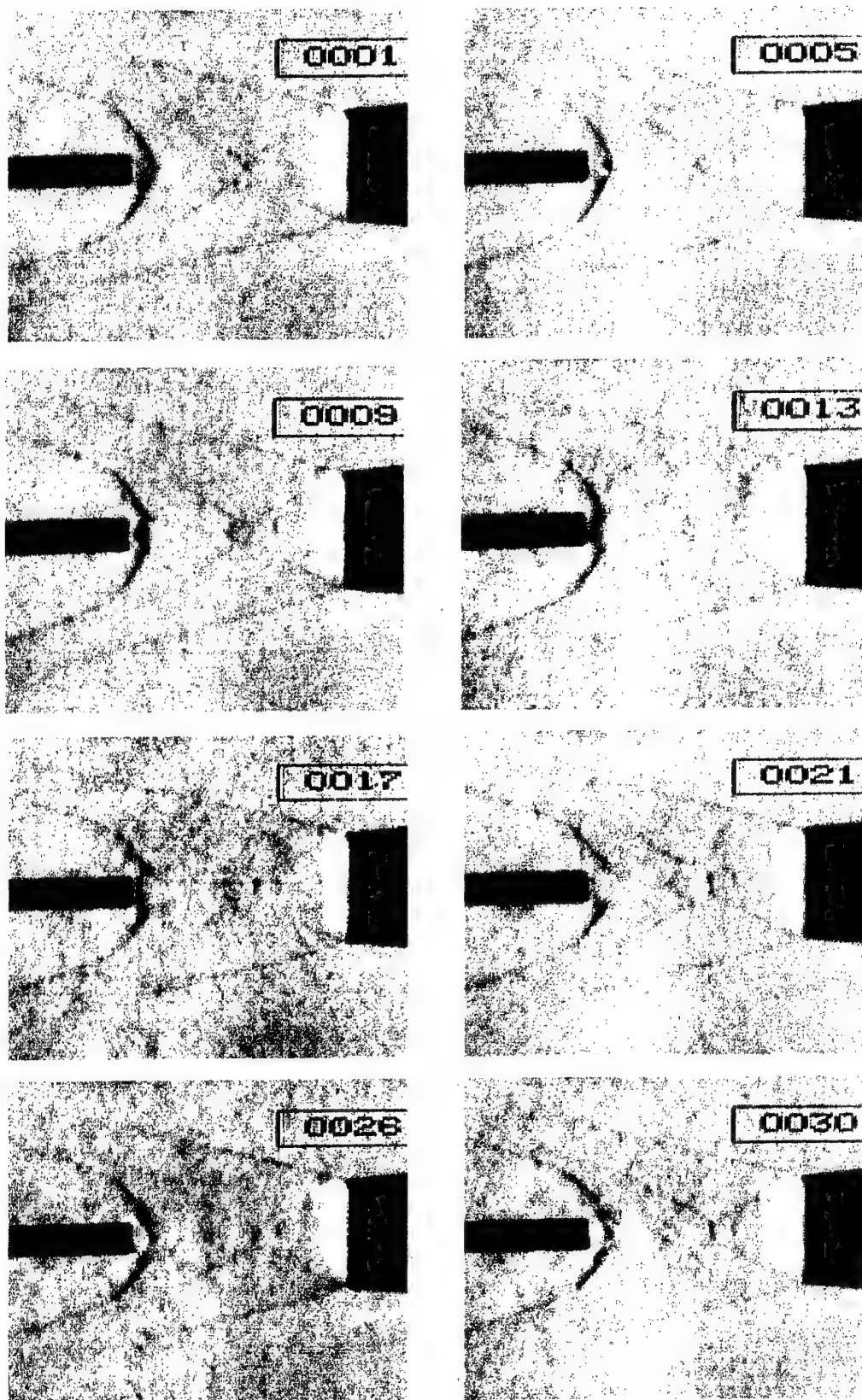
Fig.14. The dynamics of flow in CO2 for Z-polarization of MW field.

Conclusions

The complex diagnostic system for investigation of MW - plasma - body interaction processes has been made. Methods of measurement, being used in this system include as intrusive ones - sensors of stagnation and static pressure and temperature, AD balances, as non-intrusive - spatial-temporal registration and analysis of the emitted light radiation from MW discharge and wide-dynamic-range impulse digital Schlieren system. The essential part of the presented diagnostic system is MW sensors group, which allow to control the parameters of MW power both at the enter in the test gas-dynamic section and after absorption and scattering there. By the present time the created system has allowed to obtain new interesting data on MW discharge physics in supersonic flows and, undoubtedly, will be very useful in further investigations.

Acknowledgments

References

1. Workshop on Weakly Ionized Gases, USAF Academy, Colorado, 9-12 June 1997. Proceedings.
2. 2nd Workshop on Weakly Ionized Gases, AIAA, Norfolk, 24-25 April 1998. Proceedings. P.193.
3. V.G.Brovkin, Yu.F.Kolesnichenko, S.B. Leonov et. al. "Study of Microwave Plasma-Body Interaction in Supersonic Airflow", 30th AIAA Plasmadynamics and Lasers Conference, June 28-July 1, 1999 / Norfolk, Virginia, AIAA 99-3740.
4. V.G.Brovkin, Yu.F.Kolesnichenko, A.A.Gorynya et. al. "Microwave Plasma - Body Interaction in Super-sonic Airflow", Proceedings of Workshop "Perspectives of MHD and Plasma Technologies in Aerospace Applications", Moscow, IVTAN, 1999, pp. 78-81.
5. Yu.F.Kolesnichenko, D.V.Khmara. "Plasma-Chemical Composition of Airflow in MW Discharge, Relaxation Zone, and Under Interaction with Bow Shock Wave of AD Body". Second Workshop "Magneto and Plasma Aerodynamics in Aerospace Applications", Moscow, IVTAN, 5-7 April, 2000.
6. Yu. F. Kolesnichenko, V.G. Brovkin, A. A. Gorynya et. al. "Investigation of AD-Body Interaction with Microwave Discharge Region in Supersonic Flows", 39th AIAA Aerospace Sciences Meeting & Exhibit, 8-11 January 2001 / Reno, Nevada, AIAA 2001-0345.
7. V.G.Brovkin, Yu.F.Kolesnichenko. "Structure and dynamics of stimulated microwave gas discharge in wave beams". J. Moscow Phys. Soc. 5 (1995) 23 - 38.
8. A.M.Pravilov. Photoprocesses in Molecular Gases. Moscow: Energoatomizdat, 1992 (in Russin).
9. J.D.Kelley, G.V.Candler. "Flowing Air Plasmas: Kinetics, Relaxation Rates, and Flow Dynamics". Second Workshop "Magneto and Plasma Aerodynamics in Aerospace Applications", Moscow, IVTAN, 5-7 April, 2000.
10. Kantserov A.I., Krylov A.A.,Lashkov V.A.,Mashek I.Ch. "Digitally Shlieren diagnostic system for plasma-body interaction processes in supersonic flows of weakly ionized gases". V International Conference "Optical Methods of Flow Investigation" Moscow,1999, MPEI(TU), p.131-132
11. Kantserov A.I., Kosych N.B., V.A.,Mashek I.Ch "Measurements of the phase profile of a gaze stream using spatial spectrum filtration" The Second International Conference on Problems of Physical Metrology, Abstracts, St-Petersburg 1996, p.19-21.

08. DISCHARGE PLASMA INFLUENCE ON FLOW CHARACTERISTICS NEAR WALL STEP IN A HIGH-SPEED DUCT

S. Leonov, V. Bityurin, A. Bocharov, E. Gubanov, Yu. Kolesnichenko, K. Savelkin
Institute of High Temperatures, Russian Academy of Sciences, Moscow, Russia

A. Yuriev, N. Savischenko
Mozhaisky Space University

Abstract. At the present time numbers of theoretical and experimental works have been published, which show that energy release to airflow near/fore streamlined bodies can reduce a total drag of these bodies. It occurs at high level of energetic efficiency (sometimes, much more than 1) [1-5]. Several works are described efforts in a field of plasma influence on a viscous friction and separation zone properties [6-7]. As was shown by last investigations an energetic method of boundary layer control (volume energy release to gas near surface by means of electrical discharge) leads to non-trivial response. Wall steps and cavities are offered as a constructive element in supersonic combustors. Such an element can provide an artificial separation zone for a flame front stabilization and a fuel-air mixture burning initiation. Last time a plasma assisted combustion technology is discussed for purpose of a high-speed combustor development [8].

This paper analyses and discusses results of experimental work on influence of energy release from special organized electrical discharge on characteristics of separation area near wall step and profiled plate. The experiment was conducted in transonic short-time wind tunnel with closed test section at Mach number M=0.7-1.1 and static pressure P_{st}=50-500Torr. During the test a pressure distribution measurements and optical observations (natural and spectroscopic) were fulfilled. Quasi-continuous multi-electrode surface discharge was used for a plasma excitation. Electric energy input to the plasma volume was up to 5kW at width of discharge plate 10cm. The discharge structure and parameters in depends on airflow parameters are measured.

Experimental results have shown that the volume and structure of separation zone are changed significantly due to plasma influence as well as gas parameters inside the zone depending on parameters of electrical discharge. The effect of surface discharge transition to a separation area is described. The discharge structure correspondence with a gas vorticity has been considered. The data on a gas temperature inside of a separation area are given. Possible variants of electrical discharge arrangement are discussed as well as a needed power input.

The results of inviscid simulation are also presented.

Motivation.

Several important aerodynamic situations can be enhanced by means of discharge plasma interaction with airflow near the bodies. Some of them have to be considered as an active plasma influence on the position and the parameters of separated zones. They are listed below as the following:

• Base drag reduction. (Fig.1.a)

• Reduction of the drag due to aerodynamic and additional elements and theirs interference. (Fig.1.b)

• Control of the shocks in a supersonic and hypersonic diffuser. (Fig.1.c)

• Stabilization and flameholding in supersonic combustor. (Fig.1.d.)

• Control of the λ-shocks at transonic modes of airflow.

• Control of the structure and parameters of 3-D separated flows.

• Control of instabilities at external and internal flows, etc
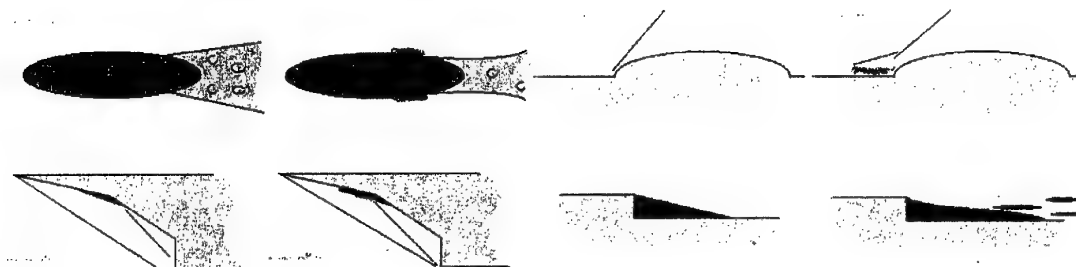
Fig.1. a b c d. Samples of possible schemes of plasma effect.

The energy deposition by means of the discharge plasma gives additional "gear" for the flows control. Such a control has important advantage in comparison with mechanical systems. This method is the inertia-less. Samples of such an influence are presented in Fig.1 schematically. The experimental results, which are described here, are actual demonstration of plasma technology possibilities in a practical aerodynamics.

Control of separation zones parameters.

New experimental data on plasma generation near the body's surface and influence on parameters and volume of stabilized separation zone downstream of a wall step have been obtained last time. Wall steps and cavities are offered as a constructive element in supersonic combustors. Such an element can provide an artificial separation zone for a flame front stabilization and a fuel-air mixture burning initiation.

The experiment has been conducted under the condition of transonic airflow in short time blow-down test installation PWT-10 of IVTAN at the following main parameters: test section 20×100mm, static pressure 60-300Torr, steady-stage operation 0.3-1sec, typical input electric power about 5kW (up to 10kW), type of plasma – quasi-DC multi-electrode surface discharge.

The experimental arrangement is shown in Fig.2. Rectangular duct with a wall step has been connected to a supersonic pipe from left side and subsonic vacuum diffuser from right side. The duct has been equipped by electrodes' plate, pipes of static and full pressure distribution measurements, and quartz window for natural and spectroscopic observations. Original power supply has been used for a plasma excitation. Typical duration of plasma switching on was 70-100ms.

The scheme of the discharge excitation and pressure measurements is presented in Fig.3. Two different modes of the discharge location have been found. They differ by the direction of an electric current. Under the first, standard, mode the current flows from positive (hot) electrodes to grounded electrodes, which are located on an insulating plain plate. At the second mode electric current changes

the direction and flow to a grounded metallic wall of the test section. At that the current flows through a separation zone. Process of the first mode transformation to the second one started from one electrode current displacement. After this all other electrodes connected through a separation zone immediately.

If a separation zone is disappeared due to flow weakening, the discharge can transform back to the first mode through the period of strong instability. The discharge appearance under the second mode is shown in Fig.4 as well as fragment of plasma cords connecting to a separation zone.
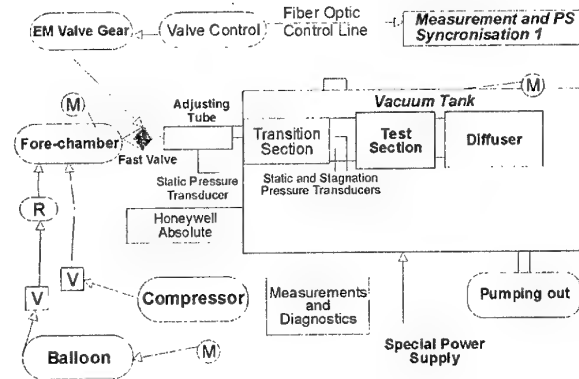
Fig.2. Layout of the experimental installation PWT-10 of IVTAN
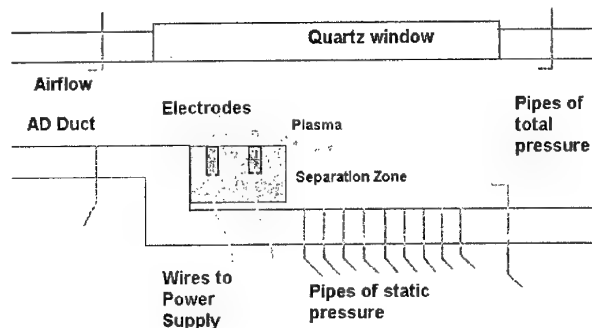
Fig.3. Scheme of the surface discharge excitation.
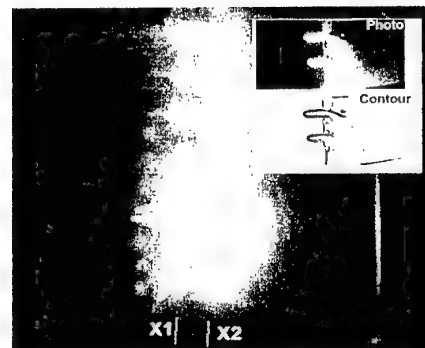
Fig.4. Discharge appearance at the second mode. Small insertion presents how discharge current connects to wall.

Spectroscopic measurements of rotational and vibrational temperatures have been done. Rotation temperature has been measured by molecular spectroscopy of the second positive band of nitrogen. An input lens of a quartz fiber line has a sharp focus. So, we could obtain the spectra from any defined point of observation. Three following basic conditions of the spectra getting have been chosen: Area between electrodes on a plane plate; Area in a separation area in 5mm downstream; and Area on an electrode plate when an artificial separating obstacle has been installed in 5mm upstream of electrode plate.

Thus, we can review three different situations: plasma generation in a free stream, plasma in separation zone at upstream generation and plasma generation in a small artificial separation zone. Summarizing the experimental data we can conclude the following values of a rotation temperature:

Electrode plate in a free stream	$T_r=1600\pm 200K.$
Standard separation zone, modes 1&2	$T_r=1400\pm 200K.$
Discharge in an artificial separation area	$T_r=3300\pm500K.$

Vibration temperature of gas has been measured in a standard separation zone downstream a wall step when the discharge current flows through it on a back wall. Such a data, probably, is the most important for applications. As was described above, the measurements were made by means of CN molecular bands analysis. A small addition of a C-contained impurity is enough to see such a spectra. The analysis of CN spectra allows us to getting a typical value of a vibration temperature of plasma inside of a separation zone $T_v=6000\pm1000K$. At some cases the temperature was less than this value - up to 4000K. Thus, a vibration temperature, at least, is 3 times more than a rotation (translation) temperature.

Plasma excitation near and inside of a separation zone effects on a static pressure distribution in this zone. Nine pressure pipes were installed on a back wall of a test section with a gap 5mm each from other downstream. Additional pipes are installed upstream discharge area and in a separation zone in 8mm from a wall step. Data from the last point are presented in Fig.5a. The chart includes also graphs of discharge current to synchronize a time period of discharge switching on. At observation of them it can be considered, that at different conditions the result for this point is the same: plasma excitation leads to increase of a static pressure near wall step approximately on 10%. Generally, this statement is correct for the

standard and the second mode of the discharge spacing both. The Fig.5b shows a sample of record of the pressure in all points.
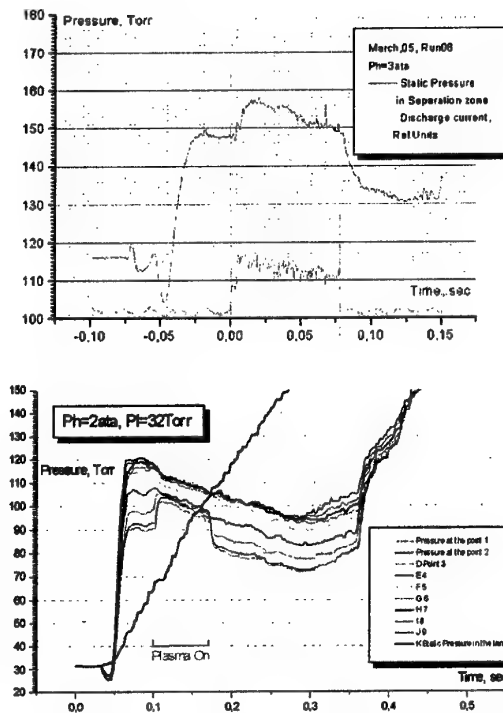
Fig.5. Static pressure temporal behavior at plasma excitation.

Results of pressure redistribution measurements are presented in Fig.6. Standard behavior of pressure in different points in a separation zone is shown at different initial conditions. It can be considered that the pressure distribution in a separation zone is change significantly. The pressure gradient occurs much less than in the case without plasma. Such an effect can lead to increasing of gas exchange between a separation zone and a main flow.

Lambda-shocks and boundary layer control.

The experiments on transonic flow control and boundary layer control have been conducted in transonic wind tunnel under the following parameters: total pressure about 1Bar, Mach number 0.5-1.1, test section 200*300mm, surface discharge up to 15kW of input power. Image of the model is presented in Fig.7.

Surface multi-electrode discharge looks like in Fig.8 where it is excited in transonic airflow. Types of the experimental arrangement are shown in Fig.9.
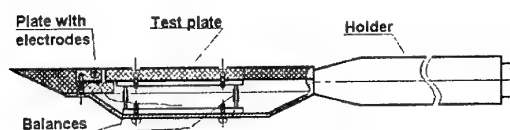
Fig.7. AD model. Test plate plain and profiled 100×120mm. Balances and pressure distribution measurements.
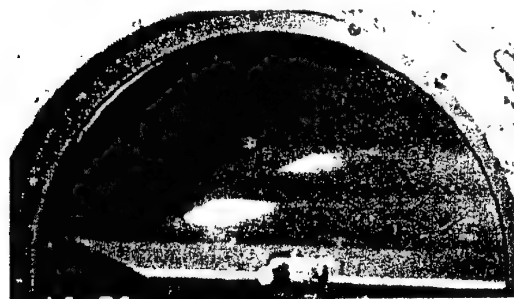
Fig.8. Surface discharge appearance at transonic airflow.
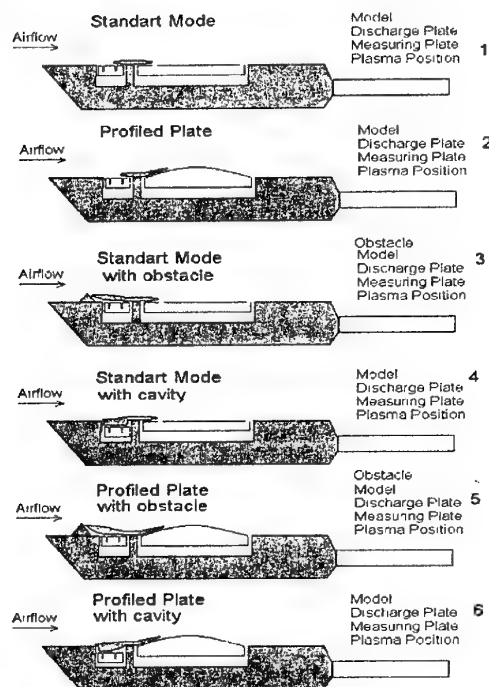
Fig.9. Experimental arrangements at different cases.

The generation of an electric discharge near the surface allows shifting a position of direct transonic shock upstream and decrease it amplitude sufficiently. The mechanism of such a shifting is the following: energy input to a near-surface layer increase a sonic velocity there. It means that an effective Mach number of the flow falls and the shock moves upstream. A sample of such a case is presented in Fig.10 by processed Schlieren photos.
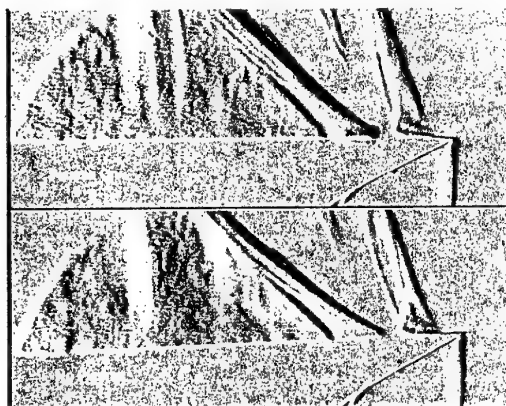
Fig.10. Schlieren photos of surface plasma effect on the direct shock position above the plain plate at transonic airflow.

At this case the visible splitting of a main shock takes place. Actually, we see two shocks: first ("old") shock is from a part of model, which is without plasma generator; second shock is from a test plate and plasma excited area. Thus, the plasma influents on whole supersonic zone by decreasing of effective Mach number inside of it. "Lambda"-shock has been stabilized by means of artificial obstacle. The effective power deposition in this case is more due to increase of power input and more time of a heated gas presence inside of an interaction area. As the result the intensity of a direct shock near the surface drops. A similar result and change of wave structure of airflow has been obtained when a special cavity on the surface has been applied for the discharge stabilization.

The experiment on BL control was conducted in transonic wind tunnel at Mach number M=0.7-0.9 (see Figs.7, 8). In dependence with Mach number a Reynolds number (on length 1m) was in range $1-1.5 \times 10^7$. During the test a balance measurements of friction drag (tangential force), pressure distribution and optical observations (natural, shadow and Schlieren) were fulfilled. Shadow photos show a structure of airflow and a separation line location. Quasi-continuous multi-electrode surface discharge was used for a plasma excitation.

Typical balances signal for a plain test plate is shown in Fig.11. Plasma switching on was 1.5sec of duration. Well seen that the tangential force reduction was about $\Delta F_{fr}=0.4N$ or in a range 10%. In case when an artificial separation has been applied and/or profiled test plate the tangential force reduction was much more, up to 100%.

61
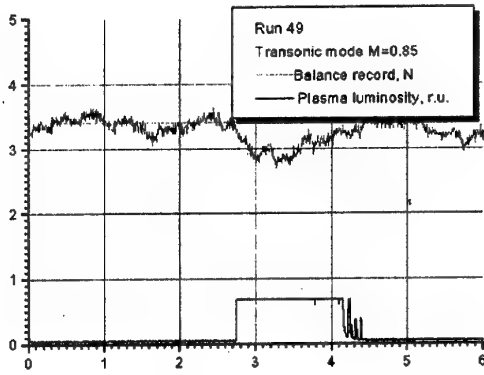
Fig.11. Sample of the balances record (tangential force) at surface plasma excitation upstream plain test plate.

The analysis of pressure distribution data allows dividing the balance's measurements on the viscous friction effect, including transition, and plasma influence through the separation. Sample of such a distribution for profiled plate with the obstacle is presented in Fig.12. One can see that static pressure along the test plate is change slightly. At the same time the total pressure of flow near the surface drops.
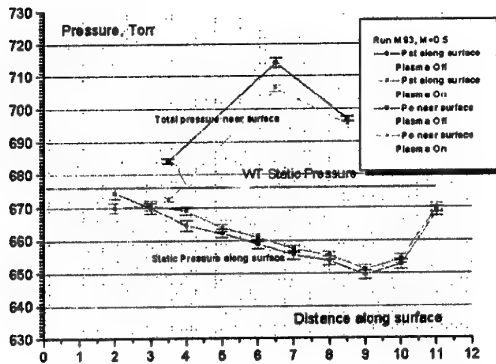
Fig.12. Pressure distribution along the test plate and upstream surface plasma effect.

The plasma effect on a tangential force in subsonic and transonic airflow depends on input power. The input power to the electric discharge depends not only on the parameters of the power supply but also on conditions of the plasma excitation. Observations of plasma luminosity show that plasma in high-speed airflow is non-homogeneous. Using of cavities and obstacles of the different type gives additional method of plasma control in airflow, including control of input power.

Mathematical simulations.

It is well known that if there is a gas flow in the channel with the step expansion profile the vortex is formed down stream off the step. The goal of this work is to numerically investigate the influence of the energy release on the vortex characteristics (form, pressure and temperature distribution). The energy release is takes place in the vortex region and is caused by Ohm's dissipation due to gas discharge.

Mathematical model.

The system of equations describing investigated flow is the system of Euler's equations with the heat source in the energy equation:

$$\frac{\partial \rho}{\partial t} + \frac{\partial}{\partial x}(\rho u) + \frac{\partial}{\partial y}(\rho v) = 0 \tag{1}$$

$$\frac{\partial}{\partial t}(\rho u) + \frac{\partial}{\partial x}(\rho uu) + \frac{\partial}{\partial y}(\rho uv) = -\frac{\partial p}{\partial x} \tag{2}$$

$$\frac{\partial}{\partial t}(\rho v) + \frac{\partial}{\partial x}(\rho uv) + \frac{\partial}{\partial y}(\rho vv) = -\frac{\partial p}{\partial y} \tag{3}$$

$$\frac{\partial}{\partial t}\left(\rho(\varepsilon + \frac{u^2 + v^2}{2})\right) + \frac{\partial}{\partial x}\left(\rho u(\varepsilon + \frac{u^2 + v^2}{2})\right) +$$

$$+ \frac{\partial}{\partial y}\left(\rho u(\varepsilon + \frac{u^2 + v^2}{2})\right) =$$

$$= -\frac{\partial}{\partial x}(up) - \frac{\partial}{\partial y}(vp) + \alpha Q \tag{4}$$

where ρ, u, v, p, ε – density, longitudinal and transversal component of velocity, static pressure and specific internal energy respectively. It is supposed that volume source Q in the right part of the energy equation (4) are caused by heat release in the gas discharge. Coefficient α modulates the intensity of the heat release. System (1)-(4) are closed by the equation of state of ideal gas:

$$\varepsilon = \frac{1}{\gamma - 1}\frac{p}{\rho} \tag{5}$$

where γ - specific heat ratio is equal to 1,4.

Scheme of the flow and boundary conditions.

Scheme of the flow is represented in Fig.13.

The computational region ABCDOF has following dimensions: AB=0.02m, BC=0.203m, OF=0.015m. The beginning of coordinate system is placed in the point O. The "supersonic" boundary condition - u_1=367m/s, v_1=0, p_1=32.99kPa, ρ_1=0.494kg/m^3, M=1.2, T=233K, p^0=10^{5}Pa is placed on the AB. The "not passing" conditions - U_n=0 are placed on AF, OF, BC, OD.

The "soft" boundary condition - $\partial/\partial n=0$ are placed on CD.
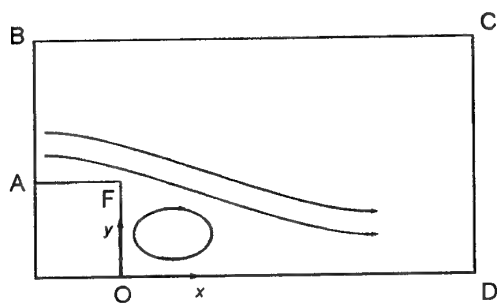
Fig.13. Scheme of the flow.

The distribution of source Q in equation (4) has been taken as follows:

$$Q = \frac{W}{Lc}\left\{\sin\left(\frac{2\pi}{L}y - \frac{\pi}{2}\right) + 1\right\}\exp\left(-\frac{x}{c}\right) \qquad (6)$$

$$x \geq 0, \ y \leq L,$$
$$Q=0 \qquad x<0 \text{ or } y>L$$

where $W=50\text{кW/m}$, $L=OF$, $c=3\cdot10^{-3}\text{m}$. Corresponding profiles of $Q(x,y)$ distribution are presented in Fig.14.
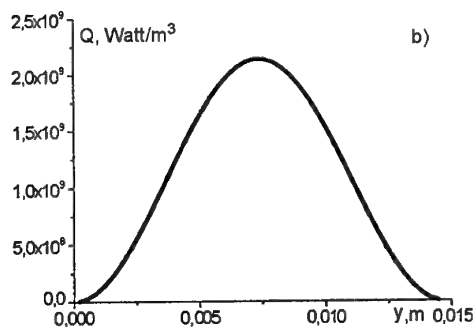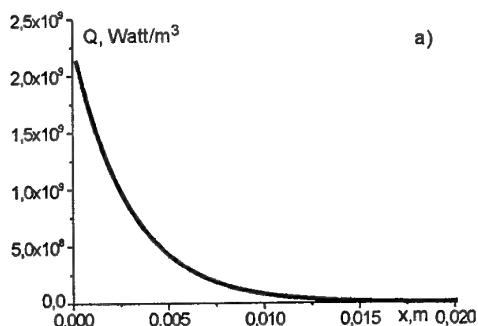
Fig.14. Distribution of Q:
a- $Q(x,7.5\cdot10\text{-3m})$, b- $Q(3.5\cdot10\text{-4m},y)$

The series of numerical calculations with coefficient α equal to 0,1,2,5 has been made in this work.

Numerical solutions.

Streamlines and pressure contours for $\alpha=0,1,5$ are presented at Fig.15-17 respectively.
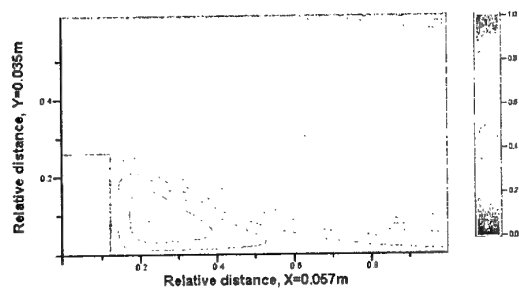
Fig.15a. Flow streamlines, $W=0$. Step = 0.345, 50 contours.
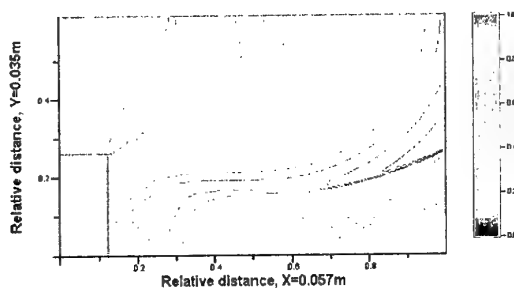
Fig.15b Pressure contours, $W=0$. $P_{min}=46.75$ Torr, $P_{max}=250.7$Torr, 50 contours.
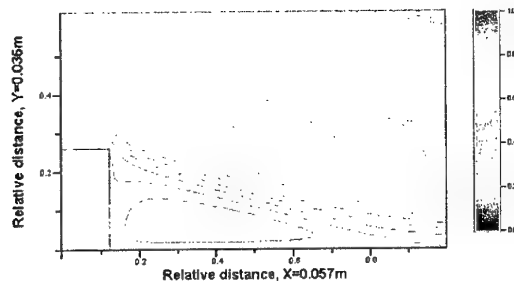
Fig.16a. Flow streamlines, $W=50\text{kW/m}$. Step = 0.340, 50 contours.
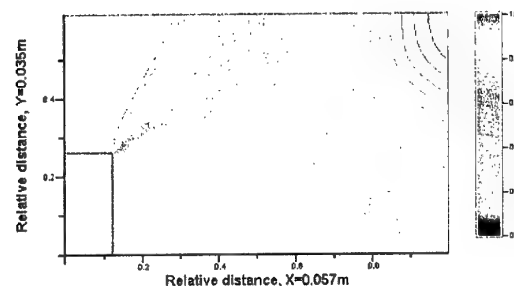
Fig.16b. Pressure contours, $W=50\text{kW/m}$. $P_{min}=63$. Torr, $P_{max}=250.7$Torr, 50 contours.
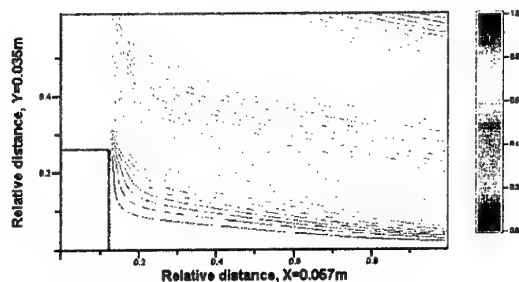
Fig.17a. Flow streamlines, W=250kW/m. Step = 0.347, 50 contours.
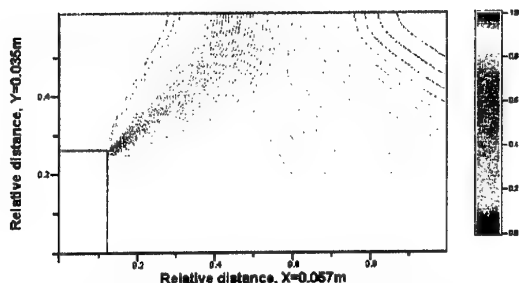
Fig.17b. Pressure contours, W=250kW/m. P_{min}=89. Torr, P_{max}=250.7Torr, 50 contours.

The important results have been obtained under the mathematical simulations. They can be formulated as the following. Energy release changes a shape and volume of a separated zone. Increase of input power leads finally to a separated zone disappearance i.e. to separation-less streamlining of a wall step.

Moderate energy release effects in a change of pressure redistribution inside of the zone. Pressure gradients are reduced. It means that the vorticity is decreased. This result appropriates to the experimental measurements not only qualitatively, but also quantitatively. The increase of level of energy release leads to increase of the temperature in a separated zone. Exceeding of the power over some level effects in transform the airflow to separation-less mode and fall of temperature consequently. Temperature value at 50kW/m of the energy release corresponds to experimental data.

The numerical modeling showed that a heat deposition to the vortex region near the wall step of the channel gives decreasing of vortex intensity. If the heat release is sufficiently high the gas flows over the step practically without vortex structure. In that case the releasing heat energy pass away by convective gas flow.
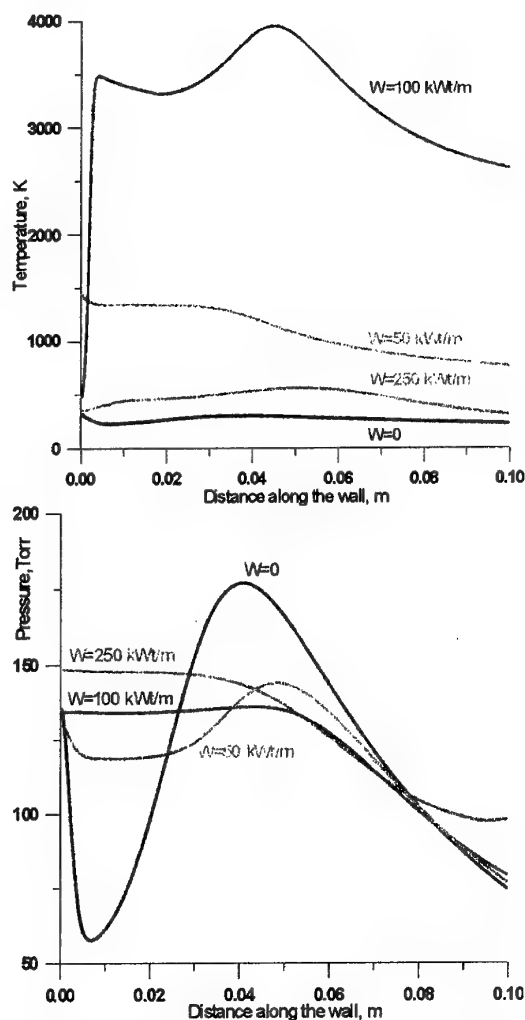
Fig.18. The distribution of temperature and pressure along the wall for different power values.

Conclusions.

The study has demonstrated the fact of considerable influence of surface plasma formations on characteristics of flow around developed surface models. The rule of the most response on an external influence when applying in the area of maximal mechanical energy losses is confirmed. The mechanisms of plasma influence are resolved. The dependence of plasma effects on power release is obtained.

The work has demonstrated the change of a transonic flow structure with plasma formations created in the flow closed to the model surface. The energy supply to the boundary layer in transonic modes may cause the reformation of shock wave structure resulting in either increasing or decreasing of the friction drag depending on particular flow conditions. The displacement of a

64

normal shock wave above the surface has been observed in a result of plasma influence. Under conditions of the subsonic flow around a contoured plate the total drag reduction in several times is observed while a surface discharge creating.

For maintenance of stable discharge excitation the electrodes should be placed behind shelves or in cavities, if the surface design allows. On flat surfaces it is necessary to apply discharges with high propagation velocity such a high frequency or pulse streamer/filament discharge. The design of a plasma generator and the definition of operation modes depend on specific flow conditions (no universal decisions).

Two modes of discharge spacing near fixed separated zone (back step type) are described: (1) current localized between the "hot" and grounded electrodes, and (2) current from "hot" electrodes to back wall of the test section. Plasma excitation in separation zone (mode 2) causes the pressure redistribution. The longitudinal pressure gradient in separation zone is decrease significantly. Translational temperature in a separation zone is achieved the value 1500K. At the same conditions the vibrational temperature can be in a range of 5000K. A mathematical simulation shows results qualitatively closed to the experimental ones. The pressure and temperature behavior in the separated zone are in accordance with experimental data and correspond to the significant modification of separated flow structure. Moreover, the simulation predicts a separation-less mode at higher energy release. This effect observed at the first in the present study needs more experimental and analytical efforts to evaluate its practical importance.

Acknowledgement.

References

1. Workshop on Weakly Ionized Gases. USAF Academy, Colorado, 9-13 June 1997; Second Workshop on Weakly Ionized Gases. Proceedings. Norfolk, 24-25 April 1998, Third Workshop on Weakly Ionized Gases. Proceedings. Norfolk, 1-3 November 1999.

2. V.Bityurin, A.Klimov, S.Leonov "Assessment of a Concept of Advanced Flow/Flight Control for Hypersonic Flights in Atmosphere." Suggested to be presented to 3rd Workshop on WIG. November 1-5, 1999 / Norfolk, Virginia, AIAA 99-4820.

3. T. Cain, D. Boyd "Electrodynamics and the effect of an electric discharge on cone/cylinder drag at Mach 5", 37th AIAA Aerospace Sciences Meeting and Exhibit, January 11-14, 1999/Reno, NV, AIAA 99-0602.

4. S. Leonov, V. Nebolsin, V. Shilov "Effectiveness of plasma jet Effect on Bodies in an Airflow", Proceedings of Workshop "Perspectives of MHD and Plasma Technologies in Aerospace Applications", Moscow, IVTAN, 1999, pp. 58-65.

5. G.G.Chernyi, The impact of electromagnetic energy addition to air near the flying body on its aerodynamic characteristics. 2-nd WIG Workshop, proceeding, Norfolk, VA, April 24-25, 1998. Levin V. A., Afonina N. E., Gromov V. G., Influence of Energy Input by Electric Discharge Supersonic flows around bodies. 2nd WIG Workshop, Proceedings, Norfolk, VA, April 24-25, 1998.

6. Kazakov A., Kogan M., Kuriachi A., Influence on the friction of local heat addition to the turbulent boundary layer. Mech. Of Fluids and Gases, N1, 1997. Kurjachi A. P., Boundary layer transition by means of electrodynamics method. Prikl. Math. I Mech., vol.49, issue 1,1985. A.V. Kazakov, A.P.Kuryachii, Electrogasdynamic influence on the development of the small diturbances in a boundary layer in the thin profile Izv. AN USSR, Mekhanika zhidkosti i gaza, 1, 1986

7. S. Leonov, V. Bityurin, V. Gromov, N. Savischenko, A.Yuriev "Influence of Surface Electrical Discharge on Friction of Plate in Subsonic and Transonic Airflow". 39th AIAA Aerospace Sciences Meeting & Exhibit, 8-11 January 2001 / Reno, NV, AIAA 2001-0640.

8. Klimov A., Byturin V, Brovkin V., Vinogradov V., Van Wie D.M. "Plasma Assisted Combustion", 39th AIAA Aerospace Sciences Meeting & Exhibit, 8-11 January 2001 / Reno, NV, AIAA 2001.

09. SUPERSONIC FLOWS WITH LONGITUDINAL GLOW DISCHARGE

V.M.Fomin[1], Th. Alziary de Roquefort[2], A.V.Lebedev[1], A.I.Ivanchenko[1]

[1]ITAM SB RAS, 630090 Novosibirsk, Institutskaya str., 4/1
[2]Laboratoire d'Etudes Aérodynamiques UMR CNRS 6609, 43, rue de l'Aérodrome, 86036 Poitiers CEDEX,
France

Abstract. The results of investigation of longitudinal glow discharge interacted with the supersonic flow (M = 3,2) are given in this work. The discharge was generated both before blunted axially symmetrical bodies and in the free flow. It is found that the high-current glow discharge reconstructs the wave flow pattern around blunted bodies. It appears, in particularly, in dissipation of a direct shock wave separated from the body and arising system of sidelong shock waves in the periphery of a cathode part of glow discharge. It is obtained that the generated glow discharge behaves as a certain virtual body, capable to generate shock waves, and its form can continue the form of a real supersonic flow body.

It is shown that the presence of the high-current glow discharge in the supersonic flow brings about essential reducing stagnation pressure, which can decrease several (5-6) times in contrast with its value after the direct shock wave. The obtained temperature distributions in the plasma discharge and used simple models allow to assume that the mechanism of interaction between non-equilibrium plasma of glow discharge and the supersonic flow has a thermal nature.

Previously, it was established that a stationary glow discharge with a high density of the electric current could be initiated in supersonic and hypersonic gas flows. It this case, the discharge exerts a profound influence on both free flows and flows around bodies. In particular, such a discharge can drastically change the wave pattern and physical parameters of supersonic flows [1-4]. It was also found that the interaction between a glow discharge and a supersonic flow is a complex process that requires a detailed study. It is the very research area the present work deals with.

A streamwise glow discharge was initiated both in front of blunted axisymmetric bodies and in a free flow. The bodies were cylinders 6mm in diameter with the nose part having the shape of a hemisphere, truncated cone or blunted cone. The nose parts were prepared from metals and used as cathodes. The anode had the shape of a 0.2-mm-thick plate with a triangular ledge on its trailing edge. The anode was installed in front of the body at a distance L from it; the distance could be varied. Both the cathode body and the anode were installed at zero incidence. A schematic of the model is shown in Fig.1. During the experiments, the model was immersed into an air supersonic flow. The Mach number of the flow was 3.2, the static pressure in it ranged from 6 to 20mbar, and the static temperature was 96K. The discharges in all experiments were similar in appearance; a representative photograph is shown in Fig.2. In the volume occupied by the discharge, a cone-shaped cathode region and a main region having a cylindrical shape and closing the cathode region and the anode can be distinguished. On the cathode surface, a cathode layer develops and the normal current density effect is observed typical of all glow discharges, namely: with increasing discharge current, the cathode surface area occupied by the discharge grows in size. The experiments were carried out under conditions in which the cathode layer covered the whole area of the electrode, which made the discharge axisymmetric. The current-voltage characteristics of the discharges were weakly descending. The characteristic voltage across the discharge was largely dependent upon the inter-electrode separation and nearly independent of the static pressure in the experiments. As the inter-electrode separation varied from 14 to 44mm, the voltage across the spark gap increased from 750 to 1250V.

Fig.1. Schematic of the model.

Fig.2. Visual appearance of a discharge.

The distribution of the electric potential over discharge plasma was examined. In the experiment, the static pressure in the flow was 10.1mbar, the distance between the electrodes was 44mm, and the forebody of the cathode had the shape of a blunted cylinder. To measure the electric

66

potential, the probe method was used. The probe in the form of a thin wire 0.05mm in diameter stretched across the flow was used to probe the main part of the discharge. To study the planar potential distribution in the cathode region, a point probe was used with the outer diameter 0.5mm, which was a compromise between mechanical strength and spatial resolution. The measurements were carried out with respect to the anode. The distribution of the potential over the axis of the «main» part of the discharge is shown in Fig.3. A considerable voltagedrop is observed across the near-electrode regions. This voltage drop is 200V across the anode region and 600 to 760V, depending on the current strength, across the near-cathode region. It should be noted that the cathode voltage drop observed in our experiments was unexpectedly high for glow discharges, where it is known to be usually lower than 250V. The latter means that a considerable portion of energy was releasing in the cathode region. An increase in the discharge current resulted in an increased fraction of the voltage falling across the cathode region. Simultaneously, the voltage drop across the «main» part of the discharge was found to decrease. This clearly indicates that the electrical resistance of this part of the discharge decreases with increasing discharge current. The resistance decreases from 13.5 to 2.9kOhm as the current increases from 35 to 105mA. Figure 4 shows the planar electric-potential distribution over the cathode region. In this experiment, the electric current was 75mA. The measurements were carried out in the symmetry plane of the discharge. The results are indicative of the following. The potential with respect to the anode increases as we move from the peripheral part of the cathode zone to its center. Almost all the voltage drop occurs across a thin near-cathode region as thin as 1mm. This thickness is in line with the cathode-layer thickness deduced from photographs.

The temperature is an important characteristic of any discharge. In this study, the stagnation temperature in the region occupied by the discharge was measured using a Chromel-Alumel thermocouple made from a 0.1-mm wire. It is known that in non-equilibrium discharge plasma the fraction of energy stored in the oscillatory degrees of freedom of the exited molecules may be rather high. The relaxation of this energy at the thermocouple surface can cause an additional heating of the thermocouple and bring about additional measurement errors. The transformation of the energy of the oscillatory motion of gas molecule into the energy of their translatory motion on the surface is characterized by the accommodation coefficient ε [5]. This coefficient is defined as the probability of oscillatory-energy

inactivation at the surface per one collision. In the case of nitrogen, the coefficient ε for metals is of the order of 10^{-3}–10^{-2}. This small value of ε convincingly proves that the temperature measured by thermocouples cannot be notably affected by the relaxation processes at the thermocouple surface. Another factor capable, in principle, of affecting the indications of the thermocouple is the intense electric field in some parts of the discharge. The results reported in [6] prove that the effect due to the strong electric field is negligibly small.
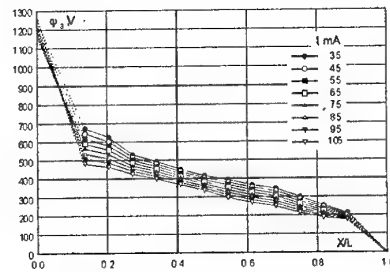
Fig.3. Electric-potential distribution over the discharge axis
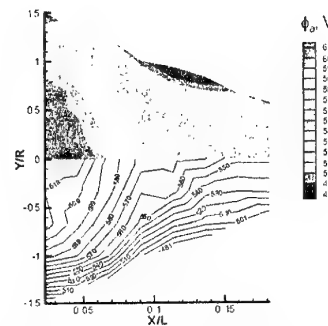
Fig.4. Electric-potential distribution over the cathode zone

The configuration of the model and the free-flow parameters were identical to those in the experiments in which the electric-potential distribution was examined.

The distribution of the stagnation-temperature over the discharge axis for various discharge powers is shown in Fig.5. Here, ΔT_0 is the difference between the stagnation temperature in the region occupied by the discharge and that in the free flow. The temperature increases with increasing discharge power. It also monotonically increases along the direction from anode to cathode, except for the central part of the discharge, where it slightly decreases. A temperature jump is observed near the cathode. The width of the zone in which the temperature displays

67

the abrupt jump is far in excess of the width of the cathode-layer where, as shown above, the electric potential displays a jump and an intense electric field arises. The latter means that the increase in the temperature gradient takes place outside the layer with an increased energy release. Figure 6 shows the distribution of the stagnation temperature over the symmetry plane of the cathode zone (here R is the cathode radius). The temperature increases from periphery to center, which is just what is expected. The following fact is noteworthy: The heat-releasing zone coincides with the luminous part of the discharge. The latter means that the electric current flows only across this region.
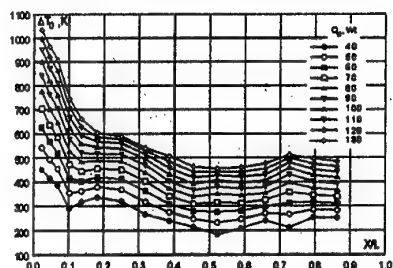
Fig.5. Stagnation temperature distribution over the discharge axis
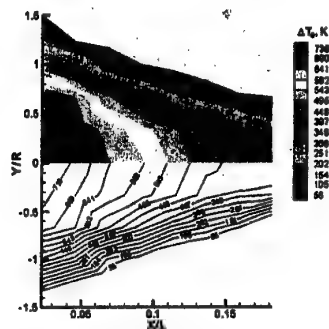
Fig.6. Stagnation temperature distribution over the cathode zone
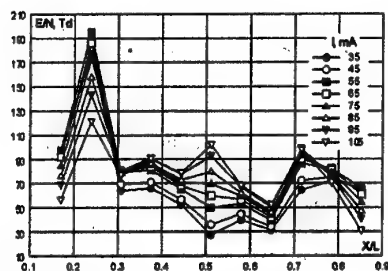
Fig.7. Distribution of the E/N ratio along the symmetry axis of the «main» part of the discharge

Assuming that the static pressure in the main part of the discharge is close to its value in the free flow, from the measured electric-potential and temperature distributions over the volume occupied by discharge we found the distribution of the parameter E/N (E is the electric-field intensity and N is the concentration of gas molecules) over the axis of the main part of the discharge (Fig.7). With this parameter and the experimental data of [7,8], we deduced the plasma characteristics in the main part of the discharge. The drift velocity of electrons under the action of the electric field was found to roughly equal 10^5m/sec, which far in excess of the flow velocity in the experiment. On the contrary, the velocity of ions was 300 to 400m/sec, which is lower than the free-flow velocity. Due to ambipolar diffusion, the plasma remains electrically neutral in its bulk (the concentrations of positively and electrically charged particles are identical), except for the region immediately adjacent to the electrodes. Since the ion velocity is negligibly small compared to the electron velocity, a predominant part of the discharge current is due to electrons. The latter fact allowed us to determine one of the main parameter of the plasma, electron concentration N_e. The current strength in the «main» part of the discharge is given by the formula

$$I = N_e V_d^- Se \,,$$

where I is the discharge-current density, V_d^- is the electron drift velocity, S is the discharge cross-sectional area, and e is the elementary charge. The electron concentration resulting from this formula is of the order of 10^{12}cm^{-3}. The ionization degree in this case is 10^{-6}. The mean electron energy amounts to 2.5eV.

Of considerable interest is the interaction between an intense shock wave with a volume glow discharge and a supersonic flow. Such a shock wave can be initiated by the frontal surface of the blunt cylinder. However, the plate-shaped anode located upstream, even having a thickness as small as 0.2mm, generates an aerodynamic wake that induces disturbances into the normal bow compression shock even in the case without discharge. For obtaining a possibility to determine the self-action of the electric discharge, it is required to eliminate or considerably diminish this disturbance. In a series of experiments, we have found that the normal compression shock suffers no changes unless the anode-induced wake does not arrive at the frontal surface of the cylinder normal to the approaching flow. Besides, the wake induces no notable changes into the cone-generated oblique compression shock it traverses. The geometry of the cathode forebody was chosen with due regard for the above observations. The forebody was made

in the form of a truncated cone. The surface area was such that the discharge occupied the whole surface beginning from its very initiation. To prevent coming of the anode-generated wake to the frontal surface normal to the axis of the flow, the anode was offset upward. The frontal-surface diameter was chosen so that the offset of the anode from the axis was small and the discharge remained nearly axisymmetric. Preliminary experiments showed that displacement by 1–2mm had not caused any changes in the visual appearance of the discharge provided that the distance between the electrodes was 40–50mm. The distance over which the anode was displaced was chosen with due regard for the results of calibration tests, in the course of which we monitored the general appearance of the bow shock and the stagnation pressure at the center of the frontal surface of the cathode. The anode was being displaced until the shock-wave pattern and the stagnation pressure became identical to those in the flow around the body but without an anode located upstream. In practice, the displacement was smaller than 2mm. The electrodes' geometry described above-was used in supersonic-flow (M=3.2) and hypersonic-flow (M=7.1) studies.

To study the influence of the discharge on the bow shock, we used the shadow technique. The slot of the device was always oriented normally to the flow direction, which made the system sensitive to streamwise gradients of gas density. Shown in photographs (Fig.8) are the flow patterns under conditions without and with discharge (photos a and b, respectively) for M=3.2. There is a substantial difference between the two photographs, which is manifested in a drastic change of the bow shock. An ordinary normal compression shock clearly observable in the flow around body without a discharge disappears after initiation of the discharge. Also, a stalled oblique shock wave is observed. It has a diffude front, which can be a consequence of either integration (over time) of the wave-front oscillations by relatively long time of exposure or real physics of the interaction between the shock wave and the non-equilibrium discharge plasma. To gain a better insight into the actual reason of this phenomenon, we used shadow photographing with a pulsed source of light. The technique was capable of ensuring the time of exposure 2μsec. The results are shown in Fig.9. The photographs 9, a and 9, b were obtained for the flows without and with discharge, respectively. Comparison between photographs 8 and 9 shows that they are nearly identical. The latter provides indication for the fact that the visual appearance of the shock-wave front does not depend on exposure duration and reflects the true distribution of density in the region of

Fig.8. The wave flow pattern under the conditions with a discharge (a) and without it (b)
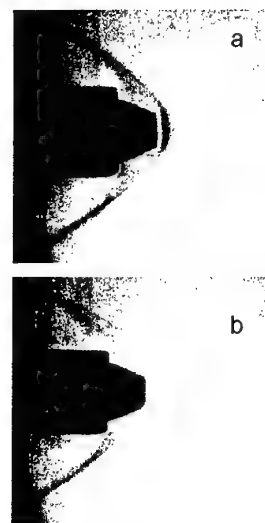
Fig.9. The wave flow pattern as revealed by observations with a pulsed source of light: a) with a discharge, b) without it

interest. This phenomenon agrees well with the numerical results of [9], where it was shown that a supersonic flow around a heat source of large aspect ratio may contain no jumps of gas parameters (density, pressure, or velocity) that usually occur during formation of a shock wave. Comparison between the wave pattern of the flow and the visual appearance of the discharge, together with examination of simultaneously taken photos of the discharge and shock waves, allowed a conclusion to be made that the cathode part

behaves similarly to a body of identical shape. Indeed, measurements of the inclination angle of the outer boundary of the shock front and that of the boundary of the cathode part of the discharge to the flow axis yielded the values 31^0 and 21.5^0. Let us consider a supersonic flow with a Mach number identical to that in our experiments (M=3.2) and a conic body, immersed into this flow, with the semi-vertex angle equal to that of the cathode region. The inclination angle of the oblique compression shock in this case is 30^0, which is very close to the value 31^0 obtained in our experiment. The latter means that the discharge plasma plays the part of a virtual body the shape of which is added to that of the streamlined body.

The considerable transformation of the shock wave caused by the discharge should in turn cause a change in the pressure at the body surface; the latter is related with the aerodynamic drag. To measure the pressure at the center of the frontal surface of the model, a hole of 0.5 mm in diameter was provided in itr. Figure 10 shows the distribution of the dimensionless stagnation pressure for various discharge powers and static pressures for M=3.2. Here, P_{02} is the pressure measured at the stagnation point at the body surface, P'_{01} is the stagnation pressure behind the normal shock measured in the flow without discharge, and Q_d is the electric power of the discharge. In the case of a supersonic flow the discharge causes a drop of the stagnation pressure that may be six-fold compared to the stagnation pressure behind the normal compression shock. The stagnation pressure decreases withincreasing discharge power. However, the decrease in the stagnation pressure becomes insignificant from a certain value of discharge power on, which is analogous to the saturation of the flow with heat revealed numerically in [10]. The results for a hypersonic flow (M=7.1) are shown in Fig.11. Theincreasing discharge power. However, the decrease in the stagnation pressure becomes insignificant from a certain value of discharge power on, which is analogous to the saturation of the flow with heat revealed numerically in [10]. The results for a hypersonic flow (M=7.1) are shown in Fig.11. TheTo compare the energy performance of the discharge action on the pressure at the frontal surface of model, the discharge power was nondimensionalized using, as normalization factor, the power of the approaching gas flow

$$Q_d = \frac{1}{2}\rho U_\infty^3 S,$$ where ρ is the gas density, U_∞ is the free-stream velocity, and S is the area of the midship section of the model. The parameter Q_d/Q_f defined in this manner has the sense of the relative energy supply. The results are shown in Fig.12. The experimental data for M=7.1 are coincident

almost for all values of the static pressure. The latter is also true for the results obtained at M=3.2. The electric power of the discharges in the hypersonic flow was far greater than that of the discharges in the supersonic flow. However, the energy of the hypersonic jet, which was higher than the energy of the supersonic jet, has made the relative energy-input in the hypersonic flow lower than that in the supersonic flow. In the flow with M=3.2, the energy input could be greater than the energy of the jet, the ratio Q_d/Q_f could run into 1.5, whereas the Q_d/Q_f ratio in the hypersonic flow was always lower than 0.6.
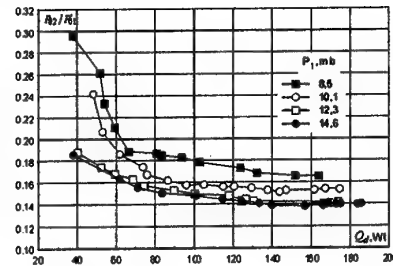
Fig.10. Stagnation pressure. M=3.2
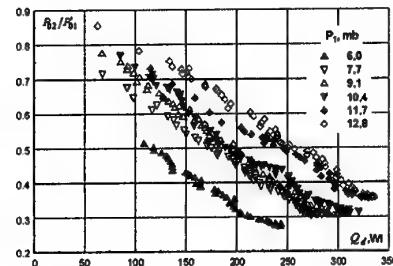
Fig.11. Stagnation pressure. M=7.1
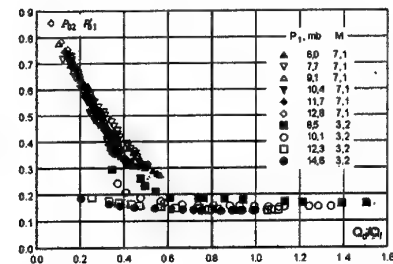
Fig.12. Stagnation pressure versus relative energy input

For generating ionized zones in the free flow, we used a model that consisted of a ring-shaped cathode and an anode installed upstream of it. The anode was identical to that described above. The ring had the diameter 10 mm and the height 2.5mm; its wall thickness was 0.3 mm. The visual

appearance of the plasma formation formed under these conditions is shown in Fig.13. As the discharge current was increased from 50 to 150mA, the voltage drop across the spark gap has changedfrom 1400 to 1000V. Photographs of the wave structure of the flow were taken. Under condition without discharge, only insignificant disturbances induced by the ring and its strut were observed. In the flow around the plasmoid formed by plasma, an oblique compression shock appeared on the front part of the plasmoid (Fig.14). Comparison of the visual appearance of the discharge with the wave pattern shows that the oblique shock wave was generated by the conic part of the cathode zone. Consequently, the discharge plasma forms a virtual body similarly as it did in the supersonic flow around the blunt body (see above). The semi-vertex angle of the conic part of the cathode zone was 22^0, and the inclination angle of the oblique shock wave equaled 29.5^0. A conic body with the semi-vertex angle identical to that of the head part of the cathode zone, when placed in a flow with M=3.2, gives rise to an oblique shock wave with the semi-vertex angle 29.6^0, which is very close to the value obtained in our experiments (29.5^0). The latter provides further indication for the fact that the discharge plasma forms in a supersonic flow a body, characteristics of which resemble the characteristics of real bodies.
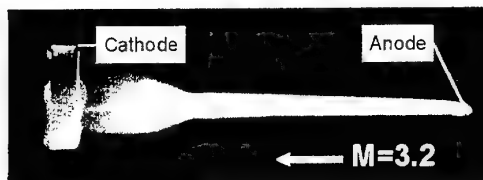
Fig.13. Visual appearance of a discharge
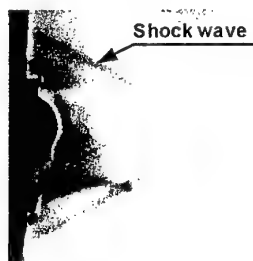
Fig.14. Wave flow pattern

To examine the radial distribution of the stagnation pressure over the cathode region of the discharge as a function of the discharge power, we used a Pitot tube with 0.8-mm diameter installed 2 mm upstream of the leading edge of the ring. The results are shown in Fig.15. Here P_{02} is the stagnation pressure behind the normal compression shock measured in the discharge, P'_{01} is the stagnation pressure behind the normal compression shock measured at the same point under the conditions without discharge, and R is the ring radius. As in the case of a flow around a blunted body, the stagnation pressure is seen to decrease. The pressure also decreases with increasing discharge power. Inside the discharge, the stagnation temperature is nearly uniform, but it rapidly increases as we move toward the discharge periphery.
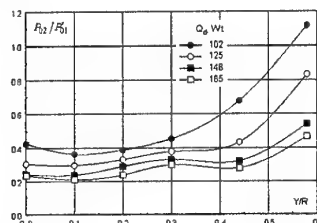
Fig.15. Stagnation pressure in the cathode zone
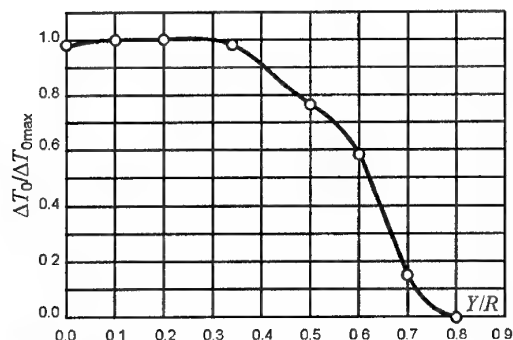
Fig.16. Stagnation temperature in the cathode zone

We measured also the radial distribution of the stagnation pressure across the flow in the cathode area of the discharge 4 mm upstream of the discharge. The discharge power was 125W. In these experiments, the Chromel-Alumel thermocouple described above was used. The result is shown in Fig.16, where ΔT_0 is the difference between the stagnation temperature in the discharge and that in the free flow, and ΔT_{0max} is the maximum value of this difference. We may conclude that the stagnation temperature is nearly uniform at the center of the discharge, and it gradually decreases toward the periphery. The region in which the temperature is higher than the free-stream temperature, is nearly coincident with the luminous zone of the discharge.

71

To give possible explanation to the discharge/supersonic flow interaction mechanism, the following simple model was used. We assume that the static pressures P and flow velocities U in the discharge and in the free flow are identical; from the known temperature T_2 in the region occupied by the discharge, it is possible to estimate the velocity of sound in the heat-releasing region and the Mach number: $a_2 = \sqrt{\gamma R T_2}$ and $M_2 = U / a_2$, respectively. The new stagnation pressure in this case may be calculated as $P_{02} = P(1 + \frac{\gamma-1}{2} M_2^2)^{\frac{\gamma}{\gamma-1}}$; from here, provided that M_2 is higher than unity, we may estimate the stagnation pressure behind the normal compression shock. The stagnation pressure distribution determined in this way from the temperature profile shown in Fig.16 is shown in Fig.17 (curve 1). This curve is compared with curve 2 that shows experimental data. Evidently, this model, although being extremely simplified, provides a satisfactory correlation with the experimental data for the central part of the discharge.
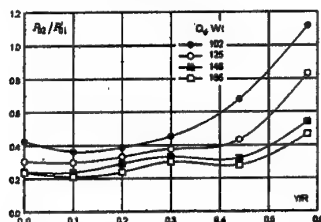
Fig.17. Radial distribution of the stagnation pressure
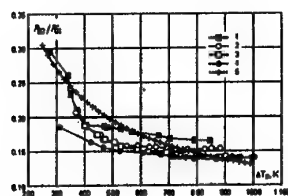
Fig.18. Stagnation pressure versus stagnation temperature

The same model was used to study the supersonic flow (M=3.2) around the blunted bodies described above. Experimental curves 1–4 of Fig.18 were deduced from the graph shown in Fig.10. Curve 5 shows the predicted dependence obtained using the model proposed above. It should be noted that curve 5 fits experimental dependences 1–4 fairly well.

Since the model under consideration, although it takes into account only the effect due to gas heating in the volume occupied by the discharge, furnishes an adequate description to experimental data, we believe the interaction between the discharge and the supersonic flow may be of thermal nature.

References

1. Fomin V.M., Lebedev A.V., Ivanchenko A.I. Spatial-energetic characteristics of electric discharge in a supersonic gas flow. // Dokladi akademii nauk. 1998. V.361. No.1. P. 58-60. (in Russian)
2. Fomin V.M., T. Alziary de Roquefort, Lebedev A.V., Ivanchenko A.I. Self-sustaining glow discharge in a hypersonic gas flow. // Dokladi akademii nauk. 2000. V. 370. No 5. P. 623 – 626. (in Russian).
3. Fomin V.M., T. Alziary de Roquefort, Lebedev A.V., Ivanchenko A.I. Cathode phenomena in a self-sustaining glow discharge in a supersonic gas flow // Diokladi akademii nauk 2000. V. 374, No 3. P. 340 - 342. (in Russian).
4. V.M. Fomin, T. Alziary de Roquefort, A.V. Lebedev, A.I. Ivanchenko. Gasdynamics and electric phenomena on glow discharge in supersonic air flow // 10th International Conference on the Methods of Aerophysical Research (ICMAR'2000): Proc.-Novosibirsk, 2000.-Pt. 1.-P. 79-84.
5. Rozenshtein V.B., Ushansky S.Ya., Gershenzon Yu.M. Heterogeneous relaxation of a vibrational energy of molecules // Plasmochimics processsesion. -Moscow.- 1979.-P. 44-63.
6. Alferov V. I., Bushmin A. S. Experimental research of effect of an electrostatic field on the indication of the thermocouple // Injenerno-phisicheskij zournal 1964. Vo. 7. Vo. 6 P. 135 – 136.(in Rusian).
7. W.Mc Daniel Collision fenomena in ionized gases. N-Y, 1964.
8. L.G.H.Huxley, R.W. Crompton. The diffusion and drift of electrons in gases. N-Y, 1974.
9. Georgievsky P.Yu., Levin V.A. Gas dynamics effects for supersonic flow over space-distributed energy sources of high power // The second workshop on magnetic and plasma aerodynamics in space applications.-Moscow, April 5-7 2000.
10. Georgievsky P.Yu., Levin V.A. Supersonic flow of volumetric sources of energy release // Mechanics: modern problems. Moscowю MSU. 1987. P.93–99.

10. THE MODIFICATION OF AERODYNAMIC CHARACTERISTICS OF DIFFERENT BODIES BY MEANS OF ENERGY INPUT TO UPSTREAM FLOW

P.Yu.Georgievsky
Institute of Mechanics MSU, Moscow

V.A.Levin
Institute for Automation and Control Processes FED RAS, Vladivostok

Yu.L.Ivanov
Sukhoi Design Bureau, Moscow

Abstract. An action of a powerful space–distributed energy sources, including pulse periodic ones, on the flow over different bodies, located downstream, is discussed. The effect of reorganization of the flow over blunt bodies, when the relatively small portion of energy input into a local region leads to the significant modification of the flow regime, is pointed out. The flow over Su–27 fighter nose radome of ogival shape close to an optimal is investigated. It is shown, that an active action on the ambient flow by an energy input is an effective method of a wave drag reduction.

In experimental investigations the possibility of nonelectrode energy input into a supersonic flow due to the absorption of an electromagnetic radiation by the gas discharge plasma is confirmed. The real processes, accompanying this phenomena, are very complicated both from physical and mathematical points of view. However, regardless of true mechanism, the significant part of effects of an action of energy input on the flow and bodies, located in the flow, can be explained simply by the temperature increasing as a result of heating. In this situation the mathematical description of a whole range of physical phenomena is not necessary. On the contrary, an application of simple models allows one to concentrate efforts on detection and investigation of qualitative gasdynamic effects.

In theoretical papers [1-12] the energy input was modeling by a predetermined function of coordinates and time. It was shown, that the active action on the ambient flow by energy input is an effective way of improvement of aerodynamic characteristics of constructional elements of flying vehicles.

For steady regimes the infinite high temperature wake is formed behind the energy source. In paper [3] the effect of "saturation of the flow with energy" was pointed out. For spherical sources some parameters of the wake (in particular Mach numbers and total pressure) could not be "improved" by forcing of the energy source intensity. In papers [11–12] the effect of "continuous deceleration of the flow" under the longitudinal energy source size increasing was detected for the first time. In this case the bow shock wave is disappeared, the wake Mach numbers are continuously decreased and the remote wake is subsonic. The effect of "saturation of the flow with energy" can be negotiated this way and

the additional total pressure reduction by several times can be reached. In [9–12] the flows over energy sources in pulse-periodic regimes that are typical for experimental installations were investigated. The quasi-stationary regimes, when the resulting flow is not depended on the pulse duration and form is determined only by the total energy input during the period, are registered.

In present paper the comparative analysis of an action of powerful energy sources, including pulse periodic ones, on the flow over blunt and sharpen bodies is carried out.

The non-steady motions of an ideal gas with a distributed energy input are described in cylindrical coordinates r, z by Euler equations:

$$\frac{\partial}{\partial t}\begin{pmatrix} \rho \\ \rho u \\ \rho v \\ e \end{pmatrix} + \frac{\partial}{\partial r}\begin{pmatrix} \rho u \\ p+\rho u^2 \\ \rho uv \\ (e+p)u \end{pmatrix} + \frac{\partial}{\partial z}\begin{pmatrix} \rho v \\ \rho uv \\ p+\rho v^2 \\ (e+p)v \end{pmatrix} =$$

$$= \frac{1}{r}\begin{pmatrix} -\rho u \\ -\rho u^2 \\ -\rho uv \\ -(e+p)u \end{pmatrix} + \begin{pmatrix} 0 \\ 0 \\ 0 \\ \rho\dot{Q} \end{pmatrix}$$

The total energy of a volume unit is determined for an ideal perfect gas as follows:

$$e = \frac{p}{\gamma-1} + \frac{\rho}{2}\left(u^2+v^2\right)$$

The energy input density (to a mass unit per time unit) is assumed to be the predetermined function of coordinates and time:

$$\dot{Q}(r,z,t) = Q_0 f(t)\exp\left(-\left(\frac{r}{\Delta r}\right)^2 - \left(\frac{z-z_0}{\Delta z}\right)^2\right)$$

For pulse-periodic regimes the rectangular pulses of duration τ with a period T were applied:

$$f(t) = \begin{cases} 1, & \mod(t,T) \leq \tau \\ 0, & \mod(t,T) > \tau \end{cases}$$

All gasdynamic parameters are referred to p_∞, ρ_∞ and typical length L_∞. The dimensionless energy input intensity Q_0 is referred to $(p_\infty/\rho_\infty)^{3/2}/l_\infty$. The total power input $W(t)$ depends on the complete task approach and can be calculated numerically.

$$W(t) = \left(\int_V \rho\dot{Q}dV\right), \quad \tilde{W}(t) = W(t)p_\infty l_\infty^2\sqrt{\frac{p_\infty}{\rho_\infty}}$$

On bodies surfaces the condition of impermeability was applied. The numerical calculations were carried out for non-steady Euler equations even for steady energy sources $(f(t)\equiv 1)$ – method of an establishment with time for stationary tasks. The MacCormac method of second order accuracy with coordinates and time was used.

The energy input effectiveness as an instrument of wave drag reduction was estimated by special criteria:

$$k = \frac{\Delta F_x v_\infty}{\tilde{W}} = \frac{\gamma^{3/2}M_\infty^3 S_m \Delta c_x}{2W}$$

were S_m – midsection.

In [7] an action of energy sources of moderate intensity on the flow over sphere for $M_\infty=3$ was considered. The energy source radius and intensity were varied in such a way, that the criteria of similarity $Q_0\Delta r$=const for the flow over source was hold. Depending on Δr value different regimes of flows over sphere are possible (Fig.1). For relatively large energy sources the quasi-uniform flow is observed (Fig.1a). In this case the significant region of the sphere is positioned in the temperature wake. So the flow over sphere with reduced Mach number is realized. Correspondingly the bow shock distance increase and the static pressure on the surface decrease. For small energy sources the effect of reorganization of the flow is observed: the front separation zone and complicated shock wave structure are formed (Fig.1b). Thus, even relatively thin temperature wake provide a finite action on the flow over sphere. Table 1 contains calculated integral characteristics for different energy sources: wave drag reduction and energy input effectiveness. When decreasing Δr the wave drag gain Δc_x reduce, but remain finite due to the effect of reorganization of the flow. Taking into account that $W\sim\Delta r^2$, the saved power can multiple exceed the expended one. Thus, for bad-streamlined bodies, the effective wave drag reduction by an upstream energy input is possible.
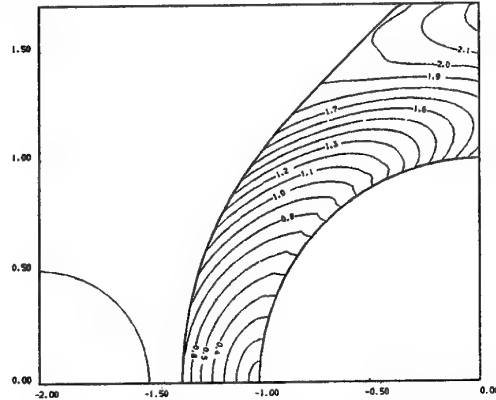
Fig.1a. Quasi uniform flow over sphere (Mach number isolines – Sf_04)
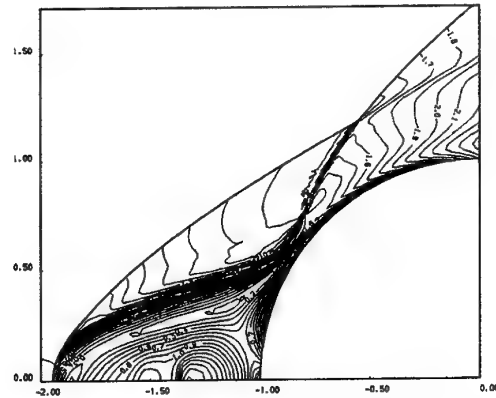
Fig.1b. Flow over sphere with a front separation zone (Mach number isolines – Sf_02)

Table 1. Wave drag reduction and the effectiveness of energy input for sphere

Variant	Description	c_x	Δc_x	$\Delta c_x\%$	W	k
Sf_00	$Q_0=0$, $M_\infty=3$, $\gamma=1.4$	1.007				
Sf_01	$Q_0=400$, $\Delta r=0.05$	0.846	0.161	15.98	0.278	40.7
Sf_02	$Q_0=200$, $\Delta r=0.1$	0.792	0.215	21.35	1.113	13.6
Sf_03	$Q_0=80$, $\Delta r=0.25$	0.710	0.297	29.49	6.960	3.00
Sf_04	$Q_0=40$, $\Delta r=0.5$	0.645	0.362	35.94	27.84	0.91

For estimation of an action of energy input on aerodynamics of well-streamlined bodies, the numerical simulation of Su–27 fighter nose radome was carried out. The technical documentation provided by Sukhoi Design Bureau was used for surface approximation. The radome was optimized for moderate supersonic flight speeds and is characterized by extremely low wave drag c_x=0.14 for M_∞=2. Calculations were executed for steady and pulse–periodic regimes of energy input into regions of different geometry.

Basic features of flows over radome are reflected by Fig.2. Shock waves are formed both ahead of the energy source and the body surface (Fig.2a). The "disappearing" of shocks in the temperature wake region (Fig.2b) can be explained by major density decreasing. The isolines step is optimized for shock wave fixation in the ambient flow, so it is insufficient when the absolute shock value in the high temperature wake is reduced. In contrast to the flow over sphere, the flow remains regular and separated zones are not formed.

a) pressure isolines

b) density isolines
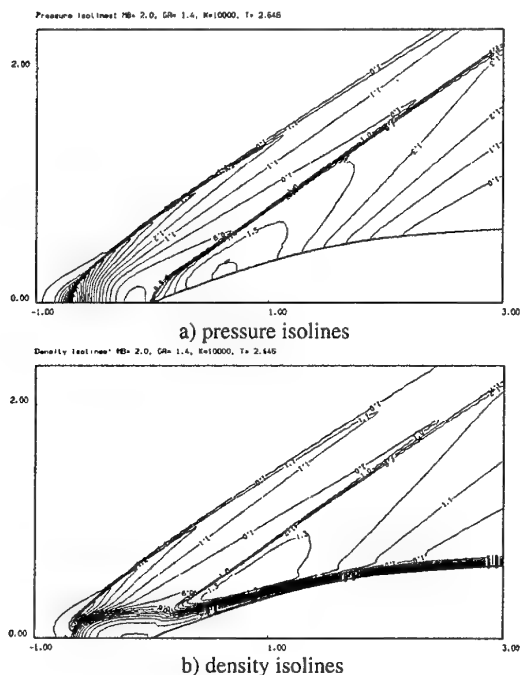
Fig.2. Steady flow over Su-27 fighter nose radome (Var06)

For verification of the effect of "saturation of the flow", the action of forcing of energy source intensity Q_0 on the assumption of conservation of geometry parameters is investigated. Distributions of parameters with z on the symmetry axes and than along the body surface are presented on Fig.3 and integral characteristics summarized in Table 2. An action of the energy input on the pressure

a) pressure distribution on the surface

b) density distribution on the surface
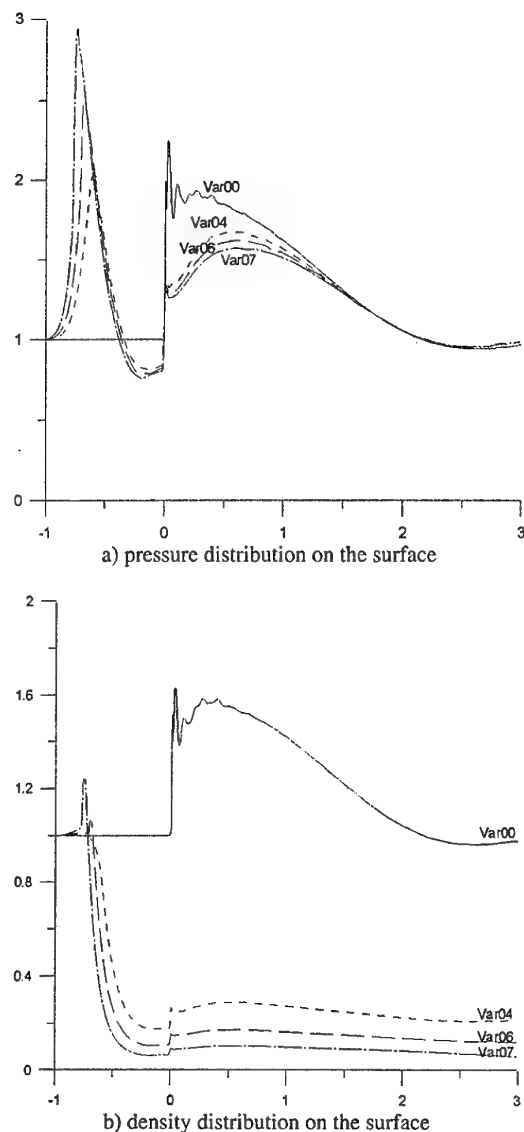
Fig.3. Steady flow over Su-27 fighter nose radome for ellipsoidal energy sources of different intensity Q_0.

Table 2. Wave drag reduction of Su-27 fighter nose radome and effectiveness of energy input (ellipsoidal energy sources of different intensity Q_0).

Variant	Description	c_x	Δc_x	$\Delta c_x\%$	W	k
Sf_00	Q_0=0, M_∞=2, γ=1.4	0.140				
Sf_04	Q_0=100, Δr=0.1, Δz=0.2	0.120	0.020	14.28	0.775	0.208
Sf_06	Q_0=200, Δr=0.1, Δz=0.2	0.113	0.027	19.28	1.220	0.179
Sf_07	Q_0=80, Δr=0.1, Δz=0.2	0.108	0.032	22.85	1.790	0.144

75

Variant	Description	c_x	Δc_x	$\Delta c_x\%$	W	k
Sf_00	$Q_0=0$, $M_\infty=2$, $\gamma=1.4$	0.140				
Sf_03	$Q_0=400$, $\Delta r=0.05$	0.134	0.006	4.28	0.240	0.202
Sf_01	$Q_0=200$, $\Delta r=0.1$	0.122	0.018	12.85	0.926	0.151
Sf_02	$Q_0=100$, $\Delta r=0.2$	0.087	0.053	37.85	3.850	0.111

distribution is restricted by the temperature wake region (Fig.3a). The dimension of this region is not varied and static pressure decrease slightly when forcing Q_0 above some critical value (the effect of "saturation of the flow"). Consequently, wave drag c_x reduction is "saturated" (Table 2). On the contrary, the power input W increase and so the effictiviness k decrease. According to analysis of fig.3b the conclusion can be made that the extra power is spend for multiply temperature increasing (density decreasing) in particular on the body surface. This circumstance must be taking into account when planning application of an energy sources for wave drug reduction of real flying vehicles.

Flows over spherical energy sources of different radious were investigated. The criteria of similarity $Q_0\Delta r$=const for the flow over sources was hold. As it was previously pointed out, the flows over sharpen bodies remain regular and the influence of energy source on the pressure distribution is restricted by a local region of temperature wake. Table 3 accumulates integral characteristics of flows. For energy sources of relatively large size the significant wave drag reduction can be obtained, when $\Delta r \to 0$ the action of energy input is infinitesimal. The effectiveness k of energy input is stably low though increasing slightly for source radius decreasing.

In [11–12] the positive action of the energy source longitudinal size Δz (Δr=const) icreasing was underlined. Energy sources referred to as "equivivalent" if $Q_0\Delta z$=const (the same power in assumption that $\rho=\rho_\infty$ in formula for W). The comparison of Var04 (Table 2) and Var01 (Table 3) confirm the conclusion [11–12]. For ellipsoidal energy source the larger wave drag reduction Δc_x can be reached with smaller energy input W.

The pulse–periodic regime of energy input into a supersonic flow is typical for experimental installations. Numerical simulations was carried out for rectangular pulses with different period T and constant factor $T/\tau=2$. On Fig.4 the essentially

unsteady and quasistationary regimes are presented in comparison. The regimes are equivalent by power input during the period to Var06 (Fig.2). In the first case (Fig.4a) every new pulse is similar to the "blust" in the flow and generates shock waves and local temperature regions, wich than drifts down along the body surface. In the second case (Fig.4b) the flowfield picture is similar to the steady one (Fig.2b). The quasistationary shock wave structure and high temperature wake are formed. The dependenses of wave drag coefficient c_x with time for spherical and ellipsoidal energy sources are presented on Fig.5. For essentially unsteady regimes the pulsing dynamic action on the body is typical for both cases. Curves for steady and quasistationary regimes are practically identical. Thus, in experiments the steady energy source can be replaced by pulse-periodic one with equivalent action on the flow and bodies, located downstream.

a) essentially unsteady regime

b) quasi-stationary regime
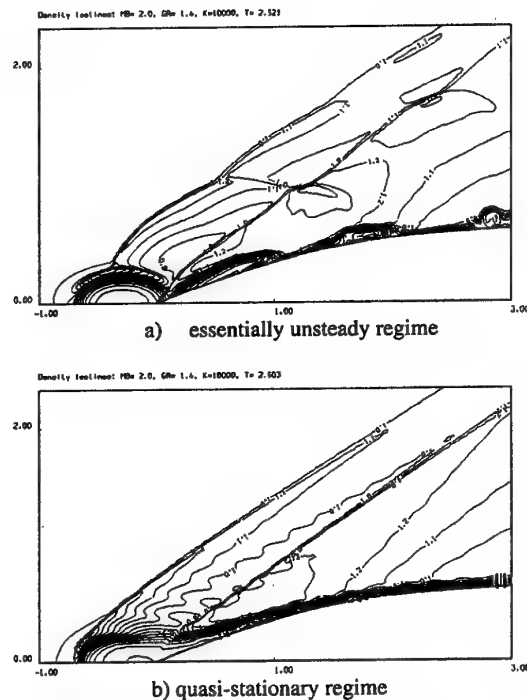
Fig.4. The flow over Su-27 fighter nose radome for pulse-periodic energy sources (density isolines).

The basic conclusion. An action on a ambient supersonic flow by localized energy input, even in pulse-periodic mode, allow one essentially improve aerodynamic characteristics of different bodies. The effectiveness of this method depends on many factors: body and energy source geometry, input power, time characteristics.

Var02 – $Q_0 = 100, \Delta r = 0.2$
Var13 – $Q_0 = 200, \Delta r = 0.2, T = 0.5, \tau = 0.25$
Var14 – $Q_0 = 200, \Delta r = 0.2, T = 0.1, \tau = 0.05$

a)   spherical energy sources

Var06 – $Q_0 = 200, \Delta r = 0.1, \Delta z = 0.2$
Var11 – $Q_0 = 400, \Delta r = 0.1, \Delta z = 0.2, T = 0.5, \tau = 0.25$
Var12 – $Q_0 = 400, \Delta r = 0.1, \Delta z = 0.2, T = 0.1, \tau = 0.05$

b) ellipsoidal energy sources
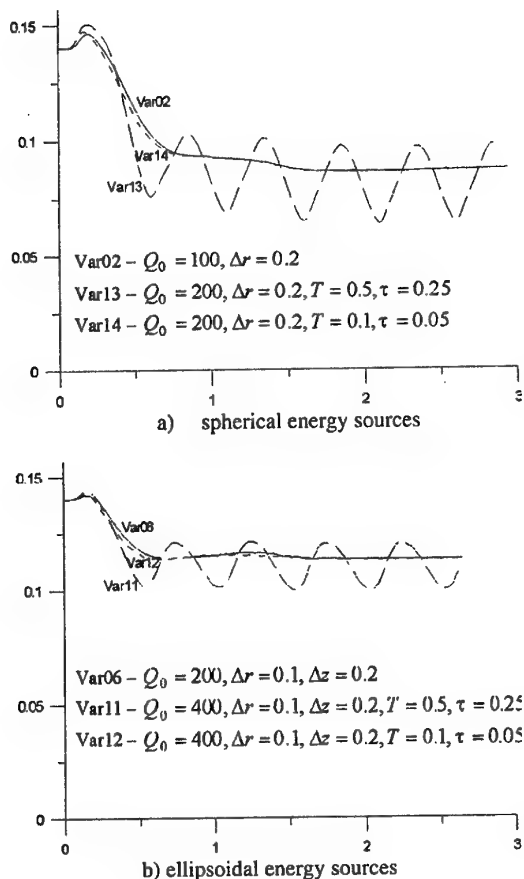
Fig.5 Wave drag coefficient c_x dynamic with time

References

1. Georgievsky P.Yu., Levin V.A. Supersonic flow over space-distributed energy sources // Mechanics, modern problems. Moscow. MSU Pub. 1987. Pp.93–99 (in Russian)

2. Arafailov S.I. The influence of an energy input in the shock layer on supersonic flight of bodies // Izv. AN SSSR, MGG. – 1987. – No.4. – P.178–182 (in Russian).

3. Georgievsky P.Yu., Levin V.A. Supersonic flow over bodies in presence of external heat supply sources // Pisma v GTF. – 1988. – Vol.14, No.8. – P.684–687 (in Russian).

4. Bazhenova T.V., Liahov V.N., Pankova M.B., Kharitonov S.M. Numerical modeling of an influence of a heat nonuniformity in a supersonic flow on the drag coefficient of spherical body // Numerical modeling of unsteady gasdynamic and MHD flows. – Moscow: IVTAN Pub, 1989. – P.53–64 (in Russian).

5. Levin V.A., Terentieva L.V. Supersonic flow over a cone in the presence of a heat supply in the vicinity of its vertex // Izv.RAN, MGG. – 1993. – No.2. – P.110–114 (in Russian).

6. Borzov V.Yu., Ribka I.V., Yuriev A.S. The influence of a local energy supply into a hypersonic flow on the drag of bodies with different blunting // IFG. – 1994. – Vol.67, No.5–6. – P.355–361 (in Russian).

7. Georgievsky P.Yu., Levin V.A. Modification of regime of the flow over a sphere by means of local energy supply upstream // International Conference on the Methods of Aerophysical Research: Proc. Pt III. - Novosibirsk, 1996, pp.67–73.

8. Korotaeva T.A., Fomin V.M., Shashkin A.P. Numerical investigation of the local energy supply action on the 3-D flow over sharpen bodies // ITAM RAN Pub. Novosibirsk 1996. No.1, 36 p. (in Russian)

9. Guvernyuk S.V., Samoilov A.V. Control of supersonic flow around bodies by means of pulsed heat source // Pisma v GTF. 1997. Vol.23. No.9, pp.1–9 (in Russian).

10. Georgievsky P.Yu., Levin V.A. Unsteady effects for a supersonic flow past a pulsing energy source of high power // International Conference on the Methods of Aerophysical Research: Proc. Pt II. – Novosibirsk, 1998, pp.58-64.

11. Georgievsky P.Yu., Levin V.A. Gas Dynamics Effects for Supersonic Flows over Space-Distributed Energy Sources of High Power // The 2nd Workshop on Magneto-Plasma-Aerodynamics in Aerospace Applications: Proc. – Moscow, 2000, pp.94–97.

12. Georgievsky P.Yu., Levin V.A. Supersonic Flow over Sharpen Bodies in Presence of an Unsteady Energy Supply Upstream // International Conference on the Methods of Aerophysical Research: Proc. Pt III. – Novosibirsk, 2000, pp.45–50.

11. GAS DYNAMICS OF SUPERSONIC WAKE BEHIND A PLANAR ENERGY SOURCE

D.I. Goryntsev, A.A. Ignatiev, G.A. Lukianov
Saint-Petersburg State Technical University
195251, Russia, Saint-Petersburg, Politechnicheskaya street, 29

Abstract. Gas dynamic structure and parameters of supersonic wake behind a planar energy source were investigated. The subcritical regimes of energy input (regimes of weak detonation or supersonic combustion) are considered. The planar and the axisymmetric flow of a monoatomic gas were analyzed. Two numerical approaches: the direct simulation Monte Carlo and the complete Navier-Stokes equations were used for the investigation. The investigation was carried out for the range of Mach number M=5-20 and Reynolds numbers Re=1-10^5 of undisturbed flow.

The peculiarity of this kind of supersonic flows is small velocity variation in the flowfield. For Re>Re_k ($Re_k \approx 100$ - for planar, $Re_k \approx 10^4$ - for axisymmetric flow) this fact leads to the formation of a very long high-temperature region with almost constant parameters near the axis behind the initial gas dynamic region. In this region density and dynamic pressure are significantly lower than in the undisturbed flow. This effect may be used for reduction of drag and thermal loadings of an object by energetic influence on supersonic flow in front of the object.

Introduction

The works [1-3] were focused on the investigations of supersonic flow behind a planar energy source, which constitutes the gas dynamic discontinuity with energy input. Supersonic wake behind such energy source represents the supersonic under-expanded jet in the supersonic concurrent flow. Under certain conditions in the paraxial zone of the wake the value of dynamical pressure can be considerably lower than in undisturbed flow. The object's drag in this wake zone is lower than in undisturbed flow. The effect of the object drag (and heat loading) decrease, naturally, depends on the wake gas dynamic structure and position of the object in the wake.

This work continues the investigations [1-3]. Here, the results of the numerical flow investigations in the wake behind a planar discontinuity with energy input, in the weak detonation regime (supersonic combustion) are discussed. The planar and axisymmetric monoatomic gas (argon) flow is considered. The investigation is carried out for the numbers M=5-20, characteristic Reynolds numbers Re=1-10^5 (from free-molecular to continual flow regimes) and different values of energy input.

1. Parameters of the energy source

Parameters behind a planar energy source are determined by the mass, energy and impulse conservation laws, amplified with the state equation

$$\rho_i \cdot u_i = \rho_\infty \cdot u_\infty , \qquad (1)$$

$$p_i + \rho_i \cdot u_i^2 = p_\infty + \rho_\infty \cdot u_\infty^2 , \qquad (2)$$

$$\rho_i u_i \left(\frac{u_i^2}{2} + c_p T_i \right) = \rho_\infty u_\infty \left(\frac{u_\infty^2}{2} + c_p T_\infty \right) + \\ + \rho_\infty u_\infty q , \qquad (3)$$

$$p = \rho \cdot R \cdot T . \qquad (4)$$

Here ρ - density, p - pressure, T - temperature, u - longitudinal velocity component, R - gas constant, c_p - specific heat capacity at constant pressure, q - energy input to the mass unit at time unit in the source, indexes ∞ and i are related to the parameters on front of and behind the source accordingly.

Solution of the system of equations (1)-(4) for the weak detonation regime can be presented in the following way [1].

$$\lambda_i = \frac{1}{2(1+\beta)^{1/2}} \times$$

$$\times \left\{ \lambda_\infty + \frac{1}{\lambda_\infty} \pm \left[\left(\lambda_\infty - \frac{1}{\lambda_\infty} \right)^2 - 4 \cdot \beta \right]^{1/2} \right\} . \qquad (5)$$

$$\frac{\rho_i}{\rho_\infty} = \frac{\lambda_\infty}{\lambda_i} \qquad (6)$$

$$\frac{T_i}{T_\infty} = \frac{1 - \lambda_i^2}{1 - \lambda_\infty^2 / \varepsilon} (1 + \beta) \qquad (7)$$

$$\frac{p_i}{p_\infty} = \frac{\rho_i \cdot T_i}{\rho_\infty \cdot T_\infty} . \qquad (8)$$

Here, $\lambda = u/u_*$ - velocity coefficient, u_* - critical velocity, $\beta = q/c_p T_{0\infty}$ - heating parameter, $T_{0\infty}$ - the stagnation temperature of the flow at the infinity, $\varepsilon = (\gamma+1)/(\gamma-1)$, γ - ratio of heat specific capacities.

The important peculiarity of the gas flow through the gas-dynamic discontinuity with energy input is relatively small variation of u and ρ with considerable change of T and p [2]. For the monoatomic gas the change of u at the discontinuity is in the limit $1 > u_i/u_\infty > \gamma/(\gamma+1)$. The limit value of energy input in the weak detonation regime for monoatomic gas corresponds to $\lambda_i = 1$, M_i=1 and $\beta = 0.56$ [1].

2. Computation methods

For the simulation of the flow in the wake two methods are applied: direct Monte Carlo simulation method (DSMC) and numerical method of solving the complete system of Navier-Stocks equations (NSE). For DSMC the program of direct simulation, based on the Bird's version [4], was used. The DSMC algorithm is described in [5]. In the terms of molecular gas dynamics the wake flow is determined completely by the set of the following basic parameters: M, Re, heating parameter β and particles model [5]. The model of particles is the model which determines the section and mechanics of particles collisions. The collisions were supposed to be elastic. For the collision partners selection the NTC Bird's scheme was used. The mechanics of intermolecular collisions corresponded to the VHS model [4]. The algorithm of data parallelization of DSMC for multiprocessor computers with shared memory [6] were used for computation.

In NSE approximation the calculation algorithm is based on the method of physical factors splitting. In accordance with this method within one time iteration the whole problem is replaced with two more simple problems - inviscid gas flow problem and problem which incorporates viscous momentum transfer processes, energy dissipation and thermal conductivity. For numerical solution of non-viscous problem explicit ENO scheme of the second precision order was used [7], and for the solution of the viscous problem explicit scheme with the use of central differences was used [8]. The perfect gas flow was simulated. In the NSE approximation wake flow is completely determined by the values M_∞, Re_∞, β and ratio of specific heat capacities γ (here γ=1.67).

Setting of M_∞, T_∞ and β determines gas dynamics parameters of the gas behind energy source (x=0, $y \le R$) uniquely. The rectangular simulation region was used. At the input (x=0, y>R) undisturbed flow parameters were settled. Transverse region size was selected rather big in order to exclude the impact of side bounds on the flow. In DSMC the "condensable" wall condition (particles that reached the exit bound, were excluded from consideration) at the exit boundary was used, in NSE approximation traditional "soft" conditions were used. The problem was solved by the time-asymptotic approach.

3. Computation results and analysis

The computations in the range of numbers $Re = \rho_\infty u_\infty R/\mu_\infty = 1 - 10^4$ were carried out by DSMC, in the range of numbers $Re_\infty = 10^3 - 10^5$ by NSE (R - radius or half-width of energy source, μ_∞ - dynamical viscosity). In the range of numbers $Re_\infty = 10^3 - 10^4$ the results of the computation by both methods correlate with each other successfully. The main attention is paid to the jet flow gas dynamic structure specifications behind energy source. As it was already mentioned this flow is considered to be laminar under-expanded supersonic jet in the supersonic concurrent flow. The simulation region includes initial gas dynamical and transitional stream segments. For the initial segment the presence of shock-wave structure and strong pressure non-uniformity in longitude and transversal direction is typical. On transitional segment the viscosity impact gradually becomes determinative. Longitude and transversal pressure gradients decrease considerably. At the end of the transitional segment the isobar flow establishes.

In the Fig.1 (on the left) gas dynamic structure and parameters of the axisymmetric jet initial segment behind energy source (qualitative picture corresponding approximately to the ideal gas flow, i.e. $Re \to \infty$) are shown. The gas heating in energy source leads to increase of pressure and consequent gas expansion. In the wake behind the source there is a formation of the structure which incorporates several surfaces of strong discontinuity: head shock wave 1; tangential discontinuity 2, which divides cold and hot gases; hanging shock ACA etc. In the free ACA expansion region, which is limited by the hanging shock, gas expands intensively. This process is accompanied with decrease of p, ρ, T and increase of u, M. Dynamical pressure $p_D = \rho u^2/2$ drops to the value that is considerably smaller than $p_{D\infty} = \rho_\infty \cdot u_\infty^2/2$. Analogous gas dynamic structure and parameters of the planar flow behind energy source are shown in the Fig.1 (on the right).
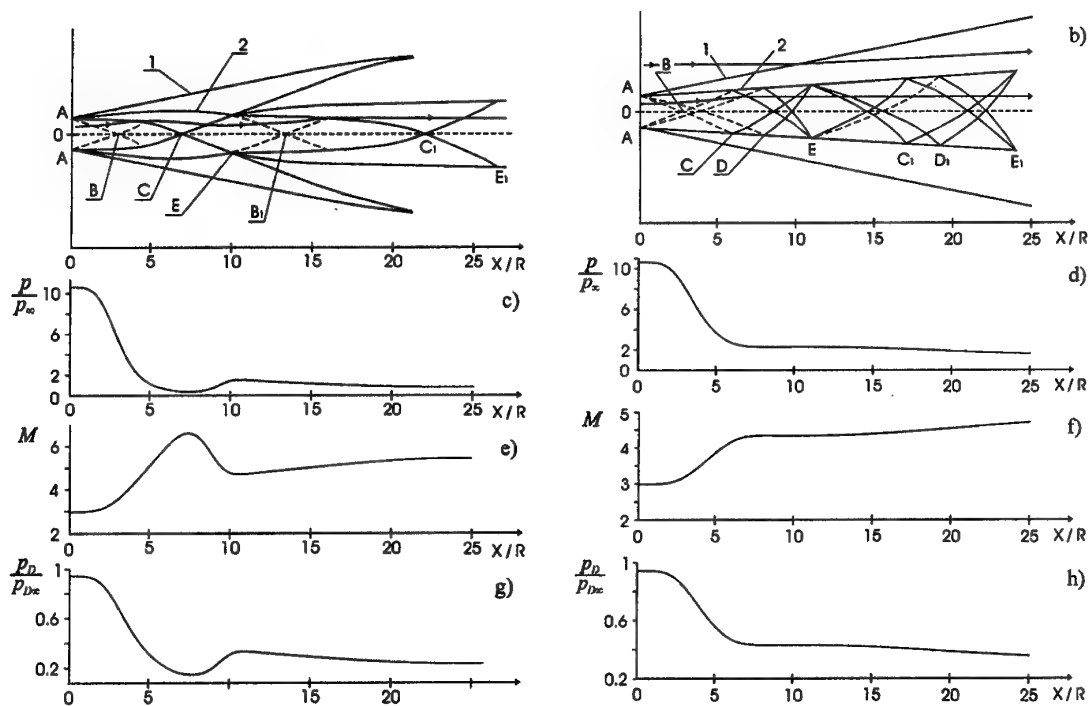
Fig.1. Gas dynamic structure of the initial segment (a, b) and axial profiles p/p_∞ (c, d), M (e, f) and $p_D/p_{D\infty}$ (g, h) for axisymmetric (on the left) and planar (on the right) flow behind an energy source; Ar, $M_\infty=10$, $\tau=10$, $\beta=0.15$, $Re=6.5\times10^4$.
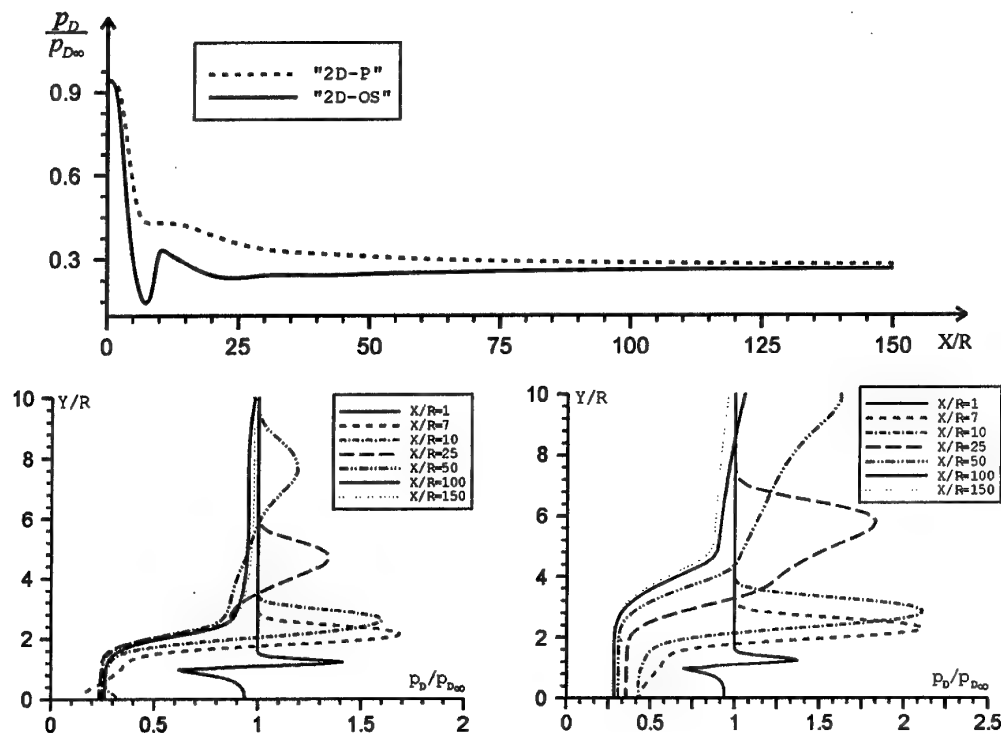
Fig.2. Axial (a) and transversal profiles $p_D/p_{D\infty}$ for axisymmetric (b) and planar (c) flow behind energy source; Ar, $M_\infty=10$, $\tau=10$, $\beta=0.15$, $Re=6.5\times10^4$.

80
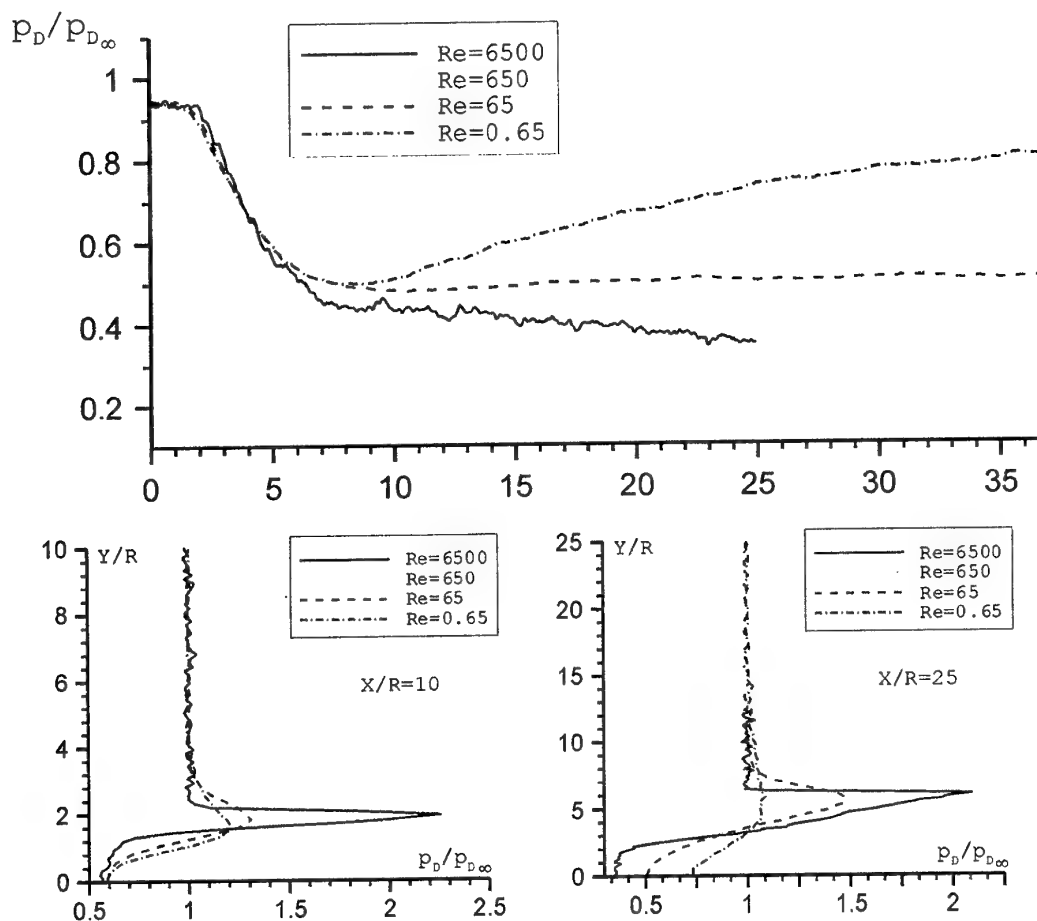
Fig.3. Axial (a) and transversal (b, c) profiles $p_D/p_{D\infty}$ in planar flow behind energy source under different numbers Re_∞.

The planar flow structure differs from the axisymmetric flow structure significantly. The main difference consists in the absence of strong inner compression shocks in the heated gas planar flow.

Gas dynamic structure of the inner segment determines the flow on the transitional jet segment. In the Fig.2 axial and transversal profiles p_D on the initial and transversal segments for the axisymmetric (b) and planar (c) flow behind energy source are shown. The simulation results demonstrate the effect of anomaly big long "range" - unusually long transitional segment with maintainance of paraxial zone with almost invariable parameters and transversal size. For the computation variant which is represented in the Fig.2, the transversal size of the axisymmetric zone is approximately $3R$, for the planar − $6R$. The stability of the parameters in paraxial zone is kept within the whole simulation region.

Regimes with large "range" realize in planar flow at $Re>10^2$ and axisymmetric flow at $Re>10^4$. At smaller numbers Re there is no paraxial area with stable parameters on the transitional segment. In the Fig.3 axial and transversal profiles $p_D/p_{D\infty}$ for planar flow under Re=0.65-6500, obtained by DSMC, are shown.

As it is shown by the present investigations supersonic jet flows behind planar energy source form the separate class of jet flows with their special features. The presence of extended regions with decreased dynamical pressure in these gets can be used to obtain the drag decrease and object's heat loading, placed in the wake behind energy sources of this type.

81

References

1. Lukianov G.A. On the resistance of a body in supersonic flow with planar source located in front of the body. Technical Physics Letters, Vol. 24, Issue 24, 1998, p.76-82
2. Lukianov G.A. On the resistance and the heat exchange of a body in supersonic flow with planar source located in front of the body. Preprint № 04-98, IHPCDB, St. Petersburg, 1998, p.19.
3. Lukianov G.A. Drag and heat exchange of an object in a supersonic flow with a source of energy in front of the object. The 2-nd workshop on magneto-plasma-aerodynamics in aerospace applications, Moscow, 5 April - 7 April 2000, IHTRAS, pp. 133-137.
4. Bird G.A. Molecular gas dynamics and the direct simulation of gas flows.- Clarenton Press. Oxford. 1994, pp. 451.
5. Grishin I.A., Zakharov V.V., Lukianov G.A. Algorithm of parallel direct simulation Monte Carlo in molecular gas dynamics (data parallelezation). Preprint № 3-98, IHPCDB, St. Petersburg, 1998, p.32.
6. Khanlarov G.O., Lukianov G.A., Malashonok D.Y., Zakharov V.V. Parallel DSMC on Shared and Hybrid Memory Multiprocessor Computers. M. Bubak et al. (Eds.): NPCN'2000, LNCS 1823, pp. 584-587, 2000. Springer-Verlag-Berlin Heidelberg 2000.
7. 7. Yang J.Y., Hsu C.A. High-Resolution, Nonoscillatory Schemes for Unsteady Compressible Flows // AIAA J., v.30, № 6, 1992, pp. 1570-1575.
8. Varentsov V.L., Ignatiev A.A. Numerical investigations of internal supersonic jet targets formation for storage rings. // Nuclear Instruments and Methods in Physics Research A 413 (1998), pp. 447 - 456.
9. Dulov V.G., Lukianov G.A. Gasodinamika processov istecheniya, Nauka, Novosibirsk, 1984, p.234.

12. ESTIMATION OF POWER EFFICIENCY OF HEAT APPLICATION BEFORE A BODY IN A SUPERSONIC GAS FLOW

A.F. Latypov, V.M. Fomin
Novosibirsk.

Abstract. The criteria for an estimation of power efficiency of heat application before a body in a supersonic gas flow are obtained. On the basis of functional purposes of vehicles and thermodynamic model of process the estimations for vehicles "bullet" and "airplane" types are executed. The estimations of the minimal Much numbers, since which heat application before a body is expedient are given. The estimations of increase of range of flight on cruise regime for the vehicle "airplane" such as and on an active part of trajectory for the vehicle "bullet" are executed. The estimations of economy of fuel are obtained at ascent the air-space "airplane" on near-Earth orbit. Is shown, that for reception of real effect it is necessary an essential part of spent fuel to put on reception of energy on heating of gas. Therefore realization of such way of the vehicle airflow control will require, apparently, essential change of the engine installation circuit. The estimation of minimal required "efficiency coefficient" of transformation of energy of fuel to energy of heating of gas is given also.

The numerous experimental researches of the aerodynamic characteristics hypersonic vehicle (HV) testify, that their maximal lift-drag ratio in hypersonic range of speeds makes about $K_{max} \approx 4$. This value fail to increase by means of aerodynamic designing of HV configurations. Therefore last years the significant attention is given to a problem of active control of a airflow by means of power and /or of force influence on approach flow, in particular, - by means of heat application before a body in a supersonic gas flow. The significant number of works are devoted to this problem, only small part from which is given in the list of the quoted here literature. For technical realization use laser and microwave - radiation is supposed. The aerodynamic effect - reduction of resistance - communicates, mainly, with reduction of gas density in approach flow, that proves to be true by direct measurements [15]. The additional effects are probable because of change of a flow regime owing to reduction of Much number, change of Reynolds number, ionization of a flow. In the majority theoretical and experimental researches the problem of aerodynamic drag reduction is studied. In theoretical work [2] on an example of a hypersonic gas flow of a tapered airfoil the significant influence of heat application on lift is shown. Is established, that optimum for a condition of the maximal lift-drag ratio is a gliding regime.

Traditionally efficiency of heat application in the steady flight is estimated by value ([1])

$$\eta = \frac{A_0 - A}{Q} \qquad (1)$$

where A_0 - initial thrust power, A - thrust power at thermal action, Q - heat application power. In this parameter the complete power balance and functional purpose of the vehicle is not taken into account. In the given work the efficiency is estimated in view of the named circumstances.

Mathematical model.

It is supposed, that heat application in approach flow is carried out at constant value of pressure and speed so, that the infinite thermal trace with parameters before a body is realized as follow:

$$P = P_\infty, \quad V = V_\infty, \quad \frac{T_\infty}{T} = \frac{\rho}{\rho_\infty} = \frac{F_\infty}{F_0} = \varepsilon. \qquad (2)$$

Here P - pressure, V - velocity, T - temperature, F - cross-section of a trace, ρ - density, F_0 - middle of the vehicle, "∞"- gas parameters on infinity, ε - in subsequent predetermined parameter.

Thermal power of a trace:

$$Q = \rho_\infty V_\infty F_0 c_p T_\infty (1-\varepsilon), \qquad (3)$$

c_p - heat capacity of air.

It is supposed also, that the vehicle with lift, carries out flight in a gliding regime the lift basically is created by the bottom vehicle surface, streaming by no disturbance flow of air, i.e.

$$Y_0 = c_y^0 q_\infty^0 S, \qquad (4)$$

c_y^0 - initial lift coefficient, $q_\infty^0 = \frac{1}{2}\rho_\infty V_\infty^2$ - velocity head, S - area of vehicle in the plan.

Approximately aerodynamic drag we shall share into two components:
1-st - longitudinal component of normal force acting on the bottom surface $X_1 = c_{x1}^0 q_\infty^0 S$, **2-nd** - drag of a body which is taking place in a thermal

trace $X_2 = c_{x2}^0 q_\infty S$. In a supersonic range of speeds at small attack angels α_A is proved the follow relationship: $c_{x1}^o = c_y^0 \alpha_A$, and for the second components let's assume $c_{x2} = c_{x2}^0 \xi$, where ξ - factor which account change of drag coefficient because of the mentioned above possible change of a regime of a airflow. Then

$$X = (c_{x1}^0 q_\infty^0 + \xi c_{x2}^0 q_\infty) S. \tag{5}$$

At the made assumptions concerning structure of aerodynamic drag for an initial regime we shall obtain

$$\bar{c}_{x2}^0 = \frac{c_{x2}^0}{c_x^0} = 1 - \alpha_A K_0, \tag{6}$$

Where $c_x^0 = c_{x1}^0 + c_{x2}^0$, K_0 - lift-drag ratio in an initial regime. At thermal action for relative lift-drag ratio we shall obtain an estimation

$$\frac{1}{\bar{K}} = \frac{K_0}{K} = 1 - (1 - \varepsilon \xi) \bar{c}_{x2}^0 \tag{7}$$

Cruise flight of the plane

The equations of movement at cruise flight look as follow:

$$\dot{L} = V_\infty;$$
$$\dot{m} = -\frac{R}{I} - \frac{Q}{\eta_Q Hu};$$
$$R = \frac{X_0}{\bar{K}}; \tag{8}$$
$$mg = Y_0;$$

Here L - range of flight; R- draft of the engine; m - weight of the plane; I - specific impulse of the engine; Hu - caloricity of fuel; η_Q - factor of transformation of energy of fuel to energy absorbed by air. For range of flight we shall obtain follow expression:
$$L = -\eta_L Br \ln(1 - g_T)$$
$$Br = \frac{V_\infty K_0 I}{g}$$

$$\frac{1}{\eta_L} = \frac{RV_\infty + \dfrac{Q}{\eta_Q}}{R_0 V_\infty} = \tag{9}$$
$$= \frac{1}{\bar{K}} + \frac{1-\varepsilon}{\eta_Q} \cdot \frac{\bar{F}_0}{c_x^0 \dfrac{\kappa-1}{2} M_\infty^0} \cdot \frac{Ia_\infty}{Hu}$$

$$\frac{1}{\bar{K}} = 1 - (1 - \varepsilon \xi) \bar{c}_{x2}^0$$

Here: Br - Breget factor for an initial regime of flight; a_∞ - sonic speed in approach flow on infinity; k - adiabat parameter; η_L - factor of increase of range of flight owing to thermal action to approach flow equal to the ratio of initial engine power to the sum of engine power at action to a flow with energy of fuel, spent on creation of the absorbed radiation Q. Also important characteristic is the ratio of expenses of fuel g_{TQ} for create the energy of radiation to expenses of fuel g_{TR} for create the draft R:

$$z = \frac{g_{TQ}}{g_{TR}} = \frac{1-\varepsilon}{\eta_Q} \cdot \frac{\bar{F}_0 \bar{K}}{\dfrac{\kappa-1}{2} c_x^0 M_\infty^0} \cdot \frac{Ia_\infty}{Hu} \tag{10}$$

Estimations

For performance of estimations the following initial values of parameters, typical for HV with ramjet engine on hydrogen are used:

$K_0=4$; $\alpha_A=2°\div3°$ $\Rightarrow$ $\bar{c}_{x2}^0 = 0.8$; $c_Y^0 = 0.1$; $\xi = 1$;

$\beta = \dfrac{Hu}{Ia_\infty} \approx 10$.

Parameter η_Q is accepted equal $\eta_Q=0.2$, since at smaller values such control of a flow is poorly effective. We receive the following values of increase of lift-drag coefficient at various degrees of air heating $1/\varepsilon$:

$\varepsilon =|$ 0.10 0.20 0.30 0.40

$\dfrac{1}{\bar{K}} =|$ 0.28 0.36 0.44 0.52

These results on increase of lift-drag coefficient are close to the data from work [2]. At $\varepsilon=0.4$ for Mach numbers $M_\infty^0 = 10; 15$ the estimations for factor η_L have the following values $\eta_L=1.22$; 1.39. Value z at $M_\infty^0 = 10$ equally $z\approx0.4$, that testifies to significant expenses of energy for a flow control.

From a condition $\eta_L=1$ determine the value of minimal Mach number, since which it is expedient to heat up approach flow:

$$M_\infty^{0\min} = \frac{\bar{F}_0}{\dfrac{\kappa-1}{2} c_{x2}^0 \eta_Q} \cdot \frac{Ia_\infty}{Hu}. \tag{11}$$

For conditions of estimations we shall obtain $M_\infty^{0\min} \cong 6$.

Limiting relations

Under condition of $\varepsilon \to 0$ we shall obtain:

$$\overline{K} \to \frac{1}{\alpha_A K_0}; \quad z \to \frac{\overline{F_0}\,\overline{K}}{\eta_Q \beta \frac{\kappa-1}{2} c_x^0 M_\infty^0}; \quad \eta_L \to \frac{\overline{K}}{1+z}$$

At $M_\infty^0 \to \infty$ accordingly we have $z \to 0$; $\eta_L \to \overline{K}$, i.e. with increase of speed of flight the efficiency of control is increased, and with this a part of energy spent for control, decreases.

Range of flight of a "bullet" body on an active journey leg

The equations of motion have a follow form:

$$L = V_\infty t;$$
$$\dot{m} = -\frac{R}{I} - \frac{Q}{\eta_Q Hu}; \tag{12}$$
$$R = X.$$

And the relative range of flight $\overline{L} = L/L_0$ is determined from the following expressions

$$\overline{L} = \eta_L (1 - \frac{\Delta \overline{m}_k}{g_T});$$

$$\frac{1}{\eta_L} = \frac{RV_\infty + \dfrac{Q}{\eta_Q}}{R_0 V_\infty} = \tag{13}$$

$$= \varepsilon\xi + \frac{1-\varepsilon}{\eta_Q} \frac{1}{c_x^0 \frac{\kappa-1}{2} M_\infty^0} \frac{Ia_\infty}{Hu}$$

Here g_T - initial relative fuel reserve in the vehicle; $\Delta \overline{m}_k$ - relative increase of weight of a design of an additional source of energy. For this variant the minimal value of Mach number, since which it is expedient to heat up an approach flow, is determined from expression:

$$M_\infty^{0\min} = \frac{1}{\dfrac{\kappa-1}{2} c_x^0 \eta_Q} \frac{Ia_\infty}{Hu} \tag{14}$$

Estimations.

For performance of estimations the following reference values of parameters are used: $c_x^0 = 0.3; \eta_Q = 0.2; \beta = 30; \varepsilon = 0.4; \xi = 1$. We shall obtain: the minimal Mach number $M_\infty^{0\min} = 2.8$;

factor of increase of range at $M_\infty^0 = 4.0$ is equal $\eta_L = 1.22$.

Flight with acceleration.

The equations of motion in a two-dimensional case have a follow form:

$$\frac{V_{op6}}{g}\dot{w} = \frac{R}{mg} - \frac{1}{K}\frac{Y}{mg} - \sin\theta = n_V$$
$$\dot{m} = -\frac{R}{I} - \frac{Q}{\eta_Q Hu}$$
$$\frac{Y}{mg} = \cos\theta(1 - w^2); \tag{15}$$
$$w = \frac{V}{V_{op6}}; \quad V_{op6} = \sqrt{g\,R_{земли}}.$$

The relative mass consumption on unit of increment of relative velocity is equal

$$\frac{1}{\overline{m}}\frac{d\overline{m}}{dw} =$$
$$-\frac{V_{op6}}{I}\left[1 + \frac{1}{Kn_V}\cos\theta\left(1-w^2\right) + \sin\theta\right] - \tag{16}$$
$$\frac{2\overline{F_0}c_p T_\infty^0(1-\varepsilon)}{\eta_Q Hu} \frac{q_\infty}{m_0 g/S} \frac{1}{n_V \overline{m} w}$$

Estimations.

For an example we execute an estimation of the relative mass consumption at the following values of parameters: $M_\infty^0 = 10; \quad q_\infty^0 = 0.5[bar]; \quad n_V = 0.5; K_0 = 3.5; \varepsilon = 0.4; \overline{K} = 2; I = 1.5\cdot10^3[m/s]; \overline{F_0} = 0.1; \dfrac{q_\infty^0}{m_0 g/S} = 10; ; \eta_Q = 0.2$. We shall obtain

$$\left(\frac{1}{\overline{m}}\frac{d\overline{m}}{dw}\right)_Q \cong \frac{3}{4}\left(\frac{1}{\overline{m}}\frac{d\overline{m}}{dw}\right)_0$$

As have been numerically obtained, that the consumption of fuel for a aerocapture trajectory of air-space plane height 200kms, at thermal action to approach flow in a range of Mach numbers $M_\infty^0 = 6 \div 17$ can be reduced approximately by 3%.

References

1. Ф. Бартльме. Газодинамика горения. Пер. с нем. Москва, Энергоиздат, 1981.

2. Л.В. Гогиш, С.Г. Дашевская. Обтекание трапециевидного крыла профиля сверхзвуковым неравномерным потоком. Изв. Ан СССР, МЖГ, 1990, №3.

3. В.Ю. Борзов, И.В. Рыбка, А.С. Юрьев. Оценка энергозатрат при снижении лобового сопротивления тела в сверхзвуковом потоке газа. ИФЖ, 1992, т.63, №6.

4. В.Ю. Борзов, И.В. Рыбка, А.С. Юрьев. Влияние локального энергоподвода в гиперзвуковой поток на лобовое сопротивление тел с различным затуплением. ИФЖ, 1994, т.67, №5-6.

5. В.И.Артемьев, В.И.Бергельсон, И.В. Немчинов, Т.И.Орлова, В.А.Смирнов, В.М. Хазинс. Эффект «тепловой иглы» перед затупленным телом в сверхзвуковом потоке. ДАН, Гидромеханика, 1990, т.310, №1.

6. В.В. Витковский, Л.П. Грачев, Н.Н. Грицов, Ю.Е. Кузнецов, В.В. Лебеденко, В.В. Скворцов, К.В. Ходатаев, В.П. Янков. Исследование нестационарного обтекания тел сверхзвуковым потоком воздуха, подогретым продольным электрическим разрядом. ТВТ, 1990, т.28, №6.

7. Л.Мирабо, Ю.П.Райзер, М.Н.Шнейдер. Расчет и теория подобия эксперимента, моделирующего эффект "AIR-SPIKE" в гиперзвуковой аэродинамике. ТВТ, 1998, т.36, №2.

8. С.В.Гувернюк, А.Б.Самойлов. Об управлении сверхзвуковым обтеканием тел с помощью пульсирующего теплового источника. Письма в ЖТФ. 1997, т.23, №9.

9. П.Ю. Гергиевский, В.А. Левин. Нестационарные явления при сверхзвуковом обтекании импульсного источника энергии большой мощности. ICMAR-98.

10. В.А. Белоконь, О.В. Руденко, Р.В. Хохлов. Аэродинамические явления при сверхзвуковом обтекании лазерного луча. Акустический журнал, 1977, т. XXIII, вып. 4.

11. Г.А.Лукьянов. О сопротивлении и теплообмене тела в сверхзвуковом потоке при наличии перед телом плоского источника энергии. Письма в ЖТФ, 1998, т. 24, № 24.

12. Г.А. Лукьянов. О сопротивлении тела в сверхзвуковом потоке при наличии перед телом изобарической области энерговыделения. Письма в ЖТФ, 1999, т.25, №1.

13. П.К. Третьяков, А.Ф. Гаранин, Г.П. Грачев, В.Л. Крайнев, А.Г. Пономаренко, А.И. Иващенко, В.И.Яковлев. Управление сверхзвуковым обтеканием тел с использованием мощного оптического пульсирующего разряда. ДАН, 1996, т.351, №3.

14. П.К.Третьяков, В.И.Яковлев. Формирование квазистационарного сверхзвукового течения с импульсно-периодическим плазменным теплоисточником. Письма в ЖТФ, 1998, т.24, №16.

15. П.К. Третьяков, В.И. Яковлев. Волновая стуктура в сверхзвуковом потоке с лазерным энергоподводом. ДАН, 1999, т.365, №1.

13. EFFECT OF AN OPTICALLY INITIATED PLASMA ON THE COMBUSTION OF HOMOGENEOUS AIR-FUEL MIXTURES

P.K. Tretyakov, S.S. Vorontsov, A.F. Garanin, A.V. Tupikin, V.I. Yakovlev
Institute of Theoretical and Applied Mechanics SB RAS, 630090, Novosibirsk, Russia

G.N. Grachov, A.L. Shmirnov
Institute of Laser Physics SB RAS, 630090, Novosibirsk, Russia

Abstract. The influence of a plasma initiated by an optical pulsed-mode discharge on the propagation velocity and stability intervals of turbulent flames in homogeneous air-fuel mixtures (hydrogen and hydrocarbons) is experimentally studied for various intensities of the initiating laser beam. Traditional means (formation of flow-separation regions) were used to stabilize the combustion. Burning characteristics were compared with those obtained during initiation of the process with the optical discharge, all other experimental conditions being identical.

It is found that, during the burning initiated by the laser beam, the burning rate increases and flame stability intervals (with respect to the velocity and chemical composition of the mixture) become wider. The effect is predominantly caused by gas-dynamic factors (turbulization of flow) and by high energy added to the flow. It is established that there are two mechanisms underlying the ignition and combustion processes. For hydrogen-air and methane-air mixtures, a thermal mechanism is operating. For complex hydrocarbon fuels, a transition from one mechanism to another is possible under the action of the laser-beam energy. In the latter case, pre-flame chemical reaction proceed, and the burning may develop without any optical break-down.

Data on the effect of flow parameters, chemical properties of the combustible mixtures, and the repetition frequency of laser-irradiation pulses on the flame velocity are reported.

Introduction

Nowadays research of the optical pulsated discharge (OPD) in supersonic gas flow [1–3] shows the possibility to apply new methods of stabilizing the flame and control the combustion in gaseous flows. OPD formation in the reactive flow can cause new effects conditioned by the influence of the gasdynamic and kinetic factors on this flow. Non-stationary gasdynamic disturbances appear at optical breakdown which forms quasistationary wave structure consisting of a shock wave and thermal wake under certain conditions [3]. Besides, an optical breakdown plasma, emitting in a wide spectral range can considerably change pre-flame processes in the reactive medium, leading mechanisms of kinetic processes, respectively, the rate of heat release in the flow till ultimate determining the explosive character of the process.

Experimental study of a combustion initiation by laser radiation (laser spark) started with a laser technique development. A large number of works were fulfilled (by the end of 70-th) in a field of a IR-photochemistry. Pulsed and cw laser sources with relatively high power were used.

The possibility of various fuel/air mixtures combustion control in flows by focused radiation of a pulsating CO_2-laser was studied in present paper. Such possibility may occur when radiation energy, absorbed effectively by reactive medium, initiates pre-flame reactions and changes leading mechanisms of a combustion.

Application of the optical pulsated discharge for a flame initiating and stabilization in homogeneous hydrogen/air and hydrocarbon/air flows was studied for the first time. To provide a medium's optical breakdown an argon was injected into the focused laser beam region along the axis of the main flow. Inert gases have a breakdown threshold several times lower than used mixtures. However, this additional factor of an optical discharge stabilization (by argon injection) is not a matter of principle and can be excluded using laser power increased by several times.

Experimental set-up and registration methods

Gasdynamic section of the set-up (Fig.1) provides the formation of subsonic jet of the working mixture by confusers and the argon wake (through the hole of 3mm in a tube of 4mm) along the flow axis. Hydrogen/air exit diameter confuser was 8mm, and 20mm for different mixtures. Air and hydrogen are mixed in the working chamber 1, air and hydrocarbons are mixed before it in gas supply system. Argon is supplied from the plenum chamber 2. Laser radiation is focused by the lens 3 in the argon jet at a distance of 10mm from the outlet section and blocked up by absorber 4. The pulse-periodic CO_2-laser LOK-3MSI developed in ILP SB RAS and applied in the previous our experiments was used.

Optical scheme of flow visualization is presented in Fig.1 too. The flow region with OPD 5 was lighted using He-Ne – laser 6. The spherical wave front (converging beam) with the demanded

aperture of the object under investigation was formed by micro-lens 7 and large focusing distance (450mm) lens 8. The application of the spherical wave front allowed one to use interferometer 9 with the inlet aperture 16mm, which is less than the visualization field's dimention (50mm). Interferometer was set up at a certain distance from the object. The applied scheme of interferometer with the separated regulation of the fringe's width and sensitivity allowed one to determine reliably the boundaries of the turbulent combustion zone. Information was registered through light filter 10 and objective 12 by television camera of technical vision 11 with the exposure time 0,1ms. It was recorded by video-player 13 and displayed by monitor 14 during process in study. After experiment the selected frames were numbered and processed by the standard graphic methods
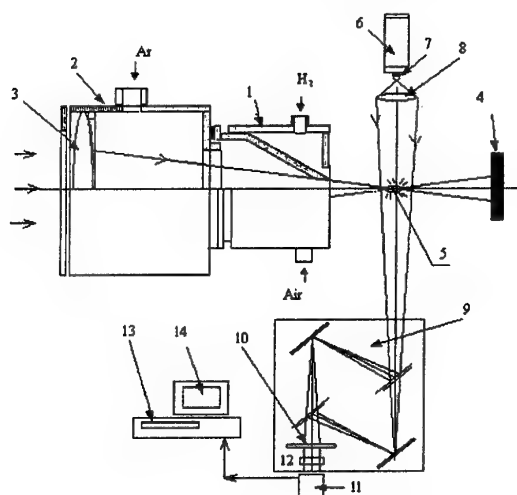
Fig.1. Experimental set-up and optical scheme.
1 – mixture chamber; 2 – plenum chamber; 3, 8 – lens;
4 – absorber; 5 – OPD; 6 – He-Ne - laser;
7 – microobjective; 9 – interferometer; 10 – light filter;
11 – TV-camera of technical vision; 12 – objective;
13 – video-recorder; 14 – monitor.

Hydrocarbons/air flame boundaries in a flow were determined by light emission visualization of a spectrum region for CH radicals.

Parameters for reactive flow (velocity, equivalence ratio), laser radiation (pulse repetition frequency and power), also argon velocity (consumption) in the case of optical breakdown were varied in experiments.

Experimental results for the flame, stabilized by separation zone behind argon supply tube (4mm of outer diameter, in a center of confuser exit), were used as the basic ones in a comparative analysis.

Experimental results for hydrogen

All experiments were conducted with the homogeneous mixture hydrogen/air jet at subsonic exhaustion into ambient atmosphere. The range of air consumption varied within 1.5–8g/s, hydrogen 0.045–0.1g/s. Argon consumption varied little and made up 2.3–2.5g/s. Velocities of the mixture and the argon flows were determined by known data about gas consumption and throat areas of the outlet holes. Equivalence ratios was determined by the relation of air and hydrogen consumption taking into account stechiometric coefficient, equal to 34.5.

Experiments were performed in two stages. At the first stage without supply of laser power (OPD) and argon supply two regimes of combustion were established: (1) – "attached" flame stabilized at the outlet confuser hole, which at increasing of the flow velocity was transferred into (2) – "detached" from the hole's edge flame with the following it's breakdown. Argon supply decreases the breakdown parameters, this effect depends on the argon consumption. In average according to the total measurements conducted in the range of the argon velocities 150–210m/s the characteristics of breakdown were: mixture velocity 60–70m/s and equivalence ratio 0.6–0.8. Thus, the first regime of combustion was realized at argon supply without OPD.

The second stage of the experiments was performed with the OPD formation in the flow. Argon exhaustion velocity was 190m/s. This parameter determines the choice of pulse repetition frequency f of the laser. As it is shown in [3] the upper limit of this parameter is determined by the value $f=u/l$ (where l is the optical break-down plasma extension), which is not more than 30kHz for the conditions of the experiment. The experiments were performed also for the frequency of 8kHz.

Figure 2,b–f shows the results of visualization of hydrogen/air mixture combustion supported by OPD when the flow velocity (from 60m/s till 200m/s) and equivalence ratio (from 0,5 till 1.9) increase. Interferometer is adjusted to the fringes of the unlimited width. OPD plasma is registered as the great lighting region showing the length 8–10mm and diameter two times smaller, whereas the diameter of the focused laser beam was not more than 0.3mm. Figure 2,a shows mixture combustion flow without OPD at low velocity and equivalence ratio values (60m/s and 0.5 respectively) and argon supply, i.e. in the regime of the "attached" flame. Argon jet in the axis part of the flow is traced poorly. The feature of this flow is that the interference fringes vary regularly at a distance not less than two diameters of the

88
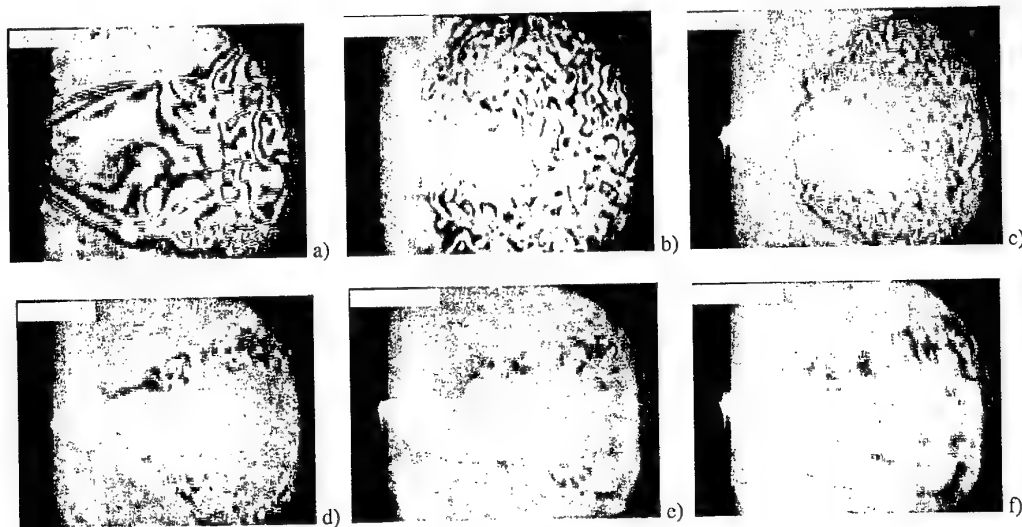
Fig.2. The results of hydrogen/air combustion visualization.

confuser. Density and other parameters in the considered flow vary regularly, that characterizes the laminar flow and combustion process. Downstream parameters vary not regularly which indicates transition to the turbulent regime. Therefore the determination of the Reynolds numbers range at which the experiments were performed is of particular importance. This parameter varied in the range of $Re=(0.5-3)\times10^4$ (at $\alpha\gg1$, considering the characteristic scale of 2mm – the circular slot which forms the mixture flow).

Thus, the optical pulsated discharge effects considerably the reactive flow and stabilizes the flame near the place of radiation focusing. The variation of the parameters of the flow at combustion in the whole range of the Reynolds numbers corresponds to the turbulent one even at low Re (see Fig.2,a and 2,b). Besides, combustion was performed even at the highest flow velocities. The ultimate values of the parameters of it's breakdown were not reached. Figure 2,b in which there is not plasma lighting should be paid attention to. It is caused by the fact that at the given laser's pulses repetition frequency of 8kHz the time interval between them (0.12ms with the frame frequency $25s^{-1}$) exceeds a little the exposition time (0.10ms). That is why in some (not frequent) cases the optical breakdown is not registered (when the opening of the lock is during the time interval between pulses). Poor lighting is conditioned by after lighting of the discharged plasma. Nevertheless the combustion process is registered which shows that it is sustained even during the period between pulses. The angle of inclination of the flame decreases monotonously when the velocity and the equivalence ratio increase. Thus,

one can make a conclusion that quasistationary process of combustion is formed by pulsated optical discharge at used frequencies of radiation 8 and 30kHz.

Propagation velocity of the turbulent hydrogen/air flame

Measured flame velocities u_r in the reactive flow hydrogen/air is considerably greater than the velocity of the laminar flame propagation whose quantity does not exceed 2,6m/s, that is evidence of a turbulent combustion also.

A number of physical models were proposed to describe the propagation velocity of turbulent flames in various mixtures [4]. As a rule, all of them boil to establishing a relation between the turbulent flame velocity and mixture parameters (normal flame velocity U_H, or characteristic time of particle residence in the laminar flame front τ_Γ), on the one hand, and turbulence parameters of the flow (mean value of turbulent velocity pulsation U', or turbulence-exchange coefficient D), on the other. Experimental data favoring this or that model are always available. For instance, in [5], a one-to-one experimentally measured dependence of the dimensionless turbulent velocity (U_T/U_H) on U'/U_H was reported for flame propagation in a channel in which the mixture flow was ignited near the channel exit.

To analyze the obtained data on on U_T, one may invoke a turbulent-combustion model based on the assumption about some limiting conditions of flame propagation [6].

Since, for turbulent flows, occurrence of arbitrary values of local velocity gradients $gradU=U'/\lambda$ are typical (where λ is the turbulence

89

scale), it is apparent that only some fraction of all pulsation is capable of promoting flame propagation. Pulsation to which velocity gradients above a certain critical value correspond do not help the flame move. Adopting, as a characteristic time of combustion, the reciprocal of the critical velocity gradient, we may write that $U_*'/\lambda_* = 1/\tau_{\Gamma}$. With the maximum value of U_*' for which the turbulent-assisted flame propagation is still possible taken as a characteristic flame propagation velocity (i.e., $U_T=U_*'$), one may determine U_T assuming that a certain definite relation between U' (RMS value), integral turbulence scale (λ), on the one hand, and U_*'' and λ_*, on the other, exists which cam be written in the form $D=U'\lambda=U_*'\lambda_*$; then $U_T=(D/\tau_{\Gamma})^{1/2}$.

This model used for description of integral characteristics of turbulent combustion in leading and trailing flame edges, intervals of parameters in which burning is possible (flame-stall characteristics) and flame front oscillation frequency (see [6-8]) showed a good agreement with experimental results obtained for various operating conditions of real technical apparatus. With no stilling devices (e.g., grids) provided for changing turbulence parameters, one may assume that the turbulence-exchange coefficient is proportional to the product of flow velocity and jet cross-sectional area: $D=ud$, [9]. The data concerning the influence of α and initial temperature on the characteristic duration of combustion for hydrogen-air mixtures was reported in [10].
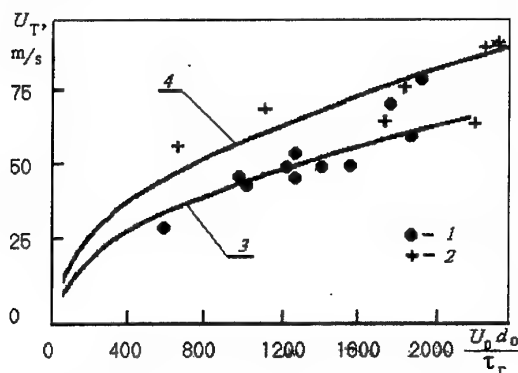
Fig.3. The data on hydrogen/air combustion –
1,2 – experiment; 3,4 – calculations

The data obtained in this study are shown in Fig.3. Various reasons can be invoked to explain the observed scatter of the measured values (within a factor of 1.3). The main one is the registration technique used. In our experiments, the oscillation frequency of the flame front amounted to several tens of Hz, while the exposure time was 10^{-4}sec; therefore, instantaneous (random) positions of the flame front between two extreme positions were probably registered. The visualization method could also add some detrimental contribution. Data obtained by two methods of registration are shown in Fig.3. The extreme positions of the flame front were determined either from infinite-thickness fringes in flow interferograms (dots 1) and from finite-thickness fringes (dots 2). As follows from the figure, the extracted data differ appreciably from each other. It should be noted that no appreciable effect of the pulse repetition frequency on U_T was found. The latter is likely caused by the fact that the characteristic time of particle combustion in our experiments was longer than the period between pulses ($\tau_{\Gamma} \geq 10^{-4}$sec), although at frequencies below 8kHz one may expect the quasistationary regime of the development of the process to be violated.

Thus, stable combustion occurs for a wider range of initial conditions. The appearance of the obtained dependence of U_T on the flow velocity and τ_{Γ} is indicative of the fact that one and the same mechanism of flame propagation is operating under conditions of flame initiation with an optical discharge and with traditional means.

Experimental results for hydrocarbons

The first experiments is devoted to reveal the main mechanisms of combustion development effected by pulsated laser radiation (with and without optical breakdown). Its have a qualitative character.

Methane/air mixture

All experiments were conducted with the homogeneous methane/air mixture jet (with 20mm diameter) at subsonic exhaustion into ambient atmosphere. The range of air consumption was within 0.3–1.7g/s, methane 0.01–0.09g/s. Velocity of a reactive mixture varied within limits 1.8–5.4m/s. Argon consumption was 0.2m/s and was increased two times in some experiments. Equivalence ratios was determined by the relation of air and methane consumption taking into account stechiometric coefficient, equal to 17.24.

Presented in Fig.4 pictures of combustion zone at laser energy supply but without optical breakdown (a) and with it (b) in a flow shows, that the velocity of a flame propagation is higher in the second case, also an argon was used to get the condition for breakdown. Despite of dilution of the reactive mixture by inert gas a flame front angle increase in a value and is close to 90°. Range of a mixture composition, where stable combustion take

a place, is widened. Range of values of α changed from 0.85–1.16 (without radiation energy supply) up to 0.61–1.35 in a presence of the OPD with frequency 17kHz and absorbed power 1.2kW. It worth to notice that an argon jet effects sufficiently (in comparison with hydrogen/air mixture) these parameters. The argon velocity increased the initiation of stable combustion had became worse. Probably, this effect is caused by dilution of the reactive mixture and decreasing of the energy, heating this fuel mixture.
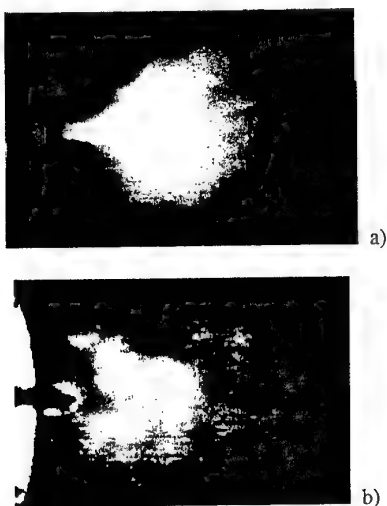
Fig.4. Combustion in a flow of a methane/air mixture.
a) – without OPD, α=1.05; b) – with OPD, α=1.10.

Preliminary analysis of the obtained results shows, that velocity of a flame propagation has the same conformity as for hydrogen/air mixture.

Propane/air mixture

The range of methane consumption varied between 0.046–0.09g/s, and air between 0.77–1.5g/s. Velocity of a reactive mixture was 2.2–4.5m/s. An argon consumption had the same values, mainly 0.2m/s as in experiments with a methane. Velocity of an argon jet was no less than 17m/s and exceeded the mixture velocity. Equivalence ratios was determined by the relation of an air and propane consumption taking into account stechiometric coefficient, equal to 15.67. One can mark the same character of combustion process which was founded out in experiments with methane. The range of mixture composition and velocity for a stable combustion was widened in a comparison with the basic regimes. For example, for velocity value 3 m/s range of α 1.02–1.18 widened to 0.95–1.5.

But in contrast to a methane/air mixture the effect of a propane/air combustion initiated by focused CO_2-laser radiation without an optical breakdown (discharge) was revealed. The same effect of a flame initiation by focused laser beam without an optical discharge was founded out for evaporated alcohol/air mixtures. Typical results of the visualization of these combustion regimes supported by laser radiation (17kHz, 1.3kW) but without optical discharge are presented in Fig.5a,b. The range of mixture composition for a stable combustion was widened in a comparison with the basic regimes also. Despite of the limited data on turbulent flame velocity for these regimes obtained one can say with certainty about changing of conformity to the natural law for flame propagation in comparison to combustion supported by optical pulsating discharge.
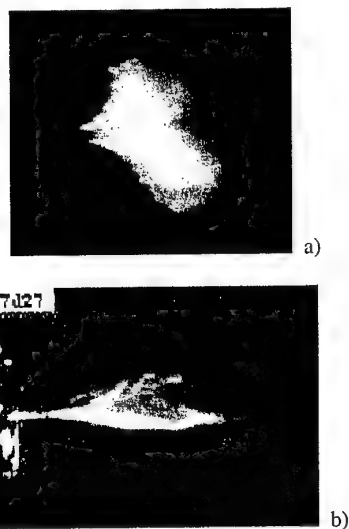
Fig.5. Combustion of propane (a) α=1.18 and vaporized alcohol (b) supported by laser radiation but without OPD.

Conclusions

Experimental results on homogeneous mixtures of a hydrogen/air and hydrocarbon/air combustion initiated by OPD showed that pulsating optical discharge effects considerably the reactive flows. It was proved by measurements in the whole range of Reynolds numbers Re=(0.5–3)×10^4 that stable hydrogen/air combustion is supported in a wider range of initial conditions; scale of a density fluctuation sufficiently changes also. High flame propagation velocities testify to development the process of a turbulent combustion.

Under conditions of an optical pulsating discharge, the flame for all used fuels was found to be stable in a wider range of initial conditions in comparison with traditional method of stabilization

91

(separation zone in flow). For hydrogen/air mixture the general appearance of the obtained dependence of U_T on the physical and chemical properties (τ_T) and hydrodynamic parameters (u,d) is the same under conditions of flame initiation with an optical pulsating discharge and with traditional means. Probably, the same conclusion one can say about methane/air mixture with lesser reactivity and, consequently, sufficiently effected by argon's dilution.

The effect of a flame initiation and supporting by focused CO_2-laser pulsating radiation without an optical breakdown (discharge) was founded out. Probably, the mechanism of this process is connected with pre-flame reactions initiated by absorbed laser radiation.

References

1. P.K. Tretyakov, A.F. Garanin et al.. Control over the supersonic flow around applying powerful optical pulsated discharge // Dokl. Akad. Nauk. 1996. Vol.329. No.3. P.329–332, (in Russian).
2. P.K. Tretyakov and V.I. Yakovlev, Formation of the quasi-stationary supersonic flow with the pulsated - periodic plasma heat source // Pis'ma v ZhTF. 1998. Vol.24. Iss. 6. P.8-12. (in Russian).
3. P.K. Tretyakov and V.I, Yakovlev, Wave structure in supersonic flow with laser energy supply // Dokl. Akad. Nauk. 1999. Vol.365. No.1. P.58–60, (in Russian).
4. E.S. Shchetinkov, Physics of Combustion and Explosion, Moscow, 1965.
5. T.W. Lee and S.I. Lee, Investigation of turbulent premixed flame propagation in one-dimensional isotropic turbulence, in: 3ht Int. Symposium on Tarbulence, Heat and Mass Transfer. Y.Nagano, K-Hanjalic' andT.Tsuji (Editors). 2000 Aichi Shuppan, p.831-838.
6. V.K. Baev and P.K. Tretyakov, Predicting exact position of a flame front in a turbulent flow, Izv. SO AN SSSR, ser. Tektm. Nauk, Issue I, .№3,1969, (in Russian).
7. V.K.Baev, Yu- V. Serov, and P.K. Tretyakov. On the oscillation frequency of a turbulent flaame front, Fizika Goreniya Vziyva, No.2, p-246-248.1970, (in Russian).
8. V.K.Baev and P.K. Tretyakov, Criterial description of burning stability in a turbulent flow of a homogeneous mixture, Fizika Goreniya Vzryva, No.1, p.46-51, 1972, (in Russian).
9. J.O.Hinze. Turbulence, McGraw-HiU,New York, 1959.
10. V.K. Baev and P.K. Tretyakov, Characteristic times of combustion of air-fuel mixtures, Fizika Goreniya Vzryva, No.3, p.367-376, 1968 (in Russian).

14. EXPERIMENTAL AND NUMERICAL INVESTIGATION OF SUPERSONIC FLOW AROUND MODEL N WITH SURFACE ELECTRIC DISCHARGE.

Klimov A. (IVTAN), *Lutsky A.* (KIAM RAS)

Introduction

Supersonic flow around model N with a longitudinal electric discharge was studied during plasma aerodynamic (PA) experiments in the wind tunnel T-113 (TsAGI), [1]. Schematic of this model is shown in Fig.1.1. Electric discharge was created by direct current plasma generator (DC PG, or a AC PG). It was revealed that this electric discharge near model N was non-stationary and non-homogeneous (structural plasma formation consisted from a number of thin plasma filaments) in a supersonic flow. In a result of these plasma instabilities considerable voltage HF fluctuations were recorded in this discharge Fig.1.2. Parameters of these voltage fluctuations were the followings:

Maximal amplitude	1-2 kV
Pulse repetitive frequency	10-100 kHz
Characteristic pulse duration	10-100 mcs
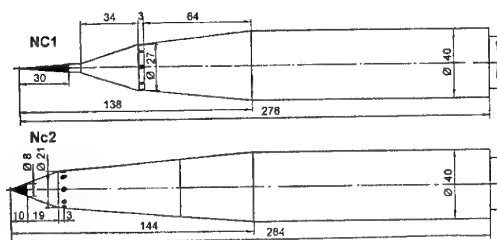
Fig.1.1. Different design of model NC. Electrodes are marked by black color

Note that discharge current modulation was not a large one. Its value was not higher than 5-10%. So, power modulation was about 200% in pulsed discharge in airflow. Entropy turbulent boundary layer with large width (about 2-10mm) was created by this pulsed discharge near model surface.

Non-stationary power input into a supersonic gas flow near model N was taken into account in the present numerical simulation. Influence of non-stationary power input on model drag and gas flow parameters was studied in this simulation. Note that non-equilibrium plasma properties are not considered in this work. This paper is devoted to analysis of these simulation results and a comparison of theoretical and experimental ones.

Two aerodynamic models NC were used during wind tunnel tests, Fig.1.1. Model NC consists of a metal cylindrical body and conical dielectric (nylon-6 or ceramic) head part. Material erosion was minimal in the case of ceramic head part namely. Diameter of a metal body is 40mm. Eight electrodes were located in a dielectric head part of a model. Note that electric gap between these electrodes and axis needle-electrode could be changed in a range of 10-30mm. Polarity of these electrodes could be changed in the case of DC discharge also.
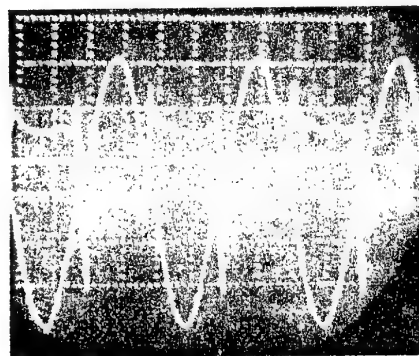
discharge without airflow, $P_{st} \sim 30$Torr, top signal- voltage-500V/div, down signal- current, 1Amp/div
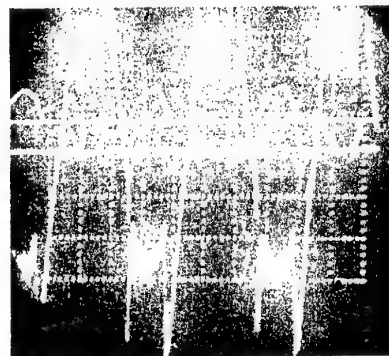
discharge with airflow, $P_{st} \sim 30$Torr, top signal- current, 2Amp/div, down signal- voltage- 500V/div

Fig.1.2. Current and voltage signals in longitudinal discharge near model NC. M~4, $P_{st} \sim 30$Torr, time-5ms/div.

Characteristic photos of AC discharge near model N in a supersonic flow and without it are shown in Fig.1.3. Characteristic signals of voltage and current in AC discharge in a supersonic

flow and without it are shown in Fig.1.4, (M=4, P_{st}=30torr).

Fig.1.3. Supersonic flow around model NC with longitudinal AC discharge.
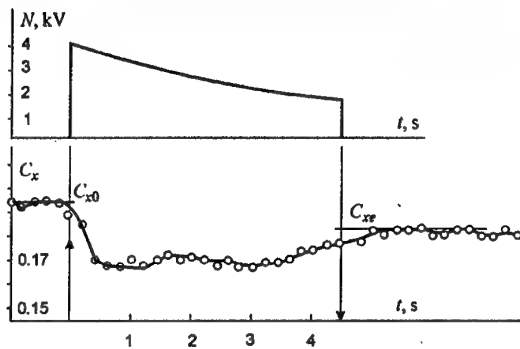
Fig.1.4. Temporal evolution of drag coefficient, (model NC). ↑- switch on AC discharge, ↓- switch out it, I_d=4Amp, M=4, P_{st}~30torr.

Parameters of airflow during plasma aerodynamic experiment were the followings:

Mach number	M~ 4
Static pressure	P_{st}~30 torr

Main experimental results

1. The following experimental results were obtained in wind tunnel test:
2. Drag decrease at electric discharge creation in a head part of model NC. Its value was 5-10%
3. Final drag coefficient value C_{de} was not equaled to initial value C_{do}. Note that analogous result was obtained in [2].
4. It was revealed that there was the following relation $C_{de}> C_{do}$ in the case of axis needle-electrode was anode. There was opposite result $C_{de}< C_{do}$ in the case of axis needle- electrode was cathode.
5. Drag coefficient C_{de} was depended on discharge power and electrode polarity.

6. Base drag decrease was a very small (about 1%) in this wind tunnel experiment.
7. Gas temperature distribution was measured in gas discharge plasma (I_d~2,6 Amp) near model N in a supersonic flow. It was revealed that maximal gas temperature in a gas discharge was about 2000K [1].

Numerical simulation

The calculations were executed within the framework of 2D (axisymmetrical) non-steady Euler's equations (without regard of viscosity and heat conduction). The numerical algorithm is based on the generalized Godunov's scheme with piesevise linear representation of the flow functions. The multi-block regular grid , containing 618 - cells along the body surface, 40 - between a body and external shock wave was used.

Two variants of energy supply location and various variant of energy supply mode are considered.
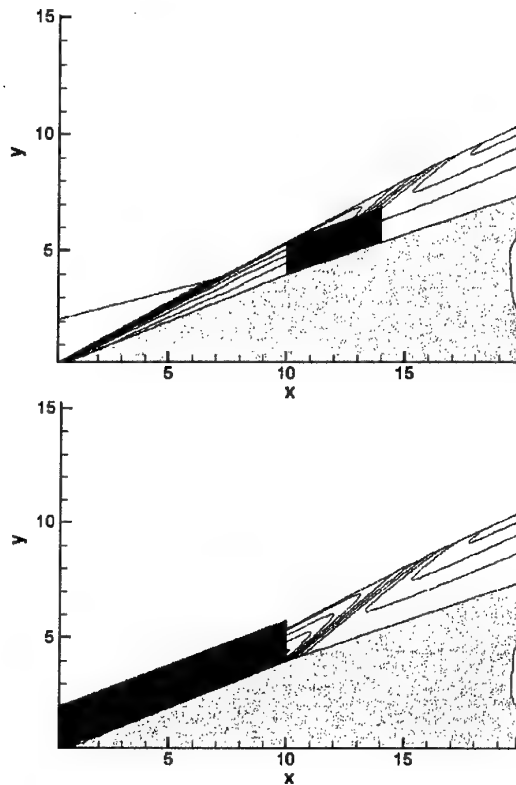
Fig.2.1. Variants of energy source location.

Variants of energy supply location is shown in Fig.2.1:

1. Between the electrodes: $10 < x < 14.75$
2. Near a model nose: $0 < x < 10$.

94

These versions are correlated with regard to the experimental data.

For each of location versions the following temporary power modes are considered:
1. Steady one with constant power 3kW
2. Periodic one with a constant level about 1kW. Total time period between two pulses is about 100mcs. Time interval t_q of energy input 5kW is equaled to:
   2.1 $t_q = 12.5$ mcs,
   2.2 $t_q = 25$ mcs,
   2.3 $t_q = 50$ mcs.
3. Periodic one with zero base level and the same total period and times of energy input.

The mean power of steady energy supply corresponds to the mean value for version 2.3.

Numerical results. Steady energy supply

The influence of steady energy supply is illustrated by Fig.2.2-2.3, where the pressure and temperature distributions in flow field are shown. Pressure increase inside energy supply region and subsequent pressure reduction in a downstream are observed in this case. The area of reduced pressure is located near model surface segment, where the main part of wave drag is realized (version 2). Therefore there is wave drag reduction (in comparison with undisturbed flow) in the case of version 2 with steady energy supply. On the contrary, the wave drag increase is observed in the case of version 1.

It was revealed that for
• undisturbed case ($Q = Q_f = 0$) the drag value is $C_{d0} = 0.0816$,
• var.1: $C_{de} = 0.0910$, $Q = 3$ kW
• var.2: $C_{de} = 0.0748$, $Q = 3$ kW

The flow function distributions on the model surface are shown on Fig.2.4-2.5. Gas temperature near energy supply region is increased by factor 10-12 for version 2. For version 1 gas temperature grows by factor 4. The special interest represents the influence of energy supply on the skin friction. Distributions of Reynolds number and local skin friction coefficient are shown in Fig.2.5. Energy input results in a Reynolds number reduction and skin friction increase in the considered cases. This result is agreed with one obtained in [3]. It is necessary to note that skin friction reduction was revealed in theoretical and experimental works [3,4].
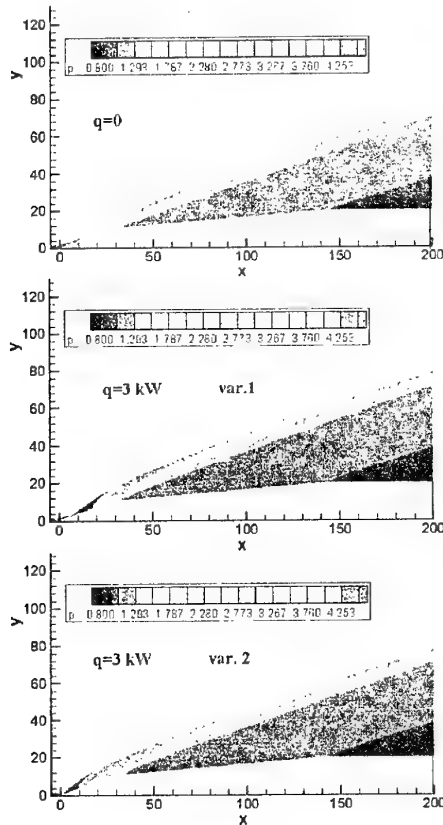
Fig.2.2. Pressure distribution for steady energy input.
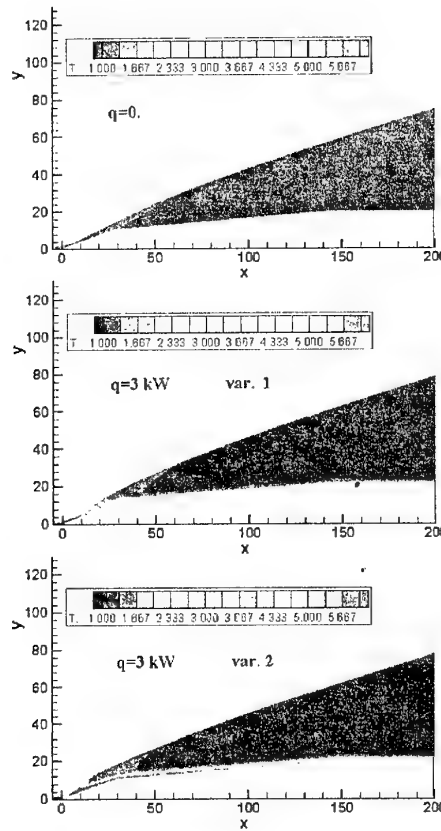
Fig.2.3. Temperature distribution for steady energy input.

95
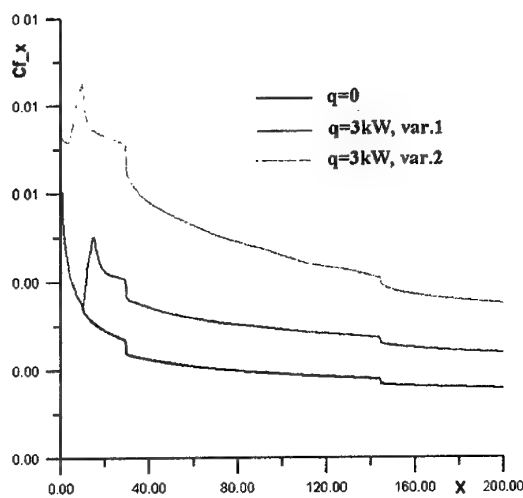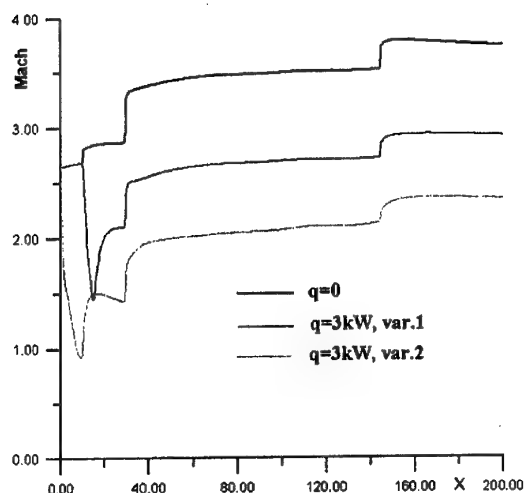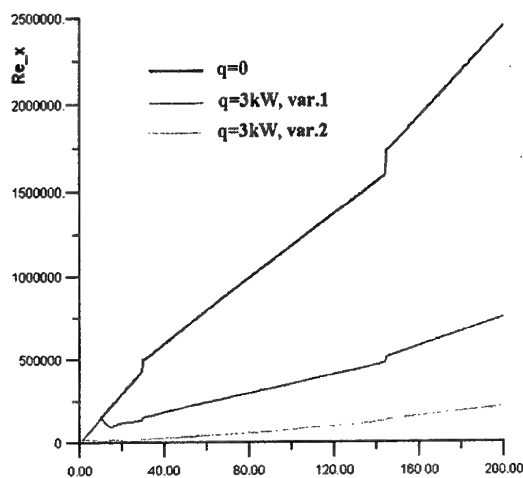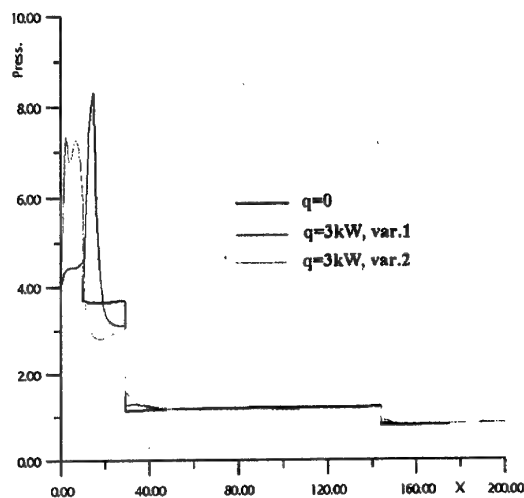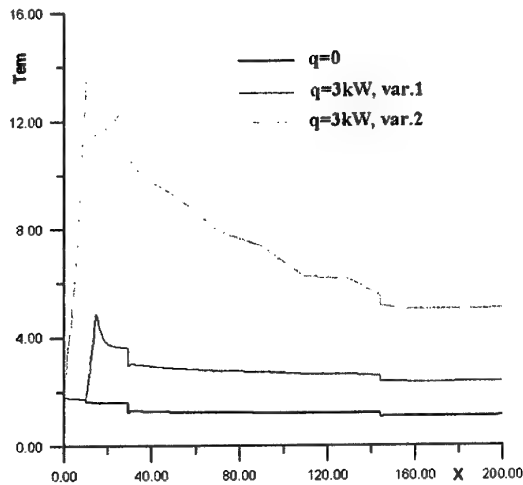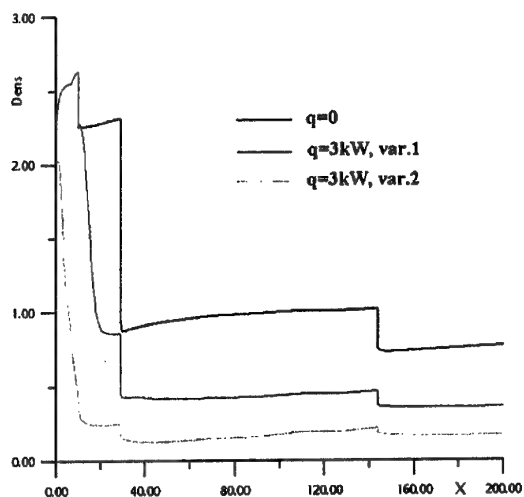
Fig.2.4. Flow function distributions on the model surface.

Fig.2.5. Flow function distributions on the model surface.

96

Numerical results. Periodic energy supply.

The distributions of gas temperature during 4 periods are shown in Fig.2.6. High temperature is observed near model surface. It is interesting to note that disturbed wave-shaped bow shock front is created near model. Pressure increase in a surface segment $10 < x < 30$ and wave drag increase are observed in the case of version 1 (steady energy source). Pressure reduction is observed during some time after cutoff energy supply, Fig.2.7. The temporal evolution of wave drag is shown in Fig.2.8-2.9. The analysis of the obtained results allows us to make a number of conclusions:

- There is a time interval, when wave drag is decreased, for all periodic energy sources,
- Base energy level gives adverse effect in the most cases.
- Drag reduction is stronger than others versions for the second version.
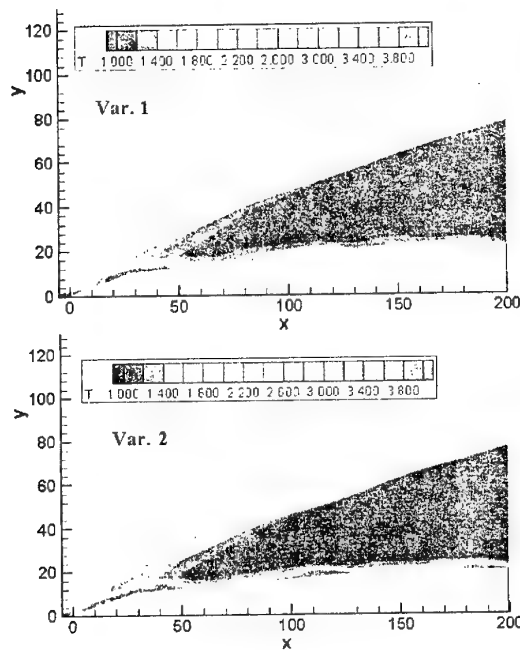
Fig.2.6. Temperature distribution for periodic energy input.
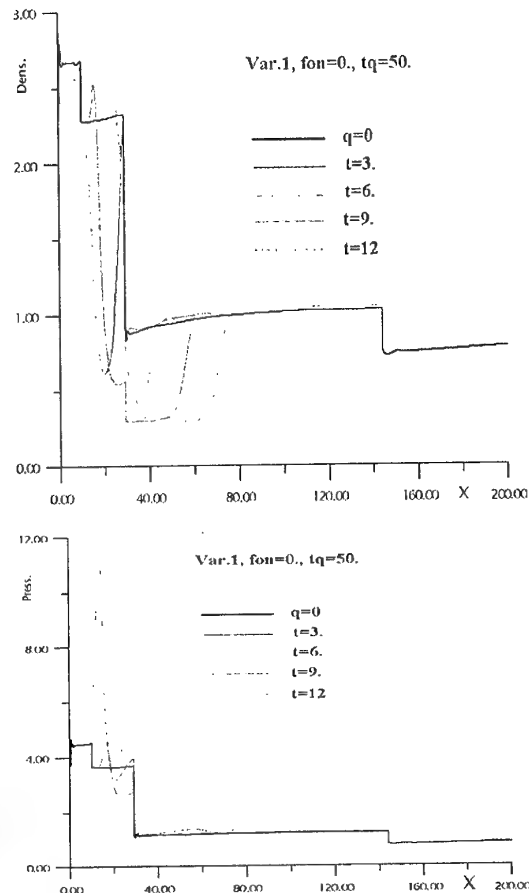
Fig.2.7. Flow function distributions on the model surface (periodic input).

The mean values of wave drag are shown in the Tables 1, 2 (periodic cases).

Table 1

t_q	$Q_f=1$ kW	$Q_f=0$
12.5 ms	0.0872	0.0841
25 ms	0.0892	0.0864
50 ms	0.0929	0.0910

Table 2

t_q	$Q_f=1$ kW	$Q_f=0$
12.5 ms	0.0788	0.0804
25 ms	0.0793	0.0806
50 ms	0.0792	0.0796

97
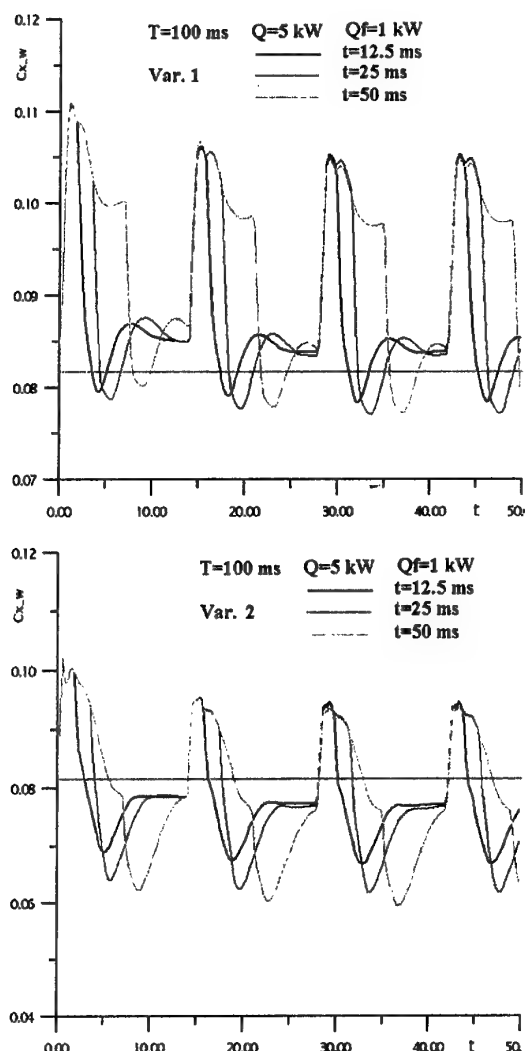
Fig.2.8. Time histories of drag for constant base level.
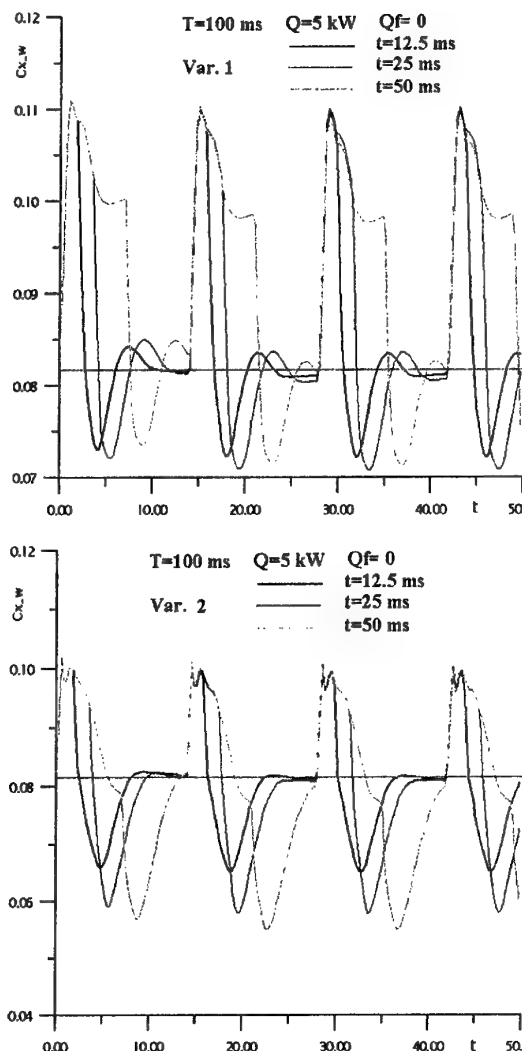
Fig.2.9. Time histories of drag for zero base level.

One can see that wave drag increase is observed in the version 1. For the case of short pulses the drag increase is less than one in the case of steady energy supply. For the second version the appreciable drag reduction is observed. The greatest effect is reached in the case of steady energy supply and short pulses.

References

1. Ershov A.P., Klimov A.I., Timofeev I.B., et.al. Flow Around Body and Characteristics of AC/DC Discharges in Plasma Aerodynamic Experiment, Proc. 2nd WIG Workshop, Norfolk, April 24-25, 1998, P.59.
2. A.U.Gridin, B.G.Efimov, A.V.Zabrodin, A.I.Klimov, K.A.Kuzin, Yu.E.Kuznetsov, A.E.Lutsky, A.V.Severin, V.V.Skvortsov, N.N.Sukovatkin, K.V.Hodataev, V.A.Cherkashin. Numerical and Experimental Research of Supersonic Flow over Blunt Nose Body with the Needle in Presence of Electric Discharge at its Head, KIAM RAS Preprint No.19, Moscow 1995, P.31. (in Russian).
3. Kazakov A.V., Kogan M.N., Kurjachii A.P. The Local Heat Input in Boundary Layer Influence on Skin Friction, Izv. RAN, MGG, 1997, No 1, P.48-56 (in Russian).
4. O.B.Larin, V.A.Levin. Energy Input into Turbulent Supersonic Boundary Layer, AMTP, 2001, V.4, No 1, P.98-101, (in Russian).

98

15. THE SHOCK WAVE STRUCTURE IN IONIC PLASMA WITH THE PRESENCE OF NEGATIVE CHARGED NANO-PARTICLES

V.Yu.Velikodnyi

Institute for Applied Mechanics RAS, Moscow, Leningradskyi pr., No 7

V.A.Bityurin

Institute for High Temperatures of Russian Academy of Sciences,
13/19 Izhorskaya Str., 127412 Moscow, Russia

Abstract. The shock wave structure in weakly ionized ionic plasma with the presence of negative charged nano-particles is studied on the base of a complex approach including the solution of the Boltzmann's equation and the Poisson's equation applied to the region of fast variation of the microscopic parameters (at the distance of several free path lengths) and the solution of the set of equation for the multi-temperature, multi-velocity gas dynamics of the chemically reacting weakly ionized plasma. It is found that in such a plasma where the major portion of electrons is bound (i.e. the conditions $n_e \ll n_{i-} \leq n_{p-} \leq n_{i+}$ ared valid) a 'super-bulldozer' effect can be observed. This effect is that the shock propagating through such a media captures the free electrons. In the region of several tens of free path length the fast compression of the electron up to $\sim 4n_{i+}(-\infty)$ gas has occurred resulting in electron number density elevation in four order of magnitude. Consequently its temperature increases in approximately 1000 times. Behind this region a zone of high concentration of electrons is formed. The electron temperature approach the equilibrium level at the distance of $\sqrt{\dfrac{m_e}{m_n}}\lambda_{en}$ (where me – the electron mass, m_n – the neutral carrying gas mass, λ_{en} – the free path length of electrons). In this rather extended region the intensive physical-chemical processes (such an electron excitation of molecules) resulting in molecule dissociation and primary radicals formation take place. In particular, these processes can affect significantly on induction time of chain reaction.

Inroduction

Even in pioneering works by N.Tesla it was found that the plasma containing the electrode erosion products or specially evaporated wax substrates reveals unique properties. In particular, the long life duration (0.1-1sec) of plasma formations was outlined. Later such results were confirmed in a number of experimental studies (see, for example, [1,2]) where besides of long life duration many others interesting features taking place in these physical environment are found.

In theoretical studies [3-5] the description of the shock wave structure in ionic dusty or cluster plasma has been given first on the base of complex approach involving the solutions of Boltznmann's and Poisson's equations along with the solution of multi-temperature multi-velocity gas dynamics. Such a plasma is considered occurring in erosion of electrodes or substrates. A number of new 'anomalous' effects in such plasmas were predicted in that study. It is notable that the important condition of the ionic plasma: $n_e \ll n_{i-} \leq n_{p-} \leq n_{i+}$ (where n_e and $n_{i\pm}$ – electron and ion number densities, -, $n_{p\pm}$ – the number density of positive and negative charged particles (clusters)). The most important results reported in [3-5] is the prediction the effect of cumulative energy – the mechanism of high kinetic energy (100keV – 10MeV) transfer from heavy particles (clusters) to ions and/or electrons through the self-sustain electric field. The latter is created by charged separation at the flow discontinuity. This effect can lead to the breakdown and/or (depending on the plasma and shock wave parameters) to the initiation of intensive physical-chemical processes that, in turn, can result in the chain avalanche reactions [6]. It was shown [3-6] that the shock wave front could play a role of an effective plasma-chemical reactor. The important feature of multi-scale nature of the shock wave front under such conditions has been found for several particular cases in paper [4]. Zones of fast parameter variation $\delta_1 \leq 10\lambda_e$ and one-two zones of slow variations $\delta_2 \leq 100\lambda_e$, $\delta_3 \leq 10^3 \div 10^4 \lambda_e$ are specified where δ_i – zone size, λ_e – electron free path length. The partial temperature and velocities of the gas components could significantly differ in different zones.

On the base of the results obtained in [4] authors have developed an approach of the description of the shock wave structure in a weakly ionized cluster plasma consisting of the solution of the Boltzmann's equation in fast variation zone and utilization of this solution as initial and boundary conditions for the multi-velocity multi-temperature gas dynamics equations and chemical kinetics equations for zones of slow variation. It provides to describe the shock wave structure in complex

chemically reacting mixtures including more that 50 reactions and many components. It was reported in paper [6] that the presence of charged particles or clusters in ionic reacting plasma could results in significant reduction of the induction time of chain reactions important for practical applications. It is known [7] that clusters can get charge of different polarity. For the case of positive charged particles it was found in [3-4] that electrons are accelerated in shock wave front. For the negative charged particles the electrons are decelerated and accumulated upstream the shock wave front. Thus, depending on particle charge the shock wave reveals the different structure. The shock wave in weakly ionized ionic plasma with negative charged particles is characterized by three zones: a zone of fast variation and two zones of slow variation. The thickness of these zones depends on flow and mixture parameters.

Approach.

In this paper two slow variations zones: - δ_2, where the electron number density increasing to compensate excessive electrical space charge, and δ_3, where the cluster concentration reaches the equilibrium level: are described with the multi-temperature, multi-velocity gas dynamics equations (compare [5,6])

$$\frac{\partial n_s}{\partial t} + \frac{\partial n_s u_s^\alpha}{\partial r_\alpha} = \frac{1}{2} \sum_{a,b,c} (k_{ab} n_a n_b - k_{ds} n_d n_s) \quad (1)$$

$$\rho_s \frac{du_s^\nu}{dt} + \frac{\partial}{\partial r_\beta} p_s^{\beta\nu} - e_s n_s E^\nu = \Delta Q_s^\nu \quad (2)$$

$$\frac{3}{2} n_s k \frac{dT_s}{dt} + p_s^{\beta\alpha} \frac{\partial u_s^\alpha}{\partial r_\beta} + \frac{\partial q_s^\alpha}{\partial r_\alpha} = \Delta Q_s^{ll} \quad (3)$$

$$\text{div } \mathbf{E} = \frac{1}{\varepsilon_0} \sum_s n_s e_s \quad (4)$$

where n_s, u_s, T_s – partial concentration, velocity, and; $p_s^{\beta\nu}$ – pressure tensor; $p_s^{\beta\nu} = \delta^{\beta\nu} p_s - \sigma_s^{\beta\nu}$; p_s – partial pressure; $\sigma_s^{\beta\nu}$ – viscous tension tensor; q_s^α – heat flux ; $m_{si} = \frac{m_s m_i}{m_s + m_i}$, m_i – particle mass; ρ_s – partial density; e_s – particle charge; k_{sd} – rate constant of non-elastic process:

$$\Delta Q_s^\nu = \sum_{s \neq \tau} m_{s\tau} n_s n_\tau \Omega_{s\tau}^{(1.1)} (u_\tau - u_s) \xi_{s\tau} \quad (5)$$

$$\Delta Q_s^{ll} =$$
$$= \sum_{s \neq \tau} m_{s\tau} n_s n_\tau \Omega_{s\tau}^{(1.1)} \left[\frac{3k(T_\tau - T_s)}{m_s + m_\tau} \xi_{1s\tau} + u_{s\tau}^2 \xi_{s\tau} \right] +$$
$$+ \frac{1}{2} \sum_{a,b,d} (\mu_{ba} E_{ba} n_b n_a k_{ba} - \mu_{ds} E_{sd} n_s n_d k_{ds}) \quad (6)$$

where $\Omega_{sd}^{(1.1)}$ – Chapman-Enskhog's omega integral, E_{sd} – non-elastic process activation energy . The others references related to (1)-(6) can be found in [5,6]. In fast parameter variation region $\delta_1 \leq 10\lambda_1$, the Boltzmann's equation along with the Poisson's equation are utilized:

$$\mathbf{v}_s \frac{df_s}{dx} + \frac{e_s \mathbf{E}}{m_s} \frac{\partial f_s}{\partial \mathbf{v}_s} =$$
$$= \sum_\tau \iiint [f_s' f_\tau' - f_s f_\tau] |g| \sigma(\chi, y) d\Omega d^3 V_\tau \quad (7)$$

$$\frac{dE}{dx} = \sum_i \frac{n_i e_i}{\varepsilon_0} \quad (8)$$

where E – electric field strength, g – relative velocity, $d\Omega$ – space angle, $\sigma(\chi,y)$ – collision cross-section, v_s – molecular particle velocity, ε_0 – electric permeatibility. Due to the small thickness of this zone δ_1, a small but still finite portion of particles reacts there. For this reason the influence of the chemical transformation on the flow can be neglected as the first. This fact is reflected in equation (7) where the terms responsible for chemical transformation are omitted. The influence of the flow on the chemical transformation is important and it is taken into account by the distribution function derived from (7) in the expression k_{sd}:

$$k_{sd} = \int f_8(x, \mathbf{v}_s) \cdot f_\beta(x, \mathbf{v}_s) \cdot P_{sd}^{ab} \sigma(g, \chi) |g| d\Omega d^3 V_\alpha d^3 V_\beta$$

The latter are used later in source terms of continuity. This approach is described in all details in paper [8].

The description of weakly ionized plasma in the upstream part of the shock wave front is based on successive approximations process (see [8] for details). In this case the reduced equations derived from (1-8) are as:

$$\frac{dP_e}{dx} = -eEn_e \quad (9)$$

100

$$T_e = \left(\frac{n_e}{n_{1e}}\right)^{2/3} T_1 \qquad (10)$$

$$\frac{dE}{dx} = \frac{1}{\varepsilon_0}\left(-n_e e + e z_i n_{1i} f(x) + e z_p n_{1p}\right) \qquad (11)$$

$$f(x) = \frac{1}{1+e^{Bx}} + \frac{u_1}{u_2}\frac{e^{Bx}}{1+e^{Bx}} \qquad (12)$$

where $P_e = n_e k T_e$ – electron partial pressure; n_{1e}, n_{1i}, n_{1p} – electron, ion, cluster number density in oncoming flow; z_i, z_p – charge numbers of ion and clusters; $f(x)$ – the function characterizes the ion and neutral particle variation derived from analysis of (7), (8) [5,6] and [9]; u_1 – flow velocity at $-\infty$, u_2, T_2 – velocity and temperature behind the fast variation zone (note that u_2, T_2 – are not equal to $u_{+\infty}$, $T_{+\infty}$, where the mixture is in equilibrium). The expressions for u_2, T_2 and the method of its definition are presented in [5,6]. The value B, used in (12) $B=4/\delta$, $s=4\lambda_1/\delta=0.8\div1.2$ (see.[9]). The solution of (9)-(12) can be found numerically. In order to start numerical integration an analytical solution in the vicinity of singular point at ($-\infty$) should be obtained. The analytical solution is found by standard linearization of (9)-(12) and neglecting of non-linear members in the ε–vicinity of singularity. This yields:

$$\psi = c_1 e^{\sqrt{A}t} + \frac{Az}{A-s^2}e^{st} \qquad (13)$$

where $A = \frac{3}{5}\frac{\kappa_e n_{1n} e^2 \lambda_1^2}{\varepsilon_1 k T_{1e}}$, $z = z_i \kappa_i \left(\frac{u_1}{u_2}-1\right)$,

$\kappa_e = \frac{n_{1e}}{n_{1n}}$, $\kappa_i = \frac{n_{1i}}{n_{1e}}$, n_{1n} – neutral particle concentration in oncoming flow, e – electron charge, $t=x/\lambda_1$, λ_1 – free path length, $n_e/n_{1e}=1+\psi$. An unknown constant c_1 is presented in (13). This reflects the fact that the values T_e and E behind the fast variation zone are unknown instead the values of $T_e(+\infty)$, $E(+\infty)$ in downstream equilibrium zone are specified. For this the equations (9)-(12) are to be integrated along with the full set of (1)-(4) (in zone of slow variation δ_3), utilizing the results of solution of (9)-(12) as the boundary conditions for (1)-(4). The solution of (9)-(12) with (1)-(4) is found by probe and faults method.

Discussion

A 'super-bulldozer' effect is predicted on the base of the solution of the problem on the shock wave structure in the weakly ionized ionic cluster plasma for the case of negative charged clusters. The essence of the effect is that for the condition $n_{1e} \ll n_{1i\pm} \sim n_{1p\pm} \ll n_{1n}$, the electrons are raked up by the shock wave. The electron number density can increase by several order of magnitude up to ($n_e \sim n_{i+}$), in depending on the initial n_e. In limiting cases the compression of electrons in the upstream part of the shock wave front δ_2 can occur adiabatically and isothermally as well. For practice the adiabatic compression is more interesting because of the strong electron temperature elevation resulting in intensive physical-chemical processes. It is notable that the electron velocity is practically equal to the shock wave velocity. Thus, the shock wave carries not only momentum and energy but mass as well. The calculation of the shock wave propagation in a weakly ionized ionic plasma with negative charged clusters has been carried out for the parameters specified in the Table 1.

				Table1
N	1	2	3	4
κ_1	10^{-6}	10^{-8}	10^{-8}	10^{-7}
. R	1	1	0.42×10^{-5}	4×10^{-6}
$\tilde{d}$	10	10	0.14	36
z	1	1	-1	-10

Here numbers $N=1,2$ stand for positive ions, $N=3$ - for electrons, $N=4$ – for clusters, $\kappa_i = \frac{n_i}{n_{1n}}$ – charged particle number density reduced to carrying gas number density, $R = \frac{m_i}{m_n}$; $\tilde{d} = \frac{d_i}{d_n}$ – the ratio of the effective diameter of charged particle and carrying gas molecule, z_i – charge numbers. The shock wave Mach number is M=3.1.

In Fig.1 and Fig.2 the electron number density $\frac{n_e}{n_{1e}}$ variations over the shock wave front are presented in different scale versus x/λ_1, where x – distance, λ_1 – the free path length in oncoming flow. It is seen from the figures that the electron number density increases in two order of magnitude. The thickness of the upstream part of the shock wave front is about $\delta_2 \sim 40\lambda_1$. For comparison in Fig.3 the variation of the reduced number density $\frac{n-1}{n_2-1}$ vs $\frac{x}{\lambda_1}$ for carrying gas (solid curve) and clusters (dashed curve) are presented. A two-side structure is clearly recognized from the Fig.3: δ_1 – the fast variation zone, δ_3 – the slow variation zone.

101
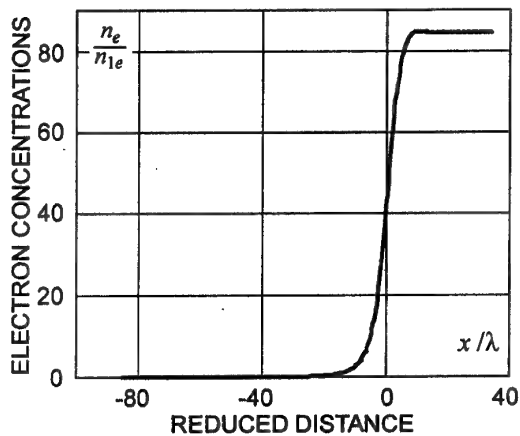
Figure 1 The electron number density distribution in close-up scale
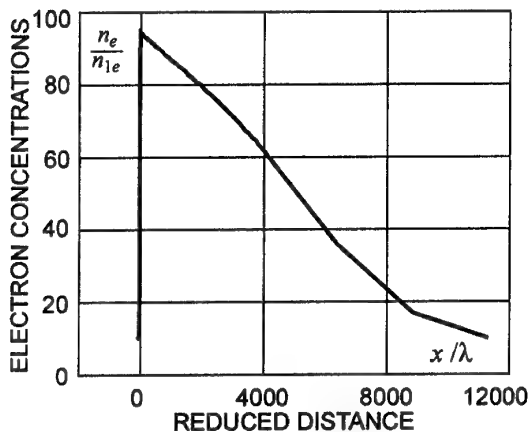
Figure 2 The electron number density distribution over the whole region
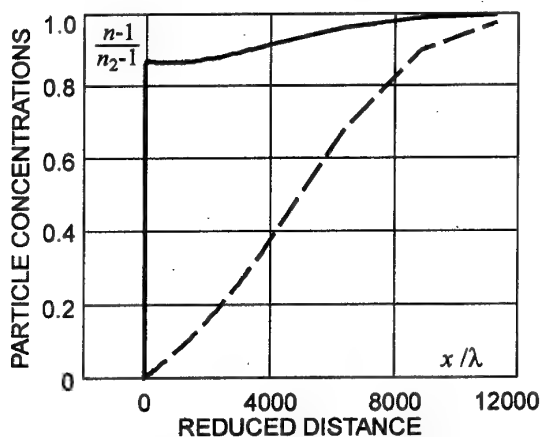
Figure 3 The carrying gas number density (solid curve) and clusters (dashed curve) distributions

The reduced $\dfrac{T_e-1}{T_2-1}$ temperature variation in the shock wave front is exampled in Fig.4. It is clearly seen that the electron compression is practically adiabatic (for the case specified in Table 1). The electron temperature excess the equilibrium level behind the shock in 35 times. In Fig.5 the variation of the reduced temperature of ions and neutral carrying gas (curve 1) and clusters (curve 2) are presented. The two-scale feature of the distribution is obvious.
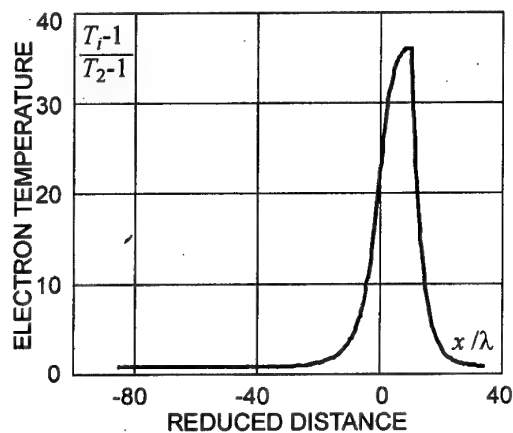
Figure 4 The electron temperature distribution
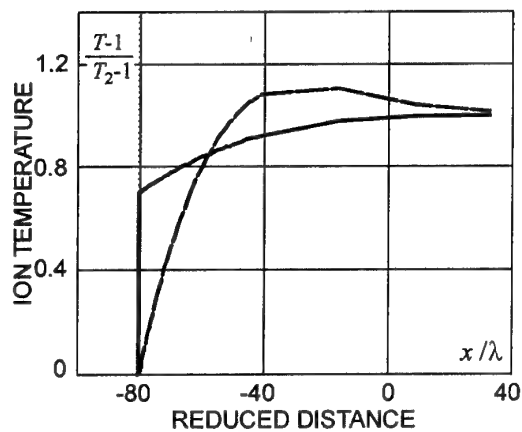
Figure 5 The neutral carrying gas molecule and ion temperature distributions

The electric field (in Td) variation is presented in Fig.6. The characteristic details is that the sign change in the shock wave front. This result differs from the earlier obtained [6] for the case of

102

positive charged clusters when the electric field sign was unchanged.
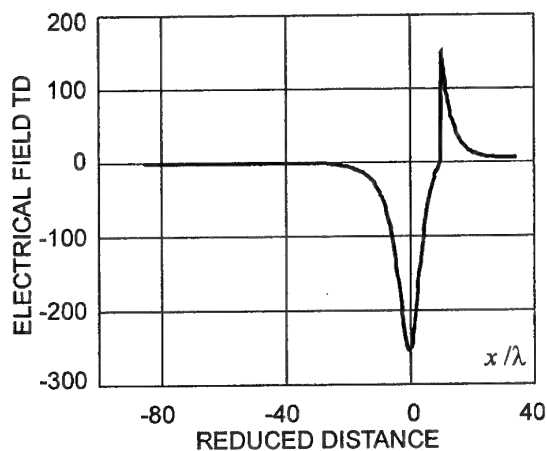
Figure 6 The reduced electric field strength distribution

At the same time the space charge distribution presented in Fig.7 looks similar to the previously considered cases..
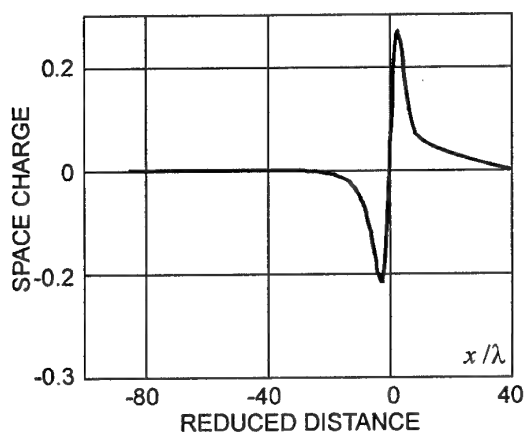
Figure 7 The space charge distribution

The corresponding potential distribution is shown in Fig.8 where the potential maximum reflects the fact of the electric field sign change.
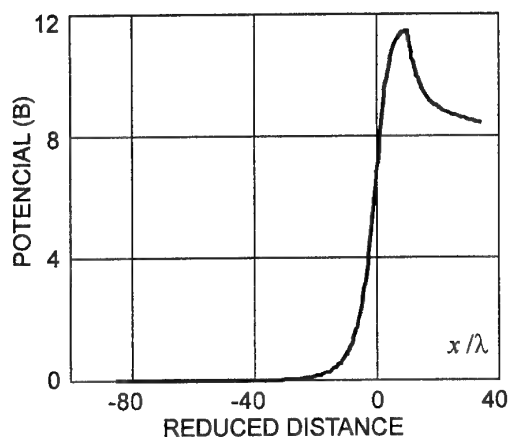
Figure 8 the electrical potential distribution
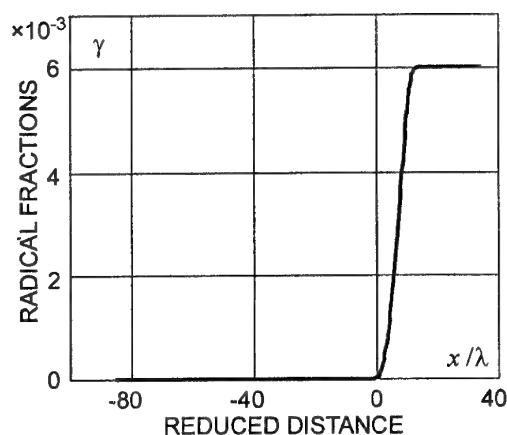
Figure 9 The o atom distribution

The variation of the reduced oxygen atom number density $\gamma = \dfrac{n_O}{n_{O_{21}}}$ produced by the oxygen molecule dissociation in the process of electron excitation and further flying away:

$$O_2 + e \Leftrightarrow O_2^* + e \Leftrightarrow O + O + e \qquad (14)$$
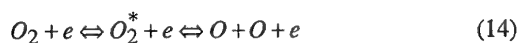
is presented. The analysis of the hydrogen-oxygen combustion, for example, has shown that the O radical production under such condition could be enough to decrease the induction time in order(s) of magnitude.

103

Concluding Remarks.

1. The structure of the shock wave in a weakly ionized ionic plasma with clusters differs significantly for the cases of negative and positive charged clusters:

   a) in the case of negative charged clusters the electrons are decelerated and its concentration increases in the shock wave front;

   b) in the case of positive charged clusters the electrons are accelerated and its concentration drops.

2. The 'super-bulldozer' phenomenon is predicted. The phenomenon is that the electrons are reflected by the negative potential barrier created by the shock wave propagation through such plasma, and accumulated in the upstream zone of the shock wave front.

3. The electron compression can occur as adiabatic and isothermal as well depending on the flow conditions.

4. The electrons move with velocity practically equal to the shock wave velocity so the shock wave carries not only the momentum and energy but and the mass as well. The shock wave character is similar in some way to the case of a single wave – solution.

Acknowledgement

References

1. Ball Lightning in a Laboratory. Collection of Papers. Chemistry, 1994, 256p.(in Russian)

2. A.Klimov, V.Nikolaeva. R.Avramenko and Development of Plasma Aerodynamics in Russia. // In: Prospective on 2nd Workshop on Magneto- and Plasma- Aerodynamics for Aerospace Application, IVTAN, Moscow, April 5 – 7, 2000, p.30-33.

3. Velikodny V.Yu., Bityurin V.A. On structure of a plane shock wave in weakly ionized plasmas // Nonequilibrium processes and their applications. IV Int. Sch.-Seminar. Minsk. 1998. P.72-75.

4. Velikodny V.Yu., Bityurin V.A. Shock nave structure in ionic plasma. // Ac. Of Sc. Reports, 1998, v.361, No.3, p.325-328 (in Russian).

5. V.Yu.Velikodny, V.A.Bityurin. Shock wave structure in long-lived plasma formations // In: Prospective on 2nd Workshop on Magneto- and Plasma- Aerodynamics for Aerospace Application, IVTAN, Moscow, April 5 – 7, 2000, p.301-306.

6. J.T.Lineberry, V.Yu.Velikodny, V.A.Bityurin, Influence of Charged Nano-Particles on Shock Wave Structure. Chain Reaction Initiation in Shock Wave Front in Cluster Ionic Plasma // AIAA 2001-0638, 39th AIAA Aerospace Sciences Meeting and Exhibit, 8-11 January 2001, Reno, Nevada, 6p.

7. Smirnov B.M. The processes in cluster plasma and cluster // JETP Letter, v.68, No.10, pp.741-746.

8. Velikodny V.Yu., Bityurin V.A. The effect of transnational non-equilibrium on the kinetic of physicochemical conversions in the shock wave front// Chem. Phys. Reports. 1997, vol.16, No.19, p.1521-1531.

9. Struminskyi V.V.., Velikodnyi V.Yu. The shock wave structure // SSSR Academy of Sciences reports, 1982, V.266, No1, pp.28-31.

16. CHARACTERISTICS OF SHOCK-WAVE UNDER LORENTZ FORCE AND ENERGY EXCHANGE

H. Yamasaki, M. Abe and Y. Okuno
Graduate School at Nagatsuta,
Tokyo Institute of Technology
4259, Nagatsuta, Midori-ku, Yokohama, Japan
E-mail: Yamasaki@es.titech.ac.jp

Abstract. Results of analytical study on characteristics of the supersonic flow under various conditions are presented. The imposed conditions are the energy addition to the flow, the energy extraction and the Lorentz force acting as acceleration or deceleration of the flow. Relations for shock strength, Mach number and total pressure loss were derived from the one-dimensional simple analytical model. The relations are similar to those of Rankine-Hugoniot, but they include the energy exchange and the MHD effects. The relations can explain observed phenomenon of the shock weakening by heat addition. It can also explain the measured relation between the enthalpy extraction and the isentropic efficiency of the disk MHD generator and the appearance of shock wave.

1. Introduction

Recently, the control of shock wave by heat addition into the supersonic flow or by an application of a magnetic field has received interest in the field of supersonic vehicle [1-2]. The concept of shock wave control by heat addition is based on experimental observation of anomalous phenomena such as the shock weakening, the change of Mach angle and the shock acceleration. In order to explain these phenomena, numerical and experimental studies were carried out [1-4]. Results of them suggest that the observed anomalous phenomena could be ascribed to thermal effect (=gas heating effect) [3-4].

The control of supersonic flow by magnetic field is an extension of MHD power generation technology. A numerical study [1] was made to know possibility of the control of supersonic flow at an intake of scramjet engine. And, it is pointed out that the position of shock intersection point shifts upstream with an increase of magnetic field and that total pressure loss increases with a magnetic field.

The behavior of supersonic flow under a magnetic field is also important in the MHD power generation. In the past, a high enthalpy extraction was accompanied by an appearance of shock wave due to the Lorentz force. However, a recent experimental study at Tokyo Institute of Technology has shown for the first time that the high enthalpy extraction is possible without an appearance of shock wave.

As described here, the knowledge of supersonic flow under the heat addition, the heat removal (enthalpy extraction) and the magnetic field (Lorentz force), is very important from the viewpoint of both the flow control and the efficiency of MHD power generation.

In this paper, an analytical study was carried out in order to explain the shock behavior under various conditions without doing a complex numerical simulation. The imposed conditions are the energy addition to the flow, the energy extraction from the flow and the Lorentz force acting as an accelerating force or a decelerating force. Relations for shock strength, Mach number and total pressure loss were derived from the one-dimensional simple model. They were adapted to the supersonic flow inside a channel with constant area along the flow direction.

2. Derivation of Shock-Relation for the Flow with Energy Exchange and Lorentz Force

Rankine-Hugoniot shock relations are well known as equations that relate fluid-dynamical properties behind the shock wave with those before the shock wave. The relations can be applied to the flow without energy exchange and the Lorentz force. But, in the present paper, an interest is focused on shock relations for the channel flow under energy exchange and the Lorentz force. Shock relations under these conditions were derived. In order to derive the relations, the ordinal one-dimensional basic equations were used. They are one-dimensional continuity equation, momentum equation and energy equation, and they can be written as follows:

$$\frac{d}{dx}(\rho u A) = 0 \tag{1}$$

Mass conservation

$$\frac{d}{dx}\left\{(\rho u^2 + p)A\right\} = p\frac{\partial A}{\partial x} + A(\mathbf{j} \times \mathbf{B}) \tag{2}$$

Energy Equation

$$\rho u \frac{d}{dx}\left\{\left(c_p T + \frac{u^2}{2}\right)A\right\} = A\mathbf{j}\cdot\mathbf{E} \qquad (3)$$

Here, ρ, u and A denote a gas density, a flow speed and an area of channel, respectively. P and T are a gas static pressure and a static temperature, respectively. $\mathbf{J}$ is a current vector and $\mathbf{B}$ is a magnetic flux density. $\mathbf{E}$ is an electric filed vector and c_p is a gas specific heat at constant pressure.

In the momentum equation (2), the Lorentz force $\mathbf{j}\times\mathbf{B}$ is included, and the energy exchange between the flow and the outside is expressed by $\mathbf{J}\cdot\mathbf{E}$ in the energy equation (3). These equations were applied to the control volume shown in Fig.1. Here, we specify fluid-dynamical properties of the flow at the inlet and those at the exit by subscript 1 and 2, respectively.
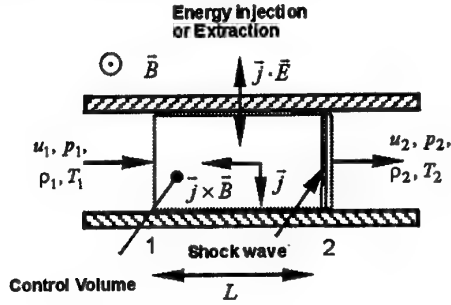
Fig.1. Flow calculation model

The basic equations were integrated from the surface 1 to the surface 2. In the integration, A was assumed constant along the flow direction. Furthermore, the Lorentz force $\mathbf{j}\times\mathbf{B}$ and the energy addition $\mathbf{J}\cdot\mathbf{E}$ were replaced by their spatially averaged non-dimensional parameters S and EA, respectively, and they are defined as follows:

$$S = \frac{<\mathbf{j}\times\mathbf{B}>\cdot L}{<\rho u^2>} \qquad (4)$$

$$EA = \frac{<\mathbf{j}\cdot\mathbf{E}>AL}{<\rho u A c_p T_0>} \qquad (5)$$

Here, $<\ >$ denotes an average along the distance L. The non-dimensional parameter S is known as the interaction parameter and the sign of S is negative when the Lorentz force acts upstream and it is positive for the Lorentz force directing downstream. EA defined by Eq. (5) is the energy addition. It is positive for energy addition from the

outside into the flow and negative for energy extraction from the flow. The negative EA is known as the enthalpy extraction ratio ($=E.E$) in the MHD power generation.

The derived shock relations

Integrating the basic equations from the surface 1 to the surface 2, we can derive relations between fluid properties at the surface 1 and those at the surface 2. Typical two relations are written below.

$$\frac{p_2}{p_1} = \frac{M_1}{M_2}(1+EA)^{\frac{1}{2}}\left[\frac{(\kappa-1)M_1^2+2}{(\kappa-1)M_2^2+2}\right]^{\frac{1}{2}} \qquad (6)$$

$$\frac{p_{02}}{p_{01}} = \frac{M_1}{M_2}(1+EA)^{\frac{1}{2}}\left[\frac{(\kappa-1)M_2^2+2}{(\kappa-1)M_1^2+2}\right]^{\frac{(\kappa+1)}{2(\kappa-1)}} \qquad (7)$$

Here, P_0 is a total gas pressure and κ is a ratio of specific heat. Eq. (6) expresses the shock strength for $M_2<1$, and total pressure loss along the channel can be estimated from Eq. (7). Mach number M_2 included in the Eqs. (6) and (7), is given as a function of M_1, EA and S. When the energy addition EA is zero, these equations agree with the Rankine-Hugoniot relations. The authors would like to call these relations MHD Rankin-Hugoniot relations or Rankin-Hugoniot-Yamasaki relations and they are applicable to the flow with and without energy addition and Lorentz force.

3. Results of Calculation

3.1 Flow Control by Heat Exchange

At first, behavior of the channel flow with heat exchange and without the Lorentz force is described. In this case, the heat addition term EA in the above equations becomes positive for heating the flow from the outside and negative for cooling, respectively.

Figure 2-(a) shows calculated static pressure ratio P_2/P_1 for three inlet Mach numbers M_1 of 1.5, 2.5 and 3.5. We notice in this figure that there are two solutions when energy addition EA is given, and for example, two solutions Sol.1 and Sol.2 exist for $EA=0$ and $M_1=1.5$. Sol.1 and Sol. 2 are the supersonic solution and the subsonic one, respectively, and they correspond to two solutions calculated from the Rankine-Hugoniot relations. The supersonic solution Sol.1 is a trivial one and it indicates that the static pressure P_2 is kept constant ($=P_1$) for the flow without heat addition. The

106

subsonic solution Sol.2 represents the shock wave solution and the static pressure ratio P_2/P_1 denotes the strength of shock wave.

heating exceeds 0.265, the flow with M_1 less than 2.5 does not exist at the channel inlet.
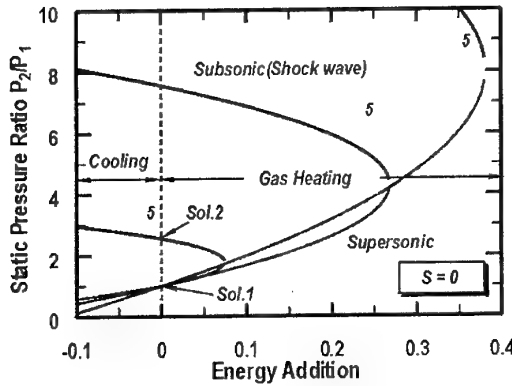
Fig.2-(a). Effect of heat addition on static pressure ratio for $S=0$
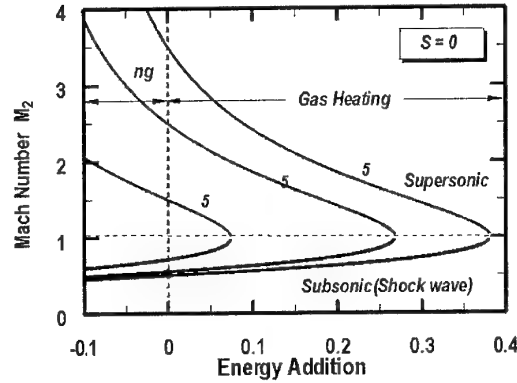
Fig.2-(b). Effect of heat addition on Mach number M_2 for $S=0$

Fig.2-(a) indicates that with an increase of heat addition EA, the static pressure ratio of subsonic solutions decreases. For example, the static pressure ratio P_2/P_1 for $M_1=2.5$ decreases with gas heating and it becomes about 4.2 at $EA=0.265$. On the other hand, the ratio P_2/P_1 for supersonic solution increases with gas heating and it becomes also 4.2 for the same EA. Thus, it is noted that in the case of $M_1=2.5$, any solutions can't be found for larger EA than 0.265. This can be explained as follows. One-dimensional equation which expresses a change of Mach number along the flow, is expressed by

$$\frac{1}{M}\frac{d\mathrm{M}}{dx}=\frac{\left\{1+\frac{\kappa-1}{2}\mathrm{M}^2\right\}\left(1+\kappa\mathrm{M}^2\right)}{1-\mathrm{M}^2}\frac{1}{2}\frac{1}{T_0}\frac{dT_0}{dx} \qquad (8)$$

Here, T_0 is a total gas temperature. In deriving this equation, the area of the channel A was assumed constant and the Lorentz force was neglected. Eq. (8) indicates that dT_0/dx has a similar role to that of dA/dx. In the convergent and divergent nozzle, flow is accelerated from subsonic to supersonic. In this case, a throat corresponds to a singular point mathematically. Thus, dA/dx should be zero at the throat where flow Mach number becomes 1. Considering this phenomenon, we can know that when the flow Mach number becomes equal to 1, dT_0/dx should become zero. In other word, heating or cooling of gas should be terminated at a location, where the flow Mach number becomes 1.0. In fact, it can be seen from Fig.2-(b) that Mach number M_2 at the heat addition of 0.265 is 1.0 for $M_1=2.5$ and the flow is choked. Therefore, if gas

It is noted in Fig.2-(a) that with an increase of gas heating, the strength of shock wave $(=P_2/P_1)$ is weakened and Mach number behind shock wave M_2 is increased (Fig.2-(b)). The weakening of shock wave has been pointed out in reference (3) and (4), and it is suggested that the weakening occurs when the gas heating exists in the flow.

As shown here, the present simple model can also explain the weakening of shock wave by the heat addition. Furthermore, it is suggested that the acceleration of the flow behind shock wave may be related with the shock acceleration found in reference (3).

3.2 Flow Control by Negative Lorentz Force

In this section, the flow control by the Lorentz force is described. Static pressure ratio P_2/P_1, Mach number M_2 and total pressure ratio P_{02}/P_{01} were calculated as a function of interaction parameter S. Here, the interaction parameter was selected negative. The negative interaction parameter indicates that the Lorentz force $\mathbf{j}\times\mathbf{B}$ acts toward negative x-direction. In order to apply the negative Lorentz force, there two methods; 1) applying current from an external electrical power supply, 2) use of current induced by an electro-motive force inside the flow. In applying current from the external power supply, the current should be applied in the negative y-direction (Fig.1) to impose the negative Lorentz force on the flow. The current induced by the electro-motive force flows automatically along the negative y-direction, and as a result, the Lorentz force $\mathbf{j}\times\mathbf{B}$ acts toward negative x-direction. This corresponds to MHD

107

power generation. The application of the Lorentz force indicates an occurrence of energy exchange between the flow and the outside. In order to estimate this energy exchange, an electrical efficiency η_e defined by the following equation was used.

$$\eta_e = \frac{<j \cdot E>}{<j \times B \cdot u>} \qquad (9)$$

When the current is applied from the outside, the electrical efficiency becomes negative and it is positive for MHD power generation. Combining Eq. (9) with Eq. (5), we can estimate the energy exchange, and the energy addition EA is related to the interaction parameter S and to the electrical efficiency η_e.

$$EA = \frac{2(\kappa - 1)M_1^2}{2 + (\kappa - 1)M_1^2} S\eta_e \qquad (10)$$

Figure 3 shows results of calculation for $M_1 = 2.5$. Fig.3-(a) indicates that when the electrical efficiency η_e is constant, Mach number M_2 in supersonic solution decreases with the negative interaction parameter. On the other hand, M_2 in subsonic solution increases with the negative S.

The increase of Mach number M_2 in subsonic solution suggests the weakening of shock wave and in fact, the static pressure ratio shown in Fig.3-(b) is decreasing with the negative S for constant η_e. If we look a change of M_2 along the broken line plotted in Fig.3-(a), we notice that with a decrease of electrical efficiency, M_2 increases. At the same time, the strength of shock wave is weakened (see Fig.3-(b)). Here, it should be recalled that at low electrical efficiency, most of the work done by the flow against the Lorentz force is converted into Joule dissipation. The Joule dissipation results in gas heating. In order to illustrate the gas heating, the energy addition is plotted in Fig.3-(c). The negative energy addition EA denotes an extraction of thermal energy from the flow and it is an enthalpy extraction in the MHD power generation. Along the broken line (S is fixed) shown in Fig.3-(c), the negative energy addition is decreasing with the decrease of electrical efficiency, and this indicates a rise of gas temperature. Therefore, in order to reduce the shock strength, the flow should not be cooled by the enthalpy extraction, but be heated.

Total pressure ratio is plotted in Fig.3-(d). It should be noted in this figure that the total pressure is lost by the impose of the negative Lorentz force. For example, the total pressure ratio for $S=0$ is 0.576 whereas it is 0.51 at point P1

Fig.3. Effect of the negative Lorentz force on Mach number (a), static pressure ratio (b), energy addition (c) and total pressure (d)
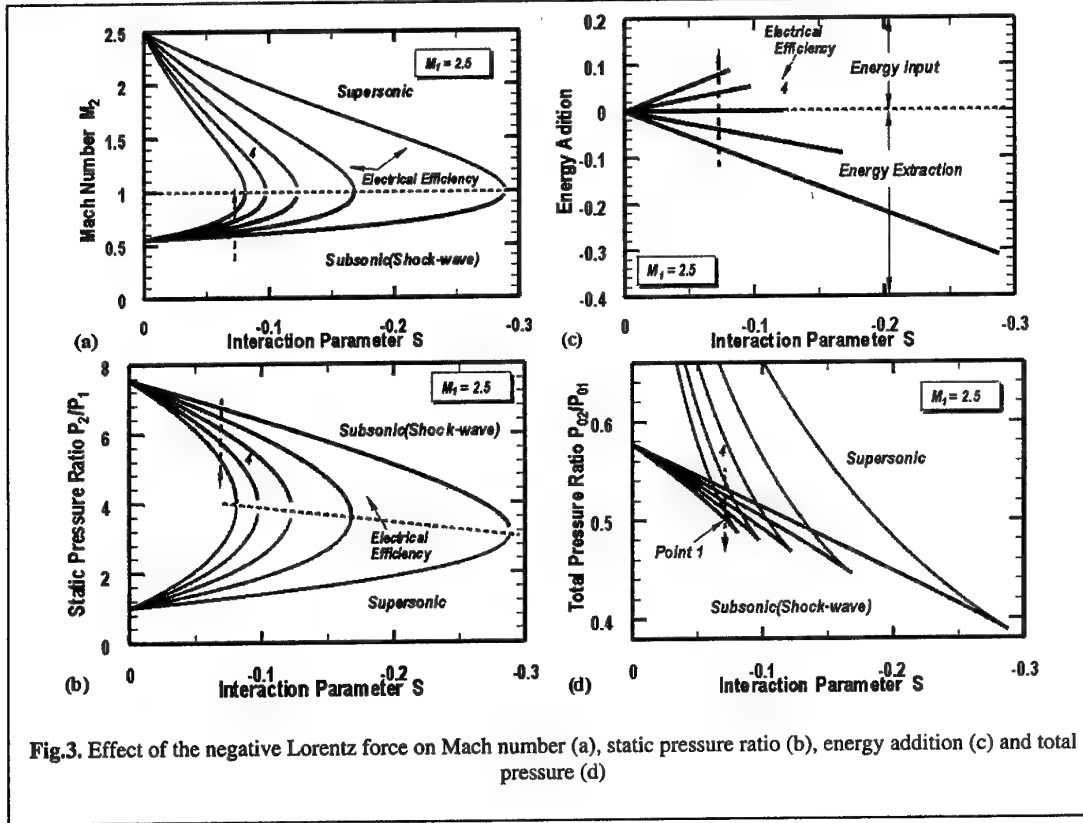
($S=-0.065$ and $\eta_e=-0.8$). This indicates a very important fact that the weakening of shock wave by the negative Lorentz force is accompanied by total pressure loss. From Fig.3-(d), it can be seen clearly that the total pressure loss increases with the decrease of electrical efficiency. Therefore, it is said that although the low electrical efficiency or the energy addition is useful for reducing the shock wave strength, a remarkable total pressure loss is induced. Particularly, in the case of energy addition, the energy is injected into the flow through the current supplied from the external power supply. This accompanies the total pressure loss in an electrical power generation. Concequently, the total pressure is always lost in the energy injection as a whole.

3.3 Flow Control by Positive Lorentz Force

Effect of the positive Lorentz force ($S>0$) on the flow is shown here. For this purpose, we introduce an acceleration efficiency η_{ac} defined by

$$\eta_{ac} = \frac{<j \times B \cdot u>}{<j \cdot E>} = \frac{1}{\eta_e} \tag{11}$$

(a)

(b)
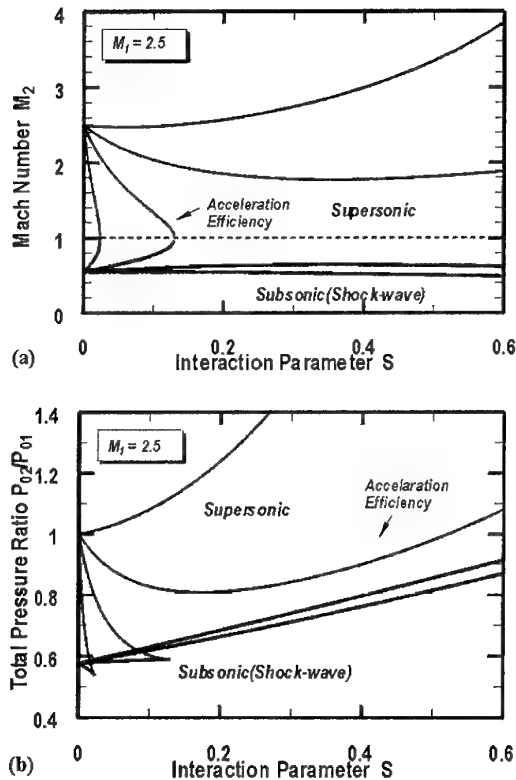
Fig.4. Effect of the positive Lorentz force on Mach number (a) and total pressure (b)

In this case, the energy addition into the flow is expressed by the following equation.

$$EA = \frac{2(\kappa-1)M_1^2}{2+(\kappa-1)M_1^2} S \frac{1}{\eta_{ac}} \tag{12}$$

Calculated results are shown in Fig.4-(a) and (b). Supersonic solutions in Fig.4-(a) indicate that for acceleration efficiency of 0.1, 0.3 and 0.5, the supersonic flow is not accelerated but decelerated even if the Lorentz force is acting as flow acceleration. This is because the gas heating which results in the flow deceleration (see Fig.2-(b)), is dominant compared with the acceleration due to the Lorentz force. Therefore, η_{ac} must be high for an efficient acceleration. Looking at subsonic solutions, we notice the remarkable flow acceleration for $\eta_{ac}=0.1$ and 0.3. In the case of $\eta_{ac}=0.3$, the total pressure is not decreased, but increased slightly since the work done by the Lorentz force is added into the flow. Therefore, it seems that the energy addition under the positive Lorentz force is the best way to reduce the shock wave strength without total pressure loss. But, it requires as mentioned above, the additional energy.

4. Experimental Observation of Supersonic Flow with and without Shock Wave under Lorentz Force

The above analytical results indicate that when S and η_e are given, there exist two solutions: the supersonic flow and the subsonic flow with shock wave. In order to know which flow appears in an actual situation, experimental data obtained at Tokyo Institute of Technology, are reviewed in this section. At T.I.Tech, experimental studies on the closed cycle MHD power generation have been carried out using shock-tube driven disk MHD generators. Through the experimental studies, many photographs of the flow under the Lorentz force and the negative energy addition (=enthalpy extraction) were taken. Figure 5 shows typical two photographs taken by a high speed-framing camera. Fig.5-(a) shows a photograph of the flow at low seed fraction (=S.F.) of 1.9×10^{-4}. Although the Faraday current j_0 along the azimuthal direction of the disk MHD channel has not be measured in this experiment, the interaction parameter $S = j_0 B / \rho u^2$ is regarded small because of the low seed fraction. In this photograph, we can see many luminous layers at the MHD channel and they extend downstream. These layers are weak compression waves originating from the rear edges of swirl vanes installed in the nozzle. But, it is noted in this photograph that there is no shock

wave in the disk MHD channel. This is confirmed also by measured static pressure distribution along the radial direction.

Nozzle   MHD channel

(A) S.F.=1.9×10⁻⁴   (B) S.F.=5.2×10⁻⁴
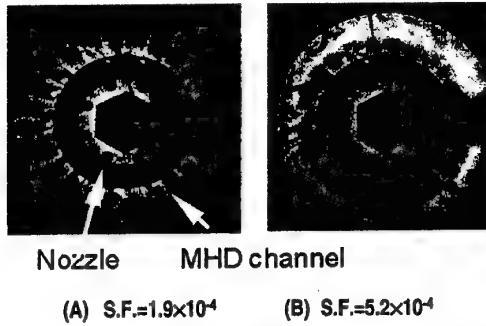
Fig.5. Photographs of flow taken by high speed camera
(B=3.0 Tesla , P_0 =0.32MPa, R= 0.14ohms)

On the other hand, we can see a circular bright layer in the photograph (b) taken at high seed fraction of 5.2×10^{-4}. The measured static pressure distribution indicates that the bright circular layer is a shock wave. In this case, the interaction parameter is regarded large and thus, this shock wave is ascribed to the strong Lorentz force. From many photographs and measured static pressure distributions, we can plot a map of shock formation on the relation between the negative energy addition and the isentropic efficiency. Here, the isentropic efficiency is defined by Eq. (13).

$$\eta_{isen} = \frac{|EA|}{\left\{ 1 - \left(\frac{P_{02}}{P_{01}} \right)^{\frac{\kappa-1}{\kappa}} \right\}} \qquad (13)$$
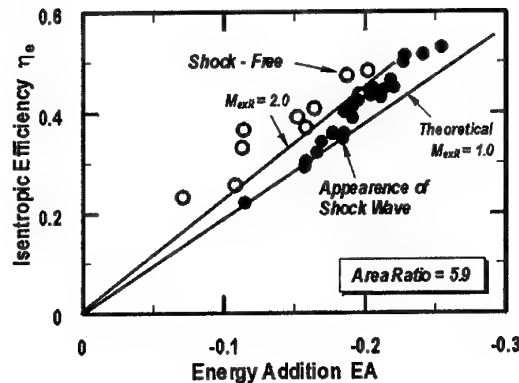
Fig.6. Experimental relation between isentropic efficiency and appearance of shock wave

The result is shown in Figure 6. Solid circles denote the appearance of shock wave and circles denote the shock-free flow. From this figure, it seems that at the same negative energy addition (=enthalpy extraction), there are two flow types of the supersonic flow and the subsonic flow with shock wave. This point is discussed later.

It is noted in Fig.6 that the isentropic efficiency is kept higher in the shock-free flow for the same negative energy addition. According to Eq. (13), the isentropic efficiency decreases with a decrease in the total pressure ratio of P_{02}/P_{01}. Therefore, the low isentropic efficiency in the flow with shock wave is ascribed to larger total pressure loss due to shock wave.

5. Explanation of Experimental Result by the Present Analytical Model

Here, we try an explanation of experimental results shown in Fig.6. For this purpose, the analytical model described in Sec. 2 was used. In order to explain the experimental data quantitatively, an area change of the channel should be included in the present model. This is because the area of the disk MHD channel used in the experiment, increases along the flow direction and an area ratio (=exit/inlet) is 5.9. But, the objective of the present simple model is to explain the experimental data avoiding a complex mathematical procedure. Therefore, the area ratio was assumed 1.0. Furthermore, the inlet Mach number M_1 was assumed 2.0. In the calculation, the interaction parameter S and the electrical efficiency η_e were changed as parameters.
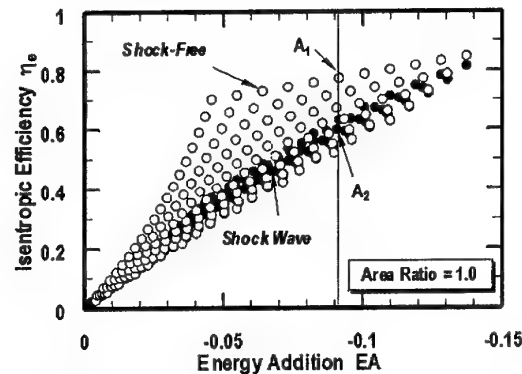
Fig.7. Calculated relation between isentropic efficiency and appearance of shock wave

The calculated result is shown in Figure 7. In this figure, the supersonic and the subsonic (shock wave) solutions are plotted by circles and by solid circles, respectively. By comparing Fig.7 with Fig.6, we notice a significant difference in

110

values of both the negative energy addition and the isentropic efficiency. And, a larger negative energy addition (=enthalpy extraction) is achieved in the experiments. This is ascribed to the large area ratio in the experiments.

As shown in Fig.3, the present analytical relations provide two solutions at the same EA for given S and η_e, These two solutions are denoted by A_1 and A_2 in Fig.7. However, in the actual situation, the flows corresponding to these two solutions do not exist simultaneously, but one of them exists. Consequently, it is suggested that S and/or η_e were different in the observed two flows.

Here, the very important and interesting question is still left. Which flow does appear in an actual situation ? Concerning this question, the authors do not have a definite answer and therefore this point should be investigated further. However, the present calculated results explain qualitatively the experimental data of shock formation under the Lorentz force and the negative energy addition.

Conclusion

The analytical study on characteristics of supersonic flow under the energy addition, the energy extraction and the Lorentz force was carried out. The followings are drawn as conclusions.
1. The simple relations for fluid-dynamical properties under the energy addition, the energy extraction and the Lorentz force were derived.
2. The derived relations can explain the observed phenomenon of shock weakening by the heat addition. The heat addition is found also to make the Mach number behind shock wave high.
3. The weakening of shock wave by the negative Lorentz force is always accompanied by the total pressure loss.
4. The simple relations can explain well the measured relation between the negative energy addition(=enthalpy extraction) and the isentropic efficiency of the MHD generator and shock formation.

References

1. J.Poggie, "Energy Addition for Shockwave Control", AIAA 99-3612, 30th Plasmadynamics and Lasers Conference, Norfolk, VA, 1999
2. Y.P.Golovachov, et., al, "Numerical Simulation of MGD Flows in Supersonic Inlets", AIAA 2000-2666, 31st Plasmadynamics and Lasers Conference, Denver, CO, 2000
3. S.Merriman, "Shock Wave Control by Nonequilibrium Plasma in Cold Supersonic Gas Flow", AIAA200-2327, Fluids 2000, Denver, CO, 2000
4. R.B. Miles, "Flow Control by Energy Addition in to High-Speed Air", AIAA200-2324, Fluids 2000, Denver, CO, 2000

17. REARRANGEMENT OF SHOCK WAVE STRUCTURE IN REACTING GASES

Baryshnikov AS, Basargin IV, Chistyakova MV
Ioffe Phisico-Technical Institute, S.Petersburg, RUSSIA

Abstract. Among shock wave instability effects conditioned by endothermic processes one should distinguishes: flow instability in front of bow part of body in polyatomic gases at regimes of gas molecular dissociation, flow instability behind ionizing shock wave in monatomic gases and rearrangement of flow with shock waves in plasma of glow and decay discharges in air, last results of which were presented in this paper.

Experimental data of rearrangement of shock wave during moving of them across plasma column of glow and decay discharges is presented. It was obtained that integral pressure impulse in wave was not changed. Nonmonotonic distribution across the discharge column of so called "sound" speed (the shock wave speed at which full dispersion arise) was observed. Moments of time at which after switching of discharge rearrangements arise were corrected. On the base of experimental data and results obtained earlier conclusion about effect mechanism was made that it connected with dispersion of shock wave disturbances spreading in relaxing media. It is well known that plasma of glow discharge is the same media. Using dispersion theory of shock wave in relaxing medium, experimental data and comparing of energy and time parameters of inner states of plasma studied with ones of sound disturbances mode, responsible in according with experiment for effect arising, it succeeded to find state, $O_2(a^1\Delta_g)$. It is relaxation of this state which determines the effect arising in air plasma.

Instability of shock wave due to the exothermic reaction is well known [1]. To-day shock wave instability connected with endothermic reactions is of great interest, for instance shock flow instability in dissociating gases [2,23,24,27], in air weakly ionized plasma or behind the ionizing shock wave [3,24-34]. Experimental results were obtained not only on shock tube installations, but for bodies in free flight on ballistic installation [2,28]. The effect was observed nearly at the regimes corresponding to begin of dissociation CCl_2F_2 (Mach number M~4), CF_4 (M~10), CO_2(M~10), O_2 (M~7) at pressures near 30 Torr (shock tube experiments carried out under the pressure p < 5 Torr) [27] in reacting gases and to begin of ionization behind strong shock waves for Ar, He, Xe (M~20, p~ 1-25 Torr and for some tests up to 100 Torr) in ionizing gases. Instability in reacting gases is more convenient for application of the effect, but now there are no experimental evidence of the effect in air and no catalysts were found in air. At the same time the analogous effect was found in glow discharge in *Ar* and air for not strong shock wave for nearly the same pressures p~10-40 Torr [3,28-33]. There is a discussion about mechanism of this effect of shock flow rearrangement in reacting gases and in plasma. In plasma first hypotheses were related with chemical processes and excitations of particles [26,27,29], but further investigation made it obvious that those hypotheses were not available [34]. The second ones deal with ion-sound transfer of energy [4]. However besides the experiment, which shows independence of effect existing on the electron concentration [5], there are simple estimations of ion-sound speed (in experiments Mach number close to 1) showing that ion-sound speed is greater than sound speed near discharge boundary in three

times and at center in five times. Such great increasing haven't been observed in experiment and at center of discharge increasing is almost absent. Ion-sound soliton is doubtful too because maximum dimensions of it should be of length $l=r_D$ $(\rho_0/\Delta\rho)^{1/2} \approx 0,3$мм , where ρ_0 – plasma density in front of shock, $\Delta\rho$ - jump of density on it, r_D – Debye radius [6]. This length is in two orders of amount less than observed. At greater amounts ion-sound cavity must be converged. Hypothesis about rearrangement due to radiation of plasma energy could be described by Carteveg-de-Vries-Burgers equation [7], solution of which as for ion-sound waves performs oscillations of density and other characteristics behind the shock wave. For small disturbances amplitude of them will be 2/3 of shock front amplitude. Such behavior isn't observed in experiments. Another model [8] suggests an mechanism of not large but very rapid cooling of plasma as result of radiation from so called pseudo-metastable states of atomic oxygen. It should be mentioned the flushes of radiation in number of experiments [9]. In [10] some kinetical scheme was suggested based on the number of sufficiently slow secondary processes (10-100s). Thanks to peculiar close metastable and resonance states in argon (res 11.83eV, met 11.72eV, or res 11.62eV, met 11.55eV) radiation has effective order 3 on concentration of species which leads to dissimilar radiation. And oxygen has got a similar pseudo-metastable state: res 9.51eV $(3^0S_1^0)$, met 9.13eV $(3^0S_2^0)$. At this mechanism pressure increasing should be nearly 20% [8]. However in experiment much more increasing is observed. So up to date there was no hypothesis explained fully the effect in plasma. Single fact that should be recognized is the fact of common reason for effect in plasma and

in reacting gases, namely, that physicochemical processes initiate the instability (the effect doesn't disappear up to almost 100sec in decaying plasma after switching the glow discharge in experiments [5]). At the same time the mechanism in reacting gases is more clear.

Shock wave instability and rearrangement of flow behind it in reacting gases have been good studied. Mechanism of shock wave instability in real media is good investigated too [35]. For interested effect mechanism is conditioned of baroclinity of reacted gas flow independently of absorption or release of energy in reactions [11]. As a result the vortex mode of disturbances shall amplified. In spite of small value of pressure disturbance it is sufficiently large in comparison with pressure in front of shock to destroy shock wave. Computations [12] shows that amplitude and development time of front disturbances coincides with experimental ones. Further investigations of planed-parallel flow layer of compressed reacted gas in front of body indicates instability for disturbances of high frequency [13].

If physicochemical processes are modeled by volume source of heat production (or absorption) Q, while the curvature of current lines is modeled by the gradient of longitudinal velocity, U', along the transverse coordinate Y, the problem reduces to single differential equation:

$$\pi'' = \pi' \frac{2U'}{Uc} + \pi a^2 \left(1 - \frac{(U-c)^2 \gamma M^2 [a(U-c)\rho + idQ/dT]}{T[\gamma a(U-c) + idQ/dT(1-\gamma)]} \right)$$

(1)

Here the pressure perturbation is $\Delta p = \exp[ia(X-ct)]$, $T(Y)$, $\rho(Y)$ and $P(Y)$ are the dimensionless temperature, density and gas-pressure distributions, M is the Mach number, and i imaginary unit (the square root of minus one). A solution of (1), as in the theory of boundary-layer stability, is sought in the form $\pi = \pi_0 \exp(ibY)$. Then the study of the stability reduces to the study of the roots of a fourth-degree polynomial in $z = -ia\rho(U-c) / (ks)$:

$$z^4 + \kappa z^3 + z^2 + \left[\frac{\kappa(1-d)}{\gamma} + g \right] z + \frac{g\kappa(1-d)}{\gamma} = 0,$$

(2)

which depends on four parameters:

$$d = \frac{\rho \, dQ/d\rho}{T \, dQ/dT}, \ g = 2ab\frac{U'\rho}{ks}, \ \gamma = \frac{c_p}{c_v}$$

$$d = \frac{T \, dQ/dT}{ks}, \ (s^2 = P\frac{\rho}{M^2}, \ k^2 = a^2 + b^2)$$

(3)

In the case of ionization in air [14] the ionization goes through a process of associative ionization with the participation electronically exited levels and the high-frequency boundary of stability ($\lambda < 0.05$m, frequency $f > 8$kHz) corresponds to the beginning of ultrasonic range in air (20 kHz).

It should be mentioned that (1) is the right part of well known Orr-Sommerfeld equation for viscid case, which gives instability only if second derivation of velocity distribution across the layer is equal zero. It could be realized behind the body at detach point of flow off the body surface. Investigated effect is a case when instability can take the place up to the body for high-frequency perturbations in shock layer of reacting gas without bend point in distribution of velocity, only with velocity gradient.

Experiment [5] shows that the effect doesn't disappear up to almost 100 sec in decaying plasma after switching the glow discharge. Deionization time after switching the discharge of the same parameters [16] is 10^{-5}sec, and cooling time is about 10^{-4} sec. In experiments [5] the time of first essential rearrangement of flow structure is 10^{-2} sec. It is a time of deexcitation of vibration mode of inner energy. So as for the effect in reacting gases and in plasma physicochemical processes do lead to instability. It is this characteristics in common which units two effects together.

To go into the mechanism of effect in plasma it should be mentioned another result of experiments that full pressure impulse doesn't change at rearrangement of flow structure. It means that at rise of the effect only dispersion of wave takes place because there is only rearrangement of distribution of pressure. High-frequency component of sound waves leave behind the low-frequency one forming shock wave of so called "precursor", while the second part causes the relatively slowly pressure increasing behind it. Investigations of such kind dispersion were carried out as in theoretical and in experimental works [17-19]. The general equation describing such kind dispersion in reacting gases was obtained in [17]:

$$\Theta^2 u_{\xi\xi} - u = -m\Theta\frac{v_{\xi\xi}}{2} - m\Theta^2 \frac{v_{\xi\xi\xi}}{2},$$

(4)

here $u = v_t + vv_\xi \beta$, subscripts mean derivations, $\Theta = \tau/T$ - relation of relaxation time to sound wave period, v - sound wave velocity (or for compressible media – inverse density), $\xi = (x - c_0 t)/c_0 T$ - "wave" variable (x – distance, t – time), c_0 - low-frequency sound speed (without dispersion), $\beta = (\gamma+1)/2$, γ - relation of specific heat capacities, $m = (c_\infty^2 - c_0^2)/c_0^2 = (\partial P/\partial \eta)_\rho$ – so called "dispersion

113

force" (P – pressure, ρ -density, η - relaxation parameter), c_∞ - high-frequency sound speed.

After not complicated computations and Laplace transformation equation takes the form:

$$p(\Theta^2 v_{\xi\xi} - v) = v v_\xi + m\Theta \frac{v_{\xi\xi}}{2\beta^2} - 3\Theta^2 v_{\xi\xi} v_\xi -$$

$$- \Theta^2 v_{\xi\xi\xi} v - m\Theta^2 \frac{v_{\xi\xi\xi}}{2\beta^3} \qquad (5)$$

One can see that there is a resonance situation when Laplace parameter goes to infinity at ($\Theta2v\xi\xi$-v) equal to zero. It can be shown that electron relaxation would give only resonance for "hypersound" frequency, waves of which effectively fading even in a distance less than 1mm. So it can't be a base of mechanism of investigated effect. Found experimental times correspond to vibration processes or to secondary processes with a number of complicated and complex ions specific for low temperature plasma.

The results of measurements of local sound velocity (minimum velocity, at which effect is not disappeared yet) was measured in experiment in plasma in inhomogeneous non equilibrium discharge plasma and presented on Fig.1.
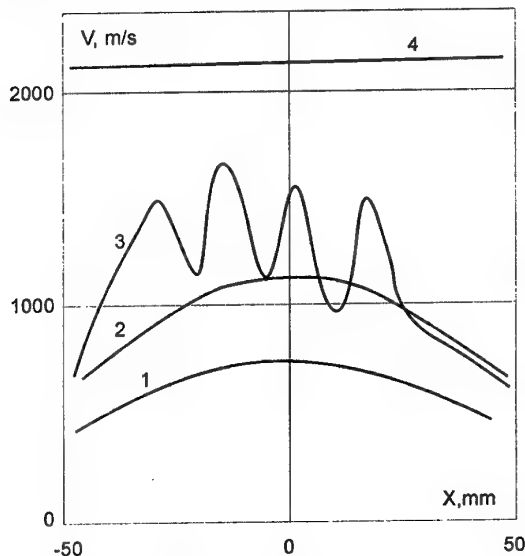
Fig.1: 1 - sound velocity, 2 - velocity calculated [4], 3 - experimental velosity, 4 - ionic sound velocity.

One can see nonmonotonous character of it. Its values lye down between the thermal and the ionic velocities. Thus measured sound velocity couldn't be classified not as thermal nor as ionic sound be determined. It should be emphasized too that smooth alteration of gas temperature at constant pressure did not can explain nonmonotonic character of experimental results. The single thermodynamic parameter which can such abruptly alter across he discharge is the plasma composition.

Measured values are the velocity of small disturbances spreading of that mode, which is responsible for appear of effect. From these values the mode energy can be calculated. From another side this energy must correspond to the mode of inner process, which is responsible for the effect. Calculated for single particle this energy is $3{,}7 \cdot 10^{-20}$J or in spectroscopic units - 1880sm^{-1} or 0,23 eV. This value is more close to value of vibration quanta than to energy of electron levels. At the same time the coupling energy of such complex ions as NO^+-N_2, O_2^+-H_2 (0,2eV) is close to the same energy value too. However it should be mentioned that number density of exited molecules is in a ten times less at study regimes than the all particles density [14], consequently the exited levels energy near 1eV should be found. It corresponds to such metastable levels of oxygen as: $O_2(a^1\Delta_g)$ - 0,98eV, $O_2(b^1\Sigma_g^+)$ - 1,63eV [22]. For instance, other metastable levels of air have following energies: $NO(b^4\Pi)$ – 4,7эB, $N_2(A^3\Sigma_u^+)$ – 6,17eV. It should be emphasized that, in accordance with [14], it is the number density of $O_2(a^1\Delta_g)$ is less in a ten times than all particle density while the concentration of $O_2(b^1\Sigma_g^+)$ – is less in a hundred times. It's came out that attention should be paid to state $O_2(a^1\Delta_g)$. It obtains not only high concentration (due to the low excitation energy) but and very long radiation time of existing – $2{,}7 \cdot 10^3$c [22]. Furthermore it is consequent from calculations [14] that time of thermal excitation (it means that and time of deexcitation), nearly at the same regimes of glow discharge, is measured in millieseconds. It corresponds to the time of essential rearrangement of flow after the switching off the discharge. Thus conducted experimental investigations able us to determine that the effect mechanism is caused by dispersion of high frequency component of sound disturbances, which occur obviously through physicochemical relaxation of excited state of oxygen in plasma $O_2(a^1\Delta_g)$.

References

1. Zeldovich YaB, Barenblat GI, Librivich VB, Mahviladze GI. Mathematical theory of burning and explosion. M: Nauka, 1980
2. Baryshnikov AS, Bedin AP, Maslennikov VG, Mishin GI. About instability of bow shock wave. Tech.Phys.Lett, v.5, p.281, 1979
3. Basargin IV, Mishin GI. Shock wave precursor in glow discharge plasma. Tech.Phys.Lett, v.15, p.55, 1989

4. Bedin AP, Mishin GI. Ballistic investigations of aerodynamic drag of sphere in ionized air. The letters in ZTF, v.21, 1995, p.14

5. Baryshnikov AS, Basargin IV, Dubinina EV, Fedotov DA. Rearrangement of shock wave structure in decaying discharge plasma. Tech.Phys.Lett., v.23, p.259, 1996

6. Arcimovich LA, Sagdeev RZ. Plasma physics for physicists. M.: Atomizdat. 1979

7. Zaslavskii GM, Sagdeev RZ. Introduction in nonlinear physics. M.: Nauka. 1988

8. Baryshnikov AS. Intensive plasma energy release behind a shock wave and flow pattern.Rarefied gas dynamics, Ed. by Beylich AE Proc. 17th Int.Symp. on Rarefied Gas Dynamics, VCH, Weinheim - N.Y. - Basel – Cambridge, p.263, 1991

9. Sufian A, Ryazin AP. Experimental investigation of strong shock wave structure in argon. Moscow University Bulletin. Physics, Astronomy, v.25, p.94, 1984

10. Baryshnikov AS. Physicochemical mechanism for rearrangement of shock wave structure in a decaying discharge plasma., Tech.Phys.Lett , v.23, p.881, 1997

11. Baryshnikov AS, Vasiliev NYu, Safonov AB. Study of flow peculiarities behind shock wave at dissociation and ionization of gas. Physics of burning and explosion, N 1, p.101, 1987

12. Baryshnikov AS, Vasiliev NYu. Vortex formation at dissociation in shock layer and disturbances on bow shock wave front. Numerical methods of continuous medium mechanics. v.17, p.3, 1986

13. Baryshnikov AS. Physical method for controlling the flux in hypersonic air intake. Tech.Phys.Lett, v.22, p.667, 1996

14. Akishev YuS, Deryugin AA, Napartovich VB, Kochetov IV, Napartovich AP, Trushkin NI. Experimental investigation and numerical simulation of glow discharge of direct current of atmosphere pressure. Plasma Physics, v.20, p.571, 1994

15. Maicopar GI. Nonequilibrium physicochemical processes in aerodynamics. M.: Mashinostroenie, 1972

16. Zarin AS, Kuzovnikov AA, Shibkov VM. Free localized radio-frequency discharge in air. M.: Neft i Gas, 1996

17. Nakoryakov VE, Borisov AA. Disturbances spreading in medium with relaxation or chemical reaction. Physics of burning and explosion, v.12, p.414, 1976

18. Pischalnikov YuA, Sapozhnikov OA, Hohlova VA. Modification of spectral approach for description of nonlinear acoustic waves with ruptures. Acoustic journal, v.42, p.412, 1996

19. Andreev VG, Klivland RO, Pischalnikov YuA, Sapozhnikov OA, Hohlova VA. Diagnostic of relaxing medium using acoustic impulse with shock front. Acoustic journal, v.45, p.13, 1999

20. 20. Artamonov KI. Thermohydroacoustical stability. M.: Atomizdat, 1991

21. Physical amounts. Ed. Grigoriev IS, Meilihov EZ. M.:Atomizdat, 1991

22. Radcig AA, Smirnov BM. Handbook on atomic and molecular physics. M.: Atomizdat, 1980

23. Hilton W.F. High-speed aerodynamics. London, 1952

24. Griffiths RW, Sandeman RJ, Hornung HG The stability of shock waves in and dissociating gases.- J.Phys.D.: Appl. Phys., v.9, p.1681, 1976

25. Glass II, Liu WS Effects of Hydrogen Impurities on Shock Structure and Stability in Ionizing Monatomic Gases. Part I. Fluid Mech., v.84, p.55, 1978

26. Tumakaev GK, Maslennikov VG, Serova EV. About instability of flow behind shock wave of great intensity in monatomic gases. Tech.Phys.Lett, v.6, p.354, 1980

27. Mishin GI, Bedin AP, Juschenkova NI and others. Anomalous relaxation and instability of shock waves in gases. Tech.Phys , v.51, p.2315, 1981

28. Mishin GI, Serov YuL, Yavor IP. Experimental Investigation of Supersonic Flight of a Sphere in Weakly Ionized Air. In: Proc. of the 2 nd International Conference on Experimental Fluid Mechanics, 1994, Torino, Italy, p.750

29. Baksht FG, Mishin GI. Influence of vibration relaxation on parameters of shock wave in molecular gases. ЖТФ, v.53, p.854, 1983

30. Gridin AJu, Klimov AI Shock wave structure in plasma (release of energy reserved in discharge plasma behind shock wave). Chemical Physics, v.12, p.363, 1993

31. Gridin AJu, Klimov AI, Hodataev KV. Investigation of shock wave spreading in heterogeneous transversal impulse discharge. High Temperature Thermotechnics, v.32, p.486, 1994

32. Mishin GI, Klimov AI, Gridin AJu. Measurement of pressure and density in shock wave gas discharge plasma. Tech.Phys.Lett., v.17, p.84, 1991

33. Serov JuL, Yavor IP. Ablation at supersonic body moving in plasma. Tech.Phys.Lett., v.65, p. 38, 1995

34. Houwing AFP, McIntyre TJ, Taloni PA, Sandeman DJ On the population of the metastable states behind unstable shock waves in ionizing argon. J.Fluid Mech., v.170, p.319, 1986.

35. Kuznetsov NM. To theory of shock waves instability. Journal of experimental and theoretical physics, v.88, p.470, 1985

115

18. SHOCK WAVE STRUCTURE AT THE CRITICAL LEVEL OF HEAT ADDITION.

V.Yu. Galyatin and V.S.Sukhomlinov
Research Institute for Physics Saint-Petersburg State University, Saint-Petersburg, Russia

V.A. Sheverev and M. V. Otugen
Polytechnic University, Brooklyn, NY, USA

This work is a continuation of the theoretical study of the shock wave structure with heat addition in the shock region that was reported at the Workshop a year ago (V.V.Kuchinsky, V.S. Soukhomlinov, V.A. Sheverev and M.V. Otugen "Effect of directed heat addition on the formation and subsequent structure of a shock wave around a body in a low temperature plasma", The 2nd Workshop on Magneto- and Plasma Aerodynamics for AeroSpace Applications, Moscow, 5-7 April 2000, p.p. 307-312).

Aerodynamic effects occurring near a body placed in a supersonic flow with heat addition into the boundary region, are adequately described in the developed theoretical model. Earlier results predicted the so-called "critical" power of the heat addition above which the shock wave moves away from the body into the upstream flow region. It was also shown that when the heat addition level is smaller than the critical value, the shock wave weakens and widens, and, depending on the spatial profile of the heat addition source, the bulk velocity distribution in space is either monotonous or has a single maximum.

In this report, the structure of a shock wave at a critical rate of heat addition is analyzed. In particular, the analysis shows that spatial profiles of the bulk velocity and local Mach number always have a maximum, i.e. the spatial profiles at the critical heat addition are always non-monotonous.

Efficiency of transferring shock wave into a "critical" state was analyzed for various spatial distributions of the heat addition. It is shown that the critical level of energy necessary to transfer gas into critical state decreases noticeably if a certain part of energy is deposited upstream from the shock. This tendency strengthens with increased Mach number.

19. THE RADIATIVE SUBSTRUCTURE IN THE INTENSE SHOCKS

Dr. Valentine A. Belokogne
Institute of Mechanics at the Moscow State University,
Academia Cosmonautica, Russian Academy of Natural Science.
<valentine_belokogne @ mtu-net.ru>

The local equilibrium radiation effects induces many peculiarities in gasdynamics phenomena i.e. shock structure depending on relation of radiation pressure to matter pressure (here n_r = mean photons number local density)

$$P_r/p_m = (n_r kT/1.11)(1/n_m kT) \approx n_r/n_m \sim T^3/\rho_m.$$

Therefore, importance of radiation is evident for the intense impact and explosive processes – not only in Nature: in energetics also, essentially fusion one, which are feasible for the flying machines of XXI Century.

The prominent peculiarity of radiative shock structure consists in the disappearing and appearing of **isothermal discontinuity** inside of the total structure (Belokogne 1959, 1968). The recent (Astrophysical Journal Supplement 2000, April) discussion on such subshock contained some instructive blunders.

§1. The peculiarity of permanent shock wave structure [1] in the considered two-component media consists in the peak of light (photons of equilibrium radiation or other ultrarelativistic bosons [2]) component concentration ahead the main subshock of the matter density.

The methodological approach of this paper is like one by Rayleigh (1910 [1]), while the like cumulative effect was pointed by Cowling (1942 [4]) and Sergey D'yakov (1954 [6]) for the case of both material components.

My very first attempt here consisted essentially in search any pluasible condition for p o s t s h o c k (!) Mach number $M_+ > 1$. Prof. Georgy Pokrovsky insistently (long ago) stimulated my efforts for such problem almost evidently incorrect. The search was marked by the derivation of algebraic criterium for $M_+ \geq 1$ in the photon-matter mixture and i s o t h e r m a l ("newtonian") postshock sound – during of student vacation, summer 1954. The followings was more complicated, with search of potential applications (less surprising, however [7]).

The rivalry to S. Belen'ky (cf [12]) was no serious, because his considerations means only qualitative statement (let rigorous), without distinct mathematical criterium. The result like my own was obtained later [10] by Vladimir S. Imshennik

(close colleague of S. Belen'ky) already for two-temperature material component and, even later, for the relativistic material plasmas (compare with interesting generalization of my work by my frend George Chapline [17]).

Extensive and partly profound research in same direction was published recently by specialists of Los Alamos (LANL) and of University of Michigan [22] with remarkable ignorance of my widepublished results. The most recent consideration of the problem [23] contains the other serious misunderstanding.

Some refinements in fundamental preconditions, and potential applications of obtained results are contained in numerous publications, partly mentioned in our reference list.

§2. The general principles necessary for the thermo- and hydrodynamic considerations of shock ware structure were developed around years 1870-1910 (Rankine, Rayleigh, Taylor) by 90 %.

The statistical-thermodynamics refinements (mainly by works of Gibbs, Plank, Bose, Heisenberg, Tolman and, in something, by Bridgman) appeared up to 1941 [2-3]. The specific role of radiation was pointed by Baron Rayleigh in 1910 correctly, let in a very general form, and more recently – much more elaborately – for the problems like the astrophysical and "extremal" technology processes. Our paper is the attempt in this direction. Let's start generally.

One – dimensional processes in a variety of media corresponds to the identity for work W, internal energy E, and "heat" Q

$$dQ \equiv dE + dW \equiv dE + p^{xx} dV \equiv dE + p^{xx} d(1/\rho), \qquad (1D)$$

where p^{xx} used for hydrodynamic and like phenomena with applicability of "Earnshaw line" on $\{p^{xx}-V\}$ diagram valid for stationary flows $(\partial/\partial t = 0)$:

$$dp^{xx}/dV = \Delta p^{xx}/\Delta V \text{ (with } u/V \equiv \rho u = \text{const).} \qquad (E)$$

Then

$$\Delta Q \equiv \Delta E + \int_0^1 p^{xx} \frac{dV}{dp^{xx}} dp^{xx} =$$

$$= \Delta E + \frac{\Delta V}{\Delta p^{xx}} \frac{1}{\int_0} p^{xx} dp^{xx} \equiv \Delta E + \frac{\Delta V}{\Delta p^{xx}} \frac{\Delta(p^{xx})^2}{2}$$

$$\rightarrow \Delta E = \Delta Q - \frac{1}{2}(p_1^{xx} + p_0^{xx})\Delta V. \qquad \text{(RH)}$$

As soon as coefficient of heatconducivity χ is here include in form

$$dQ/dt \equiv V(\partial/\partial x)(\chi \partial T/\partial x),$$

which means (at $\partial/\partial t = 0$):

$$udQ/dx = V(d/dx)(\chi dT/dx) \qquad \text{(F)}$$

$$\rightarrow \Delta Q = (1/\rho u)\, \Delta(\chi dT/dx),$$

"where coefficient of conductivity may be a function of condition of the gas, here dependent on one variable" (Baron Rayleigh, 1910).

The importance of radiation in (conductive) heat transfer in the shock structure was the evidence for Rayleigh. Meantime, the role of radiation in equation of state wasn't understand until appearance of works by Arthur Eddington – dosen years later, when the theory of stars was created.

In order to use the equation of state (EOS), it is necessary to write the fundamental thermodynamic "Gibbsian Identity" corresponding to the conditions of local thermodynamic equilibrium (LTE) valid in our model:

(GENERAL)[1] $dE \equiv dQ + dW \equiv dQ - p^{xx}dV$

(LTE) $\qquad dE = TdS - pdV$

In our present model, the media consists in matter (m) and radiation (r) in the mutual state of LTE:

$$p^{xx} \equiv p_m^{xx} + p_r^{xx} \equiv (1+P^{xx})p_m^{xx};\; p \equiv p_m + p_r \equiv (1+P^{xx})p_m;$$

$$p_m = n_m kT/V \equiv N_m kT/V \equiv 2E_m/fV \equiv (\gamma-1)E_m/V;$$

$$p_r = 0.902 n_r kT \equiv CT^4 \equiv E_r/3V,$$
$$E_r = 3p_r V = 2.7N_r kT, N_r kT = 1.11 p_r V;$$

and also $S_m(f=3) \approx 3N_m k \cdot \ln\{\frac{1}{h}\left(\frac{V}{N_m}\right)^{1/3}\sqrt{m_m kT}\} \equiv$

$$\equiv 3N_m k \cdot \ln\{<\delta x \cdot \delta p_x>/h\} \qquad \text{(EOS)}$$

S_r (photons etc: $f=6$)=$3.6k<N_{ph}>$=$3.6k<\delta N_{ph}>$=
$\qquad$ =$3.6 \cdot k<\ln \exp \delta N_{ph}>$=$4p_{ph}V/T \equiv (4/3)<E_{ph}>/T$;

---

[1] (GENERAL) $(p^{xx}-p)dV = dQ - TdS \le 0$ → $p^{xx} \ge p$ at $dV < 0$ (compression) – irrespective to the particular form of EOS!

$<N_{ph}>/V \equiv <n_{ph}>$=$20.3T^3$=$<\delta n_{phot}>$.
$\qquad$ (cm^{-3}) (°K)

Therefore,

$$P \equiv p_r/p_m = 0.902 < n_{ph} > /n_m \sim S_r/N_m.$$

Digression. Specific equilibrium radiation (photon) entropy is very much unlike specific equilibrium matter entropy: S_r/N_m=$3.6k$= universal constant, i.e. 3-rd ("Nernst") Law of thermodynamics is valid here "simply" because of N_r $(T \rightarrow 0)$ → 0, while (ordinary) matter specific entropy

$S_r/N_m \sim k \cdot \ln[T^{1/2}/(N_m/V)^{1/3}] \rightarrow 0$
at both $(n_m \approx const, T \rightarrow 0)$,
and $(n_m \rightarrow \infty, T \approx const)$.

The **nonequilibrium** radiation (photon) beam may be abundant by radiation "particles" (photons) in (practically) pure quantum state, thermodynamically describable by, let to say, T (laser beam) = 0 (like T (ideal pendulum) $\equiv$ 0 according to Ervin Schroedinger). The ultrafast laser-induced cooling is understandable by this argument, and superfast laser-induced heating (plasmenization) does not contradicts to one.

§3. Strong shocks may be specified by the conditions like

$$E_1 >> E_0, p_1^{xx} >> p_0^{xx}.$$

Let the media belongs to the class E_1=$(f/2)p_1V_1$, then the strong shock compression is $\rho_1/\rho_0 \equiv V_0/V_1$=$1+f_1(p/p^{xx})_1$ at ΔQ=0, i.e. nonequilibrium condition $(p \neq p^{xx})_1$ means undercompression (see above!), and the dominance of radiation (f_1 = 6) means compression = 7. More elaborate consideration of shock condition (R) with EOS (above) leads to

$$V_0/V_1 (\Delta Q=0) \rightarrow 1 + (p/p^{xx})_1(f_1+6P_1)(1+P_1)$$

$$\rightarrow 7 \cdot (P_1 \rightarrow \infty), \text{ or } \rightarrow f_{m1} + 1 \; (P_1 \rightarrow 0) \qquad \text{(RRH)}$$

irrespective to the conditions (let nonequilibrium!) of the initial ("0") state of media, and ever to initial composition (i.e. of degree of freedom: f_0).

§4. Our derivation of the rigorous solution for the radiative structure of shock with determination condition of disappearing (and appearing also!) isothermal discontinuity is convenient to begin by remember the equations for the straight "Earnshaw line" (here D is the shock velocity in the system of u_0= 0):

$dV/dp=(\Delta V/\Delta p)_{shock}=-(V/u)_E^2=-(V_0/D)^2$ (E)

- **if** the **continuous** dissipation within the structure of the shock is due to heat exchange only. Then, as soon as $TdS=dQ$, whence $p^{xx}=p$ **outside** the discontinuities, and for the "adiabatic shocks" we have (inside the continual part of the process): $(Q-Q_0)_{a.sh.} \geq 0$ because (compare, for instance, ref.10) on the "E-line" can be only a maximum meaning single extremum $(Q-Q_0)_{max}$. In the case of pure conductivity $(P_r=0, etc)$ temperature inside a.sh. structure increases strictly monotonically:

$(dQ = TdS)/dx = (V/u)(d/dx)(\chi dT/dx)_E,$

whence $dT/dx = (Q-Q_0)D/(V_0\chi) > 0$ **outside the discontinuities**. Consequently, the sign of the

$dp/dx = (dp/dT)E(dT/dx)$

is determined by the sign of the expression

$(dp/dT)_E = (D/V_0)^2(Nk + S_r)/(V(u/V)^2 + 2p_r - p_r),$

the sign of which changes if $p(T_{max})<p_1$, i.e. the single-valuedness of the flow parameters is violated (by overturn) until

$P_1 < (V_0/V_1) - 2 + (p_0/p_{m1})$ (cf ref. 7).   (B55)

For condition $dp/dx<0$ the continuous evolution $p \rightarrow p_1$ corresponds to the "overturn" with peculiar triple-valuedness of hydrodynamic parameters (in contrast to the "normal" single-temperature evolution $T \rightarrow T_1$).

§5. The single-valuedness of the flow parameters inside shock structure is achieved (restored!) by the **postulated** (Stokes classical idea of 1848, see Rayleigh, ref. 1) introduction of **isothermal discontinuity (i.t.d.).** In passing through **i.t.d.** the condition

$T(S_+ - S_-) \geq Q_+ - Q_-$

obviously should be valid – by the 2-nd Law of Thermodynamics (see below).

An **i.t.d.** can be considered to be degenerate case of a shock structure generated by the viscosity, or some like dissipation mechanisms. Here the matter is found to be the dissipative component, and the radiation transfer role is reduced to the isothermal heat exchange.

Inside the total **a.sh.** structure, an **i.t.d.** transforms the medium from the presubshock state "-" to the final mechanically equilibrium state "1" of the same temperature $T_1=T_-$, obviously (let, "by

definition"). Otherwise, the total **a.sh.** structure is subdivided into a "zone of heating" and **i.t.d.**:

$0 \equiv \Delta Q_{a.sh.} = (Q_- - Q_0) + (Q_1 - Q_-).$

For **any** permanent radiative shock which separates the equilibrium states "-" and "+" with identical temperatures, taking account of (RH) and (EOS), we have

$X \equiv \rho_+/\rho_- \equiv V_-/V_+ = p^+_m/p^-_m = E^-_r/E^+_r = P^-_r/P^+ = q \pm (q^2+1)^{1/2};$ (ITD)

$T(S^+_r - S^-_r)=Q^+_r - Q^-_r = 4p_r\Delta V; \ S^+_m - S^-_m = -N_mk\ln X;$

$Q^+_m - Q^-_m = (N_mkT/2)(1/X-X) \equiv qN_mkT,$

from which it follows that (for i.t.d.)

$\int(p-p^{xr})dV = \int(TdS_m - dQ_m) = \int(TdS-dQ)_{total} =$ (IRR)

$= (N_mkT/2)(X-1/X-2\ln X)=Z.$

Thus, permanent front of isothermal rarefaction with $X<1$, $\Delta Q>0$, $Z<0$, and $\Delta S>0$ is prohibited (ref.7), while permanent front of isothermal compression is irreversible ($Z>0$ for $X>1$, $\Delta Q<0$, $\Delta S<0$) !

Therefore, isothermal shock presents the instructive example of the open thermodynamic system.

Now, the appropriate substitution from (RH), (RRH) and (ITD), let us obtain the final equation for the effect of radiation on the amplitude of the isothermal subshock. Here we denote $P_1 \equiv P$, at $f = f_1 \equiv f$:

$X^2(P+1)^2 - X[(P+1)^2+6P+f]+6P+f=0$, or otherwise,

$[(P+1)^2X-(6P+f)]\cdot(X-1)=0$, therefore trivial solution is $X' = 1$, and nontrivial one is our basic result:

$X'' = (f + 6P)/(1 + P)^2 \begin{cases} \geq 1 \ \text{at} \ 2+(3+f)^{1/2} = P = 2(3+f)^{1/2} \\ \approx 0 \ \text{at} \ P \gg f^{1/2} \end{cases}$

The first root corresponds to the total continual shock structure, values $X''<1$ denoting rarefaction isothermal front are "nonphysical". When $X''\gg1$, then the first root X' corresponds to a "overturn" structure, here discarded.

The specific effect, not mentioned by other authors, is the **increase of i.t.d.** amplitude: from $X=f$ to $X_{max}=9/(6-f)$ for radiation increase over the range $0 \leq P \leq 1 - f/3$. This effect requires matter components of

$-3 < f < 3; \ -\infty < \gamma < 1/3; \ 1.67 < \gamma < \infty.$

The radiation enhancement up to $P=(6/f)-2$ reduced i.t.d. amplitude to nonradiative level $X=f$ (cf. Rayleigh 1910!).

The disappearance and appearance of an i.t.d. is a consequence of EOS – not of heat transport nature! In the specific case of $f = 1$ ($\gamma = 3$) even an arbitrary small radiation contribution in pressure leads to the formation of i.t.d., which cannot, certainly, exist in such a gas without radiation: here the radiation increases the compressibility of the medium and leads to i.t.d. over the range $0 < P < 4$ when $X_{max} = 1.8...$

As far as the effect like "Cowling's" one, let us indicate the presubshock relations

$Y_{r/m} \equiv (<n_r>/n_m)_-/(<n_r>/n_m)_+ = (n_+/n_-)_m \equiv X_m$ with maximum

$Y_{r/m}^{max} = 9/(6 - f) = 3$ for $c_p/c_v = 5/3 = 1.67.$ END
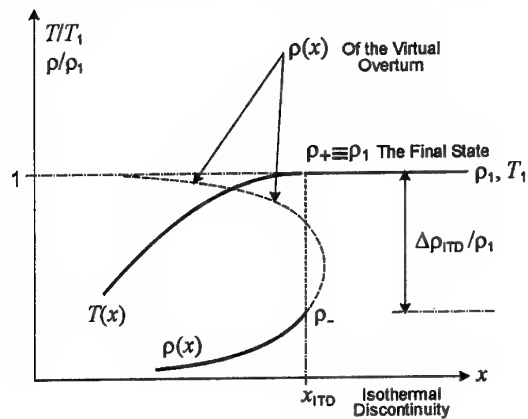
The nomenclature in the radiative shock structure.

References

1. Baron Rayleigh: Aerial plane waves of finite amplitude, Proc. Roy. Soc. (London), Ser. A v.84, pp 247-284 (1910) (Sci. Paps, Art. 346). J. Broadwell: J. Fl. Mech. v.347, p 375 (1997).
2. S. Bose: papers (in german), Berlin 1923. Ph. Morse: Thermal Physics, NY 1964.
3. Richard Tolman: The Principles of Statistical Mechanics, Oxford University Press 1938, reprinted in 1942-1962; Percy Bridgman: The Nature of Thermodynamics, Harvard UP. 1941;Harper, NY 1961.
4. T.G. Cowling: The influence of diffusion on the propagation of shock waves, Phil. Mag. v. 33, 7th Ser., pp 61-67 (1942).
5. R. Sachs, Physical Review, v.69, p514 (1946).
6. S.P. D`yakov: Shock waves in binary mixtures, J. Experim. Theor. Phys. v. 27, 283-287 (1954).
7. V.A. Belokogne: student competition papers 1954,55, Moscow Physics –Technological Institute; Soviet Phys. JETPh v.6 p 235 (1959); in Collected Papers of MPhTI: Moscow 1958, 1962, rus.; pap. at all-union Congress of Mechanics, Moscow 1968; Sov. Phys. Doklady. v.202 n6 (1972) in rus., v.17 n2 (1972) in English – incorrect translation.
8. H. Sen, A. Guess: Physical Review v.108 p.560 (1957).
9. W.Hayes: Gasdynamic Discontinuities, Princeton University 1960.
10. V.S. Imshennik: Sov. Phys. JETPh (engl.) v.15, 167-174 (1962).
11. V.A. Belokogne: The overturning of a compression waves and the connection between a shock thickness and the principles of statistical thermodynamics (papers in MHD meetings at Riga, Latvia 1960, 1962; all-union congress of mechanics, Moscow 1964); Journ. Appl. Mech. Techn. Physics 1965 n 6 in rus.
12. Ya.B. Zeldovich, Yu.P. Rayzer: Physics of Shock Waves and High-Temperature Hydrodynamic Phenomena. Moscow 1966 (rus.), vv.I,II NY-L AP 1966, 1967 (engl. transl. by Wallace Hayes and Ron Probstein); paper in Ann. Rev. of Fluid Mechanics vl (1970).
13. George Gamow: in «Property of Matter under Unusual Conditions», pp 11-22, Interscience NY-L 1969.
14. G.R. Fowles: Subsonic – supersonic condition for shocks, Phus. Fluids, July 1975.
15. S. Bruenn et al: Shock structure and neutrino radiation in stellar collapse, Astrophys. J. April 15, 1978, pp L83-L86.
16. V.A. Belokogne: Shock Compression of Layered Structures, in «Energy storage, compression, and switching», paps of 2nd Internat. Conf. Italy 1978, Plenum Press, NY 1983, pp 745-779.
17. George Chapline and A. Granik: The occurrence of isothermal discontinuities in relativistic fluids, Phys. Fluids v 27, n8, august 1984.
18. C. Fransson: The early evolution of supernova remnants, p.146 in «Radiation Hydrodynamics in Stars and Compact Objects», Copenhagen 1985, ed. by Springer Berlin 1986.
19. V.A.Belokogne, report at conference on the Physics in Explosion and Detonation, Estonia-Tallinn, autumn 1985, in russian.
20. V.A.Belokogne: On Generation of Gravitation Radiation by Fusion Explosions, in Collected papers, Moscow University – 1989, in russian.
21. Nuclear Energy and Radiation Dictionary, Chambers, NY 1992, pp 68-70. R. Rhodes: Dark Sun (The Making of the Hydrogen bomb), NY 1995.
22. R.B.Lowrie, J.E.Morel and J.A.Hittinger: The Coupling of Radiation and Hydrodynamics, Astrophysical Journal v.521, pp.432-450 (1999).
23. S.Bouquet, R.Teyssier, J.P.Chieze: Analytical study and structure of a stationary radiative shock, Astrophys. J., Supplement, april 2000, pp 245-252.

20. PECULIARITIES OF ELECTRIC DISCHARGE IN HIGH-VELOCITY AIR FLOW WITH GREAT DENSITY GRADIENTS

V.I.Alfyorov

Central Aero-Hypdrodynamical Institute — TsAGI
Zhukovskii, Moscow Region, 140160, Russia
Tel+7(095)5563179
Fax+7(095)5564337

Abstract. The paper presents the results of theoretical and experimental investigations of electric discharge between two electrodes in a wide range of flow velocities (M=0÷4.5), currents (I=10^{-3}÷5A) and gas densities (0.135÷1kg/m^3). It is shown that different discharge forms are realized depending on the current. At small currents (from 10^{-2}A to $5 \cdot 10^{-1}$A), the prebreakdown discharge occurs with the characteristics similar to the corona discharge, at $I \approx (5 \cdot 10^{-1} \div 1)$A the nonstationary constricted discharge develops and at I>2A the diffusion discharge is realized. Visual patterns of discharge glow and relevant volt-ampere characteristics are presented. For the diffusion discharge, the dissociated atom temperature and concentration fields, the potential distribution, and the radiation spectrum of its different regions are investigated. It is experimentally established that the shock wave front in the gas-discharge plasma is a region of increased electrical conductance. The obtained results are theoretically validated.

Introduction

Investigations of the corona or low-current discharge in subsonic flow basically aimed at developing diagnostic methods to measure the velocity in vacuum devices were started back in the 30s. In the 40s–50s, the corona discharge in flow was studied in connection with the problem of reducing aircraft electrization, while in the 70s–80s the high-current glow or diffusion discharge in gas flow was under study as applied to the construction of lasers with high-velocity gas. For this purpose, a uniform discharge shape in space was realized at much greater pressures than without flow, thus providing a considerably greater energy input to gas. The results of these investigations are presented in extensive publications devoted both to technical and physico-kinetic aspects [1]. It is shown, in particular, that a major portion of energy applied to gas (50÷80%) is accumulated in internal degrees of freedom. Some papers reveal that a relatively small increase in the discharge power can lead to a step change in the gas heating conditions and, accordingly, in the discharge shape. Current flow peculiarities in the presence of great gas density nonuniformities were beyond the consideration because they did not comply with the stated problem, namely production of uniform gas-discharge plasma.

Publications on decreased aerodynamic drag of bodies in nonequilibrium weakly-ionized gas-discharge plasma have inspired a renewed interest expressed by aerodynamicists in the electric discharge in gas flow. It is shown, in particular, that there exist effects of changes both in the position of shock waves near bodies in the region glow discharge region and their intensities.

Investigations carried out in shock wind tunnels and ballistic range facilities, as well as in classical wind tunnels have shown that decrease in aerodynamic drag, especially for ill-streamlined bodies, and smearing of the shock wave front during its motion in the gas-discharge plasma accompanied by gas dynamic and electrodynamic effects are really the case [2,3]. The gas dynamic effects are caused by heat emission and great density gradients in flow, while the electrodynamic effects are due to the formation of spatial discharge and electromagnetic fields, as well as changed current flow conditions.

The discharge in flow by itself is also investigated [4]. We believe, however, that the effect of aerodynamic peculiarities of flow on the discharge physics has not received proper attention. It is inferred from the analysis of extensive publications devoted to electric discharge in gas flow that a universally accepted model of self-sustained discharge to describe, at least indirectly, the discharge properties and their relation to internal processes in gas-discharge plasma has yet to be elaborated.

The present paper considers the discharge structure in air flow at M=(0÷4.5), P=($2 \cdot 10^{-2}$÷10^5)Pa and I=(10^{-3}÷5)A investigated in the TsAGI intermittent wind tunnel. The results obtained are used to analyze flows over simple bodies and vehicle models in industrial wind tunnels in the presence of electric fields and current flow in the gas-discharge plasma over them.

Description of wind tunnel and test procedure

The electric discharge by itself is investigated in a (0.15m×0.15m) intermittent atmosphere-exhaust wind tunnel equipped with a set of 2D nozzles providing Mach numbers M=0÷1; 1.5; 2.0; 2.5; 3.0; 4.0; 4.5. In all nozzles, the velocity field has a high uniformity level ($\Delta M/M \leq 0.005$). To extend the static pressure range, two supersonic ejectors with a total compression ratio of ~12 are used. The working pressure range is given in Fig.1.

For density fields to be determined, the pressure distribution on the electrode surface and the base pressure in the electrode wake are measured. Total pressure fields behind the normal shock wave are obtained using a Pitot probe rake in two mutually perpendicular directions. Simultaneously, shadow pictures of flow are taken. As follows from these investigations, the flow disturbance is intense in the electrode plane and especially in the base wake. In the interelectrode zone, the flow disturbance is much less and its

Schematic of wind tunnel to study discharge

Range of operating parameters

Fig.1

The flow parameters are obtained using standard gas dynamic methods based on measurements of pressure P_0 and temperature T_0 in the plenum chamber, as well as total pressure fields behind the shock wave by a total-pressure-probe rake and static pressures in flow. The value T_0 corresponds to normal conditions (T_0=290°C), the measurement accuracy being ~1%. The wind tunnel is equipped with a shadow facility to take pictures of the fine flow structure, shock waves, separation zones, the boundary layer. The discharge is ignited by two cylindrical molybdenum electrodes 5mm in diameter placed in rhombic fluoroplastic fairings.

A special mechanism enables the distance between the electrodes l to be changed during the tests (l=5÷40mm). Power for the electrodes is supplied from a ~100kW high-voltage rectifier providing maximum electrode voltage ~20kV and current 5A. Ballast resistances $(10^3÷10^4)\Omega$ and special filters to smooth current fluctuations are installed in the electric power circuit.

A main difference of the electric discharge in a high-velocity air flow from the discharge in fluid at rest is the presence of pressure (density) gradients in the cathode and anode regions, as well as in the region of its positive column.

attenuation proceeds faster.

With M_∞=3.0 and the electrode gap ~35mm, the flow field at a distance of 50mm or more from the electrodes can be considered as essentially uniform.

The procedure of studying the discharge properties is as follows. Initially, the discharge ignition voltage is investigated at different Mach numbers M_∞ and flow densities. Maintenance of constant free-steam flow density required to compare the experimental results proves to be possible for ρ_∞=0.135kg/m^3 within M_∞ (0.15÷4.5). At ρ_∞=0.27kg/m^3, we have M_∞=(0.1÷3.0).

Over the above range, oscillograms of discharge current and voltage are recorded, volt-ampere characteristics are obtained, the optical spectrum of discharge radiation is analyzed and visual pictures of discharge glow are taken. These experiments are carried out both in the electrode plane and in the plane perpendicular to it.

To investigate potential distributions in the discharge zone, the probe technique is applied. Temperature fields in the discharge zone are measured using calorimeters, and catalytic transducers are used to determine air dissociation level in the afterdischarge zone.

Experimental results

The presence of high-velocity and especially supersonic flows significantly changes the discharge characteristics. When the discharge is ignited in the electrode gap, intense violet glow initially occurs on the background of which electrode-induced shock waves can be clearly noted. At a density of ~0.127kg/m^3 (P_{st}~4kPa, M_∞=3), the glow is of diffusion nature, while at a high density (~0.508kg/m^3) the glow concentrates in the region of shock waves. At subsonic velocities (M_∞<0.7) and at the same gas density, the glow is much less intense or is not seen at all. The volt-ampere characteristics of such discharge correspond to the corona discharge. The values of current and voltage at which the spark gap breakdown takes place when M_∞=3 are, however, twice as great as similar values for subsonic flow (M_∞=0.5).

The glow brightness rises actively with the Mach number M_∞. Comparison of the volt-ampere characteristics of such discharge with those obtained in constructing gas-discharge lasers based on subsonic flow has revealed that they are identical.

Further increase in the current between the electrodes results in the electrode gap breakdown. Note that at supersonic velocities the breakdown proceeds not along the shortest path as is the case at subsonic velocities but along the front of electrode-induced shock waves. As the current rises, the rate of breakdowns increases and another discharge form is set at a certain mean current, namely a stationary discharge The stationary discharge is characterized by intense gas diffusion glow between the bright anode and cathode bands.

The voltage depends on the Mach number to a great extent. As the M_∞ number rises, the breakdown voltage distinctly increases at a fixed value of $\rho_\infty \cdot l$, where 1 is the distance between the electrodes [9].

The ratio of the breakdown voltage in the presence of flow to respective breakdown voltage without flow at the same density increases with rising density.

The effect of the flow velocity starting with small values (V~5m/s) up to M~4.5 is investigated on the facility under discussion. The results of these investigations are presented in [5]. Here we note only that at small velocities the discharge having a constricted shape is periodically blown out from the discharge gap with following spark breakdown resulting in shunting the previous arc channel. Starting with a velocity of ~30m/s, the discharge channel acquires diffusion nature. It is worthy of note that the discharge stability at the same free-stream flow density increases as the Mach number M_∞ rises. Over the test range of air densities and currents (ρ_∞=0.135÷1kg/m^3 and I=0.1÷5A), the discharge glow voltage depends only slightly on the current (Fig.2). As is obvious from the filming data, the cathode and anode bands begin directly in the region behind the electrodes. At subsonic velocities, their boundaries are rather smeared to be more and more distinct as the Mach number M rises (Fig.3). The extent of the glow region behind the electrodes increases as the current, flow density, Mach number M and distance between the electrodes rise. In particular, at M_∞=3.0, ρ_∞=0.27kg/m^3, I=3A and l=20mm the extent is L~1.0m. Judging from the discharge pictures taken in the direction perpendicular to the electrode plane, its smearing is insignificant. The pictures show spark channels similar to streamer discharges which retract on the electrode-induced shock waves. As follows from the analysis of the Teopler flow pictures taken at a special position of the Foucault knife to exclude the natural gas glow, the discharge-caused flow disturbance is not great. The electrode-induced shock waves are noted over the entire discharge region except for the cathode

Prebreakdown discharge
1,2 – ℓ = 10, 15mm, P_∞ = 4·10^{3}Pa
3,4 – ℓ = 10, 15mm, P_∞ = 1,2·10^{4}Pa

Diffusion discharge
ℓ = 10mm,
1– P_{st}=4·10^{3}Pa; 2– P_{st}=1,2·10^{4}Pa
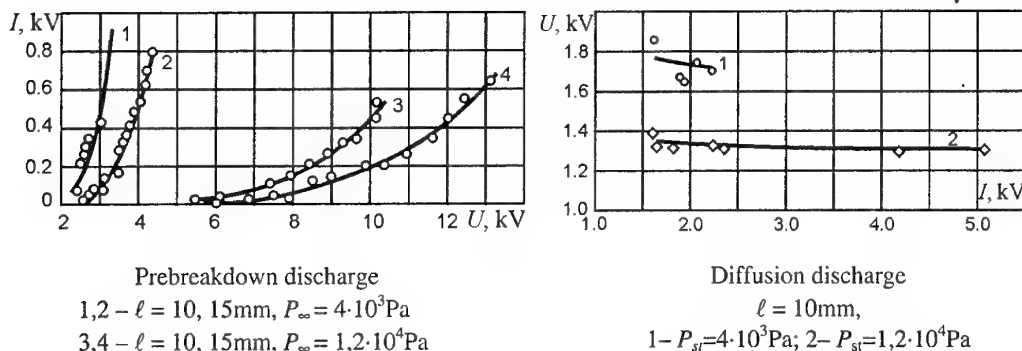
Fig.2. Volt-ampere characteristics at supersonic flow velocities (M_∞ =3)

123
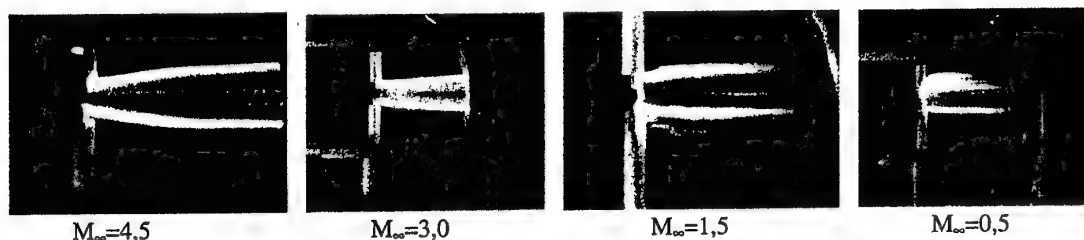
Fig.3. Visual discharge glow pattern at different free-stream Mach numbers M_∞, ℓ =10mm, ρ_∞=0,135kg/m³

and anode bands. The absence of noticeable disturbances caused by a discharge of a rather high power ($N\sim50\div70$kW) is likely to be explained by the fact that the discharge energy is basically put into the internal degrees of freedom which is confirmed by experiments of other investigators.

The potential distributions in the electrode wake are measured using a rake of probes made of molybdenum wires 0.3mm in diameter. The voltage between the wires is recorded by a cathode voltmeter. According to the measurement data, the cathode and anode bands are peculiar gas electrodes which carry a current. As the current rises, the potential difference between the bands increases in proportion. When the distance from the electrodes rises, it decreases according to an almost exponential law to be sufficiently great up to distances exceeding l>1m. For example, when M_∞=3.0; I=1.5A; ρ_∞=0.135kg/m³; l=20mm the potential difference between the centers of the anode and cathode bands is U=300 (Fig.4).
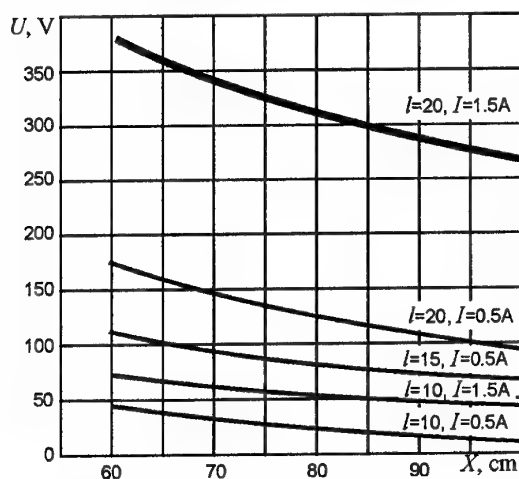
Fig.4. Potential difference between the anode and cathode bands versus current and distance from the electrodes M_∞=3, ρ_∞=0.135kg/m³

Of great importance for proper understanding of physical processes proceeding in

such discharge is the analysis of the discharge radiation spectrum [6]. For this purpose, a spectrograph ИСП-51 with a long-focus camera УФ-84 and a collimator is used. The analysis shows that the nature of radiation for all conditions is mainly the same. In view of this, most stable conditions at M_∞=3.0 are chosen for a detailed analysis. The spectra are recorded at ρ_∞=0.135kg/m³ and 0.270kg/m³, the distance from the electrodes being L=0, 10, 15, 20, 30, 50, and 75mm. The radiation spectrum over the model made of insulator at a distance of ~90mm from the electrodes is considered as a particular case.

Three regions can be clearly seen on the spectrograms:

1. The central region between the electrodes. The spectrum for this region is characterized by the presence of lines of ionized nitrogen N_{II} and oxygen O_{II}. The spectrum distinctly reveals the continuous radiation background most likely due to the recombination radiation. The fact that the observed spectrum is similar to the spectrum of a high-intense spark discharge in air is noticeable. Of particular interest is the current amplitude not in excess of 3A in the case under study.

2. The cathode and anode bands. The presence of intense glow of the first and the second positive nitrogen systems with the first one less distinctive is inherent for them. The heads of bands with wavelengths of 3943 (2÷5); 3998 (1÷4); 4059 (0÷3); 4094 (4÷8); 4141.8 (3÷7); 4205 (2÷6); 4269 (1÷5); 4343 (0÷4); 4416 (3÷8); and 4490 (2÷7)Å can be clearly seen. Quantum numbers corresponding to the present transition are given in brackets. The intensity of these bands decreases as the distance from the electrodes rises. The presence of pronounced lines of the electrode material (molybdenum) is obvious in the spectrum of the cathode band at small distances (L<16mm). These lines are absent in the spectrum for the anode band.

3. The radiation of N_2^{+2} is characteristic of the gas glow spectrum between the bands, only their

124

intensity is much less to decrease in the direction from the cathode to the anode and with rising distance from the electrodes.

Discharge region directly between the electrodes

Discharge region at a distance of 15mm downstream of the electrodes
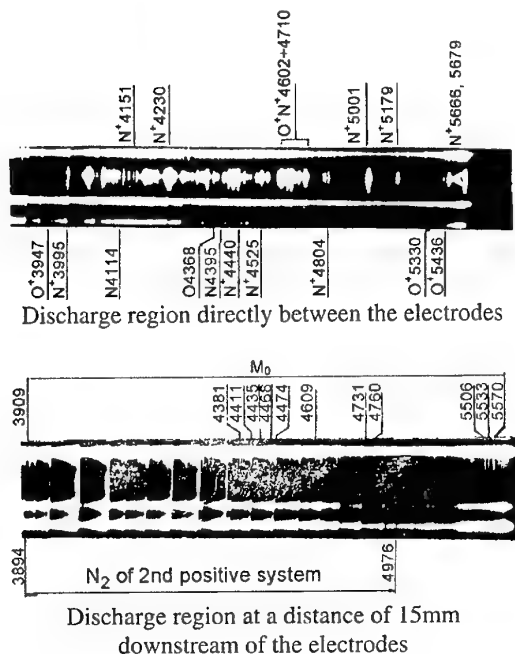
Fig.5. Discharge region radiation spectrum
M_∞=3, ρ_∞=0,135kg/m^3, I=2A, l=10mm

Relying on the obtained spectrograms, temperatures in the central region and in the region of diffusion glow are assessed qualitatively. Temperatures in the central region are determined by measuring the ratio of intensities of spectral lines N_{II} 3095A° and N_I 4137A° for which the pyrometric relationship is known. Based on these measurements we obtain $T\sim(18000\pm1500)$K. These temperatures are typical for the spark channel, but
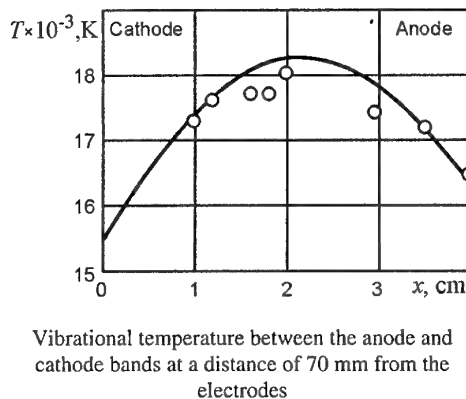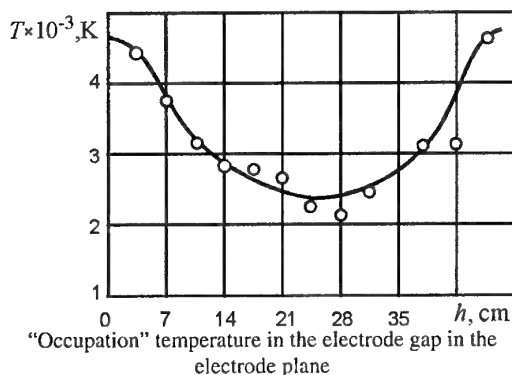
shock waves due to the spark channels are not observed.

The radiation of the anode and the cathode bands is attributed to the presence of excited N_2^{+2} molecules. The N_2^{+2} bands correspond to the intercombination transition $C^3\pi \div B^3\varepsilon$. Population of the level $C^3\pi$ is caused by excitation of N_2 molecule in the main state by electron impact, while additional excitation proceeds basically as a result of radiative decay $\tau_{rad}\sim 10^{-8}$s. Quenching by heavy particles can be neglected. The effective occupation temperature for the ground vibrational level can be assessed in detail using the occupation temperature for state $C^3\pi$. It is seen that the vibrational temperature in the discharge zone center has a minimum and decreases with rising distance between the electrodes (Fig.6).

It is well known from the literature that the probability of dissociation by electron impact is one or two orders of magnitude higher than the probability of the dissociative adhesion or ionization, and the energy of ionization of O_2 and N_2 molecules is high in comparison with the mean electron energy. In view of this, decay of O_2 and N_2 molecules can basically occur after several excited states. The presence of the above-outlined high vibrational temperatures of N_2 molecules affect the nonequilibrium dissociation rate for O_2 and N_2 molecules in two ways. On the one hand, the high vibrational temperature favors the dissociation process and, on the other hand, the portion of high-energy electrons increases. In this case, the nonequilibrium dissociation degree is represented by a sharply increasing function of E/N and power put into the discharge. The rates of inverse processes are small, therefore an appreciable concentration of dissociated N and O atoms can be expected.

For the concentration of dissociated

"Occupation" temperature in the electrode gap in the electrode plane

Vibrational temperature between the anode and cathode bands at a distance of 70 mm from the electrodes

Fig.6. Test conditions: $M_\infty = 3$, $\rho_\infty = 0,135$kg/m^3, $I = 2$A, λ=10mm

particles to be determined, the method of catalytic probes is chosen which enables the temperature field in the discharge to be obtained, as well. Knowing also the temperature field and concentration fields for dissociated atoms, vibrationally and electron-vibrationally excited molecules, it is possible to construct the energy balance for the discharge under study.

The method of catalytic probes is based on the catalytic effect of the surface material on the molecule recombination reaction. The probes are made as semispherical bodies with a thin layer of different coatings applied to their surfaces. Platinum, silver, nickel and tungsten are used as catalytic coatings, while quartz, gallium and antimony serve as noncatalytic ones. Diverse methods of coating application provide a durable film with the thickness of $(5 \div 100)\mu k$ depending on the application method. The temperature is fixed by calorimeters placed in a glass-cloth laminate holder. The sizes of the calorimetric elements are chosen so that the Damkohler number is $\Gamma_q < 10^{-1}$ behind the shock wave in gaseous phase and $\Gamma_w \geq 10^4$ on the catalytic surface. As for the noncatalytic surface, the Damkohler number is $\Gamma_w \leq 10^{-2}$. At these values, the concentration error for dissociated particles (atoms) is reduced to a minimum. Most detailed temperature fields are obtained for $M_\infty = 3.0$, $\rho_\infty = 0.27 kg/m^3$, with the electrode voltage of 7.2kV and electrode gap of $l = 15mm$.

A typical temperature field distribution in the zone behind the discharge is shown in Fig.7. It is seen that the highest temperatures are noted in the base wake behind the cathode band $(T \sim 350°C)$.

In the anode band, the temperature is lower $(T \sim 150°C)$ and in the discharge zone center it is $T \sim 100°C$.
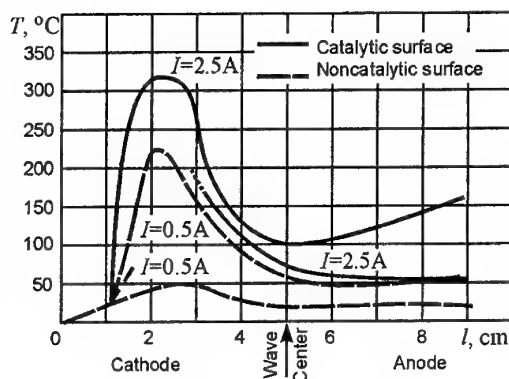
Fig.7. Temperature distributions in the wake center in the plane perpendicular to the electrode plane, $x=130mm$

The temperatures obtained using a transducer with a noncatalytic surface is accordingly much smaller. The calculated dissociation degree is given in Fig.8. The energy accumulated in the electron-vibrational nitrogen degrees is fully released when molecules collide with any solid surface irrespective of the degree of its catalyticity.

Possible errors of the dissociation degree are assessed in more detail. They basically depend on systematic errors, i.e., valid absence of recombination in the shock layer behind the shock
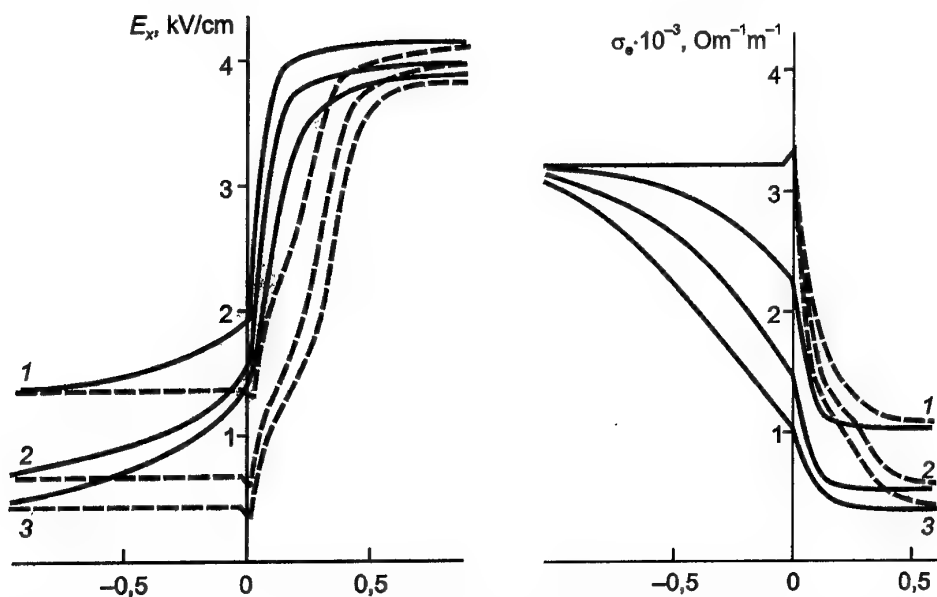
Fig.8. Distributions of normal electric field component E_x and electrical conduction at the shock wave front. $E_1 = E^2_{x1} + E^2_{y1} = 1.35 kV/cm$, $N_1 = 1.7 \times 10^{18} cm^{-3}$, $n_{e1} = 2.8 \times 10^{10} cm^{-3}$; solid lines: $E_x > 0$, dash lines: $E_x < 0$

126

wave ahead of the probe and the atom recombination degree on the catalytic surface. The assessment of the confidence interval α $(1.8 \times 10^3 \leq \alpha \leq 2.2 \times 10^{-3})$ and the analysis of random errors make it possible to believe that the presented nonequilibrium atom concentration degrees are rather reliable. At a specific energy input of ~10^3 J/g, based on approximation of the complicated geometric structure of the temperature field in the discharge zone, ~300 J/g is put into the translational and rotary degrees of freedom and electron states,, ~600J/g into the vibrational degrees of freedom and ~100J/g into dissociation. The above data are in agreement with values obtained in gas-discharge lasers.

The above-considered investigations of discharge in gas flow are carried out in strictly controlled gas-dynamic facilities within a much wider range of current densities and flow velocities than in [4,7,8].

In conclusion, the discharge under study can be characterized as follows. The discharge that we called the prebreakdown discharge [9], has the same main parameters as the glow discharge considered in [1]. When a certain limit energy input J^2/σ is exceeded, a nonstationary constricted discharge is realized, while at values of J^2/σ much higher than a critical current density of the prebreakdown discharge a stationary form occurs once again that we called the diffusion discharge. Topologically, the discharge channel in the discharge of this kind consists of two branches not closed by a pronounced section. The space between them is filled with illuminating gas. The region between the electrodes features a bright blue-violet glow the spectrum of which corresponds to that of the spark discharge. In the region far from the electrodes the glow spectrum is due to excitation of N_2 of the second positive system. Stubs behind the electrodes are peculiar gas electrodes.

At a fixed free-stream flow density, the discharge stability increases with rising Mach number. The volt-ampere characteristics are also gently sloping, while the required voltage level is almost 3 times less than in the prebreakdown discharge.

A distinctive feature of the electric discharge in gas flow is the presence of density and pressure gradients in the region of its existence due to the gas dynamic field: disturbances induced by the electrodes, channel walls etc. Behind the electrodes protruding into the flow, there occur base wakes with separation zones on their surfaces. Most drastically these nonuniformities manifest themselves at great and especially at supersonic velocities. In these cases, the pressure difference between individual regions in the discharge zone can exceed the free-stream flow static pressure level.

In the boundary layer, a maximum particle concentration gradient is

$$\text{grad } N/N \approx (5 \cdot 10^{-1} \div 1) \text{ 1/cm}$$

at a nonuniformity size of $l=0.1\text{cm} \div 1.0\text{cm}$. In the base wakes, separation zones and vortex lines we obtain grad$N/N \approx (5 \cdot 10^{-2} \div 1)1/\text{cm}$, $l=0.1\text{cm} \div 1.0\text{cm}$, while in the shock waves grad$N/N \approx 10^{-4}1/\text{cm}$, $l \sim 10^{-4}\text{cm}$. Deviations from the plasma quasineutrality for characteristic sizes of the above nonuniformities can be assessed as follows:

$$e\Delta N_i l \approx \varepsilon_0 (E/N)N$$

at $E/N \approx 10^{-15}\text{Vcm}^2$. $\Delta N_i l/N \approx 10^{-9}$ i.e., the deviation from quasineutrality will take place on the characteristic size of the shock wave, as well as at the boundaries of vortex and separation zones at a very small current density 10^{-4}A/cm^2. It is easy to show that under these conditions it is also necessary to consider diffusion of charged particles.

$$\frac{D\Delta N_1}{\mu E N_1} \approx \frac{\overline{\varepsilon}}{eEL}$$

Here D is the diffusion coefficient, μ is mobility, ε is electron mean energy.

The nonuniform fluid density results in a considerable gas conductivity nonuniformity σ and, accordingly, in current redistribution. It should be taken into account that the electron energy distribution function $\Phi(\varepsilon)$ changes because of great density gradients [10,11]. Therefore, ordinary macroscopic equations for electron motion should be handled with care. Various effects caused by the density gradient are possible depending on the ratio of the characteristics nonuniformity level l to different characteristic physical scales (ionization length l_α, Debay radius r_D, electron or ion free path length λ_e).

At the shock wave front, values of E/N; λ_e; r; $\Phi_1(\varepsilon)$; $\Phi_2(\varepsilon)$ change most sharply.

We have carried out a detailed analysis of current flow through the shock wave front in air as applied to parameters characteristic of the experiment under discussion.

The calculation technique is considered in [12], so we confine our consideration only to the results of its application to the prebreakdown discharge. We analyze the flow at $M_\infty=3.0$ and $N_2/N_1=2.83$, which corresponds to an oblique shock with an angle to the velocity vector of about 45°. The calculation results are given in Fig.8. It is seen that layers with a spatial discharge form at the shock wave front in which the electric field strength, charged particle concentration and gas conductivity change. The behavior of these values greatly depends on the electric field polarity. The electrical conduction σ (ionic conduction is 2% of σ_e) in these

Fig.9. Pictures of prebreakdown discharge glow, M_∞ =3, P_{st} =30Hg mm, distance between the electrodes:
I – ℓ=10 mm, II – ℓ=15 mm, III – ℓ=20 mm, IV – ℓ=30 mm

layers is not only function of E/N, but it also depends on the relationship between the velocity vector and electric field vector. With the direct polarity ($E>0$, $V_x>0$, a zone with an increased value of E/N forms ahead of the shock wave and, accordingly, with a decreased value of E/N behind the shock wave, thereby resulting in a region of increased activity ahead of the shock wave and a dark region behind it. With the inverse polarity, there exists only a region with a decreased value of E/N, i.e., the shock wave front is visualized in the form of a dark strip on the background of a brighter glow. These effects are clearly seen in pictures of the prebreakdown discharge (Fig.9).

Similar relaxation zones at the shock wave front should be taken into account in considering current flow through the shock wave front to analyze its stability. The presence of the zone of increased conductance results in the fact that the spark discharge breakdown proceeds along the shock wave front which is validated experimentally [9].

Unfortunately, no consideration has been given to this effect in the analysis of motion of fired (thrown) bodies through the region occupied by the electric discharge. In this case, the shock wave from the flying body shunts the electric discharge region, thus acting as an effective conductor terminating the region of electric discharge or its electrodes. In our case, this phenomenon is noted when a body of electrical insulating material is placed into the discharge region. The current from the gas electrodes is short-circuited through the shock wave front ahead of the body, thus causing the shock wave to be unstable.

References

1. Glow Discharge in Gas Flow, Velikhov E.P., Golubev V.S., Pashkin S.V., 1982, UFN, issue 1, p.117.

2. Investigation of Aerodynamic Effects at Electrical Discharge Creation of the Models of Different Geometry. V.Skvortsov, Yu.Kuznetsov et al, The 2-nd Workshop on Magneto-Plasma-Aerodynamics in Aerospace Application, Moscow, 5-7 April 2000, pp. 102-106.

3. Anomalous Supersonic Flow and Shock Wave Structure in Weakly Ionized Plasmas. A. Klimov. 1-st Workshop on Weakly Ionized Plasmas USAF Academy, Colorado, June 9-13, 1997.

4. Features of Transversal Gas Discharge in Supersonic Gas Flow. S.A. Dvinin, A.P. Ershov, I.B. Timofeev et al, The 2-nd Workshop on Magneto-Plasma-Aerodynamics in Aerospace Application Moscow, 5-7 April 2000, pp. 169-174.

5. Investigation of Discharge Glow Process in High-Velocity Gas Flow. Alfyorov V.I., Bushmin A.S., Kalachev B.V., ZhETF, 1966, vol. 51, № 5, pp. 1281-1287.

6. Spectral Analysis of a Wake behind the Electric Discharge in Supersonic Flow, Alfyorov V.I. Bushmin A S., TVT (Bulletin), № 6, 1963.

7. Electric Discharge in Supersonic Air Flow. Alfyorov V.I., Bushmin A.S., ZhETF, 1963, vol.44, № 6, p. 1775.

8. The Particle Kinetics of Plasmas. I.P.Shkarofsky, T.W.Johnston, M.P.Bachynski. RCA Victor Research Laboratories. Montreal,Canada, 1966

9. Determination of Gas Density in Vortex Line by High-Voltage Discharge Method, Alfyorov V.I., Trudy TsAGI, № 1421, 1971.

10. Electric Discharge in Spatial Nonuniform Gas Flow, Alfyorov V.I., Dmitriev L.M., TVT, vol. 23, № 4, 1976.

21. EXPERIMENTAL AND THEORETICAL RESEARCH OF DC TRANSVERSAL GAS DISCHARGE IN A SUPERSONIC GAS FLOW

V.Chernikov, S.Dvinin, A.Ershov, V.Shibkov, I.Timofeev
MSU, Faculty of Physics, Moscow, Russia

D.Van Wie
JHU, USA

Abstract. The results of transversal gas discharge in a supersonic gas flow experimental investigation are given. The formation features of DC and pulsed-periodic gas discharges are discussed. An initial air pressure range is 40-200 Torr, flow Mach number is 1,5 - 3. It is shown that characteristic fluctuations frequency is defined by value power put in discharge and flow Mach number flow.

The elementary model which is taking into account electron and ion kinetics and transfer processes in plasma, and also equation for direct current vector potential yields that the gas discharge can exist in the several shapes, depending on neutral gas flow rate.

1. The reference stationary discharge similar to discharge in fixed gas is implemented, when the plasma boundary travel velocity (in diffusive model it is a defined by relation $V_f = 2\sqrt{D_a v_i}$) exceeds gas flow rate C_s.

2. Otherwise discharge takes the form of two plasma wakes shaped accordingly by the cathode and the anode, which surface is guided under angle α ($\sin\alpha = V_f/C_s$) to gas flow.

3. If discharge maintaining voltage U_{steady} relation to breakdown voltage U_{break} exceed $\sin\alpha$, discharge becomes pulse wise - periodic shape, when the forming of cathode and anodic plasma wakes structure interrupts by a new gas breakdown.

The numerical modeling of discharge properties in two-dimensional model is carried out.

Introduction

The researches of various type of gas discharges in supersonic flows are caused large interest in connection with a problem of nonequilibrum environment creation in plasma aerodynamics [1,3]. Besides an opportunity of the boundary layer modification and influence on stream with the purpose of aircraft drag decrease, the gas discharges can be used for ignition of supersonic fuel mixture flows in ramjet engines also. The transversal electrode gas discharge in the supersonic flow in the present paper is considered. The basic attention in this paper is given to discussion of possible physical model of the transversal electrode gas discharge in supersonic flows.

Experimental setup and some experimental data

The experimental setup scheme is given in Fig.1.

The experimental setup represented the cylindrical vacuum chamber made of stainless steel, length 3 and diameter meter 1. Along its vertical diameter the forming supersonic channel terminating converging-diverging nozzle was mounted. The outside end of the channel was connected with the compressor through the electrodynamic vacuum valve. The experiments were carried out at static pressure of air $P_{st} \approx 40$-500Torr, the pressure of air in the compressor changed within the range 2-9atm, Mach number of a flow is equal to 1,5-3.
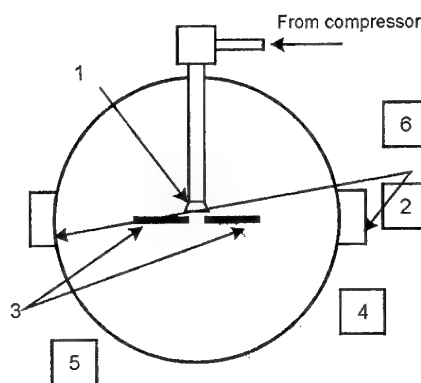
Fig.1. Scheme of experimental setup: 1 - converging-diverging nozzle, 2 - spectrograph, 3 - electrodes, 4 - power supply, 5 - probe scheme of measurements, 6 - windows.

Electrodes were settled down in the flow below the converging-diverging nozzle at the distance 1-1,5cm from it.

The pulse, pulse-periodic and direct current gas discharges in supersonic airflow were investigated. The integrated photo of the transversal direct current gas discharge in a supersonic flow of air with static pressure ~ 40Torr is given in Fig.2 as an example.

Fig.2. Transversal DC discharge in supersonic airflow
(M = 2, P_{st} = 40 Torr, I = 4,5 A)

The typical oscillograms of current and voltage for direct current discharge in Fig.3 are submitted. One can see that both the discharge current and voltage on a discharge gap are characterized by strong oscillations. The depth of modulation of current and voltage is determined by external conditions (Mach number, discharge current value, interelectrode distance, static pressure etc.).
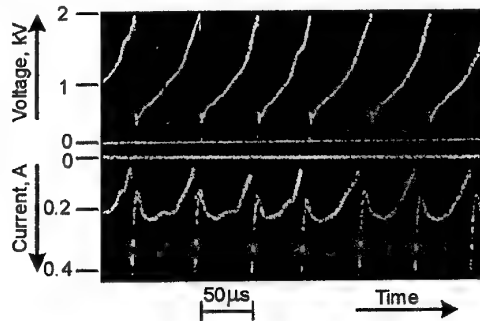
Fig.3. Typical oscillograms of discharge current (lower beam) and voltage on the discharge gap (upper beam). M= 2.

The diagrams of oscillations period as functions of interelectrode distance L and value of discharge current I in Fig.4 (a,b) are given. One can see that the period of oscillations with small currents (I<1A) grows linearly with increase of interelectrode distance practically. The period of oscillations also grows linearly with increase of current at small discharge currents. The growth of oscillations period at the fixed interelectrode interval at currents of order 2A is slowed down and at currents more than 4A the curve $T(I)$ is equal constant. The discharge in supersonic flow at small discharge currents can be qualified as glow discharge and at large currents as arc with the cold cathode probably.
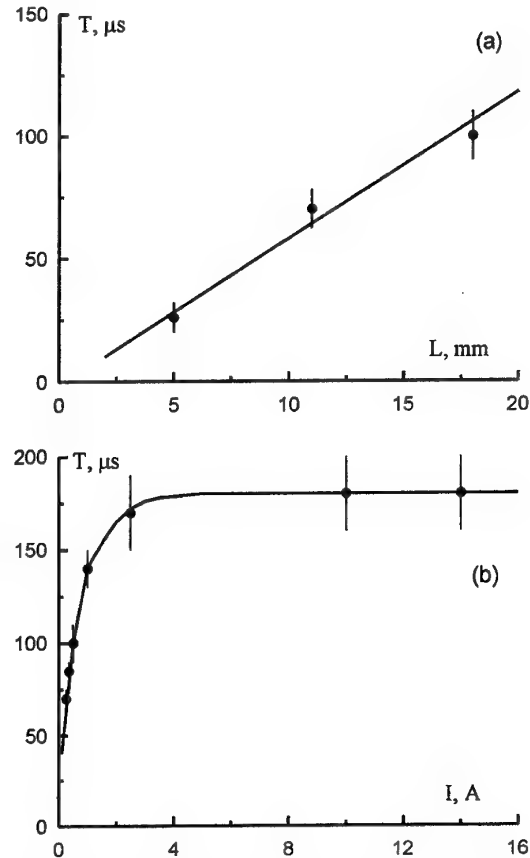
Fig.4. Period of oscillations as interelectrode distance L function (Fig.4a, I = 0,5A) and discharge current volume I (Fig.4b, L = 10 mm): P_{st} = 40 Top, P_r=2atm., M=2

The possible physical model of the electrode transversal gas discharge in supersonic flows

The geometry used for discharge numerical modeling is given in a fig. 1. The discharge forms between two electrodes (cathode C and anode A). The neutral gas stream moves along an axis OX.

The main problems of discharge model in a supersonic gas stream are connected with a diversity of ionization transfer types in space causing the motion of discharge towards to a flow. At low pressures (< 30 Torres) this transfer can be connected with

1. Drift of charged particles in an electrical field,
2. Ambipolar diffusion,
3. Free electron diffusion,
4. Transfer of radiation (photo ionization of gas before front, Penning ionization caused by a resonance emission, etc.).
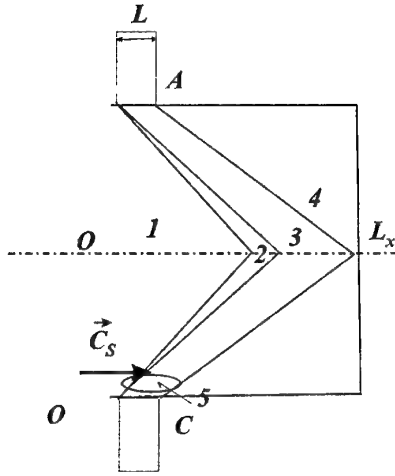
Fig.5. Structure of discharge in a crossed gas flow. A – Anode, C – Cathode, 1– Neutral gas area, (2-4) - area filled by plasma, 2– cathode and anode ionization fronts, 3– area supporting electric current (qualitatively), 4– decaying plasma, 5– cathode layer area, where the ions drift velocity exceeds gas flow rate.

At high pressures equilibrium discharge the transfer is connected with thermal conductivity, and the heat conduction can be caused by the neutrals, electrons, or radiation, depending on discharge degree of ionization.

At intermediate pressures, the rise of pressure leads to overheating instability, when the discharge development is connected with growth of frequency of ionization at reduction density of the neutrals. The neutrals density falling is caused by heavy components heating and subsequent pressure equalization with ambient gas. Thus, the electrons temperature essentially exceeds temperature of heavy components. In this case, the gas warm-up can be connected with

1. Heat conduction of neutrals,
2. Diffusive or photoionizating electrons offset from heated high-ionized gas area with weakly ionized "preplasma" creation. Electric field heats the caused "preplasma" electrons with the subsequent thermal energy transmission from electrons to the neutrals. The neutrals warm-up leads to further falling of their density in new area of space.

Discharge mathematical model and equations

In the elementary discharge model considered below, we shall keep only one type of ionization transfer (ambipolar diffusion) and at the analysis current distribution in space, we shall consider plasma quasi-neutral. The deviations from quasi-neutrality are essential near to boundary of

plasma and will be taken into account as appropriate boundary conditions. We shall neglect heating of the neutrals[1]. The photo ionization does not play an essential role in maintenance anodic and cathode ionization fronts, because high energy photons, emitted by plasma, are absorbed by electrodes, or result in occur appearance of photoelectrons far from front, bearing to new non-steady third fronts of ionization.

The equations set for quasineutral discharge area can be obtained from double-fluid hydrodynamics for electrons and ions, and Maxwell equations. We consider, that the electrons n_e and ions n_+ densities are equal $n_e = n_+ = n$, that means a series development on small parameter $\eta = r_{De}/L$, where r_{De} – Debye length, L – the characteristic size of plasma inhomogeneity.

The set of equations, used in calculations, looks like.

$$\frac{\partial n}{\partial t} + \mathrm{div}(n\vec{C}_S) - \vec{\nabla}D_a\vec{\nabla}n = F \tag{1}$$

$$\vec{E} = -\frac{D_e - D_+}{\mu_e + \mu_+}\vec{\nabla}\ln(n) + \frac{\vec{G}}{(\mu_e + \mu_+)n} \tag{2}$$

$$\vec{G}_e = n\vec{V}_e = n\vec{C}_S - D_a\vec{\nabla}n - \frac{\mu_e\vec{G}}{(\mu_e + \mu_+)} \tag{3}$$

$$\vec{G}_+ n\vec{V}_+ = n\vec{C}_S - D_a\vec{\nabla}n + \frac{\mu_+\vec{G}}{(\mu_e + \mu_+)} \tag{4}$$

In (1) – (4) and below we use denotations: V_e, V_+, C_S – speeds of electrons, ions and neutrals, μ_e, μ_+ – mobility of electrons and ions, D_e, D_i - coefficients of a free electron and ion diffusion, e - elementary electric charge, E - electric field strength in plasma, F - expression for sources of electron and ions, which are taking into account that they are born by pairs only, j - current density in plasma. The addends, containing C_S, take into account motion of a gas stream concerning electrodes resulting in to ions and electrons drift downstream. In the formulas (1) the denotation for an ambipolar diffusion coefficient

$$D_a = \frac{\mu_e D_+ + \mu_+ D_e}{\mu_e + \mu_+} \qquad .$$

is entered. The standard expression for F is

---

[1] However, the heavy components heating can be essential (experiment gives heating up to 2000K), but it is insufficient to supply equilibrium ionization. The space extension of heated area, which one can influence frequencies of elementary processes, happens downstream, where the density of charged particles and plasma conductivity are great, and, therefore, the heating of electrons by electric field is minute, and the frequency of ionization is small. The gas heating effects on ionization process should be expected at pressure above 200Torr, when the composite models of front of ionization are needed.

$$F = \nu_i n_e - \alpha n_e n_+ - \beta n_e^2 n_+ \qquad (5)$$

The expression (5) takes into consideration a straight-line ionization by electronic impact (ν_i – frequency of ionization), and two and three - partial recombination (α and β – recombination coefficients). Frequency of ionization and the frequencies of a recombination are functions of temperature of electrons.[2] At pressure of the neutrals 30Torr and above elastic energy losses of electrons predominate, and the character size of a non-uniformity is higher than character distance of heat transfer $\lambda_{Te} = \lambda_e (M/2m)^{1/2}$, where m and M – electronic and ion mass, λ_e - the free length of an electron, therefore in the elementary models of discharge is possible to consider the temperature of electrons T_e to be a local function of an electrical field E in the given point of space. To determine this function we use electron density balance equation. This equation accounts energy transfer from electric current to electrons, energy transfer from electrons to neutral particles (elastic ant nonelastic collision) and loss of energy, expended to electric ambipolar field creation. At a record (3) and (4) we have limited by sluggish processes with reference frequencies less then collision frequency an ion the neutral. It is possible, because the character time of electrons density change is determined by ionization frequency and usually on some order below.

Maxwell equation yields
$$\vec{G} = rot\vec{A} \qquad (6)$$

$$rot\left(\frac{1}{(\mu_e + \mu_+)n} rot\vec{A}\right) = 0 \ (7)$$

where A – vector potential of an electric current (it is proportional to a magnetic field, created by a current).

In the field of photo ionization (1 - in a fig.1) it was supposed, that the photoelectrons disappear due to attachment and consequently do not play any roles in discharge propagation. This requirement is possible so long as a field between the cathode and anode less breakdown one. At the solution of equation (1) in this area, we use a relation $F(\vec{r}) = -\nu_a n < 0$. Thus, numerical model could not describe processes of a secondary breakdown of a discharge gap.

The equations (1) and (7) should be supplemented by boundary conditions. The different views of boundary conditions can be obtained by integration a Poisson equation both dynamical equations and particles chemical kinetics equations on a surface. Hereinafter we shall consider boundary conditions at a plasma contact to a rigid body, which one can be dielectric or conductive.

1. Requirement of normal current density persistence on a cathode and anode surface.
$$\vec{j}_n = e\vec{G}_n = e\left|rot\vec{A}\right|_n = j_0 \qquad (8)$$

2. Assumption of ions current absence on the anode
$$\vec{G}_{+n} = 0 \qquad (9)$$

3. The part of electric current, transferred by electrons on the cathode is given [5]
$$\vec{G}_{en} = \gamma j_0/e \qquad (10)$$

The set of equations (1-10) was solved in rectangular area $0 < x < L_x$, $0 < y < L_y$. The cathode and anode placed on boundary of computation area. The requirements of a current absence through boundary, and requirement of plasma density symmetry concerning boundary were set on a remaining part of boundary
$$\vec{j}_n = e\vec{G}_n = e\left|rot\vec{A}\right|_n = 0 \qquad (11)$$
$$\left|\vec{\nabla}n\right|_n = 0 \qquad (12)$$

Computational results

1. At the identical geometry and neutral gas environmental conditions, the same discharge state will be realized, despite arbitrary initial plasma density (Fig.2).
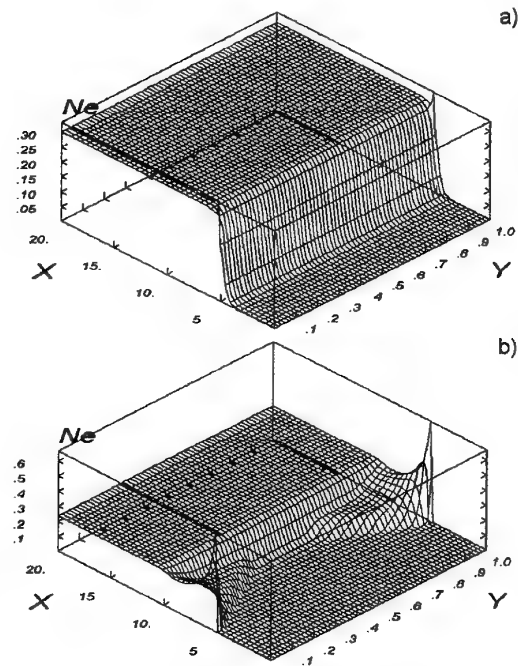
[2]On can use the model relation $\nu_i = \nu_{i0}(T_e/T_{e0})^{\varepsilon_I/T_{e0}}$, [4].

c)
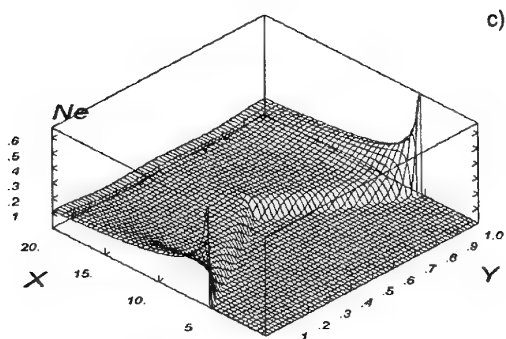
Fig. 2. Temporary discharge, maintained by the current J=1A/cm, evolution. Cathode length – 1cm. X and Y - actual discharge sizes in cm, neutral gas flow rate 50000cm/s, Ne - charged particles density in 10^{14}cm^{-3}. The calculation corresponds to neutrals pressure 200Torr. The figures a,b,c correspond to time value t=6, 225, 500µs

2. The cathode and anodic ionization fronts represent not separate areas near to the cathode and anode, but also all boundaries between plasma and no ionized area lying upwards on neutral gas fluxion.

3. The current in plasma flows past on a narrow bandwidth by the size about electrode separation adjoining to front ionization. (Fig.3).
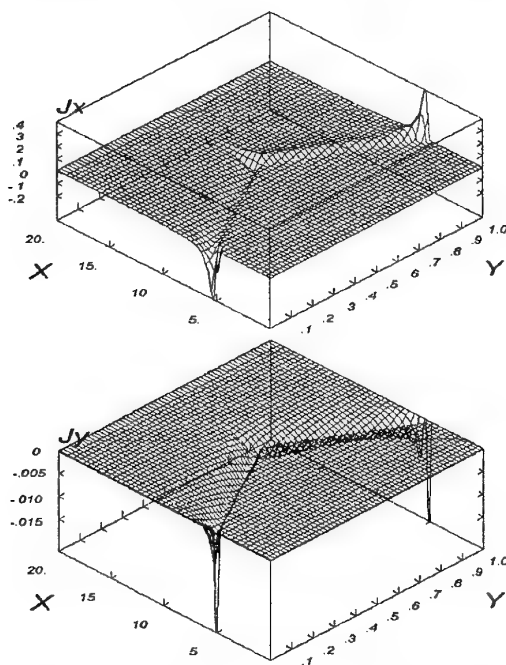
Fig.3. Direct current density J distribution (relative units). The figures correspond to fig. 2d)

4. The maximum ionization happens near to electrodes, where the current density has maximum too. As the current weep path between the cathode and anode has the least value near to ionization front, in any plasma cross-sections, parallel to axis 0X, an electrical field, tangential to ionization front surface, has maximum value near front. An electrical field, normal to front is generated by plasma non-uniformity and has maximum at plasma boundary. Thus, in any plasma cross-section lengthwise axis 0X the ionization frequency has maximum value at plasma boundary. This current stipulates a heating of electrons and ionization as at the front and near to plasma boundary.

5. Sharp boundary (by the size of the order $\sqrt{D_a/v_i}$) between space area held by plasma and free from it (so-called front of ionization) is formed. The conducted analysis yields, that boundary between plasma and not ionized gas behavior is subject to an equation similar to Kolmogorov–Petrovsky–Piskunov equation [6].

6. As the diffusive ionization front speed is perpendicular to its surfaces and is peer $V = 2\sqrt{D_a/v_i}$ and the front simultaneously communicates downstream with flow rate of the neutrals C_s, that the angle α_0 between front and a flow rate direction can be used for an of ionization frequency estimation on plasma boundary

$$\sin(\alpha_0) = V/C_s = 2\sqrt{D_a v_i}/C_s \qquad (13)$$

Equation (14) yields

$$v_i = C_s^2 \sin^2 \alpha_0/4D_a \qquad (14)$$

Thus, the ionization tracks both cathode, and anode represents a wedge (in flat geometry), and the angle between tangent to ionization front boundary and neutral hydrodynamic flow rate is determined by the formula (13). Behind ionization front, plasma density is great enough and the recombination processes can be essential. Thus, it is possible to expect, that in this area the balance of particles can be local, and the diffusion processes are incidental. It means that the set of equations behind front can be abbreviated for neglecting transfer processes in plasma.

In area behind plasma forward boundary the role of diffusion is small and we can use Raizer and Paschenko [6] analysis for discharge description, supplementing it by relation between plasma cross-sectional area on which one the current flows past and longitudinal coordinate (See equation (13)). Ionization frequency and longitudinal electric field in (13)–(14) (far from electrodes, in flowing plasma) is determined by local particle balance equation.

$$n_e\left(v_i(E_C) - \alpha(E_C)n_+\right) = 0 \qquad (15)$$

133

However, since the gas flow is perpendicular to a straight line connecting the cathode and anode (transversal discharge in a gas stream, fig.1), a positive column has a point, where its boundary is perpendicular to flow velocity, and charged particles drift is also perpendicular to a flow, therefore both electrons, and ions will move downstream at any speed of neutral gas. That completely corresponds) to outcomes of the numerical score (see fig. 3 and 4).

Thus, in absence of the transfer processes, the transversal d.c. discharge is always «supercritical». Therefore, we have the transitions from «up to stream» to «over stream» charged particles drift velocities towards to a flow near each electrode.

To obtain real space form of transversal discharge one have to take into account transfer properties (Ambipolar diffusion coefficient in our case).

Table I

The direct current discharge in transversal gas flow Classifications

Sub critical discharge similar to discharge without transversal flow $C_S < V_f \approx \approx 2\sqrt{D_a v_i}$	Super critical discharge as two sphenoid ionization tracks behind the cathode and anode $C_S > V_f \approx 2\sqrt{D_a v_i} \quad \sin\alpha \approx V_f/C_S$	
	Stationary discharge	Alternating discharge
	$\dfrac{U_{steady}}{U_{break}} < $ $< \sin\alpha$ $\approx \dfrac{V_f}{C_S}$	$\dfrac{U_{steady}}{U_{break}} > \sin\alpha \approx \dfrac{V_f}{C_S}$
	The anodic positive column	The cathode positive column
	Always sub critical (in Raizer and Paschenko sense [6])	Sub critical if $C_S \cos\alpha <$ $< u_+$	Supercritical, if $C_S \cos\alpha >$ $> u_+$

Experiments described earlier, (in accordance with [1]–[2]) shows that discharge in transversal gas flow is periodic (not stationary), as it predicted by numerical results. Apparently, it is connected with electric field growth between cathode and anode when plasma moves downstream, before the steady state is achieved. After the sufficient Voltage between cathode and anode is achieved, the breakdown is watched. The model of this breakdown must take into consideration gas photo ionization and capability of current closing between the cathode and anode by displacement current. As the angle between a plasma surface and flow rate after a breakdown

exceeds α_0, that the part of plasma removed from electrodes starts to communicate downstream and steady front begin to forms according to numerical results. Then the fixed front formation process is again interrupted by a new breakdown, and thus discharge passes in the periodic form.

For building-up alternating discharge theory it is necessary to view not only strongly ionized area, but also the weakly ionized plasma area.

In the whole requirement of embodying of the different shapes of discharge in a cross flow of gas can be formulated as the table I.

Presence of the different kinds of an alternating discharge (arc and diffuse) at different rates of flow marked in [1], can be explained by change of the discharge propagation mechanism towards to a stream. At low speeds (strong heating of gas, feeble fields in a positive column) - it may be the mechanism connected with heat conductivity, at major - (feeble heating of gas, diffusive discharge) it may be mechanism circumscribed in the present work.

References

1. Alferov V.I., Bushmin A.S., Kalachev B.V. Experimental Study of electric discharge properties in airflow. ЖЭТФ, 1966, т.51, №5(11), p. 1287-1287.
2. Dvinin S.A., Chernikov A.P., Ershov A.P., Shibkov V.M., Timofeev I.B, Features of transversal gas discharge in a supersonic gas flow. Russian Academy of sciences, Scientific Council for Direct Energy Conversion Scientific council for Fluid Mechanics. The 2nd workshop on Magneto-Plasma- Aerodynamics in Aerospace Applications. Moscow, 5 April - 7 April 2000. Organized by Institute of high Temperature of RAS In co-operation and sponsorship by PFBR, EOARD, ILG MHD, SEAM, p. 169-174.
3. Georgievsky P.Yu., Gromov V.G., Ershov A.P., Levin V.A., Timofeev I.B., Chernikov A.V., Chernikov V.A., Shibkov V.M. Gas discharge in a supersonic gas flow. Russian Academy of sciences, Scientific Council for Direct Energy Conversion Scientific council for Fluid Mechanics. The 2nd workshop on Magneto- Plasma- Aerodynamics in Aerospace Applications. Moscow, 5 April - 7 April 2000. Organized by Institute of high Temperature of RAS In co-operation and sponsorship by PFBR, EOARD, ILG MHD, SEAM, p. 169-174.
4. Smirnov B. M. Ions and excited atoms in plasma. М.: Энергоиздат, 1978.
5. Raizer Yu.P. Gas discharge physics. М.: Наука, 1982.
6. Pashenko N.T., Raizer Yu.P. A glow discharge in a longitudinal gas stream. Физика плазмы, т.8, 1982, c. 1086–1092.
7. Kolmogorov A.N., Petrovsky I.G., Piskunov N.S. MSU Bulletin. Mathematics and Mechanics. 1937, v.1, p.1.

22. PARAMETERS OF A PLASMA IN THE CHANNEL OF INITIATED UDERCRITICAL AND DEEPLY UNDERCRITICAL MICROWAVE DISCHARGE OF HIGH PRESSURE

K.V.Khodataev

Moscow Radiotechnical Institute, RAS, Moscow, Russia
113519 Moscow, Warshavskoe shosse, 132, MRTI
Tel: (095) 280-1274 (h) Fax: (095) 314-1053 E-mail: khodataev@glasnet.ru

Abstract. The work is devoted to the simulation of the initiated discharge in the air high-speed flow. The modeling have confirmed that initiated discharge can be in two different forms: the simply undercritical discharge, named by "separated" and the deeply undercritical one named by "attached". The high-speed flow influence on the discharge is not catastrophic. The temperature of the hot wake channel at any case is more than 3000 K. The power included into discharge is defined. The simulation results are compared with experimental data obtained for undercritical discharges in a motionless air.

1.Introduction

Earlier the theoretical and experimental study was performed for supercritical discharge in a gas of high pressure [1]. The present work had the goal to investigate the discharge in the presence of initiator at microwave field that is much smaller than critical one and to study the influence of a supersonic flow on the discharge parameters. The data obtained by modeling is rather useful for formulating of the experimental program and forecast of the application areas of the microwave plasma technology.

As it is well known the discharge in presence of an initiator can be excited at the microwave (MW) field which is many times smaller than critical one [1]. Meaning the different applications of initiated discharge in particular for ignition of combusting gas mix [2] it is important to know the discharge parameters in a supersonic flow in dependence from a different degree of udercriticality.

The complete understanding of the investigated processes is possible only in the comparing of the experimental measurements with the theoretical simulation results. It is namely simulating because the investigated process is too complicated and nonlinear for design the analytical theory. It is indeed modeling because the researched process is rather complicated and is nonlinear. The model of the undercritical discharge must be able to describe not only the ionizing and heating of a gas of discharge channel with wide diapason of temperature of gas and separately of temperature of the electrons but microwave field with the finite wavelength at the presence of the very thin discharge and initiator. In general case the Maxwell equation the thermodynamically not equilibrium plasma gas dynamical equations in 3D geometry must be used. But it is too complicated model for achieving of the practical results. Therefore the row of simplifications had been applied. Firstly it is supposed that microwave field

is periodical in time: $E \sim \exp(-i\omega t)$. So the field can be described by the Helmholtz's equation which will be used below. For simplicity we will suppose that the electric field has a linear polarization and is directed along the body of initiator.

The following formulation of the task was used for simulation. The initiator is a thin metallic cylinder. The initiator is placed along the electric field of the linear polarized MW field and along the gas flow. The wind velocity is 1 km/s. The gas is air. The pressure is 1 atmosphere at room temperature. The field amplitude is a bit more than breakdown at presence of the initiator.

2.The method of the field calculation at presence of the initiator and plasma channel

The modeling of the initiated discharge requests the solving of electrodynamic task which consists from finding of the field amplitude distribution in space fulfilled by arbitrary distributed electrical conductivity of plasma at presence of initiator. This task can be solved by means of Helmholtz's equation. The code [1] allows to do it. But it is difficult way because it demand the much time of calculation. For more quick solving of this task the Pocklington's equation was modified into the integral equation of 2-nd kind for arbitrary distribution of conductivity in the channel. The application of this equation supposed that the conductivity is significant only in the thin channel. The initiated streamer discharge satisfies this demand.

Earlier the simulation of the overcritical discharge was executed [2,3]. The overcritical discharge is developing very quickly so the simulation model need not take into account the gas dynamics. But undercritical discharge do not able to develop without the gas dynamic with decreasing of gas density. It strongly complicates the task. The original simulation of an initiated undercritical microwave streamer discharge was

performed by author [2] with using the said integral equation.

The modified integral equation has a view

(1)

$$E(z) = E_0(z) + ik \int_{-\infty}^{\infty} S(z')E(z')F(S(z'),a')G(z,z',a') \cdot dz',$$

(1)

$$G(z,z') = \frac{\exp(ikR)}{k^3 R^3} \cdot \left((1 - ikR) \cdot \left(2 - 3\frac{a^2}{R^2} \right) + k^2 R^2 \right),$$

$$R = \sqrt{a^2 + (z - z')^2}.$$

$$F(S) = \frac{ka}{2\sqrt{1+iS}} \cdot J_1\left(\sqrt{1+iS}\right)$$

- function taking into account the skin –effect.
where E(z) – electric field complex amplitude at axis (r=0), σ - electrical conductivity, S=4πσ/ω- normalized conductivity, ω - circus frequency of microwave field, 1/s, k – wave number.

The Eq.(1) is being solved on each step of time together with the plasma-gasdynamic equations.

3.The model of the plasma-gas dynamics

The plasma of discharge is not thermodynamically equilibrium. The electron temperature is defined by the relation of the electric field to gas density |E|/N so that the two-temperature model must be used. The gas dynamic equations for dissociating and ionizing diatomic electronegative gas mix are strongly simplified. It is supposed that dissociation coefficient f_d is defined by the gas temperature by the Saha equation and the ionization coefficient f is the same for molecules and atoms. The equations of continuity and movement is exchanged on the simple differential equations for channel radius a.

$$\frac{da}{dt} = V$$

(2)

$$\frac{dV}{dt} = \frac{P_0 - P}{\rho_0}$$

(3)

$$C_v(T_g,N)\frac{dT_g}{dt} =$$

$$= -(1 + f_d(T_g,N))(T_g + fT_e)\frac{2V}{a} +$$

(4)

$$+ \frac{\sigma(f,N,T_e,T_g)|E|^2\Phi(\sigma,a)}{N} - Q_{rec}(f,N,T_e)$$

$$\frac{dn}{dt} = N(K_i(T_e) - K_a(T_e))n + \frac{d}{dz}\left(D(N,T_e)\frac{dn}{dz} \right)$$

(5)

$$T_e = T_{e0}\frac{[E]}{E_{cr}(N)}$$

(6)

$$f = \frac{n}{N(1 + f_d(T_g,N))}$$

(7)

where n - electron number density, N =ρ/M, M – averaged molecular number of unperturbed gas mix.

4.The results of simulation

The system Eq. (2) – (7) has allowed to investigate the different regimes of the initiated discharges and the wind influence on them.

Below two calculated variants present the typical regimes of the initiated undercritical discharges. The variants correspond to the same conditions: wave length λ=8.9cm, air pressure p_g=760Torr, the initiator's diameter 2a=0.2cm and the wind velocity W=1km/s. The variants differ one from another by the length of initiator 2L=4cm and 2cm. These parameters of initiator correspond to values of a field increasing coefficient Q=21 and 6. The electric field amplitude have been elected a bit more than breakdown at the presence of the given initiator. Correspondingly it was E_0=1.9kV/cm and 6.8kV/cm. These parameters relate to the deeply-undercrirical (attached) discharge and the undercritical (separated) discharge. The results of modeling are presented on the Fig.1 – Fig.6. From all calculated variables only something are presented.

4.1. The deeply-undercritical (attached) discharge

The Fig.1 - Fig.4 demonstrate the results of modeling of the discharge initiated in the room air by the initiator with almost resonant length 2L=4cm and diameter 2a=0.2cm at the wind presence. The wind velocity W=1 km/s is directed along the initiator. The external field amplitude is 21 times less than the critical one, E_0=2kV/cm. The mentioned conditions correspond to deep undercritical discharges.

Initially the discharge arise on the both ends of the initiator. The plasma conductivity is not enough for field increasing aside the initiator. During the first microsecond the ionization front has some small velocity but than stops and begins to move with the wind flow (see Fig.1). Through a couple of microseconds the discharge at the forward end of initiator being influenced by the

136

wind is over. The Fig.2 shows the location of the streamer's ends in dependence upon time. On initial stage the streamer develops with the velocity more than 2km/s during the time less than 1 μs. Then the forward streamer have stopped but back streamer is moving slowly with the wind flow on some distance being slowly cooled.
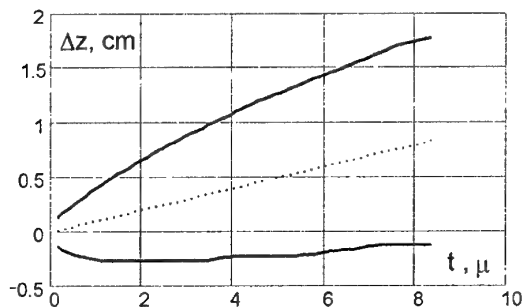
Fig.1. The streamer head outstanding from the initiator's end. The below line –of the forward streamer, the upper line –of the back streamer, dash line - W·t. (λ=8,9cm, 2L=4cm, 2a=0.2cm, air pressure – 760 Torr, E_0=1.9kV/cm, Q=21).
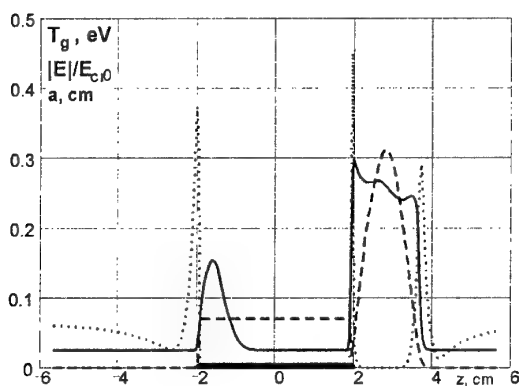
Fig.2. The gas mix temperature T_g (red solid line), microwave field amplitude $|E|/E_0$ (blue dot line) and the channel radius a (black dash line) distributions along axis z. The bold black solid line at the z axis is the initiator body. The wind velocity along the axis z - W=1 km/s. The time after discharge start - t=8.2 μs. λ=8,9cm, 2L=4cm, 2a=0.2cm, air pressure – 760 Torr, E_0=1.9kV/cm, Q=21

This process is viewed very well on the gas temperature distributions. The Fig.2 demonstrates the parameters distribution at the time t=3.2 μs. The region of the hot gas exists only on the back end of the initiator in the wake of discharge which moves with the wind together. Let us point that the field amplitude at the ends of the initiator have maximums. The maximums are approximately the same. But the field at the forward end do not cause the ionization because the gas at this end is cold and density is almost normal

so the parameter E_{max}/N is less than critical one. Other situation arise at the back end. There the gas is hot and its density is small enough (see Fig.3.) so the parameter E_{max}/N is more than critical one and ionization continues despite of the wind. The heated gas expands so the radius of the hot channel can be more than initiator's one. Note that the gas temperature is maximum on the back top of the initiator and is able to exceed the 3000-4000K. So it must not surprise us that ends of the initiator is evaporating during the discharge. Of course the wind cools the initiator. It is doing the problem not such desperate.

The process development in the time is demonstrated by the Fig.4 where the spatial-temporal gas temperature distribution $T_g(z)$ is presented. One can see the boundary of the initiator and the hot gas regions development. The picture is not symmetry because the wind influence. The forward streamer is shorter than back one. The heated gas is going with wind flow but the wind do not break the discharge.

The wind brings out the discharge from the forward end and creates the long wake of the hot gas beside the back end. It is important to note that in the case of the attached deeply-undercritical discharge which can be created in very weak microwave field the gas temperature of the wake is quite high and possibly this hot wake will be able to ignite a combustible mix in a supersonic flow.

The important result of the simulation is a high gas temperature T_g in the discharge and large radius of the channel (see Fig.3). Both parameters must be enough for the fuel mix ignition. It is important too that wind with velocity 1 km/s is not able to influence this high values of parameters of a deeply undercritical discharge.
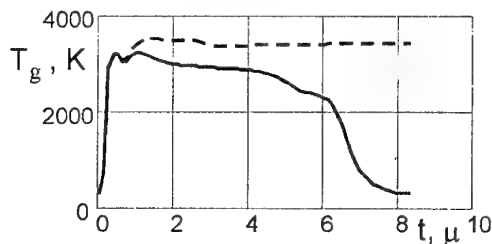
Fig.3. The gas temperature T_g near the top of the initiator. The red line – the forward end, the blue line – wake end. λ=8,9cm, 2L=4cm, 2a=0.2cm, E_0=1.9 kV/cm, air pressure – 760 Torr, Q= 21

4.2.The undercritical (separated) discharge

This variant differs from the first by the circumstance that both streamers, forward and back, continue the development despite of the supersonic wind. The streamers have stopped only

137

after the moment when sum of their length and length of the initiator have significantly exceeded the resonant value $\lambda/2$. Both streamers have the almost same length (4).

In the real process at this moment the next generation of the separated streamers goes away from the initiator. The designed model is unable to describe these next steps of the process. It can only show that the streamers length is rising up to value that exceeds the resonant value. The next step of the streamer development demand a more advanced model. But we may declare that the streamers of the next steps will have the same values of parameters that the streamers of first generation have.
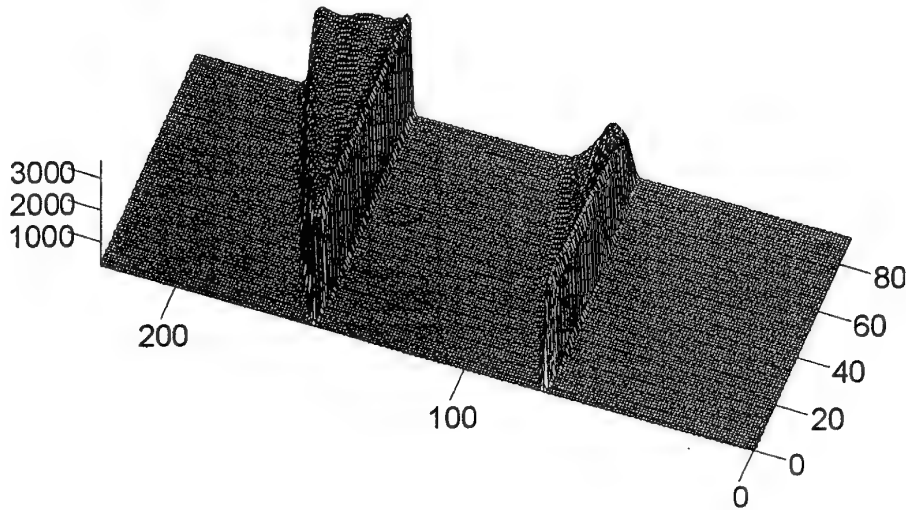
Fig.4. The spatial-temporal distribution of the air temperature T_g, K of the undercritical discharge. The numbers 0-90 – the number the time steps (0<t<8.2 μs). The numbers 0-226 – the numbers of the spatial steps (-5.7cm <z<5.7cm). λ=8,9cm, 2L=4cm, 2a=0.2cm, air pressure – 760 Torr, E_0=1.9 kV/cm, Q=21
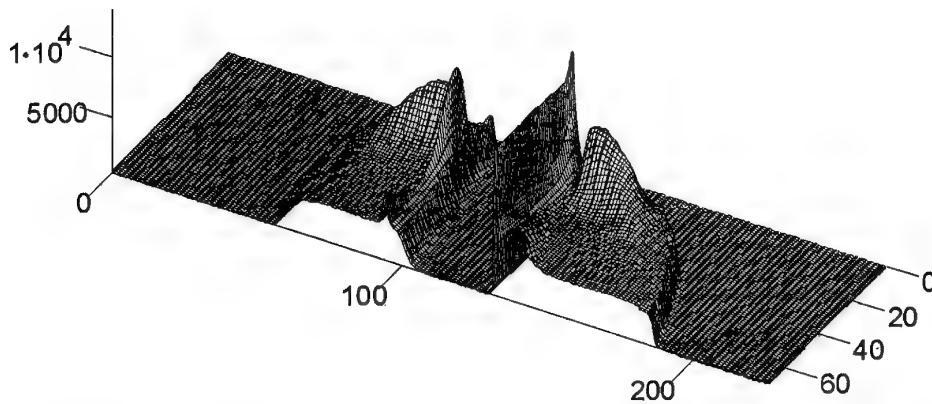
Fig.5. The spatial-temporal distribution of the air temperature T_g, K of the undercritical discharge. The numbers 0-70 – the number the time steps (0<t<4.05 μs). The numbers 0-226 – the numbers of the spatial steps (-5.7cm <z<5.7cm). λ=8,9cm, 2L=1cm, 2a=0.2cm, air pressure – 760 Torr, E_0=6.8 kV/cm, Q=6.
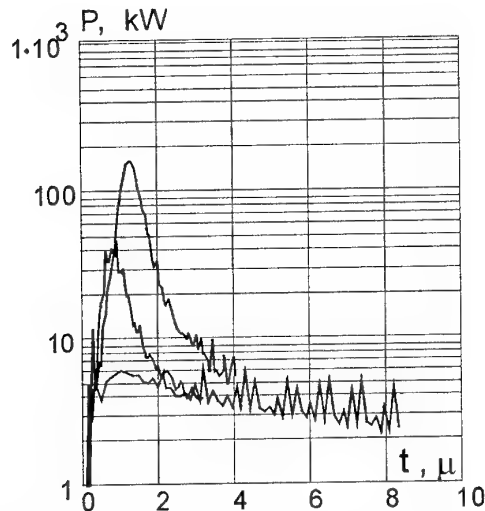
Fig.6. The power included into the discharge, red line – variant with Q=21, blue line – variant with Q=11, black line – variant with Q=6.

5. Summary of modeling

The performed modeling allows to accept for farther designing that
1) gas temperature in the initiated discharge channel is more than 3000 K,
2) a supersonic wind with velocity 1 km/s do not cut the initiated discharge,
3) said properties relates to both types of discharge, separated and attached.

The point 1) is well correlate with the experimental fact that initiated discharge of both types ignites the combustible gas mix.

It must be noted that at start of the discharge the power of heating is relatively high and proportional to $\sim E_0^2$. But 3-4 ms later the power of heating equals to 3kW approximately independently from type of discharge (Fig.5).

The simple estimation gives the value of the hot wake radius in quasi-stationary regime for attached discharge:

$$a_{ch} = \sqrt{\frac{P}{\pi \cdot W \cdot w_0} \cdot \left(\frac{T_{g0}}{T_g}\right)^{\gamma-1}} \qquad (8)$$

where W-wind velocity, w_0 and T_{g0} – unperturbed gas enthalpy and temperature, P – power of heating, T_g – temperature of the heated gas in the wake.

The Eq. (8) gives for calculated power P = 3 kW at wind velocity W=1 km/s and temperature of the channel 3000 K the size of the radius 0.123 cm. This value of radius relates to far distance from the initiator for attached discharge.

Acknowledgment

References

1. L.P.Grachev, I.I.Esakov, K.V.Khodataev. Parameters of plasma in the resonant channel microwave streamer discharge of high pressure. Proc. of the 2-nd Workshop on Magneto-Plasma-aerodynamics in aerospace applications. Moscow 5-7 April 2000, pp.154-162.
2. G.M.Batanov et all. // Proc. of IGP RAS, 1985, v.160, p. 174-203.
3. K.V.Khodataev, A.Ershov. Experimental investigation of a possibility of a MW streamer gas discharge application for fuel ignition in jet engine. // Proc. supplement of 2-nd Weakly Ionized Gases Workshop. Waterside Marriott Hotel, Norfolk, Virginia, USA, 24-25 April, 1998, pp. 339-350.
4. O.Woskoboynikova. Preprint of tThe Keldysh Applied Mathematics Institute RAS. 1998
5. V.B.Gildenburg. In the book "Nonlinear waves. Propagation and interaction." Moscow. "Nauka". 1981 P.V.Vedenin, N,E.Rozanov. //JETF, 1994, v.105, No.4, p.868-880.
6. P.V.Vedenin, N,E.Rozanov. //JETF, 1994, v.105, No.4, p.868-880.
7. K.V.Khodataev. Physics of super undercritical streamer discharge in UHF electromagnetic wave. //Proc. XXIII ICPIG, 17-22 July 1997, Toulouse-France, Contributed papers, IV-24.

139

23. PULSATING GAS DISCHARGE IN SUPERSONIC FLOW

A.Ershov, V.Chernikov, V.Shibkov, I.Timofeev
(MSU, Faculty of Physics, Moscow, Russia)

P.Georgievsky, V.Gromov, V.Levin
(MSU, Mechanics Institute, Moscow, Russia)

D.Van Wie
(JHU,USA)

Abstract. Results of the pulse-periodic transversal gas discharge investigations in a supersonic airflow are discussed. Mach number of a flow is equal 2. Static pressure of air is 100-300Torr. Average power supplied to the discharge is 50-400W. Pulse duration is 50 - 300 μs. Frequency of repetition of pulses is 500-10Hz.

A numerical simulation of a supersonic flow over pulse-periodic electric discharge is carried out. On the basis of the analysis of pressure, temperature and other parameter distribution dynamics, the classification of flows depending on the pulse frequency is proposed. The physical experiment conditions are corresponding to the single pulse regime, which is characterized by the high temperature region formation with the length depending on the pulse duration. At pulse repetition frequency increasing the regime of a pulsing temperature trace with a pulsing heading shock wave is realized. The further frequency increasing leads to the quasisteady regime, when the resulting flow is not depended on the pulse form and duration and is identical to the steady solution.

On the basis of the submitted results the conclusion about an opportunity of an ignition of air-fuel mixture flown with supersonic speed by the pulse-periodic electric discharge is done.

Introduction

Researches of various types of gas discharges in supersonic flows of air and fuel mixtures are represent large interest in connection with ample opportunities of their practical use in plasma aerodynamics for improvement of aircraft aerodynamic characteristics and volumetric ignition of supersonic flows of fuel in ramjet engines.

Some results of experimental researches of transversal pulse and pulse-periodic discharges, integrated characteristics in supersonic flows of air at Mach number M=2 in a wide range of changes of discharge current and electrical power input into the discharge are given in this paper. Discharges of this type were tested as ignition systems of supersonic flows of a fuel mixture (air-propane) in direct-flow supersonic combustor with M=1,5-3 [1].

Numerical simulation of a supersonic flow over an electric discharge region is carrying out for inviscid formulation. The energy supply is interpreted as an energy source of predetermined intensity. Steady and pulse-periodic energy sources are examined. The results of experiment are compared with the data of computation. Their quite good consent is shown.

Experimental setup and results of researches

The experimental setup represented the cylindrical vacuum chamber made of stainless steel, length 3 and diameter meter 1. Along its vertical diameter the forming supersonic channel terminating converging-diverging nozzle was mounted. The outside end of the channel was connected with the compressor through the electrodynamic vacuum valve. The experiments were carried out at static pressure of air P_{st} to 40-500Torr, the pressure of air in the compressor changed within the range 2-9atm. Mach number of a flow is equal to 1,5-3. Electrodes were settled down the flow below the converging-diverging nozzle at the distance 1-1,5cm from it.

The pulse, pulse-periodic and direct current gas discharges were investigated in supersonic flows of air. As an example in Fig.1 the integrated photos of transversal gas discharge and pulse discharge in supersonic flow of air at static pressure 40Torr are given. One can see that at large currents discharge the appearance of the discharge is essential different. The discharge has more complex structure. The discharge is hot zone occupies essentially greater volume.

a) DC discharge   b) τ = 1000 μs
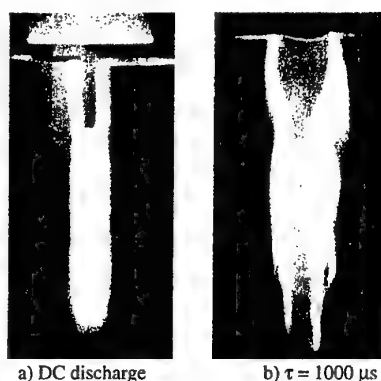
Fig.1. Typical appearance of the DC and pulse-periodic transversal gas discharges (a: P_f=1atm., P_{st}=40Torr, I=1,5A; b: P_f=2atm., P_{st}=40Torr, I=20A.)

The typical current-voltage characteristics of transversal pulse discharge in a supersonic airflow are submitted in Fig.2.
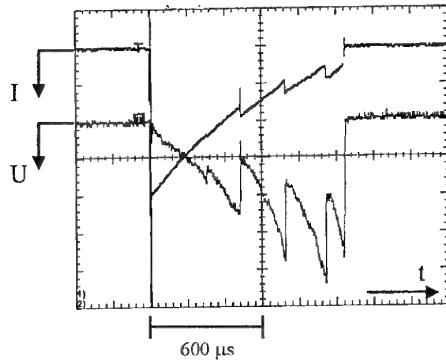
Fig.2. Typical current-voltage characteristics of transversal pulse discharge in a supersonic airflow (current is upper beam, scale factor is 10A/div, voltage is lower beam, scale factor is 840V/div; P_{st}=100Torr, P_r=2 atm, M=2).

One can see that both the discharge current and voltage on a discharge gap are characterized by strong oscillations. The depth of modulation is determined by external parameters (Mach number, magnitude of a current discharge, interelectrode distance etc.).

In Fig.3 the temporary graphs of power supplied to the discharge channel for the glow discharge ($I\approx0,2A$) "of a direct current" and pulse-periodic arc ($I\approx20A$) at Mach number M=2 of a flow are given as an example.
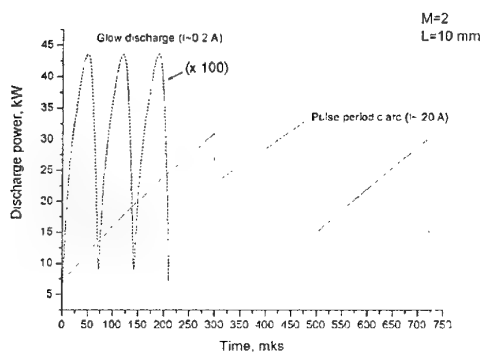
Fig.3. Dependence of electrical power supplied to the discharge on time for glow discharge ($I\approx0.2A$) and pulse periodic arc ($I\approx20A$), M=2.

One can see that the power supplied to the discharge is characterized by strong pulsations. At small discharge current (mode of the glow discharge) the frequency of power pulsations is much higher, than in the mode of the arc discharge.

The characteristic values of gas temperature of the discharges in the investigated modes lay within the range of 1000-3000K. The temperature slowly decreases along the discharge channel downstream.

Numerical simulation of an inviscid supersonic flow over an electric discharge region.

Numerical simulation of a supersonic flow over an electric discharge region is carrying out for inviscid formulation. The energy supply is interpreted as an energy source of predetermined intensity. Previously such approach was used for the computation of an action of local energy sources on the flow over different bodies [2,3]. In present paper the possibility of organization of appropriate conditions for the supersonic air-fuel mixture ignition is investigated. Correspondingly the obtaining of highest possible temperature in the wake and new principles of deceleration of the supersonic flow are a subject of particular interest.

The non-steady motions of an ideal gas with a distributed energy supply are described in cylindrical coordinates r, z by Euler equations:

$$\frac{\partial}{\partial t}\begin{pmatrix}\rho\\\rho u\\\rho v\\e\end{pmatrix}+\frac{\partial}{\partial r}\begin{pmatrix}\rho u\\p+\rho u^2\\\rho uv\\(e+p)u\end{pmatrix}+\frac{\partial}{\partial z}\begin{pmatrix}\rho v\\\rho uv\\p+\rho v^2\\(e+p)v\end{pmatrix}=$$

$$=\frac{1}{r}\begin{pmatrix}-\rho u\\-\rho u^2\\-\rho uv\\-(e+p)u\end{pmatrix}+\begin{pmatrix}0\\0\\0\\\rho\dot{Q}\end{pmatrix}$$

The total energy of a volume unit is determined for an ideal perfect gas as follows:

$$e=\frac{p}{\gamma-1}+\frac{\rho}{2}\left(u^2+v^2\right)$$

The energy supply density (to a mass unit per time unit) is assumed to be the predetermined function of coordinates and time:

$$\dot{Q}(r,z,t)=Q_0 f(t)\exp\left(-\left(\frac{r}{\Delta r}\right)^2-\left(\frac{z-z_0}{\Delta z}\right)^2\right)$$

The supersonic stream in actual experiment is formed by an outflow throw the nozzle from an open space into the low-pressure chamber. For numerical computations the flow is assumed to be "unbounded", that is effects of a real stream are neglected. Undisturbed flow parameters p_1, T_1 (initial data for numerical approach) are determined by given Mach number M_1 on a nozzle outlet and critical stagnation parameters p_0, T_0 in the open space.

141

$$\frac{p_0}{p_1} = \left(1 + \frac{\gamma-1}{2}M_1^2\right)^{\frac{\gamma}{\gamma-1}}, \quad \frac{T_0}{T_1} = 1 + \frac{\gamma-1}{2}M_1^2$$

For all computations: $\gamma=1.4$; $M_1=2$; $p_0=101320 \text{N/m}^2$; $T_0=300\text{K}$. Density is determined by an equation of state: $\rho = p/RT$, where $R = R_0/\mu$, $R_0=8314.32\text{J/(Kkmol)}$ – universal gas constant, $\mu=28.964420\text{kg/kmol}$ – molecular mass of an air. Thus: $\rho_0=1.176\text{kg/m}^3$, $p_1=12950\text{N/m}^2$, $T_1=166.7\text{K}$, $\rho_1=0.270\text{kg/m}^3$. The procedure of reduction of formulation to the dimensionless form using p_0, ρ_0 and typical length $l_0=10^{-2}\text{m}$ was applied. Pressure is measured by p_0 density – by ρ_0, velocity – by $\sqrt{p_0/\rho_0}$, distances – by l_0, time – by $l_0/\sqrt{p_0/\rho_0}$, energy source intensity Q_0 – by $(p_0/\rho_0)^{3/2}/l_0$. The total power input $W(t)$ depends on the complete task solution and can be calculated during the computation process.

$$W(t) = \left(\int_V \rho \dot{Q} dV\right) p_0 l_0^2 \sqrt{\frac{p_0}{\rho_0}} \quad \text{(Watt)}$$

a) regime with a local subsonic region (3)

b) regime with infinite subsonic trace (4)
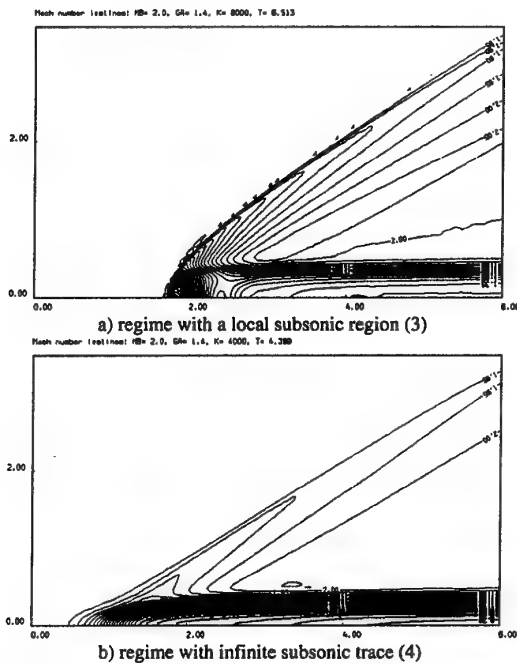
Fig.4. Steady regimes of flows over energy sources (Mach number isolines).

When similarity conditions (by γ, M_1, Q_0) are fulfilled the same numerical decision can be applied. Formula for $W(t)$ shows, that under the decreasing of energy source size (equivalent to l_0 decreasing) the same parameters, in particular

temperature, can be obtained for a narrow wake for indefinitely small energy input.

An action of a steady energy supply on the supersonic flow structure can be estimated by comparison of different energy sources of the same cross size $\Delta r = 0.15$:

(1)– $\Delta z=0.15$, $Q_0=40$, power $W=475$Watt
(2)– $\Delta z=0.15$, $Q_0=100$, power $W=913$Watt
(3)– $\Delta z=0.15$, $Q_0=200$, power $W=1340$Watt
(4)– $\Delta z=0.75$, $Q_0=40$, power $W=828$Watt

Intensities Q_0 for spherical (3) and ellipsoidal (4) energy sources were selected so that.

Flow pictures and distributions of different parameters in longitudinal and cross directions for computations (1)–(4) are presented on figures 1–5. For spherical energy sources of high power (1)–(3) existence of a local subsonic region (remote wake is supersonic) and a bow shock wake are typical (Fig.4a). For "equivalent" (by $Q_0\Delta z$) ellipsoidal energy source (4) the continuous deceleration of the flow down to a subsonic speed is taking place (Ffig.4b). The infinite subsonic wake and hanging shock wave are formed in this case.
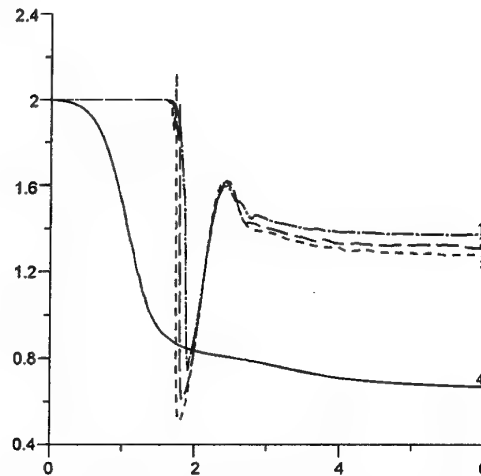
Fig.5. Mach number distribution along the symmetry axes for different energy sources.

Mach number distribution (Fig.5) demonstrates the effect of "saturation of the flow with energy", previously observed in [3]. At conservation of the spherical shape of the energy source (curves 1–3) it is impossible to decrease the Mach number in the remote wake by increasing the energy source intensity Q_0. For ellipsoidal energy sources the restrictions of this effect can be negotiated – the subsonic remote wake is formed. It is necessary to underline qualitative differences for longitudinal velocity component v (Fig.6) and static pressure p (Fig.7) behavior for examined flows. For ellipsoidal energy source (4) static pressure is

changed slightly and smoothly, while for spherical ones (1–3) the occurrence of a distinctive peak, corresponded to the bow shock wave, is typical. The remote wake velocities are determined by the energy source intensity Q_0 (curves 1,4). The greater is Q_0, the higher wake velocity observed. Thus, the energy input is consumed for kinetic energy increasing, which is unfavorable for high temperature obtaining.
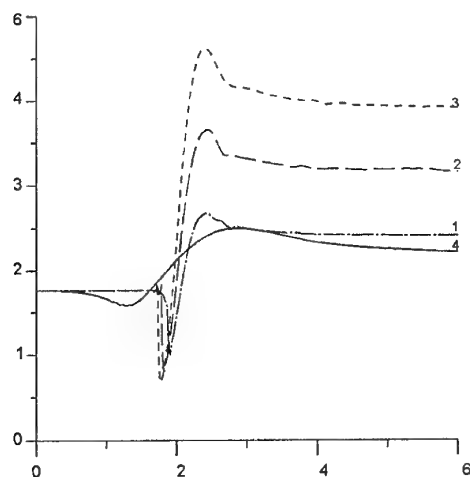
Fig.6. Velocity $v/\sqrt{p_0/\rho_0}$ distribution along the symmetry axes for different energy sources.
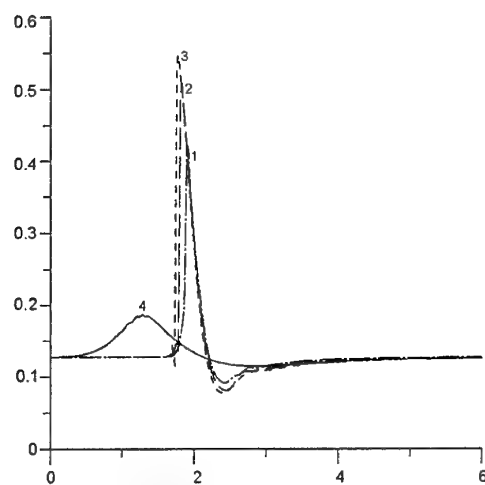
Fig.7. Pressure p/p_0 distribution along the symmetry axes for different energy sources.

The supersonic flow over pulse-periodic energy As a result of numerical computations it is shown that such critical quantity (for the air-fuel mixture ignition) as temperature is determined by synthetic parameter $Q_0\Delta z$. Temperature profiles for "equivalent" computations are closed to each other (curves 3,4 on Fig.8). For ellipsoidal energy source (4) the temperature in the remote wake is two times

greater than for spherical ones (2), in spite of smaller steady power input. Thus, the increasing of the longitudinal energy source size is the preferable method of an optimization of the energy supply. Ellipsoidal energy sources provide continuous deceleration of the flow down to a subsonic speed and high temperatures in the remote wake.
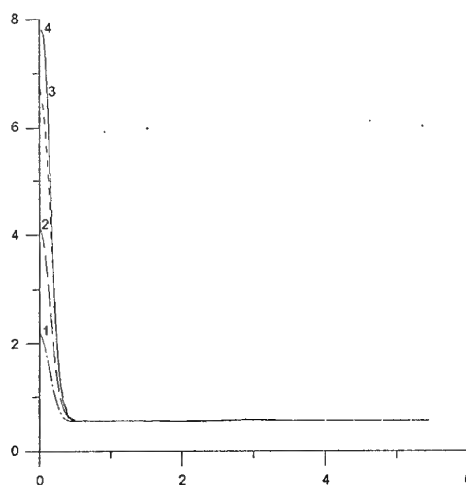
Fig.8. The cross distribution of temperature T/T_0 in the remote wake.

a) typical density isolines

b) temperature T/T_0 oscillogram for $z=6$.
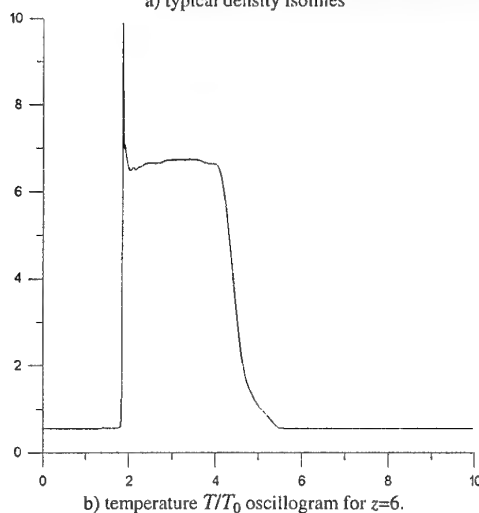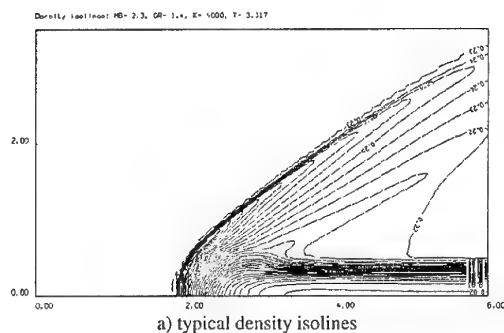
Fig.9. Regime of "long single pulses".

143

The supersonic flow over pulse-periodic energy sources was investigated. For determinacy the spherical energy source Δr=0.15, Δz=0.15, Q_0=200 with steady power input W=1340Watt was selected. It was assumed that pulses are rectangular: energy supply is powered on during the time t_0 in the beginning of every period of duration T_q. Correspondingly function $f(t)$ that modulate energy supply density $\dot{Q}(r,z,t)$ with time looks as follow:

$$f(t) = \begin{cases} 1, & \text{mod}(t,T_q) \leq t_0 \\ 0, & \text{mod}(t,T_q) > t_0 \end{cases}$$

Computation results will be presented as distributions by space for typical time moments and time oscillograms in selected point z=6 on the symmetry axes.

On the first stage the conditions of the real experiment were approximated: T_q=1msec (T_q=29.3 for dimensionless form), t_0=0.1T_q. The regime of "long single pulses" is realized (Fig.9). The formation of ellipsoidal high temperature region with size depended on the ambient flow velocity and pulse duration is typical for this case. The elongation of the region due to the ejection of hot particles outside the source by the flow is taking place when energy supply is powered on. After the energy source is down the high temperature region is drifted downstream with the velocity of ambient flow and the bow shock wave transforms to a characteristics. The pulse duration t_0 is long enough so that flow picture (Fig.9a) in observed region $0 \leq z \leq 6$ is in agreement with the steady regime. Time oscillograms (Fig.9b) have typical horizontal segments with steady values of parameters. The main conclusion: time characteristics of the energy sources, chosen for experiments, allow simulating the results of an action of the steady energy sources on a supersonic flow during the shot time period.

a) typical density isolines

b) temperature T/T_0 oscillogram for z=6.

Fig.10. Regime of "short single pulses".

a) typical density isolines

b) temperature T/T_0 oscillogram for z=6.
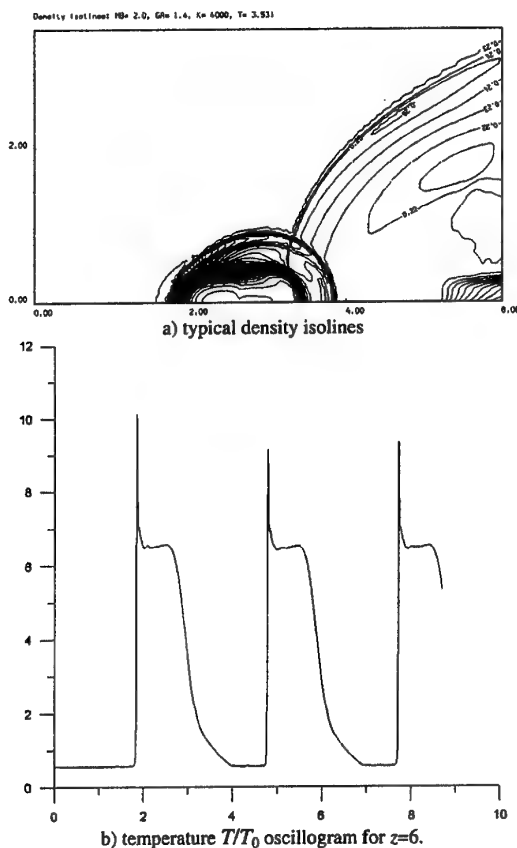
Fig.11. Regime "with quasi-stationary bow shock wave".

For investigation of the action of a pulse repetition frequency on processes dynamic the computation series with t_0=0.5T_q was carrying out.

For period T_q=0.1ms the regime of "short single pulses" is observed (Fig.10). In this case every new pulse is still realized in undisturbed region. The bow shock wave is drifted by the

144

ambient flow downstream the source center before the end of every period. The short ellipsoidal high temperature region is formed (Fig.10a). Horizontal segments with steady values of parameters are still presented on oscillograms (Fig.10b). The flow dynamics in the observed region $0 \leq z \leq 6$ is essentially unsteady.

a) typical density isolines

b) temperature T/T_0 oscillogram for $z=6$.
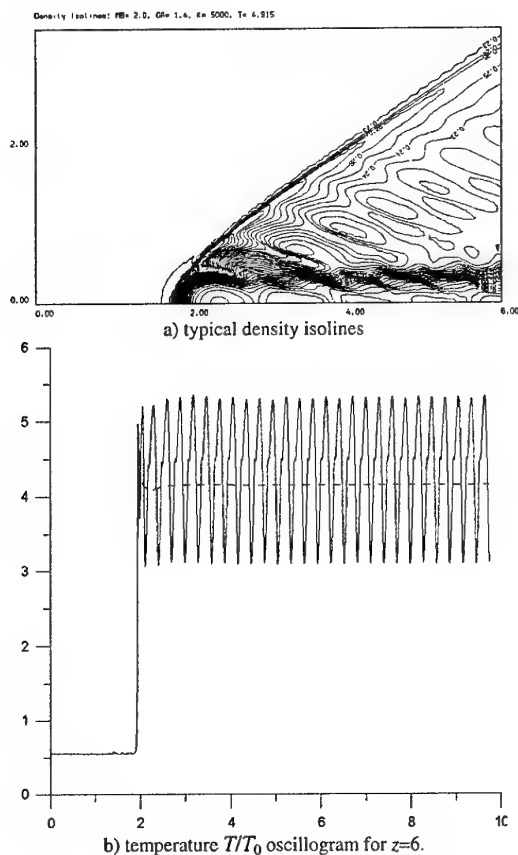
Fig.12. "Quasi-stationary" regime.

In [4] the criteria of quasi-stationary flow is determined from the condition that the upstream front of the shock wave, induced by the energy impulse, isn't drifted downstream the energy source center. This regime is corresponds to the period $T_q=0.04$ms (Fig.11). The complicated pulsing shock wave structure is formed in this case. The pulse duration is short and ellipsoidal high temperature region is not identified on fig8a. Temperature oscillogram is composed by typical

sharpen peaks with sudden fore front and gently sloping back front (Fig.11b). Thus the action of such a source on the flow is unsteady. The appropriate title for this case – "regime with quasi-stationary bow shock wave".

"Quasi-stationary regime" is realized for period $T_q=0.01$ms (Fig.12). In this case the practically steady shock wave and the pulsing high temperature wake are formed (Fig.12a). The flow field is close to steady one (fig.1a). However, as distinct from the steady case, the energy source is powered on for half of a period ($t_0=0.5T_q$). So the correct comparison by absolute values will be for $Q_0=100$ (computation (2)). Temperature oscillogram (Fig.12b) illustrates quasi-steady action of the energy source on the flow structure. The temperature oscillates near new value, determined by the steady regime $Q_0=100$. For intervals between pulses when the power is off the temperature not drop down to undisturbed values, as it was for all previous cases. For further increasing of pulse repetition frequency the temperature oscillation amplitude will decrease. Thus, pulse-periodic energy input in quasi-stationary mode not only simulate the steady source for a short time interval, but is completely equivalent to the steady source by an action on a supersonic flow.

References

1. P.Georgievsky, V.Gromov, A.Ershov, V.Levin, I.Timofeev, A.Chernikov, V.Chernikov, V.Shibkov. Gas discharge in supersonic flow. The 2nd workshop on magneto-plasma-aerodynamics in aerospace applications, pp. 143-149, Moscow, 5-7 April 2000.
2. Georgievsky P.Yu., Levin V.A. Supersonic flow over space-distributed energy sources // Mechanics, modern problems. Moscow. MSU Pub. 1987. Pp.93–99
3. Georgievsky P.Yu., Levin V.A. Supersonic flow over bodies in presence of external heat supply sources // Pisma v GTF. – 1988. – Vol.14, No.8. – P.684–687
4. Tretyakov P.K., Grachev G.N., Ivanchenko A.I., etc. Stabilization of an optical discharge in a supersonic flow of argon // DAN. 1994. Vol.336, No.4. P.466–467

24. DYNAMICS OF AIR HEATING IN PULSED MICROWAVE DISCHARGES

G.V.Naidis, N.Yu.Babaeva and V.A.Bityurin

Institute for High Temperatures of Russian Academy of Sciences,
13/19 Izhorskaya Str., 127412 Moscow, Russia

Abstract. In this work the results are presented of theoretical analysis of gas heating dynamics in pulsed discharge in microwave fields of centimeter wavelength range in air. The conditions are considered when the discharge is formed as a thin plasma channel – streamer elongated in the direction of the electric field vector. On the base of the dependencies of plasma parameters on air pressure, microwave wavelength and power the calculations are made of the rate of gas heating in plasma channel. It is shown that in some conditions the strong gas heating in the channel takes place at times much less than the typical gas-dynamic time.

Introduction

The development of discharges in high-pressure gases in static and high frequency fields is often accompanied by the formation of thin plasma channels – streamers. A streamer is an ionization wave in which front charge separation occurs with the subsequent increase of electric field and intense impact ionization. The streamer formation has been investigated most completely for static fields - homogeneous and inhomogeneous (see [1,2] and the references therein). Streamer dynamics in microwave (MW) fields has its own distinctive features. The MW discharges are intensively studied nowadays due to their possible use in plasma aerodynamics (see, e.g. [3-5]). Such discharges initiated in the beams of electromagnetic fields in millimeter and centimeter wavelength range tends to propagate towards the source of MW radiation. The character of discharge propagation and the parameters of developing plasma are determined mainly by the gas pressure and the value of electromagnetic energy flow density $S=(c/4\pi) E^2$. At low values of S the discharge front motion is continuous while at high values of S the discharge propagates by jumps. In the latter case it has a form of separate plasmoids or streamers elongated in the direction of the electric field. In previous paper [6] the possibility of appearance of $\lambda/2$ and $\lambda/4$ structures of MW discharges in nitrogen has been demonstrated. However, the details of the streamer development were not presented.

Basic equations and initial conditions

In this paper, we use 1D model of a single MW streamer in air similar to that used to investigate streamer dynamics in HF fields [7]. We consider the initial stage of streamer development in fields with linear polarization when streamer is formed in the focal plane of the electromagnetic beam (Fig.1). We assume that the streamer length L is small compared the wavelength λ, that is $L < \lambda/\pi$, and that the transverse dimension is much less than the thickness of the skin layer. Under these conditions the electric field E can be calculated in the quasi-static approximation. The distribution of electric field E is given by the Poisson equation for the potential U:
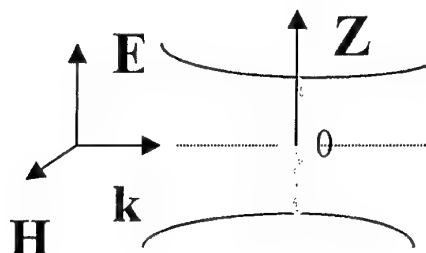
Fig.1. Experimental set-up.

$$E = -\nabla U; \qquad \nabla^2 U = -4\pi\rho \qquad (1)$$

where ρ is the space charge density. The concentrations n_j of plasma components (electrons, ions, radicals, excited molecules, etc) are determined in the framework of drift-diffusion approximation

$$\partial n_j / \partial t = \nabla(n_j \mu_j E) = F_j + S_j \qquad (2)$$

where μ_j are the mobility coefficients for charged particles of sort j , the sources F_j are the sums of contributions of local kinetic processes: ionization, attachment, ion-ion and electron-ion recombination, excitation, dissociation and ion-molecule reactions. Terms S_j in the equations for electrons and positive ions describe the generation of precursor charged particles ahead of the streamer front due to volume photo-ionization by radiation of the streamer head. The values of the constants of the processes described by F_j are assumed to

146

correspond to the local values of the reduced electric field. We consider conditions under which $\omega \ll \nu_u$, where ν_u is the frequency of energy exchange between the electrons and the molecules. In air this inequality corresponds to the range $p_0\lambda \geq 3$ atm·cm (p_0 is the gas pressure corresponding to the temperature 300K). In this case the constants of the kinetic processes can follow the variation in time of the electric field E.

The model also includes the equations for gas temperature T_g and the vibrational energy ε_V of nitrogen molecules:

$$\frac{n}{\gamma-1}\frac{\partial T_g}{\partial t} = \eta_T\, jE + \frac{\varepsilon_V - \varepsilon_{V0}(T_g)}{\tau_{VT}} \qquad (3)$$

$$\frac{\partial \varepsilon_V}{\partial t} = \eta_V\, jE - \frac{\varepsilon_V - \varepsilon_{V0}(T_g)}{\tau_{VT}} \qquad (4)$$

where $\gamma = 1.4$ is the specific heat ratio, η_T and η_V are the fractions of energy input transferred to gas heating and to vibrational excitation of N_2 molecules, j is the current density, τ_{VT}^{-1} is the rate of vibrational-translational (VT) relaxation, $\varepsilon_{V0}(T_g)$ is the equilibrium value of ε_V .The vibrational temperature of the oxygen molecules is taken to be equal to T_g , because of their relatively quick VT relaxation. The model used here also accounts for the MW streamer channel expansion in radial direction, based on solution of three Euler equations for density, velocity and temperature.

As initial conditions we specify the following form of the electron distribution which is determined by the physical formulation of the problem:

$$n_{eo}\,(z) = 10^{10}\exp\{\,-(z/0.03)^2\,\}, \text{ cm}^{-3} \qquad (5)$$

The characteristic streamer development time is many periods of the MW field, and this leads to the formation of a streamer that is almost symmetric with respect to the z=0 plane. As a result we can restrict the calculations to the region z>0. The axis z is directed upward along the vector of the electric field as shown in Fig.1. In this case the derivatives of the densities vanish on z=0. We also introduce the image of the space charge in the plane z=0 for the calculation of the field. The external field is varied according to the following expression:

$$E_L = E_0\, f(z)\cos\{(2\,\pi/T)\,t\}, \qquad (6)$$

where the function f(z) has the Gaussian profile ($|f(z)|\leq1$), T is the period and E_0 is the amplitude (at z=0) of MW radiation. The amplitude E_0 was

varied in the calculations in the range of 30–35kV/cm.

The kinetic model includes 14 components: neutral particles N_2, N, O_2,O, NO, $N_2(A^3\Sigma)$, $N_2(a'^1\Sigma)$, $O_2(a^1\Delta)$; ions O^-, O_2^- , O_3^-, O_2^+, O_4^+, and electrons. The rate constants of reactions including electrons are taken as functions of the reduced field E/n and the vibrational energy ε_V analogous to [8].

Gas heating in the MW streamer

One of the main characteristics determining the interaction of plasma regions with gas flows is the dynamics of heavy-particle temperature in plasma. The rate of increase of the temperature depends on such parameters as the type of discharge, the gas pressure, etc. In Fig.2 the approximations of the results of work [9] are presented showing the fractions of electrical energy input distributed between translational, vibrational and electronic degrees of freedom. It is seen that at moderate values of the reduced electric field the significant amount of energy goes into vibrations. However, when E/n exceeds the critical value (characterized by the equality of attachment and ionization) the energy fraction stored in electronically excited molecules increases significantly. In this paper at the calculation of the gas temperature using equation (3) the concept of 'fast' heating [10,11] is taken into account: it is assumed that at the quenching of electronically excited N_2 molecules about 40% of the excitation energy goes to gas heating. Note, that in equation (3) the term η_E is implicitly included into η_T. The rate of VT relaxation is taken from [12].

Thus, we have three channels of gas heating – characterized by the fractions η_T, η_V and η_E. All these channels act simultaneously, but their relative contributions depend on the external conditions and the particular time moment.
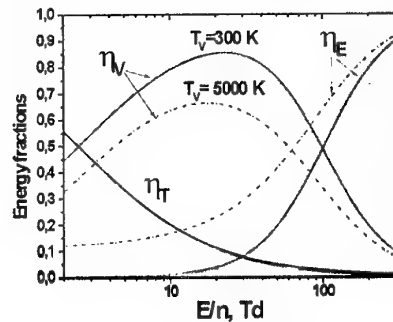
Fig.2. Energy input fractions distributed between translational (η_T), vibrational (η_V) and electronic (η_E) degrees of freedom [9]. Solid and dashed lines correspond to the vibrational temperature 300K and 5000K, correspondingly.

Results and discussion

In Fig.3 the distributions of the electron density on the streamer axis are given for 5 various time moments, corresponding to the field with the amplitude value E_0=32kV/cm. Only the upper part of the streamer (z>0), which is symmetric to the lower part (z<0) is shown. It is seen that the electron density in the channel increases with time. The abrupt streamer front is observed.
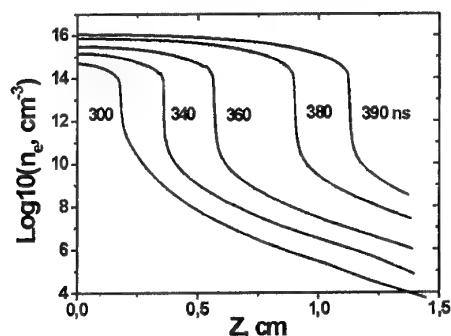
Fig.3: Distribution of the electron density on the streamer axis for 5 various time moments (E_0=32kV/cm).

Photoionization gives a long gently sloping tail of n_e in front of the discharge where the birth of precursor electrons takes place. The profiles of gas temperature on the axis of the streamer are presented in Fig.4 for the same time moments as in Fig.3. The comparison of these two figures shows that gas heating occurs gradually and rapidly behind the streamer front. Note, that for the given variant the temperature attains 4000K during ~ 400ns. Dependence of gas temperature on time recorded at the center of the streamer is presented in Fig.5. Three solid curves represent the calculation performed for various E_0 (λ=3cm).
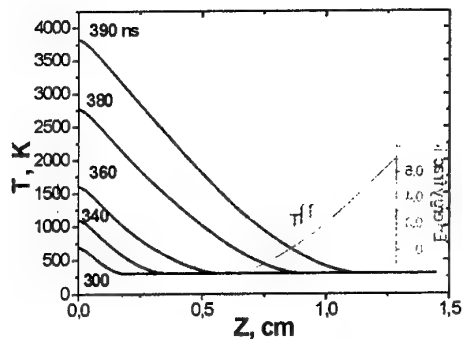
Fig.4: Evolution of gas temperature on the streamer axis for the same time moments as in Fig.3 (E_0 = 32 kV/cm).

The exponential temperature increase is observed after some time delay within the nanosecond time scale. Such temperature dependence on time is connected with the corresponding increase of electron concentration (Fig.6) and, as a result, with the increase of energy absorbed by plasma. The streamer plasma is in a state of VT non-equilibrium. It is seen from Fig.7 that the value of T_g approaches to T_V, due to acceleration of VT relaxation with the growth of the gas temperature.
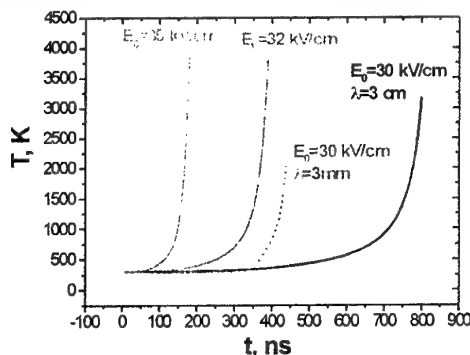
Fig.5: Dependence of gas temperature on time recorded at the center of the streamer for various E_0.
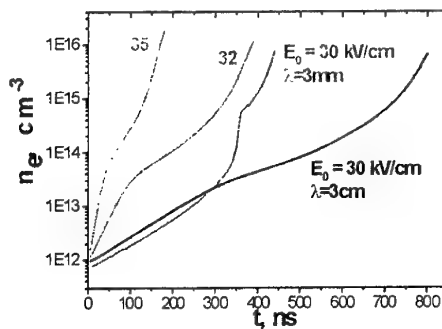
Fig.6: Dependence of electron density on time recorded at the center of the streamer for various E_0.
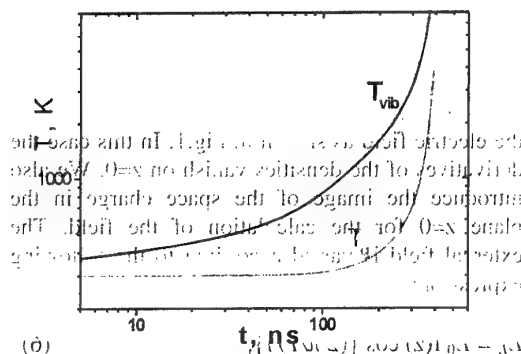
Fig.7: Vibrational and translational temperatures recorded at the center of the streamer for E_0 = 32 kV/cm.

148
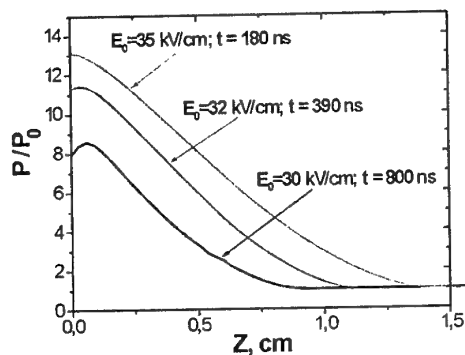
Fig.8: Pressure profiles for λ=3 cm
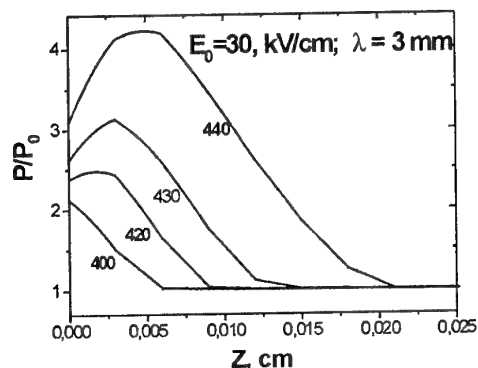
Fig.9: Pressure profiles for λ=3 mm
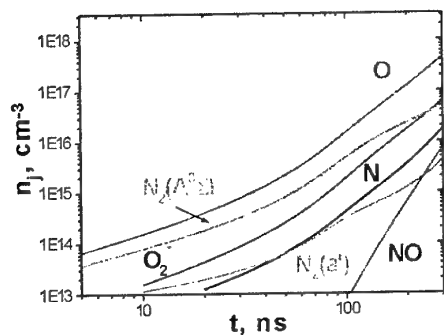
Fig.10: The concentration of neutral plasma components recorded at the center of the streamer for E_0 = 32 kV/cm.

It is interesting to analyze the case of shorter wavelengths, when greater electron number densities in the streamer are attained. The energy absorbed by the plasma is proportional to electron concentration ($W = \sigma E_e^2 \sim n_e E_e^2$), and the use of radiation in the millimeter range will result in greater energy input (at the constant value of E_0). In Fig.4 the character of temperature evolution is compared for λ = 3 cm (solid line) and λ = 3 mm (dashed line) for the same value of E_0 = 30 kV/cm. For shorter wavelength more rapid gas temperature

increase is observed. Such temperature behavior can be explained by the lowering of the gas density which takes place at times approximately equal to the ratio of the streamer radius to the sound velocity. These times are shorter for the millimeter wavelength range due to smaller streamer radius. It leads to the growth of the reduced field and, hence, to an increase of the ionization coefficient. In Fig.8 and 9 pressure profiles are compared, presented for centimeter and millimeter wavelength range. Fig.8 shows the essential increase of pressure in gas discharge region. However, the formation of shock waves does not occur during the time observed. In Fig.9 essential pressure disturbances are seen, which give rise to a noticeable lowering of the gas density and shock wave formation. Thus, using shorter wavelengths of the MW radiation it is possible to attain high gas temperatures during shorter time. Additional gas heating may be related with the accumulation of particles (radicals and excited molecules) active in acceleration of the detachment, stepwise and associative ionization, etc. Fig.10 shows the monotonous growth of the concentration of O atoms, excited O_2 molecules and other particles.
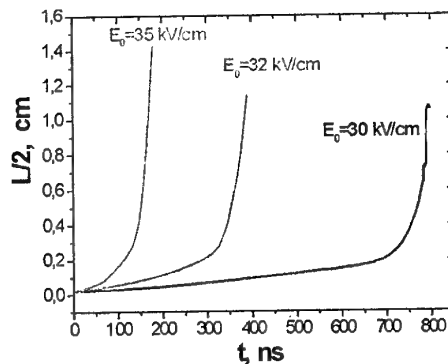
Fig.11: Dependence of the streamer length on time.

Note, that the condition $L < \lambda/\pi$ sets the restrictions on the maximal streamer length and, hence, on the maximal value of gas temperature. Fig.11 shows that the calculated streamer lengths approach the values where the validity of quasi-static approximation is violated.

Conclusion

In powerful pulsed discharges the gas heating may occur at times much less than the time of gas-dynamic scatter of molecules. Such pattern of heating leads to essential increase of pressure in gas discharge region and, hence, to formation of strong shock waves.

149

References

1. Babaeva N.Yu. and Naidis G.V., J.Phys.D: Appl.Phys. 29, 2423, 1996.
2. Babaeva N.Yu. and Naidis G.V., *IEEE Trans.Plasma Science* 25, 375, 1997.
3. Bityurin V., Klimov A., Leonov S., Lutsky A. and Van Wie D., AIAA Paper 99-4940.
4. Esakov I., Grachev L. and Khodataev K., AIAA Paper 99-4821.
5. Kolesnichenko Yu.F., in: The 2nd Workshop on magneto- plasma -aerodynamics in aerospace applications, p.150, Moscow, April 5-7, 2000.
6. Babaeva N.Yu. and Naidis G.V., in: The 2nd Workshop on magneto- plasma -aerodynamics in aerospace applications, p.175, Moscow, April 5-7, 2000.
7. Naidis G.V. Tech.Phys.Lett. 23, 493, 1997.
8. Naidis G.V., J.Phys.D: Appl.Phys. 32, 2649, 1999.
9. Alexandrov N.l., Konchakov A.M. and Son E.E., Fiz.plasmi, 4, 169, 1978.
10. Berdyshev A.V. et al. High Temp., 26, 496, 1988.
11. Devyatov A.M., Kuzovnikov A.A., Lodinev V.V. and Shibkov V.M. Vestn. MGU, ser.3, Fiz., Astron. 32, 29, 1991 (in Russian)
12. Mnatsakanyan A.Kh. and Naidis G.V. *High Temp.,* 23, 506, 1985.

25. MHD CONTROL OF SCRAMJET INLETS AND ON-BOARD POWER GENERATION

S.O.Macheret, M.N.Shneider, and R.B.Miles
Princeton University
Department of Mechanical and Aerospace Engineering
D-414 Engineering Quadrangle
Princeton, NJ 08544, U.S.A.
E-mail: macheret@princeton.edu

The paper examines the possibility of controlling scramjet inlets in off-design conditions by a near-surface MHD system upstream of the inlet. The required electrical conductivity is created by electron beams injected along magnetic field lines. A simple model of beam-generated ionization profile is developed and coupled with plasma kinetics, MHD equations, and 2D inviscid flow equations. Calculations show that an MHD system with reasonable parameters can bring shocks back to the cowl lip at Mach numbers higher than those for which the inlet was optimized. The MHD effect is not reduced to heating only, as the work by $\mathbf{j} \times \mathbf{B}$ forces plays an important role. Power requirement for ionizing e-beams is lower than the electrical power extracted with MHD, so that a megawatt-scale net power will be generated. Issues associated with high Hall parameters, chemistry, and vibrational excitation are discussed.

Internal hypersonic MHD power generators are analyzed. Ionization of the cold air is shown to be a critical issue, determining overall design, geometry, operating conditions, and performance envelope. KeV-class electron beams represent the most efficient method of ionization. In some cases, repetitive nanosecond pulses can also be used. Low electrical conductivity restricts performance and calls for very strong magnetic fields, making ion slip and near-anode processes first-order issues. Problems caused by hypersonic boundary layers and electrode sheaths, including anode sheath instability and ways to avoid it, are discussed. Calculations of MHD power generators for flight Mach numbers between 4 and 10 and altitudes of 15-40km are quite promising.

26. MHD CURRENT GENERATION IN SUPERSONIC FLOW.

S.V.Bobashev, T.A.Lapushkina, V.G.Maslennikov, V.A.Sakharov, K.Yu.Treskinskii
A.F.Ioffe Physicotechnical Institute, Russian Academy of Sciences, St. Petersburg, Russia

D.M.Van Wie
Johns Hopkins University, Laurel, Marylend, USA

Abstract. In the process of magnetohydrodynamic (MHD) interaction between a supersonic flow of xenon plasma and an external magnetic field, the dependence of the induced current through the plasma on the initial plasma ionization has been studied. The equilibrium plasma at the temperature up to $1.2 \cdot 10^4$K, the pressure up to 2.5MPa, and the ionization degree α=0.03-0.11 was formed in a shock tube in the area behind the reflected shock wave. The test section, located at the shock tube end, forms a nonequilibrium supersonic flow of the weakly ionized plasma which interacts with a transversal magnetic field of 1T inside a plane MHD channel. Changing the flow ionization degree is performed by varying the initial shock wave strength in a range of Mach numbers from 7.7 to 9.4. A comparison between the experiment results and numerical calculation data has been fulfilled.

The problem of control of a supersonic flow of low-temperature plasma is being intensively discussed in connection with designing aircraft of new generation. In particular, a possibility of air flow control in the inlet assembly—air intake—of an aircraft is being considered. Some years ago, it was proposed to use for this purpose the effect of magnetohydrodynamic (MHD) interaction between weakly ionized air and magnetic field [1,2].

Experimental modeling of the interaction of a supersonic conducting air flow with a magnetic field is a very difficult problem. Here are two partial tasks.

1. Forming and maintenance of the conduction of a bulk of air during a long time.
2. Study of gasdynamic properties of the flow.

The Physical Gasdynamics Laboratory of the Ioffe Institute has necessary equipment and the experience of years of work with shock tubes. It seems reasonable as the first step to focus one's efforts on solving the second task – study of gasdynamic properties of an inert gas flow. Using the inert gas in a shock tube allows one to avoid additional efforts for the maintenance of the plasma conduction. At the laboratory, such investigations were carried out at the small shock tube during the last few years. However, the performance of this installation cannot provide higher parameters of plasma, let alone modeling the MHD effects in molecular gases.

At the Ioffe Institute, Physical Gasdynamics Laboratory has developed experimental complex for investigations of interaction of supersonic flows of ionized gases with an external magnetic field using designed earlier big shock tube [3].

As compared with the small shock tube this installation have manifold possibilities by the parameters of height pressure chamber. Hydrogen is used as driver gas with temperature up to 750K and pressure up to 500atm. In this case the store of energy is about 4MJ.

Besides, the double diaphragm regime allows making flow with tailored contact surface. In this case the work time of the setup may be increased and reaches 1.5ms.

The system generating the pulse magnetic field comprising two coils positioned horizontally, capacitor bank by 30 mF, a current switching assembly, as well as control and supervision means. The store of energy reaches 0.4MJ. The half-cycle of the capacitor bank discharge is 4ms. The magnetic field induction reaches its maximum of 1.5T in the center between the coils.

The lateral walls of the test section are equipped with two co-axial windows of 140mm in diameter. These windows serve for observation of the flow pattern in the interaction area with the help of an optical device (10).

In the experiments carried out earlier in the small shock tube [4], the electromotive force induced by the magnetic field turned out to be less than the near-electrode potential drop, what made it impossible to obtain the induced current sufficient for detecting the MHD effect. In that case, the MHD interaction was achieved by applying a voltage from an external source to the electrodes.

In the present study was used the MHD channel allowing one, under the same flow parameters, to obtain the magnetically induced electromotive force approximately doubled as compared with [4] due to the larger distance between the electrodes. The first test of the experimental complex was aimed at detection of the scale effect by experiment investigation of MHD effect in the supersonic flow of xenon plasma.

The test section showed at fig.1 is a dielectric chamber (*1*) of the rectangular cross section of 75 mm in width and 140 mm in height and located in between two coils (*2*) positioned horizontally. At that, the induction vector of the magnetic field is perpendicular to the flow symmetry plane.
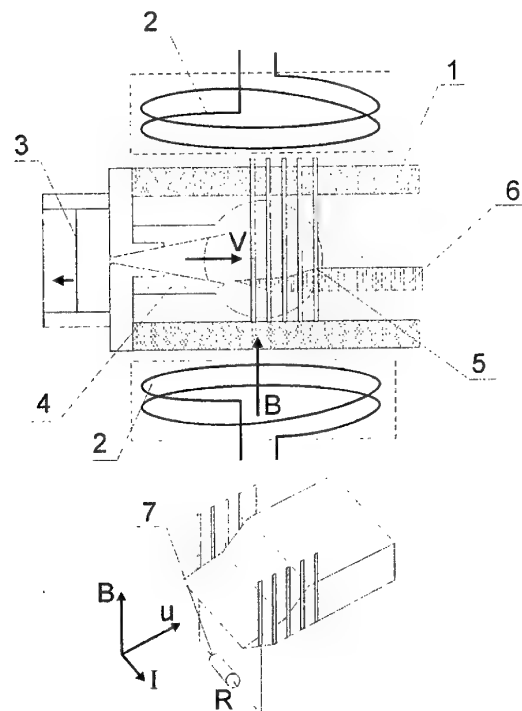
Fig.1. Draft of the MHD section and current switching.

As a result of heating the working gas by the reflected shock wave, a thermally equilibrium plasma of the high-density is formed at the end of the shock tube channel (*3*). Beginning from the time instant of the shock wave reflection from the tube end, the supersonic flow starts to form what terminates in reaching a quasi-steady state of nonequilibrium flow within the nozzle (*4*) featured by various temperatures of the electron and heavy component. The nozzle of 75mm in width, with the full angle of 22°, and heights of the critical and output cross sections of 10 and 60mm, respectively. The supersonic nozzle section is 130mm in length. The supersonic stream of the nonequilibrium plasma flowing from the nozzle is directed into the test section where MHD interaction is realized. The MHD channel is a dielectric chamber of the rectangular cross section of 75mm in width intersticed with a set of electrodes (*5*) at the inner surface of the vertical walls normally to the flow symmetry plane. In the space between the

electrodes near the output edge of the nozzle a double wedge (*6*) is housed. The wedge surfaces make angles with the mainstream velocity vector about 10 and 20°.

The induced current was determined as measurement results of a voltage drop across the resistor (*7*) $R=0.1$ohm connecting the first couple of electrodes. The distance between the nozzle inlet and the test cross section was 180mm. The magnitude of the magnetic field induction was kept to be constant and equal to $B \approx 1$T.

Changing the plasma parameters was implemented by variation of the initial gas parameters within the shock tube channel. The initial conditions of the experiments, the measurement results, and the calculated flow parameters are given in Table 1.

Table 1

Regime	P_1, (torr)	M_{s1}	U_m, (V)	ε, (V)
1	40	7,7	1	131
2	25	8,2	2	132
3	12	9,5	6	135

The notations used in Table 1 are:

P_1 is the initial xenon pressure in the low-pressure chamber of the shock tube,

M_{s1} is the Mach number of the incident shock wave,

U_m is the peak value of the voltage at the resistor, and

ε is the magnetically induced electromotive force being calculated using the formula

$$\varepsilon = BuL,$$

where

B is the magnetic field induction;

u is the plasma velocity in the test cross section, calculated by the formula of isenthropic flow; and

L is the distance between the electrodes.

From Table 1 is seen that with changing the flow regime, that is, the Mach number M_{s1}, the magnetically induced electromotive force practically does not vary. One can suppose that under the conditions of carrying out the experiment just the initial ionization of the working gas governs the plasma conduction in the test cross section.

In Fig.2, the points depict peak values of the current I_m through the measuring circuit varying with the gas ionization degree at the nozzle inlet. The measurement error does not exceed 15%. The α magnitude was determined on the basis of the

153

calculation of nonequilibrium xenon ionization behind the shock waves.
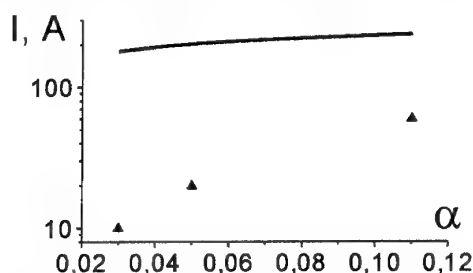
Fig.2. Variation of the current inside the MHD channel with the initial plasma ionization.

The specialists on numerical simulation of the Ioffe Institute carried out a calculation of interaction between the nonequilibrium supersonic flow of the shock-heated xenon and magnetic field. The calculation was conducted within the frame of a model of inviscid gas flow. The calculation results are shown in the graph by the solid line. As it was just expected, the calculated current values are considerably larger than the measured ones, inasmuch as in the calculations the near-electrode phenomenon was not taken into account.

Resume.

In the course of experimental investigations of the interaction between supersonic pulse flow (M= 4) of weakly ionized xenon plasma and magnetic field ($B\approx1T$) in an MHD channel it was detected an induced current. The dependence of this current magnitude on the flow ionization degree has been investigated. The comparison between the experimental results and the numerical calculation data has been performed.

References

1. Gurijanov E.P., Harada P.T. // AIAA Paper 96-4609. 7 [th] Aerospase Planes and Hipersonic Technology Conference. Norfolk, VA, 1996.
2. Brichkin D.I., Kuranov A.L., Sheikin E.G. // AIAA-98-1642, 8 [th] International Space Planes and Hypersonic Systems and Technologies Conference. April 27-30, 1998. Norfolk, VA.
3. Maslennikov V.G., Sakharov. Technical Physics. 1997, v.42, N11, pp. 1322-1328.
4. Bobashev S.V., D'yakonova E.A., Erofeev A.V., Lapushkina T.A., Maslennikov V. G., Ponyaev S.A., Sakharov V.A., Vasil'eva R.V., Van Wie D. M., Technical Physics Letters. 2001, v.27, N2, pp. 63-69.

27. NUMERICAL INVESTIGATIONS OF MGD INTERACTION IN NON-EQUILIBRIUM PLASMA FLOWS IN THE MODELS OF SUPERSONIC INLETS

Golovachov Yu.P., Kurakin Yu.A., Schmidt A.A.
Ioffe Physical Technical Institute, RAS,
194021, 26 Politekhnicheskaya, St.Petersburg, RUSSIA

Van Wie D.M.
The Johns Hopkins University, Applied Physics Laboratory,
Laurel, Maryland, 20723-6099, USA

Abstract. The effects of applied magnetic field on non-equilibrium three-component and two-temperature plasma flows in the models of supersonic intakes are investigated. Numerical simulation is performed within the framework of a MGD approach using an inviscid gas model. Numerical solutions are obtained with a high-resolution Godunov-type finite-volume scheme. The attention is focused on accounting for the real thermodynamic and electrophysical properties of non-equilibrium plasma. The geometry of the diffuser models and the input data correspond to the shock tube experiments being conducted at the Ioffe Institute.

Introduction

The idea of controlling an electrically conducting flow with an applied magnetic field is considered as a promising way for development of controlled intakes of supersonic aircraft which would ensure the rated operating regime with variation of the flight conditions [1,2]. The method to be discussed supposes preliminary ionization of incoming gas and subsequent control the ionized flow by applied magnetic field. To estimate the prospects of such a mode for flow control both experimental and numerical investigations were conducted at the Ioffe Institute. Preliminary calculations using the simplest physical and gas dynamic models [1,3] proved the possibility of controlling the flow structure in supersonic intakes with an applied magnetic field. However, more accurate analysis coupled with evaluation of plasma thermodynamic state and the electrophysical properties is obviously needed. To separate the problems of preliminary ionization of oncoming stream and the Magneto GasDynamic (MGD) flow control, the shock tube experiments were conducted with rare gases which are characterized by far greater recombination time as compared with air flows. The paper presents a numerical investigation of non-equilibrium rare gas plasma flows subjected to applied magnetic field for the range of conditions of the above experiments.

Basic assumptions

In general, collisional plasma flows subjected to a magnetic field are governed by the coupled set of gas dynamic equations complemented with the terms that take into account ionization and magneto-gas-dynamic interaction

(MGI) and Maxwell equations, see [5]. Fortunately, the flows under study may be analyzed with essential simplifications of the problem.

In accordance with the conditions of the shock tube experiments, the calculations are carried out for rare gas plasma which is assumed to consist of atoms (a), singly ionized positive ions (i), and electrons (e). The analysis is conducted using the two-temperature model and assuming plasma quasi-neutrality. The magneto-gas dynamic interaction is taken into account within the framework of the MGD approach neglecting the induced magnetic field. Validity of these assumptions follows from the inequalities:

$$l_D \ll L, \quad V_o \ll c, \quad L/V_o \gg \omega_p^{-1}, \quad Re_m < 1$$

which certainly hold for the flows under study. Here, l_D is the Debye length, L is the flow length scale, c is the light speed, ω_p is the plasma frequency, Re_m is the magnetic Reynolds number, subscript (o) denotes the scales for gas velocity, electric field strength and induction of magnetic field. Beside, we neglect the viscosity, heat conductivity, and diffusion which allows us to use an inviscid gas model described by the Euler equations. The latter assumption is substantiated, to some extent, by high Reynolds numbers of the flows under study but makes impossible an analysis of separated flows.

Governing equations

With above assumptions, non-equilibrium three-component and two-temperature plasma flows subjected to an applied magnetic field are governed by the following equations, where (1,2)

are the total and electron continuity equations, (3) is total momentum balance equation, (4,5) are the total and electron energy balance equations:

$$\frac{\partial \rho}{\partial t} + \nabla \cdot (\rho \vec{V}) = 0 \qquad (1)$$

$$\frac{\partial n_e}{\partial t} + \nabla \cdot (n_e \vec{V}) = \dot{n}_e \qquad (2)$$

$$\frac{\partial \rho \vec{V}}{\partial t} + \nabla \cdot (\rho \vec{V}\vec{V} + p) = \vec{j} \times \vec{B} \qquad (3)$$

$$\frac{\partial}{\partial t}\left(\frac{\rho V^2}{2} + \frac{3}{2}p\right) + \nabla \cdot \left[\left(\frac{\rho V^2}{2} + \frac{5}{2}p\right)\vec{V}\right] =$$
$$= \vec{j} \cdot \vec{E} - \dot{n}_e \varepsilon_{ion} \qquad (4)$$

$$\frac{\partial}{\partial t}\left(\frac{3}{2}p_e\right) + \nabla \cdot \left(\frac{5}{2}p_e \vec{V}\right) = \vec{V} \cdot \nabla p_e +$$
$$+ \vec{j} \cdot (\vec{E} + \vec{V} \times \vec{B}) - \dot{n}_e \varepsilon_{ion} -$$
$$- 3\frac{m_e}{m}kn_e(\nu_{ei} + \nu_{ea})(T_e - T) \qquad (5)$$

Here, $\vec{V}$ is the mass-averaged flow velocity; ρ is the plasma density; p is the plasma pressure; $p_e = n_e kT_e$ is the partial pressure of the electrons; n_e is the number density of the electrons; m, m_e is the mass of a heavy particle and an electron; k is the Boltzmann constant; $\vec{j}$ is the electric current density; $\vec{B}$ is the induction of magnetic field; $\vec{E}$ is the electric field strength; ε_{ion} is the ionization energy per atom; $\dot{n}_e$ is the number rate of electron production per unit volume; ν_{ei}, ν_{ea} are the collision frequencies; T_e, T are the temperatures of the electrons and the heavy particles.

The collision frequencies are calculated using the cross-sections presented in [7]. The number rate of electron production is supposed to be determined by ionization through electron impact and three-particle recombination. The recombination rate constant is calculated following the theory of non-equilibrium low-temperature plasma developed by Biberman et al. [6].

Equations (1)-(5) apply both to non-stationary and stationary plasma flows. Stationary solutions are obtained using a time-asymptotic technique. In most calculations, all plasma parameters are prescribed on the inflow boundary of the computational domain. If the outflow velocity is subsonic, the pressure should be prescribed on the downstream boundary. On the duct walls, the impermeability conditions are imposed.

MGI models

To close the set of equations (1 - 5) one has to determine the electric current density and the electric field strength. With that end in view one can use the generalized Ohm's law:

$$\vec{j} + \beta_e \vec{j} \times \vec{b} = \sigma\left(\vec{E} + \vec{V} \times \vec{B} + \frac{\nabla p_e}{en_e}\right) \qquad (6)$$

where β_e is the Hall parameter for electrons, $\vec{b} = \vec{B}/|\vec{B}|$.

The electric field strength is found through specification of the external load coefficient k: $\vec{E} = -k(\vec{V} \times \vec{B})$. The above Magneto Gasdynamic Interaction (MGI) model is widely used in calculations of MHD generators, see [8].

A more accurate way to determine the electric field strength uses the equation for the electric field potential. Under the above assumptions it looks as follows:

$$\nabla \cdot \left[\tilde{\sigma}\left(-\nabla \varphi + \vec{V} \times \vec{B} + \frac{\nabla p_e}{en_e}\right)\right] = 0 \qquad (7)$$

where $\tilde{\sigma}$ is the tensor of electric conductivity.

Wall boundary conditions for equation (7) are given by the fixed electrode voltage and by zero electric current normal to insulated walls. The inflow and outflow boundary conditions depend on the duct geometry and the electrode system design.

Numerical method

The method for solving equations (1)-(5) is based on the Godunov-type high-resolution finite-volume scheme, the ionization and collision terms being evaluated with the simplest two-layer implicit scheme. The computational procedure is second-order accurate with respect to both spatial coordinates in the flow regions with smooth function behaviour. The admissible time step is limited by the CFL stability condition. More detailed description of the computational procedure is presented in [9]

Results

The results of calculations pertain to xenon plasma flows in the MGD sections of the experimental facilities using Small and Big Shock Tubes of the Ioffe Institute.

Let us consider, at first, the results for plasma flows in MGD section of the Small Shock Tube (SST) setup which consists of a nozzle and a model of a diffuser with rectangular cross-sections, see [3, 4]. The electrode system includes several pairs of electrodes (filled rectangles on figures) mounted in the lower and upper walls of the diffuser model separated by insulated inserts. The induction of applied magnetic field $\vec{B}$ is normal to the side walls of the MGD section. This being the case, the flows under study are planar both with and without an applied magnetic field. The plasma parameters in the critical cross-section of the nozzle are the following:

M=1.00, T=7700K, T_e=8700K,
α=0.013, n_0=0.9·10^{25}m^{-3},

where M is the Mach number, α is the ionization degree, n_0 is the neavy particle number density.

Fig.1. Mach number in SST setup, (a-b) at B=0.5T, $\Delta\varphi$=±100V; (c) - without magnetic field.

Figs.1 (a-c) display the Mach number contours calculated with (a,b) and without (c) the magnetic field. Here and below cases (a) and (b) correspond to the applied electric field directed along (a) and opposite (b) the electromotive force induced by plasma flow in the applied magnetic field B=0.5T. Corresponding distributions of the electric field potential and the electric current streamlines are shown in Fig.2. As it is seen from Figs.1(a,b) the direction of the applied electric field determines the electric current direction and the direction of ponderomotive force, which, effects drastically the flow stucture. Case (a), in contrast to

(b), is characterized by stronger flow deceleration and inner subsonic zones (shaded on the figure).

Fig.2. Electric field and electric current streamtraces in SST setup at B = 0.5 T, $\Delta\varphi$ = ±100V.

Distributions of the heavy particle and electron temperatures are shown in Figs.3 and 4.

Fig.3. Heavy particle temperature (Kelvins) in SST setup at B = 0.5 T, $\Delta\varphi$ = ±100 V.

Fig.4. Electron temperature (Kelvins) in SST setup at B = 0.5 T, $\Delta\varphi$ = ±100 V.

It is seen that the flow is essentially non-equilibrium down to the outlet of the MGD section. Intensive variation of the electron temperature (see Fig.4) due to the Joul heat release leads to successive heating of the heavy particles resulting in the flow deceleration (see Fig.1). Diffrent

distributions of the Joul heat release in cases (a) and (b), see Fig.4, determine different location of flow regions where the most plasma deceleration occurs.

Figs.5 and 6 present the elecrtic conductivity and the Hall parameter distributions. The Hall effect results in asymmetry of the flow noticeable in Figs.1-6.
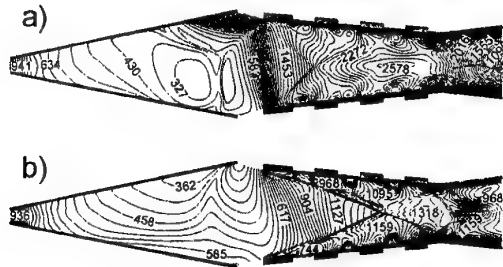
Fig.5. Electric conductivity (mho/m) in SST setup at $B = 0.5$ T, $\Delta\varphi = \pm100$ V.
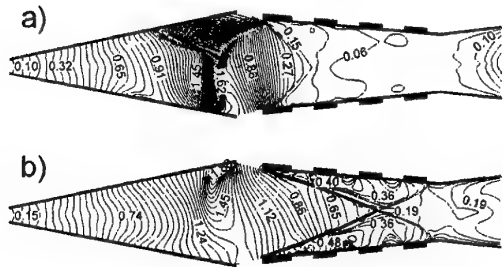
Fig.6. Hall parameter in SST setup at $B = 0.5$ T, $\Delta\varphi = \pm100$ V.

The MGD section of the Big Shock Tube (BST) setup consists of a supersonic nozzle and a two-step wedge. Fig.7 presents Mach number distribution in MGD section of the BST setup without magnetic field. The working gas is heated by the shock wave reflecting from the shock tube end wall which has a small outlet to the supersonic nozzle. The experiments have been performed with the following shock tube incident Mach numbers:

1) $M_o = 7.8$;   2) $M_o = 8.2$;   3) $M_o = 9.5$.

Plasma behind the reflected shock was assumed to be in equilibrium with the following parameters:

1) $M_o = 7.8$: T = 9978 K, $\rho = 0.00265$ g/cm^3, $n_e = 4.192 \cdot 10^{23}$ m^{-3};
2) $M_o = 8.2$: T = 10106 K, $\rho = 0.00173$ g/cm^3, $n_e = 3.715 \cdot 10^{23}$ m^{-3};
3) $M_o = 9.5$: T = 10558 K, $\rho = 0.00116$ g/cm^3, $n_e = 4.166 \cdot 10^{23}$ m^{-3};
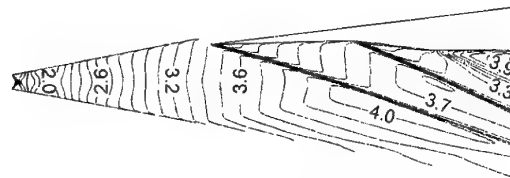
Fig.7. The Mach number contours in MGD section of the BST setup without magnetic field.

The initial data for calculation of non-equilibrium flows in supersonic nozzle and diffuser model were obtained from preliminary calculation of plasma flow through the nozzle throat.

In the BST experiments, the magnetic field is applied along the vertical y-axis, so that the electrodes are mounted in the parallel side walls of the diffuser model. To eliminate the Hall effect which has been found to impede plasma deceleration by magnetic field, the electrodes were separated with insulated inserts. The calculations were carried out assuming the scheme of Faraday generator with ideally segmented electrodes. In this case, the MGD flow remains planar. The induction of applied magnetic field, $B = 1$T, and the loading factor, $k=0.5$ was assumed.

Fig.8 presents the Mach number distributions in the diffuser model. One can see quite different flow structures for the above variants of the experimental conditions. The magnetic field decelerates the plasma flow down to subsonic speed resulting in rather complicated shock interactions.

Fig.8. Mach number in the diffuser model of the BST setup at $B = 1$ T.

Fig.9 shows the electric current through the first pair of the electrodes of the experimental setup versus Mach number of the incident shock. A considerable difference between the measured (circles) and calculated (solid curve) values is attributed, apparently, to oversimplification of the real electrode system with the model of Faraday generator with ideally segmented electrodes and to the neglect of the near electrode phenomena in the computational model.
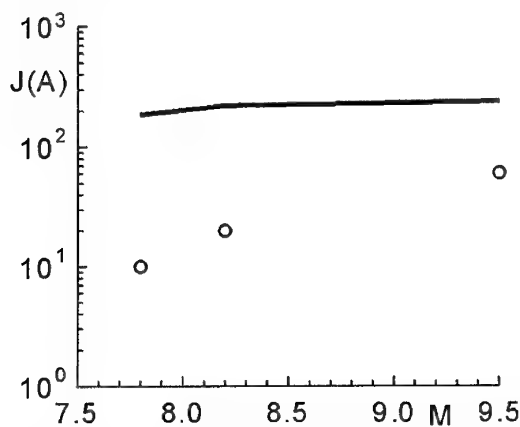
Fig.9. Variation of the electric current in the inlet of the diffuser model of the BST setup with Mach number of the incident shock wave.

Conclusions

Numerical simulation of non-equilibrium xenon MGD flows in the models of supersonic intakes has been carried out over the range of conditions of shock tube experiments.

The effects of applied electric field on the flow structure and plasma parameters has been investigated.

The results of numerical simulation provide evidence of the possibility for plasma flow deceleration by applied magnetic field down to subsonic speed.

Further improvement of the computational model is requested to bring together the computational and experimental results.

References

1. Golovachov Yu.P., Il'in S.A., and Sushchikh S.Yu. "Magnetic Field Control of Gas Flow in a Supersonic Intake", Tech.Phys.Lett., 1997, Vol.23, No.8, P.615-616.
2. Brichkin D.I., Kuranov A.L., Sheikin E.G. "MHD-technology for Scramjet Control", AIAA Paper 98-1642.
3. Golovachov Yu.P., Sushchikh S.Yu., and Van Wie D.M. "Numerical Simulation of MGD Flows in Supersonic Inlets", AIAA Paper 2000-2666.
4. Bobashev S.V., et al. "Shock Tube Facility for MGD Supersonic Flow Control", AIAA Paper 2000-2647.
5. Mitchner M. and Kruger C.H. Jr. Partially Ionized Gases. Wiley & Sons, 1973.
6. Biberman L.M., Vorob'ev V.S., Yakubov I.T. Kinetics of Low-temperature Non-equilibrium Plasma, Moscow, Nauka, 1982 (in Russian).
7. Volkov Yu.M., Zinov'ev O.A., Maluta D.D. "Measurement of the diffusion cross-sections of low-energy electrons in rare gases using the microwave technique", Teplofizika Vysokikh Temp., 1968, Vol.6, No.2, P.209-218 (in Russian).
8. Breyev V.V., Gubarev A.V., Panchenko V.P. Supersonic MHD Generators. Moscow, Energoatomizdat, 1988 (in Russian).
9. Golovachov Yu.P., Kurakin Yu.A., Schmidt A.A., and Van Wie D.M. "Numerical Investigation of Non-Equilibrium MGD Flows in Supersonic Intakes.", AIAA Paper 2001-2883 (to be published)

28. MHD-CONTROL OF GAS FLOW IN THE TRACT HYPERSONIC RAMJET ENGINE

E.N.Vasilyev, V.A. Derevyanko, A.N.Mierau
Institute of Computational Modeling, Krasnoyarsk

Nowadays in leading countries of the world active research has been conducted on developing the perspective hypersonic aerospace aircraft. One of the key directions of research on this problem is the development highly efficient hypersonic ramjet engine (HRE). It is known that the efficiency of HRE with supersonic flow velocities in the combustion chamber decreases with the increasing of flight velocities. The basic losses take place in the combustion chamber as firstly the relative losses of working capacity of gas is considerably increasing at the heat supply, secondly because of high speed of the flow the quality of fuel confusion with the air on the bounded length considerably deteriorates and the completeness of combustion declines. The remarks of estimates demonstrate that for this reason the application of HRE is bounded evidently with the Mach numbers of flight that doesn't exceed 11-12. At the same time the thermodynamic estimates demonstrate the considerable reserve on the specific characteristics. This reserve can partly be realized by the reconstruction of the structure of the current using MHD-interaction.

In the Institute of Computational Modeling and Institute of Theoretical and Applied Mechanics a principle of MHD-control of gas flow in the channel HRE has been worked up. It is based on the creation of local plasma areas with temperature 10^4K in the flow that would interact with an external magnetic field so as to increase the specific characteristics of engine [1]. The use of the effect of T-layer in HRE would also allow to get the electric energy on the board of an aircraft. Some part of this energy would be used in the initialization of T-layers and creation of the magnetic field, another part for the useful energy.

The principle of MHD-control of the gas flow is based on the following physical processes (Fig.1). The filling current is broken and contracted in the air intake whereupon it proceeds to the entrance of the combustion chamber, constructively combined with MHD - channel. Here the system of initialization with the high-voltage break-down of gas creates periodically the high-temperature current layers. The mode of MHD interaction is selected so, that the Joule dissipation would compensate the power losses and the mode of the self-sustaining T- layer is installed. The self-sustaining T - layer in a flow of gas is the peculiar plasma's piston to which the braking electromagnetic force reconstructing the structure

of the current in the combustion chamber of HRE is applied. When the T-layer brakes in the HRE channel the non-stationary structure of the flow is formed, consisting of the following zones: 1-undisturbed gas current, 2 - shock compressed gas, 3 - T-layer, 4 - area of the wave of exhaustion. Changing the specific characteristics of MHD-interaction (K-load factor, B- induction of the magnetic field) we may control the value of the electromagnetic force applied to the T-layer, the extension of the zones and the value of their physical parameters. We offer to conduct the combustion of the fuel in the area of shock compressed gas which is characterized with higher pressure, and the velocity of the flow is considerably lower than that at the input that promotes the more effective burning of fuel. Moreover the combustion of the fuel in this area is profitable for thermodynamics as the average temperature of the heat supply increases while the average temperature of the flow stays unchanged. In the nozzle part the gas flow accelerates, creating the propulsion impulse.

Fig.1. The scheme of hypersonic ramjet engine and the structure of the stream.

The principle of MHD-control of the gas flow is based on the following physical processes (Fig.1). The filling current is broken and contracted in the air intake whereupon it proceeds to the entrance of the combustion chamber, constructively combined with MHD - channel. Here the system of initialization with the high-voltage break-down of gas creates periodically the high-temperature current layers. The mode of MHD interaction is selected so, that the Joule dissipation would compensate the power losses and the mode of the self-sustaining T- layer is installed. The self-sustaining T - layer in a flow of gas is the peculiar

plasma's piston to which the braking electromagnetic force reconstructing the structure of the current in the combustion chamber of HRE is applied. When the T-layer brakes in the HRE channel the non-stationary structure of the flow is formed, consisting of the following zones: 1- undisturbed gas current, 2 - shock compressed gas, 3 - T- layer, 4 - area of the wave of exhaustion. Changing the specific characteristics of MHD-interaction (K-load factor, B- induction of the magnetic field) we may control the value of the electromagnetic force applied to the T-layer, the extension of the zones and the value of their physical parameters. We offer to conduct the combustion of the fuel in the area of shock compressed gas which is characterized with higher pressure, and the velocity of the flow is considerably lower than that at the input that promotes the more effective burning of fuel. Moreover the combustion of the fuel in this area is profitable for thermodynamics as the average temperature of the heat supply increases while the average temperature of the flow stays unchanged. In the nozzle part the gas flow accelerates, creating the propulsion impulse.

In the works [2,3] the structure of the current in the HRE channel with one T-layer has been investigated on the basis of solution of the one-dimensional system of equations of gas dynamics in Lagrange coordinates with the regard of the heat of fuel combustion in the area of shock-compressed gas. The calculation of structure of current was added with the definition of balances of energy and impulse for all zones of the flow and general efficiency of MHD-process. With the help of functional mathematical model the specific propulsion characteristics of the engine for each zone of a gas flow were estimated, and then the average characteristics during a running cycle (the flight time of T-layer) were found. The given estimates have shown, that the application of MHD-control with a T-layer can increase the value of the specific HRE impulse up to 50%.

The estimates have shown the basic opportunity of the use of MHD-control with a T-layer for the extension of range of work of the engine on Mach's numbers and the improvement of specific propulsion characteristics. To define of an opportunity of practical use of MHD-control it is necessary to solve a set of various problems, including the research of periodic mode of work.

One of major factors influencing the structure of the current in HRE channel with MHD-control are the shock waves and waves of underpressure, that are formed in the interaction of a T-layer with a magnetic field. Here the wave disturbances cooperate with each other and with T-layers, created in periods by the system of

initialization, and, thus, they influence considerably on the structure of a T-layer and the characteristics of the current in the HRE channel.

The numerical modeling of the structure of the non-stationary gas dynamic current in HRE channel was conducted on the basis of the solution of the system of non-stationary equations of gas dynamics in the Euler coordinates.

$$\frac{\partial \rho F}{\partial t} + \frac{\partial \rho u F}{\partial x} = 0, \tag{1}$$

$$\frac{\partial \rho u F}{\partial t} + \frac{\partial \rho u^2 F}{\partial x} + \frac{\partial p F}{\partial x} = jBF + p\frac{\partial F}{\partial x}, \tag{2}$$

$$\frac{\partial \rho F(e + \frac{u^2}{2})}{\partial t} + \frac{\partial \rho u F(e + \frac{u^2}{2})}{\partial x} + \frac{\partial p u F}{\partial x} =$$
$$= (jE + q_{in} + q_f - q_R)F , \tag{3}$$

$$j = \sigma E, \quad E = (1 - K)uB, \tag{4}$$

$$p = R\rho T, \quad E = c_V T. \tag{5}$$

Here j - current density, $F(x)$ - the section of the channel, t - time, x-coordinates, p –pressure, e –internal energy, E - electric field tension, q_{in} - the power of heat apportionment of the initialization, q_R - radiation energy losses, q_f - specific heat of combustion of fuel, σ - electroconductivity, T - temperature, ρ - gas density,

The boundary condition on the entrance are the parameters corresponding to the parameters on the exit from the air intake, that were preliminarily estimated with the regard of irreversible losses on the oblique leaps, and the boundary condition on the exit corresponds to the free departure as the derivative parameters are set as zero. The initial condition is the hypersonic undisturbed current of gas.

The value of radiation losses of energy was defined in the approximation of the volumetrical radiator in the form $q_R=2\sigma_R\varepsilon(T,p,\delta)T^4/\delta$. Here σ_R - the Hermann-Boltzman constant, ε - the blackness factor of the flat emanating layer, δ - the sickness of the emanating layer. The thermophysical and radiation properties of the gas were calculated with the help of software package MONSTR [4] and were entered into the program in the tabular form $\sigma(T,p)$, $\varepsilon(T,p,\delta)$, $\mu(T,p)$, $\gamma(T,p)$.

The system of equations (1.1-1.5) was solved with the obvious method of MacCormack [5]. Due to the fact that the current contains the

161

areas with the large gradients of parameters (T-layers and shock waves) the method of the flow correction FCT [6] was used to eliminate oscillations and to increase of the precision of the estimates.

In the figure below the results of the modeling of the current are introduced with the following parameters on the entrance of the hypersonic flow to the combustion chamber: T=600K, p=4.5·10^4Pa, u=1500m/s. The parameters of MHD-interaction are: K=0.8, B=2T. In the course of the numerical modeling the periodical mode of work was investigated, when the T-layers are initialized in the entrance to the combustion chamber with the frequency of 500Hz.

The non-stationary process starts at the initial moment of time with the initialization of the first T- layer, which is simulated by the setting of q in the form of sinusoidal impulse with duration of 10^{-4} seconds on the entrance to the channel. The power of thermal apportionment is set so that, that for this time the temperature in a local area of the flow would achieve 10^4K, which is accompanied by the corresponding increase of the pressure. At the same time the electroconducting gas starts to interact with the magnetic field, so the shock wave goes up the flow while the wave of the rarefaction goes down (Fig.2).
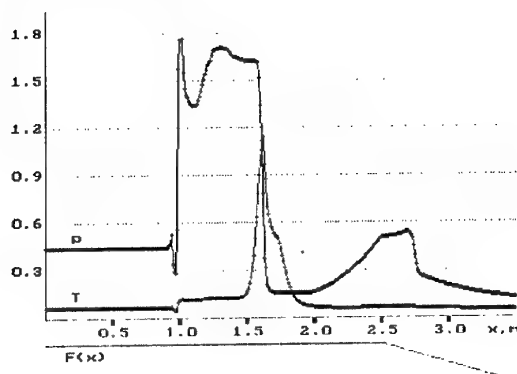
Fig.2. Distribution of temperature (scale 10^4K) and pressure (10^5Pa) in the channel at the moment of time t=10^{-3}s.

At the expense of the inducted electric field the current starts to flow in the gas, that compensates the radiation losses of the energy and provides the mode of self-sustaining T-layer. Behind the front of the shock wave the apportionment of the heat in the combustion of the fuel is simulated. The apportionment of the heat raises the temperature of the gas in the area of shock-compressed gas up to 1150K, and the extension of this area increases approximately on

50 % and to some insignificant extent it leads to the increase of the pressure and speed of T-layer. For the moment of time 10^{-3}s the T-layer forms the stabilized structure, i.e. its' parameters stay further constant before the exit in the nozzle part. At an entrance of a T-layer in the nozzle temperature of gas in it declines (Fig.3.), but this of mass of gas accelerates. The application of effect of T-layer in HRE has its' positive side in comparison to the pure generator process, as in this case energy spent on initialization, isn't lost, and contributes considerably to the propulsion impulse of the engine.
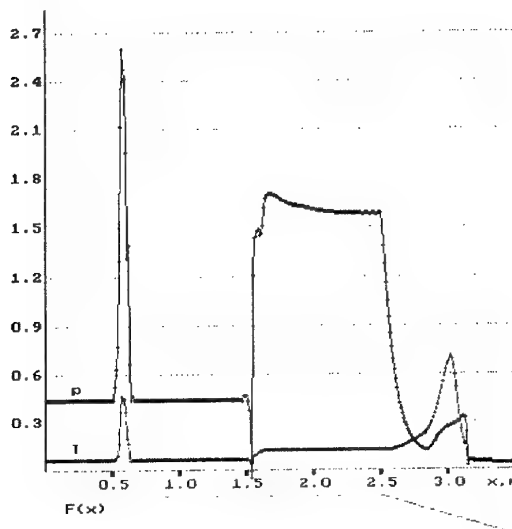
Fig.3. Distribution of temperature (scale 10^4 K) and pressure (10^5 Pa) in the channel at the moment of time t=2.05 10^{-3}s.

At the moment of the entrance of a T-layer in the nozzle part the initialization of the subsequent T-layer occurs (Fig.3). Here in the combustion chamber still remains shock -wave disturbance, that goes up along the flow and at the certain parameters of MHD-interaction the front of this shock wave can achieve the newly initialized T-layer within the limits of the chamber of combustion, changing radically its' power balance. In this case the radiation losses of the energy increase in the direct proportion of pressure, and speed of gas with the corresponding Joule heat apportionment decrease, that leads as a result in to the fast loss of electroconductivity, the stopping of MHD-interaction and break of the mode of the engine work. This effect is the feature of a periodical mode and it is necessary to be considered. For the elimination of the disintegration of a T-layer it is necessary to select parameters of MHD-process excluding interaction

162

of a T-layer with a shock wave. This condition imposes the additional restrictions in comparison with process with an isolate T-layer [3].

In the considered periodical mode there is an interaction of a shock wave with the wave of rarefaction departing from the new T-layer, but there is no interaction of a T-layer with the shock wave, as it has time to be brought out from the combustion chamber (Fig.4.).
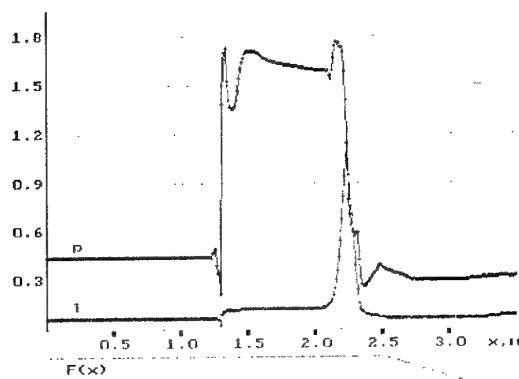
Fig.4. Distribution of temperature (scale 10^4 K) and pressure (10^5 Pa) in the channel at the moment of time $t=3.8 \cdot 10^{-3}$.

At decrease of factor of loading up to 0.7 and other parameters of process being constant the interaction of a T-layer with a shock wave occurs already within the limits of the combustion chamber at the moment of time $t=3.2 \cdot 10^{-3}$ s, and further the temperature, the electroconductivity of gas and the overfall of pressure in a T-layer decrease, and the MHD-interaction practically stops.

One of the major characteristics of MHD-process is the efficiency of transformation enthalpy, which is defined as the ratio of useful power selected in the loading, to the thermal power of the flow, brought in through entrance section, of combustion chamber. For the considered mode the value $\eta_N=17\%$ (when $q_f=0$ $\eta_N=15\%$). Taking into account in the definition of, that in the chamber of combustion the heat content of the flow is increased at the expense of heat of combustion of fuel, we set the value $\eta_N=7.5$ of %. The major requirement for organization of a periodical mode is the reproduction of electrical energy powerful enough for the initialization of T-layers. In this case to initiate one T-layer $1.6 \cdot 10^5$J were spent on one unit of the cross section of the channel, and for flight time one T-layer produces $2.4 \cdot 10^5$J/m^2 of the useful energy. Thus it is necessary to note, that the parameters of MHD-interaction were not optimized on the production of useful energy.

One of the basic criterion of the efficiency of the engine is specific impulse - I_{ud}. Granting essential non-steadily-state of flow impulse in the outflow face of nozzle was calculated with using averaging of the period, using following ratio.

$$I_{ud} = \frac{1}{\Delta t m_f} \int_0^{\Delta t} \left(\rho u^2 F_c + p_c F_c \right) d\tau \qquad (6)$$

Here: I_{ud} - specific impulse, F_c - the area of exit section of the nozzle, τ - time, p – the gas pressure in the exit section of the nozzle, ρ - gas density, u_c – velocity of gas in the exit section of the nozzle, m_f – fuel mass, Δt – period of initialization of T-layers.

In the estimates of periodic power setting, basic efforts were are directed on the search of optimum values of parameters of an external magnetic field B and the load factor K and also on the selection of optimum frequency of initialization of T-layers, at which the front of shock wave disturbance extending up the flow doesn't achieve the newly initialized T-layer within the limits of the combustion chamber. Otherwise there is a disintegration of a T-layer owing to the change of its' power balance and the stopping of MHD-interaction.

In figure 5 the diagrams of dependence of a specific impulse of the engine from the Mach's number of flight at the values of period of initialization of T-layers $5.5 \cdot 10^{-3}$c $-$ $4.5 \cdot 10^{-3}$c. For the comparison the values I_{ud} for ramjet engine without MHD-control are given.
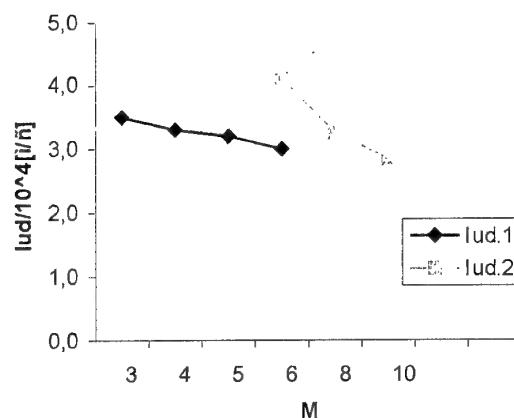
Fig.5. I_{ud1} is specific propulsive impulse for ramjet, I_{ud2} is specific propulsive impulse for HRE with MHD – control.

163

From the diagram we can see, that the use of MHD-control of a gas flow allows to increase the value I_{ud} on 20-25 of % at the Mach's number 6 in comparison with the traditional circuits of ramjet engines and to advance in the area with Mach's numbers of flight 6-10.

The further increase of the efficiency of an engine is possible at the expense optimisation of geometry of the channel and other parameters of MHD-interaction.

References

1. Latypov A.F., Derevyanko V.A., Vasilyev E.N., Ovchinnikov V.V Ramjet and method it of operation. The patent of Russian Federation № 1803595 from 03.01.96.
2. Vasilyev E.N., Derevyanko V.A., Latypov A.F., Mathematical simulation of gas flow in hypersonic ramjet with MGD control. In: 7th. International Conference on the Methods of Aerophysical Research. - Novosibirsk, 1994.
3. MacCormak R. W. The effect of viscosity in hypervelocity impact creating.// AIAA Paper 69-354,Cincinnati, Ohie,1969.
4. Book D.L., Boris J.P., Hain K. Flux-Corrected Transport II. Generalization of the Method // Journ. of Comput. Phys. - 1975. - 18. - P. 248 - 283.

29. INTERACTION OF DIAMAGNETIC PLASMA FLOW WITH STRONG TRANSVERSAL MAGNETIC FIELD

A.F.Pal, V.M.Strunnikov.
The State Scientific Center of Russian Federation
Troitsk Institute for Innovation and Fusion Research
Tel.: (095) 334-0675, e-mail: afpal@triniti.ru

Introduction

Studying the features of interaction of plasma flows with transversal magnetic field is of interest for creating the picture of the stationary magnetosphere of the Earth and for the dynamics of this picture during Solar flares, for fabricating MHD generators, facilities for magnetic surface isolation from thermal overload as well as for fuel injection into the thermonuclear reactors.

The interaction feature is, first of all, determined by magnetic Reynolds number $R_\sigma = vL/v_H$ [1]. Here, v and L are the characteristic stream flow velocity and inhomogeneity size, v_H is the coefficient of magnetic diffusion.

In laboratory experiments with fast plasma streams, such as [2-8], most detailed investigation was performed for streams with small Reynolds numbers, when $R_\sigma \ll 1$. In this case the primary magnetic field was not practically disturbed by the stream as the field had enough time to diffuse into the moving plasma. The magnitude of the disturbance did not exceed 10% [4,8].

For large Reynolds numbers the stream behavior should sharply change. In this case there should occur formation of thin skinning boundary between plasma and magnetic field, and hence that of stream channel with new shape and with flexible walls on which the pressure of magnetic field is balanced by gas-dynamical p and dynamical $\rho v^2/2$ plasma pressures. This problem was first theoretically solved without taking into consideration the limitedness of transverse size of the stream [9-11]. According to Tuck criteria [10] the behavior of stream penetration into transverse magnetic field depends on the value of $H_c = (12\pi\rho v^2)^{1/2}$, where ρ is the mass density. When $H > H_c$, the stream stops for some time, and then due to Rayleigh-Taylor instability out of plane boundary of plasma there forms a thin leaf-like structure moving along the former direction. L.A.Artsimovich [12] solved the problem about the movement of such a structure having formed along lines of magnetic force with conductivity σ and thickness h. Internal plasma pressure was not taken into account, it was assumed that the field increased up to value H within distance L. The condition for the stream with such a form to pass is as follows: $\rho v > \sigma h^2 H^2/12c^2 L$.

In [12] there is a film about movement of high conductivity plasma through a strong transverse magnetic field. There occurs a strong deformation of the stream. Under a small excess of magnetic pressure above dynamic one the stream crosses the field area as a strongly bent leaf-like structure oriented along lines of magnetic force. Under 30-fold excess plasma stops with forming a sharp luminous boundary from field side. The results produced did not contradict Artsimovich criterion.

Experimental conditions

This work was performed to investigate the dynamics of magnetic field under conditions of the revealed great deformations of stream. The same co-axial injector with pulsed working gas input system (Marshall plasma gun) [14,15] was powered with a capacitor battery of 42μF. The injector produced and directed short streams of hydrogen plasma into a glass tube of 95mm in diameter (Fig.1). The used stream flowed into a vacuum reservoir with great volume. A new magnetic field rectangular coil with internal dimensions of $20 \times 22 cm^2$ was fabricated. Five turns without axial shift of layers made of long copper band of 32cm in width were wound. The center of the coil was 110cm from the injector, in this case glass tube passed through holes of 10cm in diameter which were made in the walls of the coil. Magnetic field with the strength up to 18.5 kOersted was created during the process of discharging the same capacitor battery of 1500μF in capacitance. However, now the change in magnetic field strength could be ignored for the discharge period was increased from 80 to 540μs. Within the tube axis the field grew from $0.1H_{max}$ up to $0.9H_{max}$ over the distance of 8cm, the scattered field of the opposite sign did not exceed $0.1H_{max}$ and slowly decreased towards the injector. Initial pressure in the vacuum reservoir was not greater than $10^{-3}Pa$.
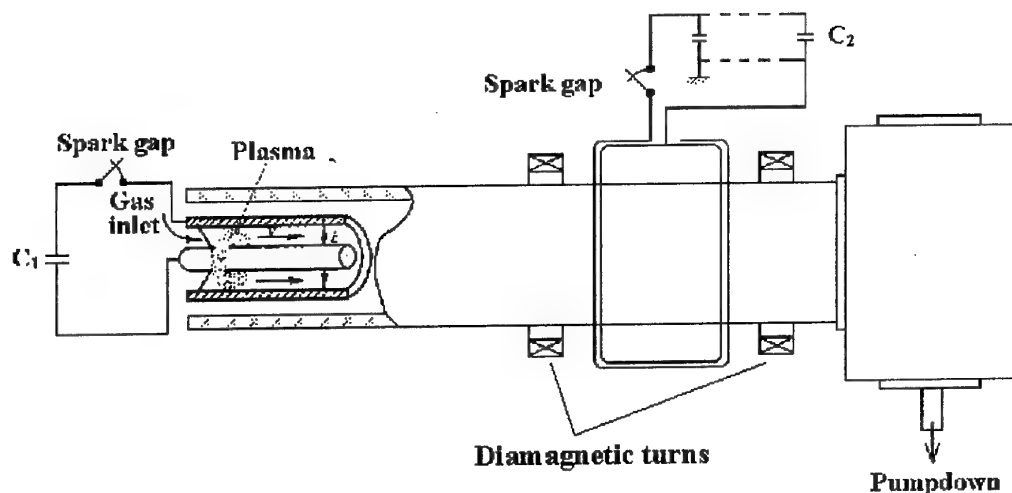
Fig.1. The scheme of the setup. C_1=42 mF, C_2=1500 mF

The glow of the stream of plasma within visible spectrum was photographed with high-speed photocamera. Time interval between shots was 3.2μs. Plasma was simultaneously photographed from two views. The bottom view was produced with mirrors placed under the tube at an angle of 45 degrees with the horizontal plane. The current in the injector was measured with Rogovsky loop. Two diamagnetic turns wound on both sides of the coil of transverse field, 24.5cm from the coil center, were used for measuring the stream velocity and time length. Weak magnetic fields were created in these sites by the battery current in the coils of 15cm in diameter. Plasma density in the flow was measured with accuracy up to 50% [16] with floating electrical probe. All basic investigations of magnetic field dynamics were performed with a magnetic probe. The probe was a coil of 3mm in diameter with 200 turns of copper wire. The coil was placed inside a glass tube of 5 mm in diameter near the face end. The probe could easily be moved to any site of the tube without breaking vacuum. Signals from the probe and diamagnetic turns were integrated with RC-circuits with time constant of 2.4ms. Electrical probe signals, injector current and synchronization signals from high speed photocamera were recorded with oscillograph.

According to measurement data, electron density in the incident stream was $2 \cdot 10^{15} cm^{-3}$, the stream velocity was ~$7 \cdot 10^6$cm/s. Further, z-axis was assumed to coincide with the direction of transverse magnetic field, and x-axis was directed toward the stream motion. All distances were measured from the center of the coil, and time intervals were measured from the end of the first half-period of injector current.

Experimental results

Fig.2 presents oscillograms of signals from two diamagnetic turns for a number of magnetic field strength values. The value of the signal is proportional to magnetic flux displaced from tube area by plasma. It is clearly seen that the
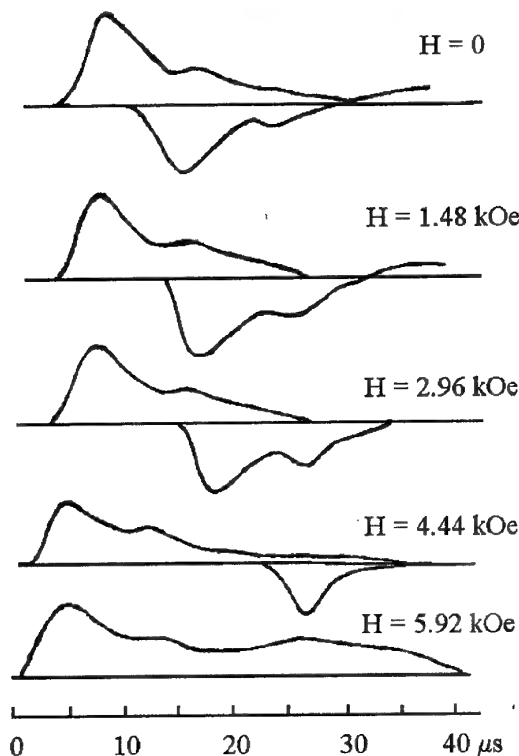
Fig.2. Signals from diamagnetic turns

166

head part of the stream with strong diamagnetic properties consists of two plasmoids continuously flowing into each other and moving with practically the same speed. The total length of these plasmoids is about 1.5÷2.0m. With the growth of field strength the speed is linearly decreased and tends to zero for $H_{max} \approx 5.6$kOe. The value of the signal from the turn placed behind the coil with field is also decreased. For $H_{max} \approx 5.9$kOe ($H^2_{max}/4\pi\rho v^2 \approx 17$) this signal disappears and on the signal for $H_{max} \approx 5.2$kOe from the other turn there forms a broad maximum created by a shock wave in the plasma stopped in front of the coin.

The shots of the film show that the glow of primary stream is non-uniform within the tube cross section. Within the coil area the head brightly luminous part has a cone-like shape. Bright radiation increases its diameter from 2cm up to 6.5cm in 13μs and then, fainting, gradually fills the whole tube.

During the interaction of the stream with the field of 0.7kOe in strength there occurs noticeable stream compression. It is maximal within the center of the coil. There appears a sharp luminous boundary between the field and the bright stream core. This boundary is clearly seen when the plasma passes through the field of $H_{max} \approx 1.85$kOe in strength (Fig.3, shots 3 and 4). Here, $H^2_{max}/4\pi\rho v^2 \approx 1.7$. Not the whole stream probably penetrated to the field. Upper and lower layers of the stream are reflected from the steep magnetic channel wall. In shot 4 one can see a shift of the luminous boundary both against the stream and from the axis of the tube. Within the stream axis the glowing is considerably weaker, what may be due to lower plasma density. On entering the coil, 5cm from the coil edge the stream is compressed towards the tube axis in the vertical plane xy down to the size of 1.5cm. Then for about 15μs the stream thickness increases up to 3.5cm and keeps practically this size till the end of the process.

In horizontal plane xz plasma dynamics is different. First of all no reflection and broadening of the incident stream can be seen through the mirror. Instead, there occurs a strong compression of the stream along z-axis what is probably due to features of the field structure. It happens immediately behind the plane of the input hole of the coil and is clearly seen during the first 25μs. After the compression zone there begins a zone where the stream becomes broadened along the lines of force. The boundary of this zone moves with the speed of ~10^6cm/s up to the tube walls. Plasma forms leaf-like structure with thickness mentioned above. Since the moment 30μs, after stream's hot part has passed, plasma compression along z-axis can hardly be seen, the sheet in the whole coil is limited by the tube walls and keeps its shape. The sheet is bent and up-shifted towards the coil outlet.
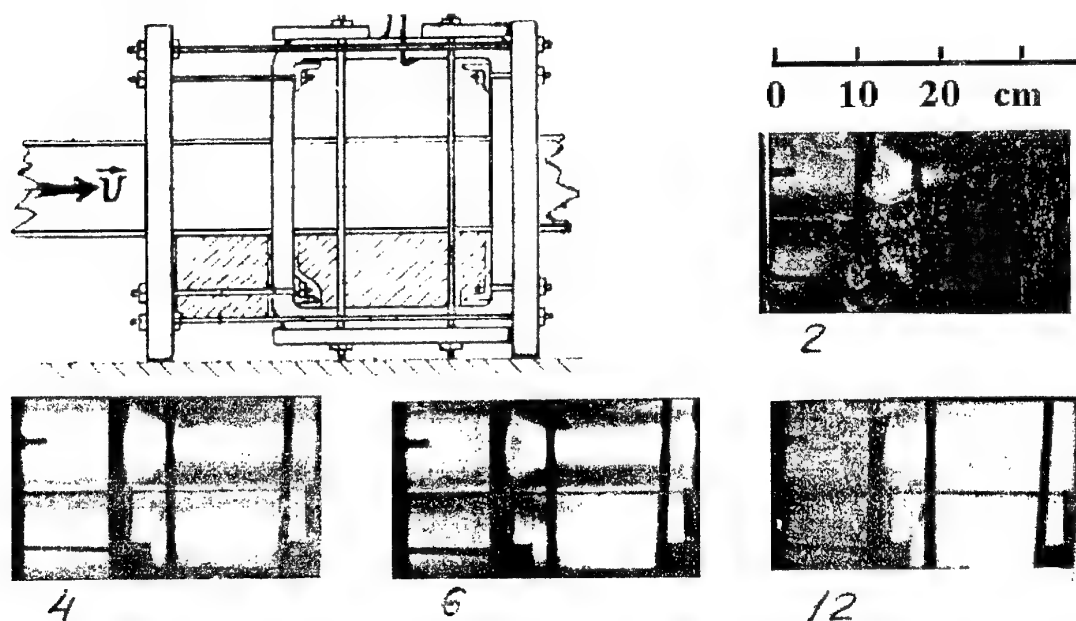
Fig.3. Stream flow in the field of $H_{max} \approx 1.85$kOe. Film shots No.2,4,6 and 12.

167
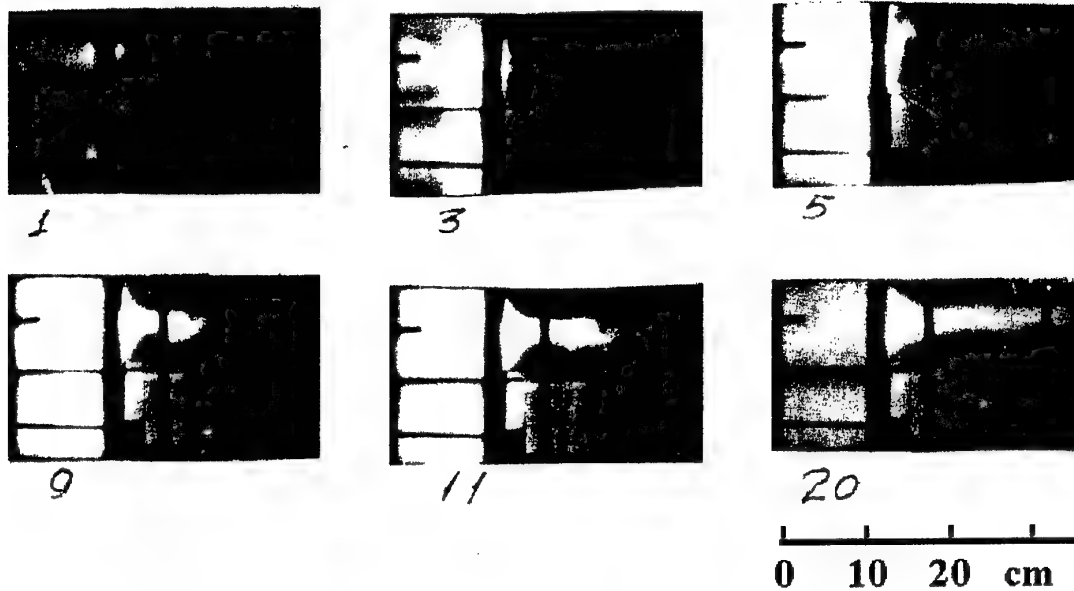
Fig.4. Stream flow in the field of $H_{max} \approx 7.4$ kOe. Film shots No.1,3,5,9,11 and 20.

When $H_{max} \approx 3.7$kOe the flow picture inside the coil is practically the same except two features. On the first eight shots there is a greater reflection of external in relation to the axis layers of the stream, and before the coil outlet there occurs a sharp down-bend what is immediately followed by a bright illumination filling the whole section of the tube in the site. When $H_{max} \approx 5.5$kOe the sheet twice bloats during the first 10μs.

The shots in Fig.4 were made for $H_{max} \approx 7.4$kOe ($H^2_{max}/4\pi\rho v^2 \approx 28$). Plasma stops. First, during the time interval between the second and third shots it fills the tube before the coil as a washer-like structure of about 7cm in thickness. During the process the plasma movement back is clearly seen as streams pressed to the walls. This movement is observed only in xy plane. In a perpendicular plane the movement near the walls is absent, there being rather increase in stream transverse size here. On the other side of the washer the primary boundary between the stream and the field is smooth and clear (shot 3). The boundary is hooped so that in xz plane along the tube walls (or the far wall, as the near one cannot be seen in the mirror) the plasma got inside the coil $1 \div 2$cm further than in xy plane. Then, from shot 5, when plasma before the coil filled at least 10cm area of the tube and magnetic field according to the measurements restored primary distribution, there begins slow plasma movement along initial direction. Above the axis out of the boundary there forms a leaf-like structure along the field. Then this structure gets nearer to the axis. The hook on the front further moves along the axis with the speed of
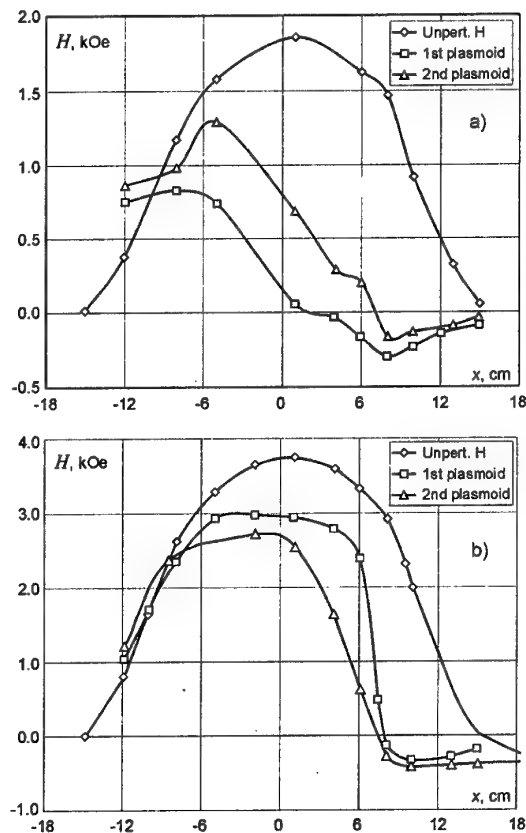
Fig.5. The dependence of magnetic field strength along the axis of the first and second plasmoids upon their penetration depth into the coil.
a: $H_{max} \approx 1.85$kOe, b: $H_{max} \approx 3.7$kOe.

168
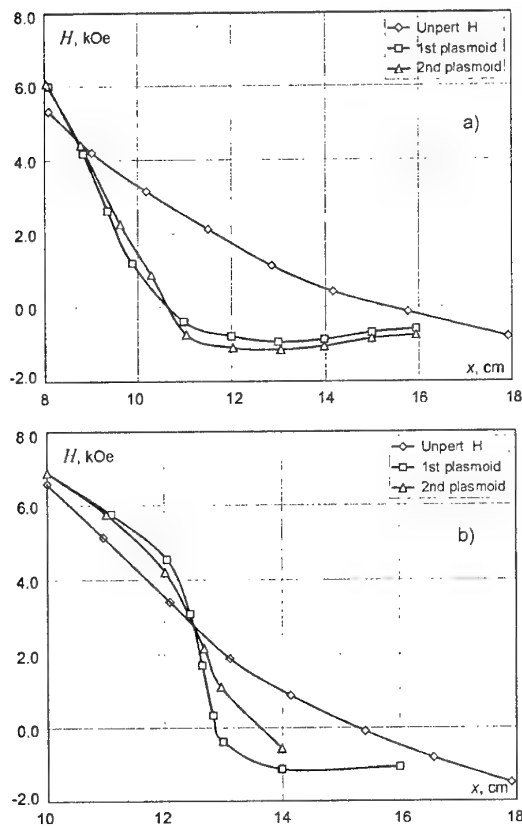
Fig.6. Distribution of magnetic field strength along the axis of the tube during the field being maximally disturbed by the first and second plasmoids.
a: $H_{max} \approx 7.4$kOe, **b:** $H_{max} \approx 14.8$kOe

5×10^5cm/s. The leaf-like structure reaches the outlet of the coil only by the end of the film. It is important that by this time the flow becomes steady and close in shape and size to steady flows in weak fields.

When $H^2_{max}/4\pi\rho v^2 \approx 110$ and $H^2_{max}/4\pi\rho v^2 \approx 175$ the dynamics differs in the penetration process into the field only after 20μs time interval. Plasma gets into the field as a wedge-like structure with a base equal to the tube diameter, bent but clear walls and getting more acute apex angle in the course of time. A thin front leaf-like structure of a few mm in thickness reaches the coil center by 40μs and does not pass any further till the end of the observation at 65 μs.

In Fig.5÷7 there is a behavior picture of magnetic field in the first and second plasmoids when they move along the axis. The curves are made according to the results of measurements with magnetic probe and correspond to maximal signal peaks in every axis point. The total duration of the signal does not exceed 30 μs. Then local magnetic fields obtain their primary values. While moving to the coil the stream is saturated with the opposite

sign scattered field, the value of the captured field exceeding the primary one.

When $H_{max} \approx 1.85$kOe plasma carries this field nearly up to the center of the coil (Fig.5a) and only then is the plasma penetrated by the basic field, with which the stream leaves the coil. With the field strength increasing, the point of sign change is shifted towards the injector, saturation of plasma with the basic field occurs within shorter distances and up to greater relative values, and on leaving the coil the stream is quickly degaussed (Fig.5b, $H_{max} \approx 3.7$kOe). It should be noted that the processes are faster rather in the first plasmoid than in the second one, what is probably due to the following: in making the channel the first plasmoid has greater loss in speed in strong fields. If the field stops the plasma then the point of the field sign change is shifted to the plane of the inlet coil hole and is the same both for the two plasmoids and for the luminous boundary visible in pictures (Fig.6, $H_{max} \approx 7.4$ and 14.8kOe).
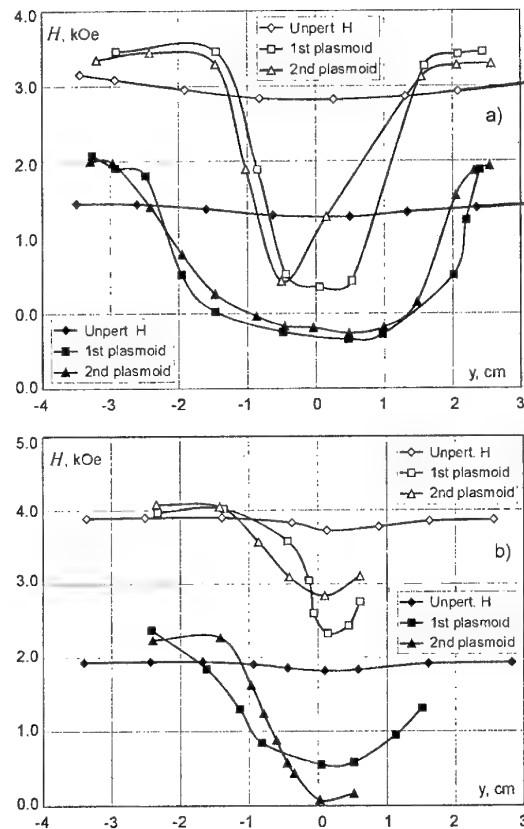
Fig.7. Distribution of magnetic field strength along the direction perpendicular to the velocity and field vectors during the field being maximally disturbed by the first and second plasmoids. **a:** $x=7.5$cm, **b:** $x=0.5$cm. $H_{max} \approx 1.85$kOe is for lower curves, $H_{max} \approx 3.7$kOe is for upper curves.

In Fig.7 there are field distributions along vertical axis for the discussed parts of the stream. Measurements were performed for $H_{max} \approx 1.85$ and 3.7kOe at the inlet region of the coil and near its center, at points $x=7.5$ и 0.5cm. It is seen that the thickness of the skin-layer is close to 1cm. There is excess of field strength over the primary one beyond the stream. In the first section at $H_{max} \approx 1.85$kOe in plasma there still exists opposite sign scattered field. In the picture in this site of the coil there is greater brightness of plasma luminosity within the field boundary. This stripe appeared to pass through the point of the sign change of the disturbed field. On the presumption that the total pressure of field and plasma along the vertical axis is constant, plasma pressure distribution transverse to the stream was calculated according to the field distribution, and plasma conductivity and temperature were estimated according to the field diffusion rate into the stream. The value of the primary electro conductivity is 4×10^{13} in ab-units. Temperatures of 2.5 and 13eV correspond to fields of 1.85 and 3.7kOe, and the pressure at $x=7.5$cm under such temperatures correspond to plasma densities of $\sim 2 \times 10^{16}$cm^{-3} and $\sim 1 \times 10^{16}$cm^{-3}. In calculating the densities dynamical pressure was considered negligible. At $x=0.5$cm the pressure becomes 1.5 times less in a weak field and 2.5 times less in the field of 3.7kOe. Such calculations result in a little, only 10% greater density at the point of field sign change in comparison with the density within the axis, what is hardly sufficient to understand bright luminosity within the stream boundary. There probably occurs non-stationary process of collecting plasma by magnetic field, the process being accompanied by the formation of shock waves and being analogous to the phenomenon of "snow plough" in fast pinches. Any case, two conditions among the ones required for this are fulfilled: relatively thin skin-layer and a great stream speed in comparison with sound velocity.

When greater than 3.7kOe regardless of the field value in the coil center there is hardly any change in the undisturbed field strength in the point where the value of the opposite sign scattered field captured by plasma becomes zero. It corresponds to Tuck criteria and is close to 2.5kOe. Here, $H^2_{max}/4\pi\rho v^2 \approx 3$. However, under supposition that the boundary of the stopped plasma is the point, farthest from injector, where disturbed field steepness changes, then the ratio of pressures becomes greater. Defined this way, the local

magnetic field holds back the total dynamic and gasdynamic pressure of the stopped stream in the cross section $x=12$cm in front of the coil (Fig.6b) when $H_{max} \approx 14.8$kOe, the pressure being 12 times greater than the dynamic one of the incident flow. For $H_{max} \approx 7.4$kOe such a cross section is shifted inside the coil, the mentioned ratio exceeding 18 (Fig.6a). However, as it was shown above, stopping the stream does not mean stopping the plasma movement into the region with a strong field. After the process of field diffusion into the stopped plasma there begins a slow process of plasma diffusion into the field. To terminate the process of plasma diffusion within the axis of the transverse magnetic field in our experiment the magnetic pressure was required to be 100 times greater than the dynamic pressure of the stream.

References

1. Bai Shi-i, Magnetic gasdynamic and plasma dynamics. Mir, M., 1964 (in Russian).
2. Harris et al., Phys. Rev., 1957, 105, p. 47.
3. Baker D.A., Hammel J.E., Phys. Rev. Letters, 1962, 8, n. 4, p. 157.
4. Baker D.A., Hammel J.E., Phys. Fluids, 1965, 8, n. 4, pp. 713-722.
5. Baker D.A., Hammel J.E., London, 1965, report CN-21/85.
6. Demidenko I.I. et al., ZhTF, 1964, 35, issue 7 (in Russian)
7. Demidenko I.I. et al., ZhTF, 1965, 35, issue 5, p. 823. (in Russian)
8. Beckner E.H., Phys. Fluids, 1964, 7, No. 4, pp. 586-595.
9. Chapman S., Ferraro V.C.A., Terr. Mag. (J. Geophys. Res.) 1931, 36, p.77.
10. Tuck J.L., Phys. Rev. Letters, 1959, 3, p.313.
11. Rose D.J., Clark M.C., Plasmas and Controlled Fusion, Techn. Press, 1961.
12. Demichev V.F., Strunnikov V.M., DAN USSR, 1963, 150, No.3, pp. 523-526. (in Russian)
13. Artsimovich L.A., Controlled thermonuclear reactions, FM, M., 1961 (in Russian).
14. Marshall J., Phys. Fluids, 1960, 3, No.1, p.134-135.
15. Demichev V.F., Matyuhin V.D., DAN USSR, 1963, 150, No.2, pp. 279-282.
16. Demichev V. F. et al, Atomic energy, 1965, 19, issue 4, pp. 329-335 (in Russian).

30. FLOWS OF SUPERSONIC PULSED PLASMA STREAMS IN THE CONFUSER WITH MAGNETIC INSULATION

N.V.Goriacheva, V.V.Sidnev, V.M.Strunnikov, N.S.Zhitlukhina
State Scientific Centre of RF Troitsk Institute of Innovation and Fusion Research (TRINITI)
Phone: (095) 334-0675, E-mail: toporkov@triniti.ru

Among the others, the magnetic fields application for controlling supersonic plasma jets and heat fluxes is the topic of this workshop. These questions are ordinary in nuclear fusion tasks.

A goal of this experiment is a suitable plasma preparation to fill a long magnetic trap with minimum B [1] by using the powerful electrodynamical accelerators of MK-200 type [2]. It is necessary to match the accelerator outlet of a big diameter with a not great inlet of the magnetic trap as well as to reach the high value of number $G=[(N_i/1.4\cdot10^{17})(1+z\theta_e/\theta_i)(2/A)]^{1/2}z(2r/R_c)(\rho_i/\delta)$. Here, $N_i[\text{cm}^{-2}]$ is a linear ion density of the trap plasma; z, A and ρ_i are a charge, a mass number and a gyroradius of an ion; θ_e and θ_i are electron and ion temperatures; r and R_c are a radii of a plasma cylindrical body and ring slits of cusps as well as δ is a width of the ring slit. The long cusp-trap has no advantages over a θ-pinch when $G\leq1$. The goal has been fulfilled and the principal results have been announced in a short report [3]. This paper presents the discussion of these experimental results.

The results of both V.F.Demichev and A.M.Zhitlukhin are a background to setting up this experiment. The investigations [4] have been carried out to test the L.A.Artsimovich criterion [5] of a passage through a longitudinal magnetic field by a pulse plasma stream generated with a coaxial injector (a plasma gun). In deducing of the criterion, it have been assumed a possibility of a radial compression of the stream having a high conductivity. But in advanced manner, the criterion take into account only correlation of the pressures as well as of the geometrical sizes of the magnetic field and the plasma. A relation of values of a directional velocity to heat one does not used. Experimentally, the local magnetic field of H up to 30kOe in strength can not stop the stream with initial a mass density ρ and a velocity v up to $H^2/4\pi\rho v^2\approx200$, what is 4 times higher the critical value. But yet the experiment validates the strong radial compression of the stream at a field entrance with the result that its pressure increases by the orders of the magnitude. The phenomenon is due to the strong diamagnetism of the plasma. Clearly the compression makes the penetration conditions much easier. A stream front is not braked during the process whereas the velocities of next stream parts are lowered by a factor of $2\div3$.

The next step in the process understanding has been made in [6]. Here, it has been shown the flow in a magnetic field lack of a collisional plasma stream generated with the MK-200 accelerator is in accordance with the well-known rules of supersonic aerodynamics. Then, a $50\div60$-fold increase of the particle density up to the level in excess of 10^{18}cm^{-3} has been fixed in a long narrowing conical diffuser with the relatively slow longitudinal magnetic field. Evidently the process approaches the isentropic one but no corroborations by magnetic measurements have been made. The stream moving with $2\cdot10^7$cm/s velocity and Mach number M=5 has been used in $H^2/4\pi\rho v^2\approx10\cdot$conditions.

Experimental facilities.

The supersonic hydrogen plasma streams at a near-atmospheric pressure but of a high conductivity flowing in a narrowing conic plasma drift tube (Fig.1) being filled with a longitudinal magnetic field are investigated. Pulsed streams of some metres length have been generated with the MK-200 electrodynamical plasma accelerator (1) with its external electrode being ~70cm long and ~30cm in diameter. Its energy generator has 720mcF capacity. Operation of the pulsed valve, which provides an initial dose of a gas in the accelerator, is forced in this experiment to reach the high G-values. The drift tube (2) 2.9m in length has been made from stainless steel 2.5mm thick. Its inlet area is ten-fold as much as the outlet area.
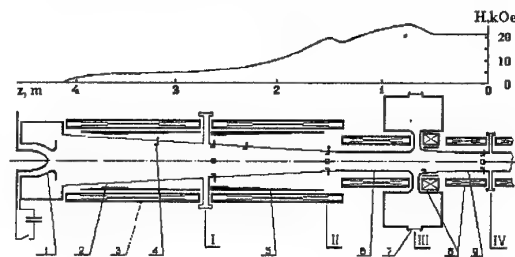
Fig.1. The design of the experimental installation and the magnetic field distribution. (1) plasma gun; (2) conic drift tube; (3, 8) solenoids; (4) magnetic probe; (5) magnetic screen; (6, 9) cylindrical drift tubes; (7) window. (I÷IV) are the measurements' sites: (I) interferometer, (I and II) magnetic probes, (III) CIII and CIV lines as well as X-ray intensities, (IV) neutrons.

The cone outlet is matched with a long cylindrical tube (6 and 9). The vacuum drift-tube is pumped to a pressure of ~$3 \cdot 10^{-3}$ Pa before every shot.

A magnetic flux has been established constant along the axis to have 1.8Tl outlet magnetic induction. The field geometry is formed from a field geometry of solenoids (3 and 8) with help of brass cylindrical screens (5) having a profiled thickness of walls. A front rise time of solenoid currents ranges from 3ms to16ms in different parts of the drift tube. A time of the drift-tube filling with a magnetic field is not less then 100mcs. It is much smaller then the current rise times, but much bigger then a duration of a plasma-field interaction. That is why the magnetic flux inside the cone remains constant both in the space and in the time.
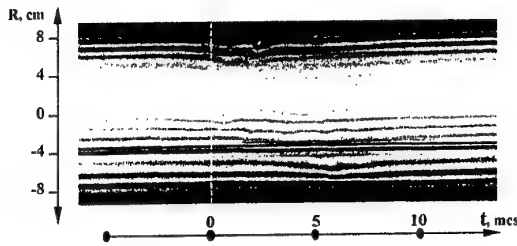
Fig.2. The temporal interferogram of the plasma flowing through the section I of 16 cm in diameter of the conic drift tube. U=25 kV.
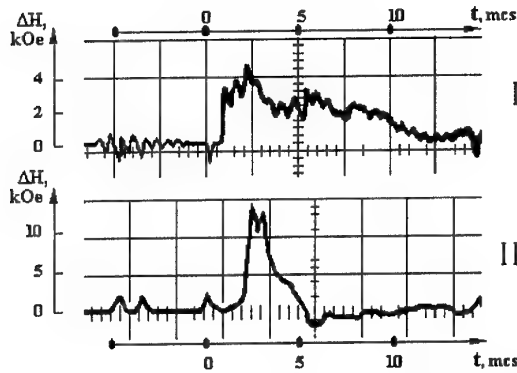
Fig.3. The oscillograms of magnetic probe signals from the sections I and II of the conic drift tube. U=25 kV.

The principal measurements have been carried out at two cone cross-sections (I and II) which areas differ by four times. The second of them is the outlet of 8cm in diameter. Magnetic probes, a laser interferometer, a visible line spectroscopy as well as soft x-ray and neutron detectors in the cases of deuterium plasma have been used. The interferometer of Mach-Tsender with a ruby laser as an illuminant has been used to measure an electron density n_e at the cross-section

I. An ordinary temporal foto-scanning of a flow interferogram is shown in Fig.2. The closely pressed to wall magnetic probes (4 in Fig.1) in the form of plane multiturn coils 5mm thick are placed evenly along the tube axis. Oscillograms of their signals recorded simultaneously with the interferogram are illustrated in Fig.3. Magnetic probes 5mm in diameter disposed at various radii inside the tube give the analogous signals, but with a reverse polarity. These probes are mounted in a holder and can be located at any point of the drift-tube. CIII and CIV lines of carbon impurities have been photographed in the section III with a LV-03 high-speed elektronooptical camera. The use of their intensities allows the electron temperature calculating by a procedure described in [7]. To obtain electron and ion temperature points of a reference the soft x-ray and neutron radiation from the deuterium plasma with much like characteristics are used.

Measurement results

The comprehensive measurements have been made at an accelerator voltage U of 12kV and 25kV, when storage capacitor energies $CV^2/2$ have been 50kJ and 225kJ and energies of stream head protons have been 0.2keV and 2.5keV accordingly. As is evident from the result analysis, the moving plasma displaces the magnetic field from its own volume and presses it to the cone walls forming a ring layer of a magnetic insulation. The table 1 lists the measured at the two cone sections at the points in time corresponding to a diamagnetic signal maximum values of a magnetic insulation field H_e and a field H_i inside the bulk of plasma in comparison with the initial magnetic field H_0 as well as n and θ_e. Here, the stream velocities v and diamagnetic signal widths $\Delta t_{0.5}$ are also given. They are used to calculate $\beta = p/(p + H_i^2/8\pi)$, a plasma heat pressure p, an effective stream radius r, a sum temperature $\theta_e + \theta_i$, the Mach number M, an effective thickness of the magnetic insulation layer $\Delta r = R - r$ and the ion gyroradius ρ_i inside this layer. Here, R is a drift tube radius. It is suggested that

$$\frac{H_e^2}{8\pi} = p + \frac{H_i^2}{8\pi}, \quad H_0 R^2 = H_e(R^2 - r^2) + H_i r^2,$$
$$p = n(\theta_e + \theta_i), \quad \theta_i >> \theta_e.$$

The densities and the velocities alike are measured with the least exactness. Errors of density determination account for a deviation of an actual plasma geometry from ideal one of an Abel model and are estimated by ~2 factor. It is difficult to estimate the velocity measurement errors. The velocity is measured on a delay of signals of the

172

two magnetic probes located in different sites. In table 1 the velocities are given for fronts of such signals, i.e. they are for stream fronts. They do not change with a high degree of accuracy along the axis. The velocities of next parts of the stream is lower, but it is impossible to measure they exactly when the signal oscillogram is smooth and without features. Moreover, these stream parts are prone to a strong deceleration up to a total stoppage. That is why the shape of the probe signal changes drastically. Its width in the second section is some times less than in first one. As a result, the velocity of the stream part giving the diamagnetic signal maximum can be estimated with the same uncertainty factor of ~2.

It is seen from the table 1 that the plasma indeed behaves as diamagnetic. The magnetic field is appreciably driven out of the stream and raises by 1.5 times outside it. The value of β does not fall below 0.96. The ratio of the pressures in the sections I and II is most closely measured. In both cases it is over ten. These ratios are taken as basis to compare the remaining experimental values with calculated ones.

Result discussion

Ignoring the stream deceleration ($v_1=v_2$) and assuming that the compression process is adiabatic ($p_1 r_1^{2\gamma}=p_2 r_2^{2\gamma}$), one obtains in the magnetic flux conservation and thin skin-layer conditions:

$$\frac{H_{e1}}{H_{01}} = \frac{1-(p_2/p_1)^{(1-0.5\gamma)/\gamma}}{1-(R_2/R_1)^2(p_2/p_1)^{1/\gamma}} .$$

A graphical representation of this relationship for the $(R_2/R_1)^2=4$ and $\gamma=5/3$ cases is shown as a solid line in Fig.4. The sections I and II
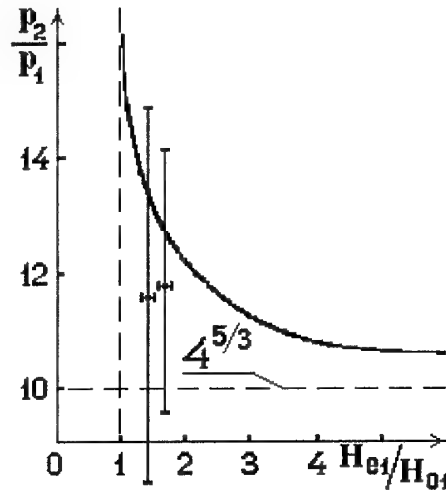
Fig.4. The compression ratio of plasma pressures in the sections I and II of the conic drift tube upon the strengthening factor of magnetic field in the section I of S_1 area. $S_1/S_2=4$, $v_1=v_2$.

		Table 1
Measured values of plasma properties in magnetic confuser.		

Gas	Hydrogen			
U, kV	12		25	
$CU^2/2$, kJ	50		225	
Section No.	1	2	1	2
R, cm	7.8	4.2	7.8	4.2
H, kOe	5.2	18	5.2	18
H_e, kOe	7.3±0.3	25±3	9±0.4	31±1.7
H_i, kOe	0.05	4.6	$7 \cdot 10^7$	6
v, cm/s	$2 \cdot 10^7$	$2 \cdot 10^7$	~10	$7 \cdot 10^7$
$\Delta t_{0.5}$, mcs	~10	~5	$(2\pm_1^2) \cdot 10^{16}$	1.75±0.25
n, cm^{-3}	$(2\pm_1^2) \cdot 10^{16}$			
θ_e, eV	$1\text{-}5 \cdot 10^{-5}$			20
β	$(13\pm1) \cdot 10^{17}$	1-0.03		1-0.04
p, eV/cm^3	4.3±0.4	$(15\pm4) \cdot 10^{18}$	$(20\pm2) \cdot 10^{17}$	$(24\pm3) \cdot 10^{18}$
r, cm		2.1±0.4	5.3±0.35	2.6±0.2
$\theta_i+\theta_e$, eV	$65\pm_{32}^{65}$		$100\pm_{50}^{100}$	
M	2±0.8		5.4±2	

173

U, kV	12		25	
№, (R, cm) of cone section	1 (7.8,e)	2 (4.2,e)	1 (7.8,e)	2 (4.2,e)
p, eV/cm^3 (p, MPa)	$1.3 \cdot 10^{18}$,e (0.21, e)	$1.5 \cdot 10^{19}$,e (2.4, e)	$2 \cdot 10^{18}$, e (0.32, e)	$2.4 \cdot 10^{19}$,e (3.84, e)
v, cm/s	$2\ 10^7$, e	$1.2\ 10^7$	$7\ 10^7$, e	$5.75\ 10^7$
n, cm^{-3}, e	$(2\pm_1^2)10^{16}\ 4\ 10^{16}$		$(2\pm_1^2)10^{16}$	
theory	32.5	$1.8 \cdot 10^{17}$	$1 \cdot 10^{16}$	$4.4 \cdot 10^{16}$
$\theta_i + \theta_e$, eV		83	200	550
θ_e, eV	2.8			20, e
M	4.3, e	1.1	3.8	1.9
r, cm	0.13	2.7	5.3, e	2.8
ρ_i, cm	28	0.06	0.25	0.12
$\Delta r/\rho_i$	$3.3 \cdot 10^{18}$	25	10	11.7
N, cm^{-2}	5.5	$4.1 \cdot 10^{18}$	$0.9\ 10^{18}$	$1.1 \cdot 10^{18}$
G		7.5	3.5	3.8
$W_\parallel$, kJ		5		29
$W_\perp$ kJ		11.5		19
$\sum W$ kJ		16.5		48
η, %	0.1	33		21
λ_{ii}, cm	10^{-8}	0.15	16	28
τ_{ii}, s		10^{-8}	$6 \cdot 10^{-7}$	$7\ 10^{-7}$

Table 2.
The results of calculations at nvr^2=const, γ=5/3. (e) is the experimental value.

are indicated by indexes 1 and 2. A horizontal dotted line notes the result of the adiabatic compression in a cone in the lack of magnetic field. Here too experimental values of a compression coefficient for U=12kV (p_2/p_1=11,6) and U=25kV (p_2/p_1=11,8) are entered. They lie above the dotted line and in error bars coincide with calculated values. A finite value of a skin-layer thickness alone can be the main reason of their incomplete agreement. The remaining characteristics for the second section have also been calculated within a framework of this model. The result of $M_2<1$ has been obtained for U=12kV. In another way, according to the model the total thermalization of this stream can be observed long before the second section. This picture is possible, but the taken measurements are poor to discuss it. And with it a calculated efficiency η of electric-plasma energy transformation for U=25kV seems to be too high.

The mentioned difficulties can be got around using as before at γ=5/3 the same averaged experimental data of just as the pressures p_1 and p_2, so and an initial stream radius r_1, but taking in the error bars n_1=$4 \cdot 10^{16}$cm^{-3} for U=12kV case and n_1=$1 \cdot 10^{16}$cm^{-3} for U=25kV one. Calculations are carried out in accordance with supersonic aerodynamic equations for narrowing diffusers [8] in isentropical process suggestions and a strict condition of continuity: nvr^2=const. When the flow is reversible adiabatic, the energy equations take the form:

$$\theta^*/\theta = 1 + (\gamma-1)M^2/2, \quad (v_s^2/\gamma - 1) + v^2/2 = v_s^2/\gamma - 1.$$

Here, v_s is a sound velocity and the index (*) is related to the stoppage point where M=0. The remaining characteristics are bound by the following relationships:

$$n_2/n_1 = (\theta_2/\theta_1)^{1/\gamma-1} = (p_2/p_1)^{1/\gamma}.$$

The calculation results are given in Table2. At the chosen calculation scheme, the single characteristic, namely, the cross dimension of a stream in the second section remains the main criterion of the model applicability. A very good agreement between the theory and the experiment is observed for the stream generated at U=25kV. The calculated radius fits in the error bars and differs by no more then 8% from the average

measured value. With efficiency, the value of $\eta \approx 20\%$ is possible. The stream having a high enough value of the initial Mach number ($M_1 \approx 4$) is subjected to a slight deceleration, no more than 20%. Because of this, its motion may not strong differ from flows in cylindrical drift-tubes. Here, η reaches 35% in the cases of a good accelerator tuning, from which namely about one half is due to the investigated head stream part with the high value of M.

In the case of the stream generated at U=12kV, an accord between the theory and the observations is not so good. The calculated radius fits even in the bars of sum errors of radii in both sections and now exceeds the average measured value of r_2 by almost 30%. The put in the equations limit of a possible plasma density in the first section permits an increase of the initial Mach number up to M_1=2.8. This is just the minimum value, which results in $M_2 \geq 1$. The velocity of the stream passed through the cone is calculated to be almost halved, and two thirds of its combined energy ($\sum W$) is to transform to the sum W_T of a heat plasma energy and an energy of the compressed magnetic field. This is a limiting case in the frames of the data on hand. It is not inconceivable that a shock wave already stands inside the cone and in actuality a flow of early-thermalized plasma through the second section is observed.

Conclusion

By this means the applications of the supersonic aerodynamic equations to the pulse stream flows inside the narrowing diffusers of a high β plasma is justified. The good enough fit of the theory and the experiment is observed for both collisional and weakly-collisional plasma. A free path length λ_{ii} and a time of ion-ion collision τ_{ii} alike are slow varied along the cone (Table 2). In the first case (U=12kV) they are less by the order of magnitude then the characteristic stream values, in the second case (U=25kV) they are comparable or some times the last mentioned. The correctness of the isentropic process use is supported by not only the agreement between the theory and the experiment but a big enough relative thickness of

the ring layer of magnetic insulation. A $\Delta r/\rho_i$ value is kept constant along the axis and does not fall bellow ten in both cases. What is more, there is a visual verification of such heat-insulation efficiency. In the absence of magnetic field, a cone wall surface is strongly eroded.

The importance of the confuser with the longitudinal magnetic field once exceeds far beyond the simple limits of aperture concordance. First and foremost, a usually magnetizing inside cylindrical drift-tubes stream acquires the diamagnetic properties in the confuser. The experiment shows the possibility of receipting the high G-values. They are attained not only by a suitable control-point setting of an accelerator, but through a stream deceleration in the confuser as well. In this way in the course of the active stream deceleration (U=12kV) the G-value increases 1.5 times and reaches 7.5. Lastly the confuser use softens or it may be that solves the task of the straight magnetic traps filling with contrary streams raising the Coulomb collision probability by the stream velocity lowering. To fill the trap with plasma fully thermalized inside the confuser would be the ideal limit variant.

References

1. Alipchenkov V.M. et al. Preprint IAE-2753, M., 1976 (in Russian).
2. Skvortsov Yu.V. Phys.Fluids, 1992, B4(3), pp.750-756.
3. Gavrilov V.V. et al. Proc. 10th Europ. Conf. On Controlled Fusion and Plasma Physics, Moscow, 14-19 Sent. 1981,V II, p.146.
4. Demichev V.F., Strunnikov V.M. DAN USSR, 1963, 150, No.3, pp.523-526 (in Russian).
5. Artsimovich L.A. Controlled thermonuclear reactions, M., FM, 1961, 468p.
6. Zhitlukhin A.M. et al. Preprint IAE-2749, M., 1976 (in Russian).
7. GervidsV.I. et al. Plasma Accelerators and Ion Injectors. Abstr. Vth All-Union Conf. M., Science, 1982, pp.164-165 (in Russian).
8. German R. Supersound inlet diffusers. M., FM, 1960, 290p. (in Russian).

31. FLYER ACCELERATION BY INTENSE PULSED ION BEAM ABLATION

Nob. HARADA†, M.Yazawa†, W. Jiang‡, and K. Yatsui‡

† Department of Electrical Engineering,
‡ Extreme Energy Density Research Institute
Nagaoka University of Technology
1603-1 Kamitomioka, Nagaoka 940-2188, Japan
nob@nagaokaut.ac.jp

Abstract. Flyer acceleration by ablation plasma pressure produced by irradiation of intense pulsed ion beam has been studied. Acceleration process including expansion of ablation plasma was simulated based on fluid model. And interaction between incident pulsed ion beam and a flyer target was considered as accounting stopping power of it. In experiments, we used ETIGO-II intense pulsed ion beam generator with two kinds of diodes; 1) Magnetically Insulated Diode (MID, power densities of $<100J/cm^2$) and 2) Spherical-focused Plasma Focus Diode (SPFD, power densities of up to $4.3kJ/cm^2$). Numerical results of accelerated flyer velocity agreed well with measured one over wide range of incident ion beam energy density. Flyer velocity of 5.6 km/s and ablation plasma pressure of 15GPa was demonstrated by the present experiments. Acceleration of double-layer target consists of gold/aluminum was studied. For adequate layer thickness, such a flyer target could be much more accelerated than a single layer. Effect of waveform of ion beam was also examined. Parabolic waveform could accelerate more efficiently than rectangular waveform. Applicability of ablation propulsion was discussed. Specific impulse of 7000~8000 seconds and time averaged thrust of up to 5000~6000N can be expected.

Introduction

We have been studying on thin film flyer acceleration by ablation plasma using intense pulsed ion beam.[1-4] So far, we could achieve 5.6km/s of flyer velocity and 15GPa of ablation pressure in experiment. Further, fairly good agreement between experimental data and analyses has been obtained. Although the major purpose of these studies is application of this process to materials science such as production of new material, improvement of material surface by collision of an accelerated film to another materials, and so on, another and direct possibility may be ablation propulsion.

In the present paper, previous fundamental results are reviewed firstly. Then recent results on acceleration of multi-layer target and effect of waveform of incident ion beam on acceleration process are presented. Finally, capability of thrust and specific impulse of ablation propulsion is discussed.

Principle Concept of Flyer Acceleration by Ablation

Figure 1 shows the basic concept of flyer acceleration by ablation plasma that is produced by irradiation of an intense pulsed ion beam. Incident ion beam can penetrate into the target within a certain depth so-called "range" and deposits its energy. Deposited energy is so high that the part within the range evaporates, ionized, and finally forms high-temperature and high-pressure ablation

plasma. Thus residual part of the target is highly accelerated by the reaction of this ablation plasma expansion.
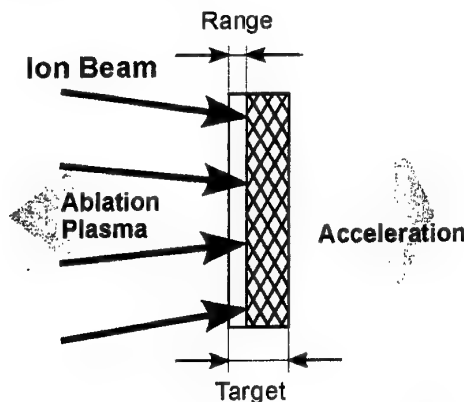
Fig.1. Principle of ablation acceleration by ion beam.

Experimental Facility

Ion beam is produced by the intense pulsed ion beam facility "ETIGO-II" that is installed at the Extreme Energy Density Research Institute (EDRI) at the Nagaoka University of Technology. We have been using two kinds of diode to produce ion beam: 1) Magnetically Insulated Diode(MID) with the energy density of up to $100J/cm^2$ and 2) Spherically-shaped Plasma Focus Diodes(SPFD) with up to $4.3kJ/cm^2$. Typical operating conditions are listed in Table 1.

Table 1. Experimental Conditions and Accelerated Target

Diode	MID			SPFD	
Ion Source	Poly-ethylene			Nitrocellulose Alkyd Resin	
Ion Beam Energy density [J/cm²]	51, 61, 77, 100	120	152	2000	4300
Voltage [MeV]	~0.95	~1.1	~1.3	~0.7	~0.85
Pulse Width [ns]	~60	~70	~70	~70	~50
Ions	H^+ (O^+, C^+)				
Target material	Aluminum				
Size and Weight	10mm×10mm, t=50μm (13.5mg), 100μm (27mg)				

Numerical Analysis

We applied 1-dimensional fluid model to this ablation process as for numerical simulation. Simple basic equations were used as follows.

Mass conservation:

$$\frac{\partial \rho}{\partial t} + \frac{\partial \rho u}{\partial x} = 0 \tag{1}$$

Momentum conservation:

$$\rho \left(\frac{\partial u}{\partial t} + u \frac{\partial u}{\partial x} \right) = -\frac{\partial (P+q)}{\partial x} \tag{2}$$

Energy equation;

$$\rho C_v \left(\frac{\partial T}{\partial t} + u \frac{\partial T}{\partial x} \right) = -(P+q)\frac{\partial u}{\partial x} + S + H \tag{3}$$

where interactions of ion beam with target and ablation plasma can be taken into account as so-called stopping power S. Term of H denotes energy loss due to thermal conduction. In addition to the above basic equations, ideal equation of state was used.

$$P = (n_e + n_i)kT \tag{4}$$

Above set of equation were solved a finite difference method in the Lagrange scheme.[4]

Results and Discussions

Acceleration of Mono-Layer Target

At first mono-layer targets of aluminum is used. Accelerated flyer velocity is shown in Fig.2 against incident ion beam energy density. For measurement of flyer velocity, we adopt the Time-of-Flight method with the electric probe located at the distance of 1mm from the target. So, measured flyer velocity is averaged one over the flight distance of 1mm.

We can see that fairly good agreement of experimental data with the results of numerical analysis over the wide range of incident beam energy density.

Figure 3 shows time trend of flyer velocity for various beam energy densities. Although duration of ion beam irradiation is about 60ns, flyer is rapidly accelerated and its velocity becomes almost constant afterward. Initial rapid acceleration is due to the formation of ablation plasma and following rather gradual increase in velocity is mainly due to the reaction of ablation plasma expansion.
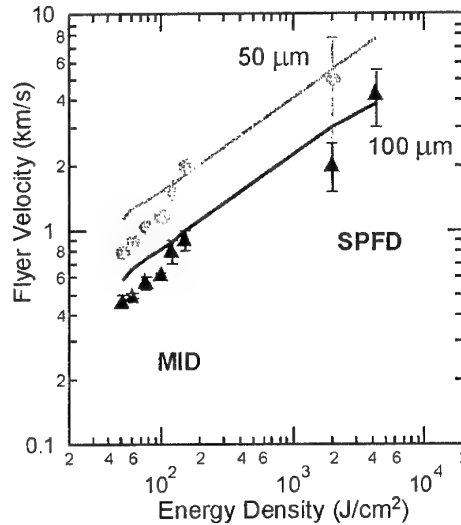
Fig.2. Flyer velocity against incident ion beam Energy density.
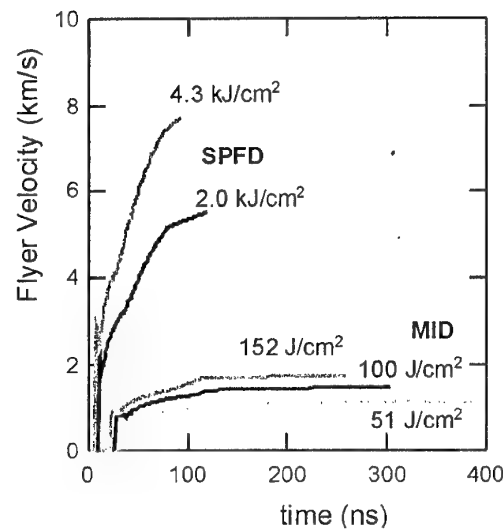
Fig.3. Velocity trend for various incident ion beam.

We can recognize certain delay time before start of acceleration. Delay time depends on beam energy density. The higher energy density results in the longer delay.

Pressure of ablation plasma is shown in Fig.4. Experimental data are estimated under the assumption of constant acceleration, which is averaged over about 1μs in this particular case. On the other hand, results of numerical analysis show the maximum pressure for each condition. Difference between experimental data and numerical ones is about slightly more than an order. This fact can be understood as the difference of averaging period. For example, for the case of 100J/cm^2, integrated ablation pressure is 30GPa x 60ns from analysis, which corresponds to 0.3GPa x 1000ns from measured data. Therefore, we can understand that these differences must be reasonable.
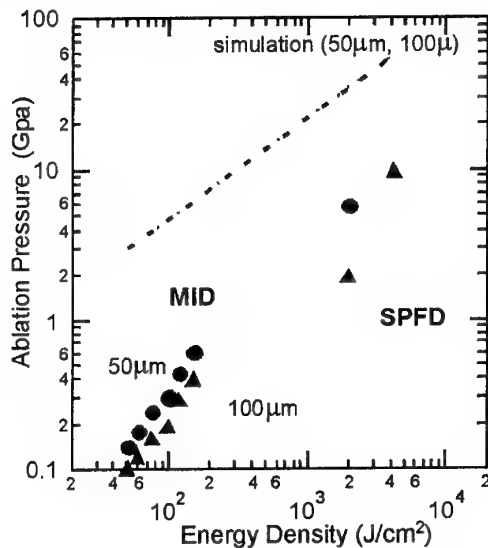
Fig.4. Ablation plasma pressure vs. energy density.

Acceleration of Multi -Layer Target

If we use multi-layer target that consists of heavier material to be ablated and lighter material to be accelerated, the flyer velocity can be increased easily. However, heavier material part must be completely ablated or flyer velocity may decrease due to increase in mass of flyer.

We examine acceleration experiments using aluminum target with the thickness of 50μm plated with various materials such as Au, Pb, Ag, Cu, and C. Figure 5 shows the results of flyer velocity as a function of plated layer thickness. Experimental data for Au/Al target are shown in the sane figure. We can see that the heavier material is obviously effective to increase velocity.

We have to note that too thick plated material results in decrease the velocity.
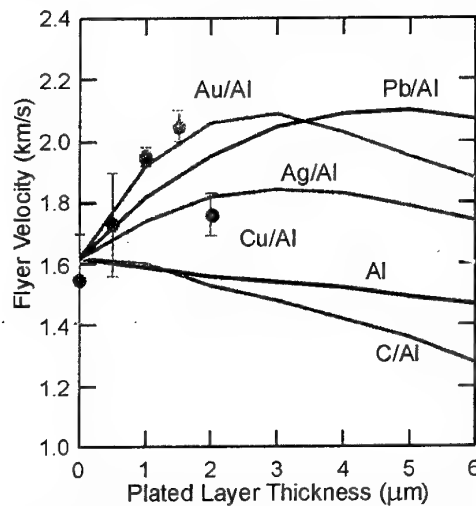
Fig.5. Velocity of multi-layer flyer for various plated materials.

For the case of Au/Al target, numerically analyzed tendency of increase in flyer velocity with the increase of plated layer thickness agrees well with the experimental data. Further maximum obtained velocity also agrees in spite of discrepancy of tendency in decrease for thick plated layers. This may be ascribed to the uncertainty of layer thickness of plated layer in experiments.

Influence of Ion Beam Waveform

In order to understand phenomena of flyer acceleration by ion beam ablation, we have to examine influence of ion beam waveform. So far, numerical analyses are done at 60ns of pulse width and 120J/cm^2 of energy density, for example.

Figure 6 shows velocity trends for various pulse widths at the same total energy density of 120J/cm^2. The shorter pulse width means the higher beam power per unit time. It can be seen that the same final velocity can be obtained owing to the same beam energy density, though acceleration period depends on pulse width or on beam power. Also delay time depends on beam power. The higher power results in the shorter delay.

Figure 7 shows velocity trends for various pulse widths at the same beam power density of 2J/ns·cm^2. So 60ns of pulse width corresponds to 120J/cm^2. Final velocity increased with the increase of pulse width, i.e. increase of total energy density. On the other hand, acceleration and delay are the same for various pulse widths.

178
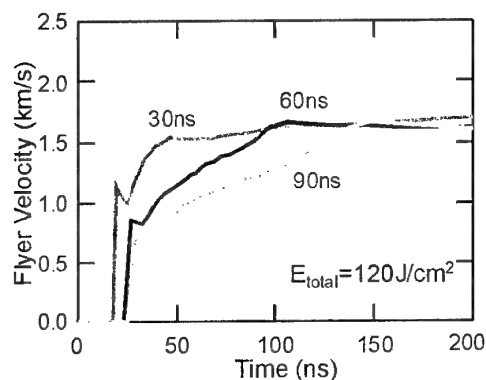
Fig.6. Flyer velocity vs. pulse width at the constant total deposition energy.
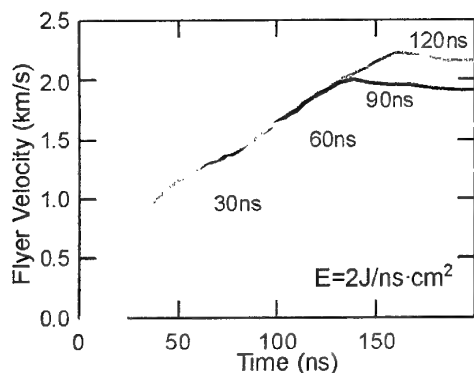
Fig.7. Flyer velocity vs. pulse width at constant ion beam power.

From these results, we can understand that final flyer velocity is decided by total deposition energy density by ion beam. Delay time and acceleration are decided by beam power density per unit time.
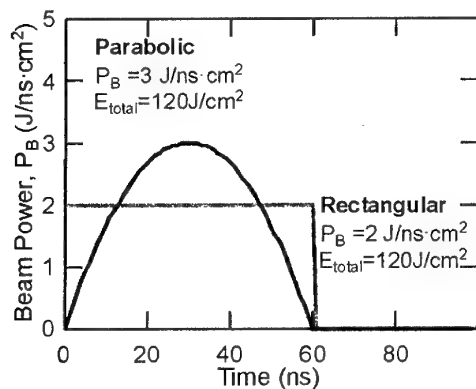
Fig.8. Beam waveform examined in this analysis.

Generally, intense ion beam is produced by capacitor discharge and beam power is not rectangular. We examine influence of waveform of ion beam by compare rectangular and parabolic forms, which are shown in Fig.8. For both cases, total deposition energy is the same as $120J/cm^2$.

Figures 9 and 10 show changes of pressure distribution and of temperature distribution in time for the case of parabolic waveform. Figures 11 and 12 show changes of pressure distribution and of temperature distribution for the rectangular waveform. We can see that the ablation pressure more gradually increases for the case of parabolic waveform because of more mild increase of deposition power. Maximum ablation pressure reaches up to 5.3GPa for parabolic case. This value is higher than that for rectangular case. Comparing temperature distributions, increase of temperature for the case of parabolic waveform is not significant than that for rectangular case. This can be understood that the parabolic waveform can convert beam energy into ablation pressure or kinetic energy of flyer more efficiently rather than into temperature, i.e. internal energy. This suggests that the existence of optimum waveform with maximum acceleration efficiency.
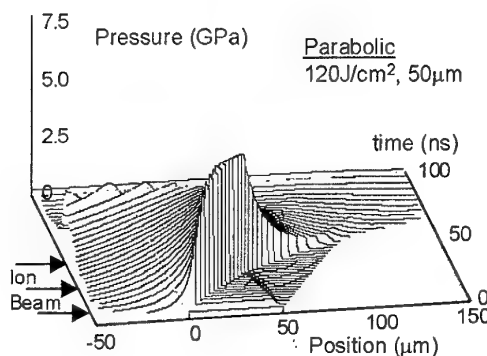
Fig.9. Time-dependent pressure distribution for parabolic waveform.
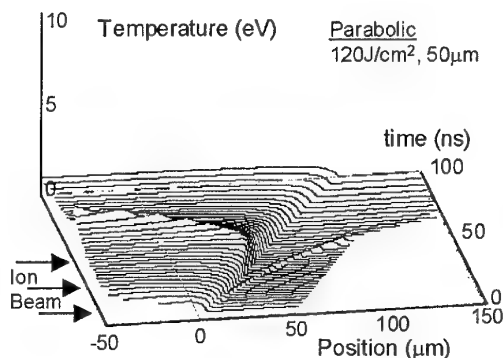
Fig.10. Time-dependent temperature distribution for parabolic waveform.

179
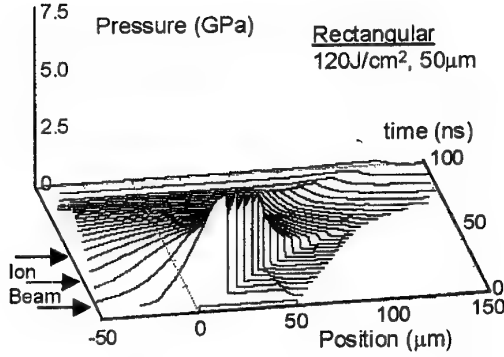
Fig.11. Time-dependent pressure distribution for rectangular waveform.
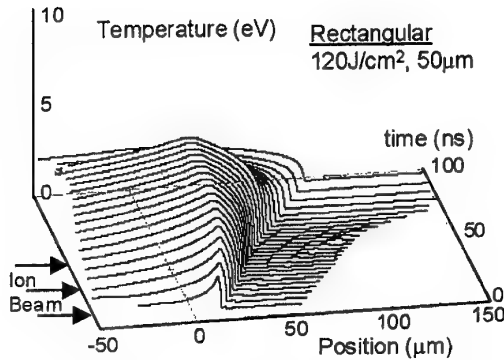
Fig.12. Time-dependent temperature distribution for rectangular waveform.
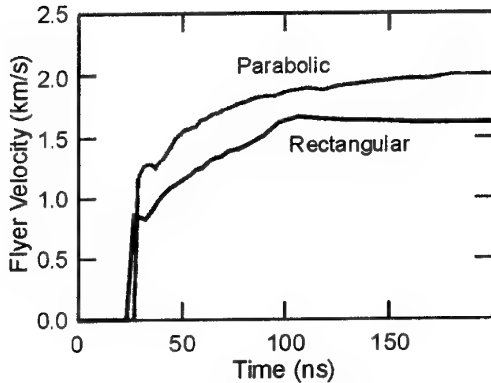
Fig.13. Effect of waveform on flyer velocity.

Figure 13 shows comparison of flyer velocity trend between parabolic and rectangular waveform. We can see that longer delay time due to small beam power at initial period for the parabolic case. However, velocity increase with formation of ablation plasma and with its expansion process is reflected by the change of beam power with time for the case of parabolic waveform. Final velocity in this case is higher by 25% compared with that for rectangular case. This fact shows again the higher acceleration efficiency by parabolic waveform.

Applicability of Propulsion by Ablation Plasma

We have to examine applicability of this acceleration process by ablation plasma to propulsion system. Specific impulse and thrust are discussed. We have to note that the maximum power level of the present experiments of $4kJ/cm^2$, which corresponds to $40MJ/m^2$ if ablation area is assumed to be $1m^2$. If this process is performed once a second, required electric power becomes 40MW and this corresponds to electric propulsion power for transportation from lower Earth orbit to Mars proposed by Dr.Ron Litchford.[5]

Specific Impulse

Total momentum balance cab be written as:

$$m_{ion}v_{ion} = m_f v_f - \overline{m}_{ab}\overline{v}_{ab} \qquad (5)$$

where f and ab denote flyer and ablation plasma. Because of momentum of incident ion beam is small and is negligible, ion beam only transfer its energy not its momentum. From this point of view, ion beam has the same role as lasers, electron beams and so on. Advantages of ion beam are relatively high-efficiency to produce intense beam, short range, i.e. penetration depth, and higher-pressure and higher–temperature of ablation plasma produced by ion beam. Therefore, averaged ablation plasma velocity can be written:

$$\overline{v}_{ab} = \frac{m_f}{\overline{m}_{ab}}v_f \approx \frac{t_f - t_r}{t_r}v_f \qquad (6)$$

where t_f and t_r denote initial thickness and range.

In the present experiments, flyer velocity v_f of ~8 km/s can be expected as shown in Fig.2. And the factor $(t_f - t_r)/t_r$ are around 6. Therefore, averaged ablation plasma velocity that corresponds to effective exhaust gas velocity is about 50km/s and specific impulse will be 5000 seconds. Further, it can be increased 7000~8000 seconds by optimization of waveform of ion beam as shown in the previous section.

Thrust

We can expect ~20GPa of ablation pressure as shown in Fig.4 at $4kJ/cm^2$. Duration can be estimated as ~100ns. This corresponds to averaged value over 1 second of 2000N for $1m^2$ of ablation area. If we use heavier material, thrust can be increased even with the same beam energy

180

density. We just started to accelerate tungsten flyer. Comparison of energy with the same deposition energy density:

$$\frac{1}{2}m_{Al}v_{Al}^2 = \frac{1}{2}m_W v_W^2 \tag{7}$$

and relation between each momentum is:

$$m_W v_W = \sqrt{\frac{m_W}{m_{Al}}} \cdot m_{Al}v_{Al} \tag{8}$$

We can expect that the thrust may be increased by 2.6 times and the average thrust reaches up to 5000~6000N for the case of tungsten target.

Concluding Remarks

Flyer acceleration process by intense pulsed ion beam has been experimentally and numerically studied. We can summarize the following concluding remarks:

- Numerical results of accelerated flyer velocity agreed well with measured one over wide range of incident ion beam energy density.

- Flyer velocity of 5.6 km/s and ablation plasma pressure of 15 GPa was demonstrated by the present experiments.

- Acceleration of multi-layer target was studied. For adequate layer thickness, such a flyer target could be much more accelerated than a single layer.

- Influence of waveform of ion beam was also examined. Parabolic waveform could accelerate more efficiently than rectangular waveform.

- Applicability of ablation propulsion was discussed. Specific impulse of 7000~8000 seconds and time averaged thrust of up to 5000~6000N can be expected.

References

1. Nob.Harada, et al., Proc. 12th Int. Conf. High-Power Particle Beams, Vol.2, p.1048, 1998.
2. Nob.Harada, et al., AIAA Paper, 99-3485, 1999.
3. K.Yatsui, et al., Jpn. J. Appl. Phys. Vol.40, pp.955-959, 2001.
4. Nob.Harada, et al., Jpn. J. Appl. Phys. Vol.40, pp.960-964, 2001.
5. Ron Litchford, et al., AIAA paper, AIAA 2001-0961, 2001.

32. ONBOARD MHD GENERATOR USING THE ELECTRON BEAMS FOR THE MAINTENANCE OF THE CURRENT LAYERS IN THE SUPERSONIC AIR FLOW

V.S. Slavin, K.A. Finnikov
Krasnoyarsk State Technical University

V.A.Bityurin
IVTAN, Moscow, Russia

M.V.Kraev
SAA, Krasnoyarsk

1. Introduction

The aerospace craft working out is the basic direction of the hypersonic flight use. The airplane-type start of this device will allow to carry out its acceleration up to $M \approx 12$ by the means of jet engine consuming the oxygen from the air. It will decrease the start weight sufficiently because during the rocket-type start of Space Shuttle the weight of oxygen in tanks exceeds 9 times weight of oxygen. Besides, the one time used elements of rocket start: the start boosters, thrown away fuel tank, are absent, which also reduces the price of system. As a result, the estimations show that the aerospace craft as a carrier may reduce the expenditure for the cargo delivering to the orbit approximately 100 times, which as compared with the current level 20000$/kg will amount to 200$/kg. The realization of the aerospace craft program will allow to start the industrial developing of space which can't repay itself with the current cost of transportation. Presumably, the most prospective space technologies are: manufacturing of ultra-pure semiconducting materials; manufacturing of glass for the fiber-optic cables; production of electrical power, transmitted to the Earth by the microwave channel and so on. The development of these programs will require the organization of large-tonnage transportation from the Earth to the space and back.

In a number of problems that must be solved during the development of aerospace craft the problem of stable fuel combustion in the supersonic flow and the problem of the drag reduction would be emphasized. The method of solution of these problems lies in the active influence on the air medium. So, it is supposed to switch on the stationary UHF discharge in the tract of jet engine, that will stabilize the combustion of hydrogen in the supersonic air flow. For the purpose of the drag reduction it is supposed the plasma injection to the forward air flow. An active influence on the air medium will require sufficient electrical power expenses. According to the estimations, it will be necessary to install the onboard energy source with the power level on the order 3-10MW. There is no turbine in the channel of jet engine and consequently, nothing can rotate the electric generator rotor. An evident solution of problem can be the MHD generator that can accomplish the derect conversion of the kinetic energy of forward flow to the electric energy. In this way, the problem of utilization of the MHD generator on the board of hypersonic aircraft becomes the central problem of the development of the aircraft itself.

The conventional MHD generational MHD generator working with the uniform of molecular gas requires rather high flow temperatute about 3000K, achieved at the expense of the heat emission on the fuel combustion, and besides, at the expense of alkali used to create the electrical conductivity in the flow. However, even in this case the electrical conductivity doesn't exceed $10\Omega\text{-}1\text{-}m\text{-}1$, which dictates the use of the superconducting magnets with the magnetic field induction about 4T. the weight and dimension characteristics of such magnets don't accord the capability of aircraft. Another approach is the use of uniform forward flow of cold air. The electrical conductivity in this case is created by the outer source (electron beams). Here the air flow transforms to the flow of cold nonequilibrium plasma in that the molecules ionization by the injected high energy electrons compensates the electron loss in the pair collisions with the positive molecule ions and also the process of three-body attachment of electron to the oxygen molecule. The problem of such generator is that the energy expenses to the conductivity maintenance in the cold air plasma are comparable or even higher that the useful energy outcome.

The way out of this deadlock may be the idea of the rejection of a uniform flow. If the air flow is organized as a stratified one, where the sections of cold and not ionized flow alternate with the high temperature (3000-4000K) layers with non-equilibrium ionization, the maintenance of electrical conductivity ($\sim 100\Omega^{-1}\cdot m^{-1}$) in these layers will require much less energy, than in a uniform

flow. It may explained by that in the air at the temperature >3000K the detachment of electrons flow the negative oxygen molecular ions occurs and besides, the thermal dissociation of oxygen and nitrogen molecules begins. In this way, high energy electrons ionize not only molecules but also atoms, for that the recombination process comes by the triple collision scheme. The rate of electron loss in the triple collision process at the temperature 3000-4000K approximately 10^4 times less than the rate of loss in the pair collision with molecular ions. Hence in such plasma the number of ionization acts and consequently, the electron beam power must be decreased proportionally to keep the needed value of electrical conductivity.

2. problem formulation

The parameters of gas flow in the MHD channel may be derived from the known temperature and density of air at the altitude 35km [1]:

$\rho=0.00689\rho_n$; $p=0.0057p_n$,

when ρ_n and p_n correspond the zero altitude. Let's set the velocity of vehicle equal to 1.76km/s, which corresponds to the Mach number of forward air flow M=6. Let's consider that the forward air flow is braked by two oblique shocks after which enters the MHD channel with Mach number M=3. During the braking the irreversible loss of the flow stagnation pressure occurs. According [2], the braking from M=6 to M=3 by two oblique decreases the stagnation pressure 2.5 times. Using the adiabatic relations for $\gamma=1.4$, one can obtain the parameters of air flow entering the MHD channel:

1. stagnation temperature – T_s=1870K,
2. stagnation pressure – p_s=0.37MPa,
3. flow velocity – u=1.55km/s,
4. temperature – T=667K,
5. density – ρ=0.052kg/m^3.

The electric field in the MHD channel is determined by the following conditions. The magnetic field in the considered case is supposed to be created by a permanent magnet and its induction would be about 1T. the load factor must correspond the maximum extracted electrical power, K=0.5. Thus, the electric field in the flow reference system will be about 0.8kV/m, and the relation between the field and gas concentration will be on the order 2×10^{-17}V·cm^2, which is much less than the characteristic field of the breakdown development $\approx10^{-15}$V·cm^2. Thus we can say that the electron temperature gap $\Delta T/T_0 \ll 1$.

As one can see, the temperature of gas flow at the inlet of MHD generator is quite low. In a cold air the effective processes of free electron loss occur: the dissociative recombination of the electron with the molecule ion N_2^+, O_2^+, NO^+,

$e+AB \rightarrow A+B$,
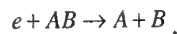
and besides, the three-body attachment of electrons to the oxygen molecules:

$e+2O_2 \rightarrow O_2^- +O_2$.
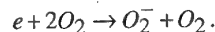
The constants of dissociative recombination processes amount to ~10^{-7}cm^3/s, the constant of three-body attachment – ~10^{-26}cm^6/s [3]. At the pointed gas temperature the three-body electron-electron-ion recombination is also strong. The recombination constant, which temperature dependency in our case accords the "9/2" law, has the value – ~10^{-21}cm^6/s.

Let's find the characteristic time of electron loss in the above-mentioned reactions. The needed conductivity value about $100\Omega^{-1}\cdot$m^{-1} determines the electron density n_e~10^{13}cm^{-3}. according the known density of flow, the molecular oxygen concentration is n_{O_2}~10^{17}cm^{-3}. The characteristic time of electron loss is:

in the dissociative recombination
$$\tau_{dr}=(k_{dr}n_e)^{-1}=10^{-6}\text{s};$$

in the three-body attachment
$$\tau_a=(k_a n_{O_2}^2)^{-1}=10^{-8}\text{s};$$

in the three-body recombination
$$\tau_r=(\alpha n_e^2)^{-1}=10^{-6}\text{s}.$$

As one can see, the electron loss at a low gas temperature occurs most due to the process of the three-body attachment. With the increase of temperature the reverse process of detachment begins to influence. As far as the bound energy of ion O_2^- amounts to 0.44eV, at the temperature about 3000-4000K the attachment is practically completely suppressed.

The ionization is created mostly by the electron beam. To accomplish the ionization act, certain quantity of electrical energy must be spent, that amounts to 30eV in the optimal case. Lets estimate the quantity of electrical energy produced by an electron during its lifetime.

The stratified structure of flow prevents from the Hall current running and therefore the
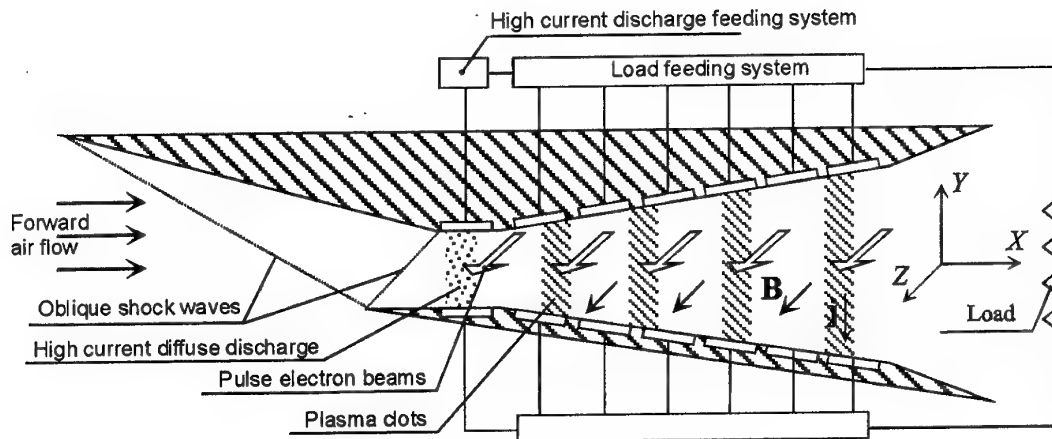
Fig.1. Scheme of MHD energy conversion/

electron drift velocity is perpendicular to the flow. In this way the work produced by the electron is

$$\varepsilon = \left| eE_y \right| v_d \tau .$$

Due to the absence of the Hall current, electron drift velocity is defined by the electric field in the flow reference system:

$$v_d = \frac{eE'_y}{m_e v_e^p} \approx 2 \cdot 10^4 \text{m/s},$$

where v_e^p is the frequency of electron momentum loss.

With the magnetic field $B=1$T and load factor $K=0.5$ the electrical energy produced by the electron amounts

$$\varepsilon \approx (4 \cdot 10^7 \tau) eV.$$

One can derive from this estimation that the energy generated by the electron detached from a molecule and lost in the process of dissociative recombination has the same order as the energy expenses for the ionization. Hence the MHD generator working with the cool air that full consists of the molecules isn't expedient from the point of view of energy efficiency.

The temperature increase to 3000-4000K provides the condition of thermal dissociation of air molecules (within this temperature range the oxygen dissociates mainly). In the heated air the electron beam ionizes the both molecules and atomic oxygen. The dissociation recombination

constant keeps its order value $\sim 10^{-7} \text{cm}^6/\text{s}$ at the pointed temperature and thus the process of dissociative recombination comes with the intensity. In the same the ions O^+ take partipation in the process of three-body recombination only, the process constant of that amounts to $\sim 10^{-26} \text{cm}^6/\text{s}$ at the given temperature, which is less by 4 order as compared with the case of cold air. It leads to the increase of the mean electron lifetime and consequently, the work produced by it. In fact, at a high temperature the ionization and accumulation of free electrons comes due to the ionization of atomic oxygen, whereas the ionization of molecules is quenched fast by the dissociative recombination and leads only to the addition expenses of electron beam power.

The temperature increase is expedient when a local sections of flow (not more than 10% of flow mass) are heated. For these purpose the section of periodical plasma clots creation must be set at the inlet of MHD channel. The process of plasma clot creation involves the primary ionization of the local flow section by the electron beam and the following heating by the means of the high current diffuse discharge. The scheme of onboard MHD installation is presented on Fig.1. The ionization maintenance in the plasma clot requires to switch on the electron beam sources synchronously with the plasma clot passing through. To simplify the problem formulation the ionization by the electron beams may be considered as a persistent electron sources which action zones are connected with the high temperature regions locations.

184

3. Physical model

The physical model is based on the quasi one-dimensional MHD equations system including the radiation and the electron density equation.

The size of plasma clot is about several centimeters and the gas mass density in plasma clot is ≤0.1kg/m^3. The data on the radiation emittance of the air [5] testify that the integral emissivity factor of a hemispheric volume of air with such parameters ε≤0.02. In this way, we can consider the radiation as volume one. Proceeding from the definition of the emissivity factor of a hemispheric volume with the radius R

$$\varepsilon = \frac{\pi}{\sigma T^4} \int_0^\infty B_V (1 - \exp(-k_V R)) dv ,$$

that in the case of optically thin layer ($k_v R$<<1 in the region of wavelength at which the most part of power emits) comes to the form

$$\varepsilon = \frac{\pi}{\sigma T^4} \int_0^\infty j_V dv ,$$

we can obtain the connection between the emissivity factor and the total radiation power, emitted by the unit of volume q_r:

$$q_r(T,p) = 4\pi \int_0^\infty j_V dv = \frac{4\varepsilon(T,p,R)\sigma T^4}{R} .$$

As the data on the emissivity factor of hemispheric show [5], within our limits of temperature (2000-8000K), pressure (10^{-4}-1Mpa) and the radiating layer thickness (up to 10cm) ε∝R with a deviation not more than 5%. Hence the power of radiation emitted by the volume unit practically doesn't depend on the size of radiating region.

In this way we can write the system of MHD equations in the following form:

$$\frac{\partial}{\partial t} \begin{pmatrix} \rho A \\ \rho u A \\ A(\varepsilon + \rho u^2/2) \end{pmatrix} + \frac{\partial}{\partial x} \begin{pmatrix} \rho u A \\ A(p + \rho u^2) \\ A(\varepsilon + p + \rho u^2/2) \end{pmatrix} =$$

$$= \begin{pmatrix} 0 \\ pA'_x + jBA \\ A(jE - q_r) \end{pmatrix}.$$

In the equation for the electron concentration we take into account the gas ionization by the electron beam, the ionization by the electrons being in the thermal equilibrium with gas and three-body recombination:

$$\frac{\partial(An_e)}{\partial t} + \frac{\partial(An_e u)}{\partial x} - \Gamma_{beam} - \Gamma_{therm} + \alpha n_e^3 = 0 .$$

The electron beam creates the non-equilibrium electron concentration that is formed by the processes of impact ionization of the atomic oxygen and three-body recombination. As far as the beam power is selected such that the ionization ratio is ~10^{-4}, the non-equilibrium value of electron density practically doesn't affect the neutral particles. Within the frameworks of that supposition the thermodynamic properties of the air will be defined as the equilibrium ones. In this way the system of MHD and electron density equations is closed by the equilibrium relationships

$$T(\rho,\varepsilon); \ p(\rho,\varepsilon); \ n_e^{eq}(\rho,\varepsilon); \ \sigma(\rho,T,n_e),$$

When $n_e^{eq}(\rho,\varepsilon)$ is the equilibrium electron density necessary to define the rate of ionization by thermal electrons Γ_{therm}.

Within the framework of present consideration the following model of ionization by the electron beam is chosen:

$$\Gamma_{beam} = \sum_k G(x) I_k(x,t)\rho_0$$

Here $G(x)$ – is the amplitude of electron beams distributed along the MHD channel; $I_k(x,t)$ – distribution of beam ionization intensity within the certain (k^{th}) plasma clot,

$$I_k(x,t) = \begin{cases} 1 - \left(\dfrac{x - x_k(t)}{\delta}\right)^2 , & |x - x_k(t)| < \delta, \\ 0 \end{cases}$$

$x_k(t)$ – the coordinate of gas particle in which the temperature is maximum for this plasma clot; δ – half-width of region of electron beam action; ρ_0 – partial density of atomic oxygen. The function $G(x)$ is defined by the distribution of electron beam current density in the MHD channel, besides, it depends on the energy of beam electrons and cross-sections of various ionization and radiation collisions with atoms and molecules. Now we down concentrate on the consideration of these processes and merely choose the form of $G(x)$ in such way that the ionization in the plasma clots would have a value ~10^{-4}.

The power spent to the ionization by the electron beam can be estimated as following:

$$W_{beam} = \varepsilon_0 \int A\Gamma_{beam} \frac{\rho}{\rho_0} dx,$$

where ε_0 is the mean energy spent to the creation of electron-ion power, which will be accepted equal 30eV. Here we suppose that the frequency of neutral particle ionization is proportional its electron quantity and hence, its mass. In this way total ionization rate relates to the atomic oxygen ionization rate as ρ/ρ_0.

The rate of ionization by thermal electrons Γ_{therm} depends on the concentrations of neutral particles. As far as an electron temperature gap is absent, we can consider that the electron energy distribution is Maxwell and therefore, $\Gamma_{therm} \propto n_e$. Lets derive Γ_{therm} from the detailed balance relationship. At the equilibrium electron density

$$n_e = n_e^{eq}$$

$$\Gamma_{therm}^{eq} = \alpha(n_e^{eq})^3,$$

and correspondingly, at a non-equilibrium n_e

$$\Gamma_{therm} = \alpha(n_e^{eq})^2 n_e.$$

In this way, two terms in the equation for the electron density may be written in the following form:

$$\Gamma_{therm} - \alpha n_e^3 = \alpha n_e \left((n_e^{eq})^2 - n_e^2 \right).$$

To find thermodynamic relationships it is necessary to calculate the concentrations of several kids of atomic and molecular neutral and ionized particles. As the results of calculation of equilibrium air properties, at a temperature below 15000K the basic components of air plasma are N_2, O_2, NO, N, O, N^+, O^+, e. Besides, at a low temperatures the most part of positive ions are the molecular ions NO^+. In this way, for finding the above-mentioned relationships the system of equations for the equilibrium concentration of N_2, O_2, NO, N, O, N^+, O^+, NO^+, e, had been solved. The system consists of the Saha equations for the dissociation of N_2, O_2, NO, ionization of NO, N, O, condition of quasineutrality and equation for the concentration of nitrogen and oxygen nuclei density, that is connected with the air mass density. In this way the energy as function of temperature and mass density could be obtained. For the solution of the inverse problem – finding the

temperature and pressure as a functions of energy it is necessary to find a root of obtained equation $\varepsilon = \varepsilon(T, \rho)$. As one can see, the procedure of finding the temperature and pressure is quite long and machine resources consuming. Since that the two-dimension tables $T, p(\rho_i, \varepsilon_j)$ were calculated primarily and interpolation had been used in the time of MHD equations solution.

For the calculation of electrical conductivity with consideration of electron collision with the ions, electrons and different kinds of neutral particles the Frost's formula had been used. The data of FTR-archive of A.V.Phelps and collegues (ftr://ftr.jila.Colorado.edu) were taken for the momentum transfer cross sections of electron collision with N_2 and O_2. The cross sections of collision with other neutrals were taken in [4].

4. Numerical simulation results

In the course of numerical simulation the characteristics of MHD installation and its working regime had been set up:

MHD channel length	2 m
Input cross section (open to the atmosphere)	0.4 m^2
Inlet MHD cross section	0.14 m^2
Channel expansion ratio	3
Magnetic field	0.8 T
Load factor	0.5

The intensity of electron beam ionization had been set up by the means of selection of electron beam power profile $G(x)$. The function $G(x)$ is shown on the Fig.2 by the dash curve. The instant distribution of ionization rate per the unit of mass of atomic oxygen is shown by the solid curve. The locations of peaks correspond the maximums of temperature in plasma clots.
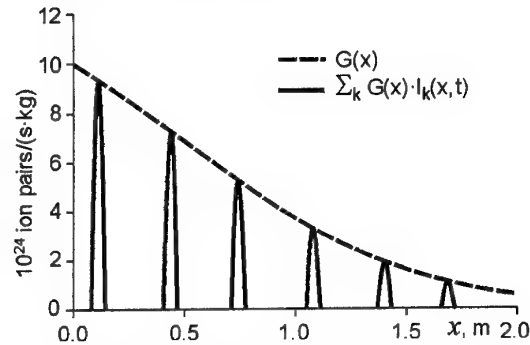
Fig.2. Instant distribution of electron beam intensity (quantity of electron-ion pairs generated by the electron beam per the time unit per 1 kg of atomic oxygen).
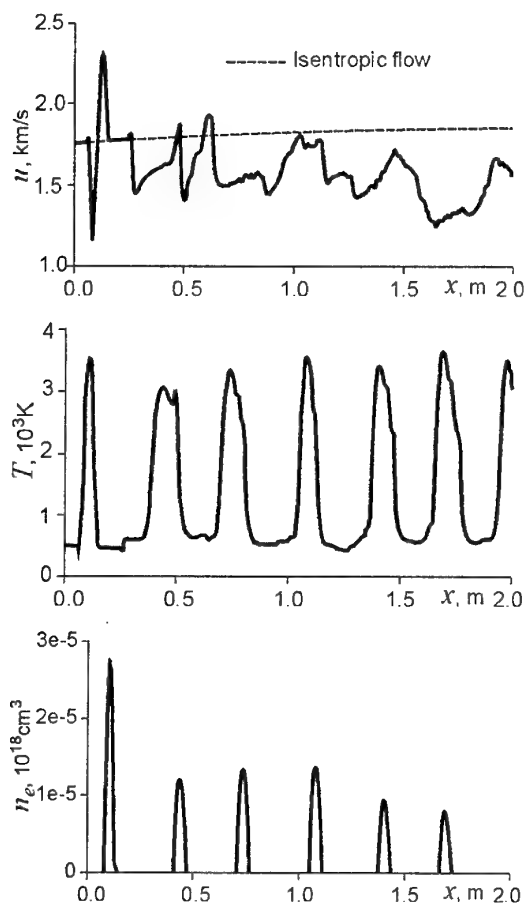
Fig.3. Instant distribution of the flow velocity, temperature and electron density in the MHD channel.

The energy characteristics of MHD installation are listed below.

Input enthalpy flux	20 MW
Useful electric power	3 MW
Enthalpy extraction ratio	0.148
Power spent to the electron beam ionization	7 kW
Mean power spent to the primary heating of plasma clots	1.2 MW

The instant distribution of flow velocity, temperature and electron density are shown on the 3. The temperature keeps practically constant value ≈4000K. The high-temperature zones are larger than the regions of high ionization because these zones are formed at the primary stage of diffuse high current discharge, during that the effect of gasdynamic expansion happens. In this regime the thermal ionization is practically absent, which must provide the stability of plasma clots.

References

1. A.P.Babichev, N.A.Babushkina, A.M.Bratkovskii et al. Physical values. Moscow, Energoatomizdat, 1991 (in Russian).
2. L.G.Loytsanskii. Liquid and gas mechanics.
3. U.P.Rizer. Gas discharge physics. Moscow: Science, 1987 (in Russian).
4. Physics and technology of low-temperature plasma / ed. S.V.Dresvin. Moscow, atomizgat, 1972 (in Russian).
5. V.A.Kamenxhikov, U.A.Plastinin, V.M.Nikolaev, L.A.Novitskii. Radiation properties of gases at high temperatures. Moscow, Machinostroenie, 1971 (in Russian).

33. SIMULATION OF SHOCK WAVES AND SOUND OF A MOVING LASER SOURCE

V.N.Tischenko[+)], G.N.Grachev[+)], A.I.Gulidov[*)], V.I.Zapryagaev[*)], V.G.Posukh[+)]

+) - Institute of Laser Physics of the Siberian Branch of the Russian Academy of Sciences. 630090, Novosibirsk, 13/3 Lavrentyev ave.

*) - Institute of Theoretical and Applied Mechanics of the Siberian Branch of the Russian Academy of Sciences. 630090, Novosibirsk, 4/1 Institutskaya st.

At present the schemes of control of flowing over supersound bodies are under consideration. These schemes are based on a pulse-periodic introduction of energy into an incident gas flow (see, for example, [1-5]). Here both a thermal trace with low gas density and shock waves (SW) filling in the conical area, limited by the surface of a resultant (SW) are being created. Investigation of properties of such SW is very urgent as they carry away a major part of the power introduced into the flow (~ 25-50 %) and might affect the flowing over bodies. Single or periodic (with small repetition rate) laser sparks create a SW that is described by the point explosion theory. Many publications are devoted to the investigation of dynamics of SW propagation (see, for example, [6-9]). In paper [10] is described an optical pulsating discharge (OPD) with repetition frequency of sparks F up to ~ 100kHz. In the present paper it is shown that sparks at large values F can generate a SW the profile of which depends not only upon the energy (Q) of sparks but on F as well. The investigation was carried out within the scope of the problem on transformation of a laser beam into plasma one in a free gas space [11].

The gas dynamics equations were solved numerically, taking into account the properties of air at a high temperature. It is assumed that a pack of N pulses having repetition frequency F heats coaxially-symmetrically the region, the length of which L is much larger its radius (a cylinder). Time of heating $t_0 \approx 1$ μs, air pressure $P_0 = 1$ atm., radius of the first wave $- R_0 \approx 0.1 \div 0.5$ cm, the energy introduction is close to the experiment [12]. As an energy parameter we accepted a value that is equal to the relation of the energy absorbed in the spark to the energy of cold gas in spark volume $E=Q/Q_0$. SW was investigated at the fixed value of total spark energy in the pack $Q_S = \sum_1^N Q_i$. If the sparks in the pack have equal energy Q, then parameter $E_S \equiv Q_S / Q_0 \approx E \cdot N$ describes a SW being created by one powerful spark with energy Q_S. In the given paper we accepted value $E_S = 1000$.
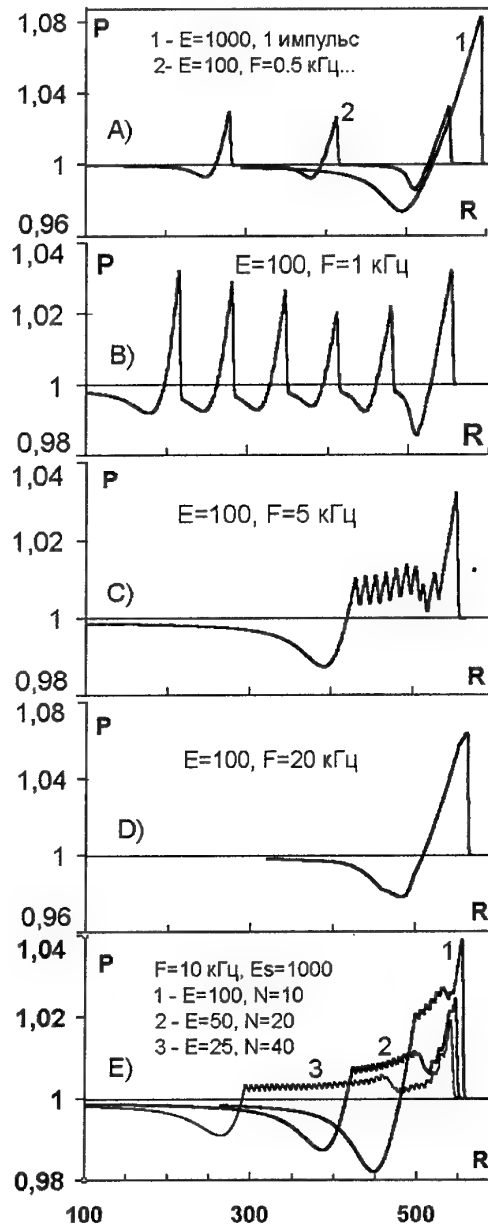
Fig.1. Distribution of pressure behind SW front (moment of time t=8 mcs)

188

In Fig.1 one can see SW created at different repetition frequencies of sparks. Here R_0 = 0.5cm, N=10 and E=100. The pressure and distance in radius are normalized on P_0 and R_0, respectively. If the time between sparks $T_S \approx F^{-1}$ is less the time (T_R) of relaxation of a high pressure in the area of heating (depends on E and R_0), then the pack of sparks forms a SW that is slightly distinguished from the SW generated by one spark with energy $Q_S=Q_0 \cdot Es$ (see Fig.1a and Fig.1d). While decreasing F, a SW with large extension of a pressure phase $R_+ \sim C_0 \cdot N/F$ (Fig.1c) is being created. The phase of a lower pressure is approximately the same one as for the case $E=Es$ (C_0 is the sound velocity in air). A high frequency component behind the front corresponds to disturbances from each SW (ultrasound at small E or R_0). Shock waves do not interact if for the time T_S every SW goes away from the plasma channel at the distance that is larger than SW extent, created by one spark (Fig.1a). From the calculations it follows (see Fig.1e) that at the equal value E_S it is possible to generate a SW of large extension, at decreasing E and increasing N. The repetition

frequency of sparks at which SW interact, depends upon energy and space characteristics of laser sparks. The calculation for sparks with the parameters close to the experiment described in the present paper can serve as an example for the fact mentioned above (Fig.2).

To investigate dynamics of SW characteristics and their dependences upon energy and sizes of a spark we have carried out a number of calculations where an energy contribution per unit length was equal to q =5 and 50J/cm and the values E and R_0 varied.
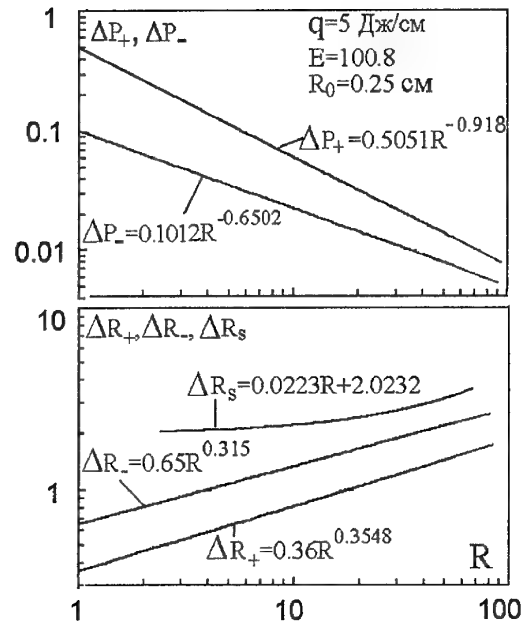
Fig.3 Dependence of the parameters of a single cylindrical SW upon the radius of its front. Pressure is normalized on P_0, and radius – on R_d .

Fig.2. Distribution of pressure in radius in SW generated by a tandem of sparks (P and R are normalized on P_0 and R_0).

In Fig.3 depending upon the location of SW front one can see the dynamics of SW characteristics. Pressure is normalized on P_0 and space characteristics – on dynamic radius $R_d \sim 3.14(q/P_0)^{1/2}$ [cm] (q[J/cm], P_0 [atm]). Here $\Delta P_+ = (P_+ - P_0)/P_0$ and ΔR_+ are pressure at SW front and the length of SW pressure phase, respectively; $\Delta P_- = |P_- - P_0|/P_0$ and ΔR_- are the pressure and length corresponding to minimum pressure P_- in the phase of lower pressure of SW; ΔR_S is a SW length. Reading of ΔR_+, ΔR_-, and ΔR_S starts from SW front (ΔR_S is a distance up to the point in which $|P_- - P_0|/\Delta P_- = 0.2$). In the range mentioned above ($E = 3 - 1000$ and $R_0 = 0.1 \div 1.5$ cm) the maximum and minimal values of the specified values are

189

described by the following dependences obtained by approximation of the calculation data.

$(\Delta P_+)_{max}=$
$=0.6453 \, R^{-0.9134}$
$(\Delta P_+)_{min}=$
$=0.5051 \, R^{-0.9175}$ $R=1\div100$

$(\Delta P_-)_{max}=$
$=0.116 \, R^{-0.6386}$
$(\Delta P_-)_{min}=$
$=0.0924 \, R^{-0.6748}$ $R=1\div100$

$(\Delta R_+)_{max}=$
$=0.4245 \, R^{0.3743}$
$(\Delta R_+)_{min}=0.328R^{0.3837}$ $R=1\div100$

$(\Delta R_-)_{max}=$
$=0.637 \, R^{0.358}$
$(\Delta R_-)_{min}=0.58 \, R^{0.345}$ $R=2\div100$

$(\Delta R_S)_{max}=$
$=0.02 \, R+2.12$
$(\Delta R_S)_{min}=$
$=0.0246 \, R+1.83$ $R=3\div100$

On the right from the formulae is shown a range of their applicability. A maximal value R is limited by the range of the performed investigations and at R being less than its minimal value, SW or separate SW phases haven't been formed yet. Approximation error is less than 5 %.
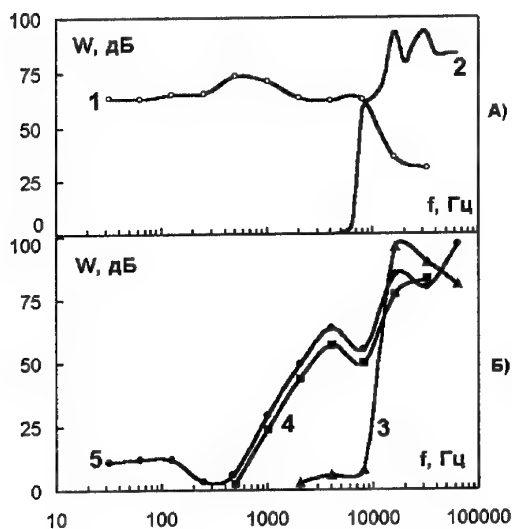
Fig.4. Experimental data. Spectrum of the sound created by the optical pulsating discharge at different repetition frequencies of laser radiation pulses: 1 – background spectrum; 2,3,4,5 – F=8, 20, 40, 60 kHz.

Experiment. Argon under high pressure flew into a chamber from which it entered into a tube (length – 4 cm, diameter – 0.7 cm, gas velocity – 20 m/s) and after that into the atmosphere. An optical pulsating discharge (OPD) was being formed at the tube axis while focusing a periodic radiation of CO_2 –laser [13] (pulse duration was 1 µs, OPD absorbed ~ 650 W). OPD formed a thermal "cork" that resulted in a stoppage of OPD combustion and periodic formation of a

tandem of laser sparks. We have determined the effect of repetition frequency of laser sparks $F \approx 8 - 64$ kHz upon the sound spectrum created by OPD. In Fig.4 are shown the spectrums of OPD sound at different repetition frequencies of sparks. The measurements were mainly octave (average value in the frequency range $f \pm f/2$), ignoring the background signal. A total intensity of sound makes up ~ 125 and background – 85 decibel. At $F = 8$ and 20 kHz an ultrasound prevails and at large F OPD formed both ultrasound and low frequency sound. The calculations have shown that a sound with frequency $f >> F$ is created at the expense of pulsation of shock waves inside the tube. At the tube exit a plasma jet emits. The radiation of a lateral tube surface was greatly absorbed. The tadems of sparks at repetition frequency $F > 25$kHz created a sound with frequency $f << F$ that is in the agreement with the calculation (see Fig.2).

So, while introducing energy at high repetition frequency into gas, there can be created shock waves of different types, namely: periodic, low frequency, simultaneously with low and high frequency.

References

1. G.G.Chernyi, 2nd Weakly Ionized Gases Workshop Proceedings, Norfolk, Published by the American Institute of Aeronautics and Astronautics, 1998.
2. Myrabo L.N., Raizer Yu.P. Laser-Induced Air Spike for Advanced Transatmospheric Vehicles. AIAA Paper. №.94-2451, 1994.
3. Yuriev A.S., Savschenro N.P., Mosraletz G.N., Tsvetkov O.V., Ryizhov E.V. Some Problems of Energy Addition Applications for Control of Streaming. The 2nd Workshop on Magneto-Plasma-Aerodynamics in Aerospace Applications. Moscow, IVTAN, 2000, p.121.
4. Levin V.A., Afonina N.Ye., Georgievsky P.Yu., Gromov V.G., Terentyeva L.V. The Influence of an Energy Extraction Source upon Supersonic Flow over Bodies. Paper № 36-98, Moscow, Institute of Mechanics of Moscow State University, 1998 (In Russian).
5. Tretyakov P.K., Garanin A.F., Grachev G.N., Krainev V.L., Ponomarenko A.G., Tischenko V.N., Yakovlev V.N. Reports of the Academiy of Sciences, 1996, v.351, p.339 (In Russian).

6. Bunkin F.V., Komissarov V.M. Acoustic Journal (Russian journal), 1973, n. 3, p.307.
7. Nemchinov I.V., Artem'ev V.I., Bergelson V.I., Khazins V.M., Orlova T.I., Rybakov V.A. Shock Waves, 1994, n. 4, p. 35.
8. Anisimov V.N., Vorobiev V.A., Grishina V.G., Derkach O.N., Kanevsky M.F., Sebrant A.Yu., Stepanova M.A., Chernov S.Yu. Quantum Electronics (Russian journal), 1995, v.22, No.8, p.862.
9. Bukatyi V.I., Gaskova O.V. Optics of Atmosphere and Ocean (Russian journal), 1998, No.1, p.43.
10. Tretyakov P.K., Grachev G.N., Ivanchenko A.I., Krainev V.L., Ponomarenko A.G., Tischenko V.N. Reports of the Academiy of Sciences (Russian journal). 1994, v.336, p.466.
11. Tischenko V.N., Gulidov A.I. Letters to the Journal of Technical Physics (Russian journal), 2000, v.24, n.19, p.77.
12. Tischenko V.N., Antonov V.M., Melekhov A.V., Nikitin S.A., Posukh V.G., Shaikhislamov I.F. Letters to the Journal of Technical Physics (Russian journal), 1996, v.22, p.30.
13. Grachev G.N., Ponomarenko A.G., Smirnov A.L., Shulyat'ev V.B. Multifunctional 3 kW CO2-Laser with Controllable Spectral and Temporal Characteristics for Industrial and Scientific Applications. Proc. Of SPIE, 2000, v.4165, p.185.

34. GLOBAL THERMAL-BARO-DIFFUSION EFFECT IN WEAKLY IONIZED NONEQUILIBRIUM SHOCK LAYER

Anatoly F. Kolesnikov
Institute for Problems in Mechanics RAS
Prospect Vernadskogo 101/1, 117526 Moscow, Russia
E-mail: koles@ipmnet.ru

Abstract. A numerical study of the weakly ionized shock layer structure is carried out through a stagnation line flow analysis with an accurate treatment of ambipolar diffusion phenomena (= zero electric current) in two-temperature argon plasma. Computations have been performed for the free stream conditions related to a ballistic range test. It is shown that baro-diffusion and thermal diffusion caused by the separation of the electron temperature and gas temperature in the bow shock affect the entire shock layer structure and provide the "anomaly" diffusion of the charged particles. The ratio of the electron partial pressure and gas pressure in the free stream is found as a factor of the bow shock standoff and weakening. The two-peak structure of the ambipolar thermal-baro-diffusion-induced electric field inside the bow shock is discovered.

Nomenclature

c_I	mass fraction of ions
$D_{IA}(1)$	binary ion-atom diffusion coefficient in first approximation
$D_{Iamb}(1)$	ion ambipolar diffusion coefficient in a three-species mixture in first approximation
e	electron charge
$\vec{E}_A$	ambipolar electric field
$\vec{J}_I$	ion mass diffusion flux
k	Boltzmann constant
k_{pI}	ion ambipolar baro-diffusion factor
k_{TI}	ion ambipolar thermal diffusion factor
M	Mach number
p_e	electron partial pressure
p	pressure of the mixture
Re	Reynolds number
R_w	nose radius
T_h	gas temperature
T_e	electron temperature
V	flow velocity
y	dimensionless distance from the body

Greek symbols

$\theta = T_e/T_h$	
ρ	mass density of the mixture

Sub- and superscripts

e	*indicates* the electrons in the mixture
h	indicates the heavy particles in the mixture
w	wall
∞	free stream

Introduction

Since prior Russian data [1-3] indicating the bow shock weakening in the weakly ionized supersonic flow, many researches have focused attention on this phenomena and on the accompanying ill-understood effects such as an increase in shock standoff distance. The questions associated with nonuniform heating, molecular relaxation processes and proper plasma physics have been discussed, novel ballistic range plasma experiments in air and argon have been conducted and new measurement technique has been developed [4,5]. But so far the weakly ionized supersonic plasma remains an open issue. An adequate fluid dynamic model with the key thermodynamic and plasmadynamic features should be developed in order to explain the data and to predict aerodynamic drag reduction. We believe that such a model must include an accurate mathematical theory of transport processes in plasmas [6]. In Refs. 7 and 8 a rigorous formalism of the ambipolar diffusion in multi-component two-temperature plasmas was developed and an application of the Stefan-Maxwell relation for ions in the three-species plasma was given through CFD analysis of the supersonic weakly ionized argon plasma flow along the stagnation line. It was indicated that thermal diffusion caused by the separation of the electron and heavy particle temperatures and coupled baro-diffusion effect provided the global effect on the ions in entire

192

shock layer. In the present paper the same 1-D model of the weakly ionized frozen three-species two-temperature supersonic plasma flow along the stagnation line is applied to study the weakly ionized shock structure for conditions related to a ballistic range test in argon. Some results of CFD analysis of the shock layer structure and details of the ion diffusion inside the bow shock and boundary layer are presented. The special attention has been paid to the ambipolar electric field switching due to tendency of charge separation within the bow shock structure and boundary layer as well.

1-D Fluid Dynamic Model

The supersonic nonequilibrium argon flow past a blunt body is supposed to be weakly ionized in the free stream with different gas and electron temperatures and the shock layer is considered as a frozen one. The governing equations for the 3-species two-temperature plasma in the case of ambipolar diffusion include the simplified 1-D Navier-Stokes equations, the electron energy equation, the heavy particles energy equation, and the ion diffusion equation. According to Ref. 8, the expression for the diffusion flux of ions was used in the "field-free" form and it included contributions due to the concentration diffusion, the baro-diffusion effect, and a novel thermal diffusion term linked to the gradient of the ratio of the electron and heavy particle temperatures:

$$\vec{J}_I = -\rho D_{Iamb}(1)\left(\nabla c_I + k_{pI}\nabla \ln p + k_{TI}\nabla\theta\right)$$

$$D_{Iamb}(1) = (1+\theta)\frac{1+c_I}{1+c_I\theta}D_{AI}(1)$$

$$k_{pI} = \theta\frac{1+c_I\theta}{1+\theta}\frac{c_I(1-c_I)}{(1+c_I)^2}$$

$$k_{TI} = \frac{1}{1+\theta}\frac{c_I(1-c_I)}{(1+c_I)^2}$$

$$\theta = T_e/T_h$$

The ambipolar electric field can be expressed in the form

$$\vec{E}_A = -\frac{kT_e}{e}\left(\frac{1}{1+c_I\theta}\nabla \ln c_I + \nabla \ln p + \frac{1}{1+c_I\theta}\nabla \ln\theta\right)$$

In the present approach the thermal diffusion connected to particles collision in the plasma is neglected and diffusion is described at

the first approximation in terms of Sonine polynomials [6]. The average cross sections for the pairs Ar-Ar, Ar$^+$-Ar and e-Ar were taken in Ref. 9.

We consider a wall as a thermally isolated one to the electron heat flux due to thermal conductivity and as a non-catalytic one to the ion-electron recombination.

Results and Discussion

Computations were carried out at $M_\infty=3$, $Re_\infty=5330$, $p_\infty=3.25\cdot10^3$N/m^2, $R_w=5\cdot10^{-3}$m, $T_{h\infty}=600$K, $T_w=300$K, $c_{I\infty}=10^{-3}$, and $T_{e\infty}/T_{h\infty}=20$, 100 and 200. Some of these parameters were close (more or less) to conditions of the ballistic range tests in weakly ionized argon reported in Ref. 5.

Our computations have not indicated any influence of the ionization on the aerodynamics at $c_{I\infty}\leq10^{-4}$ as far as $T_{e\infty}/T_{h\infty}<2\cdot10^2$. A gasdynamic shock layer structure is found to be sensitive to the ionization at $c_{I\infty}\geq10^{-3}$. Figure 1, where dimensionless profiles of the pressure $p=p/(\rho_\infty V_\infty^2)$ are presented, shows some evidence of the shock standoff increasing at $c_{I\infty}=10^{-3}$, if the electron temperature in free stream increases. The ratio of electron and gas partial pressures in free stream appears to be a factor of the bow shock standoff and weakening, because electron temperature changes rather smoothly across the shock [10].
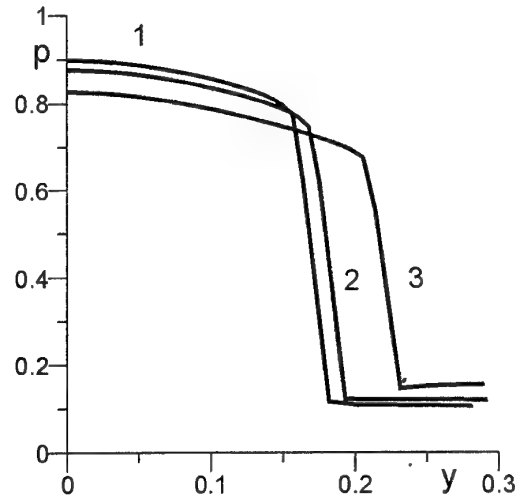
Fig.1. Pressure distribution along stagnation line:
1- $T_{e\infty}/T_{h\infty}=20$, 2 – 100, 3 - 200

Figure 2 shows the distribution of the normalized ion mass fraction $c_I/c_{I\infty}$ along the stagnation line for the case $c_{I\infty}=10^{-3}$. If the thermal-baro diffusion effects are not taken into account, the ion diffusion equation has an exact solution for a non-catalytic wall case as $c_I/c_{I\infty}=1$. Keeping this

in mind, we see that the thermal and pressure gradients cause global changes of the ion distribution inside the boundary layer, shock layer and bow shock. The ions and electrons, reaching the bow shock, are braked by the strong gradients of the pressure and gas temperature. As a result of interference of the ion mass fraction, pressure and temperatures gradients, the ion fraction reaches a local minimum just outside gasdynamic shock and local maximum inside the bow shock. At the present free stream conditions ion distribution looks even more complicated than observed in our prior computations [8], where a single maximum of the ion fraction was indicated. Inside the boundary layer, the ions being affected by the strong gas temperature gradient near the wall, are forced out in the direction of the ion fraction gradient. At the specified wall conditions the strong "anomalous" ion fraction gradient near the non-catalytic wall compensates exactly the gas temperature gradient and the interference of these gradients leads to the second maximum of the ion fraction inside the shock layer. So, the entire shock layer structure is affected by the ambipolar baro-thermal diffusion.
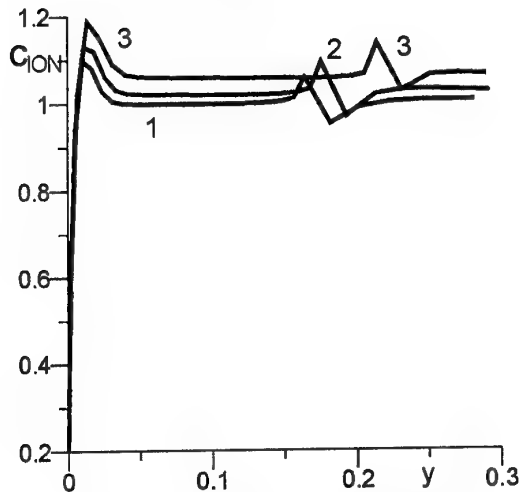
Fig.2. Ion mass fraction along stagnation line: 1- $T_{e\infty}/T_{h\infty}$=20, 2 – 100, 3 - 200

Figure 3 shows the distributions of the dimensionless ion diffusion flux along the stagnation line with the fine details concerning global ion diffusion: the ions accelerate just in front of the bow shock toward a body and brake inside the shock structure. The increase of the electron temperature in free stream shifts the peaks of the ion diffusion flux upstream, though it does not affect much the peak magnitude. If, again, thermal-baro-diffusion of ions is neglected, the ion diffusion flux equals zero along the stagnation line in the non-catalytic wall case.
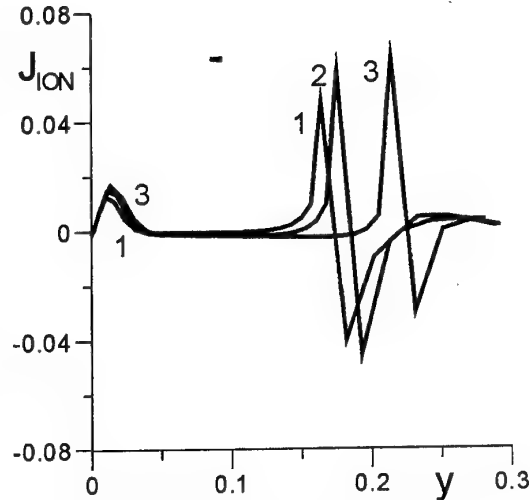
Fig.3. Dimensionless ion mass diffusion flux along stagnation line: 1- $T_{e\infty}/T_{h\infty}$=20, 2 – 100, 3 - 200

Figure 4 indicates the switching of the ambipolar electric field inside the bow shock structure and inside the boundary layer as well. This electrostatic field prevents the charge separation due to diffusion of the electrons and ions. The distribution of the ambipolar electric field exactly follows the behavior of the ion diffusion flux: the directions, the peaks positions, and locations of the points where both functions equal zero within shocks are the same. The analysis of the ambipolar electric field reveals two main findings: 1) The structure of the ambipolar electric field does not depend on the degree of ionization, and 2) The electric field amplitude reaches a level ~2·10^{4}V/m. If the thermal-baro-diffusion phenomena is excluded from the fluid dynamic model, there is not any computational evidence that the electric field exists inside the shock structure.

In order to understand better how the electric field caused by charge separation can affect the shock structure, the parameter E_A/p, which characterizes the efficiency of ionization in a glow discharge [11], is shown in Fig.5. The two-peak structure of this factor is discovered. The electron temperature in free stream controls the location of the peaks. The increase of the electron temperature in free stream causes the shifting both peaks upstream. The amplitude of the outer peak is essentially higher than the amplitude of the inner one due to a pressure jump in the shock, while the electric field itself is higher at the inner layer.

194
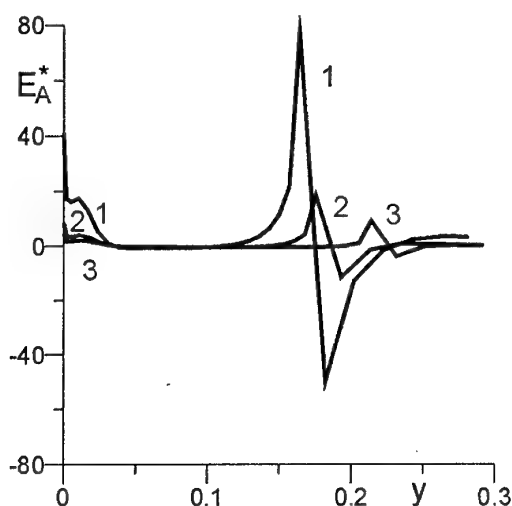
Fig.4. Dimensionless ambipolar electric field along stagnation line: 1- $T_{e\infty}/T_{h\infty}=20$, $2-100$, $3-200$
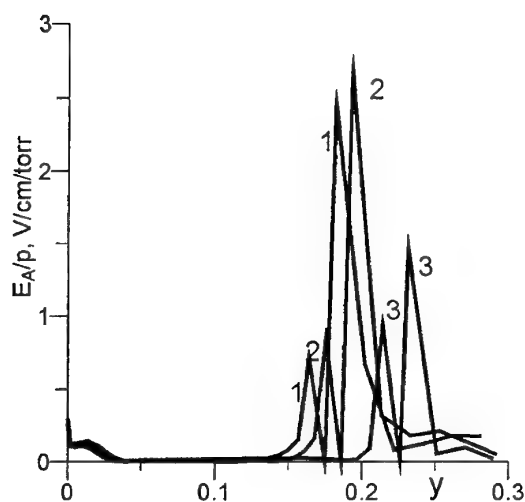
Fig.5. Factor E_A/p along stagnation line: 1- $T_{e\infty}/T_{h\infty}=20$, $2-100$, $3-200$

Conclusions

The developed fluid dynamics model with an accurate treatment of the ambipolar diffusion in two-temperature plasmas is found to be sufficient to explain some "anomalous" effects of the bow shock standoff decreasing and the shock weakening in the weakly ionized supersonic argon flow, though at the degree of ionization above 10^{-3}.

The noticeable ambipolar thermal-baro-diffusion-induced electric field in shock structure is indicated. In order to enhance the sensitivity of our model to the lower ionization degree the effect of the charge separation-induced electric field should be implemented in the above fluid dynamic model.

References

1. Klimov, A.I., Koblov, A.N., Mishin, G.I., Serov, Yu.L., and Yavor, I.P., "Shock Wave Propagation in a Glow Discharge," Sov. Tech. Phys. Lett., Vol. 8, No. 7, 1982, pp. 439-443.
2. Mishin, G.I., Serov, Yu.L., and Yavor, I.P., "Flow Around a Sphere Moving Supersonically in a gas Discharge Plasma," Sov. Tech. Phys. Lett., 17, June 12, 1991, pp. 65-71.
3. Bedin, A.P., and Mishin, G.I., "Ballistic Studies of the Aerodynamic Drag on a Sphere in Ionized Air," Sov. Tech. Phys. Lett., 21, January 12, 1995, pp. 14-19.
4. Lowry, H., Smith, M., Sherrouse, P., Felderman, E., Drakes, J., Bauer, M., Pruitt, D., and Keefer, D., "Ballistic Range Tests in Weakly Ionized Argon," AIAA 99-4822, Nov. 1999.
5. Felderman, E.J., Limbaugh, C.C., Scott, W.M., Pruitt, D.W., and Drakes, J.A., "Analysis Of Ballistic Range Plasma Shock Measurements," AIAA 2000-2568, June 2000.
6. Ferziger, J.H. and Kaper, H.G., Mathematical Theory of Transport Processes in Gases, North-Holland Publishing Company, Amsterdam-London, 1972.
7. Kolesnikov, A.F., "Self-Consistent Stefan-Maxwell Relations for Multi-Component Ambipolar Diffusion in Two-Temperature Plasma Mixtures," von Karman Institute for Fluid Dynamics, TN 196, Rhode Saint Genese, Belgium, Jan. 1999.
8. Kolesnikov, A.F., "Stefan-Maxwell Relations for Multicomponent Ambipolar Diffusion and Thermal-Baro Diffusion Effects in Two-Temperature Plasmas," AIAA 2000-2570, June 2000.
9. Devoto, R.S., "Transport Coefficients of Ionized Argon," Phys. Fluids., Vol. 16, No. 5, 1973, pp. 616-623.
10. Zel'dovich, Ya.B., and Raizer, Yu.P., *Physics of Shock Waves and High Temperature Hydrodynamic Phenomena*, Academic Press, New York, 1967.
11. Raizer, Yu.P., Physics of Gas *Discharge*, Nauka, Moscow, 1987, 592 p.p. (in Russian).

195

35. STRUCTURE OF AN ION-ACOUSTIC PRECURSOR OF A SHOCK WAVE IN PLASMA

V.A.Pavlov
State University, St-Petersburg

Yu.L.Serov
Ioffe PTI RAS, St-Petersburg

Abstract. Structure of an ion-acoustic precursor in weakly ionized collisional plasma is investigated. Formation of ion clots, in which a strong influence of charges on a neutral component of plasma is realized, is numerically investigated. Is shown, that simultaneous influence of nonlinearity, dispersion and dissipation results in formation of oscillatory structure of a precursor.

An ion-acoustic precursor is an area of perturbation before a shock front,which will be formed owing to nonlinear processes when a strong shock wave propagates in weakly ionized plasma [1-4]. High speed motion even in rather dense collisional plasma of gas discharge in some conditions is accompanied by the anomalies, which is not described by the thermal model in limits of gas dynamics [3-5].

We consider the conditions of formation of ion-acoustic precursor and will determine its parameters which make it possible for precursor to influence on a neutral component of plasma and on a shock wave. We shall be based on following idealization of process. The field is one dimensional and stationary (it depends on a combination of parameters z-ct, where z is the coordinate; t, time; c=const, speed of a shock wave.) The condition of ion-acoustic approximation for electron and ion temperatures in plasma is carry out. Taking into account of nonlinearity, elastic collision, dispersion, viscosity and thermal conduction it is possible to receive the equation for dimensionless speed $V_i = V/C$, where V is speed of ions, before a front of a shock wave[2]:

$$\frac{d^3V_i}{dx_i^3}d^2 = (1-V_i)\frac{d^2V_i}{dx_i^2}MA +$$

$$0.5\left[M^2(1-V_i)-(1-V_i)^{-1}\right]\frac{dV_i}{dx_i}-0.5V_iM \qquad (1)$$

$x_i = \xi_1^{-1}(z-ct)$, $\xi_1 = V_s\nu^{-1}$; V_s, speed of ion sound, ν, effective frequency of elastic collision of ion with neutral particles; an influence of electron conductivity is taken into account [1], $d = D\xi_1^{-1}$; D, electronic Debye length; $A = 0.5\sqrt{5}T_iT_e^{-1}$, dimensionless factor of ion viscosity; $M = cV_s^{-1}$ is an ion Mach number. The dimensionless concentration of ions in a stationary wave has representation $n_i = (n/n_0)_i = (1-V_i)^{-1}$, here an index the zero marks a nonperturbed state. The equation (1) is received at an assumption, that the converse influence of charges to neutral particles is negligible. We shall show below that under certain conditions formation of areas with increased degree of ionization is possible. It is an area of strong return influence of charges on a neutral component and on a shock wave. For the solution of the equation (1) it is necessary to formulate three boundary conditions. For analytical solution one condition corresponds to limiting transition to nonperturbed state $V_i(\infty) = 0$. Yet two condition can be received from the solution of a closed problem in area behind of front ($x_i < 0$). But we shall be lower to proceed from idealization of complete blowing away of charges by front of a strong shock wave $V_i(0) \approx 2(\gamma+1)^{-1}$, where $\gamma \approx 1,4$ is the ratio of specific heat. The formulation of the third condition represent some difficulties. For example, it can be a principle of selection of the solution, satisfying to some attribute. At numerical integration of the equation (1) (for example by a method of Runge-Kutt) it is necessary to set all three boundary conditions at $x_i = 0$, but so that at $x_i \to \infty$ transition $V_i \to 0$ is realized. Thus, two conditions on derivatives $V_i'(0)$, $V_i''(0)$ should simultaneously provide limiting transition to undisturbed state and rule of selection of the solution. It is necessary to note, that at $d = 0$, $A = 0$ the equation (1) turns to the equation of the first order and in this case the solution of a physical problem should satisfy to two boundary conditions $V_i(0), V_i(\infty)$. In a case when M<1 there is the continuous solution, and when M≥1 the condition $V_i(\infty) = 0$ can be carried out only due to introduction of rupture [2]. Influence of dispersion $d \neq 0$ and viscosity A>0 results in smoothing of rupture in a plasma precursor.
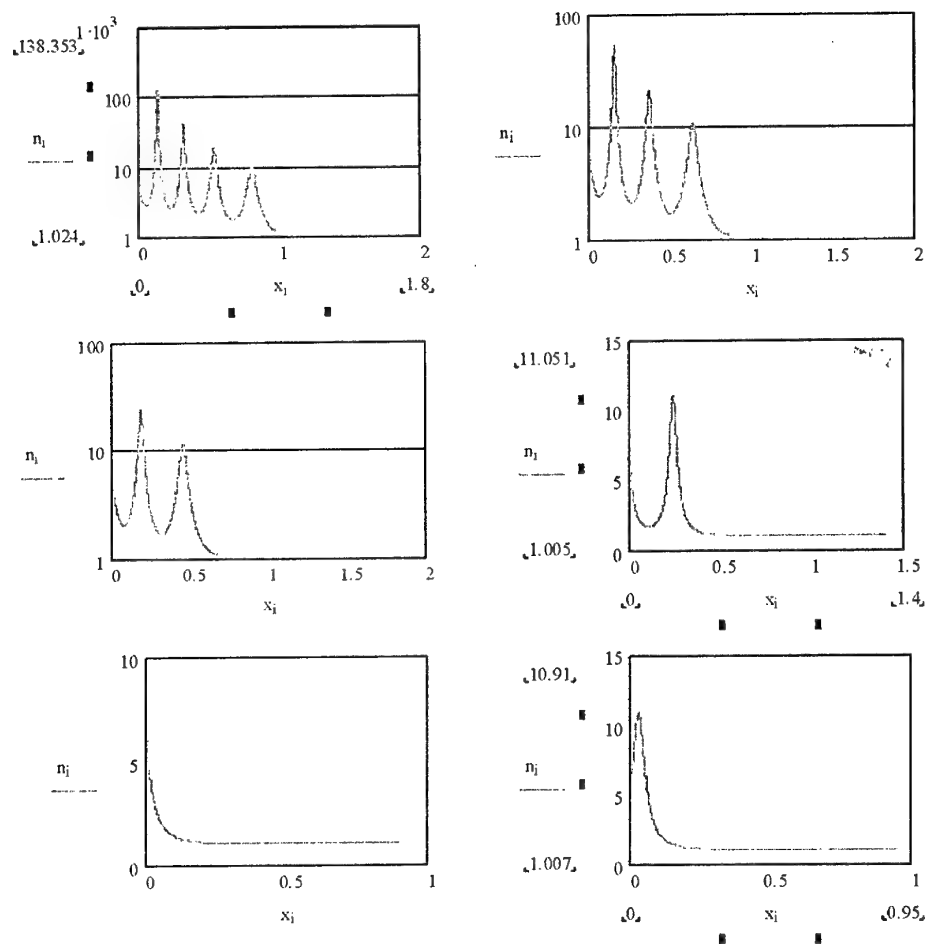
Fig.1. Precursors of different type; M=1.5, d=0.05, A=0.
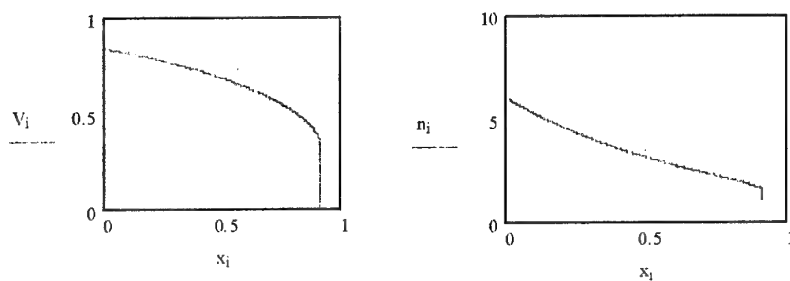
Fig.2. M=1.5, d=0, A=0

Construction of soliton can be ambiguous when a rule of selection was not used. In Fig.1 dependences $n_i = n_i(x_i)$ for a case of M=1.5, $d = 0,05$, $A = 0$ are presented. These diagrams show a basic opportunity of creation of precursors of a various type (with various number of maxima) at identical Mach numbers, identical dispersion and viscosity. Different precursors are realized at the different ways of excitation at the expense of creation of various boundary conditions on front $x_i = 0$. But these boundary conditions must secure nonperturbed state at $x_i = \infty$. Practical creation of various precursors at identical parameters d, A, M was not yet investigated. It is possible to formulate the rule of selection of the solution of this physical problem on the basis of analysis of properties of the

197

strict analytical solution of the equation (1) when $d=0$, $A=0$. In such situation representation $V_i(0)=5/6$, $V'_i(0)=-5M(36-M^2)^{-1}$, $V''_i(0)=30M^2(36-M^2)^{-2}$, takes place in front and functions $V_i(x_i)$, $n_i(x_i)$ are presented in Fig2.
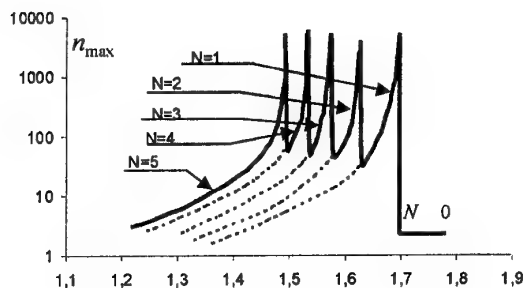
Fig.3. Precursor; d=0.05, A=0
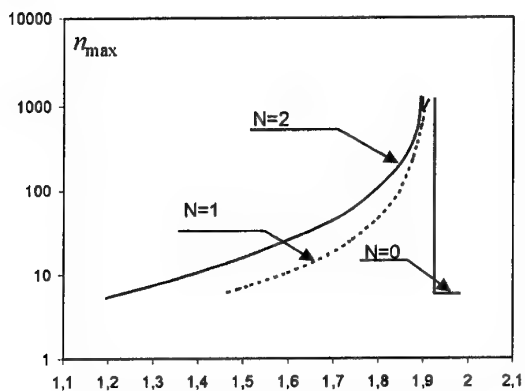
Fig.4. Precursor in glow discharge; d=0.13, A=0.05

There is the rupture of function V_i, x_i when $x_i \approx 0.9$. The role of senior derivatives in equation (1) has the most essential means for smoothing of a rupture in a situation when $d \neq 0$, $A \geq 0$. Hence a structure with the greatest steepness should be formed in a precursor here. There is the point of an inflexion of the diagrams here. Variant in Fig.1.1 corresponds to this condition. We shall look after evolution of this solution when ion Mach number increases. In Fig.3 dependence of size of the maximum value of dimensionless concentration n_{max} from M is shown. Parameter $N=5,4,3,2,1,0$ is represented number of maxima in a precursor. There is the precursor with five maxima when M<1.49. In a range of $1.49 \leq M \leq 1.52$ such perturbation is not present. It is probably to create a structure $n_i(x_i)$

with four maxima in this range of Mach number when the boundary conditions are changed sharply. For adopted idealization there is no smooth continuous transition from one solution to other. It is necessary jump change of a boundary condition for $V_i''(0)$. Thus a structure of perturbation is sharply reconstructed, a number of maxima decreases per unit, value of n_{max} sharply decreases. It is plasma analogue of hydrodynamic effect of "Houston horse". For the first time this effect for plasma was predicted in [2] on the basis of analytical estimations. There is the opportunity to construct the solution with three maxima when $M \geq 1.52$. Further increase of ion Mach number up to value $M=1.58$ results in the similar phenomenon, n_{max} is increased then due to sharp change of a boundary condition for $V_i''(0)$. When $M \geq 1.58$ creation of a structure with two maxima and so on is possible. At last a final collapse is occurs when $M \geq 1.72$ and monotonous structure will be formed. The dashed lines in Fig.3 represents situation which is realized at reduction of ion Mach number (there is original "hysteresis" concerning to change of parameter M). The account of influence of viscosity displaces effect to area of large ion Mach number. Thus a situation of a "main" maximum varies, it can place at in a forward and back part of precursor. Dependences $n_{max} = n_{max}(M)$ for specific conditions of the stationary glow discharge (pressure, P=40Torr; factor of ionization, $\alpha \sim 5 \cdot 10^{-6}$; $T_i \sim 1500K$, $T_e \sim 1ev$) are brought in Fig.4. These parameters correspond to values d=0.05, A=0.13. The real interaction of a supersonic body with plasma is more complex process, than interaction of a shock wave with plasma. In particular, trans-ion-acoustic regime of streaming over a body can be realized. Besides, perturbations of electrical field, created by a moving body, can generate an ion sound. The dependences in Fig.1-4 demonstrate a structure of an ion-acoustic precursor, created only by a bow shock wave. Its show that the bow shock wave in specific conditions can really be a source of a powerful ion-acoustic precursor, which have a strong influence on streaming over a body. It is necessary to note, that at the stage of previous to effect of "Houston horse" an area with increased degree of ionization will be formed. Therefore here display of strong influence of the charges on a neutral component of plasma is possible. Of course, thus an assumption about neglect by such influence, made at statement of a problem is broken. Construction of the solution in view of such interaction is the following stage of investigations.

198

References

1. V.A. Pavlov, Plasma Phys. Report, v.22, №2, 2000.
2. V.A Pavlov, Plasma Phys. Report, v.26, №2, pp.507-511, 2000.
3. V.A. Pavlov, Yu.L. Serov. Ion-acoustic model of streaming over body by weakly ionized plasma (pure and dusty plasma). The 2nd Workshop on magneto plasma- aerodynamics in aerospace applications. Moscow, 5 - 7 April 2000, pp. 125-127.
4. Y. Serov. Experimental Investigation of a Supersonic Sphere Motion in Plasma on Ballistic Apparatus. 2nd Weakly Ionized Gases Workshop. Norfolk, USA, 1998 pp32-44.
5. V.A. Pavlov, Yu. L. Serov. Supersonic Motion of a Body in Weakly Ionized Plasma: Phenomena of Trans-Ion-Acoustic Plasma Dynamics. 3rd Weakly Ionized Gases Workshop. Norfolk, USA, 1999, AIAA-99-4852.

36. A PRELIMINARY STUDY OF MICROWAVE, ITS GENERATION AND ITS APPLICATION ON SHOCK WAVE MODIFICATION

Xiujun Tang and J.D.Mo
The University of Memphis
Memphis, TN 38152

Alan S.Chow
NASA/Marshall Space Flight Center
Huntsville, AL 35812

K.X.He
Alabama A&M University
Normal, AL 35762

A preliminary study has been conducted on the microwave, its generation and its application to weakly ionize air for alternating shock characteristics in supersonic and hypersonic flight. A systematical review will be presented in the workshop on the feasibility of the shock wave modification of potential microwave length range and its related energy consumption. A one-dimensional shock wave modification model of weakly ionized air has been developed and the preliminary results well demonstrate the concept of shock wave modification.

37. TRANSONIC STREAMLINING OF PROFILE AT ENERGY ADDITION IN LOCAL SUPERSONIC ZONE

Yuriev A.S., Korzh S.K., Pirogov S.Yu., Savischenko N.P.
Mozhaisky Space Engineering University, St.-Petersburg

Leonov S.B.
IVTAN, Moscow

Ryizhov E.V.
SSRI, Moscow

Abstract. The aerodynamic characteristics of bodies change strongly at transonic speed range. These changes, as a rule, are negative and are determined by intensity and position of shock waves on a surface of streamlined bodies, mainly. At the same time several works have shown that the energy addition to supersonic undisturbed flow allows changing an intensity, form and position of shock waves significantly. Last circumstance has defined the purpose of the research - controlled modification of aerodynamic performances of bodies at transonic airflow by means of an energy addition to the local supersonic zones.

The outcomes of this examination, which have been made on the base of a numerical simulation of streamlining profile NASA - 0012 within the framework of model of inviscid gas, is presented in this paper. Some outcomes are confirmed by an experimental data. The streamlining of profile was investigated at Mach numbers 0.8-0.9. The distribution of gasdynamic parameters on a surface of profiled body has been obtained at different values of power of energy release, sizes of area of energy release and its position in local supersonic zone. Their influence on the form and position of shock waves is determined. It is shown, that in dependence on Mach number of a undisturbed flow the drag of the profiled body can increase and decrease at energy addition. The influence of an energy addition on lift, pitch moment and position of a center of pressure distribution for the body is explored also.

In [1-3] the analysis of physical processes happening at interaction of transonic stream of ideal gas to local area of heat release from a laser beam is executed. Besides in [1] it is scored, that at passing of a laser beam near to a surface of a plate located in transonic stream of gas, on it there is a force which is capable to influence on the aerodynamic moments. In [4] is shown, that at energy supply by means of homogeneous condensation of a water vapour in a local supersonic zone about a profile at M=0.8 and 0.87 can take place both growth, and reduction of drag depending on position of a shock wave. But, when the energy is brought thus, origin, the increase and quantity of allocated heat is determined by flow. Therefore in this case it is possible rather precisely to designate only coordinates of a beginning of condensation in a local supersonic zone at a profile. In same paper is concluded that the decrease of profile drag in transonic stream of ideal gas can achieve and at any other mode energy supply in a local supersonic zone. This decrease of drag is stipulated by deformation of shock-wave structure called by moving of the main shock wave upstream. Such moving is possible to see on photo 1, obtained in optical experiment executed by authors of this paper at study of influence of energy supply of surface electrical discharge in a local supersonic zone on transonic streamlining of a flat plate.

We investigated influence of parameters of an energy supply which is carried out in strictly restricted area in a local supersonic zone about a profile NACA-0012 at transonic velocities of an approaching flow, on distribution of gasdynamics parameters, position and shape of a shock wave, and also on aerodynamics coefficients. As varied parameters of the energy supply were received: value of a brought energy, coordinates and sizes of energy supply zone. The computational algorithm was under construction on the basis of a greed-characteristic method [5] and explicitly is described in [8]. It is necessary to mark satisfactory convergence of outcomes with the data of [6,7] (Fig.1).

During the conducted examinations dimensionless longitudinal coordinate and thickness of energy supply zone x_Q and h_Q varied in ranges 0.38-0.66 and 0.032-0.263 accordingly. The dimensionless specific power of energy supply $Q=q \cdot b/V_\infty^3$ ranged 0.156-1.248, which ensured saving a supersonic velocity after supply of a thermal energy. Here q - power brought to a mass unit of gas, b - chord of a profile.

201

a) without discharge ($M_\infty \approx 0,95$)

b) with discharge ($M_\infty \approx 0,95$)

a) without discharge ($M_\infty \approx 0,75$)

b) with discharge ($M_\infty \approx 0,75$)

Photo.1.

202
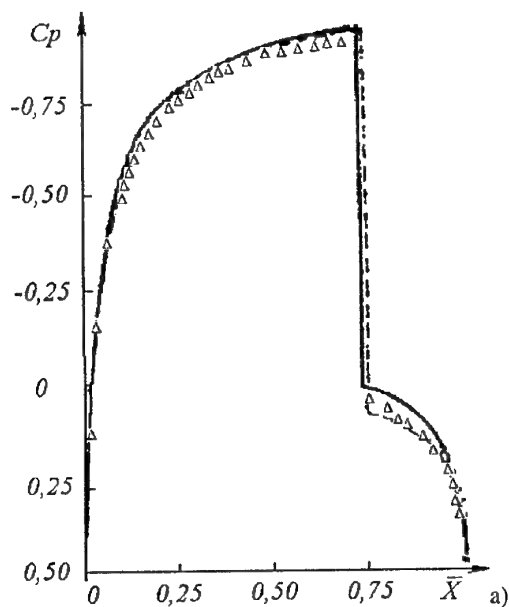
——— This method: grid 75×35 C_{x0}=0,0395
– – – Method [6]: grid 128×32 C_{x0}=0,0431
△ Method [7]: grid 188×24 C_{x0}=0,0387

——— Without energy supply
········· $\overline{O}_Q = 0,56$
– – – $\overline{O}_Q = 0,44$ $Q = 0,624;\ h_Q = 0,138$
– – – – $\overline{O}_Q = 0,38$
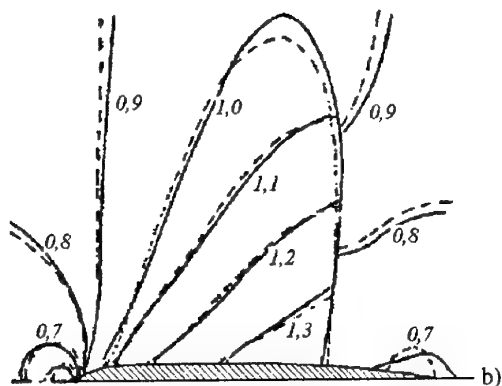
Fig.1. Comparison date of calculation and results of other studies at Q=0 for NACA - 0.012 and M=0.85, α=0 on a coefficient of pressure and levels of Mach numbers.

Fig.2. Influence of an energy supply zone place on distribution of parameters on a profile (M and ρ).

Discussion

The numerical studies have shown, that the supply of a thermal energy in a local supersonic zone about a profile reduces in formation of the channel with low density. The pressure in supply region varies unessentially (grows on 1-2%) owing to small values Q. Energy supply was executed at M_∞=0.8 and 0.85 at α=0, when local maximum Mach numbers in a supersonic zone about a profile lays within the limits 1.25-1.36. Because of a falling of a density there is a decrease of local Mach numbers before a shock wave and its displace upstream (Fig.2). The decreasing of shock

wave intensity reduces in pressure drop behind it (Fig.3). Thus, the modification of profile drag will happen owing to influence of two major factors: reduction of sizes of low pressure zone on central part of a profile (decrease of drag) and pressure decrease in its tail part (increase of drag).

As is known, at streamlining a profile NACA-0012 by transonic stream of ideal gas at M_∞=0.8 and α=0 the shock wave on a profile is in a point with coordinate x_{sw}=0.5. The conducted numerical examinations have shown, that in this case at any parameters of energy supply the drag coefficient of profile grows, as the pressure-fall area behind a shock wave affects a majority of a

203

Cp

-0,75

-0,50

-0,25

0

0,25

0,50

0   0,25   0,50   0,75 $\overline{X}$ a)
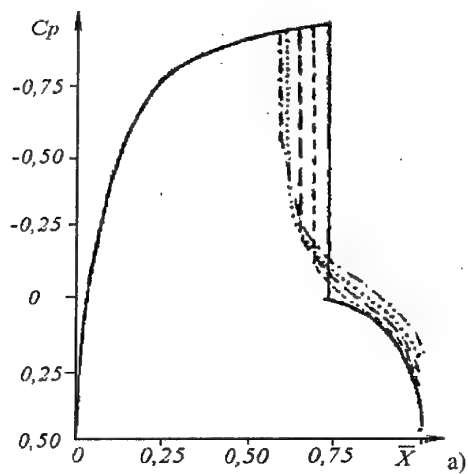
——— Without energy supply
- - - $Q = 0,312$
- - - . $Q = 0,624$
.... $Q = 0,936$ } $\overline{X}_Q = 0,44; h_Q = 0,138$
—·— $Q = 1,248$

b)

ρ

1,25

1,00

0,75

0,50

0,25

0   0,25   0,50   0,75 $\overline{X}$ c)

Cp

-0,75

-0,50

-0,25

0

0,25

0,50

0   0,25   0,50   0,75 $\overline{X}$ a)
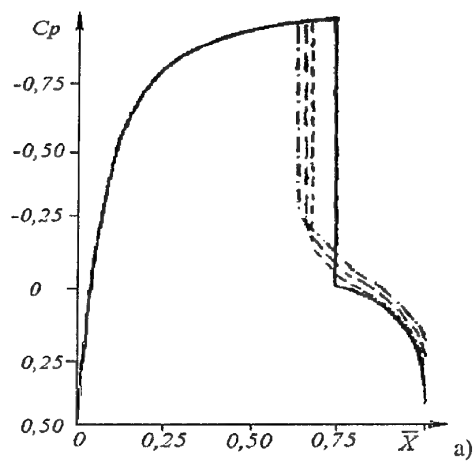
——— Without energy supply
.... $h_Q = 0,072$
— - - $h_Q = 0,138$ } $\overline{X}_Q = 0,44; Q = 0,624$
—·— $h_Q = 0,263$

b)

ρ

1,25

1,00

0,75

0,50

0,25
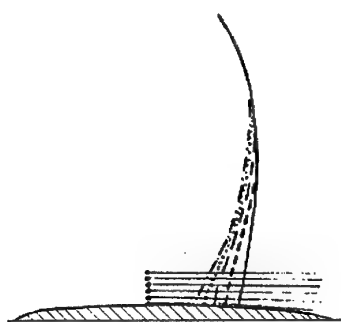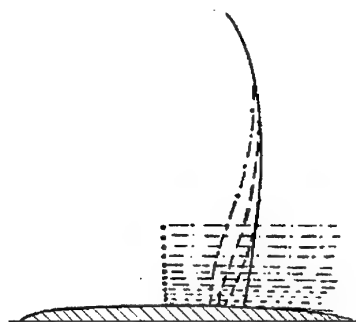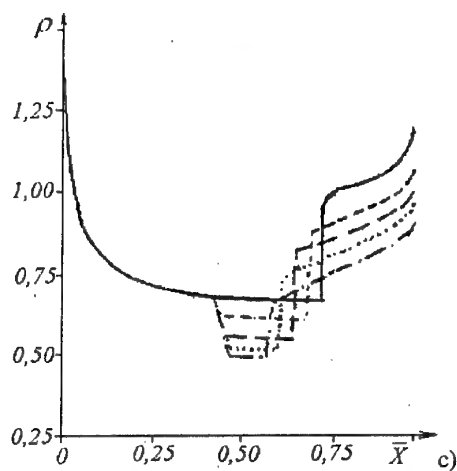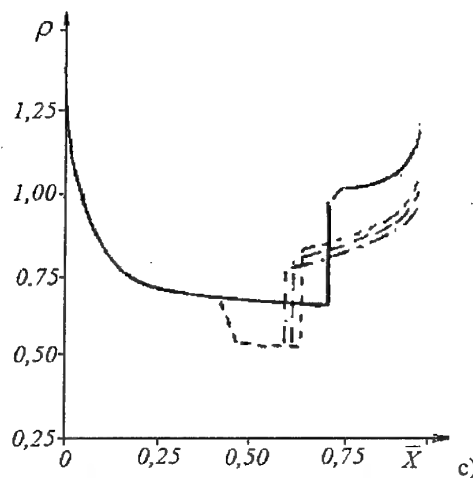
0   0,25   0,50   0,75 $\overline{X}$ c)

Fig.3. Influence Q on distribution of a coefficient of pressure on a profile, position and shape of a shock wave and distribution of a density.

Fig.4. Influence h_Q on distribution of a coefficient of pressure on a profile, position and shape of a shock wave and density distribution.

profile and exceeds influence on a drag coefficient of the first factor. The similar outcomes for this profile under the same conditions are obtained and in [4], at implementation of nonequilibrium condensation of a water vapour in a local supersonic zone. The outcomes of calculations on definition of influence of longitudinal coordinate x_Q on distribution of parameters on profile are shown in a Fig.2. It is visible, that value of a decreasing of a density and local Mach numbers weakly depend on this coordinate. Therefore in consequent calculations this coordinate was received constant and equal 0.44. Such value was selected with the purpose to shun interception of shock wave and energy supply zone in case of maximum displace of a shock wave upstream. Besides the numerical experiments were conducted which have shown, that in a case energy supply in several points on axis x, distribution of parameters on a profile and position of a shock wave are determined by value of increase of an entropy behind last point.

The character of influence Q on distribution of a coefficient of pressure on profile, density and on position of a shock wave is shown

in a Fig.3. On figure it is visible, that at increase Q the density before a shock wave (and also local Mach numbers and intensity of a shock wave) decrease, that promotes more strong deformation shock wave in its lower part and pressure decrease behind it. The central part of a shock wave displaces to a lesser degree. But if increment of a falling of a density and displacement of shock wave in a zone of influence energy supply, since some threshold Q, decrease, the pressure behind a shock wave decrease stronger. It determines character of relation ΔC_x and x_{sw} from Q (Fig.5).

The influence of energy supply zone thickness h_Q on gasdynamic parameters is exhibited a little otherwise. On Fig.4 can see, that at Q=const with growth h_Q the shock wave displaces upstream, but the change of its coordinate is stipulated by not so decreasing of a density, and deformation on a major part of a shock wave. The falling of pressure behind shock wave happens owing to a drop of its intensity the same as and in case of influence Q. The dependency parameters from energy supply zone thickness are shown in a Fig.6.
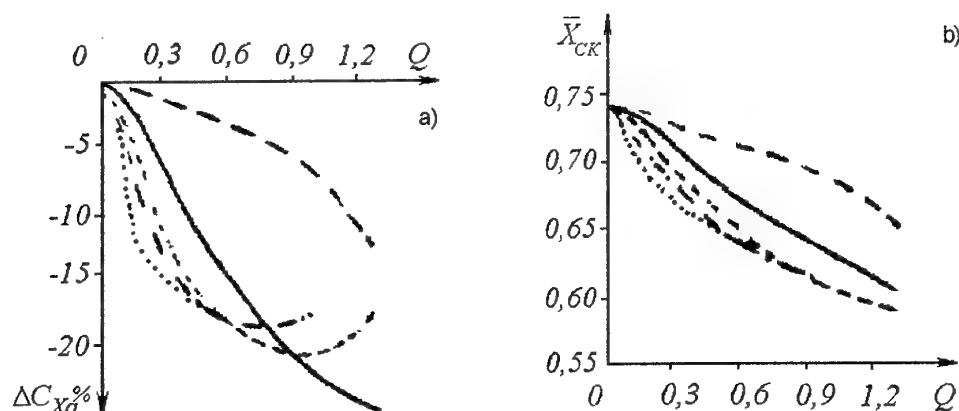
Fig.5. A modification $\Delta C_x=[(C_{xQ}-C_x)/C_x]\times100\%$ and coordinates of a shock wave on a profile x_{sw} depending on Q.
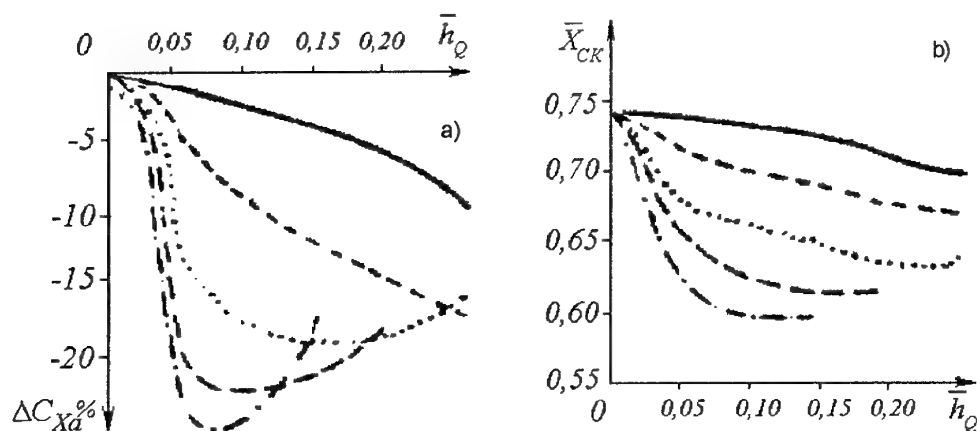
Fig.6. A modification ΔC_x and x_{sw} depending on h_Q.

205
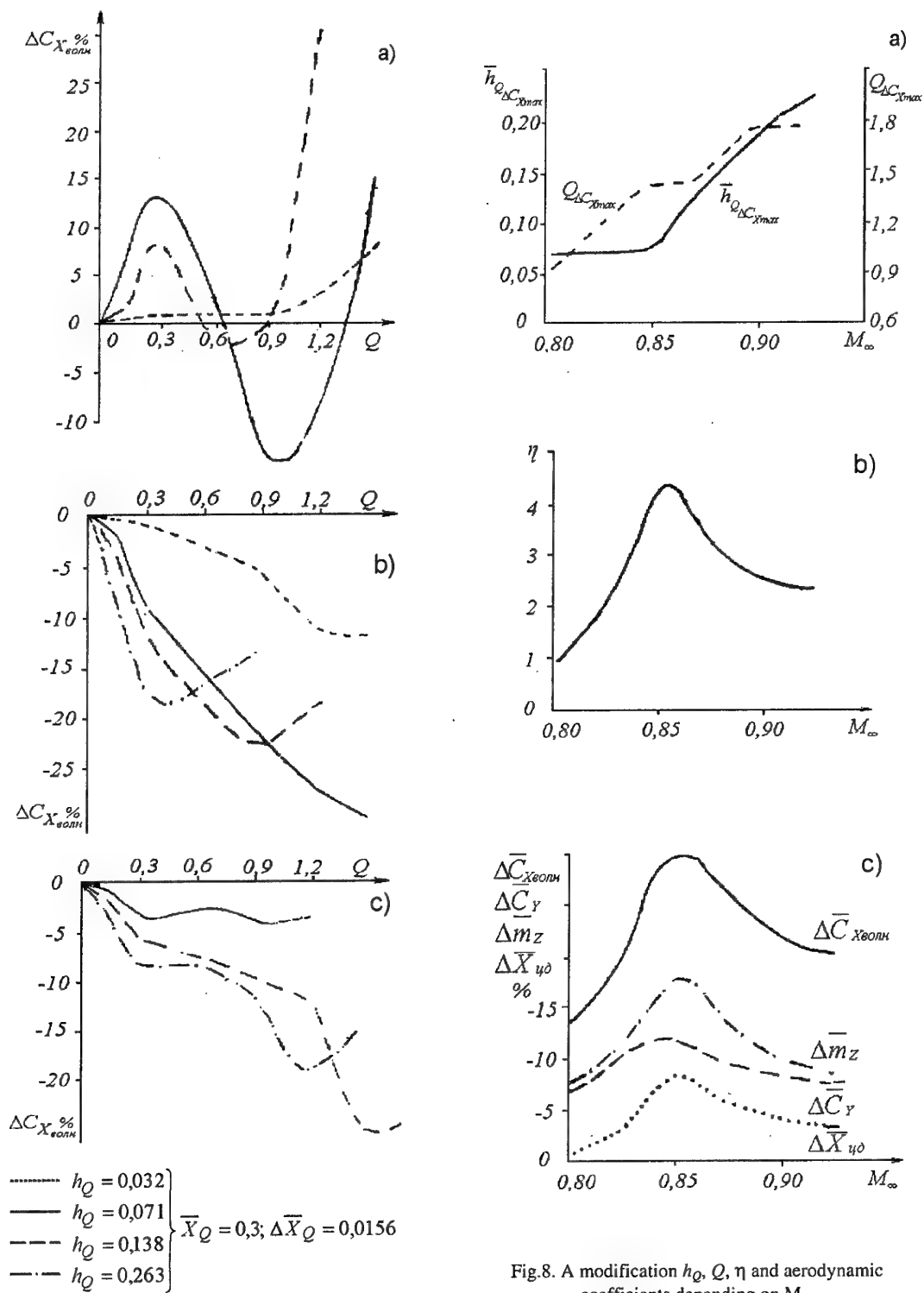
Fig.7. Influence Q on ΔC_x at different number M_∞

$$\begin{array}{l}
\text{.........} \quad h_Q = 0{,}032 \\
\text{———} \quad h_Q = 0{,}071 \\
\text{- - -} \quad h_Q = 0{,}138 \\
\text{-·-·-} \quad h_Q = 0{,}263
\end{array} \right\} \; \overline{X}_Q = 0{,}3; \; \Delta\overline{X}_Q = 0{,}0156$$

Fig.8. A modification h_Q, Q, η and aerodynamic coefficients depending on M_∞.

View of dependencies ΔC_x from Q and h_Q (the Fig.5 and 6) speaks about a capability of selection of best values of parameters energy supply, at which the increase of a scoring in drag with minimum energy expenditure is ensured. So, for reaching noticeable decreasing of a drag coefficient on 15-25% it is most expedient to execute energy supply at $h_Q=0.07$ and $Q=0.6-1.2$. The similar character of dependency ΔC_x from value of a brought energy Φ_0 (parameter of a relative humidity) is obtained and in [4] for a profile as a circular aerofoil with $C=0.1$ at M=0.87 and $\alpha=0$. There maximum scoring in drag made about 30% at $\Phi_o=50\%$.

Thus, the conducted numerical experiment has confirmed conclusions [4] that for a decrease of profile drag in transonic stream of ideal gas at energy supply in a local supersonic zone it is necessary, that the shock wave in initial flow placed closer to a trailing edge. In the present study it was possible to receive a decrease C_x on 25% at arrangement of a shock wave on a profile in a point with coordinate $x_{sw}=0.75$ (NACA - 0.012, $\alpha=0$, M=0.85).

The total dependencies energy supply parameters, index of energy effectiveness and relative modifications of aerodynamic coefficients of a profile from a Mach number are shown in a Fig.7,8. From figure it is visible, that for reaching maximum ΔC_x, specific power and thickness of energy supply area with increase of a Mach number should be augmented, though the rate of their increase at big M_∞ decrease because of stabilization of values of local Mach numbers. The index of energy effectiveness $\eta=\Delta X \cdot V_\infty / N$ (N - power energy supply) reaches values 2.5-4 on conditions, where the crisis phenomena and wave drag become essential. It allows to make a conclusion about presence of a principled capability of reaching of energy profits at enough high coefficient efficiency of energy sources. To the greatest degree on all Mach numbers the wave drag varies. Decreasing m_z

and the displacement of centre of pressure upstream can promote a decrease of expenditures on balance, and decrease C_y should be indemnified to other tools (for example, increase of an angle of attack at value about fraction of degree). Maximum values η and ΔC_x are reached at $M_\infty=0.85$, that is explained by an optimum ratio between position of a shock wave and its intensity in this case.

Referancies

1. Belokon V.A., Rudenko O.V., Hohlov R.V. Aerodynamic phenomena at supersonic streamlining of a laser beam // Acoustic Journal, V.23, 4, 1977.
2. Fedorchenko A.T. About generation of nonlinear waves in a supersonic stream by a volumetric source of heat release // Acoustic Journal V.32, 2, 1986.
3. Krasnobaev K.V. Supersonic streamlining of feeble sources of radiation. // Izv. ÀS USSR, MLG, No.4, 1984.
4. Shnerr G.H., Dormann W. Transonic flow about profiles at presence of processes of a relaxation and energy supply called by homogeneous condensation // Aerospacc technics, No.2, 1991.
5. Magometov K.M., Holodov A.S. Greed-characteristic methods.- M.: "Nauka", 1988.
6. Computational methods of flow (streamlining) of devices of flight vehicles at transonic velocities. // ONTI TsAGI, Reviews. No.685, 1988.
7. Dadone A., Moretty J. An effective computational method transonic streamlining of profiles on the basis of equations of the Euler // Aerospace technics.-1989, No.4.
8. Korzh S.K., Yuriev A.S. Influence of thermal energy supply parameters on drag of a profile in transonic stream of ideal gas. // Scientific notes of TsAGI, No.3-4, 1995.

38. ACOUSTIC-ELECTRIC CARCINOTRON IN NONSTEADY SUPERSONIC PLASMA AERODYNAMICS

V.M. Gubchenko, V.G. Bondarenko, M.L.Khodachenko, V.E. Semenov, V.P. Denisov, A.V. Kozlov
Institute of Applied Physics RAS, Nizhny Novgorod, Russia
(ua3thw@appl.sci-nnov.ru)

Abstract. We proposed the AEC (acoustic –electric carcinotron) - a new wavy flying device for unsteady supersonic plasma aerodynamic development. Main feature of the AEC is an active role of internal degrees of freedom of a body in a supersonic flight. The AEC strongly interact with sonic modes of air by MHD forces. As a result new media with new wave and dynamical properties forms around and at resonance conditions we have radical change of drag-jet characteristics of a body.

1. We are studying theoretically and in a laboratory experiment the idea to create a new supersonic device which we call an acoustic-electric carcinotron (AEC) which in a supersonic regime of motion or supersonic flows inside a nozzle with $M = 2 \div 10$, does not radiate acoustic waves, or forms a shock around and shock wave wake inside and has a decreased and variable in value and sign drag force. Traditional way of steady ($\partial / \partial t = 0$) supersonic aerodynamics has natural limits in growing pressure, heating at the body and shock wave radiation losses. Steady MHD has very limited affect on aerodynamics with tuning of a given mechanical system to optimal conditions of a flight. New possibilities opens unsteady ($\partial / \partial t \neq 0$) supersonic plasma aerodynamics MHD.

2. According to a liner approach the value of the wave energy losses by an ideal thin supersonic body in ideal gas is defined by an aerodynamic coefficient $c_x = \delta / \sqrt{M^2 - 1}$ (δ - is a form factor of the body). The dimensionless coefficient c_x is a ratio of a drag force F_x and dynamical pressure of a flow $F_V \propto V^2$ on a body. In particular, c_x shows absence of losses in a subsonic regime, $M = V / c_s \ll 1$. This effect is known as a d'Alambere limit. Besides, similar regime can also be realized by increase of the sound velocity c_s via local heating by dissipation or ionization in a supersonic regime of flight and it is now a traditional way to decrease a drag force on a body in plasma aerodynamics.

In our device we try to reproduce somewhat more interesting and new limit, $M \gg 1$, where again we are in a regime with no energy losses ($F_x \to 0$) and a value of aerodynamic coefficient $c_x \to 0$. The regime with $M \gg 1$ can be realized in two ways. The first, evident, but with no practical interest way is to increase the velocity of a body $V \to \infty$. This will increase the dynamical

pressure and as a result $F_x \to \infty$. The second and a new way is to decrease locally the sound velocity in a medium $c_s \to 0$ while keeping velocity of a body V corresponding to the supersonic range, $M = 2 \div 10$, for parameters of the medium on a far periphery. In this case, which we call a hypersonic d'Alambere limit we have $F_x \to 0$.

To realize hypersonic d'Alambere limit $M \gg 1$ flying in range $M = 2 \div 10$, we propose a supersonic unsteady ($\partial / \partial t \neq 0$) system which we call as the AEC, and which is formed by coupling via plasma envelope of air sonic modes and a body through activation of a body internal degrees of freedom. As a newly formed media this system has its special dispersion properties $\omega(k)$ different from dispersion properties of initial background ideal gas $\omega = \pm k c_s$. We consider the AEC formed by a hypersonic body with a long wave line of electromagnetic oscillators onboard surrounded by a weakly ionized gas. Due to conductivity we have inductive interaction of fast (+) and slow (-) modes of the long line $\omega = \pm \omega_0 + kV$ in the AEC with direct (+) and return (-) acoustic waves. Under the resonance conditions when phase velocity $V_{ph} = \omega / k$ of a gas mode and one of the line mode are the same we have strong linear and nonlinear interaction and strong modification of dispersion properties of the system. In particular, strong decrease of group velocity of waves $V_{gr} = \partial \omega / \partial k$ in comparison with sound velocity c_s takes place which corresponds to the limit $M_{eff} \to \infty$ realized near the body. In this case we have slippage of the wavy body through a gas.

There are four interesting resonances with sonic modes (we exclude here consideration of resonances with curl modes of a gas). The most important among them is a resonance of a fast wave of the line with a return wave of the gas (a carcinotron case). In our theoretical study as an AEC we consider a special travelling wave type
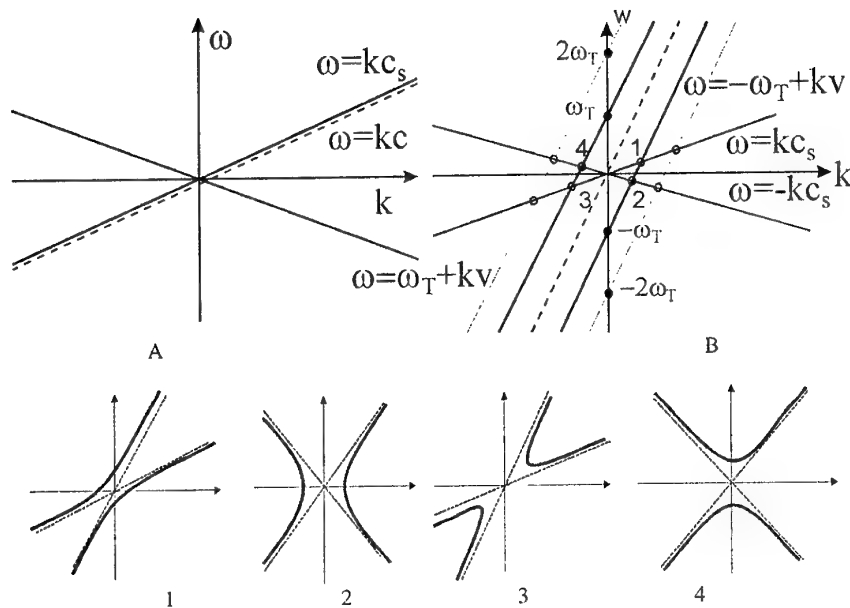
Fig.1. Dispersion curves $\omega = \omega(k)$ of the system formed by gas and a body. (A). Dispersion curves of direct (+) and return (-) sound waves $\omega = \pm k c_s$, dotted line correspond to a steady body $\omega_b = k V_b$. (B). Dispersion curves of direct and return sound waves with lines corresponding to a dynamical body including harmonics of $\omega_b = \pm \omega_0 + k V_b$. Resonances of wave phase velocities are in points 1,2,3,4. Structure of dispersive curves in resonant points shown on corresponding figures1,2,3,4.

body in a working regime turned to this type of resonance. In other resonances different limiting cases can be realized, including, in particular, the case of $M_{eff} \to 0$ but with no dissipation and heating. The main feature of the AEC with traditional hypersonic system is its dynamical (unsteady) nature ($\partial / \partial t \neq 0$) with internal degrees of freedom activated ($\omega_0 \neq 0$) – flow of a gas remains non-stationary and oscillating in any coordinate system and its complex dynamics gives possibility for the resonance interaction.

Our AEC is an acoustic analog of the EMC – the electromagnetic carcinotron. As an analog of the EMC's oscillating electron beam in the AEC appears the onboard long line. The electromagnetic analogs of sound modes in the AEC are slowed electromagnetic modes of the EMC resonator.

For modeling of the AEC idea, described above, we constructed plasma aerodynamic set-up of a standard type. The set-up consists of a Lavale nozzle, producing a supersonic flow in a tube where experiment is organized. The supersonic flow is ionized by a HF discharge and after that the flow interacts with LF travelling wave fields from phased coils around a tube. We discuss our former, current and planned future experiments with our set-up.

3. From principles of basic physics we argued a possibility for a new trend in supersonic aerodynamics with radiation free dynamical devices and propose a way for its realization in a particular type of such device.

Acknowledgements

References

1. V.M. Gubchenko et all. Proc. of the 2nd Workshop on Magneto-Plasma Aerodynamics in Aerospace Applications, IVTAN, Moscow 2000, p.313-317
2. M.V. Nezlin. Uspekhi Fiz. Nauk, Vol. 120, No 3, p.481-495, 1976.
3. A.V. Gaponov-Grekhov, I.S. Dolina, L.A. Ostrovsky. Doklady AN,Vol 268, No 4, p.827-831, 1983.
4. G.B.Whitham. Linear and Non-linear Waves. John Wiley & Sons, 1974.
5. M.I. Rabinovich, D.I. Trubetskov. Introduction to Theory of Oscillations and Waves. "Nauka", Moscow, 1984.

209

39. ANOMALOUS RELAXATION OF SHOCK WAVES AND ANOMALOUS STREAMING OVER BODY BY WEAKLY IONIZED COLLISION PLASMA

V.A.Pavlov
State University

Yu.L.Serov
Ioffe Institute, St-Petersburg

Abstract. Ion-acoustic model of nonthermal plasma influence on a shock wave and streaming over a body by plasma is considered. Proposed model permits to explain a phenomenon of anomalous relaxation of a strong shock wave and to calculate a range of Mach number in which this phenomenon exists. An explanation of effect of anomalous streaming over a body by plasma is offered. An experimental confirmation of the effects of nonlinear plasmadynamics is received.

At the moment many researchers undertake unsuccessful attempts of plasma (nonthermal) influence on shock waves (SW). However, such influence is possible only at fulfilment of some conditions. At a movement of a weak shock wave plasma behaves as usual heated up gas. Some weak effect, connected with additional internal energy of atoms and molecules, can also be observed. However, plasma is dispersion medium and the strong nonlinear effects begin to be displayed at large amplitudes of perturbation when a strong shock wave propagates. These effects influence on structure of a shock wave and its have been observed in practically important range $V \geq 700 m/s$.

The stratification and instability of a strong SW was observed by many researches(see for example[1-5]). This phenomenon was accompanied also by strong turbulization and instability of a flow behind a shock wave [3]. Anomalous streaming over a supersonic body was observed also in ballistic experiments at plasma formation in result of excitation and dissociation of freon in a bow shock. Anomalous streaming over a body in discharge plasma was observed in ref [6,7]. The presence of dusty particles in plasma results in even more strange nonlinear effects at a movement of a body in plasma. The specified effects have a nonthermal nature and can be explained within the framework of ion-acoustic plasma dynamics, taking into account strong nonlinearity of dispersion medium, which is plasma. In a neighbourhood of sharp front system of equations of three component plasma dynamics in view of nonlinearity, ion-neutral collisions, viscosity and dispersion results in the equation of Sagdeev for potential of electrical field [8,10]. This equation has a soliton solution when $1 < M_i \leq M_*$, where M_i is the ion Mach number, $M_* \approx 1,6$. In usual Mach numbers this condition looks like $\theta \leq M \leq 1,6\theta$; $\theta = V_{is}/V_s$;

$V_{is} = \sqrt{T_e/m_i}$, where V_s is speed of a sound; T_e is electronic temperature, m_i is mass of ion.

The amplitude of soliton grows and there is the explosive instability when ion Mach number approachs to the value of 1,6 (see [8,10]). There is the stratification, instability and destruction of a shock wave in result of strong interaction of charged particles in soliton with a neutral component. Soliton collapse takes place and the shock wave assumes a usual state when $M > 1,6\theta$. Concentration of electrons, ions and exited particles grows in zone of relaxation at a movement of a strong shock wave. There is a photoionization in area of shock front. Kinetics of excitation, ionization and heating of electrons at a movement of a strong SW in inert gases is well known . The main channel for reception of fast electrons($\varepsilon > 4ev$) is collision of atoms exited on a resonant level. Additional heating of electrons occurs at the expense of collision of electrons and exited atoms. The basic equations, resulting in formation of fast electrons at a movement of shock wave in inert gases are wrote in table 1. It is possible to neglect by the doublet structure of terms of argon atoms. Here at the collision of two exited atoms we take into account basically the first resonant level with much above settling, then settling of the second resonant level. Each of reactions results in occurrence of group of fast electrons with certain energy, and it results to swing of oscillations in plasma. The certain ion-acoustic speed and range of Mach number, in which an ion-acoustic soliton can exist, corresponds to group of electrons with identical energy (see tab.1). The concentration of exited atoms on the second resonant level can be significant at large Mach numbers, and then this level should be taken into account. Thus, the certain ion-acoustic mode corresponds to each of reaction. An amplitude of soliton increases in

Table 1. Ionization of atoms and electron heating in a shock wave.

	V_{is} km/s	Area of soliton existence ΔM
Xenon		
$A^* + A^* \rightarrow A^+ + A + e$ [4.73ev]	1.84	10.5 16.8
$A^* + e \rightarrow A + e$ [8.4ev]	2.5	14.3÷23
e [9.52ev]	2.62	15÷24
$A^+ + e$ [4.73ev] $\rightarrow A + e$ [13.07ev]	3.1	17.7÷28.4
e [14.25ev]	3.22	18,4÷29.5
Argon		
$A^* + A^* \rightarrow A_2^+ + e$ [8.74ev]	3.24	10.3÷16.2
$A^* + A^* \rightarrow A^+ + e$ [7.48ev]	4.2	13.1-21
$A^* + e \rightarrow A + e$ [11.62ev]	5.3	16.6-26.4
$A^* + e$ [7.48ev] $\rightarrow A + e$ [19.1ev]	6.75	21-33.7
Neon		
$A^* + A^* \rightarrow A^+ + e$ [11.66ev]	7.45	16.8-27
$A^* + e$ [11.66ev] $\rightarrow A^+ + e$ [6.71ev]	5.65	12.7-20.4
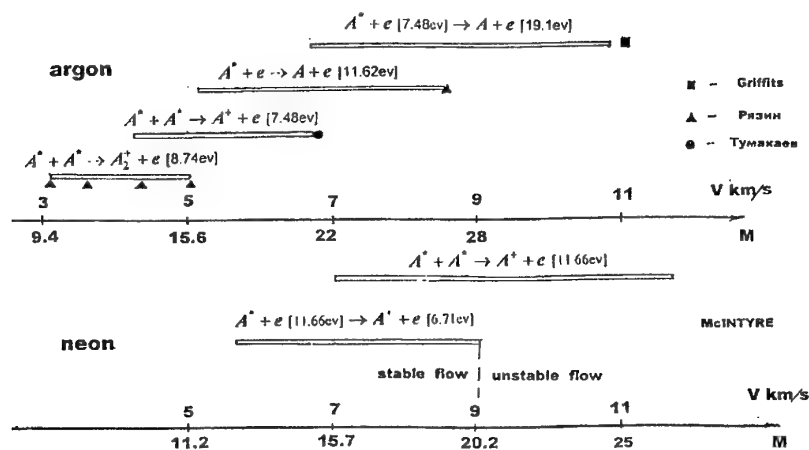
Fig.1a. Structure of ion-acoustic modes in argon and neon; points-[Griffiths et al. J.PhysD:Appl.Phys.1976,9, p.1681], [5], [3] , [Tumakaev,Zh.Tech.Fiz.52(11), 1982, pp.2305-2306].
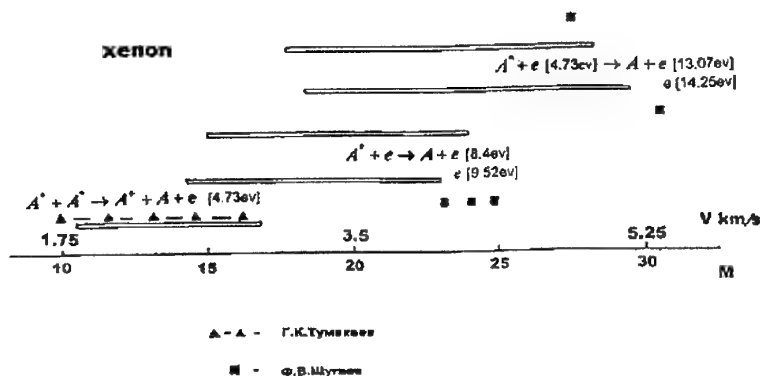
Fig.1b. Structure of ion-acoustic modes in xenon; experimental points from ref.[4] (Г.К.Тумакаев) and from report of MSU №277 (1979),theme 29\79 (Ф.В.Шугаев)

211
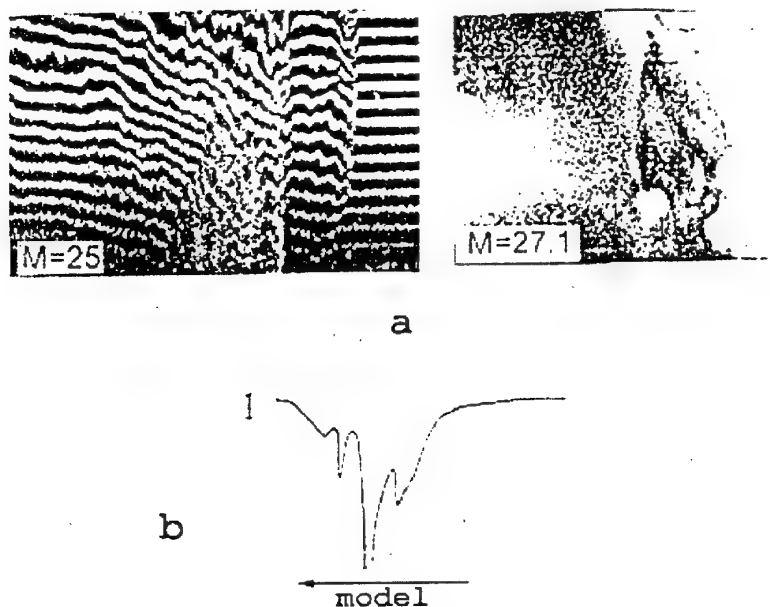
Fig.2. Anomalous phenomena in shock heated xenon plasma
a)   shock tube, photo of F.V. Shugaev (1979); shock wave moves from the left
b)   ballistic apparatus; signal of radiation from photomultiplier, sphere, $M = 13$, soliton package on a front (from the left) of a bow shock.

accordance with increase of speed of SW. The concentration of charged particles in soliton grows on many orders and it begins to interact with a neutral component of plasma. The diagram in Fig.1 shows a mutual arrangement of ion-acoustic modes on axis of speeds for each of considered reactions. It appears that the borders of ion-acoustic modes coincide with the borders of "anomalous relaxation" of strong shock waves.

Anomalous relaxation.

The name "anomalous relaxation" usually mean a complex of the phenomena, accompanying the propagation of strong shock waves [1-5]. These phenomena are observed in plasma, formed at ionization of medium by a shock wave. There are the flares of radiation, nonmonotonous distribution of electron concentration and of medium density behind a front of SW, there are the precursors, then there is the stratification and even destruction (Fig.2a) of shock front [4,5]. The specified effects have threshold character and are observed in certain ranges of Mach numbers. However, it is possible to note that the beginning of a range is diagnosed in rare cases, and usually the high-speed border is determined, where there are strongest "anomalies" resulting in a stratification and destruction of a shock wave.

On the diagram in Fig.1 the experimental points indicates the borders of ranges of anomalous relaxation received by the various authors. The borders of ranges concur with the borders of ion-acoustic modes with accuracy ~ 4%. This concurrence and also character of processes testify that "anomalous relaxation" is display of strongly nonlinear dynamic properties of plasma [8,10] in a range of ion Mach number $1 < M_i \leq 1,6$. In experiments [4,5] it was possible to determine rather precisely the top and bottom borders of the first range of "anomalous relaxation", connected with collision of two atoms exited on the first resonant level. The flares of radiation, observable at "anomalous relaxation" actually represent the ion-acoustic solitons, arising at interaction of a SW with plasma. A burst of concentration of charged particles and a growth of density, connected to interaction of soliton with a neutral component of plasma begin to be registered when an amplitude of soliton increases [8]. The bursts of radiation (ion-acoustic solitons) are registered by the authors in ballistic experiment at Mach number M=13 (Fig 2b). There are soliton package, consisting from two ion-acoustic soliton on forward front of a signal from photomultiplier. The waves of charge in similar conditions are registered also in our work [9]. The large Debye lenght on significant distance from a body has allowed directly to observe an ion-acoustic soliton in collision dense plasma. The top value of ion Mach number $M_i \approx 1,6$ is not quite exact and depends on viscosity of medium and on

frequency of ion-atom collisions. The range of pressure, at which experiments of the various authors were made, is rather wide. There fore the observable deviation C~ 4% of borders of calculated ion-acoustic modes from the borders of anomalous relaxation is quite allowable. Moreover the experimental measurements are discrete and not always precisely coincide with border of effects. Plasma forms by the shock wave in a case of propagation of a strong shock wave. However, it is possible to create plasma by the gas discharge on a way of a shock wave. In this case the similar "anomalous" effects can be observed at lower speed, if we shall get to a range $1 < M_i \leq 1{,}6$.

Ballistic experiment.

We fulfiled an experimental investigation on ballistic apparatus in xenon plasma of glow discharge. The results of measurements of standoff distance of a bow shock wave in ion-acoustic mode are presented in Fig.3. An anomalous streaming over a body is observed. The standoff distance in plasma much exceed this in xenon, heated up to appropriate temperature ~1000K in plasma. The normal flow is restored on a border of ion-acoustic mode when =2,2 ev. It is measured electron temperature. T_e. It is possible to note some distinctions. In experiments with the strong shock waves an anomalies are accrued at increase of shock speed. In ballistic experiments a standoff distance decreases. This distinction is connected to reduction of electron temperature near a surface of a body. Actually in ballistic experiment we should consider not one ion-acoustic mode, but ion-acoustic continuum of modes, appropriates to distribution of electron temperature near a body. In accordance with increase of speed we gradually leave some modes of continuum and the effect weakens, though inside of one mode it accrues. It is necessary to note, that for realization of anomalous regimen of streaming over a body a combination of a number of conditions is necessary. Thus an anomalous relaxation of strong shock waves and anomalous streaming over a body by plasma have an identical nature and are connected to display of nonlinear dynamic properties of plasma. These nonlinear effect can be displayed also at a movement of meteors (head echo, flares, splitting) and in any technical devices with the high-speed

movement of pure plasma V>700m/s, or in low – speed plasma(V>0) with heavy ions or with dusty particles (engines, MHD-channels).
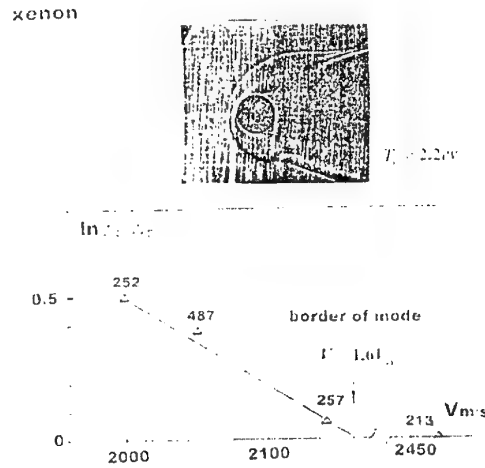
Fig.3.Anomalous streaming over a body by plasma of a glow discharge; xenon + 10% air; Δ_p is a standoff in plasma, Δ_T is a standoff in hot air.

References

1. R. Fowler, G. Paxton, H. Hughes, Phys. Fluids 4, 234 (1961)
2. Houwing A. F., McIntyre T. J., Taloni P. A., Sandeman R. J. 1986, J. Fluid Mech. 170, 319-337
3. T.J.McIntyre, A.F.Houwing, R.J.Sandeman, H.-A.Bachor, J. Fluid. Mech. (1991), 227, 617-640
4. G.K.Tumakaev, Z.A.Stepanova, P.V.Grigorev, Sov. Phys. Tech. Phys. 31(1), 1992, 37-41.
5. S.Aslam, A.Rjazin, Vestnik Mosc. Universit. Ser.3, 1984, 25 (1), 94-96
6. G.I.Mishin, Y.L.Serov, I.P.Yavor, Sov. Phys Tech. Phys. 36, 972 (1991)
7. Yu. Serov, Proc. 2nd Weakly Ionized Gases Warkshop, Norfolk, 1998, pp. 32-34.
8. V.Pavlov, Yu.L.Serov, AIAA-99-4852.
9. Yu.Serov, I.Yavor, Tech.Phys. 41(11) 1996, 1183-1185
10. V.Pavlov, Plasma Phys. Rep. v.26,6, 2000,507-511

213

40. INVESTIGATIONS OF PLASMA JET INTERACTION WITH POLYMERIC MATERIALS

Bychkov V.L.

Institute for High Temperatures of Russian Academy of Sciences,
13/19 Izhorskaya Str., 127412 Moscow, Russia

Bychkov A.V., Timofeev I.B.

Lomonosov Moscow State University, Moscow, Russia

Abstract. Investigations have been carried out on the purpose of studies of plasma interaction processes with polymeric materials and vapors of high polymeric substances. Two types of plasma generators, namely plasma dynamic and capillary have been applied. Experiments on creation of long-lived luminous objects (LLO) at application of these plasma generators have been carried out. Different modes of plasma interaction with the polymer material surfaces have been realized. An ignition of paraffin vapors has been realized. Two types of LLO were obtained.

Introduction

Questions of plasma jet interaction with polymeric materials are of interest in connection with applications at plasma jet use for an ignition of different organic materials and at creation of long - lived luminous objects (LLO) [1-4]. However experimental information on interaction of plasma jets with such materials as paraffin, organic resins, cellulose and their vapors is practically absent. Questions of LLO nature and their creation are relevant during last twenty years, they require development of new experimental approaches based on heterogeneous, in particular polymeric, nature of these objects.

The target of this work is the investigation of such plasma jet interaction at the application of two types of plasma generators, namely, the plasmadynamic and erosive capillary ones. Also the possibility of LLO creation at their application has to be investigated.

Experimental Studies

Plasmadynamic discharge with the following characteristics was used as the first plasma generator: I_{max}~20kA, U_{work}=4.5kV, τ_{pulse}~20μs, detailed information about this plasma generator is represented in [5]. Interaction of this discharge with the cellulose surface (a paper with density 80g/m^2, 80μm thick), plates of paraffin, 0.5-5mm thick, and aluminum foil 50μm thick took place from the distance 5-50mm between the nozzle and the sample's surface.

At interaction of its jet from the distance 5-30mm the destruction of the paper sample with the appearance of 1 mm diameter hole took place, the same interaction with the aluminum foil sample lead to melting of its surface and creation of ~0.5mm diameter hole. Destruction of the paraffin sample took place at the sample's width smaller than 1mm, at the bigger thickness the paraffin's surface was melted without other observed traces. The thickness of the evaporated paraffin layer was 0.4-0.5mm.

A number of experiments was devoted to investigation of paraffin's vapor ignition. In experiments paraffin's vapor was obtained at heating of paraffin up to boiling temperature. During experiments the temperature of the air-paraffin's vapor mixture was about 50-70°C in the place of plasma jet-mixture interaction 5cm over the paraffin surface.

Ignition of the mixture took regularly place during τ_{ig}<< 20 ms in experiments with plasmadynamic discharge. Its combustion took place over the dish during τ_{comb} ≤20 ms. In a number of experiments the motion of flame up to height $h\approx$ 50 cm in open air was observed. It indicated the height of vapor's mixture ascending.

The capillary erosive discharge was used as the second plasma generator. Its characteristics were the follows: I_{max}~100-150A, U_{work}~340V, τ_{pulse}~6-14мc, $W\approx$200J. Detailed information about this plasma generator and some properties with capillary in PMMA is represented in [1-3]. PMMA (organic glass), paraffin, mixture of paraffin with resin and with milled wood, mixture of technical wax with milled (pine-tree) wood in ratio of components (over volume) 1:1 were used as the dielectric material in capillary of which the creation of plasmas took place. The channel's length is 3-4 mm and diameter is ~1-2mm. In the Fig.1. the scheme of plasma source and experiment is represented. In this case we developed the approach of [4], where the wax was used as the evaporating substance, energy of the capacity storage was 5.6kJ.

In particular we were interested in the lifetime and size jet's characteristics at the application of different high polymer natural materials.
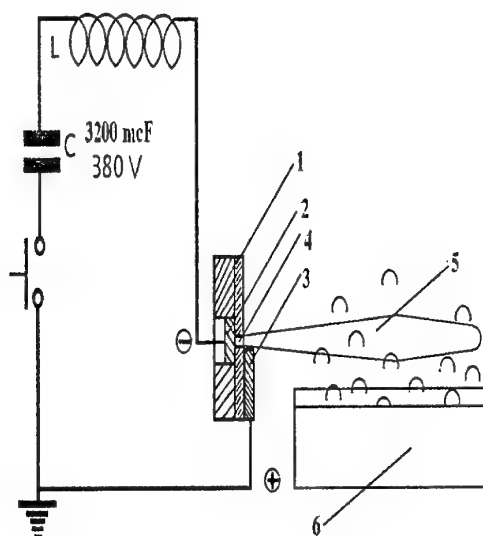
Fig.1. Scheme of experiments with erosive capillary Discharge
1. -dielectric ; 2,3-electrodes; 4-capillary; 5- Plasma region; 6 -a dish with melted polymeric material

In the Fig.2. a,b,c are represented the photos of luminescent plasma regions obtained at application of PMMA, mixture of technical wax with milled wood, and also of medical paraffin ($T_{melting} = 52°C$).

In all the cases the length of the luminous region was 10-12cm, PMMA based jet has a form of a knife with the radius at the base ~2mm. In other cases jets have the torch like form with the radius at the base ~7-10mm and the radius of the widest part 30-40mm.

In the case of mixtures of paraffin with resin and milled wood, technical wax with milled wood and paraffin with milled wood the luminous regions usually consisted of two definite parts. The first one consisted of orange-yellow and white colors (see Fig.2) and the second one of bright yellow color. But in the case of medical paraffin applications we did not observed bright yellow regions. The lifetime of the bright regions was at least ~2 times greater than of orange-yellow-white regions, which lifetime was about 14-20ms. Formation of such regions could be connected with the destruction of paraffin vapor with creation of CH_4, C_2H_2 and melted lignin (from the milled wood) and their following polymerization in plasma [6-7]. In this case the typical colors and time of region appearance have to differ significantly.

In experiments with erosive capillary discharge interacting with paraffin vapor the luminous regions of spherical or complex forms (see Fig.3) were created during the pulse time.

Their effective diameter 10-15cm, lifetime (burning time) up to 200ms. Video movie of the process allowed to determine the typical time of the ball's ascending for $x \approx 5$ cm during $t \approx 40$ ms.
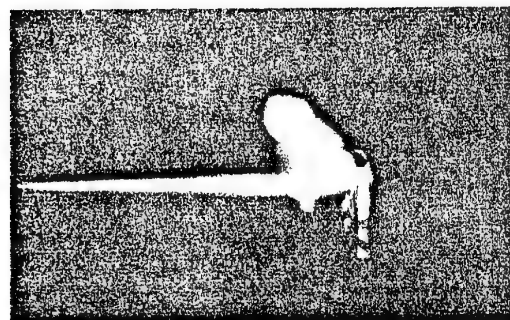
Fig.2.1. Erosive discharge with the capillary of PMMA
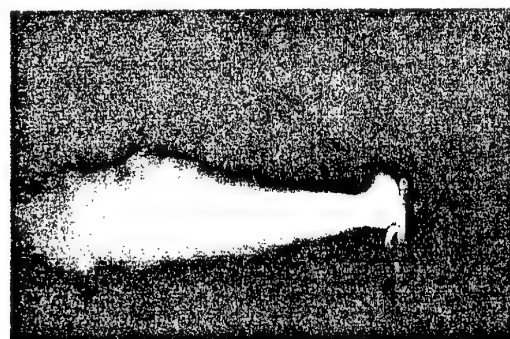
Fig.2.2. Erosive discharge with the capillary of medical paraffin
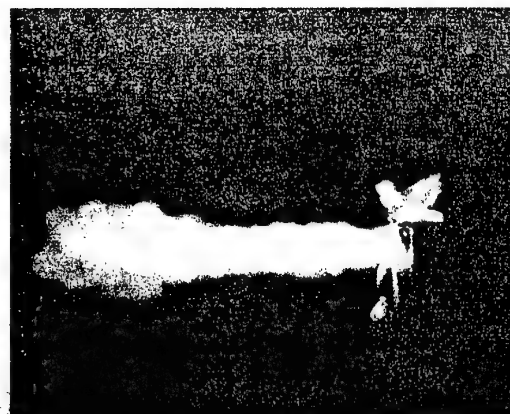
Fig.2.3. Erosive discharge with the capillary of mixture of technical wax with milled wood

In a number of experiments with the capillary discharge with the dielectric of wax or paraffin with milled wood the LLO were formed. Their observation size was up 1 cm and the lifetime was up 1.5s. They appeared during 20-40ms after the discharge realization.

215
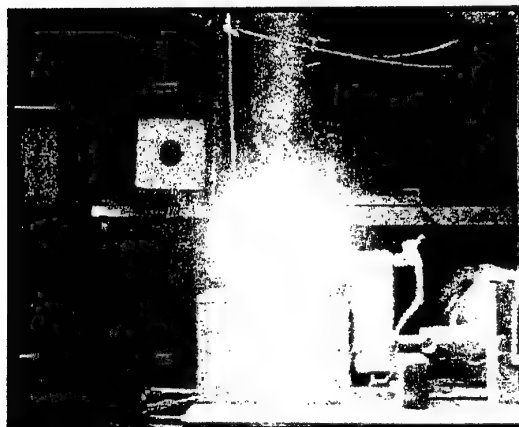
a)
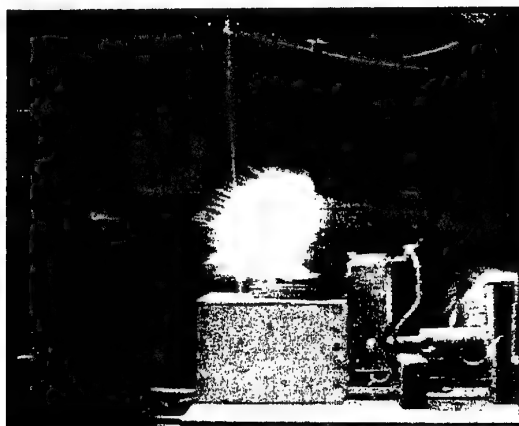
b)
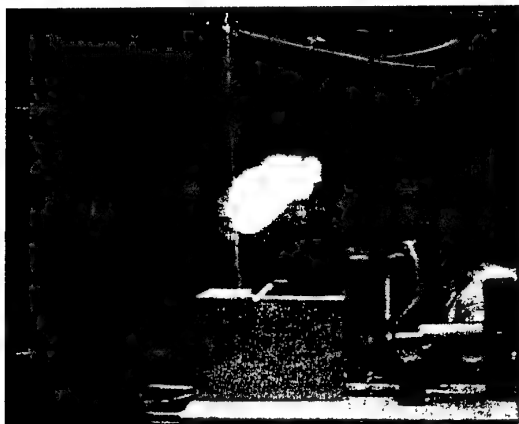
c)

Fig.3. Erosive discharge with the capillary of mixture of paraffin with milled wood over paraffin vapor

Conclusions

Theoretical estimates allow making some conclusions. During the interaction of the plasmadynamic discharge with the wax or paraffin surface their quick heating takes place, it is accompanied with the evaporation of the material. Estimates of energy necessary to evaporate experimentally observed paraffin layer from the sample of 40× 40×4 sizes at the distance from the nozzle to the sample ~5 mm give the value of the released energy $W \approx 500$ J, which is in agreement with the value obtained from the ampere-volt characteristics of this discharge.

This energy exceeds at least by two times the energy necessary for the heating of the methane region (obtained at the paraffin's heating) of about 20 cm in diameter up to 2000 K. So this discharge is effective for the ignition and combustion of the paraffin vapor.

In experiments with the erosive discharges, interacting with the paraffin vapor, the typical time and height of the ascending of the luminous ball allow to detect the gas temperature in a ball $T \approx 2000$ K, it indicates the full combustion of paraffin vapor [8]. Supposing that methane is the main component of the paraffin destruction at heating one can evaluate the ratio of molecular components over the surface of the heated paraffin $CH_4 : O_2 : N_2 \approx 1:1:4$. In this case the energy realized in the discharge does only to the ignition of the mixture.

Luminous regions with the lifetime $t \approx 200$ ms can be attributed to LLO and a conducted analysis indicates their chemical nature. They can appear in natural conditions near the surface of heated trees, lead to the fires at the manufacturing and storing of paraffin, resins and waxes.

LLO of another type requires additional investigations, however our previous studies allow to characterize them as LLO of the polymeric nature.

References

1. Avramenko R.F., Bakhtin B.I., Nikolaeva V.I. et al. Zhurnal Tekh. Fiz. V.. T.60. N. 12. P.57-64.
2. Avramenko R.F., Nikolaeva V.I., Poskacheeva L.P. in a book: Ball lightning in laboratories. Eds. R.F.Avramenko, V.L.Bychkov, A.I.Klimov, O.A.Sinkevich Moscow. Khimia. 1994. P.15-55.

216

3. Ershov A.P., Timofeev I.B., Chuvashev S.N., Shibkov V.M. Ibidem. P.112-118.

4. Bychkov V.L., Gridin A.Yu. Klimov A.I. Ibidem. P.66-72.

5. Chernikov A.V., Chernikov V.A. et al. 2-nd Workshop on magneto-plasma-aerodynamics in aerospace appl. Moscow 5-7 April. 2000. IVTAN. P.215-220.

6. Egloff G. Destruction and Polymerization of Hydrocarbons. ONTI-Khimteoret. Leningrad. 1935.

7. Yasuda H. Plasma Polymerization. M. Mir. 1988.

8. Ravich M.B. Simplified method of thermal-technical calculations. Academy of Science USSR Publishers. M. 1961.

9. Bychkov V.L., Bychkov A.V., Stadnik S.A. Physica Scripta. V.53. P.749-759

217

41. LOCALIZED FLOW CONTROL IN SUPERSONIC FLOWS BY PULSED LASER ENERGY DEPOSITION

Russell G. Adelgren *, Gregory S. Elliott **, Doyle D. Knight ***
Rutgers – The State University of New Jersey
98 Brett Road
Piscataway, NJ 08854-8058

Alexander A. Zheltovodov +
Institute of Theoretical and Applied Mechanics
Siberian Branch of Russian Academy of Sciences
Novosibirsk 630090, Russia

Thomas J. Beutner
Air Force Office of Scientific Research
801 N. Randolph St
Arlington, VA 22203-1977

Abstract. Localized flow control in supersonic flows by pulsed laser energy deposition is investigated experimentally for Mach 3.45 flow past a sphere without and with a separate oblique shock. The objective is to determine the capability of a laser pulse (spark) to favorably modify the flowfield for a brief period of time, e.g., to reduce the peak pressure on the surface of the sphere. The laser spark is generated using a focused Nd:YAG laser (10ns pulse, and incident laser beam energy levels ranging from 13 to 258mJ/pulse). Experimental data include Schlieren images and high frequency response surface pressure measurements. For the isolated sphere, tests for three different energy levels and two different incident laser beam diameters were performed. The interaction of the laser-generated plasma with the blunt body shock exhibits a complex shock structure reminiscent of the simulations of Georgievsky and Levin (Mekhanika Zhidkosti I Gaza, No.4, June 1993, pp.174-183); however, the surface pressure shows an initial compression not observed in their simulations. Experiments were also performed wherein an Edney IV interaction was generated at the sphere using a separate oblique shock. The effects of laser energy deposition were examined for sparks located at two different positions upstream of the sphere. Schlieren images display the complex shock structure associated with the interaction of the plasma with the Edney IV interaction. Surface pressure measurements indicate a significant reduction in surface pressure over a portion of the sphere.

Introduction

Researchers have recently studied the possibility of using energy deposition as a means of global flow control, i.e., drag reduction of a supersonic body by means of energy deposition [1-5]. On the other hand, energy deposition could also be used to modify localized flow problems. Such an example of localized flow control with energy deposition would be the mitigation of the detrimental effects of a shock/shock interaction on an air vehicle during maneuver. Shock/shock interactions can occur on supersonic and hypersonic aircraft during maneuver and sustained flight. For example, oblique shock waves propagating from the nose of an aircraft or missile

---

can interact with the bow shock of any body protruding from the fuselage, i.e., stabilizing fins, weapon stores, booster rockets, engine cowls, and inlets. Some shock/shock interactions can lead to severe and often catastrophic events for aircraft.

Such catastrophic damage was the case for a 1968 Mach 6.7 test flight of the X-15 aircraft [6-8]. In this test flight an oblique shock generated from the leading edge of a dummy ramjet model impinged on the model support pylon. The subsequent Edney IV interaction led to severe burn damage of the pylon skin. This damage occurred approximately 160 seconds into the test flight and completely burned through the Inconel skin (Iconel has a melting temperature of 2800 degrees Fahrenheit). Fig.1 shows the X-15 with model ramjet and the severity of the burn damage caused by the shock impingement. Energy deposition applied to the mitigation of such an extreme pressure and heat load associated with the Edney IV phenomena would be an example of localized flow control via laser discharge into the flow region.
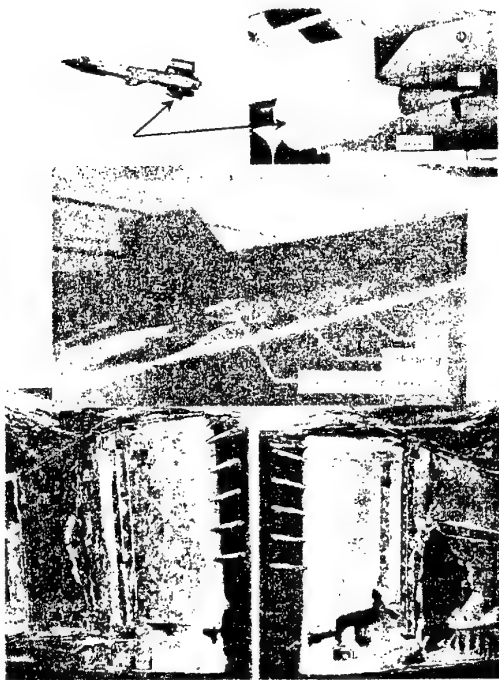
Fig.1. X-15 with ramjet model and post flight test pylon burn damage (photos courtesy of NASA)

The application of energy deposition for local flow control would require low power in terms of the energy deposition into the flow. These lower power requirements translate to small, low weight energy generation systems, i.e. small lasers with optics or small electric arc units both with

their appropriate control systems. Therefore, these smaller systems have real near-term potential applications for localized flow control. In addition, the use of a laser facilitates the ability to modify the flow remotely from a vehicle. For instance, it would eliminate the need to have electrodes protruding into the flow to induce an electrically generated discharge.

The objective of this paper is to summarize some of the recent experiments completed by the representatives of the USA and Russian scientific centers at the Rutgers University Gasdynamics Laboratory investigating the effect of depositing laser energy upstream of a sphere in Mach 3.45 flow as well as experimentally explore the effect of depositing energy into a flow to ameliorate the adverse Edney IV condition [9]. In the first case, experiments are performed for three different laser energy deposition levels upstream of the bow shock of the sphere. Secondly, the laser energy is deposited at two locations upstream of the same sphere subject to an Edney IV interaction.

Background

Laser-induced Discharge

The deposition of energy into a gas medium with a focused laser beam has been studied since the discovery of a laser induced spark in 1963 [10]. Subsequent research since the discovery has led to an extensive list of publications, and this research has been detailed and summarized quite nicely by Raizer [11-12], Morgan [13], and Smith [14]. The overall process, described in greater detail by Raizer, starts when a laser beam with sufficient power is focused down, and a sufficient radiation flux density is achieved, leading to a discharge (somewhat similar to the discharge induced by a sufficient electric field between the electrodes of a spark plug in a standard automobile engine). The pressure and temperature of the gas in the region of this discharge will be increased significantly as the energy of the laser is absorbed to cause this so called laser induced optical breakdown. The energy deposition into a gas by a focused laser beam can be described by four progressive steps: 1) initial release of electrons by multi-photon effect, 2) ionization of the gas in the focal region by the cascade release of electrons, 3) absorption and reflection of laser energy by the gaseous plasma, rapid expansion of the plasma and detonation wave formation, and 4) the propagation of the detonation wave into the surrounding gas and relaxation of focal region plasma.

Various models have been developed for the laser-induced breakdown process. Dors, Parigger, and Lewis recently analyzed the

asymmetric effects of the breakdown process in quiescent nitrogen gas [15]. The asymmetric effects are caused by the non-spherical volume of the plasma formation, and the plasma propagation up the focal axis during the laser pulse. Dors et al numerically solve the viscous equations with assumed initial conditions, based on a physical model for the gas at the termination of the plasma phase, for the velocity, temperature, and pressure. Output from their model was substantiated with experimental data. A major item to note is the formation of a vortex ring in the focal region due to the asymmetric breakdown process. A similar vortex ring formation was observed by Adelgren et al. [9] Similarly, Svetsov et al have experimentally and numerically analyzed the post fluid motion of a laser discharge [16]. Jiang, et al [17] and Stiener, et al [18], have also numerically analyzed laser-induced blast waves. These latter two models mentioned assume a symmetric sphere shape for the initial region.

Energy Deposition in Supersonic Flows

Much of the research involving energy deposition into gas flows was pioneered in Russia. Chernyi [4,19] and Tretyakov et al [5] have provided brief summaries for energy deposition in different gasdynamic flows. Georgievsky and Levin [20,21] have studied the effect of pulsed energy deposition in a supersonic flow. The lens effect and blooming of a bow shock in front of a sphere was analyzed with an Euler code simulation for various shaped energy deposition regions. The temperature discontinuity created by the energy deposition creates an interface. This interface, in turn, propagates into the bow shock upstream of the sphere, and the temperature discontinuity across the interface causes the shock to bloom forward. This shock blooming effect takes the shape of a lens in front of the spherical model. Levin et al [22] have also analyzed the energy deposition effects on drag reduction numerically with a Navier-Stokes code. They define a heat source parameter that governs the overall effect on the flow from the energy deposition.

Tretyakov et al have performed experimental study of the supersonic flow over a powerful pulsating laser discharge and its influence on the aerodynamic drag reduction [23,24]. They have shown the aerodynamic drag reduction of axisymmetric body up to 50 percent with increasing the discharge frequency. A similar problem was considered recently by Levin and Georgievski on a basis of numerical studies with the Euler computations [25]. Tretyakov and Yakovlev considered a simplified analytical approach for estimation of quasistationary flow parameters in the thermal wake after a optical pulsating discharge [26,27].

Research has also been conducted in the area of energy deposition in supersonic flows as a means of flow control. Korotayeva, Fomin and Shaskin have analyzed the effect of a local energy source on the aerodynamics performances of axisymmetric body and delta wing in a framework of the Euler computations [28]. Riggins, Nelson and Johnson have shown focused power deposition upstream of blunt bodies at Mach 2.5, 6.5, and 10 can reduce the wave drag by as much as 50 percent [29]. Their numerical studies with a Navier-Stokes computational fluid dynamics code included axisymmetric as well as two dimensional blunt bodies.

Other investigators have studied the gas dynamic effect of depositing energy in supersonic flows. Krasnobaev developed a velocity potential function, analogous to supersonic slender body theory, for supersonic flow past small energy perturbations [30]. Kogan et al have analyzed the effect of moving energy sources for subsonic, supersonic, transonic, and hypersonic cases [31]. Vlasov et al have numerically analyzed with an Euler model the effects of varying the frequency of pulsing energy sources in subsonic and supersonic flows [32]. Moreover, Jagadeesh, et al have shown the effect of pulsed energy deposition inside of a jet impinging on a wall [33].

In addition, other researchers have proposed the use of changing the bow shock structure upstream of blunt bodies through the use of energy depositions. Nemchinov et al analyze the effect of a "hot spike" in front of a blunt body [34]. Shang et al have also demonstrated a flow modification with radio frequency plasma generation ahead of a blunt body and with a jet-spike shock bifurcation [35].

Edney IV Interaction

We decided to determine the effects of depositing energy upstream of the Edney IV interaction as an example of a detrimental local flow phenomena where energy deposition might be used as a mitigation flow control technique. Even though damage due to shock/shock interactions was observed prior to Edney's 1968 report [36], he was the first to categorize and fully characterize the shock/shock interactions. He studied the effect of an oblique shock interacting with a blunt body shock and developed six categories of interactions. The fourth, known as the Edney Type IV interaction, is the most severe case leading to localized regions of high surface pressure and heat transfer rates on the body. When the oblique shock propagating from an upstream compression turn

intersects the bow shock of the blunt body within the sonic region, i.e. the subsonic region behind the bow shock, an Edney Type IV interaction occurs (see Fig.2). A supersonic jet embedded in the subsonic region behind the blunt body bow shock develops and impinges on the blunt body. This impinging, embedded supersonic jet causes high, localized heat transfer regions and high, localized surface pressures on the blunt body. These surface thermal and pressure stresses can be 10 to 20 times greater than stagnation conditions, thus leading to catastrophic failure of the blunt body material, e.g. the X-15 ramjet test mentioned above.
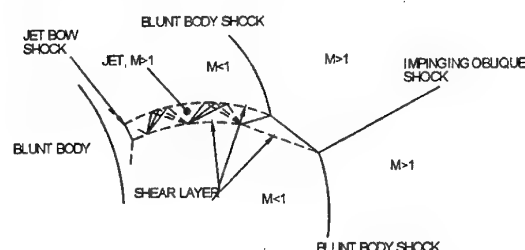
Fig.2. Edney Type IV shock/shock interaction

For the second test case presented here, the energy was deposited upstream of an Edney IV shock/shock interaction with the desired effect of perturbing the Edney IV interaction in a localized fashion, and therefore, reducing the high surface heat flux on the body downstream of the embedded supersonic jet. However, in these initial tests the heat flux was not measured (such measurements are in progress). Instead the surface pressure distribution was measured using available equipment. The literature to date indicates a correlation of the pressure and heat flux in the interaction. The goal here is to perturb the embedded supersonic jet with energy addition and thereby decrease the thermal and pressure loads on the body subjected to the Type IV interaction.

Test Apparatus

The energy deposition tests upstream of a 25.4mm diameter sphere with and without the Edney Type IV interaction were conducted in the Rutgers University Mach 3.45 supersonic wind tunnel [9]. Fig.3 is a photograph of the model and test section of this supersonic wind tunnel facility, and Table 1 lists the operating parameters for this facility [37].

The beam of a pulsed (10Hz) frequency doubled Nd:Yag laser (532nm wavelength) was focused in the wind tunnel test section to generate

the energy deposition. The pulse width of the laser is 10 nanoseconds, and the transit time for flow about the spherical model is on the order of microseconds. Therefore, the energy deposition will be instantaneous as compared to the flow timescale. In addition, the 10Hz pulse frequency ensures that the flow interaction phenomena are associated with the unsteady nature of the single energy deposition pulse and its effect on the flow structure.
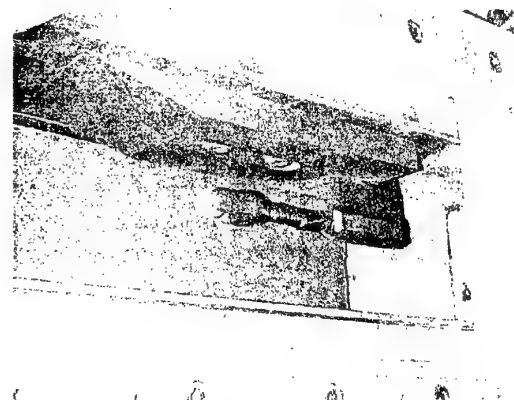
Fig.3. The 25.4mm diameter sphere model, sting, sting support, and 15 degree compression ramp mounted in the test section the wind tunnel

Table 1. Operating Parameters for the Rutgers Mach 3.45 Supersonic Wind Tunnel

Mach Number	3.45
Operating Stagnation Pressure	1.4 MPa
Typical Stagnation Temperature	290 K
Mass Flow Rate	9.8 Kg/s
Total Run Time	1.8 minutes
Test Area Cross Section	15 cm × 15 cm
Test Area Length	30 cm

The bow shock stand-off distance for the undisturbed model at Mach 3.45 was measured and compared to the Lobb [38] approximation to Van Dyke's [39] shock stand-off model. The model predicted the stand-off distances within 3 percent of the measured distances.

Experimental Results

Laser-induced Discharge

A preliminary study of the laser-induced discharge in quiescent air as well as in Mach 3.45 flow has been performed [9]. Fig.4 is a series of three photographs of a laser generated spark for three different incident beam energies and two different incident beam diameters. All three clearly

indicate the elongation of the spark along the direction of laser incidence. Rayleigh scattering [40,41] images were taken of the laser induced energy deposition for a discharge in quiescent air with ambient pressure of one atmosphere, and ambient temperature of 295 K. Fig.5 is a time sequence of images following the laser induced optical breakdown. Each image is an average of 150 images taken. The laser beam is incident from top-to-bottom in these images. The intensity in these images is, to a first order, proportional to the density. The darker regions are qualitatively lower density regions. The time given is the delay time from laser discharge pulse to the pulse of the laser sheet used to image the Rayleigh scattering. The asymmetry of the heated region of the optical breakdown is elongated along the axis of laser propagation as seen in Fig.4. The blast wave is
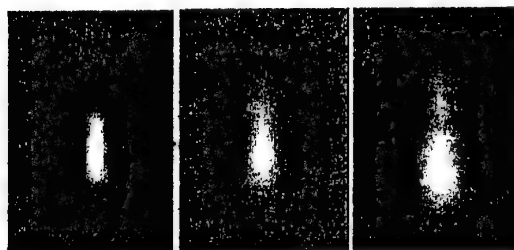
Fig.4. Pictures of laser sparks in quiescent air for a) 13mJ/1$\pm$0.5 mm^3, b) 127mJ/1.3$\pm$0.7 mm^3, and c) 258mJ/3$\pm$1 mm^3. Laser incidence is from bottom to top.
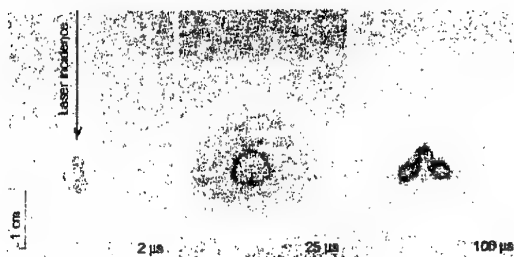
Fig.5. Rayleigh scattering images following laser induced optical breakdown of quiescent air at 2, 25, and 100 microseconds after laser excitation pulse

clearly observed propagating away from the discharge region in Fig5. It is also deduced, that a vortex ring is formed from the asymmetric plasma formation caused by the laser discharge. Dors et al [15] discuss the asymmetric breakdown process in the focal region and the onset of vorticity due to this process. The image at 100 microseconds in Fig5 shows the formation of the vortex ring. The lower density regions at the core of the ring separate along the axis and also grow in diameter. The examples with a laser spark discharge in Mach 3.45 are considered also in Adelgren et al.[9]

Upstream of Bow Shock of Mach 3.45 Sphere

The frontal pressure distribution is recorded as a function of time for three different laser energy deposition levels at 25.4mm upstream of the sphere. The pressure was measured on the vertical symmetry plane of the sphere. The pressure is nondimensionalized with the freestream pitot pressure. The surface pressure was measured across 120 degrees of the frontal face.

The time histories of the surface pressure on the centerline (see Fig.6) for the three energy levels show a common behavior comprised of an initial pressure rise (1), expansion (2), compression (3) and transient decay (4). The expansion (2), compression (3) and transient decay (4) are similar to the ideal gas Euler simulations of Georgievski and Levin[21] for the interaction of a thermal spot with a sphere at Mach 3. The expansion lowers the surface pressure at the centerline by 40%. The initial compression (1) was not observed by Georgievski and Levin. The interaction of the thermal spot, generated by the laser discharge, with the bow shock (Fig.6, in the time interval of 40-90 microseconds) causes a blooming of the bow shock (Georgievski and Levin call this the lensing effect). This behavior is consistent with the simulations of Georgievski and Levin[21] and Aleksandrov et al. [42] It can be noted that the energy deposition effects the flow over a period on the order of 50 microseconds. This flow transient effect is much greater than the energy deposition whereby the excitation laser has a pulse width of 10 nanoseconds.
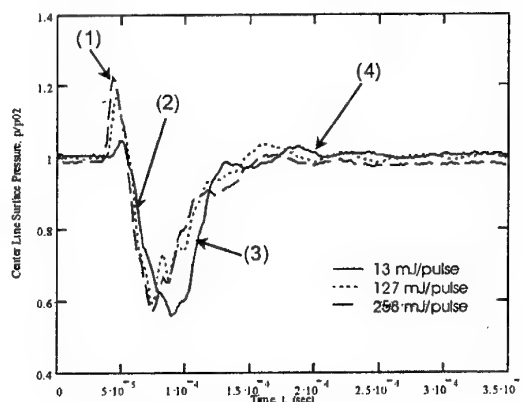
Fig.6. Centerline pressure traces for sphere

In Fig.7 the pressure distribution before the energy deposition (the continuos black line trace) and the instantaneous pressure distribution (the dotted line trace) are correlated with the Schlieren image. Thus, these traces superimposed on the Schlieren images show the effect of the

energy deposition on the flow structure about the model as a function of time. In addition, Fig.8 gives the pressure traces for all of the port locations of the pressure transducer. The effect on the surface pressure about the sphere can clearly be seen as the thermal spot created by the laser discharge propagates into the sphere. The zero coordinate on the time axis of Fig.8 corresponds to the time of the laser excitation pulse.
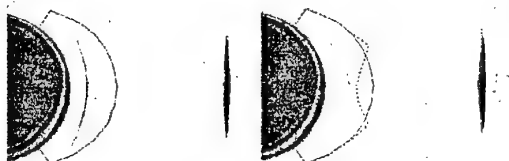
Fig.7. Energy deposition interaction with Mach 3.45 sphere at 10 and 80 microseconds after discharge
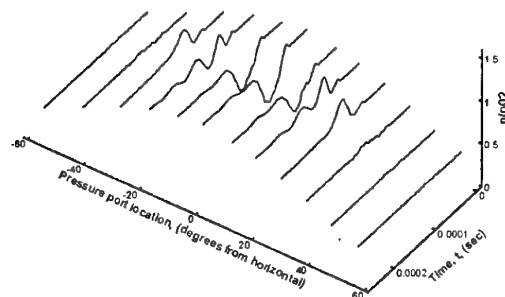
Fig.8. Surface pressure traces for various pressure port locations on the vertical symmetry plane around front of sphere with laser energy deposition (incident laser beam energy at 13mJ/pulse) 25.4mm upstream and focused on model centerline

Upstream of Mach 3.45 Sphere with Edney Type IV Interaction

The frontal pressure distribution is recorded as a function of time for two different energy deposition locations for the Type IV shock/shock interaction tests. In Fig.9 the pressure distribution before the energy deposition (continuos black trace) and the instantaneous pressure distribution (dotted line trace) are correlated with the shadowgraph image. The traces superimposed on the shadowgraph images show the effect of the energy deposition on the flow structure about the model as a function of time. Likewise, Fig.10 gives the pressure traces for all of the port locations of the pressure transducer. The effect on the surface pressure about the sphere can clearly be seen as the thermal spot created by the laser discharge

propagates into the sphere and disrupts the Edney IV shock interaction structure. The zero coordinate on the time axis of Fig.10 corresponds to the time of the laser excitation pulse.
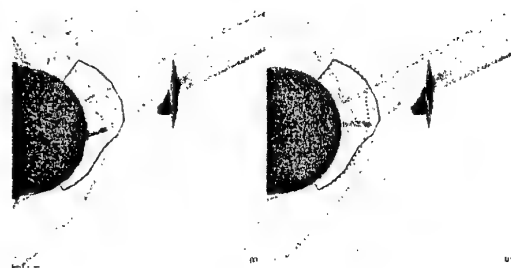
Fig.9. Energy deposition interaction with sphere and Edney IV shock/shock interaction at 1 and 70 microseconds after discharge
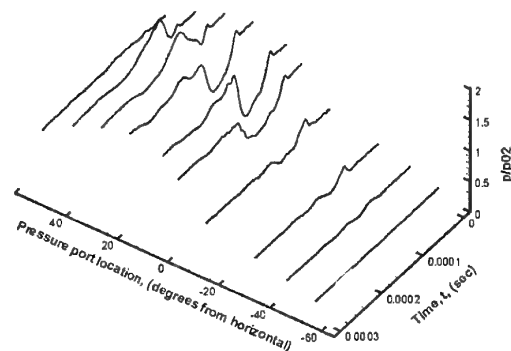
Fig.10. Surface pressure traces for various pressure port locations on the vertical symmetry plane around front of sphere in an Edney IV interaction with energy deposition 17.0mm upstream and 7.1 mm above model centerline

The disturbance in the surface pressure due to the interaction of the thermal spot can be clearly seen in the images (see Fig.9 and 10). For the first laser spark location, the surface pressure begins to decrease from 40 to 70 microseconds after an initial pressure rise at 40 microseconds. This initial pressure rise was also seen in the test case without the oblique shock interaction. The decrease in pressure is due to the relaxation of the embedded supersonic jet as the rarified region from the thermal spot reacts with the shock structure in front of the sphere. A pressure spike then appears at 80 microseconds and then decays by approximately 130 microseconds. The pressure spike is due to the re-formation of the supersonic embedded jet due to the Type IV interaction. The jet can be seen forming in the shadowgraph images and then sweeping across the sphere surface. The same phenomena is seen for the second energy deposition location. An initial pressure rise is observed at 40 microseconds, and then the pressure

223

decreases from 50 to 100 microseconds. However, with this laser spark above the centerline axis, the pressure spike upon re-formation of the embedded supersonic jet is less severe. In both cases, the surface pressure in the region of the embedded jet is reduced by 30% during the time interval of the interaction with the thermal spot.

Conclusions

The objective of this research effort is to demonstrate the feasibility of reducing the peak pressure (and, ultimately, peak heat transfer) associated with the Edney IV shock impingement condition through the use of laser energy deposition.

Surface pressure measurements show a 40% decrease in surface pressure during the 50 microsecond thermal spot interaction time as observed for the case of a sphere in Mach 3.45 flow with varying levels of energy deposition upstream of the bow shock. The laser excitation pulse width is 10 nanoseconds versus the 50 microsecond transient effect on the flow. An initial compression during the lensing of the bow shock has also been observed.

The peak surface pressure associated with the Edney IV interaction was reduced by 30% momentarily by the flow perturbation created by the upstream laser discharge.

References

1. Riggins, D., Nelson, H.F., Johnson, E., "Blunt-Body Wave Drag Reduction Using Focused Energy Deposition," AIAA Journal, Vol. 37, No. 4, April 1999.

2. Myrabo, L. N., Raizer, Y. P., "Laser-induced Air Spike for Advanced Transatmospheric Vehicles," 25th AIAA Plasmadynamics and Lasers Conference, June 20-23, 1994, Colorado Springs, CO.

3. Pilyugin, N., Talipov, R., Khlebnikov, V., "Supersonic Flow over the Bodies by the Flow with Physical-Chemical Heterogeneity", Thermophysics of High Temperatures, 1997, Vol. 35, No. 2, pp. 322-336 (in Russian).

4. Cherniy, G. G., "Some Recent Results in Aerodynamic Applications of Flows with Localized Energy Addition", AIAA 99-4819, 19p.

5. Tretyakov, P.K., Fomin, V.M., Yakovlev, V.I., "New Principles of Control of Aerophysical Processes. Research Development", Proc.: International Conference on the Methods of Aerophysical Research, September 2-6, Novosibirsk, Russia, 1996, Part 2, pp. 210-220.

6. Watts, J.D., Olinger, F. V., "Heat-transfer Effects of Surface Protuberances on the X-15 Airplane," NASA TM-1566, May 1968.

7. Watts, J.D., "Flight Experience with Shock Impingement and Interference Heating on the X-15-2 Research Airplane," NASA TM X-1669, October 1968.

8. Burcham, F. W. Jr., Nugent, J., "Local Flow Field around a Pylon-mounted Dummy Ramjet Engine on the X-15-2 Airplane for Mach Numbers 2.0 to 6.7," NASA TN D-5638.

9. Adelgren,R., Elliott, G., Knight, D., Zheltovodov, A., Beutner T.J., "Energy Deposition in Supersonic Flows," AIAA Paper No. 2001-0885, Jan. 2001.

10. Maker, P.D., Terhune, R.W., Savage C.M., "Optical Third Harmonic Generation," Quantum Electronics, Proceedings of the 3rd International Congress, Paris, 1663, ed. Grivet P., Bloembergen, N., Vol.2, Columbia University Press, New York, 1964, p. 1559-1572.

11. Raizer, Y. P., "Breakdown and Heating of Gases Under the Influence of a Laser Beam," Soviet Physics USPEKHI, Volume 8, Number 5, 1966, pp. 650-673.

12. Raizer, Y. P., Laser-Induced Discharge Phenomena, Consultants Bureau, New York, NY, 1977.

13. Morgan, G. C., "Laser-induced breakdown of gases," Rep. Prog. Phys., 38, 1975, pp. 621-665.

14. Smith, David C., "Laser Induced Gas Breakdown and Plasma Interaction," 38th Aerospace Sciences Meeting and Exhibit, January 10-13, 2000, Reno, NV.

15. Dors, I., Parigger, C., and Lewis, J., "Fluid Dynamic Effects Following Laser-Induced Optical Breakdown," 38th Aerospace Sciences Meeting and Exhibit, January 10-13, 2000, Reno, NV.

16. Svetsov, V., Popova, M., Rybakov, V., Artemiev, V., Medveduk, S., "Jet and Vortex Flow Induced by Anisotropic Blast Wave: Experimental and Computational Study," Shock Waves, Springer-Verlag, 7, 1997, pp. 325-334.

17. Jiang, Z., Takayama, K., Moosad, K.P.B., Onoreda, O., Sun, M., "Numerical and Experimental Study of a Micro-Blast Wave Generated by Pulsed-laser Beam Focusing," Shock Waves, Springer-Verlag, 1998, pp. 337-349.

18. Stiener, H., Gretler, W., Hirschler T., "Numerical Solution for Spherical Laser-driven Shock Waves," Shock Waves, Springer-Verlag, 1998, pp. 139-147.

19. Cherniy, G.G., "The Impact of Electro-Magnetic Energy Addition to air near the Flying Body on its Aerodynamic Characteristics", Proc.: 2nd Weakly Ionized Gases Workshop, 1998, Norfolk, VA., 31p.

20. Georgievsky, P.Yu., Levin, V.A., "Unsteady Effects for a Supersonic Flow Past a Pulsing Energy Source of High Power," Proc.: International Conference on the Methods of Aerophysical Research, 29 June – 3 July, 1998, Novosibirsk, Russia, 1998, Part 2, pp. 58-64.

21. Georgievski, P., and Levin, V., "Unsteady Interaction of a Sphere with Atmospheric Temperature Inhomogeneity at Supersonic Speed", Mekhanika Zhidkosti i Gaza, No. 4, June 1993, pp. 174-183.

22. Levin, V. A., Afonia, N. A., Gromov, V. G., "Navier-Stokes Analysis of Supersonic Flow with Local Energy Deposition," AIAA Paper 99-4967, 1999.

224

23. Tretyakov, P.K., Kraynev, V.I., Yakovlev, V.I., Grachev, G.N., Ivanchenko, A.I., Ponomarenko, A.G., Tischenko V.N., "A Powerful Optical Pulsating Discharge as the Source of Energy Release in a Supersonic Flow", Proc.: International Conference on the Methods of Aerophysical Research, August 22 - 26, 1994, Novosibirsk, Russia, 1994. Part 2, pp. 224-228.

24. Tretyakov, P.K., Garanin, A.F., Kraynev, V.L., Tupikin, A.V., Yakovlev, V.I., "Investigation of Local Laser Energy Release Influence on Supersonic Flow by methods of Aerophysical Experiments", Proc.: International Conference on the Methods of Aerophysical Research, September 2-6, 1996, Novosibirsk, Russia, 1996, Part 1, pp.220-204.

25. Gergievskyi, P. Yu., Levin, V. A., "Supersonic Flow over Shapen Bodies in Presence of an Unsteady Energy Supply Upstream", Proc.: International Conference on the Methods of Aerophysical Research, 9-16 July, 2000, Novosibirsk – Tomsk, Russia, 2000, Part III, pp. 45-50.

26. Tretyakov, P.K., Yakovlev, V.I., "Formation of the Quasi-Stationary Supersonic Flow with the Pulse Periodic Plasma Heat Source, DAN, 1999, Vol. 365, No. 1, pp. 466-467 (In Russian).

27. Yakovlev, V.I., "Developmentt of a Method of Estimation of Quasistationary Flow Parameters in a Wake of an Optical Pulsating Discharge", Proc.: International Conference on the Methods of Aerophysical Research, 9-16 July, 2000, Novosibirsk – Tomsk, Russia, 2000, Part III, pp. 139-145.

28. Korotaeva, T.A., Fomin V.I., Shashkin, A.A., "The Effect of a Local Energy Source on the Aerodynamics Characteristics of Pointed Bodies at Supersonic Flow", Proc.: International Conference on the Methods of Aerophysical Research, 9-16 July, 2000, Novosibirsk – Tomsk, Russia

29. Riggins, D. W., Nelson, H. F., "Hypersonic Flow Control Using Upstream Focused Energy Deposition," 37th AIAA Aerospace Sciences Meeting and Exhibit, January 11-14, 1999, Reno, NV., 2000, Part I, pp. 111-116.

30. Krasnobaev, K.V. "Supersonic Flow Past Weak Sources of Radiation," Fluid Dynamics, Plenum Publishing Corporation, 1985, pp. 629-632.

31. Kogan, M.N., Kucherov, A.N., Mikhailov, V.V., Fonarev, A.S., "Planar Gas Flows with Weak Energy Supply," Fluid Dynamics, Plenum Publishing Corporation, 1979, pp. 711-717.

32. Vlasov, V.V., Grudnitskii, B.G., Rygalin, V.N., "Gas Dynamics with Local Energy Release in Subsonic and Supersonic Flow," Fluid Dynamics, Plenum Publishing Corporation, Vol.30, No.2, 1995, pp. 275-280.

33. Jagadeesh, G., Jiang Z., Onodera, O., Ogawa, and Takayama, K., "Experimental Investigation of Micro-Shock Waves Generated Inside a Fluid Jet Impinging on Plane Wall," 38th Aerospace Sciences Meeting & Exhibit, 10-13 January 2000, Reno, NV.

34. Nemchinov, I.V., Artem'ev, V.I., Bergleson, V.I., Khazins, V.M., Orlova, T.I., Rybakov, V.A., "Rearrangement of the Bow Shock Shape Using a 'hot spike'," Shock Waves, Springer-Verlag, 4, 1994, pp.35-40.

35. Shang, J.S., Ganguly, B., Umstattd, R., Hayes, J., Arman, M., Bletzinger, P., "Developing a Facility for Magnetoaerodynamic Experiments," Journal of Aircraft, Vol. 37, No. 6, Nov.-Dec. 2000, pp. 1065-1072.

36. Edney, B., "Anomalous Heat Transfer and Pressure Distributions on Blunt Bodies at Hypersonic Speeds in the Presence of an Impinging Shock," FFA Report 115, Aeronautical Research Institute of Sweden, 1968.

37. Stroehle, Eric J., "The Design and Construction of a Wind Tunnel for Education and Research," Masters Thesis, Rutgers University, New Jersey, Oct 1999.

38. Lobb, R.K., "Experimental Measurement of Shock Detachment Distance on Spheres Fired in Air at Hypervelocities," The High Temperature Aspects of Hypersonic Flow, Pergamon, 1964, pp. 519-527.

39. Van Dyke, M.D., "The Supersonic Blunt-Body Problem - Review and Extension," Journal of the Aerospace Sciences, Aug. 1958, pp.485-496.

40. Elliott, G.S., Beutner, T.J., "Molecular Filter Based Planar Doppler Velocimetry," Progress in Aerospace Sciences, Pergamon, 35, 1999, pp.799-845.

41. Miles, R.B., Lempert, W.R., "Flow Diagnostics in Unseeded Air," AIAA Paper 90-0624, 1990.

42. Alexandrov, A., Vidyakin, N., Lakutin, V, et al, "On a Possible Mechanism of Interaction of a Shock Wave with the Decaying Plasma of a Laser Spark in Air", Zhurnal Technicheskaya Phyzika, 1986, Vol.56, p.771.

225

42. COMPARISON OF ENERGETIC AND DYNAMIC DEVICES OF NON-UNIFORMITY FORMATION IN THE SUPERSONIC FLOW AROUND A BLUNT BODY

S.V. Guvernyuk

Lomonosov Moscow State University, Institute of Mechanics,

E-mail: guv@imec.msu.ru

Introduction

The influence of localized sources of energy *(SOE)* on supersonic aerodynamics of bodies located downstream has been investigated by many researchers [1]. One practical method of energy supply to gas flow is the formation of a zone of low-ionized plasma with microwave structure, generated by a powerful optical pulsing discharge [2] or electron beams [3]. The comparison of the known experimental data with the results of numerical modeling shows that all the experimentally observed aerodynamic effects, caused by *SOE*, may be explained by ordinary gas dynamics [3,4]. The role of *SOE* reduces to the influence of a gas-dynamic non-uniformity, induced in supersonic flow due to non-uniform heating. Downstream *SOE* there is formed a hot wake with a lesser total pressure and greater velocity than in supersonic undisturbed flow [5]. Due to the interaction with the blunt body, this wake can result in flow reconstruction: in the shock layer ahead of the body the separation zones are formed, the bow shock becomes weaker and the wave drag of the body decreases [1,5]. However, it is well known that similar effects may be produced by a cold wake, formed due to the interaction of dynamic supersonic flow with the solid obstacle [6]. This wake from the dynamic-interaction zone *(DIZ)* differs in structure in comparison with the *SOE*-wake. In the *DIZ*-wake the total pressure and flow velocity are smaller than in that without disturbances, but the total temperature is approximately the same as outside the wake. Due to the interaction with the blunt body *DIZ*-wake may also change the flow structure and decrease the wave drag of the body [6,7]. Although the mechanisms of energetic *(SOE)* and dynamic *(DIZ)* methods of influence on the supersonic flow seem to have different physical nature, but the mechanisms of the influence of the *SOE* and *DIZ* wakes on aerodynamic characteristics of the bodies may be similar. There arises a fundamental question: which of the two methods of control of the flow near the body, dynamic or energetic, is preferable

This paper presents some theoretical ideas (in particular, the theorem of comparison of asymptotic wakes) and examples of numerical modeling of a supersonic flow around bodies with the presence of a non-uniformity of the *SOE* or *DIZ* type ahead the bodies. The results [7,8], in which the classes of different shear non-uniformity in supersonic flows, however, leading to the same flow structures when interacting with the bodies, are used. The calculations have been carried out using the standard *GDT* *(Gas Dynamic Tools*, created by A.V.Zibarov [9]) codes. For taking the external energy supply into account the mechanism of *SOE* has been added to the set of *GDT* tools using the method [4].

1. The causes being different, the results are similar

Figure 1 shows the results of physical (Fig.1,b) and numerical (Fig.1,c,d) simulation of the non-uniform supersonic flow of air ($\gamma=1.4$) around a concave axisymmetric body at Mach number M=3. In the experiment, performed in the A-8 wind tunnel of the Institute of Mechanics of MSU the non-uniformity represented the wake behind a small cylindrical body, located on the symmetry axis upstream the main body.

The ratio of diameters of the forward and the back bodies was $d_1/d_2=0.29$ and the distance between them was $l_2/d_2=2.6$ (Fig.1,a). The velocity profile in the wake behind the forward body had the usual configuration with a minimum near the symmetry axis. The total temperature was equal to the total temperature in the main stream. The Reynolds number, based on d_2 and the parameters of the flow without disturbances, was $5 \cdot 10^6$. The flow regime was turbulent.

In the numerical calculations, the non-uniformity was created by distributed periodic pulsing energy supply *(SOE)* in small cylindrical volume Ω on the symmetry axis ahead of the body (Fig.1,a). The volume Ω had the aspect ratio $l_1/d_1=1.76$, the ratio of the diameters was $d_1/d_2=0.075$, the relative distance between Ω and the body was $l_2/d_2=1.31$, the time-averaged power of SOE in the volume Ω was equal to $0.16d_1^2\rho_\infty u^3_\infty$, and the pulse frequency was $11.8u_\infty/d_1$ (here, ρ_∞, u_∞ are the density and the velocity of the flow without disturbances; the physical viscosity was not taken into account). The

226
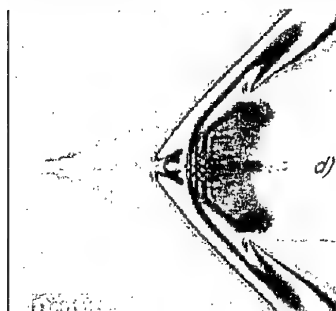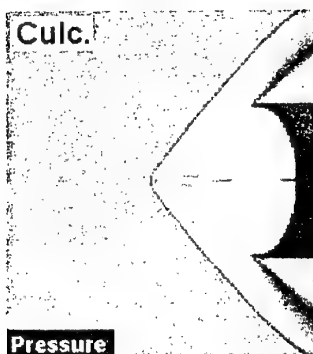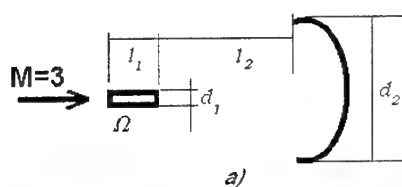
Fig.1. Non-uniform supersonic flow around a concave body.

wake behind the source *SOE* was hot, and the velocity in it exceeded the velocity of the main flow. So, there were many differences between the conditions of the experiment and the calculation. However, it is not difficult to observe an analogy of the flow patterns behind the thermal and the dynamic obstacles (Fig.1,b,c). Moreover, not only the configurations of the flows with the disturbances were found to be close, but also the relative decreases in the wave drag of the body X in

comparison with the uniform flow: $\mathcal{S}(X-X_0)/(\rho_\infty u^2_\infty \pi d_2^2) \approx 0.7$. The unique common property of the non-uniformities (for both flow types) was the closeness of the Mach numbers in the wake core ahead the bow shock: $M_0 \approx 2.3$. As will be shown further, it is not an accidental circumstance, but the decisive factor of the similarity of the flow patterns.

2. Dynamic-invariant quantities

Let us consider the typical boundary-value problem of supersonic flow around the head part of an axisymmetric body [10]. In the inlet section $x=x_1$ (see Fig.2), the supersonic stream without disturbances is described by the formulas:

$$x=x_1: \quad V_x=u_\infty, \ V_r=0, \ p=p_\infty, \ \rho=\rho_\infty ; \qquad (1)$$

$$M_\infty=u_\infty(\gamma p_\infty/\rho_\infty)^{-1/2}>1$$

(here, ρ is density, p is pressure, V_x, V_r are axial and transverse velocity components, γ is the specific heat ratio). On the symmetry axis ($r=0$) and on the body surface, the no flow conditions are specified. The outlet section $x=x_2$ is located in the region, where the axial velocity component is supersonic and, hence, in this cross-section the boundary conditions are not required. In the zone $x_1<x<x_2$, the existence of surfaces of discontinuity is admitted (shocks, tangential discontinuity, etc), on which the suitable compatibility condition must be satisfied. In the regions of flow with out discontinuities the parameters are described by the Euler equations. The presence of a shear non-uniformity in the supersonic flow may be taken into account by means of specifying at the inlet section instead of (1) the generalized conditions:

$$x=x_1: \quad V_x=f(r)u_\infty, \ V_r=0, \ p=p_\infty, \ \rho=g^{-1}(r)\rho_\infty, \qquad (2)$$

where the functions $f(r)$, $g(r)$ specify an arbitrary axisymmetric distribution of the non-uniformity [6,7].

Fig.2. Flow diagram

227
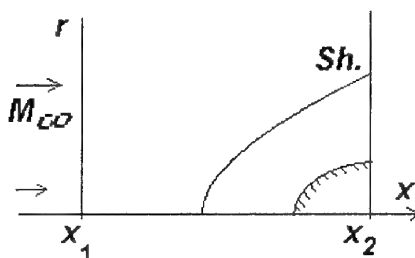
The next *theorem concerning the dynamic invariant quantities* is valid:

if in the region $x_1 < x < x_2$ there is some steady flow, which satisfies the boundary conditions (2) for f, $g>0$, $(fM_\infty)^2>g$, then there is an infinite set of other solutions satisfying the boundary conditions

$$x=x_1: \quad V_x=D^{-1/2}(r)f(r)u_\infty, \quad V_r=0,$$
$$p=p_\infty, \quad \rho=D(r)g^{-1}(r)\rho_\infty, \quad (3)$$

for arbitrary positive function $D(r)$.

The proof of this and the more general [8] theorem is based on the application of one group property of the gas-dynamical system of equations, known in the literature as "the substitution principle" [11, 12]. Further generalizations are possible for the equation of state $\rho=P(p)S(s)$ (here, s is entropy) and for some specific types of unsteady flows [12].

The solutions, which may be obtained by varying the function $D(r)$ in (3), have the property of invariance of the dynamic characteristics of the flow [8]. In particular, everywhere in the region $x_1 < x < x_2$ the pressure, the Mach number, the total pressure and the velocity pressure vector are maintained. However, the distributions of such physical parameters as the temperature, the total enthalpy, the velocity of sound, the entropy, the vorticity vector, the number and the intensity of tangential discontinuity surfaces may change. The main point is that from two functions $f(r)$, $g(r)$, determining the non-uniform structure in the stream ahead of the body, in fact, only their combination f^2g^{-1} is important [7,8]. It means that the critical parameter, determining the influence of the non-uniformity on the flow structure near the body and on its aerodynamic characteristics, is the transverse distribution of the dynamic pressure $q(r)=\rho V_x^2$. It is by this criterion it is necessary to compare the hot and the cold wakes behind the zones of energetic or dynamic influence on the supersonic flow. In particular, if non-uniformity (2) is such that $f^2g^{-1}\equiv1$, then the flow will be dynamically equivalent to the uniform flow. In other words, such non-uniformity must behave as a passive impurity, which does not change the streamline pattern and makes no dynamical impact on the body. In Fig.3 an example of the calculation of non-uniform transverse supersonic flow around a cylinder for $M_\infty=3$ is given.

The non-uniformity "N" (Fig.3,a) is localized in a narrow zone, displaced upper from the symmetry plane. In this zone, the flow velocity is two-fold greater and the temperature is four-fold greater, then in surrounding space. However, it is clear that there is no dynamic interaction of this non-uniformity with the shock layer near the cylinder: both the configuration of the bow shock front and the pressure distribution remain symmetrical (Fig.3,b), as in the uniform flow. The zone of "hot" non-uniformity "N" (Fig.3,a) penetrates through the shock front, as a passive impurity and does not distort the flow symmetry.

a   b
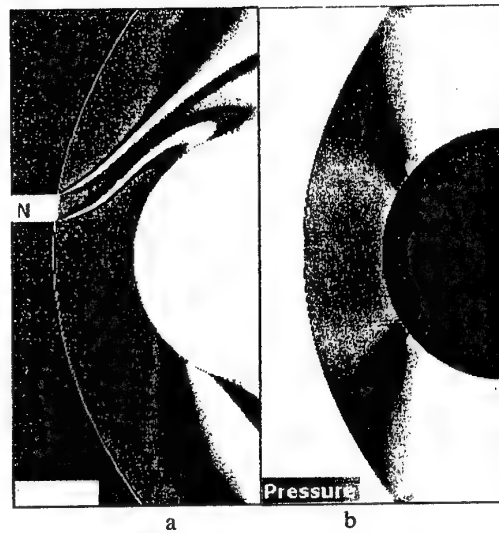
Fig.3. Distributions of the density (a) and the pressure (b) in the pseudo-non-uniform supersonic flow around the cylinder; $M_\infty=3$, $\gamma=1.4$, $f=2$, $g=4$.
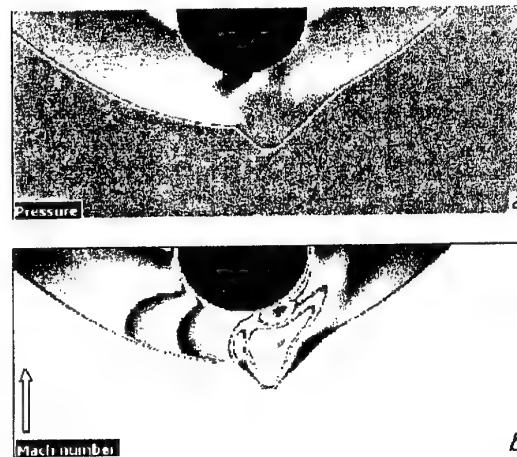
Fig.4. Distributions of the pressure (a) and the Mach number (b) in the non-uniform supersonic flow around the cylinder; $M_\infty=3$, $\gamma=1.4$, $f^2/g=0.44$.

Another flow pattern is found for different parameters of the non-uniformity. In Fig.4, the obvious dynamic interaction of the non-uniformity with the shock layer ahead of the body is shown.

228

For a viscous medium and also for unsteady flows, the dynamic-invariant quantities are not exact solutions, but in some cases they give a good approximation to the solution. In Fig.5, the results of solving the non-stationary problem of penetration of the body through the shear pseudo-non-uniformity are shown (the velocity of the main flow is 994m/s, the body moves in the transverse direction from left to right and crosses the zone of non-uniformity 10% from the body caliber wide with the velocity 60 m/s). It is clear that in the given non-stationary flow the consequence of the theorem concerning the dynamic invariant quantities is valid.
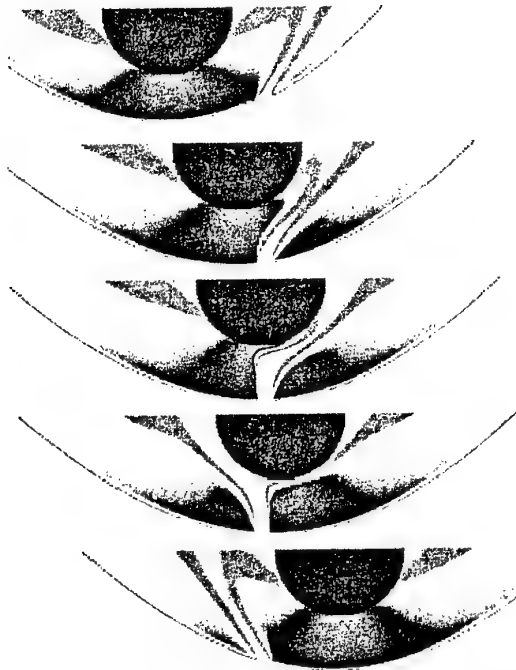
Fig.5. Distribution of the density in non-stationary flow around the body, crossing the shear non-uniformity; $M_x=3$, $\gamma=1.4$, $f=2$, $g=4$.

3. The integral relations

Assume that in a uniform supersonic flow (along the axis x), there is a region of *SOE* (with the power of energy supply W) or *DIZ* (with the drag force X), localized in some volume Ω. The centre of Cartesian coordinate system x,y,z is situated inside Ω (Fig.6).
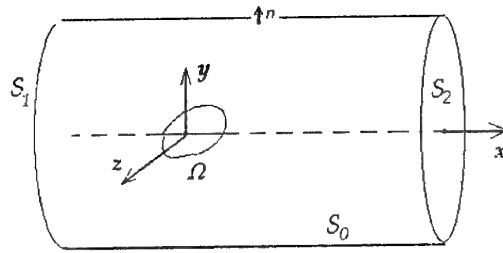
Fig.6. A control volume, including the region Ω of energy supply or dynamic-interaction zone

All the disturbances from the region W expand with the asymptotic Mach cone with the law of expansion $r \sim x^1$. In this cone near the axis x there is dissipative subzone of the wake with the asymptotic law of expansion $r \sim x^k$, $0<k<1$, where the degree k depends on the dimensionality of the space and the mechanisms of dissipation (laminar or turbulent wake, the type of turbulence) [13].

Let us surround the region Ω by the closed cylindrical surface $S=S_1+S_0+S_2$ (Fig.6), distant from the Ω so that the pressure everywhere at S may be considered as constant and equal to the pressure p_∞ in the flow without disturbances. Then the general integral equations of the mass, impulses and energy balance [10] may be written:

$$- \int_{S_1} \rho u d\sigma + \int_{S_0} \rho v_n d\sigma + \int_{S_2} \rho u d\sigma = 0 \ ,$$

$$- \int_{S_1} \rho u^2 d\sigma + \int_{S_0} \rho u v_n d\sigma + \int_{S_2} \rho u^2 d\sigma = -X - \int_{S_1+S_0+S_2} p\cos(n,x)d\sigma \ ,$$

$$- \int_{S_1} \rho u H d\sigma + \int_{S_0} \rho v_n H d\sigma + \int_{S_2} \rho u H d\sigma = W \ ,$$

from which by the known way [10,13] the following two main relations for the wakes can be obtained:

$$\int_{S_2} \rho u(u - u_\infty)d\sigma = -X \quad , \quad \int_{S_2} \rho u(H - H_\infty)d\sigma = W$$

Here $H = \dfrac{u^2}{2} + \dfrac{c^2}{\gamma-1}$ is the total enthalpy, c is the velocity of sound, $c^2 = \gamma\, p/\rho$, $u=V_x$.

The wake non-uniformity decreases because of influence of viscosity, heat-conducting and turbulent transfer. Let us accept the usual for the asymptotic wakes [13] assumption concerning the small value of $u_* = u-u_\infty$ and $\rho_* = \rho-\rho_\infty$ in comparison with u_∞ and ρ_∞. Then, neglecting the

229

values $(u_*/u_\infty)^2$ and $(\rho_*/\rho_\infty)^2$, we can calculate the asymptotic value of integral

$$I = \int\limits_{-\infty}^{+\infty} \int\limits_{-\infty}^{+\infty} (\rho u^2 - \rho_\infty u_\infty^2)\,dy dz$$

far downstream:

$$I = -2X - (\gamma - 1)\, M_\infty^2\, X - (\gamma - 1)\, M_\infty\, c_\infty^{-1}\, W \tag{4}$$

If the region Ω (Fig.6) is a region of the energy supply SOE, then $X=0$, and from (4) it follows

$$I_{SOE} = -(\gamma - 1)M_\infty\, c_\infty^{-1}\, W . \tag{5}$$

If in the region Ω there is no energy supply, but there is a dynamic interaction *DIZ*, then $W=0$, and we also have

$$I_{DIZ} = -2X - (\gamma - 1)\, M_\infty^2\, X . \tag{6}$$

As it follows from the dynamic-invariant quantities theorem (see the part 2), every shear non-uniformity with the same distribution of the Mach number are dynamically equivalent. The concrete profile of the Mach number in the wake behind *SOE* or *DIZ* may depend on the shape of Ω and the distance from Ω, and the distribution of the intensity of interaction in the Ω, and also from the mechanisms of transverse turbulent transfer in the wake. The same distribution of the Mach number in some chosen cross-section of the supersonic flow may be obtained by means of suitable location of *SOE* as well as by means of *DIZ*. Hence the equation $I_{SOE}=I_{DIZ}$ will be valid. Taking into account (5)-(6), we'll obtain:

$$(\lambda - 1)M_\infty^2 W = (2 + (\gamma - 1)M_\infty^2)Xu_\infty \tag{7}$$

It gives us a key to comparison of energetic and dynamic methods of non-uniformity formation.

The product Xu_∞ in (7) may be interpreted as the device power needed for keeping the dynamic-interaction zone ahead of the flying body. Then the following *theorem of comparison* of *SOE* or *DIZ* energetic expenditures is valid: for ensuring the same dynamic action on the bodies due to the wake behind the artificial source of non-uniformity the power W_1 of the thermal (*SOE*) and the power

$W_2=Xu_\infty$ of dynamic (*DIZ*) sources must be in a ratio

$$\frac{W_1}{W_2} = 1 + \frac{2}{(\gamma - 1)\, M_\infty^2} \tag{8}$$

Conclusion

There are different technologies of formation the artificial sources of non-uniformity, interacting dynamically with the shock layer ahead of the body. The *SOE* technologies are convenient in many aspects, but they are not the most advantageous from the point of view of the supplied power. In this paper it is shown that the dynamic method (*DIZ*) may be more profitable. In the Table the result (8) concerning the possible relative power decreasing $(W_1-W_2)/W_1$ (in percents), by the transition from energetic to dynamic method of non-uniform formation is presented.

TABLE. Possible decrease of the energy expenditures (%) by the transition from *SOE* to *DIZ*

M_∞	air ($\gamma=1.4$)	CO_2 ($\gamma=1.3$)	SF_6 ($\gamma=1.1$)
2.0	55.6	62.5	83.3
3.0	35.7	42.6	69.0
6.0	12.2	15.6	35.7
10.0	4.8	6.25	16.7

There are different technologies of formation the artificial sources of non-uniformity. The SOE technologies are convenient in many aspects, but they are not the most advantageous from the point of view of the supplied power. In this paper it is shown that the dynamic method (*DIZ*) may be more profitable. In the Table the result (8) concerning the possible relative power decreasing $(W_1-W_2)/W_1$ (in percents) due to transition from energetic to dynamic non-uniformity formation method is presented.

The keeping in the flow ahead of a body the leading solid obstacle may be realized by different ways: mechanical contacting (e.g. an aerodynamic solid string or spike) or MGD-technologies. In the latter case it is possible to keep a compact set of the small magnetic particles or an ionized gas bunch by the electromagnetic field. Also it may be interesting to use the combined technologies, i.e. *SOE* and *DIZ* simultaneously.

Acknowledgments

References

1. Chernyi G.G. The Impact of Electromagnetic Energy Addition to Air Near the Body On Its Aerodynamic Characteristics. // 2-nd WIG Workshop, proceeding, Norfolk, VA, April 24-25, 1998, pp. 1-31.
2. Tretyakov P. Supersonic Flow around Axisymmetric Bodies with External Supply of Mass and Energy. // 2-nd Workshop on Magneto-Plasma-Aerodynamics in Aerospace Applications, proceeding, Moscow, April 5-7, 2000, pp. 128-132.
3. Macheret S.O., Ionikh Yu.Z., Chernysheva N.V., Yalin A.P., Martinelli L., McAndrew B., Barker P.F., Shneider M.N. and Miles R.B. Shock Propagation in Weakly Ionized Gases and Plasma Control of High-Speed Flows. // 2-nd Workshop on Magneto-Plasma-Aerodynamics in Aerospace Applications, proceeding, Moscow, April 5-7, 2000, pp. 34-42.
4. Guvernyuk S.V. and Samoilov A.B. Control of Supersonic Flow Around Bodies by Means of a Pulsed Heat Source. // Tech. Phys. Lett. 23(5), May 1997, pp. 333-336. // [S1063-7850(97)00105-5 – American Institute of Physics].
5. Levin V.A., Afonina N.E., Gromov V.G., Georgievsky P.Yu. and Terentjeva L.V. Influence of Energy Input by Electric Discharge on Supersonic Flows around Bodies. // 2-nd WIG Workshop, proceeding, Norfolk, VA, April 24-25, 1998, pp. 201-231.
6. Lin T.C., Reeves B.L. and Siegelman D. Blunt-Body Problem in Non-Uniform Flowfields. // AIAA J., 1977, vol. 15, no. 8, pp. 1130-1137.
7. Guvernyuk S.V. and Savinov K.G. Generalization of the Blunt-Body Problem in Non-Uniform Supersonic Flowfields. // Fluid Dynamics, vol. 31, № 2, March-April, 1996, pp. 302-307.
8. Guvernyuk S.V. Dynamical Invariants in Problems of Steady Inviscid-Gas Flow around Bodies. // Physics-Doklady, vol.41, № 8, 1996, pp. 361-364.
9. Guvernyuk S.V. and Zibarov A.V. About Modeling of the Gas-Dynamic Effects of the Sources of Impulse-Periodical Energy Supply in the Problems of Flow Structure Control. // Mathematical Models and Methods of their Investigation. International conference, Krasnoyarsk 1999, August 18-24. Abstracts, pp. 84-85 (in Russian)
10. Chernyi G.G. Gazovaya dynamica. – Nauka, Moscow, 1988, 424 p. (in Russian).
11. Oliveri F. and Speciale M.P. Exact Solutions to the Equations of Ideal Gas-Dynamics by Means of the Substitution's Principle. // Int. J. Non-Linear Mechanics, 1998, vol. 33, № 4, pp. 585-592.
12. Munk M. and Prim R. On the Multiplicity of Steady Gas Flows Having the Same Streamline Pattern. // Proc. Nat. Acad. Sci. USA. 1947. Vol. 33. pp. 137-141.
13. Birkhoff G. and Zarantonello E.H. Jets, Wakes and Cavities. – Academic Press inc. Pub. N.Y. 1957.

43. THE THERMAL CORRECTION OF SCRAMJET INTAKE

T.A. Bormotova, V.V. Golub, V.V. Volodin
IHED IVTAN

I.N. Laskin
CIAM

I. Introduction

Supersonic combustion ramjet (scramjet) technology is expected to provide the propulsion for future hypersonic vehicles. The successful development of such technology were achieved by means of ground based wind tunnel testing, computational fluid dynamics (CFD), and flight tests.

One of the actual problems of supersonic flying device aerodynamics is the maintenance of appropriate mode of air-breather operations under changing of flight conditions [1]. The system of the shocks is realized in the scramjet diffuser. Scramjet diffuser operates under an optimum mode, when the shocks hit to an engine cowl. Changing of flight Mach number the oblique shocks deviate from the engine cowl. For the maintenance of the first oblique shock angle to be a constant the rejection angle of incident flow from an initial direction varies by changing an angle of the diffuser wall inclination. In this paper the opportunity of the flow Mach number that to be supported constant before the first oblique shock by the heat-supply in a region before the air-breather (Fig.1) is considered.

Fig.1. A sketch of an intake correction by the volumetric heat-supply before first oblique shock

Using the constant flow Mach number before the first oblique shock the Mach numbers distributions before the following shocks also remains constant and, thus, optimum shock-wave configuration is statement.

One of the flow Mach number reduction ways is a volumetric heat-supply to the flow in the region before the scramjet diffuser first oblique shock. The supersonic flow gas parameters are changed at the homogeneous volumetric heat-supply.

The dependence of flight Mach number on the scramjet flight height is shown on Fig.2. [2]. The atmospheric gas parameters were used depending on a flight height.
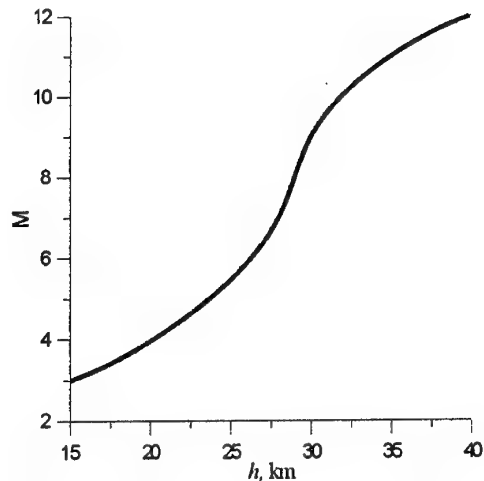
Fig.2. The Mach numbers dependence on the flight height.

The analytical prediction of useful energy losses in the first oblique shock was carried out depending on flight height and it results are shown on Fig.3. The sum of energy losses in shock and in heat-supply origin is less those using the mechanical correction.
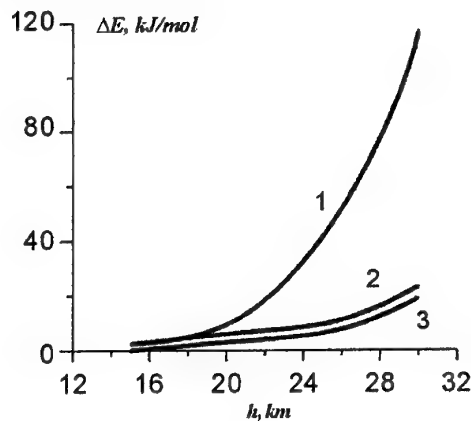
Fig.3. The energy losses in first oblique shock using the mechanical correction (1), thermal correction (2) and the heat-supply energy (3) dependencies on a flight height.

232

II. Numerical calculation of supersonic gas flow structure in the heat-supply region

The numerical calculation of gas flow structure and parameters in the region of the volumetric heat-supply was carried out. The calculation of structure in the wake of energy source also carried out in [3]. The formation of a contact surface between the heated up and cold gas behind oblique shock, a temperature, a pressure and a Mach number of the flow are considered. The flow gas expansion (Fig.4) is caused by the volumetric heat-supply to the supersonic flow if there are no walls.
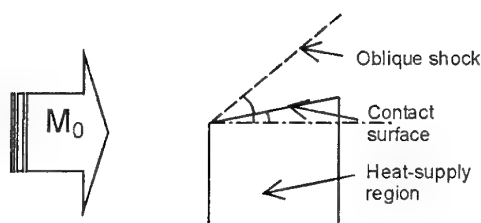
Fig.4. An ideal gas flow structure in the heat-supply region.

Table 1. M_i, P_i and T_i – gas flow initial parameters, P_f and T_f – gas flow parameters on the out of the energy supply region and Q - the heat-supply energy.

M_i	Q, J/mol	T_i,K	T_f,K	P_i,Torr	P_f,Torr
3	0	217	217	90.8	90.8
7	$2.8*10^4$	224	1145	12	50
9	$5.2*10^4$	230	1946	8.9	59.6

The supersonic gas flow outside of heat-supply region is deviated from the initial upstream. The formation of oblique shock should be carried out. On the beginning of the heat-supply region the oblique shock is a Mach line. It is being transformed in a shock wave towards the end region of heat-supply. The static pressure behind it is increased up to one in the heat-supply region. On the both sides of the contact surface the static pressures should be equal, provided the static temperature, the density and the Mach number of flow are changed.

Experimentally the similar structure was observed in the argon flow with the pulse laser energy source [4].

The task is to support the constant Mach number behind heat-supply source. It was numerically solved in a plane stationary case for the heat-supply region 1m*1m for the air flow of the different external flow Mach numbers. The static temperatures and pressures of the flow with the isotropic heat-supply were calculated. The

results are represented in table 1 and plots in Fig.6-8.
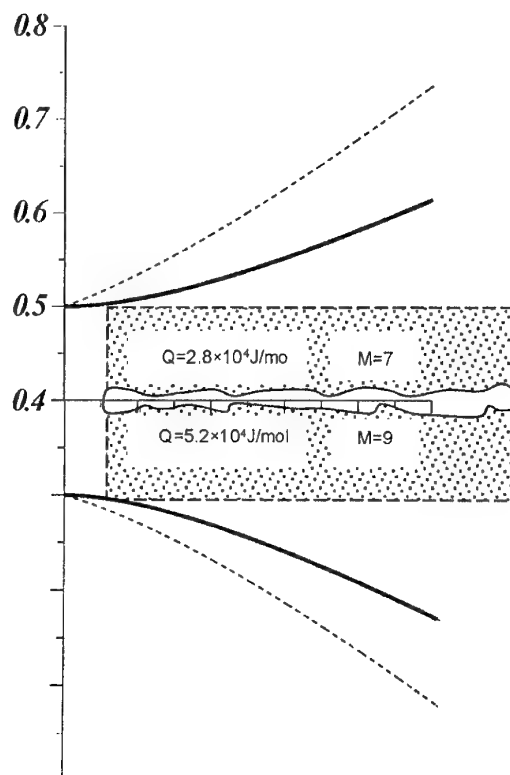
Fig.5. The contact surface (solid line) and oblique shock (dashed line) dependencies on
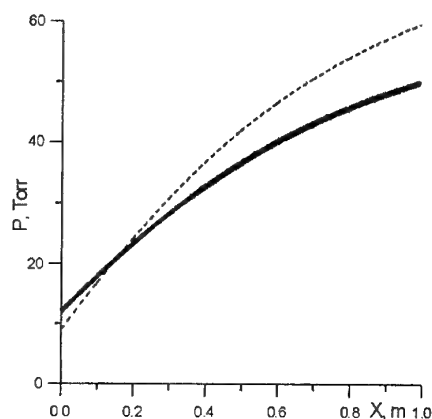
Fig.6. The static pressure downstream distributions for the external flow Mach numbers 7 (solid line) and 9 (dashed line).

Increasing the external flow Mach number the pressure on the output from the heat-supply region is increased. In the case of diffuser mechanical correction the static pressure on the input of an air-breather is the same as the beginning of heat-supply region. When the upstream Mach

233

number is increased the temperature in the heat-supply region is essentially increased (fig. 7). When the Mach number is reduced from 7 to 3 the temperature is increased in 3 times, and from 9 to 3 in 10 times. Practically the ambient temperature isn't changed with a height. According to statement of the task, the Mach number on an output from heat-supply region remains constant and it is equal 3 (Fig. 8).
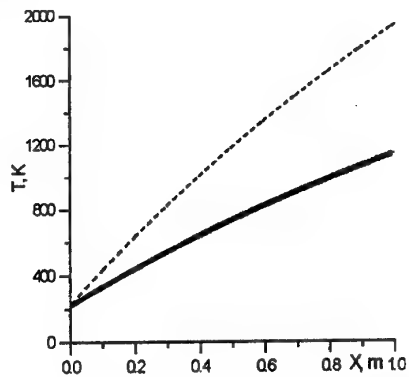
Fig.7. The static temperature distributions on the downstream coordinate for the flow Mach numbers 7 (solid line) and 9 (dashed line).
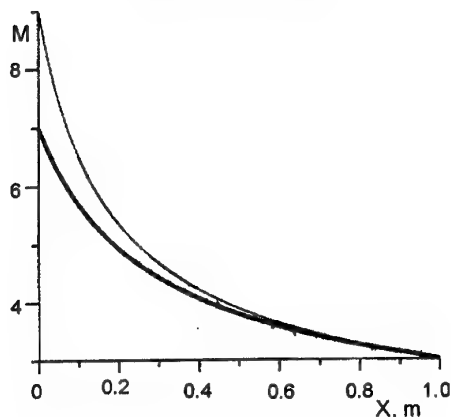
Fig.8. The flow Mach numbers dependencies in the region of volumetric heat-supply on the downstream coordinate for the initial Mach numbers 7 (solid line) and 9 (dashed line).

III. The flow in the scramjet diffuser calculation

The obtained data were used in the 1m-height plane scramjet diffuser numerical modeling for different flight Mach numbers with correction of the first diffuser oblique shock by a mechanical method and by the volumetric heat-supply in the region before the air-breather. The different requirements to mathematical models and computer codes can be formulated for the flow description in these elements. One of the most important problem is connected with the boundary layer in the scramjet duct. In traditional approach, it is anticipated that forces and heat transfer loads can be evaluated in the process of successive calculations of inviscid flow and boundary layer. Such approach is not applicable for the hypersonic propulsion because of the strong viscous/inviscid interaction, shock wave/boundary layer interaction etc. All these difficulties might be overcamed if the full Navier-Stokes equations are used for the flow description. Unfortunately, the applications of the codes developed on the basis of these equations, are limited, especially at the stage of design.

Parabolized Navier-Stokes (PNS) methods provide an efficient alternative to full Navier-Stokes techniques for high Reynolds numbers, supersonic and hypersonic flows with local subsonic regions when employing the space-marching methods.

The PNS equations are used for the description of steady flow in the scramjet duct. The Reynolds averaged system of equations is used in the case of turbulent flows. The differential turbulence model for turbulent viscosity [5,6] developed in CIAM and tested on high speed boundary layers and jets problems has been incorporated into the CFD code. Regularization techniques of Cauchy initial value problem in subsonic regions is carried out with analogy of [7,8].

The explicit and semi-implicit marching schemes [9] are developed for the modified system of equations. This upwind scheme is used both in supersonic and subsonic regions. The developed upwind marching scheme is an adaptation of supersonic steady analogy of Godunov's scheme [10]. The higher order of accuracy with conservation of monotonicity is realized with the aid of principle of minimal derivatives [11].

The gas parameters on an energy supply region output were used as the initial data in numerical modeling of a scramjet diffuser for different flight Mach numbers. The comparison of gas parameters in an air-breather using the mechanical and thermal corrections of the first oblique shock was carried out.

In an air-breather the static pressures using the mechanical and thermal corrections (Fig. 9) are approximately the same at the appropriate ambient Mach numbers. The Mach numbers fields using the thermal correction in the diffuser practically are not varied under changing of ambient Mach numbers (Fig.10). The shock-wave configurations are constant. The changes are caused by effects of a boundary layer thickness reduction and a dissociation by temperature increasing. It facilitates a construction of the scramjet combustion chamber.

234
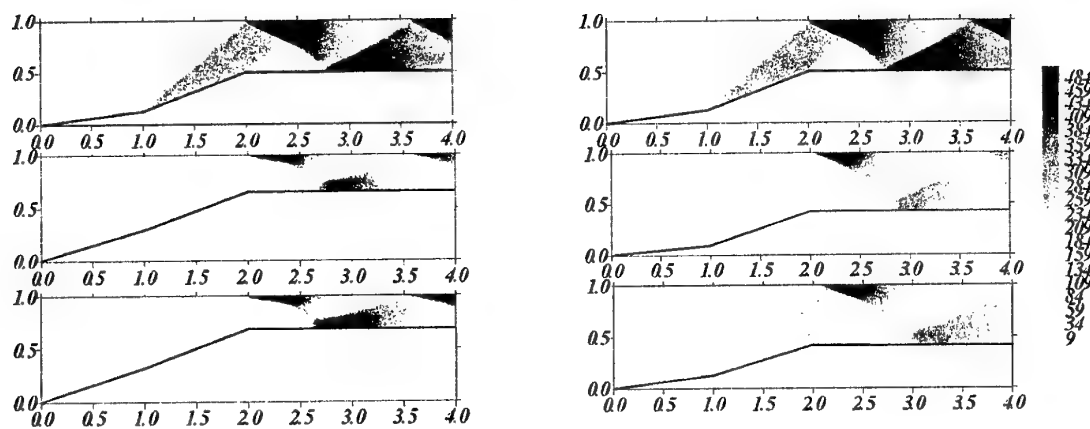
Fig.9. The static pressure distributions in the scramjet diffuser for the flight Mach numbers 3, 7 and 9 (from up to down) in the cases of mechanical and thermal (left and right) corrections of the first oblique shock.
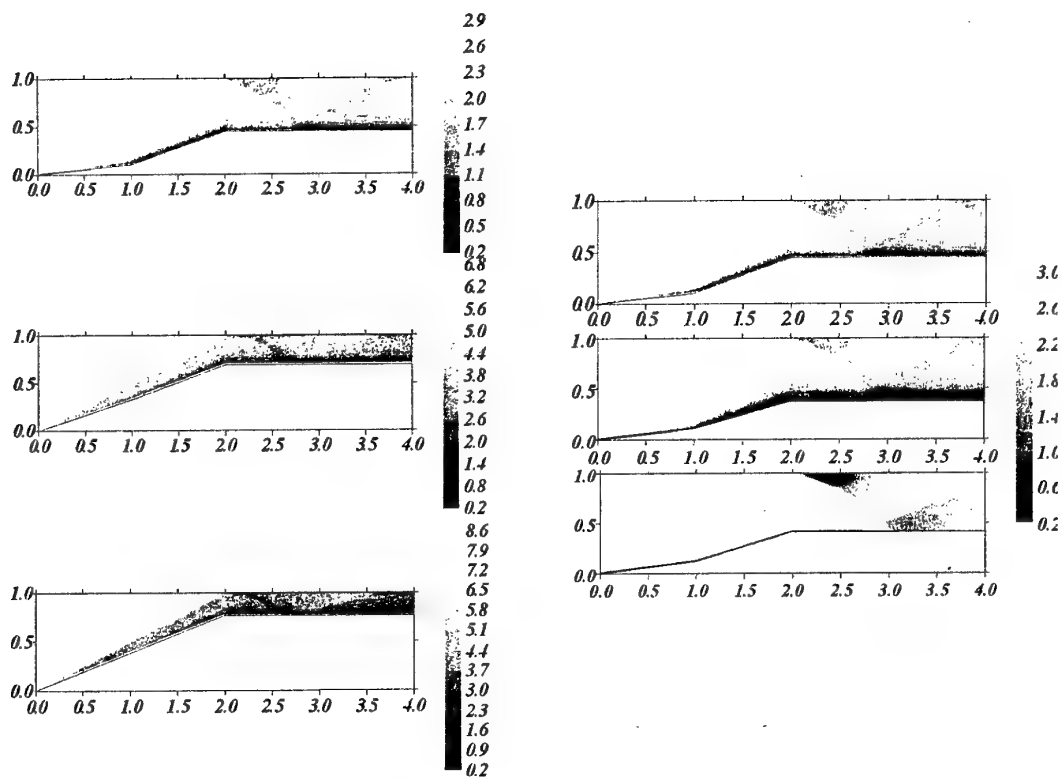
Fig.10. The Mach number fields in the scramjet diffuser for the flight Mach numbers 3, 7 and 9 (from up to down) in the cases of mechanical and thermal (left and right) corrections of the first oblique shock.

235
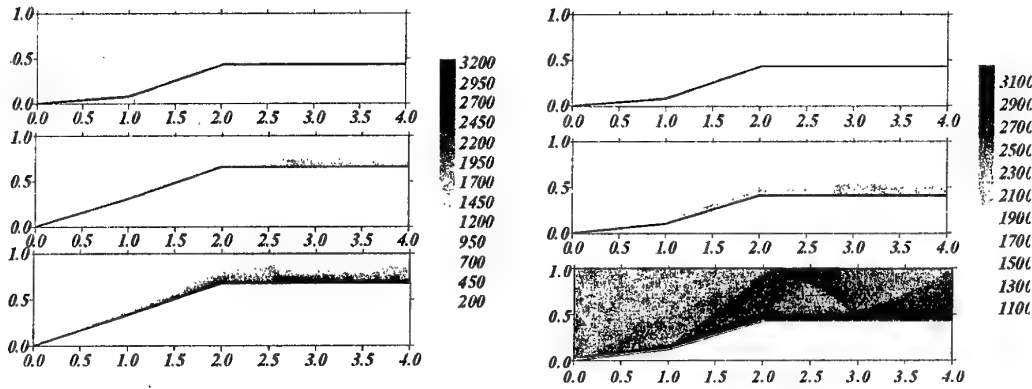
Fig.11. The static temperature distributions in the scramjet diffuser for the flight Mach numbers 3, 7 and 9 (from up to down) in the cases of mechanical and thermal (left and right) corrections of the first oblique shock.

The temperature in an air-breather is more than twice of the one using mechanical correction under the appropriate ambient Mach number (Fig.11). It will increase thermal loading in the combustion chamber.

According to obtained data it were obtained the flight Much number dependencies of a substance flow passed through the scramjet diffuser (Fig.12), diffuser drag (Fig. 13) and power spent for drag overcoming (in case of thermal correction with power of a heat-supply) (Fig.14).

Fig.13. The dependence of drag in the cases of mechanical correction (solid line) and thermal correction (dashed line) on flight Mach number.

Fig.12. The dependences of substance flow in the cases of mechanical correction (solid line) and thermal correction (dashed line) on flight Mach numbers.
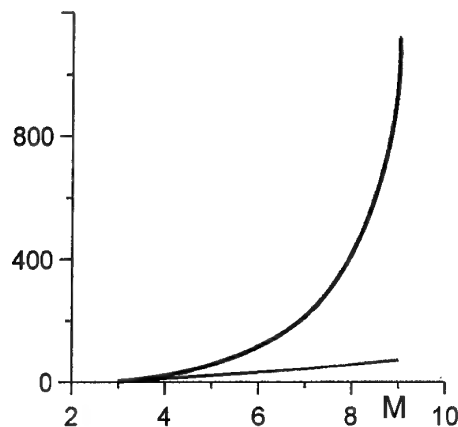
Fig.14. The dependence of full power of drag in the cases of mechanical correction (solid line) and thermal correction (dashed line) on flight Mach number.

IV. Summary

1. Using the thermal correction of a scramjet diffuser the drag force and power spent for drag overcoming are strongly decreased.
2. The static pressure and Mach number in air-breather are not changed under changing of ambient Mach numbers
3. The temperature increased is more than twice and a heat flux into the combustion chamber walls is also increased.
4. Using the thermal correction of a scramjet diffuser the substance flow through the air-breather is reduced.

References

1. R. Hermann Supersonic inlet diffusers and introduction to internal aerodynamics.
2. J.J. Erdos Scramjet testing in shock-heated tunnels, ISSW21, vol. 1, pp. 41-50.
3. Lukianov G.A. Drag and Heat Exchange of an Object in a Supersonic Flow with a Source of Energy in Front of the Object, 2-nd Workshop on Magneto-plasma-aerodynamics in Aerospace Applications, 2000, pp.133-137.
4. Tret'akov P.K., Yakovlev V.I. Wave structure in supersonic flow with the laser energy source, DAN.-1999.-Vol.365, №1.-pp. 58-60

5. Kozlov V.E., Secundov A.N., Smirnova I.P. The Turbulence Models for Compressible Gas Flows Jets. Fluid Dynamics. No. 6, 1986. p.38-44.
6. Gulyaev A.N., Kozlov V.Ye., Secundov A.N. A Universal One-Equation Model for Turbulent Viscosity. Fluid Dynamics, V.28, No.4, 1993, p.485-494.
7. Kovenya V.M., Chernyi S.G. Method of Solution of Steady Simplified Equations for Viscous Gas. Institute of Theoretical and Applied Mechanics, Preprint 42-81, 1981.
8. Vigneron Y.C., Rakich J.V., Tannehill J.C. Numerical Simulation of Steady Supersonic Viscous Flow. AIAA 79-0130, 1979.
9. Kopchenov V.I., Laskin I.N. A Finite-Differenece Scheme for Numerical Solution of Parabolized Navier-Stokes Equations, Comp. Maths Math. Phys., Pergamon, Vol.36, No. 2, pp.235-245, 1996
10. Godunov S.K., Zabrodin A.V., Ivanov M.Ya., Kraiko A.N., Prokopov G.P. Numerical Solution of Multidimensional Gas Dynamics Problems. M., Nauka, 1976.
11. Kolgan V.P. The using of minimal derivatives principle under construction of finite-difference schemes for calculation of discontinuous gasdynamics solutions. TsAGI Scientific Notes (in russian), V.3 , No.6, 1972.

44. PULSATING LASER PLASMA IN A SUPERSONIC FLOW: EXPERIMENTAL AND ANALYTICAL SIMULATION

Yakovlev V.I.

Institute of theoretical and applied mechanics SD RAS, 630090, Novosibirsk

Abstract. The stabilization of an optical pulsating discharge in a supersonic flow for the first time realized in [Tretyakov P.K. et al //Physics-Doklady.- 1994, v.39, No.6; and 1996, v.41, No.11] gave new possibilities to simulate and study experimentally gas flows with an external energy supply. In addition to experimental data on the wave structure, the work presents the results of an analytical study of energetic and gasdynamics parameters correlation, allowing one to estimate effects of laser plasma/supersonic flow interaction in a broad range of initial conditions.

Two different quasistationary flow conditions formed by proper laser beam focussing are studied herein. One regime is characterized by the limited rate of energy supply behind a light-supported detonation wave, the other one, by instantaneous energy deposition (point explosion).

The dependence of gasdynamic parameters and thermal wake boundaries on the free-stream flow Mach number and laser power was determined. For example, the relative values of the total pressure different for both regimes at the same power absorbed decrease suffitiently, more than by an order of magnitude, with Mach number increasing between 1-10. Besides, as integrated effects depend on the body and thermal wake dimention ratio, these effects are strengthened by increasing power up to certain limits.

1. Introduction

Stabilization of a pulsating optical discharge in a supersonic flow first achieved in [1-3] offered wide potentialities for experimental simulations and studies of flows with external energy supply. The problem of achieving nearly steady (quasistationary) energy deposition into the flow was solved (by ITAM in cooperation with Institute of Laser Physics, SD RAS) using a pulsed-periodic radiation emitted by a CO_2-laser with a mean output energy of 1 to 2.5kW at a repetition frequency $f=12,5-100$kHz. The power density of each focused pulse is greater than the threshold value for the breakdown (over 10^8 W/cm^2), which provides stabilization of the pulsating plasma in an argon supersonic flow. Experimental data showed that, at a high frequency, the pulsating plasma thermal source generates a quasistationary wave structure consisting of a shock wave in its nose part and of a thermal wake spreading far downstream [2-6]. On the basis of available laser plasma dynamics concepts [7,8] for the region behind the light-supported detonation wave (LDW), flow parameters in the thermal wake were also determined [9] under condition of large length l of the breakdown plasma (with respect to its diameter d). In experiments the above indicated condition was ensured by proper focusing of the laser radiation. In the case of short focusing, i. e., at $l\sim d$, the conditions for light-supported detonation wave are lacking and the character of the energy deposition processes suits better the condition for an instantaneous local release of energy. The latter condition is usually used in numerical studies [10,11] of interrelation between space-time energy parameters of the heat source and the flow structure

in the vicinity of streamlined bodies. An analytical model of an intense point explosion was also used in [12] for predicting desired configuration of the shock wave that can be initiated by a series of laser pulses. As shown below, the potential of the analytical approach within the limits of this model can be substantially widened. Indeed, apart from the space-time scales of the process, it becomes possible to find correlation between its gasdynamic and laser radiation energy parameters using generalized results of numerical studies of a point explosion with allowance for counter pressure [13,14].

The purpose of the present work is to perform a comparative analysis of the wave structure and thermal wake parameters in a supersonic flow with a pulsating plasma thermal source for two utmost focusing conditions for the laser beam (either extended at $l>>d$ or local at $l\sim d$). This analysis is based on a developed approximate method for evaluation quasistationary parameters behind the breakdown region in dependence on frequency-energy characteristics of the laser radiation and on the flow Mach number. To reveal specific features of the two flow conditions and differences between them, the comparative analysis is carried out at identical mean power of laser radiation and initial conditions of the experiments performed (at $l>>d$).

2. Extended plasma heat source. Physical models used and assumptions adopted.

Among known regimes of discharge propagation along a laser beam [7] in the case of its sharp focusing, only the light-supported detonation regime can be operative [15]. The light emitted by

laser is absorbed in a thin layer behind the front of the LDW with a certain characteristic absorption length smaller than the beam diameter (the condition for the existence of an LDW). The propagation velocity V of the LDW front is given by the following equation [7]: $V=[2(\gamma^2-1)W/s\rho]^{1/3}$, where γ is the ratio of specific heats, W is the radiation power (in the pulse), s is the beam cross-sectional area, and ρ - the initial gas density. In the power-density range $W/s=10^8-10^{10}$W/cm^2 typical of LDW conditions this velocity is hypersonic (several km/sec). The flow parameters behind the LDW front (denoted with the subscript W), namely: the density, pressure, internal energy (or enthalpy), flow velocity and velocity of sound, are given by the following well known relations for detonation waves: $\rho_W/\rho_\infty=(\gamma+1)/\gamma$, $P_W/\rho_\infty V^2=1/(1+\gamma)$, $\varepsilon_W/V^2=\gamma/(\gamma+1)^2(\gamma-1)$, and $u_W=c_W=\gamma V/(\gamma+1)$. Here the subscript ∞ refers to the free-stream parameters. In the optical breakdown plasma with a high degree of ionization (~1) and temperature of about 25000K, the apparent adiabatic index is expected to lie in the range 1.15-1.25 with an average value $\gamma=1.2$. Under the experimental conditions of [2,3], at a repetition frequency of laser pulses 100kHz $V=5.7$km/sec, the pressure behind the LDW front is $P_W=34$MPa, $\varepsilon_W=40$MJ/kg, and the argon temperature is 24500-25000K (and $\gamma\cong1.21$). The peak values of the above-indicated parameters are attained in a narrow zone the length of which is no greater than the laser beam diameter, 0.2-0.25 mm.

The pulsed-periodic regime of energy supply is characterized by rapid (the pulse duration is $\tau\ll t=1/f$) formation of an extended plasma, which is removed downstream over the distance $l=ut$ until the next breakdown begins. The measured lengths of the glow region are about 5-8 mm, in line with the values predicted by the formula $l=\int Vdt$ or $l\approx V\tau$ from the measured power dynamics of laser pulses $W(t)$ (or respective average values of W and τ). Visualization data showed that, as the repetition frequency of the pulses increases (in excess of $\sim u/l$), a continuous and extended thermal wake was formed behind the breakdown region. The nonstationary shock waves generated by each breakdown give rise to a quasistationary shock wave around the nose part of the thermal source as it happens in a flow around solid body. The threshold frequencies given by the relation $f_1=1/t_1=u/\int Vdt$ for the experimental conditions with repetition frequencies of laser pulses $f=12.5$, 25, 45, and 100kHz are shown in Fig.1 as normalized values f/f_1 ($=t_1/t$) for the range $\gamma=1.15-1.25$. The main result is the following: the working and threshold frequencies coincides (i.e., $f/f_1=1$) in the frequency range 45-65kHz in which the measured decreasing relative values of the

aerodynamic drag C_x/C_{x0} of streamlined models attains an almost constant value. In view of the fact that the range of mean radiation power is rather narrow, this result confirms that the condition for the transition to the quasistationary flow regime has the form $V\tau=u/f_1$ or $f_1=u/l$.
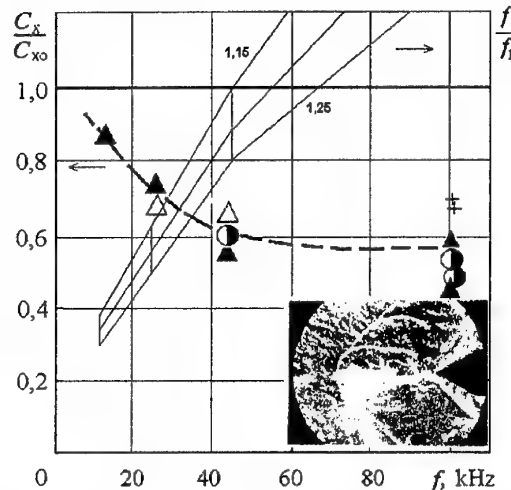
Fig.1. Experimental data on aerodynamic drag reduction C_x/C_{x0} and calculated normalized frequency f/f_1.

The problem of determining quasistationary flow parameters in the thermal wake can be solved using the well known results of numerical and experimental studies [8,16] of breakdown plasma dynamics. In the coordinate system attached to the LDW, the plasma flow detaches from the front with the local velocity of sound. Therefore, the flow pattern corresponds to an underexpanded sonic nozzle outflow of expanding plasma into a co-current hypersonic flow. The interaction between the two flows results in appearance of an adiabatic shock wave, and the heated gas expands and gets acceleration in the axial direction, forming a high-temperature jet ranging over a distance up to several hundreds of the "nozzle" diameter. In this case, as the numerical study [8] showed, the radius of the shock wave and the pressure distribution in the asymptotic region (over a distance far in excess of the diameter of the energy-releasing region) can be determined from the point explosion model. Simultaneously, the high-temperature gas flow in the flow core (jet) with good accuracy is isentropic owing to weak intensity of oblique shocks in the internal region of the flow. Thus, determination of the pressure distribution behind the optical breakdown region is the main problem. Its solution should permit determination of other flow parameters in the thermal wake also.

239

We used the solution of the problem about point explosion with allowance for counter-pressure [13] for a cylindrically symmetrical geometry with ignored edge effects since the diameter of the energy-releasing region is far smaller than the characteristic spatial scale.
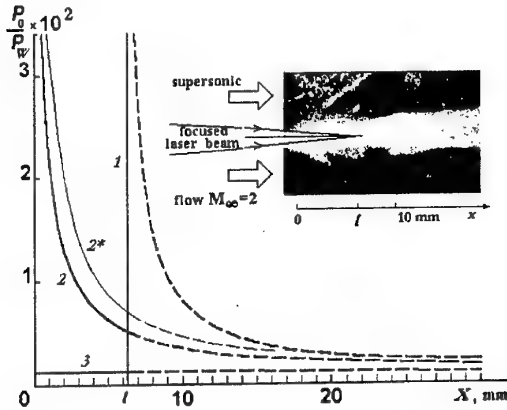
Fig.2. Pressure profiles in the optical discharge region (0 – 6.3 mm) at various times after breakdown: $1 – t = 0$, laser impulse starting ; $2 – t=\tau$, finishing ; $3 – t=1/f$, to the next laser impulse. 2^* – non-one-dimensional flow.

According to the adopted model, the radius of the wave $r(x)$ at a distance x from the LDW front was determined at the time $t=x/V$ after explosion of a linear charge with a specific (per unit length) energy $E_0=W/sV$. Figure 2 shows the distributions of the relative pressure P_0/P_W in the central part of the flow at different moments. The vertical line 1 corresponds to the beginning of a laser pulse ($P_0=P_W$ at $t=0$), pressure profile 2- to its end ($t=\tau=1.1\mu sec$), and profile 3 - to the beginning of the next laser pulse (at $t=1/f=10\mu sec$ for $f=100kHz$). The axis x is in the direction of a gas flow and laser beam, the latter being focused at $x=6.3mm$ ($t=0$). The LDW propagates in the counter direction, and at $t=\tau$ $x=0$. The dashed lines continue the respective solution into the expanded region of x and t; they show the spatial profiles of pressure for the conditions of stationary radiation at the above indicated moments. In reality, the breakdown region is limited by the range $x=0$-6.3mm ($=V\tau$); it is why the actual pressure profiles differ from the predicted ones. Nevertheless, these results give all necessary data on dynamics and characteristic scales of the process in the breakdown region. At a small (several diameters of the laser beam, or ~1mm) distance behind the LDW front there occurs an abrupt pressure drop from several tens of MPa down to a level comparable with a pressure in the flow (56kPa). At every position of the LDW, the pressure profiles differ more weakly from one another as we moves farther from the breakdown region; these profiles come close together at a distance no greater than the length of the breakdown zone l, where the flow becomes isobaric. Thus, a certain quasistationary pressure distribution weakly nonuniform along the downstream direction (and, hence, similar distributions of other parameters) is attained behind the nonstationary region of the optical breakdown. The repeated breakdown in a cold gas with "entrained" plasma maintains the steady flow regime. The glow behavior is indicative of rapid transition from nonstationary flow conditions to stationary ones (see photo in Fig.2); here, the bright region (breakdown plasma) is followed by a region with weakly varying glow intensity in the thermal wake.
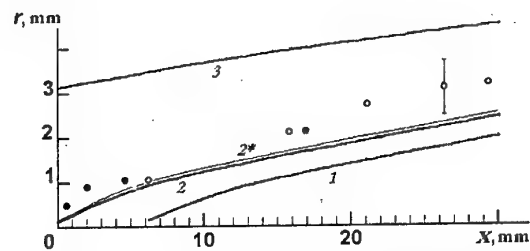
Fig.3. Experimental data on the thermal wake configuration in comparison with the results of calculations for different times after optical breakdown ($1-3$, $t = 0$, τ, $1/f$)

The question about the magnitude of the quasistationary pressure can be solved by comparing visualization data and the natural glow of the wake, on the one hand, and the predicted radius $r(x)$ at various times from the beginning of laser pulse, on the other. In figure 3, these solutions are shown (by curves 1–3) for three (analogous to Fig.2) moments: $t=0$, τ, and $1/f$ after the breakdown. The experimental data are close to curve 2, i.e., for $t=\tau$, when the maximum amount of gas is "entrained" into the motion. It is why the pressure profile at the end of laser pulse was used to calculate other wake flow parameters. Quantifying the reduction of pressure with the parameter $p=P_0/P_W$ and using formulas for an isoentropic flow, we immediately obtain the following relations for the relative enthalpy and density in the central part of the wake flow:

$h_0/h_W =p^n$, $\rho_0/\rho_\infty = p^{1-n} (1+\gamma)/\gamma$,

where $n = (\gamma - 1)/\gamma$.

The flow velocity and the Mach number are obtained by similar manner:

$u_0/V = [1+2(1 – p^n)/(\gamma - 1)]^{1/2} \gamma/(1 + \gamma) + u_\infty/V$,

$M = (u_0/V – 1)(1 + \gamma)/\gamma \, p^{n/2}$,

where u_∞ is the main flow velocity.

240

Figure 4 shows the distributions of the relative enthalpy (a) and total pressure (b), and also the distribution of the thermal wake Mach number M_0 for the conditions of a main argon $M_\infty=2$ flow. In the region occupied by the quasistationary flow, the enthalpy amounts to 0.4 of its extreme (behind the LDW front) value, which corresponds to a temperature drop from 24500K to 12500K. It is essential that the gas density turned out to be diminished by two orders of magnitude. Owing to high local velocity of sound, the Mach number is relatively low, $M_0 \approx 1.4-1.6$ at high flow velocity. The interrelation between these parameters results in a decrease in the total (stagnation) pressure $(P_0)^*$ with respect to its value $(P_\infty)^*$ in the main flow.

a)
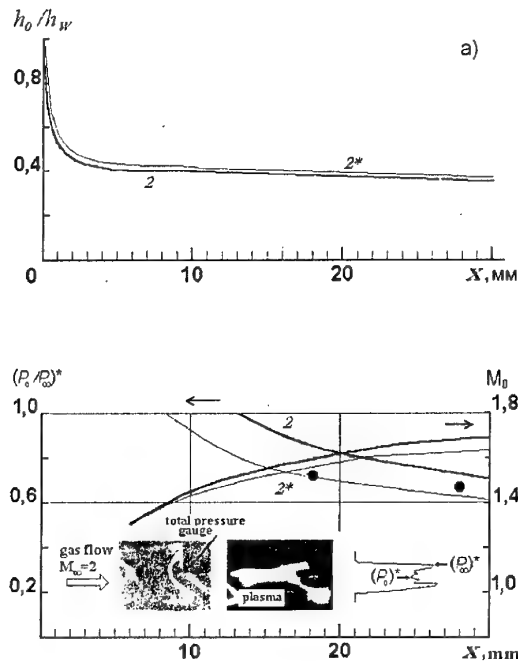
Fig.4. Flow parameters axial distribution in a quasistationary thermal wake.

In the frame of this model, it is possible to evaluate the effects due to flow non-one-dimensionality caused by the radial divergence of the flow and plasma radiation losses. The first effect can be estimated like in [7] by introducing an additional parameter δ and using in the calculation, instead of W/s, the effective value $\delta(W/s)$. In the experiments, the power density was little more than its threshold value; therefore, the value $\delta=0.5$ was used to obtain a rough estimate. The results are shown in Figs.2-4, 7 with respective curves 2*. The change in the flow parameters is relatively small owing to the fact that the dependence $V \sim W^{1/3}$ is weak and the decrease in P_W is small.

The radiation losses can be estimated from the ultimate value of the total radiant flux $S_R(x)= 4\pi \int \varepsilon_S(T,n_E,n_1)dx$ of the breakdown plasma extending over the distance x from the LDW front. An approximate expression for the integral (over spectrum) emission capacity ε_S of dense argon plasma was obtained in [16] when studying a continuous optical discharge. Also used was the predicted distribution of parameters behind the LDW front. Comparison between the radiant flux with the mass energy flux $S_M \approx \rho_0 V h_W$ permits gaining a better insight into the contribution of the radiation energy losses to the total energy balance. Under the experimental conditions, $S_M \approx 6.3 \cdot 10^7 \text{W/cm}^2$, which well correlates with the laser radiation flux $W/s \approx (0.5-1) \cdot 10^8 \text{W/cm}^2$ that provides for the heating and the gas motion in the breakdown region. The predicted distribution of the integral emission capacity of argon plasma behind the LDW front displays an abrupt decay (by three orders of magnitude) over a distance comparable with the beam diameter. It is this region that contributes predominantly $(2.2 \cdot 10^6 \text{W/cm}^2)$ to the total radiant flux $S_R=2.24 \cdot 10^6$ W/cm^2 throughout the entire length (6.3mm) of the breakdown region. Hence, $S_R/S_M=0.036 \ll 1$ and, consequently, the effect due to radiation losses is negligible.
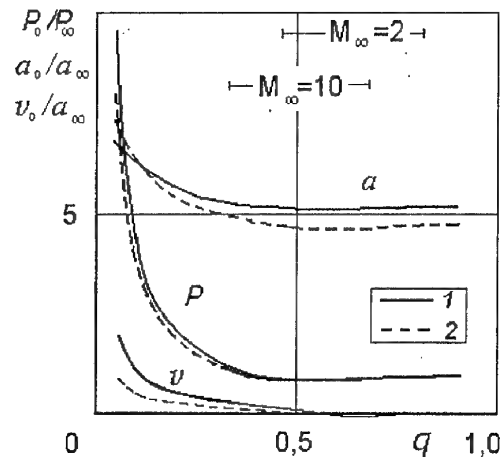
Fig.5. Gasdynamic parameters behaviour in central part of point explosion.

Thus, the obtained solutions show that the quasistationary thermal wake is a high-temperature rarefied supersonic flow. An indirect indication for this is provided by the photographs (in Fig.4) of the flow around pressure gauge, which indicate the presence of a compression shock in front of them. The large extension of the wake (no less than 150d) observed in experiments gives grounds for ignoring

241

dissipative processes caused by, say, vortex formation processes in mixing flows, at least, on the initial stage of development. The validity range of this condition can be clarified by measuring the radial distribution of the total (also static) pressure in the flow behind the plasma thermal source. By now, no systematic studies of this matter have been carried out. Only limited data are available obtained by measuring the total pressure with a Pitot tube 1.8mm in diameter installed behind the breakdown region (18 and 28mm). These data for close to quasistationary conditions (f=35kHz) are shown in Figs.6 and 7; they agree well with the predicted values.
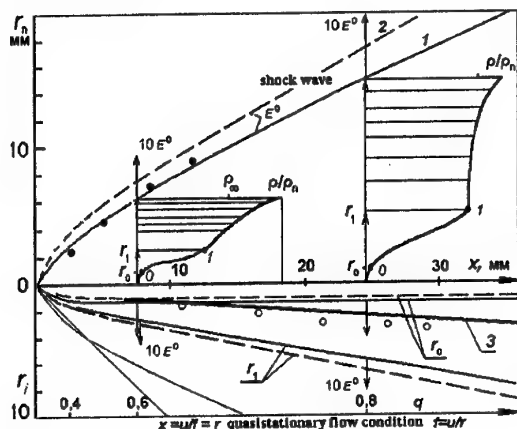
Fig.6. Wave structure and radial density distribution in supersonic M_∞=2 flow caused by point (x=0) energy deposition.
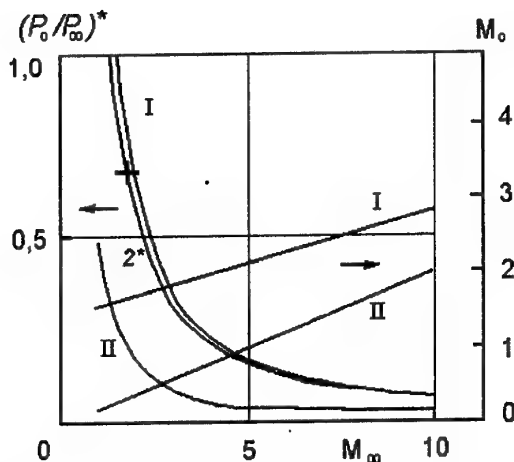
Fig.7. Results of the comparative analysis: relative total pressure and Mach number M_0 in thermal wake in dependence on main flow Mach number M_∞.
I - extended plasma thermal source ($l >> d$),
II - point explosion model ($l \sim d$)

3. Point source of heat in a supersonic flow.

In contrast to an extended source, here we assume that the energy is absorbed instantaneously at the point where the radiation is focused, i.e., the main assumptions of the point explosion model are assumed fulfilled. Assuming also that the repetition frequency of laser pulses is sufficient for initiating a quasistationary flow (this condition is given below), we determine the initial energy parameter (energy per unit length) $E^0=N/u_\infty$. Here u_∞ is the main flow velocity and N is the measured mean power of the absorbed laser radiation $N=W\tau f$, which gives N=1.6kW for f=100kHz. The value E^0=4 J/m obtained for these experimental conditions characterizes the space-time scales of the point explosion of cylindrical symmetry [13]: $r^0=(E^0/P_\infty)^{1/2}$ and $t^0=r^0(\rho_\infty/P_\infty)^{1/2}$ (8.4mm and 54μsec). In the analytical consideration of the radial distribution of parameters at different moments after the explosion, tabulated data on gasdynamic parameters of [14] were used. These data are represented as functions of dimensionless variables ξ and q, where $\xi=(r_i/r_n)^2$, r_i and r_n are the radii of the points of interest and shock wave; $q=(a_\infty/c)^2$, a_∞ is the velocity of sound in the free stream, and c is the velocity of the shock wave. For a fixed distance x from the point where the explosion happens $t=x/u_\infty$, and the dimensionless parameter t/t^0 determines the value of q.

Figure 5 shows the variation of the relative pressure P_0/P_∞ , velocity of sound a_0/a_∞ and radial (expansion) velocity of medium v_0/a_∞ (1 and 2 for γ=1.3 and 1.67) in the central part (x=0) of explosion with increasing q (time after explosion). The same figure shows the ranges of q for the flow Mach numbers M_∞=2 and 10 in the interval x=5-30mm. The common feature of these solutions is establishing, at q larger than 0.35, of almost constant (within several per cent) values of P_0/P_∞ $\cong$1, $a_0/a_\infty\cong$5 and $v_0/a_\infty\cong$0 (and the change of the sign of the velocity at q=0.6-0.8). The isobaric quasistationary flow is determined by the coordinate $x^*= u_\infty (t/t^0)t^0$ (where $t/t^0\cong$0.11-0.13, depending on γ for q=0.35).

The radial profile of the relative density ρ/ρ_n in the argon flow with M_∞=2 (it is shown for γ=1.3, the behavior for other γ is similar) for two fixed values of q, q=0.6 and 0.8 (x=7.6 mm and 24.4mm, respectively), are shown in Fig.6. The behavior of this parameter allows one to obtain the following estimate of its mean value in the central region: $\rho_0 \cong$0.03-0.04ρ_∞ (the estimated velocity of sound is $a_0\cong5a_\infty$) at the point r_0, the nearest one to the axis, thus eliminating the singularity of the point explosion theory solution at r=0. This choice is also justified by the fact that the energy release

242

takes place at the spatial scale $d<r_0$. The inner and outer boundaries of the characteristic low density (and high temperature) region are shown below the x-axis by lines r_0 and r_1. With increasing x, the first boundary remains nearly unchanged (r_0 is smaller than 0.9–1.2mm), whereas the radius of the outer boundary appreciably (by several times) increases, clearly showing the expansion of the region with a nearly constant density gradient. The latter is a feature that distinguishes the process under study from the energy release behind the LDW front, where the thermal wake boundary (curve 3) is a weak shock that separates the high velocity plasma flow from the main stream. Also shown in this figure are the predicted (r_n - 1,2 for both values of a γ 1,3 and 1,67) and measured (points) configurations of the bow shock wave. This shock wave results from superposition of unsteady waves generated by different breakdowns: it is nearly independent of focusing conditions for $r_n >> d$.

The dependence of flow parameters on the power N manifested itself in the interrelation between E^0, r^0 and t^0, which shows that the latter quantities increase proportionally to $N^{1/2}$. Simultaneously, the values of t/t^0 and q decrease, whereas the radius of the shock wave and the gasdynamic characteristics grow in value. Also shown in Fig.6 (with arrows $10E^0$) is evolution of r_0, r_1 and r_n with a tenfold increase in the power. Most pronounced is the increase in r_0 (by a factor of 2.5-3) and less pronounced is that in the shock wave radius. Thus, the effect due to increasing power is manifested in the enlargement of the low density region with earlier attainment of the quasistationary values of flow parameters ($q>0.35$).

The condition for the formation of a quasistationary flow acquires the form $x=r_0(x)$ (or $r_1(x)$). Graphic solution is a cross point of corresponding lines in Fig.6, then $f=u_\infty/r_0$. As compared to the case of an extended source, for which $u_\infty/f \sim l$, at a short beam focusing a higher (by factor l/r_0) frequency is required. For the less stringent requirement $u_\infty/f \sim r_n$ (here, spherically symmetrical solutions should be used) the value of f turns out to be several times (r_n/r_0) decreased; however, here again the spatial non-uniformity of flow parameters becomes more pronounced. In both regimes of energy supply, the required frequency increases with increasing flow velocity (Mach number).

4. Results of the comparative analysis.

To determine the mean values of velocity characteristics of the quasistationary flow (such as Mach number or total pressure), we used the following general property of the solution for the expansion velocity of medium in the central part of the explosion: $v_0/a_\infty \cong 0$. This means that in the region occupied by the isobaric flow the mean axial velocity of the medium u_0 at the center of the flow (i.e., in the region of radius r_0) is close to the main flow velocity, i. e., $u_0 \cong u_\infty = M_\infty a_\infty$. The velocity of sound under these conditions is nearly constant: $a_0 = Ka_\infty$ with the coefficient $K \cong 5$ (within 10% for different γ). As a result, we determine the Mach number in the central part of the flow: $M_0 = M_\infty/K \cong M_\infty/5$. This result is compared in Fig.7 (curve II) with the data (curve I) obtained for an extended energy source (with identical initial conditions and the mean radiation power), also in the range where the isobaric condition holds. These data show that in the range $M_\infty=1-10$ the Mach number of the flow in thermal wake M_0 is always lower than that in the main flow; it is the lowest one in the regime with explosion for which the flow for $M_\infty<5$ is subsonic.

From the known correlation between the gasdynamic parameters in the flow, we have also determined the relative profile of the total pressure $(P_0/P_\infty)^*$ for the two quasi-stationary energy supply conditions. The results are shown in Fig.7. Here, the frequencies may differ appreciably from each other. For the first time it is shown that, for identical mean values of power, the stagnation parameters differ considerably (they are three times smaller at short focusing and at low M_∞). Simultaneously, their values decrease markedly throughout the whole range explored (by more than ten times) with increasing main flow Mach number. The established, for the case under study, steeper variation of the ratio $(P_0/P_\infty)^*$ at low M_∞ implies that the effects due to energy supply (for instance, in the flows around bodies), with all other conditions kept unchanged, should change only slightly in the velocity range from $M_\infty \cong 5$ on. Besides, since the integral effects due to the energy supply are also determined by the relationship between the crossflow dimensions of streamlined bodies and those of the region in which the flow parameters change appreciably (of a radius smaller than r_1), these effects become more distinctly pronounced with increasing power only up to a certain limit, which depends on the ratio between the above dimensions.

5. Conclusion.

In contrast to a point (or by volume) explosion the plasma behind a light-supported detonation wave front gains high velocity in the direction of a main flow. For all that, there is the same wave structure by formal resemblance, including a bow shock wave and a thermal wake flowdown in a supersonic flow with energy deposition. The bow shock wave configuration is

243

identical for both regimes because it is shaped by superpositions of nonstationary shock waves caused by each optical breakdown; but the thermal wake's boundary dinamics have the difference. To a greater degree both regimes differ in velocity parameters (Mach number, total pressure).

The approach used herein may be developed and adopted for analysing the effects of a local energy deposition in a supersonic flow (for determination of a wave structure and estimation of flow parameters) with application of other kinds (and methods of supply) of radiation energy. It takes to know general mechanisms (models) only, which determine the plasma expansion in a region of energy absorption.

References

1. Tretyakov P.K., Garanin A.F. et al. // Dokl. Akad. Nauk. 1994. V.336. No.4. P.466-467. (in Russian).
2. Tretyakov P.K., Garanin A.F. et al. // Int. Conf. on the Methods of Aerophys. Research: Proc. Pt 1. Novosibirsk, Russia 2-6 Sept., 1996. P. 200-204.
3. Tretyakov P.K., Garanin A.F. et al. // Dokl. Akad. Nauk, 1996. V. 351. No.3. P. 339 – 340, (in Russian).
4. Yakovlev V.I. // Int. Conf. on the Methods of Aerophys. Research: Proc. Pt 3. Novosibirsk-Tomsk, Russia 9-16 July, 2000. P. 139-145.
5. Tretyakov P.K., Yakovlev V.I. // Pis'ma v ZhTF,. 1998. V.24. No.6. P.8-12, (in Russian).
6. Tretyakov P.K., Yakovlev V.I. // Dokl. Akad.Nauk, 1999. V.365. No.1. P.58-60, (in Russian).
7. Raizer Yu.P. Gas Discharge Physics. - New York, Berlin:Springer-Verlag, 1991.
8. Thomas P.D. // AIAA-Journal. 1977. V. 15. №10. P.1405-1409.
9. Yakovlev V.I. // Pis'ma v ZhTF. 2001. V.27. №9. P.13-19, (in Russian).
10. Georgievsky P.Yu., Levin V.A. // Pis'ma v ZhTF. 1988. V.14. №8. P.684-687, (in Russian).
11. Guvernyuk S.V., Samoilov A.B. // Pis'ma v ZhTF. 1997. V.23. №9. P.1-8, (in Russian).
12. Myrabo L.N., Raizer Yu.P. AIAA Paper №94-2451. 1994.
13. Korobeinikov V.P. Problems in the Theory of Point Explosion, Moscow, Nauka, 1985, (in Russian).
14. Korobeinikov V.P., Chushkin P.I., Sharovatova K.V., Point Explosion Gasdynanic Functions.-Moscow, Computing Center, USSR Acad. Sci., 1969.-47 p., (in Russian).
15. Fisher V.I. // ZhTF. 1983. 1983. V. 53. №11. P. 2143-2147, (in Russian).
16. Pirri A.N. // Physics of Fluids. 1973. V.16. №9. P.1435-1440.
17. Kozlov G.I., Kuznetsov V.A., Masyukov V.A. // ZhETF. 1974. V. 66. № 3. P. 954-964, (in Russian).

45. INFLUENCE OF ACTIVE RADICAL CONCENTRATION ON SELF-IGNITION DELAY OF HYDROCARBON FUEL/AIR MIXTURE

Buriko, Yu., Vinogradov, V., Goltsev, V.
Central Institute for Aviation Motors, Moscow, Russia

Waltrup, P.
John Hopkins University Applied Physics Laboratory, Laurel, MD, USA

Abstract: Evaluation results of required active radical concentration to decrease the time of self-ignition delay t_{ind} of hydrocarbon fuel/air mixture are presented. The effect of initial radical concentration on t_{ind} was investigated under assumption of one-dimensional combustion process model with the use of verified kinetics schemes of combustion processes. Calculations were carried out under flow pressure P and temperature T values equal to P=0.05-0.15MPa, T=500-1500K and fuel temperature T_f = 900K correspondingly. It is following from the calculation data, that initial flow radical concentration effects on t_{ind} significantly only when the value of initial concentration is close to radical concentration on flame front. Radical concentration is practically constant on flame front and combustion process is realized according to generally accepted scheme in spite of t_{ind} is decreased very strongly at large initial radical concentration. Also it was considered the effect of initial radical concentration along with the air temperature changing and individual effect of typical radicals on t_{ind}. It is shown that radical O has strongest influence than another ones. Further, next radicals H, OH, CH$_2$OH, HCO и CH$_3$O are following as to respect of influence.

Nomenclature

t	- time,
C	- concentration,
P	- pressure,
T	**- temperature,**
β	- fuel/air equivalence ratio

Subscripts

a	- air,
f	- fuel,
ind	- induction

Introduction

Numerous experimental investigations and computations show there are serious difficulties concerning ignition and combustion of hydrocarbon fuels in the whole raw of technical devices, such as, combustion chambers of ground power plant, main and afterburner combustion chambers of gas turbine engines and ramjet combustors [1-3]. Now various ways of fuel reactivity improvement for combustion intensification in ramjet combustor entry are being considered.

One of the promising ways for the burning improvement is fuel destruction product utilization instead of original fuel. It is supposed that fuel will be used for airframe and engine construction elements cooling. As a result fuel will be warm up and fuel destruction will occur in fuel line. It is expected that thermo-destruction products are more chemically active than original fuel because of changing of chemical composition and presence of active radicals and this chemical property would intensify combustion process. The second way to improve air-fuel mixture reactivity is saturation of air and fuel with active radicals. This can be achieved, for example, by the mean of initiating a discharge into one or both reactants. Another approaches deals with injection of combustion products containing radicals in high concentrations or photochemical method of active-species injection, when additional radicals are formed as a result of radiation-induced decomposition of reagents. Our analysis will be restricted by the consideration of the effect of these active species on ignition delay t_{ind} without details of the nature of active species formation and mechanism of their injection into the system. In this paper one effect have been investigated numerically, namely, impact of the radical concentration rise in the air/fuel mixture on the characteristic ignition time delay which specifies the fuel reactivity. Currently, there is lack of evidence for the matter in question and, therefore, further research is required.

Static pressure and temperature at the combustor entrance for typical flight trajectories of vehicle powered by air breathing engine under M=4-7 are in the range P=0.08-0.12MPa and T=500-950K correspondingly. Flow velocity V are equal to $(0.9-1.6)\times10^3$m/s. Consequently, residence time of air/fuel mixture for the combustor length of 1-2 m is not more, than 1-2ms. In such a manner, for effective operation process under assumption of diffusion combustion mechanism the value of t_{ind} has not be higher pointed meanings. However, for stoichiometric (β=1) hydrogen/air mixtures the value of t_{ind} under above mentioned flow parameters is 10-0.1ms, that it is resulted to impossibility of combustion initiation, basing only on self-ignition of mixtures. Addition of silane (SiH$_4$) in the limit of 20% into the hydrogen decreases this value down to t_{ind}=0.4-0.05ms. In

case of hydrocarbon fuels, for example, kerosene the value of t_{ind} is increased up to 10^2-10 ms, that is, leads to unacceptable combustion organization, when engine operation is considered under the regime of fuel self-ignition. That is why for high speed engines the special devices, such as plasma jet generators [4], electric discharge spark plugs [5] or pilot flames using self ignited components [6] and et al are considered for application. As a rule, these devices affect locally and so they are installed in regions of flow recirculation (regions of combustion stabilization). Dimensions of stabilization zone are defined by the local velocity V, flow parameters – pressure P and temperature T, fuel/air equivalence ratio β in flow and in stabilization zone and by dimensions of stabilizator. In this case the regimes of "residual flames" or "flame spreading" are realized [7]. And so, results of this research could be applied not only to whole flow in engine, but also to the flow incoming into the stabilization zone.

Statement of work

One of the main effect of above mentioned devices is an increase of active radical concentration in the vicinity of such devices. Effect of initial radical concentration on characteristic self-ignition time of the mixture has been examined as well on the base of one-dimensional combustor model [8]. The model is founded on the assumption of instantaneous mixing of fuel (original fuel or fuel with radical additives) with air. At such premise, characteristic ignition time delay is defined by the chemical reactions kinetics only and by this it is simulated only kinetic, more important, aspect of active radical effect on ignition of complex chemical mixtures. Combustion performance (temperature, reactant concentrations) is defined from the solution of equations (1)-(2). Mechanism of radical concentrations increasing in the air/fuel mixture is not a question of this paper.

Following equations describe combustion and distribution of reactant concentration and temperature along the combustor length:

$$U\frac{dC_i}{dx} = W_i \qquad (1)$$

$$U\frac{dH}{dx} = q_R, \qquad (2)$$

where $t=X/V$ - time, X - coordinate directed along the combustor length, C_i - i_{th} reactant concentration, W_i - i_{th} reactant formation (or consumption) rate, H - mixture enthalpy, n – total number of reactants, V - flow velocity.

To simulate combustion process for both original fuel and mixture with radicals, the simplified kinetic scheme was applied for

hydrocarbons oxidation [9-12]. Main demand to kinetic scheme required in frame of present research is correct description of initial phase of combustion process. The scheme comprised 311 reactions between 60 components, including atoms H, O, C, N and also Ar. Rate constants of elementary reactions are adopted mainly from [9-12]. To test and to specify values of rate constants, experimental data presented in work [13] were used. In work [13] ignition time delay behind shock wave for mixtures $C_3H_8/O_2/Ar$, $CH_4/O_2/Ar$ and other were measured. The set of rate constants are chosen which provides the best correlation with: experimental data [13] and thermodynamic parameters of combustion products (at $t\rightarrow\infty$) in frame of one dimensional model of equations (1)-(2).

Discussion

Calculations were performed mainly for pressure p=0.05MPa, as this value corresponds to typical one, under assumption that temperature of fuel is T_f=900-1200K. Propane C_3H_8 was considered as a fuel. During first stage of calculations values of t_{ind} were found under variation of fuel (T_f) and air (T_a) temperatures and fuel/air equivalence ratio β at fuel and air radical concentration level close to equilibrium state (original fuel). For the second stage it was obtained the effect of significantly overequilibrium contents of radical in fuel/air mixture (original fuel with radicals).
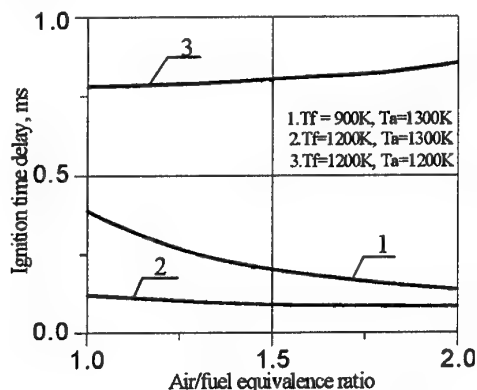
Fig.1. Effect of air/fuel equivalence ratio on ignition time delay vs T_f and P=0.05Mpa.

Effect of equivalence ratio on characteristic ignition time is presented in Fig.1. At the first glance, an unexpected result was achieved. However, if the air temperature is higher than fuel temperature (curves 1 and 2), then characteristic ignition time delay drops when value of $1/\beta$ varies

246

from 1 (stoichiometry mixture) to 2.0 (lean mixture). At the same time, if air temperature is lower or equal than fuel temperature then characteristic ignition time delay diminishes with equivalence ratio β rise. Revealed relationships are caused by the fact that in the first case mixture temperature increases with equivalence ratio $1/\beta$, but in the second case it drops.

Therefore, only few influence of equivalence ratio on ignition time delay can be expected. The effect of mixture temperature on characteristic ignition time delay is more important at mixing of air/fuel flows distinguished by initial temperatures. Effect of air temperature variations only on changes of t_{ind} is shown in Fig.2 (curve 1). As it was proposed, the increase of T_a has large effect on t_{ind}. For example, increase of T_a in 400K causes to decrease of t_{ind} by three order of magnitude.
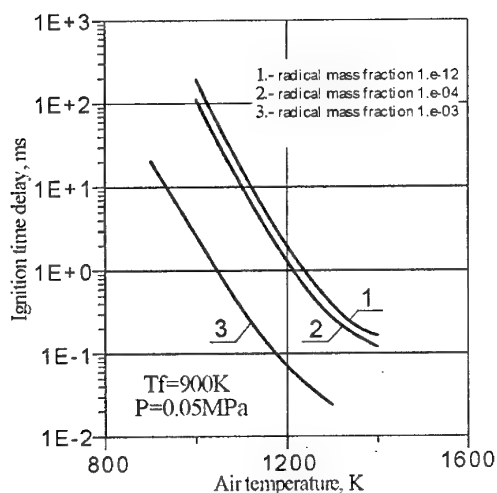
Fig.2. Characteristic ignition time delay versus air temperature under combustion of stoichiometric air/fuel mixture combustion at different radical concentration in mixture.

It was considered the effect of initial level of radical concentration O, H and OH in mixture on pre-flame process in combustor. Radical OH was chosen to generalize behavior of all active species within combustor. It resulted by the fact that radical OH more reliable mark to characterize of the flame front location. Fig.3 shows time history for radical OH concentration distribution along the combustor length.

Considered time interval corresponds to the pre-flame stage of original fuel combustion. As it is seen the initial radical concentration increase from 10^{-12} to 10^{-6} has no influence on characteristic ignition time delay of the air/fuel mixture. It should

be noted that over initial pre-flame stage ($t<10^{-4}$s) radical concentration history distinguishes essentially between two cases under consideration. When the initial radical concentration is equal 10^{-12}, then radical concentration into mixture increases further monotonically till ignition. In a case when initial radical concentration is 10^{-6} and more, change of radical concentration is nonmonotonous.
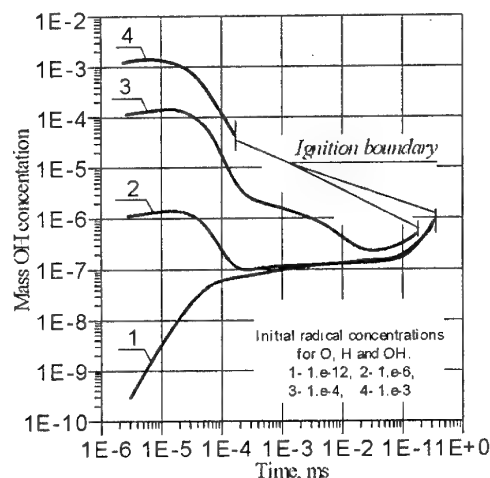
Fig.3. OH mass fraction vs time over preflame stage. Stoichiometric air/fuel mixture $P=0.05$Mpa, $T_f=900$K, $T_a=1300$K.

At the beginning of the process radical concentration is decreased and after some time begin to increase. If the initial radical concentration varied in range from 10^{-12} to 10^{-6}, concentration profiles coincide in fact for time more than 0.01 ms. Increase of initial radical concentration up to 10^{-4} causes some decrease of the characteristic self-ignition time. Steep drop of self-ignition time is observed when the initial radical concentration reaches 10^{-3}.

Fig.4 demonstrates full time history profiles of OH concentration over the region preceding flame front. An important fact resulting from the present calculations is necessary to be noted. Though characteristic self-ignition time drops severely at high initial concentration of radicals, its value near the flame front remains unchanged. This result is very important from practice point of view, as it argues possibility to conduct calculations of combustion process under simulation of developed operation process without taking into account of mixture satiation by additional radicals. The second important conclusion from the calculations is in the fact that initial concentration of radicals can not effect essentially on characteristic ignition time except for the case when this initial concentration corresponds

well with the radical concentration over the flame front.
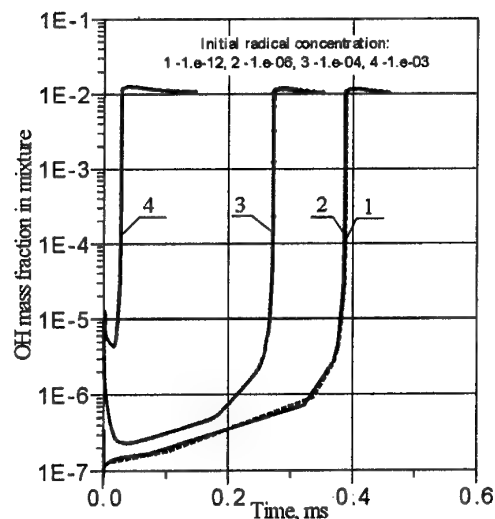
Fig.4. OH mass fraction vs time under combustion. Stoichiometric air/fuel mixture P=0.05Mpa, T_f=900K, T_a=1300K.

Particular influence of every species fraction on characteristic self-ignition time is demonstrated in Fig.5. It is seen that radical O has strongest influence on characteristic self-ignition time. It is followed by the group of radicals in order of significance as to respect of influence H, OH, CH_2OH, HCO and CH_3O.
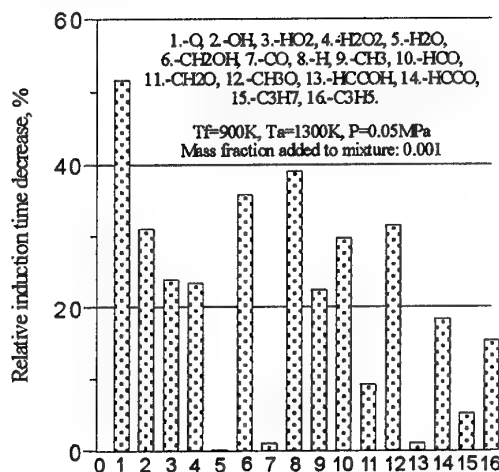
Fig.5. Comparative estimation for an effect of extra components added to mixture on induction time decrease under combustion of stoichiometric air/fuel mixture

Fig.6 shows calculated results which indicate an influence of radicals added to fuel on characteristic self-ignition time separately from

ones added to air. In this figure characteristic self-ignition time is presented in relative manner. Characteristic self-ignition time to be calculated for high radical concentration is referred to characteristic self-ignition time for initial radical concentration equal to 10^{-12}. As it was shown, such initial concentration of radicals injected into the flow eliminates, in fact, the effect of radicals on self-ignition and combustion of mixture.
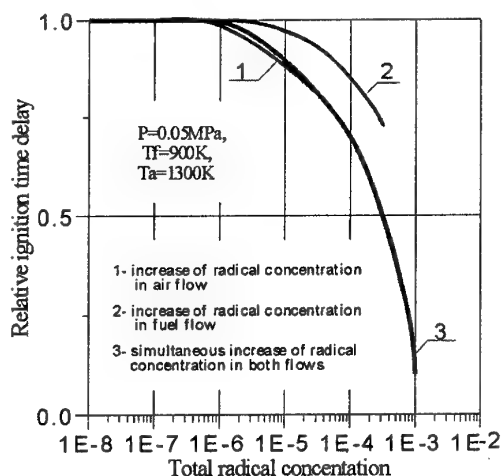
Fig.6. Decrease of charscteristic ignition time delay under combustion of stoichiometric air/fuel mixture saturated with radicals separately both in air and fuel flows.

Such representation of calculated results allows to compare three basically different variants for injection of radicals into combustor. It is seen that in case of stoichiometric combustion, a generation of radicals in fuel is less productive than generation in air. The effect is quite realizable. Indeed, though initial radical concentration in air was the same as that in fuel initial radical concentration in air was the same as that in fuel there would be much more radicals in air/fuel mixture if they had initially been added into air. This results from the fact that stoichiometric mixture comprises much more air than fuel.

Conclusion

Presented results show that addition of radicals to original fuel C_3H_8 has strong effect on self-ignition time in comparison with the time for original fuel if injected radical concentrations are comparable with the flame front radical concentration. In this case decrease of t_{ind} can reach to one and half order in comparison with original fuel.

Injection of active radicals into the air gives more effect at the same fuel/air equivalence

248

ratios in comparison with the case when radicals injected into the fuel.

In general, obtained results have shown that kinetic calculations based on one-dimensional model of combustor are very useful instrument which give us possibility to clarify role various effects on ignition and combustion processes and therefore to diminish extend of the expensive experimental investigations.

References

1. Vinogradov, V.A., Kobigsky, S.A., Petrov. M.D., Experimental Investigation of Kerosene Fuel Combustion in Supersonic Flow. // J of Prop. and Power, 11, 1, 130-134 (1995)
2. Ortwerh, P., Vinogradov, V., Grin, V., Mathur, A., Goldfeld, M., Starov, A., Experimental and Numerical Investigation of Hydrogen and Ethylene Combustion in a Mach 3-5 Channel with a Single Injector. // AIAA Paper 96-3245, Lake Buena Vista, USA, (1996).
3. Kurziner, R.I., Jet Engines for High Supersonic Speeds. Moscow, Mashinostroenie, 119-120 (1989).
4. Yatsuyanagi, N., Chinzei, N., Mitani, N., Wakamatsu, Y., Masuya,G. at al, Ramjet Engine Test Facility (RJTF) in NAL-KRC, Japan. AIAA 98-1511, Norfolk, USA (1998).
5. Ogorodnikov, D.A., Vinogradov, V.A., Shikhman, Yu.M., Strokin, V.N., Design and Research Russian Program of Experimental Hydrogen Fueled Dual Mode Scramjet: Choice of Conception and Results of Pre-Flight Tests. AIAA-98-1586, Norfolk, USA (1998).
6. Hueter, U., Rocket-Based Combined-Cycle Propulsion Technology for Access-to-Space Applications. AIAA 99-4925, USA (1999).
7. Strokin, V.N., Grachev, V.A., Possible schemes of flameholding in hydrogen fueled scramjet combustors, Proc of the Second Inter. Aerospace Congr., v.1, Academy, Moscow, 630-633 (1997).
8. Volkov, D.V., Zaitcev, S.A., Goltsev, V.F. Numerical investigation of the NOX formation under combustion of the homogeneons methane-air mixture. J Fizika Gorenia and Vzriva, 35, 2, 9-15 (1999).
9. Miller, J.A., Bowman, C.T. Mechanism and modeling of nitrogen chemistry in combustion. Prog. Energy Combust. Sci., 1989, v.15, pp.287-338.
10. Warnatz, J., in: Combustion chemistry, ed. by W.C. Gardiner, Jr. Springer Verlag, New York, Berlin, Heidelberg, Tokyo (1984).
11. Wilk, R.D., Cernansky, N.P., Pitz, W.J. and Westbrook, C.K. Propane Oxidation at Low and Intermediate Temperatures: A Detailed Chemical Kinetic Study. J of Combustion and Flame, 77, 145-170 (1989).
12. Kojima, S., Detailed Modeling of n-Butane Autoignition Chemistry. J of Combustion and Flame, 99, 87-136 (1994).
13. Burcot, A., Scheller, K., Lifshitz, A., J of Combustion and Flame, 16, 1, 29-34 (1971).

46. COMPACT PLASMA ANTENNA FOR FLYING VEHICLES

E.E. Dyunin, A.V. Kostrov, G.V. Permitin, A.I. Smirnov, M.V. Starodubtsev

The problem of remote radiocommunication with flying vehicles requires compact efficient low-frequency airborne (onboard) emitters. Development of such antenna systems mainly concerns matching an emitter with the feeding line. Standard matching networks consist of discrete reactive elements. Basic drawbacks of such networks are connected with their extremely narrow frequency bandwidth. Besides, in the low-frequency range matching devices composed of discrete elements are rather bulky. The aforesaid stimulates development of novel methods of matching compact low-frequency antenna systems.

This report presents first experimental results of laboratory modeling of compact plasma antenna systems intended for low-frequency radiocommunication in the frequency range from 100kHz to 5MHz. The antenna system is made as a short (1m length) electric dipole surrounded with a magnetized plasma shell.

The results of the laboratory modeling show the prospective of a plasma antenna system as an efficient, compact, sufficiently wideband, easily tunable, low-frequency emitter. It has been shown experimentally that radiating efficiency of a short electric dipole antenna surrounded with a magnetized plasma shell grows by three to four orders as compared to the case of no plasma around the antenna.

47. AERODYNAMIC AND HEAT EXCHANGE OF AN OBJECT IN A SUPERSONIC FLOW BEHIND A PLANAR ENERGY SOURCE

D.I. Goryntsev, G.A. Lukianov

Saint-Petersburg State Technical University
195251, Russia, Saint-Petersburg, Politechnicheskaya street, 29

Abstract. The investigation by the direct simulation Monte Carlo of resistance and heat exchange of an object in a wake behind a planar energy source (gas dynamic discontinuity with given energy input) was carried out. Supersonic flow of monoatomic gas past a wedge, cone and etc. in the range of Mach numbers M=4-20 and Reynolds numbers Re=65-1000 corresponding to the flit conditions at high altitude was analysed.

The influence of energy source power, M and Re numbers and reciprocal location of the object and the energy source on the aerodynamics characteristics and thermal loadings of the object was investigated. There's shown a possibility of significant reduction of drag and thermal loading of an object. The energetic efficiency of such way of control of aerodynamic characteristics was studied.

Introduction

This work continues the investigations [1-3] on the drag and heat exchange of the objects in supersonic wake behind planar energy source that constitutes the gas dynamic discontinuity with energy input to the gas in the weak detonation (supersonic combustion) regime. Gas heating in the source leads to increase of pressure and formation of the wake with the structure of supersonic underexpanded jet in concurrent supersonic flow behind the source. Detailed investigations of gas dynamic structure of the wake behind such energy source (planar and axisymmetric flow) showed that its gas dynamic structure has some important peculiarities [4]. At considerably high values of characteristic Reynolds number Re_∞ behind the initial gas dynamic segment in paraxial zone a very long high-temperature region with low density ρ and low dynamical pressure $p_D = \rho u^2/2$ (u - gas velocity) forms. Transversal sizes of this zone are equal to several transversal sizes of energy source. Parameters of gas along this zone remain almost constant. The "range" effect is observed at $Re_\infty > 100$ for planar and $Re_\infty > 10000$ for axisymmetric flow ($Re_\infty = \rho u_\infty R/\mu_\infty$, R - radius or half-height of energy source, μ - dynamic viscosity, index ∞ corresponds to the parameters of the undisturbed flow).

In the present work the results of the investigation on drag and heat-exchange of the objects in planar and axisymmetric wake behind energy source are given. The by-pass of wedge and cone with half-angle 20° by supersonic flow of monoatomic gas (argon) in the range of Mach number $M_\infty = 4-20$, number $Re_\infty = 65-1000$ under various values of energy input and object's position in the wake is considered.

1. Calculation method and problem setting

For the investigation DSMC method, based on Bird's version [5] is used. Geometric parameters of the problem and calculation grid are shown in Fig.1.
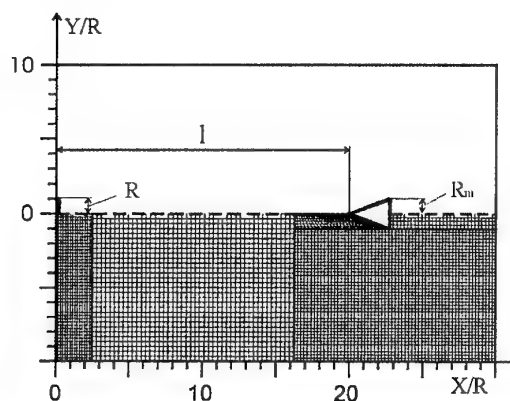
Fig.1. Geometry of task and calculation gird.

In terms of DSMC method the nondimensionalized characteristics of the flow are determined by the following numbers: M_∞, Re_∞, the temperature ratio T_w/T_∞, heating parameter $\beta = q/c_p \cdot T_{0\infty}$ (q - energy input to the mass unit at time unit in the source, c_p - specific heat capacity, $T_{0\infty}$ - the stagnation temperature of the flow at the infinity). Parameters are also determined by the model of the surface interaction and model of the particles. In the present work it is suggested that all collisions are elastic. The Bird's NTC scheme was employed to choose collision partners. The mechanism of molecular collisions corresponds to VHS model [5].

The initial and boundary conditions are stated as follows: at $t=0$ the simulation domain is

251

empty; the supersonic flow of monoatomic gas is set on the left boundary $x=0$. The velocity distribution function on the boundary $x=0$ is Maxwellian.

for $y>R$

$$f_\infty = \frac{n_\infty}{(2\pi R T_\infty)^{3/2}} \cdot \exp\left[-\frac{(V_x-u_\infty)^2+V_y^2+V_z^2}{2\cdot R\cdot T_\infty}\right],$$

for $y\leq R$

$$f_i = \frac{n_i}{(2\pi R T_i)^{3/2}} \cdot \exp\left[-\frac{(V_x-u_i)^2+V_y^2+V_z^2}{2\cdot R\cdot T_i}\right],$$

where n_∞, u_∞ - numerical density and velocity of the flow at infinity; n_i, T_i, u_i - numerical density, temperature and velocity of the flow behind the energy source; R - gas constant. The conditions of specular reflections are set on the top and bottom boundaries of the computational domain. The diffuse reflection with accommodation coefficient equal to 1 is set on the body surface. The particles which reach the right boundary are excluded from simulation.

The parallel algorithms of DSMC for multiprocessor computation systems with shared memory [6,7] were used for computations. The blocked 4-corner non-uniform grid with number of nodes from 10^4 to $2\cdot10^5$ was used for the simulation. The maximum number of particles being at the given moment in the domain was from $5\cdot10^5$ to $4\cdot10^5$. The calculations were carried out on supercomputer CONVEX SPP-1600.

2. Computation results and analysis

The flow over a wedge is illustrated by the density fields shown in Fig.2 for the computation variant $M_\infty=10$, $T_w/T_\infty=1$, $Re_\infty=65$, $\tau=T_i/T_\infty=10$ ($\beta=0.15$), (T_i - temperature behind energy source). The forepart of wedge is at the distance of $8R$ from energy source. On the Fig.2a energy source is on, on the Fig.2b energy source is off. Energy release in the source leads to gas expansion, density and dynamic pressure decrease in front of the object. Decrease of p_D leads to reduction of the object drag and heat flows forwards the object.

For estimation of drag change F and total heat flux to a body Q parameters $\omega=F_1/F_\infty$ and $m=Q_1/Q_\infty$ were used. Here indexes 1 and ∞ are related to parameters in wake behind an energy source and undisturbed flow correspondingly.

$$C = (N_1+N_i)/N_\infty, \quad K = (N_\infty-N_1)/N_i.$$

Here N_i - energy source capacity, $N_\infty=F_\infty u_\infty$, $N_1=F_1 u_\infty$. The scheme provides energy gain if $C<1$ and $K>1$.
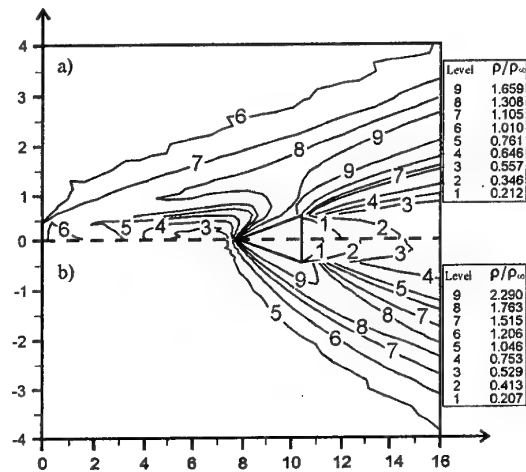
Fig.2. Structure of flow over the wedge with $M_\infty=10$, $Re_\infty=65$, $X/R=8$, $T_w/T_\infty=1$, a) source is on ($\tau=10$), b) source is off ($\tau=1$).

The investigation of the factors that influence on drag and heat flux towards the object (for the wedge and cone) was carried out. These factors are: position of the object with respect to energy source l/R, relative object size R_m/R, temperature factor $\tau=T_i/T_\infty$, numbers Re_∞ and M_∞. In Fig.3 the dependence of ω, m, C and K from l/R and R_m/R are represented (for a wedge in a planar wake) under $M_\infty=10$, $Re_\infty=65$, $T_w/T_\infty=1$, and $\tau=10$. Values of ω, m and C reduce, values of K increase when moving away from the source. Thus, resistance and thermal flows towards the object reduces at the increase of l. This conditions lead to the increase of the scheme energy efficiency. Increase of R_m/R results to certain increase of ω, m, C and K.
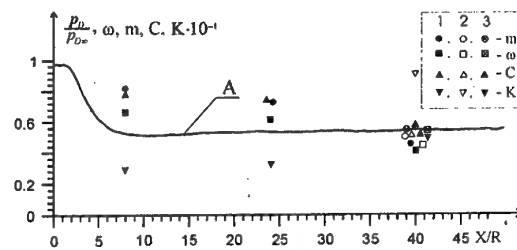
Fig.3. Axis profile $p_D/p_{D\infty}$ (A) and dependence ω, m, C and K from location of wedge relatively energy source with $M_\infty=10$, $Re_\infty=65$, $T_w/T_\infty=1$, and $\tau=10$; 1 - $R_m/R=1$, 2 - 2, 3 - 4.

Dependence of ω and m from τ is shown in the Fig.4. Increase of the energy contribution leads to decrease of ω and m. Under $\tau>10$ decrease of ω and m is insignificant. All regimes seem to be

energetically beneficial $(C<1, K>1)$. Regimes with the lowest waste realize under $\tau\approx10$.
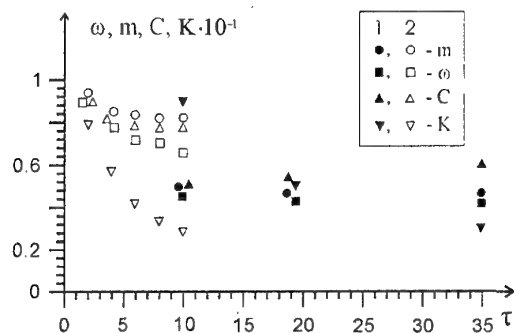
Fig.4. Dependence of ω, m, C and K from τ under $M_\infty=10$, $Re_\infty=65$, $T_w/T_\infty=1$; 1 - $R_m/R=2$, $l/R=40$, 2 - $R_m/R=1$, $l/R=8$.

In Fig.5 the dependence of ω, m, C and K from Re_∞ under $M_\infty=10$ for two computation variants are shown. Increase of Re_∞ results in decrease of ω, m, C and K. Decrease of F and Q is bound up with the reduction of forces and drag operation.

Fig.5. Dependence of ω, m, C and K from τ under $M_\infty=10$, $Re_\infty=65$, $T_w/T_\infty=1$; 1 - $\tau=10$, $R_m/R=1$, $l/R=8$; 2 - $\tau=35$, $R_m/R=2$, $l/R=40$.

References

1. Lukianov G.A. On the resistance of a body in supersonic flow with planar source located in front of the body. Technical Physics Letters, Vol. 24, Issue 24, 1998, p.76-82
2. Lukianov G.A. On the resistance and the heat exchange of a body in supersonic flow with planar source located in front of the body. Preprint № 04-98, IHPCDB, St. Petersburg, 1998, p.19.
3. Lukianov G.A. Drag and heat exchange of an object in a supersonic flow with a source of energy in front of the object. The 2-nd workshop on magneto-plasma-aerodynamics in aerospace applications, Moscow, 5 April - 7 April 2000, IHTRAS, pp. 133-137.
4. Goryntsev D.I., Ignatiev A.A., Lukianov G.A. Gas dynamics of supersonic wake behind a planar energy source (look at this collection of works).
5. Bird G.A. Molecular gas dynamics and the direct simulation of gas flows.- Clarenton Press. Oxford. 1994, pp. 451.
6. Grishin I.A., Zakharov V.V., Lukianov G.A. Algorithm of parallel direct simulation Monte Carlo in molecular gas dynamics (data parallelezation). Preprint № 3-98, IHPCDB, St. Petersburg, 1998, p.32.
7. Khanlarov G.O., Lukianov G.A., Malashonok D.Y., Zakharov V.V. Parallel DSMC on Shared and Hybrid Memory Multiprocessor Computers. M. Bubak et al. (Eds.): NPCN'2000, LNCS 1823, pp. 584-587, 2000. Springer-Verlag-Berlin Heidelberg 2000.

253

48. PULSE VOLUME DISCHARGE INFLUENCE ON SUPERSONIC FLOW OVER BLUNT MODEL

Znamenskaya I.A. Mursenkova I.V.
Moscow State Aviation University, Moscow

Lutsky A.E.
KIAM RAS, Moscow

The presented method of pulse energy deposition is based on use of pulse volumetric discharge preionized by UV radiation. The method allows investigating different problems of gas dynamics, bound with pulse (pulsewise - periodic) input of energy in gas flow [1-3].

The problems of influencing of energy deposition on gas flow around varies bodies were studied in a number of works [4-10]. In the present paper experimental and numerical analysis of pulse volumetric energy input influence on supersonic flow near blunt model are given.

The experiments were conducted on a shock tube with pulse discharge chamber. The duration of supersonic flow around a model depends on a Mach number, and it was in experiments 180-300µs. The pulse volume discharge was originated in a supersonic flow behind a plane shock wave 30-60µs after arrival of this shockwave to model, (i.e. when the supersonic flow near model with a bow shockwave had been formed. The energy deposition into supersonic flow was during 150-200ns. Discharge area was 4-14cm streamwise model (blunted cylinder, diameter 9mm) (Fig.1).

The scheme of a pulse volume discharge preionized by a ultraviolet radiation from plasma sheets was used. The discharge area was 100mm; cross-section 48×24mm. Discharge gap size was 24mm, voltage U=30-40kV; maximum value of electric field E/N=500Td. The discharge homogeneity and fast current increase was provided due to preliminary illumination of a volume with UV radiation from plasma sheets along top and bottom surfaces of discharge volume during (60 ns).
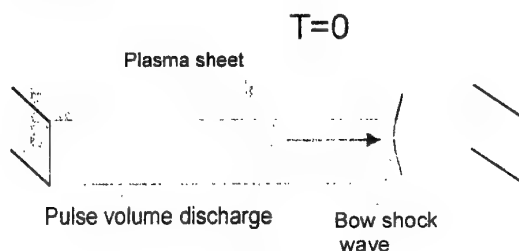
The energy input created in an instant T=0 extended homogeneous area of nonequilibrium exited gas. That area of nonequilibrium gas drifted to the model, interacted with bow shock wave, shock layer, model surface. The supersonic nonequilibrium flow over model (M=1.34-1.75) was investigated. Gas density was 0.07-0.22kg/м³. Volume pulse discharge energy was converted to heating, ionization, dissociation, an excitation of internal degrees of freedom of molecules and atoms, and also to radiation. The sliding surface discharges produce disturbances in cross-sectional flow directions (owing to the energy input into thin layers in short time).

20-30µs after initiation of discharge the disturbance, which has arisen at pulse volume energy input in gas, interact bow shock wave, shock layer and surface of model. Pressure dynamics in stagnation point, curvature of bow shock front, distance X between model and bow shock were studied in experiments.

The shadowgraphy showed, that at pseudo-steady flow streamlining of model by exited air, the maximum increase of shock layer size X along flow zero line reached 20% to the value of unexcited flow. On Fig.2 the X dependence against Mach number for a undisturbed flow and X values at the pseudo-steady flow in non-equilibrium flow are presented. The curvature of a wave front was less, than in a flow without discharge excitation.

Gas pressure measurements in stagnation point in pseudo-steady exited flow were conducted. The essential pressure variations in stagnation point were revealed on the initial stage of nonequilibrium area interaction with shock layer; low level of stagnation pressure was at pseudo-steady exited flow [10]. The oscillogram of pressure obtained in experiments with excitation of flow area by a pulse discharge, is on Fig.5. T=0 - moment of initiation of a pulse discharge.

Stagnation pressure measurements showed, that the pressure decline at pseudo-steady flow depends on energy input level and air humidity.

In order to refine the mathematical model and analyze the processes under consideration

T=0

Plasma sheet

Pulse volume discharge   Bow shock wave

Fig.1

some numerical researches were executed. The calculations of non-steady flow, perturbed by pulse energy input over the blunt model were conducted. The calculations were held within the framework of mathematical model of 3D non-steady Euler equations without regard of viscosity and heat conduction. The numerical algorithm is based on the generalized Godunov scheme with piecewise linear representation of flow functions. The multi block grid (14 blocks, 35600 cells) was used.

Фиг. 2
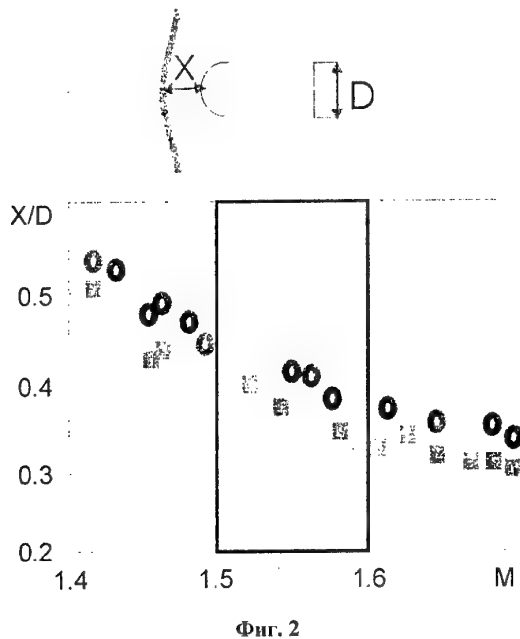
The energy input into undisturbed flow upstream the model was simulated (according to an real process) in 2 stages. At first stage energy ($W/8$) was enclosed during 67ns in narrow layers near each of plasma electrodes; $W=0.16h$, h-enthalpy of undisturbed flow. Then during 200ns the energy W was enclosed in all area of discharge. To study influence of disturbances introduced by plasma electrodes on flow, the calculation without plasma sheets energy input were performed also. The case M=1.61 was considered.

Some analytical estimations were done in order to control numerical data and reveal the main details of the flow pattern. In the case of 1D Euler equations with the source term q=const in the equation for energy conservation there exist the solution of the form:

ρ=const, u=const, $p=p(t)=(\gamma-1)qt+p(0)$

After t=200 ns the pressure for the exact solution is p=1.22. For the present numerical 3D solution it was obtained p=1.23. The pressure

increase with constant speed and density leads to decrease of the Mach number from 1.61 to 1.46.

Computer simulation showed, that originally homogeneous area of discharge stratifies with time. The borders of layers with different speeds move downstream towards model and interact with it. Area 4 with high pressure does not interact directly with model.

During energy input time flow particles shift on spacing interval ~ 0.003 lengths of discharge area, so at approximated estimations it is possible to consider, that the energy input is instantaneous. On right and left borders of discharge area there is decay of gap between a undisturbed flow and flow of high pressure. X-T configuration are presented on Fig.3. The solid vertical line marks stagnation point of model. Up to certain instant the flow upstream bow shock consists of zones of constant parameters, separated with shock waves, contact discontinuity and rarefaction waves. Each of these zones has its value of stagnation pressure: P_{01}=3.85, P_{02}=4.51, P_{03}=3.98, P_{04}=3.97.
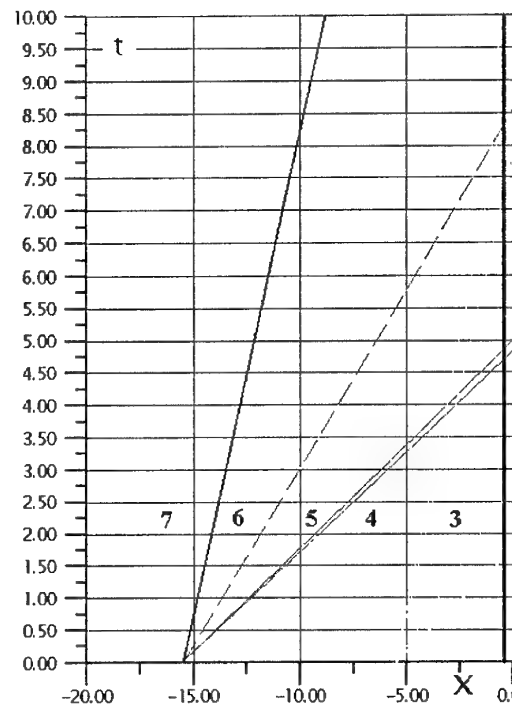
Fig.3.

Area 4.2 is formed as a result of a rarefaction wave coupling (see of Figs.3); density here ρ~0.87 is lowered. Pressure and speed are close to values in a nonperturbed flow. The stagnation pressure P_{04_2}=3.42 corresponds to these flow parameters. Analytical estimations predict,

255

that in the process of interaction of these perturbed areas with the model stagnation pressure against time the listed P_0 values will be watched.
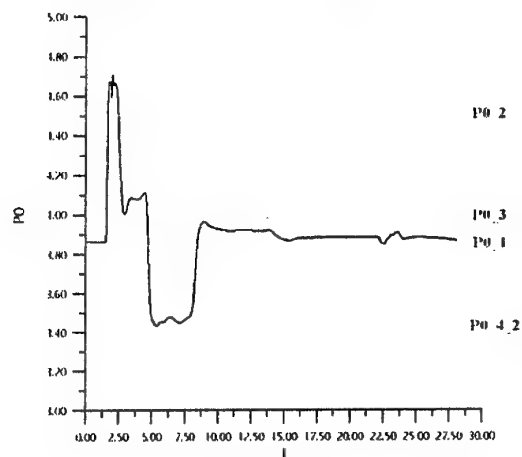
Fig.4

On Figs.4 the computational time histories of stagnation pressure for two models of energy input are shown (with boundary energy deposition and without it). It is shown, that in some zones of constant rate has time to.be formed a pseudo-steady mode. For example, in zone 4.2, there is long interval of low pressure. The matching of two calculated curves demonstrates, that the initial input of energy near two boundaries influences a flow weakly.

Computed and experimental oscillograms of pressure in stagnation point and of shock layer X time histories were matched (Fig.5). On Fig.6 calculated three-dimensional pressure flow field 14μs after an energy deposition is presented. The numerical three-dimensional animation of studied process demonstrates spatial interaction of non-equilibrium area with a bow shockwave and dynamics of flow parameters.

0   20 μs
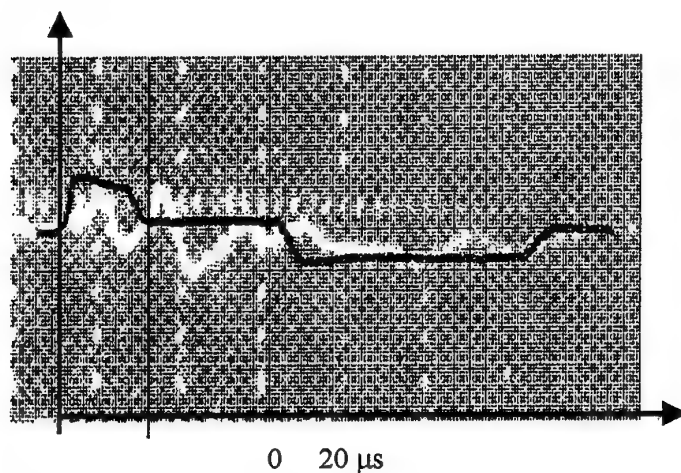
Fig.5
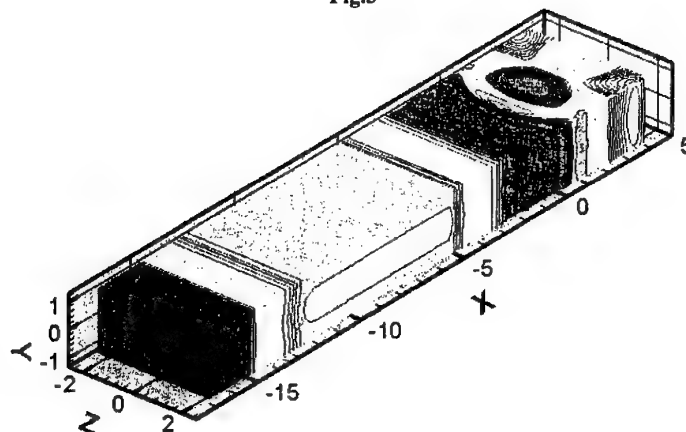
Fig.6

256

Numerical and experimental data comparison has shown, that the disturbances from plasma sheets do not influence non-equilibrium model streamlining. The calculation of instant energy deposition coincides with experimentally registered changes in a flow.

References

1. Znamenskaya. Discharge imaging technique for shock tube studies. In: Proc 21th Int Symp on Shock Waves. 1997. Keppel p. 489-491.
2. I.A.Znamenskaya, T.A.Gulu-zade. Quick Ionization of Supersonic Gas Flow. XXIV International Conference on Phenomena in Ionized Gasas. 1999, Varshava.
3. I.A. Znamenskaya, I.E. Ivanov, T.A. Gulu-Zade, N.N. Sysoyev Pulse Volume Ionization of Complex Channel Flow. Workshop Perspectives of MHD and plasma techologies in aerospace applicatios. 1999,Moscow, IVTAN P.123.
4. Beaulieu W, Bityurin V.A, Klimov A.I, Leonov S.B, Paschina A.S, Timofeev B.I. Aerodinamics WT Test of the 1/6 Scale Model of the F-15 Nose Part. Workshop Perspectives of MHD and plasma techologies in aerospace applicatios. 1999, Moscow, IVTAN:P 44-46.
5. Levin V.A., Afonina N.E., Gromov V.G.,Georgievsky P.Yu., Terentieva L.V. Influence of Energy Input by Electric Discharge on Supersonic flows around bodies. IM MSU Preprint N 36-98. Moscow. 1998. 93p .
6. Bityurin V.A., Klimov A.I., Leonov S.B., Lutsky A.E. Numerical Simulation of the Flow with Energy Supply Region Around the Model with a Needle. Workshop Perspectives of MHD and plasma techologies in aerospace applicatios. 1999,Moscow, IVTAN P. 47-52
7. A.Kh.Mnatsakanyan, G.V.Naidis and S.V.Rumyantsev. Shock Wave Propagation Through Nonuniform and Nonequilibrium Gase Regions. Proceedings of the Sixteenth International Symposium on Shock Tubes and Waves. Aachen, Germany, July 26-31,1987.
8. G.V.Candler and J.D.Kelley. Effect of Internal Energy Excitation on Supersonic Blunt-Body Drag. AIAA 99-0418. 37th AIAA Aerospace Sciences Meeting and Exhibit. January 11-14, 1999. Reno. NV.
9. V.M.Fomin, Th. Alziary de Roquefort, A.V.Lebedev, and A.I.Ivanchenko. Gasdynamic and electric phenomena on glow diccharge in a supersonic air flow. //X International Conference on the Methods of Aerophysical Research. Proceedings. Part I. Novosibirsk. 2000. pp 79-84.
10. Tretyakov P.K., Yakovlev V.I. Wave structure in supersonic flow with laser energy supply // Dokl. Akad. Nauk. - 1999. - Vol. 365, No.1. - P. 58 - 60 (in Russian).
11. Andreev S.I., Znamenskaya I.A.,Stepanets I.V. Udarnyi sloi v vozdukxe, vozbuzhdennom ob'emnym razpyadom. // Kximicheskaya fizika, 1993. vol.12. No.3. pp.392-393 (in Russian).

49. MECHANISMS OF THE DRAG FORMING IN A SUPERSONIC FLOW OF THE LOW-IONIZED GAS

I.P.Zavershinskii.
Samara State AeroSpace University

1. The construction of the analytical models, which assigned some mechanisms of drad force damping in a nonequilibrium gas flow, caused several interest. The set of the experimental papers and numerical models in this region is very noticeable, for example, [1-6], but analytical models are practically absent.

The main factors of changing of the wave resistance in a acoustically active media are changing of the amplitude and structure of radiated shock waves. There are exist two main mechanisms: the possibility of shock wave amplification in the nonequilibrium media and wave scattering on media fluctuations. The first mechanism is prevailed at weak turbulent phone

$$\langle v_x(\vec{r})v_x(0)\rangle << \sqrt{\mu_{0;\infty}k_y}\,; \frac{k_x^2 u_{0;\infty}^2}{k_y^{-2}}$$

whereas the secomn mechanism in the opposite limit. Here $v_{x,y}$ and $k_{x,y}$ are perturbances of velocity and wave vector, $\mu_{0;\infty}$, $u_{0;\infty}$ are whole viscosity coefficient and sound velocity in low-frequency and high-frequency limits, symbol $<...>$ means averaging.

Under condition of stationary acoustic field of radiation, taking place if number of Strouchal $S >> 1$

$$S = \frac{U\omega^{-1}}{l_x} >> 1,$$

or dispersion ratio $\omega = u_s k + \vec{U}\vec{k}$ is allowed the existance of stationary perturbances with $\omega = 0$. Let u_s supposed that the sound velocity has the fluctuated component c $u_s=u_s[1+\zeta(\vec{r})]$, where $\vec{r} = (x,y)$, $\zeta(\vec{r})$ is homogeneous chaotic function ($<\zeta>=0$) and radiated acoustic waves are belongs to high-frequency part of spectrum $\omega\tau >> 1$, where τ is time of relaxation of the internal degree of freedom.

2. The set of standard transformations, described in [7], for the high-frequency perturbances from accuracy to $\sim \varepsilon^2 << 1$ is lead to equation

$$\left(\frac{\partial}{\partial t}+U\frac{\partial}{\partial x}\right)^2 \varphi - u_\infty^2\left(1+\varsigma(\vec{r})\right)^2\nabla^2\varphi =$$

$$= b\left(\frac{\partial}{\partial t}+U\frac{\partial}{\partial x}\right)\nabla^2\varphi - \alpha_\infty u_\infty\varphi + R[\varphi],$$

where
$$R[\varphi] =$$

$$= \frac{1}{2u_\infty^2}\left(\frac{\partial}{\partial t}+U\frac{\partial}{\partial x}\right)\cdot\left\{\left(\frac{\partial}{\partial t}+U\frac{\partial}{\partial x}\right)\frac{\partial\varphi^2}{\partial t}+u_\infty(\nabla\varphi)^2 + \right.$$

$$\left. +(\Psi_\infty -1)\left[\left(\frac{\partial}{\partial t}+U\frac{\partial}{\partial x}\right)\varphi\right]^2\right\}-\nabla\left[\nabla\varphi\left(\frac{\partial}{\partial t}+U\frac{\partial}{\partial x}\right)\varphi\right]$$

After presentation of function φ in form of the superposition of coherent and chaotic components $\varphi=<\varphi>+\varphi'$, where $<\varphi'>=0$ in the coordinate system U, $t=t$, $\xi=x-Ut$, $y=y$ can lead to equation

$$\frac{\partial^2 <\varphi>}{\partial t^2}-u_\infty^2(1+\sigma^2)\nabla_\xi^2 <\varphi>=b\nabla^2\frac{\partial <\varphi>}{\partial t}-$$

$$-\alpha_\infty u_\infty <\varphi>+R[<\varphi>]+4u_\infty^2 GB*\frac{\partial^2}{\partial t^2}\nabla_\xi^2 <\varphi>$$

where
$$GB = \frac{\delta(t-t')B(\vec{r}_\xi -\vec{r}'_\xi)}{u_\infty^2} + F^{-1}[\Xi].$$

$$B(\vec{r}_\xi -\vec{r}'_\xi) =<\zeta(\vec{r}_\xi)\zeta(\vec{r}'_\xi) >$$

is correlator of velocity perturbances.

The evolution if the average field $<\varphi>$ is defined by ratio L/λ, where λ is wave length, L is correlation scale. In the limit $L/\lambda << 1$ we have

$$\frac{\partial^2 <\varphi>}{\partial y^2}-(M^2-1)\frac{\partial^2 <\varphi>}{\partial x^2}-$$

$$-\alpha_\infty M\frac{\partial <\varphi>}{\partial x}++\frac{(\mu_\infty+\mu_{TX})M^3}{u_\infty}\frac{\partial^3\varphi}{\partial x^3}+. \quad (1)$$

$$+\frac{\mu_{TY}M^3}{u_\infty}\frac{\partial^3\varphi}{\partial x^2\partial y}+R[<\varphi>]=0$$

where

$$\mu_T = \frac{2}{\pi} \int_{-\infty}^{\infty} (\vec{r}_\xi - \vec{r}'_\xi) B |\vec{r}_\xi - \vec{r}'_\xi| d\vec{r}'_\xi$$

is turbulent viscosity coefficient, $\mu_{TX;Y}$ are its components, α_∞ is linear sound increment. This equation is must be added by boundary condition

$$n_x \left(U + \frac{\partial \varphi}{\partial x} \right) + n_y \frac{\partial \varphi}{\partial y} \Bigg|_{y \to \pm 0} = 0 . \qquad (2)$$

After substitutions

$$\frac{\partial \varphi}{\partial y} = F_{2;1}(u) , \quad u = \frac{\partial \varphi}{\partial x},$$

$$F_{2;1}(u) = \pm \beta_\infty u \pm \frac{\Psi_\infty M_\infty^3 u^2}{2u_\infty \beta_\infty},$$

where $\beta_\infty = (M_\infty^2 - 1)^{1/2}$ for the longitudinal velocity we lead to equation

$$\frac{\partial u}{\partial y} \pm \beta_\infty \frac{\partial u}{\partial x} \pm \frac{\Psi_\infty M_\infty^3}{2\beta_\infty u_\infty} u \frac{\partial u}{\partial x} =$$

$$\left[\pm \frac{(\mu_\infty + \mu_{TX}) M_\infty^3}{2\beta_\infty u_\infty} - \frac{\mu_{TY} M_\infty^3}{2u_\infty} \right] \frac{\partial^2 u}{\partial x^2} \mp \qquad (3).$$

$$\mp \alpha_\infty M_\infty u$$

2.1. In the limit $\mu_{TX;Y} k_{X;Y}^2 \ll \alpha_\infty$ the stationary radiated acoustic disturbances are strengthen along the Mach lines into $\alpha_\infty l_x$ times. As a result the gradients of pressure up and down of the streamlinied body are smoothed over. Since the wave resistance and lifting force coefficients is damped on a value $\delta^2 \alpha_\infty l_x$. l_x is the body length, δ is an attack angle

$$C_X = \frac{2\delta^2}{\beta_\infty} \left[2 + \frac{M_\infty \delta}{2\beta_\infty} \alpha_\infty l_x + \frac{k_{3\infty} M_\infty^3}{\beta_\infty u_\infty} \delta \right].$$

$$C_Y = \frac{2\delta}{\beta_\infty} \left[2 + \frac{M_\infty}{2\beta_\infty} \alpha_\infty l_x - \frac{k_{3\infty} M_\infty^3}{\beta_\infty u_\infty} \delta \right]. \qquad (4)$$

Thus, the changing of these coefficients caused by described factor is small.

2.2. In the limit $\mu_{TX;Y} k_{X;Y}^2 \gg \alpha_\infty$ the radiated shock waves are damped in a fluctuated media at great values of turbulent viscosity. The drag and lifting force coefficients for symmetrical body are defined by following expressions

$$C_X = \frac{4}{\beta_\infty} \left[\delta^2 + \frac{4}{3} \varphi^2 - \mu_{TX} \frac{\varphi^2 M_\infty^3}{2l_x u_\infty} \right],$$

$$C_Y = \frac{4}{\beta_\infty} \left[\delta - \mu_{TX} \frac{\varphi M_\infty^3}{l_x u_\infty} \right] \qquad (5).$$

where φ is integral average value of a tangent line from the contour of profile with respect to its chorde. These expressions demonstrated the well accordance with experiment [8], where considered the supersonic motion of conical body with angle $\psi = 35°$ by flow of He-N$_2$, plasma under conditions $P=70$Top. $E/P=5$Td, $T=400$K. The Mach angle is growed from the value $\beta = 95°$ to value $\beta_p = 119°$. As a result the Mach number is damped from M=2 to =1.8. The drag force coefficient is damped on 18%, Fig.1.

3. The heterogeneous heating of the bounds ant boundary layers at most experimentally popular middle pressures $P<100$Torr has the lower characteristic time then the homogeneous. It is lead to decreasing of the radial gradient of a longitudinal velocity $\partial u_x / \partial y$ and increasing of scale of a a boundary layer $\delta(x)$. As a result the turbulent drag force coefficient is decreased [10]

$$C_{XT} = \frac{(\mu + \mu_T) u^{1/2}(\infty)}{\left(\frac{\mu}{\sigma} + \frac{\mu_{T-}}{\sigma_T} \right)^{3/2}} \left(\frac{T(\infty)}{T} \right)^{1/2} \cdot$$

$$\cdot \left[1 + \exp \left(\frac{\alpha - \beta}{kT} h\omega_0 \right) \right]^{3/2} \qquad (6)$$

The boundary layer width in such conditions is defined by expression

$$\delta \approx \sqrt{\tau_H \left(\frac{\mu}{\sigma} + \frac{\mu_T}{\sigma_T} \right)}$$

Under conditions [9] at $N=0.7$кВт, $P=55$Top we have $\delta \approx 1.6$mm, the experimental result is $\delta \approx 2$mm.
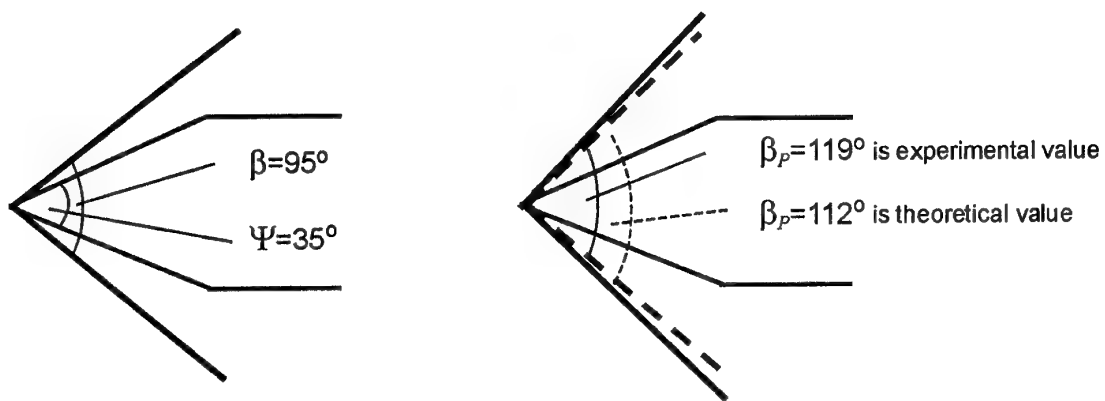
Fig.1. The Mach lines in experiment [8] (continuous line) and in accordance of Eq. (5) (stroke line).
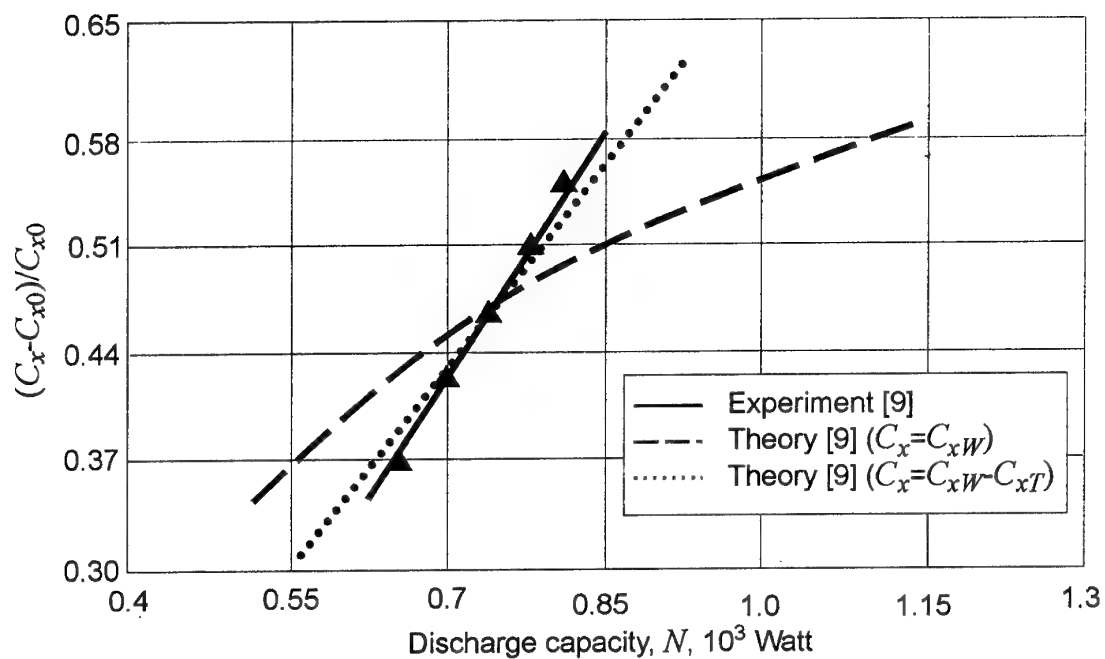
Fig. 2. The changing of the turbulent resistance coefficient.

References

1. Becker E. Chemically reacting flows. Annual review of fluid mechanics. 1972. V.4. P.155-194.
2. Homentchvschi D. Chemically reacting flow of an inviscid gas past a thin profile. ZAMM. 1977.V.57. P.461-469.
3. Bityurin V., Brovkin V., Klimov A., Kolesnichenko Yu., Leonov S., Savelkin K., van Wie D.M. Features of shock wave propagation through a longitudinal pulse dischrge. The 2nd WSMPA. Moskow. 5-7 April 2000. P. 263-268.
4. Soloviev V.R., Krivtsov V.M., Konchakov A.M., Malmuth M.D. Supersonic body drag reduction during forebody filamentary discharge temporal evolution. The 2nd WSMPA. Moskow. 5-7 April 2000. P. 98-101.
5. Ganguly B.N., Bletzinger P. Shock wave damping and dispersion in nonequilibrium low pressure argon plasmas. Phys. Letters. A230. 1998. P.218-224.
6. Merriman S., Ploenjes E., Palm P., Adamovich I. Shock wave control be nonequilibrium plasmas in colf supersonic gas flows. Nonequilibrium processes and their applications. V International School-seminar. Contr. papers. Minsk. 2000. P.70-72.
7. Zavershinskii I.P., Kogan E.Ya. Flow of the nonequilibrium gas past bodies. High Temperature. 1999. V.37. N.5. P. 749-753.
8. Merriman S., Ploenjes E., Palm P., Adamovich I. Shock wave control be nonequilibrium plasmas in colf supersonic gas flows. Nonequilibrium processes and their applications. V International School-seminar. Contr. papers. Minsk. 2000. P.70-72.
9. Bychkov V.L. Grachev L.P, Esakov I.I. et al. Numerical and experimental investigation of supersonic flow aroun blunt body at the existance of the longitudinal discharge // G.Keldysh's Institute of Applied Mathematics Prepr. N27. 1997. P.1-50.
10. Zavershinskii I.P., Kogan E.Ya. The influence of heterogeneous processes on streamlinied bound in the nonequilibrium gas on gasdynamic resistance // Tech. Phys. Letters. 2000 V. 26 N.5. P.76-79.

50. A NEW CONCEPT FOR THE PROSPECTS OF HUMAN MARS MISSIONS BASED ON APPLICATION OF THE MHD METHOD FOR ENERGY CONVERSION IN POWER AND PROPULSION INSTALLATION

V.S. Slavin, K.A. Finnikov, A.A. Gavrilov, T.A. Milovidova, K.U. Litvintzev
Krasnoyarsk State Technical University

M.V. Kraev
Siberian Aero-Space Academy

Introduction

Among the project of the XXI century emphasis should be on the Mars missions project having been intensively discussed over 2 recent decades. Specially for realization of the this project developments of nuclear thermal engines [1] allowing to make the Mars mission vehicle reusable thus reducing the cost of each flight were being conducted in USA [2] and USSR in the 1970's - 1980's. In this version the launch from the near-earth orbit is accomplished and the spacecraft mass will make about 1000 tons with the working medium mass 600 tons. The estimated cost for this program is 500-1000 billion, which makes it unlikely to be realized in the foreseeable future.

Another approach is based on application of expendable vehicle systems which would be end, like the Moon expeditions, with the recovery of the manned capsule. In this case the launching mass on the near-earth orbit makes 330 tons for chemical rocket engines, so does with electrical rocket engine (ERE). This result comes from application of the spaceborne equipment based on perspective solar cells with specific power 200W/kg and the area $32 \cdot 10^4 m^2$. In this project the mass of the vehicle is determined by the script of the expedition intending to land man on the Mars surface. The landing module will have the mass about 50 tons correspondingly, while the mass of the Mars orbit spacecraft together with the landing module makes 90 tons.

However man landing can be rejected as suggested in the recent planetary explorations concept (project "Space Rover" - SR) [3] by means of interplanetary spaceship supplied with handling robots operating under the "effect of presence". This mode eliminates the contradiction between the need of human presence at the point of contact with the "novel" and requirements for his safety. Crew attendance on the orbit of the celestial body explored provides a small distance between the operator and the handling robots on the surface. Everything taken by robot sensors will be transmitted to the spaceship for further investigation and distribution. According to this strategy human landing on the surface of celestial bodies loses its meaning. So the mass of spaceship can be considerable reduced.

A solar spaceborne closed-cycle MHD-generator based power plant can have, as said below, a specific power index 500W/kg order, which also reduced the mass of a spaceship. Thus, in the context of SR concept, a space vehicle can be reusable with a small launching mass, which will make this project financially reasonable.

Solar spaceborne closed cycle MHD generator based power plant

The most commonly used notion now is that solar space power plants are limited in power by the level of 100 kW, so that only nuclear multimegawatt plants are available [4]. A gas cooled nuclear reactor is considered as a source of thermal energy, after which the gas is expanding in the gas turbine operating from Brayton closed cycle. Calculation [5] of this type of cycle has shown that the temperature of radiation panels cooling the working medium has the optimum value 350K. In terms of the mass of these panels specific power of a nuclear power plant would not exceed the level 300 W/kg.

The MHD closed cycle generator, operating with noble gas at the temperature 2000K order, will maintain high thermodynamic efficiency at high ($\approx$ 500-700K) temperatures of a "cooler". Radiation panels used as "cooler" release thermal energy into space in the form of thermal radiation. Specific power of thermal radiation $\sim T^4$ hence the high "cooler" temperature make possible to considerable reduce the mass radiation panels, which is the chief advantage of space MHD application over gas turbines. However the condition of maintenance of non-equilibrium conductivity in an MHD channel limits the gas stagnation pressure at the channel inlet at the level of 1MPa, which is an order below the required level in the active reaction zone. Due to this reason, the Sun as thermal power source in closed cycle of MHD generator offers the advantage over a nuclear reactor.

The solar film parabolic mirror concentrating the radiation on thermal adapter has

been proposed as a source of thermal energy for a spaceborne power plants. Fig.1. shows the overall scheme of the mirror-adapter system.
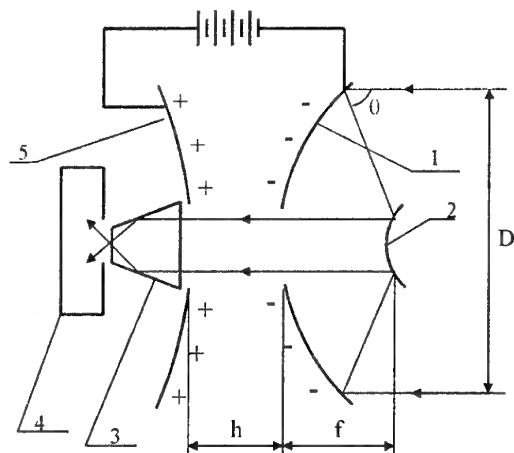
Fig.1. System of solar film parabolic mirrors. 1 – primary mirror, 2 – secondary mirror, 3 – mirror funnel concentrator, 4 – radiation parabolic adapter, 5 – capacitor film cover involved in formation of parabolic form for the primary mirror.

The electrostatic field with the voltage determined by an order excess of electrostatic forces over the inertia force gives parabolic form to the film. The latter arises due to accelerating impact of ERE, its level being $\sim 10^{-3}$ m/s^2. With the mirror's diameter of 120m and focusing angle 60° the distance between the film capacitor plates should be the order of minimum 20m that determines the voltage 200kW. The section of equipotential surface should be placed on the back surface of the mirror film. Their potential set up, one can control the mirror's curvature. The second convex mirror and reflection condensing funnel of the light stream allow to attain the concentration $\geq 10^4$. The concentrated light flux passes through the transparent glass surface and enters the vortex chamber, where it reflects once again from the mirror cone directing the radiation flow onto the ball bed made up of ceramics balls (ball's diameter 5mm). The working medium of the power plant, noble gas neon, is supplied tangentially in circular over the entire bed layer and creating centrifugal forces in it. Radial component of the gas velocity, at which it flows through the bed, produces the effect of boiling layer and every ball is being in the balance of centrifugal forces and those of flow resistance. The boiling layer is a loose semi-transparent structure, where the radiation would be absorbed over the entire volume of the ball filling. Heat exchange between gas and ball bed, which is in the state of a boiling layer, occurs very

intensively and allows to minimize the mass of the heat adapter.

Mirror calculation

The solar radiation concentrator diameter is selected so that to obtain the electric power ≈10MW. The expected efficiency of the power plant ≈30%. Thus a heat adapter is to collect ≈30MW from the mirror. Considering that the mirror systems will have a common 80% order efficiency we can determine the power of the solar radiation collected by mirror as 30/0,8=38MW. When the solar constant I_0=1,4kW/m^2 the area of primary mirrors will make ≈ 27100m^2. When distributing this area between three mirrors their diameters will be ≈110m. Allowing for an error of these assessments as well as inaccuracy of focusing on the adapter we choose the diameter value D=120m. In what follows the calculation for a single mirror will be offered.

To evaluate the mirror mass assume a mirror accuracy parameter to be $\Delta\alpha$=2.5°, then according to [6] the specific mass will be determined as m=50g/m^2, which corresponds to the level for promising film mirrors techniques. The mirror mass equal $M \approx m\pi D^2/4 \approx$ 570kg. The solar energy power brought in the mirror focal plane considering the reflection factor for primary and intermediate mirrors (η=0.95) will equal $W_0=\eta^2 \cdot I_0 \pi D^2/4 \approx$ 14,3MW. The power falling on the adapter will be evaluated.

The main property of the mirror is its concentration determined as a relationship between the power illumination in the given point of the adapter and the normal power illumination from the Sun. The maximum concentration of solar radiation for a perfect parabolic concentrator is determined from relationship [6] $C=\eta \cdot 4,8 \cdot \sin^2(2\theta)/tg^2\alpha_0$, where α_0 =30′ - visible angle Sun dimension. An actual concentrator makes concentration K_c times lower, where $K_c=1/(1+\Delta\alpha/\alpha_0)^2$, $\Delta\alpha$ mirror accuracy constant evaluating an increase in the area of the actual mirror focal spot compared to perfect mirror focal spot.

Adopt the accuracy constant value for a film concentrator equal 2.5° which corresponds to a fairly rough mirror that does not offer any special difficulties for its realization. Thus the actual concentration of solar radiation in the center of the focal spot on the adapter will make $C_1=K_c C \approx 1000$.

To asses the focal spot diameter on the adapter the relationships [6] are used, defining the distribution of radiation energy stream in the focal plane

$$I(r) = C_1 \exp(-C_2 r^2),$$

263

where

$$C_1 = (180/\pi)^2 I_0 \eta \sin^2\theta h_a^2 \ ,$$

$$C_2 = [(180/\pi)(h_a/2f)(1+\cos\theta)]^2 \ , \ h_a = 4{,}11\sqrt{K_c}$$

The focal length of the mirror is determined from the concentration of the rays path in a parabolic mirror,

$$\frac{D}{f} = \frac{4\sin\theta}{1+\cos\theta} \ .$$

At the optimal angle focusing [6] $\vartheta=66°$ we obtain f=52m.

Considering that the radiation intensity on the boundary of the focal spot makes 10% of that in its central part, we have the radius of the focal spot $R\approx2.7$m. The total power of the Solar radiation, concentrated in the focal spot is determined as

$$W = \int_0^R I(r)2\pi r dr = 11{,}4 \ \text{MW}.$$

The obtained heat power source will be applied as an initial parameter for calculation of receiver radiation entered the eddy chamber through the mirror funnel considering a light stream, its output radius being R_a=0.5m. Due to the funnel converge of solar radiation attains $C_r\approx3\cdot10^4$.

Radiation adapter calculation

In the radiation adapter, which scheme is shown in Fig.2, the light stream is absorbed by the "boiling" layer of ball bed, which temperature being 210° higher than that of the gas (obtained from he heat balance condition). Consequently, if the outlet gas temperature makes 2000K, the temperature of balls in the inner radius of the ball

gas

gas   gas
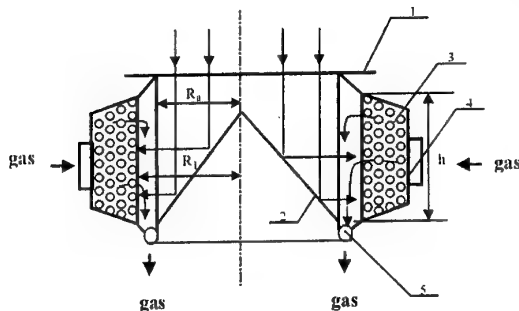
Fig.3. Radiation receiver – vortex chamber. 1 – transparent glass partition, 2 – reflecting mirror cone, 3 – ball bad, 4 – input pipes for gas, 5 – output collector for gas. (R_1=0,8 m, W_{heat}= 9 MW, M ≈1 ton)

bed will make 2210K. The inner surface of the bed which dimensions h=20cm and R=70cm will radiate as a black body. That radiation is dissipating in space that leads to the reduction of the of the adapter efficiency. With given dimensions and parameters the parameter efficiency can be determined as η_a=79%.

The consumed heat power for the radiation adapter ($Wd=W\cdot\eta_a$=9MW) and the input and output temperature (T_1=1100K, T_2=2000K) of the working medium have been the initial data for its calculation. Neon heat capacity in the given temperature interval is a constant equal C_p=1040J/(kg·K). Mass consumption for the working medium has been determined from the heat balance equation $G=W_a/(C_p(T_2-T_1)) \approx9.6$kg/s. Tangential flow velocity in the eddy chamber will be determined from the condition ω^2R_1=2g, g=9,8m/s^2, where an angular velocity of bed particles ω=4.6s^{-1} and a linear tangential velocity 3.7m/s can be found. A radial component of the bed balls velocity is to be chosen so that the pressure loss force acting on them would be balanced by a centrifugal force that is

$$\xi\frac{\rho_g U_r^2}{2}\cdot\frac{\pi d^2}{4} = m_1\omega^2 R_1 \ ,$$

where ξ – resistance factor (for Re$\geq10^3$ $\xi\approx$1), ρ_g – gas density, u_r – radial component of gas velocity, m_1 – a single ball mass.

An average gas density will be determined from the relationship $\rho_g= P\mu/R_0 T\approx1{,}6$kg/m^3, where P=10$^6\cdot$Pa – gas pressure in adapter, T=1500K – average gas temperature.

A single bed ball mass with a diameter d=5mm is determined through ceramics density =3970kg/m^3 (Al$_2$O$_3$) of which the balls are made determine that m_1=0,26g. Thus the radial velocity value $U_r\approx18,$1m/s has been obtained.

Define the Reynolds and Nusselt numbers by equations [7]

$$\text{Re} = U_r d/\nu \approx 1837{,}3$$
$$\text{Nu} = 2 + 0{,}16\cdot\text{Re}^{2/3} \approx 26{,}6$$

The value of convective heat transfer factor can be found as α=Nu$\cdot\lambda/d$=915,1W/m$^2\cdot$K (cinematic viscosity value ν=4,9$\cdot$10^{-5}m^2/s and heat conductivity value λ=0,172W/m·K is taken for neon at the temperature T=1500K).

We determine the surface of heat exchange

$$F = W_a/\alpha\,\Delta T \approx 47 \ \text{m}^2$$

using the equation of heat balance and assuming the temperature difference between the bed and flowing around gas = 210 K.

Specifying the dimensions of an eddy chamber we select the thickness for a bed so that to obtain a specified surface of heat exchange at a radial velocity of heat transfer medium $U_r \approx 18,1 \text{m/s}$. The average radius of the bed layer $R_c \approx 0,8\text{m}$ at the average height $h=0,2\text{m}$. The area of the chamber cross–section without bed on radius R_c is defined as $S_0 = 2 \cdot \pi \cdot R_c \cdot h \approx 1,0 \text{m}^2$. With bed we find that the cross–section is to be equal $S = G/\rho_g \ U_r = 0,33\text{m}^2$ from the equation of continuity. This determines the distance between the centers of adjacent bed balls $a=0,006\text{m}$. Here from we find a relative volume fraction of boiling bed voids

$$\varepsilon = 1 - V / V_0 \approx 0,62 \ ,$$

where V – dense material volume in boiling layer, V_0 – general bed volume. (presumable thickness of a bed layer 0.1m). Specific area of particles surface is being calculated

$$f = 6 \ (1 - \varepsilon) \, / \, d \approx 456 \ \text{m}^2/\text{m}^3.$$

Substituting this value in a relation for the area of heat exchange surface get

$$F = 2\pi f R_c \, \delta \, h = 47 \ \text{m}^2 \ ,$$

whence it follows that the filling layer thickness $\delta \approx 0,1$ m.

To assess working medium pressure loss in the eddy chamber the relation [7]

$$\Delta P \approx \left[150 \frac{(1-\varepsilon)^2}{\varepsilon^3} \frac{\nu \rho U_r \varepsilon}{d^2} + 1.75 \cdot \frac{1-\varepsilon}{\varepsilon^2} \cdot \frac{\rho \varepsilon^2 U_r^2}{d} \right] \cdot \delta$$

is used. It follows that $\Delta P \approx 84$ kPa.

Calculation of thermodynamic cycle of MHD plant

A new type of MHD generator with non–uniform gas–plasma flow of unseeded noble gas has been suggested as a converter of thermal energy into electric one. Electric conductivity in flow is provided by nonequilibrium plasma current layers (P–layers) being at the state of slow recombination – "frozen ionization".

The distinctive properties of this generator type are as follows:
- High enthalpy conversion ratio ($\eta_N \approx 0,4$) is realized in the gas flow with P–layers.

- Low Joule dissipation level, required for maintaining "frozen ionization", allows to attain a high value of adiabatic efficiency ($\eta_S \approx 0,8$).
- Non–using alkali seed enables to eliminate numerous problems related to the input, uniform ionization and output of seed.
- Using P–layers, where the gas temperature is 3–4 times higher than that in surrounding "cold" flow, allows to bring the level of optimal value of the input stagnation pressure up to 1MPa instead of 0.3MPa for conventional closed–cycle Hall MHD generator.

Based on these peculiarities one can suggest a thermodynamic cycle (see Fig.3).
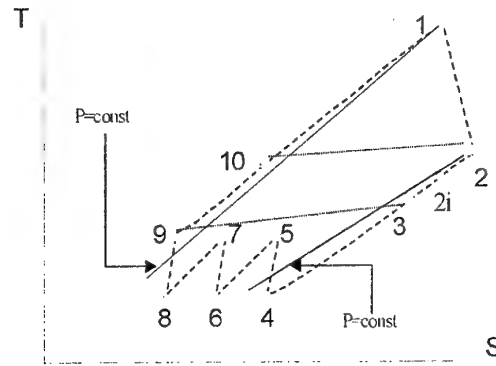
Fig.3. Diagram of thermodynamic cycle for MHD power plant

On the T–S plane working medium states at the MHD generator input and output correspond to the points 1 and 2. The point 2i would be the ending of an ideal process of isentropic gas expansion in the MHD generator. Taking MHD generator efficiency factors to be $\eta_N \approx 0.4$ and $\eta_S \approx 0.8$, that are find as

$$\eta_N = (T_1 - T_2) \, / \, T_1 \ ; \ \eta_S = (T_1 - T_2) \, / \, (T_1 - T_{2i}) \ ,$$

we can find that $T_2=1200\text{K}$, and $T_{2i}=1000\text{K}$. Correspondingly pressure differential on the MHD generator will be determined as

$$\beta = \frac{P_1}{P_2} = \left(\frac{T_1}{T_{2i}} \right)^{\frac{\gamma}{\gamma-1}} = 5.64 \ .$$

The output MHD temperature 1200K allows to use a tubular recuperation heat exchanger for preliminary heating of working medium before radiation adapter. Heat exchange running with counter flows at a temperature difference on a tube wall $\Delta T=100\text{K}$ is being used. After cooling in recuperation heat exchanger the gas is finally

265

cooled in a radiation cooler at temperature T_3 and supplied onto the input at temperature T_4. To reduce the power consumed by the compressor a three–step compression with intermediate cooling in the radiation "cooler" is utilized. Temperatures at the compression steps input, as well as those at the output, are the same, i.e. $T_4=T_6=T_8$ and $T_5=T_7=T_9$. Adiabatic efficiency of a compressor is considered to be equal $\eta_c=0,9$.

Thermal efficiency of the given power plant is determined as a relationship

$$\eta = \frac{W_g - W_c}{W_a},$$

where W_g – thermal (heat) energy converter power, W_c – compressor power, W_a – heat source power.

Expression for efficiency can be represented through temperature values in characteristic points of thermodynamic cycle

$$\eta = \frac{T_1 - T_2 - 3(T_5 - T_4)}{T_1 - T_{10}}.$$

Here the value $T_{10}=T_2 - \Delta T$, while the temperature T_5 is will be defined from the relationship

$$T_5 = T_4 + \frac{T_4}{\eta_c}(\pi^{\frac{\gamma-1}{\gamma}} - 1),$$

where defining the parameter $\pi=P_5/P_4=(P_1+\Delta P_1)/(P_2 - \Delta P_2)$ requires the pressure losses in high and low pressure tracts to be given. Let $\Delta P_1=130$kPa, $\Delta P_2=50$kPa.

Temperature growth of radiation panel of the cooler reduces their area and hence their mass. Together with the growth of the cooler temperature thermal efficiency reduces, i.e. electric power generated by the plant lowers.

The objective of the thermodynamic calculation is to determine the optimal temperature value T_4, that provides the maximum value of specific power. One must set mass of the aggregates, forming the power plant, to carry out this calculation.

To access mass characteristics the data of space technique will be used. Thus the compressor steps mass together with electric engine can be defined as 500kg while that of pipe heat exchanger as 300kg. The MHD generator mass together with superconducting magnetic system can be evaluated just by convention through the method of analogies. It is exemplified by the paper 10 analyzing space application of MHDG. At the electric power level of 100MW the total mass of MHDG together with magnetic system is being assessed as 4000kg. In our case, at electric power at

10MW, the mass value for this equipment with the safety margin will be chosen 1500kg.

The mass of radiation cooler depends on the quantity of the heat power dissipated. The mass of a square meter of heat dissipating panels surface will be considered to equal $\tau=1$kg/m^2, while the energy flow from their surface corresponding to the law of blackbody radiation. In this case the cooler mass

$$M_{cool} = \tau\, W_a \cdot (1-\eta) / (\sigma_0 T_4^4), \text{ kg}$$

where $W_a=9\cdot10^6$W, $\sigma_0=5.67\cdot10^{-8}$W/m^{2}K^4 – Stefan-Boltzmann constant.

Specific power capacity will be determined as the relationship of the electric power to the total mass ratio:

$$\varphi = W_a\eta / M,$$

where M=3870[kg]+ M_{cool} - overall mass of plant.

The peak value of the plant capacity $\varphi=450$W/kg is being attained at the cooler temperature $T_4=450$K. A thermal efficiency value in this case will make $\eta \approx 0,32$.

Pulse action ERE with azimuthal current layers.

The peak thrust values at electrodynamic acceleration of working medium in the rocket engine have been obtained under stationary plasma discharge conditions in cross electric and magnetic fields within the so-called stationary plasma engines (SPE) [11]. This level for SPE is 0,1N now and will be able to attain 1N in future. Specific impulse for such engines lies within the range from 15 to 20km/s and mass flow of working medium does not exceed 10^{-2}g/s. Requirements of stable burning of stationary discharge in SPE determine a low mass flow for of the working medium. In attempting of its increase the mass flow density is growing as the result, the plasma temperature is dropping and plasma is coming into a low ionized state. In such plasma the electric conductivity dependence on the temperature is close $\sim T^8$ which results in the developments of overheating instability and makes the engine operation ineffective. Clearly a system with such a low thrust level can be used just as an attitude control and orbit stabilization engine. At the same time plans of the space industrial assimilation including the orbital injection of space system on geostationary orbits, transportation cargoes to the Moon, where a lunar base is supposed to be set, and manned flights to the solar system planets anticipate that the electric rocket engines of high thrust will be produced.

266

A magnetic plasma engine [12], which is to meet the requirement for thrust level of march space engines is being under development in USA. This engine offers an open magnetic system for high temperature plasma to be heated to the temperature $\geq 10^6 K$ by a high frequency energy source. The magnetic field line form a magnetic nozzle and the charged particles, moving along the field lines, form a propulsive jet of the working medium. Plasma acceleration in such an engine proceeds mush in the same way as in a thermal engine but high efflux velocities (~100-200km/s) achieved through a high temperature. For flight to the nearest planets (Mars and Venus) these velocities lie in the optimal velocities range which boundaries (see the following section) can be defined as 40km/s $\leq u_{efflux} \leq$ 3km/s. The drawback of this engine type is that for effective plasma heating in the volume of open magnetic system it should be in a collisionless state which will determine large volumes of system and hence large overall dimensions and mass of the engine. For a manned flight to Mars harnessing of the nuclear power plant with machine converter (gas turbine) being of 30MW power and 100 tons order mass has been suggested.

Trying to achieve optimum conditions for the manned flight to Mars (launch from the near-earth orbit) in the context of minimizing the product of a launching mass and flight duration, it has been found that the acceptable values are attained at the engine thrust ~500N and a specific impulse 40km/s (4000s). This engine will allow spacecraft with payload 60 tons at the power plant mass 20 tons and the launch supply of propellant (hydrogen) 135 tons to reach the Mars in less than 4 month and to spend much the same time to return.

In the paper [13] magnetohydrodynamic (MHD) process in the channel of hypothetic electric engine, based on the T-layer phenomenon, had been analyzed. T-layer is a stable structure arising on a non-linear phase of overheating instability development. By virtue of this a working medium flow carrying T-layers will be stable with reference to overheating instability at the sufficiently higher values of mass flow than that in SPE. The [13] was founded on the electrode circuit of MHD accelerator where a plasmoid was being formed by means of a periodic impulse discharge of an external energy source in the gas stream at the MHD channel input. The flow brought that plasmoid into the channel with a transverse magnetic field where it shorted the electrodes connected with the main sources of energy. The discharge current from the main source interacted with magnetic field, which resulted in appearance of accelerating electrodynamic force in the plasma

volume. A sequence of plasmoids (T-layers) filling the MHD channel effectively accelerates the gas flow up to ≈50km/s, the thrust level ≈1500N is reached in the channel with a cross-section $1 \times 1 cm^2$ and working flow 30g/s.

In an interplanet flight the engine will be working the most part of the flight time, therefore its operational life time should be about a year. In T-layer the discharge current corresponds to the high current arc operation which must rule out application of any electrode circuit due to inevitable arc erosion of electrodes. In this paper an MHD accelerator of induction circuit is being analyzed. Here the current in T-layers would close by itself and energy transmission from an external source would be performed through inductive coupling.

Induction MHD accelerator

Scheme of ERE with T-layers forming azimuthal current rings can be shown according to Fig.4. Here the MHD channel makes a cylindrical space between coaxial magnetic poles, which are made from ferromagnetic material. The winding is connected to the external source of alternative EMF setting up an alternating current in the winding and alternating magnetic field in the MHD channel. In its turn, the increasing with time magnetic filed generates the vortex (φ-direction) electric field, which induces the current in plasma in a direction opposite to that of the current in the winding. The resulting repulsive forces between coils cause the plasma flow to accelerate. The problem of plasma coil release out of MHD channel is being solved by
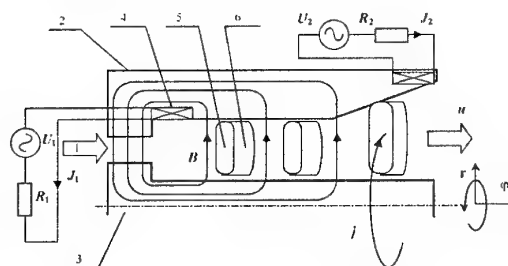
Fig.4. Scheme of induction MHD accelerator with the current layers: 1 - working medium flow; 2 - external magnetic circuit; 3 - internal magnetic circuit; 4 - current coil; 5 - current layers; 6 - mass clots of cold gas.

means of a diffuser at the channel outlet and with the second auxiliary winding placed at the channel outlet. Channel expansion result in plasma cooling and conduction loss. In the calculations the channel dimensions were set up as following: channel length 30cm, channel height 1 cm, diffuser length 7cm. Hydrogen was chosen as a working medium. Parameters of gas flow at the channel inlet were:

stagnation pressure 0,1MPa, stagnation temperature 10^3K, flow Mach number 1,5.

Simulation the MHD process in ERE channel

Modelling had been performed on numerical solution of a complete system of one-dimensional magnetohydrodynamic equations appearing as:

$$\frac{\partial}{\partial t}\begin{pmatrix} \rho \\ \rho u \\ \rho(\varepsilon + u^2/2) \end{pmatrix} + \frac{\partial}{\partial z}\begin{pmatrix} \rho u \\ p + \rho u^2 \\ (p + \rho\varepsilon + \rho u^2/2)u \end{pmatrix} =$$

$$= \begin{pmatrix} 0 \\ -j_\varphi B_r \\ j_\varphi E_\varphi - q_{rad} \end{pmatrix}$$

$$\frac{\partial}{\partial t} B_r - \frac{\partial}{\partial z} E_\varphi = 0, \quad j_\varphi = \frac{1}{\mu_0}\frac{\partial}{\partial z} B_r = \sigma(E_\varphi + uB_r),$$

where μ_0 – magnetic constant, E_φ- electric filed, B_r – magnetic filed, j_φ - current density, q_{rad}.- volume radiation losses.

In this case the circuit equation with external EMF source inductively related to the plasma circuit has been solved to determine boundary conditions for the magnetic filed. Thus equation appears as:

$$RJ(t) - U(t) = -\frac{d}{dt}\Phi(t),$$

$$2\pi aE(z = 0, t) = -\frac{d}{dt}\Phi(t),$$

$$J(t) = a\ln(\frac{r_1}{r_0})\frac{B(z=0,t)}{\mu_0},$$

$$a = \sqrt{\frac{r_1^2 - r_0^2}{\ln(r_1/r_0)}}$$

where R – circuit resistance, U – external EMF, Φ – magnetic flux, r_0, r_1 – internal and external magnetic circuit radii.

Volume radiation energy losses are considered by the most simple model $q_{rad} = q_0 T^4$, where factor $q_0 = 10^{-7}$W/m^3·K^{-4} has been chosen from a stabilization condition of T-Layer at temperature ~3·10^{4}K. Radiation losses calculation by the more exact models when defining plasma temperature, shows no more than 20% difference compared to the procedure. To describe a plasma condition of the working medium assume the availability of thermodynamic balance.

The optimum time dependence of voltage at the source had been found after a number of modeling calculations. It is shown in Fig.5a.
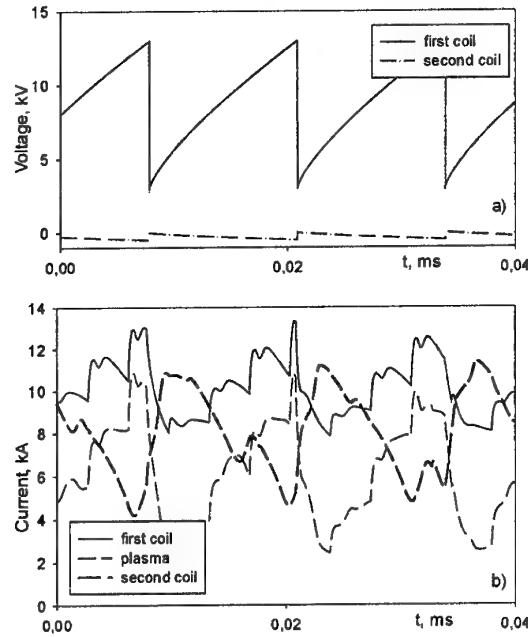
Fig.5. Oscillograms of currents and voltages.

Duration of the stage of the build-up of voltage makes 26 µs. In this time interval, seven plasma clots given as isobar temperature disturbances in the computation process model are being initiated. In actual practice those disturbances can be generated at regular intervals by a high frequency induction discharge. In Fig.5b current oscillograms both in the primary and secondary excitation winding as well as in the plasma circuit are shown. We notice that on the whole, the currents in the primary winding and plasma circuit qualitatively repeat the voltage oscillogram in the EMF source, the current it the secondary winding being in the opposite phase. Hence the secondary winding plays the part of an absorbent of electromagnetic energy of the T-layer issuing the MHD channel, which solves the problem of a plasma clot release from MHD channel. Dynamics of temperature distribution and that of mass density is represented as space dependencies $T(x,t)$ and $\rho(x,t)$ (see Fig.6 and 7).

The temperature distribution corresponds to the periodic steady state. By the curves nature one can see that the temperature peak in T-layers attains the values $\approx 35\cdot 10^3$ K, which is much lower than the plasma temperature in SPE and magnetoplasma engines. From the area of T-layers the secondary disturbances are separated, which appear as compression waves transforming into

268

ionizing shock waves. The temperature growth due to shock compression results in "pick up" of secondary disturbances which temperature is built up through electric heating. In the diffuser T-layers are cooled and their plasma recombinated, that is, the flow at the engine outlet will consist of the non-ionized gas.
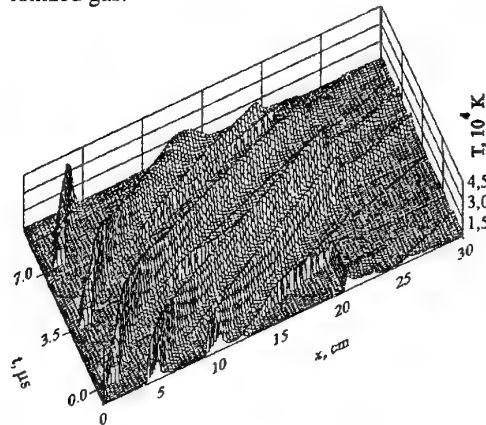
Fig.6. Temperature distribution dynamics.
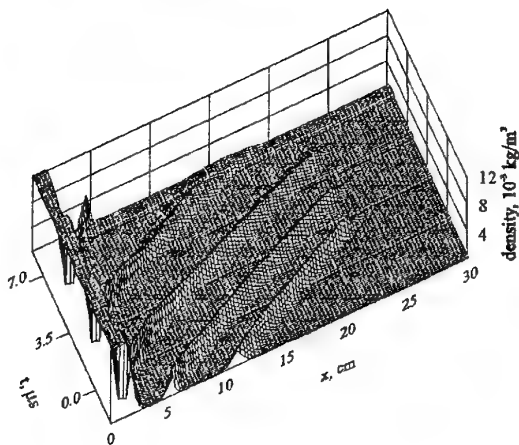
Fig.7. Mass density distribution dynamics.

The density distribution has a shape of mass clots pushed ahead by T-layers as if they were pistons. Mass clots decay in diffuser like T-layers that forms a uniform flow at the ERE outlet.

Distribution of magnetic filed in the channel and that of flow velocity are shown in the form of instantaneous distributions in Fig.8. As seen from the curves nature in Fig.8a the magnetic field has a uneven drop on T-layers. Here effect of the Lorentz force on the T-layers reduces to the action of magnetic pressure gradient. Distribution of velocity over the channel is of a non-monotone nature But as a whole tendency of velocity increasing is observed, which shows to be "exhausted" before T-layers decay. The flow gains

additional acceleration through the heat expansion of T-layers in diffuser.
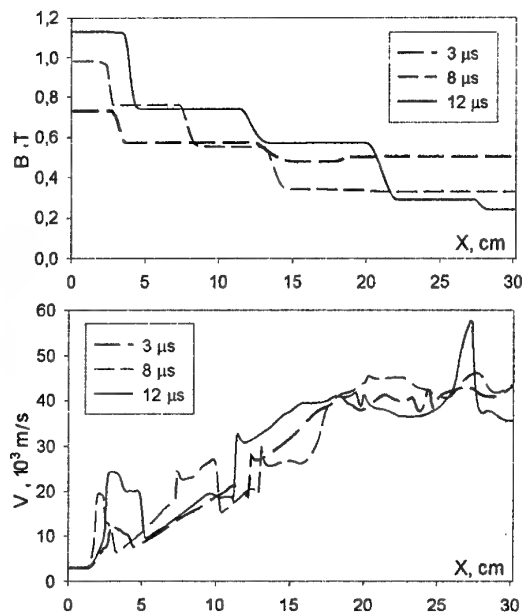
Fig.8. Steady state of induction MHD accelerator with periodic structure of T-layers
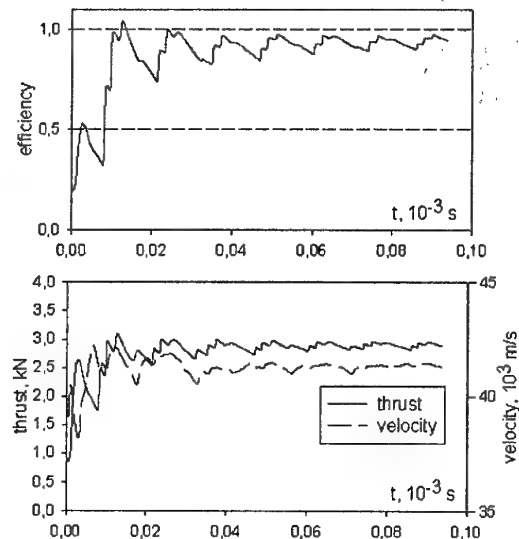
Fig.9. Parameters defining ERE efficiency.

To define parameters determining ERE efficiency, namely, average value of specific impulse, thrust and efficiency numerical integration has been performed, its results being shown in Fig.9. It is seen from Fig.9a that the engine efficiency makes ≈95%. Fig.9b shows that average specific impulse makes 42km/s and the engine thrust 2800N. High efficiency can be explained by the fact that only a part of the gas in ERE with T-

269

layers is being ionized, that one in volume of T-layers. Therefore, unlike SPE with its complete ionization of the flow, consumption of energy not for acceleration will be much less. The process in the engine involved proceeds under high pressure and in small volume, i.e. this device will be much more compact in size and its mass smaller than that of a magnetoplasma engine.

Script of human Mars mission based on a new power and propulsion installation

Consider the opportunities arising in Mars missions project with the solar MHD power plant and ERE with T-layers. Assume that the power plant has a specific power 500W/kg and ERE exerts propulsion of 500N at specific impulse 4000s. Relationships below enabled to calculate the characteristics of the Mars expedition, which will proceed the following script.

1. Spaceship launch from the near-earth orbit.
   Mass parameters at launch:
   - Accommodation unit for 3–4 astronauts with life-support system including stocks of water and oxygen and a closed system with greenhouses for growing vegetative food and air and water regeneration. It will have radiation protection screen with hydrogen tanks as an element of protection. Altogether – 40 tons.
   - Spaceborne research equipment and communication systems – 10 tons.
   - Lowered unmanned non-returned capsule with research robots and laboratory for sample analysis — 10 tons.
   - Power plant together with propulsion system — 20 tons.
   - Stock of propellant – hydrogen — 135 tons.
   - Overall launching mass – 215 tons.
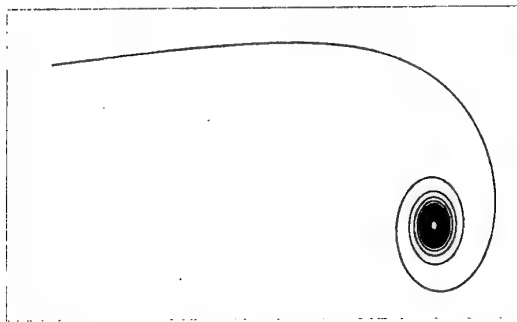
Fig.10. Spiral trajectory of vehicle acceleration from the near-Earth orbit.

2. Untwisting of helical trajectory around the Earth by means of ERE. This stage duration ≈

35 days. Propellant consumption — 40 tons. Fig.10 shows the result of numerical calculation of the trajectory at this stage.

3. Flight to the Mars. At this point, the engine in-service time is determined by requirement to minimize the product of launching mass by flight duration. Calculation showed that the spaceship velocity (relative to the Sun on the Earth orbit radius) would best make ≈35,5km/s. Hence additional velocity make ≈5,5km/s. At this stage, the time in flight, which includes th section of braking prior to passing to the helical trajectory will make 115 days. The calculation result at this stage is shown in Fig.11.
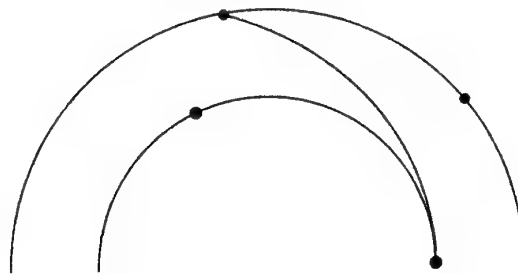
Fig.11. Trajectory of flight from the Earth orbit to the Mars one.

4. Braking at flying up to Mars, motion over a helical trajectory passing to a circular orbit. Stage duration – 15 days. The propellant residual is 51 tons.

5. Mars exploration using robots. Stage duration is about one year. Time of this stage is determined by the orbital periods of Earth and Mars. The remained propellant mass is used for organization of effective radiation defense.

6. Return to Earth. This stage ends with recovery to the circular near–Earth orbit. Stage duration – 105 days. The rest part of propellant ≈7 tons will be used for automatic orbit stabilization till the next expedition to Mars.

7. Crew recovery to the Earth by means of a shuttle Earth–orbit device.

According to the similar script a number of flight modes have been calculated with the preset of engine thrust level and specific pulse. Correspondingly those two parameters determined the propellant consumption per second, power plant capacity and its mass (500W/kg specific power was taken). Resulting from the fact, that the optimal trajectory is diverse for various types of motive systems, fuel supply was taken considering the following: continuous engine operation for low consumption engines and operation time determined by optimization conditions for high consumption engines. Further transportation time

270

for the overall expedition (without the time on Mars orbit) has been found. While determining the optimal mode (or areas of optimal modes) one should result from the requirement of the launching mass on the one hand, and the need of decreasing the exposure time of space radiation on astronauts. As far as these requirements lead to the opposite results, decision was made to search for the optimal value through a minimum value of the product of the launching mass by the expedition time flight.

The relationships used to determine the launching mass and the time in–flight by means of iterating till the complete combustion of propellant are given:

$$\dot{r} = V_r ;$$

$$\dot{\varphi} = \frac{V_\varphi}{r} ;$$

$$\dot{V}_r = r \cdot \varphi^2 - \frac{f \cdot M}{r^2} + V_{noz} \cdot V_r \cdot \frac{\dot{m}}{m \cdot \sqrt{V_r^2 + V_\varphi^2}} ;$$

$$\dot{V}_\varphi = -\dot{r} \cdot \dot{\varphi} + V_{noz} \cdot V_\varphi \cdot \frac{\dot{m}}{m \cdot \sqrt{V_r^2 + V_\varphi^2}} ,$$

where V_{noz} – gas outflow velocity from the nozzle, $\dot{m}$ – propellant consumption, V_r and V_φ radial and angular velocity components, M – mass of planet (either Earth or Mars), m – spaceship mass.

The result of optimization task solution is shown in the diagram thrust–specific impulse (see Fig.12), where the isolines of optimization parameter – product of the launching mass [tons] by the flight time [days] are drawn.
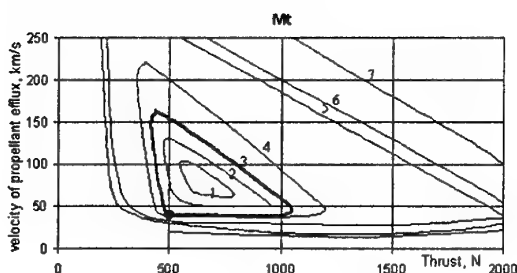
Fig.12. Isolines of the optimised parameter (launching mass multiplied by the transfer time), 10^3 days·tons: $1 - 55, 2 - 58, 3 - 63, 4 - 66, 5 - 80, 6 - 94, 7 - 117$.

As seen from the plot, there is an area of optimal modes limited by isoline 3, inside of which the optimization parameter changes no mor than 10%. Beyond this area the parameter value sharply increases. The chosen mode for a Mars expedition script, based on MHD method of electrical energy generation from the solar radiation and MHD

method of working medium acceleration, is shown in the plot by the point lying within the area of optimal modes.

Conclusion

As a conclusion we refer to the main concept of the paper involved.
1. Feasibility of realizing a multimegawatt space power plant based on a solar radiation concentrator, volume adapter in the form of eddy chamber and closed cycle MHD generator with recombining plasma layers has been demonstrated.
2. Thermodynamic and mass–dimension analysis has shown that the essential index of efficiency for a space power plant, that is, specific power could make 500 W/kg.
3. Numerical simulation of MHD process within the ERE channel with azimuthal current layers receiving energy from a spaceborne source through inductive coupling has revealed that at the channel length ≈30cm a velocity ≈40km/s can be available. ERE of this type can operate at high consumption of working medium (to 50g/s) which allows to attain thrust up to 2000N.
4. Analysis of a possible script of a manned flight to the Mars suggested that a reusable spaceship based on the solar space power plant with MHD generator can be created. It is launched from the near–Earth orbit and its launching mass ≈215 tons. The overall expedition time in–flight for this vehicle will make ≈8–9 months.

References

1. Gatland, K. (consultant and principal author) et al. "Space Technology", London, Salamander Books Ltd., 1982.
2. Feoktistov, K.P. "Space engineering. Prospects of development". Moscow, N.E. Bauman MSTU, 1997 (in Russian)
3. Gitelzon I.I., Bartsev S.I., Mezhevkin V.V., Okhonin V.A. Distant Space: People or Automation? Vestnik RSA, v.70, N. 7, 2000, pp. 611-620 (in Russian).
4. V.N. Akimov, A.A. Gafarov, A.S. Koroteev, A.B. Prishletsov. "Nuclear Power in the XXI Century Astronautics", Flight Journal, 2000, No.10, pp.3-11.
5. V.S. Slavin, V.V. Danilov, M.V. Kraev, A.V. Romashko, K.A. Finnikov, U.M. Ermoshkin, "T-layer MHD in Aerospace Applications", Proc. of Workshop "Perspectives of MHD and Plasma Technologies in Aerospace Applications", Moscow, March 1999, pp. 31-43.

271

6. Kudrin, O.I. "Solar high temperature space power and propulsion installations". Moscow, Mashinostroenie, 1987 (in Russian).

7. "Industrial heat and mass exchange processes and installations"/edited by Baklastov A.M./ Moscow, Energoatomizdat, 1986 (in Russian).

8. V.S. Slavin, K.A. Finnikov, "Nonequilibrium Plasma Layer Evolution in a Pure Noble Gas Flow in the MHD Generator Channel", Proc. "The 2nd Workshop on Magneto-Plasma-Aerodynamics in Aerospace Applications", Moscow, April, 2000, pp. 246-250.

9. Reference book."Engines 1944–2000, aircraft, rocket, naval, industrial". Moscow, "AKS-Conversal", 2000 (in Russian)

10. W.D. Jackson, et al., "Non-equilibrium MHD Disk Generator Using Cesium-Seeded Hydrogen", Proc. of 11-th Intern. Conf. on MHD Electrical Power Generation, Beijing, October, 1992, Vol. 4, pp. 1224-1231.

11. O.A. Gorshkov, A.S. Koroteev. "Electrical plasma rocket engines: today and tomorrow", Flight Journal, 2000, No.1, pp.14-23.

12. F.R.C. Diaz, "Research Status of the Variable Specific Impulse Magnetoplasma Rocket", Proc. of Intern. Conf. on Open Systems, Novosibirsk, July, 1998, pp. 87-93.

13. Slavin V.S., Danilov V.V., Kraev M.V., "Space Transport System on the Basis of MHD Generator and Electric Rocket Engine", Proc. of Intern. Conf., "MHD Power Generation and High Temperature Technologies", Beijing, October, 1999, Vol. 2, pp. 694-708.

14. Tikhonov A.N., Samarsky A.A., et al., "A Non-Linear Effect of Formation of the Self-Maintained High Temperature Electrically Conducting Gas Layer in Unsteady Process of Magnetohydrodynamics", DAN USSR Journal, Vol. 173, No. 4, 1967, pp.808-811.

51. FEASIBILITY STUDY OF APPLICATION OF PULSED MHD GENERATORS FOR POWER SUPPLY OF NASA MAGLEV LAUNCH-ASSIST ELECTROMAGNETIC TRACKS

V.A.Novikov, V.I.Okunev, V.Yu.Rickman
Institute for High Energy Densities of IVTAN-Association
Russian Academy of Sciences

Abstract. A power supply system is considered for the NASA full-scale experimental electromagnetic track designed for acceleration of aerospace plane of mass of 54-68 ton and dimensions closed to airplane SR-71 up to velocity of 179 – 268 m/s). It is shown that the power supply may be developed on a basis of two power units of pulsed MHD facility "Sakhalin".

Introduction

An anticipated growth of amount of the space launches needed to maintain a serviceability of the orbital stations and the space power systems requires reducing the cost of the orbital injection of a payload.

One of directions of solving the problem is an increase of the flight weight and reducing the fuel mass by rejection of on-board oxidant. The supersonic and hypersonic ramjets developed using an ambient air as the oxidant allow increasing the payload mass by several times.

However, an operation of such ramjets requires an acceleration of the launcher up to velocity of sound to provide the air flow rate needed in the intake.

It is proposed to apply a supersonic inductive storage for the power supply of the electromagnetic accelerator (linear electric motor) that will allow using the cheap industrial electric power. It is noted [1], that the cost of electricity consumed for acceleration of the aircraft similar to SR-71 will be 75$ only. Nevertheless, this superconductive inductive storage should provide large amount of the energy accumulated. For example, to accelerate the carrier with the spacecraft of total mass of 2000ton with acceleration of 30m/c^2 up to velocity of 300m/s the total accumulated energy of the storage should be $1.2 \cdot 10^{11} \text{J}$ [2]. It is clearly evident that such inductive storage will be very complicated electric device requiring high investments and large self-repayment period. In this connection for the power supply of experimental electromagnetic launch systems closed to the full-scale accelerators it is expedient to apply the less expensive and simple high-power source of electric energy like pulsed MHD generator proposed in this feasibility study. Due to the total self-sufficiency of this power source it may be used as a standby power supply for the electromagnetic launch system.

1. NASA full-scale 1.5 mile experimental electromagnetic track

NASA plans to build in 2004-2005 the full-scale 1.5 mil (2413m) in the Kennedy Space Center[1]. It is supposed that it will accelerate within 9.5s the reusable launch vehicle (RLV) with the spacecraft of total mass of 120,000–150,000 lb (54–68ton) and dimensions closed to SR-71 aircraft up to velocity of 400–600mph (179–268m/s) along 1/2 length of the experimental track. In this case the carriage mass will be 60,000 lb (27 ton) [1,5].

The electrical power of the power source for the track may be estimated by the following formula:

$$N = (ma + c_\chi \rho a S x) v / \eta$$

where m is the total mass of RLV and the carriage, a - acceleration, c_χ – aerodynamic drag coefficient, ρ – air density, S – total maximum cross-section of RLV and carriage, x – traveled distance, v - velocity, η – total efficiency of linear electric motor and conversion system.
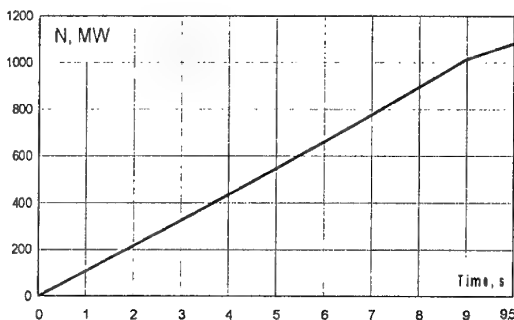
Fig.1. Power consumed by the track versus time.

The experimental track under study has he following parameters: accelerated mass of 95ton, acceleration duration of 9.5s, and final velocity of 268m/s. The consumed electrical power calculated by formula above versus acceleration time is shown in Fig.1. In this case the total maximum cross-section of the carriage and RLV was taken at a first approximation as proportional to mass ratio in the power of 2/3 maximal cross-section of moving part of the electromagnet launch system[4]. The total efficiency was taken as 0.7.

2. Power supply system for NASA experimental tracks

The operation duration of the linear electric motor and the power consumed are typical for performances of the pulsed MHD generators that allows considering these devices for the power supply system.

All variety of MHD power systems developed in Russia is based on five types of power units. The power unit consists of electrical magnet, MHD channels, plasma generators, and switching and control equipment). The power unit

performances are shown in Table 1. As the table indicates the highest power in the load (400MW) is generated by "Sakhalin" power unit, which was tested in a composition of the pulsed power system of the same name supplying the inductive storage of capacity of 600MJ. Therefore, according to the power generated this power unit is the most suitable as a basis for development of the power supply system of the linear electric motor. Basic parameters of the power unit are given in Table 2 [4].

Design of the power unit is given in Fig.2.

According to the consumed power dependence given in Fig.1 it is clear that this performance may be provided by MHD power system based on two modified power units "Sakhalin". The modification will consist of development of plasma generators fueled by advanced plasma-generating propellant providing increase of the power generated by 60% [6] with operation duration required. Considering the gradual increase of the power consumed these plasma generators for the propellant saving may have the similar increased pressure dependence in the combustor.

Table 1. General performances of the power units of pulsed MHD facilities

Power unit	Pamir	Pamir 3U	Soyuz	Ural	Sakhalin
Number of MHD channels	2	3	1	1	1
Working fluid of mass flow rate, kg/s	24-27	~24	~40	70-100	720-1000
Maximal power generated, MW	20	30	32	40	500
Maximal power in the matched load, MW	10	15	16	30	400
Operation duration in the load, s	2.5-10	2.5-10	up to 10	~6	5-6
Mass of the power unit, ton	14	18	25	16	50

Table 2. General parameters of "Sakhalin" power unit

Parameters	Value
Mass flow rate	720-1000 kg/s
Duration of power generation	5-6 s
Electric power of MHD channel	510 MW
Rated current of MHD channel	200 kA
Rated voltage	2.5 kV
Maximal induction of magnetic field	up to 2.5 T
Power consumed by magnet system	25 %
Power unit mass	50 ton
Power unit dimensions (L × W × H)	13.5m×3.8m×2.8m
Efficiency of energy conversion	12 %
Power density in the MHD channel volume	90 MW/m^3
Specific power per the propellant mass unit	0.65 MJ/kg
Specific mass of the power unit	0.1 ton/MW
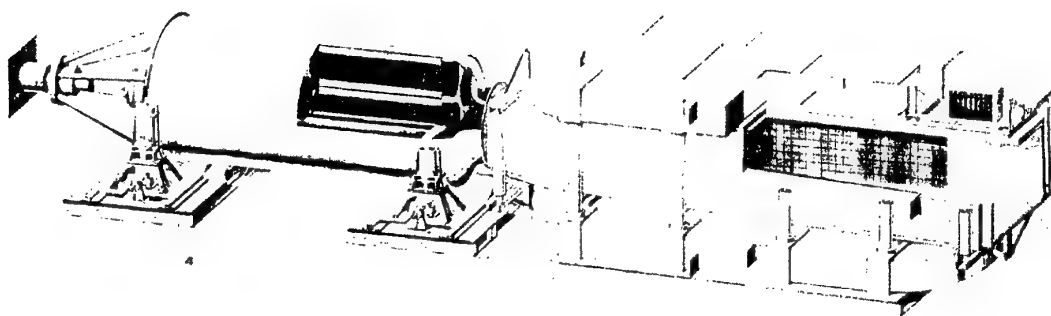
Fig.2. Design of the power unit "Sakhalin": 1- plasma generator (combustor); 2 – MHD channel; 3 - magnet; 4 – supports.

An electrical circuit diagram of the MHD facility is given in Fig.3.
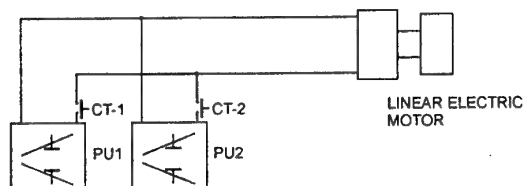
Fig.3. Electric circuit diagram of MHD facility PU1, PU2 – power units, CT-1, CT2 – contactors

Table 3 shows the time of connection of each power unit, duration of generation of pulses in the load, and corresponding operation duration of plasma generators considering the periods of heat loss stabilization and achievement of the self-excitation mode.

Table 3. Time parameters of the power unit operation

Power unit No.	Time of the power unit connection, c	Duration of pulse generation in the load, s	Operation duration of plasma generator, s
1	0	9.5	14.0
2	6.5	3.0	7.5

Conclusion

As a result of the analysis performed it is concluded that the power supply system for the NASA full-scale track may be developed on a basis of existing and experimentally proved MHD equipment.

References

1. MagLev Tested as Launch Aid//Aviation Week & Space Technology, V. 13, 1999, p.78.
2. A.M.Rubinraut, N.V.Burbaeva, A.S. Veselovskiy, V.B.Zenkevich, I.A.Kir'enin. Operation of Linear Synchronous Electric Motor Powered by Superconductive Inductive Energy Storage // Electricity, No.2, 1998, P.28-37 (in Russian).
3. D.W.Swallom, V.M.Goldfarb, V.A. Zeigarnik et al. Pulsed Portable Magnetohydrodynamic Power System Program. J. Propulsion and Power, 1998, v.14, N6, pp1049-1058
4. V. M. Batenin, V. A. Bityurin, G. S. Ivanov, P.A.Gorozhankin, V.A.Novikov, V.Yu. Rickman, Yu.V.Andreev, A. M. Paradovskiy. Advanced reusable space transportation system with horizontal launch of air-space plane. 51st Int. Astrounautical Congress, Rio de Janeiro, Brazil,October2-6,2000 IAF-00-V.3.09
5. Advanced Space Transportation Technology Summary. Magnetic Levitation. (from Internet site of Marshall Space Flight Center: http://www.msfc.nasa.gov/)
6. Yu.P.Babakov, V.A.Polyakov V.A.Novikov, V.I.Okunev, V.Yu.Rickman Experimental Study of Energetic Performances of Advanced Solid Plasma-Generating Propellants for Pulsed MHD Generators, The 3nd Workshop on Magneto-Plasma-Aerodynamics in Aerospace Applications, 24-26 April 2001, Moscow

275

52. PRELIMINARY ANALYSIS OF LARGE PULSED MHD GENERATOR

Motoo Ishikawa and *Yuki Koshiba*

Institute of Engineering Mechanics and Systems,
University of Tsukuba
Tsukuba 305-8573, Japan
(e-mail: misikawa@kz.tsukuba.ac.jp)

Abstract. The present report intends to study preliminarily the performance of "SAKHALIN", a large pulsed MHD generator constructed in Russia, operated with solid fuel with the electric power output of 510 MWe, by time-dependent quasi-one-dimensional anal- yses in order to obtain data needed for multi-dimensional analyses. A preliminary analysis has indicated that the magnetic Reynolds number is about 0.58 for run No.1, which is much different from many other MHD generators. The induced magnetic flux density is about 20% at the entrance and the exit of MHD channel. The flow field experiences the shock wave when the operation voltage becomes low, while the shock wave becomes stronger when the induced magnetic field is taken into account. The electric power output results in 511 MW when the induced magnetic field is not included, while it becomes 509 MW when the induced magnetic field is taken into account. The effects of the induced magnetic field are cancelled out with each other between the first and the second half part of MHD channel.

1. Introduction

Large pulsed MHD generators can be used as an adequate energy source of assistance of the rocket propulsion, because the large DC current can be produced and then a large electro-magnetic force can be induced. Many pulsed MHD generators operated with solid fuel were constructed in Russia [1]. The largest pulsed MHD generator was called "SAKHALIN" with the channel length of 4.5m. The MHD generator could demonstrate the electric power output of 510 MWe [2]. There was no report that analyzed the large MHD generator "SAKHALIN". On the other hand, the authors have carried out time-dependent one- and two-dimensional analyses with the assumption of mono phase flow and two phase flow, and time-dependent three-dimensional analyses with the assumption of mono phase flow [3-8]. The present study intends to study preliminarily the performance of "SAKHALIN" by time-dependent quasi-one-dimen -sional analyses in order to obtain data needed for planned multi-dimensional analyses.

2. Numerical Scheme

2.1 Gasdynamics

The basic equations used for the gasdynamics are time-dependent one-dimensional compressible conservation equations along the x direction, the main flow direction. The working fluid is weakly ionized plasma which contains about 40 wt% of Al_2O_3, because the fuel consists of the metal Al. In the present study, however, the assumption of mono phase flow is used, while two phase flow analyses will be carried out as a near future work. The gasdynamic equations are solved with the 1969 MacCormack method [9]. Even meshes are used along the x direction with 711 mesh points of 1 cm mesh.

2.2 Electrodynamics

The basic equations used for the electrodynamics are the steady Maxwell equations and the generalized Ohm's law with quasi-one-dimensional approximation [9].

2.3 Thermodynamical Properties

Thermodaynamical properties of the working gas of "SAKHALIN" was not reported and therefore the values used for analyses of Pamir-3U are used as:

Gas constant [J/kgK]

$$R(T) = 359.9 + 0.3459 \times 10^{-2} T^2 \qquad (1)$$

Enthalpy [J/kg]

$$h(T) = -733600 + 649.9T + 0.3105T^2 \qquad (2)$$

Electrical conductivity [S/m]

$$\sigma(p,T) = \exp\{(-0.1569 + 0.3194 \times 10^{-4} T)\, p + (-2.020 + 0.2122 \times 10^{-2} T) + (-3.297 + 0.1408 \times 10^{-2} T)/p\}/G_F \qquad (3)$$

Hall parameter

$$\beta(p,T,B) = (0.3937 + 0.3025 \times 10^{-2} T^{1/2}) B/p/G_F \qquad (4)$$

where p and T stand for the static pressure and the static temperature of the working gas, and G_F the G-factor indicating the nonuniformity effect of

plasma, being assumed to be 1.1 in the present study.

3. Performance of "SKHALIN"

3.1. Brief Summary of Large Pulsed MHD Generator "SKHALIN"

The channel length of the large pulsed MHD generator is 4.5m, the cross section of entrance is 0.9m×1.0m and 1.6m×1.0m at the entrance and the exit, respectively, where the height along the magnetic field is kept constant with 1.0m. The nominal mass flow rate is 1000 kg/s. The combustor temperature is 3800 to 3900K, while the combustor pressure is 4.0 to 5.6Mpa. The generator was quite powerful, light (only 50tons), and compact, which could demonstrate the electric power output of 510MWe, the specific mass of 0.1 ton/MWe, and the specific volume of $0.3m^3$/MWe. The air-core magnet was activated to more than 2 T by the MHD generator itself, which is the Faraday type with continuous electrodes made from glass-reinforced plastic plates with graphite [2].

3.2 Design of Air-Core Magnet

The report [2] informs that the design value of magnetic flux density is 2.5 T and the ampere-turn of the magnet is $8.4×10^3$kA. The number of turn results in 56, because the excitation current of design is 150kA. Our three-dimensional code of magnetic field analysis has, however, shown that the number of turn of 56 is too large, resulting in much higher value of magnetic flux density. Our analyses have indicated that the number of turn must be 33, which can give 2.5T. The number of turn is, therefore, assumed to be 33 in our analyses.

The experimental results indicated that the constructed magnet could not produce the designed value and we have introduced a modification coefficient which can produce the value of magnetic flux density obtained at the experiment. The modification coefficient used in the present study is shown below:

Run No.	Coefficient	Maximum B
1	0.590	2.09 T
2	0.622	2.20 T
3	0.424	1.50 T
4	0.435	1.54 T
5	0.435	1.54 T
	0.438	1.55 T

This table shows that the electric circuit may have changed between Runs 1 & 2 and Runs 3 through 6.

3.3 Induced Magnetic Field

A preliminary analysis has indicated the magnetic Reynolds number is about 0.58 for Run No.1, which is much different from many MHD generators. The induced magnetic field, therefore, cannot be neglected. Then the one-dimensional approximation has been applied to Ampere's law.
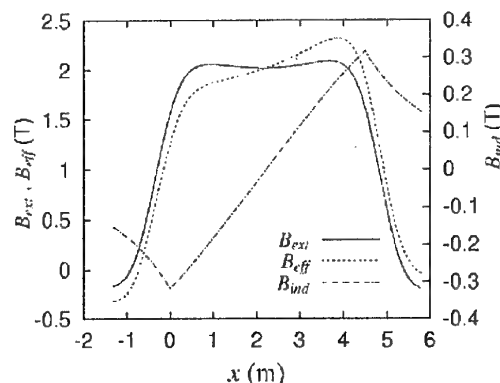
Fig.1. Distributions of magnetic flux density (Run No.1, solid line: external field, dashed line with dots: induced field, dotted line: effective field).

Figure 1 depicts distributions of the magnetic flux density for Run No.1, where the solid line shows the externally applied field, the dashed line with dots does the induced field, and the dotted line does the effective field. It is revealed that the induced magnetic flux density is about 20% at the entrance of MHD channel, while it becomes about 19% at the exit for Run No.1, being rather large.

3.4 Estimation of Electrode Voltage Drop

The value of electrode voltage drop can be automatically calculated in the case of multi-dimensional analyses, but the present one-dimensional analysis requires estimation of the electrode voltage drop. It has been well known that the electrode voltage drop is nonlinear and shows a complicated behavior [10]. The present work, however, assumes rather a simple relation. At first the electrode voltage drop is assumed to be constant without the induced magnetic field. It has been shown that the estimated constant electrode voltage drop ranges from 700 to 1200 volts (except for run No.5), which is much larger than the originally estimated value of 200 volts [2], as listed below.

277

Run No.	Average Current $(J_y, kA/m^2)$	Electrode Voltage Density Drop (V)
1	44.45	1035
2	42.89	1199
3	43.33	1165
4	46.44	790
5	40.00	487
6	44.44	732

where J_y is the y-component of the electric current density.

Then a simple linear relation to the local electric current density J_y is assumed as:

$$\Delta V = - r_{drp} J_y + \Delta V_0 \qquad (5)$$

where ΔV is the electrode voltage drop and ΔV_0 is the constant, and the value of constant of the linear relation r_{drp} is estimated so as to agree with the electric output power as shown below:

Run No.	r_{drp}	Run No.	r_{drp}
1	0.0143	2	0.019
3	0.0175	4	0.00836
5	0.0022	6	0.0074

The value of ΔV_0 is assumed to be 400 volts, which must be estimated with experimental data and/or multi-dimensional analyses. The rather large electrode voltage drop indicates that there were thick boundary layers. This relation is used for all further calculations with or without induced magnetic field.

3.5 Effects of Induced Magnetic Field

The operation voltage of experiment of run No.1 is 2550 volts and our calculation has shown that the electrical conductivity has a peak of about 120S/m at the first half part of the MHD channel, while the Hall parameter experiences a
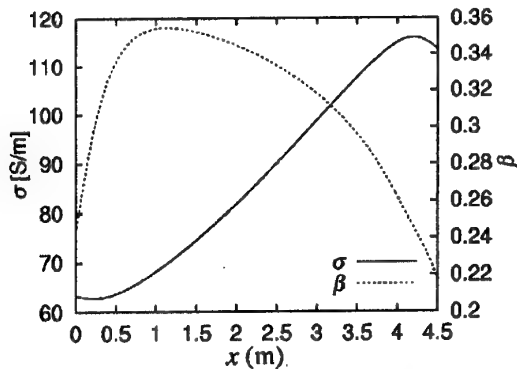
Fig.2. Distributions of electrical conductivity and Hall parameter (Run No.1, 2550 [V]; solid line: conductivity, dotted line: Hall parameter).

peak of 0.35 at the second half part, as shown in Fig.2, where the operating condition is for Run No. 1 and the load voltage is 2550 volts.
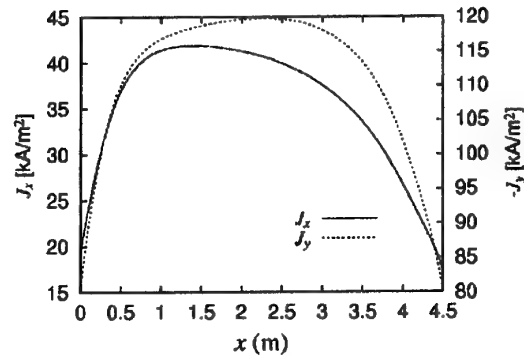
Fig.3. Distributions of electrical current density (Run No.1, 2550 [V]; solid line: J_x, dotted line: J_y).

Figure 3 depicts distributions of electric current density (J_x and J_y), showing that the peak value of J_y is about 120 kA/m^2, while the maximum value of J_x is about 40 kA/m^2 for Run. No.1. The existence of large J_x suggests that the strong three-dimensional phenomena may be induced on the y-z plane, indicating that three-dimensional analyses are required to understand phenomena in detail.

Figures 4 and 5 indicate distributions of the flow velocity and the Mach number when the induced magnetic field is not taken in account and taken into account, respectively. It is shown that a smooth acceleration to Mach number of 2.35 along the nozzle, a strong deceleration to Mach number of 1.7 at the end of MHD channel, and a slight acceleration to Mach number of 1.75 along the diffuser, showing the supersonic flow along the whole channel after the nozzle when the induced magnetic field is neglected. When the induced
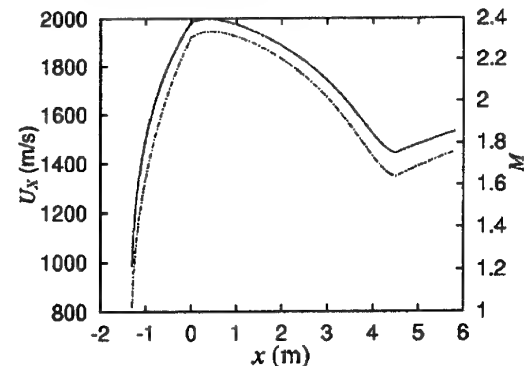
Fig.4. Distributions of velocity and Mach number without induced magnetic field (Run No.1, 2550 [V]; solid line: velocity, dotted line: Mach number).
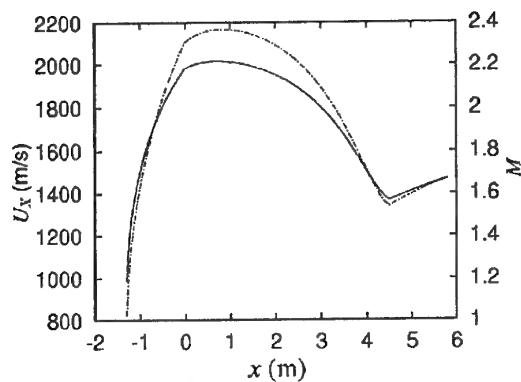
Fig.5. Distributions of velocity and Mach number with induced magnetic field (Run No.1, 2550 [V]; solid line: velocity, dotted line: Mach number).

magnetic field is taken into account, these values of Mach number become about 2.38, 1.55, and 1.65, showing that a slight acceleration along the first half part of MHD channel because of reduced magnetic field and a slightly stronger deceleration along the second half part due to the enhanced magnetic field.

Figure 6 depicts distributions of the static pressure and the static temperature of the working gas for Run No.1, operated with the load voltage of 2550 volts, showing that the pressure and the temperature decrease rapidly along the nozzle because of the strong acceleration, then almost constant pressure and temperature is maintained along the MHD channel, and finally the flow is slightly accelerated again along the diffuser.
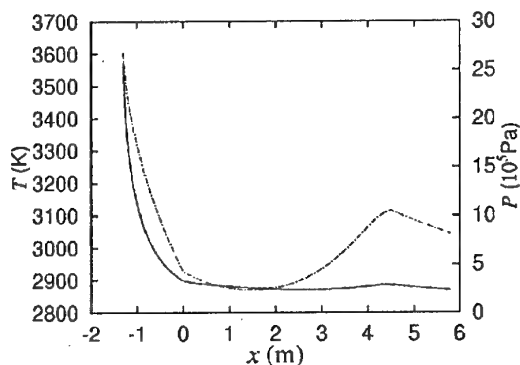
Fig.6. Distributions of pressure and temperature with induced magnetic field (Run No.1, 2550 [V]; solid line: pressure, dotted line: temperature).

Figure 7 shows distributions of Mach number, indicating effects of the induced magnetic field, where the load voltage is decreased to be 1900 volts and the larger current density and stronger deceleration result. Even when the supersonic flow

can be maintained along the whole channel without the induced magnetic field, a shock wave is induced at the end region of MHD channel when the induced magnetic field is considered. This is because the flow is less decelerated along the first half of MHD channel since the induced magnetic field reduces the effective magnetic field there, whereas the flow experiences stronger deceleration along the second half of MHD channel due to the enhanced magnetic field when the induced magnetic field is taken into account.
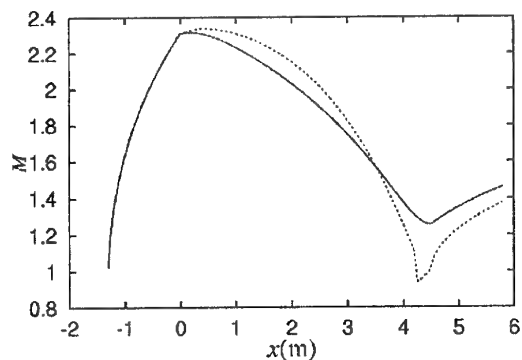
Fig.7. Distributions of Mach number (1900 [V]; solid line: without induced magnetic field, dotted line: with induced magnetic field).

Figure 8 depicts distributions of Mach number, where the MHD generator is operated with a lower load voltage of 1600 volts, showing that a slight shock wave is induced at the end region of MHD channel, even when the induced magnetic field is not taken into account, whereas a stronger shock wave is produced and the position of shock wave moves upwards when the induced magnetic field is taken into account.
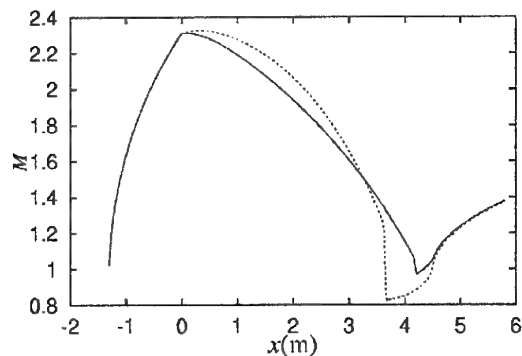
Fig.8. Distributions of Mach number (1600 [V]; solid line: without induced magnetic field, dotted line: with induced magnetic field).

279
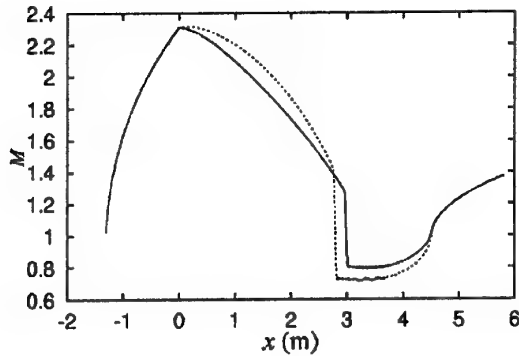
Fig.9. Distributions of Mach number (1000 [V]; solid line: without induced magnetic field, dotted line: with induced magnetic field).

Figure 9 shows distributions of Mach number, when the MHD generator is operated with a load voltage of 1000 volts, telling that a strong shock wave is induced, a subsonic region is produced at the second half region of MHD channel, and the flow is again accelerated into the supersonic flow along the diffuser even when the induced magnetic field is not taken into account.

In summary, the flow field experiences the shock wave when the operation voltage becomes low in both cases, while the shock wave becomes stronger when the induced magnetic field is included. The flow is less decelerated along the first half channel and the stronger shock wave is induced at the second half part of channel, when the operation voltage becomes lower such as 1000 volts. Our experiences [5,7] tell that the strong shock wave always occurs together with the boundary layer separation, indicating that two- and tree-dimensional analyses are required to understand the MHD interaction in detail.
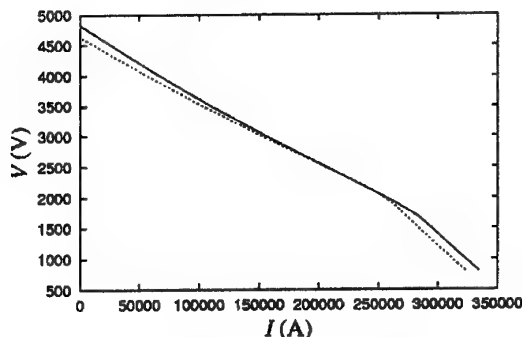
Fig.10. Voltage-current characteristics (conditions of Run No.1; solid line: without induced magnetic field, dotted line: with induced magnetic field).

Figure 10 depicts the voltage-current characteristics of the large MHD generator under the operation conditions of Run No. 1. The electric power output results in 511 MW when the induced magnetic field is not included, while it becomes 509 MW when the induced magnetic field is taken into account. The effects of the induced magnetic field are cancelled out with each other between the first and the second half part of MHD channel.

4. Concluding Remarks

The large pulsed MHD generator "SAKHALIN" was studied preliminarily by time-dependent quasi-one-dimensional analyses in order to obtain data needed for planned multi-dimensional analyses. The following results were obtained.

(1). The magnetic Reynolds number is about 0.58 for run No.1, which is much different from many other MHD generators. The induced magnetic flux density is about 20% at the entrance of MHD channel, while it becomes about 19% at the exit.

(2). The estimated value of electrode voltage drop becomes 700 volts to 1200 volts, which is much higher than the originally estimated value of 200 volts.

(3). The flow field experiences the shock wave when the operation voltage becomes low, while the shock wave becomes stronger when the induced magnetic field is taken into account.

(4). The electric power output results in 511 MW when the induced magnetic field is not included, while it becomes 509 MW when the induced magnetic field is taken into account. The effects of the induced magnetic field are cancelled out with each other between the first and the second half part of MHD channel.

Acknowledgements

References

1. V.A.Zeigarnik and M. Ishikawa, "Key- note Presentations K-04: Pulsed MHD Power Systems", Proc. of Int. Conf. on MHD Power Generation and High Tem- perature Technologies, Vol. III, pp. 775- 792, 1999.
2. E.P.Velikhov et al., "Pulsed MHD Power System "SAKHALIN": The World Largest

Solid Propellant Fueled MHD Generator of 500 MWe Electric Power Output", Proc. of Int. Conf. on MHD Power Generation and High Temperature Technologies, Vol. II, pp. 387-398, Beijing, 1999.

3. T. Matsuo, H. Sugita, M. Ishikawa and V. A. Zeigarnik, "Preliminary Analysis of Gas-Liquid Two-Phase Flow in Pulsed MHD Generator", 28th AIAA Plasmadynamics and Lasers Conference☐AIAA 97-2374,1997.

4. H.Sugita, T. Matsuo, Y. Inui and M. Ishikawa, "Two-Dimensional Analysis of Gas-Particle Two-Phase Flow in Pulsed MHD Channel", 30th AIAA Plasmadynamics and Lasers Conference, AIAA 99-3483, 1999.

5. H.Sugita, T. Matsuo, Y. Inui and M. Ishikawa, "Two-Dimensional Analysis of Gas-Particle Two-Phase Flow in Pulsed MHD Channel", 30th AIAA Plasmadynamics and Lasers Conference, AIAA 99-3483, 1999.

6. H.Sugita, T. Matsuo, Y. Inui and M. Ishikawa, "Analysis of Pulsed MHD Generator Considering Collision-Coalescence and Fragmentation of Liquid Particles", 30th AIAA Plasmadynamics and Lasers Conference, AIAA 99-3661, 1999.

7. T. Matsuo, H. Sugita, M. Ishikawa and V. A. Zeigarnik, "Boundary-Layer Separation and Generator Performance of Self-Excited Pulsed MHD Channel with Strong MHD Interaction", Int. Conf. on MHD Power Generation and High Temperature Technologies, Vol.2, III-2, pp.399-408, 1999.

8. H.Sugita, T. Matsuo, Y. Inui and M. Ishikawa, "Analytical-Study of Self -Excited, Pulsed MHD Power System Using Two-Fluid Model", Int. Conf. on MHD Power Generation and High Temperature Technologies, Vol.2, III-11, pp.463-474, 1999.

9. M. Ishikawa, "Unsteady Phenomena in High-Interaction MHD Generators", Technical Report of Institute of Atomic Energy, Kyoto University, No.192, 1982.

10. A.A.Yakusheev, V.P.Panchenko et al., "Recent Experimental Researches of Combustion Products Plasma of Com- bined (Protechnic) Propellant for Pulsed MHD Generators", Proc. of Int. Conf. on MHD Power Generation and High Temperature Technologies, Vol. II, pp. 423-434, 1999.

53. ON MODERN PROGRESS IN DESIGN OF FUSION POWERED FLYING MACHINES

Dr. Valentine A. Belokogne
Institute of Mechanics of Moskow State University
Russian Academia Cosmonautica
valentine-belokogne@mtu-net.ru
tel / fax (Russia, Moscow) 445 38 81

Abstract. Inertial confinement fusion (ICF) can, in principle, be gained in the form of technologically effective microexplosion of plasma with peak density $\rho(D+^3He) > 1000$ g/cm^3 necessary for limitation the explosive yield of tiny capsules to $Y < 10^9$ joules applicable in spacecraft, aero- and ecrano-planes propulsion, and the pumping superlasers. The key problems of lowentropy implosional supercompression remains partly unresolved. The scarceness of helium-3 may be overcome by the proper conversion of warheads test. ICF-planes and alike machines (including ones of our own layout) are feasible by years 2020-2030, and will be certainly more ecologically safe than the atomic U-boats, atomic power facilities and even the beautiful excellent Concorde, Airbus 3XX, American superjumbo and like fueled vehicles – especially against terrorism and the stupid incompetence.

Introduction

The august 2000 catastrophic failure of the first SST "Concorde" crashed near Paris is important and for stimulation new wave of reflections on the future world transport in general, and aviation progress especially. Consequently, the more attention draws to the future air- and spaceborne energetics, to global energetics. Here is the clear imperative: we need the radical decision on the perspective fuel. Then, what is the inexorable arguments against the use of fuels based on oil processing, especially for rocket and jet engines in big flying machines? Consider some well-known arguments:

- oil prices increasing, especially in ten-twenty forthcoming years
- imminent progress in processing of oil and gas for the sake of nonfuel needs as synthetic materials (not only for dress-making, for aerospace technology also; pharmaceutics; why not the artificial food also?)

What is the typical element in such argumentation?

Please, it is the market-style approach and therefore is neither decisive nor imperative enough. Let me reply firstly by the weak argument – historical: natural oil shortage is not imperative factor, since during the 2-nd World War German engineers was able to fabricate lots of "artificial" fuel from oil shales, possibly even from coals. The German fuel then was more expensive than "natural" benzene or kerosene only *twice...* Moreover, there is more vital and global argumentation applicable both to products of oil proceedings and to hydrocarbons in general, hydrogen, and also to on-board oxidizers, up to oxygen and fluorine. The crux of matter consists in the vulnerable nature of modern vehicles based on the internal combustion engines or turbojets: aeroplanes are "simply" flying cisterns – now, and tomorrow. Its much more great dimensions will be market with hydrogen fuel which is assessed by noisy prophets. Concretely: the famous "Concorde" flying in the sky and rolling along aerodromes with 117 000 litres of kerosene viz. 92 tonnes of substance capable on 4.4×10^{10} joules per tonn i.e. 4×10^{12} joules per one "Concorde" or (equvalently) thousand tonnes of TNT! Attention: the next generation "Superconcorde" (feasible literally today) will be flying and rolling with twice more load of fuel, i.e. future SST(mass production assessed on 2020-2025 years) will be equvalents to 2 kilotonnes each in the kerosene case and around 5kt in hydrogen fuel case. Moreover, newest Airbus 380, and his counterpart in US are more dangerous "flying and rolling bombs" – at least from the point of the terror risk rising implacably. The next generation subsonic Jumbo promised with start mass up to 2000 t around year 2025, if not even more tonnes. To the point, Ukrainian special Jumbo "Mriya" (with composite materials for wing structure) reached take-off mass of 600 tonnes at winter 1988/89, and there was no serious obstacles to design and built "Twin-Mriya" with mass of 1200-1400 tonnes ten years ago, also. Otherwise, the our common future promises the "Flying Hirosimas" almost certainly. Even worse, let read "Daily Telegraph", page 21, february 2, 2000: "... fatal airliner crashes will double to an average of one a week by 2007 as air travel grows rapidly...". This conclusion, almost the plan, by competent experts was given without pessimistic-realistic correctives by terror factor, of course.

Now, WHAT CAN WE DO? I think so: let start design of ICF-planes *immediately*!

For the beginning it is useful to study the symptomatic results of engineering in XX Century:

The ultimate idea is even more radical: to arrange coherent **gravitons** beam generator – **Laser analogue for gravitons** (mentioned in our publication in 1989,MGU). With the scenario to assist space travel by the coherent beam of gravitons capable to change Local area of space-time, of course in the controllable mode of action.

Simple classification for schemes of supercompression potentially interesting for iCF mobile system
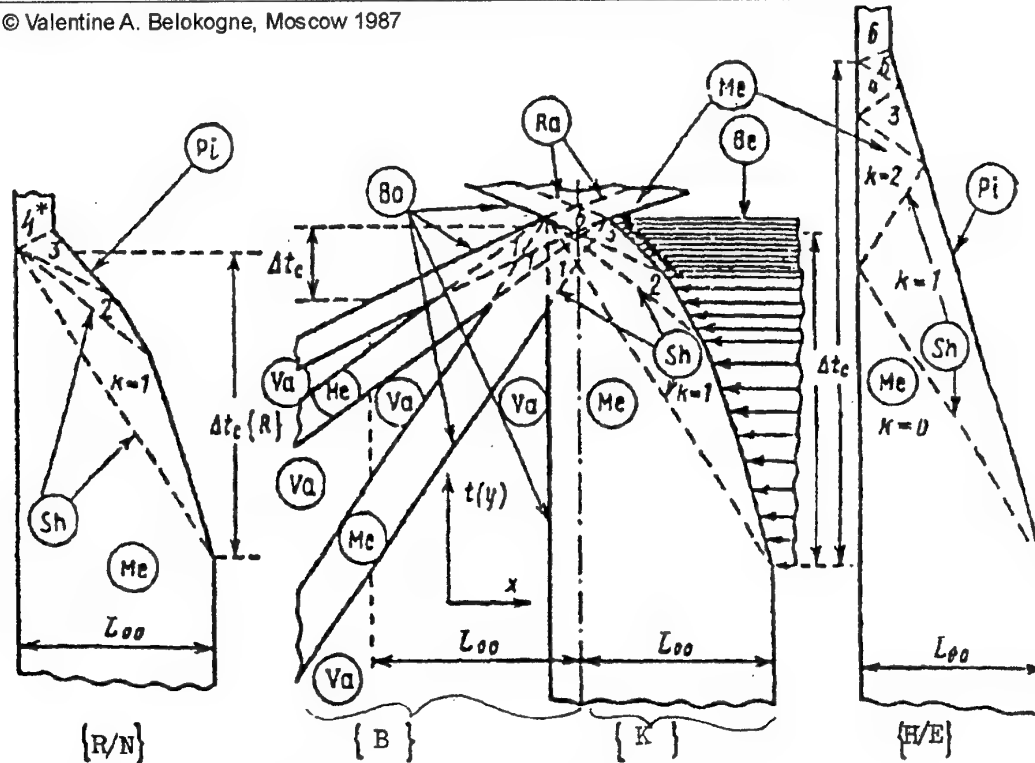
SYMBOLICS: /Me/ - medium, fluid (perfect gas) undergoing compression;
/Sh/ shock fronts, shock and sound waves of compression;
/Ra/ rarefaction waves;/Bo/ boundary between medium (matter) and vacuum;
/Va/ vacuum,especially for scheme {B};
/Pi/ boundary, face of real, ideal or imaginable piston;
/Be/ beam or similar pushing interaction (piston-like, ablation etc) driving compression for cases {R/N}, {K}, {H/E} and indicated only for case {K} here;
L_{oo} thickness of uncompressed medium layer;
$k = 1,2, \ldots$ number, index of medium state behind the preceding shock front. Here $k_{max}=6$ for the visuality, so total number of medium layers in the case {B} amounts to $N=k_{max} +1 = 7$
D velocity of shock front the relative the medium ahead the front; e a c h shock gives the same jump of medium velocity $= \Delta u$ here for cases {B}, {K}, {H/E};
$D/a = M$ Mach number of the shock front: here in perfect gas with sound velocity a ahead the front at the permanent Poisson exponent $\gamma = 1+2/f$ where f=number of freedom degree in the equipartition approximation . Here is Moo ($\gamma=3$) >> 1 or Moo($\gamma =2$) ≈ 2.

As soon as the specific internal energy of medium (matter, perfect gas, fluid) has a form $E= (f/2)(p/\rho) = a^2/\gamma (\gamma -1)$, the multilayerness secure very high compression: at N=kmax+1 >> 1
Assessed compression is $\rho_{max}/\rho_{oo} \approx (N/f)^f$ in time span $= \Delta t_c$ minimal for our case **{B}:**
$\Delta t_c\{H/E\} \approx (Loo/ \Delta u) > \Delta t_c\{K\} > \Delta t_c\{R/N\} \approx (Loo/Doo) >> (Loo/N \Delta u\} \approx \Delta t_c\{B\}$.
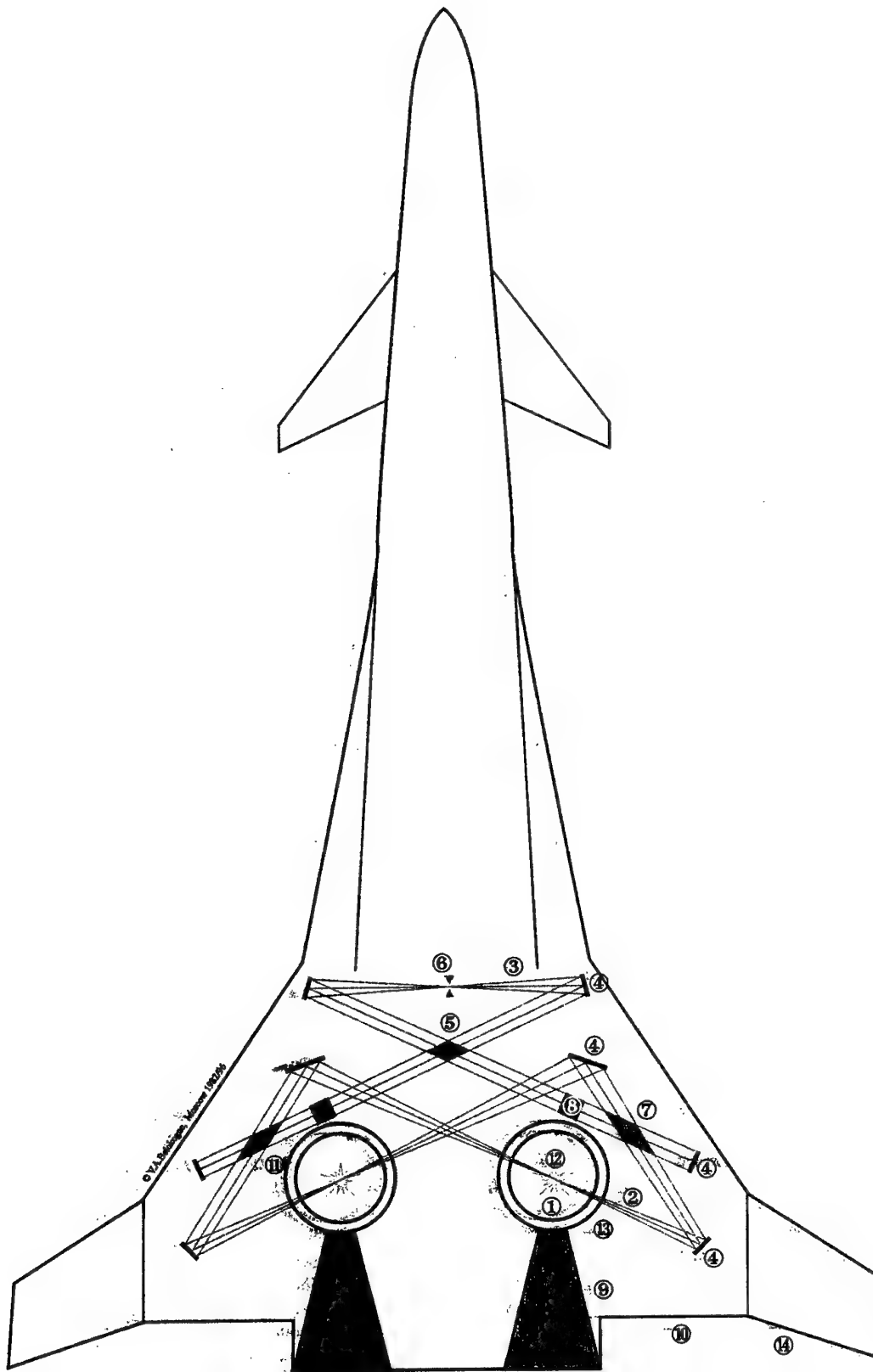
Twin laser-Driven reactor for monofuzelage hypothetical plane of Dr. V.A.Belokogne design 1980.
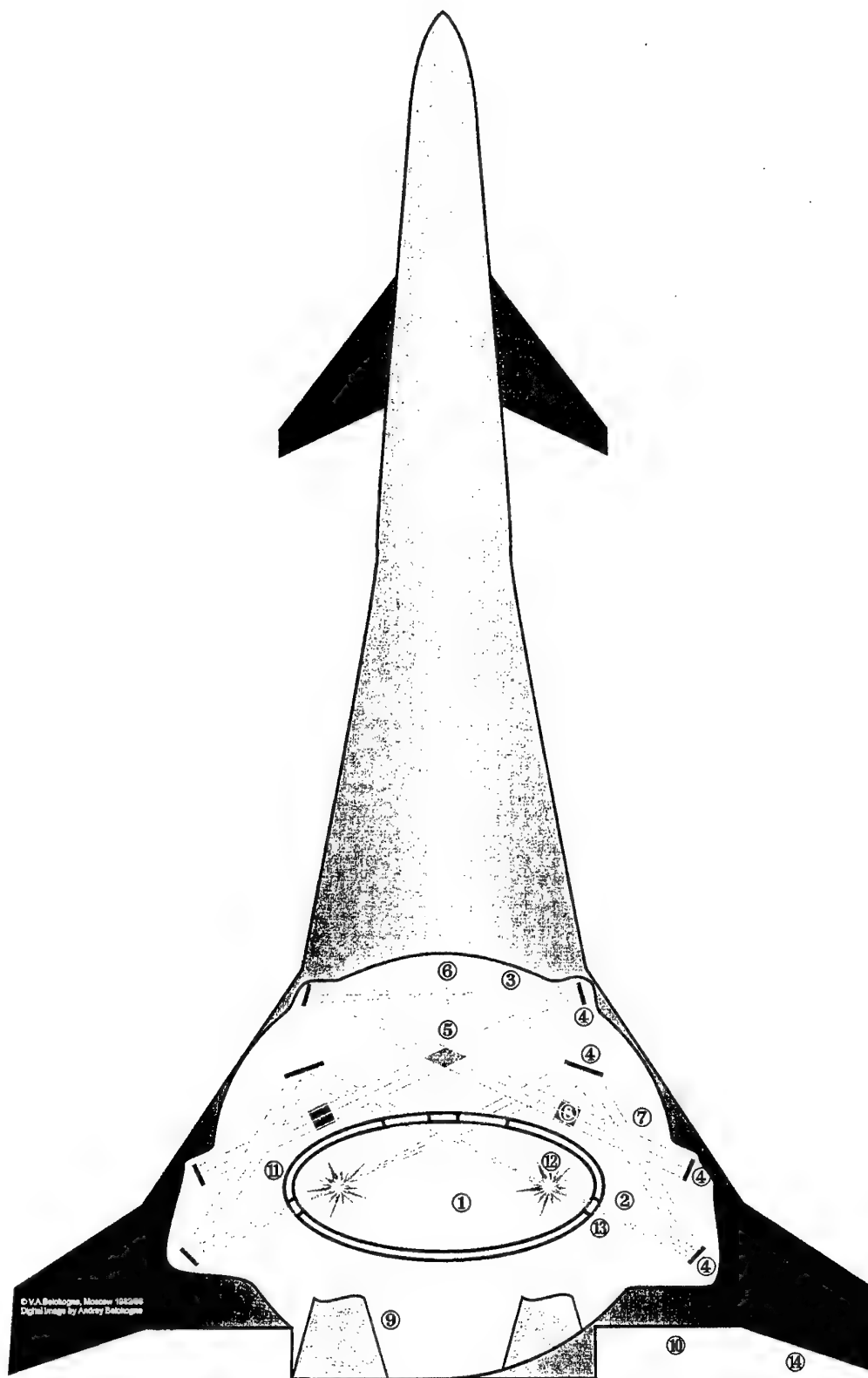
Double microexplosion monoreactor for monofuzelage ICF-plane. Dr.A.Belokogne design 1998.

MONOFUSELAGE ICF – LINER

© Valentine A. Belokogne 1999

1) microexplosion reactor chamber
2) laser beam focused on fuel containing target
3) beam washed by spatial coherence filter
4) laser beam mirror
5) part of active lasing media
6) spatial coherence filter
7) input of beam from master oscillator
8) polarization filter (faraday rotators etc)
9) jet nozzle etc. propulsion subsystems (i. e. MHD devices, electromotors as drive for propellers fans and compressors up to $M \cong 3.5\text{-}4$, ar MHD – assisted superramjets)
10) contour of aerodynamics design
11) tuning, switching laser (inside and outside) etc subsystems
12) place of delivered target (center of microexplosion)
13) flickering porthole
14) winglet as fin and/or radiator

288
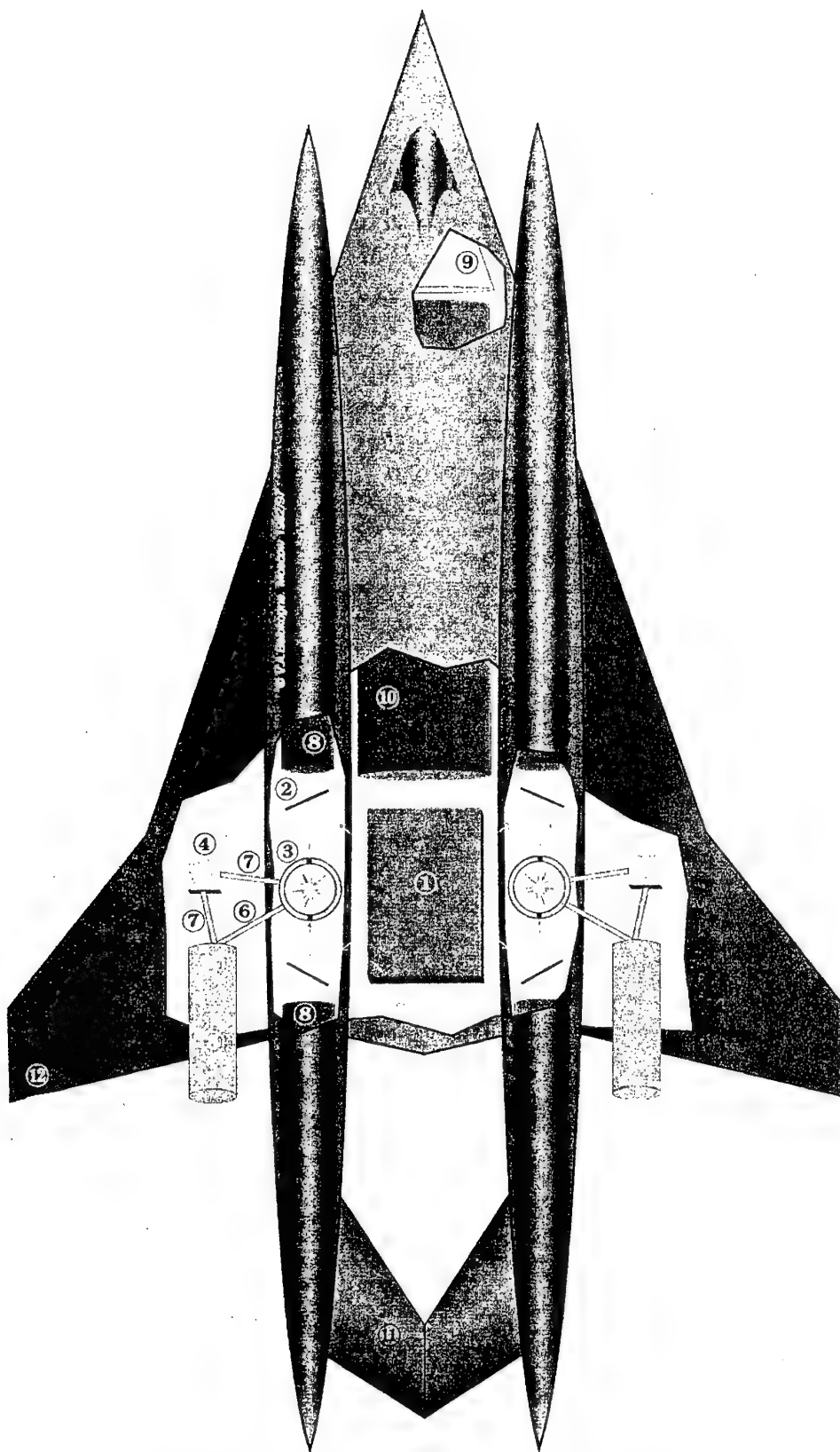
Twinfuzelage twin-reactor ICF-plane. Dr.A.Belokogne design 1982.

[1] Main module of laser driver in fusion microexplosion system

[2] mirror for laser beam

[3] microexplosion reactor chamber

[4] module of power transformation from reactor to propulsion system (and subsystems), i.e. electrogenerator (possibly MHD) feeding electromotor (possibly superconductive) driving compressor of the t u r b i n e l e s s jet engine

[5] channel of the power transformation (i.e. MHD) from microexplosions

[6] channel of heat and mass transfer to propulsion system, i.e. propeller, air-breathing compressor (both blade- and MHD –assisted, simple and sophisticated ramjet etc) or rocket-like pulsed engine with the direct blow-off of the fusion (D + He-3 = = H + He-4+ neutral expellant) – during missions in outer space

[7] propulsive (main engine) systems creating thrust

[8] auxiliary systems

[9] crew cockpit or piloteless guidesystem module

[10] module (possibly changeable) for transportable payloads, i.e. passengers, researchers, instruments and apparatus, testing devices, and so forth

[11] tail, i.e. in roof-like form of overturned "butterfly"

[12] deflective outer part of wing – at angle as function of the Mach Number (M) of flight

The hypothetical aeroplane electrofan configurations with L/D, i.e. favourable for subsonic ICF propulsion

Rombus V A,B (L/D ≥ 40, 400-600km/h).
Rombus I : 1952; II : 1955; III : 1992;
© Valentine A. Belokogne; Moscow 1996
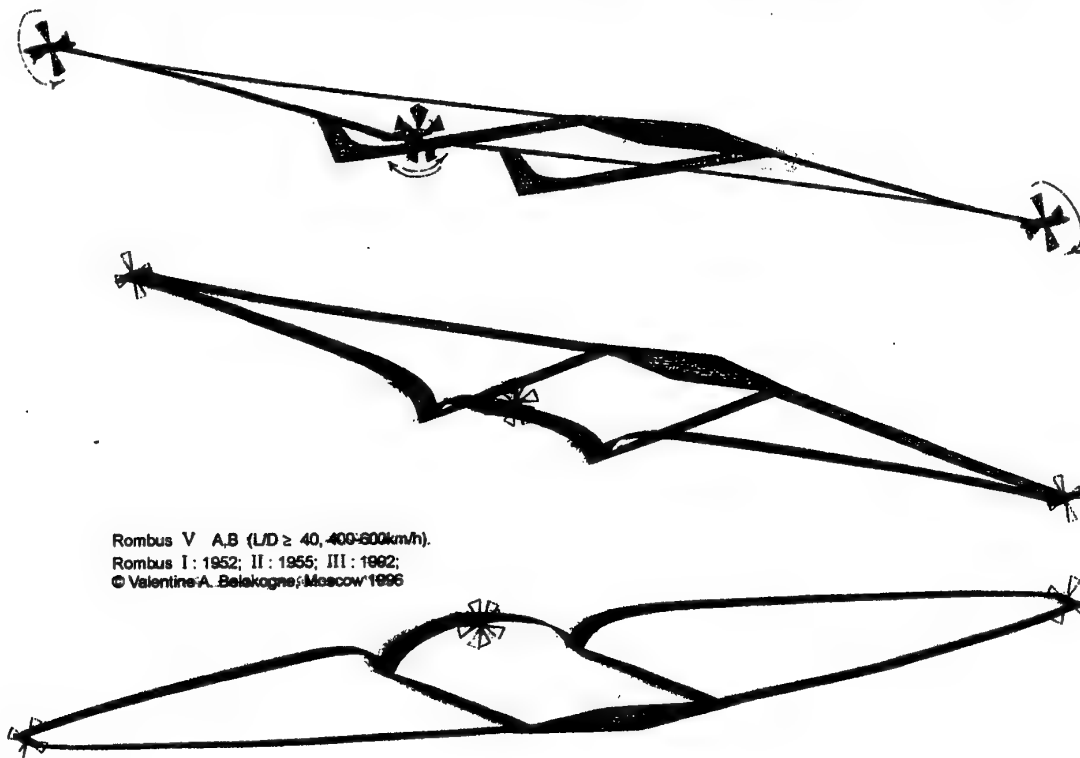
References

1899: Wells H.G. WHEN THE SLEEPER WAKES London.

1907: Goddard R. Paper of Wooster Polytech.Institute (NY 1977,M.1979)
　　　Bogdanoff A.{Malinovsky} KRASNAYA ZVEZDA (in rus.)
　　　　　　　　　　　= RED STAR {MARS}, Peterbourg 1908, M. 1987.

1909: Soddy F. THE INTERPRETATION OF RADIUM, London; M.1924.

1926: Eddington A.S. THE INTERNAL CONSTITUTION OF STARS Cambridge.

1934: Eddington A.S. NEW PATHWAYS IN SCIENCE Cambridge.

1958-1961 : U.S. and S.U. papers on projects of ORION class.

1961: LLL paper by John Hopkins Nuckolls on fusion microexplosion propulsion.

1970: Belokogne V.A. Aviatsya i cosmonavtika (rus.) № 6.

1974: LLL Laser Program Annual Report UCRL-50021-74; pap. UCRL-75363.

1975: Belokogne V.A. Sov.Physics DOKLADY; JTP LETTERS.

1976: Belokogne V.A., Ilynsky Ju., Khokhlov R.V. JETP LETTERS.

1977: LLL Laser Program Annual Report UCRL-50021-77(1979).
　　　Belokogne V.A., Roudenko O.V., Khokhlov R.V. AERODYNAMIC EFFECTS
　　　OF LASER BEAM ILLUMINATION, Acustich. Z. N 4 (rus.) (english translation, by APhS U.S.,
　　　contains flaws!).

1978: Kuchemann D. AERODYN.DESIGN OF AIRCRAFT London;
　　　Bond A. et al: PROJECT DAEDALUS, JBIS Supplement.

1979: Martin A.,Bond A. J.Brit. Interplanetary Society p.283
　　　Belokogne V.A. MULTIFOIL SUPERCOMPRESSION –
　　　Paper for Venice (Italy) meeting published by Plenum NY 1983.

1979, 1982: AIAA conferences on VERY LARGE VEHICLES.

1983 : Hyde R. LLL paper on ICF space propulsion craft to Mars.
　　　Belokogne V.A. Sov. Physics DOKLADY n 1.

1984: Dyson F. WEAPONS AND HOPES NY (rus.M.1990).
　　　Belokogne V.A. pap. (rus.) for TSIOLKOVSKY READING, Kalouga.

1985: Belokogne V.A. paps (rus.) for CONFERENCE ON EXPLOSION AND DETONATION, Tallinn,
　　　Estonia.

1986: Belokogne V.A. THERMONUCLEAR AEROPLANE OF XXI CENTURY -
　　　interview (rus.) to "NTR" newspaper (partly published by "Nauka i Technika"
　　　(bolgar.) n 56; "Air et Cosmos" (fra.) febr. 14 1987; "Sci. et Vie" (fra.)
　　　avril 1989).

1987: Gloushko V.P. (rus.) "Progress in rocket propulsion design and cosmonautics in
　　　Soviet Union", Moscow.
　　　FUSION ASSESSMENT, AIR FORCE STUDY, Washington.

1988: Broad W. NY TIMES on Halite/Zenturion Program, march 21.
　　　Aviation Week & ST, march 21, Scott W. "USAF PREDICTS ANTIMATTER
　　　PROPELLANTS BY XXI CENTURY".
　　　MINICOURSE ON FUSION APPLICATION IN SPACE, ed. by G.Miley
　　　(Salt Lake Sity, Utah 9 october) U. of Illinois, USA.
　　　Zababahin E.I., Zababahin I.E. PHENOMENA OF UNLIMITED
　　　IMPLOSION (rus.), Moskwa.

1989: Hansson P. ON THE USE OF VACUUM FOR INTERSTELLAR TRAVEL
　　　IAA pap. - 89-667.
　　　Belokogne V.A. ON GRAVITATION WAVES GENERATION BY FUSION
　　　EXPLOSION OF SUPERDENSE FUEL, in collected paps (in rus.) on
　　　experimental tests for gravitation, M.G.U.; paps for Conf. (rus.)
　　　FUTURODESIGN-89, publ. Moskwa 1990.

1990: Hirsh D., Mathews W. HISTORY OF US H-BOMB Bulletin of Atomic
　　　Scientists, n february, (transl. and comments by V.Belokogne in rus. ed. of Sov. Physics
　　　USPEHI, n may 1991).
　　　Orth Ch. TRAVEL TO MARS WITH ICF, LLNL-NASA pap. on "VISTA",
　　　octob. 1990.

1992: Nuckolls J. SHAPING THE FUTURE, LLNL.
　　　Belokogne V.A. pap. Conf. Perspectives in cosmonautics, Zelenograd;

Belokogne V.A., Karabutov A.A. Paper Aerospace Conference, Zelenograd
Raymer D. AIRCRAFT, DESIGN, AIAA, Washington.
1993: Belokogne V.A. pap. Conf. 90 Years of the first flight: ON AROUND –
THE – WORLD RACE AIRCRAFT (MGU); RED STAR newspaper 28.08.93,
09.09.95, 12.07.97.
1995: Lindl J. INDIRECT – DRIVE ICF, Physics of Plasmas, n. November.
Rhodes R. DARK SUN, NY.
Sidorov A.F. MATHEMATICAL MODELLING OF THE PROCESSES OF UNSHOCKED
GAS COMPRESSION, Rus.J.Numerical Anal.Math.Modelling.v.10 n3 pp 255-277.
1996: Orth Ch. et al, Nucl. Fus. January.
Tabak M. TRITIUM – POOR FUELS IN ICF, Nucl. Fus., February.
Belokogne V.A. THERMONUCLEAR FUSION: A VIEW FROM RUSSIA,
EIR (Washington), march 1 pp. 14-19.
Caruso A., Pais V. THE IGNITION OF DENSE DT FUEL BY INJECTED
TRIGGERS, Nucl. Fus. june.
FUSION ENERGY IN SPACE PROPULSION, AIAA. (v. 167 of Progr. Astr. & Aeron.)
1997: Lindl J., Levendahl W. Nuclear Fusion n. 2, p. 165.
LLNL ICF Annual Reports – 95, 96, 97.
Belokogne V.A. ON ICF FLUING MACHINES, pap. of the International
Aerospace Meeting, Moscow State University, September
Feoktistov L.P. THE SPACE RUOKETS BASED ON THE HYBRID
FISSION-FUSION REACTOR, pap. of the International Aerospace Meeting,
Moscow State University, September
1998: Basko M. Nuclear Fusion n. 12, pp. 1779-1788.
Yonas Gerry: Scientific American
Belokogne V.A. pap. XVI Mendeleev Congress (Peterbourgh) ICF OF ALL ELEMENTS?
"ONCE AND FOREVER'(rus.) Coll.paps.in honor of Valentine P.Gloushko, Moscow.
1999: AEROSPACE SOURCE BOOK, AW&ST, January 11.
FIGHTING AIRCRAF OF RUSSIAN AIR FORCE (in rus.)-Coll.paps of Techn.
Information, TsAGI, pt.2-3,august.
Belokogne V.A. preprints of Academia Cosmonautica for Zvenigorod Fusion meeting
and Podolsk nuclear energy conference.
2000: Basko M.,Kemp A.,Meyer-ter-Vehn: IGNITION CONDITIONS FOR MAGNETIZED
TARGET FUSION IN CYLINDRICAL GEOMETRY, Nuclear Fusion n1,59-68.
Willi O. et al ICF AND FAST IGNITOR, Nuclear Fusion n. 3Y.
Nevins W., Swain R. THE THERMONUC. FUS. p – ^{11}B. Nuc. Fus. n. 4.
Wall R.: Aviation Week & Space Techn., august 28.
Belokogne V.A.: preprints of Academia Cosmonautica for 2nd Workshop of MHD-
Aerodynamics (Moskow), and 3rd International Aero-Space Congress (Moscow);
Assessment of Science and Technology for XXI Century, Nov. Izvestiya October 14,
Nzavis. Gazet. Dec. 20.
Linhart J.G ORION REVISED, preprint, University of Ferrara, taly.
2001: Herrmann M., Tabak M., Lindl J.: A GENERALIZED SCALING LAW FOR THE IGNITION
ENERGY OF ICF CAPSULES, Nucl. Fus. January. pp 99-112.

APPENDIX A-I

THERMONUCLEAR MICROEXPLOSION DRIVEN AEROPLANES UP TO 2035 YEAR
<H Y P O T E N T I A L>

	1974*	1977*	–	1979*	1995**
ASSESSMENT GIVEN TO YEARS					
FOR YEARS	??	2000		2015	2025 – 2035
CRUISE, km/hour	800	800	800	800	2200 - 4400
CEILING, km	10	10	10	10	15 - 25
START MASS, tons	200	450	900	4500	2000 – 3000
PRIMARY CRUISE (EXPLOSIVE)					
ICF POWER, MWt	200	370	660	3000	2000 – 6000
REACTORS numb.	1	1	1-2	2	1 - 2 - 4?
«MECHANICAL» CRUISE POWER MW OF PROPULSION	80	70	130	600	1000 – 3000
CRUISE THRUST t	40	35	65	300	140 – 300
Lift/Drag L/D	5-6	14	15	16-17	14 – 10
PAYLOAD % IN START MASS		20 - 25			20 - 10

© Valentine A. Belokogne, Moscow 1995.
 * LLNL
** Valentine A. Belokogne

APPENDIX B
FUSION. GENERAL INFORMATION
FUSION FUELS: SPECIFIC ENERGY OUTPUT AND RADIACTIVITY (*)

I. FUEL OF SUN (CORE)

(slow burn at $T_{max} \approx 15 \cdot 10^6$ °K, $\rho^{max} = 100\text{-}150$ g/cm^3, $p^{max} \approx 2\text{-}2.5 \cdot 10^{11}$ atm)

$$\underline{H+H} + H + \underline{H+H} + H \rightarrow \underline{D+H} + \underline{D+H} \rightarrow {}^3He + {}^3He \rightarrow {}^4He + 2H(+\upsilon + 2e^+)$$

as if $\quad 4^1H \quad \rightarrow \quad {}^4He\ (+\upsilon + 2e^+) + \underline{q \approx 4 \cdot 10^{11}}$ Joules/gram

(1920)   (1930th)

II. FUEL FOR NOBEL LAUREATE PRETENDERS:

$$D+T^* \rightarrow {}^4He + n^* + \underline{q = 3.37 \cdot 10^{11}}\ \text{J/g}$$
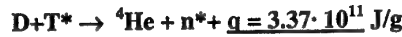
III. MAIN FUEL FOR THE FIRST H-BOMB «MIKE» (1952: ≈ 100 g/cm^3):

$$D+D \rightarrow \quad ({}^3He + n^*) + \underline{q \approx 10^{11}}\ \text{J/g}$$
$$({}^3H^* + H)$$
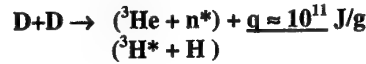
IV. MODERATELY SAFE «URBAN FUEL» PROPOSED FOR FUSION PROPULSION (1972-78)

$$D + {}^3He \rightarrow {}^4He + {}^1H + \text{trace } T^* + \text{trace } n^* \text{ from DD reaction} + \underline{q = 3.52 \cdot 10^{11}}\ \text{J/g}$$

V. ABSOLUTELY SAFE ADVANCED PROPULSION FUEL
(too expensive up to 2010-2025 years)

$$^3He + {}^3He \rightarrow {}^4He + 2\ {}^1H + \underline{q \approx 2 \cdot 10^{11}}\ \text{J/g}$$
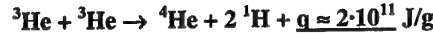
VI. MORE HYPOTHETICAL SAFE FUSION FUEL

$$^1H + {}^{11}B \rightarrow 3\ {}^4He\ (+\text{trace } {}^{14}C^* \text{ from } {}^{11}B + {}^4He) + \underline{q \approx 7 \cdot 10^{10}}\ \text{J/g}$$

VII. ANNIHILATION

$$(e^- + e^+ = \Sigma\gamma \text{ etc}): (\Delta m)c^2/m_o \equiv mc^2/m_o \geq m_o c^2/m_o \equiv c^2 = q = 9 \cdot 10^{13}\ \text{J/g}$$

APPENDIX C

FUSION ENERGY OUTPUT: MICROEXPLOSION YIELD

$$Y(\text{Joules}) \equiv \Phi(\text{burn fraction})\ qm\ (g\ \text{fuel}) \equiv \Phi q (4\pi/3)\rho R^3(\text{sphere}) \approx q\rho R^3 \equiv q(\rho R)^3/\rho^2$$
$$(\Phi = 0.3)$$

$$\approx 10^{13}/\rho^2\ (\text{DT}: T_{ign} = 5\text{-}10 \cdot 10^7\ °K) \leq 10^9\ J \rightarrow \rho \geq 100\ \text{g/cm}^3$$
$$(\rho R = 3;\ T_{burn} \approx 40 \cdot 10^7\ °K)$$

$$\approx 10^{15}/\rho^2 (D^3He, {}^3He^3He : T_{ign} \approx 40 \cdot 10^7\ °K) \leq 10^9\ J \rightarrow \rho \geq 1000\ \text{g/cm}^3$$
$$(\rho R = 14,\ 17;\ T_{burn} \approx 100 \cdot 10^7\ °K)$$

54. SUPER - VELOCITY RAILGUNS: THE STRUCTURE OF AN ENERGY AND CURRENT INPUT INTO THE CHANNEL, THE MAGNETIC GEOMETRY OF THE CHANNEL AND THE CURRENT TRANSPORT IN THE ANCHOR AREA

M.P. Galanin
KIAM of RAS

M.K. Krylov, V.V. Kuznetsov, A.P. Lototskii, Yu.A. Khalimullin
SSC RF TRINITI

Abstract. The development of electromagnetic accelerators for a direct launch of small artificial satellites from the Earth surface takes the important place in studies of many experts in various countries. The first spacevelocity (8km/s) for objects of masses of several grams had been reached and exceeded [1] with the help of a railgun. With the increase of a projectile mass and the decrease of a magnitude of acceleration, admissible for the equipment, the length of an accelerating channel must increase many times compared to that of a channel in laboratory facilities (up to 200-1000 meters). Linear current densities in rails can be reduced. The life time of the channel, which in laboratory installations is 3-5 pulses, should become much longer.

The paper presents the outcomes of the researches into operation of a large railgun. The velocity limit and small efficiency of energy transformation were taken into account. The last parameter in a laboratory railgun does not exceed 3-5% for a plasma and 10 - 15 % for a metal armature.

The work has been done under partial financial support of the Russian Fund for Basic Researches (project N 00-02-16130).

1. The structure of an electrical part of power supply systems for large railguns

The classical circuits of current input into the railgun channel from a breech side [2, 3] are common and differ among themselves by the "degree" of uniformity of a current pulse shape. In this scheme it is necessary to fill the channel by a magnetic field. This is a shortcoming, which has the two sides: 1. unproductive expenditures of an energy, which can not be used for acceleration of a projectile; 2. maintenance of a high potential difference at entire length of the channel during acceleration. In 1982, R. Marshall [4] offered a new scheme with a distributed energy input. Parker [5] tried to optimise the parameters of such a circuit with capacity storage of an energy. However, in the case of large railguns the use of inductive storage of an energy is preferred more. The principal diagram of the electrical circuit for the power supply system is shown on Fig.1. In it, the railgun sections, which finish the acceleration regime, are automatically included into the structure of the segmented inductive power supply. Thus the "transfer" of the magnetic energy into the acceleration zone is carried out not only from the nearest inductive storage, but also from all previous areas of the railgun channel.

Supposing the non - dissipation system and instantaneous switching and using the law of conservation of a magnetic flux we can obtain the following system of equations

$$I_{1n}[L+(n-1)l+\Delta l]+$$
$$+I_{2n}[(n-2)l+\Delta l]+...+I_{nn}\Delta l = LI_0$$

$$I_{1n}[(n-2)l+\Delta l]+$$
$$+I_{2n}[L+(n-2)l+\Delta l]+...+I_{nn}\Delta l = LI_0 \qquad (1)$$

$$I_{1n}\Delta l + I_{2n}\Delta l + ... + I_{nn}(L+\Delta l) = LI_0$$

Here $\Delta l = b\Delta a$. The second index in unknown currents designates the amount of "on - switch" sources in accordance with projectile motion and depends on coordinate x.

The solution of system (1) has the form

$$C_{im} = C_{mm}(L/l)^{m-1},$$

$$C_{mm} = C_{m-1,m-1}(L/l) + \sum_{i}^{m-1} C_{i,m-1}, \qquad (2)$$

$$D_m = C_{m+1,m+1}(L/l)^{-1}, \quad i < m.$$

from which we see, that in an acceleration system and sources no currents inversion occurs: $C_{im} > 0$ and $d_m > 0$. Therefore the magnetic field $B(x)$ distribution shown on Fig.1 (b) is valid for any ratios L/l. The form of $B(x)$ distribution corresponds to the forming of the magnetic piston following the projectile. At some distance, equal to 2–3a, the magnetic energy from the channel flows into the acceleration zone together with the unused

295
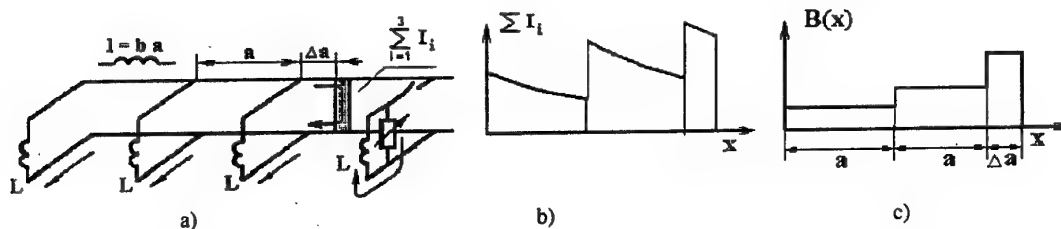
Fig.1. a) Scheme of distributed current input in the railgun channel, b) current through the armature versus projectile coordinate, c) distribution of the magnetic induction in the channel.


```
m    = 1.0000
r    = 3.00E-04
i0   = 2.0E+06
Lx   = 3.0E-07
tk   = 0.000100
dt   = 0.000010
Lint = 0.000
Tk/E0 = 0.382
Wom  = 8.57E+06
Tk   = 9.18E+06
E0   = 2.40E+07
lend = 0.000
Msi  3.28E+06

x = 10.0  m
u =   4285 m/s
t = 0.00617
```
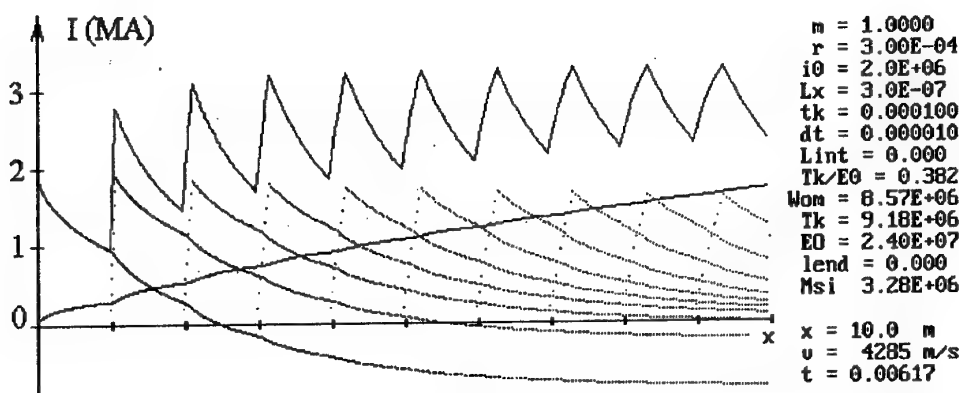
Fig.2. The result of the numerical calculation

energy of appropriate stores. The total initial energy in stores being NW_0, the magnitude of useful kinetic energy $\eta=W_{kin}/(NW_0)=(NW_0-W_{magn})/NW_0=1-L/(L_eN)$. This system principally differs from classical ones by the absence of precise separation between the power sources and the acceleration part.

The next stage of the analysis is determination of an active losses in the armature and power losses in the current switches. There has been carried out the evaluation of critical magnitude R, affecting automatic localisation of magnetic energy. For various systems $R_{cr} \approx 0.25$-0.30mOhm. In Fig.2, the calculated currents, I, and velocity of a projectile of 1kg mass for the 10 - meter accelerator with high magnitude of a resistance of a armature $R > R_{cr}$ are presented.

The curves show, that even in case $R=R_{cr}$ the current inversion in an initial part of the channel takes place, but the current remains localised in the first section of an accelerator (the first source). It is easy to estimate, that the Joule's losses and the kinetic energy of the projectile are 0,37 and 0,39 from initial energy store, respectively. Thus, the final magnetic energy of the system at the moment of a projectile exit does not exceed 0,25 of the initial energy store and is essentially lower than W_{kin}. This value is unattainable in a railgun of an ordinary

configuration where the constant current amplitude is maintained.

2. The "muzzle-fed" - railgun: the magnetic configuration of the channel and the stability of the plasma projectile

How is it possible to save the compactness of the plasma projectile? In [6], it was noted, that it is possible to provide a negative gradient of voltage on the channel using the inverse connection of the current into the projectile with the help of additional current feeds, as shown in Fig.3.
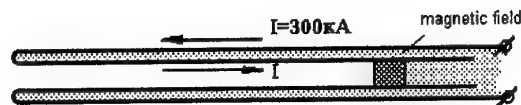
Fig.3 The scheme of acceleration channel with the inverse connection of the current.

The 3D numerical simulation [7, 8] of current distributions in rails and a metal projectile has been carried out for an evaluation of performance capabilities of an experimental "muzzle - fed" – railgun. The cross – section of such a railgun is shown in Fig.4. Relative magnitudes of the acceleration force and its time variations have been determined too.

296
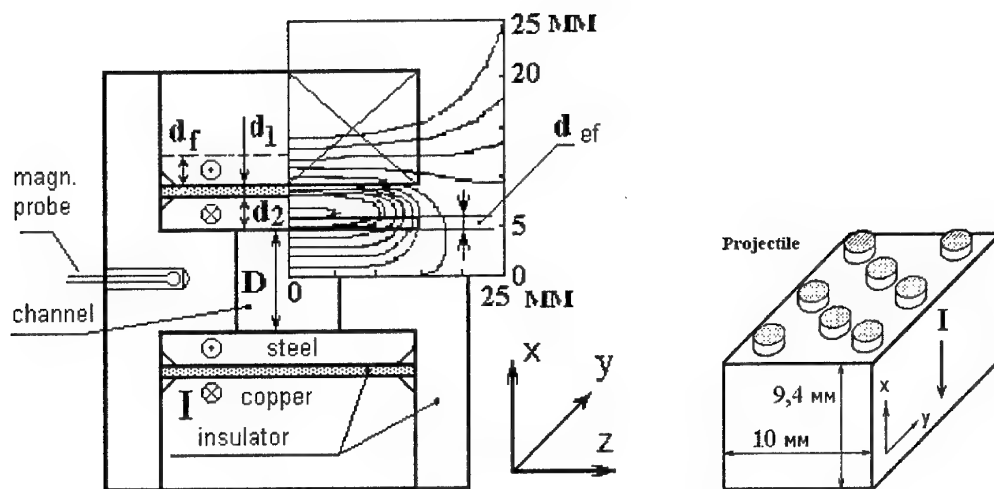
Fig.4. The cross-section of the railgun channel with inverse current connection. Caliber D=10mm. The part of a magnetic configuration, where the force lines are constructed from points z=0, x=N<15mm, are shown. The projectile with separate conducting rods.

The typical distribution of the magnetic field induction in a plane of the cross - section z=const, through-passing 2 average rods (Fig. 4), is shown on Fig.5. The total current through the accelerator I=10kA. The presence of a magnetic field Bz in front of the projectile is seen well. This field leads to the decrease of an accelerating force compared with railgun of a ordinary construction. The field with a high magnitude of flux density is generated between direct and inverse rails. Here, the presence of the field results in an additional magnetic pressure, which keeps the lower rail closer to a projectile and improves the electrical contact with the metal projectile. The field distributions on front and rear (on x) boundaries of the area vary in time because of diffusion of the magnetic field (and currents) into the rail. We present only experimental data on the velocity of a plasma piston versus the rate of the energy input into the railgun at range of maximum working currents of 220kA, omitting the consideration of all factors influencing formation of shunting current structures. At di/dt=5·10^8-10^{10}A/s the function V (di/dt) is nearly linear V=1.3·10^{-7}di/dt+2300 (m/s; A/s). The analysis of this dependency and the discharge circuit equation for the first cascade shows that the plasma piston can effectively work only at a rising section of a current shape. (di/dt > 10^{10}A/s).

The authors carried out the cycle of investigations of the plasma piston stability in the "muzzle – fed" railgun [9]. We present the main results. In Fig.6 the time dependency of the geometric centre position of the plasma piston is shown at negative magnitude di/dt (after reaching the maximum amplitude of a current I_{max}=220kA).

The profiles of signals of magnetic probes are shown here too. On the basis of them the time dependency $x(t)$ of projectile position was determined.
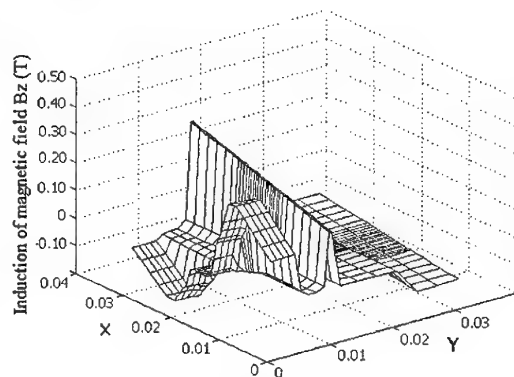
Fig.5. The component B_z of the magnetic induction vector in the projectile region.
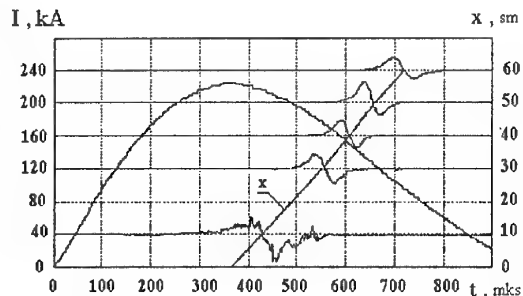
Fig.6. The current oscillogram and the association of the plasma piston position versus time in the "muzzle - fed" channel.

297

When acceleration begins at a time moment, corresponding to the maximum current, the plasma piston status destabilises and this leads to the more stretched and non - compact discharge (see the first magnetic probe signal). In a conventional railgun, it is impossible to bring such a structure back to the compact form. After the current structure enters the "muzzle - fed" channel, the compactness of the plasma structure completely restores at a short distance (~ 20cm.), which is seen well by the second magnetic probe signal. The length of the plasma structure is 6-7cm at velocities in the range of 1.6-2km/s. The maximum velocity of a plasma piston is 2.1km/s. Under similar conditions of acceleration in a classical railgun with the same current amplitude, the maximum velocity was 2.96km/s (reached at the growing part of the current curve only).

Thus, by the results of investigations of a "muzzle - fed" railgun with the plasma armature one can make a conclusion on a much higher level of stability. This happens due to the decrease of Ohmic resistance gradient of the channel.

The observed increased stability of the plasma armature in these channels allowed one to offer a new system for the launch of dielectric projectiles in the multi - cascade accelerator [10]. Its configuration is shown in Fig.7. The scheme is supplemented by the third cascade, which accelerates the dielectric projectiles by the compact plasma armature. Operation of the system was investigated experimentally.
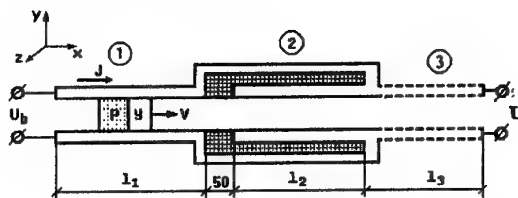
Fig.7. The schematic diagram of the two - cascade accelerator.

In Fig. 8, the current, I, and the voltage, U, oscillograms, and in Fig.9, - the diagram of magnetic probes and dependency of the plasma armature position in the channel are shown. The projectile of the mass of 1.4 grams had initial velocity of 500m/s, travelling between the 1-st and 2-nd magnetic probes.

Heterogeneity of the discharge in the first cascade was made deliberately by using insulating walls, which caused the formation of two parallel current circuits (see Fig.9) and decrease of the armature velocity. The compression of the discharge happened in the "muzzle - fed" cascade. It finished completely at the length of 15-20cm,

that was reflected in the character of the discharge VAC ($U{\sim}I$). Further the process of acceleration continued in the next classical cascade, which was the last in the three-cascade accelerator. This procedure can be repeated several times. The efficient system of the distributed power supplies for such a multi - cascade accelerator can be constructed on the basis of inductance - capacitor power sources. In this case the initial cascades with the metal armature being accelerated are fed from inductive stores which permit to return the accumulated magnetic energy into the accelerator completely and don't fill the entire accelerator channel with a magnetic flux. In the case of the change of a type of an armature (from metal to plasma), the "classical" cascades must be fed from fast capacity sources ($di/dt{>}0$). Taking into account the equation $dx=Vdt$ one can see that for maintaining the acceleration process it is necessary to increase the charge voltage on capacity modules by a magnitude of $L'I_lV_b$ at least. The "muzzle - fed" compensatory cascades can be fed from inductive stores with $di/dt{<}0$.
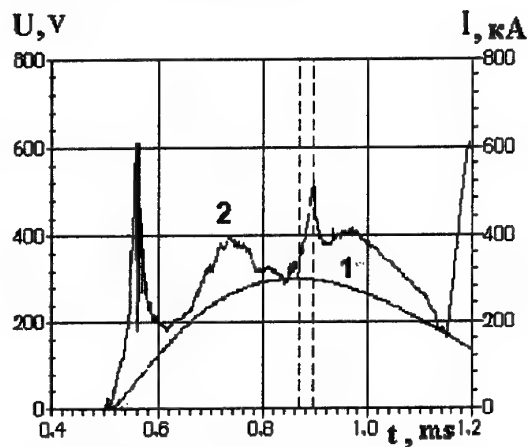
Fig.8. The current and voltage oscillograms in the two - cascade accelerator.
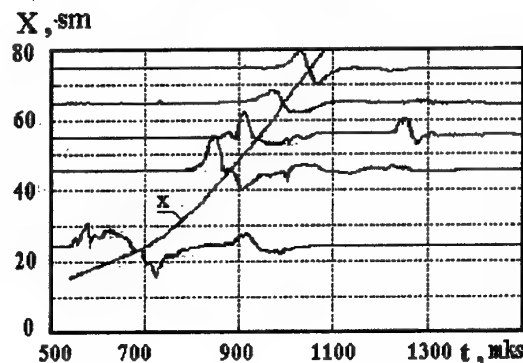
Fig.9. The summary diagram of magnetic probes signals and time association of a position of a plasma armature.

298

Some additional details of the presented results are in [11].

Conclusion

The railgun systems considered, with distributed current feeds from magnetic stores, differ from the "classical" accelerating system by high efficiency of the energy transformation and quasi - stationary waveform of the accelerating current.

The forthcoming necessity to solve the problem of reaching space velocities ($V>10$km/s) with the help of railguns will require the use of the plasma armature. Therefore it is necessary to prevent the plasma armature from destruction for output cascades or renewing its compact configuration.

The main conclusion of the paper is that the big system must be multi - modular for satisfactory power efficiency of a super - velocity accelerating machine. The design of modules (armature, feed, input of the current, length) must match the achievable velocity on every channel part. There is no doubt, that the problem of development of such an accelerator can be solved with the help of the appropriate system approach and experimental modelling.

References

1. N. Kawashima, Akira Yamori. Improvement of High Velocity and Stable Railgun (HYPAC) in ISAS. 5 - th Europ. Symposium on EML Technology. Toulouse. April 10 - 13, 1995. Proc. Conf. Report N 57.
2. Proceedings of I All-Union Conference on High Current Arc Discharge Dynamics in Magnetic Field (Novosibirsk, 10-13 April 1990), Novosibirsk, 1990, 350 pp. (In Russian).
3. Proceedings of II All-Union Conference on High Current Arc Discharge Dynamics in Magnetic Field (Novosibirsk, 4-6 December 1991), Novosibirsk, 1992, 367pp. (In Russian).
4. R.A. Marshall. Railguns. Proc.9 - th US nat. Conf. \ Appl. Techn. Ithaca, N 4, 21 - 25 June. 1982. P.p. 361 - 366.
5. J.V. Parker. Electromagnetic Projectile Acceleration Utilising Distributed Energy Source. J. Appl. Phys., 1982, v. 53, No 6. P.p. 6710 - 6723.
6. I.E. Shrader, A.J. Bohn, J.C. Thompson. Rail Guns Experimental Results due to Varying Bore and Arc Materials, and Varying Number of Barrel turns. IEEE Transaction on Magnetics. V.22. 1986. No 6. P.p. 1739–1741.
7. M.P. Galanin, Yu. P. Popov. Quasi - stationary electromagnetic fields in non - homogeneous media. Mathematical modelling. Moscow, Nauka, Fizmatlit, 1995, 320 pp., in Russian.
8. M.P. Galanin, A.P. Lototsky, Yu.P. Popov, S.S. Khramtsovskii. Numerical modelling of spatially three - dimensional phenomena at electromagnetic acceleration of conducting armatures // Mathematical modelling. 1999. V. 11. N 8. p.p. 3 - 22.
9. J.V. Parker. The SRS Railgun: A New Approach to Restrike Control. IEEE Transaction on Magnetics. V. 25. 1989. No.1, p.p. 412 - 417.
10. Lototsky A.P., Kotova L.G., Halimullin Yu.A. Re- establishing of compact current structure of a plasma armature in railgun // 6th European Symposium on electromagnetic launch technology. Hague, 1997, p. 322 - 329.
11. Krylov M.K., Kuznetsov V.V., Lototsky A.P., Halimullin Yu.A., Galanin M.P., Savitchev V.V. Large railguns: a structure of an energy and current input into the channel, magnetic geometry of the channel and the current flow in the zone of a projectile. // Preprint of SSC of Russian Federation TRINITI, 2001, 53 p, in press.

55. COMBINED POWER SYSTEMS FOR SPACE APPLICATION

Osipov M., Mojarov A., Samsonov V.
Bauman Moscow State Technical University,
Russia, e-mail:osipov@power.bmstu.ru

The concept of designing and development of solar and nuclear power systems (CPS) for generation of output power in the range of Ne =10kw → 10000Mw has been considered with taking into account the progress in the development of gas cooled nuclear reactors and solar equipment (concentrator, heat receiver). The results of comparing of parameters and performances of autonomous closed cycle gas turbine units (CGTU) and combined power systems including magneto hydrodynamic generator and gas turbines with helium-xenon mixture, argon, neon, hydrogen (temperature 1100...1800K) showed the advantages of heat exchange closed cycle gas turbine units for output power 5...50kw for conversion of solar energy and heat of nuclear reactor. Increasing of working medium temperature to 2000...3500K and output power of power units till Ne=10...10000Mw showed that combined closed cycle MHD-generator and gas turbine power facilities –are preferable because of high efficiency ($\eta \geq 55\%$) and acceptable dimensions of heat-exchangers, MHDG, compressors and turbine. The electrical power in these schemes is generated by MHD-channel and whole output power of gas turbine is transmitted to compressors. The gas cooled core reactors for temperature of working medium (H_2, He-Xe, Ar) ~ 3000...3500K in close cycle MHDG, gas turbines and gaseous laser system for transmission of energy to the cart will be able to generate the output power Ne =1000...10000Mw.

Influence of working processes for gas turbine, compressor and showed the ways for increasing of efficiency and reliability of combined closed cycle power systems.

56. THE PULSED MAGNETO - CUMULATIVE POWER SHARPENER WITH THE ELECTROMAGNETIC LINER ACCELERATION

V.P. Smirnoff
RSC «KI»

E.V. Grabovskii, A.M. Gytlukhin, V.V. Kuznetsov, V.F. Levashov, A.P. Lototskii
SSC RF TRINITI

M.P. Galanin, Yu.P. Popov
KIAM of RAS

1. Introduction

The explosion – magnetic generators (EMG) [1], which were developed, are the pulsed energy converters and allow one to get pulses of electric current with the amplitude of 10^4-10^8A and power of up to $5 \cdot 10^{12}$W. Complete destruction of such devices in each pulse prevents their wide use. This is stipulated not only by the essential device cost, but by particular conditions of usage as well. At the same time EMG has a very high power gain factor K_w=30-100, the value of which is defined as the ratio of the acceleration time of conductors and the time of their slowing down by the pressure generated by a magnetic field in a high–current output electrical circuit. This EMG characteristic is attractive for realisation in a laboratory power amplifier, where it is possible to realise an acceleration of a conducting armature by electromagnetic forces. The inductive store or capacitor bank can be used as primary energy sources for the acceleration. Thus, the electrical pulse generator can be trasnformed into a pulsed power sharpener – magnetic compressor (MC).

As a basis, the authors of the designed laboratory device have taken the system of flat accelerating liners, launched towards each other. In the paper, the concept of a device is substantiated. According to preliminary estimates it will allow one to get on output a current pulse of duration of 3-5μsec and amplitude of 10MA at the voltage of up to 100kV.

The physical and two - dimensional mathematical models of the process of electromagnetic acceleration of a laminar metallic liner have been constructed. The numerical algorithm has been realised in a software code for a PC. The programs developed are for the simulation of versions of the device, with which the experiments on the study of energy compression have been conducted. There were investigated some special features of motion of the liners, which during acceleration and slowing down in a magnetic field change shape from flat one. In the paper, the results of simulations of launches of flat shells are of compared with experimental results, obtained on a small test sharpener model with the liner of 30 mm width and 250mm length.

2. The geometric concept of the electromagnetic power sharpener

The TRINITI Centre acquired an experience in an electromagnetic launch of heavy cylindrical shells (liners) to velocities of 1-5km/s [2-4] for compressng magnetic field and plasma in thermonuclear Θ-pinch traps. They have some backlog of calculations of stability of shells in different regimes of their loading. However, in this problem, the geometry of liners was chosen to be a strip, under which the area of compressed magnetic flow is limited by plates launched towards each other, these plates being at the same time the conductors of an output circuit. The geometry of the sharpener is shown in Fig. 1.

In contrast with the cylindrical geometry, where for the output of generated current we have to insert a fixed central conductor, this system has the following advantages:

1. The compression circuit is completely formed by single use elements, which are easily replaced after each operation cycle. It is unlikely that a fixed conductor of output circuit won't be heavily damaged at liner velocities of 1-1.5km/s.

2. The analysis of a pumping system of an initial magnetic flow in the compression circuit has shown that in the case of a strip geometry the initial flow can be delivered by the accelerating circuit itself, saving the device from extra storage and switching circuits.

The magnetic configuration for generating a magnetic flow in the MC output circuit during acceleration of liners, is shown in Fig. 1B. The flow can be captured in the compression circuit at the moment of switching on a load.
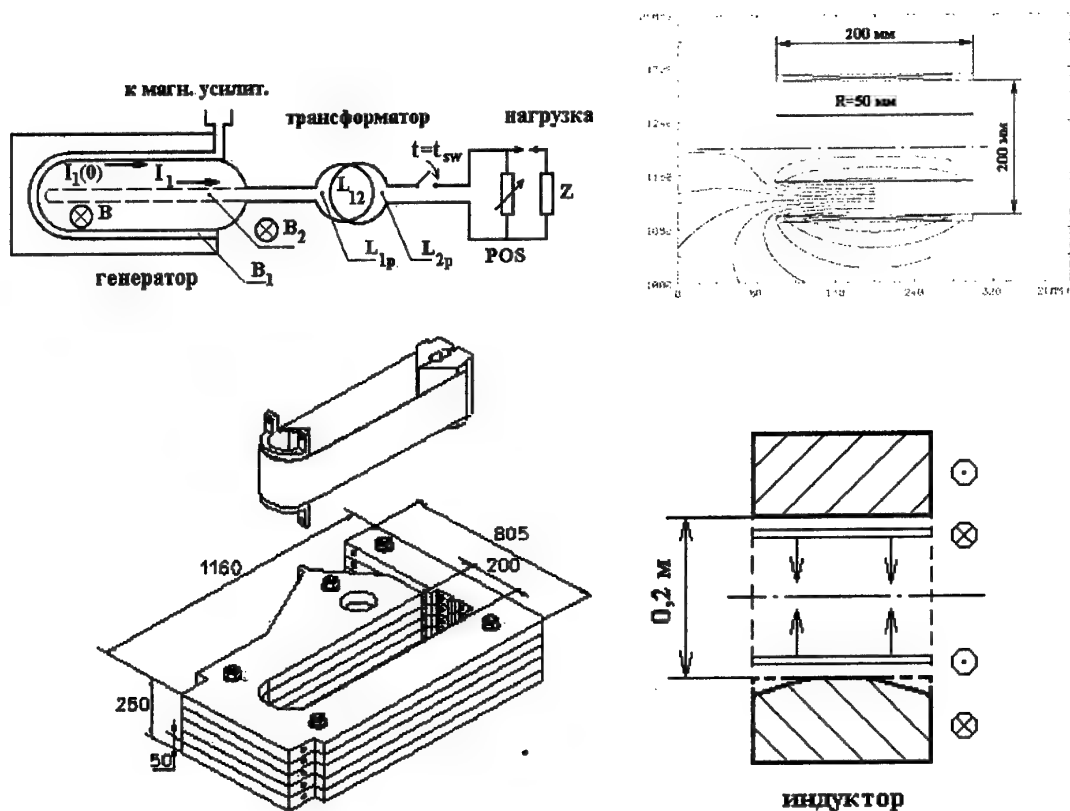
Fig.1. The outline of scheme (A) and main details of the current generator, cross - sections (B) of the devices; C – the flat tape being accelerated with a tightening device and a turn of an inductor of an accelerating magnetic field; D - the cross-section of the generator, directions of currents and accelerations are shown.

3. Special features of power sharpening in the MC system.

In general, the conditions of the process are the following. The liner must be flat. Profiles of liner velocities are unknown. With certain approximation, the stage of compression can be considered as a reverse stage of acceleration with its own transport factors. So there is a need in the numerical simulation of both processes - acceleration and compression.

4. The electromagnetic model for the acceleration of parallel conductors

In MC of this type, there are a motionless inductor and accelerated plate, returning current (see Fig.2). The influence of the second pair (the oncoming accelerated system) can be neglected decause of its remoteness. Let us divide the plate into N conductors carrying currents I_i and having masses of $dx \cdot h \cdot r$ each, then find a distribution of currents. Because we don't know the current distribution in the inductor, we use reflection currents (see Fig.2) and suppose that the

conductors with currents I_i and I_i' belong to one of N parallel circuits, connected to a common power source.
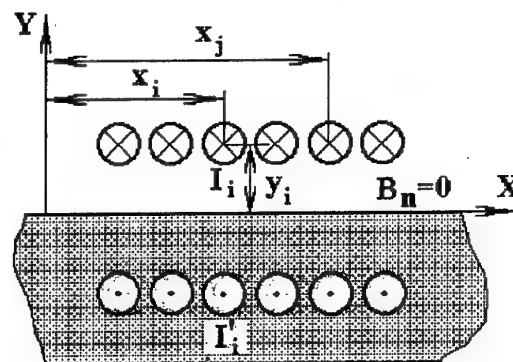
Fig.2. The scheme of currents in the plate-liner and continuous inductor.

Since on a surface of an ideal conducting inductor the normal component of a magnetic flux density vector $B_n = 0$, this picture adequately reflects the distribution of inductance between

302

parallel conductors of the liner connected to the common source. Knowing dimensions $dx \cdot (j-i)$ and using arbitrary R_i and R_j, which are not equal to each other, one can calculate a mutual inductance for any pair of conductors, and after that obtain all L_{ij} (R_i, R_j). Their determination means that the problem of finding a distribution of currents is solved, and, consequently, the magnetic field in the accelerating gap at the moment of a switching on of a source of accelerating current becomes known. Then it isn't hard to find forces F_{yi}, acting on conductors, and acceleration of the plate element at the initial stage of a launch. The acceleration of the liner and the change of R_i later on lead to the change of L_{ij} and necessity to take into account their derivatives in an electrical circuit. At this stage we can neglect forces F_{xi}, assuming a thin plate to be flexible, but non-stretched and incompressible.

The results of calculations of currents, acting forces and velocity profiles of $N=20$ conductors and profiles of a liner plate at different moments of time $t=10\text{-}50\mu\text{sec}$ are presented on Fig.3. The transverse dimensions (20×1mm) of Al plate correspond to dimensions of a small specially made test device (the length of a strip system is 300mm), fed with current of 300kA amplitude.

It is well seen in Figures that the motion of the plate begins from edges, departing from the motionless surface of an inductor. The edges gain an essential velocity before the observable displacement of the central part of plates. With the further motion of the whole plate, the edges "run away" forward and get into the zone of a weak action of the force $F_{y1,N}$ generated by the magnetic field. The maximum of the velocity profile starts to move from the edge to the middle of the plate, until

the clearly distinctive central maximum of the velocity profile at 30μsec is formed.

From this moment, the originally formed deflection of the plate begins to straighten, the plate of the liner restores a flat shape at $t=30\mu\text{sec}$, and to the moment $t=50\mu\text{sec}$ the direction of sagging changes. It should be noted that the changing of a direction of sagging is accompanied not only by a reduction of acceleration, but also by a weak slowing down of the central conductors. this is well seen by the decrease of the absolute velocity. The described above picture of plate oscillations was observed experimentally in the device with the above mentioned dimensions.

Photos of the accelerating plate were taken by SPR in the mode of "magnifying glasses of time". Two distinctive frames corresponding to different moments of time in one cycle of acceleration are shown in Fig.4. In the first frame at $t=20\mu\text{sec}$ from the beginning of current input , there is observed the spreading of a "shade" of a plate profile, which gets thin (~ 1mm) in the second frame at $t=40\mu\text{sec}$.

So, both calculations and experiment show the waves of the plate oscillations in the transverse direction, along the magnetic field. The natural explanation of this effect is the development of Alfven magnetohydrodynamic waves [5], in which the role of restoring forces is played by inertia forces mdV/dt. An initial disturbances here are the "running away" edges in the cross - section. The estimation of the Alfven velocity at characteristic parameters of the experimental device (used in the calculation) gives a value $V_a = H\sqrt{\mu_0\rho} = 400\text{m/s}$.

t=42 mks

50 mm

t=80 mks

50 mm
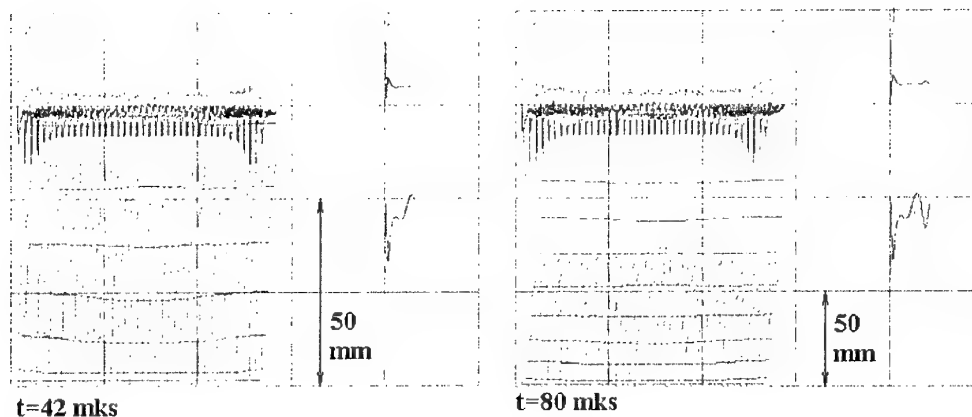
Fig.3. The field of velocities of the point conductors of the liner and the profile of the plate.

Fig.4. SPR - grams of the plate profile. The right edge of the device. The maximum velocity $V_{max} \sim 500m/s$.

When at the beginning of the launch calculations give the first maximum of the velocity profile in the middle of the plate at t = 40 µsec, there is a good agreement with the Alfven velocity: $V_{calc}=(dx \cdot N/2)/t=500$м/s. In Fig.3, at $t=80$µsec one can see the development of the second harmonics of the Alfven waves, which is marked as a "darkness" (overcrowding of spots) on the diagram of velocities field in the area $X=(dx \cdot N)/4$ and $X=(dx \cdot N)3/4$. It should be noted that the marginal area of the slot is a permanent disturbance source for the generation of Alfven waves, ending when the value of the opening slot becomes equal to the half – width of the plate. The results of the calculations show that in the phase of acceleration the relatively low calculated value of the plate deflection is provided, if the Alfven wave has the time to pass the whole width of the plate.

4. The two - dimensional electromagnetic model of the plate launch taking into account non - linear field diffusion

The 200mm liner plate acceleration in a big machine is different to the above considered in the next three things: 1. a comparatively small length of the acceleration length, thus the Alfven wave does not manage to run the whole width of the plate; 2. an aspect ratio d/h in this case reaches 100 thus intensifiying the role of marginal effects; 3. a special emphasis should be placed on the simulation of the compression process, resulting in high current density and magnetic flux density $B_{max} \sim 100Tl$.

Due to non – uniformity of the currents distribution and the accelerating field typical for strip line edges, there is no warranty that the accelerated plates will move in a plane – parallel way at this choice of a flat geometry. The achievement of high output power at the compression of the flow requires small distortions of the liner flat geometry, since the transformation of the liner kinetic energy into the magnetic energy must occur as simultaneously as possible on all surfaces of a closing slot. The value of deflections from a plane, Δx, must be smaller than the characteristic length X_{ret} of the plate slowing down by the compressed magnetic flow. Supposing the launch length of the plate is X and the gain factor of power for device is $K_p=50$, we obtain $\Delta x<X_{ret} \approx X/K_p=2mm$. Seemingly, it is possible to reduce distortions of the plate shape by profiling an inductor plane, making it convex, as shown in Fig.1 (or with the inverse curvature), and make an initially non – uniform slot. Other measures could be undertaken.

On the other hand, due to the same reasons the liner shape perturbations, which occur during acceleration, will have the tendency to restore a shape in the slowing down phase. However, the joule heating of conductors renders the significant influence on these processes, and effects of joule heating are different in the acceleration and the slowing down phases.

That is why there was stated the problem, and specified the task of the software development for the numerical simulation of electromagnetic launch of flat plates and compression of magnetic flux in the output circuit of pulsed power amplifier before the fabrication of an experimental device.

304
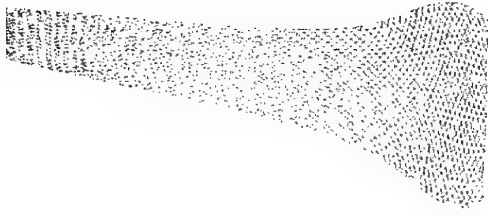
Fig.5. The finite – element grid in the field of the liner at the time moment $t = 0.09377$.

Fig.6. The distribution of H_y component at the time moment $t = 0.1085$.

In model [6] it is assumed that the liner material is incompressible conducting liquid. On each liner particle the Lorentz force, hydrodynamic and viscous pressures act. Thus, in connection with characteristic phenomena of transport, the calculation grid is taken to be changing its shape in accordance with the viscous liquid flow. The self – consistent problem for finding magnetic fields and currents distribution in conductors and in space (see also [7,8]) was solved, taking into account the non-linear resistance caused by the joule heating by the currents in an inductor and in a liner.

The calculation grid in the zone of the liner, presenting its shape at the respective moment of time at low assumed viscosity (kinematic viscosity 0,01), is shown in Fig.5. It is seen that there is an essential distortion of the initial rectangular shape of the liner. Such a distortion is accompanied by the transport of the liner material together with the magnetic field diffused in there. In Fig.6, the level lines of H_y component show the presence of areas with the increased strain in the liner.

It should be noted that the real ratio of the liner dimensions for better graphic presentation is changed in the figures. True liner sizes on abscissas and ordinates axis are distinguished approximately in 50 times.

When the viscosity is increased to 0.1, the characteristic shape of ends of the accelerating plate changes. This is shown in Fig. 7.

Fig.7. The finite – element grid in the field of the liner at the time $t = 0.127$.

While in the previous two cases the widths of an inductor and liner were equal, and that led to the higher acceleration of the ends, the increase of the liner width to 1 cm resulted in the fact that the direction of deflection had a reversal in flight. It is clearly seen in Fig. 8, where the density of the Lorentz force distribution is shown as well.
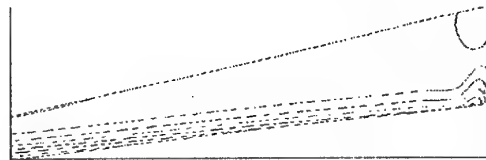
Fig.8. The Lorentz force F_{1x} component distribution in the liner at the time $t = 0.1502$.

In general, the presented results realistically agree with an expected qualitative picture of flat liners acceleration up to the moment of full stop of converging parts (edges or middles).

This stage of the software development, which is connected with the fact of the reversal of a velocity vector is currently under testing and adjustment.

5. Conclusion

The results of the studies of special features of acceleration of flat plates with the current are presented. The qualitative picture of processes for the duration of acceleration of 50-100μsec and the nature of the plates deformation on edges of the equivalent strip line are determined. Further works will concentrate on the actual experimenting with acceleration of broad plates (200mm) and the analysis of special features of fast (2-3μsec) compression of a magnetic flux at the magnetic flux density about 80 Tesla, at which case the processes of diffusion of the field play the main role.

305

References

1. V.K. Tchernyshov, V.N. Mokhov, A.M. Buyko et al. The main types of explosive – cumulative generators and their application. // In Megagauss and megaamper impulse technology and applications. V.K. Tchernyshov, V.D. Selemyr, L.N. Plyashkevitch (Ed.). V. 1, Sarov, VNIIEP, 1997. In Russian.

2. V.G. Belan, S.T. Durmanov, I.A. Ivanov, V.F. Levashov, V.L. Podkovyrkov. The compression of magnetic flow by multi – layer liner. // In Superhigh magnetic fields. Physics, technique, application. V.M. Tytov, G.A. Shvetcov (Ed.). M., Nauka. 1984. P. 218-220. In Russian.

3. S.G. Alykhanov, V.P. Bahtin, D.A. Toporkov. Some particularities of manufacturing of superhigh magnetic fields by means of Z – pinch liner. // In Superhigh magnetic fields. Physics, technique, application. V.M. Tytov, G.A. Shvetcov (Ed.). M., Nauka. 1984. P. 213-217. In Russian.

4. A.P. Lototsky. The physical mechanisms of magnetic energy output from inductive storage in power impulse systems. Doctor in pHs. and math. tes. Abstract. IVT of RAS, 2000. 55 p.p. In Russian.

5. H. Alfven, K. – G. Felthammar. Cosmic electro - dynamics. M. Mir. 1967. 260 p.p. In Russian.

6. M.P. Galanin, A.P. Lototsky, V.F. Levashov. The calculation of electromagnetic acceleration of flat plates in the laboratory magneto - cumulative generator. // prepr. of KIAM of RAS. 2001. № 3. 30 p.p. In Russian.

7. M.P. Galanin, Yu. P. Popov. Quasi - stationary electromagnetic fields in non - homogeneous media. Mathematical modelling. Moscow, Nauka, Fizmatlit, 1995, 320 pp., in Russian.

8. M.P. Galanin, A.P. Lototsky, Yu.P. Popov, S.S. Khramtsovskii. Numerical modelling of spatially three - dimensional phenomena at electromagnetic acceleration of conducting armatures // Mathematical modelling. 1999. V. 11. N 8. p.p. 3 - 22. In Russian.

57. POWER-INTENSIVE PLASMA FORMATION INVESTIGATION

V.A.Epurash, A.V.Krasilnikov
Central Research Institute of Machine Building
141070, Korolev, Moscow Region, Russia

Abstract. The experimental investigation of power-intensive plasma formation (PIPF) with energy up to 1Mdj is conducted. The exposition of a designed construction of a pulsing plasma generator of an erosive type and of the power supply are given, and the results of experiments are presented. The exotic PIPF properties are explored. The new phenomenon - ability of copper as a result of powerful thermal and electromagnetic action to gain ferromagnetic properties is revealed.

For obtaining PIPF with total energy up to ~1Mdj the construction of a pulsing plasma generator designed on the basis of the longitudinal discharge of an electric arc in the channel from a gas-making material. As the prototype the device, presented in [1], and usual way of an ignition of a longitudinal arc "cathode - anode" in a plasma generator of a stationary type by a copper thin wire was used.

The construction of a pulsing plasma generator is shown in a Fig.1, where:

The relations of the sizes of the bush internal passage 1, the minimum anode diameter d_a were selected from a requirement: $l/d=5\div6$; $d_a/d=5\div6$, where d - the discharge channel diameter.

To make airtight of discharge gases the cathode fastening (5) from the back side realized with the help of the housing - hoop thread and back cover of the cathode fastening(16) with bolts (15). The igniting wire (9) was fixed on the cathode with the help of a copper tip (15) and bolt (6), and on the anode by a bolt of wire fastening (12). The fastening of current leads (2) was yielded from the back side of a plasma generator (for elimination the exhaust plasma hit) by bolts (10) on the cathode and bolts (11) on the anode.

The anode (3,4), arranged with an obverse of installation, consists of a steel disk to an exterior diameter of 170 mm. and interior one of 50 mm. The fastening of the anode (3) to a plate is yielded by bolts (11) and is joined to a replaceable ring (4) by thread. The fixation and fastening of the gas-making bush (8) was yielded with the help of an exterior thread and follow-up by cover (17). The cathode tip (15) fastened in a bolt (6) by thread and had an output diameter of $6\div10$ mm relevant to a passage diameter of the bush (8), in which it entered.

The making airtight of discharge gases follow-up was executed by a strong rubber spacer (14), pushed by a bolt (6). The linking of the anode replaceable ring (4) and the housing - hoop (7) was yielded by a thread, that reinforced an output part of the housing - hoop.

As a power supply the drosselling transformer including following leading particulars was applied: a saturation drossel, power transformer having six voltage steps, and semiconductor rectifier. A rated power of the transformer was 16500 kVA, circuit voltage - 10000V, output voltage -1250, 2500, 3750, 5000, 6500, 8600V.

The load current was regulated by change of saturation drossel guidance current. The short-circuit impedance of the drosselling transformer, reduced to the party 10000V, is equal 1.35Ohm.

Feature of the drosselling transformer is that in the first time of engagement the drossel magnet are saturated, its induced drag is not enough, that predetermines a considerable current throw. The transient process presents aperiodic signal dieing away, formed by summarizing of the first and sixth harmonicses of frequency 50Hz.

The amplitude of the first peak depends on a guidance current a little. The ratio of the subsequent peaks amplitudes to first is increased at increasing of a guidance current. The transit time depends on a loading quantity, but does not exceed 0.2s with at a loading resistance close to null. The shape of curves of transient also depends on a guidance current as a result of a phase change and amplitude of their component harmonics.

At realization of experiments one of four drosselling transformers was used, the step with voltage output 3750V. A guidance current I_g was chosen equal 0, 400 and 600V. The current cutout implemented by the operating cutout on the side 10kV, approximately through 0.2s after switching on.

Current and voltage during experiments were registered by an oscillograph HO71 with velocity 250cm/s. In Table 1 the maximum and mean parameters after initial runaways of a current and voltage for six experiments are shown. Besides in the table the duration t and the total discharge energy Q_Σ are shown.

307
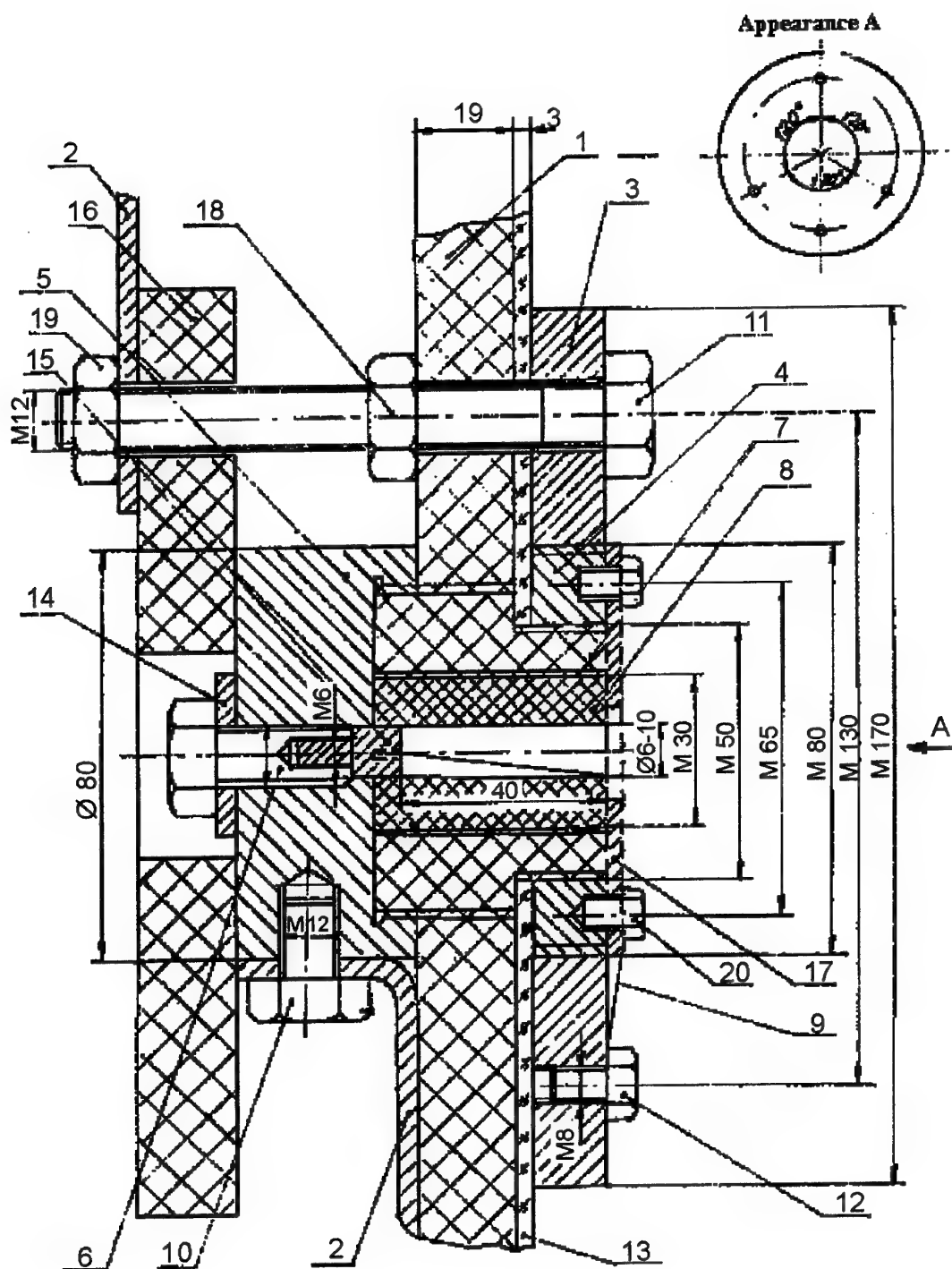
Fig.1. Impulse plasmotron construction.

1 - insulation plate (organic glass), 2 - current leads (copper), 3 - anode (steel), 4 - replaceable ring of the anode (copper), 5 - cathode (copper), 6 - bolt of igniting wire fastening (steel), 7 - housing - hoop (organic glass), 8 - replaceable gas-making bush (organic glass), 9 - igniting wire (copper), 10- bolts of the cathode fastening (steel), 11- bolts of the anode fastening (steel), 12- bolts of a wire fastening (steel), 13- walls of the exterior channel working section (organic glass), 14- spacers of compression (rubber), 15- tip (copper), 16- back cover of the cathode fastening (organic glass), 17- forward cover of the bush fastening (copper), 18- nuts of the anode current lead fastening (steel), 19- nuts of a back cover fastening (steel), 20- bolts of a cover fastening (steel).

Table 1

No. exp.	I_y A	I_{max} A	U_{max} V	I_{cp} A	U_{cp} V	t s	Q_Σ Mdj
232	0	9000	1000	410	560	0.180	0.10
233	600	8300	1130	1100	1040	0.174	0.40
234	600	7150	1030	1500	1200	0.168	0.46
235	600	11490	753	1300	660	0.176	0.30
236	400	8750	1160	850	660	0.171	0.24
237	600	6050	1030	1380	565	0.164	0.30

The PIPF filming realized by a movie camera KCK-1 with velocity 48 frame/s and movie camera CKC-1-M with velocity 700 frame/s. By handling photos was spotted, that the PIPF exit velocity from the channel makes ~ 100m/s, and apart 1.5÷2m are reduced up to 30÷40m/s.

The PIPF sizes up to a separation makes in length of ~ 1m and 20÷30 cm in a diameter. At the exit moment PIPF has the shape of the sharpen cylinder in a diameter ~ 8cm with rather legible outlines in a frontal part, and a kern - centre punch in the diameter ~ 2cm inside is was transparent.

After a breaking of a jet the PIPF has the shape, close to spherical dimensioned ~ 0.4÷0.5m, rough outlines of a contour in stern and rather legible in a nose part.

Owing to formation PIPF in air the smell of ozone apart up to 5÷10m from a plasma generator was felt.

Inside a plasma generator bush during the discharge the considerable pressure developed, therefore the outbreak of gas near to the cathode and arcuation of an insulation plate by width of 19 mm implemented. The process of PIPF formation and disappearance in all experiments was escorted by a sharp sound crack.

In a series of experiments the interaction of a PIPF jet with different screens manufactured of stainless non-magnetic steel, magnetic steel and press-spahn was studied. As well as in operation [1] the considerable difference in PIPF interaction with conductive and non-conducting materials was revealed. On steel screens a dimple up to ~ 0.3mm in diameter of ~ 20mm was formed, and on a reverse tracks a blueing in diameter of ~ 100mm, that indicates a heating up to temperature more than ~ 1000K. On a press-spahn the concentrated centers of interaction of the PIPF jet were not watched, the surface was plated with equal gray - black color without charring.

For definition of a PIPF electron concentration the procedure grounded on a double electrostatic probe was used. The probes were made of a carbon material and represented hemispheres of radius 10mm, and center distance of probes was 25mm. On measuring probe a

negative potential - 9V a rather basic probe was moved, that allowed to work in a mode of an ionic saturation current.

The measuring probe placed on one axis with the plasma generator erosive bush apart 400mm from it. The probe holder is made of fluoroplastic and fastened on a dielectric (dry tree) plate.

The measuring of electron concentrations at the presence of strong electromagnetic fields has demanded padding safety precautions for a decoupling of a metering circuit from "ground". With this purpose the probe currents amplifier with the optical isolator grounded on usage of a optron pair was applied. The designed amplifier, except for this function, moved simultaneously stabilized potential on a double electrostatic probe. The signal from the probe currents amplifier, was registered on the magnetic recorder and was handled through a remembering oscillograph C9-8.

Previously, before realization of experiments, the amplifier calibration was yielded. With usage of calibration the translation of the registered voltage drop, recorded on the magnetic recorder, in values of a probe current implemented.

At recalculation of an ionic saturation current in an electron concentration, it was supposed, that the probe shaped of a hemisphere, is streamlined by a subsonic flow with formation a boundary layer on the probe surface.

The observed dates in two experiments are submitted in Table 2.

Table 2

No. exp.	Signal length s	I_3 mA	N_e cm^{-3}
240	0.264	64.5	$4.94 \cdot 10^{14}$
242	0.256	76.6	$5.86 \cdot 10^{14}$

During realization of experiments some of a plasma generator parts were exposed to fracture under activity of extreme physical properties of electric discharge. So, for example, the width of the organic glass bush with an internal passage of a diameter 6÷8mm varied on quantity > 1mm, copper electrodes and igniting copper wire smelted.

The analysis of these phenomena has allowed to find out unexpected effect. As a result of a smelting of copper electrodes , igniting thin copper wire and the actions of powerful electromagnetic fields inside the erosive channel were formed copper fragments by the size ~ 0.1÷5mm and possessing ferromagnetic properties (ones are dragged up to a magnet). The basic

309

material has no ferromagnetic properties. The acquired copper fragments ferromagnetic properties are maintained within already 8 years after realization of the first experiments.

References

1. Р.Ф.Авраменко, Б.И.Бахтин, В.И.Николаева, Л.П.Поскачеева, Н.Н.Широков. Исследование плазменных образований, инициируемых эрозионным разрядом. Журнал технической физики, 1990, том 60, в.12, с.57-64.

58. ABOUT THE BASIC PARAMETERS OF THE PLASMOID STRUCTURES

A.S.Paschina, V.I.Nikolayeva
Scientific Research Institute of Radio Instrumental Devices,
Leningradsky pr., 80, Moscow, 125190, Russia
E-mail: *niirp@online.ru*

Abstract. The model of the plasmoid structures formation, corresponds to a quantum-field problem of the formation of the wave packet in 4-dimensional closed hyperspace, is considered. The formation of de Broglie wave packet is stipulated by the space-time phase displacement operator's action on conjugate (relative of the reverse of time) components of the wave field of electrons.

In a quasi-classical approximation, the case relevant to symmetric time phase displacement is surveyed. The structure of a wave packet appears to be an equivalent to the coherent state of electrons with equal and opposite impulses, concentrated in a narrow energy interval. The total energy of a wave packet appears to be much more the energy of time phase displacement, initiated its formation.

The parameters, obtained for a wave packet (characteristic size, energy of formation, total energy etc.), are agreed with experimentally observed parameters of the plasmoid structures.

1. The necessity of the quantum approach for the plasmoid structures explanation is stipulated, first of all, by the numerous experimental data's showing the defining role of macroscopic quantum processes in their formation, observed properties, interaction with substance and subjects etc. In the considerable part of articles, devoted to a mentioned problem, next conception is dominated: the plasmoid structures are the electronic formations generated as a result of particular physical processes. Thus a spectrum of viewed processes and their further physical interpretation are depend of the initial backgrounds of the concept, in which basis the interpretation of the electron's wave function, tightly bounded with a problem of the "wave-particle" dualism, is lay.

There are, at least, two points of view on this problem. One of them grounded on the probability interpretation of a wave function and the conception of a local electron. The second point of view is ground on the idea of a nonlocal electron, to which the waves of a substance (de Broglie waves) are correspond. In the latter case, the processes, bounded with the change of phase relations of the electron's wave function, are on the foreground.

2. The wave nature of the electron and bounded with it the opportunity of nonlocal interactions is a consequence of the quantum theory fundamentals, which has revealed the primacy of a wave function conception, its space-time evolution for explanation of observed processes. The relativistic generalization of a quantum theory gives the necessity of specification the concept of a wave function, instead of which the more adequate concept of a wave field is introduce. The state of a wave field is describe by Laplace-Beltramy generalized equation:

$$\Psi = \frac{1}{\sqrt{-g}}\partial_\mu g^{\mu\nu}\sqrt{-g}\partial_\nu\Psi = \frac{m_0^2 c^2}{\hbar^2}\Psi ,\qquad (1)$$

where Ψ - a wave field; $g^{\mu\nu}, g$ - a metric tensor and its determinant, accordingly.

The general solution of Laplace-Beltramy equation looks like

$$\Psi = \Psi_+ + \Psi_-^+ ,\qquad (2)$$

where Ψ_+ - the operator of birth of a particle, described by this field, and Ψ_-^+ - the operator of birth of its antiparticle, to which de Broglie wave packets, as is known, are compared.

The wave packet formation, which corresponds to the general solution (2), is stipulated by the action of the space-time displacement operator $\left(\dfrac{1}{\sqrt{-g}}\partial_\mu g^{\mu\nu}\sqrt{-g}\partial_\nu - \dfrac{m_0^2 c^2}{\hbar^2}\right)$ to unperturbed components of a wave field, conjugate relative of the reverse of time. Each of unperturbed components of a field can be submitted as a Fourier series expansion on a complete gang of eigenfunctions in 4-dimensional space with a volume element $\sqrt{-g}\,d\Omega$. From this point of view, the general solution (2) can be considered as a result of an interference of the time-versed components of a wave field, each of which has been acted by the space-time displacement operator.

As is known, in a quantum electrodynamics the expansion of a wave field in a series on eigenfunctions gives the problem of "divergences".[1] It is simple to note, that it is a result of the selection of the space volume, occupied by a field, which aspires to perpetuity in

---

[1] On a fair note of the authors [1] "this is owing to the lack of a complete logic closure of the existing theory" (p.25).

311

the Universe with the Euclidean metric. It is obvious, that for spaces with closed geometry, the similar problem does not arise.

The space of a hypersphere is one of such spaces [2], infinite in direction, but having restricted volume. In a wave equation (1) the properties of space are determined by a metric tensor $g_{\mu\nu}$, specifying "the boundary conditions" on a surface of a hypersphere, that allows, basically, to completely determine a field, relevant to waves of substance (see, for example, [3], p.p.62-73).

Similar reasons were put on a basis of the concept, formulated by R.Avramenko, about existence of a natural background of an electronic Bose-condensate [3] – a wave field of electrons filling the Universe. This concept fills by the concrete physical content the existing ideas about a nature of a physical vacuum, which follows from the quantum-field theories [4]. With the account (1), (2) a ground states of an electronic wave field can be determined, as the state, at which the space-time phase displacement of the conjugate field components is absent. In this case, the high harmonics of Fourier-expansion of the conjugate field components (except of a harmonic with n=0) are mutually cancelled. The energy of a ground state is determined by the zero term of expansion, which is, within a constant factor, equal to m_0c^2.

The fact, that the wave field occupies the volume of the Universe, cause the necessity of the supposition about the strong connection of processes in the conjugate points of 4-hyperspace, which reflects the principles of symmetry in a quantum theory (CPT-invariance, etc.), representing a well known conservation laws. It is possible to see, that the strong connection is present in general solution (2), where to the operator of birth of a particle there corresponds the operator of birth of an antiparticle, which concerns to a conjugate 4-hyperspace area. In another words, the formation of object and antiobject in the closed geometry of a hypersphere can be considered as a result of a self-focusing of the waves of a substance. This is automatically solved the problem about a wave packet stability, bounded with de Broglie waves dispersion.

The opportunity of existence of standing waves of substance in requirements of the closed geometry of the Universe allows concretizing the opportunity of connection of microscopic objects (fundamental particles) with the processes in the Universe. Within the framework of the considered approach, it is appear, that the processes of formation and evolution of the wave packets (including fundamental particles) are accompanied by the adequate change of the wave field state. Account of the restricted volume of the Universe (and, hence, of the restricted number of the terms of Fourier-expansion of a field components) spread this change to all volume of 4-hyperspace. Somewhat it is possible to consider the change of a state of a wave field as "a reaction of a physical vacuum" on perturbation, bounded with the formation of a wave packet (formation of area with heightened concentration of a field). It is obvious, that in a considered situation the approach of small perturbation ([2], p.71), i.e. when the perturbation action on a field can be neglected, appears to be inapplicable for as much as small perturbations. Accounting the quantum character of a wave field, the minimum value of perturbation is determined by the fundamental constants, characterizing a sectional type of a field, such as - a Plank's constant h, the mass of the field carrier (electron) m_0, gravitational potential c^2 etc.

It is obvious, that the nonlocal character of connection of a wave packet and state of a wave field should be taken into account in the equation of a wave field state (1), that is necessary for security the conservation laws, for example, energy-impulse conservation.[2] It can be reached in several ways. For example, if to assume, that the change of a state of a wave field (reaction of a wave field to perturbation) expresses in the change of the space-time metric, there is obvious a necessity of the account of this connection by the relevant components of a metric tensor, which is included in a wave equation (1). For example, the time component of a metric tensor, featuring the influence of the time displacement operator, can be submitted as $g_{00}=1-\varphi/c^2$, where $c^2 = \gamma M_U / R_U$ - gravitational potential of the Universe, and φ - scalar potential relevant to the time displacement operator (here γ - a gravitational constant, M_U, R_U - mass and radius of the Universe, accordingly).[3] This supposition means the dependence of the spatial metric (and, hence, of gravitational field) from a state of a wave field. From this supposition follows, that any change of a state of a wave field should be accompanied by gravitational effects (and on the contrary).

3. As an example we shall consider the properties of a wave packet generated as a result of the action of time displacement operator to conjugate components of a wave field. On the basis of the Ehrenfest theorem [4, 5] the field equations

[2] For satisfaction of the wave equation (1) to the equation of a condition of a wave field, it is necessary to satisfy the conservation law of energy-impulse. The given requirement can be taken into account by additional conditions, or immediately in the equation - by the account of "reaction of a wave field" in the terms, defining boundary conditions (the metric of 4-hyperspace).

[3] The respective changes should touch also the spatial components of a metric tensor.

(1) can be reduced to classical equations of motion of a particle if to consider, that energy and impulse of a particle correspond to root-mean-square of the relevant operators

$$<E>^2-<p>^2c^2=m_0^2c^4, \qquad (3)$$

where $<E>=m_0c^2/\sqrt{1-\beta^2}$ - total energy of a particle, relevant to the time displacement operator,

$<p>=m_0c\beta/\sqrt{1-\beta^2}$ - impulse of a particle, relevant to the spatial displacement operator. Parameter $\beta=v/c$ is the energy performance of the spatial and the time displacement operators.
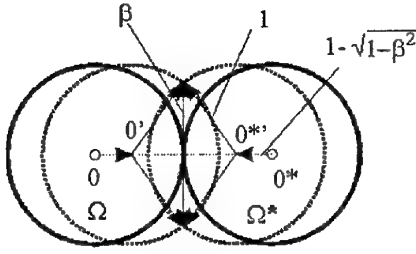
Fig.1.

It is convenient to use the energy representation of 4-dimentional space of a hypersphere with a unit radius of curvature to be equal to the gravitational potential c^2 (Fig.1). Thus, the radial direction corresponds to the action of the time displacement operator, and the tangential direction – to the action of the spatial displacement operator.

The equation (3) is establishing the strong connection between the time and the spatial phase displacements. The restrictions, concerning to the classical case, allow to consider only symmetric processes, to which there is correspond the identical change of the "interior" Ω and the "exterior" Ω^* hypersphere volumes. Thus, the "interior" and the "exterior" volumes are corresponding to conjugate components of a wave field. The symmetric time phase displacement can be conventionally presented as the change of a distance between centers 0 and 0* of the "interior" Ω and the "exterior" Ω^* volumes with their simultaneous squeezing (tension). If we use the potential, relevant to the time phase displacement, to be equal to $1-\sqrt{1-\beta^2}\approx\beta^2/2$, the equivalent change of a hypersphere surface, corresponds to spatial phase displacement, is β.

Comparing the root-mean-square values of the time and the spatial displacement operators to the corresponding changes of the sizes of a hypersphere phase volume, we gain the parameters describing a wave packet.

A. Parameters relevant to the time displacement operator:

• bandwidth of a wave packet

$$h\Delta\nu\cong m_0c^2(1-\sqrt{1-\beta^2})\approx m_0c^2\beta^2/2 \qquad (4)$$

• size of a spatial domain, occupied by a wave packet

$$r_B=c/\Delta\nu \qquad (5)$$

• electromagnetic wave length r_m, which corresponds to the interaction of electrons inside a spatial domain r_B

$$r_m=e^2/2\varepsilon_0h\Delta\nu \qquad (6)$$

• number of electronic energy levels of a wave packet n_S, relevant to time phase displacement (number of the terms of a wave field Fourier-extension), gained from a requirement $n_S\cdot h\Delta\nu=m_0c^2$

$$n_S=1/(1-\sqrt{1-\beta^2})\approx2/\beta^2 \qquad (7)$$

B. Parameters relevant to the spatial displacement operator:

• impulse, defined as a phase gradient of a wave function

$$\hbar\nabla\theta=mc\beta \qquad (8)$$

• number of impulse electronic levels n_p, difiniendum by a requirement $n_p\hbar\nabla\theta=mc$

$$n_p=1/\beta \qquad (9)$$

In a considered case, concerned to symmetric squeezing of phase volume of a hypersphere, the total amount of all tangential impulse components (8) on a hypersphere surface should be equal to zero. The situation appears to be the equivalent to the coherent state of the paired electrons on the Fermi surface (Fig. 2), with equal and opposite impulses mcβ, concentrated in the energy range, defined by the expression (4). It is simple to see, that the total number of electronic levels in an energy interval (4) is equalz

$$n_\Omega=n_p n_s=1/\beta(1-\sqrt{1-\beta^2})\approx2/\beta^3 \qquad (10)$$
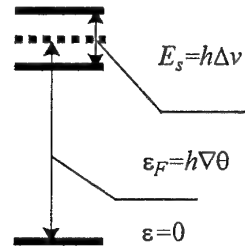
Fig.2.

The total number of electronic levels n_Q defines the total energy of a wave packet. It is obvious also, that the amount of total energy to be in n_Q/n_S times greater, than the energy of time phase displacement (4), initiated process of a wave packet formation.

It is obvious, that a state, relevant to the time phase displacement, and surface state are conjugate and, in particular sense, are orthogonal. Conjugation of states means, that any change of energy of time phase displacement is accompanied by adequate change of energy of a surface state (total energy of a wave packet). As the energy values of the relevant states are essentially various, the cross correlation of the indicated states will be determined by the minimum value, i.e. the value of the time phase displacement energy. In this sense, the considered states are orthogonal. Another point of view, why the indicated states are orthogonal, is that these states refers to various components of a metric tensor $g_{\mu\nu}$, namely: the state, relevant to time phase displacement, refers to a time component, and surface state - to a spatial component of a metric tensor. It means, that the change of the parameters of the state, relevant to the time phase displacement, results the major changes of parameters of the surface state, than it takes place in the inverse situation.

$r_B = c/\Delta\nu$

$\xi = 1/\nabla\theta$

$\varepsilon_F = h\nabla\theta$

φ_{inter}　　φ_{exter}
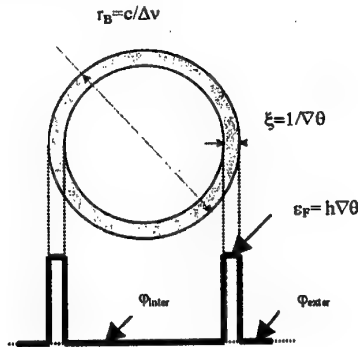
Fig.3.

Connection between the energy and the geometrical parameters of a wave packet is determined by the relations (4), (5), (8). To a case of symmetric phase displacement a spherical spatial configuration of a wave packet (Fig.3) with the reference size of r_B (5) is correspond.[4] Thus the size $\xi = 1/\nabla\theta$, defined by the relation (8), which is traditionally compared to de Broglie wavelength [5], characterizes a spatial domain, in which the

energy of a wave packet is concentrated. It is natural to assume, that the abovementioned spatial domain is concentrate on a wave packet border and represents a high-energy shell.[5]

Thus, the spatial configuration of a wave packet is somewhat similar to the structure of a potential pit with the wall height, defined by the expression (8). The feature of such spatial configuration is that the high-energy shell on border of a package, which separates the interior space of a package from the exterior space, corresponds to a coherent electronic wave. It does not allow connecting uniquely the potentials of exterior and interior space, relevant to an initial energy level. The initial levels of potentials are not in strong interrelation and generally can be defined by the processes, which take place in the interior and the exterior areas separately. It is obvious, that such configuration of the electronic wave field can exhibit a variety of properties, the small number of which is observing in natural and laboratory plasmoids.

The potential structure of a wave packet, probably, supposes the processes, bounded with "entrapment of mobile electrons", for example, into the interior area, with the energy spectrum, corresponding to Fermi distribution. As was shown [6], the requirements of formation of condensed fermi-state in the interior package area are determined by the balance of energy of a surface state and energy of free electron state. The difference of a surface state energy and the free electrons energy can be considered as the surface-tension energy. Thus the positive values of the surface-tension energy corresponds to the condensed state - such as fermi-liquid, and negative values – to the state of fermi-gas [6].

4. The above-defined parameters of a wave packet allow considering the correspondence of the processes of the wave packet formation to the observed processes with plasmoid structures participation.

The energy parameters of a wave packet, namely: the energy, relevant to time phase displacement, the energy of a surface state, and the energy of a surface tension - are the basic criteria of the plasmoid structures stability to exterior perturbations. It is obvious, that the maximum efficiency of a wave packet interaction with exterior perturbations can be reached in the case, than the energy parameters of exterior perturbation and one or more of the relevant parameters of the

---

[4] It is simple to see, that the size of a wave packet is correspond to Pippard coherence length in the theory of a superconductivity $r_B = hc/[mc\beta^2/2]$, where $mc\beta^2/2$ is correspond to "a breadth of a energy gap".

wave packet are coincide, i.e. in resonance conditions. Thus, the influence degree on a wave packet parameters and its stability should depend of a type of exterior perturbation.

In the requirements of laboratory experiments the energy parameters, describing exterior action, essentially exceed the energy, relevant to time phase displacement. Therefore, the basic stability criterion of a wave packet in experimental requirements is the structure (and energy) of the surface state.

First of all the experiments deal with mechanical, contact, thermal interactions, and interactions caused by the scalar and the vector potentials.

The mechanical interaction, first, results in the change of parameters of a surface state. The reaction of a surface state can express in the change of the internal-impulse's phase relations of a wave function, describing a surface state that is equivalent to the redistribution of the plasmoid surface energy. The expression of such redistribution is the occurrence of the impulse component, the value and the direction of which is such to cancel the influence of exterior action.

The most brightly mechanical interactions, bounded with the change of the internal-impulse's phase relations, are exhibited during the interaction of the plasmoid structures with a stream of gas. In this case, the distribution of such structures is observed to the direction of a perturbing source, i.e. against the direction of a stream [6]. In the plasma aerodynamic experiments the occurrence of a "canceling" impulse results in the diminution of a drug of a streamlined body.

The contact of the plasmoid structures with substance should depend of physical properties of the contacting substance in a strong degree. First of all there are the properties, defined the electronic structure of substance - electrical conductivity, a work function, Fermi level etc. The contact phenomena, obviously, should be accompanied by smoothing of electrochemical potentials of the contacting substance and wave packet. For a wave packet the electrochemical potential (Fermi level) is determined by a relation (8). It is known, that the process of smoothing of electrochemical potentials is accompanied by redistribution of electrons between the contacting objects ("electronic reservoirs"). For a wave packet the "impeding breadth of a barrier", relevant to energy of time phase displacement, is much less than a contact potential difference on a demarcation, which value, basically, corresponds to a work function of substance. Therefore, the process, bounded with redistribution of electrons, should take place, practically, while plasmoids contact with all materials. The intensity of the

process of redistribution of electrons is defined by the extent of contact area.

In experiments, the contact phenomena are express in selective interaction of plasmoids with a substance. So, for plasmoids generated by the erosive discharge (see p.p.212-240 in [3]), the contact with metal is accompanied by the plasmoids fracture with liberation of energy in local area of metal. The energy influence of a plasmoid to the insulator surface is expressed much less.

With reference to a gas medium, the interaction of a wave packet with atoms or molecules results in redistribution of their electronic structure (structure of electronic shells, polarization etc.). It can be accompanied by the processes of ionization, excitation of atoms and molecules, dissociation of molecules etc. that is observed experimentally. It is necessary to note, that the secondary effects, bounded with high-level plasma-chemical reactions, formations of associates etc., can also take place on a surface of plasmoids [7].

It is possible to consider the interactions with thermal oscillations of medium (gas, fluid, crystalline lattice) as an exchange of energy between oscillators, one of which corresponds to a medium, and another – to a surface state, and also the state, relevant to time phase displacement. The essential difference of the energies (and relevant resonant frequencies) of indicated states results that the interaction with these states should correspond to different frequency ranges.

As a stability criterion of a coherent state to thermal fluctuations a relation between the Debye frequency (or relevant temperature) and the frequency of thermal fluctuations is usually used, i.e. $h\nu_D > kT$. It seems, that more exact is to use a criterion, which characterizes a degree of interaction of oscillators. The mutual correlation function of oscillators, which value is restricted on the reasonable level, can be used as such criterion i.e.

$$\chi = \frac{1}{\sqrt{E_1 E_2}} \int_{-\infty}^{\infty} S_1(\omega) S_2(\omega) d\omega < 1/Q \qquad (11)$$

where $S_1(\omega)$, $S_2(\omega)$ – the spectral density of the relevant oscillators, E_1, E_2 – the energy of oscillators, Q – parameter, having sense of the minimum quality factor of system.

For coherent oscillators the requirement (11) becomes simpler

$$(1/Q)\omega_1 < \omega_2 < Q\omega_1 \qquad (12)$$

It is obvious, that for plasmoids of the macroscopic sizes in a wide range of requirements the thermal interaction will render the influence to a surface state. This deduction follows from that the energy value, relevant to time phase

315

displacement, appears to be comparable with a thermal energy of oscillations (hundred degrees of a Kelvin) only then, when the reference size of a wave packet is of an order of interatomic distances [6]. Therefore, for macroscopic plasmoids (the order of millimeters – ten's centimeters), gained in experiments, the level of temperature, corresponds to the plasmoid destruction, is ~1000K.

A most strong influence to a wave packet should be rendered by fields of scalar φ and vector (convectional) A_k potentials. According to well-known relations - $h\partial\theta/\partial t=e\varphi$ and $h\nabla\theta=(e/c)A_\kappa$ - these fields results in the amplitude-phase modulation of the electron's wave function. As against of the mechanical and the contact interactions, rendering the local influence to a wave function of a surface state, the action of scalar and vector potentials is integrated. Bounded with it the restructuring of a surface state, which is, according to a principle of a minimum of a free energy should correspond to the allocation of the potential's field, generally accompanied by the change of a space-time configuration of the wave packet. Thus, the action of the scalar potential field results in non-stationary processes, and the vector potential field – in the stationary processes.

In the experiments, the influence of vector potential is exhibited in the change of a spatial configuration of plasmoids. For example, in known experiments with plasmoids, generated by an erosive discharger [3, 8], the influence of vector potential of convectional currents expresses in the change of length of a plasmoid. The construction of a discharger is those, that there is a site between electrodes, that is perpendicular to the axes of the discharge channel. This site is a source of the vector potential of convectional currents. In experiments, the dependence of a plasmoid length from the discharge current etc. is detected. The similar influence of the convectional vector potential was also observed in the experiments with a dusting of a torch discharge [6].

The range of electromagnetic radiation of plasmoids is determined by the energy values of the state, relevant to time phase displacement, and the surface state. Thus the energy, relevant to time phase displacement, determines a low-frequency level of electromagnetic radiation, and energy of a surface state - high-frequency level. For the majority of laboratory plasmoids the high-frequency level of electromagnetic radiation

corresponds to an optical range. Therefore, in the optical range of the plasmoids radiation there is a line, which wavelength coincides with energy of a surface state (8), i.e. $\nu{-}c/\xi$ (see, for example, [3,8]) and corresponds (depending on the size of plasmoids) to the ultraviolet radiation.

5. Thus, the surveyed approach allows to reveal a nature of the processes, responsible for the plasmoid structures formation and their properties, which are observed in experiments, and to estimate their basic parameters (the formation energy, total energy amount of a wave packet, reference sizes etc.).

Within the framework of the offered approach, it is appear, that the formation energy of a wave packet is much less than its total energy.

The surveyed physical mechanisms, responsible for the wave packet formation, and which follows from the quantum approach, allows from new positions to approach the problem of the high-performance plasmoid generators design, and also to the methods of the experiments statement.

References

1. Berestetsky V.B., Lifshitz E.M., Pitaevski L.P. Kvantovaya electrodynamika. M.: Nauka, 1989. 728 p.
2. Landau L.D., Lifshitz E.M. Teoria polya. M.: Nauka, 1988. 512 p.
3. R.F.Avramenko. The Future is Opened by a Quantum Key. M.: Chemistry, 2000. 352 p. (in Russian).
4. Bogolyubov N.N., Shirkov D.V. Kvantoviye polya. M.: Fizmatlit, 1993. 336 p.
5. Blokhintsev D.I. Osnovi kvantovoj mekhaniki. M.: Nauka, 1983. 664 p.
6. Paschina A.S., Nikolaeva V.I., Grishin V.A.. The Influence of the Medium Parameters to the Plasmoids Performances/ The Second Workshop on Magneto-and Plasma Aerodynamics for Aerospace Applications. Moscow, IVTAN, 5-7 April 2000.
7. Sharovaya molniya v laboratorii. M.: Khimija, 1994. 256 p.
8. et al. Experimental Investigations of Plasma Formations, Initiates by the Erosive Discharger//Journ. Tech. Phys.(Soviet), 1990, N1. P.17.

59. THE SPACE ELECTRIC FIELD DISTRIBUTION IN THE THERMOIONIZATION STRONG JETS

M.S. Apfelbaum

IHED RAS. e-mail:msa@hedric.msk.su, fax- 485-79-90
127412, Izhorskaia 13/19, Moscow.

Abstract. It was shown [1] that the shock –wave may be caused the strong electric field in a low temperature plasma. Many years ago [2] the strong thermoionization jets analogous effect was optioned by as theoretically too. Poisson equations for potential of this field were decided both [1] and [2]. But the kinetic Boltzman equations were used in [1] and electrodynamic charge conservation equation was used in [2]. And the space charge transfer by Shlichting jets [3] was described by our methods. The electric current as an integration constant of this charge conservation law equation was found for previous our calculations [2] from measurement. In this work one of the theoretical methods for this current calculation was carried out.

Introduction

The shock wave can cause the strong electric field in low temperature plasma [1]. Many years ago analogous effect for the strong thermoionized jets was obtained theoretically too [2]. To describe the field the Poisson equation for its potential was solved both [1] and [2]. There was also used the kinetic Boltzman equation to describe charge transfer in shock waves [1], and the macroscopic charge conservation law together with Shlichting solution the jet [2]. The electric current trough the jet is initial condition for the methods proposed in [2], and thus far this constant has been known from measurements. In this work one of the theoretical methods for calculation of this current is described.

Theoretical model

For the mathematical description of the charge transfer by strong jets we used the same macroscopic model as the model of our previous works. But for this problem we may consider the more general thermoionization model than in [4]. We suppose that the electrical conductivity σ of the media in hand is depended on their absolute temperature T, but we do not define exactly such dependence. (For example in our previous works we used Arrhenius type equations for the rate of ionization). We also neglect the diffusion terms in electrodynamics equations because we showed in [5] that influence of these terms is important only in the thin layers on the boundary of media in hand. The preheated jets move from cone metallic surface S into the same cold media. The jet temperature is not greater than the weakly ionized plasma temperature. For this case the density ρ and the velocity v of the neutral components are the density and the velocity of the whole medium. So, we may use for axes-symmetrical stationary jets the simple formulae obtained by Shlichting [3]. The debit of the strong turbulent jet J was determined analytically [3]. This expression is:

$$J = 0.404\sqrt{P/\rho} \cdot x \qquad (1)$$

Here P is the jet momentum; x is the axial jet coordinate. So, let us come to electrodynamics equations. The relation for the electric current density j is:

$$\mathbf{j} = \sigma\,\mathbf{E} + q\mathbf{v} \qquad (2)$$

Here q is the density of the volume charge; E is the electric field intensity. And the volume charge can be caused by two ways. The first way is the thermoemission from the surface S. The second way is the volume charge formation by the conductivity gradient. This gradient was caused by the temperature gradient. Both ways described in [4]. And in [5] we obtained that the momentum P is the jet draught.

The well-known Poisson equation for q is

$$\frac{d^2\varphi}{dx^2} = -\frac{q}{\varepsilon\,\varepsilon_0} \qquad (3)$$

Here ε is the dielectric permittivity, φ is electric potential. We postulated that

$$\left|\sigma\,\vec{E}\right| << \left|q\vec{v}\right| \qquad (4)$$

And we may be used the relations (1)-(4) for the obtaining of the electric field distribution. So, the equation for the potential is

$$\frac{d^2\varphi}{dx^2} = -\frac{I}{0.404\varepsilon\,\varepsilon_0\sqrt{P/\rho x}} \qquad (5)$$

And the boundary conditions are:

317

$\varphi(S)=0, \varphi(d)= \varphi_0$ (6)

Here d is maximum distance from S, φ is empirical potential over the distance d [2].

The dimensionless solution of this equation with given conditions is:

$$\tilde{\varphi}(\tilde{x}) = \tilde{x}(1 - \tilde{I} \ln \tilde{x})$$

$$\tilde{I} = \frac{Id}{0.404\varepsilon\,\varepsilon_0\sqrt{P/\rho}}, \quad \tilde{\varphi} = \frac{\varphi}{\varphi_0} \qquad (7)$$

The current I determined from Richardson formulae. The theoretical maximum value for the potential is of order 100 V. The empirical maximum [2] is 110V. So, our theoretical model is in agreement with an experiment, and may be proposed for the jet electrification diagnostics.

References

1. Velikodnyi V. Yu., Bityurin V.A. The 2ND workshop on magnetoplasma-aerodynamics in aerospace application, Moscow, IVTAN, 2000, p 97.
2. Apfelbaum M. S. IVTAN Proc. "Ekstremalnye sostoyaniya veshestva" (Ed. V.E. Fortov, in russian) Moscow, 1991, p.p. 358-364.
3. Shlichting H. "Boundary layar theory" New - York, Mc. Grow-Hill, 1968.
4. Apfelbaum M.S., Apfelbaum E.M Chem. Phys., Report, vol.18, 2000, p 2313-2329
5. Apfelbaum M.S., ApfelbaumE.M. J. Of Electrostatics, v. 50, 2001, p 129-142

60. LASER SCHLIEREN METHOD FOR MEASURING DENSITY DISTRIBUTION OF GAS-DYNAMICAL DISTURBANCES

A. V. Filippov, D. A. Mazalov, A. F. Pal
The State Scientific Center of Russian Federation
Troitsk Institute for Innovation Fusion and Fusion Research

Abstract. For a few decades a lot of investigators have been involved in studying closely the interaction of gasdynamical disturbances, like shock waves, with non-equilibrium medium. This is due to both scientific and especially practical applications. For parameters of gasdynamical disturbances to be determined laser schlieren-method is widely used. Precise computing of the signal in this method runs into common mathematical problems, therefore, it is necessary to use one approximate method or another, for example, Fresnel zone method. The present work reports the sequential schlieren-system calibration procedure, which includes determining the parameters of laser beam (intensity and divergence), frequency and amplitude characteristics of the schlieren-device used, as well as the results of computing the schlieren-signal by the method of partial beams. There is also a comparison of computing results with huge experimental data that shows perfect agreement of the computed and measured schlieren-device signals. Therefore, applicability of the laser-schlieren method is firmly proved for performing quantitative measurements of gasdynamical disturbances' parameters.

1. Introduction

Recent years studying the interaction of shock waves (SW) with low temperature plasma has been of high interest. It is firstly due to the fact that in various gas discharge systems there occurs spontaneous formation of shock waves, which effect upon the operation of the systems. Secondly, some experiments resulted in the observation of interesting phenomena in the behavior of shock waves in low temperature plasma. These phenomena are increase of SW rate in SW entering a discharge region, formation of two-stage front structure etc (see reference paper [1] and papers cited in [2]). At present, in studying gas density inhomogeneity in gas dynamical disturbances and plasma structures a laser schlieren method is widely used due to high sensitivity and good time resolution [3-5]. Quantitative computation of the results produced by this method was rather well developed for the laser beam diameter being much smaller than the characteristic size of inhomogeneity [3,4]. But using the laser schlieren method for determination of shock wave structure for the characteristic size of gas density inhomogeneity much smaller than the laser beam diameter results in serious mathematical difficulties [6,7] owing to the necessity to solve the problem of propagation of laser radiation in strongly non-homogeneous medium. Therefore, approximate calculation methods are widely used. For example, in paper [6] method of Fresnel zone was described. In [7] a solution algorithm was developed for ill-posed problem about reconstructing gas density distribution in SW. In this algorithm equations in second order partial derivatives of parabolic type were numerically solved according to Green function method. In the present work to calculate response of schlieren system for SW crossing laser beam we used the partial beam method, which was proposed in [8], where it was applied to measurement of VT-relaxation rate of vibration-excited molecules. To calculate the signal it is also necessary to know the frequency response, the schlieren system sensitivity, to determine laser beam parameters, i.e. it is necessary to perform calibration. In this work detailed description of the laser schlieren-system calibration method and the method for calculating the signal from this system are presented.

2. Laser schlieren system

Laser schlieren system scheme for measuring shock front density is shown in Fig.1. He-Ne laser beam was refracted by shock wave and deflected from initial direction. Beam deflection was registered by section quadrant photo device. Differences between output signals from photo device's upper and lower sections diagonally situated were found, then the two differences were summed up. This resulted in the photo device signal being proportional to laser beam shift only within up-down direction.

Spherical shock waves were created by two spark sources: low voltage one (further, source No.1) with discharge voltage up to 1.6kV, discharge gap of 0.4cm, discharge capacitor capacitance of 10µF, and high voltage one (source No.2) with 12.5-35kV discharge voltage, discharge gap of 0.5cm, discharge capacitor capacitance of 0.75µF. In source No.1 a spark was initiated by a low power burning pulse.

Fig.1. Laser schlieren system scheme and the scheme of section quadrant photo device (the circle shows position of laser beam with radius of a=0.2cm for t=0 or h=0)
The size is given in cm; d=40 cm, L=100 cm.
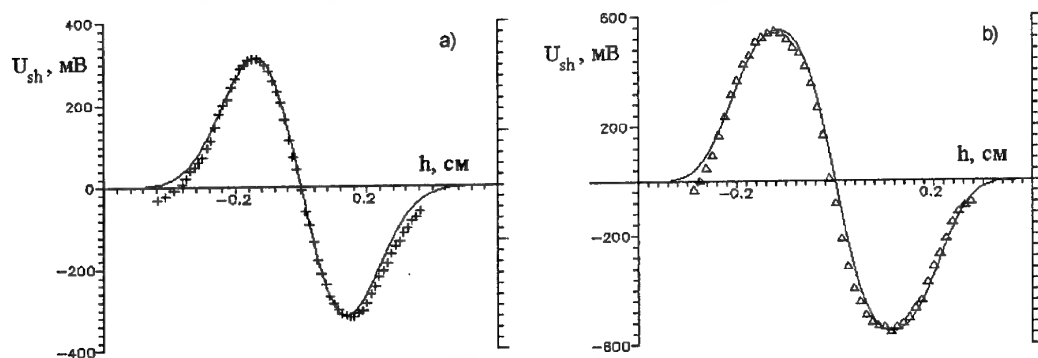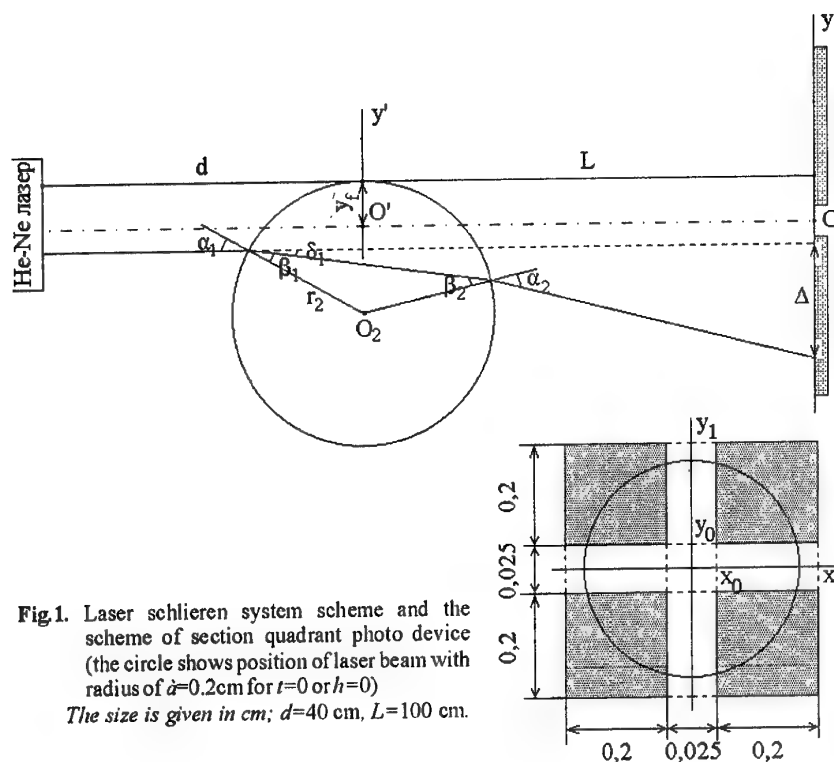
Fig.2. Experimental (dots) and calculated (solid lines) dependences of schlieren signal amplitude U_{sh} on laser beam shift h. $a)$ is for non diaphragmed laser beam; computing was performed for a=0.2cm, K_1=28.8 mV; $b)$ is for diaphragmed laser beam; computing was performed for a=0.1cm, K_1=31.6mV.

3. Frequency response and sensitivity of schlieren device

Frequency response of the photo device was produced with photo diode, which in our scheme performed glow pulse fronts no longer than a few tens of nanoseconds. Computing the schlieren device response from photo diode glow pulse of about 5 µs in duration resulted in the photo device frequency response being determined by two sequentially connected RC filters with about identical time constants, the sum of which is equal to 0.55µs. One of the filters was joined to the capacitor of the photo device, the other one being joined to the amplifier of the device's signal. ±0.1µs variations in the time constants (so that their sum should be constant) did not practically result in any change of the shape of the computed schlieren device signal, therefore, in further computations of schlieren device signals we assumed the time constants of RC-filters to be equal to each other: $\tau_1 \approx \tau_2 \approx 0.275$µs.

Photo-device sensitivity was determined by experimental dependence of photo-device signal U_{sh} on He-Ne laser beam shift h in the experiment, the distance between the laser and the device being 1.4m in our scheme. The dependence is shown in Fig.2a. Fig.2b shows the dependence $U_{sh}(h)$ for the

case of laser beam being diaphragmed with aperture of 0.6 mm in diameter. The amplitude of schlieren device signal for laser beam shift along Y-axis is expressed as follows:

$$U_{sh}(h) = K \int_{-x_1}^{x_1} \int_{-y_1}^{y_1} sign(y) \cdot \zeta(x, y) \cdot W(x, y - h) dxdy, \tag{1}$$

where h is the shift of He-Ne laser beam along OY-axis; K is the sensitivity of a photodiode; $\zeta(x,y)$ is the function equal either to 1 for the partial beam with (x,y) coordinates hits the photodiode (Fig.1), that is for two simultaneous conditions $|x| \in [x_0, x_1]$ and $|y| \in [y_0, y_1]$, or otherwise to 0; $W(x,y)$ is the Gaussian profile of laser beam:

$$W(x, y) = \frac{2W_0}{\pi a^2} exp\left[-\frac{2}{a^2}(x^2 + y^2) \right], \tag{2}$$

where a is the laser beam radius on the surface of the section photodiode; W_0 is the laser radiation power.

Double integral in expression (1) was numerically computed by dividing a laser beam into partial rays with square cross-sections of $0.008 \times 0.008 cm^2$ in size, each photo diode section catching 25×25 partial rays. Fig.2 shows computed dependence curves calculated for laser beam radius a and $K_1 = 2KW_0/\pi$, which were taken according to the condition of calculation results best agreeing with experimental ones. Fig.2 demonstrates good agreement of computed dependences with experimental points, and the values of K_1 for non diaphragmed laser beam ($K_1 = 28.8mV$) and diaphragmed one ($K_1 = 31.6mV$) nearly coincide, the difference allowing the accuracy of the schlieren device sensitivity to be evaluated. In further calculations K_1 was assumed to be equal to 30mV.

4. Determination of the dependence of shock front density on spherical SW

Both the dependence of SW front density on SW radius and the law of SW motion in a polytropic gas for one dimension case are determined by the parameter r_0 being the characteristic dynamical length [9,10], which is expressed as follows:

$$r_0 = \sqrt[3]{E_0/P_0} , \tag{3}$$

where E_0 is the explosion energy (of electrical breakdown) taken by SW; P_0 is the primary gas pressure in explosion area. Therefore, after

calculating this parameter due to dependence of SW arrival time on the distance it is possible to determine the dependence of SW front density on SW radius r_2.

Fig.3 shows experimental and calculation dependences of SW arrival time on distance r_2. The value of the parameter r_0 was determined according to the method proposed in [2]. This method consists in the following. Approximation by iteration results in selecting the parameter r_0 minimizing the sum of squares of differences of experimental SW arrival times and calculation ones performed on the base of work [11], where there are results of numerical solution of one-dimension spherical problem about point explosion (PPE) in a gas with backpressure taken into account. The value of sound velocity in air under room temperature was assumed to be equal to 345m/s [12]. Fig.3 shows that experimental values of SW arrival time well agree with one-dimension theory. Therefore, to estimate the jump in SW front density the results of numerical solution in [11] were used for up to $r_2 = 2r_0$.
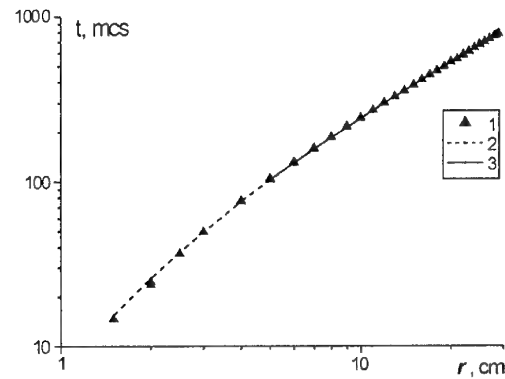
Fig.3. Time dependence of the SW arrival instant on the distance. 1 is the experimental points in air with source No.1 with $U = 1.4kV$; 2 is the calculation dependence performed on the base of numerical solution [11] of PPE with backpressure taken into account for $r_0 = 2.58cm$ ($E_0 = 1.8J$); 3 is formula (4) for $r_0 = 2.58$ cm.

The motion of SW and the parameters of SW for $r_2 \geq 1.5 \cdot r_0$ are determined by asymptotic law [10]:

$$\tau = \tau^* + \frac{R_2}{\sqrt{\gamma}} - \frac{\overline{k_3}}{\gamma\sqrt{\alpha}}\sqrt{\ln(R_2/R^*)} , \tag{4}$$

$$\frac{\rho_2}{\rho_1} = 1 + \frac{2\overline{k_3}}{(\gamma+1)\sqrt{\alpha\gamma} \cdot R_2 \sqrt{\ln(R_2/R^*)}} , \tag{5}$$

321

where $\tau = t/t_0$ is the nondimensional time; $t_0 = r_0\sqrt{\gamma}/a_s$ is the characteristic dynamical time; a_s is the adiabatic sound velocity; $R_2 = r_2/r_0$ is the nondimensional length; ρ_1, ρ_2 are the gas densities in front of SW and behind SW respectively; γ is the adiabatic exponent; α is the parameter in the solution of auto-model problem about high point explosion in perfect gas; $\bar{k}_3$, R^*, τ^* are some constants. According to [10] for $\gamma=1.4$ these constants are as follows: $\bar{k}_3=0.322$, $R^*=0.692$, $\tau^*=-0.22$. The value of the parameter α was calculated according to [10]. Fig.3 shows asymptotic dependences (4) for $r_2 \geq 2r_0$, with r_0 defined above. Fig.3 shows that formulae (4) well agrees with the experiment. Therefore, evaluation of the SW jump in density for $r_2 \geq 2r_0$ was performed with asymptotic formula (5).

5. Calculation of schlieren signal by the method of partial rays

Let us allow the coordinate system $x'y'$ ($O'x'$ axis is perpendicular to the plane of schlieren system scheme in Fig.1), which is in the plane containing point O_2 with a spark source of SW and is perpendicular to the laser beam, with origin of coordinates being on the axis of the beam. When there is no SW, the laser beam axis passes through the central point of schlieren device (Fig.1). On the surface of the schlieren device let us allow the coordinate system xy, being coaxial to the $x'y'$ system and having a simple relation with it as follows: $x = x' \cdot (a/a_0)$, $y = y' \cdot (a/a_0)$, where a_0 is the radius of the laser beam in $x'O'y'$ plane. Let us divide laser beam into partial rays with square cross section of $0.008 \times 0.008 \text{cm}^2$ in size (on the surface of schlieren device). Hitting the point with xy coordinates on the schlieren device surface during the absence of SW, the partial ray with $x'y'$ coordinates is deflected by SW and hits the point with $(x, y-\Delta)$ coordinates (negligible deflection of laser beam along x axis is ignored). In geometrical optics approximation the angle of partial ray deflection can be expressed as follows:

$$\delta = 2\delta_1 = 2\sqrt{2(1 - n_0/n_1) + ctg^2\alpha_1} - ctg\alpha_1, \qquad (6)$$

where n_0, n_1 are the gas indices of refraction in front of the SW and behind the SW respectively; α_1 is the incidence angle of the considered partial laser beam to the SW. The incidence angle depends on time as follows:

$$\alpha_1 = \arcsin(1 - (Ma_s t - y')/r_2), \qquad (7)$$

where M is the Mach number of SW; t is the time. The gas index of refraction depends on the density according to the Gladstone-Dale law: $n = 1 + A\rho$. Gladstone-Dale coefficients for the used gases were determined according to indices of refraction for the wavelength of He-Ne laser radiation under normal condition [13]. In all experiments performed for the current work the maximal angle deflection of laser beam within SW front did not exceed 0.1 radian, therefore partial ray deflection was determined according to the relationship as follows: $\Delta = L \cdot \delta$.

Schlieren device signal was computed as follows. For each instant from $t = -3\mu s$ with time spacing of $\Delta t = 0.005\mu s$ there performed numerical calculation of integral (1) with using relations (2),(6),(7) and the values of jump in SW front density, partial rays up to до $(x^2+y^2)^{1/2} = 3a$ having been taken into account. Then there performed smoothing of calculated values with schlieren device frequency response taken into account.

Fig.4 shows the difference, both experimental and calculated according to the described above method, between maximal and minimal values of schlieren device signal, and also the maximal values of schlieren device signal for source No.1. It should be noted that the difference between maximal and minimal values of the calculated signal (unlike the maximal value) does not practically depend on ± 0.1 cm shift of laser beam axis in any direction within the central point of the schlieren device. Fig.4 shows that experimental and calculation values well agree with each other.
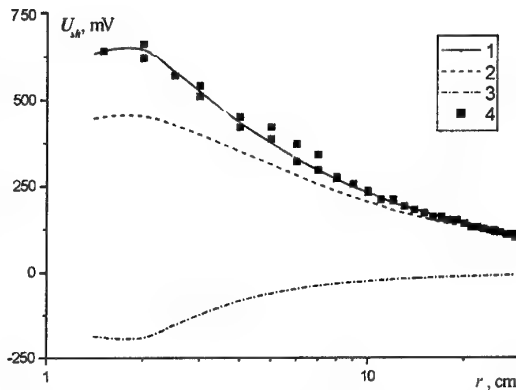
Fig.4. Experimental and calculation values of schlieren signal amplitude in dependence on SW radius. 1 is the calculation values $U_{sh} = U_{max} - U_{min}$; the calculation was performed for $a = 0.2$ cm, $a_0 = 0.075$ cm, $K_1 = 30$; 2 is for U_{max}; 3 is for U_{min}; 4 is the values U_{sh} in experiments with source No.1.
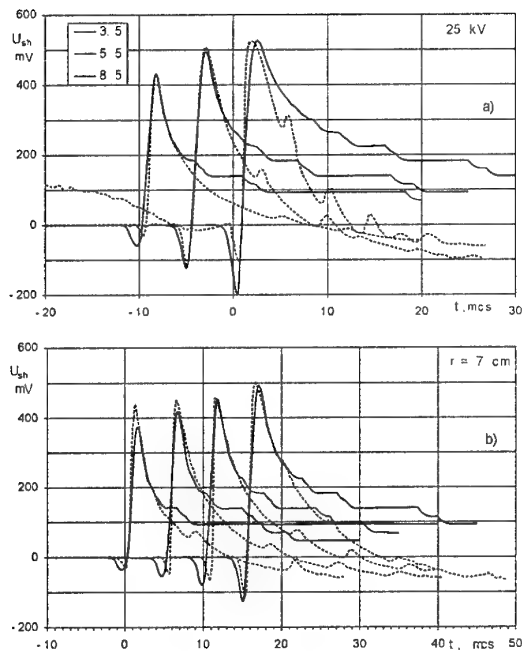
Fig.5. Calculated and experimental shapes of schlieren signals in experiments with source No.2 for various distances with breakdown voltage value of 25kV *(a)* and for distance of 7cm with various breakdown voltage values *(b)*.

Fig.5 shows the comparison of calculated schlieren device signals with experimental ones for source No.2 used for generation of spherical SW. Fig.5 demonstrates good agreement of calculation curves with experimental ones for maximal and minimal values of signals. Disagreement behind the maximum are due to calculations non taking into account the deflection of laser beam within inhomogeneity behind the SW. That deflection is about 100 times smaller than the one within the SW. When the front point of SW has crossed the laser beam, what happens $\Delta t \sim a/a_s \approx 5\mu s$ after the minimal signal of the schlieren device, the deflection owing to that inhomogeneity becomes greater, however this effect is observed only after the signal has passed the maximum. Taking into account this effect would have allowed the agreement of the calculation with the experiment to be enhanced, but this problem did not belong to the field of our interests so only the maximal amplitude of the schlieren device signal was used.

6. Conclusion

Reconstructing the jump in density of spherical SW in the present work was performed with the use of the new calibration method and the calculation of the signal of laser schlieren system including experimental determination of schlieren device frequency response and sensitivity; reconstruction of the SW jump in density in dependence on SW radius from experimental values of SW arrival instant in air for various distances on the base of numerical solution of one-dimensional problem about point explosion in gas with backpressure taken into account and on the base of asymptotic laws of SW motion; calculation of schlieren signal system by the method of partial rays. Comparison of calculations with extensive experimental material was performed what resulted in excellent agreement of the calculated schlieren device signals with the measured ones. Thus, it was well shown that the laser schlieren method could be applied for quantitative measurements of the parameters of gas dynamical disturbance.

References

1. Osipov A.I. And Uvarov A.V., Usp. Fiz. Nauk, 1992, vol.162, No.11, p.1.
2. Bystrov S.A., Mazalov D.A., Pal' A.F., Filippov A. V., Shugaev F. V.// Plasma Physics Reports, Vol.24, No.1, 1998. pp.37-44.
3. Kiefer J.H.// Shock waves in chemistry./ Ed. by Lifshitz A. N.Y.: Plenum Press, 1981. P. 219-277.
4. Woolsey G.A., MacGregor S.J., Farish O.// Proc. R. Soc. Lond. A. 1986. V.405. P.355-367.
5. Yakushev G.G., Kolpakov V.I., Zhukova E.N., Pyatnitskii L. N., Kul'beda V.E., Preprint of IVTAN, No.5-221, Moscow: 1987, 49 pages
6. Panda J., Adamovsky G. // Phys. Fluids. 1995. V. 7. No. 9. P. 2271.
7. Bystrov S.A., Honma H., Ivanov V.I. et al. //Density reconstruction from laser schlieren signal in shock tube experiments, Shock Waves, (1998), No.8, pp.183-189
8. Dove J.E., Teitelbaum H.// Chemical Physics. 1974. No.6. P. 431-444.
9. Sedov L. I., Metody podobiya i razmernosti v mekhanike (Methods of Similarity and Dimensions in Mechanics), Moscow: Nauka, 1978

10. Korobeinikov V.P. Zadachi teorii tochechnogo vzryva (Problems of Theory of a Point Explosion), Moscow, Nauka, 1985.

11. Korobeinikov V.P, Chushkin P.I., Sharovatova K.V., Gazodinamicheskie functsii tochechnogo vzryva (Gas Dynamic Functions of a Point Explosion), Moscow: Computation Center, Acad. Sci. of the USSR, 1985

12. Vargaftik N.B., Spravochnik po teplofizicheskim svoistvam gazov i zhidkostei (Handbook on Thermophysical Properties of Gases and Liquids), Moscow: Fizmatgiz, 1963

61. ABOUT ACCURACY OF TEMPERATURE MEASUREMENT FOR THIN FIBER OF NON-HOMOGENEOUS NON-EQUILIBRIUM ELECTRIC-DISCHARGE PLASMA

Bityurin V.A., Bocharov A.N., Brovkin V.G., Kolesnichenko Yu.F., Kolpakov A.V., LeonovS.B.
Institute for High Temperatures of Russian Academy of Sciences,
13/19 Izhorskaya Str., 127412 Moscow, Russia

Abstract. For widely used experimental technique for measurement of plasma translational temperature [1-3], based on analysis of viewed spectrum of molecular nitrogen, calculation estimation has been obtained for upper bound of measurement error for maximum translational temperature for non-homogeneous fiber of non-equilibrium dissociating plasma.

Scope of parameters has been considered, which is characteristic of electro-discharge plasma [3-5]. Probe dependencies on radial coordinate have been used for temperature and concentration. Calculations of spectral dependence of radiation intensity have been carried out for 0-0 transition of second positive system of molecular nitrogen.

Strict conditions for accuracy of measurement of plasma translational temperature have been considered, when dependence of temperature on radial coordinate does not have the only strong maximum, and vibrational temperature of plasma exceeds the translational temperature strongly, so that dissociation of plasma is very significant.

It has been shown for non-equilibrium plasma, that plasma maximum translational temperature can differ from measured effective temperature more than by 500K, when measured temperature of plasma is on the level of 2300K. Such error of measurement is substantially greater, than 50K level, which has been obtained previously for non-dissociating plasma and for temperature dependence on coordinate with the only strong maximum [1-3].

It has been shown also, that for plasma at equilibrium, error of measurement can mount ~15000K, when intensity radiation of very thin hot kernel with temperature 20000K is substantially less, than intensity of radiation of relatively cold 1mm radius envelope.

1. Introduction

A purpose of this work is to find numerical level for maximum error of measurement of temperature for non-homogeneous fiber of non-equilibrium dissociating plasma of nitrogen for a case of widely used experimental technique [1-3], which is based on analysis of viewed molecular spectrum of nitrogen. When this technique is used, maximum translational temperature of plasma is determined by means of comparison of experimental spectrum with a number of spectrums, which have been calculated for different temperatures. The temperature, for which the spectrum calculated is close at most to experimental spectrum, is usually considered to be equal to maximum translational temperature for plasma fiber.

Strictly speaking, technique described above gives a possibility to find not maximum translational temperature, but some effective temperature of plasma, which depends on temperature dependence on coordinate along ray of observation [1,2]. Nevertheless for some important cases effective temperature and maximum temperature are practically equal to each other.

For example, it has been shown at [1,2], that when dissociation can be neglected, and temperature dependence on coordinate has the only strong maximum, then intensity of radiation for hot volumes of plasma with temperature near to maximum overwhelms intensity of radiation emitted by volumes, which are less heated. Overwhelming of contribution to intensity of radiation from volumes with temperature near to maximum temperature is due to exponential dependence of radiation intensity on temperature [1,2].

Maximum temperature of plasma in this case is near to effective temperature, which can be find with accuracy not worse, than 50K, - also due to exponential dependence of radiation intensity on temperature [3]. Correspondingly, the same high is an accuracy of measurement of maximum translational temperature of plasma. Cases, when effective temperature strongly differes from maximum temperature, as it is known by authors, have not been considered previously.

At this work more strict conditions have been considered, as compared with previous works. At first we have considered high temperatures, when dissociation of plasma is strong. It has been supposed also, that dependence of temperature of plasma on coordinate does not have the only strict maximum. Level of measurement error, which has been found for these conditions, can be considered as an estimation for upper bound for error of measurement of maximum temperature.

2. Basic assumptions

Similar to [1-3], it has been supposed, that populations of energetic levels at non-equilibrium plasma can be described by Boltzman relation;

translational and rotational temperatures are equal to each other, and can strongly differ from vibrational temperature.

Scope of physical parameters has been considered, which is typical of electric-discharge [1-3]: translational temperature of plasma is 300-20000K, vibrational temperature of plasma is 300-10000K, initial pressure is on the level of 10Torr. Electric field is in the range $3 \cdot 10^{-16} < E/N < 6 \cdot 10^{-16} \text{Vcm}^2$, concentration of electrons is on the level of 10^{10}-10^{12}cm^{-3}. Mean energy of electron is 0,5-3eV. Typical viewed dimension of plasma fiber is 1-2mm.

Calculations of spectral intensity of radiation have been carried out for 0-0 transition of second positive system of molecular nitrogen. Intensity of radiation, which is due to electron-vibrational-rotational transitions, has been calculated on a base of known classic formulae [6,7], tabulated data [8], and under assumption, that plasma is transparent. Width of apparatus function has been assumed to be equal to 1-1,2 angstrems, similar to [3].

Probe dependencies of temperature and concentration on radial coordinate have been used. Theoretical modeling of non-homogeneous, non-equilibrium plasma based on numerical solution of system of kinetic equations for populations of energetic levels, together with system of equations of gas dynamics is not in the scope of this investigation.

At this work two-steps dependence of temperature on radial coordinate has been considered. Such dependence does not have obligatory the only strong maximum, and can be used as an example to obtain upper estimation for error of experimental technique under consideration. It is due to at this case intensity of radiation from hot internal kernel of fiber can be of the same order of magnitude, or even less, than intensity of radiation of relatively cold envelope, which can have substantially greater value of volume, as compared with the kernel.

At the case of equilibrium plasma with temperature, which is not greater, than 3000K, dissociation can be neglected indeed [9], as it has been done at previous works [1-3]. But on a practice plasma can be substantially non-equilibrium one, because main part of energy, which is passed into plasma, transforms to excitation of vibrational levels, and it gives rise to a situation, when vibrational temperature can exceed translational temperature by some times, or even by the order of magnitude [4,5].

It is known, that for pressure greater, than 1,5 Torr, for conditions of electric-discharge plasma, dissociation of molecular nitrogen is near to entirely due to excitation of vibrational levels of

basic electron state [5]. At this work calculations have been carried out using [10], which have shown, that for vibrational temperature near to 10000K, and for translational temperature 3000K, dissociation of molecular nitrogen can be the same strong, as equilibrium dissociation for temperature 10000K. So that, even when translation temperature is substantially less, than temperature of equilibrium dissociation, for non-equilibrium electric-discharge plasma dissociation should be taken into account obligatory.

To estimate numerical value of concentration of molecules of dissociating plasma, we have used an expression for equilibrium constant [9].

For the case of non equilibrium plasma we have used the same expression, as for equilibrium plasma, where temperature has been supposed to be equal to vibrational temperature of plasma.

This approach seems to be adequate, when a time of VV-relaxation at discharge is substantially less, than a time of dissociation, and, in turn, a time of dissociation is substantially less, than a time of VT-relaxation. For some ratio of physical parameters at electric-discharge such relation between characteristic times can take place. Indeed, in accordance with [4] (Table 11.3), for electric field $E/N=3 \cdot 10^{-16}$ Wt cm^2, for concentration of electrons $n_e=10^{11}\text{cm}^{-3}$, for $T_{gas}=500K$, for initial pressure of molecular nitrogen 5Torr we have: time of VV-exchange $5.5 \cdot 10^{-4}$s, time of eV-exchange $2 \cdot 10^{-3}$s, time of dissociation $1,6 \cdot 10^{-1}$s, time of dissociation due to direct electron collision 0,5s, time of VT-relaxation $2,5 \cdot 10^2$ s. For electric field $E/N=6 \cdot 10^{-16}$Wt·cm^2, and for the same concentration of electrons, temperature of gas and initial pressure of molecular nitrogen we have: time of VV-exchange $5.5 \cdot 10^{-4}$s, time of eV-exchange 10^{-3}s, time of dissociation $1,6 \cdot 10^{-1}$s, time of dissociation due to direct electron collision 0,5s, time of VT-relaxation $2,5 \cdot 10^2$s.

Calculation of intensity of radiation

As an example, we consider 0-0 transition of band $C^3\Pi_u - B^3\Pi_g$ of molecular nitrogen (second positive system). For transparent plasma spectral intensity of radiation is defined by following relation:

$$I_\lambda = \int_0^{R_{viewer}} \sum_{lines} j_{J'J} r f(\lambda) dr$$

Here $j_{J'J}$ - radiation coefficient, $f(\lambda)$ - contour of line ($\int f(\lambda)d\lambda = 1$), $r=0$ corresponds to

326

the axe of plasma fiber, R_{viewer} - distance from the axe of fiber to registering apparature.

Radiation coefficient for electron-vibrational-rotational (eVR) line of band can be calculated using following known formula [6]:

$$J_{J'J} = \frac{16\pi^3 c}{3}\omega^4 N \frac{g_e' g_n}{Q Q_n} S_{J'J} q_{v'v} \frac{S_e}{g_e} \times$$

$$\times \exp\left[-\frac{hc}{kT}(E_e' + E_v' + E_J')\right]$$

Here c - speed of light, ω - frequency of radiation, cm^{-1}, N - number of molecules inside radiating volume, g_e', g_n - electron and nuclear statistical weights, Q, Q_n -whole and nuclear statistical sums, $S_{J'J}$ - Henle-London factor, $q_{v'v}$ - Frank-Kondon factor, S_e -strength of electron transition, E_e', E_v', E_J' - energy of upper electron level, energy of upper vibrational level, energy of upper rotational level.

At the case of non-equilibrium plasma, rotational temperature should be put in formula for intensity of radiation, and here the rotational temperature is practically equal to translational temperature during all time of discharge.

$^3\Pi$ state of nitrogen molecule refers to a case of a-bond in terms of Gund [6], when $J=\Omega, \Omega+1, \ldots$, where Ω - sum of projection of whole spin on axe between nuclei and projection of orbital moment of electrons on the same axe. Following numerical data have been used [7]:

E_e' =89105 cm^{-1}, E_e=59583,4 cm^{-1}

$$E_v' = hc\omega_e\left(v+\frac{1}{2}\right)$$

$E_J' = B_e J'(J'+1)$, ω_e' =2035cm^{-1}, ω_e=1734cm^{-1},

B_e' =1.826cm^{-1}, B_e=1.638cm^{-1}

For Frank-Kondon factor of 0-0 vibration we have used value 0.455, which has been tabulated at [8].

For both energetic states $C^3\Pi_u$ and $B^3\Pi_g$ projection of whole orbital moment of electrons on an axe of molecule is characterized by quantum number $\Lambda=1$, so that $\Delta\Lambda=0$. In this case for Frank-Kondon factors we have [6]:

$$S_J^{J+1} = S_J^R \frac{(J+1+\Lambda)(J+1-\Lambda)}{J+1},$$

$$S_J^{J-1} = S_J^P \frac{(J^2-\Lambda^2)}{J},$$

$$S_J^J = S_J^Q \frac{(2J+1)\Lambda^2}{J(J+1)}$$

Here J – rotation quantum number for down energetic level.

Coefficient of radiation for spectral line represents integral of spectral intensity of radiation over spectrum. Estimations of width of eVR-lines show, that characteristic width of lines is of the order of 0.01 angstrem. Indeed, for doppler broadening we have [6]:

$$\gamma_D = 4.3\times10^7 \lambda \left(\frac{T}{\mu}\right)^{1/2} \approx$$

$$\approx (\lambda=3300A°, T=3000K, \mu=28) \approx 0.015A°$$

Collisional resonance broadening can be estimated using formula [6]:

$$\gamma = \frac{e^2}{m\omega}\left(\frac{g_{J'}}{g_J}\right)^{1/2} f_{J'J} \approx$$

$$\approx (e=2.8\times10^{10} \text{sgs}, m=91\times10^{28}\text{g}, f\approx0.09,$$
$$\omega\approx3\times10^4\text{cm-1}\sim9\times10^{14}\text{s}^{-1}) \approx 10^{-7}\text{s}^{-1}$$

Characteristic width of apparatus function for experimental equipment [3] is of the order of 1A, and hence it is substantially exceeds the width of spectral lines. Thus, apparatus, which is used at [3], resolves spectral lines partially.

At Fig.1,2 spectral dependencies of radiation intensity are shown, which have been calculated for different translational temperatures. Comparison of calculated spectra with experimental spectra, which are also shown at the same figures, gives the possibility to find effective temperature, which is usually considered, as maximum translational temperature at plasma fiber [1-3].
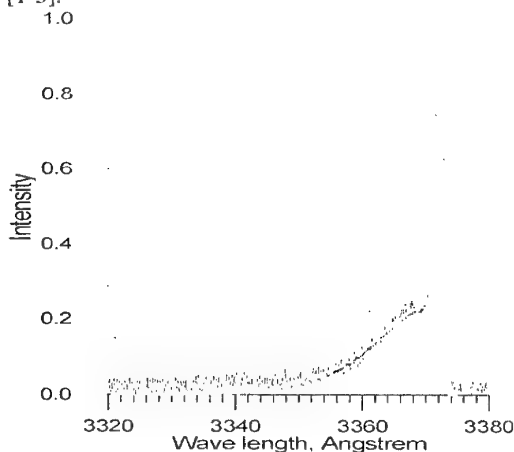
Fig.1. Spectral dependencies of intensity calculated for T=500, 550, 600 K as compared with experimental data (black).

327
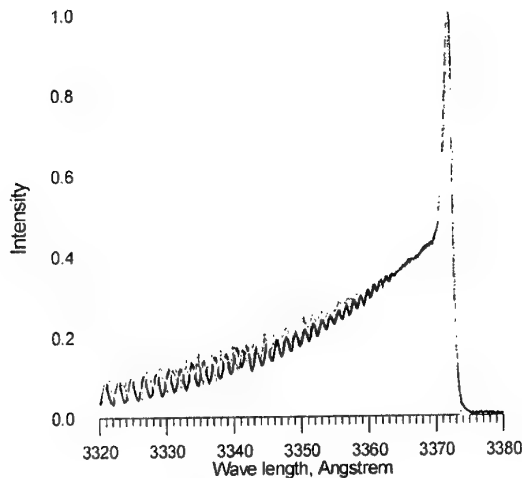
Fig.2. Spectral dependencies of intensity calculated for *T*=2500, 2800K as compared with experimental data (black).

Effective temperature can be determined using such technique with an accuracy of the order of 50K due to strong, exponential dependence of radiation intensity on temperature. At the same time assumption, that effective temperature is very close to the maximum temperature, can be wrong for some cases. At this work two examples will be demonstrated, when effective temperature differs from maximum temperature substantially greater, than by 50K.

4. Calculation of dissociation rate of nitrogen

Dependence of relative concentration of nitrogen molecules on temperature, as it has been described at *2.Basic assumptions*, are shown at Fig.3. For temperature dependence of equilibrium constant empiric relation [9] has been used. It can be seen, that for temperature 10000K concentration of nitrogen molecules is by 4 orders of magnitude less, as compared with concentration for temperatures, which are less, than 3000K.

When translational temperature of electric-discharge plasma does not exceed a level of 3000K, as at [3-5], dissociation of equilibrium nitrogen plasma can be neglected (Fig.3).

Plasma of electric-discharge can be non-equilibrium one, so that vibrational temperature of plasma strongly exceeds translational temperature. It is due to the fact, that a main part of energy of electromagnetic field is passed to excitation of vibrational energetic levels of molecules, and a time of vibration-translation exchange is relatively large [4,5]. As it has been pointed out at [5], for pressures more than 1,5 Torr and for conditions, which are typical of electric-discharge, dissociation

of N_2 is only due to excitation of vibrational levels of basic electron state. At this work calculations have been carried out to find rate of equilibrium dissociation and to find non-equilibrium coefficient correction factor $Z(T,T_v)$ using formulae [10], which have shown, that for vibrational temperature of the order of 10000K, and for translation temperature 3000K, dissociation of nitrogen can be of the same significance, as compared with equilibrium dissociation for 10000K. Results of calculations are shown at Fig.4.
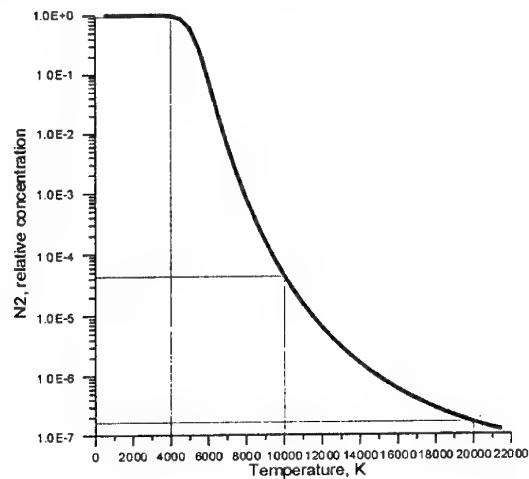
Fig.3. Temperature dependence of concentration of nitrogen molecules for equilibrium dissociation and recombination

Thus, even when translational temperature is significantly less, than the temperature of equilibrium dissociation, it is necessary to take into account dissociation for non-equilibrium plasma of electric-discharge.

An extent of dissociation of nitrogen for known constants of rates of dissociation and recombination can be found by means of solving system of kinetic equations, but approximate solution can be found using more simple algorithm. To find approximate solution, it is sufficient to take into account relation of characteristic times of processes of VV- and eV-exchange, time of dissociation and time of VT-relaxation.

In accordance with [4] (Table 11.3), for electric field $E/N=3\times10^{-16}$Wt·cm^2, for concentration of electrons $n_e=10^{11}$cm^{-3}, for $T_{gas}=500$K, for initial pressure of molecular nitrogen 5Torr we have: time of VV-exchange 5.5×10^{-4}s, time of eV-exchange 2×10^{-3}s, time of dissociation 1.6×10^{-1}s, time of dissociation due to direct electron collision 0.5s, time of VT-relaxation 2.5×10^2 s. For electric field $E/N=6\times10^{-16}$ Wt cm^2, and for the same concentration of electrons, temperature of gas and

initial pressure of molecular nitrogen we have: time of VV-exchange 5.5×10^{-4}s, time of eV-exchange 10^{-3}s, time of dissociation 1.6×10^{-1}s, , time of dissociation due to direct electron collision 0.5s, time of VT-relaxation $2,5 \cdot 10^2$s.

Fig.4. Temperature dependence of dissociation rate and of non equilibrium factor

Thus, a time of VV-relaxation at electric-discharge is substantially less, than a time of dissociation, and in turn a time of dissociation is substantially less, than a time of VT-relaxation. Hence to estimate the extent of dissociation of nitrogen at discharge it is proposed to use an expression for equilibrium rate of dissociation, in that in place of translational temperature vibrational temperature should be passed.

5. Examples, when error of temperature measurement is large

Previously, as it has been done at [1-3], by the estimation of the level of measurement error for maximum translational temperature of plasma, a situation has been considered, when intensity of radiation for "hot" volumes of plasma with a temperature, which is close to the maximum, practically overwhelms intensity of radiation from "cold" volumes of plasma with temperature, which considerably less, than maximum temperature of plasma.

Such situation is realized, when a number of radiating molecules with a temperature, which is near to the maximum temperature, is not considerably less, than a number of relatively cold molecules, as compared with difference of radiation intensities per one molecule:

$$N_{hot} / N_{cold} >\sim \exp(-E (1/T_{cold} - 1/ T_{hot}))$$

Here E – quantum of radiative transition, T – translational temperature.

At this case spectral intensity of radiation, which is registered by apparatus, being a value, integrated along a ray of observation, nevertheless with a good accuracy equals to intensity of radiation from only "hot" volumes of plasma, which temperature is near to the maximum one. Registering apparatus practically does not "see" "cold" volumes of plasma.

A situation, which is different in the main, as compared with the situation described above, can be realized, when intensity of radiation from "cold" volumes is not less, than the intensity of radiation from "hot" volumes. For this, a number of radiating molecules inside "cold" volumes should be much larger, than a number of molecules inside "hot" volumes:

$$N_{hot} / N_{cold} << \exp(-E (1/T_{cold} - 1/ T_{hot}))$$

Temperature dependence of intensity of radiation for molecular nitrogen, integrated over spectrum range 3320-3380 angstrems, is shown at Fig.5. Curve 1 corresponds to the dissociating nitrogen, and curve 2 corresponds to the case, when dissociation has not been taken into account by calculations.
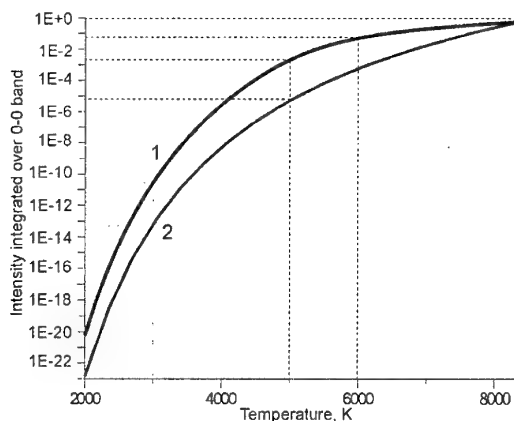
Fig.5. Temperature dependence of intencity, integrated over spectrum region 3320-3380A

This dependence is proposed to be used to obtain approximate estimation for N_{hot} / N_{cold}. For example, it can be seen at Fig.5, that intensity of radiation for 2500K is approximately by 4 orders of magnitude less, than intensity of radiation for 3000K. It means, that, when a number of "cold" emitters with temperature 2500K is by 4 orders of magnitude larger, than a number of "hot" emitters with temperature 3000K, intensity of radiation from "cold" emitters is approximately equal to intensity of radiation from "hot" emitters, and apparatus registers not only intensity from "hot" emitters, but some substantially different intensity, which can be obtained by means of integration along the ray of observation.

For a case of two-steps dependence of temperature on radial coordinate, a number of "cold" emitters can be significantly larger, than a number of "hot" emitters due to the following two circumstances:
- -value of volume of "cold" plasma is considerably larger, than the value of "hot" plasma volume; concentration of "cold" plasma and concentration of "hot" plasma are of the same order of value;
- the main part of molecules of "hot" plasma have been dissociated.

If we take into account all circumstances, which have been pointed out above, we can demonstrate examples, when measurement error for maximum translational temperature is large.

First example

At Fig.6 spectral dependencies of intensity of radiation are shown for following three cases:
1— homogeneous plasma fiber with radius 1mm, translational and vibrational temperatures do not depend on radial coordinate and $T=T_{vibr}$ =3000K. At this case we can assume, that plasma does not dissociate; in addition, we have the only strong maximum for coordinate dependence of temperature.
2— non-homogeneous plasma fiber with radius 1mm, having hot kernel with radius 0,1mm, translational temperature of the kernel is: T_{kernel}=3000K, vibrational temperature of the kernel is much larger, than the translational one: $T_{vibr\,kernel}$=10000K; translational and vibrational temperatures of envelope for 0.1mm $< r <$ 1mm are equal to each other: $T_{envelope}$=2400K;
3— the same, as for 1, except following: $T=T_{vibr}$=2300K.

As it can be seen at Fig.6, spectrum of intensity of radiation for case2 is very close for spectrum, obtained for case 3. This takes place, because at the case 2 volume of "cold" envelope is

by 2 orders of value larger, than the volume of "hot" kernel, and concentration of molecules in the kernel, which have not dissociated for $T_{vibrcenter}$=10000K, is by 4 orders of magnitude less, than it takes place for cold envelope (Fig.3). Thus, as it can be seen at Fig.5, larger intensity per molecule for translational temperature 3000K is compensated by a large number of molecular emitters, which have translational temperature 2300K.
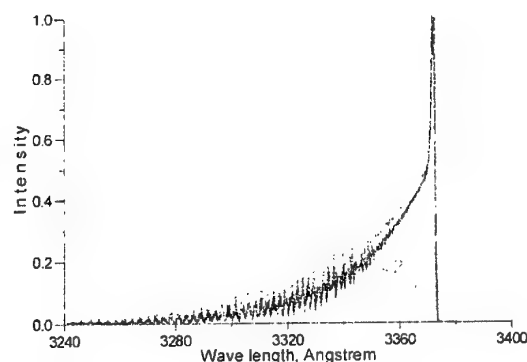
Fig.6. Spectral dependencies of intensity: 1– $T=T_{vibr}$ =3000K; 2– T_{center}=3000K, $T_{vibrcenter}$=10000K, T_{out}=2400K; 3– $T=T_{vibr}$ =2300K

Interpretation of spectrum shown at Fig.6 in the way, that spectrum 2 corresponds to the maximum translational temperature of plasma 2300-2400K, would give rise to the error 600-700K by the determining maximum translational temperature of plasma, because in this case, as it has been shown above, maximum translational temperature of plasma is 3000K.

Second example

Temperature, that is measured, can be substantially less, than maximum temperature inside plasma fiber not only for the case of non-equilibrium plasma.

To demonstrate this, we have considered plasma at equilibrium. We have calculated intensity for non -homogeneous plasma fiber with hot kernel, and relatively cold envelope. Radius of kernel is 0.05mm, radius of envelope is 1mm. Temperature of kernel is 20000K, temperature of envelope is 4000K. We have compared results for calculation of intensity, that have been obtained for non-homogeneous plasma fiber, with similar results for homogeneous fiber with radius 1mm for different temperatures: 2000K, 2100K, 4000K, 5000K. The results of such comparison are shown at Fig.7.

330
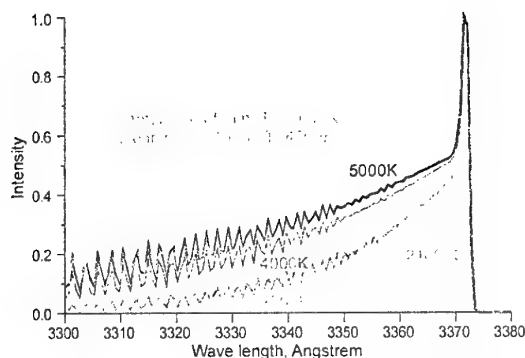
Fig.7. Spectral dependencies of intensity

It can be seen, that neglecting plasma non-homogeneity can result to measurement error of the order of 15000K for maximum plasma temperature. Indeed, spectrum dependence of intensity for non-homogeneous plasma fiber with 20000K for hot kernel is between spectrum dependences for 4000K and 5000K homogeneous plasma fibers.

Conclusions

For widely used experimental technique for measurement of plasma translational temperature [1-3], based on analysis of viewed spectrum of molecular nitrogen, calculation estimation has been obtained for upper bound of measurement error for maximum translational temperature for non-homogeneous fiber of non-equilibrium dissociating plasma.

Scope of parameters has been considered, that is characteristic of electro-discharge plasma [3-5]. Probe dependencies on radial coordinate have been used for temperature and concentration. Calculations of spectral dependence of radiation intensity have been carried out for 0-0 transition of second positive system of molecular nitrogen.

Strict conditions for accuracy of measurement of plasma translational temperature have been considered:

— dissociation of plasma is very significant;
— dependence of temperature on radial coordinate does not have the only strong maximum;
— -vibrational temperature of plasma can exceed the translational temperature strongly.

It has been shown, that:

1. At the case of equilibrium and non dissociating plasma, when vibrational and translational temperatures are near to each other, the accuracy of temperature measurement is not worse, than 50K. Such result is in accordance with results of previous investigations of other authors.
2. Dissociation of non-equilibrium plasma, that is due to high vibrational temperature, when translational temperature is low, can result to considerable decrease of accuracy of temperature measurement. An example of non-equilibrium nitrogen plasma has been demonstrated, when error of measurement is greater, than 500K.
3. For plasma at equilibrium, error of measurement can mount ~15000K, when intensity radiation of very thin hot kernel with temperature 20000K is substantially less, than intensity of radiation of relatively cold 1mm radius envelope.
4. Experimental technique under consideration, which is widely used to measure translational temperature of non-equilibrium plasma, is recommended to be amplified, to take into account dissociation and non-homogeneity.

References

1. Rusanov V.D., Fridman A.A. Diagnostika neravnovesnoj himicheski aktivnoj plazmy. Moskva, EAI, 1985. (in Russian).
2. Zhivotov V.K., Kalachev I.A., Krasheninnikov E.G., Samarin A.V., Rusanov V.D., Fridman A.A., Tarasov Yu.V. Spektralnye metody diagnostiki plazmohimicheskogo prostranstvenno-neodnorodnogo razrjada. Preprint IAE im. I.V.Kurchatova, 3704/7, Moskva, 1983.(in Russian).
3. S.Leonov, V.Bityurin, V.Brovkin, A.Klimov, Yu.Kolesnichenko, C.Savelkin, D.M.Van Wie Features of shock wave propagation through a longitudinal pulse discharge. – The 2-nd workshop on magneto-plasma-aerodynamics in aerospace applications, Moscow, 5-7 Apr., 2000, p.263-268.
4. Neravnovesnaja kolebatelnaja kinetika. Per. s angl. / redakz. M.Kapitelli.-Mir, 1989, 392s. (in Russian).

331

5. Rusanov V.D., Fridman A.A. Fizika himicheski aktivnoj plazmy. – Nauka, 1984, 415s.

6. Kamenshikov V.A., Plastinin Yu.A., Nikolaev V.M., Novizkij L.A. Radiazionnye svojstva gazov pri vysokih temperaturah. M., Mashinostroenie, 1971, s.440.

7. Zeldovich Ya.B., Rajzer Yu.P. Fizika udarnyh voln i vysokotemperaturnyh gidrodinamicheskih yavlenij. M., Nauka, 1966, s.688.

8. Kuzmenko N.E., Kuznetsova L.A., Kuzjakov Yu. A. Faktory Franka -Kondona dvuhatomnyh molekul. M., MGU, 1984, 344s.

9. Chul Park, R.L.Jaffe, H.Partridge Chemical-kinetic parameters of hyperbolic earth entry. – AIAA 00-0210, 38thAerospace Sciences Meeting & Exhibit. 10-13 Jan. 2000/ Reno, NV.

10. Fiziko-himicheskie processy v gazovoj dinamike. Pod red. G.G.Chernogo, S.A.Loseva, t.1, MGU, 1995, 350s.

62. SPATIAL EVOLUTION OF THE EMISSION SPECTRUM AND TEMPERATURES OF HIGH ENTHALPY NITROGEN PLASMAS JETS

A.A. Belevtsev, V.F. Chinnov, A.V. Fyodorov, E.Kh. Isakaev, A.V. Markin, S.A. Tereshkin
Associated Institute for High Temperatures, Russian Academy of sciences
Moscow, 127412 Izhorskaya 13/19, Russia

Abstract. The paper reports on the 200-1000nm emission spectrum of high enthalpy atmospheric pressure plasmatron-produced nitrogen plasma jets. The longitudinal profiles of the electron, rotational and mass-averaged temperatures and of the electron number density as well as the influence of the inlet nozzle diameter on the plasma parameters are investigated. A double-peaked structure of the N2+ B2Σu+-X2Σg+ (0-0) band in the region of the energy deposition and a strong overcooling of the electron gas in the far relaxation zone are revealed.

1. Introduction

Because of displaying hundreds of atomic and ionic lines of different stages of ionization, the emission spectra of highly ionized plasma jets offer great potentialities for accurate determination of the electron temperatures and number densities and estimating the populations of atoms and ions in different electronic states. Besides, these spectra are abundant in tens of vibronic molecular bands thus making it possible to derive rotational and vibrational temperatures and reasonably assess kinetic temperatures of heavy species. As well as being of great interest in studying the plasma kinetics in transonic flows of highly heated molecular gases, the obtained data allow some conclusions to be drawn about their thermodynamic states.

The present paper reports on the longitudinal evolution of the emission spectra of high enthalpy atmospheric pressure nitrogen plasma jets. The Abel inverted intensities of NI, NII, and NIII lines are used to determine electron temperatures T_e, whilst the electron number densities n_e are derived from the Lorentz constituents of the spectral line profiles. Much attention is given to the (0-0), (0-1) bands of the first negative $B^2\Sigma_u^+$-$X^2\Sigma_g^+$ system of N_2^+ and their evolution downstream from the plasmatron cathode. By the spectral simulation technique the distribution of the rotational temperatures T_r along the jet is determined, which is used to assess the mass-averaged temperature T. The influence of the nozzle inlet diameter, D_{in}, on the plasma parameters is examined. The data are used to analyze the thermodynamic state of the plasma at different segments of the jet.

2. Experimental setup and measuring systems

High enthalpy nitrogen plasma jets are produced by a high current (I=150-400A) plasmatron with vortex stabilization by the working gas [1]. The specific power depositions are as high as 50kW/cm^3. The plasmatron is essentially comprised of a tip cathode made of a thoriated/lanthanated tungsten rod, a copper interelectrode spacer and the anode with a divergent channel, the angle of divergence being 12^0. The inlet nozzle diameter can be varied from 2mm to 6mm, whilst the outlet diameter is 26mm. In the anode, there exist windows of 10mm in height and 1mm in width placed at different distances Z from the cathode for observation of the plasma jet transversely. The working gas is fed tangentially into the interelectrode spacer zone at flow rates G=1÷6g/s. The plasma streams show high hydrodynamic stability and their geometric and thermophysical parameters are firmly reproducible.

For spectral measurements two recording systems were used, one of which involves diffraction grating DFS-452 with two photodiode arrays Toshiba 1250A and the other is based on monochromator MDR-41 with photomultiplier FEU-100 [2]. The emission spectra were taken in the 200-1000nm region with high spectral resolution (~0.01nm) at different distances Z from the cathode. Note that the spin-splitting of $N_2^{+2}\Sigma$ terms and Λ-doubling of $N_2^3\Pi$ terms remained, however, unresolved because of an appreciable broadening of rotational lines under the present conditions. To process spectrometric data an automated system SPEC_MCD.100 based on package Mathcad 7.03 Professioonal was developed [3]. It allows creation of extensive data files (up to 10Mb per experimental cycle) as well as securing of a great body information on physical characteristics of spectral lines emitted by atoms, singly and doubly charged ions, primarily on radiation transition probabilities A_{ik} and Stark constants w_{St}. The system also permits the Abel inversion and simulation of rovibronic molecular spectra.
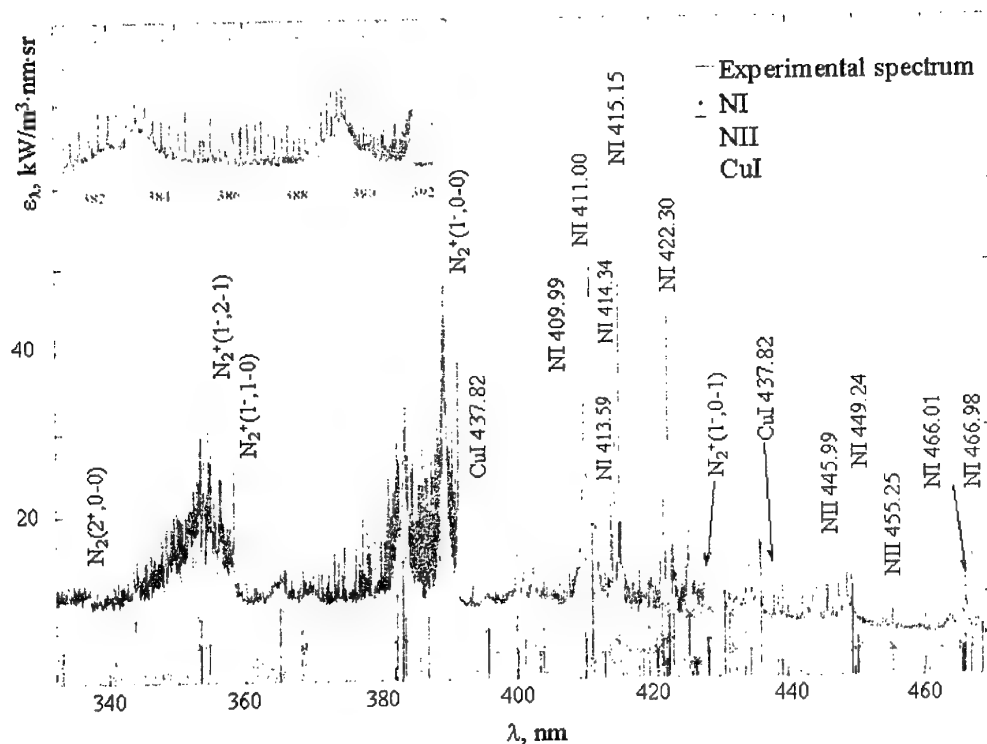
Fig.1. Emission nitrogen spectrum at $Z=34$mm. $I=400$A, $G=1.5$g/s, $D_{in}=5$mm. The positions of NI, NII, and *CuI* lines are given as the reference points. In the upper left part of the figure, the (0-0) band of N_2^+ I system is shown on an enlarged scale.

3. Emission spectra

Fig.1 presents a typical spectrum of high enthalpy nitrogen plasma jet taken in the near relaxation zone. The most prominent atomic and ionic lines as well as N_2 and N_2^+ vibronic bands are labeled in the figure. A number of *CuI* lines appearing due to evaporation of anode walls are also observed. In the upper left part of the figure, the band (0-0) of N_2^+ I system is shown on an enlarged scale. A double-peaked "relief" with two maximums at 389.5nm and 383.2nm is clearly seen. Of considerable interest is to follow the evolution of the nitrogen spectrum in the 380-392nm region downstream from the cathode. In the near-cathode region the band (0-0) is faintly visible against the continuum background and strong NII lines. The (0-0) band contribution to the total spectrum gradually increases with distance from the cathode, the band beginning to display a double-peaked structure. This structure is most pronounced in the near-anode arc region. At larger Z-values, the "peak" intensities diminish and the band exhibits a usual rotational structure. It should especially be stressed that the double-peaked
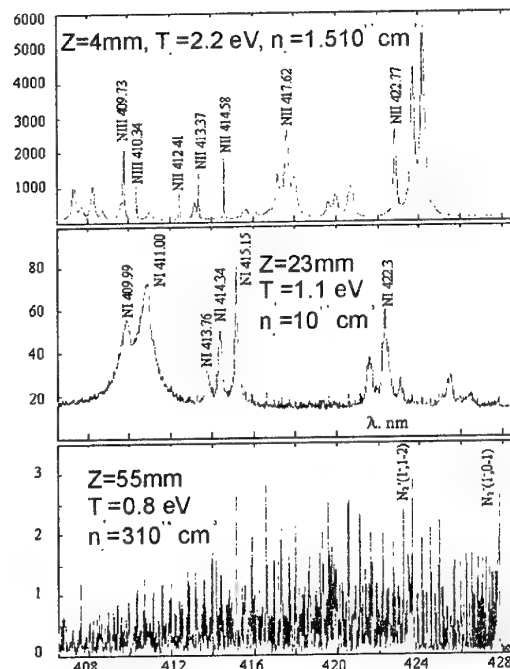
Fig.2. Evolution of the nitrogen plasma jet spectrum $I=400$A, $G=1.5$g/s, $D_{in}=5$mm. The axial magnitude of n_e, T_e and T_r are shown for different z-values

spectra were obtained using three different types of plasmatrons at various gas flow rates. Besides, the double-peaked structure was also observed in the experiments employed the plasmatrons with axially symmetrical gas flows. So there are strong grounds for believing that the existence of the mentioned "relief" in the spectrum of the N_2^+ 1' (0-0) band in the region of the energy deposition is a distinguishing feature of the studied nitrogen plasma jets generated by divergent channel plasmatrons. A spectroscopic analysis [4] does not allow the observed feature of the N_2^+ 1' (0-0) band structure to be attributed to neither possible singularities in the distribution of N_2^+ molecules over the rotational levels nor the contributions of other N_2 and/or N_2^+ bands. The actual nature of the phenomenon remains yet to be understood.

4. Spectral simulation. Determination of rotational temperature Tr

To determine rotational temperature T_r the bands (0-0) and (0-1) of N_2^+ 1' were numerically simulated with the line-by-line code. The spectroscopic constants are taken from [5,6]. The positions of P and R doublets are chosen in accord with [7,8]. Account is generally taken of the spin-splitting effect, although it becomes noticeable only for sufficiently large rotational levels. The temperature determination technique consists in performing a global fit of the spectral regions 388-391.5nm and 423-428nm, respectively, involving the method of least squares. Fig.3 illustrates this procedure as applied to the far relaxation zone (Z=70mm) of the jet. It is seen that the value $T_r=7000K$ gives the best agreement between the measured and simulated spectra for both bands.
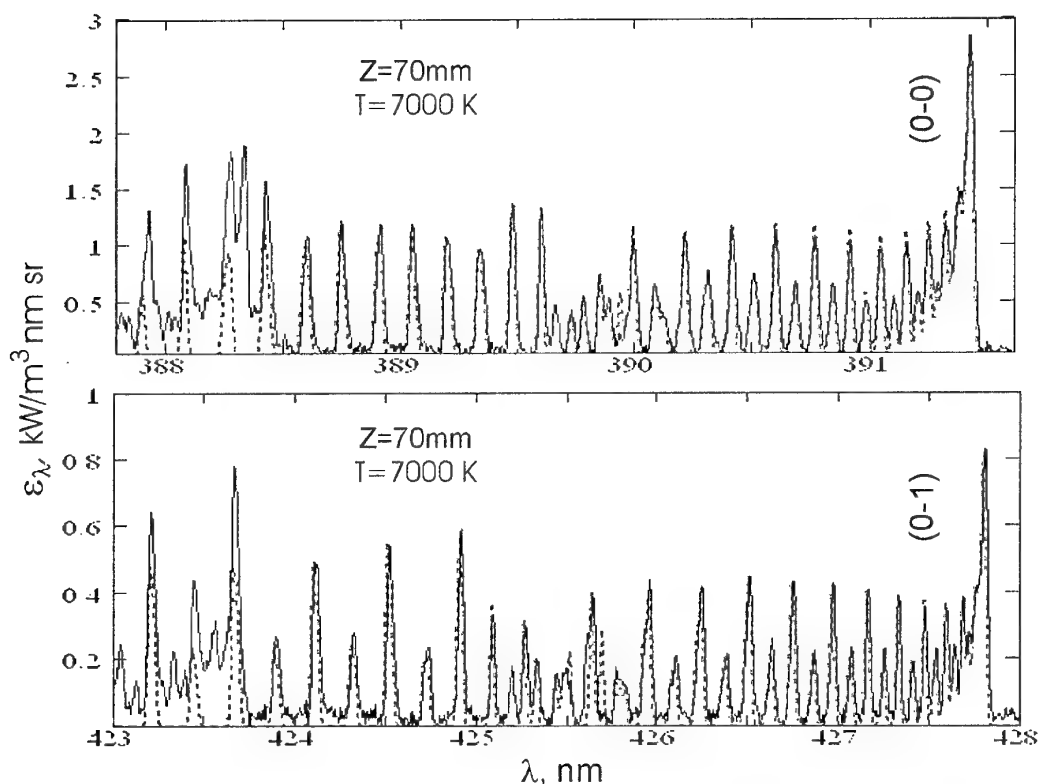
Fig.3. Spectral simulation of the (0-0) and (0-1) bands of the first negative system of N_2^+. I=400A, G=1.5g/s, D_{in}=5mm.

5. Determination of electron temperature T_e and number density n_e

Different techniques were used for deducing the values of axial electron temperatures throughout the length of the jet. In the near-cathode region (Z=4-5mm) and in the near relaxation zone (Z=16-34mm), the method of relative intensities of lines originated from different stages of ionization was employed. It shows a great efficiency in the present conditions because of appreciable differences ΔE in the excitation energies of the

lines to be compared (for I_{III}/I_I ΔE ~50eV, for I_{II}/I_I ΔE ~30eV). The electron temperatures in the near-cathode region attain magnitudes of~2.5÷3eV. Therefore the radial distributions of intensities of NI lines and even some NII lines take their maximal values not at the jet axis. In this connection two points should be mentioned. First, the use of NI lines offers considerable difficulties because their intensities are often less than that of the continuous background. Second, an accurate performance of the Abel inversion procedure is growing in importance.
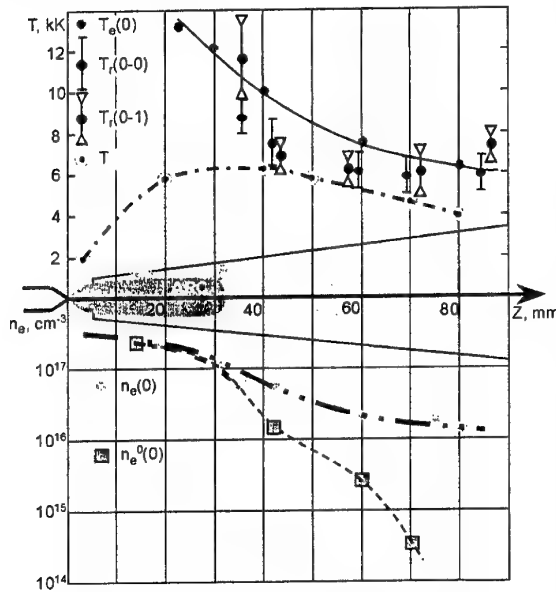
Fig.4. The longitudinal profiles of the basic plasma parameters. I=400A, G=1.5g/s, D_{in}=5mm.

In the far relaxation zone (Z~70-75mm), the electron temperatures have been determined using CuI lines with the excitation energies lying in the range 5.6-7.7eV. All resonance transitions and those to the lower metastable levels with energies of 1.39-1.64eV were left out of consideration for the radiation reabsorption can be neglected. In our conditions the chosen irradiating levels are in equilibrium with the electron continuum even at distances well removed from the cathode. Therefore the use of the Boltzmann-plot technique

allowed T_e-values to be derived with a high degree of accuracy.

Electron number densities n_e were generally determined from the half-widths of NI and NII lines with known Stark broadening constants w_{St}. The exception is the far relaxation zone where NI lines are observed only in the 810-860nm region and, therefore, Doppler broadening can appreciably influence the total half-widths of these lines. In this case n_e-values were determined by the Stark constituents extracted from the Voigt profile.

Fig.4 shows the profiles of the axial values of the electron temperature $T_e(0)$, of the rotational temperatures $T_r(0,0)$ and $T_r(0,1)$ determined by two vibronic bands and of the mass-averaged temperature T downstream from the tip cathode. T-values are of considerable interest for thermophysical studies and estimating the efficiency of the plasmatron as a whole. The kinetic temperatures of the heavy species within the plasma torch are assumed to be close to the rotational temperatures. Also shown are the profiles of the axial electron number density. One curve represents values $n_e(0)$ derived from the Stark half-widths and the other corresponds to the equilibrium values $n_e^0(0)$ calculated using the determined $T_e(0)$. It is seen that in the far relaxation zone the electron and rotational temperatures are fairly close. Conversely, there is great difference between the magnitudes of $n_e(0)$ and $n_e^0(0)$ at large distances from the cathode. For example at Z=70mm $n_e(0)/n_e^0(0)>50$. Thus a strong overcooling of the electron gas is observed in the far relaxation zone. This phenomenon does not seem to be of a local nature and needs the plasma kinetics to be considered throughout the length of the jet as a whole.

Effective cooling of all parts of the plasmatron permits a noticeable decrease in the inlet nozzle diameter down to 2mm. This significantly changes the jet plasma characteristics in the near-cathode region. For comparison the emission spectra taken at Z~6mm composed of NI and NII lines are presented for D_{in}=5mm (Fig.5a) and D_{in}=3mm (Fig.5c) along with the associated radial intensity distributions (Fig.5b and Fig.5d, respectively). It is clearly seen that the ratio between the intensities of NIII and NII lines increases with diminishing D_{in}-value, which gives firm evidence that, the electron temperature rises.
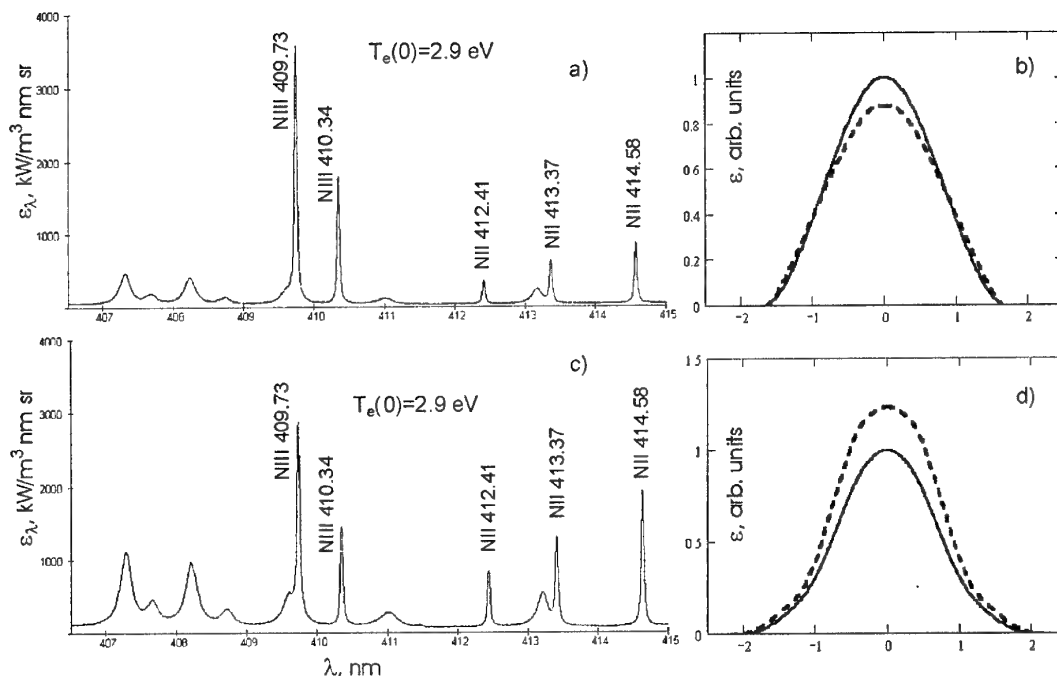
Fig.5. Nitrogen emission spectra and radial intensity distributions taken at distance Z=4mm downstream from the cathode for two values of the nozzle inlet diameters: a,c - D_{in}=5mm; b,d - D_{in}=3mm. I=400A, G=1.5g/s. Solid lines represent the side-on records. Dashed lines - the profiles reconstructed through the Abel inversion.

6. Conclusion

A spatial evolution of the emission spectrum and some plasma parameters in high enthalpy nitrogen plasma jets at atmospheric pressure has been investigated. The double-peaked structure of the (0-0) band of the first negative system of N_2^+ in the region of the 7energy deposition is revealed. The axial electron temperatures in the far relaxation zone are close to the rotational ones and those of heavy species. Nevertheless the axial electron number densities are more than an order of magnitude higher than the equilibrium values. Thus the electron gas is strongly overcooled in the far relaxation zone. This seems to come from a non-local nature of the plasma kinetics in the jet. Diminishing the inlet nozzle diameter leads to increasing the electron temperature in the near-cathode region.

References

1. E.Kh.Isakaev, R.R.Grigor'yants, N.O.Spector, A.S.Tyuftyaev, High. Temp. **32** (1994), 588-590.
2. A.A. Belevtsev, E.Kh.Isakaev, A.V.Markin, V.A.Khaimin, V.F.Chinnov, High Temp. **38** (2000), 667-674.
3. E.Kh.Isakaev, A.V.Markin, V.A.Khaimin, V.F.Chinnov, Instr. Exper. Techn. **44** (2001), 1-7.
4. A.A.Belevtsev, V.F.Chinnov, E.Kh.Isakaev, A.V.Markin, Proc. of 25th ICPIG, Warsaw, July 11-16, 1999, 306-307.
5. F.Michaud, F.Roux, S.P.Davies, A-D. Nguyen, Appl. Opt. 35 (1996), 2867-2873.
6. F.Michaud, F.Roux, S.P.Davies, A-D. Nguyen, C.O.Lax, J.Molec. Spectrosc. 203 (2000), 1-8.
7. K.A.Dick, W.Benesch, H.M.Crosswhite, S.C.Tilford, R.A.Gottscho, R.W.Field, J. Molec. Spectrosc. 69 (1978), 95-108.
8. L.Klynning, P. Pages, Phys. Scripta 25 (1982), 543-560.

63. SHORT PULSE PROPAGATION IN DISSIPATIVE AND ACTIVE MEDIA WITH RESONANT RELAXATION

Larichev V.A., Maksimov G.A.
Moscow State Engineering Physics Institute (MEPhI)

Abstract. The new analytical representation of fundamental solution (Green's function) describing the short pulse propagation in medium with single process of resonant relaxation is presented. This analytical solution is based on the generalized local response function of linear media [3]. It contains well-known Lorentz's and Debye's models of relaxing media, like particular cases. The changing of pulse shape at propagation, described by obtained solution, shows a variety of forms of pulse propagation and general lows of pulses dynamics beginning from pure relaxation behavior and up to resonant one. The derived solutions are correct and for active media for linear regime of the pulse propagation.

The analysis of dynamics of small perturbations, propagating in non equilibrium media is presently the subject of many theoretical and experimental investigations. The interest to this problem is dealt with wide field of applications concerning of sound propagation in gases and plasma. [1,2]. For description of non equilibrium media behavior the model with negative second viscosity is often used.

In the paper [3] the state equation, describing local response of arbitrary linear medium in vicinity of thermodynamic state, is derived by use of thermodynamic approach. This state equation (1) at corresponding values of parameters describes as a particular cases an exponential relaxation processes in medium (Debye's model), as well as resonant relaxations (Lorentz' model):

$$\sigma(t) = \rho_0 c_\infty^2 \left(\varepsilon(t) - \frac{\Delta\rho}{\tau} \int_0^t dt\, \varepsilon(t-t') e^{-t/\tau} \cos(\Omega t' - \varphi) \right)$$

(1)

where σ - stress, ε - strain, ρ_0 -density, c_0, c_∞ - high and low frequency limits of phase velocity in medium, and the basic parameters, which determines attenuation-dispersive properties of medium, are τ - relaxation time, Ω - resonant frequency, φ - inertial phase. Besides, the following notations are introduced for normalizing multiplier $\rho = (1+\Omega^2\tau^2)/(\cos\varphi + \Omega\tau\sin\varphi)$ and for dispersion jump of phase velocity $\Delta = 1 - c_0^2/c_\infty^2$.

Taking into account the state equation (1) for the case of an arbitrary single process of resonant relaxation, the Green's function of propagating pulse is presented by the Laplace integral:

$$I(x,t) = \frac{1}{2\pi i} \int_{\delta-i\infty}^{\delta+i\infty} dp \exp(pt - xK(p))$$

(2)

with wave number of following view

$$K(p) = \frac{p}{c_\infty} \left(1 - \Delta\rho \frac{(p\tau+1)\cos\varphi + \Omega\tau\sin\varphi}{(p\tau+1)^2 + (\Omega\tau)^2} \right)^{-1/2}$$

(3)

For small dispersion of phase velocity $\Delta \ll 1$ it is possible to expand the wavenumber $K(p)$ by Δ and to take into account two first terms only.

$$K(p) \approx \frac{p}{c_\infty} \left(1 + \frac{\Delta\rho}{2} \frac{(p\tau+1)\cos\varphi + \Omega\tau\cos\varphi}{(p\tau+1)^2 + (\Omega\tau)^2} \right)$$

(4)

Note, that in the case $\varphi = \pi/2$ the expression (4) is analytically equivalent to dispersion low for Lorentz's model, and for the case $\Omega = 0$ is equivalent to the one for the Debye's model.

With use of Efros's theorem about generalized convolution, the following new analytical representation of the Green's function (2) with wave number (4) is obtained [4]:

$A>0$

$$I(x,t) = \frac{e^{-\beta\cos\varphi - (1-B)t'}}{\tau} \Big(\delta(t') -$$
$$- \sqrt{\frac{|A|}{t'}} J_1\big(2\sqrt{|A|t'}\big)\Theta(t') + \int_0^{t'} d\xi \sqrt{\frac{C|A|}{\xi}} e^{-2B\xi} \cdot$$
$$\cdot J_1\big(2\sqrt{|A|(t'-\xi)}\big) J_1\big(2\sqrt{C\xi(t'-\xi)}\big) \Big)$$

(6)

Where the following notations are introduced
$\beta = \Delta x \rho / 2\tau c_\infty$, $t' = (t - x/c_\infty)/\tau$,
$A = \beta(\cos\varphi - \Omega\tau\sin\varphi)$,
$B = \Omega\tau(\cos\varphi - \Omega\tau\sin\varphi)/(\sin\varphi + \Omega\tau\cos\varphi)$,
$C = B^2 + (\Omega\tau)^2$.

The representation (5), (6) is pure real. The elastic (delta-function) precursor and high-frequency Sommerfeld's precursor (for $A<0$) are extracted in analytical forms in this representation. The relatively low-frequency component,

338

corresponding to Brillouin's precursor is expressed in a form of real integral in finite limits. Thus, the obtained expressions allow us to analyze the short pulse propagation for whole region of distances in any medium, which dissipative-disprsive properties is described by single resonant relaxation process. The type of pulse propagation is determined in this case by two values: $\Omega\tau$ and φ. In dependence on these values the phase velocity and attenuation coefficient can have different features. It is possible to obtain from (4) the following expressions for attenuation coefficient $\alpha(\omega) = \operatorname{Re} K(i\omega)$ and phase velocity $c^{-1}(\omega) = \operatorname{Im} K(i\omega)/\omega$:

$$\alpha(\omega) = \frac{\Delta\rho}{2c_\infty\tau} \cdot$$

$$\cdot \frac{(\omega\tau)^2 \left((\omega\tau)^2 \cos\varphi + \left(1 - (\Omega\tau)^2\right)\cos\varphi + 2\Omega\tau\sin\varphi\right)}{\left((\omega\tau)^2 + \left(1 - (\Omega\tau)^2\right)\right)^2 + 4(\Omega\tau)^2}$$

$$c(\omega) = c_\infty \left(1 - \frac{\Delta\rho}{2} \cdot \right.$$

$$\left. \frac{\left(\omega^2\tau^2\left(\cos\varphi - \Omega\tau\sin\varphi\right) + \left(1 + \omega^2\tau^2\right)\left(\cos\varphi + \Omega\tau\sin\varphi\right)\right)}{\left((\omega\tau)^2 + \left(1 - (\Omega\tau)^2\right)\right)^2 + 4(\Omega\tau)^2} \right)$$

The features, which the attenuation coefficient and phase velocity can have at various values of $\Omega\tau$ and φ for stable, dissipative media, are shown on Fig.1 and Fig.2. The attenuation coefficient can monotonically increase with frequency or can have maximum. The phase velocity also can be monotonic, or it can have maximum or minimum or the both together.
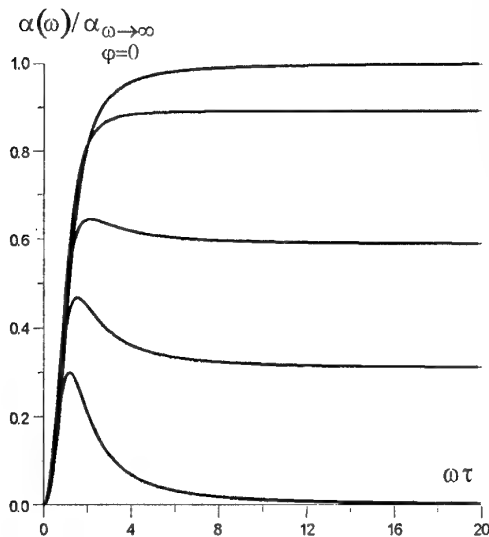
Fig.1. The attenuation coefficient in dependence on dimensionless frequency for different values of $\Omega\tau$ and φ
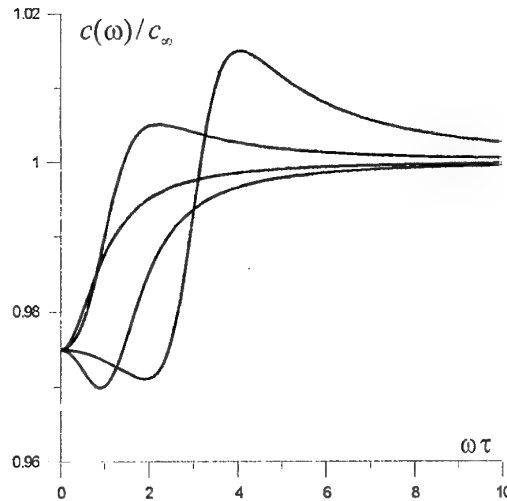
Fig.2. The phase velocity in dependence on dimensionless frequency for different values of $\Omega\tau$ and φ

On the plane $\Omega\tau$ - φ the domains, in which the attenuation coefficient and phase velocity have different features, and which correspond to different pulse dynamics, are shown on the Fig.3.
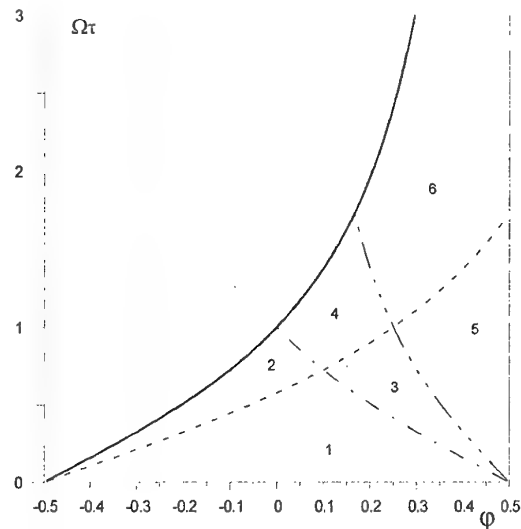
Fig.3. The domains of parameters $\Omega\tau$ and φ, corresponding to different pulse dynamics (phase φ is measured in parts of π): 1 – monotonic phase velocity and attenuation coefficient. 2 – minimum of phase velocity and monotonic attenuation coefficient. 3 – monotonic phase velocity and maximum of attenuation coefficient. 4 – maximum of phase velocity and attenuation coefficient. 5 – minimum of phase velocity and maximum of attenuation coefficient. 6 – minimum and maximum of phase velocity and maximum of attenuation coefficient.
$A>0$ in domain 1, 2, 3 and 4
$A<0$ in domain 5 and 6

339
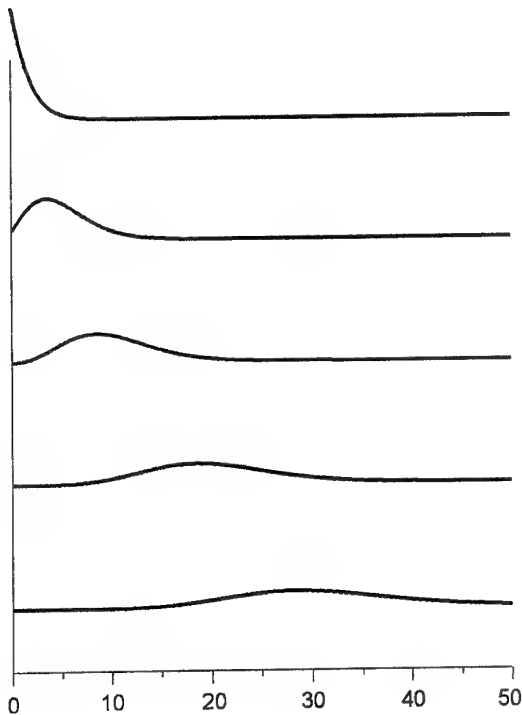
Fig.4. Time profiles of the pulse for different distances from source. Relaxation type of pulse propagation. $\varphi=0.0\pi$, $\Omega\tau=0.3$.
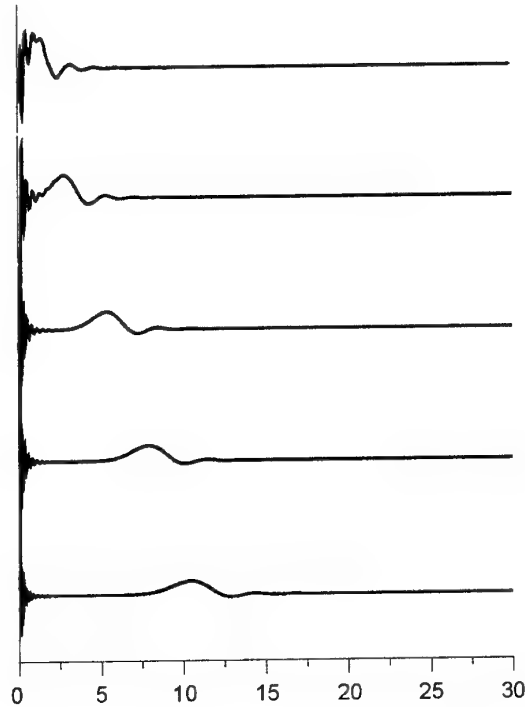
Fig.5. Time profiles of the pulse for different distances from source. Resonant type of pulse propagation. $\varphi=0.49\pi$, $\Omega\tau=7.0$.

The analysis of phase velocity and attenuation coefficient and direct numerical calculations of pulse dynamics allow us to image the following picture of different types of pulse dynamics for different domains of values of parameters $\Omega\tau$ and φ.

The pulse dynamics for parameters values on the line $\Omega\tau=0$, correspond to the pure relaxation Debye's model. In that medium the pulse body of gaussian form with power low of decay (Brillouin's precursor) follows for exponentially decaying elastic precursor. Qualitatively the same type the pulse dynamics exists for values of parameters in domains 1 and 3, corresponding to monotonic behavior of phase velocity, where the Brillouin's precursor also has the gaussian form. The mentioned pulse dynamics (without elastic precursor) is shown on the Fig.4.

In domains 2 and 4, where phase velocity has minimum, the Brillouin's precursor begins to oscillate. Need to note, that all variation of pulse dynamics occurs smoothly with variation of parameters. In domains 5 and 6 the phase velocity has maximum, and high-frequency components propagates with phase velocity greater then c_∞, that

leads to appearance of Sommerfeld's precursor propagating with pulse front. The oscillation frequency of Sommerfeld's precursor increases with passed distance and its amplitude decrease exponentially. In the limit case, corresponding to the Lorentz's model ($\varphi=\pi/2$) the exponent index vanishes and the power gross of the precursor appears. More low-frequency part of spectrum is responsible for formation of Brillouin's precursor, which is related with both the extremes of phase velocity and minimum of attenuation coefficient at zero frequencies. The qualitative behavior of pulse dynamics for parameters belong to domains 5 and 6 is shown on the Fig.5.

Above the features of short pulse dynamics in stable, dissipative media with positive attenuation coefficient in whole frequency domain were considered. However, the obtained solution (5), (6) proves to be correct and for non stable, active media on the beginning stage of pulse propagation, while its amplitude is enough small and it is possible to use the linear approximation. In this case the frequency dependencies of attenuation coefficient and phase velocity are more variety as it is shown on Fig.6, Fig.7.

340
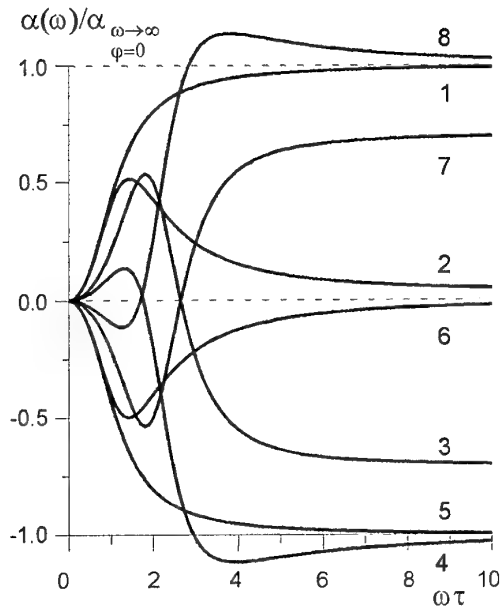
Fig.6. The attenuation coefficient in dependence on dimensionless frequency for different values of $\Omega\tau$ and φ.
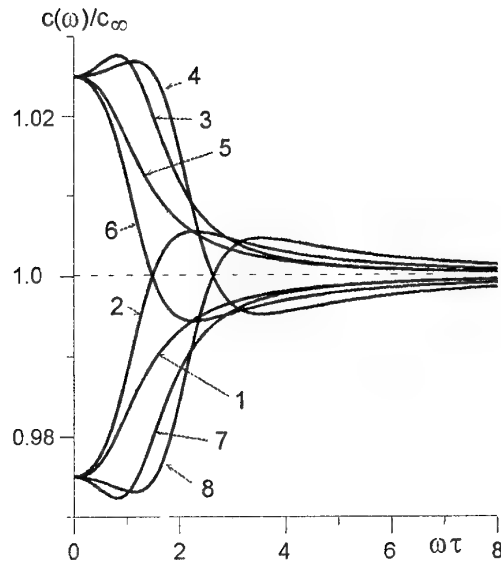
Fig.7. The phase velocity in dependence on dimensionless frequency for different values of $\Omega\tau$ and φ.

On the plane $\Omega\tau$ - φ the domains, in which the attenuation coefficient and phase velocity have different features corresponding to different pulse dynamics, are shown on Fig.8, Fig.9 for arbitrary active or passive media.
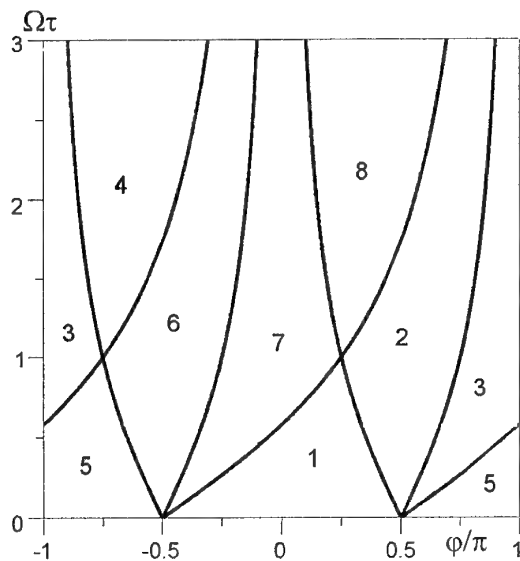
Fig.8. The domains of parameters $\Omega\tau$ and φ, corresponding to different behavior of phase velocity (The region numbers correspond to number of curves on Fig.7).
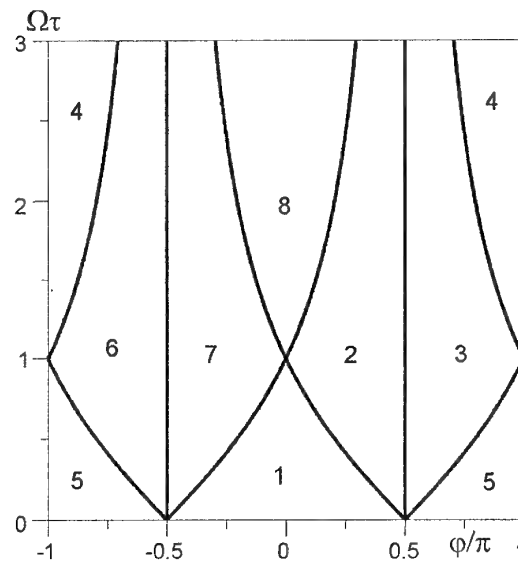
Fig.9. The domains of parameters $\Omega\tau$ and φ, corresponding to different behavior of attenuation coefficient (The region numbers correspond to number of curves on Fig.6).

341
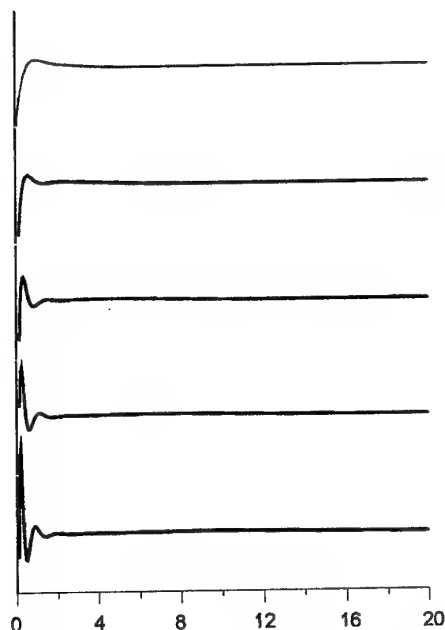
Fig.9. Time profiles of the pulse for different distances from source for domain 3: $\varphi=0.51\pi$, $\Omega\tau=1.5$.
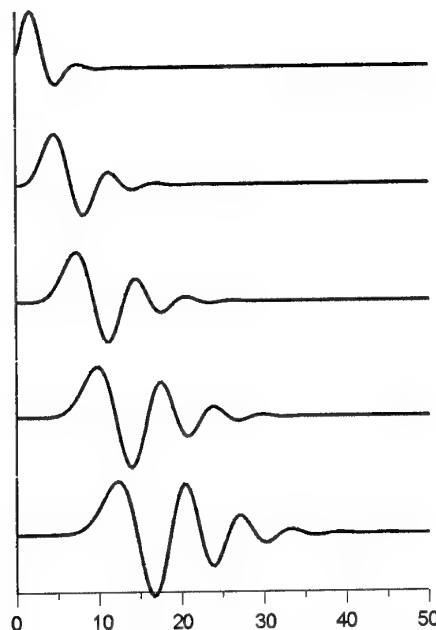
Fig.10. Time profiles of the pulse for different distances from source for domain 8: $\varphi=0.0\pi$, $\Omega\tau=1.5$.

As it seems on Fig.6, Fig.7, for pure active media 5, 6, for which the attenuation coefficient is negative in whole frequency domain, its frequency dependence, as well as frequency dependence of addition to phase velocity, differ only by sign from pure dissipative media 1, 2. For that media the basic forms of pulse dynamics will be determined by frequencies with maximal amplification coefficient. At this, if the maximum is achieved at high frequencies, then the pulse dynamics will be determined by Sommerfeld's precursor, if the maximum is achieved at finite frequency, then the pulse dynamics will be determined by Brillouin's precursor.

However, the most interesting case, as it seems, is the case of active-dissipative media 3,4,7,8, when on some frequencies medium is amplified, but on another frequencies it is dissipative. There are two basic regimes: amplification at low frequencies and dissipation at high frequencies 7,8, and versus 3,4. The pulse dynamics for two last cases is shown on Fig.10, Fig.11. As it seems on the figures, the pulse behavior is determined by frequencies, corresponding to the maximum of amplification coefficient.

References

1. Oughstun K.E., Sherman G.S. Electromagnetic pulse propagation in casual dielectrics. Berlin.: Springer-Verlag, 1994.
2. Kelbert M.Ya., Sazonov I.A. Pulse propagation in liquids. M.: Nauka 1991. (in Russian)
3. Larichev V.A., Maksimov G.A. Relaxation and resonance properties of acoustical media in the thermodynamic approach: the problem of uniform description. // Acoustical Physics 1998, V.44, N 6, p.709-716
4. Larichev V.A., Maksimov G.A. The general laws of short pulse propagation in resonant relaxation medium. / Proc. of 10-th session of Russian Acoust. Soc., V.1, p.69-73, Moscow, GEOS, 2000. (in Russian).

342

64. ABOUT SOME POSSIBLE MECHANISMS OF INTENSIVE WHIRL EXCITATION IN NONEQUILIBRIUM MEDIA

N.E.Molevich

Samara state aerospace university, Moskovskoe sh. 34, 443086 Samara, Russia
E-mail:molevich@mb.ssau.ru

Abstract. It is discussed two possible mechanisms of the whirl excitation in nonequilibrium media with the negative second viscosity. The examples of such media are gases with excited molecular states, nonisothermal plasma, chemically active mixtures. The first mechanism is connected with Reynolds number decrease. The second is stimulated by parametric interactions of sound waves with the noise whirl waves. In equilibrium medium the parametric increment has the linear dependence on propagation length x. In difference from it the parametric increment of acoustically active media has an exponential dependence on x. Moreover this interaction has no threshold in active media.

1. Introduction

It is known that the media in thermodynamic nonequilibrium can be acoustically active. The universal criterion of their acoustical activity is the inversion of the second (bulk) viscosity coefficient $\xi < 0$. In [1-4] it is shown that at $|\xi|/\eta \gg 1$ (η is shear viscosity coefficient) the influence of the relaxation phenomenon on laminar – turbulent transition can be important (at $\xi > 0$ Reynolds critical increases, at $\xi < 0$ it decreases). Intensive whirl excitation was observed e.g. in the glow discharge tube [5] and also in boundary layers of nonequilibrium gas flows [6]. The whirl dimensions were many less than the sound wave length.

In present work it is theoretically investigated another mechanism of whirl structure excitation, connected with the stimulated sound scattering.

2. The nonstationary theory of the stimulated sound scattering by whirls (SSW).

An acoustical scattering by noise whirls is even possible in homogeneous immovable media [7]. Let us consider the stimulated scattering of high-frequency sound ($\omega\tau \gg 1$) by the whirls in the immovable vibrationally excited gas with the simple relaxation model:

$$\frac{dE}{dt} = \frac{E_e - E}{\tau(T,\rho)} + Q ,\qquad (1)$$

where E, E_e is the vibrational energy and its equilibrium meaning per one molecule; τ is relaxation time; Q is the power of the pumping source ensuring the stationary nonequilibrium degree $S = Q\tau_0/T_0$; $\tau_0 = \tau(T_0,\rho_0)$; T, T_0, ρ, ρ_0 is the temperature, density and their stationary meanings.

The sound field is represented as the superposition of the pumping wave (Π_0) and scattered wave (Π_1):

$$\Pi = \frac{\Pi_0}{2}\exp[i(\vec{k}_0\vec{r} - \omega_0 t)] +$$
$$+ \frac{\Pi_1}{2}\exp[i(\vec{k}_1\vec{r} - \omega_1 t)] + c.c.$$

where $\Pi = P'/\rho_0 u_\infty^2$; P' is the pressure disturbance in the sound wave; u_∞ is the frozen sound speed.

The vortical mode ($\vec{W} = \text{rot } \vec{V}$, $\vec{V}$ is the velocity disturbance) is also represented in the wave form with the frequency $\Omega = \omega_0 - \omega_1 \ll \omega_0$, $\omega 1$ and the wave vector $\vec{q} = \vec{k}_0 - \vec{k}_1$:

$$\vec{W} = \frac{1}{2}\vec{W}_0 \exp[i(\vec{q}\vec{r} - \Omega t)] + c.c.$$

After the standard shortening procedure of the initial gasdynamics equations we receive the following set of equations

$$\frac{\partial \Pi_1}{\partial t} + u_\infty \cos\theta \frac{\partial \Pi_1}{\partial x} + g_1 u_\infty \Pi_1 = \vec{A}\vec{W}_0^*\cos\theta \Pi_0 ,$$

$$\frac{\partial \vec{W}_0^*}{\partial t} + \alpha_W \vec{W}_0^* = \vec{B}\,\Pi_1 \Pi_0^* ,$$

$$\Pi_0 = \Pi^{(0)}\exp(-g_0 x)\qquad (2)$$

This system of equations describes the amplification of the weak scattered sound and vortical waves in the given strong field of the dissipating pumping wave, which propagates along x. Here θ is the angle of scattering; $\vec{A} = [\vec{k}_0 \times \vec{k}_1]/2q^2$; $\vec{B} = -i2[\vec{k}_0 \times \vec{k}_1]g_1 u_\infty^2/k_1$; $g1 = \alpha_\infty + \delta(\omega_1)$; $\alpha_W = i\Omega + \nu q^2$; $g_0 = \alpha_\infty + \delta(\omega_0)$;

$\delta(\omega) = \omega^2 \left(2v/3 + \chi/2C_{V\infty}\right)/u_\infty^3$; v, χ are the kinematic viscosity and temperature conductivity coefficients; $\alpha_\infty = C_{V0}^2 \xi_0 / 2\rho_0 C_{V\infty}^2 \tau_0^2 u_\infty^3$ is the high-frequency sound decrement (if $\alpha_\infty > 0$), connected with the relaxation processes, forming the second viscosity; $\xi_0 = \tau_0(u_\infty^2 - u_0^2)\rho_0 C_{V\infty}/C_{V0}$ is the low-frequency coefficient of the second viscosity; $C_{P\infty}$, $C_{V\infty}$ are the frozen (high-frequency) specific heats at constant pressure and volume; $C_{P0} = C_{P\infty} + C_K + S(\tau_T - \tau_0)$,
$C_{V0} = C_{V\infty} + C_K + S\tau_T$ are the equilibrium (low-frequency) specific heats in vibrationally excited gas with relaxation law (1) [8]; $\tau_T = \partial \ln \tau_0 / \partial \ln T_0$; $\tau_\rho = \partial \ln \tau_0 / \partial \ln \rho_0$;
$C_K = dE_e/dT$; $u_0 = (C_{P0}T_0/C_{V0}m)^{1/2}$ is the equilibrium sound speed; m is the molecular mass. The second viscosity coefficient ξ_0 and α_∞ become negative at $S(C_{V\infty}\tau_\rho + \tau_T) + C_K < 0$ [8]. At $g_0, g_1 < 0$ such media is acoustically active. All coefficients of (2) take no account of the inhomogeneity of a stationary nonequilibrium medium. The additive corrections to decrement α_∞ in weakly inhomogeneous media (in longitudinal direction) were obtained in [9]. The qualitative view of system (2) is conserved.

We supplement the system (2) for case of the forward scattering ($\theta < \pi/2$) with the conditions $\Pi^{(0)}$=const, $\Pi_1(0,t) = P_1(t)$, $W(x,0) = 0$, $\Pi_1(x,0) = 0$. The solutions of the system (2) is obtained in form

$$\Pi_1(x,t) = P_1(y)\exp(-g_1 x/\cos\theta)\eta(y)$$

$$-\frac{1}{2}\int_0^t P_1(t-t')\frac{Z(x,t')}{y'}\cdot \qquad (3)$$

$$\cdot\exp(-\alpha_W y' - g_1 x/\cos\theta)\cdot J_1[Z(x,t')]\eta(y')dt',$$

$$\vec{W}_0^* = \vec{B}\,\Pi^{(0)*}\int_0^t P_1(t-t')\cdot$$

$$\exp(-\alpha_W y' - g_1 x/\cos\theta - g_0 x)\cdot \qquad (4)$$

$$\cdot J_0[Z(x,t')]\eta(y')dt',$$

where
$$y = t - x/u_\infty \cos\theta; \quad y' = y(x,t') ;$$

$$Z(x,t) = \left\{-2\vec{B}\vec{A}\left|\Pi^{(0)}\right|^2 \frac{y[1-\exp(-2g_0 x)]}{u_\infty g_0}\right\}^{1/2} ;$$

J_n is a Bessel function of the first kind of the order n; η is a saltus function of Hevisaid.

Accordingly to (3), (4) the intensities of the scattered sound and generated vortical waves

$\left|\Pi_1\right|^2 \sim \exp G_1(x,t)$, $\left|W_1\right|^2 \sim \exp G_W(x,t)$, where at forward scattering and $Z \gg 1$ the nonstationary increments are equal to

$$G_1 = -2vq^2 y - \frac{2g_1 x}{\cos\theta} + \left\{\frac{4\left|\vec{A}\vec{B}\right|\left|\Pi^0\right|^2 y[1-\exp(-2g_0 x)]}{g_0 u_\infty}\right\}^{1/2}$$

$$G_W = G_1 - 2g_0 x \qquad (5)$$

The stationary regime of SSW is established at $t \geq |t_S|$ where

$$t_S = \frac{x}{u_\infty \cos\theta} + \frac{\vec{A}\vec{B}\left|\Pi^{(0)}\right|^2 [1-\exp(-2g_0 x)]}{2\alpha_W^2 g_0 u_\infty}. \qquad (6)$$

The stationary increments have (at $Z \gg 1$) forms

$$G_{S1} = -\frac{2g_1 x}{\cos\theta} -$$

$$-\frac{\left|\vec{A}\vec{B}\right|\left|\Pi^{(0)}\right|^2 [1-\exp(-2g_0 x)]\Omega}{g_0(\Omega^2 + v^2 q^4)u_\infty}\,sign\,g_1 \qquad (7)$$

$$G_{SW} = G_{S1} - 2g_0 x \qquad (8)$$

The obtained results can be easily generalized on another boundary conditions. E.g., we must simply change in the expressions (5)-(8) $x \to x-L$, $AB \to AB\exp(-2g_0 L)$ for the backward scattering ($\pi/2 < \theta < \pi$) and condition on boundary $x=L$ in form $\Pi_1(L,t) = P_1(t)$.

3. SSW in dissipative media ($g_1, g_0 > 0$)

Accordingly to (7), (8) the forward scattering amplification is possible at $g_1 > 0$ only in anti stokes region ($\Omega < 0$). The stationary parametric increments (7), (8) are linear functions on x at $g_0 x \ll 1$.

The threshold intensity of the pumping sound wave is determined by condition

$$\left|I^{(0)}\right|^2 \geq \frac{g_0\rho_0 u_\infty^2 q^2 k_1 (\Omega^2 + v^2 q^4)x}{[1-\exp(-2g_0 x)]\Omega[\vec{k}_0 \times \vec{k}_1]^2 \cos\theta}. \qquad (9)$$

SSW is the resonance process. The amplification has a maximum at vortex frequency $\Omega_w = -vq^2$, where $q \approx 2k_0\sin\theta/2$. At $g_0 x \ll 1$ the condition (9) coincides with [7]. We can obtain the estimation of the threshold intensity $I^{(0)} \approx 2\text{mW/cm}^2$ for the normal conditions of gas medium and $\omega_0 =$

344

$2\pi 10^4$Hz, $\theta=10°$. The characteristic whirl dimension $\Lambda=\pi/q\approx 10$cm. At $\Omega=\Omega_W$ the threshold intensity $I^{(0)}$ increases with the scattering angle and sound frequency $\sim\omega_0\sin^2(\theta/2)$. The whirl dimension decreases with a increase of this quantities~ $1/\omega_0\sin(\theta/2)$.

4. SSW in acoustically active media $(g_1, g_0 >0)$

The negative second viscosity changes the properties of SSW cardinally. Accordingly to (7) in acoustically active media this process has not threshold. At the weak parametric connection when the second item in (7) is less than the first one the vortices excitation can be observed due to both the stokes and antistokes scattering independently on scattered sound direction. For the forward scattering at $t>x/u_8\cos\theta$ we have

$$\vec{W} = \frac{\vec{B}\Pi^{(0)*}P_1}{\alpha_W}\exp[-g_0 x - \frac{g_1 x}{\cos\theta}], \qquad (10)$$

that is at $\cos\theta \sim 1$ the whirl wave increases with the double sound increment. In literature such transfer of the linear increment of the instable wave on the weak signal wave is sometimes named by superheterodyne amplification[10].

If transverse dimension of the nonequilibrium medium d is greater than Λ the stimulated scattering is more effective in the forward direction as $|B/\alpha_W|\sim(\sin\theta/2)^{-1}$. Moreover $|B/\alpha_W| \sim \xi/\eta$ at great values of ξ, that is it increases with the second viscosity coefficient increase.

The possible length x in (10) can not be more than the break length $x\le L_B$, where
$$L_B = -\ln(1-\alpha_\infty L_B^E)/\alpha_\infty \qquad [11],$$
$L_B^E = 2C_{V\infty}/\Pi^{(0)}k_0(C_{P\infty}+C_{V\infty})$ is known expression of the break length at $\alpha_8=0$ [12]. At $x\sim L_B$ the high-frequency sound transformed into the saw-toothed wave. In dissipative media the decrement sharply increases at such length and parametrical interactions become impossible later on. In active media the saw-toothed wave can exist as the stationary structure, which propagates without amplitude change [13,14]. That is why at $x>L_B$ parametrical interactions are not stopped similar to theirs in dissipative media, but become more complicated and the plane wave approximation is not further correct.

At great $I^{(0)}$ the second item in (7) can be important. In this case (if $d>\pi/2k_0\sin\theta/2$), the vortex amplification results from the forward stokes scattering as $G_{SW} \sim \Omega\sin^{-2}(\theta/2)$. The taking into account the pumping sound wave amplification $(g_0<0)$ leads to the exponential dependence of the stationary increment on x instead of the linear one

in dissipative media. Analogous result (the exponential increment) was obtained for stationary parametric amplification ultrasonic waves in piezosemiconductors [15]. The time of the stationary regime establishment (6) is also exponential function on x $(t_S \sim |G_{S1} + 2g_1 x/\cos\theta|/8\nu k_0^2\sin^2\theta/2)$. Hence the law-angle scattering will be nonstationary.

We can estimate the nonstationary increment G_W (5), e.g., for parameters $I^{(0)}=1$mW/cm^3, $\theta=10°$, $\omega_0=2\pi 10^4$Hz and normal conditions of acoustical active gas media with $g_0 \sim 0.01$cm^{-1}. At $x\sim L_B \sim 2$m, $t=1$min $(t_S\approx 14$min) we have $G_W\approx 25$. In this case the intensity of the whirl wave, developing from the thermal noise level $(I_t\sim 10^{-18}\div 10^{-16}W/cm^2)$, $I_W\sim I^{(0)}$. As the active media noise can be significantly more than thermal noise of an equilibrium medium the propagation of the strong sound wave can be accompanied by the intensive vortex excitation even at $G_W<25$. The forward sound scattering leads to excitation of the macroscopic whirls with Λ greater than sound wave length.

Conclusion

It is considered first the nonstationary theory of the stimulated sound scattering by the whirls in the dissipative and active media. In the acoustically active medium this process has not threshold and the whirl excitation can be intensive.

References

1. Emanuel G. Bulk viscosity of a dilute polyatomic gas // Phys. Fluids A. 1990. V.2. No.12. P. 2252-2254.
2. Kogan E.Ya., Molevich N.E. Sound wave propagation in a nonequilibrium fluid// Acoustical Physics. 1995. V. 41. No.4.
3. Nerushev O.A., Novopashin C.A. Transition to turbulence for N2 и CO in a circular tube// Abstracts of the 4th Siberian Workshop [in Russian]. 1997. P.76-77.
4. Molevich N.E. Asymptotic analysis of the syability of a plane – parallel compressible relaxing boundary layer// Fluid Dynamics. 1999. V34. No.5. P. 675-680.
5. Galechyan G.A. Acoustical waves in plasma // Uspehi fizicheskih nauk [in Russian]. 1995. V. 165. No.12. P. 1357-1379.
6. K Beaulieu W., Klimov A.,Bityurin V., and et.al. Plasma Aerdynamic WT tests with 1/6 Scale Model of Nose Part of F-15 // AIAA-99-4825 Paper, Proc.WIG-3, Norfolk, 1999.
7. Pushkina H.И., Hohlov R.V. About stimulated sound scattering by whirlwaves //

Akusticheskii Zh. [in Russian]. 1971. V.17. No.1. P. 167-169.

8. Kogan E.Ya., Molevich N.E. Sound wave collapse in nonequilibrium molecular gas// Zh. Technical Fiziki [in Russian]. 1986. V. 56. No.5. P. 941.

9. Molevich N.E. Sound amplification in inhomogeneous flows of nonequilibrium gas// Acoustical Physics. 2001. V. 47. No.1. P.119-122.

10. Gulyaev Yu.V., Ziljberman P.E. To theory of sound waves parametric interaction in piezosemiconducter // Fizika i technika poluprovodnikov[in Russian]. 1971. V.5. P.126-133.

11. Molevich N.E. To question of break length in acoustically active medium // Tecnical Physics Letters 2001 (in Print)

12. Rudenko O.V., Soluyan S.I. Theoretical principles of nonlinear acoustics [in Russian]. M.: Nauka, 1975.

13. Ott E., Manheimer W.M., Book D.L. et al. Model equations for mode coupling saturation in unstable plasmas // Phys. Fluids. 1973. V.16. No.6. P.855-862.

14. Makarian V.G., Molevich N.E. Stationary high-frequency structures in vibrationally excited gas // V Int. School-Seminar Nonequilibrium Processes and their Applications (September, 2000): Contrib. Papers. Minsk, Belarus. 2000. P.20-23.

15. Zemon S., Zucker J., Wasko J.H., Conwell E.M., Ganguly A.K. Parametric amplification of ultrasonic waves in CdS// Appl. Phys. Lett., V.12. P.378 .

65. PLASMA JET AERODYNAMICS INFLUENCE ON THE ARRANGEMENT OF CORRECTION THRUSTERS OF A SPACECRAFT

U.M.Ermoshkin, A.E.Chugunov
NPO PM, Zheleznogorsk

M.V.Kraev
SAA, Krasnoyarsk

V.S.Slavin
KGTU, Krasnoyarsk

For geostationery spacecrafts with the rotation axis of solar batteries passing through the mass center, the interaction of plasma jet with solar battery panels inevitably results in thrust losses and disturbance momentum, which is usually compensated by orientation thrusters. The mass of the propellant necessary for this should be taken into account.

There were carried out optimization calculations of a correction thruster system at the angle of 10-15°, the non-uniformity of plasma jet being considered. Compared to the angle of 40-45°, this reduces thrust losses down to 3-4%, decreases disturbance momentum by two thirds and allows removing the working time limits through design steps only.

66. OPTIMIZING THE TECHNOLOGY OF PLASMA THRUSTERS FIRING TESTS

U.M.Ermoshkin, A.V.Nikipelov, A.V.Romashko, V.B.Serogodskiy, V.V.Christich
NPO PM, Zheleznogorsk

V.M.Kraev
MAI, Moscow

The use of stationery plasma thrusters (SPT) for the orbit correction propulsion system (PS) of a geostationery satellite with service life of 10-15 years allows to considerably reduce necessary fuel supply. At transition from liquid propellant engines to SPT, the saved mass makes up hundreds of kilograms for a long life spacecraft.

The integration of SPT in a spacecraft is determined by a comprehensive task complex, which is related to carrying out of firing and docking tests, development and acceptation tests of PS with the control system and the onboard voltage converter with parameters needed for PS.

There were carried out firing tests of technological samples of correction units, that include an M-100I SPT used for spacecrafts "Express" and "Sesat".

The firing was conducted in a special cryogenic chamber at the condition of high vacuum (10-5mm.hg.p.) and successive command controlling. Working medium consumption was regulated by thermal chokes by the discharge current. The nominal consumption was 5,5mg/sec, the discharge voltage and discharge current were 300±15V and 4,5±0.1A respectively. The chamber had internal cryogenic screens cooled by liquid nitrogen, which imitated "cold outer space".

The analysis of PS firing test results proved the working capacity of SPT at the conditions realized in the test-bed to be true. The test characteristics were maximally close to the real situation.

67. DEVELOPMENT OF METHODS OF MONITORING AND CONTROL OF THE CONDITIONS OF ELECTRODE DISCHARGE IN PLASMA POWER FACILITIES

N. N. Baranov

United Institute for High Temperatures of Russian Academy of Sciences,
13/19 Izhorskaya Str., 127412 Moscow, Russia

Abstract. A comparison is made of the conditions of electrode operation in plasma power facilities (PF) of different types such as magnetohydrodynamic generators and thermionic converters. The results are given of an experimental check of a universal electrophysical method of fluctuation diagnostics for monitoring electric-discharge processes, as well as for revealing and preventing irregular (pre-emergency) conditions in the PF operation. It is demonstrated that the methods of fluctuation diagnostics may be used to advantage in developing devices for monitoring (in real time) and control of plasma PFs of different types for the purpose of increasing their reliability and service life.

Introduction

The problem of developing highly efficient plasma power facilities, whose operation is based on the methods of direct energy conversion (DEC PF), such as magnetohydrodynamic generators (MHDG) and thermionic converters (TC), is associated both with attaining high specific energy performance (which makes them competitive with energy sources of other types) and with ensuring a high reliability and a long service life of the PF. For this purpose, it is first of all necessary to monitor the conditions of electrode discharge in DEC PFs, because the discharge conditions represent one of the major factors defining the reliability of operation of a plasma power facility [1].

The conditions of current flow to the electrode (or the form of discharge on the electrode) in plasma PFs depend largely on the magnitude of the current being extracted, on the type and parameters of the electrode (material, configuration, temperature), on the parameters of the working medium of the interelectrode gap (temperature, pressure, concentration of plasma components), and on a number of other factors.

In accordance with the adopted terminology, the following types of electrode discharges are identified in plasma PFs:
— diffuse or diffusive (a discharge distributed uniformly over the entire electrode surface is characteristic, as a rule, of low values of current density);
— microarc (several microarcs with an overall current of several to tens of amperes are simultaneously present on the electrode surface);
— high-current arc (a single high-current arc with a current of several tens to a hundred amperes burns on the electrode surface).

An electrode discharge may be stationary or moving. A diffuse discharge is stationary, while microarcs move at random over the electrode surface. High-current arcs are usually stationary and located at the electrode edges.

As a rule, the standard (rated) operating conditions of a plasma PF have a certain type of discharge corresponding to them, which provides for a long-term trouble-free operation of the power facility.

The results of investigations performed at DEC PFPs of different types demonstrate that the methods of fluctuation diagnostics, which involve the recording and analysis of fluctuations of the electrical parameters of PFs (potentials and voltages or currents), present a reliable means for identifying the electrode discharge and precluding the emergence of irregular (pre-emergency) conditions in the PF operation.

The methods of fluctuation diagnostic do not require any additional complication of the PF design; therefore, the use of these methods does not affect the reliability of the PF.

1. Operating conditions of electrodes in plasma power facilities

1.1. MHD Generator

The basic electrophysical processes at the channel walls of an MHDG are associated with the transport of current between a solid and a plasma. Basically, these are the same processes as those occurring in a classical gas discharge. However, the pattern of discharge phenomena in an MHDG exhibits singularities which are defined by the presence, as a "second electrode," of a plasma with a relatively high equilibrium concentration of charged particles and high rates of ionization and recombination.

In full-scale MHD generators, the electrode walls are not observed visually, one can judge the processes on the electrodes only indirectly, i.e., by the output electrical parameters (current, voltage, output power of the MHDG).

The phenomenological investigations of the electrode processes in model MHD facilities have revealed that different modes of current flow to the electrodes (diffuse, microarc, high-current arc) have different regions of the curve of the electrode current-voltage characteristic (CVC) with different slopes corresponding to them. When the high-current discharge conditions are realized, a considerable increase in the current density is caused by a small variation of the voltage drop in the electrode boundary layer (see Figs.1 and 2).
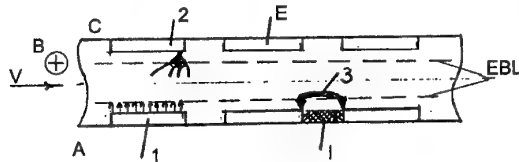
Fig.1. Different modes of discharge on electrodes in a flow of plasma: (1) electrode operating in the diffuse mode, (2) electrode operating in the arc mode, (3) interelectrode Hall breakdown; C – cathodes; A – anodes; E – electrode; I – insulator; EBL – electrode boundary layer.
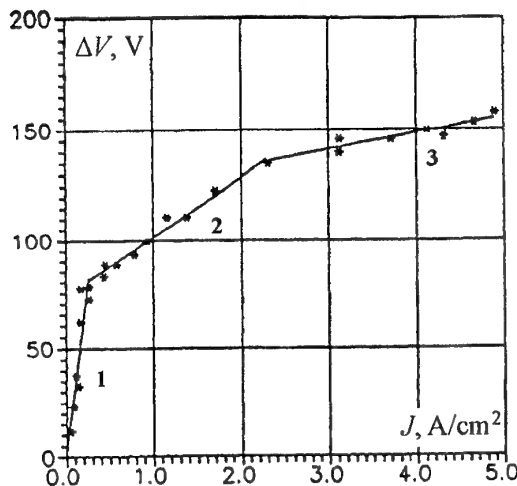
Fig.2. A typical current-voltage characteristic of the electrode layer in a model MHD channel: (1) diffuse flow of current, (2) microarc mode, (3) high-current arc mode.

The results of experiments in model MHD facilities were supported by the results of processing of the current-voltage characteristics of large-scale MHD channels [2]. It has also been found that high-current arcs located on the electrode edges in the vicinity of interelectrode insulators may cause emergency failure of the structure of the electrode walls of MHD channels (see Figs.3 and 4).
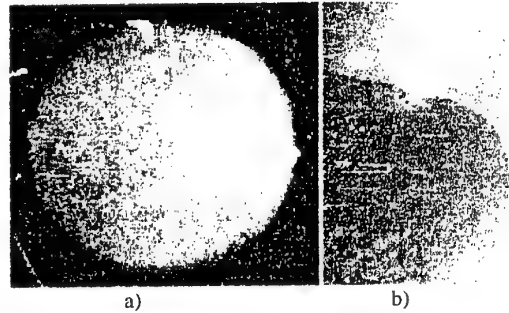
Fig.3. Photographs of electrodes operating in the (a) microarc and (b) high-current arc modes.
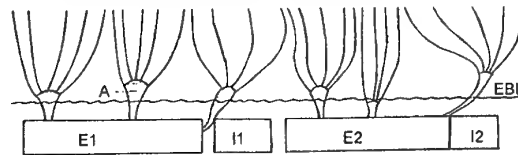
Fig.4. A model image of current flow to electrodes in the arc mode: A– arc; E– electrode; I– insulator; EBL– electrode boundary layer.

Therefore, the current-voltage characteristic of an MHDG may serve as a means of diagnostics. However, in the course of continuous operation of an MHDG, the level of insulation between some of its elements may decrease, and leakage currents may arise in the structure. The CVC is distorted and exhibits no characteristic slope kinks. As a result, it is difficult to identify the discharge conditions by the form of the CVC.

Along with high-current arcs on the electrodes, emergency situations in MHDGs are caused by the interelectrode Hall breakdown, i.e., the emergence of arcs between adjacent electrodes (cathodes or anodes) separated by an interelectrode insulator (Fig.1).

The arc arises under the effect of a longitudinal (Hall) electric field E_H in the MHD channel when the voltage ΔV_H between adjacent electrodes reaches the value of the Hall arc ignition voltage, $V_{ign} = \Delta V_H = E_H \cdot S$, where S is the segmentation pitch between electrodes.

Therefore, special importance in the operation of an MHD generator (in the absence of visual observation of the electrodes) is assumed by the development of the methods of monitoring high-current arcs on the electrodes and the interelectrode Hall breakdown; should these arcs and breakdown arise, prompt measures must be taken to eliminate the pre-emergency conditions.

350

1.2. Thermionic Converter

The operation of thermionic converters (TC) is based on the effect of emission of charged particles from a heated electrode.

A TC scheme involves two electrodes placed in a hermetic casing, namely, a high-temperature emitter and a less heated collector, which are separated by an interelectrode gap (IEG) filled with a cesium vapor; during the operation of the instrument, this vapor generates a weakly ionized plasma, i.e., a conducting medium with a relatively high coefficient of thermal emf.

The emission current density (that is, the maximum number of electrons that may be extracted per unit time per unit surface of the electrode) increases abruptly with increasing emitter temperature and decreasing work function of the emitter.

The presence of an electrically conducting plasma, as well as the decrease in the work function of the electrodes in cesium vapors (a cesium-barium mixture is also used for the purpose), provide for an economical operation of the instrument at the specific power on the electrodes ranging from 1 to $10W/cm^2$ (specific power values of up to $150W/cm^2$ could be obtained in demonstration facilities), whereby compact energy sources may be developed with a small relative weight of the thermionic system proper.

Modern TCs are instruments with refractory metal-based electrodes (single-crystal tungsten or molybdenum alloys for the emitter and niobium or molybdenum for the collector, sometimes provided with coatings improving the electronic and optical properties of the surface). The emitter temperature ranges from 1400K in a cesium TC to 2500K in a cesium-barium TC. Owing to the adsorption of cesium on the emitter surface, a decrease in the work function of the electrodes may be attained to a level required for efficient operation of the instrument, namely, 2.6–2.8eV on the emitter and 1.4–1.6eV on the collector.

A thermionic converter is a dc source. Arbitrary values of voltage and current strength are obtained by using series-parallel connections of TCs. Inverters are used to produce alternating current. However, connection schemes and conditions exist, in which a TC generates a pulsating current, which enables one to isolate the variable component. TCs combine most conveniently with nuclear reactors and isotope sources of heat to provide for a greater independence than in the case of systems utilizing the heat of organic fuels and solar energy.

Figure 5 gives a schematic view of a TC built in a nuclear reactor, where the heat source is provided by the fission reaction of uranium nuclei.
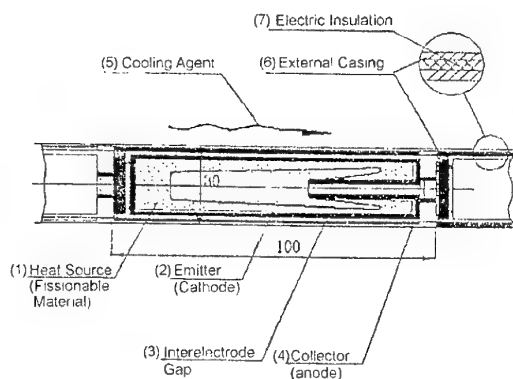
Fig.5. A thermionic electricity-generating cell: (1) heat source (fissionable material), (2) emitter (cathode), (3) interelectrode gap, (4) collector (anode), (5) cooling agent, (6) external casing, (7) electric insulation.

Life duration tests of TCs incorporated in nuclear power plants have revealed the possibility of attaining a reliable continuous TC operation of 20 thousand hours and more.

The electrodes in a thermionic converter, depending on its parameters (temperature, work function), magnitude of the IEG, and the parameters of the interelectrode medium (composition, pressure, etc.), may operate in a distributed (diffusion) or in a contracted (discharge) mode.

The diffusion mode is realized provided the Knudsen number for plasma $Kn=d/\lambda>>1$ (where d is the interelectrode gap, and λ is the electron free path), and the electric field in the plasma is lower than the threshold of emergence of contracted discharge. In so doing, classical conditions are realized in the IEG of electron transport due to the mechanism of ambipolar diffusion in a plasma forming as a result of surface ionization of cesium.

The transition to the discharge mode occurs at a relatively high concentration of plasma formed in the IEG due to the mechanism of stepwise ionization upon electron collision with atoms of the interelectrode medium. This mode is characterized by high values of current density (up to $20A/cm^2$ and higher) and of efficiency of TC (10–12% and higher).

The discharge mode of the electrodes is used most frequently in TC devices.

During the TC operation, the electrodes are not observed visually (similar to the case of MHD generator). Therefore, the development of reliable methods of monitoring the conditions of discharge on the TC electrodes is an urgent scientific-and-technical problem.

2. Development and application of methods of fluctuation diagnostics for monitoring electric-discharge processes in plasma power facilities

2.1. Experiments with MHD Generators

The diagnostic procedure for detection of the interelectrode gap was developed on the basis of recording and analysis of fluctuations of interelectrode Hall voltage. This procedure was used in experiments to find that the emergence of interelectrode arcs is characterized by the appearance, in the fluctuation spectrum of interelectrode Hall voltage, of intense high-frequency noise with a frequency of the order of 100kHz. This procedure was evaluated when studying Hall breakdown in MHD channels in both applied and induced electric field. Figure 6 gives, by way of illustration, oscillograms of fluctuations of voltage between adjacent electrodes of an MHDG in the absence (a) and presence (b) of an interelectrode Hall arc.
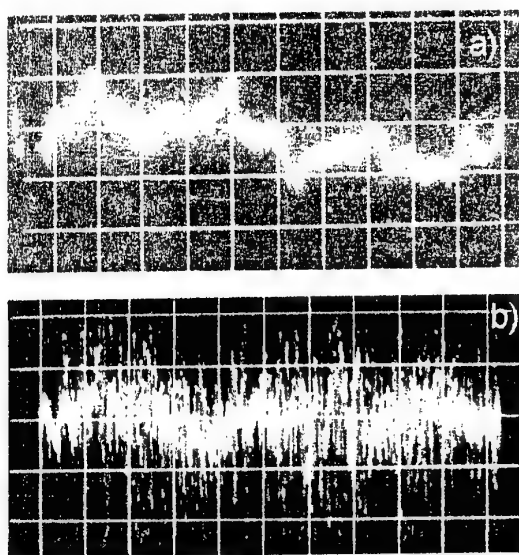
Fig.6. Oscillograms of fluctuations of voltage between neighboring electrodes of an MHDG (a) in the absence and (b) in the presence of an interelectrode Hall arc: a mode with B=1.7T and V_{1-2}=100V; (a) I_1=50A and I_2=30A, (b) I_1=66A and I_2=35A; time base of 1ms per scale division and sensitivity of 4V per scale division.

Experiments in MHD facilities of different scales and power levels have revealed that the development of interelectrode Hall breakdown in an MHD generator is largely defined both by the magnitude of interelectrode Hall voltage and by the mode of discharge on the electrodes: the arc mode of electrode operation promotes the development of interelectrode breakdown. In addition, the arcs on

electrodes, especially, high-current arcs, bring about intense erosion and reduced reliability of operation of the MHD generator. Therefore, the diagnostics and monitoring of the arcs assume critical importance.

For this purpose, the correlation between the fluctuations of electrode voltage drop and the mode of current flow to the electrode was determined. As an illustration, we will examine the results obtained at the U-25 BM Facility with a thermal power of about 25MW (Fig.7).
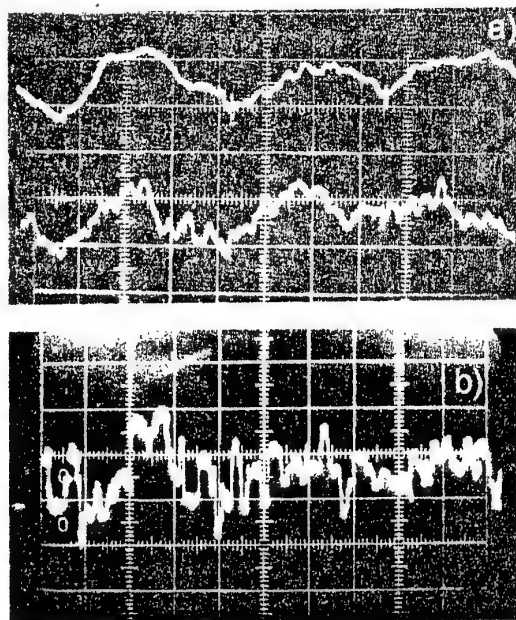
Fig.7. Oscillograms of fluctuations of cathode voltage drop on electrodes operating in (a) the diffuse and microarc modes and (b) in the high-current arc mode; time base of 1ms per scale division and sensitivity of 2V per scale division.

With the diffuse mode of discharge on the electrodes, 300-Hz fluctuations due to the electric load (inverter) were observed in the fluctuation spectrum of electrode voltage drop. A variation of the discharge mode (emergence of microarcs on the electrodes) was accompanied by the appearance of components with a frequency from 1 to 10kHz in the fluctuation spectrum of electrode voltage drop. The development of a high-current arc on the electrodes was accompanied by an increase in the fluctuation frequency to tens of kHz.

Therefore, the methods of fluctuation diagnostics involving the recording of fluctuations of interelectrode Hall voltage and fluctuations of electrode voltage drop in an MHD channel enable one to reveal, in real time, the development of the interelectrode Hall breakdown and of the arc mode of discharge on the electrodes.

352

2.2. Experiments with a Gas-Discharge Thermionic Device – Cesium-Barium Tacitron

The possibilities of using the fluctuation diagnostic methods for monitoring the efficiency of thermionic converters were studied in experiments with a high-current tacitron, a thermionic device for controlling the current in electric circuits.

A fully controlled three-electrode cesium-barium tacitron provides for a high current density of 10 to 20A/cm^2 in an electrode discharge at a low voltage of 1.7-2.5V and low pressure of 10^{-2} torr in the discharge chamber [3].

The modulation of anode current in the tacitron, as well as the current control (both the ignition and quenching of the discharge), are accomplished by delivering heteropolar voltage pulses with an amplitude of 10 to 40V to the control electrode (grid) located between the cathode (emitter) and anode (collector).

The experimental methods employed for monitoring the conditions of tacitron operation and for measuring the discharge plasma parameters in the tacitron are mainly probe and optical methods. Probes are used to determine the plasma density and potential and the electron temperature and distribution function. An analysis of the optical spectra of plasma radiation enables one to determine the electron density and temperature.

The investigation results have demonstrated that a discharge in a tacitron is very sensitive to the pressure of working gas, i.e., cesium vapors, in the interelectrode gap. At low and medium values of current, a discharge takes up only a part of the electrode area and moves continuously along the electrode surface. In spite of the constancy of the total anode current, the local current density varies continuously.

Probe measurements of the plasma parameters, performed in different discharge regions (in the cathode and anode regions and in the grid meshes), revealed fluctuations of the local density of plasma from almost zero to a maximum value with a frequency of 10 to 20kHz.

The fluctuations of the local density of plasma reflect on the probe characteristic. Figure 8 gives (in its bottom part) the variations in time of the electron current to one of the probes located in grid meshes at different points along the electrode surface and of the probe potential. One can see that the fluctuations of the local plasma density bring about fluctuations of the current and potential of the probes with the same frequency (of the order of 10 to 20kHz).

In its top part, Fig.8 gives the variation in time of the total anode current and voltage. The fluctuations of the local plasma density do not show up in the graph of the anode current;

however, the graph of anode current exhibits a slight modulation with the same frequency (10 to 20kHz) as the fluctuations of the local plasma density. The frequency of fluctuations of the local plasma density increases somewhat with the anode voltage and anode current.
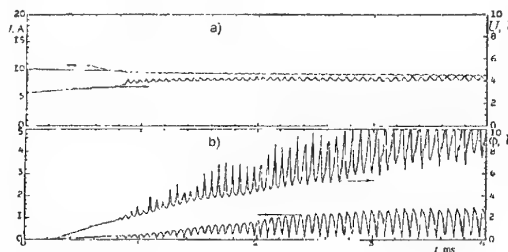
Fig.8. Standard conditions of tacitron operation (in the absence of control pulses on the grid): (a) anode current and voltage, (b) current to the probe and probe potential in the cathode region.

The foregoing characteristics correspond to a discharge that "travels" on the electrode surface. Owing to continuous displacement of the discharge along the electrode surface, the concentration of neutral atoms in the discharge region increases, thereby providing for an increase in the ionization rate and for the maintenance of the balance between this rate and the rate of escape of ions from the discharge region. In this mode, a stable modulation of current begins when control voltage pulses are delivered to the grid.
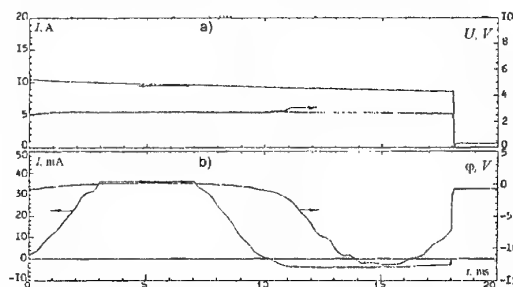
Fig.9. Nonstandard conditions of tacitron operation at a high pressure of cesium vapors (in the absence of control pulses on the grid): (a) anode current and voltage, (b) current to the probe and probe potential in the cathode region.

As the pressure of cesium vapors increases, the fluctuations of the local plasma density disappear, and the discharge becomes stationary. Figure 9 shows in its top part the behavior in time of the anode current and voltage, and in its bottom part, of the electron current and probe potential in the stationary mode of the

353

discharge. The fluctuations of the probe current and voltage, as well as the noise at anode voltage, cease when the fluctuations of the local plasma density disappear. The stability of current modulation in this mode deteriorates.

When the pressure of cesium vapors decreases, the escape of the heavy component of plasma from the discharge zone brings about a spontaneous quenching of the discharge. A new ignition of the discharge becomes possible after a certain time during which the concentration of cesium atoms in the discharge gap is restored to the adequate value. The processes of ignition and quenching cease to be regular, skipping of the discharge phase in the process of modulation is observed, and the stability of modulation also deteriorates (Fig.10).
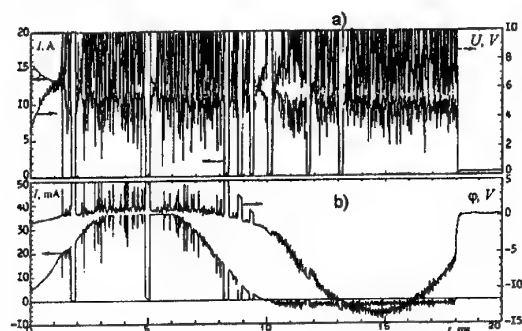
Fig.10. Nonstandard conditions of tacitron operation at a low pressure of cesium vapors and in the absence of control pulses on the grid: (a) anode current and voltage, (b) current to the probe and probe potential in the cathode region.

Therefore, the frequency-response characteristic of the anode voltage may be used for choosing the desired pressure of cesium vapors at which a stable tacitron operation is possible in the mode of current modulation.

The fluctuations of the anode voltage and current of a tacitron may be used to monitor the tacitron operation and the discharge mode (with the standard and nonstandard conditions revealed without using the probe or spectral methods of diagnostics), namely,

— low-amplitude regular fluctuations of the anode voltage (with a frequency of 10 to 20kHz) (Fig.8) correspond to a nonstationary discharge traveling on the electrode surface (standard conditions);

— simultaneous strong irregular fluctuations of the anode voltage and current (Fig.10) correspond to unstable combustion of a discharge with spontaneous disruptions and repeat ignitions (characterize nonstandard conditions); and

— the total absence of fluctuations of the anode voltage (Fig.9) corresponds to a stationary discharge taking up the entire area of the electrode (nonstandard conditions).

3. Options of practical realization of automatic systems of monitoring and prevention of emergency conditions in plasma power facilities

The results of experiments performed with plasma power facilities of two types, namely, MHD generator and thermionic tacitron, have demonstrated that the method of fluctuation diagnostics enabling one to monitor electric-discharge processes on electrodes and register the emergence of nonstandard conditions may be a basic method in developing devices for monitoring and improving the reliability and extending the service life of power facilities.

3.1. Device for Recording an Arc Breakdown and Prebreakdown States

As an example, we will examine the engineering solution of the problem of automatic control of the operating conditions of an MHD generator (as the most electrically and thermally stressed plasma PF) for the purpose of prevention of emergency conditions caused by electric effects (development of a high-current arc discharge on the electrodes or the emergence of Hall breakdown).

The detection and monitoring of the above-identified undesirable effects require the recording and analysis of fluctuations of interelectrode and electrode voltage drops in an MHD channel.
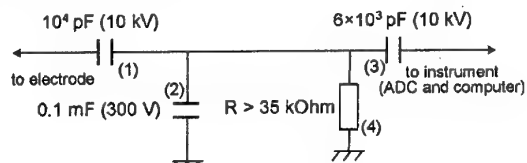
Fig.11. A scheme of recording the potentials in an MHD channel.

One of the developed schemes for recording potential fluctuations in an MHD channel is given in Fig.11. The scheme comprises a capacitive divider 1, 2 attenuating the signal to safety level, as well as elements 3, 4 of a system of high-voltage protection of the measuring circuit. The capacitance in the divider upper arm 1 is rated for twice the working voltage, and that in the lower arm 2, for a voltage of the order of several hundred volts, proceeding from the conditions of

354

measurement of a variable signal with a minimal frequency of several hertz.

When voltage fluctuations are to be measured, two similar dividers are connected to a recorder in a differential circuit. In so doing, the capacitances in the divider arms must be calibrated with a high accuracy (at least 0.1%).

In the input circuits of the measuring instrument, provision is made for protective capacitances 3 rated for a higher-than-working voltage.

The recorded signals are delivered via an ADC to a computer input for spectral-correlation processing.

For monitoring the potentials from a large number of electrodes in the process of MHDG operation, one must use a scanning device providing for automatic connection of the recorder via capacitive divider in series to the potential outputs of all electrodes being investigated.

The foregoing scheme (Fig.11) has provided a basis for developing a device which enables one to automatically perform, in real time, the recording and analysis of fluctuation spectra of electrical parameters with a view to identifying groups of electrodes in an MHD channel, on which a high-current arc discharge mode is developed or interelectrode (Hall) breakdown, as well as to produce respective signals to the control system (as described in [4]).

3.2. Control of the Mode of PF Operation for Prevention of Nonstandard Conditions

(a) MHD generator

In the case of nonstandard (pre-emergency) conditions, an MHD generator may be controlled with the aid of regulators of the output voltage or current of the MHDG (for example, inverter settings of the MHDG loading system).

For prevention of an emergency situation in the case of prebreakdown condition (or condition of unstable Hall breakdown) between adjacent electrodes of the MHDG, it is necessary to reduce the interelectrode voltage ΔV_H, i.e., the Hall field intensity E_H in the MHD generator, because $\Delta V_H = E_H \cdot S$, where S is the electrode segmentation pitch.

The Hall field E_H is proportional to the transverse current density j_y and to the magnetic field-dependent Hall parameter β: $E_H \sim \beta <j_y>/<\sigma>$, where $\beta \sim B$, and $<\sigma>$ is the average electrical conductivity of the plasma.

Therefore, in order to reduce the Hall field intensity, one must reduce the current density (total current) on the electrode where a prebreakdown

condition is observed, or on a group of one-two electrodes adjoining the latter electrode (Fig.12).
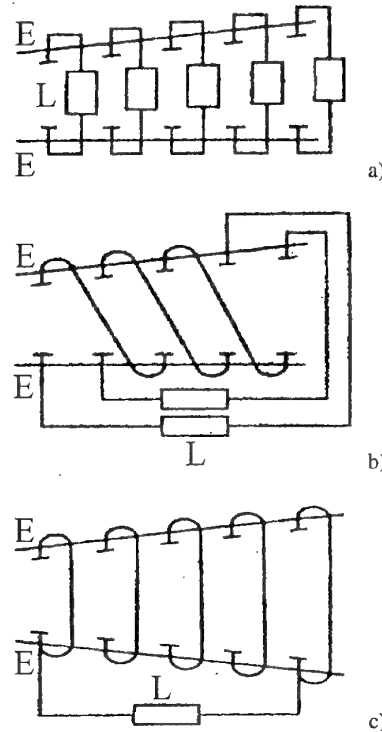
Fig.12. A scheme of connection of an MHD generator to load: (a) Faraday-type MHD generator, (b) MHD generator with diagonal connection of electrodes, (c) Hall-type MHD generator; E– electrodes; L– load.

In the case of the Faraday scheme of loading an MHD generator, this reduction of current must be provided for by changing the settings of inverters connected to opposite electrodes (or by varying the resistance in the load circuit). In order to reduce the Hall field intensity E_H in the case of the diagonal loading scheme, one must increase the longitudinal current I_H in the MHD generator (by reducing the longitudinal voltage),

$$E_H = \beta <j_y>/<\sigma> - <j_H>.$$

In the single-load MHDG scheme, the total current of the MHD generator is reduced, while in the multiload scheme, the longitudinal current of the inverter is regulated in the region where electrodes in the prebreakdown state are located.

When an unstable breakdown between electrodes is detected (because this state is not yet critical to the channel operating efficiency), the Hall field reduction may be performed discretely until the termination of prebreakdown effects, i.e., until the disappearance of high-frequency

fluctuations of voltage with a frequency of the order of 10kHz.

When recording an arc Hall breakdown (high-frequency fluctuations with a frequency of the order of 100kHz), it is necessary to reduce the potential difference between neighboring electrodes to a value below that of the Hall arc extinction voltage (up to 15–20V [5]). The methods of reduction are the same as those discussed above, but at the cost of immediate reduction of the transverse (Faraday) current.

When a high-current discharge characterized by electrode voltage fluctuations with a frequency of 10kHz and higher arises on the electrode, the current to this electrode must be reduced either by adjusting the inverter setting in a scheme with Faraday loading, or by increasing the overall longitudinal load current in the case of diagonal loading.

We will treat, by way of example, the principle of construction and operation of an automatic system affecting the load inverters and designed to reveal and prevent nonstandard (pre-emergency) conditions in an MHD channel. The block diagram of such a system may have the form shown in Fig.13.
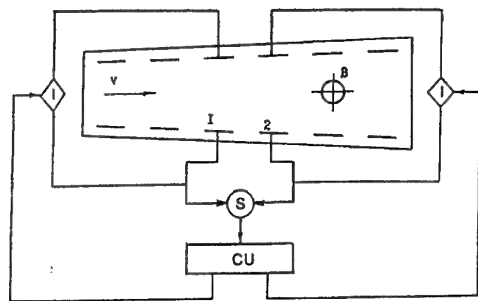
Fig.13. Block diagram of an automatic system for detection and prevention of nonstandard conditions in an MHD channel:
(1, 2) MHD-generator electrodes; S– sensors of signals from the electrodes; CU– control unit; I– inverter.

When electrical fluctuations arise which characterize the prebreakdown state or breakdown (high-frequency noise with a frequency of the order of 100kHz), a control signal is generated which is delivered to the inverter settings of the respective electrodes with a view to reducing their currents and the gradient of potential between them (up to the moment of disappearance of high-frequency noise from the spectrum of interelectrode fluctuations).

The monitoring and control of the mode of electrode operation in an MHD channel are performed in a similar manner (using the current values of current to the electrode and of the fluctuations of the electrode potential drop being measured).

(b) *Thermionic converter – tacitron*

A tacitron operation may be controlled depending on the type of fluctuations of its output electrical parameters, i.e., voltage and current:
— regular fluctuations (Fig.14a) correspond to the standard conditions of tacitron operation, when a stable modulation of anode current is possible;
— irregular fluctuations (Fig.14b) correspond to nonstandard conditions of tacitron operation, when no modulation of anode current is possible.

Strong irregular fluctuations of voltage U and current I arising simultaneously in some modes of tacitron operation (in particular, with a lower emitter temperature) and shown in Fig.14b indicate that the discharge burns unstably; spontaneous disruptions and repeat ignitions of the discharge occur. No stable and reliable modulation of anode current is possible in modes with such irregular fluctuations.
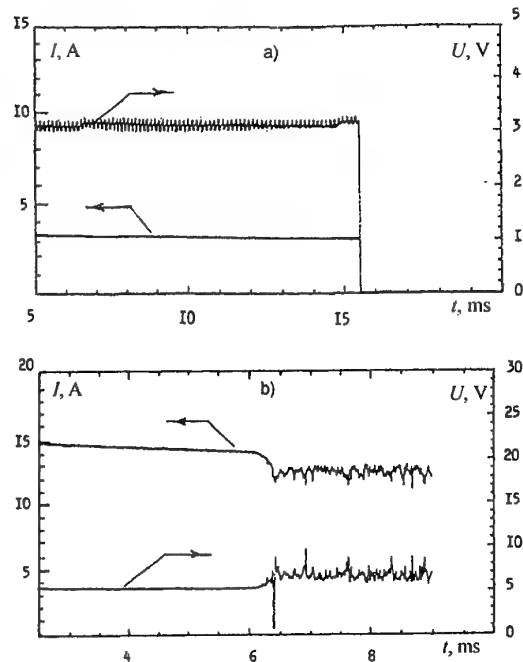
Fig.14. Characteristic fluctuations of the output electric parameters (voltage and current) during operation of a thermionic converter - tacitron: (a) standard conditions; (b) nonstandard conditions.

In order to eliminate the nonstandard mode of tacitron operation and change it over to

356

standard mode, when strong irregular fluctuations of anode voltage arise, it is necessary (for example, using an automatic control system) to deliver respective control signals to raise the emitter temperature (or to raise the pressure and concentration of barium and cesium in the interelectrode gap) until the moment of disappearance of irregular and emergence of regular fluctuations in the anode voltage spectrum, of the type given in Fig.14a.

Discharges of two types are possible in the standard mode of tacitron operation:
— a nonstationary discharge traveling over the electrode surface is characterized by low-amplitude regular fluctuations of anode voltage (with a frequency of 10 to 20kHz). A modulation of anode current and stable tacitron operation are possible in this mode;
— a stationary discharge taking up the entire area of the electrode is characterized by a total absence of fluctuations of anode voltage (see Fig.9). No modulation of anode current and, accordingly, no stable tacitron operation are possible in this mode.

For the tacitron to operate stably, a nonstationary discharge traveling over the electrode surface and characterized by regular fluctuations of anode voltage must be maintained (for example, using an automatic control system) in its interelectrode gap.

The absence of such fluctuations points to the emergence of a stationary discharge. In this case, it is necessary to deliver control signals to reduce, for example, the concentration of cesium or barium in the interelectrode gap (by decreasing the respective temperatures of cesium or barium thermostats) until the moment of emergence of regular fluctuations in the anode voltage spectrum, of the type given in Fig.14a.

Conclusions

The development of methods of fluctuation diagnostics and experiments with plasma PFs of different types (MHD generators and thermionic tacitron) led to the following conclusions.
1. The methods of functional diagnostics enable one to reliably monitor electrophysical effects in electrode boundary layers and on electrodes in the absence of "optical" openings in the PF

walls and of the possibility of visual observations of electrodes.
2. The recording and analysis of fluctuations of interelectrode Hall voltage and fluctuations of electrode voltage drop in an MHD channel enable one to reveal, in real time, the development of nonstandard (pre-emergency) conditions associated with the interelectrode Hall breakdown and with the high-current arc mode of discharge on the electrodes.
3. The use of the methods of fluctuation diagnostics in a high-current thermionic converter such as tacitron enables one to monitor the mode of discharge on the electrodes and reveal standard and nonstandard conditions of tacitron operation. In so doing, this monitoring (and subsequent control in real time) may be performed using the fluctuations of the anode (total) voltage and current of the tacitron without using the probe or spectral methods of diagnostics.
4. The methods of fluctuation diagnostics were used to develop options of practical realization of automatic monitoring and measuring devices which are also capable of control and protection of PFs against nonstandard (pre-emergency) conditions in the process of their operation with a view to improving the reliability and extending the service life of power facilities.

References

1. Baranov, N.N., Izv. Ross. Akad. Nauk Energ., 1997, No. 2, p. 28.
2. Baranov, N.N., Benilov, M.S., Bochkarev, G.G. et al,.Teplofiz. Vys. Temp., 1986, vol. 24, No. 2, p. 370.
3. Kaibyshev, V.Z., Kuzin, G.A., and Mel'nikov, V.M., Zh. Tekh. Fiz., 1972, vol. 42, No. 6, p. 1265.
4. Baranov, N.N., Buznikov, A.E., and Kaibyshev, V.Z., Izv. Ross. Akad. Nauk Energ., 1999, No. 2, p. 64.
5. Kovbasyuk, V.I., Baranov, N.N., Iserov, A.D., and Klimovskii, I.I., Teplofiz. Vys. Temp., 1977, vol. 15, No. 6, p. 1294.

68. CATALYTIC COOLING OF OVERHEATED SURFACES

S.I.Serdjukov, N.M.Voskresenskii, V.K.Bel'nov, M.S.Safonov, T.N. Danilchuk, L.G.Izmailov,
S.L.Levchenko

Department of Chemistry, Moscow State University, 119899 Moscow, Russia

Flying vehicles, the speed of which reaches 5 M and more, require compulsory cooling of overheated surfaces. The necessity of cooling can arise in some units of a engine, as well as in a forward side of flying vehicle as a result of friction in dense layers of atmosphere.

There is a number of the programs of development of flying vehicles, including catalytic method cooling of overheated surfaces [1-5]. The most complete the project "Ajax" is at present considered, important making which is thermocatalytic cooling with the help of process of methane steam conversion. In the given message is considered processes of methane steam conversion

$$CH_4 + H_2O \Leftrightarrow CO + 3H_2 - Q_1; \qquad (I)$$

$$CO + H_2O \Leftrightarrow CO_2 + H_2 + Q_2, \qquad (II)$$

carbon dioxide conversion of methane

$$CH_4 + CO_2 \Leftrightarrow 2CO + 2H_2 - Q_3; \qquad (III)$$

$$CO_2 + H_2 \Leftrightarrow CO + H_2O - Q_2 \qquad (IV)$$

and ammonia decomposition

$$2NH_3 \Rightarrow N_2 + 3H_2 - Q_5 \qquad (V)$$
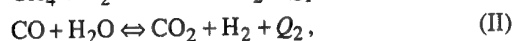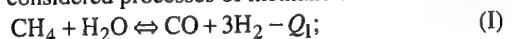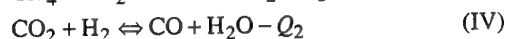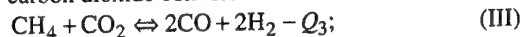
and their efficiency in cooling of overheated surfaces is compared.

Urgent problem is creation of unified catalytic modules (blocks), effectively working in extreme conditions. Traditional catalytic modules with a granular catalyst bed feature low efficiency of catalytic mass use as well as high gasodynamic resistance. Catalysts implemented as coverings applied to regular constructional elements of a module (planar catalysts) are more promising [6].

The paper considers such a module which is a set of plane-parallel plates made of heat-conducting material with catalyst divided by transport channels wherein gas flows (see Fig.1). Heat is supplied to the plates from the reaction mixture outlet due to high thermal conductivity of the carrier.

Experimental researches of the developed Ni-containing and Fe-containing planar catalysts, prepared by a plasma method, have shown their high catalytic activity in reactions (I), (II), (III), (IV) and (V), respectively.

Offered processes in a repeating fragment of a catalytic block can be described by the following system of differential equations:

$$\varepsilon\frac{\partial\rho}{\partial t}+\frac{\partial\dot{m}}{\partial z}=0; \quad \varepsilon\rho\frac{\partial x_1}{\partial t}+\dot{m}\frac{\partial x_1}{\partial z}=-AW;$$

$$\varepsilon c_p\rho\frac{\partial T}{\partial t}+c_p\dot{m}\frac{\partial T}{\partial z}=\alpha A(T_k-T);$$

$$(1-\varepsilon)\rho_k c_{pk}\frac{\partial T_k}{\partial t}=$$

$$=(1-\varepsilon)\lambda_k\frac{\partial^2 T_k}{\partial z^2}-\alpha A(T_k-T)-AW\Delta H, \qquad (1)$$
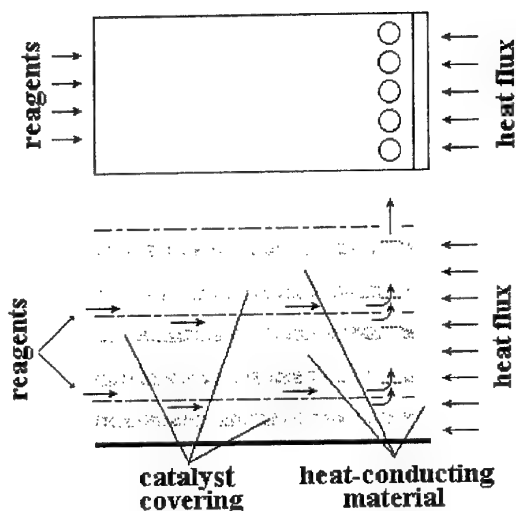
Fig.1. A fragment of the catalytic block

where A - solid material surface area in one unit of package volume, 1/m; b - channel half-width, m; c_p specific heat capacity of gas, J/(kg·K); c_{pk} - specific heat capacity of the carrier, J/(kg·K); ΔH - increase of gas mixture enthalpy due to chemical reaction per one kilogram of converted methane or ammonia, J/kg; l - half-thickness of the carrier with catalytic covering, m; $\dot{m}$ - gas mass rate per one unit of reactor cross section, kg/(m² s); t - time, s; T - gas mixture temperature, K; T_k - temperature of the carrier and catalyst, K; x_1 - fraction by mass of methane or ammonia in the mixture; z - axial distance along the package in gas flow direction, m; W - rate of methane or ammonia transformation per one unit of contact surface area, kg/(m²·s); α - heat transfer coefficient, J/(m²·s K); $\varepsilon=b/(b+l)$ – fraction of void section in package; λ_k - heat

358

conductivity coefficient of the carrier, J/(m·s·K); ρ - gas mixture density, kg/m^3.

Initial conditions (at $t=0$):

$$x_1 = x_0; \quad T = T_0; \quad T_k = T_0. \qquad (2)$$

Boundary conditions:

at $z=0$ ($t \geq 0$)

$$\dot{m} = \dot{m}_0; \quad x_1 = x_0; \quad T = T_0; \quad \frac{\partial T_k}{\partial z} = 0; \qquad (3)$$

at $z=L$ ($t \geq 0$)

$$-\lambda_k (\partial T_k / \partial z) + (1-\varepsilon)^{-1} \varphi = 0, \qquad (4)$$

where L - length of reactor, m; φ - thermal flux per one unit of reactor cross section, J/(m2·s).

To close the equations system (1), let us use the equations connecting gas mixture density ρ to the current mass fraction x_1 of methane or ammonia.

We shall designate through β mole ratio carbon dioxide ÷ methane and through β' mole ratio of water steam ÷ methane at the inlet of the catalytic block. Then for steam conversion methane

$$x_0 = \frac{1}{1 + \dfrac{M_{H_2O}}{M_{CH_4}} \beta'} \qquad (5)$$

and for carbon dioxide conversion of methane

$$x_0 = \frac{1}{1 + \dfrac{M_{CO_2}}{M_{CH_4}} \beta} \qquad (6)$$

According to equations (I) and (II), the mass fractions of H_2O, H_2 and CO mixture components will:

$$x_2 = (1 - x_0) - \frac{M_{H_2O}}{M_{CH_4}}(x_0 - x_1) - \frac{M_{H_2O}}{M_{CO_2}} x_5;$$

$$x_3 = \frac{M_{H_2}}{M_{CH_4}}(x_0 - x_1) + \frac{M_{H_2}}{M_{CO_2}} x_5; \qquad (7)$$

$$x_4 = \frac{M_{CO}}{M_{CH_4}}(x_0 - x_1) - \frac{M_{CO}}{M_{CO_2}} x_5,$$

and according to equations (III) and (IV), the mass fractions of H_2, CO and CO_2 mixture components will be

$$x_3 = 2\frac{M_{H_2}}{M_{CH_4}}(x_0 - x_1) - \frac{M_{H_2}}{M_{H_2O}} x_2;$$

$$x_4 = 2\frac{M_{CO}}{M_{CH_4}}(x_0 - x_1) - \frac{M_{CO}}{M_{H_2O}} x_2; \qquad (8)$$

$$x_5 = (1 - x_0) - \frac{M_{CO_2}}{M_{CH_4}}(x_0 - x_1) - \frac{M_{CO_2}}{M_{CO_2}} x_2,$$

where M_{CH_4}, M_{H_2O}, M_{CO}, M_{H_2}, M_{CO_2}, M_{NH_3} - molecular masses of the components, kg/mol. The value of x_5 was calculated based on quasiequilibrium condition of the reaction (II), and

the value of x_2 was calculated based on quasiequilibrium condition of the reaction (IV) using the expression for equilibrium constant $K_{p2} = 1/K_{p4}$ /7/

$$K_{p2} = \frac{M_{H_2O} M_{CO}}{M_{H_2} M_{CO_2}} \frac{x_3 x_5}{x_2 x_4}. \qquad (9)$$

Using (6), we can derive the equation for reaction mixture density

$$\rho = \frac{P}{RT} \frac{M_{CH_4} + \beta' M_{H_2O}}{3 + \beta' - 2x_1 \left(1 + \dfrac{M_{H_2O}}{M_{CH_4}} \beta'\right)}, \qquad (10)$$

or

$$\rho = \frac{P}{RT} \frac{M_{CH_4} + \beta M_{CO_2}}{3 + \beta - 2x_1 \left(1 + \dfrac{M_{CO_2}}{M_{CH_4}} \beta\right)}, \qquad (11)$$

where P total pressure, R - gas constant.

In the case of ammonia decomposition to the inlet of reactor comes pure ammonia and $x_0 = 1$.

The ratio of nitrogen and hydrogen (reaction products) is 1:3, hence

$$\rho = \frac{P M_{NH_3}}{RT(2 - x_1)} \qquad (12)$$

In calculation of heat transfer coefficient α the known Reynolds analogy between heat exchange and friction was used, which can be expressed by /8/

$$\text{St} = \frac{\alpha \varepsilon}{c_p \dot{m}} \approx f, \qquad (13)$$

where St - Stanton number, f - friction resistance factor. For completely developed laminar flow in a flat channel the friction resistance coefficient is described by the formula

$$f = \frac{12}{\text{Re}}, \qquad (14)$$

and for turbulent flow

$$f \approx 0.039 \,\text{Re}^{-0.25}, \qquad (15)$$

where $\text{Re} \equiv \dot{m} d_{_3} / \varepsilon \eta$, $d_{_3}$ − equivalent diameter (for a flat channel $d_{_3} = 4b$), η - dynamic viscosity, kg/(m s).

Thus, from (10) and (11) we have under laminar modes

$$\alpha = 3\frac{c_p \eta}{b}. \qquad (16)$$

Let us enter the dimensionless variables:
$G = \dot{m}/\dot{m}_0$, $\theta = T/T_0$, $\theta_k = T_k/T_0$, $\sigma = \rho/\rho_0$,
where for methane steam conversion

$$\rho_0 = \frac{P}{RT_0} \times \frac{M_{CH_4} + \beta' M_{H_2O}}{1+\beta'}, \qquad (17)$$

for carbon dioxide conversion of methane

$$\rho_0 = \frac{P}{RT_0} \times \frac{M_{CH_4} + \beta M_{CO_2}}{1+\beta}, \qquad (18)$$

and for ammonia decomposition

$$\rho_0 = \frac{M_{NH_3} P}{RT_0}, \qquad (19)$$

dimensionless coordinate $Z = z/L$ and time $\tau = \frac{\lambda_k t}{\rho_k c_{pk} l^2}$. Using dimensionless variables, let us transform the system and additional conditions (1) - (4) to the form:

$$\frac{\partial \sigma}{\partial \tau} + \frac{\rho_k c_{pk}}{\lambda_k \rho_0} \frac{\dot{m}_o}{\varepsilon} \frac{l^2}{L} \frac{\partial G}{\partial Z} = 0;$$

$$\sigma \frac{\partial x_1}{\partial \tau} + \frac{\rho_k c_{pk}}{\lambda_k \rho_0} \frac{\dot{m}_o}{\varepsilon} \frac{l^2}{L} G \frac{\partial x_1}{\partial Z} = -\frac{\rho_k c_{pk}}{\lambda_k \rho_0} \frac{l^2}{b} W;$$

$$\sigma \frac{\partial \theta}{\partial \tau} + \frac{\rho_k c_{pk}}{\lambda_k \rho_0} \frac{\dot{m}_o}{\varepsilon} \frac{l^2}{L} G \frac{\partial \theta}{\partial Z} =$$

$$= \frac{3\rho_k c_{pk}}{\lambda_k \rho_0} \eta \frac{l^2}{b^2}(\theta_k - \theta); \qquad (20)$$

$$\frac{\partial \theta_k}{\partial \tau} + 3\eta c_p \frac{l}{b}(\theta_k - \theta) =$$

$$= \left(\frac{l}{L}\right)^2 \frac{\partial^2 \theta_k}{\partial Z^2} - \frac{\Delta H}{\lambda_k T_0} l W,$$

$$\tau = 0; \quad x_1 = 1, \quad \theta = 1, \quad \theta_k = 1;$$

$$Z = 0; \quad x_1 = 1, \quad \theta = 1, \quad G = 1, \quad \frac{\partial \theta_k}{\partial Z} = 0; \qquad (21)$$

$$Z = 1; \quad \frac{\partial \theta_k}{\partial Z} = \frac{1}{\lambda_k} \frac{\varphi L}{(1-\varepsilon)T_0}.$$

For numerical calculations were used average temperature-independent parameter values of a steel carrier for planar catalysts:

$$\rho_k = 8 \times 10^3 \frac{kg}{m}; \quad c_{pk} = 0.046 \frac{J}{kg \cdot K}; \quad \lambda_k = 46 \frac{J}{msK},$$

the known empirical relations for ΔH and c_p /7/.

Gas mixture viscosity was calculated by the approximation formula of the kinetic theory of gases /9/:

$$\eta_m = \sum_{i=1}^{n} \frac{x_i M_i^{-1} \eta_i}{\sum_{j=1}^{n} x_j M_j^{-1} \Phi_{ij}},$$

$$\Phi_{ij} = \frac{\left[1 + (\eta_i/\eta_j)^{0.5}(M_j/M_i)^{0.25}\right]^2}{\left[8(1 + M_i/M_j)\right]^{0.5}},$$

$$\eta_i = \eta_{ic}^* T^{0.71 + 0.29/T}, \qquad (22)$$

where $\eta_m(T)$ – gas mixture viscosity, $\eta_i(T)$ – viscosity of i-th pure component of the mixture, η_{ic}^* – viscosity of the i-th component at the critical temperature T_{ic} and critical pressure P_{ic}:

$$\eta_{ic}^* = \frac{3.5 M_i^{0.5} P_{ic}^{2/3}}{T_{ic}^{1/6}}. \qquad (23)$$

For reactions (I), (II) and (III), (IV) on Ni-containing catalyst the equations derived in /10/ was used:

$$W = M_{CH_4} \frac{kP_{CH_4} P_{H_2O}\left(1 - \frac{1}{K_{p1}} \frac{P_{CO} P_{H_2}^3}{P_{CH_4} P_{H_2O}}\right)}{P_{H_2O} + k_1 P_{H_2}} \qquad (24)$$

and

$$W = M_{CH_4} \frac{kP_{CH_4} P_{CO_2}\left(1 - \frac{1}{K_{p3}} \frac{P_{CO}^2 P_{H_2}^2}{P_{CH_4} P_{CO_2}}\right)}{P_{CO_2} + k_1 K_{p2} P_{CO}}, \qquad (25)$$

respectively, where $P_{CH_4}, P_{H_2O}, P_{H_2}$ and P_{CO} - partial pressures of components, K_{p1} – reaction (I) equilibrium constant, K_{p3} – reaction (III) equilibrium constant /7/

$$k = \gamma T_k e^{\left(-\frac{E}{RT_k}\right)}, \quad \gamma = 0.23 \frac{mol\ s}{kg\ m\ K},$$

$$\frac{E}{R} = 1.58 \times 10^4\ K, \quad k_1 = 1.99 \times 10^3. \qquad (26)$$

Relation between partial pressures and mass fractions of components was defined by the formula

$$P_i = P \frac{x_i M_i^{-1}}{\sum_i x_i M_i^{-1}}, \quad i = 1,..,5, \qquad (27)$$

where P_i and M_i – partial pressures and molecular masses of components.

For the reaction of ammonia decomposition on Fe-containing catalyst the known relation was used

$$W = M_{NH_3} K \exp\left(-\frac{E}{RT_k}\right), \qquad (28)$$

wherein the constants values for the developed catalyst type were /11,12/:

$K = 7.10 \times 10^{11} mol/m^2 s$; $E = 1.9 \times 10^5 J/mol$. (29)

360

In numerical solution of equation (16) values of parameter l, b, L, T0, P, mo, β and β' were varied.

The calculation results for steady state processes of methane conversion and ammonia decomposition in a catalytic block for some specific values of design parameters are presented in Fig.2 and Fig.3.
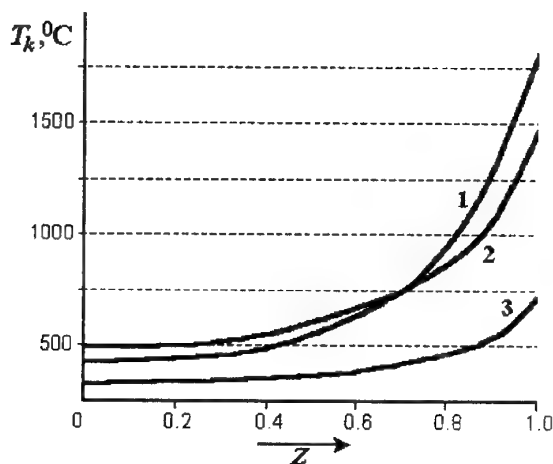
Fig.2. Temperature distribution T_k along the block length (L=0.1m, φ=1MW/m^2):
1 – methane steam conversion (m_0=1кг/м^{2}c, β'=4);
2 – carbon dioxide conversion of methane (m_0=1кг/м^{2}c, β=4); 3 - ammonia decomposition (m_0=0.25кг/м^{2}c).
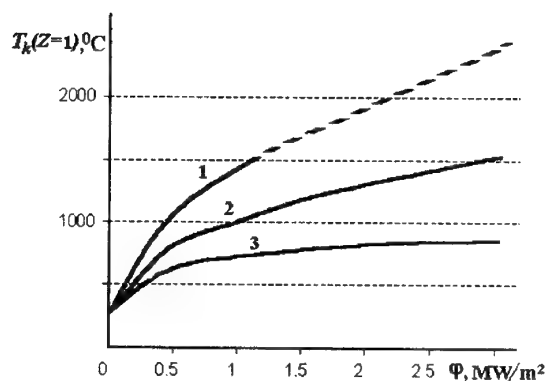
Fig.3. Relations between the temperature of a catalytic block wall (L=0.1m) and the value of heat flux:
1 - methane steam conversion (m_0=4 кг/м^{2}c, β'=4); 2 – carbon dioxide conversion of methane (m_0=4кг/м^{2}c, β=4); 3 - ammonia decomposition (m_0=1кг/м^{2}c).

From Fig.2 it can be seen that the length of a catalytic block (determined particularly by the value of thermal flux) for ammonia decomposition process is much less than in case of methane conversion.

Fig.3 shows that the level of thermal load allowable for heat-resistant steel (T_k (Z=1) < 1000°C), for the process of methane conversion does not exceed 1 MW/m^2. Further increase of the thermal flux results in significant growth of catalytic block wall temperature.

For ammonia decomposition the allowable thermal flux may achieve 3MW/m^2.

These results demonstrate a significant advantage of ammonia decomposition over methane conversion in chemothermal cooling of overheated surfaces.

References

1. Nosach V.G. Thermochemical insulation. Doc. AN USSR, Ser. A. 1979. № 11. pp. 941-953.
2. Anikeev V.I., Bobrin A.S., Kirillov V.A. Collected volume of the 1-st All-Russia Conf. Chemical regeneration of heat in air vehicles. 1989. pp 281-294.
3. Anikeev V.I., Hanaev V.M., Bobrin A.S., Kirillov V.A. Analysis of heat removal efficiency from catalyst surface in carrying out perspective thermochemical reactions under diffusion restrictions. Sib. Chem. J. 1991. B. 2. pp. 130-135.
4. Kurganov B.A., Zejgarnik J.A., Korabel'nikov A.V., Maslakova I.V. A thermochemical principle of cooling on the basis of steam methane conversion. Teploenergetika. № 3. 1996.P. 18-29.
5. Korabel'nikov A., Kuranov A. Thermochemical conversion of hydrocarbon fuel under the concept "AJAX". AIAA-99-4921.
6. Safonov M.S., Serdyukov S.I., Voskresenskij N.M. A device for heterogeneous catalytic processes. Patent № 2055635 // 1996. Bul. No.7.
7. Gurvich L.V., Vejts I.V., Medvedev V.A. et al. Thermodynamic properties of individual substances. /Edited by V.P.Glushko. M.: Nauka, 1978. v.1.
8. Heat exchange manual. V. I. M.: Energatomizdat, 558 p.
9. Reid R., Prausnitz J., Sherwood K. The properties of gases and liquids. L.: Chem. 1982. P. 360.
10. Makunin A.V., Bel'nov V.K., Safonov M.S., Serdyukov S.I., Suris A.L. Experimental research and mathematics modeling of a coaxial tubular reactor of steam methane

conversion. Teor. Osnovy Chim. Technol., 2000. v.34. No.6. P. 618-625.

11. Ostoshevskaja O.Yu., Serdyukov S.I., Safonov M.S., Plasma-covered catalyst of ammonia decomposition. I. Influence of preliminary processing conditions on catalytic

properties. Kinetika i kataliz, 1996. v. 37. No.6. P. 927-930.

12. Ostoshevskaja O.J., Serdyukov S.I., Fabrichnii P.B. Plazma-covered catalyst of ammonia decomposition . II. Research of phase transformations. Kinetika i kataliz, 1996. v. 37. No.6. P. 931-934.

69. EXPERIMENTAL STUDY OF ENERGETIC PERFORMANCES OF ADVANCED SOLID PLASMA-GENERATING PROPELLANTS FOR PULSED MHD GENERATORS

Yu. P. Babakov, V. A. Polyakov
Federal Center of Dual Technologies "Soyuz"

V. A. Novikov, V. I. Okunev, V. Yu. Rickman
Institute for High Energy Densities of IVTAN-Association Russian Academy of Sciences

Abstract. Results of experimental study of advanced solid plasma-generating propellants of double-based (BP-15C) and composite (CPP) types in the pulsed self-exciting MHD power system "Pamir-1" are presented. The power generated by Faraday MHD channel was obtained of 10.15MW to 10.83MW for the BP-15C propellant, and of 11.31MW to 14.64MW for the composite propellant application. Thus, an increase of the output power of the MHD generator by 10-60% was obtained only by application of the novel plasma-generating propellants without modification of main components of the MHD power system (MHD channel and magnet system). An application of these propellants for the pulsed MHD power systems will provide an increase of their power performances and efficiency for solving different problems of science and engineering.

Introduction

The self-contained, self-exciting pulsed MHD power systems should provide the high level of power density, which depends on the power complex σu^2. In addition, the maximal energetic performances (electric power, current, and voltage) of the solid-propellant pulsed MHD generators of "Pamir" type are obtained in the flow mode with strong MHD interaction (St ~ 0,2) [1]. These modes are accompanied by an occurrence of perturbations of the supersonic flow at the outlet of the conversion area of the MHD channel. These perturbations move upstream under further increase of magnetic field that results in stabilization of electric current, voltage, and power. An alternative of the process noted from the point of view of raising the power generated is the pressure increase in the plasma generator at the moment of the crisis occurrence of the supersonic flow.

The study presented is purposed to assist the development of new compositions of the plasma-generating propellants providing increased power parameters of the MHD generator. The double-based propellant BP-15C [2] differs from the standard plasma-generating propellant BP-10F by increased content of ionized seed $CsNO_3$ (15%), that provides a growth of electrical conductivity σ of combustion products at the inlet of MHD channel up to 100S/m (for BP-10F propellant σ=80S/m). The composite propellant is based on the advanced oxidizer KDNA (potassium salt of dinitramide) [3] providing the raised temperature in combustor (4100K) and increased electrical conductivity of combustion products at the inlet of MHD channel up to 140S/m. These advanced propellants were test-fired in the plasma generators GP-81 and GP-83L having the combustor pressure increase during operation.

Pulsed MHD power system "Pamir-1"

The experimental MHD facility consists of the following components:

- Plasma generator (GP-77, GP-81, or GP-83L);

- Standard Faraday type MHD channel IM-112-5 [1] with volume of conversion zone of $0.033m^3$ and Mach number of 2.4 at the inlet of this zone;

- Air-core magnet system consisting of four standard sections IM-114-1 [1] with total inductance L_M=9mh, resistance R_M=10.2mOhm and the magnet constant α=0.105T/kA; the magnet system in the series of firings discussed was used simultaneously as a load of the MHD channel;

- Initial excitation system consisting of capacitor bank of capacity C=0.2F;

- Commutating, protective, and control devices;

- Multi-purpose test bench equipment;

- Control, measurement, and recording system.

The electrical circuit diagram of the experimental MHD facility is given in Fig.1.

The study of the advanced double-based propellant BP-15C was performed with application of the plasma generator GP-81. The plasma generator case design and shape of the propellant grain provide a growth of the combustor pressure from 3.0 to 5.0MPa. The standard plasma generator GP-77 for geophysical MHD power systems of "Pamir" type with a charge of the solid plasma-generating propellant BP-10F provides the constant

pressure in the combustor on a level of 4.0–4.5MPa and mass flow rate of combustion products of about 25kg/s. In the firing testing of the composite propellant the special-designed plasma generator GP-83L was used with a growth of the combustor pressure during operation from 4.0 to 6.0MPa Typical curves of the pressure for the three types of the plasma-generating propellants are shown in Fig.2.

Fig.2. Combustor pressure versus operation duration of the plasma generator

Fig.1. Electrical circuit diagram of the experimental MHD facility. R_C – resistance of the capacitor bank; R_b=11mOhm – ballast resistance; I_C, I_K, I_M – currents of the capacitor bank, MHD channel, and magnet, relatively; V_C – the capacitor bank voltage; B_1, B_2 –diode units; K_1, K_2, K_3 – commutating switches

To exclude an influence of declining of performances of the MHD channels and plasma generators after multi-run operation only new MHD channels IM-112-5 and cases of the plasma generators.

The experiments for all three types of the propellants were performed with application of the same timing diagram. The pre-charged capacitor bank is discharged to the magnet about 1.5 s after ignition of the plasma generator creating an initial magnetic field of about 1 T for starting the self-excitation process. The typical variations of the electric power, current, and voltage generated by Faraday MHD channel versus operation duration for the propellants above mentioned are shown in Figs. 3, 4, 5, relatively.

Fig. 3

364
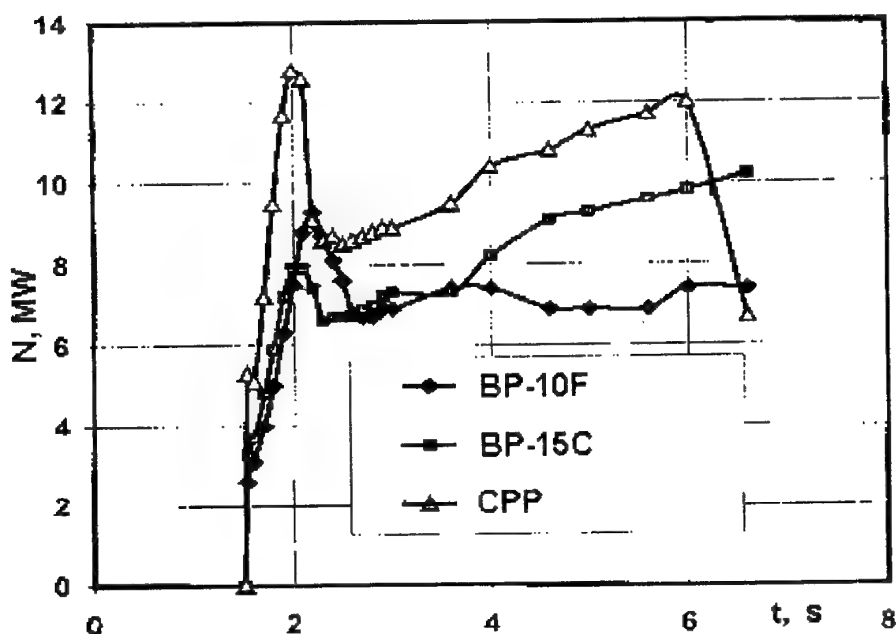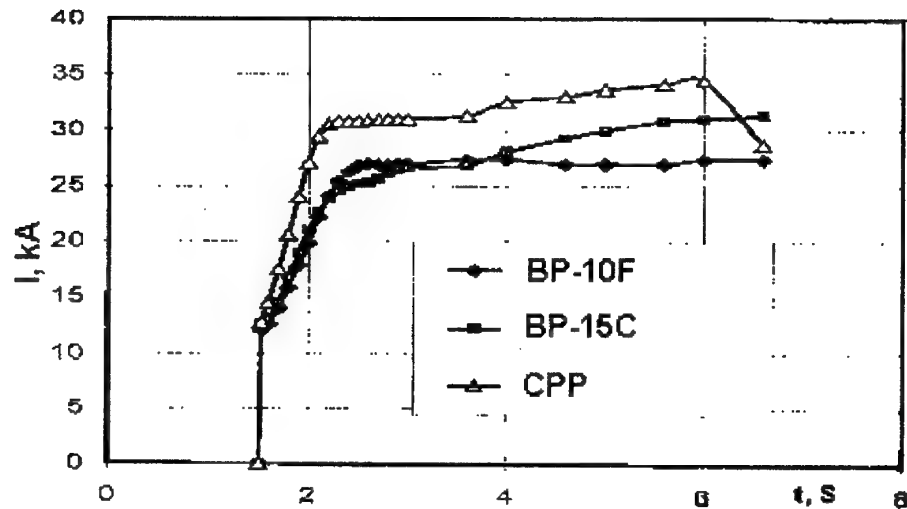
Fig. 4
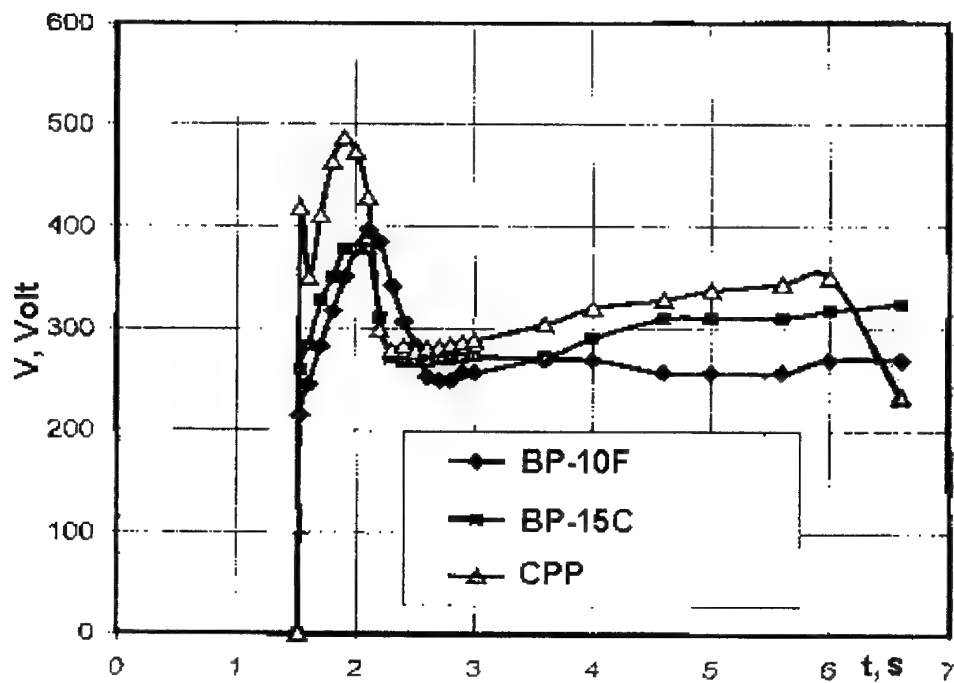
Fig.5

As shown in Fig.3, the maximal level of the power of 13.0MW is obtained faster in the firing of composite propellant, then 10.1MWe in the firing of BP-15C double-based propellant, and 9.3MW in the firing of BP-10F double-based propellant. After occurrence and development of the crisis of the supersonic flow the power generated by MHD channel dropped significantly (approximately by 33%). After that the power generated is at the quasi-stable level in the firings of propellants BP-10F and BP-15C, whereas in the firings of the composite propellant the power rises to the end of the plasma generator operation approximately by 46% in spite of the flow crisis.

Main output parameters obtained by application of the plasma-generating propellant BP-15C and composite propellant CPP, as well as standard propellant BP-10F are given in the table below.

365

Parameters of MHD generator "Pamir-1"

Plasma-generating propellant	BP-10F	BP-15C	CPP
Тип генератора плазмы	GP-77	GP-81	GP-83L
Combustor pressure, MPa	4.6	5.1–6.0	5.7–6.5
Electric current of Faraday MHD channel, kA	24.1	31.3–32.2	27.12–33.0
Voltage of Faraday MHD channel, V	384.4	324.2–336.5	342.8–539.9
Maximal power of MHD generator, MW	9.3	10.15–10.83	11.31–14.64

Thus, only by application of advanced plasma-generating propellant without modification of another main components of the MHD generator (MHD channel and magnet system) an increase of the maximal output power of the pulsed MHD generator by 10 – 60% was obtained.

Conclusion

1. The advanced plasma-generating propellants BP-15C of double-based type and CPP of composite type were successfully tested in the series of firings of the pulsed MHD power system "Pamir-1".

2. The power generated by MHD facility fired by BP-15C propellant varied from 10.15 to 10.83 MW, and from 11.31 to 14.64 MW when the facility was fired by composite propellant that exceeds the maximal power obtained with standard propellant BP-10F by 10 – 60%.

3. An application of the advanced composite and double-based propellants will provide the growth of their power performances and efficiency for solving the problems of science and engineering.

References

1. Pulsed MHD converters of chemical energy into electricity//Editors A.E.Sheindlin, V.E.Fortov, Energoatomizdat, Moscow, 1997.
2. Energetic condensed systems. Abridged encyclopedia//Editor B.P.Zhukov, Yanus-K, Moscow, 1999.
3. O. A. Luk'yanov, V. A. Tartakovskiy O.A. Chemistry of dinitramide and its salts//Russian Chemical Journal, V. 41, No.2, P.P. 5-13, Moscow, 1997.

70. COMPUTER SIMULATION OF LAMINAR FLOWS IN PLASMATRONS WITH VARIABLE ARC LENGTH

V.V.Glazkov, S.E.Chikunov, E.Kh.Isakaev, P.P.Ivanov, A.G.Khachaturova, O.A.Sinkevich
Science and Engineering Center for Energy Efficient Processes and Equipment,
Associated Institute for High Temperatures, Russian Academy of Sciences,
Izhorskaya 13/19, Moscow, 127412, Russia
Tel: (+7) 095 484 1833
Fax: (+7) 095 484 1833
e-mail: agni@aha.ru

Abstract. New specific method is proposed for numerical modelling of the two-dimensional plasma flow in plasmatrons with the cylindrical and expanding channel as an electrode. Within the framework of this program a simplified two-dimensional mathematical model of electrical arc was created for the cooled channel with self-settled length and axial injection of working gas. A change of laminar flow regime to turbulent one is discussed.

1. Introduction

Widespread use of high current cylindrical or divergent channel flow stabilized plasmatrons claim for computer simulation and for a comprehensive knowledge of the electron component parameters as functions of the arc current and the working gas flow rate. For the numerical modelling of laminar and turbulent plasma flows in plasmatrons several codes were developed by our research team.

The first approach is quasi-one-dimensional. Considering well-known kinds of non-uniformity in the cross-section – uniform arc channel and standard boundary layer, - and additional energy equation governing core temperature and radius by joule heating and radiative and convective heat transfer from the arc core, there is a possibility to incorporate real thermodynamic and transport properties of working gas, radiation in a complex continuum and linear spectrum and approbated convective heat transfer data. A good agreement with limited experimental data was reported in [1].

Second one is based on boundary layer approximation. The gas flow profile is supposed to be symmetrical, mode of gas flow is laminar, all processes are supposed to be stationary, the external magnetic field is absent, the plasma is quasi-neutral, in a condition of local thermodynamic equilibrium, heat radiation is volumetric. It was supposed also, that within the arc the gas flows mainly in an axial direction, radial gradients of both temperature and velocity are much greater than axial ones, viscous dissipation is small in comparison with joule heating, the gravitational force is negligible. Joule heating is determined mainly by axial component of electrical current density, the intensity of an electrical field is essentially constant over cross-section of the channel but it's axial component changes along the axis. The magnetic field has only azimuthal component. All these specified assumptions allow using the equations of heat and mass transfer in a boundary layer approximation. Equation of state of plasma and dependence of transport coefficients on temperature and pressure are incorporated in the numerical code. The boundary conditions are set in initial section, on an axis of symmetry and on cold walls of the channel. To exclude influence of an electrode and of near-electrode area on the characteristics of a flow of plasma a supposition is made that the internal electrode has extended cylindrical nozzle. On the nozzle exit one-dimensional asymptotic flow of arc plasma is realized, and the distribution of temperature is defined by means of analytical solution of the Elenbaas-Heller equation. The plasma enters in the cylindrical channel of plasmatron and is stabilized by circular axial flow of gas.

And at last a third approach is the newly created code based on the system of automation of numerical experiment (ANES), developed in the Heat Physics Department of the Moscow Power Engineering Institute, and generalized including Maxwell equations.

2. Plasmatron configurations

We studied an electrical arc burning in the plasmatron channels shown in Figs. 1a and 1b. This design of plasmatron is the simplest and is widely used in laboratory researches. The plasma forming gas is injected axially through the annular gap along the cathode, as indicated by arrows. The plasma column develops between the cathode and the anode wall. We considered the long plasmatron channel in which the fully developed gas flow is realized.
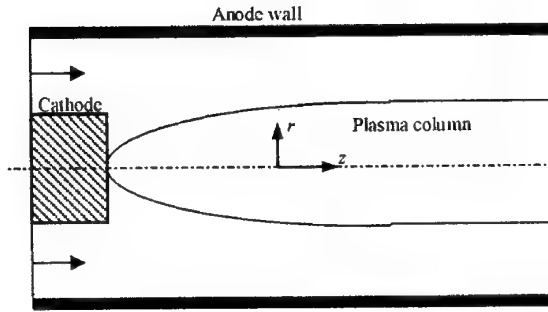
Fig.1a. Plasmatron with cylindrical channel.
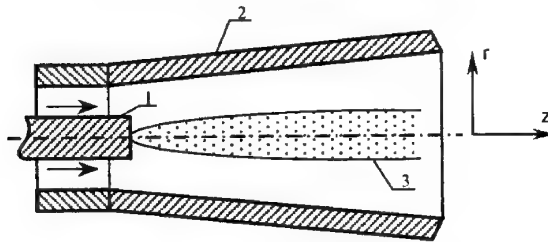
Fig.1b. Plasmatron with divergent channel: (1) – cathode, (2) – anode wall, (3) – plasma column.

3. Governing equations

In numerical analysis, assumptions of steady state, axisymmetry, local thermodynamic equilibrium and optically thin plasma are adopted for the two-dimensional MHD modelling of thermal plasma. A control volume method and the SIMPLE algorithm are used as the numerical scheme for solving the governing conservation equations of mass, momentum, energy, coupled with Maxwell's equations and the Ohm's law. These equations can be written as follows:

$$\text{div}(\rho \mathbf{V}) = 0$$

$$\text{div}(\rho \mathbf{V}\mathbf{V} - \mathbf{\Pi}) = -\text{grad}\,P + \mathbf{j} \times \mathbf{B}$$

$$\text{div}\left(\rho \mathbf{V}h - \frac{\lambda}{c_p}\text{grad}\,h\right) = \frac{\mathbf{j}^2}{\sigma} - Q_{ray}$$

$$\text{div}\,\mathbf{j} = 0$$

$$\text{rot}\,\mathbf{E} = 0$$

$$\text{rot}\,\mathbf{B} = \mu_0\mathbf{j}$$

$$\mathbf{j} = \sigma\mathbf{E}$$

Here $\mathbf{V}$, $\mathbf{j}$, $\mathbf{B}$, $\mathbf{E}$ are the velocity, current density, induced magnetic field and electrical field vectors respectively; ρ, λ, σ are the density, the thermal conductivity and the electrical conductivity respectively; $\mathbf{\Pi}$ is the viscous stress tensor; P is the pressure; h and c_p are the enthalpy and the specific heat at constant pressure respectively; μ_0 is the

permeability of free space; Q_{ray} is the net radiation from the plasma.

4. Modelling of plasma flow and transition from the laminar to the turbulent regime in plasmatrons

Modelling are carried out for electrical arc burning in the cylindrical channel and for plasmatron with the expanding channel as an electrode for the plasma in a state of local thermodynamic equilibrium. As a result of numerical experiments the two-dimensional distributions of plasma temperature, gas flow velocity and current density in plasmatrons were obtained. Using before mentioned ANES method the numerical calculations were carried out in order to determine the stabilizing lengths (the thermal stabilizing length L_T, the dynamical stabilizing length L_U and the electrical stabilizing length L_E). Experimental dependencies of critical Reynolds numbers for transfer from the laminar flow regime to turbulent one are checked in order to establish the hydrodynamic Kelvin-Helmholtz instability as a possible cause of this transfer.

The knowledge of stabilizing lengths allows us to find for the each plasmatron experiment the minimum length of the plasmatron channel needed to reach the stabilized regime of plasma. As a result dependencies of these stabilizing lengths on regime parameters: the total electric current, mass flow rate and the diameter of the channel were found. The dependencies for an electrical arc, stabilized by the wall, demonstrate that the average temperature on the stabilized part of plasmatrons does not depend on the convective heat transfer. Stabilizing lengths grow nearly linearly with increase of the flow rate. Influence of viscous and magnetic forces, as well as of conductive heat transfer in the plasma flow is less for the higher flow rates. Dependencies of L_T, L_U, and L_E demonstrate the stabilizing lengths decrease, with the tendency to constant values, when an electric current grows.

The electric arc burning in plasmatron channel is producing a large band of noise that may be generated by the current-convection instability due to Ampere force and (or) Kelvin-Helmholtz instability. The threshold of the current-convection instability is characterized by the critical electrical Rayleigh number Ra_e [2]. The critical electrical Rayleigh number $Ra_{e,cr}$ for plasmatrons is about $3.19 \cdot 10^3$ (see [2]). When $Ra_e < Ra_{e,cr}$, the hydrodynamic instability predominates over the current-convection instability in a plasmatron.

We used the experimental dependence of the longitudinal gradient of pressure in the channel on gas flow rates, obtained in [3,4] and represented

368

in Fig.2. Experimental data were obtained for an argon arc burning in a cylindrical channel with an axial injection of the plasma-forming gas. Operation conditions were the following: pressure P is between 10^5 and $20 \cdot 10^5$Pa, current I is between 5A and 400A, gas flow rate G is between 0.1 and 15 grams per second (g/s), d_w is between 5 and 10 millimetres, L/d_w is between 70 and 150. The experimental set-up is described in [3].
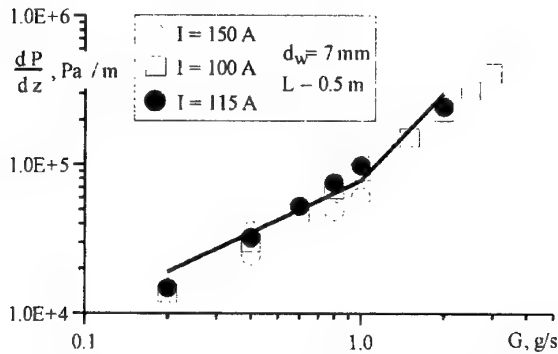
Fig.2. Comparison of results of numerical solution of two-dimensional equations (marked points) with experimental data from [3,4] (line).

One could see from experimental data shown in Fig.2 that there is point of inflection in the graphs representing the longitudinal gradient of pressure in the channel versus gas flow rate. Here an inflection point is located against the flow rate G value about 1gps. We suppose that on the left side of the point of inflection ($G<1$g/s) the laminar regime prevails while on the right side ($G>1$g/s) the turbulent one predominates. So the point of inflection could give us the value of critical Reynolds number. For a definition of this critical Reynolds number in case of variable viscosity it is, however, necessary to know the radial distribution of the temperature in the plasmatron channel. The Reynolds number is defined as Re=$4G/(\pi d_w \eta_m)$, where $\eta_m = \eta(T_m)$, T_m - the bulk temperature that could be found from numerical calculations for a given gas flow rate G and a channel internal diameter d_w. Such numerical calculation has been realized. From numerical experiments the dependence of the gradient of pressure on gas flow rate was studied. The results are represented in Fig.2. It is clear that all the calculated points are located along the line corresponding to the laminar regime. For the investigated range of electrical currents, $I=112$-$129A$, the electrical Rayleigh number $Ra_e=339$ is well below the critical electrical Rayleigh number for the plasmatron. Under this assumption laminar models of flow can be used and the flow properties of the plasma can be determined at the point of inflection as the

dependency of the longitudinal gradient of pressure on the gas flow rate. At the end of these calculations, the critical Reynolds numbers have been determined.
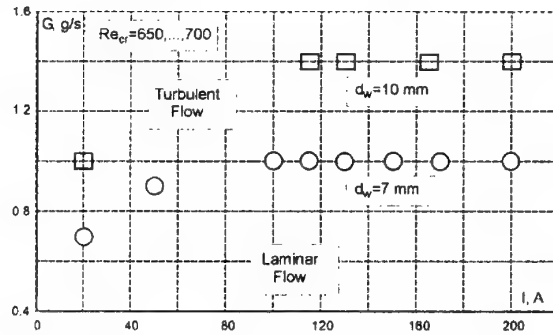
Fig.3. The marginal curve, which separates laminar regime of flow and turbulent one in the space of following parameters: a gas flow rate G, electrical current I and internal diameter d_w for cylindrical channels.

As shows in Fig.3, for $P=10^5$Pa, the parameters of the point of inflection are $G=1$g/s, and $dP/dz=8 \cdot 10^4$Pa/m. For all experimental results represented in the range of electric currents $I=(112$-$129)A$ the critical Reynolds numbers predicted by calculations are in the range 650–700. The numerical calculations of the critical Reynolds number allow plotting pairs of G and I for various d_w. This marginal curve for plasmatrons with cylindrical channel is represented in Fig.3. This curve could be approximated by the following equation: Re=$4G/(\pi d_w \eta_m)$=Re$_{cr}$=const. It is represented in Fig.3 for two channel diameters. In this figure, the area located below the marginal curve corresponds to the laminar regime; the area located above the curve corresponds to the turbulent regime. For the case of plasmatron with the expanding channel as an electrode we recommend to use the equivalent diameter of the divergent channel.

5. Diffuse model of short circuit of an electrical arc in the plasmatron channel

For the calculation of current-voltage characteristics of plasmatron an external algorithm is required to determine a length of the arc self-settled in the plasmatron channel. Within framework of two-dimensional model it is impossible to simulate process of short-circuiting of an electrical arc on a channel wall. In this connection the diffuse model of an electrical arc short-circuiting in the plasmatron channel is proposed (an electrical arc length definition). It is supposed, that the electrical arc moves downwards

the flow and, simultaneously, makes casual wandering on cross section of the channel. Wandering occurs under the action of whirlwinds having the characteristic size about the diameter of the arc. Further is supposed, that these whirlwinds are generated by the gas flowing around arc areas inclined to plasmatron axis, i.e. each bent arc area generates in a flow behind itself something like a Karman vortex path (the similar phenomenon takes place when a flag trembles on a wind). The action of whirlwinds on an arc is supposed to be non-correlated. The whirlwinds being quite "large", they do not influence over transport properties of a medium, and in "average" gas flow remains laminar. This model of short-circuiting of the arc on the anode wall describes quite satisfactorily such a complex physical phenomenon as self-settled electric arc in the channel of plasmatron.

Gas mean velocity inside the whirl relative to the mean gas flow is supposed to be $v_{whirl}=(8/\xi)^{1/2}<w>$. Whirl interaction with the arc lasts for R_{arc}/v_{whirl}, during the interaction arc center shifts by $(1/4)R_{arc}$ in casual direction. After N consecutive interactions a root-mean-square deviation of the arc from the center of channel exceeds a backlash between a wall and border of the arc, and the arc touches the channel walls. This happens on the distance $L_{Arc} \sim N <w> (R_{arc}/v_{whirl})$ downstream from cathode. Within these assumptions, finally the following formula for L_{Arc} is obtained

$$L_{Arc}/R_W = C (8/\xi)^{1/2}(1-R_{Arc}/R_W)^2$$

In a case of a laminar flow $\xi=64/Re$, $Re=2G/(\pi R_W \eta)$ is calculated using mean mass temperature of gas within the end of the arc; R_{Arc} is calculated as radius of channel area, through which passes the main part of arc current (for $Re<700$ - it is 95% I, for $Re>700$ - 99.9% I); C - constant, characterizing a ratio between the size of whirlwinds and radius of the arc. Theoretical value of constant C is within the range of 10-30, its precise value has to be defined by experimental data analysis. For $C\approx20$ divergence between the generalized experiment data [3] and calculated data is quite moderate and for the channel with the radius 8 mm the divergence does not exceed 25% in the range of I=50-400A and G=0.0005-0.003kg/s.

6. Conclusions

Special methods for numerical modelling of the two-dimensional plasma flow in plasmatrons with the cylindrical and expanding channel as an electrode including process of short-circuiting of the electrical arc on a channel wall are discussed. Within the framework of this program simplified two-dimensional mathematical model of electrical arc was created for cylindrical cooled channel with self-settled length and axial injection of working gas.

New method for calculation of the critical Reynolds number (the transfer from the laminar flow regime to turbulent one when turbulence is caused by the hydrodynamic Kelvin-Helmholtz instability) was developed. This method is based on numerical calculations and the experimental dependencies of the longitudinal gradient of pressure in the channel on gas flow rate. The critical Reynolds number for gas flow in plasmatrons under $Ra_e<Ra_{ecr}$ has been obtained using precise plasmatron experiments [3-4] and our new developed code for numerical calculations. The marginal curve, which separates laminar regime of flow and turbulent one has been established in the space of following parameters: gas flow rate, plasmatron diameter and electrical current.

References

1. A.A.Belevtsev, L.G. D'yachkov, E.Kh. Isakaev, P.P. Ivanov, Nitrogen plasma radiation in a quasi-one-dimensional flow code for axially symmetric plasmatron, International Symposium on Electron-Molecule Collisions and Swarms, 18-20 july 1999, Tokyo, Japan, pp.147-148.
2. V.I.Artemov, Y.S.Levitan, O.A.Sinkevich, Plasma instabilities and turbulence in low temperature plasma; Moscow, MPEI Publishing House, 1994 (in Russian).
3. G.Frind, B.L.Damsky, USA Air Force, Wright-Patterson Air Force Base, Ohio, Tech. Rep., 1 (1964), 64 - 148; 2(1966), 66 - 0073; 3 (1968), 68 - 0067, 4 (1970), 70–0001.
4. P.W.Runstadler Jr., Harvard University, Dept. Eng. and Appl. Phys., Tech. Rep., No 22, 1965.

71. USING OF SEPARATION FLOW AT THE HYPERSONIC FLIGHT VELOCITIES

A.F. Savvateev, A.V. Budin, V.A. Kolikov, Ph.G. Rutberg

Institute of Problems of Electrophysics of Russian Academy of Sciences (IPE RAS)

Abstract. The problems of plasma aerodynamics are connected to projection of hypersonic flight vehicles. At the Mach number more than 8 the temperature of stagnation gas stream becomes sufficient for partial ionization of gas. In this case except necessity of reducing aerodynamic drag of vehicle there is a need in diminutions of thermal loads. It is known, that the nose needle installation on a hypersonic flight vehicle reduces in a significant modification it aerodynamic characteristics due to the organization the separation flow of its head part.

In the present work the results of an experimental research of aerodynamics of hypersonic flight vehicles with front separation zone formed in space between tank of vehicle and nose disk tip are represented. The use nose disk tip allows essentially reducing pressure at the front end face of tank, that results in a significant diminution of a drag coefficient C_x. It is shown, that for body of such configuration the magnitude C_x, close to C_x of an acute cone can be reached. Taking into account tight correlation of aerodynamic drag of body and acting on it of thermal loads, it is possible to make a conclusion that the installation of the nose disk tip will allow to reduce the heat flows to tank of vehicle. Just one more virtue of flying vehicle with nose disk tip is the raise of their aerodynamic stability.

In work the obtained experimental dependencies of aerodynamic characteristics of bodies with nose disk tip on geometric sizes of tip and angle of attack are presented.

1. Introduction

From point of view of interior arrangement of flying vehicles the most convenient form is the cylinder. The traditional methods of the aerodynamic stabilization of cylindrical bodies assume use of tail or of base cone in combination with a necessary displacement of a center of masses. However such methods have a series of shortages. They concern, mainly, to the bore hypervelocity accelerators, such as railguns, light-gas accelerators and induction accelerators. One basic directions of use of these accelerators is the research of high-speed impact. In such experiments the impactors of the complicated shape, installed in a fairing, made from an easy material, are usually used. The application of a base cone for the stabilization rather short of accelerated assembly (elongation $\lambda \approx 2$) is not acceptable way due to the following reasons:

- for short impactor the mass and dimensions of
- base cone are commensurable with ones of impactor itself. It leads to the distortion of interaction process.
- applying of base cone limits the maximum impactor size for the fixed bore caliber.

Therefore, another way has been chosen for the stabilization of short impactor supersonic flight. The separated flow of projectile head part was created by means of spike or disk tip set on its front face. In [1] is shown that it causes the significant changing of aerodynamic characteristic of projectile. For example, value of aerodynamic resistance coefficient C_x depends very strong on dimensions and shape of spike as it shown in Fig.1. Obviously, that C_x of cylindrical spiked body with the flat front face is several times less than C_x of

body without spike (0.27-0.4 and 1.6 correspondingly). The spike dimensions and shape give a strong influence on stability characteristics of spiked body [2] Fig.2.
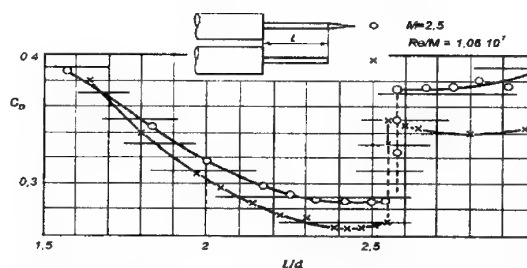
Fig.1. Dependence of aerodynamic resistance coefficient C_x on dimensions and shape of spike [1].

The significant pressure decreasing on the body front face [2,3,4] causes all effects connected with the separated flow of spiked body. The pressure on spiked body front face is equal to (0.2-0.4)P_f (where $P_f = \rho \cdot V^2/2$ - dynamic head pressure, here: ρ - gas density, V - velocity of body) in dependence on supersonic flow characteristics (Mach M and Reynolds Re numbers). In case of unsymmetrical flow (attack angle does not equal zero) the line of aerodynamic resistance force acting does not conform to the projectile axis due to the unsymmetrical pressure distribution on the front face of body. It results in appearance of negative pitch moment, which value depends on gas dynamics parameters of flow and on spike dimensions too. This phenomenon was named as 'head stabilization' effect.

371
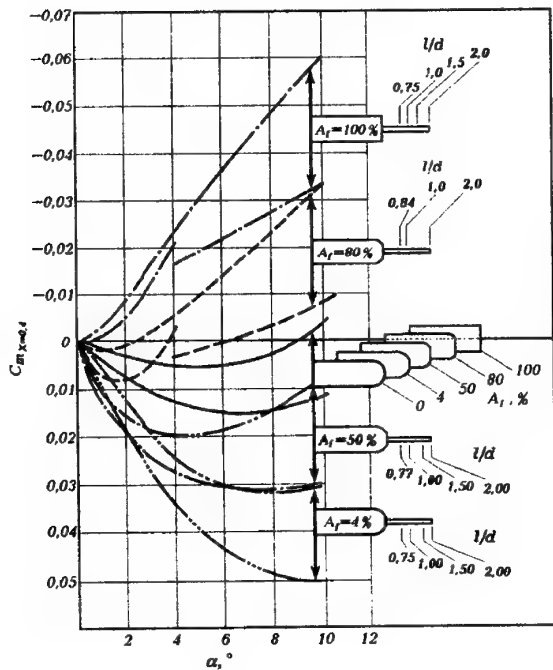
Fig.2. Dependence of pitching moment coefficient relative point of 0.4 body length from one front face on attack angle α. A_f – blunt degree, l – spike length, d – body diameter [1].

In [5,6,7,8] are shown that all effects caused by the separated flow of body increased when the spike was replaced with the disk tip, which consists of spike and disk on its front end. For the body of such shape the closed circulation zone appears in the space between the disk and the front face of body. The type of flow and gas dynamics flow characteristics inside the zone are defined by the relative dimensions of disk tip ($\bar{l}$ =l/D and $\bar{d}$ =d/D, where l - spike length, d - disk diameter, D - body front flat face diameter) and by the parameters of undisturbed flow (M and Re). Static pressure inside the circulation zone at the supersonic velocity of flow approximately equals to $0.1 \cdot P_f$. The drag coefficient C_x of body with the disk tip is close to the one of body with the nose cone, which includes the disk tip of such dimensions Fig.3. In both cases (spike and disk tip) the critical spike length l_{cr} exists. If $\bar{l}$ exceeds l_{cr} the flow rebuilding appears. For the spiked body it expresses in moving of flow separation point from spike nose lower the stream [3,4]. For the body with the disk tip it means the destroying of circulation zone. In any case it leads to the increasing of pressure on body front flat and, consequently, to the spasmodic C_x increasing (Fig.1). Value of l_{cr} depends on flow characteristics and attack angle.

2. Results of Experiment

Experiments on the hypersonic wind tunnel at Mach number M=17 had permitted to define the quantity pressure distribution on front face of body with the disk tip and values of its aerodynamic coefficients. The dependence of C_x on disk tip dimensions (see Fig.3 and 4) has the same view as one for the spiked body (see Fig.1).
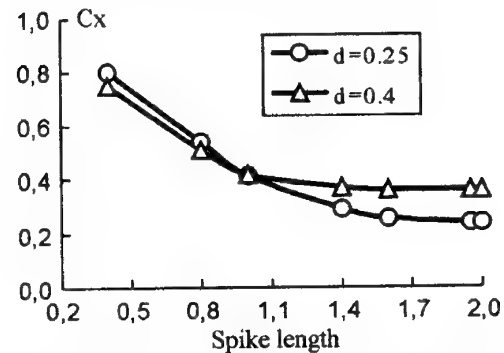
Fig.3. Dependence of drag coefficient of projectile on relative disk tip dimensions.
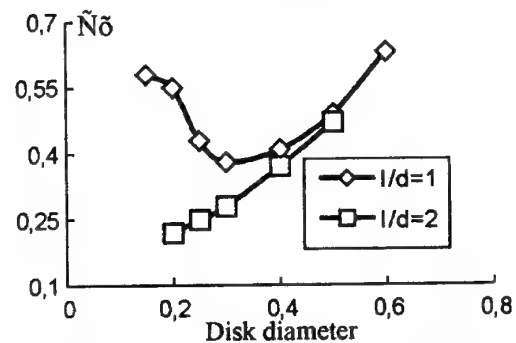
Fig.4. Dependence of drag coefficient of projectile on relative disk diameter.

When circulation zone does not destroyed the enlarging of spike length and the decreasing of disk diameter leads to the reducing of C_x. The least obtained value of projectile C_x is equal to 0.24 when $\bar{l}$ =1.8 and $\bar{d}$ =0.25 (at the zero attack angle). In Fig.5 and 6 the pressure distribution P/P_f on the front face of body with the disk tip dimensions $\bar{l}$ =1.425 and $\bar{d}$ =0.4 at the different attack angles is presented. Magnitude of pressure peak on attack edge of front face can exceeds one inside the circulating zone fifteen times. Obviously, 'head stabilization' effect is a result of pressure increasing on attack edge of body front face. This effect has place only if attack angle does not exceed the critical value α_{cr}, at which the circulation zone destroying appears. In contrary case the pressure distribution on the projectile front

372

face changes very strong (curve α=20° on Fig.6) and the values of lift (C_n) and pitching moment (C_{mz}) coefficients become **undefined** (attack angle 15° in Fig.7).

Fig. 5. α=11°
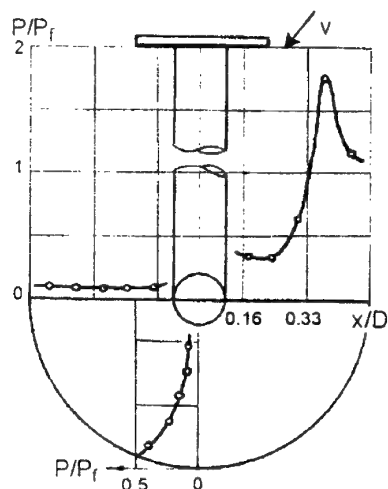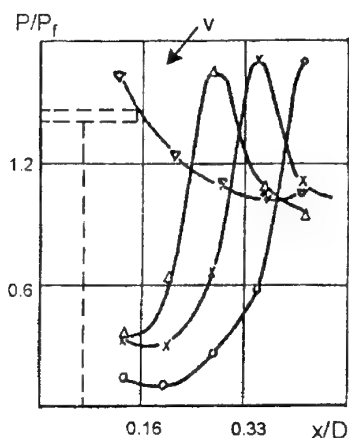
Fig. 6 o - α=8°, x - α=11°, Δ - α=14°, ∇ - α=20°
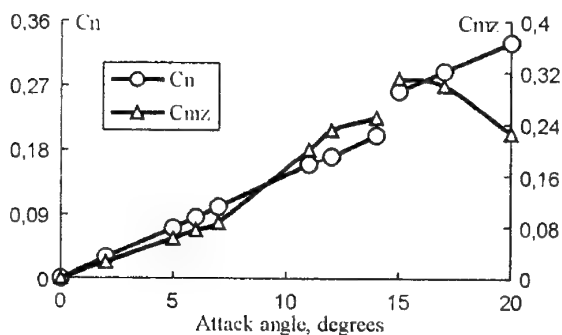
Fig.7 Dependencies of lift and pitching moment coefficients on attack angle for the body with the disk tip

$$\bar{l} = 1.425, \quad \bar{d} = 0.4$$

This phenomenon means that the value of pitching moment derivative C_m^a is decreasing spasmodically. Value of α_{cr} depends basically on the disk tip dimensions and M. Result of experiment shows that the increasing of $\bar{d}$ and M and the decreasing of $\bar{l}$ causes the increasing of α_{cr}.

One of the most important features of spiked bodies and bodies with the disk tip is the increasing of circulating zone steadiness at the high supersonic velocity. Disadvantage of 'head stabilization' effect is low value of demping moment. It means that the projectile stabilization completion (when the oscillations finish and the attack angle becomes close to zero) needs in relative long time (several oscillations [9]). Value of pitching moment derivative influences on the oscillation period duration:

$$T = 2\pi / v\sqrt{\alpha} \quad (1)$$

here: $\alpha = \rho S l C_m^a / 2A$, C_m^a -pitching moment derivative, A - inertia moment, ρ - air density, S – projectile cross-section area.
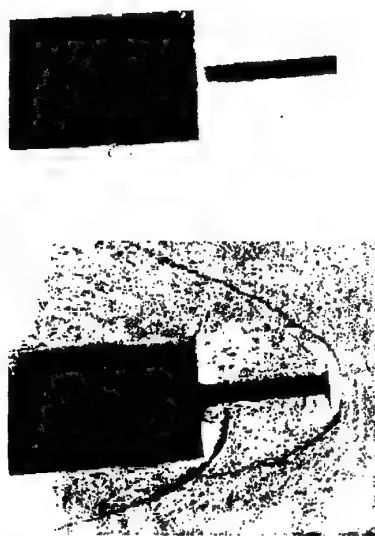
Fig. 8 Spiked body and body with the disk tip in hypersonic flow (M=16.8).

For the defining disk tip sizes which providing steady flight of body the series of experiments on the ballistic range of 50м length at the velocities of 0.7-3.0km/s (M=2.2-9.0) was conducted. These accelerated bodies were equipped with the spike or disk tip of different dimensions and had the different ballistic coefficient value $\sigma = C_x S/m$ (where, S – body cross-section area, m –

projectile mass). The photos of spiked body and projectile with the disk tip in supersonic flow are shown in Fig.8. The area of high pressure appears on attack edge of front face of projectile equipped with the disk tip. This area corresponds to the glowing zone in Fig.8, which testifies about the high gas temperature (and, consequently, high pressure) of stagnant flow. Obviously, that such unsymmetrical pressure distribution on body front face creates the negative pitch moment relative the body mass center. The experiment results show that disk tip stabilizes body better than nose needle.

The main goal of this experiment was to define the dimensions of disk tip that provide the most reliable projectile stabilization. Postaction of EDL exhausting gases and sabot separation results in initial projectile attack angle up to $11°$. It was defined that for the stabilization of cylindrical projectile at the Mach numbers M=5-17 the most acceptable way is using the disk tip of following dimensions: spike length $\bar{l}$ =1.2-1.4 and disk diameter $\bar{d}$ =0.3-0.4. The results of experiment shown, this disk tip configuration provides the reliable stabilization of cylindrical projectile with the body elongation (L/D) up to 2.5 and the ballistic coefficient from $1,3\cdot10^{-3}$ up to $3.4\cdot10^{-3}$ m^2/kg at the such M. Projectile mass influences on duration of its full stabilization only.

3. Conclusion

Thus, for want of hypersonic velocities of flight disk tip allows essentially to improve the aerodynamic characteristics of hypersonic vehicles. Disk tip installation on blunt body results in reducing aerodynamic drag (C_x disk tip is closed to C_x of acute cones) and thermal loads. For want of it the characteristics of stability of such bodies are much higher, than at a conic bodies, due to the effect of "head stabilization". The reliable aerodynamic stabilization of the body with disk tip can be supplied for want of initial angles of attack up to $20°$ in dependence on elongation of tank and transversal moment of inertia. It was estimated that steadiness of circulating zone is increasing as the Mach number of flow.

With reference to light-gas accelerators or railguns the cylindrical shape of accelerated body enables to locate inside him some separate impactors, that is a necessary condition for want of realizations of experiments on high-speed impact.

References

1. Paul K. Chang "Separation of flow," v.2 Pergamon Press 1970.
2. Crawford D. H. "Investigation of the Flow over a Spiked- nose Hemisphere- cylinder at a Mach Number of 6,8," NASA TN D-118, Dec 1959.
3. Wood C. J., " A Study of Hypersonic Separated Flow," Ph. D. thesis, University of London, Oct. 1961 (available as DDC AD 401652).
4. Maull D. J., "Hypersonic Flow over Axially Symmetric Spiked Bodies," J. Fluid Mech., 8, Part 4, 584-592 (Aug. 1960).
5. Hunt G. K., "Supersonic Wind-tunnel Study of Reducing the Drag of a Bluff Body at Incidence by Means of Spike," Royal Aircraft Establishment, Rept. Aero. 2606 May 1958.
6. Album H. H. Spiked Blunt Bodies in a Supersonic Flow," Air Force Office of Scientific Research, Washington 25, DC, Rept. AFOSR 307, June 1961.
7. 7.Belov I.A., Dementev I.M. "Analyze of results and methods of Modeling Substantiation of bodies with the front separated flow" Preprint 1353 PhTI Academy of Sciences USSR 1989.
8. Isaev S.A. "Numerical Exploration of Aerodynamic Resistance Decreasing of Bodies with Front separated Flow" Engineer-physics journal, vol.68, #6, p.p. 975-9826 1995.
9. Savvateev A.F, Budin A.V, Zakharenkov S. V, Kolikov V.A, Rutberg Ph.G. "Launch Package for Multiple- Rod Hypervelocity Impact Investigation," IEEE Transactions on Magnetics, vol. 35, Num. 1, part 1, pp. 90-94, January 1999.

72. WALL SPUTTERING BY PLASMA STREAMS WITHIN LINEAR AND TOROIDAL MAGNETIC FIELDS

V.A. Alekseev, V.I. Vasil'ev, B.N.Kolbasov, P.V.Romanov
Kurchatov institute, TRINITI, IZMIRAN. Fax:(095) 334 01 24

In a plasma accelerator or in T-10 tokamak chamber, the interaction between the walls and the flow of heated plasma give rise to wale-matter sputtering. We investigate the particles generated in the presence of corresponding magnetic field. The report describes data of the measurement of particles sizes together with results of studying the composition of these particles.

The destruction of metallic wall surface appears as on complicated process producing fine dust. The elements composition of the dust depends on the sizes of dust particles.

73. SIMULATION OF TURBULENT FLOWS IN CHANNELS WITH GAS INJECTION IN NEAR WALL REGIONS

M.Osipov, V.Shuchkin
Bauman Moscow State Technical University,

Yu.Eliseev
Federal Scientific Centre "Salut"

W.Shyy, S.Takyyr
University of Florida
USA, e-mail:wss@aero.ufl.edu

The basic problem in the analysis of improvement of working processes efficiency, time service and reliability while designing of gas flow ducts (nozzles, channels, diffuses, combustion chambers) for high temperature engines and aerospace power generation systems (MHD-generators, gas turbines) is the problem of simulation of turbulent high temperature flows with operation of near wall process for avoiding of separation and decreasing of friction, heat and in some cases electrical losses. The problem is of theoretical interest and it has many practical implication. One of perspective methods for solution of this problem is the heat and mass transfer protection by porous blowing through the porous section (porous insulation walls) and tangential injection (film cooling) through slots, perforation or porous steps (nozzles, combustion chamber, electrode walls of MHDG).

Theoretical and experimental studies presented in this paper devoted to simulation of subsonic and supersonic turbulent flows in restangular channels with operation of boundary layer development by gas blowing through separation cooling elements with taking into consideration compressibility, nonisothermal conditions, intensity of blowing or injection, MHD-interaction and roughness. Methods of calculation are based on the solution of system of equations written in integral relation forms and in Navier-Stokes equations with using of k-ε model of turbulence. The boundary conditions were accepted from experimental investigations conducted in BMSTU. The results of calculations showing the dynamic and heat transfer processes, position of shock, Max number, pressure and temperature, turbulence energy, distributions along the channel and across the boundary layers with variation of intensity of blowing are presented. The distributions of temperature across the porous matures have been analysed.

The problems of high temperature composite materials application in designing of permeable electrode and insolating walls of MHD-channels are considered.

74. CONICALLY SELF-SIMILAR SOLUTIONS OF THE MAXWELL'S EQUATIONS WITH AN ELECTROMAGNETIC FIELD TORSION

A. P. Byrkin, S. V. Ershkov, V. V. Schennikov

Institute for Computer-Aided Design of the Russian Academy of Sciences,
19/18 2-nd Brestskaya St., Moscow 123056, Russia
tel. +7 (095) 250-8853; e-mail: ICAD @ inapro.msk.su

Abstract. In this presentation, conically self-similar stationary solutions of the Maxwell's equations for the case of axially symmetric electromagnetic field propagation in a medium, are considered. In this context, the conicity is understood as a global topological invariance of these solutions: they are mapped to themselves upon rescaling.

As an example of solutions of that type, we may mention electromagnetic field, each component of which propagates along one of two intersecting (twisting or untwisting) conical helices with a common axis.

If variables are selected in the suggested way, a system of the Maxwell's equations can be reduced to a system of 2nd order ordinary differential equations, which admits a solutions of two-parameter class. As it is shown, *in the case of local charge compensation*, both field components (*electric and magnetic*) have a torsion and exhibit significant Rickatti's character.

A key feature of the representations constructed consists in explicit demonstration of invariants which allow for penetration (surmounting) through emerging singularities, in particular, that one which relates to a solution topology switching, i.e. transition from conical to cylindrical topology at the vicinity of the symmetry axis.

The latter aspect creates (*within the framework of constructed solutions*) the necessary prerequisites to appearance of the superconductivity.

First of all, let us write out the common form of the initial system of the Maxwell's equations [1] in a spherical coordinate system R, θ, φ (the origin of the coordinate system coincides with the origin of the electromagnetic field, polar axis Ox is directed normal to the field propagation in the medium):

$$div\,\vec{E} = 4\pi\rho \tag{1}$$

$$div\,\vec{B} = 0 \tag{2}$$

$$rot\,\vec{E} = -\frac{1}{c}\frac{\partial \vec{B}}{\partial t} \tag{3}$$

$$rot\,\vec{B} = \frac{4\pi}{c}\vec{j} + \frac{1}{c}\frac{\partial \vec{E}}{\partial t} \tag{4}$$

$$div\,\vec{j} + \frac{\partial\rho}{\partial t} = 0 \tag{5}$$

Here, the following notations are adopted: ρ – charge density distribution in the medium; $\mathbf{E}=\{E_1,E_2,E_3\}$ - electric field vector in the respective point of the medium; $\mathbf{j}=\{j_1,j_2,j_3\}$ - displacement current vector; $\mathbf{B}=\{B_1,B_2B_3\}$ - magnetic induction vector in the respective point of the medium, $\mathbf{B}=\mu_0\cdot\mathbf{H}$, μ_0 – permeability coefficient of the medium, $\mathbf{H}=\{H_1,H_2,H_3\}$ - magnetic field vector in the respective point of the medium; c –

light velocity in the medium; besides, the following assumptions (see [2]) are made:

$$rot\,\vec{E} = \left\{\frac{1}{R\sin\theta}\left(\frac{\partial}{\partial\theta}(\sin\theta\,E_3) - \frac{\partial E_2}{\partial\varphi}\right)\right\}\vec{e}_R +$$

$$+\left\{\frac{1}{R}\left(\frac{\partial(RE_2)}{\partial R} - \frac{\partial E_1}{\partial\theta}\right)\right\}\vec{e}_\varphi +$$

$$+\left\{\frac{1}{R\sin\theta}\frac{\partial E_1}{\partial\varphi} - \frac{1}{R}\frac{\partial}{\partial R}(RE_3)\right\}\vec{e}_\theta$$

$$div\,\vec{E} = \frac{1}{R^2}\frac{\partial(R^2 E_1)}{\partial R} + \frac{1}{R\sin\theta}\frac{\partial(\sin\theta\,E_2)}{\partial\theta} +$$

$$+ \frac{1}{R\sin\theta}\frac{\partial E_3}{\partial\varphi}$$

In this case, the statement (5) (i.e. a mathematical formulation of the charge conservation law) cannot be considered as unique. Actually, it can be derived from (1) and (4) (see [1]). In other words, entire Maxwell's electrodynamics theory can be built on the base of the first four of the above-mentioned postulates, which describe the electric and magnetic fields generated by charges and currents in the spatial region under consideration.

In this work, we'll consider solutions of the system composed of equations (1)–(4), written for the case of stationary ($\partial/\partial t = 0$) distribution of electric and magnetic fields in the medium.

In this respect, in order to extend target solutions to the case of deviations from axial symmetry ($\partial/\partial\varphi \neq 0$) (taking into account specificity of the phenomenon) and in agreement with the general concept of conical self-similarity (see [3-6]), we'll represent all functions in the initial system in a self-similar form (here, α, β, γ, ζ are self-similarity constants; a_1, a_2, a_3, a_4 - are field torsion parameters):

$$\vec{E}(R,\theta,\varphi) = \frac{\vec{E}(\theta)}{R^\alpha}\exp(a_1\varphi), \quad \vec{E} = (E_1, E_2, E_3),$$

$$\vec{B}(R,\theta,\varphi) = \frac{\vec{B}(\theta)}{R^\beta}\exp(a_2\varphi), \quad \vec{B} = (B_1, B_2, B_3),$$

$$\vec{j}(R,\theta,\varphi) = \frac{\vec{J}(\theta)}{R^\gamma}\exp(a_3\varphi), \quad \vec{J} = (J_1, J_2, J_3),$$

$$\rho(R,\theta,\varphi) = \frac{\rho(\theta)}{R^\zeta}\exp(a_4\varphi). \tag{6}$$

After substitution of the representations (6) in the initial system and choosing the following auto-similarity constants: $\zeta = \alpha+1$, $\gamma = \beta+1$ and field torsion parameters: $a_1 = a_4$, $a_2 = a_3$, we obtain the following system of ordinary differential equations ($a_1, a_2 \neq 0$):

$$(2-\alpha)E_1 + \frac{(E_2\sin\theta)'}{\sin\theta} + \frac{a_1 E_3}{\sin\theta} = 4\pi\rho \tag{7}$$

$$(\beta-2)B_1 = \frac{(B_2\sin\theta)'}{\sin\theta} + \frac{a_2 B_3}{\sin\theta} \tag{8}$$

$$\frac{(E_3\sin\theta)'}{\sin\theta} = \frac{a_1 E_2}{\sin\theta} \tag{9}$$

$$(1-\alpha)E_2 = E_1' \tag{10}$$

$$(1-\alpha)E_3 = (a_1 E_1)/\sin\theta \tag{11}$$

$$J_1 = \frac{c}{4\pi}\left\{\frac{B_3\sin\theta)'}{\sin\theta} - \frac{a_2 B_2}{\sin\theta}\right\} \tag{12}$$

$$J_2 = \frac{c}{4\pi}\left\{\frac{a_2 B_1}{\sin\theta} - (1-\beta)B_3\right\} \tag{13}$$

$$J_3 = \frac{c}{4\pi}\left\{(1-\beta)B_2 - B_1'\right\} \tag{14}$$

The system of equations (7)-(14) adopts a 4-parameters class of solutions; besides, three

functions: $E_1(\theta)$, $\{B_i(\theta)\}$, $i=2, 3$ seems to be free (i.e. functions to be adjusted in the accordance to boundary conditions of task investigated).

It means, that other necessary characteristics of the solution can be expressed via these functions (here, α, $\beta \neq 1, 2$):

$$E_2 = \frac{E_1'}{(1-\alpha)}, \quad E_3 = \frac{a_1 E_1}{(1-\alpha)\sin\theta},$$

$$B_1 = \frac{(B_2\sin\theta)'}{(\beta-2)\sin\theta} + \frac{a_2 B_3}{(\beta-2)\sin\theta},$$

$$J_1 = \frac{c}{4\pi}\left\{\frac{(B_3\sin\theta)' - a_2 B_2}{\sin\theta}\right\},$$

$$J_2 = \frac{c}{4\pi}\left\{\frac{a_2[(B_2\sin\theta)' + a_2 B_3]}{(\beta-2)\sin^2\theta} - (1-\beta)B_3\right\}$$

$$J_3 = \frac{c}{4\pi}\left\{(1-\beta)B_2 - \left[\frac{(B_2\sin\theta)' + a_2 B_3}{(\beta-2)\sin\theta}\right]'\right\}$$

Furthermore, the two latter of the above-mentioned statements can be transformed as follows:

$$E_1'' + \{ctg\,\theta\}E_1' + \left\{(\alpha-1)(\alpha-2) + \frac{a_1^2}{\sin^2\theta}\right\}E_1 + \\ + \{4\pi(\alpha-1)\rho\} = 0 \tag{15}$$

$$B_2'' + \{ctg\,\theta\}B_2' + \left\{(\beta-1)(\beta-2) - \frac{1}{\sin^2\theta}\right\}B_2 + \\ + \left\{(4\pi/c)(\beta-2)J_3 + a_2\left(\frac{B_3}{\sin\theta}\right)'\right\} = 0 \tag{16}$$

$$\rho = \frac{1}{4\pi}\left[(2-\alpha)E_1 + \frac{(E_1'\sin\theta)'}{(1-\alpha)\sin\theta} + \frac{a_1^2 E_1}{(1-\alpha)\sin^2\theta}\right].$$

Among diverse possible solutions of the system composed of equations (7)-(14), solutions, which are invariant relative to influence of the electromagnetic field carriers (i.e. electrons) themselves to the medium, are of most interest.

In particular, they include solutions, which imply local charge compensation in the medium (it is not equivalent to zero total charge, for example, as in the case of physical vacuum filled with virtual "particle-antiparticle" pairs).

Therefore, in order to achieve such an invariance, we should assume $\rho \propto 0$ in the equation (15) that leads to a conclusion that $\rho(\theta)$ is a zero-

factor [6]. In this case, the equation can be transformed into a second-order differential equation

$$E_1'' + \{ctg\,\theta\}E_1' + \left\{(\alpha-1)(\alpha-2) + \frac{a_1^2}{\sin^2\theta}\right\}E_1 = 0 \tag{17}$$

which can be further reduced to the Rickatti's type equation by substitution $f(\theta) = y'(\theta)/y(\theta)$ (where $y(\theta) = E_1(\theta)$) (see [2]). This means that the target solution is continuous only on a limited (narrow) range of θ values or, in other words, it has a discontinuity on a certain closed half-line θ_0.

In the case of $J_3(\theta) \propto 0$, $a_2 = 0$, basing on (16) we may write out

$$B_2'' + \{ctg\,\theta\}B_2' + \left\{(\beta-1)(\beta-2) - \frac{1}{\sin^2\theta}\right\}B_2 = 0 \tag{18}$$

here, the latter equation (similarly to equation (17)) can be reduced to a Rickatti's equation using a substitution $f(\theta) = y'(\theta)/y(\theta)$ (where $y(\theta) = B_2(\theta)$) [2].

After a more thorough analysis of equations (12) and (13) within the system outlined above, we may conclude that condition $B_3(\theta) \neq 0$ (or, more strictly, $B_3(\theta) = C_0/\sin\theta$, where C_0 is an integration constant) does not contradict to the equations if the following parameters are chosen: $\{J_1(\theta), J_2(\theta)\} \propto 0$ (i.e. the flow $\mathbf{J}$ should be a zero-factor in total), $a_2 = 0$ (magnetic field $\mathbf{B}$ is axially symmetric), and $\beta = 1$ (restriction of target solutions to 2-parameter class).

This conclusion could be and should be associated with the non-zero torsion of the magnetic field (magnetic induction field); thus, the constructed conically auto-similar representations *a priori* possess a torsion (magnetic field torsion).

Let us now consider a particular case with $\{\alpha,\beta\} = 1$. Such a selection of self-similarity parameters is fully equivalent to transition to a cylindrical topology of target solutions within the predefined conical topology. Thus, assuming $\alpha = 1$, we conclude basing on equation (10) that $E_1 = \text{const} = C_{01}$ that does not contradict to the equation (11) in the case of $a_1 = 0$. But in this case, from the equation (9) we may conclude that:

$$E_3 = C_{03}/\sin\theta,$$

(here, C_{03} – integration constant), and from the equation (7) we may derive the following expression for the E_2 component of the electric field:

$$E_2 = C_{01}\,ctg\,\theta + (C_{02}/\sin\theta).$$

Further assuming $\beta = 1$, basing on the equation (14) of the above system (taking into account that $J_3(\theta) \propto 0$ as in earlier cases), we may conclude that the first component of the magnetic field ($B_1(\theta)$ in this particular case) is constant: $B_1(\theta) = \text{const} = C_1$.

Besides, if we assume that $J_1, J_2 \propto 0$ (it is equivalent to assumption that the flow $\mathbf{J}$ is zero-factor in total, $\mathbf{J} \propto 0$ [6]), basing on the equation (12), we may conclude (similarly to the case with $\forall \{\alpha,\beta\} \neq 1$ considered above) that the field component $B_3(\theta) = C_3/\sin\theta$ ($C_3 = C_0$), that does not contradict to the equation (13) in the case of $a_2 = 0$, and basing on the equation (8) - that in the case $a_2 = 0$ (C_1 and C_2 are integration constants):

$$B_2(\theta) = C_1\,ctg\,\theta + (C_2/\sin\theta).$$

Now, let us consider case of $\{\alpha,\beta\} \rightarrow 1$. Basing on the equation (11), we may conclude that existence of nontrivial solutions can be guaranteed only in the case of the following limit transition condition:

$$\lim_{\substack{\alpha\rightarrow 1 \\ a_1\rightarrow 0}} \left(\frac{\alpha-1}{a_1}\right) = \text{const} \tag{19}$$

or, in other words, we should assume that $\alpha \rightarrow 1$ as rapidly as $a_1 \rightarrow 0$.

Correlating the character of the solutions at $\{\alpha,\beta\} \rightarrow 1$ with respective behavior at arbitrary values of α, β (meeting the condition $\{\alpha,\beta\} \neq 1$), we may make the following suggestions:

$$\rho(\theta) \propto (\alpha-1), \quad \bar{J}(\theta) \propto (\beta-1) \tag{20}$$

In this case, the field component $E_1(\theta)$ is still determined as a solution of the equation (15) (in which all the second order infitesimal terms are neglected thus giving rise to the equation (17) at $a_1 = 0$); the component $B_2(\theta)$ – as a solution of the equation (16) (in which $a_2 = 0$ thus giving rise to (18) at $\beta = 1$); and the magnetic field component $B_3(\theta)$ – as a solution of the equation (12) at $a_2 = 0$, which gives, similarly to cases considered above, the value $C_0/\sin\theta$ (noteworthy, it does not contradict to the equation (13) at $a_2 = 0$, $\beta = 1$).

In an analogous way we may establish a similarity between behavior of solutions in the case of $\{\alpha,\beta\} \rightarrow 1$ and $\{\alpha,\beta\} = 1$ for all electric and magnetic field components relevant to these conditions (they also retain their character).

379

Summarizing all the arguments outlined above we may conclude that all solution components in the following three cases: 1) $\forall\{\alpha,\beta\}$ ($\{\alpha,\beta\}\neq1$), 2) $\{\alpha,\beta\}=1$, and 3) $\{\alpha,\beta\}\rightarrow1$ are self-similar to each other and change over continuously upon switching the solution's topology, i.e. upon variation of the $\{\alpha,\beta\}$ parameters values.

References

1. Leon N. Cooper. *Phizika dlya vsekh: vvedenie v suschnost' i strukturu phiziki* (Physics for everyone: introduction to nature and structure of physics). Mir, Moscow, 1973, vol. 1 "Klassicheskaya phizika" (Classical Physics), in Russian.
2. E. Kamke. Spravochnik po obyknovennym differentsial'nym uravneniyam (Handbook on ordinary differential equations). Nauka, Moscow, 1971, in Russian.
3. V. V. Schennikov. Ob odnom klasse tochnyh resheniy uravneniy tipa Nav'e-Stoksa dlya sluchaya szhimaemogo teploprovodnogo gaza (On one of class of exact solutions of the Navier-Stokes' type equations for the case of compressible heat-conducting gas) // Prikladnaya matematika i mehanika, 1969, vol. 33, № 3, p. 582 – 584, in Russian.
4. A. P. Byrkin. O tochnyh resheniyah uravneniy Nav'e-Stoksa dlya techeniya szhimaemogo gaza v kanalah (On exact solutions of Navier-Stokes equations for a flow of compressible gas in channels) // Uchenye Zapiski CAGI, 1970, vol. I, No.6, p. 15 – 21, in Russian.
5. S. V. Ershkov, V. V. Schennikov. Ob avtomodel'nyh resheniyah sistemy polnyh uravneniy Nav'e-Stoksa dlya sluchaya osesimmetrichnyh zakruchennyh techeniy vyazkogo szhimaemogo gaza (On the self-similar solutions of a system of complete Navier-Stockes' equations for the case of axially-symmetric flow of a viscous compressible gas with a torsion) // Zh. vychislitel'noy matematiki i matematicheskoy phiziki, 2001, **41**, No.7, pp.1126-1133, in Russian.
6. A. P. Byrkin, V. V. Schennikov. *Konicheski avtomodel'nye techeniya neszhimaemoy zhidkosti i gaza s krucheniem* (Conically self-similar flows of an incompressible liquid or gas with a torsion). Proceedings of the XIIth School-seminar "Aerodynamics of aircrafts", March 2001, Moscow: CAGI, p. 23 – 24.

75. MHD COAXIAL THRUSTERS FOR MARINE VESSELS

Kovalev L.K., Koneev S.M.-A., Larionoff A.E., Poltavets V.N., Kovalev K.L.
Moscow State Aviation Institute (Technical University),
Russia 125871 Moscow, Volokolamskoe shosse 4, MAI
Phone/Fax: +7 (095) 9635089
e-mail: kovalev@mail.sitek.net

Abstract. Application of MHD thrusters (MHDT) will allow to increase essentially the speed, manoeuvreness and survivability of the ships, will provide practically unlimited thruster's power and noiselessness of its work, as well as give an opportunity of fast reverse of the nominal thrust. MHDT may find wide application on the boats and on the underwater vessels. Nowadays the most perspective scheme of MHDT for large-scale marine ships are MHDT of coaxial type with toroidal magnetic system. This scheme of thrusters has higher significances of power and efficiency and are well combined with modern architecture of the boats [5]. In this paper coaxial MHDT are considered. The theory of volume magnetohydrodynamic laminar and turbulent flows in coaxial MHD channels of a various shape are presented. The obtained analytical solutions allow to determine local distributions of velocity, pressure, potential and electric current density in coaxial MHD channels with different walls shapes.

1. Laminar Flows in Coaxial Channels
1.1. Problem formulation

There is a laminar axis-symmetric $v(v_r, 0, v_z)$ developed flow of a conducting liquid in the ring MHD channel (Fig.1.1), continuous impenetrable ideally conducting walls of which are slightly curved in the direction of axis z:

$$r_1' = r_0 \cdot (1 + f(\varepsilon z)); \quad r_2' = r_1' + \Delta'(\varepsilon z); \qquad (1.1)$$

Here r_1' and r_2' - equations of the forming surfaces of the wall; $f(\varepsilon z)$, $\Delta'(\varepsilon z)$ - slightly varying along axis z smooth functions, ε - small parameter ($\varepsilon \ll 1$) for the description of the wall curvature, r_0 - radius of the internal electrode at the inlet ($z=0$), $\Delta'(\varepsilon z)$ - width of the ring gap.
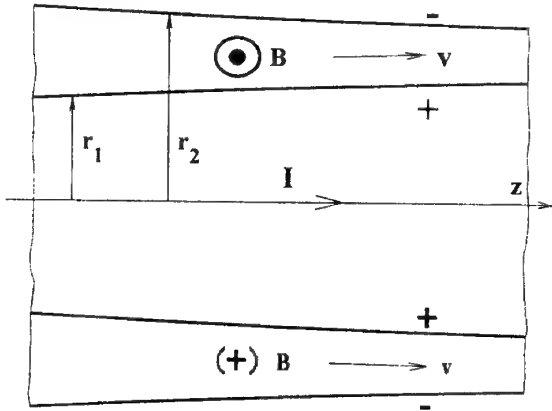
Fig.1.1. Scheme of coaxial MHD channel

At the lateral electrodes there is a difference of the potential

$\Delta U = -U_e$, and $U=0$ at $r=r_1(z)$ and $U=-U_e$ at $r=r_2(z)$.

The scalar conductivity σ_0, density ρ_0 and viscosity μ_0 are assumed constant. It is considered, that the magnetic Reynolds number $Rm = \tilde{\mu}\sigma v L \ll 1$ and the induced magnetic fields are negligible small in comparison with the external magnetic field $\mathbf{B}(0, B_\theta, 0)$, ($B_\theta \sim 1/r$). The channel length L is assumed large in comparison with the ring gap ($L/(r_2-r_1) \geq 5\text{-}7$) which allows to neglect the inlet and outlet effects.

In this case the system of magnetic hydrodynamics can be presented in dimensionless form as [2]:

$$\partial(rv_r)/\partial r + \partial(rv_z)/\partial z = 0; \qquad (1.2)$$

$$v_r \partial v_r/\partial r + v_z \partial v_r/\partial z = -\text{Eu}\,\partial p/\partial r +$$
$$+ \frac{1}{\text{Re}}\left\{\frac{\partial}{\partial r}\left[\frac{\partial(rv_r)}{r\partial r}\right] + \frac{\partial^2 v_z}{\partial z^2}\right\} - SJ_z B_\theta \qquad (1.3)$$

$$v_r \partial v_z/\partial r + v_z \partial v_z/\partial z = -\text{Eu}\,\partial p/\partial z +$$
$$+ \frac{1}{\text{Re}}\left\{\frac{\partial}{r\partial r}\left[r\frac{\partial v_z}{\partial r}\right] + \frac{\partial^2 v_z}{\partial z^2}\right\} - SJ_r B_\theta \qquad (1.4)$$

$$\partial(rJ_r)/\partial r + \partial(rJ_z)/\partial z = 0; \qquad (1.5)$$

$$J_r = \sigma_0\left[-v_z B_\theta - \tilde{K}\,\partial U/\partial r\right]; \qquad (1.6)$$

$$J_z = \sigma_0\left[v_r B_\theta - \tilde{K}\,\partial U/\partial z\right]; \qquad (1.7)$$

$$B_\theta = 1/r \qquad (1.8)$$

Here: $Re = \rho_0 <v_0> r_0 / \mu_0$ - Reynolds number, $Eu = p_0 / (\rho_0 \langle v_0 \rangle^2)$ - Euler number, $S = \sigma_0 B_0^2 r_0 / (\rho_0 <v_0>)$ - MHD interaction parameter, $v = v'/\langle v_0 \rangle$, $p = p'/p_0$, $r = r'/r_0$, $z = z'/r_0$, $B = B'/B_0$, $U = U'/U_e$, $J = J'/(\sigma_0 <v_0> B_0)$, where $<v_0>$ - average speed at the channel inlet; the index "0" corresponds to characteristic values at the channel inlet (at $r_1' = r_0$), the stroke - corresponds to the dimensionless values.

Parameter $\tilde{K} = U_e / (\langle v_0 \rangle B_0 r_0)$ determines the operation mode of MHD channel and is dealt with the local load factor K by the relations:

$$K = \frac{U_e}{<v><B> r_0 \Delta} = \tilde{K} \xi(z),$$

$$\xi(z) = \frac{(r_1 + r_2)^2}{4 \overline{\Delta}(1 + 0.5\overline{\Delta})}, \qquad (1.9)$$

Where

$$\langle v' \rangle = \frac{v_0 \Delta_0 (1 + 0.5\Delta_0)}{0.5\Delta (r_1' + r_2')},$$

$$\langle B \rangle = 2B_0 / (r_1 + r_2)$$

- accordingly average speed and magnetic induction in the section z=const; $\Delta = \Delta'/r_0$, $\overline{\Delta} = \Delta_0/r_0$ - accordingly relative width of the ring gap at z=const and at the inlet of the channel (z=0).

From (1.9) it is seen that if $\tilde{K} \geq \max(1/\xi(z))$ then at the whole length of MHD channel the acceleration mode ($K>1$) is realized.

1.2. Method of the solution

After the introduction of the hydrodynamic functions determined by the equations $v_r = \partial \psi / r \partial z$, $v_z = -\partial \psi / r \partial r$ we use new independent variables $R=r$, $\eta = \varepsilon z$, where $\varepsilon <<1$ - small parameter (see (1.1)).

Excluding pressure p from (1.3) and (1.4) and current density $J(J_r, 0, J_z)$ from (1.5)-(1.7) the system (1.2)-(1.8) can be written as two equations for ψ and U:

$$\varepsilon \frac{\partial}{\partial r} \left\{ \frac{\partial \psi}{r^2 \partial r} \frac{\partial^2 \psi}{\partial r \partial \eta} - \frac{\partial \psi}{r \partial \eta} \frac{\partial}{\partial r} \left(\frac{\partial \psi}{r \partial r} \right) \right\} +$$

$$+ \varepsilon^3 \frac{\partial}{\partial \eta} \left\{ \frac{\partial \psi}{r^2 \partial r} \frac{\partial^2 \psi}{\partial \eta^2} - \frac{\partial \psi}{r \partial \eta} \frac{\partial}{\partial r} \left(\frac{\partial \psi}{r \partial \eta} \right) \right\} =$$

$$= 2S \frac{\sigma_0}{r^3} \left[\tilde{K} \frac{\partial U}{\partial r} - \frac{\partial \psi}{r \partial r} \right] -$$

$$- \frac{1}{Re} \left\{ \frac{\partial}{\partial r} \left[\frac{\partial}{r \partial r} \left(r \frac{\partial}{\partial r} \left(\frac{\partial \psi}{r \partial r} \right) \right) \right] + 2\varepsilon^2 \frac{\partial}{\partial r} \left(\frac{\partial^3 \psi}{r \partial r \partial \eta^2} \right) + \right.$$

$$\left. + \frac{\varepsilon^4}{r} \frac{\partial^4 \psi}{\partial \eta^4} \right\} \qquad (1.10)$$

$$\frac{\partial}{\partial r} \left\{ \tilde{K} r \frac{\partial U}{\partial r} - \frac{\partial \psi}{r \partial r} \right\} + \frac{\partial \ln \sigma_0}{\partial r} \left\{ \tilde{K} r \frac{\partial U}{\partial r} - \frac{\partial \psi}{r \partial r} \right\} =$$

$$= \varepsilon^2 \partial^2 (\tilde{K} r U - \psi/r) / \partial \eta^2 \qquad (1.11)$$

The asymptotic solution (at $\varepsilon <<1$) for the system (1.10)-(1.11) is [2,3]:

$$\psi = \sum_{l=0}^{\infty} \psi_l \varepsilon^l, \quad U = \sum_{l=0}^{\infty} U_l \varepsilon^l, \qquad (1.12)$$

Where the coefficients of series (1.14) ψ_l and U_l satisfy to the boundary conditions [3]:

$$\psi_0 = U_0 = 0 \text{ at } r = r_1(\eta);$$
$$\psi_0 = -\overline{\Delta r}_{av}, \; U_0 = -1 \text{ at } r = r_2(\eta); \qquad (1.13)$$

$$\psi_l = U_l = 0, \; l \geq 1 \text{ at } r = r_1(\eta) \text{ and } r = r_2(\eta) \qquad (1.14)$$

$$v_z^l = -\frac{\partial \psi^l}{r \partial r} = 0 \; (l \geq 0) \text{ at } r = r_1(\eta) \text{ and } r = r_2(\eta) \qquad (1.15)$$

($\overline{\Delta r}_{av} = \overline{\Delta}(1 + 0.5\overline{\Delta})$ - dimensionless flow rate through the ring channel).

Introducing the (1.12) into (1.10) and (1.11) and equating members of identical ε-degrees (e.g., "0" and "1") we can obtain 2 subsystems of differential equations for $\psi_{0,1}$ and $U_{0,1}$. From these subsystems it is possible to find the axial velocity and potential for the zero and first approximations of the series (1.12) (it is clear, that this procedure can be generalized for the higher approximations):

$$v_z^0 = \frac{C_1^0 Ha^2 \ln^2(r)}{2} + \frac{C_2^0 r^2}{4} + C_3^0 \ln(\kappa \eta + C_4^0; \qquad (1.16)$$

$$v_z^1 = \frac{C_1^1 Ha^2 \ln^2(r)}{2} + \frac{C_2^1 r^2}{4} + C_3^1 \ln(r) + C_4^1 + Re\, L(r, \eta) \qquad (1.17)$$

382

$$U_0 = \tilde{K}^{-1} C_1^0 \left[\frac{\ln(r)}{\sigma_0} - \frac{Ha^2 \ln^3(r)}{6} \right] +$$

$$+ \tilde{K}^{-1} \left[\frac{C_2^0 r^2}{8} + \frac{C_3^0 \ln^2(r)}{2} + C_4^0 \ln(r) + C_6^0 \right] \quad (1.18)$$

$$U_1 = \tilde{K}^{-1} \left\{ C_1^1 \left[\frac{\ln(r)}{\sigma_0} - \frac{Ha^2 \ln^3(r)}{6} \right] + \frac{C_2^1 r^2}{8} \right\} +$$

$$+ \tilde{K}^{-1} \left\{ \frac{C_3^1 \ln^2(r)}{2} + C_4^1 \ln(r) + C_6^1 - \text{Re} \int_{r_1}^{r} \frac{1}{r} L(r, \eta) dr \right\}$$
$$(1.19)$$

Here

$$N(r, \eta) = \int_{r_1}^{r} r L(r, \eta) dr;$$

$$L(r, \eta) = \int_{r_1}^{r} \frac{1}{r} \left[\int_{r_1}^{r} P(r, \eta) dr \right] dr;$$

$$P(r, \eta) = \frac{\partial \psi_0}{r \partial r} \frac{\partial^2 \psi_0}{\partial r \partial \eta} - \frac{\partial \psi_0}{\partial \eta} \frac{\partial}{\partial r} \left(\frac{\partial \psi_0}{r \partial r} \right),$$

Where C_i^0, C_i^1 ($i = 1 \div 6$) - constants of integration of zero (top index "0") and first approximations (top index "1") which can be determined from the boundary conditions (1.13)-(1.15) (these constants are too long for this article, see [5]).

The distributions of current density $J\{J_r, 0, J_z\}$ and gradient of pressure (∇p) in coaxial MHD channel in zero and first approximation can be found from the equations (1.6)-(1.7) and from momentum equation.

1.3. Calculation Results

To investigate the influence of the channel shape on the flow in coaxial MHDT the forming lateral ring electrodes were set in the following dependencies:

1. The symmetric channel ($r_{av} \gg \Delta$):

$r_1 = 1 - 0.05\Delta$, $r_2 = 1 + 0.05\Delta$,

$\Delta = 0.5\overline{\Delta}(1 + e^{\varepsilon(z_{max} - z)})$, $\overline{\Delta} = 0.45$

$\varepsilon = 0.17$, $z_{max} = 5$ \hfill (1.20)

2. The coaxial channel with cylindrical internal electrode:

$r_1 = 1$, $r_2 = 1 + \Delta$,

$\Delta = 0.5\overline{\Delta}(1 + e^{\varepsilon(z_{max} - z)})$, $\overline{\Delta} = 0.1$,

$\varepsilon = 0.2$, $z_{max} = 5$ \hfill (1.21)

3. The coaxial channel with two curved electrodes:

$r_1 = 0.5\overline{r}(1 + e^{\varepsilon k(z_{max} - z)})$, $r_2 = r_1 + \Delta$,

$\overline{r} = 1.17$, $k = 0.7$, $\Delta = 0.5\overline{\Delta}(1 + e^{\varepsilon(z_{max} - z)})$,

$\overline{\Delta} = 0.17$ $\varepsilon = 0.24$, $z_{max} = 5$ \hfill (1.22)

On Fig.1.2-1.4 distributions of speed $v_\Sigma = v_z^0 + \varepsilon v_z^1$ in MHD channels of a various configuration ((1.20)-(1.22)) are presented at various values of Reynolds number (Re), Hartman (Ha) and MHD interaction parameter (S).

In coaxial MHD channels with tangential magnetic field ($B \sim 1/r$), radial component of current density is in inverse proportion to radius $J_r \sim 1/r$, and electromagnetic force $|JB| \sim 1/r^2$ causes the heaviest electromagnetic acceleration of the flow near the internal electrode ($r = r_1$) (see Fig.1.3-1.4). The increasing of MHD interaction parameter S causes the strong acceleration of the flow at the MHD channel inlet and results in the displacement of the flow to the external electrode, occurrence of the zones of "back flow" and induce flow separation at $r = r_2$ (Fig.1.3-1.4). In the outlet section of MHD channels, however, the distribution of axial speed becomes positive (Fig.1.2,c-1.4,c). The distributions of speed v_z show, that the increasing of Re number leads to the increasing of electromagnetic flow separation at the external electrode in the inlet section.

From Fig.1.2 it is also seen, that in symmetric channel (1.20) the distribution of axial speed is close to axis-symmetric one and "positive" on the whole channel length. For the channels (1.21)-(1.22) the maximum of speed is located closer to the internal electrode.

These distributions in various sections of coaxial MHD channels show, that at designing of MHD thrusters for it is necessary to optimize the shape of the channel and especially take into account the shape of the inlet nozzle.

383
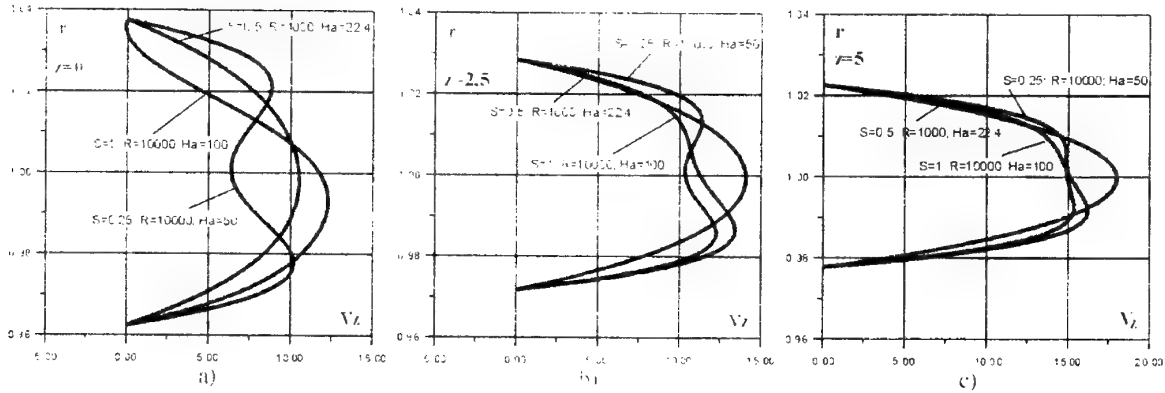
Fig.1.2. Distribution of axis velocity in symmetric coaxial MHD channel
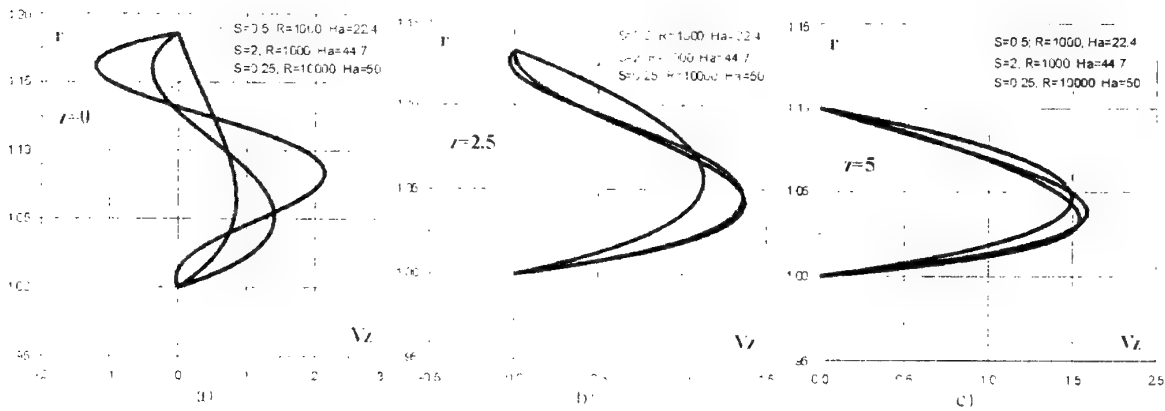
Fig.1.3. Distribution of axis velocity in coaxial MHD channel with the cylindrical internal electrode
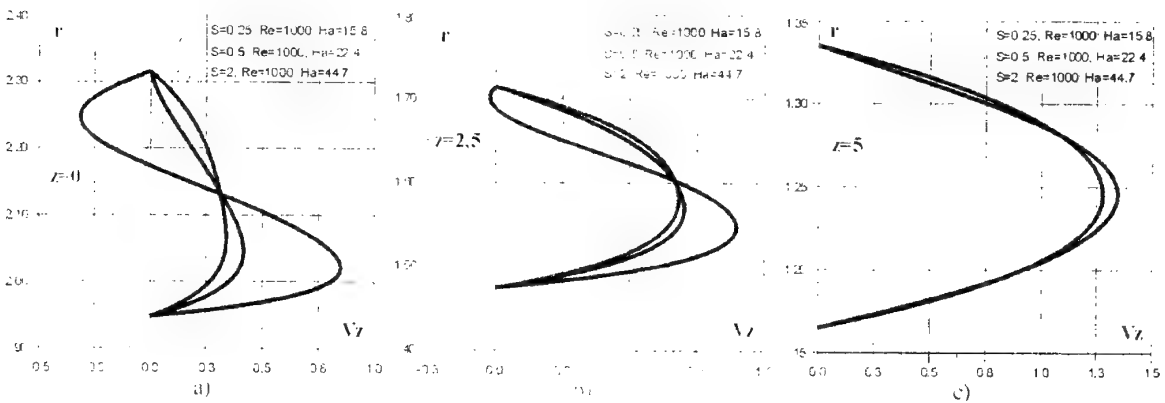
Fig.1.4. Distribution of axis velocity in coaxial MHD channel with two curved electrodes

2. Turbulent Flows in Coaxial MHD Channel
2.1. Problem Formulation and Solution

We consider completely advanced turbulent axis-symmetric one-component $\mathbf{u}(0,0,u)$ flow of non-compressing conducting liquid in MHD channel of ring cross-section with the gap Δ. It is considered, that the channel walls r_1 and r_2 are slightly curved along the axial coordinate (see Fig.1.1 and (1.1)).

At the same assumptions as in the section 1, the problem solution can be constructed by expanding of the MHD variables in asymptotic series in power of ε. Thus accurate to members $o(\varepsilon)$ the solution of a problem will be described by one-dimensional equations. With these assumptions the system of magnetic hydrodynamics of zero approximation describing the distribution of the axial velocity $\mathbf{u}$, electrical potential φ, current density J_r, magnetic

384

field B can be written in dimensionless form as follows:

$$Eu\, dp/dz = SJ_r B_j + \partial(r\tau)/r\partial r, \qquad (2.1)$$

$$\partial(rJ_r)/\partial r = 0, \qquad (2.2)$$

$$J_r = -\sigma(uB_\varphi + \partial\varphi/\partial r), \qquad (2.3)$$

$$B_\theta = 1/r \qquad (2.4)$$

Where $u = u'/u_o$, $\varphi = \varphi'/(u'_0 B'_0 r'_0)$, $J = J'_\kappa/(\sigma' u'_0 B'_{\theta 0})$, $\tau = \tau'/\rho u'^2_0$ - non-dimensional velocity, electrical potential, current density and tangential stress accordingly, the dimensional values are marked with the stroke (all other values correspond to the similar ones in section 1).

The completely advanced flow in the coaxial MHD channel represents a combination of two boundary layers. Each of these layers is located between the appropriate wall: outside (concave) and internal (convex) and point of the maximum of the speed. Thus the boundary layers differ one from another by distributions of the velocities, tangential stresses and characteristics of the turbulence. In point of a maximum of the speed ($r=r_p$) it is considered that $du/dr \approx 0$ and $\tau \sim du/dr \approx 0$.

Momentum equation (2.1) for the internal ($r_p>r>r_1$, sign "+") and external ($r_2>r>r_p$, sign "-") walls can be written as

$$\pm d(r\tau)/rdr = Eu\, dp/dz - SJ_r B_\varphi \qquad (2.6)$$

And the tangential stress in cross section of the channel can be determined from (2.6) as:

$$\tau = \pm r^{-1}\left[0.5Eu(r^2 - r_p^2)dp/dz - SJ_o\ln(r/r_p)\right] \quad (2.7)$$

From (2.7) the following relation for the friction factors $c_{f_{1,2}} = \tau'_{162}/(\rho'_0 u'^2_0/2) = 2\tau_{1,2}$ ($\tau_{1,2}=\tau(r_{1,2})$ – tangential stress on the channel walls) and longitudinal gradient of pressure can be found:

$$\frac{c_{f_1} + \xi c_{f_2}}{1+\xi} = -Eu\frac{dp}{dz}r_1(\xi-1) + \frac{2SJ_o}{r_1}\frac{\ln\xi}{1+\xi},$$

$$\xi = r_2/r_1 \qquad (2.8)$$

For the determination of a structure of axial velocity $u(r)$ in turbulent zone of the flow the formula of Prandtle for turbulent tangential stress was used (in dimensionless form):

$$\tau = l^2\left|\frac{du}{dy}\right|\frac{du}{dy}, \qquad (2.9)$$

Where $l=l'/r_0$ - length of the mixing way, y - distance from the appropriate wall ($y=r_2-r$ for the flow near to the external wall, when $r_2>r>r_p$; $y=r-r_1$ for the flow near to the internal wall, when $r_p>r>r_1$).

Length of the mixing way l is determined by the Prandtle-Nikuradze formula [1]:

$$\frac{l}{\delta_{pi}} = 0.14 - 0.08(1 - \frac{y}{\delta_{pi}})^2 - 0.06(1 - \frac{y}{\delta_{pi}})^4 \quad (2.10)$$

Where δ_{pi} - distance from the appropriate wall up to the point of speed maximum ($\delta_{pi}=|r_i-r_p|$; $i=1,2$).

By integrating of (2.9) the expression for the structure of speed near to the appropriate wall of the channel can be written as:

$$u(r) = u_{li} + \int_{r_{li}}^{r} \sqrt{\tau}/l, \qquad (2.11)$$

Where τ and l are determined from the equation (2.7) and (2.10) accordingly, r_{li} and u_{li} - thicknesses of laminar sub-layer and speed on the border of laminar sub-layer and main turbulent zone of the flow near to the appropriate wall ($i=1$ - internal, $i=2$ - external).

Characteristics of the laminar sub-layer near the external and internal walls are determined by the law of Newton for tangential stresses:

$$\tau = \pm \text{Re}^{-1} du/dr \qquad (2.12)$$

By integrating of (2.12) with taking into account (2.7) and boundary conditions: $u=0$ at $r=r_i$ ($i=1,2$) the speed structure in laminar sub-layers (at $i=1$- on internal wall, at $i=2$- on external wall) can be found:

$$u(r) = \frac{\text{Re}}{2}\left[Eu\frac{dp}{dz}\frac{r_i^2}{2}\left[\frac{r^2}{r_i^2} - 1 - 2\frac{r_p^2}{r_i^2}\ln\frac{r}{r_i}\right] - \frac{SJ_0}{r_p}\ln\frac{rr_i}{r_p^2}\ln\frac{r}{r_i}\right]$$

$$(2.13)$$

The thicknesses of viscous laminar sub-layers δ_{li} (on both walls of ring MHD channel) are determined from the condition, that on their borders the Reynolds number, calculated on local speed u_{li} and distance δ_{li}, achieves some critical value [1,4].

$$\text{Re}_{li} = u'_{li}\delta'_{li}/(\mu'_0/\rho'_0) = \alpha^2, \ \alpha\approx 11,5. \qquad (2.14)$$

Solving (numerically) the equation (2.14) with taking into account (2.13), it is possible to determine the thickness of the laminar sub-layer on the walls of the channel, further from (2.13) – the

speed structure in laminar sub-layer and its size on the border of sub-layer (at $r=r_{li}$), and then according to (2.11) - structure of the speed in main turbulent zone of the flow of non-compressing conducting liquid in coaxial MHD channel.

For the determination of the unknown gradient of pressure dp/dz an obvious integral condition of the flow rate conservation was used:

$$\int_{r_1}^{r_2} ru(r, dp/dz)dr = \Delta = r_2 - r_1 \qquad (2.15)$$

The resistance factor can be determined as

$$\lambda = -\left(dp/dx - <F_e>\right)d_\Gamma\Big/\left(r'u'_{av}/2\right) \qquad (2.16)$$

Where $\langle F_e \rangle = s_k^{-1}\int_s <J\times B> ds_k$ - average on the cross-section electromagnetic force, $d_\Gamma = 2(r_2 - r_1)$ - hydraulic diameter.

The expression (2.19) in non-dimensional form can be written as:

$$\lambda = 4\left[J_0 S \cdot \ln\left(r_2/r_1\right) - D\cdot Eu\cdot \frac{dp}{dz}\right]. \qquad (2.17)$$

2.2. Calculation Results

On Fig.2.1-2.4 the speed structures are presented for advanced turbulent flow of conducting liquid in coaxial MHD channel for wide range of the parameters $Re=10^4$-10^7, $S=0$-1, $K=1$-5 at $\xi = r_2/r_1 = 1.22$. It is seen, that the speed structures are asymmetric relative to the average radius of the channel r_o, the maximum of speed are displaced to the internal wall of the channel. This displacement is that stronger, then the significance of Re, S, K are higher. With the increasing of Re the speed structures become more filled on both walls of the channel.
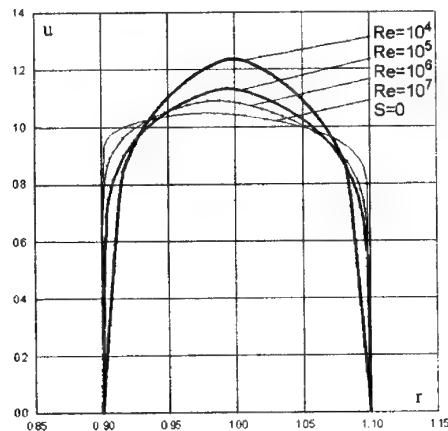
Fig.2.2

Fig.2.3

Fig.2.4

Fig.2.1
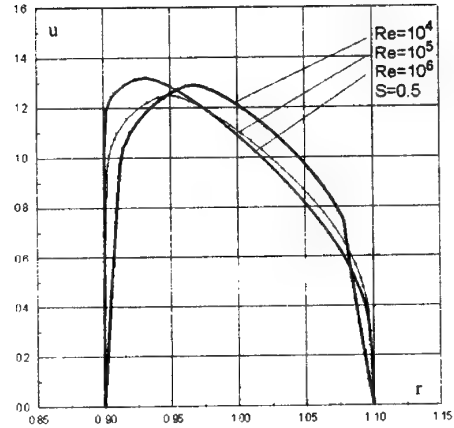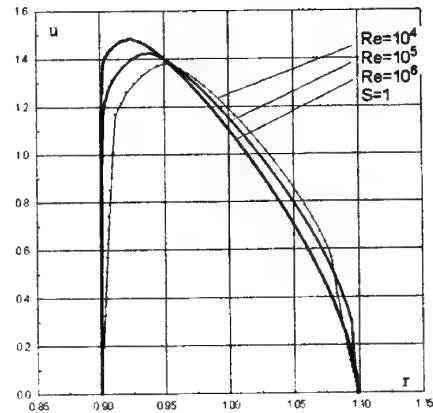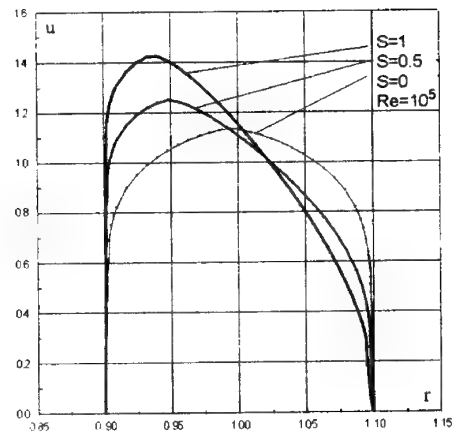
With the increase of S and K on the internal wall the filling of the speed profile increases, and on the external wall it decreases and at $S\sim 1$ and $K\sim 5$ the speed is close to power dependency with parameter $n\sim 1/2$, that is characteristic for the mode flow of non-compressing liquid before the layer separation. The increasing of MHD interaction leads to the layer separation of turbulent flow on the external wall.

386

On Fig.2.5 the resistance factor depending on the Re number is shown at various MHD interaction parameters (at $K=2$). The dotted line is a curve $\lambda(\mathrm{Re})$ for the flow in the circular pipe [1]. It is seen, that in the coaxial channels the friction factor value exceeds the similar one for the circular pipe, and that stronger then MHD interaction parameter is higher.
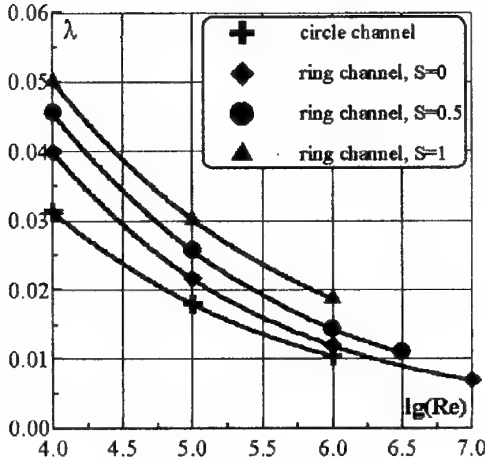
Fig.2.5

On Fig.2.6 dependencies of friction factor C_f on the external ($r=r_2$ - continuous lines) and internal ($r=r_1$ - dotted lines) surfaces of the coaxial channel on Reynolds number Re are presented at various parameters of MHD interaction and $K=2$. It is seen, that with the increase of Re the value of C_f decreases on both walls of the ring channel. It is explained by significant asymmetry of the flow with increase of S (see Fig.2.1-2.4).
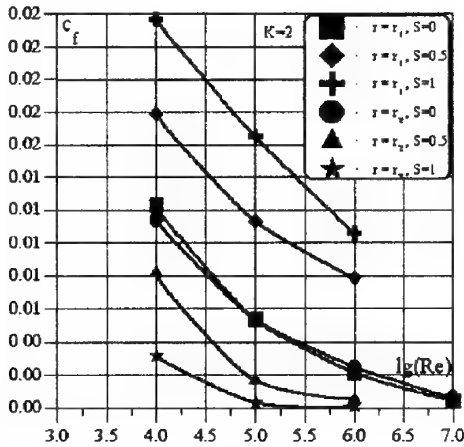
Fig.2.6

Thus, transversal magnetic field influence essentially on the characteristics of the turbulent flow

of conducting liquid in coaxial MHD channels. There is the reorganization of a flow, modes of flow, friction factors and resistance appreciably change. The above described approach allows to take into account these effects in calculations of turbulent modes of flow in MHD thrusters with coaxial channels.

3. Coaxial MHD thruster design

The first estimation of the parameters of the submarine with MHDT can be done as follows. The resistance force of the submarine motion is defined as $F_c=(1+D/2L+3(D/L)^3)C_{F_0}\rho V_s^2\Omega/2$ [1]. Where C_{F_0} - drag coefficient of the equivalent lamina, ρ - density of seawater, Ω - area of the wet surface of the vessel.

At the constant speed of the vessel the thrust force created by the MHD propulsor is equal to the motion resistance force of the vessel [1] $F_t=F_c$. Therefore the required power is $N=F_tV_s$, where V_s – the ship speed.

The thrust force of MHDT consists of two components: electromagnetic force F_e and friction force in the channel F_{fr} $F_t=F_e-F_{fr}$. The electromagnetic force can be found as $F_e=\sigma v_0 B_0^2 AL_k(K-1)$. Where σ - electrical conductivity of seawater, $A=\pi(R_0^2-R_i^2)$ - cross-sectional area of the channel, L_k - channel length, K - load factor. The friction force in the channel is determined as $F_{fr}=\lambda\rho v_0^2 S_w/8$, where $S_w=2\pi(R_0+R_i)L_k$ - lateral area of the channel walls, λ - resistance factor. The expression for the thrust force of MHDT can written finally as:

$$F_e=\sigma v_0 B_0^2 AL_k(K-1)-\lambda\rho v_0^2 S_w/8 .\qquad (3.1)$$

The MHD channel length can be defined from (3.1) as

$$L_k=8F_t\big/(8\sigma v_0^2 B_0^2 A(K-1)-\lambda\rho v_0^2 S_w) .\qquad (3.2)$$

On the basis of the developed algorithm the preliminary calculations for the submarine of 8650 ton deadweight, length $L=100$m, maximal diameter $D=11.11$m were done for the speed $V_s=10.5$m/c (the output power of the MHD thruster N_e=MW). The designed tanker-submarine is shown in Fig.3.1.

The MHDT radiuses were $r_1=0.475 \cdot D$, $r_2=r_1+\delta$, $\delta=0.75$m; magnetic induction $B_0\leq10$T, load factor $K=3.5$. From Fig.3.2 it is seen that the needed thrust force can be achieved by different set of the parameters of the coaxial MHDT. The optimization of the MHDT parameters must be carried out for the concrete project of the vessel.
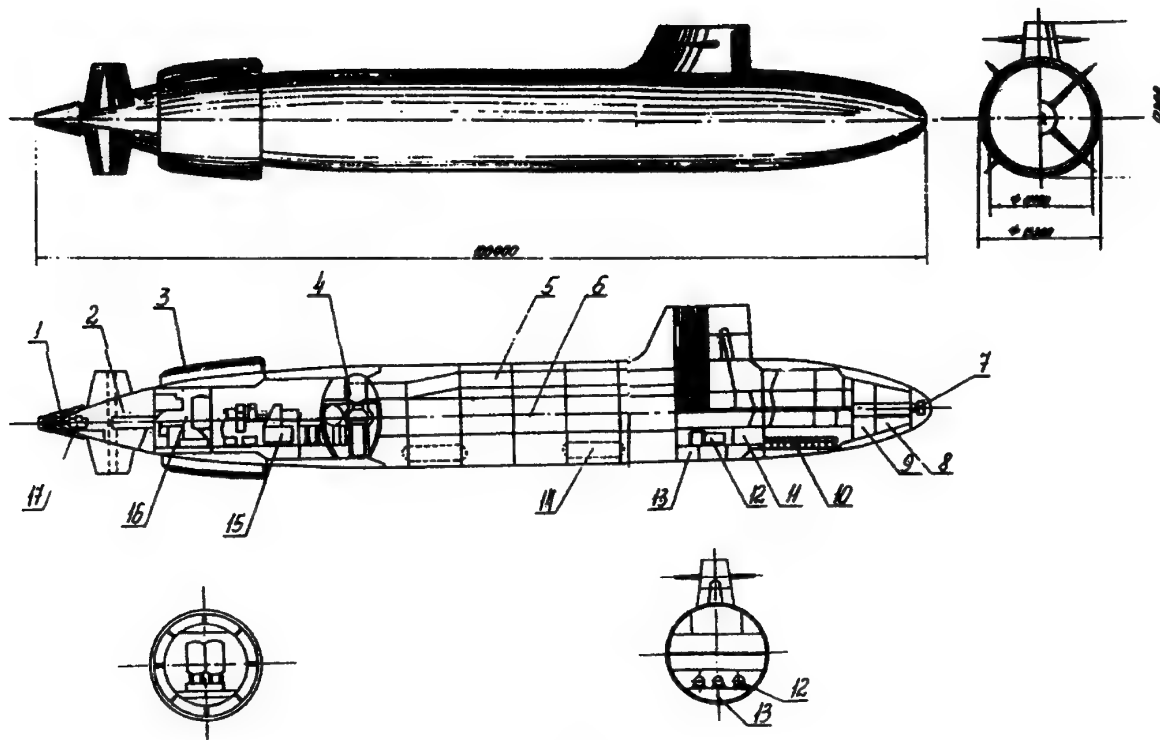
Fig.3.1
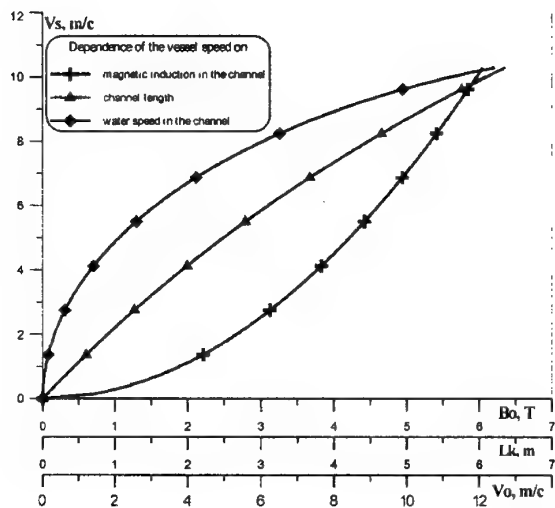
Fig.3.2

References

1. H.Schlichting. Theory of boundary layer. (Translated in Russian). M.:Nauka (1978).
2. A.B.Vatagin, G.A.Lubimov, S.A.Regirer. Magnetohydrodinamic flows in channels. M.:Nauka (1970)
3. L.K.Kovalev et al. Two-dimensional flows in coaxial channels. Magnetohydrodinamics, No 3, pp. 37-46, 1972.
4. K.K.Fedlevskiy et al. Calculation of turbulent boundary layer for non-compressing liquid. L.:Sudostroenie (1973) (in Russian.)
5. L.K.Kovalev, K.L.Kovalev. Coaxial and multi-pole thrusters with cryogenic magnetic systems for marine vessels. Proc. of 12th International conference on MHD electrical power generation, Yokohama, Japan, 1996.

76. SHOCK WAVE CONTROL BY NONEQUILIBRIUM PLASMAS IN COLD SUPERSONIC GAS FLOWS

Samuel Merriman, Rodney Meyer, Peter Palm, Elke Ploenjes, and Igor V.Adamovich
Nonequilibrium Thermodynamics Laboratory
Dept. of Mechanical Engineering
The Ohio State University, Columbus, OH 43220-1107

The paper discusses experimental studies of shock modification in weakly ionized supersonic gas flows. In these experiments, a supersonic nonequilibrium plasma wind tunnel, which produces a highly nonequilibrium plasma flow with the low gas kinetic temperature at M=2, is used. Supersonic flow is maintained at complete steady state. The flow is ionized by a high-pressure aerodynamically stabilized DC discharge in the tunnel plenum and by a transverse RF discharge in the supersonic test section. The DC discharge is primarily used for the supersonic flow visualization, while the RF discharge provides high electron density in the supersonic test section. High-pressure flow visualization produced by the plasma makes all features of the supersonic flow, including shocks, boundary layers, expansion waves, and wakes, clearly visible. Attached oblique shock structure on the nose of a 35o wedge with and without RF ionization in a M=2 flow is studied in various nitrogen-helium mixtures. The wedge extended wall-to-wall in a quasi-two-dimensional supersonic test section.

It is found that the use of the RF discharge increases the shock angle by 14o, from 99o to 113o, which corresponds to Mach number reduction from M=2.0 to M=1.8. Time-dependent measurements of the oblique shock angle show that the time for the shock weakening by the RF plasma, as well as the shock recovery time after the plasma is turned off, is of the order of seconds. Since the flow residence time in the test section is of the order of ten microseconds, this result suggests a purely thermal mechanism of shock weakening due to heating of the boundary layers and the nozzle walls by the RF discharge. Gas flow temperature measurements in the test section using infrared emission spectroscopy, with carbon monoxide as a thermometric element, are consistent with the observed shock angle change. The results suggest that the observed shock weakening in the plasma is a purely thermal effect, primarily due to the flow heating in the boundary layers adjacent to the RF discharge electrodes. To reduce the boundary layer effects, an additional series of experiments using a cone model placed into a supersonic inviscid core flow (away from the heated boundary layers), has been conducted. Preliminary results did not show any measurable shock weakening in this case. This also suggests that shock weakening by the plasma is a purely thermal effect.

The results demonstrate the feasibility of both sustaining uniform ionization in cold supersonic nitrogen and air flows and the use of transverse stable RF discharge plasmas for supersonic flow control, combustion control, and MHD energy extraction / addition in supersonic air flows.

77. EFFICIENT GENERATION OF NONEQUILIBRIUM PLASMAS BY HIGH-ENERGY ELECTRONS

S.O. Macheret, M.N. Shneider, and R.B. Miles
Princeton University, Department of Mechanical and Aerospace Engineering, U.S.A.
D-414 Engineering Quadrangle
Princeton, NJ 08544,
E-mail: macheret@princeton.edu

In a number of aerospace applications of plasmas, such as MHD flow control, sustaining a substantial degree of ionization in low temperature air with minimal power budget is crucial. Analysis of ionization physics shows that high-energy electrons represent the most energy-efficient ionization method. These electrons spend about a half of their energy on ionization cascades, in contrast to low-energy (1-3eV) electrons in conventional discharges that dissipate up to 99.9% of their energy in inelastic collisions. High-energy electrons can be injected as beams through windows or differentially pumped ports. Alternatively, they can be created *in situ* by applying a very strong electric field for a short time, with a repetition rate matching the rate of recombination. We describe a unified approach to modeling of both e-beams and repetitive pulses, combining computations of non-local, rapidly evolving in time, electron energy distribution from very low to very high energies, ionization and recombination kinetics, transport of charged particles, and self-consistent evolution of electric field. We predict new effects: field reversal, "two-cathode" effect, and interpulse ionization. The repetitive-pulse method is shown to reduce the power budget for plasma generation by as much as 2 orders of magnitude compared with that in conventional discharges. However, repetitive-pulse ionization method still requires 1-2 orders of magnitude higher power than that of e-beam plasmas.

78. MONTE-CARLO SIMULATION OF E-BEAM SPATIAL INPUT POWER DISTRIBUTION IN AIR

V.R.Soloviev, A.M.Konchakov, V.M.Krivtsov
Moscow Institute of Physics and Technology, Russia

N.D.Malmuth
Rockwell Science Center, CA

Abstract. Present work is devoted to Monte-Carlo simulation of spatial distribution of power input into Air by spike electron beam (E-beam). These data are necessary to calculate the spatial distribution of electron density and conductivity for consequent estimation of the possible MHD flow control effect. Simulation has been done by modeling the variation of electron trajectory and energy loss in each collision of the electron on the basis of experimental data for both elastic and inelastic collision cross sections. The computation of 10,000 E-beam electron trajectories for initial electron energy 100keV demands around 13 minutes on a Pentium-1 233MHz computer. The results for spatial distribution of energy deposition demonstrate good agreement with computational results of another authors obtained in the frame of enhanced collision model.

Input power distribution is extremely inhomogeneous. At the E-beam exit to the gas, the power deposition is four orders of magnitude higher than in the volume at a distance approximately one half of electron stopping range. This means the gas heating near the E-beam exit could be critically important in this "boundary layer" region, despite it being negligible in the main part of ionized volume.

MHD external flow control in AJAX hypersonic airplane concepts requires calculation of the degree of Air ionization by an electron beam (E-beam) that provides required electrical conductivity to the captured Air [1,2]. A sketch of such a system is shown in Fig.1.
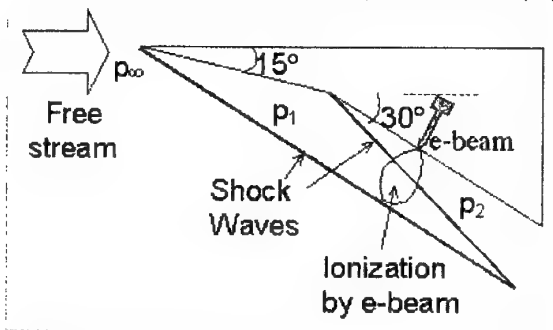
Fig.1. Schematic of E-beam ionization system.

Previous assessments [1-4] of the feasibility of this MHD flow control approach assumed homogeneous Air ionization with a planar E-beam. The E-beam electrons were assumed to be emitted from a plane surface of area approximately $1m^2$, which was necessary to create the necessary ionized volume. Furthermore, Air ionization by the E-beam electrons was assumed homogeneous over the E-beam penetration distance. Both of these simplifications are not realistic for practical E-beam systems.

Regarding the first approximation, even the planar E-beam source has an inhomogeneous distribution of energy losses over its penetration distance. In fact, this quantity increases to a maximum value at some distance from the plane and then approaches zero [5]. Accordingly, the electrical conductivity near the airplane surface (where the E-beam source is located) is much less then in the volume off the surface. This electrical conductivity inhomogeneity strongly influences the electrical current distribution in the gas volume and causes a spatial variation in the MHD effect for flow control. Thus, the anticipated Air ionization inhomogeneity for a practical electron beam system should be accounted for to obtain a more realistic assessment of the feasibility of MHD flow control.

Regarding the second simplification, planar E-beam evolution involves propagation through the thin foil separating the vacuum region where the E-beam is initiated from the ambient Air. Because of the attendant frequent destruction of the foil, this system is relevant to laboratory experiments only. For practical usage, E-beam propagation through a gasdynamic window is required. Accordingly, the E-beam diameter needs to be small (around few millimeters). With this approach the E-beam enters the Air like a needle, resulting in much more inhomogeneous Air ionization than that for the ideal planar E-beam configuration. To smooth out this inhomogeneity, numerous E-beams are required to ionize the appropriate volume.

From the foregoing, it is clear that Air ionization by a single needle-like E-beam is a key unit problem in the treatment of Air ionization by a

system of multiple E-beams. To obtain the spatial distribution of electrical conductivity in this problem, the appropriate system of kinetic balance equations for electrons and ions should be incorporated in the formulation. The input data for these equations (source terms) are the primary ionization rates by E-beam and secondary electrons, which can be expressed through the E-beam power inputs into the gas.

As a step to providing this information, this paper will describe our effort in computational modeling of the aforementioned unit problem to determine the spatial distribution of input power to Air from the single stationary needle-like E-beam. Monte-Carlo simulation of the electron trajectories was chosen as the most appropriate method to attack this problem.

The trajectory of an electron is simulated as a succession of free flights interrupted by collisions that result in deflections and energy losses. Collisions between electron and the Air constituents are classified into three categories:

a) Scattering by atomic nuclei, a process which is essentially elastic and gives only the deflection of the electron without energy loss
b) Inelastic scattering by orbital electrons resulting in ionization of the Air species, a process which determines both the deceleration and deflection of the primary electrons and is accompanied by the creation of secondary electrons
c) Inelastic scattering by orbital electrons resulting in Air species excitation, a process which does not deflect the electrons but contributes to their deceleration.

A complete description of the analysis will be given in the full paper.

As an illustration of the results of this analysis, Fig.2 shows power input contours in Air for E-beam power=10kW, Air pressure=30 Torr, and E-beam electron energy T_0=100keV. The numbers near the curves are the power-input values in units of mW/cm^3. The E-beam enters the Air at the point $x=0$, $y=0$, $z=0$ along z-axis. The boundary between Air semi-infinite domain and the solid surface is assumed to be the $z=0$ plane.

Solid lines represent the result with included modeling of secondary electron trajectories. Dashed lines correspond to the result, when the secondary electrons were assumed to lose their energy at the point of their creation. The computation of 10,000 E-beam electron trajectories for T_0=100keV needs around 13 minutes on a Pentium-I 233MHz computer.

Figure 2 indicates that the input power distribution is extremely inhomogeneous. At the E-beam exit to the gas, the power deposition is four orders of magnitude higher than in the volume at a distance approximately 1m from this point. This means the gas heating near the E-beam exit could be critically important in this "boundary layer" region, despite it being negligible in the main part of ionized volume.
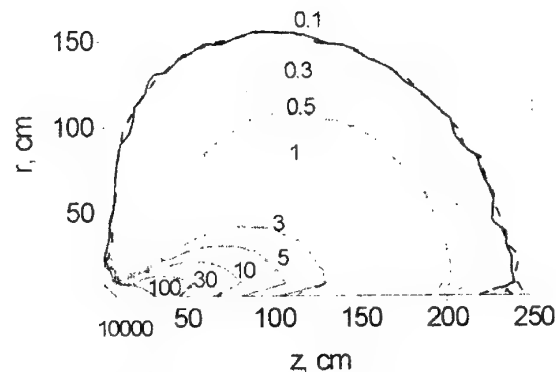
Fig.2. Input power contours for E-beam power = 10kW, Air pressure = 30 Torr, and E-beam electron energy = 100keV, number of E-beam electrons = 100,000.

To smooth out the ionization inhomogeneity, diverging magnetic and/or electric lenses at the E-beam exit are recommended. The prospects for future analysis of these improvements and the investigation of the optimal E-beam configuration will be discussed in the full paper submitted on AIAA WIG-4 Workshop, Anaheim, 2001.

Acknowledgements

References

1. Brichkin D.I., Kuranov A.L., Sheikin E.G., AIAA Paper 98-1642 (1998).
2. Brichkin D.I., Kuranov A.L., Sheikin E.G., AIAA Paper 99-4969 (1999).
3. Bityurin V.A., Bocharov A.N., Lineberry J.T., Proc. Int. Conf. on MHD Power Generation and High Temperature Technologies, Beijing, PRC, Oct.12-15, 1999, 793-814.
4. Vatazhin A.B., Gouskov O.V., Kopchenov V.I., Proc. Int. Conf. on MHD Power Generation and High Temperature Technologies, Beijing, PRC, Oct.12-15, 1999, 875-882.
5. Baranov V.F. Dozimetry of electron radiation. Atomizdat, Moscow, 1974 (in Russian).

79. MICROWAVE TORCH. CONSTRUCTION AND RESULTS OF INVESTIGATIONS

S.I. Gritsinin, I.A. Kossyi and M.A. Misakyan

General Physics Institute, Russian Academy of Sciences, 38 Vavilov str., Moscow, 119991 Russia

Abstract. The design of a microwave coaxial plasma torch is presented. This torch can operate both in the pulsed and cw modes at atmospheric pressure with any gases - both noble and molecular ones. The time evolution of the torch operating in the pulsed mode is considered. It has been revealed that that the evolution is different in noble and molecular gases. The characteristic feature of torches in noble gases is a dense core with plasma density no less than 10^{16}cm^{-3}. Plasma bunches with density of 10^{14}–10^{15}cm^{-3} successively propagate downstream from this core, which are seen as glow bursts. In molecular gases, the core is absent and the torch is formed by propagating plasma bunches.

1. Introduction

Microwave torches are widely applied as plasma sources in various plasma technologies, as well as useful instruments in physical laboratories. Most intense studies of parameters and properties of microwave torches have started nearly 20 years ago, and presently papers on this subject now are even increasing in number.

Until now, the torches of TIA-design were commonly used. The classical scheme of such microwave torches is discussed for example in [1]. The energy from a microwave generator is transmitted through a waveguide (usually, rectangular and tunable) line into a coaxial section (which also may be regulated). The inner electrode of this section also serves to supply the torch with the working gas and has a refractory nozzle. The sizes of the inner and outer electrodes of the coaxial line are nearly equal. In this case, there is the open coaxial output at the end of the line. In the presence of the torch, a considerable portion of the input microwave energy is absorbed in the formed gas-discharge plasma, whereas the remainder energy is emitted into space. When the torch quenches (occasionally, because of a certain failure), the microwave energy is almost completely emitted into space. For this reason, this design of torches does not guarantee the radiation safety. There is also another disadvantage in this design. Notwithstanding the presence of a sharp edge of the nozzle, for lower generator microwave powers (usually, on the order of 1 kW), it is difficult to ensure the enhancement of the electric field to levels required for gas breakdown at atmospheric pressure. Under these conditions, the initial ignition of the torch cannot occur spontaneously. In addition, in the torches of this design, the field is enhanced near the nozzle, but drops sharply with distance away from it because of the geometry of the device. For this reason, such torches are usually small in size, 1-2cm.

Earlier [2-4] we had proposed another design of the microwave coaxial plasma torch. From physical standpoint, a this torch can be classed among plasma waveguide discharges [5]. Characteristic of these discharges is that a gas-discharge plasma produced in the wave field is one of main components of the guiding waveguide structure for wave propagation. In this paper, we consider a special case of this class of discharges – a plasma coaxial line, when the plasma plays role of one of the electrodes of the coaxial line. The version in which the plasma acts as the outer electrodes was considered in [6,7,2-4]. Here, we consider another version, specifically, when the plasma forms the inner electrode of the coaxial line.

Experimental setup

The design of the microwave coaxial plasma torch proposed in this paper differs from the commonly used design in that the outer electrode is longer than the inner one. Such an insignificant (at the first glance) modification of the design radically changes the principle of operation of the torch. The device is shown schematically in Fig.1. A rectangular resonator is fed with microwave energy from a rod antenna coupled with a production 2.45 GHz magnetron with a mean power of ~ 1kW at half-wave rectification. From the rectangular resonator, the microwave energy is transmitted into the coaxial section of the device with the help of a current loop; continuation of this loop inside the coaxial line is the inner electrode. This loop is made of a pipe and serves for working gas supply. There is a refractory metal nozzle at the end of the inner electrode, it has the sharp edge to facilitate the gas breakdown. The outer coaxial electrode is longer than the inner one; consequently, for the electromagnetic wave propagating through the system, the coaxial transmission line terminates with a circular waveguide section. This section which has a diameter of 2–3 cm is a below-cutoff waveguide for the pumping microwaves with a wavelength of ~ 12 cm. In the absence of a torch (plasma), the microwave approaches the end of the inner electrode and reflects from the circular waveguide

inlet. For this reason, the high-power microwave in the absence of a torch cannot be emitted into space and remains inside the system. A similar picture is also observed in the presence of the torch if its size is shorter than the sizes of the outer electrode: unabsorbed radiation reflects backward and again passes through the torch plasma. Therefore, the proposed design ensure the radiation safety. For convenient observation and diagnostic purposes, a certain part of the outer electrode can be made in the form of a "basket" – a bunch of thin rods (wires) 2–3mm in diameter positioned at a distance of 0.5–1cm from each other. Since the currents in the coaxial line flow in the longitudinal direction, such a basket successively plays the role of the solid electrode.
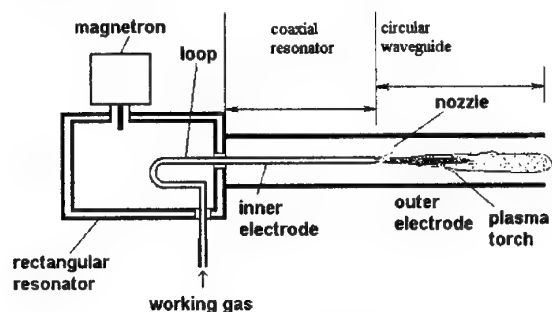
Busket type extension

copper wires
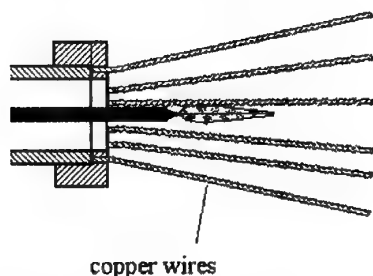
Fig.1. Microwave coaxial plasma torch design.

The microwave energy reflected from the circular waveguide is accumulated in the system of resonators, namely, the rectangular, coaxial, and magnetron resonators. The length of the inner electrode from the inlet into the coaxial section is chosen such that the nozzle exit falls to a maximum of the electric field of the standing wave which is formed due to the reflection of the running wave from the circular waveguide. As a consequence, as the energy is accumulated in the standing wave, the field at the nozzle end grows with time and ultimately reaches the threshold level. This is the reason why operating with a relatively low microwave power, we have managed to achieve the breakdown (and then the plasma formation) in the

pulsed mode (half-wave operation regime) in various gases (argon, nitrogen, air, carbon dioxide, hydrogen, methane, propane) over a wide range of pressures including atmospheric pressure.

After breakdown, the formed plasma, if it is sufficiently dense, becomes the part of the waveguide structure, as it were the extension of the inner electrode, so that the wave can propagate further and then reflect from the circular waveguide at the other point at which the breakdown conditions will be also fulfilled. Thus, as the breakdown advances inside the coaxial, the inner electrode "grows" in length. In this case, the torch length can reach 10-20cm which substantially exceeds the torch length attainable with usual design.

In our study, main attention was give to the time evolution (propagation) of the torch in the pulsed mode of operation with half-wave rectification. The discharge glow was measured with collimated photomultipliers and a photodiode, and a streak camera. Microwave radiation was probed with a half-wave antenna located at a certain distance from the torch. The plasma density was estimated from the passage of diagnostic microwaves (2.3mm and 337μm) through the torch.

Time evolution of the discharge glow

In this section, we present results from studies the time evolution and spatial structure of the plasma torch glow. In our case, the device operates in the pulsed mode (50Hz). The pulse duration was about 8 ms and pause was 12ms. This implies that the torch is initiated in every successive pulse; then it grows propagating along the guiding structure until reaches a certain size. It was reasonable to expect that, behind the front of the propagating torch, both the glow and the gas and plasma parameters should rapidly come to a steady state. However, the experimental results demonstrate a complicated temporal and spatial evolution of the glow and medium parameters.

Visually, the torch under study differs substantially from the torches of traditional TIA design. For argon and other noble gases, a bright core 1–2mm in diameter and 1–2cm in length is observed near the nozzle as in the case of usual TIA. This region corresponds to maximum values of the energy deposition and plasma density. However, in the usual torches, the core is followed by the recombination region in which the plasma density (together with the energy deposition) drops sharply because of less intense ionization processes. The reason is that the pumping wave energy is partially absorbed in the core, and then the wave field weakens because of the geometrical factor – the wave that was not completely absorbed

in the core is emitted by the core, as by a rod antenna, into space. In our case, the core is followed by a region that is substantially larger in size, but less bright, with curved boundaries. The volume of this region is 2—3 orders of magnitude greater than the core volume. This region spans over the most part of the inner plasma electrode of the coaxial line. The unabsorbed wave energy can propagate along the formed plasma electrode (i.e., through the coaxial line), thus significantly increasing the size of the glow region and maintaining the plasma density at a rather high level. The mere fact that there exist the region in which the wave can propagate through a distance on the order of the wavelength indicates that the plasma density in this region is on the order of the cutoff value for the pumping wave frequency with allowance for the high value of the frequency of electron collisions with heavy particles.

When the molecular gas (nitrogen, air) is used as the working gas, the bright core with well-defined boundaries is absent.
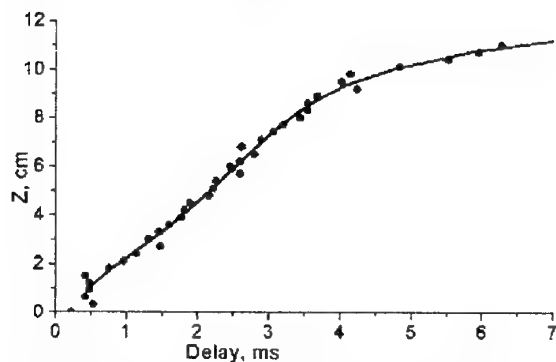
Fig.2. Delay time of the light appearance vs distance from the nozzle.

Figure 2 shows how the torch size varies with time; this dependence was obtained with the help of the collimated photodiode. It is seen that the glow front propagates at a nearly constant velocity $V=20$m/s through a maximum (under these conditions) distance of $l=10$cm. This effect is similar to the plasma (and glow) propagation along the guiding structure of the launcher in the surfatrons based on surface electromagnetic waves. It may be assumed that, in our case too, we have surface waves which make their contribution to the torch propagation mechanisms. We have carried out the following experiment. A quartz tube with a small ($D=6$mm) inside diameter was inserted into the torch along its axis. In this case, the plasma advanced inside the tube through distances of tens of centimeters, far beyond the boundaries of the outer coaxial electrode. This suggests that the plasma propagation mechanism is related to the formation of surface electromagnetic waves. This assumption is also confirmed by the fact that microwaves propagate along the torch without noticeable damping (as follows from the large size of the torch). Apparently, the propagation of surface waves along the torch is hindered by the fact that there is no sharp interface (e.g., between the plasma and surrounding gas) because the radial plasma distribution is rather flat. The appearance of the sharp interface, when the quartz tube is inserted into the torch, brings about the favorable conditions for the propagation of surface waves, in which case the plasma size increases substantially.

The process of glow propagation was studied also with the streak camera. Its slit was oriented along the axis of the coaxial system. Figure 3 illustrates the photochronograms of the torch propagation for different working gases – argon and nitrogen. The initial phase is globally traced with a time resolution of 2.5ms/div. It is seen that, in the case of argon, the processes begins with the appearance of a core glow 1–2mm in diameter and 1–2cm in length. The core glow continues throughout the microwave pulse. In Fig.3, one can notice the modulation in the core glow with a frequency of nearly 10kHz, that is, regular bursts in the core glow and variations in its size with a characteristic time about 100μs. After a certain time (0.5–1ms) after the appearance of the core glow, a less intensive glow wave arises near the core and begins to propagate along the axis of the system. The velocity of the glow front corresponds to that given in Fig.3. After the primary glow front goes away from the core, secondary glow waves arise near the core, which are associated with its periodic bursts. The secondary waves overtake the primary front which is therefore an envelope of a great number of the secondary front. One can notice that the intensity of secondary fronts is also modulated with a characteristic time about 1 ms.

With high time resolution, we detected the higher modulation frequencies in the torch-core glow at times preceding to the formation of the propagating glow. It is seen that a rather uniform burst arises along the entire core length and then the core is completely quenched with characteristic times of 5–10 μs. Simultaneously, microwaves are generated in short high-power pulses. Figure shows oscillograms with different time resolution for the torch glow measured with the non-collimated photomultiplier and for the microwave radiation received by the half-wave antenna in the vicinity of the torch. It is seen that the magnetron initially begins to generate short radiation pulses with frequencies about 100—200 kHz. After a period of several hundreds of microseconds, over which the pulse generation frequency gradually increases, the

395

first burst occurs in the core and then such bursts occur synchronously with the magnetron pulses. The pulse generation frequency gradually increases, and the generation becomes continuous. The glow intensity at the continuos-generation stage is several times lower than that for the pulsed generation stage. It is reasonable to assume that the microwave power in pulses is significantly higher than a mean magnetron power of 1 kW. Obviously, this circumstance makes the gas breakdown near the nozzle much easier. The duration of the pulse generation stage and the pulse duration depend on the magnetron load which is a complex unsteady electrodynamic load depending on the torch parameters. In the case of free generation (full matching)the generation becomes continuos after 5—10 pulses. With the closed end of the coaxial line, the generation ultimately becomes suppressed completely.

a)

b)

c)

d)
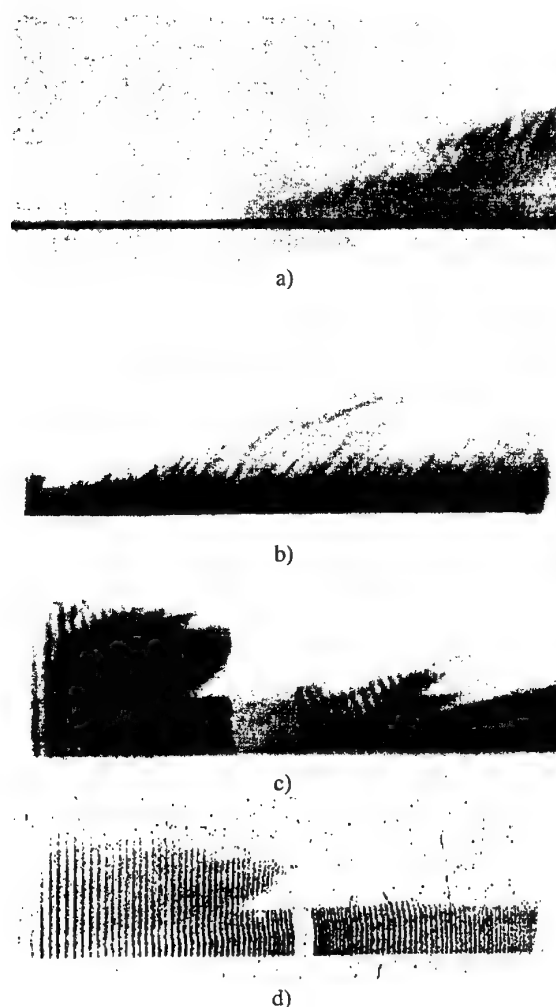
Fig.3. Streak camera photo of microwave torch for N2 (a) and Ar (b-d) as a working gas. Time scanning is 3 ms (a,b), 750 μs (c) and 250 μs (d) for full scale.

Conclusion

(1) The design is presented for a microwave coaxial plasma torch which can operate with any gases (including air).

(2) Like in torches of usual design, the fist ignition phase in noble gases is accompanied by the formation of a core – the bright glow region near the nozzle, with well-defined boundaries and length of 1-2cm. The core–formation time does not exceed 5 μs.

(3) After 0.5-1ms, glow waves begin to propagate downstream from the core, resulting in the formation of the bulk plasma extending over 1-20cm. Plasma bunches with density up to 10^{14}-10^{15}cm^{-3} propagate periodically through this plasma with a time interval about 1 ms. The volume of the bulk plasma is 2-3 orders of magnitude greater than that of the core.

(4) The mechanism governing the torch formation in molecular gases is different – the core is absent. This is dramatic, since in usual TIA and MPT, the torch per se consists of the core only. This circumstance, probably, hinders the torch formation in these devices. The advantage of the proposed design is that the torch is successively formed by propagating plasma bunches.

References

1. Moisan M., Sauve G., Zakrzewski Z., and Hubert J. An atmospheric pressure waveguide-fed microwave plasma torch: the TIA design. // PSST 1994, v 3, pp 584-592.
2. Gritsinin S.I., Kossyi I.A. at all, 14th Intern. Symp. on Plasma Chemistry, Prague, 2, 675, (1999).
3. S.I.Gritsinin, I.A.Kossyi, M.A.Misakyan., Proc. of ESCAMPIG XI, Miskolc-Lillafured, Hungary, August 2000, v. 24F, pp 216-217.
4. Gritsinin S.I., Kossyi I.A., Malykh N.I., Misakyan M.A., Temchin C.M. and Bark Y.B., Plasma Coaxial Discharge as a New Type of the Microwave Surface Wave Discharge. // Preprint GPI RAS N 1, Moscow, 1999, 24 p.
5. Yu M Aliev, I Ghanashev, H Schluter, A Shivarova and M Zethoff. Analytical estimations on the axial structure of plasma-waveguide discharges // Plasma Sources Sci. Technol. 3 No 2 (May 1994) 216-225.
6. Rauchle E. Duo-plasmaline, a surface wave sustained linearly extended discharge // 3 IWMDFA, 1997. - J. Phys. IV France, 1998, v 8, N 7, pp 99-108.
7. Walker M., Baumgartner K.-M., Schulz A., Rauchle E. Silicon nitride films from the PLASMODUL-a new microwave plasma device // Proc. of ISPC 14, Prague, 1999, v 3, pp 1427-1432.

80. ANOMALOUS GAS DYNAMIC PROPERTIES OF PLASMOIDS IN AIRFLOW

Klimov A.
Institute for High Temperature RAS
Moscow, Izhorskaya 13/19.

Generation of stable non-equilibrium high energetic structural plasma formations (PF or plasmoids) was studied in our works [1-3]. These PF were created by different types of plasma generators (PG):

- High frequency PG,
- Microwave PG,
- Erosive plasma jet PG,
- And others.

Unusual anomalous gas dynamic properties of some types of these PF were revealed in plasma aerodynamic experiments:

- Drift absence in a gas flow of some types of plasmoids,
- Plasmoid's propagation toward incoming airflow,
- Non- optimal gas dynamic shape (spherical shape) of dusty plasmoid in a supersonic flow near aerodynamic model in wind tunnel experiment,
- Bad mixing of various types of plasmoids in airflow (its independent behaviors in an airflow).
- Propagation of dusty plasmoid with anomalous small plasma recombination through a thin dielectric tube,
- Propagation fuel through streamer channel,
- Influence of electric field on plasmoid's propagation.
- PF propagation through thin ceramic plate.

Further study of these plasmoid properties could be useful for plasma aerodynamics and plasma assisted combustion.

References.

1. Ball Lightning in Laboratory. Editors: Avramenko R.F., Bychkov V.L., Sinkevich O.A., Klimov A.I., Moscow, Chimia publishers, (in Russian), 1994, P.291.
2. Beaulieu W., Byturin V., Klimov A., et. al., Plasma Aerodynamic WT Tests with 1/6 Scale Model. Proc. of the Workshop on Magneto- Plasma- Aerodynamics in aerospace applications. Moscow. March 24-25, 1999, IVTAN, P.44,
3. Klimov A.I., Nikolaeva V.I., Avramenko R. and Development of Plasma/ Aerodynamics in Russia. Proc. of the 2nd Workshop on Magneto- Plasma- Aerodynamics in aerospace applications, Moscow, 5- 7 April, 2000, IVTAN.
4. Bityurin V.A., Klimov A.I., et.al. Plasma Assisted Combustion, AIAA 2001-0491, 39th AIAA Aerospace Science Meeting & Exhibit, 8-11 January 2001, Reno, NV.

81. PRINCIPLE OF A LOCAL DIRECTIVITY OF THERMAL PROCESSES AND INADMISSIBILITY OF USAGE OF HYPERBOLIC-TYPE EQUATIONS FOR MATHEMATICAL SIMULATION OF THESE PROCESSES

B.M.Burakhanov, E.N.Lyutikova

IHED RAS. e-mail:msa@hedric.msk.su, fax- 485-79-90

127412, Izhorskaia 13/19, Moscow.

Abstract. The hypothesis on existence of a local stationary process is formulated. The function of a local deviation of temperature is introduced. The principle of a local directivity of thermal processes is formulated. The limitations imposed on heat conduction equations are obtained. The inadmissibility of usage of hyperbolic-type equations in mathematical models of processes of propagation of thermal perturbations is shown.

Introduction

There are various laws of a thermal conduction, and also there are restrictions, which are imposed on these laws [1-4]. The authors do not know papers, in which the restrictions are imposed on heat conduction equation. In this paper these restrictions are formulated. The heat conduction equation is obtained by substitution of a thermal conduction law into the law of conservation of energy [2]. Therefore restrictions imposed on heat conduction equation impact on the laws of a thermal conduction by an indirect route.

In the paper the restrictions imposed on heat conduction equation, are obtained by usage the scheme of a method of a local state [3]. The hypothesis on existence of a local stationary process is accepted. Besides the hypotheses on existence of function of a local diversion of temperature and hypothesis on existence of a principle of a local directivity of thermal processes are accepted.

The checkout of correspondence of two concrete forms of a heat conduction equation to introduced restrictions is carried out.

It has been found, that the heat conduction equation of a parabolic-type satisfies to these restrictions, and a hyperbolic-type equations does not satisfy. In this connection the reason, on which the solutions of a hyperbolic-type equations can contradict the requirements of the laws of thermodynamics, has been investigated.

1. A substantiation of a principle of a local directivity of heat exchange processes

1.1. Monothermal and polythermal processes

The processes of heat exchange discussed below will be considered in the assumption, that the hypothesis of a local state is valid [3]. Besides it is supposed that temperature $T(x,t)$ is a continuous function possessing a continuous derivative, where $\mathbf{x}=\{x_1,x_2,x_3\}$ - spatial coordinates, and t is time.

Let's consider a properties of thermodynamic systems connected to thermostats. Let's consider that the thermostat is the external (in relation to discussed system) thermodynamic system, a temperature in which is constant.

Let's assume that the thermodynamic system is connected to thermostats all of them have the same temperature T_0. In this case, independently from properties of medium an initial distribution of temperature $T(\mathbf{x},0)$ of the system should passes in isothermal stationary state $T(\mathbf{x},\infty)$ $=T^{mono}{}_{st}=T_0$. Transition processes of system from an initial state $T(\mathbf{x},0)$ to the isothermal state $T^{mono}{}_{st}$ we shall term as monothermal processes and designate as $T^{mono}(\mathbf{x},t)$.

Let's assume that the thermodynamic system is connected to thermostats having various temperature T_{0i} ($1\leq i \leq n$). Let's assume, that thise system has a stationary distribution of temperature $T(\mathbf{x},\infty)=T^{poly}{}_{st}(\mathbf{x})$, which realized independently from an initial distribution of temperature $T(\mathbf{x},0)$. Transition processes of system from the initial distribution of temperature $T(\mathbf{x},0)$ to the stationary distribution of temperature $T(\mathbf{x},\infty)=T^{poly}{}_{st}(\mathbf{x})$ we shall term as polythermal processes and designate as $T^{poly}(\mathbf{x},t)$.

Notice, that the stationary distribution of temperature $T^{poly}{}_{st}(x)$ represents a stationary thermodynamic process. This process means that the properties of medium should do not depend on time. In this connection we shall consider thermodynamic systems, which properties do not depend on time, including implicit dependence through temperature.

Let's introduce the conception of functions of a diversion of temperature $\theta^{mono}(\mathbf{x},t)$ and $\theta^{poly}(x,t)$ through relations

$$\theta^{mono}(\mathbf{x},t)=T^{mono}(\mathbf{x},t) - T^{mono}{}_{st} \qquad (1.1)$$

$$\theta^{poly}(\mathbf{x},t)=T^{poly}(\mathbf{x},t) - T^{poly}{}_{st}(\mathbf{x}) \qquad (1.2)$$

398

These functions define a diversion a current distribution of temperature into system from a stationary distribution of temperature into system. From (1.1) and (1.2) follows. that the functions of a diversion $\theta^{mono}(\mathbf{x},t)$ and $\theta^{poly}(\mathbf{x},t)$ should have the following properties

$$\partial\theta^{mono}(\mathbf{x},t)/\partial t = \partial T^{mono}(\mathbf{x},t)/\partial t \qquad (1.3)$$

$$\partial\theta^{poly}(x,t)/\partial t = \partial T^{poly}(x,t)/\partial t \qquad (1.4)$$

$$\theta^{mono}(\mathbf{x},\infty) = \theta^{poly}(\mathbf{x},\infty) \equiv 0 \qquad (1.5)$$

1.2. A directivity of thermal processes in monothermal systems

The existence of a stationary state $T^{mono}(\mathbf{x},\infty)$ for monothermal system. in which the system transfer from any initial distribution of temperature, allows to speak about a directivity of thermal process in these systems. It is easy to obttain a mathematical expression, which characterizes this directivity. For this purpose it is enough to introduce restriction, imposed by the second law of thermodynamics on a sign of time derivative of a maximum of the module of function of a diversion $\theta^{mono}(\mathbf{x},t)$.

Let's assume, that the point $\mathbf{x}^*(t)$ is a point, in which the module of function of a diversion reaches the exstremum. Naturaly, that the point $\mathbf{x}^*(t)$ can be as a point of a maximum $\mathbf{x}^+(t)$ of function $(\max\theta^{mono}(\mathbf{x},t) = \theta^{mono}(\mathbf{x}^+,t))$, and as a point of a minimum $\mathbf{x}^-(t)$ of function. Thus, it is obvious, that in a point of a maximum $\mathbf{x}^+(t)$ value of function of a diversion is positive $\theta^{mono}(\mathbf{x}^+,t) \geq 0$, and in a point of a minimum $\mathbf{x}^-(t)$ is negative $\theta^{mono}(\mathbf{x}^-,t) \leq 0$.

By virtue of the second law of thermodynamics in a point of a maximum $\mathbf{x}^+(t)$ a time derivative of temperature $(\partial T^{mono}(\mathbf{x}^+,t)/\partial t)$ should be less than zero, and in a point of a minimum $x^-(t)$ - should be more than zero

$$(\partial T^{mono}(\mathbf{x}^+,t)/\partial t) < 0 \qquad (1.6)$$

$$(\partial T^{mono}(x-,t)/\partial t) > 0 \qquad (1.7)$$

Similar inequalities are valid and for function of a diversion $\theta^{mono}(\mathbf{x},t)$ too. It means that in a point $\mathbf{x}^*(t)$ the following inequalities should be fulfilled

$$(\partial\theta^{mono}(\mathbf{x}^*,t)/\partial t)\,\theta^{mono}(x^*,t) \leq 0 \qquad (1.8)$$

$$\partial|\theta^{mono}(\mathbf{x}^*,t)|/\partial t \leq 0 \qquad (1.9)$$

It is possible to consider an inequality (1.9) as mathematical expression defined directivity of monothermal process to setting-up of a stationary isothermal state $T^{mono}(\mathbf{x},\infty) = \text{const}$.

1.3. Monothermal processes with the function of a diversion of constant signs

We shall consider monothermal processes $T^{mono}(\mathbf{x},t)$. Let's assume, that a time derivative of temperature $\partial T^{mono}(\mathbf{x},0)/\partial t$ in all points of system in an initial instant $t=0$ has an identical sign. Let's show that the function of a diversion $\theta^{mono}(\mathbf{x},t)$ in all points of system also has an identical sign, and this sign is opposite to a sign of function $\partial T^{mono}(\mathbf{x},0)/\partial t$

$$(\partial T^{mono}(\mathbf{x},0)/\partial t)\,\theta^{mono}(\mathbf{x},t) < 0 \qquad (1.10)$$

Let's assume, for example, that the function $\partial T^{mono}(\mathbf{x},t)/\partial t$ in an initial instant is more than zero

$$\partial T^{mono}(\mathbf{x},0)/\partial t > 0 \qquad (1.11)$$

In this case the following inequality at any moment of time should be fulfilled

$$T^{mono}(\mathbf{x},t) - T_0 \leq 0 \qquad (1.12)$$

where T_0 is temperature of a thermostat, and this inequality in an initial instant should be rigorous

$$T^{mono}(\mathbf{x},0) < T_0. \qquad (1.13)$$

The proof we shall conduct by contradiction. Let's assume, that there is an inside point $\mathbf{x}=\mathbf{x}_0$, in which a value of function $T^{mono}(\mathbf{x},0)$ is strict more than temperature of a thermostat, that is

$$T^{mono}(\mathbf{x}_0,0) > T_0. \qquad (1.14)$$

From the assumption that the function $T^{mono}(\mathbf{x},0)$ is continuity follows, that there should be an inside point $\mathbf{x}^+(0)$, in which the function $T^{mono}(\mathbf{x},0)$ reaches the maximum value $T^{mono}(\mathbf{x}^+,0) > T_0$. However, by virtue of the second law of thermodynamics the sign by time derivative of temperature in a point $\mathbf{x}^+(0)$ should be negative. It contradicts a requirement (1.11). By this means, that our assumption that value of function $T^{mono}(\mathbf{x},0)$ can be strict more than temperature of a thermostat is incorrect.

Let's show now, that there are no inside points, in which value of function $T^{mono}(\mathbf{x},0)$ are equal to temperature of a thermostat. Really, if such

399

point $\mathbf{x}=\mathbf{x}_1$ exists, then by virtue of expression (1.11), the time derivative of temperature in this point should be more than zero. Therefore the value of function $T^{mono}(\mathbf{x}_1,\Delta t)$ in an instant $t=0+\Delta t$ becomes strict more than temperature of a thermostat. However, by virtue of the second law of thermodynamics, to increase temperature of a body up to temperature increasing of temperature of a calefactor it is impossible. Therefore, ours assumption that there is the inside point of system, in which the value of function $T^{mono}(\mathbf{x},0)$ is equal to temperature of a thermostat, is incorrect.

Similar by a fashion it is possible to show, that in a case, when a time derivative of temperature in all points of system in an initial moment is negative, the values of function of a diversion should be plus. It proves validity of an inequality (1.10).

Taking into account (1.3) it is possible the inequalities (1.10) are presented as

$$\partial\theta^{mono}(\mathbf{x},t)|_{t=0}/\partial t \cdot \theta^{mono}(\mathbf{x},0) < 0 \qquad (1.15)$$

From expression (1.15) follows, that the follow inequality should be fulfilled

$$\partial|\theta^{mono}(\mathbf{x},0)||_{t=0}/\partial t < 0 \qquad (1.16)$$

Thus it is shown, that the change of temperature in all points of system in an initial moment of time $t=0$ is directed to the setting-up of stationary distribution of temperature T^{mono}_{st}.

1.4. Principle of superposition of polythermal processes

Let's consider a polythermal processes $T^{poly}(\mathbf{x},t)$. In the item 1.1. the hypothesis was accepted that these processes have stationary distribution of temperature $T^{poly}(\mathbf{x},\infty)=T^{poly}_{st}(\mathbf{x})$. The function of a diversion $\theta^{poly}(\mathbf{x},t)$ was introduced too.

Let's assume, that any polythermal process $T^{poly}(\mathbf{x},t)$ can be represented as a superposition of stationary process $T^{poly}_{st}(\mathbf{x})$ and monothermal process $T^{mono}(\mathbf{x},t)$.

The superposition of fields of temperature of stationary $T^{poly}_{st}(\mathbf{x})$ and of monothermal $T^{mono}(\mathbf{x},t)$ processes means the following. If the monothermal process $T^{mono}(\mathbf{x},t)$ has an initial distribution of temperature $T^{mono}(\mathbf{x},0)=\theta^{poly}(\mathbf{x},0)$ + const, and a temperature of thermostats equal T_0, and the stationary process $T^{poly}_{st}(\mathbf{x})$ has the values of temperature of thermostats equal $T_{0i}=T_i$ ($1\le i\le n$), there is a polythermal process

$$T^{poly}(\mathbf{x},t) = T^{mono}(\mathbf{x},t) + T^{poly}_{st}(\mathbf{x}), \qquad (1.17)$$

which has an initial distribution of temperature $T^{poly}(\mathbf{x},0)=T^{mono}(\mathbf{x},0)+T^{poly}_{st}(\mathbf{x})$, and at values of temperature of thermostats equal $T_{0i} = T_i+ T_0$.

From expression (1.17) follows, that the time derivative of temperature of the polythermal and monothermal processes should coincide

$$\partial T^{poly}(\mathbf{x},t)/\partial t \equiv \partial T^{mono}(\mathbf{x},t)/\partial t \qquad (1.18)$$

Comparing expressions (1.17) and (1.2) and taking into account expression (1.1), we shall receive, that the functions of a diversion of the polythermal and monothermal processes should coincide

$$\theta^{poly}(\mathbf{x},t) \equiv \theta^{mono}(\mathbf{x},t) \qquad (1.19)$$

Let's mark, that the principle of superposition extends to a distribution of a thermal stream $q(x,t)$. It means, that, if the function $\mathbf{q}^{poly}_{st}(\mathbf{x})$ is distribution of a vector of a thermal stream in the stationary process, and the function $\mathbf{q}^{mono}(\mathbf{x},t)$ is distribution of a vector of a thermal stream in the monothermal process, the function $\mathbf{q}^{poly}(\mathbf{x},t)=\mathbf{q}^{mono}(\mathbf{x},t)+\mathbf{q}^{poly}_{st}(\mathbf{x})$ is distribution of a vector of a thermal stream in the polythermal process.

Hypothesis on principle of superposition have a important argument for the benefit of this assumption. This argument is the linearity of the law of conservation of energy. This law for systems, which have the properties do not depend on time, looks like

$$C(\mathbf{x})\rho(\mathbf{x})\partial T(\mathbf{x},t)/\partial t = -\mathrm{div}\mathbf{q}(\mathbf{x},t) \qquad (1.20)$$

where $C(\mathbf{x})$ is heat capacity, $\rho(\mathbf{x})$ is density, and $\mathbf{q}(\mathbf{x},t)$ is vector of density of a thermal stream. By virtue (1.20) the following equalities is correct

$$\begin{aligned} C\rho\partial T^{poly}(\mathbf{x},t)/\partial t &= -\mathrm{div}\mathbf{q}^{poly}(\mathbf{x},t) = \\ &= -\mathrm{div}(\mathbf{q}^{mono}(\mathbf{x},t)+\mathbf{q}^{poly}_{st}(\mathbf{x})) = \\ &= -(\mathrm{div}\mathbf{q}^{mono}(\mathbf{x},t)+\mathrm{div}\mathbf{q}^{poly}_{st}(\mathbf{x})) = \\ &= C\rho\partial T^{mono}(\mathbf{x},t)/\partial t+C\rho\partial T^{poly}_{st}(\mathbf{x})/\partial t= \\ &= C\rho\partial(T^{mono}(\mathbf{x},t) + T^{poly}_{st}(\mathbf{x}))/\partial t \end{aligned} \qquad (1.21)$$

1.5. A principle of a local directivity of thermal processes

Let's assume, that in some moment of time $t=t_0$ infinitesimal the particle δv with boundary $r_{\delta v}$ mentally is extracted from system. Let's assume, that the thermostat is connected to each boundary point $\mathbf{x}'|_{\mathbf{x}'\in r\delta v}$ of the extracted particle. Distribution of temperature in the extracted particle δv at $t=t_0$ we shall designate as $T(\mathbf{x},t_0)|_{\mathbf{x}\in \delta v}$. Let's assume, that

400

temperature of each thermostat is equal to current value of temperature $T(\mathbf{x}',t_0)|_{\mathbf{x}' \in r\delta v}$ a point $\mathbf{x}'$, to which it is connected. Process of transition of a particle δv from an anitial distribution of temperature $T(\mathbf{x},t_0)|_{\mathbf{x} \in \delta v}$ to a stationary distribution of temperature $T^{loc}_{st}(\mathbf{x})|_{\mathbf{x} \in \delta v, t_0}$ we shall term as local polythermal process. Distribution of temperature in local polythermal process we shall designate as $T^{poly}_{loc}(\mathbf{x},t')$, where t' is time, in which this process executes. It is obvious, that $T^{poly}_{loc}(\mathbf{x},0)=T(\mathbf{x},t_0)|_{\mathbf{x} \in \delta v}$, and $T^{poly}_{loc}(\mathbf{x},\infty)=T^{loc}_{st}(\mathbf{x})|_{\mathbf{x} \in \delta v, t_0}$. Let's designate the function of a local diversion of temperature $\theta^{loc}(\mathbf{x},t')|_{\mathbf{x} \in \delta v}$ through a relation

$$\theta^{loc}(\mathbf{x},t')|_{\mathbf{x} \in \delta v}=T^{poly}_{loc}(\mathbf{x},t')|_{\mathbf{x} \in \delta v}-T^{poly}_{loc}(\mathbf{x},\infty)|_{\mathbf{x} \in \delta v} \quad (1.22)$$

From a hypothesis about a superposition of polythermal process is followed that the local polythermal process $T^{poly}_{loc}(\mathbf{x},t')|_{\mathbf{x} \in \delta v}$ can be represented, to within a constant, as a superposition of local monothermal $(T^{mono}_{loc}(\mathbf{x},t')|_{\mathbf{x} \in \delta v})$ and of local stationary $(T^{poly}_{loc}(\mathbf{x},\infty)|_{\mathbf{x} \in \delta v})$ processes. Let's mark, that the change of temperature in local monothermal process $T^{mono}_{loc}(\mathbf{x},t')|_{\mathbf{x} \in \delta v}$, to within a constant, should coincide with function of a local diversion of temperature $\theta^{loc}(\mathbf{x},t')|_{\mathbf{x} \in \delta v}$

$$T^{mono}_{loc}(\mathbf{x},t')|_{\mathbf{x} \in \delta v} = \theta^{loc}(\mathbf{x},t')|_{\mathbf{x} \in \delta v} + \text{const} \quad (1.23)$$

From expressions (1.22), (1.23) follows, that time derivative of temperature in polythermal and monothermal processes, and also time derivative from function of a diversion should be equal

$$(\partial T^{poly}_{loc}(\mathbf{x},t')/\partial t')|_{\mathbf{x} \in \delta v} = (\partial T^{mono}_{loc}(\mathbf{x},t')/\partial t')|_{\mathbf{x} \in \delta v} = (\partial \theta^{loc}(\mathbf{x},t')/\partial t')|_{\mathbf{x} \in \delta v} \quad (1.24)$$

Let's assume, that the sign by time derivative of temperature $(\partial T^{poly}_{loc}(\mathbf{x},t')/\partial t')|_{\mathbf{x} \in \delta v, t'=0}$ and sign by time derivative from current temperature $(\partial T(\mathbf{x},t)/\partial t)|_{\mathbf{x} \in \delta v, t=t0}$ in all points of a particle δv in an initial moment of time $t'=0$ is coincides

$$\text{sign}(\partial T^{poly}(\mathbf{x},t')/\partial t')|_{\mathbf{x} \in \delta v, t'=0}=\text{sign}(\partial T(\mathbf{x},t)/\partial t)|_{\mathbf{x} \in \delta v, t=t0} \quad (1.25)$$

Let's assume, that the function $(\partial T(\mathbf{x},t)/\partial t)|_{\mathbf{x} \in \delta v, t=t0}$ is a continuous function. Let's assume, that the particle δv contains even one point, which time derivative of temperature is equal zero. Then this function in all points of a particle should be equal zero, within infinitesimal of the first order. It means, that the local polythermal process in particles, where time derivative from

temperature is equal zero, coincides with local stationary process $T^{poly}_{loc}(\mathbf{x},t')|_{\mathbf{x} \in \delta v}\equiv T^{poly}_{loc}(\mathbf{x},\infty)|_{\mathbf{x} \in \delta v}$.

Let's select the sizes of a particle δv so small, that by virtue of continuous of time derivative of temperature the sign of function $(\partial T(\mathbf{x},t)/\partial t)|_{\mathbf{x} \in \delta v, t=t0}$ in all points of a particle is identical. Taking into account, that the signs of the functions $(\partial T^{mono}_{loc}(\mathbf{x},t')/\partial t')|_{\mathbf{x} \in \delta v, t'=0}$ and $(\partial T(\mathbf{x},t)/\partial t)|_{\mathbf{x} \in \delta v, t=t0}$ in an initial instant $t'=0$ are coincided, we shall receive, that the sign by time derivative of temperature in local monothermal process $\partial T^{mono}_{loc}(\mathbf{x},t')/\partial t')|_{\mathbf{x} \in \delta v}$ in an initial instant $t'=0$ everywhere is identical.

The processes, for which the sign of function of a diversion in all points in an initial instant is identical and is constant should be satisfy to the relations (1.15) and (1.16). Therefore the local functions of a diversion $\theta^{loc}(x,t')$ should be satisfy to the following relations

$$(\partial \theta^{loc}(\mathbf{x},t')/\partial t')|_{\mathbf{x} \in \delta v, t'=0}(\theta^{loc}(\mathbf{x},t'))|_{\mathbf{x} \in \delta v, t'=0} \le 0 \quad (1.26)$$

$$\partial|\theta^{loc}(\mathbf{x},t')/\partial t'|_{\mathbf{x} \in \delta v, t'=0} < 0 \quad (1.27)$$

Taking into account (1.22) and (1.24) we shall receive, that (1.26) is possible to describe as

$$(\partial T^{poly}_{loc}(\mathbf{x},t')/\partial t')|_{\mathbf{x} \in \delta v, t'=0}(T^{poly}_{loc}(\mathbf{x},t')|_{\mathbf{x} \in \delta v, t'=0} - T^{poly}_{loc}(\mathbf{x},\infty)|_{\mathbf{x} \in \delta v}) \le 0 \quad (1.28)$$

Taking into account, that $T^{poly}_{loc}(\mathbf{x},t')|_{\mathbf{x} \in \delta v, t'=0}$ is equal $T(\mathbf{x},t_0)|_{\mathbf{x} \in \delta v}$ and taking into account also (1.24) we shall receive

$$(\partial T(\mathbf{x},t)/\partial t)|_{\mathbf{x} \in \delta v, t=t0}(T(\mathbf{x},t)|_{\mathbf{x} \in \delta v, t=t0}-T^{loc}_{st}(\mathbf{x})|_{\mathbf{x} \in \delta v, t0}) \le 0 \quad (1.29)$$

The inequality (1.29) is equivalent to expression of a view

$$\partial|T(\mathbf{x},t)|_{\mathbf{x} \in \delta v, t=t0} - T^{loc}_{st}(\mathbf{x})|_{\mathbf{x} \in \delta v, t0}| < 0 \quad (1.30)$$

The expression (1.30) can be interpreted as a principle of a local directivity of thermal processes, according to which the local thermal process in each point infinitesimal particles is always directivity to setting-up of a local stationary process.

2. An inadmissibility of usage hyperbolic-type equations for mathematical simulation of heat exchange processes.

2.1. Properties of function of a local diversion of temperature

Let's assume, that there is a thermodynamic system, which properties are functions x and t. Let's assume, that everyone infinitesimal a particle δv of this system has a local stationary distribution of temperature $T^{loc}_{st}(\mathbf{x})|_{\mathbf{x}\in\delta v, t0}$, here t_0 - is parameter. A local stationary distribution of temperature is such distribution of temperature into a particle δv, which should be setting-up in a particle, if on its boundary r to fix temperature $T(\mathbf{x},t_0)|_{\mathbf{x}\in\delta v}$, and inside a particle to fix properties of medium $\rho(\mathbf{x},t_0)|_{\mathbf{x}\in\delta v}, C(\mathbf{x},t_0)|_{\mathbf{x}\in\delta v}$ and $\lambda(\mathbf{x},t_0)|_{\mathbf{x}\in\delta v}$, here $\lambda(\mathbf{x},t_0)|_{\mathbf{x}\in\delta v}$ is thermal conductivity. The hypothesis on existence a local stationary distribution of temperature is identical with the hypothesis on existence a local stationary process.

The hypothesis on existence of a local stationary process allows to introduce a function of a local diversion of current temperature $\theta^{loc}(\mathbf{x})|_{\mathbf{x}\in\delta v, t0}$, here t_0 - is parameter. Let's to introduce this function through a relation

$$\theta^{loc}(\mathbf{x})|_{\mathbf{x}\in\delta v, t0}=T(\mathbf{x},t_0)|_{\mathbf{x}\in\delta v}-T^{loc}_{st}(\mathbf{x})|_{\mathbf{x}\in\delta v, t=t0} \qquad (2.1)$$

where $T(\mathbf{x},t_0)|_{\mathbf{x}\in\delta v}$ is distribution of current temperature in a particle δv in an instant $t=t_0$, and $T^{loc}_{st}(\mathbf{x})|_{\mathbf{x}\in\delta v, t=t0}$ is a local stationary distribution of temperature.

As the function $T^{loc}_{st}(\mathbf{x})|_{t=t0}$ is completely determined by the assignment of functions $T(\mathbf{x},t_0)|_{\mathbf{x}\in\delta v}$, $\rho(\mathbf{x},t_0)|_{\mathbf{x}\in\delta v}, C(\mathbf{x},t_0)|_{\mathbf{x}\in\delta v}$ and $\lambda(\mathbf{x},t_0)|_{\mathbf{x}\in\delta v}$, this function can be represented symbolically as a functional ϑ of a view

$$T^{loc}_{st}(\mathbf{x})|_{\mathbf{x}\in\delta v, t=t0}=\vartheta(\rho(\mathbf{x},t_0)|_{\mathbf{x}\ni\delta v}, C(\mathbf{x},t_0)|_{\mathbf{x}\ni\delta v},$$
$$\lambda(\mathbf{x},t_0)|_{\mathbf{x}\ni\delta v}, T(\mathbf{x},t_0)|_{\mathbf{x}\ni r\delta v}). \qquad (2.2)$$

As the expression (2.1) contains the function $T^{loc}_{st}(\mathbf{x})|_{\mathbf{x}\ni\delta v, t=t0}$ and the function $T(\mathbf{x},t_0)|_{\mathbf{x}\in\delta v}$, that the function of a local diversion $\theta^{loc}(\mathbf{x})|_{\mathbf{x}\in\delta v}$ can be represented symbolically as a functional Ω of a view

$$\theta^{loc}(\mathbf{x})|_{\mathbf{x}\in\delta v, t=t0}=\Omega(\rho(\mathbf{x},t_0)|_{\mathbf{x}\in\delta v}, C(\mathbf{x},t_0)|_{\mathbf{x}\in\delta v},$$
$$\lambda(\mathbf{x},t_0)|_{\mathbf{x}\in\delta v}, T(\mathbf{x},t_0)|_{\mathbf{x}\in r\delta v}, T(\mathbf{x},t_0)|_{\mathbf{x}\in\delta v}) \qquad (2.3)$$

The hypothesis on existence of a local stationary process and the introduction of a function of a local diversion of current temperature allows to formulate a principle of a local directivity of thermal processes. Two various determine of this principle are possible.

First of these determine postulates existence a directivity of local thermal process. This determination have a following formulation. The thermal process in each particle is always directivity to the setting-up of a local stationary process. The expression of a view

$$\partial|T(\mathbf{x},t)|_{\mathbf{x}\in\delta v, t=t0} - T^{loc}_{st}(\mathbf{x})|_{\mathbf{x}\in\delta v, t=t0}|\partial t \leq 0 \qquad (2.4)$$

corresponds to this determination.

Second of this determine postulates existence an interrelation between function of a diversion and function of a time derivative of temperature. This determination have a following formulation. In each point of a particle δv the sign of time derivative of temperature $\partial T(\mathbf{x},t)/\partial t|_{\mathbf{x}\in\delta v, t=t0}$ is opposite to a sign of function of a diversion $\theta^{loc}(\mathbf{x})|_{\mathbf{x}\in\delta v, t=t0}$. The expression of a view

$$\partial T(\mathbf{x},t)/\partial t|_{\mathbf{x}\in\delta v, t=t0}\, \theta^{loc}(\mathbf{x})|_{\mathbf{x}\in\delta v, t=t0} \leq 0 \qquad (2.5)$$

corresponds to this determination. In the mathematical relation the records (2.4) and (2.5) is equivalent.

Let's consider the properties of the function of a local diversion $\theta^{loc}(\mathbf{x})|_{\mathbf{x}\in\delta v, t0}$. It was shown above, that the function $\theta^{loc}(\mathbf{x})|_{\mathbf{x}\in\delta v, t=t0}$ is completely determined by the assignment of functions $\rho(\mathbf{x},t_0)|_{\mathbf{x}\in\delta v}$, $C(\mathbf{x},t_0)|_{\mathbf{x}\in\delta v}$, $\lambda(\mathbf{x},t_0)|_{\mathbf{x}\in\delta v}$, $T(\mathbf{x},t_0)|_{\mathbf{x}\in r\delta v}, T(\mathbf{x},t_0)|_{\mathbf{x}\in\delta v}$. It means, that the function $\mathrm{sign}\partial T(\mathbf{x},t)/\partial t|_{\mathbf{x}\in\delta v, t=t0}$ can be symbolically represented as a functional Σ of a view

$$\mathrm{sign}\partial T(\mathbf{x},t)/\partial t|_{\mathbf{x}\in\delta v, t0}=\Sigma(\rho(\mathbf{x},t_0)|_{\mathbf{x}\in\delta v}, C(\mathbf{x},t_0)|_{\mathbf{x}\in\delta v},$$
$$\lambda(\mathbf{x},t_0)|_{\mathbf{x}\in\delta v}, T(\mathbf{x},t_0)|_{\mathbf{x}\in r\delta v}, T(\mathbf{x},t_0)|_{\mathbf{x}\in\delta v}) \qquad (2.6)$$

From (2.6) follows, that the function $\mathrm{sign}\partial T(\mathbf{x},t)/\partial t$ is completely determined by the assignment of the properties of medium and by the assignment of the function $T(\mathbf{x},t)$.

By virtue of continuous of function $\theta^{loc}(\mathbf{x})|_{\mathbf{x}\in\delta v, t=t0}$ and by virtue that this function on a boundary of particle is equal to constant and also by virtue of a smallness of a particle δv the function of a local diversion $\theta^{loc}(\mathbf{x})|_{\mathbf{x}\in\delta v, t=t0}$ has a following properties.

This function has the exstremum into particle. The gradient of this function in all inside points of a particle within infinitesimal of the first order should be equal to zero

$$\nabla\theta^{loc}(\mathbf{x})|_{\mathbf{x}\in\delta v, t=t0} \approx 0. \qquad (2.7)$$

The sign of this function in all inside points of a particle is identical. The sign of the function of a local diversion $\theta^{loc}(\mathbf{x})|_{\mathbf{x}\in\delta v, t=t0}$ and the sign of the laplacian of this function $\nabla^2\theta^{loc}(x)|_{\mathbf{x}\in\delta v, t=t0}$ in all inside points of a particle should be opposite. Therefore by virtue (2.5) the following inequality is valid

$$\partial T(\mathbf{x},t)/\partial t|_{\mathbf{x}\in\delta v, t=t0}\, \nabla^2\theta^{loc}(\mathbf{x})|_{\mathbf{x}\in\delta v, t=t0} \geq 0 \qquad (2.8)$$

402

Let's mark, that the function $\theta^{loc}(\mathbf{x})|_{\mathbf{x} \in \delta v, t = t0}$ in all particle where time derivative of temperature is plus should be convexity. Besides this function in all particle where time derivative of temperature is negative should be concave.

2.2 Checkout of correspondence of heat conduction equations of parabolic and hyperbolic types to restrictions which follows from existence and properties of local diversion function.

Let's consider the heat conduction equation of a parabolic type. This equation can be received, inserting the law of a thermal conduction the Fourier

$$\mathbf{q}(\mathbf{x},t) = - \lambda(\mathbf{x})\nabla T(\mathbf{x},t) \qquad (2.9)$$

in the law of conservation of energy (1.20). We have received a heat conduction equation the Fourier of a view

$$C(\mathbf{x})\rho(\mathbf{x})\partial T(\mathbf{x},t)/\partial t = $$
$$= \lambda(\mathbf{x})(\nabla^2 T(\mathbf{x},t)) + (\nabla\lambda(\mathbf{x}))(\nabla T(\mathbf{x},t)) \qquad (2.10)$$

From expression (2.10) follows, that the function of a sign by time derivative of temperature symbolically can be represented as a functional ψ of a view
$$\text{sign}(\partial T(\mathbf{x},t)/\partial t) = \psi(\rho(\mathbf{x}),C(\mathbf{x}), \lambda(\mathbf{x}),T(\mathbf{x},t)) \qquad (2.11)$$
Comparing the left-hand parts of expressions (2.11) and (2.6), we shall receive, that the heat conduction equation the Fourier corresponds to restriction imposed on totality of functions, determined of the function of a sign by time derivative of temperature.

The expression erecting interrelation between a laplacian of function of a local diversion and the time derivative of temperature can be easy received with the help of expression (2.10). For this purpose it is necessary to insert the function $T^{loc}_{st}(\mathbf{x})|_{\mathbf{x} \in \delta v, t = t0}$ in expression (2.10). In result we shall receive the elliptic equation of a view

$$\lambda(\mathbf{x})(\nabla^2 T^{loc}_{st}(\mathbf{x})|_{\mathbf{x}0 \in \delta v, t = t0} + $$
$$+(\nabla\lambda(\mathbf{x}))(\nabla T^{loc}_{st}(\mathbf{x})|_{\mathbf{x}0 \in \delta v, t = t0} = 0 \qquad (2.12)$$

Subtracting a right part of expression (2.12) from a left part of the equation (2.10) we shall have

$$(C(\mathbf{x}_0)\rho(\mathbf{x}_0)\partial T(\mathbf{x}_0,t)/\partial t)|_{\mathbf{x}0 \in \delta v, t = t0} = $$
$$= \lambda(\mathbf{x})(\nabla^2 \theta^{loc}(\mathbf{x})|_{\mathbf{x} \in \delta v, t = t0} + (\nabla\lambda(\mathbf{x}))(\nabla \theta^{loc}(\mathbf{x})|_{\mathbf{x} \in \delta v, t = t0} \qquad (2.13)$$

Taking into account, that according to expression (2.7), the gradient of local diversion

function is infinitesimal of the first order, we shall represent the equation (2.13) in the shape

$$\partial T(\mathbf{x},t)/\partial t = (\lambda(\mathbf{x})/C(\mathbf{x})\rho(x)) \nabla^2\theta^{loc}(\mathbf{x})|_{\mathbf{x} \in \delta v, t = t0} \quad (2.14)$$

Multiplying both parts of expression (2.14) on $\nabla^2\theta^{loc}(\mathbf{x})|_{\mathbf{x} \in \delta v, t = t0}$, we shall receive

$$(\partial T(\mathbf{x},t)/\partial t)(\nabla^2\theta^{loc}(\mathbf{x})|_{\mathbf{x} \in \delta v, t = t0}) = $$
$$= (\lambda(\mathbf{x})/C(\mathbf{x})\rho(\mathbf{x})) (\nabla^2\theta^{loc}(\mathbf{x})|_{\mathbf{x} \in \delta v, t = t0})^2 \qquad (2.15)$$

As the right member of expression (2.15) is plus, the following inequality is valid

$$(\partial T(\mathbf{x},t)/\partial t)(\nabla^2\theta^{loc}(\mathbf{x})|_{\mathbf{x} \in \delta v, t = t0}) > 0 \qquad (2.16)$$

Comparing the expression (2.8) and the expression (2.16) we shall receive, that the heat conduction equation the Fourier corresponds to restrictions imposed on properties of heat conduction equations.

We shall consider now heat conduction equation of a hyperbolic-type. Inserting the law of a thermal conduction Cattaneo [4]

$$\tau \partial\mathbf{q}(\mathbf{x},t)/\partial t + \mathbf{q}(\mathbf{x},t) = - \lambda(\mathbf{x})\nabla T(\mathbf{x},t) \qquad (2.17)$$

where τ is relaxation time, in the law of conservation of energy (1.20), we have received a so-called telegraph equation of a view

$$C(\mathbf{x})\rho(\mathbf{x})\partial T(\mathbf{x},t)/\partial t + \tau C(\mathbf{x})\rho(\mathbf{x})\partial T^2/\partial t^2 = $$
$$= \lambda(\mathbf{x}) (\nabla^2 T(\mathbf{x},t)) + (\nabla\lambda(\mathbf{x}))(\nabla T(\mathbf{x},t)) \qquad (2.18)$$

From expression (2.18) follows, that the function of a sign by time derivative of temperature symbolically can be presented as a functional ψ_1 view

$$\text{sign}(\partial T(\mathbf{x},t)/\partial t) = $$
$$= \psi_1(\rho(\mathbf{x}),C(\mathbf{x}),\lambda(\mathbf{x}),T(\mathbf{x},t),\partial T^2(\mathbf{x},t)/\partial t^2) \qquad (2.19)$$

Comparing the left parts of expressions (2.19) and of expressions (2.6), we shall receive, that the telegraph equation does not correspond to restriction imposed on totality of functions, determined of the function of a sign by time derivative of temperature.

On the basis of expression (2.18) it is easy to receive a relation erecting interrelation between time derivative from temperature and the function of a local diversion of a view

$$\tau\partial T^2(\mathbf{x},t)/\partial t^2(\nabla^2\theta^{loc}(\mathbf{x})|_{\mathbf{x} \in \delta v, t = t0}) + $$
$$+ \partial T(\mathbf{x},t)/\partial t)(\nabla^2\theta^{loc}(\mathbf{x})|_{\mathbf{x} \in \delta v, t = t0}) > 0 \qquad (2.20)$$

From expressions (2.19) and (2.20) follows, that the hyperbolic equation (2.18) does not correspond to restrictions imposed on properties of heat conduction equations.

2.3. An inadmissibility of usage of a telegraph equation for solution of a thermal conduction problem

In this paragraph there is an example of the physically incorrect one dimension solution obtained with the help a system of equations (1.20) and (2.17). This system of equations can be reduced to a telegraph equation (2.18). This is a problem of propagation of thermal perturbations in a bar. The physical setting of this problem was made on the basis of paper [4], in which was made the physical setting of a problem about reflection a thermal wave from a free surface. Physical setting of this task following.

There is a homogeneous rectilinear bar of length L, which up to an instant $t=t_0$ is in a state of a temperature equilibrium. The temperature of the bar is equel to T_0. To the left boundary of a bar in an instant $t=t_0$ is connected the thermostat having temperature T_1, major than T_0.

The initial conditions is

$$T(\mathbf{x},0) = T_0 \tag{2.21}$$

$$\mathbf{q}(\mathbf{x},0) = 0 \tag{2.22}$$

The boundary conditions is

$$T(0,t) = T_1 \tag{2.23}$$

$$\mathbf{q}(L,t) = 0 \tag{2.24}$$

The solution of this problem in dimensionless form was obtained by the numerical method. Let's mark that between dimensionless and dimensional parameters takes place the dependence of a view

$$t=\tau\, t^*,\ x=\tau\, c_0 x^*,\ T=T_0\, T^*,\ \mathbf{q}=\rho_0 C_0 c_0 T_0\, \mathbf{q}^* \tag{2.25}$$

On figures 1-2 the diagrams of distribution of dimensionless temperature T^*, as functions of dimensionless length x^*, in instants $t^*_1 = 0.9$ and $t^*_2 = 1.1$ are given. Thus $t^* = 1.0$ is an instant, when the discontinuity surface reaches of adiabatic boundary of a bar.
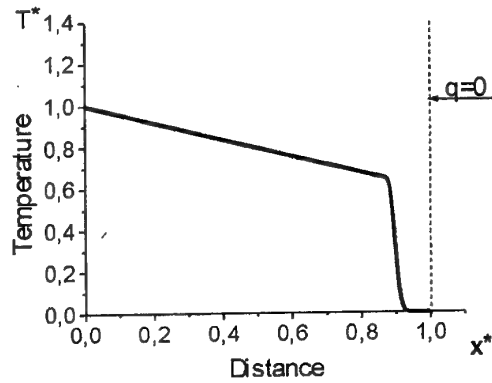
Fig.1. Temperature distribution at $t^*=0.9$
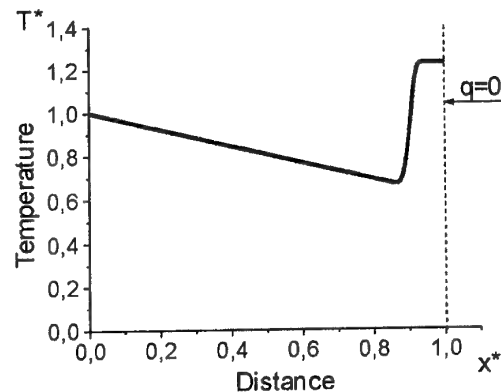
Fig.2. Temperature distribution at $t^*=1.1$

From figures 1 and 2 follows, that in an instant $t^*=1.1$ temperatures on a interval 0.9-1.0 are higher than temperature on a interval of a bar 0.8-0.9, but in an instant $t^*=0.9$ temperatures on a interval 0.9-1.0 was less than temperature on a interval of a bar 0.8-0.9. It is easy to show, that this exceeding of temperature on a interval 0.9-1.0 contradicts the requirements of the second law of thermodynamics. The heating of a bar on interval 0.9-1.0 can happen only through a interval of a bar 0.8-0.9. However, by virtue of the second law of thermodynamics a maximum of temperature a device which is heated can not exceed the maximum of temperature of a device, through which this heating was happened.

This ristriction can be represented as two following inequalities. Let's assume, that $\max T(x,t)|_{x \in \Delta V}$ is the maximum of temperature into heating part of a body ΔV. Besides $\max T(x,t)|_{x \in r\Delta V}$ is a maximum of temperature on its boundary this part of a body. Let's assume, that a maximum of temperature of a heated up part of a body in an initial instant $t=0$ was on its boundary

$$\max T_x(\mathbf{x},0)|_{x \in r\Delta V} \geq \max T_x(\mathbf{x},0)|_{x \in \Delta V}, \tag{2.26}$$

404

where the lower index x signify, that the maximum takes on spatial coordinates, then at any moment of time $t^*_0 > 0$ maximum of function $\max T_{x,t}(\mathbf{x},t)|_{x \in \Delta V}$ in a time interval $[0, t^*_0]$ is restricted to a maximum of function $\max T_{x,t}(x,t)|_{x \in r\Delta V}$

$$\max T_{x,t}(x,t)|_{x \in r\Delta V} \geq \max T_{x,t}(x,t)|_{x \in \Delta V}, \qquad (2.27)$$

where the lower indexes x and t signify, that the maximum takes both on spatial coordinates and on time.

On figures 1-2 the diagrams of distribution of dimensionless temperature T^* is broken the requirement (2.27). Therfore this solution is physically incorrect.

2.4. Restriction imposed by the laws of thermodynamics on processes of propagation of thermal perturbations in mediums.

The heat conduction equation the Fourier (2.10) belong to the parabolic-type equations. The solutions of this type equation are physically incorrect, as the thermal perturbations in these solutions are spread with infinite velocity. The hyperbolic-type heat conduction equation, an example, the telegraph equation (2.18) is correct in this respect. However, the solutions of the hyperbolic-type heat conduction equation on a surface separating a area of the thermal perturbation and the unperturbed area have a rupture of temperature and a rupture of module of a vector of a thermal stream.

Below it is shown, that, if the surface separating an area of the thermal perturbation and the unperturbed area move with finite velocity and if a normal component of a vector of a thermal stream on this surface have a rupture, then this solution is incorrect.

We shall consider the dynamics of the propagation of thermal perturbation in a homogeneous rectilinear bar of length L. The physical setting of this problem is followings. Let's assume, that the bar up to an instant $t=t_0$ was in a state of a temperature equilibrium. The value of this temperature is equal T_0. Let's assume also, that the left-hand end of a bar in an instant $t=t_0$ is associated to a thermostat. The temperature of this thermostat is more T_0 and is equal T_1. Besides we shall consider, that the thermal perturbations in a bar are propagated with a finite stationary velocity. The value of this velocity is equal to c_0.

Mentally we shall divide a bar on n of equal intervals. The length of each interval is equal $\Delta x = L/n$. Let's consider, that the instant t_0 coincides with an initial instant ($t_0=0$). Let's consider, that the origin of coordinates coincides with the left-hand

boundary of a bar. Therefore the coordinate of point x_i coinciding with the left-hand end of a interval - i is equal $x_i=(i-1)\Delta x$, where $0 \leq i \leq n$.

We shall consider the dynamics of change of inflow of quantity of heat ΔQ into the intervals $(n-1)$ and n of a bar in instants $t_1=t^*+\Delta t$, $t_2=t^*+2\Delta t$, $t_3=t^*+3\Delta t$. Here t^* is an instant, when the discontinuity surface reaches the left-hand end of the interval (n-1) of a bar. Besides here $\Delta t=\Delta x/c_0$ is a time slice, for which the discontinuity surface transits each of interval of a bar.

We shall enter the following designations. A quantity of a thermal stream between contiguous intervals $(i-1)$ and i we shall designate as $q_{i-1}(t) = \mathbf{q}(x_{i1},t)$. A difference between entering in a interval - i and leaving a interval - i of a thermal streams we shall designate as $\Delta q_i(t)=(q_{i-1}(t)-q_i(t))$. Let's consider, that the thermal stream $\mathbf{q}(x,t)$ everywhere, except for a discontinuity surface S, is continuous function. Hence we shall receive, that the quantity $\Delta q_i(t)$ is equal

$$\Delta q_i(t)=(q_{i-1}(t)-q_i(t)) = (\partial q_i(x,t)/\partial x) \, \Delta x + O(\Delta x) =$$
$$=(\partial q_i(x,t)/\partial x)c_0 \, \Delta t + O(\Delta t) \qquad (2.28)$$

In these designations the inflow of heat into a interval - $(n-1)$ to instants of time t_1, t_2 и t_3 will be accordingly equal

$$\Delta Q_{n-1}(t_1) = q_{n-2}(t_0) \, \Delta t \qquad (2.29)$$

$$\Delta Q_{n-1}(t_2)=\Delta Q_{n-1}(t_1)+q_{n-2}(t_1) \, \Delta t - \Delta q_{n-1}(t_1) \, \Delta t \quad (2.30)$$

$$\Delta Q_{n-1}(t_3)=\Delta Q_{n-1}(t_2)+q_{n-2}(t_2) \, \Delta t - \Delta q_{n-1}(t_2) \, \Delta t \quad (2.31)$$

By virtue of equality (2.28), we shall receive

$$\Delta Q_{n-1}(t_3) = q_{n-2}(t_0) \, \Delta t + O(\Delta t)^2 \qquad (2.32)$$

We shall consider now a dynamics of change of quantity of heat $\Delta Q_n(t)$, entered in a interval - n of a bar to instants t_1, t_2, t_3.

The discontinuity surface only has approached to the left-hand boundary of a interval n to an instant t_1, therefore $\Delta Q_n(t_1)=0$. The inflow of a thermal energy into a interval - n of a bar to an instant t_2 will be equal

$$\Delta Q_n(t_2) = q_{n-1}(t_1) \, \Delta t \qquad (2.33)$$

Taking into account, that the perturbations determined by boundary conditions to an instant t_3 have not time to influence on quantity of a thermal stream $q_{n-1}(t_2)$ entered into an interval - n, and also taking into account, that by virtue of boundary conditions we have $q_n(t) = 0$, and $\Delta q_n(t) = q_{n-1}(t)$,

405

we shall receive, that the inflow of warm into interval - n of a bar to an instant t_3 will be equal

$$\Delta Q_n(t_3) = q_{n-1}(t_1)\,\Delta t + q_{n-1}(t_2)\,\Delta t \qquad (2.34)$$

The assumption was made above that $q(x,t)$ is a continuous function, everywhere, except for a discontinuity surface, also the assumption was made above that on this surface value of the module of a thermal stream is rigorously plus $\|\mathbf{q}(x,t)\|_s \ge a_0 > 0$.

Taking into account, that the quantities Δt and Δx have one order, we shall receive, that the values $q_{n-2}(t_0)$, $q_{n-1}(t_1)$ and $q_{n-1}(t_2)$ is equal within of the order Δt. Therefore, by virtue of equality (2.34), we shall receive

$$\Delta Q_n(t_3) = 2q_{n-1}(t_0)\,\Delta t + O(\Delta t)^2 =$$
$$= 2q_{n-2}(t_0)\,\Delta t + O(\Delta t)^2 \qquad (2.35)$$

Taking into account, that $|q_{n-2}(t_0)|$ is rigorously more than zero ($|q_{n-2}(t_0)| \ge a_0 > 0$) also taking into account, of the asumption about a homogeneity of properties we shall receive

$$T_n(t_3) > T_{n-1}(t_3) \qquad (2.36)$$

where $T_n(t_3)$ and $T_{n-1}(t_3)$ is a value of temperature of the intervals $(n-1)$ and n of a bar in an instant t_3. However an inequality (2.36) contradicts to an inequality (2.27), and consequently contradicts the requirements of the laws of thermodynamics.

Thus, the solution of a heat conduction equation of a hyperbolic-type is physically incorrect. The reason of this incorrectness is a properties of hyperbolic-type equations. This properties is a disrupture of gradient of solution on boundary of an area of a perturbation and an unperturbed area.

Conclusions

1. The hypothesis on existence of local stationary process is formulated.
2. The concept of function of a local diversion of temperature is introduced.
3. The principle of a local directivity of heat transfer is formulated.
4. The restrictions, which are imposed on heat conduction equation, are derived.
5. It is shown, that usage of the hyperbolic-type equations is inadmissibility for mathematics simulation of processes of mathematical models of processes of propagation of thermal perturbations.

References

1. Sedov L.I. Mechanics of continua. (volume 1), Moscow, "Science", 1973.
2. Landau L.D., Lifshits E.M. Hydrodynamics. Moscow, "Science", 1986.
3. Germain P. Course of a mechanics of continuous mediums. (volume 1), Moscow, "Higher school", 1983.
4. Cattaneo C. " Sulla conduzione de calore ", Atti del Semin. Mat.e Fis. Univ. Modena 3,3.
5. Kuvyrkin G.N. Thermomechanics of a deformable solid body at high-intensively a loading. Moscow, " Publishing house MSTU", 1993.

82. A CONCEPT OF TURBULENCE

L.N. Pyatnitsky

Institute for High Temperatures of Russian Academy of Sciences,
13/19 Izhorskaya Str., 127412 Moscow, Russia

Abstract. The turbulence phenomenon is interpreted on the basis of linear theory of spherical wave layers. The flow hydrodynamic parameter pulsations form spatial-time structures resulted from superposition of the spherical waves, original and reflected from the flow boundaries. Such structures can be computed as deterministic, though they depend on many factors, and therefore look like chaotic. The simulation mechanism of turbulent processes are considered in the planar channel and tube of square cross section.

Introduction

Pulsations of flow hydrodynamic parameters arise when a laminar flow transits into a turbulent one. Since the time of Reynolds' well known experiment with fine jet dyed the pulsations have being considered as chaotic. The word turbulent itself comes from Latin 'turbulentus' which means disorder. This term has pre-determined renouncing the phenomenon mechanism search of, and promoted its description by statistical methods. At the same time, to estimate exchange processes within the flow quantitatively, turbulent transport coefficients were introduced. These are represented by expressions for molecular transport coefficients where the molecule free pathlength used to be formally substituted with intermixing path, not quite adequately determined value.

In the approach the pulsation origin is treated as the flow stability loss, or stability loss of the la-minar boundary layer, to be exact [1]. The conditions of the loss are defined by the method of weak perturbations. Even longitudinal pulsations of hydrodynamic parameters are employ as the perturbations. Now, here appears the contradiction in the approach to the turbulence phenomenon interpretation, by no means the only one: transverse pulsations are believed to be dominant in transport phenomena, however, their influence on the turbulence development is omitted. For all this, the problem of turbulence nature is left open.

In the paper the mechanism of formation of pulsations and the model of their structure is offered.

Processes accompanying gas flow in channels

The fluid motion is set in motion by compression waves which then compensate the flow friction at channel walls to support the motion. The drag leads to disturbance of hydrodynamic parameters. On the average the disturbance level depends on dynamical equilibrium between two processes: the drag which increases the structure non-uniformity, and wave emission which levels that.

The disturbances propagate in space as spherical wave packets. The problem about the propagation is solved on the basis of linear wave equation for potential f of velocity disturbance u ($u=$grad f) [1]. Here is the solution for fluid at rest, $V = 0$:

$$\phi = \frac{P\delta(r-ct)}{r}, \tag{1}$$

$\delta(ct-r)$ being Dirac-function, c – sound velocity, $u'c$, $P=$ const. It describes wavelet spherical surface of radius $r = ct$ with field which dies down while it runs away from the source point.

If the fluid is moving, the sphere surface can change its shape. The wave velocity is given by the known formula of $U = (\partial\omega(k)/\partial k)$, where $\omega(k)$ is the dispersion law which depends on the fluid velocity distribution, $V(r)$. Let the fluid move along with x axis of some flat channel, the height being $z=d$. Then the sound dispersion simple relation $\omega=ck$ should include the movement:

$$\omega = c\,k + V\,k. \tag{2}$$

Also, the wave surface propagation at the point of radius **r** is characterized by orientation in the direction of unit vector **s**, and this point trajectory changes in accordance with the equation [1]:

$$\frac{ds}{dl} = \frac{1}{c}[rot\mathbf{V}\times\mathbf{s}] \tag{3}$$

where $dl=c\,dt$ is an element of trajectory. When $V=$const, $U=ck/k+V$, the flow carries away the wave as total, and any of the point trajectories keeps its own original orientation.

Now, let the flow be profiled, $V=V(z)$, so that $V(z=0)=0$ and $dV/dz > 0$. As it follows from (3) the field $V(z)$ bends the point trajectory Total angle of the trajectory rotation can be found by

integrating (3) that gives for z component of s vector ($s_z = \cos\chi$):

$$\sin^2\chi \approx \sin^2\chi_0 - \frac{2V(z)}{c}\cos\chi_0\cos\varphi_0, \qquad (4)$$

where $\chi=\pi/2-\theta$, θ and φ are guiding angles, subscript "0" designates the initial vector s orientation. As equation (4) shows, the trajectory curvature depends on its orientation. For a wave point moving against the flow ($|\varphi_0|<\pi/2$) it recedes from the wall. otherwise ($\varphi_0 > \pi/2$) it comes nearer to the wall. Now, let us consider an example in Fig.1.
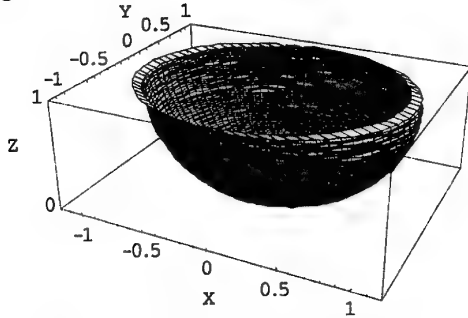

Fig.1. The disturbance wave shape in a flow

In Fig.1 the wave propagates in the flow with the velocity distribution $V=1.15\beta[z(1-z)]^{1/g}$, where $\beta=V/c=0.1$, $g=5$. The coordinates are expressed in the scale of height d, and the time scaled by d/c. Here is given the disturbance (1) at the moment $t=1$ after its onset on the upper wall.

As it can be seen from Fig.1, the wave keeps the hemisphere form almost everywhere, with the exception of some small height z^* nearby the wall. It corresponds to a 'ray' direction cornered χ_0^*, for which the wave front selvedge has horizontal s vector, and $\chi=0$. At the angles $\chi<0$ s vector bends to the wall. Accepting the equality $\chi=0$ for criterion of a whirlpool formation, and substituting $\chi=0$ into (4), we will have the condition of vortex generation:

$$\sin^2\chi_0^* \approx \frac{2V(x^*)}{c}\cos\chi_0 \cdot \cos\varphi_0. \qquad (5)$$

Condition (5) determines the ray inclination band, $\chi_0<\chi_0^*$, within which any ray moving off does not exceed the value z^*. The effect depends on Mach number, $M=V/c$. When $V/c \sim (z^*/d)^{1/2g}$ and, for example, $V/c\leq 0.2$, $g=5$, $\chi_0<20-30°$, then value z^*/d is confined to 0,05-0,07. Behold, with slowly growing function of $V(z)$ the vortices can not be successful shaped in limits

of $z \sim d$, just as in the case of V=const. The formula (5) makes it possible to estimate the disturbances layer thickness, caused by vortex making process. Notice, the disturbances in the direction along the wall form rings flying off at the velocity $c/\sin\theta$.

Superposition of these rings disturbs the drag field uniformity, and creates density local maxima of effective size a. When $r \gg a$, each of them tends to get a real spherical layer, independent of original disturbance shape. Let the shape be a half of a ball of diameter $2a$. Excessive density ρ distribution within the half-ball is the product of constant factor P by function f, $\rho=Pf$ ($r£a$). Then, in accordance with formula (1), the velocity u in arbitrary point r_n will be [2]:

$$\text{if } |r_n-t| > a,\, u = 0; \qquad (6)$$

$$\text{if } |r_n-t|\, £\, a,\; u = B(1-\alpha)^n f\left(\frac{r_n-t}{a}\right)\frac{r_n-t}{r}$$

Here n is a number of the wave reflections from the channel walls, α is coefficient of the wave reflection losses. The magnitudes scaled is used for the coordinate and time values. The factor $B=cP/2\rho_0$ is put equal to unity without generality breaking.

The reflection of these waves excites additional disturbances in the fluid structure at the wall. Indeed, while z-component of the pulsation velocity vanishes at the wall surface, $u_z=0$, the density fluctuations, accordingly, are growing. Moreover, as a result of interaction of falling and reflected waves the density pulsation amplitudes grow by two times together with simultaneous frequency twofold reduction [3]. The interaction creates the same ring disturbance moving with velocity $c/\sin\theta$. As well as above mentioned vortex formation the effects develop within the layer which height a is equal to half of the spherical wave thickness.

The features of the spherical wave propagation within narrow band of function $V(z)$ strong gradient let us interpret the region of height a nearby the wall as the boundary layer. Out of this region the function $V(z)$ grows slowly, and the velocity gradient becomes small. Therefore evaluating of the wave superposition within the flow core can be based, as the fist approximation, on the simplifying condition V=const, and const may can equal zero.

Wave propagation in channels

Structure of the disturbances depends on channel configuration. In simple cases such a channel can be represented by free space above

408

plane surface (the case of usual plate), or the planar gap confined by two plane surfaces, or internal cavity of a tube. The disturbance structure above the plate seems rather evident and can be easily computed with the help of (6). Somewhat more complicated problems happen to deal with when the reflected waves should be taken into account. Therefore we begins with the channel in the form of the gap with distance d between the two plane walls.

Let x-y axes be placed at the lower wall, and z axis directed to the upper one. It is reasonable to take the channel height d as a scale value for outlining channel processes with non-dimensional parameters. Expressing position of some point within the channel volume in scaled units we will use the former designations for x, y, z coordinates. For the process chronology, t, we employ ratio d/c as the time unit for the scaling. Due to the accepted scale values the wave propagation can be written in the very simple form: $r = t$.

With the non-dimensional parameters the place and time of the disturbance origin will be pointed out by the parameters $pr = \{px, py, pz\}$ and pt.

In the case of many disturbances the values of pr and $p\tau$ represent sequences of parameters. The parameter pz can have only two meanings, 0 (at the lower wall) or 1 (at the upper wall).

Without taking into account the reflections, and with $z > 0$ a wave originating in a point pr should move in accordance with equation $r = t - pt$ in the coordinate system. In the channel, $0 > z > 1$, the reflections deform the wave. As a result of n reflections the wave configuration $\{x, y, z\}$ relatively to zero of coordinate system can be described with the following equations:

$$t + pt < 0: \qquad + pt > 0:$$
$$x = px \qquad x = (t - pt)\sin\vartheta \cos\varphi + px$$
$$y = py \qquad y = (t - pt)\sin\vartheta \sin\varphi + py \qquad (7)$$
$$z = pz \qquad z = \{(t - pt)\cos\vartheta -$$
$$- 2IP\left[\frac{n+1}{2}\right]\}(-1)^{n+pz} + pz$$

IP operation means taking integer value of the number in the brackets, n is the quantity of wave reflections from wall (integer positive number):

$$n = IP[(t - pt)\cos\vartheta]. \qquad (8)$$

We will find the surface of wave front, a sort of snapshot, which it takes through time of $t = 6.5$ after onset. The channel volume explored are limited by dimensions: $x_2 - x_1 = y_2 - y_1 = 8$, and initial

parameters have meanings: $pt = 0$, $px = 1.2$, $py = 3$, $pz = 1$ (the initial point is on the upper wall). Equations (7) and (8) are computed for angle φ in the range from 0 to 2π, and for the angle θ from 0 to $\pi/2$. The configuration under calculation is shown in Fig.2a where z values has been multiplied by factor 2 for convenience of perception.

The front has corrugating surface with variable distance between the edges and changing orientation of normal to the surface of folds. As it can be seen from Fig.2, the propagation in the channel of the only wave creates such a structure in which the its origin simple law can not be realized at once. Still more clearly the structure formation process is seen in Fig.2b, where two waves propagate in the same channel volume. One of them corresponds to conditions of Fig.2a, the other to the parameters: $pt = 0$, $px = 6$, $py = 7.3$, $pz = 1$, $t = 7.5$.

Finally, Fig.2c demonstrates the superposition structure of eight waves which initial parameters change by chance in the ranges: $px \in [0.2, 15.9]$, $py \in [0.1, 9.9]$, $pz = \{0, 1\}$, $pt \in [0, 3.1]$. In order to descry the structure details, Fig.2c shows not the whole studied channel volume, but only a strip of width $x \in [4.5, 5.5]$ (the diagram scale value is increased twice). It is already possible to conceive structure nature of disturbances looking at the superposition picture of eight waves.

Fig.2 displays the wave configurations in the tube of square cross-section 1×1 (non-dimensional values) as well to compare structures in channels of different profiles. Fig.2d hows the wave tconfiguration in $t = 2$ after its onset at the bottom wall at the point $\{px, py, pz\} = \{2, 0.6, 0\}$. As expected, the spherical wavefront is deformed in tube much faster than in the planar gap. So that the structure in Fig.2d looks irregular as a result of only two reflection cycles of a mere wave.

It is impossible to distinguish any details in 3D image configuration with eight waves included into the process. Therefore, in Fig.2e the configuration is shown for shot time and small initiation period($t = 0.3$, $pt \leq 1$). As to developed stage of superposition, it is shown in Fig.2f only in tube cross-section of $x = 4$. In these examples of one and two waves, $k = 1$ or $k = 2$, the initial parameters of the perturbations are chosen simply from visual clearness, whereas with $k = 8$ these are set by the law of random numbers.

It is seen from Fig.2, how transient structure appears, and that size and shape of its cells have rather complex distributions. This explains, why the picture of pulsations looks chaotic. Also, there can get full explanation on the basis the intermittence phenomenon which usually is put down to boundary layer instabilities.
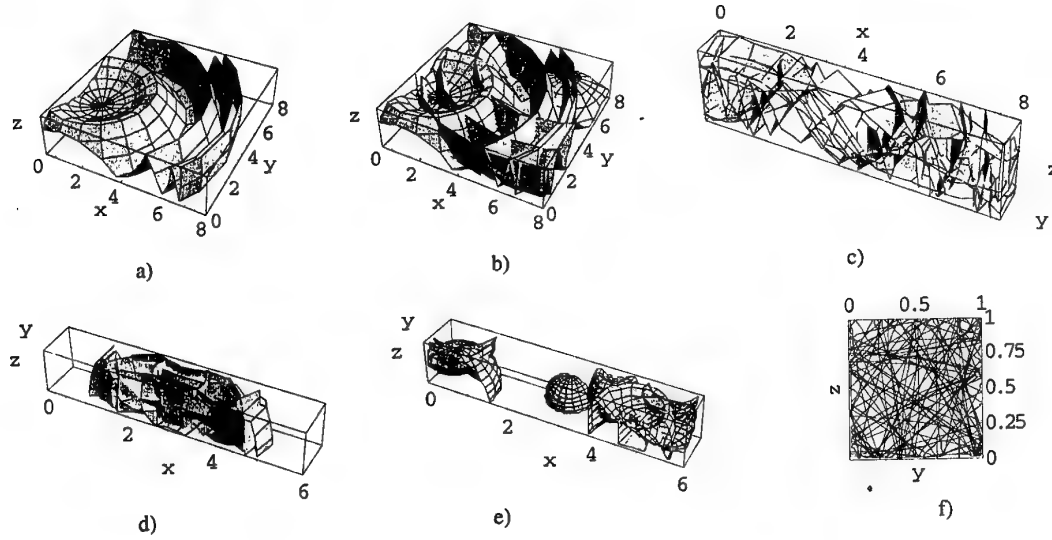
409

Fig.2. Wave configurations in the channels: plane channel – one wave (*a*), two (*b*) and eight (*c*) waves; tube – one wave, *t*=2.1 (*d*); eight waves: *t*=0.3 (*e*) and *t*=3 (*f*)

Parameter fluctuations in flow core

The parameter disturbances can be presented as consecutive passages of spherical waves through imaginary points which are looking-glass reflections of the observation real point in the walls. The transition from one such an image to the next occurs just after each reflection at one of the walls. That is accompanied by the image coordinate, *z*, increase which equal double altitude of the channel, 2*d*.

Let r_n (ξ,η, $ζ_n$) be the distance from wave onset *pr* to n^{th} imaginary point. Therein pulsations arise under the condition $|r_n{-}r| < a$, where *r* is the current radius of the spherical wave in free space. Coordinates ξ, η, ζ can be represented as functions of observation point position, *x*, *y*, *z*, in its associated reference system:

$$ξ = x - px \; ; \; η = y - py \; ;$$

$$ζ_n = 2 \; IP\left[\frac{n+1}{2}\right](-1)^{pz} + (z{-}pz)(-1)^n \; ; \qquad (9)$$

$$r_n = \sqrt{ξ^2 + η^2 + ζ_n^2} \; .$$

Formula (9) together with (6) and (8) just give the desired dependence of *u*(*x*,*y*,*z*,*t*) for alone wave. But it is necessary to set still inceptive conditions.

As an example, the original parameters are given in the following list.

$$a = 0.1; \; α = 0.1; \; f = \cos(\frac{π}{2}\frac{r-(t-pt)}{a});$$

$$\{x_1,x_2; \; y_1,y_2; \; z_1/z_2\} = \{0,20; \; 0,20; \; 0/1\]; \qquad (10)$$

$$\{x,y,z\} = \{10, \; 10, \; 0.7\}; \; N = 2000;$$

$$k = 100; \; τ = 10; \; n = 10; \; T = 50; \; t \text{IJ}[30,50].$$

It includes: the original disturbane radius *a*, losses coefficient α, kind of function *f*(*r*,*t*), point of observation {*x*,*y*,*z*}, number of resolved elements *N*, number of waves *k*, a wave lifetime τ, number of reflections considered *n*, process duration *T*, and the time interval *t* during which the searching is on, in our case it is state of dynamic equilibrium.

Time dependence of the pulsations in the field of many waves is computed by artless summing up the contributions of individual waves. But thereto the order of their arising should be set, in other words, the parameters *px*, *py*, *pz*, *pt*. are needed for that. Sequences *pr* with random and fixed distributions make real practical meaning [3]. In its turn, time moments *pt* can be represented by random and periodical (or quasi-periodical) sequences for various series of *pr*.

The pulsation spatial characteristics are found out in a similar way, however, with somewhat different entry conditions. Some parameters for determining spatial characteristics are given in the list:

410

$\{x_1, x_2; y_1, y_2; z_1/z_2\} = \{0,40; 0,40; 0/1\};$

$x∪[10,30]; \{y,z\}=\{10, 10, 0.7\};$ (11)

$N=2000; k=200; \tau=10; n=10; T=50; t=50.$

To obtain the comparable circs, in (11) the effects at the ends should be taken into account. Each of the techniques have its own peculiarities which follow. In the first of them we do fix observation place, $\{x,y,z\}$, and the parameter t varies within chosen limits in one way or another. Vice verca, to get spatial characteristics along some line or contour it is the time moment t that is fixed, and vector r stands as a variable parameter which follows the path (line or counter) of interest. In this case spatial frequency μ becomes an argument of the spectrum, and it is expressed in pulsation number per non-dimensional length in given direction.

Dependence $u(t)$ at the conditions (10), its spectrum being $A(\nu)$, and dependence $u(x)$ at the conditions (11), the spectrum being $A(\mu)$, are presented accordingly in Fig.3 and Fig.4. The graphics show functions u and spectra A for three various kinds of the disturbance sequences given by parameter set $\{px,py,pz,pt\}$. In Fig.3a, 4a sequences $\{pr,pt\}$ are entirely based on random distributions for intervals $\{r_1,r_2\}$, $\{0,T\}$. In graphics Fig.3b, 4b series pr has five fixed periodical points, whereas values pt are random. In Fig.3c, 4c series pr and pt are fixed and periodical.

In examined frequency band up to $\nu=\mu=50$ the spectra contain harmonic progression depending on distribution $f(r)$. As their amplitudes decreases quickly, the spectra are shown only in the frequencies range up to $\nu=\mu\sim15$, where the first and second harmonics are situated. The first is analysed here. Note, that the spectral density of oscillations depends on the sequence features of the initial parameters pr and pt.

When disturbances are of random distribution, one can distinguish several bands in the spectra, which contain sharp maxima [3]. The first such appreciable maximum has frequency 2 that corresponds to mean rate of the disturbance origins. One more maximum of large amplitude at frequency 3.5 coincides with the spatial mean frequency of the disturbances placing. But the outline of spectra $A[u(t)]$ falls to frequency 5 which is immediately associated with the breadth of the spherical layer, $1/2a$, above accepted. This frequency is present in spectra $A[u(x)]$ as well, though sometimes not so evidently owing to their specific [4].

For the sequences regulated partly (fig.3b, 4b) the harmonics half-width gets more narrow, and contrast of of individual lines grows. In the case of waves being well ordered (Fig.3c, 4c) spectra consist practically only of separate lines. There are 23 lines in the spectra in all. Mean frequency difference between the neighbouring is 0.4. It seems to be equal to the frequency with which the set of 5 disturbances arises.

It is seen from the plots of Fig.3, 4 that as far the disturbance sequence is ordering, the spectral lines are getting sharper, and contrast is growing. These consequences might be useful for preliminary estimation of the pulsation field development and in its structure modeling, as well as for express analysis of turbulent processes.

It is worth to emphasize, that the developed approach to the problem of the turbulence nature allows to extend pulsation mechanism to structure exploration of disturbances arising in some other conditions. For example, the disturbances might appear not due to friction at the wall, but as a result of laser radiation absorption by targets like gases, liquids, solids, or plasmas.
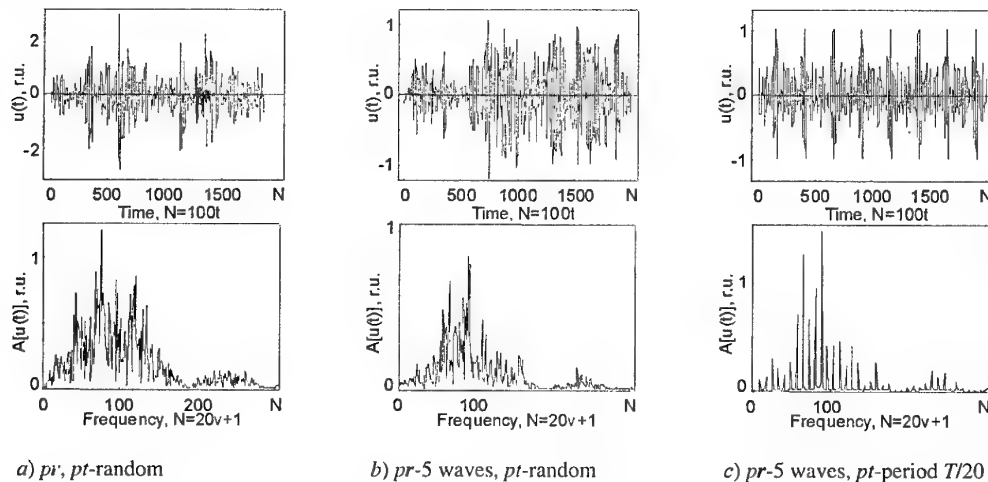

a) pr, pt-random   b) pr-5 waves, pt-random   c) pr-5 waves, pt-period $T/20$

Fig.3. Velocity pulsations at $x = y = 10$, $z = 0.7$ within $t \in [30,60]$

411

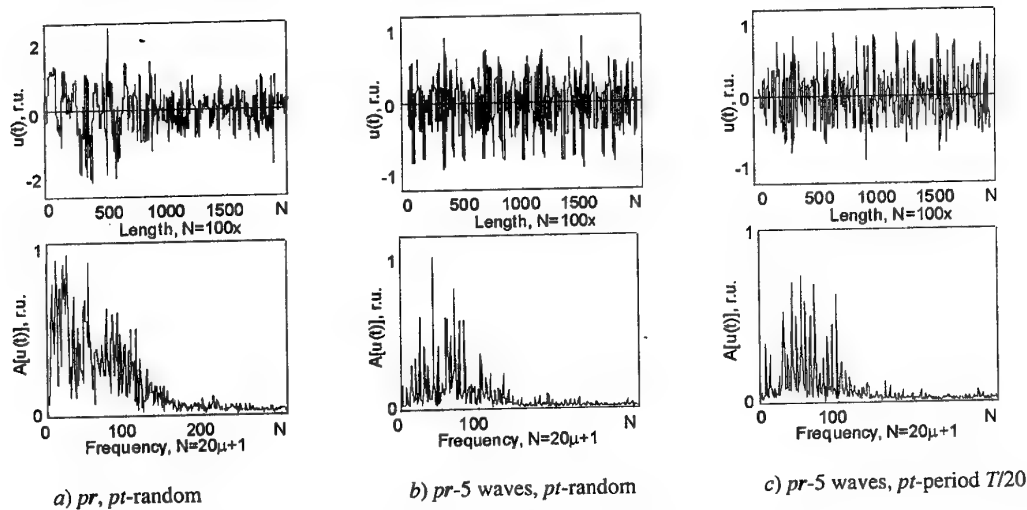*a) pr, pt*-random   *b) pr*-5 waves, *pt*-random   *c) pr*-5 waves, *pt*-period $T/20$

Fig.4. Velocity pulsation distributions along x IJ [10,20] at $y = 10$, $z = 0.7$, $t = 50$

Pulsation structure in a plasma channel

The plasma channel was created by laser impulse ($\lambda=1.06\mu m$, $E=0.6J$, $\tau=100ps$ [5]) in the beam with Besselian as the radial profile [6]. The beam had the length 1.5cm and diameter of Besselian central part $2r_b\sim2.7\mu m$. The channel interferogram (probe radiation $\lambda=0.53\mu m$ [5]) made at the middle of the beam along the length $512\mu m$ is shown in Fig.5 where figures mark the numbers of CCD-camera pixels, each of $1.6\mu m$. The channel is obtained with target of N_2O (pressure 500Torr) in 250ps after the heating pulse starts. By the moment of the snapshot the channel diameter has reached $2R=41.0\mu m$.

The power source of the channel formation is the field of Bessel beam which has a structure [6]. is specified by rings of Bessel function in the radial direction. The zeroes of the function divide the beam into coaxial cylinders which radii r_i are set by the criteria: $kr_i \sin\gamma=2.40$; 5.52; 8.65; … . Here k is wave number, γ – the angle at which the heating radiation rays fall onto symmetry axis x. With the scaling factor R these radii $a_i=r_i/R$ equal $a=0.063$, 0.145, 0.227,… . Along with axis x the field can be characterized by periodic sequence of maxima separated by interval $l=2\lambda/\sin^2\gamma$ [6]. For the channel shown in Fig.5 $l\approx21\mu m$.

It is rather difficult to get information on the data in immediate measurement. At the same time, it is possible to suggest that the gas breakdown in Bessel beam is dispersed among these maxima. Then, therein optical microdischarges beget nascent centers of the disturbances which quantity k should be about not more than 24–25. In the beam cross section such

disturbances might be confined by Bessel function zeroes have, e.g. radius of the function central part, a_0, or of one of mentioned above rings, a_1, a_2, etc.

The interferograms in Fig.5 has strips (fringes) of equal inclination. A shift δ of a strip is proportional to plasma density change ρ. In the window sight of CCD-camera falls 56 strips. Accepting them for the elements of resolution gives 56 values of distribution $\delta(x)$ which, in its turn, describes discrete distribution of function $\rho(x)$ and, in the end, the structure of disturbances in the channel.

On bottom left diagram in Fig.5 the bold curve (marked 'Experiment') presents distribution $\delta(x)$. It has been measured along the line collinear with axis x, but $r^*/R=1/2$ distant from it. Values of x and δ are scaled by h, the distance between the neighbouring strips, and $N=x/h$ is the strip number. The spectrum (bold curve on right bottom diagram of Fig.5.) is given as ratio to its maximum, just the same as all the other functions in Fig.5, frequency μ is in pulsations per the strip step.

The problem consists in determination of dimensions of the microdischarges and their location along the axis x. Developed model can be used for the purpose. However, it is necessary to look for initial parameters of using properties of pulsations known from experimental measurements. This implies the inverse problem which can be solved, in this case, by means of sorting out answers with varying initial parameter sets for the disturbances. In addition to that, there are some distinctions in conditions of process development.

In searching the plasma channel we deal with the process at unsteady stage, when the very first waves are just creating the channel. It means
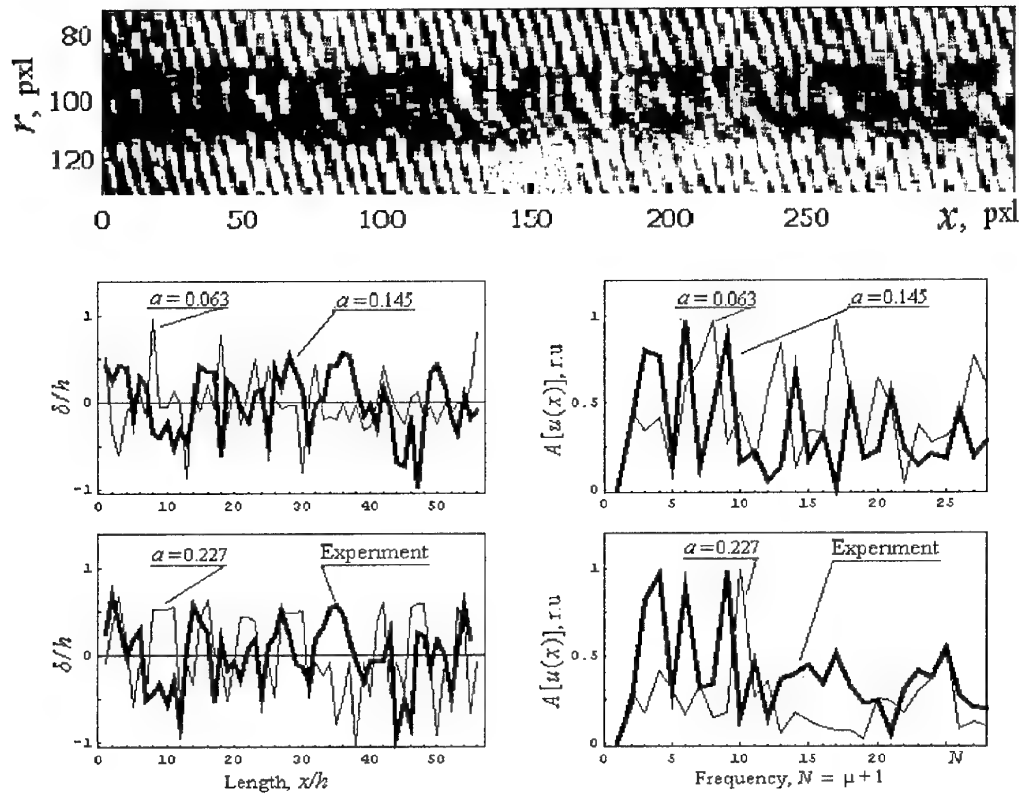
412

Fig.5. Density pulsations in plasma channel

there is no need to take into account reflected waves, and hence the structure can be characterized by parameter $T=1$. In former model parameters pr were placed at the walls, whereas in plasma channel the disturbances arise at the axis of cylinder. So, the process geometry can generally be described with two parameters – axial, x, and radial, r, (scaled by channel radius R).

On the other hand, the picture of the strip shifts appear as a achordwise average of the cylindrical channel. For the chord at the level of $r^*=1/2$ a point y of integration runs the path from – r^*tgφ to r^*tgφ, where φ is azimuthal angle. The summing over the length y of the chord has to include all the disturbances that arise at points pxIJ$[x_1,x_2]$ during laser radiation pulse, t_0, in the moments of pt.

The properties of Bessel beam allow to compile alternative conditions for initial parameters. One of the alternatives is given in list (12). Therein equable sequence px and three versions of radius a meaning are assumed.. Also, it is accepted that the disturbances appear in random sequence pt within halfwidth of laser pulse of $t_0=0.4$, which is expressed in scale of the channel lifetime, 250ps.

$a = 0.063, 0.145, 0.227$ $f(r)=1$; $k=25$;

$$\{x_1,x_2;\ y_1,y_2\} = \{-1;56;0;0.5\cdot\tan[\pi/3]\}; \qquad (12)$$

$T=1$; $t_0=0.4$; $\varepsilon=1$; $m=11$; $Q=1$; $q=0$; $\theta=0$

Apart from previously mentioned data, there are indicated in the list: function kind of parameter distribution in microdischarge $f(r)$, total quantity of disturbances k (taking into account effects at the channel ends for $T=1$), dimensions of the channel under investigation $\{x_1,x_2;\ y_1,y_2\}$, duration of structure development T, duration t_0 of heating radiation, the radiation active part ε, quantity of elements of summing up along half of the chord m, displacement Q of sequence px as a whole system, range q of random deviations of coordinates px in the case of breaking their strong periodicity, and the range of delay difference θ in moments pt at different parts of sequence px.

Results of the calculations for density fluctuations are shown in graphics of Fig.5 on the left, and the related spectra are on the right. Comparison of experimental and theoretical data on the pulsation structures reveals, it is only the case of $a=0.145$ which ratings look like the measured

413

ones. Indeed, the structure scale of pulsations for $a=0.063$ is too small to outline the data measured, whereas in case of $a=0.227$ the scale is found to be too large.

In connection with the result new computations have been made for $a=0.145$ model to define more precisely some parameters in list (12). There were varied this time: kind of function total $f(r)$, total quantity of disturbances k, duration of heating radiation being effective ε, the displacement Q of the whole sequence px with regard to CCD-camera matrix, the range of random deviation q at various point of sequence px. Bessel beam wave front runs all the channel length during about $t=0.01$ (less than 2ps), that is why delay θ was not available.

As a result the best accordance with measurements was achieved with the parameter values that follow: $a=0.145$; $k=25$; $t=0.2$; $Q=0,17$; $q=0$; $f(r)=1$. As the data say, the disturbances appear within second ring of Bessel function(radius 3µm) during laser pulse which real efficiency is restricted by $\varepsilon=0.2$ (i.e. 50ps instead of 100ps). Microdischarges situate regularly, the period being equal 21µm , and deviations from the periodicity do not exceed several percents.

Conclusion

For steady turbulent flow the hydrodynamic parameters are integral values which magnitudes do not depend on time. So that their distributions correspond to the solution of stationary hydrodynamic equation system. On the contrary, pulsations remain explicit functions of time in any case. In relation to the pulsations the steady state of turbulent flow denotes only the dynamic equilibrium. As it has been shown, that parameter pulsations can be interpreted on the basis of linear propagation of spherical wave layers and their superposition. The waves origin as disturbances at a channel walls in the process of vortex formation and the wave reflections as well.

References

1. Landau L.D., Lifsjitz E.M. Course of Theor. Physics. V.6. Pergamon Press, N-Y. 1987.
2. Pyatnitsky L.N. Sov.Phys. JETF. (Am. Inst. of Phys.). V.86, pp.107-114 (1998)].
3. Pyatnitsky L.N. Sov.Phys. JETF. (Am. Inst. of Phys.). V.92, pp.576-593 (2001).
4. Pyatnitsky L.N., Physics of Vibrations (Moscow). V.8, pp.185-207 (2000)]
5. Clark R.,. Milchberg H.M. Phys. Rev. E. V.57, pp.3417-3423 (1998).
6. Andreev N.E., Aristov Yu.A., Polonsky L.Ya., Pyatnitsky L.N. Sov.Phys. JETF. (Am.Inst. of Phys.). V.73 (6), pp.969-975 (1991).

83. ACOUSTIC WAVE-GUIDING WITHOUT HARDWARE

L.N. Pyatnitsky

Institute for High Temperatures of Russian Academy of Sciences,
13/19 Izhorskaya Str., 127412 Moscow, Russia

Abstract. Reflection of an acoustic wave by concave conical surface forms plane intensive wave at the symmetry axis, which field radial profile looks like Besselian of zero index. This profile shape persists downstream, and the wave propagates along with the extended focal length of the cone as if it is confined to an acoustic wave-guide. Therein slanting energy supply stands for the wave-guide wall. The wave reflected by conical surface with base helix line propagates as if it is confined to a hollow wave-guide, the radial profile looking like Besselian of index $m > 0$.

Introduction

Extreme, or simply high, parameters of substance states provide for energy strong concentration. They used to explore the states by means of shock waves. Such a wave is some abrupt jump of pressure from p_1 to p_2. The wave bringing the concentration with it is characterized by the pressure ratio p_2/p_1.

The shock tube in which the wave is created comprises two chambers, of low pressure p_1 and high pressure p_2. The former serves as a wave-guide for the wave propagation. The latter volume determines the length of compressed gas following the pressure jump.

Ratio p_2/p_1 can reach the magnitudes at the level of 10^3-10^4 in modern practice of the experiment. However such parameters in shock tubes can only be achieved in the case of very low pressure p_1 in the wave-guide. In addition, there are required firm high-grade optical glasses and their air-tight mounting in wave-guide that restrict dimensions of window for visualization the processes under investigation.

As it has been shown in [1], there exist wave equation accurate solutions describing wave beams in free space, that do not diverge. These solutions have no singularities, like for plane wave, and are characterized by the finite intensity. In the case of axial symmetry the wave field distribution in some cross section looks like Bessel function and is permanently reproduced in following cross sections. Experimental confirmations of such kind wave propagation of electromagnetic radiation in visible and others ranges can be seen elsewhere (see e.g. [2]).

With this background a focalizing manner of acoustic packages can be elaborated to concentrate wave energy within a 'wave-guide' however without hardware. In this way that low pressure p_1 is not limited, as well as window of observation.

Method of focalization

Let us consider such focalization with an example of the acoustic package harmonic component at frequency $\omega=2\pi c/\lambda$, the phase front being originally planar. Here c is the sound velocity and λ is the wavelength of the harmonic under consideration. In real embodying of the method the wave front can not have infinite aperture. Hence, it has to be restricted by the diameter $2R_0$, which restriction should, as it is common in diffraction theory, be added with the complementary condition $R_0>>\lambda$. Wave field is convenient in further analysis to outline using potential f of the velocity u in wave packet, introduced according $u=\text{grad}\phi$ [3]. As a matter of fact, any of the hydrodynamic parameters in the wave is easily expressed through ϕ.

Let some reflecting surface in the form of a concave circular right cone be placed in the way of the wave front propagation. The cone shape has the base angle α ($\alpha<<1$), the diameter of the directrix circular line, $2R_0>>\lambda$, and rectilinear generatrix which is described by equation $\zeta=R\,\text{tg}\alpha$. Configuration of the system designed is illustrated in Fig.1. Obviously, the incident plane wave field is concentrated round about and along with the symmetry axis z.

Combining the origin of coordinates with the top point of the cone, we can find the coordinate z at which the wave 'beam' reflected from the mirror at point of radius R crosses the symmetry axis, and all the cone focal length L (focal segment) as well:

$$z = \frac{R}{\sin 2\alpha} , \quad L = \frac{R_0}{\sin 2\alpha} \tag{1}$$

The wave field in the vicinity of the focal segment is described by the wave equation:

$$\frac{\partial^2\phi}{\partial t^2} - c^2\Delta\phi = 0 \tag{2}$$
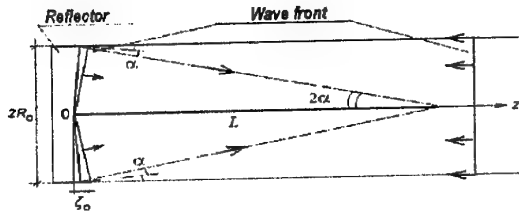
415

Fig.1. Scheme of wave-guide focal setting

As it is well known, the equation admits the factorization of its solution, and we can separate it into coordinate- and time-dependant parts to write:

$$\phi(r,z,t) = \mathrm{Re}\{f(r,z)\exp[i(kz - \omega t)]\},\qquad (3)$$

where $k=\omega/c$ is modulus of wave vector, $f(r, z)$ is the wave complex amplitude. At the time moment $t=0$ and at the coordinate $z=0$ the reflected wave can be represented as ($\alpha \ll 1$):

$$f(r,z=0) = F(R)\exp(-ik\,r\sin 2\alpha),\qquad (4)$$

where $F(R \leq R_0)$ is radial profile of the incident wave acoustic field.

Function $f(r,z,t)$ changes along the axis z rather slowly. Therefore, the derivative $\partial^2 f/\partial z^2$ can be neglected, and the substitution of dependence (3) into wave equation (2) gives for stationary distribution of the cylindrically symmetric field:

$$2ik\frac{\partial f}{\partial z} + \frac{1}{r}\frac{\partial}{\partial r}\left(r\frac{\partial f}{\partial r}\right) = 0 \qquad (5)$$

In the vicinity of axis z, $r< z\sin 2\alpha$, $r < \sqrt{z/k}$, and along the main part of the focal length $z \gg \lambda/\sin^2\alpha$, with the accuracy to small item of the order of $r/2R$ the solution (5) and (4) can be presented as the following expression [4]:

$$f(r,z) \approx f_0(z)J_0(kr\sin 2\alpha +$$
$$+ f_1(z)\exp\left(\frac{ikz(R^2 + r^2)}{2z}\right)J_0\left(\frac{kR_0 r}{z}\right),\qquad (6)$$

where $J_0(x)$ is Bessel function of the first kind and zero index,

$$f_0(z) = \sqrt{2\pi kz}\,\sin(2\alpha)F(z\sin 2\alpha)\times$$
$$\times\exp\left(-i(kz/2)\sin^2 2\alpha + \pi/4\right)\qquad (7)$$

and

$$f_1(z) \approx \frac{F(R_0)}{1 - z/L}\exp(-ikR_0\sin 2\alpha)$$

Existence of the second item with amplitude $f_1(z)$ in expression (6) is obliged to the wave finite aperture. Accordingly, it describes the wave diffraction at the boundary of reflecting mirror. It means that the second item contribution to the sum total becomes noticeable only near the end of the focal length, when $z \to L$. Analysis shows, that condition $|f_1|/|f_0| \geq 1$ is getting valid, if value z begins to satisfy the requirement of of $(L-z)/\lambda \geq 10$. In this case the intensity of the acoustic field of the wave can be approximated to assume ery simple expression:

$$|f(r,z)|^2 = |f_0|^2|J_0(x)|^2,\qquad (8)$$

in which the radial distribution of intensity is specified by the Bessel function $J_0(x)$ with the argument equal to $x=kr\sin 2\alpha$, and where the axial distribution is described by the dependence

$$|f_0|^2 = 2\pi kz\sin^2(2\alpha)F^2(z\sin 2\alpha).\qquad (9)$$

Axial intensity distribution

In accordance with (8), maximums of the radial distribution of the intensity acquire configuration of a set of coaxial cylinders with the length of $\sim L$. The cylinders have diameters practically independent of coordinate z. Thus, this kind of reflection leads to the acoustic wave formation, plane front of which does not diverge, and propagates in free space as if the process occurs in some solid wave-guide.

In this situation the role of the wave-guide fulfils the side energy supply to z-axis, thereof arrangement being similar to well known configuration of Mach reflection. It is worth to note, that the wave front propagates along the-symmetry axis at the speed, $c_z=c/\cos 2\alpha$, which exceeds the sound velocity.

Efficiency of the intensity concentration can be introduced for given profile $F(R)$ as evident ratio $b=|f_0^2/F^2$. If, for example, profile $F(R)$ has rectangular distribution, then the intensity of the wave focused at axial point, $r=0$, $z=R/\sin 2\alpha$, exceeds the corresponding value of incident wave at conjugated point R by $b=4\rho^2 (R/l)\sin 2\alpha$ times. For $R=100$cm, $l=0.1$cm, $\alpha=5°$ the efficiency value averaged over focal length L makes up approximately $b\approx 3\cdot 10^3$.

Now, let us consider the intensity distribution along the axis of z. First of all,

416

according expression (1) the length of L is not dependent on wavelength λ, and it is limited only by technical parameters of experiment. Furthermore, it follows from (9), that the axial distribution $f_0|^2$ reproduces the incident wave intensity profile $F^2(R=z\sin 2\alpha)$ with coefficient (see (7)) that linearly grows with z. Therefore, in contrast to real wave-guiding, in the case under consideration axial intensity distribution $f_0|^2$ does not leave constant, generally. On the other hand, it can be controlled by changing intensity radial profile in the incident wave.

Practically, however, varying the intensity profile of incident wave seems to represents technically rather the difficult problem. Much more easier to vary the surface shape of reflecting cone, using a generatrix with variable angle $\alpha(R)$ instead of rectilinear generatrix (α=const). With generatrix curved the magnitude of coordinate ζ depends on radius R as $\zeta \int\limits_{0}^{R} tg\alpha(R)dR$.

Necessary kind of that dependence $\zeta(R,\alpha)$ which is needed to construct the axial distribution $|f_0|^2$ expected is evidently defined by the profile of $F^2(R)$. Among others, the distribution f_0^2 at the symmetry axis, which does not depend on z value, corresponds to logarithmic generatrix. For small angles α it has the simple form: $\zeta=\alpha_0 R \ln(R_0/R)$, where $\alpha_0=\alpha(R_0)$.

Some opportunities of controlling the axial intensity distributions will be demonstrated for dependence of coefficient $b(z, r=0)$ on kind of profile $F^2(R)$ and on the configuration of generatrix $\xi(R,\alpha)$. The profiles F^2 are assumed to be some function of Gaussian type, $F^2 \sim \exp[-2(R/R_0)^{2n}]$. To compare distributions $b(z, r=0)$ having with various n and different generatrices $\zeta(R,\alpha)$ the dependences b were normalized to the same value of incident wave power, which is proportional to integral $\int\limits_{0}^{R_0} F^2(R,n)RdR$. The results are shown in Fig.2, where the dependences are presented as the ratio of $b(z, r=0)$ to its maximal value for rectangular profile $F^2(R)$ ($n=\infty$) at $z=L$ set equal 10.

Graphs 1–3 in Fig.2 correspond to rectilinear generatrix, to angle $\alpha=5°$ and numbers of $n=1$, 5, ∞. As it is seen from the diagram, gaussian profile of the incident wave intensity (curve 1, $n=1$) forms the maximum of axial distribution at $z=\frac{1}{2}L$. With gypergaussian as the distribution (curve 2, $n=5$) this maximum falls onto $z \Box 0.7L$. Finally, in case of rectangular profile of the wave field (curve 3, $n=\infty$) the intensity of

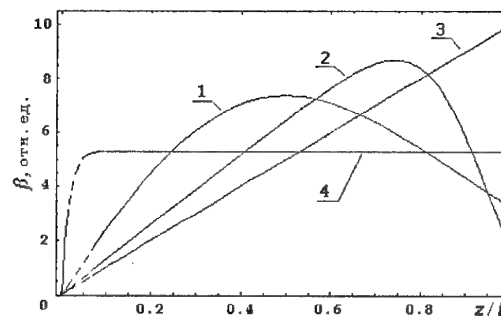focused wave grows linearly, and reaches maximum at the end of focal length, at $z=L$.

Fig.2. Intensity axial distributions

The dependence 4 in Fig.2 relates to the logarithmic generatrix of the reflecting conoidal surface with angle $\alpha_0=5°$. It is built only for number $n=\infty$, because some maximums in distribution of $b(r=0, z)$ appear in the case of other values of n. It requires additional corrections of the reflecting surface to smooth out the maximums.

Intensity radial distribution

Until now the consideration has dealt with the reflecting conical surface thereof base line is the circumference. Another kind of the line might be chosen as the base as well. It may be, for example, helix line of radius R^* which gradually grows with the polar angle to increase for quantity m of wavelength λ while one turn, $R^*=R_0(1+m\lambda)$. (Numerous other kinds of the reflecting surface give combinations of Bessel functions, which can not be considered here.)

Reflection of the wave by such a cone with linear generatrix deflects the rays of the wave propagation in the direction of azimuth for angle φ. As a result of such angular shift there appears some addition in expression for potential (3). To the radial transformation depending on argument $kr\sin 2\alpha$, should be added angular transformation, connected with variable phase $m\varphi$ of the wave.

It can be shown [5], that taking the azimuthal dependence into consideration in wave equation (2) will bring some small modifications of equation (5) and of condition (4) as well. For instance, the condition (4) will now have the following form:

$$f_\varphi(r,\varphi,z=0) = F(r)\exp[i(m\varphi - kr\sin 2\alpha)] \qquad (10)$$

The equation (5) new version and condition (10) have the solution which, with just

417

the same restrictions as for (6), changes and can now be presented in the form:

$$\left| f_\varphi(r,z,m) \right|^2 \cong \left| f_0 \right|^2 \left| J_m(x) \right|^2 , \qquad (11)$$

where $J_m(x)$ is Bessel function of the first kind with index m, $x = kr \sin 2\alpha$, and $|f_0|^2$ is the intensity axial distribution which is described, as before, by (9).

Accordingly, all above mentioned attributes of the axial distribution are true in the case of the helix base line as well. These include the transformation of $F(R)$ into $f_0(z)$, linear growth of the transformation factor, the restrictions on formula (11) application at the very extreme parts of the focal length.

However, the radial distributions circumscribed in (6) and (11) are quite different indeed. For their comparison distributions $|f(r, z=\text{const})|^2$ and $|f_\varphi(m=5)|^2$ scaled by $|f(r=0, z=\text{const})|^2$ are represented in Fig.3 for the same profile $F^2(R)$ and equal values of parameters k, α and z.

Diagrams in Fig.3 show, that in the case of linear circular cone the intensity main maximum is sited at the symmetry axis within the circle of very small radius a. The intensity main maximum for cone with helix base line is situated within narrow ring, the radii of its inner and outer boundaris being b_{in} and b_{ex} with mean value b. Inside this ring, $r < b_{in}$, the intensity goes down to zero.

Along the focal length these maximums form, accordingly, solid cylinder of radius a and hollow of mean radius b. With focalization parameters from the above example dimensions of the two configurations can be computed. The cylinder diameters are: $2a = 4.5$mm, $2b = 23.5$mm, and $(b_{ex} - b_{in}) \approx 5$mm. At the same time, each of them has the length $L \approx 5.8$m.
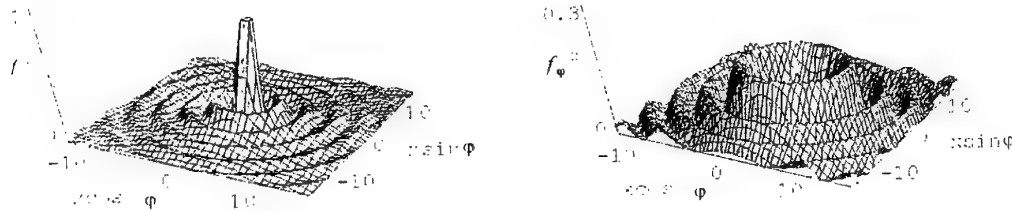

Fig.3. Intensity radial distributions

Conclusion

The conical focalization creates the plane wave of enhanced intensity, which propagates through peculiar wave-guide that has no walls. In such a wave-guide the simple wave can easily turn into the shock wave in accordance with Hugoniot mechanism. But the shock wave can be used from the very beginning, as the incident acoustic pulse. In this case there arises around axis z Mach reflection configuration with axial symmetry.

In the above consideration there were introduced no restrictions on initial pressure of gas, as well as on kind of medium in general. Therefore, the focalization method can be applied not only to gases, but also to liquids and solids.

References

1. Durnin, J. Opt. Soc. Am. A4, No.4, 651 (1987).
2. Pyatnitsky L.N., Polonsky L.Ya. ICPIG XIX, Invited Lectures. Delgrade.1989, pp.342-351.
3. Landau L.D., Lifsjitz E.M. Course of Theor. Physics. V.6. Pergamon Press, N-Y. 1987.
4. Andreev N.E., Aristov Yu.A., Polonsky L.Ya., Pyatnitsky L.N. Sov.Phys. JETF. (Am.Inst. of Phys.). V.73 (6), pp.969-975 (1991).
5. Andreev N.E., Margolin L.Ya.,Pleshanov I.V, Pyatnitsky L.N. Sov.Phys. JETF. (Am.Inst. of Phys.). V.78 (5), pp.663-669 (1994)

84. GENERATION OF A VORTICITY BY LORENTZ FORCE AT FLOW PAST A CYLINDER WITH A LINEAR CURRENT ON AN AXIS BY CONDUCTING INCOMPRESSIBLE FLUID

N.I. Klyuchnikov

Institute of High Temperatures, Russian Academy of Sciences, Moscow, Russia

1. The practical applications of magnetic hydrodynamics, in essence, are reduced to the solution of a question as in what measure Lorentz force $\mathbf{f}=\mathbf{j}\times\mathbf{B}$ ($\mathbf{j}$ is the density of the electric current, $\mathbf{B}$ is the magnetic field) changes character of flow. Below we shall keep in mind only incompressible fluid with a constant conductivity σ provided that it is possible to neglect by a magnetic field induced by motion of fluid (small magnetic Reynold's numbers). The rather obvious answer to a question on a degree of influence of Lorentz force on the flow consists in that, whether or not its curl $\nabla\times\mathbf{f}$ is equal to zero. The usual hydrodynamics deals, for the most part, with potential flows, when the vorticity $\omega=\nabla\times\mathbf{V}$ ($\mathbf{v}$ is the velocity of a fluid) is equal to zero. It is concerned with that sources of a vorticity here are or spinning of an input flow or (take into account of viscosity) diffusion of vortexes from a surface of a body. The operating on fluid external mass forces, as a rule, are (with the exception of rather special case of a rotation of fluid as whole) and are incapable to generate a vorticity by definition. Therefore typical flow pattern in usual hydrodynamics are the limited areas of a vorticity (a boundary layer, a wake behind a body), surrounded by a potential flow.

If $\nabla\times\mathbf{f}=0$ (that has a place only in very special cases) the flow having a place in usual hydrodynamics is essential to change by Lorentz force will not be. If $\nabla\times\mathbf{f}\neq0$, i.e. when the Lorentz force is not conservative, has a place the generation of a vorticity by an external force and we can expect the radical rearrangement of a flow pattern. The vortical hydrodynamics is the essentially non-linear theory even in case of an inviscid incompressible fluid [1], that causes both a difficulty of arising problems and riches of their physical contents. In magnetic hydrodynamics the situation becomes even more complicated because of non-potentiality of an external force.

In this paper the emphasis has been on vortical consequences of the action of Lorentz force as the main hydrodynamic effect and in this respect we want to give some analytical consideration of the steady flat flow past an infinite circular cylinder with a linear current on its axis by ideal incompressible conducting fluid. We reason that only a combination of analytical and numerical approaches advances a deep understanding of the physical aspect of a question.

2. Let us consider that the axis of the cylinder of a radius a coincides with an axis z of a co-ordinate system and the motion occurs in planes parallel a plane xy. An infinite fluid stream with speed U directed along a positive direction of an axis x flow around the cylinder. The current with intensity I on an axis of the cylinder creates the magnetic field equal $\mathbf{B}=(0,B_0(r),0)$ in a cylindrical co-ordinate system (r,ϑ,z) where

$$B_0(r)=\frac{\mu_0 I}{2\pi r}.$$

The density of the electric current $\mathbf{j}=\sigma\mathbf{v}\times\mathbf{B}$ in this geometry is directed along an axis z and the electrical field $\mathbf{E}$ is directed also if external sources are absence. Under these conditions from the equation $\nabla\times\mathbf{E}=0$ follows that $\mathbf{E}=$const but, as the field on an infinity should be equal to zero, it follows that $\mathbf{E}$ is equal to zero everywhere.

In two-dimensional case it is convenient to enter the stream function ψ related to a speed of a fluid by means of the formula

$$\mathbf{v}=\nabla\psi\times\mathbf{i}_3 ,$$

where $\mathbf{i}_3$ is the unit vector along an axis z. The steady equations of hydrodynamics for the stream function and the unique distinct from zero component of the vortex $\omega_z=\omega$ are

$$(\nabla\omega\times\nabla\psi)\cdot\mathbf{i}_3 = N(\mathbf{b}\cdot\nabla)^2\psi, \qquad (1)$$

$$\nabla^2\psi = -\omega. \qquad (2)$$

Dimensionless variable are used here with a and U as scales of the length and the speed respectively. The quantity N equal

$$N=\frac{\sigma b_0^2 a}{\rho\, U} \quad (b_0=\frac{\mu_0 I}{2\pi a})$$

is the parameter of the MHD-interaction and $\mathbf{b}=(0,1/r,0)$ is the dimensionless magnetic field.

There are many various versions of the potential flow around a cylinder in usual hydrodynamics. The flows without a circulation, with a circulation, with free stream lines are possible. Besides it is possible to arrange outside of

(or inside) a cylinder point vortexes that also results to possible potential flows round a cylinder [2].

This variety of capabilities is sharply narrowed at transition to vortical flows. In this case (at $N=0$) the equation of the vortex transport (1) is satisfied by the any function $\omega=\omega(\psi)$ which form is determined by conditions on an infinity. Substituting this function in (2) we obtain in the general case the non-linear equation

$$\nabla^2\psi = -\omega(\psi), \qquad (3)$$

which is required to solve. Only the rather special cases of a variable vorticity analytically are considered in the literature [3,4], besides simple case of a constant vorticity, namely such, at which ω depends from ψ linearly that results to the linear equation (3). In magnetic hydrodynamics ($N\neq0$) the problem is determined by the system of the non-linear equations (1)-(2) and there are no any particular cases causing to a linear equation.

The similar difficulty has a crucial character and it is reflection of a physical essence of the problem. The solution $\omega=\omega(\psi)$ of usual hydrodynamics is simplly formulation of that fact that the vorticity is saved along a stream line (Helmgoltz theorem). If the right-hand side of equation (1) is different from zero then this equation describes a generation of a vorticity which now is not saved along a stream line.

For further it is conveniently to introduce a logarithmic polar co-ordinates

$$r = \exp(\pi\xi), \ \vartheta = \pi\eta \ (0\leq\xi\leq\infty, \ 0\leq\eta\leq2)$$

in which equations (1) and (2) take the more simple form. The value $\xi=0$ corresponds to the surface of the cylinder, $\eta=0$ gives the mean line behind of the cylinder and $\eta=1$ - the mean line in front of the cylinder. The components of the speed $\mathbf{v}=(u,v,0)$ in these co-ordinates are expressed through the stream function as

$$u = \frac{1}{\pi}\exp(-\pi\xi)\frac{\partial\psi}{\partial\eta}, \ v = -\frac{1}{\pi}\exp(-\pi\xi)\frac{\partial\psi}{\partial\xi}.$$

The equations of hydrodynamics in the variables ξ, η has the form

$$\frac{\partial\psi}{\partial\eta}\frac{\partial\omega}{\partial\xi} - \frac{\partial\psi}{\partial\xi}\frac{\partial\omega}{\partial\eta} = Ne^{-2\pi\xi}\frac{\partial^2\psi}{\partial\eta^2}, \qquad (4)$$

$$\frac{\partial^2\psi}{\partial\xi^2} + \frac{\partial^2\psi}{\partial\eta^2} = -\pi^2 e^{2\pi\xi}\omega. \qquad (5)$$

The stream function appropriate the input flow is

$$\psi_\infty(\xi,\eta) = \exp(\pi\xi)\sin(\pi\eta). \qquad (6)$$

3. By virtue of the marked mathematical difficulties we shall consider here only stream in a vicinity (on angle ϑ) of the forward stagnation point. The region in which the solution is searched is shown schematically on Fig.1. Let us represent in accord with (6) the stream function as

$$\psi(\xi,\eta) = F(\xi)\sin(\pi\eta). \qquad (7)$$

Such stream function will not satisfy to the vortex transport equation (4). However in a vicinity of the point $\eta=1$ this expression satisfies to equation (4) in the lowest order on η-1 provided that the function $F(\xi)$. Is determined by the equation

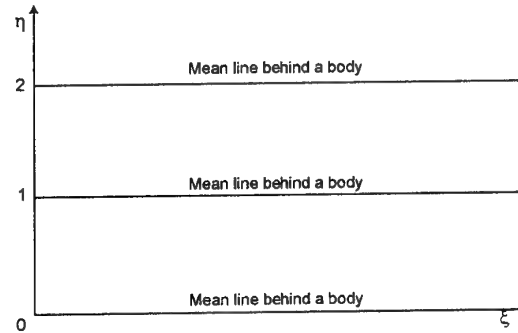$$F'F'' + 2\pi FF'' - FF''' - 2\pi^3 F^2 - \pi^3 NF = 0. \qquad (8)$$

Fig.1. Geometry of a problem in ξ, η - variables. The shaded band is the ranhge where is searched a solution.

Here and below the primed symbols of functions indicate the derivatives of functions with respect to ξ. The velocity components and vortex are given by

$$u(\xi,\eta) = e^{-\pi\xi}F(\xi)\cos(\pi\eta),$$

$$v(\xi,\eta) = -\frac{1}{\pi}e^{-\pi\xi}F'(\xi)\sin(\pi\eta),$$

$$\omega(\xi,\eta) = G(\xi)\sin(\pi\eta), \qquad (9)$$

where the function $G(\xi)$. Is determined in accord with (5) by the relation

$$G(\xi) = -\frac{e^{-2\pi\xi}}{\pi^2}\left[F''(\xi) - \pi^2 F(\xi)\right]. \qquad (10)$$

The equation (8) is a rather complex non-linear equation of the high order the analytical solution of which is not possible obviously.

420

Therefore we shall consider Lorentz force rather small, i.e. we shall believe $N=\varepsilon$, where $\varepsilon \leq 1$, and we consider a disturbance of the potential flow past the cylinder by Lorentz force. Thus we believe

$$F(\xi) = F_0(\xi) + \varepsilon\, F_1(\xi) + \varepsilon^2\, F_2(\xi) + \dots ,$$

where is the stream function of the potential non-circulation flow round a cylinder. Substituting this expansion for in the equation (8) and requiring fulfilment it in each order on ε, we shall obtain a set of equations which complexity grows with increase of the order. Here we shall restrict our consideration to the first order on ε in which the equation for F_1 has the form

$$\frac{-1}{\pi^3} F_1''' + \frac{3e^{2\pi\xi}-1}{\left(e^{2\pi\xi}-1\right)\pi^2} F_1'' + \frac{1}{\pi} F_1' - \frac{3e^{2\pi\xi}-1}{\left(e^{3\pi\xi}-1\right)\pi^2} F_1 = 1 .$$

(11)

The general solution of the equation (11) contains three arbitrary constants which are determined from the conditions of i) $F_1(0)=0$, ii) $G_1(\infty)=0$ and iii) the fulfilment of the correct asymptotic behaviour (6) of the stream function at the large distances. As a result of its we obtain the next expression for the stream function

$$F_1(\xi) = \left(-\frac{1}{16}e^{-\pi\xi} - \frac{1}{8}e^{\pi\xi} - \frac{1}{16}e^{3\pi\xi}\right)\ln(e^{\pi\xi}-1) +$$

$$\left(\frac{1}{8}e^{-\pi\xi} + \frac{1}{16}e^{\pi\xi} - \frac{1}{16}e^{3\pi\xi}\right)\ln(e^{\pi\xi}+1) - \frac{7}{8} - \frac{1}{8}e^{2\pi\xi} -$$

$$-\frac{1}{4}\cosh(\pi\xi)\ln\left(\frac{e^{\pi\xi}+1}{e^{\pi\xi}-1}\right) + \frac{1}{4}\operatorname{di}\log(e^{\pi\xi}+1)e^{\pi\xi} +$$

$$+\frac{1}{4}\left(-\frac{\pi^2}{6} + \operatorname{di}\log(e^{\pi\xi}) + \pi\xi\ln(e^{\pi\xi}-1)\right)e^{\pi\xi} +$$

$$+\left(\frac{\pi^2}{8}+1\right)e^{\pi\xi} - \frac{\pi^2}{16}e^{-\pi\xi}$$

(12)

where

$$\operatorname{di}\log(x) = \int_1^x \frac{\ln(t)}{1-t}\,dt .$$

Substituting (12) in (10) we shall obtain the expression for the vorticity in the lowest order

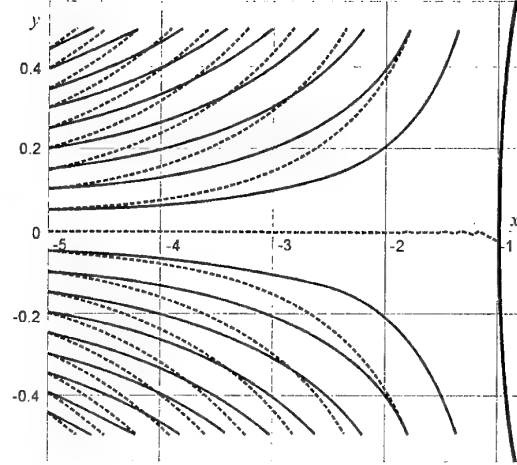$$G_1(\xi) = \sinh(\pi\xi)\ln\left(\frac{e^{\pi\xi}-1}{e^{\pi\xi}+1}\right) - e^{-2\pi\xi} + 1 .$$

(13)

Fig.2. A picture of stream lines in a vicinity of a stagnation point: solid lines are the vortical MHD-flow at $N = 0.25$, dashed lines are the potential flow.
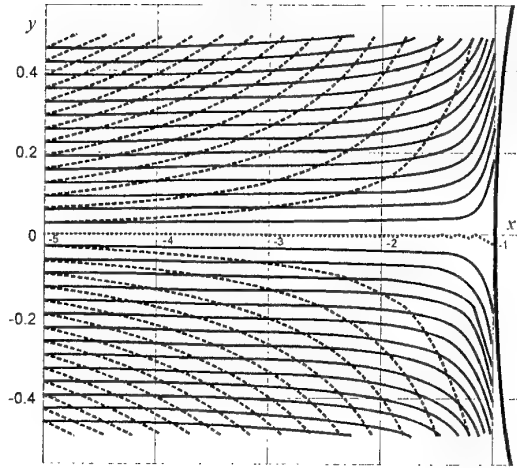

Fig.3. Lines of an equal vorticity in a vicinity of a stagnation point at $N = 0.25$. For comparison the dotted line gives stream lines.
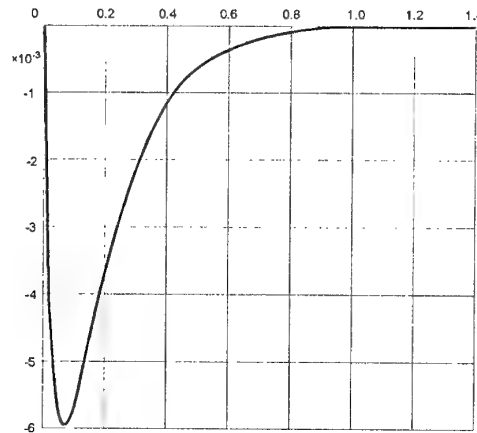

Fig.4. Change of a vorticity along a radial direction at $N = 0.25$ (10 degrees towards to an input flow).

421

The formulas (12) and (13) give the solution of the set problem. We call our attention to the analytical complexity of the first correction to the simple stream function of the potential flow that is the indirect evidence that even the weak Lorentz force causes qualitative change of the flow pattern.

The obtained solution is illustrated on Fig.2-4. On Fig.2 the stream lines of the vortical flow (N=0.25) are given in comparison with the stream lines of the potential flow. The vorticity lines (together with the stream lines) are given on fig.3. The intensity of the generation of the vorticity allows to estimate fig.4 where the change of the vorticity along a radial co-ordinate is shown. Let us note the long range character of Lorentz force: the vorticity arises on very large distance from the cylinder (order of 23 radiuses). This circumstance can have the specific appendices, for example, in the conversion of a wake behind a body, in the flow separation control and so on.

References

1. P.G. Saffman. Vortex Dynamics. Cambridge University Press, 1992.
2. L.M. Milne-Thomson, C.. B.E. Theoretical Hydrodynamics. London, New York, 1960.
3. D.S. Tsel`nik, Fluid Mechanics 3, 93, 1973 (in Russian).
4. W.D. Hayes, R.F. Probstein. Hypersonic Flow Theory. Academic Press, New York and London, 1959.

HARD X-RAYS, FAST IONS AND FUSION NEUTRONS FROM INTERELECTRODES MEDIA OF LOW-ENERGY VACUUM DISCHARGE

Yu.K. Kurilenkov,
Institute for High Temperatures of Russian Academy of Sciences,
13/19 Izhorskaya Str., 127412 Moscow, Russia
ykur@online.ru

M.Skowronek
Laboratoire des Plasmas Denses, Universite P.& M. Curie, F-75252 Paris Cedex 05, France
msk@ccr.jussieu.fr

Abstract. We study the high power density random dusty media in low energy nanosecond vacuum discharges. This ensembles (cold grains with possible small fraction of hot microplasmas) are created by an intense energy deposition into the cold solid density, low volume dust "target" collected in interelectrode space (clusters, grains, microparticles of different size from anode). Hard x-rays emission efficiency, generation of energetic ions (~1 MeV) and neutrons, trapping of fast ions or/and x-rays, laser-like behavior, some modeling for laboratory astrophysics (x-rays bursts, "clusters of stars", etc) are the subject of our interest. X-rays "random" laser scheme assumes partial diffusion of photons due to regulated level of multiple scattering and reflecting in disordered or self-organized dusty media. The neutrons from DD fusion, as well as modeling of some interstellar nuclear burning (like oxygen "burning") due to microexplosive nucleosynthesis (driven by anodes "ectons" [1]) are demonstrated and discussed. The value of neutrons yield from DD fusion in interelectrodes space is variable one being up to ~ 10^6-10^7/4π per shot under just 1 J of *total* energy deposited to create all the discharge processes[*].

Introduction

Different states of matter in unusual conditions and intriguing physics related are studying successfully during previous and recent years on the basis of vacuum discharges [1]. The present work concerns an attempt of the incorporation of plasma density, coupling (correlation), dusty, collective and anomalous effects *simultaneously* into novel efficient ways of high power density matter (HPDM) production. We study experimentally and theoretically the high power density random media (ensembles of cold grains with small fraction of hot microplasmas) generated in vacuum discharges with hollow cathode at low energy (~ 1 J). These ensembles are created by an intense energy deposition into the cold solid density, very low volume dusty "target" collected in interelectrode space (clusters, grains, microparticles of different size from anode material). The consequence of high power local density effects have been realized specially in design of our low-energy vacuum discharge [2], that will be presented in more detail elsewhere. This paper concerns the discussion namely of some novel physical phenomena obtained on this basis.

The main anomalous deposition of external energy into nucleated phase obtained in vacuum is starting up immediately after the end of breakdown (nanoseconds-scale electron beams, but mainly - Joule anomalous overheating some of small volumes solid density grains by post breakdown high density current). The percolation of current through the media of quasiconductors (grains) - quasidielectrics (vacuum) may create from part of the grains a certain number of microplasmas with extreme temperatures and densities ($T_{e,i} \approx 1$-5keV from TOF (time of flight) data [2], and electron density $n_e \sim 10^{20}$-10^{22}cm^{-3}), meanwhile, the majority of the clusters and grains will remain "cold". Correspondingly, the process of the explosive destruction of dusty grains is accompanied by x-rays radiation (during hydrodynamic expansion, cooling and recombination of the dense hot microplasmas created), as well as by ejection of hot electrons and fast ions. Their energy will be deposited into the surrounding dusty media also. The hot electrons bremsstrahlung on grains will produce additional x-rays photons, sublightning the "ball" in whole, meanwhile the fast ions stopping on the clusters and micrograins may provide another phenomena.

---

[*] This paper have been presented also at Euroconference on Hypersonic and Aerothermic Flows and Shocks, and Lasers, 23-27 April, 2001, Observatoire de Paris, Meudon .

Remark, that the mixture of "cold" grains (reflectors and scatterers) and expanding "hot" grains (HPDM as active media, or other sources of x-rays pumping like bremsstrahlung from grains) have to represent, in general, an ensemble of specific random media with x-rays amplifying properties. These properties will depend on the relation between characteristic amplifying and absorbing lengths l_{amp}/l_{abs} for a particular ensemble [4,5]. Thus, potentially the arc phase of discharge may transform the near anode "dusty" plasma into specific amplifying media [6], if the gain could overcome absorption and loses. This feature of random ensembles allows studying some lasing in hard x-rays area due to effects of multiple scattering at stochastic resonators predicted earlier [4].

Furthermore, the generation of hot electrons and energetic ions (with energies about ~ 0.1-1MeV or higher from TOF measurements [2]) is going on also simultaneously with x-rays, partially like for irradiated clusters [3]. Both electrons and ions ultimately have to reach the speed of sound in hydrodynamically expanding microplasmas, $C_s \approx (\gamma_{ad} ZkT_e/m_i)^{1/2}$ (kT_e is electron thermal energy, m_i and Z - ion mass and mean charge, γ_{ad} -adiabatic exponent) [7]. Most of the kinetic energy is contained in the ions since their mass is much greater. In a result, the interelectrodes ensembles interior may remind something like microreactors to create nuclearsynthesis microevents (like DD fusion) due to head-on collisions of fast ions or their penetration into the

dusty target and anodes edge containing deuterium. These dusty ensembles at interelectrodes space in vacuum remind the foam-like laser target systems suggested recently for efficient neutron generation [12]. Therefore, taking into account the generation of fast ions in experiment and even the possibility of fast ions trapping by interelectrodes ensembles, looks reasonable to start the studying of any microfusion events on this basis in more detail also. Some of the qualitatively new results related and obtained for our low-energy discharge are presented and discussed below.

Experiment

Few effects of high local power density were realised in experiment, that allowed to produce the different ensembles of cold grains with certain fraction of hot microplasmas (T~1KeV and n_e~10^{20}-10^{22}cm^{-3}). The source consists of a cylindrical vacuum chamber with diameter of 50 mm and having three windows closed by mylar sheets 70-100 μm thick (Fig.1). This cylinder is connected to a vacuum pump able to reach 10^{-6} to 10^{-7}mbar. Two electrodes are included on the cylinder axis: the hollow anode and the hollow cathode having different shapes. The anode is insulated from the ground cylinder by a teflon envelope. The distance between the electrodes can vary by 0.1mm steps until 6-7mm maximum. The source is included in a coaxial high voltage cable having 50Ω impedance; this cable is connected to a four-stage Marx generator delivering a 50ns pulse
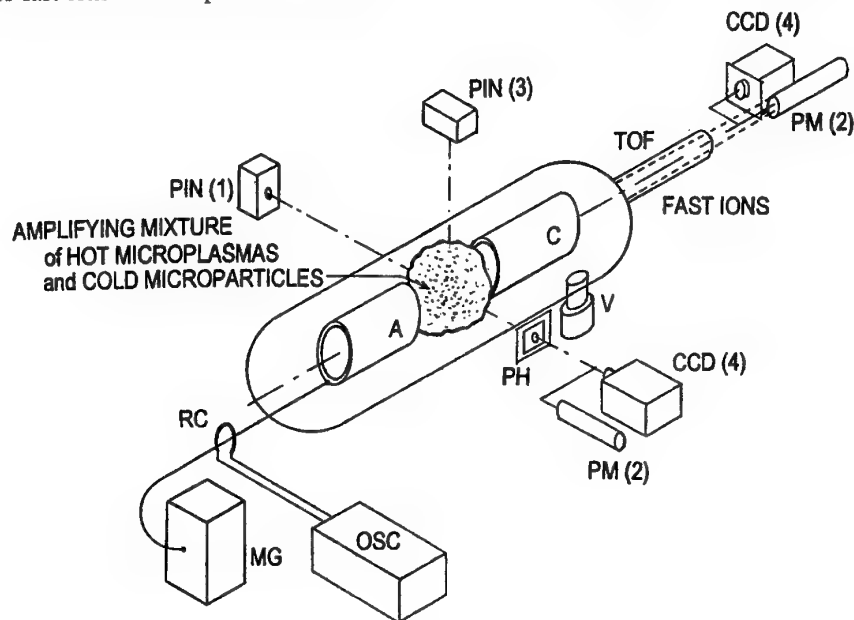
Fig.1 Schematic of the experiment for generation of ensembles of cold microparticles and hot microplasmas (plasmas «dust»): MG – Marx generator, R – Rogovskii coil, A and C – anode and cathode, PIN – PIN diodes, CCD – camera, PH – pinhole, PM – photomultiplyer, OSC – oscilloscope, V - vacuum pump.

424

of maximum voltage 70kV in a 50Ω load. Three mylar windows allow the x-ray intensity measurement in three perpendicular directions (side-on: right, left and upper) in the plane corresponding or in parallel to the anode edge. Another mylar window allows the end-on measurement through the hollow cathode. Calibrated PIN diodes having a 1 to 2ns rise-time and sensitivity maximum at 10-20keV are used to measure the x-ray yield, photo multiplier PM2 covered by set of absorbers registered usually the photons with the energy higher than 50keV. The image of the multiple x-ray sources is obtained by means of a pinhole (PH) diameter=0.1mm bored in a 1mm thick lead screen, and covered by Al foil, 0.1-0.2 mm. It is registered using a scintillator sheet (NE102A) by a low noise CCD camera, either from the end-on or the side-on right window and using the scintillator at the entrance of a low-level sensitive camera (> 2-3keV). Some of the different types of hard x-rays images deduced from analysis of database images registered are given at [2] (see also schemes at Fig.4 at the next section). Fig.2a shows the eroded edge of basic anode (grains "'factory"), and Fig.2b represents the typical collection of grains accumulated inside the anode near the edge (its structure just illustrates the character of dusty interelectrodes "target").
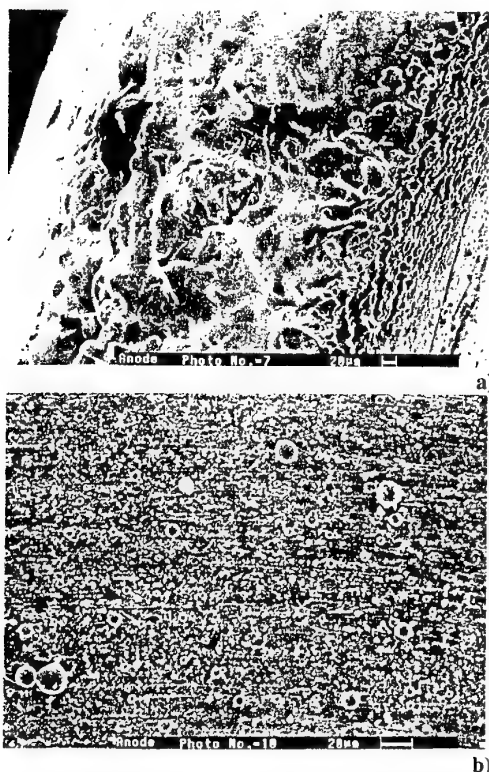
Hard x-ray yield efficiency registered and well reproduced in the vacuum discharges is about 0.1-0.3%, that is about two-three order of magnitude higher than for laser-irradiated clusters [3]. Detailed study of the TOF ion energy spectrum provides different, but important, information on the x-ray random media, including some diagnostics. In particular, this data allows us to estimate independently some of hot dusty plasma parameters. In fact, under shock wave expansion the microplasmas temperature may be related to the front velocity, $T_{e,i} \sim V^2_{ion}$ (radiation energy and pressure are vanished) [7]. For TOF measured values of ion velocity $V_{ion} \sim 5\times10^7$-10^8cm/sec, the values of temperature in curtain overheated dense microplasmas may be estimated as $T_{e,i} \sim$ 1-5keV.
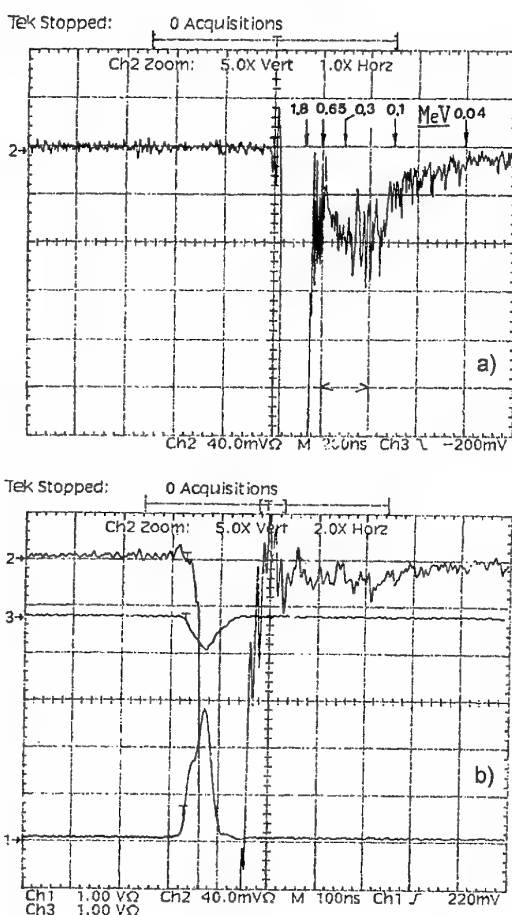

a)

b)

Fig.3. Particular time of flight distribution measured for energetic ions (a) and rather suppressed distribution of main part of fast ions due to their stopping in the x-rays «ball» interior (b) (mostly energetic ions are taking part in ambipolar flight with electrons: the spikes on right-side part of x-rays peak, where hot electrons may manifest themselves besides of x-rays).

a)

b)

Fig.2. The microrelief of surface for Fe anode edge after more than 10^3 shots (a) and micrograins pattern spectrum from anode edge interior (b).

425

Time of flight measurements have showing not only that hard x-ray production may accompanied by energetic ions like for irradiated clusters [3]. This study recognised also that fast ions (as well as x-rays) might be trapped inside the x-ray dust "ball" interior if needed (see oscillogramms presented) [2]. Transparent images (like on Fig.1 at [2]) gives usually the strong fast ion signal (like on Fig.3a), meanwhile lowering of image transparency is correlated with suppression of fast ion signal (Fig.3b). This feature has to be important for specifics of possible nuclear events at these systems. Further, looks exciting the opportunity of hard x-rays trapping that is much more complex task than ions trapping. It needs higher concentration of cold grains of specific

mean sizes and better symmetry of ensembles, but this phenomenon promises another set of interesting effects (next section).

Trapping of X-Rays.
Hard X-Rays «Random» Lasers.

To describe or analyze these mixtures we may introduce the parameters α, β (characterizing the mean inter-grain distances to their mean diameters) and η (relation between numbers of cold and hot grains): $\alpha = N_c^{-1/3}/2a_c$, $\beta = N_h^{-1/3}/2a_h$, $\eta = N_c/N_h$, where N_c, N_h are the densities of cold and hot "grains", a_c, a_h – average values of their radii, respectively. We illustrate on Fig.4 some of the qualitatively different conFigurations and regimes
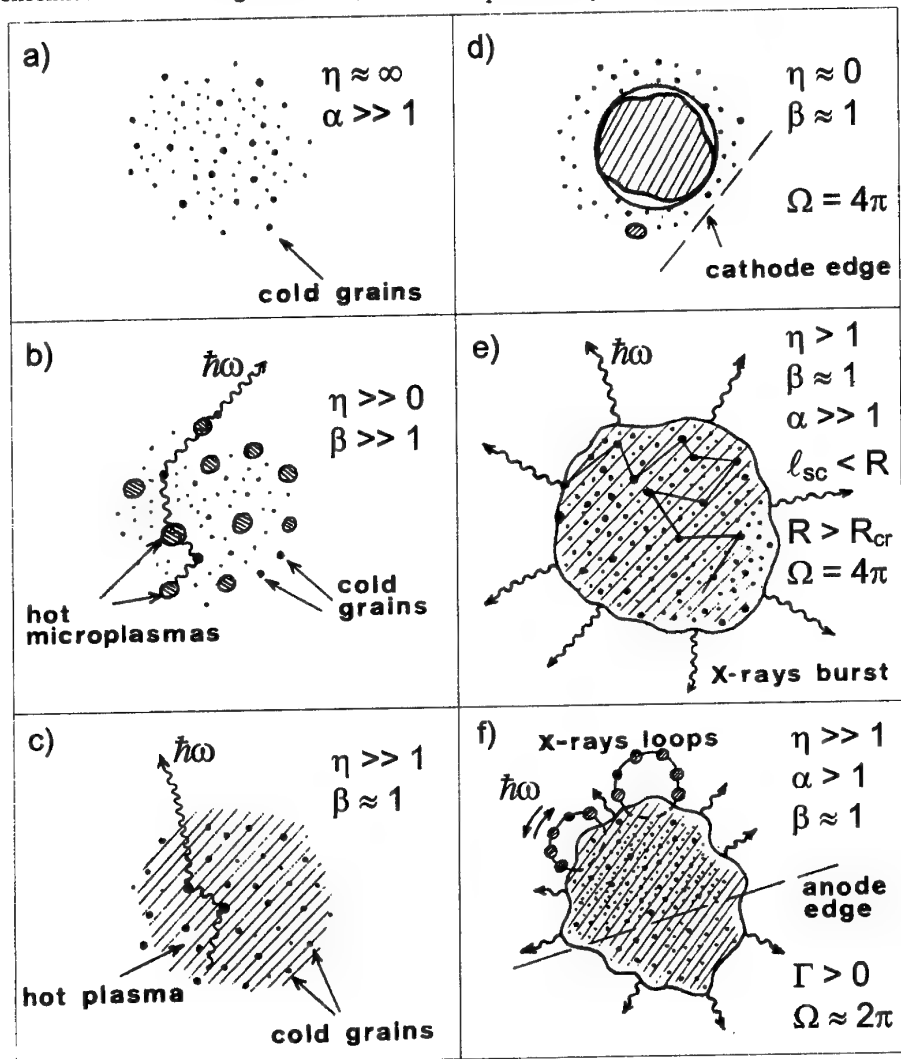

Fig.4. Schematic of different types of conFigurations of ensembles of dusty interelectrodes media, registered and identified in experiments with hollow cathode discharge [2] (see text).

426

of x-ray ensembles (identified in our experiments) in terms of parameters α, β, η. There are shown schematically, in particular, the "cold" anode flare dusty plasma before the end of breakdown (Fig.4a), initial overheating and expansion for the fraction of grains during the main current rising, when arc phase has started (Fig.4b), and the overlapping of microplasmas that transformed into rather uniform dilute hot plasma with the rest of unperturbed and cold grains immersed (Fig.4c). Note that Fig.4a qualitatively represents the effective plane of dust solid density target partially reproduced in experiments on the surface of anode interior (Fig.2b).

In principle, any experimental variation of parameters like α, β, and η may allow for different levels of reflection, scattering and pumping in ensembles of cold and hot grains. As a result, it would be possible to get even various types of x-ray lasing media or systems on the basis of these ensembles (Figs.4d-f). As an example of particular interest, we will evaluate the possibility of experimental realization of a laser scheme [4] when incoherent scattering of photons provides feedback mechanism necessary for laser action. During recent years interest and studies of this scheme were renewed, and multiple scattering as feedback for laser action has been used experimentally in the visible part of spectra, in particular, for a dye systems with including of strongly scattering medium (colloidal suspension) [8] and powder of laser crystals [9]. Recently this specific laser system was analyzed and discussed in more detail for the visible part of spectra for grinding crystals or microspheres in dye solution [9,10] Available theory developed earlier [4] provides good reference basis for understanding the problem. V.Letokhov [4] considered the case when the mean free path of photons due to scattering $l_{sc} = 1/N_0 Q_s$, ensemble dimension R and the wavelength λ are related as

$$\lambda \ll l_{sc} \ll R \qquad (1)$$

and $N_0^{-1/3} \gg \lambda$ (Q_s – scattering cross section, N_0 – volume density of scattering particles). Being trapped in disordered system, light makes a long random walk before it may leave the medium from near surface area.

The solution of the system of equations which describes diffusion of photons [4] shows that laser generation threshold may be achieved when volume gain become larger than surface losses at some ensemble volume which is above critical size, or at $R > R_{cr}$ in the case of sphere (looking forward, see Fig.5b below). The critical radius is equal to

$$R_{cr} \approx \pi \, (l_{sc} / 3\gamma_m)^{1/2} \qquad (2)$$

where γ_m is mean gain coefficient. In our case $\gamma_m = \gamma/\beta = \gamma \, 2a_h \, N_h^{1/3}$, $\gamma = Q_r \, N$. Here Q_r is cross section for induced radiation transition, N is density of inverted population that is difference of populations in higher and lower state of resonance transition. The evaluation of scattering mean free length and gain are key features, determining the possibility of laser action.

If one consider the case when hot non-equilibrium plasma, merged in central sphere (radius of which is R) is surrounded by spherical layer of cold grain media, ΔR in thick, with scattering length l_{sc}, than reflection coefficient of outer layer will be $\Delta R / l_{sc}$. Than laser threshold condition will be

$$(\Delta R / l_{sc}) \exp (\gamma R / \beta) > 1 \qquad (3)$$

Critical radius is determined by equation (3). Processes of scattering in vacuum discharge are complex, and perhaps may be defined by the specific properties not only of cold grains, but also partially by the features of boundary conditions for the radiating volume. We can change effectively the values of parameters α, β, and η in our x-ray ensembles, i.e. regulate the levels of scattering and pumping inside the system. Our x-ray mixtures have the space scale of $R \sim 0.3$-0.5cm, which is a reasonable order of magnitude of the critical radius in expression (3). Let us suggest that $\gamma = 10$cm^{-1}, $R = 0.5$ cm, $\beta = 5$, $l_{sc} = 0.1$cm, than threshold condition (3) will be valid. Note that the role of clusters surface in scattering processes (grazing angles) may essentially reduce the random laser threshold (underline, that surface/volume relation increases at small clusters sizes).

The number of "modes" coupled by scattering [4] is

$$N \approx \Omega / (\lambda / 2R) \qquad (4)$$

where Ω is the lasing solid angle. The highest degree of nonresonant feedback corresponds to maximal angle of generation $\Omega = 4\pi$. As is evident from expression (4), the number of «modes» namely in hard x-ray random laser may be extraordinary high.

The dynamics of x-ray radiation in random laser has an interesting property, differing from ordinary x-ray «balls»: there is almost no more artificial (electronic) delay (~35nsec) between photomultiplier signals and PIN diods ones [2]. In real time this means that random diffuse x-ray photons (energy less than ~ 20keV), some part of which may be attributed to laser action, appear to

427
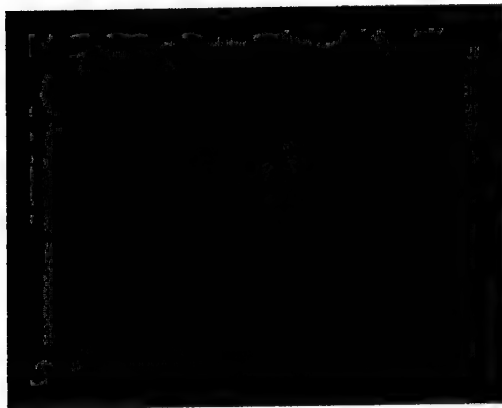
a)
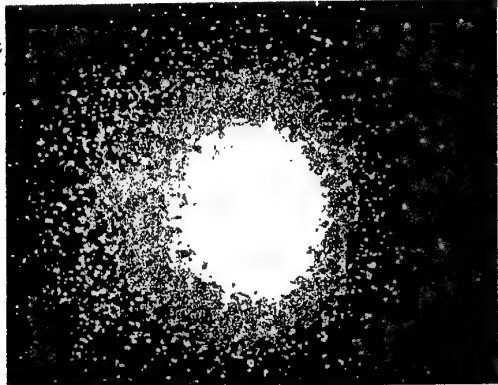
b)
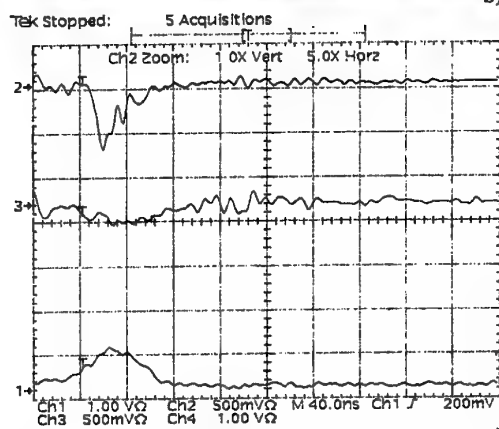
c)

Fig.5. Transparent ensemble with low concentration of micrograins (a) and image of x-rays burst after x-rays trapping at more dense ensemble (random laser) (b). Low intensity and extended signals from the x-rays "bathroom" ensemble like on Fig.5b (x-rays are trapped and dissipate inside the ball, and x-rays intensities registered by channels 1,3 originate mainly from the "ball" skin-layer) (c). Fast ions are trapped completely also (TOF regime, Ch.2)

photons with energy ~10-20keV due to their diffusion in ensemble may be about 2-3 order of magnitude less than in vacuum.

Example of ensemble beyond of any lasing and bright ensemble with x-rays delayed are shown at Figs 5a,b, correspondingly. Last example is close to the situation when volume gain becomes larger than surface and volume losses (random x-rays lasing, Fig.5b). Seems that this is x-rays analogy of random lasing at colloidal suspension in visible light observed and presented earlier [8]. Specific behavior of low level and extended PIN diodes signals for x-rays "ball" (Fig.5b) is shown properly at oscillogramme (Fig 5c, channel 3) and illustrates the delay of lower energy x-rays photons: the maximum of very hard x-rays, channel 2, have to be shifted to the left on ~35nsec to compare the x-rays yield in real time (intensity of ch.1 is lower with factor of 3 for ensemble on Fig.5b than shown). Thus, the ensembles with high level of symmetry may trap x-rays properly (~10 keV) and give almost no x-rays yield intensity (Channels 3,1), meanwhile this intensity from skin-layer is enough to create the image by sensitive CCD camera. (For very hard x-rays (> 50-60 keV) the ensemble on Fig.5b is rather transparent, channel 2). Underline, that images of type Fig.5b sometime are not accompanied by the set of oscillogramms since the needed triggering value of $U = 100$ mV at channel 1 is not available being rather less than needed to switch registration. For ordinary random disordered ensembles [2] this intensities are essentially higher (see also Figs 6,7 below). Moreover, distortion of high symmetry like on Fig. 5b may provide the strongly anisotropy x-rays burst which reminds single pass ASE lasing regime [6]. The example of this sort of oscillogramms is given at Fig. 5d and corresponds
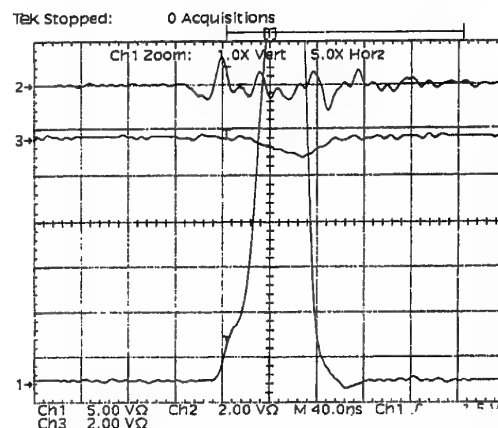
d)

Fig.5d. Ensembles with broken symmetry may accompanied by strongly anisotropy x-rays burst like single pass ASE lasing regime [6] (sensitivity of channel 1 is five times lower than at Fig.5c)

delay relative to very hard x-ray radiation (PM2, >50keV). As in the case of optical transport in scattering media [11], the transport velocity of

428

to CCD disordered image on Fig.4 at [2] (or schemes on Figs.4b,c, presented above). X-rays ensemble at Fig.5b corresponds to intermediate case between schemes presented at Figs.4e and 4f.

Nuclear Fusion Events

Finally, taking into account the properties of x-rays ensembles with fast ions, the further reasonable steps like generation of neutrons due to fusion reaction $D(D,He^3)n$ as well as some modelling of elements of interstellar burning have been done at the next stage of the present work.

Neutron generation in x-rays ensembles have been registered using the same experimental

and 4 on oscillograms below, Figs.6,7). Photomultipliers were covered by scintillators and screened by Pb plates, being located under different distances within one meter from the source. Beyond of usual x-rays signal (first strong peak), PM2 indicates the well reproducible signal with typical delay about 46,6nsec/meter [3] which may be attributed to DD fusion neutrons. Meanwhile, the special PM4 located usually at the half of PM2 distance from source, is registering under favorable conditions the moment of DD burning time, when fusion events may take place at any part of ensemble (rather narrow x-rays signal, located after strong x-rays maximum). Second PM2 peak position is a reproducible function of distance from

a)

b)
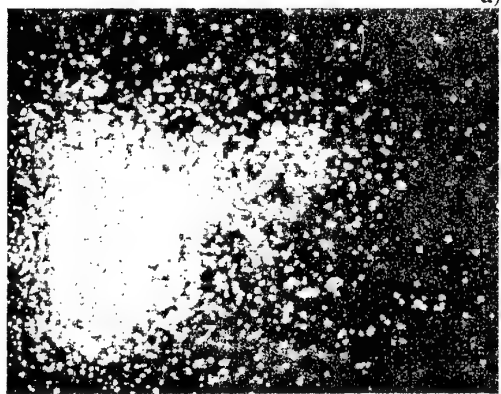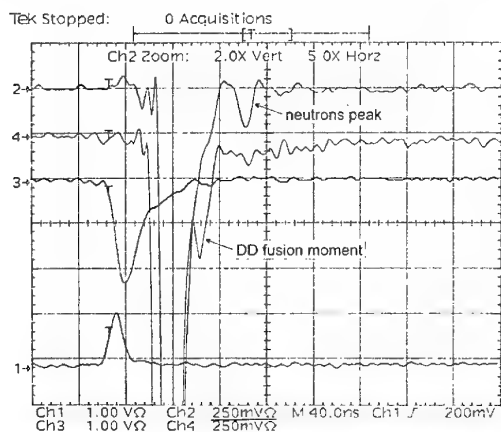
Fig.6. Oscillogrammes (a) and hard x-rays CCD camera quasitransparent image (b) of interelectrodes dusty matter with DD microfusion events accompanied by moderate neutron yield ($\sim 10^5$-10^6/4π per 1 Joule).

a)

b)
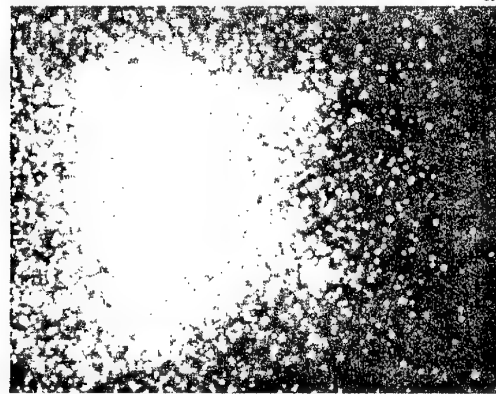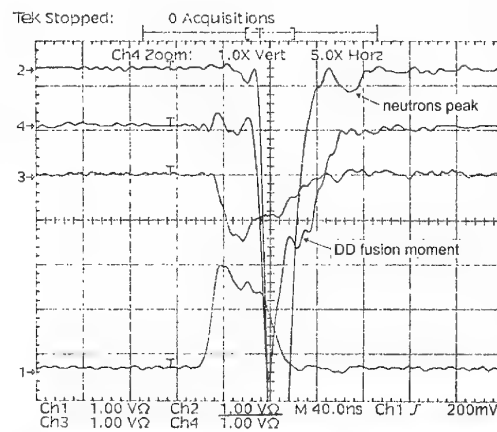
Fig.7. Oscillogrammes (a) and hard x-rays CCD camera nontransparent image (b) of interelectrodes dusty matter with higher number of DD microfusion events accompained by higher neutron yield ($\sim 5 \cdot 10^6$-10^7/4π per 1 Joule).

set-up [2] as for x-rays and fast ions studies. We have used particular modified Pd electrodes with deuterium D doped by rechargeable manner. Modified scheme of TOF measurements have been performed without any vacuum tube and with two photomultipliers, PM2 and PM4, located in the air along the axes of hollow cathode (See channels 2

source that confirms the fact of correspondence of TOF signal to neutron yield from DD reaction of nuclearsynthesis. (It partially reminds the spirit of recent experiments on nuclear fusion driven by Coulomb explosion of laser irradiated deuterium clusters [3]). For illustration, two different

429

examples of oscillograms and correspondent x-rays images from vacuum discharges are given on Figs.6,7. The changing of the distances between x-rays source and PM2 provokes correspondent moving of second peaks at PM2. The simultaneous using with TOF scheme the plates CR39 and PN3 (and the way to develop them) shows the variable number of tracks, which have to be attributed with neutrons also. Remark that the energy of deuterons estimated from the spread of arrival times of neutrons to PM2 detector is about 30keV, that essentially higher than at [3] as well as for complex fast ions [2] (Fig.3a) in comparison with laser irradiated clusters [18].

Summing up, the magnitudes of particular TOF's peaks measured by PMs, numbers of tracks related at PN3 plates, intensities of hard x-ray CCD images registered are in good and reproducible correlation. Number of tracks is growing with number of shots also. The value of neutron yield from random interelectrode "dusty" media is variable one, being about 10^5-10^7 per shot under about 1 J of *total* energy deposited to create all the discharge processes at the single shot. The typical variation of x-rays intensities of interelectrodes ensembles images with neutron yield are following from comparison of data shown at Figs.6 and Fig.7 (pay attention that sensitivity of Channel 2, PM2, is differ with factor of 4 for oscillogramms presented). Underline, that in terms of [1], we study here the specifics of ensembles of microparticles with fraction of anodes "ectons"(in our case - exploded micrograins). If the well known *cathode "ectons"* produce the packages of electrons [1], from our study *we may conclude that some of the anodes "ectons" (exploded microparticles) might be responsible for microexplosive nuclearsynthesis.*

The efficiency variated of neutron production from *fusion driven by anodes "ectons"* at our low-energy discharge (up to 10^7 per shot under about 1 J of *total* energy) is higher than for laser irradiated clusters (10^4 neutrons for 120mJ of *laser* energy [3]). One of the reason of the higher efficiency of vacuum discharge is the fact that for experiments [3] with fusion driven by Coulomb explosion the collisional free path l_D for ions D^+ is much longer than the plasma dimension d_{focal}, which is about laser focal diameter, 200μm ($l_D \gg d_{focal}$). In our case, we have *the fusion driven by anodes "ectons" where we may variate relation between l_D and R_{ball}, including even the trapping of all the deuterium fast ions* generated inside the ensemble of cold grains ($l_D < R_{ball}$), which play the role of the additional cold disperse target. In a result, the neutron yields in fact is higher for ensembles with lower transparency images (examples of images see also at [2a], www.fpl.gpi.ru). However, the stochastic nature of

x-rays ensembles may influence the reproducibility of neutron yield being a subject of further study as well as establishing of the proper diagnostics. Nevertheless, hopefully that simple nanosecond scale discharge scheme suggested to produce neutrons may supplement available novel efficient approaches like laser irradiated clusters [3], laser excitation and hydrodynamic dissipation of foam-like targets [12] as well as popular laser initiation of other nuclear reactions by energetic ions [13]. Looking forward, perhaps it is interesting also to investigate the neutron yield from the "dusty" ensembles with high symmetry, where x-rays are trapped properly also (like on Fig.5b).

Nuclear burning or transmutations of elements?

Last but not least, DD microfusion is important but particular example of well-known nuclear "burning" in astrophysics (sf.[14]). In fact, if to assume that different elements may reach similar velocity $\sim C_s \approx (\gamma_{ad} ZkT_e/m_i)^{1/2}$ during microexplosions, the energy of head-on collisions for real sorts of particles will increase with the mass of element. (Remark that this situation
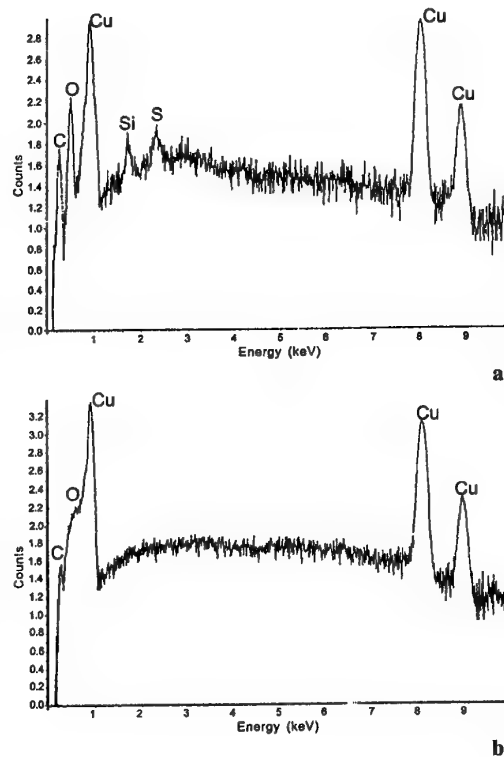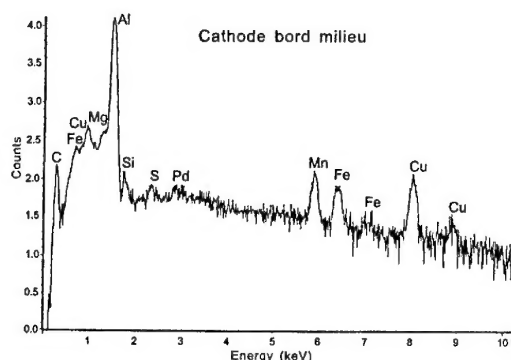

Fig.8. Electron microscope data for chemical composition of Cu side-on anode surface before (b) and after some number of shots (a): the effect of accumulation of Si and S during discharge operations.

formally corresponds to modeling of different ignition "temperatures", $T_{ign} \sim m_i v_i^2 / 2$, at the stars interiors for different shells [14]). Concerning this phenomena, note that we observe accumulation of some elements (at the electrodes edges), which are not included into electrodes materials initially (although its important to share them from any occasional available impurities at chamber interior). Systematically observed accumulation of *Si* and *S* peaks in our discharges (as well as C and O) at the anodes external surfaces and mylar windows perhaps is an example for modeling of oxygen nuclear burning [14], $O^{16}+O^{16}=(Si, S, P, Mg,$ etc.). Electron microscope data for surfaces indicated before and after some number of shots are given for illustration at Figs.8b,a correspondingly. Some results from the synthesis of iron-group nuclei, like *Mn, Fe* (probably due to the next stage of "ignition", i.e. *Si* burning) are registered also (example is given on Fig.9) but this data need further analysis.

Note that concentration of Mn is higher usually than Fe, that seems confirms the difference with potential impurities effects. However, the nature of Mn is not completely clear: is it the product of Si burning or some other transmutation product. In fact, the upper part of anode from Pd is attached to Cu basis, and intermediate layer contains some Pb, Zn, and Sn. Since the transfer of even dominating Pd to cathode is rather low (Fig.9), first version looks as the more probable one, but the final answer needs further study.

Fig.9. Electron microscope data for chemical composition of Al cathode edge surface: the appearing of noticeable Mn concentration (higher than Fe), this element is not available at anode-cathode components.

Concluding remarks and discussion.

Long-term study of vacuum discharges represents the broad and instructive basis for a large spectrum of very different physics (see reviews [1,15]). However, the complexity of data interpretations, the uncertain character and specifics of discharge phenomena themselves do not allow to incorporate directly the advanced and sophisticated knowledge from other disciplines, like dense coupled plasmas, dusty plasmas [16], target physics, driven granular medium dynamics, physics of clusters and novel cluster sources of radiation [17], power laser – clusters interactions [3,18,19], x-ray lasers and physics related [6], physics of disordered media with multiply light scattering for lasing [4,5,8-11], pseudospark discharges [20]. Our work is an attempt of making some particular steps in this direction, relying upon the "soft" physics starting from the earlier x-rays experiments [21].

Generally speaking, dusty-like random media created in the experiments described here represent a number of problems related to chaos and complexity [22,23]. Our x-ray ensembles of cold and "hot grains" correspond to particular examples of open systems with nonlinearity, which are in energy exchange with their surroundings. By exceeding some thresholds of deposited energy the state or structure of these systems may be changed, and sometimes in a violent manner. One of the manifestations of structural changing in complex systems is their self-organization, which has been partially exhibited at some stages of our ensembles evolution by different manner and scale. It is a subject of further study to try to include the specific nature of instantaneous energy pumping, which may accompanied by cascading self-organization [22] and another effects of "induced" organization of dusty ensembles in close interaction with electrodes edges.

Experimental variation of effective levels of reflectivity, scattering and pumping (and their combinations as particular sets of ensemble's parameters like α, β, η, Γ, Ω) provide *different types of x-rays lasant systems based on random amplifying media*, which have been recognized and studied in a preliminary way. In particular, single pass ASE lasing into narrow angle from plasmas "dust" (Fig.5d), ASE or near subfluorescence regime in all directions from uniformed x-ray ball (Fig.3 in [2]), diffuse regimes of x-rays photons (random laser, Fig.5b,c) and x-rays guiding (Fig.5 in[2]) have been identified.

Other fundamental physics which could be studied on the example of x-ray "ball" phenomena, is the such effect as *localization of light* [24,10]. In fact, electron transport in disordered metals and photon transport in random systems like dielectrics have unexpected similarities [24,25]. In our case an ensemble of microplasmas and grains has the "weak" disorder (since $\lambda \ll l_{sc}$), thus the optical and electronic localization are also analogously in part. If we could "introduce" in our case more

431

noticeable initial correlation between grains, $\Gamma > 0$, and increase the number of cold grains under sufficient energy deposition into exploding grains, we would get the trapping of x-ray photons not only due to diffusion regime ($l_{sc} << R$), but also due to their partial localizations ($\Gamma = U/kT$ is a coupling parameter for intergrain interactions, where U and kT are the potential and kinetic energies of cold grains, correspondingly). In this case, loop trajectories may appear, as schematically shown on Fig.4f (here some of the trajectories of photons like on Fig.4b is transformed into circular ones). This case may be realized experimentally, when the density of grains is high and the ensemble itself covers the anode surface essentially. In this case, it would be interesting to consider in more detail the transformation of the incoherent random laser into partially coherent one with closed loops paths, and with almost all deposited and created energy being trapped inside the microdust cloud.

The measured hard x-ray emission efficiency in our discharges (0.1-0.3%) as well as neutrons yields are about two order of magnitude higher than for femtoseconds laser irradiated clusters (sf.[3,18,19]). Partially, it has been realised also due to the *increasing of mean sizes of exploding grains* in our experiments up to 0.1-1μm (instead of 10^{-3}–10^{-2}μm at laser focusing on clusters) and *longer confined anomalous heating of grains*, as well as due to the role of complexes like $(D_2O)_n$ [26], which must be clarified for our conditions. However, many questions remained, and x-rays spectroscopic study of radiation, including potential redistribution along the spectrum under ensembles transformations, and other problems (like anisotropy, stochastics, etc) and diagnostics requires further work.

Some of the effects under investigation might be described reasonably in terms of explosive centres ("ectons" [1], and in our case - anodes ectons. These centers originate from the small part of micronucleations of anode material, and their certain explosions are accompanied by fast ions, hot electrons and x-rays production, that confirms the general conception of explosive centers [1]. In our opinion, in a result - the anodes ectons should be responsible for *microexplosive nuclearsynthesis* in low-energy nanosecond vacuum discharges, meanwhile the main part of micrograins may assist to optimize or variate the processes related: to keep (or not) the particles or/and photons inside of interelectrodes dusty ensembles and guide the x-rays.

Mechanisms of ion acceleration by collective fields, including current-carrying dusty plasmas need further analysis also. For example , the role of current density sharp cutting ~ dI/dt at the process of micrograins explosion, as additional mechanism to create hydrodynamic expansion looks analogously to Coulomb explosion of clusters by inverse bremsstrahlung [18,19,26]. But even the well-known mechanisms [27] allow to make some estimations. In fact, spherical drop model [27] suggests that ambipolar acceleration of ions by electrons in double layers is going on. The energy of fast ions estimated as $E_i \approx 4 \cdot 10^{-3} Z E_e^{1/2} n_{0e}^{1/2} r_0$, where E_i and E_e – mean ion and electron energy (eV), Z – mean ion charge, n_{0e} and r_0 - initial electron concentration and drop radius. Usually, this model have been applied to estimate expansion of the plasma *as a whole* [27] in a vacuum spark where $r_0 \sim 0.1$–1cm and rather low values of n_{0e}. At the same time, this results may be applied also to particular *microcondensations* in a rarefied plasmas or vacuum. For example, for ensembles of cold micrograins with "ectons" ($r_0 \sim 10^{-5}$ cm, $n_{0e} \sim 10^{22}$cm^{-3}, $E_e \approx 1$keV and $Z \approx 20$-25) we obtain $E_i \approx 250$-300keV (or approximately $E_i/Z \sim 10$-30keV), that in agreement with our estimations of deuterons or complex fast ions energies in our experiments.

In this sense, looks interesting also to check the *scaling* of some phenomena considered above at small scale low-energy vacuum discharge (with the rather high rate of energy deposition obtained ~ 10^8 J/sec) at large scales systems, for example, for high energy discharges *in the liquids* (V.Urutskoev et al, Seminar at Zvenigorod, Feb.2000). Perhaps, that similar conception of anodes ectons might be partially applied to interelectrodes processes also and predict potentially high yield of nuclearsynthesis or transmutations at longtime discharge. Remark also, that our rather high neutrons yield in vacuum discharges corresponds to low energy limit of predictions for foam-like laser targets models [12], meanwhile the situations when experiment gives much higher neutron yields than theory are known also [28]. Note that additional analysis of some alternative mechanisms of neutron generations at specific current-carrying systems [29] is needed to supply the never-ending physics of vacuum discharges.

References:

1. G.A.Mesyats, Ectons in vacuum discharge: breakdown, the spark, and the arc. -M. Nauka, 2000.
2. Yu.K Kurilenkov, M. Skowronek, G.Louvet, A.A. Rukhadze, J.Dufty. Journal de Physique IV, **10** (2000), Pr5-409; XXVII-IIII Conferences on Plasma Physics and Controlled Fusion, Zvenigorod, February,2000 and 2001.
3. T. Ditmire et al, Nature (London) **398** (1999) 489; J.Zweiback et al, Phys. Rev.Lett. **84** (2000) 2634; J.Zweiback et al, Phys. Rev.Lett. **85**(2000) 3640.
4. V. S. Letokhov. JETPh, vol. 26, no. 4, pp. 835–840, 1968
5. D. Wiersma and A. Lagendijk. Physics World, vol. 10, no. 1, pp. 33–37, 1997
6. R. C. Elton, "X-ray Lasers", New York, Academic Press, 1990.
7. Ya. B. Zel'dovich and Yu. P. Raizer "Physics of Shock Waves and High-Temperature Hydrodynamic Phenomena", Academic Press, New York, 1966.
8. N. M. Lavandy et al. Nature **368** (1994) 436.
9. C. Gouedard, D. Husson, C. Sauteret, F. Auzel and A. Migus. J. Opt. Soc. Am. **B10** (1993) 2358.
10. D. S. Wiersma and A. Lagendijk . Phys. Rev.E. **54** (1996) 4256-4265.
11. M. P.van Albada et al. Phys. Rev. Lett, **66** (1991) 3132.
12. S.Yu. Gus'kov et al, Letters to JETPh **66** (1997)521.
13. V.Yu. Bychenkov et al JETPh **115** (1999)2080-2090.
14. R.L.Bowers and T.Deeming. Astrophysics I. Stars. Jones&Barlett Publishers, Inc, Boston, 1984.
15. R. L. Boxman, S. Goldsman, and A. Greenwood. IEEE Trans. Plasma Sci., **25** (1997) 1174.
16. A. P. Nefedov, O. F. Petrov, and V. E. Fortov, Usp. Fiz. Nauk, **167** (1997)1215.
17. B. M. Smirnov. Usp. Fiz. Nauk, **167** (1997)1169–1200.
18. T.Ditmire, R.A.Smith, J.W.G.Tisch, and M.H.R. Hutchinson. Phys. Rev. Lett., **78** (1997) 3121..
19. M. Lezius, S. Dobosz, D. Normand, and M. Schmidt J. Phys. **B 30**(1997) L251.
20. K. Frank et al. XVIIIth Int. Symp. on Discharges and Electrical Insulation in Vacuum, Eindhoven, 1998, Proceedings,v.1, p.362.
21. M. Skowronek and P. Romeas. IEEE Trans. Plasma Sci.. **PS-15**(1987) 589.
22. T. Sato et al Phys. Plasmas 3 (1996) 2135.
23. K. Efetov "Supersymmetry in Disorder and Chaos", Cambridge University Press, Cambridge, 1997.
24. C.W.J.Beenakker. Rev.Mod. Phys.**69** (1997) 731.
25. F. Scheffold and G. Maret. Phys. Rev. Lett. **81** (1998) 5800,.
26. I.Last and J.Jorthner. Phys. Rev. Lett. **87** (2001)033401.
27. A.A. Plyutto. JETPh **12** (1960)1106.
28. C.Topin,E.Lefebre, and G.Bonnaud. Physics of Plasmas **8** (2001) 1011.
29. B.E. Meyerovivh. "Strong Current Channel" Moscow, "FIMA-press", 1999.

НАУЧНЫЕ ТРУДЫ

Третье совещание по магнитной и плазменной аэродинамики в аэро-космических приложениях